Ghenadii Korotcenkov *Editor*

Handbook of II-VI Semiconductor-Based Sensors and Radiation Detectors

Volume 1, Materials and Technology

Springer

Editor
Ghenadii Korotcenkov

Handbook of II-VI Semiconductor-Based Sensors and Radiation Detectors

Volume 1, Materials and Technology

Editor
Ghenadii Korotcenkov
Department of Physics and Engineering, Moldova State University,
Chisinau, Moldova

ISBN 978-3-031-19530-3 e-ISBN 978-3-031-19531-0
https://doi.org/10.1007/978-3-031-19531-0

© The Editor(s) (if applicable) and The Author(s), under exclusive license to Springer Nature Switzerland AG 2023

This work is subject to copyright. All rights are solely and exclusively licensed by the Publisher, whether the whole or part of the material is concerned, specifically the rights of translation, reprinting, reuse of illustrations, recitation, broadcasting, reproduction on microfilms or in any other physical way, and transmission or information storage and retrieval, electronic adaptation, computer software, or by similar or dissimilar methodology now known or hereafter developed.

The use of general descriptive names, registered names, trademarks, service marks, etc. in this publication does not imply, even in the absence of a specific statement, that such names are exempt from the relevant protective laws and regulations and therefore free for general use.

The publisher, the authors, and the editors are safe to assume that the advice and information in this book are believed to be true and accurate at the date of publication. Neither the publisher nor the authors or the editors give a warranty, expressed or implied, with respect to the material contained herein or for any errors or omissions that may have been made. The publisher remains neutral with regard to jurisdictional claims in published maps and institutional affiliations.

This Springer imprint is published by the registered company Springer Nature Switzerland AG
The registered company address is: Gewerbestrasse 11, 6330 Cham, Switzerland

Preface

Binary and ternary semiconductors of II-VI group (ZnS, ZnSe, ZnTe, CdS, CdSe, CdTe, HgTe, HgS, HgSe, HgCdTe, CdZnTe, CdSSe, and HgZnTe) are very popular among researchers because of their remarkable physical and chemical properties, which, as a group, are unique. II-VI compounds possess a very wide spectrum of electronic and optical properties. Most materials of group II-VI are semiconductors with a direct band gap and high optical absorption and emission coefficients. In addition, binary II-VI compounds are easily miscible, providing a continuous range of properties. As results, the II-VI semiconductors possess band gap, varying over a wide range. Therefore, II-VI compounds can serve as efficient light emitters, such as light diodes and lasers, solar cells, and radiation detectors operating in the range from IR to UV and X-ray. II-VI compound-based devices can also cover terahertz range. Besides common photovoltaic applications, II-VI semiconductors are also potential candidates for a variety of electronic, electro-optical, sensing, and piezoelectric devices. In particular, nanoparticles of II-VI semiconductors, such as quantum dots, one-dimensional structures, and core-shells structures, can be used for development of gas sensors, electrochemical sensors, and biosensors. These semiconductors, when downsized to nanometer, have become the focus of attention because of their tunable band structure, high extinction coefficient, possible multiple exciton generation, and unique electronic and transport properties. It is important that II-VI semiconductors can be easily prepared in high quality epitaxial, polycrystalline, and nanocrystalline films. The concentration of charge carriers can also vary in II-VI semiconductors in wide range due to doping. Thus, the use of II-VI films represents an economical approach to the synthesis of semiconductors for various applications. It should be noted that the range of technical applications for II-VI compounds goes beyond the better-known semiconductors such as Si, Ge, and some of III-V compounds.

Formally, metal oxides such as CdO and ZnO also belong to II-VI compounds. However, we will not cover them in this book. In recent years, these compounds have been allocated to a separate group, “metal oxides,” and many books have been devoted to their discussion, in contrast to other II-VI compounds. In particular, those who are interested in exactly these

compounds, we can recommend the Metal Oxides series which is published by Elsevier.

The aim of this three-volume book is to provide an updated account of the state of the art of multifunctional II-VI semiconductors, from fundamental sciences and material sciences to their applications as various sensors and radiation detectors, and, based on this knowledge, formulate new goals for further research. This book provides interdisciplinary discussion of a wide range of topics, such as synthesis of II-VI compounds, their deposition, processing, characterization, device fabrication, and testing. Topics of the recent remarkable progresses in application of nanoparticles, nanocomposites, and nanostructures consisting of II-VI semiconductors in various devices are also covered. Both experimental and theoretical approaches were used for this analysis.

Currently, there exist books on II-VI semiconductors. However, some of them were published too long ago and cannot reflect the current state of research in this area. Other published books focus on a limited number of topics, from which topics related to various sensor applications such as gas sensors, humidity sensors, and biosensors are almost completely excluded. When considering photodetectors, the focus is also only on the analysis of IR photodetectors. Although sensors operating in the visible, ultraviolet, terahertz, and X-ray ranges also hold great promise for applications. With these books, we will try to close this gap.

Our three-volume book *Handbook of II-VI Semiconductor-Based Sensors and Radiation Detectors* is the first to cover both chemical sensors and biosensors and all types of photodetectors and radiation detectors based on II-VI semiconductors. It contains a comprehensive and detailed analysis of all aspects of the application of II-VI semiconductors in these devices. This makes these books very useful and comfortable to use. Combining this information in three volumes, united by common topics, should help readers in finding the necessary information on required subject.

Chapters in *Handbook of II-VI Semiconductor-Based Sensors and Radiation Detectors. Vol. 1: Materials and Technologies* describe the physical, chemical, and electronic properties of II-VI compounds, which give rise to an increased interest in these semiconductors. Technologies that are used in the development of various devices based on II-VI connections are also discussed in detail in this volume.

Handbook of II-VI Semiconductor-Based Sensors and Radiation Detectors. Vol. 2: Photodetectors focuses on the consideration of all types of optical detectors, including IR detectors, visible detectors, and UV detectors. This consideration includes both the fundamentals of the operation of detectors and the peculiarities of their manufacture and use. An analysis of new trends in development of II-VI semiconductors-based photodetectors is also given.

Handbook of II-VI Semiconductor-Based Sensors and Radiation Detectors. Vol. 3: Sensors, Biosensors and Radiation Detector describes the use of II-VI compounds in other fields such as radiation detectors, gas sensors, humidity sensors, optical sensors, and biosensors. The chapters in this volume provide a comprehensive overview of the manufacture, parameters, and applications of these devices.

We believe that these books will enable the reader to understand the present status of II-VI semiconductors and their role in the development of new generation of photodetectors, sensors, and radiation detectors. I am very pleased that many well-known experts with extensive experience in the development and research of II-VI semiconductor sensors and radiation detectors were involved in the preparation of the chapters of these books.

The target audience for this series of books are scientists and researchers working or planning to work in the field of materials related to II-VI semiconductors, i.e., scientists and researchers whose activities are related to electronics, optoelectronics, chemical and bio sensors, electrical engineering, and biomedical applications. I believe this three-volume book may also be of interest to practicing engineers and project managers in industries and national laboratories who would like to develop II-VI semiconductor-based radiation sensors and detectors but do not know how to do it, and how to select the optimal II-VI semiconductor for specific applications. With numerous references to an extensive resource of recently published literature on the subject, these books can serve as an important and insightful source of valuable information, providing scientists and engineers with new ideas for understanding and improving existing II-VI semiconductor devices.

I believe that these books will be very useful for university students, doctoral students, and professors. The structure of these books offers the basis for courses in materials science, chemical engineering, electronics, optoelectronics, environmental control, chemical sensors, photodetectors,

radiation detectors, biomedical applications, and many others. Graduate students may also find the book very useful in their research and understanding of the synthesis of II-VI semiconductors, study, and application of this multifunctional material in various devices. We are confident that all of them will find the information useful for their activities.

Finally, I thank all the authors who contributed to these books. I am grateful that they agreed to participate in this project and for their efforts to prepare these chapters. This project would not have been possible without their participation. I am also very grateful to Springer for the opportunity to publish this book with their help. I would like also to inform that my activity related to editing this book was funded by the State Program of the Republic of Moldova project 20.80009.5007.02.

I am also grateful to my family and wife, who always support me in all my endeavors.

Ghenadii Korotcenkov
Chisinau, Moldova

Contents

Part I II-VI Semiconductors Properties

1 Introduction in II-VI Semiconductors
Osvaldo de Melo

2 Cd- and Zn-Based Wide Band Gap II-VI Semiconductors
Ghenadii Korotcenkov

3 Hg-Based Narrow Bandgap II-VI Semiconductors
Ghenadii Korotcenkov and Denis L. Nika

4 Ternary II-VI Alloys Promising for Application in Photodetectors
Mustafa Kurban, Osman Barış Malcıoğlu and Şakir Erkoç

5 II-VI Semiconductors Bandgap Engineering
Mustafa Kurban, Yusuf Şimşek and Şakir Erkoç

6 Electronic Structure of Mercury Chalcogenides Nanocrystals
Emmanuel Lhuillier, Tung Huu Dang, Mariarosa Cavallo, Claire Abadie, Adrien Khalili and Charlie Gréboval

7 Colloidal Nanoparticles of II-VI Semiconductor Compounds and Their Participation in Photosensitization of Metal Oxides
Roman B. Vasiliev, Artem S. Chizhov and Marina N. Rumyantseva

8 Quantum Dot (QD)-Induced Toxicity and Biocompatibility
Karishma Niveria, Priyanka Singh, Monika Yadav and Anita K. Verma

Part II Material Technology

9 Features of Single-Crystal Growth of CdTe and $Cd_{1-x}Zn_xTe$ Compounds Designed for Radiation Detectors
Ghenadii Korotcenkov and Sergiu Vatavu

10 Thin Films of Wide Band Gap II-VI Semiconductor Compounds: Features of Preparation
Vyacheslav F. Markov, Ghenadii Korotcenkov and Larisa N. Maskaeva

11 Synthesis of II-VI Semiconductor Nanocrystals
Ghenadii Korotcenkov and Igor A. Pronin

12 II–VI Semiconductor-Based Nanomaterials

Yuliana Lukan, Andrii Hotynchan, Yuliia Andriichuk, Sergii Vojtovych, Yulia Seti and Yuriy Khalavka

13 CdTe-Based Nanoparticles Synthesized in Solutions
Galyna Okrepka, Olena Tynkevych, Nataliia Doskaliuk, Ghenadii Korotcenkov and Yuriy Khalavka

14 II-VI Quantum Dots and Their Surface Functionalization
Faheem Amin, Zulqurnain Ali and Ghenadii Korotcenkov

15 HgCdTe Device Technology
Sergey Alekseevich Dvoretsky, Vladimir Vasilievich Vasiliev, George Yurievich Sidorov and Dmitriy Vitalievich Gorshkov

16 II-VI Wide-Bandgap Semiconductor Device Technology: Deposition, Doping, and Etchig
Ghenadii Korotcenkov

17 II-VI Wide-Bandgap Semiconductor Device Technology: Schottky Barrier, Ohmic Contacts, and Heterostructures
Ghenadii Korotcenkov, Nikolay P. Simonenko, Fedor S. Fedorov and Victor V. Sysoev

18 II-VI Wide-Bandgap Semiconductor Device Technology: Stability and Oxidation
Ghenadii Korotcenkov

19 II-VI Wide-Bandgap Semiconductor Device Technology: Post-Deposition Treatments
Ghenadii Korotcenkov

Index

About the Editor

Ghenadii Korotcenkov
received his PhD in physics and technology of semiconductor materials and devices in 1976 and his Doctor of Science degree (doctor habilitate) in physics of semiconductors and dielectrics in 1990. He has more than 50-year experience as a teacher and scientific researcher. For a long time, he was a leader of gas sensor group and manager of various national and international scientific and engineering projects carried out in the Laboratory of Micro- and Optoelectronics, Technical University of Moldova, Chisinau, Moldova. International foundations and programs such as the CRDF, the MRDA, the ICTP, the INTAS, the INCO-COPERNICUS, the COST, and NATO have supported his research. From 2007 to 2008, he carried out his research as an invited scientist at Korea Institute of Energy Research (Daejeon). Then, from 2008 to 2018, Dr. G. Korotcenkov was a research professor in the School of Materials Science and Engineering at Gwangju Institute of Science and Technology (GIST) in Korea. Currently, G. Korotcenkov is a chief scientific researcher at Moldova State University, Chisinau, Moldova.

Scientists from the former Soviet Union know the results of G. Korotcenkov's research in the study of Schottky barriers, MOS structures, native oxides, and photoreceivers based on III–Vs compounds such as InP, GaP, AlGaAs, and InGaAs. His current research interests since 1995 include material sciences, focusing on metal oxide film deposition and characterization (In_2O_3, SnO_2, ZnO, TiO_2), surface science, thermoelectric conversion, and design of physical and chemical sensors, including thin film gas sensors.

G. Korotcenkov is the author or editor of 45 books and special issues, including the 11-volume "Chemical Sensors" series published by Momentum Press; 2-volume "Handbook of Gas Sensor Materials" published by Springer; 15-volume "Chemical Sensors" series published by Harbin Institute of Technology Press, China; 3-volume "Porous Silicon: From Formation to Application" issue published by CRC Press; 3-volume "Handbook of Humidity Measurements" published by CRC Press; 3-volume "Handbook of II-VI Semiconductor-Based Sensors and Radiation Detectors" published by Springer; and 6 proceedings of the international

conferences published by Trans Tech Publ., Elsevier, and EDP Sciences. In addition, currently he is a series editor of “Metal Oxides” book series published by Elsevier. Since 2017, more than 35 volumes have been published within this series.

G. Korotcenkov is the author and coauthor of more than 650 scientific publications, including 9 review papers, 38 book chapters, and more than 200 peer-reviewed articles published in scientific journals (h-factor = 43 (Web of Science), h = 45 (Scopus) and h = 61 (Google scholar citation), 2022). He is the holder of 17 patents. He presented more than 250 reports at the National and International conferences, including 17 invited talks. G. Korotcenkov, as a cochairman or member of program, scientific, and steering committees, has participated in the organization of more than 40 international scientific conferences. Dr. G. Korotcenkov is a member of editorial boards in five scientific international journals. His name and activities have been listed by many biographical publications including Who’s Who. G. Korotcenkov have also been listed as one of the “World’s Ranking Top 2% Scientists” in Applied Physics/Analytical Chemistry in the Physics and Astronomy Cluster. His research activities have been honored by the National Prize of the Republic of Moldova (2022), the Honorary Diploma of the Government of the Republic of Moldova (2020), an Award of the Academy of Sciences of Moldova (2019), an Award of the Supreme Council of Science and Advanced Technology of the Republic of Moldova (2003), the Prize of the Presidents of the Ukrainian, Belarus, and Moldovan Academies of Sciences (2004), Senior Research Excellence Award of Technical University of Moldova (2001; 2003; 2005), the National Youth Prize of the Republic of Moldova in the field of science and technology (1980), among others. Some of his research results and published books have won awards at international exhibitions. G. Korotcenkov also received a fellowship from the International Research Exchange Board (IREX,

United States, 1998), Brain Korea 21 Program (2008–2012), and BrainPool Program (Korea, 2007–2008 and 2015–2017).

https://www.scopus.com/authid/detail.uri?authorId=6701490962
https://publons.com/researcher/1490013/ghenadii-korotcenkov/
https://scholar.google.com/citations?user=XR3RNhAAAAAJ&hl
https://www.researchgate.net/profile/G_Korotcenkov

OceanofPDF.com

Part I
II-VI Semiconductors Properties

OceanofPDF.com

© The Author(s), under exclusive license to Springer Nature Switzerland AG 2023
G. Korotcenkov (ed.), *Handbook of II-VI Semiconductor-Based Sensors and Radiation Detectors*
https://doi.org/10.1007/978-3-031-19531-0_1

1. Introduction in II-VI Semiconductors

Osvaldo de Melo[1] ✉
(1) Physics Faculty, University of Havana, La Habana, Cuba

✉ **Osvaldo de Melo**
Email: omelo@fisica.uh.cu

Keywords II-VI semiconductors – Alloys – CdS_xSe_{1-x} – CdZnS – $Cd_{1-x}Zn_xTe$ – $Hg_{1-x}Cd_xTe$ – Applications – Biosensors – Gamma and X-ray detectors – Gas sensors – IR detectors – Focal plane arrays – Lasers – Light-emitting devices – Phosphors – Photocatalysis – Solar cells – THz emitters and detectors – UV detectors – CdS – CdSe – CdTe – HgTe – History – ZnS – ZnSe – ZnTe – Band alignments – Band gaps – Doping – Nanostructures – Core-shells – Quantum dots (QDs) – Semiconductors – GaAs – GaN – Ge – InAs – PbS – Si – ZnO

1.1 Introduction

II-VI semiconductors are composed by elements of the groups IIB (12 in the modern classification, or Zn family group) and VIA (16 in the modern classification or chalcogen group) of the periodic table (see the relevant section in Table 1.1). Along this book, mainly compounds and alloys formed of Zn, Cd, and Hg, from the group IIB, and the chalcogen elements S, Se, and Te from the group VIA will be considered. Oxygen, an important member of the VIA group which forms semiconducting compounds with IIB elements, is often classified in the more specific group of oxides. Cn (copernicium) and Lv (livermorium) are recently discovered member of the IIB and VIA group, respectively, but they are artificial and unstable without any practical interest in materials science. Polonium, belonging to the VIA

group, is a very rare element. On the other hand, Be and Mg from the group IIA can form semiconducting compounds when mixing with chalcogen elements; they are frequently used in alloys for tuning the lattice parameter or band gap in heterostructures.

Table 1.1 Section of the periodic table where II-VI semiconducting compounds are located. Relevant elements from IIB and VIA groups are highlighted

Row ⇓ / Group ⇒	11	**12 (IIB)**	13	14	15	**16 (VIA)**	17
			B	C	N	O	F
3			Al	Si	P	**S**	Cl
4	Cu	**Zn**	Ga	Ge	As	**Se**	Br
5	Ag	**Cd**	In	Sn	Sb	**Te**	I
6	Au	**Hg**	Tl	Pb	Bi	Po	
7		Cn				Lv	

This introductory chapter is divided into four parts corresponding to aspects that, in the opinion of the author, can motivate the reader to face the book or help him to grasp the different topics in the next chapters. First, a brief journey through the history of II-VI semiconducting compounds and related materials will allow the reader to appreciate the origins and development of these important materials. In the following section, an account will be presented of the main basic properties that distinguish II-VI compounds and make them useful for fabricating different kinds of devices for a wide variety of applications. This section summarizes important topics such as the fundamentals of fabrication of alloys and heterostructures, conductivity type and dopability control, and nanostructures synthesis and properties. Finally, in the last section, the main areas in which applications have been developed or in which there is potential for applications of II-VI compounds are briefly resumed.

1.2 The History of II-VI Semiconductors: A Brief Journey

Chalcogen elements were important components of early semiconductor materials. More than 2000 years ago, in the Greco-Roman period, a hair dyeing formula used a cream composed by PbO and $Ca(OH)_2$ for blackening the hair. Today, it is known that lead reacted with the sulfur in

the amino acids of hair to form small crystals of PbS, similar to the PbS quantum dots that scientists fabricate today routinely [1]. Much later, silver sulfide was the first discovered material with semiconducting behavior (electrical conductivity increase with temperature) as early as in 1833 by Michael Faraday who described his experience in an expressive way:

> There is no other body with which I am acquainted, that, like sulphuret of silver, can compare with metals in conducting power for electricity of low tension when hot, but which, unlike them, during cooling, loses in power, whilst they, on the contrary, gain. Probably, however, many others may, when sought for, be found. [2]

What today is known as photovoltaic effect was first observed in selenium crystals in 1877 [3], while electric current rectification was detected in selenides in the same decade. PbS (with the mineral name galena) reappears in the history as the material forming the first signal detector. It was developed by Karl Ferdinand Braun [4] who shared the Nobel Prize in physics in 1909 with Guglielmo Marconi for their “contributions to the development of wireless telegraphy.”

II-VI compounds are a well-established family that celebrated their first congress in Rhode Island as early as in 1967 with the name of II-VI Semiconducting Compounds International Conference. After 15 years, the conference series was recommenced as the International Conference of II-VI compounds which has held in Durham (1983), Aussois (1985), Monterrey (USA) (1987), Berlin (1989), Tamano (1991), Rhode Island (1993), Edinburgh (1995), Grenoble (1997), Kyoto (1999), Bremen (2001), Niagara Falls (2003), Warsaw (2005), Jeju (2007), St. Petersburg (2009), and Riviera Maya (2011). From this year on, the topics of the conference were extended to include related compounds as chalcopyrites, different kinds of oxides, and 2D materials. The name of the series was modified to “International Conference of II-VI compounds and Related Materials” with the next meetings in Nagahama (2013), Paris (2015), San Juan (2017, the in-person event was affected by the occurrence of Hurricane Maria), Zhengzhou (2019), and Bath (2022).

1.3 Material Properties

1.3.1 General Trends: Chemistry, Structure and Band Gaps

As expected, according to their position in the periodic table, II-VI compounds have more ionic bonds than III-V compounds and, obviously, than elemental semiconductor of the group IV which are completely covalent materials. For example, the fractional ionic character for compounds in the fourth row CuBr (I-VII), ZnSe (II-VI), GaAs (III-V), and Ge (IV) are 0.735, 0.63, 0.31, and 0, respectively [5]. Due to the large iconicity, II-VI compounds tend to present larger band gaps than the other semiconductor groups, so, CuBr, ZnSe, GaAs, and Ge present band gaps of 2.94, 2.7, 1.4, and 0.66 eV, respectively.

Differently from III-V compounds, II-VI materials tend to evaporate congruently due to the higher vapor pressure of the group II elements compared with those of group III elements. This is the reason why simple and low-cost vapor phase techniques as thermal evaporation or close space vapor transport are widely used for preparing polycrystalline II-VI materials. In the phase diagrams, only the stoichiometric II-VI compound solid appears, while the vapor phase is composed by atomic monomers of the group II element and dimers or polymers of the group VI element.

Most frequent crystal structures in II-VI semiconductors are wurtzite, with hexagonal symmetry, or sphalerite (also called zinc blend in reference to the II-VI ZnS mineral) with cubic symmetry, which are displayed in the left panel of Fig. 1.1. In both structures, there is tetrahedral coordination, and the two different lattice sites are occupied by the IIB and VIA elements, respectively. In some compounds such as CdS and CdSe, for example, the free energy difference between both phases is quite small, and they can be found in both structures quite stably; they can even coexist in the same sample.

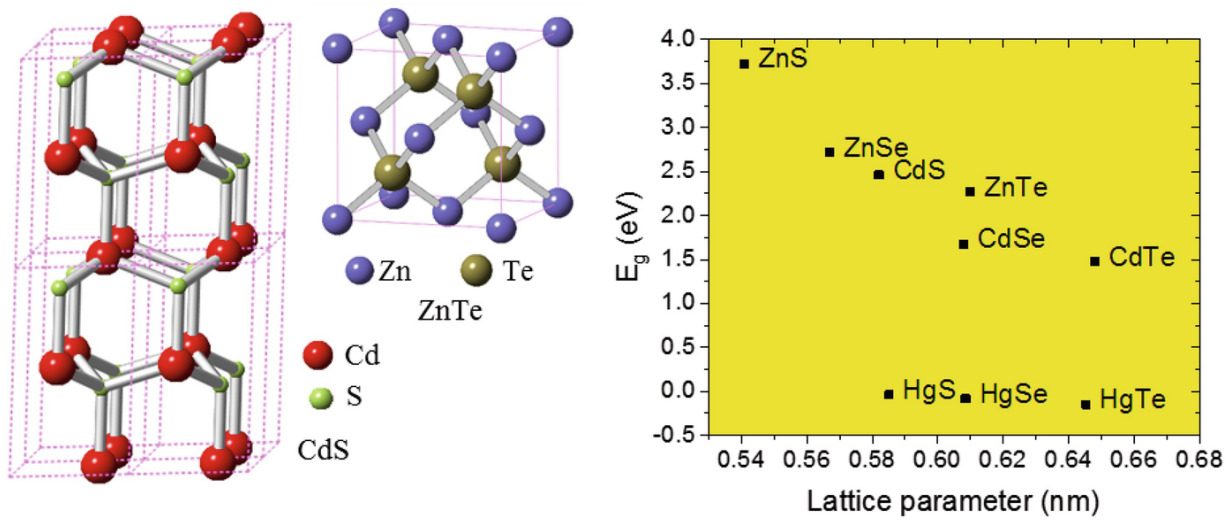

Fig. 1.1 Hexagonal wurtzite and cubic sphalerite structures common in II-VI compounds illustrated with CdS (wurtzite) and ZnTe (sphalerite) compounds, respectively (left). Room temperature energy band gap and lattice parameters for the II-VI compounds in the cubic structure (right)

Interesting features of II-VI compound can be appreciated in the right panel of Fig. 1.1 in which the room temperature band gap is plotted as a function of the lattice parameter for all the II-VI compounds [6] in the cubic structure.[1] The band gap is direct for all the compounds having a band gap and ranges from nearly zero for Hg compounds to 3.7 eV for ZnS. This allows the fabrication of photonics detectors and other devices in a large range of wavelengths: from the far infrared up to the ultraviolet and even in the X-ray and gamma ray spectral regions.

1.3.2 II-VI Semiconductor Alloys

To tune the band gap or the lattice constant (or both), alloys can be synthesized from the different compounds. In the case where the two binary extrema of these alloys are in the same crystallographic modification, solubility is expected to exist in all the composition range. Then, they can be represented as $A_xB_{1-x}C$ or AC_xD_{1-x} where A and B stand for IIB group elements while C, D for group VIA elements (alternatively, the notation $(AC)_x(BC_{1-x})$ or $(AC_x)(AD_{1-x})$ is frequently used). Although these alloys are formed by three elements, they are not considered as true ternary alloys since the composition is specified by a single parameter: one of the elements occupies one of the two sites of the crystal lattice, while the other site is shared by the other two elements. Important examples of these alloys are the semiconductors $Hg_{1-x}Cd_xTe$ and $Cd_{1-x}Zn_xTe$. In these kinds of

alloys, the lattice parameter a varies quite linearly with the composition x; so, for an alloy $A_xB_{1-x}C$, the empirical Vegard Law holds and $a = xa_{AC} + (1 - x)a_{BC}$ (a_{AC} and a_{BC} are the lattice parameters of the binary extrema compounds). Due to the similarity of the ionic radii of Hg and Cd, it is interesting to note that for $Hg_{1-x}Cd_xTe$ (or any other pseudobinary alloy containing Hg and Cd), the lattice parameter of the alloy is quite independent of the composition.[2] This fortunate issue allows using CdTe substrates for growing epitaxial films of $Hg_{1-x}Cd_xTe$ at every composition. When the mixed compounds have different crystallographic phases, solubility occurs only near the extreme compositions 0 and 1. This occurs, for example, in the CdS_xTe_{1-x} alloy, which is usually formed in the CdTe/CdS interface of the CdTe-CdS solar cells.

The band gap of pseudobinary alloys also varies with composition but not linearly; in general, a bowing parameter has to be considered and the equation relating the band gaps of the compounds $E_{g\,AC}$ and $E_{g\,BC}$ with the band gap of the alloy E_g is usually written as $E_g = xE_{g\,AC} + (1 - x)E_{g\,BC} + Bx(1 - x)$ where B is the bowing parameter. The band gap and lattice parameter of the compounds or alloys can be further modified by strain or by quantum confinement in samples in which at least one dimension is below the Bohr exciton ratio. In this case, it is common to speak of quantum wells, wires, or dots with 1D, 2D, or 3D confinement, respectively. More complex multinary alloys involving only II-VI compounds, including elements for other groups of the periodic table, or even inorganic compounds, have been also obtained and studied [7].

1.3.3 Band Alignment and Heterostructures

An important parameter for heterostructure-based devices is the band alignment that allows favoring or blocking the injection of the desired carriers (electron or holes) through the interfaces. This ability is in the heart of the operation of any electronic or optoelectronic device. Barrier materials in quantum-confined devices as quantum wells or wires, or core/shell nanostructures must have larger band gap than the confined material but also an adequate conduction and valence band alignment if both types of carriers must be confined: the conduction/valence band of the barrier lying over/below the conduction/valence band of the well. This is known as type I band alignment.

The band location for II-VI compounds (with respect to the vacuum level, taken as zero reference energy for all compounds) is illustrated in Fig. 1.2a in which electron affinity (χ_e) and band gap of the different compounds were taken from ref. [8], except for Hg chalcogenides in which case data was obtained from valence band maximum calculations [9, 10].

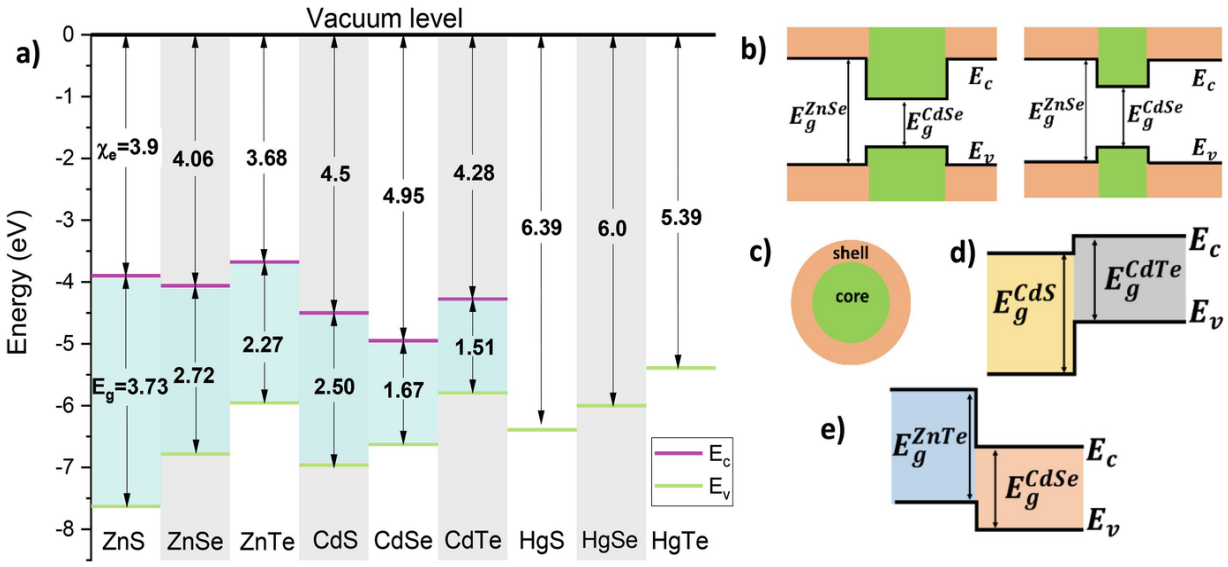

Fig. 1.2 (**a**) Band gap alignment for II-VI compounds. (**b**) Band alignment in the ZnSe/CdSe/ZnSe quantum structure. For very small well size, the band gap increases because of the quantum confinement effect. (**c**) A core-shell structure with similar shell (barrier) well (core) band alignment. (**d** and **e**) Band alignments for the CdS/CdTe heterostructure solar cell and a ZnTe/CdSe photodetector

Some examples of structures that take advantage of the band alignment are also presented in Fig. 1.2. ZnSe/CdSe/ZnSe heterostructure (Fig. 1.2b for two different wells thickness) can form a type I quantum structure in which ZnSe forms a barrier for both electrons and holes. For very thin CdSe layers, this type of structure is highly luminescent, and the characteristic emission can be varied in a wide wavelength range by changing the thickness of the CdSe layer [11]. As it will be described in the next section, the same type I configuration occurs in core/shell nanostructures with ZnSe or ZnS shells (barriers) as shown in Fig. 1.2c. It can be noted that ZnS, due to its large band gap and the energy location of its bands extrema, can be used as a barrier for practically all other II-VI compounds and even for semiconductors of other groups. ZnS has other two important advantages: it is not toxic, and both Zn and S are abundant materials in the earth crust. The band alignment in the CdS/CdTe heterostructure solar cell is shown in

Fig. 1.2d. In this structure, the alignment favors the injection of holes/electrons in the CdS/CdTe layer as needed for the photocurrent in a solar cell. Figure 1.2e shows a ZnTe/CdSe core/shell nanowire structure that use the piezo-phototronic effect [12].

1.3.4 Conductivity Type and Doping

The main problems faced in the early development of II-VI semiconducting compounds were related with the control of the conductivity and the doping ability. They arise because of self-compensation by defects, low solubility limits, or reactivity of dopants. In fact, in II-VI compounds, some intrinsic defects can lead to the formation of relatively shallow levels in the band gap which play an important role in the conductivity value, in the conductivity type, and in the compensation mechanisms. Some of the problems related to doping have been partially solved by using nonequilibrium growth techniques such as molecular beam epitaxy (MBE) or metal organic vapor phase epitaxy (MOVPE) that remove some of the equilibrium thermodynamics restrictions using lower temperatures and obtaining films with low defects density and the desired impurification. The use of plasma sources in MBE has allowed to dope with atomic elements which are not present in the equilibrium vapor species; this has been used to obtain p-type ZnSe by doping it with atomic nitrogen, for example.

Thus, for non-intentionally doped materials, as a trend, anion (element of the group II) vacancies or cation (element of the group VI) interstitials lead to n-type conductivity, while cation vacancies or anion interstitial lead to p-type conductivity. So, to a large extent, conductivity has been controlled by adequate annealing processes that modify the stoichiometry of the compound. For example, as-grown $Hg_{1-x}Cd_xTe$ is frequently encountered with p-type conductivity because of the presence of vacancies of the volatile element mercury [13]. These vacancies can be eliminated by post-growth annealing in Hg vapors of by using an adequate Hg overpressure during the growth of the films. In the case of CdS, sulfur annealing contribute to a decrease of the red luminescent band ascribed to sulfur vacancies defects and to increase the conductivity in two orders of magnitude [14]. In general, it has been observed that undoped tellurides tend to be p type and undoped sulfides tend to be n types. In the case of selenides, undoped ZnSe tends to be n-type, and CdSe has been found with both p-type and n-type conductivity.

More control of the carrier concentration and the conductivity type can be obtained using extrinsic doping. So, group I/group V elements when substituting the cation/anion lead to p-type conductivity, while group III/group VII substituting the anion/cation leads to n-type conductivity. The doping of II-VI compounds and alloys is a very exciting topic presently. The goal is to find the adequate dopants and methods that allow to obtain controlled and relatively high values of carrier concentrations and mobilities. First principles studies of defects in CdTe [15] have given valuable information about the expected level of carrier concentration for different doping elements or defect concentration. On the other hand, doping wide band gap compounds has been observed to be more difficult probably because of the presence of defect levels into the band gap, inducing compensation (carrier killers) [16].

1.3.5 Nanostructures

An important advantage of II-VI compounds is the capability to form nanostructures by simple preparation procedures. For small sizes, the quantum confinement effect allows for the modification of the band gap as a function of size. But, even at larger sizes, these nanostructures are single crystals with a very low defect density and high surface to volume ratio. These properties make them very promising to fabricate detectors and other devices in different wavelength ranges with innovative designs [17]. Nanocrystals have been fabricated using both top-down and bottom-up techniques. In the first variant, bulk materials are fractioned in small pieces with sizes smaller than around 100 nm by using different techniques as electron beam lithography, focused ion beam, exfoliation, ball milling, etc. Better quality/smaller size nanocrystals can be obtained by the bottom-up approach. For example, different bottom-up (both dry and wet) chemical methods have allowed to obtain nanocrystals of all II-VI compounds with excellent properties. When the size of the nanocrystals become smaller than the exciton Bohr ratio, circa 5–6 nm, quantum confinement results in the apparition of discrete energy levels whose position depends on the nanocrystal sizes. These objects are called quantum dots (QDs) and present unique properties like size dependent band gap, strong luminescence, large absorption coefficient, and narrow/broad emission/excitation spectrum. To enhance the luminescence properties of the QDs, different kinds of core/shell structures have been fabricated. For example, in the case of

CdSe/ZnS core/shell dot, a widely studied structure, the larger band gap ZnS with similar bond length than CdSe is used to passivate the core surface leading to an important enhancing of the luminescence while also contribute to isolate the toxic elements of the core from the environment. Intense research work is now focused on the modification of the QDs surfaces to promote hydrophilicity and stability in the biological environments and to conjugate them with biomolecules of interest for targeting.

1.4 Applications

1.4.1 Infrared Detectors and Focal Plane Arrays

The mix of CdTe and HgTe produces the alloy $Hg_{1-x}Cd_xTe$ (also known as MCT) which was discovered in 1959 and is probably the flag ship of II-VI semiconductor materials. Depending on the composition x, the band gap of the alloy can be tuned to cover the needs of infrared detection and imaging in all the characteristic infrared windows: short-wave (1–3 μm), mid-wave (3–5 μm), long-wave (8–14 μm), and very-long-wave (14–30 μm). Individual detectors on both photovoltaic and photoconductive modes and focal plane arrays (FPA) are today fabricated using liquid phase epitaxy or vapor phase nonequilibrium techniques like molecular beam epitaxy (MBE) or metal organic vapor phase epitaxy (MOVPE) [13]. Compared with III-V materials competitors like InSb/GaSb type II superlattices, for example, MCT devices present much better performance due to its high quantum efficiency and larger minority carriers lifetime. Recent developments and challenges in $Hg_{1-x}Cd_xTe$ IR FPA for military, civilian, medical, and industrial applications like night vision, reconnaissance, surveillance, missile guidance, remote sensing, firefighting, security, pollution-monitoring, leak-testing, thermography, and cancer and tumor detection are described in a relatively recent review [18]. Present trends in FPA are focusing in decreasing the pixel size and the power consumption and to increase the area, operating temperature, frame rates, and thermal resolution. $Hg_{1-x}Cd_xTe$ is today the indisputable leader in IR detection and imaging despite the disadvantage related with the toxicity of their components.

1.4.2 Devices in the THz Range

An interesting range of the electromagnetic spectra is the so-called submillimeter or THz range which goes from some tenths to a few tens of THz or equivalently for wavelengths between circa 100–1000 μm, which partially overlap the far IR region. In this range, in between microwave and optical technologies, electromagnetic waves are strongly absorbed by water and metals while are penetrating in other materials as plastics and textiles. These properties together with the fact of being a nonionizing radiation has promoted the use of this electromagnetic range for several applications as nondestructive imaging, communications, or molecular spectroscopies. II-VI materials are important protagonist in this research area, too. The high nonlinear electro-optical coefficient of some II-VI semiconductors like ZnTe [19, 20] and CdTe [21] makes them materials of first choice for the generation of pulses with a broadband spectra in the range of 0.1–3 THz, using the optical rectification of femtosecond laser pulses (Ti or Yb lasers).

HgCdTe inter-band lasers are also promising in the range 5–15 THz in which quantum cascade III-V lasers fail because their emission is absorbed by the lattice [22], while the lower phonon energies of HgCdTe avoid lattice absorption. In contrast, the main problem stopping with HgCdTe stimulated emission is the strong Auger recombination rate in this material. Unique properties of HgCdTe as the existence of Dirac semimetal or topological insulator states can be useful for THz emission or detection mainly due to the high mobility of the carriers in these “exotic” states. In [22], the authors have demonstrated both detection and imaging with radiation of some tenths of THz as well as stimulated emission in the range 20–60 THz range.

1.4.3 X-Ray and Gamma Ray Detectors

The combination of a relatively large band gap and high atomic number of its component elements (48 and 52 for Cd and Te, respectively), CdTe and $Cd_{1-x}Zn_xTe$, are widely used as X-rays or gamma rays detectors [23]. They are particularly important in the range of high-energy photons, where silicon, germanium, or GaAs detectors have very large attenuation lengths. In fact, CdTe is one of the so-called high Z materials with good energy resolution and sensitivity. Typically, the $Cd_{1-x}Zn_xTe$ alloy with x ranging from 0.08 to 0.15 has an increased band gap with respect to CdTe which leads to lower leakage currents and better resolution in spectroscopic

applications. These kinds of detectors are relatively large and are fabricated from bulk single crystals. They are widely used in medical imaging [24] and security inspections.

Today, there are commercially available cardiac image devices based on CdZnTe. These devices have been observed to increase sensitivity, contrast, and resolution with respect to scintillation based ones, this leading to an increase of the diagnostic confidence and reduced radiation exposure [25, 26]. Energy-resolved photon counters of CdZnTe, including spectroscopic features to better resolve the images details, have provided enhanced contrast in digital mammography for detecting breath tumors [27]. New generation of gamma cameras with increased spatial and energy resolution is using pixelated CdZnTe material [28]. Hard X-rays and gamma rays CdTe and CdZnTe detectors, associated with different kinds of telescopes, are widely used in the exploration of the universe [24].

1.4.4 Solar Cells, UV-VIS Detectors, and Light-Emitting Devices

In the visible range, CdTe is also a very renowned compound. As well as its III-V partner GaAs, CdTe possesses a band gap of 1.4 eV which is near to the optimal value for a solar cell absorber material. This has given rise to the development of polycrystalline thin films solar cells based in CdTe which has reached more than 20% of efficiency [29, 30]. They have been prepared by using several techniques as close space vapor transport, thermal evaporation, chemical bath deposition, or sputtering. On the other hand, CdS, ZnO, and ZnS, with larger band gaps, are frequently used as window partners of CdTe or other absorber-based solar cells. Other II-VI semiconductors as ZnTe or HgTe are often used to achieve ohmic contacts to the moderately p-type CdTe [31].

CdS nanowires, traditionally used in UV/blue detection, have been proposed to integrate multicolor detectors in combination with diamond, InGaN, or ZnO [32]. Taking advantage of the ZnS large band gap, ZnS nanobelts [33] have been used for UV “solar blind” detectors, while CdS photodetector arrays have been prepared in flexible polyethylene terephthalate (PET) substrates [34], and individual ZnSe nanobelt has been used as UV photodetector [35].

In the late 1980s and early 1990s, intense research efforts on ZnSe and related alloys were devoted to the fabrication of blue light-emitting devices,

but these efforts were truncated because of the impressive development and success of GaN-based devices. However, laser research has become an important research topic again in II-VI semiconductors, now in the MID IR range. Transition metals or rare earth doped II-VI semiconductor presents tunable wideband laser emission. For example, optically pumped (using Tm or Er fiber lasers, or directly with diode lasers) Cr or Fe doped ZnS and ZnSe lasers have been fabricated [36, 37]. Depending on the used configuration, the laser emission can be tunable in the range of 1–3 μm. They are used in several applications as remote sensing, environmental monitoring, mid-IR communications, optical coherence tomography, ophthalmology, and dermatology [38, 39].

An important contribution of II-VI materials is in the field of phosphors. Sulfides are among the first discovered phosphor materials. ZnS, whose luminescence was discovered in 1866, has been recognized as the most important phosphor material matrix [40]. Alternated current-driven electroluminescence (ACEL) is the preferred configuration in these devices. In particular, ACEL powder-based devices [41], in which luminescent particles are embedded in a dielectric binder, allow large area and colored light sources by simple screen printing techniques when using ZnS:Cu (other dopants such as Al, Cl, Mn, Ag, etc. can be used to change the emission wavelength in the range 450–690 nm; white emission has been reported using Eu as the dopant [42]). In another variant (ACTFEL), thin films of the phosphor elements are sandwiched between insulator films, and metal electrodes are deposited in both sides. In this conditions, electron tunneling from interface states to the phosphor film and impact ionization are responsible for light emission during AC cycles [43]. Displays with this technology are used in some applications due to advantages as large lifetimes, ease of manufacture, large viewing angle, and wide range of operating temperatures, among others.

On the other hand, II-VI QDs have shown excellent luminescent properties and can be used in a wide range of applications including luminescent biomarkers, light-emitting diodes, and lasers. The application of these QDs in biosensor will be the subject of the following paragraph.

1.4.5 Biosensors

II-VI QDs have found interesting biomedical applications including in vivo or in vitro chemical sensing, biomolecules targeting, luminescence imaging,

and drug delivery [44]. They have demonstrated superior properties than traditionally used organic fluorophores [45]. For example, (i) QDs have a broad absorption wavelength range which allows excitation well above the emission region and makes possible to excite, with the same source, QDs emitting at different wavelengths; (ii) they have very intense luminescence, and due to the quantum 3D confinement of electron and holes, the emission wavelength can be controlled through the size; and (iii) they are resistant to photobleaching and are in general more stable than fluorophores. For sensing, the modification of the emission wavelength or intensity in the presence of specific biomolecules is used.

QDs are generally presented in a colloidal form in organic solvents, and Cd chalcogenides are probably the most studied colloidal QDs. To be used in biological media, QDs must be hydrophilic, but after their synthesis process in organic reactants, they result with hydrophobic surfaces. In fact, the first two demonstrations of QDs ability for bio-sensing [46, 47], using CdSe/ZnS and CdSe/CdS core/shell structures, respectively, were presented once the authors implemented procedures to hydrophilize the QDs and reached to conjugate biomolecules to their surfaces. After those pioneering work, several II-VI QDs have been widely used in bio-applications. A survey of the QDs-based biosensors in the period 2013–2018 [48] included 28 sensors based on II-VI compounds or alloys as CdTe, CdS, CdS_xSe_{1-x}, CdSe, and ZnS for a long list of targets including DNA, HIV, cancer cells, glycoproteins, dopamine, cardiac troponin, etc.

QDs biosensor research is a very active field since some challenges remain. One of them, the toxicity of Cd, a component element in almost all QDs for biological applications. Visible light-emitting QDs can only be limitedly used for in vivo biological imaging because of the high absorption of tissues in the visible range. Then near-infrared (NIR) emitter composed of III-V InAs or IV–VI PbS is commonly used. Even in these cases, II-VI materials as ZnS or CdZnS are used as shells.

1.4.6 Gas Sensors

Traditionally, gas sensor devices have been dominated by metal oxide materials. However, semiconductor chalcogenides have been considered to be attractive in this area [50] after the demonstration of sensitivity, selectivity, and fast response/recovery in gas sensing at RT. For example, CdS QDs/Co_3O_4 composites have shown high sensitivity and low response

and recovery times for H_2S sensing at room temperature [51]. CdSe QDs/ZnO composites have shown sensitivity toward NO_2 under green light illumination [52]. The authors ascribe the effect to the transport of photogenerated electrons from the CdSe to the ZnO which influence the interface potential and the adsorption desorption process of NO_2.

1.4.7 Photocatalysis

In semiconductor photocatalytic technology, solar energy is used to promote chemical reactions. Typical examples of photocatalytic process are the production of H_2 fuel by the splitting of water, or the degradation of toxic contaminants, both with obvious implications in energy and environmental matters. The conventional TiO_2 catalytic material with a band gap of 3.2 eV wastes most of the solar energy spectra. For this reason, other semiconductors with lower band gaps have been tested as photocatalysts; this is the case of some II-VI semiconductor-related materials. With a band gap of 2.4 eV and excellent electrical conductivity parameters, CdS has been considered a significant candidate [53]. In fact, H_2 evolution has been demonstrated using CdS with different morphologies as nanowires, QDs, or hollows structures, among others. To resolve instability of CdS chemical properties or photo-corrosion effects, different kinds of composites have been used as, for example (among many others), TiO_2/CdS [54, 55] or n-doped graphene/CdS [56], with enhanced catalytic efficiencies. CdS catalytic properties have been also used to reduce the CO_2. a greenhouse and contaminant gas to clean hydrocarbon fuels such as CH_4. In this case, the requirement of cocatalysts is more needed, and several composites have been used; for example, reduced graphene oxide–CdS nanorod composite has shown excellent catalytic efficiencies [57]. On the other hand, the porous CdTe QDs/NTU-9 metalorganic framework nanocomposite has demonstrated rapid photodegradation of rhodamine 6G, a polluted dye [58], while CdSe nanoribbons have been used as photocatalyst hydrogen production from water in the presence of Na_2S/Na_2SO_3 as sacrificial electron donors under UV and visible light [59].

1.5 Conclusions and Outlook

II-VI compounds, with a very early presence in the history of materials and being founders of the semiconductor science and technology, represent today an active research and development area. Some examples of devices and structures developed on the basis of II-VI compounds are shown in Fig. 1.3.

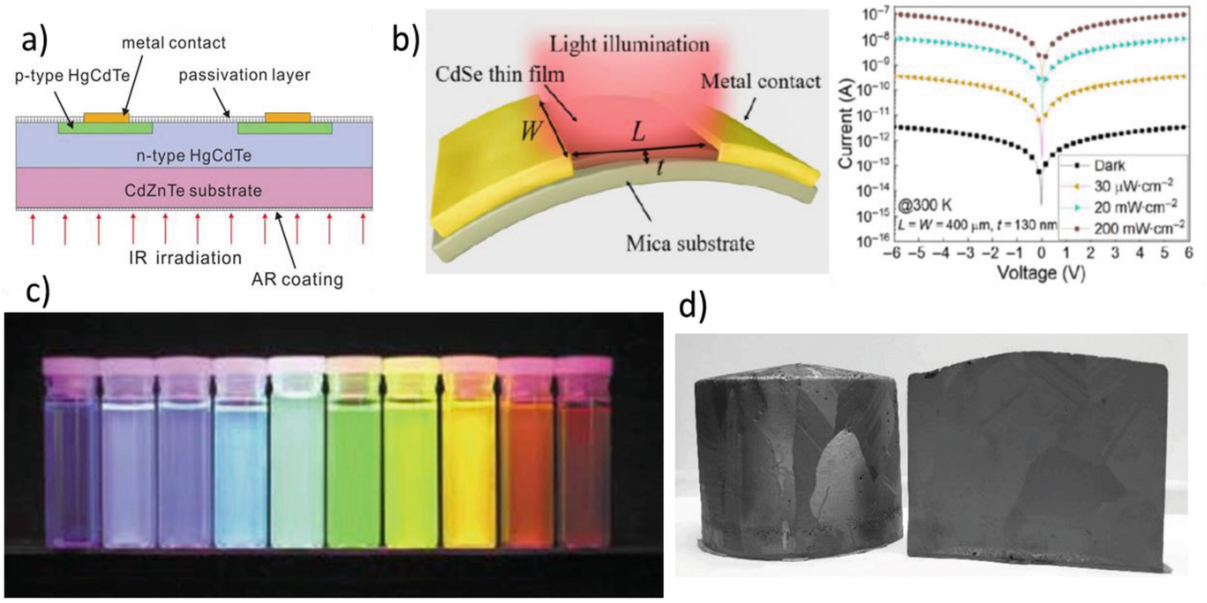

Fig. 1.3 Illustration of some kinds of detectors based in II-VI materials. (**a**) Planar structure of a p-n HgCdTe IR photodiode detector. Reproduced with permission from Ref. [13]. Copyright 2015: AIP Publishing; (**b**) schematics of a CdSe/mica flexible photodetector and its dark and illuminated I–V characteristics. Reproduced with permission from Ref. [60]. Copyright 2022: Springer; (**c**) Ten distinguishable emission colors of ZnS-capped CdSe QDs excited with a near-UV lamp. Reproduced with permission from Ref. [49]. Copyright 2001: Springer; (**d**) 8 in (24 kg) CZT ingot grown by the HP-EDG technique at eV Products, Inc. from which X-ray and gamma ray detectors are fabricated. Reproduced with permission from Ref. [61]. Copyright 2018: AIP Publishing

Several semiconductor industries use II-VI compounds or alloys, many laboratories around the world are involved in II-VI compounds research and development, and many public or private agencies devote a lot of resources for the study of this kind of materials with the purpose of making new more efficient devices. In detector technology relays most of the importance of II-VI compounds. HgCdTe and CdZnTe are excellent examples in IR and gamma/X-ray detection. Novel nanostructures as nanocrystals, quantum dots, quantum well, or nanowires have demonstrated their possibilities and potentialities in several applications.

Acknowledgments

The author thanks M. Sanchez for useful suggestions and revisions.

References

1. Walter P, Welcomme E, Hallégot P, Zaluzec NJ, Deeb C, Castaing J et al (2006) Early use of PbS nanotechnology for an ancient hair dyeing formula. Nano Lett 6:2215–2219. https://doi.org/10.1021/nl061493u
[Crossref]
2. Faraday M (1922) Experimental researches in electricity. J. M. Dent & Sons Ltd./E.P. Dutton & Co, New York
3. Adams WG, Day RE (1877) V. The action of light on selenium. Proc R Soc Lond 25:113–117. https://doi.org/10.1098/rspl.1876.0024
[Crossref]
4. Sze SM (ed) (1991) Semiconductor devices: pioneering papers. World Scientific, Singapore
5. Phillips JC (1973) Bonds and bands in semiconductors. Elsevier, New York
6. Adachi S (2005) Energy-band structure: energy-band gaps. In: Properties of group-IV, III–V and II–VI semiconductors. Wiley, Chichester, pp 103–145
7. Tomashyk V (2014) Quaternary alloys based on II–VI semiconductors. CRC Press, Boca Raton
[Crossref][zbMATH]
8. Adachi S (2005) Electron affinity and Schottky barrier height. In: Properties of group-IV, III–V and II–VI semiconductors. Wiley, Chichester, pp 195–209
9. Li Y-H, Walsh A, Chen S, Yin W-J, Yang J-H, Li J et al (2009) Revised ab initio natural band offsets of all group IV, II–VI, and III–V semiconductors. Appl Phys Lett 94:212109. https://doi.org/10.1063/1.3143626
[Crossref]
10. Wei S-H, Zunger A (1998) Calculated natural band offsets of all II–VI and III–V semiconductors: chemical trends and the role of cation *d* orbitals. Appl Phys Lett 72:2011–2013. https://doi.org/10.1063/1.121249
[Crossref]
11. Vargas-Hernández C, de Melo O, Hernández-Calderón I (2002) Photoluminescence study of ultra-thin CdSe quantum wells. Phys Status Solidi (b) 230:331–334. https://doi.org/10.1002/1521-3951(200204)230:2<331:AID-PSSB331>3.0.CO;2-9
[Crossref]
12. Rai SC, Wang K, Chen J, Marmon JK, Bhatt M, Wozny S et al (2015) Enhanced broad band photodetection through piezo-phototronic effect in CdSe/ZnTe core/shell nanowire array. Adv Electron Mater 1:1400050. https://doi.org/10.1002/aelm.201400050
[Crossref]

13. Lei W, Antoszewski J, Faraone L (2015) Progress, challenges, and opportunities for HgCdTe infrared materials and detectors. Appl Phys Rev 2:041303. https://doi.org/10.1063/1.4936577 [Crossref]
14. de Melo O, Hernández L, Zelaya-Angel O, Lozada-Morales R, Becerril M, Vasco E (1994) Low resistivity cubic phase CdS films by chemical bath deposition technique. Appl Phys Lett 65:1278–1280. https://doi.org/10.1063/1.112094 [Crossref]
15. Yang J-H, Yin W-J, Park J-S, Ma J, Wei S-H (2016) Review on first-principles study of defect properties of CdTe as a solar cell absorber. Semicond Sci Technol 31:083002. https://doi.org/10.1088/0268-1242/31/8/083002 [Crossref]
16. Woods-Robinson R, Han Y, Zhang H, Ablekim T, Khan I, Persson KA, Zakutayev A (2020) Wide band gap chalcogenide semiconductors. Chem Rev 120:4007–4055. https://doi.org/10.1021/acs.chemrev.9b00600 [Crossref]
17. Chen H, Liu K, Hu L, Al-Ghamdi AA, Fang X (2015) New concept ultraviolet photodetectors. Mater Today 18:493–502. https://doi.org/10.1016/j.mattod.2015.06.001 [Crossref]
18. Bhan RK, Dhar V (2019) Recent infrared detector technologies, applications, trends and development of HgCdTe based cooled infrared focal plane arrays and their characterization. Opto-Electron Rev 27:174–193. https://doi.org/10.1016/j.opelre.2019.04.004 [Crossref]
19. Vidal S, Degert J, Tondusson M, Freysz E, Oberlé J (2014) Optimized terahertz generation via optical rectification in ZnTe crystals. J Opt Soc Am B 31:149–153. https://doi.org/10.1364/JOSAB.31.000149 [Crossref]
20. Zhai D, Hérault E, Garet F, Coutaz J-L (2021) Terahertz generation from ZnTe optically pumped above and below the bandgap. Opt Express 29:17491–17498. https://doi.org/10.1364/OE.421282 [Crossref]
21. Ropagnol X, Matoba M, Nkeck JE, Blanchard F, Isgandarov E, Yumoto J, Ozaki T (2020) Efficient terahertz generation and detection in cadmium telluride using ultrafast ytterbium laser. Appl Phys Lett 117:181101. https://doi.org/10.1063/5.0024112 [Crossref]
22. Ruffenach S, Kadykov A, Rumyantsev VV, Torres J, Coquillat D, But D et al (2017) HgCdTe-based heterostructures for terahertz photonics. APL Mater 5:035503. https://doi.org/10.1063/1.4977781 [Crossref]
23. Pennicard D, Pirard B, Tolbanov O, Iniewski K (2017) Semiconductor materials for x-ray detectors. MRS Bull 42:445–450. https://doi.org/10.1557/mrs.2017.95 [Crossref]

24. Del Sordo S, Abbene L, Caroli E, Mancini AM, Zappettini A, Ubertini P (2009) Progress in the development of CdTe and CdZnTe semiconductor radiation detectors for astrophysical and medical applications. Sensors 9:3491–3526. https://doi.org/10.3390/s90503491 [Crossref]
25. Chakraborty M, Hashmi MSJ (2018) Cadmium telluride and cadmium zinc telluride as detector materials and their practical applications. In: Olabi A-G (ed) Encyclopedia of smart materials. Elsevier, Oxford, pp 469–475 [Crossref]
26. Ben-Haim S, Kennedy J, Keidar Z (2016) Novel cadmium zinc telluride devices for myocardial perfusion imaging—technological aspects and clinical applications. Semin Nucl Med 46:273–285. https://doi.org/10.1053/j.semnuclmed.2016.01.002 [Crossref]
27. Lee Y, Lee S, Kang S, Eom J (2017) Dose optimization for dual-energy contrast-enhanced digital mammography based on an energy-resolved photon-counting detector: a Monte Carlo simulation study. Radiat Phys Chem 132:46–51. https://doi.org/10.1016/j.radphyschem.2016.11.016 [Crossref]
28. Lee Y, Kim H-J (2015) Performance evaluation of a small CZT pixelated semiconductor gamma camera system with a newly designed stack-up parallel-hole collimator. Nucl Instr Methods Phys Res Sect A 794:54–61. https://doi.org/10.1016/j.nima.2015.05.007 [Crossref]
29. Romeo A, Artegiani E (2021) CdTe-based thin film solar cells: past, present and future. Energies 14:1684. https://doi.org/10.3390/en14061684 [Crossref]
30. Metzger WK, Grover S, Lu D, Colegrove E, Moseley J, Perkins CL et al (2019) Exceeding 20% efficiency with in situ group V doping in polycrystalline CdTe solar cells. Nat Energy 4:837–845. https://doi.org/10.1038/s41560-019-0446-7 [Crossref]
31. Afzaal M, O'Brien P (2006) Recent developments in II–VI and III–VI semiconductors and their applications in solar cells. J Mater Chem 16:1597–1602. https://doi.org/10.1039/B512182E [Crossref]
32. Sang L, Hu J, Zou R, Koide Y, Liao M (2013) Arbitrary multicolor photodetection by hetero-integrated semiconductor nanostructures. Sci Rep 3:2368. https://doi.org/10.1038/srep02368 [Crossref]
33. Fang X, Bando Y, Liao M, Gautam UK, Zhi C, Dierre B et al (2009) Single-crystalline ZnS nanobelts as ultraviolet-light sensors. Adv Mater 21:2034–2039. https://doi.org/10.1002/adma.200802441 [Crossref]
34. Amos FF, Morin SA, Streifer JA, Hamers RJ, Jin S (2007) Photodetector arrays directly assembled onto polymer substrates from aqueous solution. J Am Chem Soc 129:14296–14302. https://doi.org/10.1021/ja073675b [Crossref]

35. Fang X, Xiong S, Zhai T, Bando Y, Liao M, Gautam UK et al (2009) High-performance blue/ultraviolet-light-sensitive ZnSe-nanobelt photodetectors. Adv Mater 21:5016–5021. https://doi.org/10.1002/adma.200902126
[Crossref]
36. Sorokina IT, Sorokin E (2015) Femtosecond Cr^{2+}-based lasers. IEEE J Sel Top Quantum Electron 21:273–291. https://doi.org/10.1109/JSTQE.2014.2341589
[Crossref]
37. Fedorov V, Martyshkin D, Karki K, Mirov S (2019) Q-switched and gain-switched Fe:ZnSe lasers tunable over 3.60–5.15 mm. Opt Express 27:13934–13941. https://doi.org/10.1364/OE.27.013934
[Crossref]
38. Wang Y, Fernandez TT, Coluccelli N, Gambetta A, Laporta P, Galzerano G (2017) 47-fs Kerr-lens mode-locked Cr:ZnSe laser with high spectral purity. Opt Express 25:25193–25200. https://doi.org/10.1364/OE.25.025193
[Crossref]
39. Morgner U, Drexler W, Kärtner FX, Li XD, Pitris C, Ippen EP, Fujimoto JG (2000) Spectroscopic optical coherence tomography. Opt Lett 25:111–113. https://doi.org/10.1364/OL.25.000111
[Crossref]
40. Smet PF, Moreels I, Hens Z, Poelman D (2010) Luminescence in sulfides: a rich history and a bright future. Materials 3:2834–2883. https://doi.org/10.3390/ma3042834
[Crossref]
41. Bredol M, Schulze Dieckhoff H (2010) Materials for powder-based AC-electroluminescence. Materials 3:1353–1374. https://doi.org/10.3390/ma3021353
[Crossref]
42. Rivera-Medina MJ, Carrillo-Verduzco A, Rodríguez-Gómez A, Loi MA, Alonso-Huitrón JC (2021) White-emission from ZnS:Eu incorporated in AC-driven electroluminescent devices via ultrasonic spray pyrolysis. Mater Chem Phys 270:124866. https://doi.org/10.1016/j.matchemphys.2021.124866
[Crossref]
43. Rack PD, Holloway PH (1998) The structure, device physics, and material properties of thin film electroluminescent displays. Mater Sci Eng R 21:171–219. https://doi.org/10.1016/S0927-796X(97)00010-7
[Crossref]
44. Díaz-González M, de la Escosura-Muñiz A, Fernandez-Argüelles MT, Alonso FJG, Costa-Fernandez JM (2020) Quantum dot bioconjugates for diagnostic applications. In: Puente-Santiago AR, Rodríguez-Padrón D (eds) Surface-modified nanobiomaterials for electrochemical and biomedicine applications. Springer, Cham, pp 133–176
[Crossref]

45. Chaniotakis N, Buiculescu R (2014) 11 – Semiconductor quantum dots in chemical sensors and biosensors. In: Honeychurch KC (ed) Nanosensors for chemical and biological applications. Woodhead Publishing, pp 267–294
[Crossref]
46. Chan WCW, Nie S (1998) Quantum dot bioconjugates for ultrasensitive nonisotopic detection. Science 281:2016–2018. https://doi.org/10.1126/science.281.5385.2016
[Crossref]
47. Bruchez M, Moronne M, Gin P, Weiss S, Alivisatos AP (1998) Semiconductor nanocrystals as fluorescent biological labels. Science 281:2013–2016. https://doi.org/10.1126/science.281.5385.2013
[Crossref]
48. Ma F, Li C, Zhang C (2018) Development of quantum dot-based biosensors: principles and applications. J Mater Chem B 6:6173–6190. https://doi.org/10.1039/C8TB01869C
[Crossref]
49. Han M, Gao X, Su JZ, Nie S (2001) Quantum-dot-tagged microbeads for multiplexed optical coding of biomolecules. Nat Biotechnol 19:631–635. https://doi.org/10.1038/90228
[Crossref]
50. Galstyan V (2021) “Quantum dots: perspectives in next-generation chemical gas sensors” – a review. Anal Chim Acta 1152:238192. https://doi.org/10.1016/j.aca.2020.12.067
[Crossref]
51. Dun M, Tan J, Tan W, Tang M, Huang X (2019) CdS quantum dots supported by ultrathin porous nanosheets assembled into hollowed-out Co_3O_4 microspheres: a room-temperature H_2S gas sensor with ultra-fast response and recovery. Sensors Actuators B Chem 298:126839. https://doi.org/10.1016/j.snb.2019.126839
[Crossref]
52. Chizhov AS, Rumyantseva MN, Vasiliev RB, Filatova DG, Drozdov KA, Krylov IV et al (2014) Visible light activated room temperature gas sensors based on nanocrystalline ZnO sensitized with CdSe quantum dots. Sensors Actuators B Chem 205:305–312. https://doi.org/10.1016/j.snb.2014.08.091
[Crossref]
53. Cheng L, Xiang Q, Liao Y, Zhang H (2018) CdS-based photocatalysts. Energy Environ Sci 11:1362–1391. https://doi.org/10.1039/C7EE03640J
[Crossref]
54. Daghrir R, Drogui P, Robert D (2013) Modified TiO_2 for environmental photocatalytic applications: a review. Ind Eng Chem Res 52:3581–3599. https://doi.org/10.1021/ie303468t
[Crossref]
55. Kim JC, Choi J, Lee YB, Hong JH, Lee JI, Yang JW et al (2006) Enhanced photocatalytic activity in composites of TiO_2 nanotubes and CdS nanoparticles. Chem Commun:5024–5026. https://doi.org/10.1039/B612572G

56. Jia L, Wang D-H, Huang Y-X, Xu A-W, Yu H-Q (2011) Highly durable N-doped graphene/CdS nanocomposites with enhanced photocatalytic hydrogen evolution from water under visible light irradiation. J Phys Chem C 115:11466–11473. https://doi.org/10.1021/jp2023617 [Crossref]
57. Yu X, Marks TJ, Facchetti A (2016) Metal oxides for optoelectronic applications. Nat Mater 15:383–396. https://doi.org/10.1038/nmat4599 [Crossref]
58. Kaur R, Rana A, Singh RK, Chhabra VA, Kim K-H, Deep A (2017) Efficient photocatalytic and photovoltaic applications with nanocomposites between CdTe QDs and an NTU-9 MOF. RSC Adv 7:29015–29024. https://doi.org/10.1039/C7RA04125J [Crossref]
59. Frame FA, Carroll EC, Larsen DS, Sarahan M, Browning ND, Osterloh FE (2008) First demonstration of CdSe as a photocatalyst for hydrogen evolution from water under UV and visible light. Chem Commun:2206–2208. https://doi.org/10.1039/B718796C
60. Pan W, Liu J, Zhang Z, Gu R, Suvorova A, Gain S et al (2022) Large area van der Waals epitaxy of II–VI CdSe thin films for flexible optoelectronics and full-color imaging. Nano Res 15:368–376. https://doi.org/10.1007/s12274-021-3485-x [Crossref]
61. Prokesch M, Soldner SA, Sundaram AG (2018) CdZnTe detectors for gamma spectroscopy and x-ray photon counting at 250×10^6 photons/(mm^2 s). J Appl Phys 124:044503. https://doi.org/10.1063/1.5041006 [Crossref]

Footnotes

1 Slight increase of the band gap is observed for the wurzite structure with respect to the cubic structure. For example, wurzite CdS (a = 0.416 nm; b = 0.6756 nm) presents a band gap of 2.501 eV, slightly higher that 2.46 eV for the cubic structure.

2 In this sense II-VI alloy $Hg_{1-x}Cd_xTe$ alloys is similar to its III-V counterpart $Ga_{1-x}Al_xAs$ in which the lattice parameter is practically unchanged with composition.

OceanofPDF.com

© The Author(s), under exclusive license to Springer Nature Switzerland AG 2023
G. Korotcenkov (ed.), *Handbook of II-VI Semiconductor-Based Sensors and Radiation Detectors*
https://doi.org/10.1007/978-3-031-19531-0_2

2. Cd- and Zn-Based Wide Band Gap II-VI Semiconductors

Ghenadii Korotcenkov[1] ✉
(1) Department of Physics and Engineering, Moldova State University, Chisinau, Moldova

✉ **Ghenadii Korotcenkov**
Email: ghkoro@yahoo.com

Keywords Wide band gap II-VI semiconductors – ZnS – ZnSe – ZnTe – CdS – CdSe – CdTe – Crystallographic structure – Cubic – Hexagonal – Sphalerite – Space group F43m – Space group P63mc – Wurtzite – Zinc blende – II-VI semiconductor applications – Light-emitting devices – Optoelectronics – Photodetectors – Phosphors – Quantum electronics – Scintillators – Solar cells – Substrates – X-ray detectors – II-VI semiconductor properties – Band gap – Catalytic properties – Chemical bond – Iconicity – Chemical properties – Band structure – Elecrophysical properties – Defects – Doping – Acceptors – Donors – Self-compensation – Heat treatment – Mobility – n-type – p-type – Resistivity – Physical properties – Bulk properties – Physicochemical properties – Surface properties – Adsorption – Pinning – Oxygen – Oxidation – Surface state – Surface Fermi level – Stability – Dissociation – Oxidation – II-VI semiconductor technology – Polycrystals – Single crystals – Thin films

2.1 General Characterization

Almost all metals form compounds with elements of group VI – chalcogens – sulfur, selenium, and tellurium [121]. However, the most interesting for use are compounds formed by metals of II group, Zn, Cd, and Hg, the so-

called II-VI compounds, which include sulfides, selenides, and tellurides of zinc, cadmium, and mercury. In principle, oxygen also belongs to the chalcogens. Therefore, oxides of ZnO and CdO should also be included in II-VI compounds. However, as a rule, metal oxides, due to their specific properties, are allocated in a separate group. We will do the same, confining ourselves to considering only the ZnS, ZnSe, ZnTe, CdS, CdSe, and CdTe compounds. Mercury-based compounds will also not be considered in this chapter, since the main compounds from this group HgSe and HgTe, in contrast to the indicated wide band gap semiconductors, are characterized by a much narrower band gap and have their own specific area of application.

2.2 Crystallography

According to [6], almost all II-VI compounds crystallize in such a way that each atom is located in the center of a regular tetrahedron, at the four corners of which are atoms of another element. These tetrahedra can form two types of structures: sphalerite (cubic) and wurtzite (hexagonal). The distances between atoms in the tetrahedra of both modifications are very close to each other.

The structure of sphalerite or zinc blende is very similar to the structure of diamond but differs in the alternation of atoms in the lattice of two different elements. In the structure of sphalerite, the atoms of one element are located at the sites of the face-centered cubic lattice, and the atoms of the second element occupy the centers of four (out of eight) small cubes (Fig. 2.1a). This crystallographic structure belongs to the space group of F43m. The coordination number for the atoms of both elements is the same and equal to four. Four atoms of a different kind, arranged in tetrahedral directions, surround any atom. In particular, each Zn(Cd) atom has four S(Se, Te) atoms around it, which are located at the vertices of a regular tetrahedron. Any atom of the same kind, as already mentioned, is surrounded by 12 atoms of the same kind, which are neighbors of the second order. Six of them are located at the vertices of a hexagon lying in the same plane as the considered atom, the remaining six form a trigonal antiprism, in which three atoms are located above and the other three are below the plane of the hexagon. In view of this arrangement of atoms, the A^{II} and B^{VI} atoms exhibit the same valence equal to four, which is achieved

due to the appearance of two donor-acceptor bonds. The electron clouds in II-VI compounds are drawn toward the anion former B^{VI}.

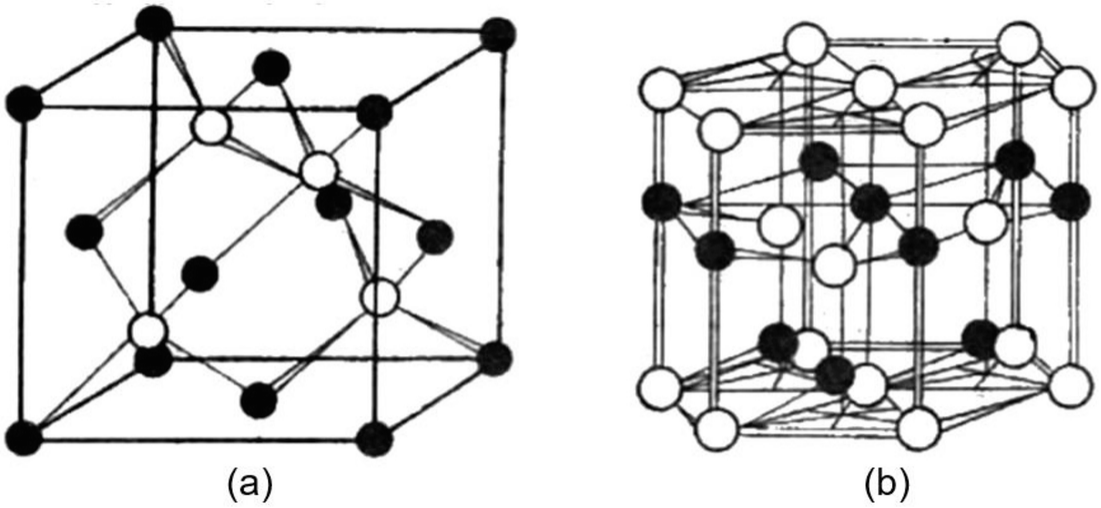

Fig. 2.1 Crystal structure of (**a**) sphalerite and (**b**) wurtzite

An important structural feature of zinc blende is the absence of a center of symmetry or inversion. The Zn–S layers (or ZnS4 tetrahedra) are oriented along the <111> directions. As a result, the crystals are polar, and the planes (*hkl*) and ($\bar{h}\bar{k}\bar{l}$) oppositely located in them, and the directions (*hkl*) and ($\bar{h}\bar{k}\bar{l}$) may have different physical and chemical properties. Therefore, crystals with a zinc blende structure exhibit piezoelectric properties. In addition, in II-VI compounds with the sphalerite structure, cleavage of the core along the (100) cube planes is observed, which is characteristic of substances with a higher proportion of bond ionicity.

Figure 2.1b shows the structural type of wurtzite. This crystallographic structure belongs to the space group of P63mc. The coordination number for the atoms of both elements is also four. This means that each atom in the lattice is bonded to four neighbors, two of which are covalent and the other two are ionic. The bond strength of atoms in the crystal lattice within each group (sulfides, selenides, tellurides) decreases with an increase in the total atomic number. According to the data of crystallographic analysis for the sphalerite and wurtzite structures, there are two types of surfaces: a layer consisting of elements of the 12th group of the periodic table of elements (Zn, Cd) and a layer ending with chalcogen atoms (S, Se, Te). The ionicity of the bond in the structure of wurtzite is higher than in the structure of sphalerite.

The structures of sphalerite and wurtzite are very close to each other. The same number of atoms determines this similarity not only in the first but also in the second coordination spheres. In both structures, in the second coordination sphere, 12 atoms of the same element surround each atom; there is only some difference in the arrangement of atoms, associated with the difference in packing according to the cubic and hexagonal laws. The difference between the two structures is essentially in the position of the atoms of the third coordination sphere, since the distances to the atoms located in the third coordination sphere in the wurtzite structure are smaller than in the sphalerite structure. Therefore, it can be expected that for compounds with a greater difference in the electronegativity of the elements, the wurtzite structure will be preferable.

From the point of view of crystal chemistry, there is a continuous transition from the sphalerite structure to the wurtzite structure. For the entire group of II-VI compounds, the sphalerite-type cubic structure is low temperature and stable, while the wurtzite modification is high temperature. In many cases, the wurtzite modification can be obtained only under nonequilibrium conditions by deposition on a cooled substrate or on a substrate of another II-VI compounds with wurtzite structure [20, 52, 101]. It is this situation, in particular, that is observed for CdTe.

As for individual semiconductor II-VI compounds, each compound has its own specifics [84]. Indeed, depending on the synthesis conditions, ZnS crystallizes in two modifications – high-temperature hexagonal and low-temperature cubic (Table 2.1). The phase transition point lies near 1020 °C. However, synthesized ZnS almost always contains a mixture of both modifications. An important feature of zinc sulfide is that it forms a continuous series of solid solutions with CdS, CdSe, and ZnSe. In this case, the addition of CdS to ZnS stabilizes the hexagonal modification, while the addition of ZnSe stabilizes the cubic modification.

Table 2.1 Crystal structures of type II-VI compounds

Compound	Structure type	Lattice constant, nm		Minimum distance between dissimilar atoms	Phase stable at 300 K
		a	c		
ZnS	S	0.541		0.236	Zinc blende + wurtzite
	W	0.382	0.626	0.235	

Compound	Structure type	Lattice constant, nm		Minimum distance between dissimilar atoms	Phase stable at 300 K
		a	c		
ZnSe	S	0.566		0.245	Zinc blende
	W	0.401	0.654	0.245	
ZnTe	S	0.610			Zinc blende
CdS	S	0.582		0.252	Wurtzite
	W	0.413	0.675	0.252	
CdSe	S	0.6084		0.262	Wurtzite
	W	0.430	0.701	0.263	
	Hexagonal 24-layer	0.4291	8.43		
CdTe	S	0.648		0.279	Zinc blende
	W	0.457	0.747		
	Hexagonal 12-layer	0.46	4.51		

S sphalerite (zinc blend), *W* wurtzite

The CdS compound is no exception to the regularities common for compounds II-VI: there are CdS crystals with both structures. Moreover, in thin films of cadmium sulfide, as well as in ZnS, both cubic and hexagonal modifications can be present simultaneously. When the pressure rises to $2.5 \cdot 10^9$ Pa, cadmium sulfide transforms into the cubic (Fm3m) structure of sodium chloride. In this case, there is a transition from tetrahedral to octahedral coordination, which is accompanied by a decrease in the volume of the substance by almost 20%. Such phases are stable only at high pressure and are also semiconductors.

The same situation is observed for other semiconductors. Cadmium selenide can crystallize both in the structure of zinc blende (β-CdSe) and in the structure of wurtzite (α-CdSe) [6]. However, unlike CdS and ZnS, the hexagonal modification of CdSe of the wurtzite type is the most stable, which determined the use of this modification of CdSe in the development of various semiconductor devices [19]. The transition from the cubic to the hexagonal modification occurs at 409 °C [50].

CdTe usually crystallizes into a zinc blende structure, but at normal pressures, CdTe can exist in two polymorphs: wurtzite and sphalerite. In

[7], the authors note that in the Cd–Te system at high temperatures (above 1100 K), there are polymorphic modifications of cadmium telluride, which differ in structure from sphalerite. Moreover, in [5], it was shown that at room temperature under pressure, cadmium telluride undergoes phase transitions from the sphalerite structure to a cubic structure of the NaCl type, accompanied by a sharp decrease in electrical resistance by several orders of magnitude.

It is important to note that, due to the proximity of both types of structures, cadmium and zinc chalcogenides during their preparation from the gas phase, in addition to crystallization in a three-layer (cubic) and two-layer (hexagonal) packing, can form structures with a violation of the order of the layers. This leads to the formation of multilayer polytype forms (modifications that differ in the type of closest packing at the same coordination number).

2.3 Chemical Bond

The atoms of group II elements on the outer shell have two electrons each with the s^2 configuration, and the atoms of the elements of the oxygen subgroup can have six electrons with the s^2p^4 configuration. In the case when metal atoms have sufficiently strong electropositive properties and can donate two external *s*-electrons to nonmetal atoms, doubly charged ions with filled *p*-shells are formed and a structure with octahedral coordination (of the NaCl type) appears, as is the case in alkaline earth chalcogenides metals. Compounds with a tetrahedral structure such as sphalerite or wurtzite are formed between the elements of the zinc and oxygen subgroups, when the metals have sufficiently high ionization potentials and the atoms do not give up their electrons, but can share them with neighboring nonmetal atoms. In this case, four elongated electron clouds are formed around each atom, which, located in the sp^3 configuration, appeared due to the hybridization of *s* and *p* orbitals, form four bonds directed to the vertices of a regular tetrahedron.

Due to the large electronegativity of group VI elements compared to group II elements (X (2) < X (6)) (see Table 2.2), the two-electron cloud shifts from atoms of group II elements to atoms of group VI elements. Therefore, in II-VI compounds, the bond is ionic-covalent, and these compounds have features characteristic of both bond types. The tetrahedral

arrangement of atoms in II-VI compounds is similar to their arrangement in crystals of group VI elements, which are typically covalent structures. At the same time, the magnitude and sign of the effective charge, the crystal structure, and the nature of cleavage in II-VI compounds indicate the presence of a significant ionic component [6]. The ionic component of the bond in these compounds reaches 45–70%. This leads to larger band gaps and lower carrier mobility in the homologous series.

Table 2.2 Atomic number and relative electronegativity of elements forming II-VI compounds

Element	**O**	**S**	**Se**	**Te**	**Zn**	**Cd**
Atomic number	8	16	34	52	30	48
Atomic weight	15.9994	32.066	78.96	127.60	65.39	112.411
Covalent radii, nm	0.066	0.104	0.114	0.132	0.131	0.148
Ionic radii, nm	0.140	0.184	0.198	0.221	0.074	0.095
Electronegativity	3.5	2.5	2.4	2.1	1.6	1.7

Table 2.3 gives the magnitude and sign of the effective charge of metal atoms in II-VI compounds. The sign of the effective charge of metal atoms is always positive, which means that the charge is shifted toward the anion. The decrease in the effective charge for cadmium telluride compared to selenide indicates a decrease in the proportion of bond ionicity within each group with an increase in the serial number of the nonmetal. This is also evidenced by the change in the crystal structure of II-VI compounds [6]. Along with a decrease in the proportion of ionicity with an increase in the atomic number of the elements that make up compounds of the II-VI type, the bonds become more and more metallic. There is an increasing blurring of the electron clouds of covalent bonds, somewhat shifted toward the anion former B^{VI}, due to the easy polarizability of large atoms, although the electrons have not yet become the property of the entire lattice [6]. In this case, the increase in the proportion of the metallic bond is carried out mainly due to the decrease in the proportion of the ionic one.

Table 2.3 Parameters of II-VI compounds characterizing the chemical bond in the compound

Compound	**Heat of formation, $-\Delta H^0$ (298 K), (kcal/mol)**	**Electron affinity, eV**	**Electro-negativity difference, ΔX**	**The value of the effective charge for metal atoms, X**
ZnS	49.0	3.9	0.9	+0.268

Compound	Heat of formation, $-\Delta H^0$ (298 K), (kcal/mol)	Electron affinity, eV	Electro-negativity difference, ΔX	The value of the effective charge for metal atoms, X
ZnSe	38.0	4.09	0.8	+0.099
ZnTe	28.5	3.50–3.53	0.5	+0.066
CdS	37.5	4.50–4.79	0.8	+0.77
CdSe	34.6	4.95	0.7	+0.55
CdTe	24.1	4.28	0.4	+0.081

2.4 Band Structure

It is known that the photoelectric and luminescent properties of semiconductors are directly related to the band structure of the semiconductor. Figures 2.2 and 2.3 show electronic band structures calculated for II-VI compounds with cubic and wurtzite structures along high symmetry directions. Local-density approximation was used for these simulations. It can be seen that the maxima of the valence band and the minima of the conduction band fall on the center of the Brillion zone (Γ-point), where the momentum κ is equal to zero. This means that II-VI compounds are direct-gap materials in the Γ direction, regardless of the material structure. Differences in both diagrams of the band structure are observed near the Γ-point. The band gaps in this point for these II-VI compounds change from 1.44 eV (CdTe) to 3.6 eV (ZnS). II-VI compounds with the zinc-blend structure contain fourfold degenerate levels of the valence band at the Γ-point, while in wurtzite, the valence band is broken by the crystal field into two twofold degenerate levels. The valence band states (Γ8 band) are mostly composed of the *p* orbitals from the chalcogen [33]. This band is strongly degenerated (eightfold) and split into light and heavy hole bands far from the Γ-point. The valence band exhibits weak dispersion, corresponding to a large hole effective mass. The conduction band (Γ6 band) is generally composed of the *s* orbital of the metal. This band is twofold degenerated and is more strongly dispersive than the valence band. Specifically, the associated effective mass is lower. The spin orbit band is located in the valence band and is responsible for increasing the splitting between the light and heavy hole bands. A general trend is an increase in the spin-orbit coupling as the mass of the chalcogenides

increases. In addition, the band gap increases linearity with pressure due to decreasing interatomic distance and decreases with increasing temperature.

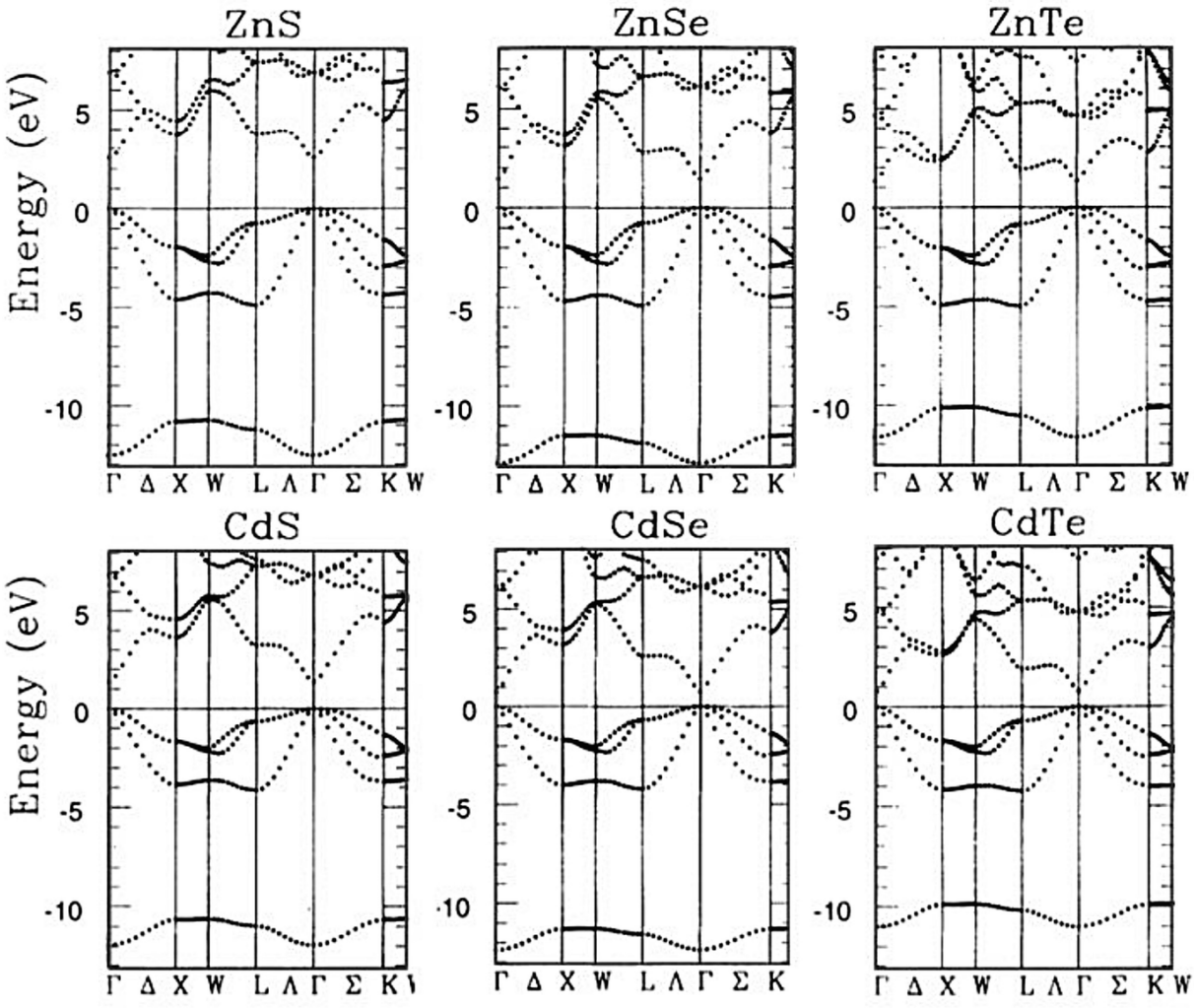

Fig. 2.2 Band diagram calculated for II-VI compounds with zinc blende structure. (Reprinted with permission from Zakharov et al. [123]. Copyright 1994: Am. Phys. Soc.)

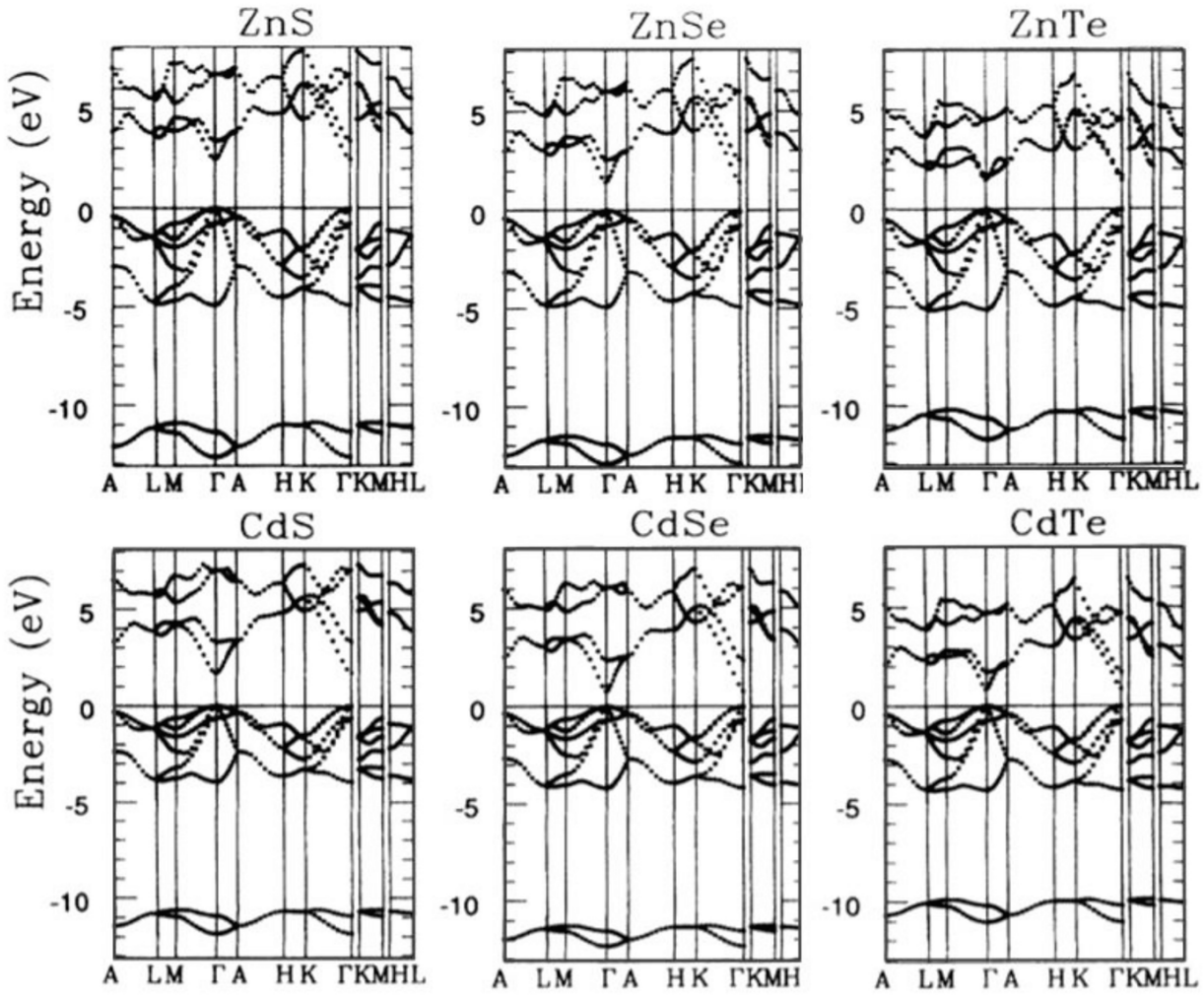

Fig. 2.3 Band diagram calculated for II-VI compounds, having a wurtzite structure. (Reprinted with permission from Zakharov et al. [123]. Copyright 1994: Am. Phys. Soc.)

2.5 Physical Properties

When studying the processes occurring in semiconductor materials and responsible for the observed characteristics of various device structures, it is necessary to take into account the various properties of a substance: chemical, physicochemical, electrical, optical, mechanical, etc., which are characterized by the arrangement of atoms of substances, their nature, and the type of connection between them (see Tables 2.4 and 2.5). It is important to know that the physical properties of diamond-like semiconductors change in a regular way depending on their composition and crystallographic structure. Despite the fact that each group of semiconductors is characterized by its own combination of properties,

nevertheless, there are regularities in the change in the properties of semiconductors both within groups and between them, common to all compounds [6]. These regularities are fulfilled also for II-VI compounds, considered in this chapter. Semiconductors related to II-VI compounds have a completely filled valence band separated from the conduction band by a band gap varying from 1.4 to 3.7 eV [6].

Table 2.4 Bulk physical properties of II-VI compounds

Compound	Atomic number (average), Z	Molecular weight	Density, g/cm^3	Micro hardness, GPa	Temperature coefficient of linear expansion, K^{-1}
ZnS	23	97.43	4.09–4.10	1.78	$(6.2–6.7)\cdot10^{-6}$
ZnSe	32	144.34	5.26–5.43	1.35	$(1.9–7.8)\cdot10^{-6}$
ZnTe	41	191.36	5.7–6.34	0.6–1.0	$8.3\cdot10^{-6}$
CdS	32	144.46	4.82	0.8–1.2	$(4.1–6.5)\cdot10^{-6}$
CdSe	41	191.36	5.81	0.5–0.9	$(2.5–4.4)\cdot10^{-6}$
CdTe	50	240.01	5.81–5.86	0.45–0.6	$(4.0–5.9)\cdot10^{-6}$

Table 2.5 Some bulk physical properties of II-VI compounds

II-VI	Теплопроводность, W/cm·K	Free exciton binding energy, meV		Dielectric constant		Refractive index, n
		Experiment	Theory	High frequency, ε_∞	Low frequency, ε_S	
ZnS	0.16–0.27	34–40	37.8	4.7–5.7	8–9.6	2.2–2.38
ZnSe	0.16–0.19	18.7–20	20.1	5.4–5.9	8.1–8.9	2.3–2.6
ZnTe	0.11–0.18	12.8 ± 2	14.2	6.9–8.2	7–10.1	2.65–2.8
CdS	0.2	27–31	16.9	5.3–5.4	7–9.8	2.3–2.6
CdSe	0.04–00.9	15.7–16.7	13	5.8–6.2	9.3–10.7	2.5–3.05
CdTe	0.062–0.075	10.5–11	10.4	7.1–10.8	9.6–12	2.7–3.1

Tables 2.3 and 2.6 show the physicochemical properties of II-VI compounds [38, 84]. Compounds-analogues are grouped according to the principle of constancy of the cation former. Within the group of analogue compounds, there is a clear dependence of properties on the atomic number

of the nonmetal (Table 2.2). With an increase in the atomic number of a nonmetal, interatomic distances increase in each row, indicating an increase in the length of directional bonds between atoms (see Table 2.1). Due to this, the bond strength decreases, as can be judged by the change in thermodynamic characteristics. Molecular weight has the same effect on the properties of semiconductor compounds (see Fig. 2.4).

Table 2.6 Physicochemical properties of II-VI compounds

Compound	T_m, °C	E_{at}, kJ/mol	E_g eV	dE_g/dT, x10^4, eV/grad	E_{EHP}, eV
ZnS	1780–1830	611	3.6–3.67	−(3.8–7.4)	10.8
ZnSe	1515–1520	477	2.73	−(4.7–7.2)	8.2
ZnTe	1239–1295	456	2.23	−(3.6–5.5)	6.7
CdS	1475–1750	532	2.4–2.57	−(4.7–4.9)	7.3
CdSe	1258–1264	423	1.7–1.85	−(4.6–6.9)	5.5
CdTe	1041–1098	402	1.44–1.51	−(3.5–5.0)	4.4

E_g band gap, T_m melting temperature, E_{at} the atomization energy, E_{EHP} energy of the formation of e-h pair, dE_g/dT band gap temperature coefficient (77–300 K)

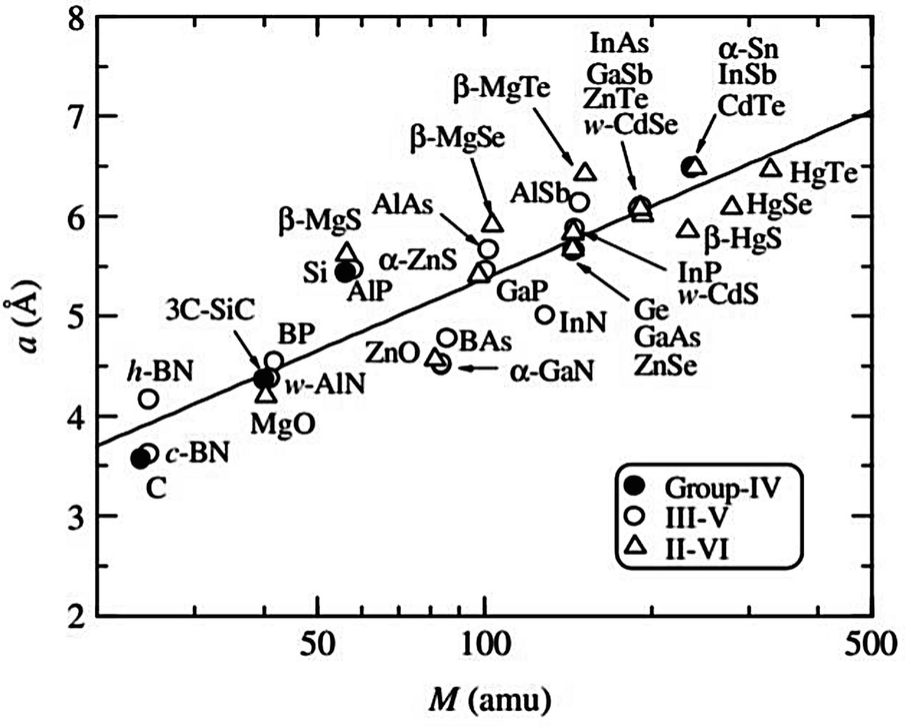

Fig. 2.4 Lattice constant *a* as a function of molecular weight M for a number of groups IV, III-V, and II-VI semiconductors. (Reprinted with permission from Adachi [2]. Copyright 2005: Wiley)

Within the group, the atomization energy, melting temperature, microhardness, and energy of formation of an electron-hole pair decrease, i.e., the main characteristics that evaluate the strength of bonds in a crystal (Tables 2.4, 2.5, and 2.6). These changes are directly related to the change in the type of bond within the group. In particular, the observed increase in the band gap in the series CdTe-CdSe-CdS and ZnTe-ZnSe-ZnS is due to an increase in the ionic component of the chemical bond [6]. Due to the increase in the proportion of the covalent-metal bond and the decrease in the ionic component in the series CdS-CdSe-CdTe and ZnS-ZnSe-ZnTe, a regular increase in the mobility of charge carriers and a decrease in resistivity are also clearly recorded. Therefore, sulfides, in which a significant proportion of ionic bonds are present, are characterized by low electron mobilities, while tellurides, on the contrary, have very significant carrier mobilities due to a small fraction of ionicity. Metal selenides of the zinc subgroup occupy an intermediate position.

The band gap E_g is one of the fundamental parameters of semiconductor materials. The larger E_g, the higher the permissible operating temperature and the more shifted to the short-wavelength region of the spectrum the operating range of photoelectrical and optoelectronic devices created on the basis of the corresponding semiconductor materials. The E_g value correlates well with dielectric constant, reflectivity, bond ionicity, and electronic polarizability. In particular, Tripathy and Pattanaik [113] have shown that dielectric constant, linear optical susceptibility, and reflectivity of II-VI and III-V group semiconductors decrease with increasing band gap. A direct relationship also exists between band gap and melting temperature. The larger the band gap, the higher the melting point, and vice versa (see Table 2.6). Both of these values increase with an increase in the binding energy of atoms in the crystal lattice. Therefore, wide-gap semiconductor materials are characterized by high melting temperatures, which create great difficulties in the way of creating pure and structurally perfect single crystals of such semiconductor materials. The band gap also decreases with an increase in the atomic mass of the elements, which are part of II-VI compounds (Table 2.4). It is important to note that a change in the crystallographic structure can also change the band gap. For example, CdS

has direct band gaps of 2.57 eV and 2.40 eV at room temperature for hexagonal and cubic structures, respectively [97].

As for other parameters of II-VI compounds, the vibrational properties of II-VI semiconductor nanostructures are described in [36], properties of II-VI semiconductors associated with moving dislocations are discussed in [86], and results of simulation and experimental study of optical and electronic properties are presented in [1, 2, 113]. Some of these properties are listed in Table 2.7.

Table 2.7 Physical parameters of II-VI semiconductors

Parameter	ZnS	ZnSe	ZnTe	CdS	CdSe	CdTe
Breakdown voltage E_{BR}, (10^5 V/cm)	43–44	20	13	16–17	6.3–7.1	4.9
Surface (cleavage) energy, J/m^2	0.85–1.225	0.75–0.98	0.84–0.96	0.69–1.06	0.88–0.94	0.58–0.85
Specific heat C_p, J/g·K	0.486	0.360	0.258	0.328	0.281	0.211
Debye temperature θ_D, K	351–440	340	260	310	135	44
Elastic stiffness, C_{ij} (10^{11} dyn/cm^2)	4.46–10.2	2.09–8.57	3.11–7.15	2.36–7.70	2.23–6.67	2.02–5.35
Young's modulus, Y (10^{12} dyn/cm^2)	0.513–0.864	0.478–0.786	0.418–0.632	0.326–0.509	0.287–0.465	0.234–0.400
Bulk modulus, B_u (10^{11} dyn/cm^2)	7.71	6.24	5.10	6.16	5.31	4.24
Long-wavelength optical phonon, meV						
LO	43.46	31.2	26.0	37.6	26.2	20.7
TO	33.73	25.4	22.4	29.4	21.0	17.2
Piezoelectric stress constant, e_{14} (C/m^2)	0.147	0.049	0.028			0.0335
Piezoelectric strain constants, d_{14} (10^{-12} m/V)	3.18	1.10	0.91			1.68
1st-orbital Bohr radius, α_B, nm	2.7–3.3	4.1	6.2	2.5–2.6	4.5–4.8	6.5

Source: Data extracted from Adachi [2]

2.6 Stability

Under normal pressure, ZnS does not melt; under a pressure of 15 MPa (150 atm), it melts at 1850 °C. At elevated temperatures, all II-VI compounds in a vacuum and neutral atmosphere decompose according to the reaction.

$$2A^{II}\ B^{VII} \rightarrow 2A^{II}{}_{(gas)} + B_2{}^{VII}{}_{(gas)} \tag{2.1}$$

The presence of $A^{II}B^{VI}$ molecules in the vapor phase is not completely excluded, but for most compounds, their concentration is low, and it can be assumed that dissociation is complete [6]. The equilibrium vapor pressure of volatile components strongly depends on temperature.

When II-VI compounds are heated in air, the formation of oxides is possible, since both the anion and cation oxides are more stable than the corresponding Cd (and Zn) selenide, sulfide, or telluride. Therefore, when II-VI semiconductor nanoparticles are heated in air, their oxidation occurs, which accelerates with increasing temperature. For example, treatment of ZnS nanoparticles at temperatures up to 400 °C led to the formation of a significant amount of sulfates fixed on the surface of particles detected by FT-IR, Raman, and XPS methods, and at temperatures above 500 °C led to the complete conversion of ZnS to ZnO [21]. This is clearly seen in the XRD patterns shown in Fig. 2.5a. Simultaneously, this process was accompanied by the growth of crystallites (Fig. 2.5) and the release of SO_2. Similar result was reported by Shanmugam et al. [100] and Park et al. [89]. They established that the annealing at 500 °C in air converts ZnS nanocrystals into ZnO as a result of oxidation. It was found that the ZnS crystallographic modifications are oxidized at different temperatures and these processes have different mechanisms. Schultze et al. [99] have found that the oxidation of wurtzite starts at a higher temperature (~560 °C), and ZnO is formed without any detectable by-products or intermediates (Eq. 2.2). The oxidation of sphalerite starts at a lower temperature (~500 °C), and $ZnSO_4$ and $Zn_3O(SO_4)_2$ are formed intermediately in side reactions with the formation of ZnO (Eqs. 2.3, 2.4, 2.5, and 2.6). It can be seen that the oxidation of sphalerite is more complex, including several stages.

Oxidation of wurtzite

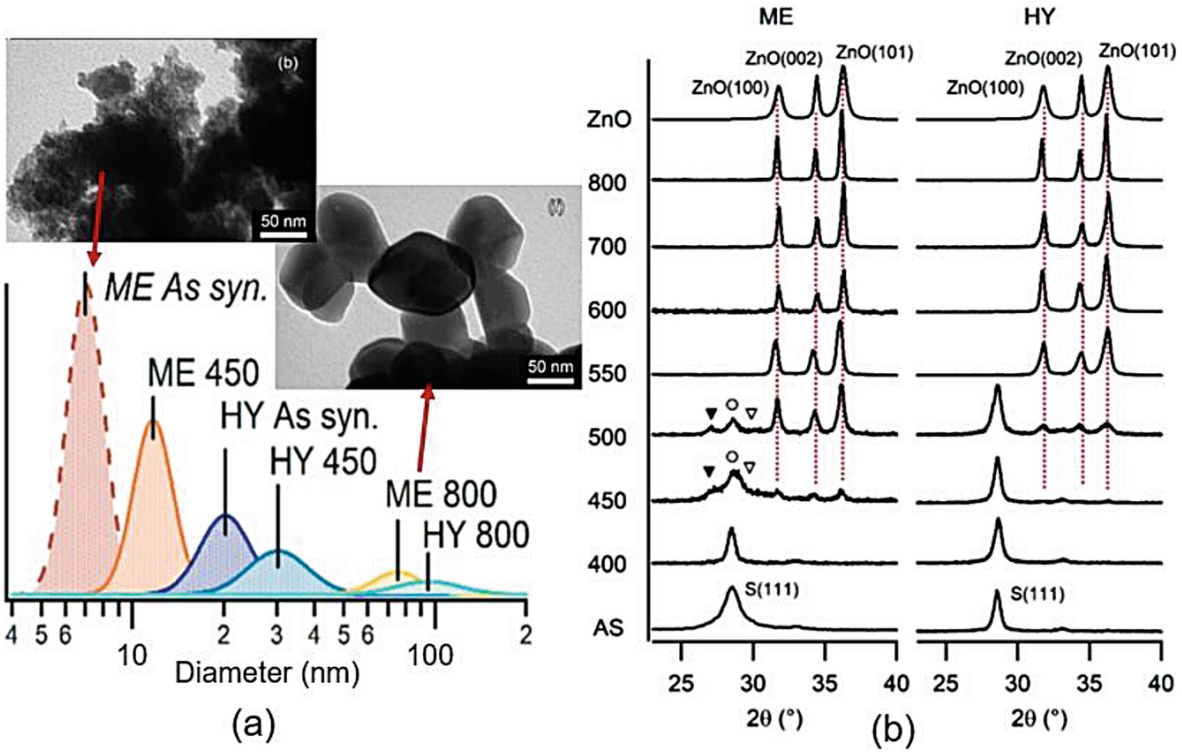

Fig. 2.5 (**a**) Log-normal approximate numerical distribution of ZnS nanoparticles diameter obtained from TEM images. (**b**) Evolution of the XRD diffractograms at different calcination temperatures. The S(111) index is referred to sphalerite-phase ZnS. The dotted lines emphasize the presence of the three main reflections of ZnO. Markers show the presence of the wurtzitic ZnS reflections: (▼) = (100), (○) = (100), (▽) = (100). *AS* as-synthesized. Temperatures are indicated in Celsius degrees. *ME* miniemulsion, *HY* hydrothermal synthesis. (Reprinted with permission from Dengo et al. [21]. Copyright 2018: ACS)

$$ZnS + 3/2O_2 \rightarrow ZnO + SO_2 \tag{2.2}$$

Oxidation of sphalerite

$$ZnS + 2O_2 \rightarrow ZnSO_4 \tag{2.3}$$

$$3ZnSO_4 \rightarrow Zn_3O(SO_4)_2 + SO_3 \tag{2.4}$$

$$Zn_3O(SO_4)_2 \rightarrow 3ZnO + 2SO_3 \tag{2.5}$$

$$2SO_3 \leftrightarrow 2SO_2 + O_2 \tag{2.6}$$

It should be noted that the conversion of ZnS to ZnO at elevated temperatures also occurs in water vapor even in the absence of oxygen. Sasaoka et al. [98] showed that ZnS can be converted to ZnO, SO_2, and H_2

with H_2O in the absence of O_2 at high temperature (>600 °C). At the first stage of oxidation, ZnS predominantly reacted with H_2O. SO_2 formed from ZnS contained oxygen from H_2O. From the experimental results, it was found that the oxidation of ZnS in the presence of H_2O can be expressed by the following two equations (Eqs. 2.7 and 2.8):

$$ZnS + 3H_2O \iff ZnO + SO_2 + 3H_2 \tag{2.7}$$

$$3H_2 + {}^{3}/_{2}O_2 \Rightarrow 3H_2O \tag{2.8}$$

Similar regularities were found for the process of oxidation of ZnSe polycrystalline films (grain size 0.2–6.5 mm) [53]. It was found that up to temperature of 300 °C ZnSe remains the dominant phase. While with further rise in temperature, its fraction appreciably decreases as compared to zinc oxide. At a temperature ~500 °C, up to 18% of zinc selenite were found. However, already at temperatures of 550 °C and above, complete conversion of ZnSe into ZnO occurs. Moreover, if at T = 550 °C this requires ~300 min, then at T = 600 °C, complete oxidation occurs in 70 min [53]. Wherein, within the whole temperature range (250–700 °C), the main reaction product in the gas phase is a mixture of selenium and its dioxide (SeO_2) [111]. It was suggested the following equation for the oxidation of zinc selenide:

$$ZnSe + (1/2 + y)\,O_2 \rightarrow ZnO + xSe + ySeO_2 \tag{2.9}$$

When CdSe is heated at T = 400 °C, the formation of metal oxide, CdO is also observed on the surface [29]. This suggests that chalcogenides can be converted into oxides through oxidation. During annealing of thin CdTe films at temperatures up to 550 °C, the main oxides formed were $CdTeO_3$, TeO_2, and Te_2O_5. However, the dominant oxide was $CdTeO_3$ [9]. In addition to oxides, Te was also observed after annealing, which arose because of the decomposition of the CdTe compound at a high annealing temperature (Fig. 2.6). At the same time, a regularity was discovered that in a densely packed film, which had a grain size of submicrometer or micrometer, the heat treatment did not provide enough energy to reorient the grains. However, films with small CdTe grains usually showed a significant increase in crystallinity after the heat treatment. This agrees with the observations for metal oxides; small grains are easy to reorient and

coalescence. The texture orientation of CdTe films did not change even after heat treatment at the highest temperature of 550 °C [9].

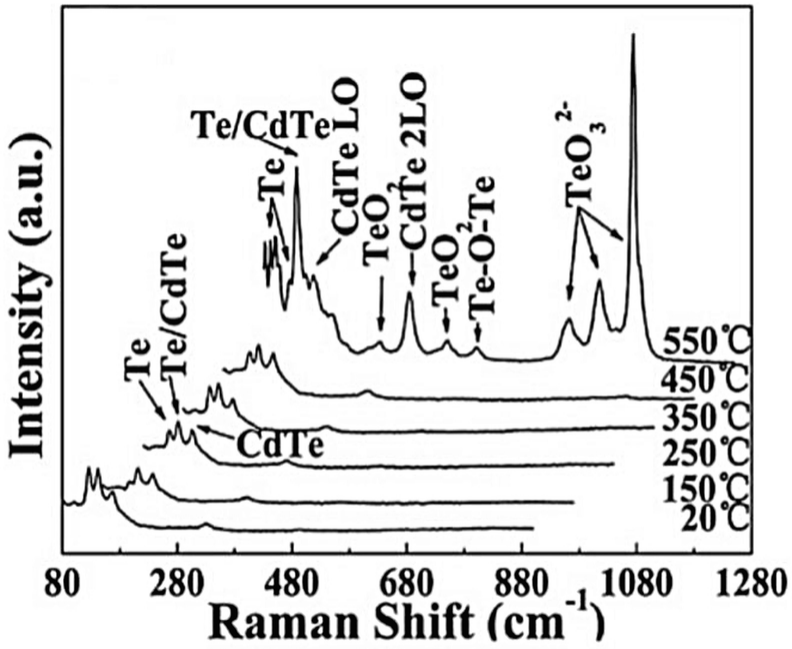

Fig. 2.6 Raman spectra of CdTe films after annealing at different temperatures (recorded at room temperature). (Reprinted with permission from Bai and Wang [9]. Copyright 2012: Wiley)

Similar studies were carried out by Trenczek-Zajaca [112]. Cadmium sulfide nanopowders were oxidized in air at temperatures ranging from 100 to 900 °C. During these experiments, it was established that no changes in composition below 400 °C were found. At higher temperatures, different oxidized phases belonging to Cd-O-S system were observed. The appearance of $Cd(S_2O_7)$ and $CdSO_4$ at 400 °C was accompanied by an increase in crystallinity. $Cd_5S_3O_6$ and Cd_3SO_6 appear at 500 and 600 °C, respectively, and, finally, CdO at 800 °C. SEM observations showed that oxidation leads to a gradual increase of CdS nanoparticles form 10 nm to more than 3.5 μm at 800 °C. As for volatile components, according to Bootsma [12], when oxygen and CdS interact, SO_2 appears at temperatures above 250 °C (Fig. 2.7a), but intense sublimation of S begins at temperatures of 500 °C (Fig. 2.7b). In humid air, zinc and cadmium sulfides are oxidized to sulfate.

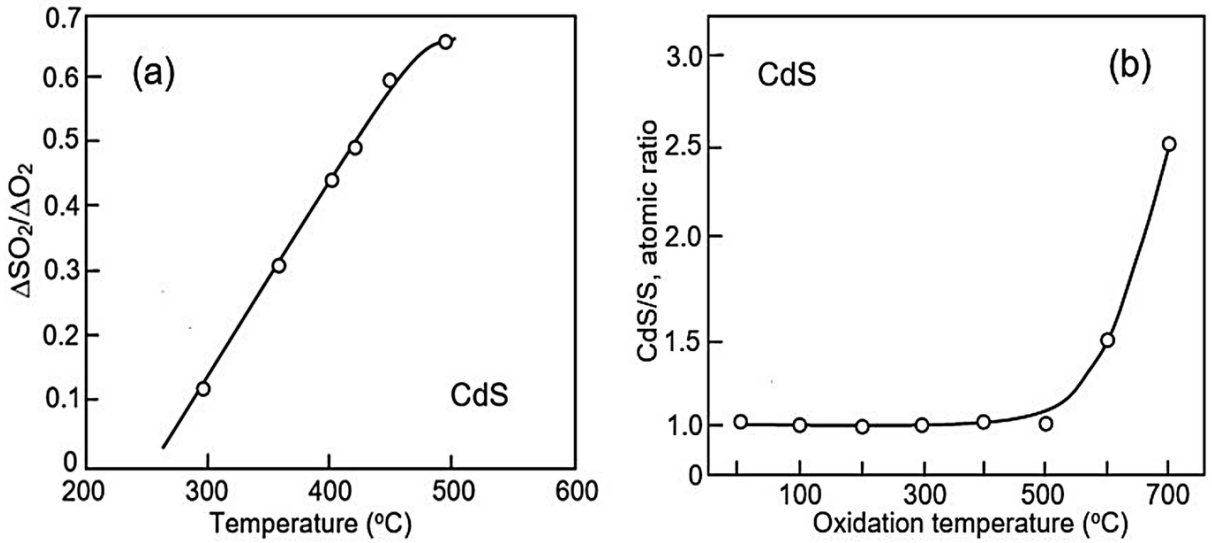

Fig. 2.7 (**a**) Relative amount of SO_2 produced during the reaction of CdS with oxygen versus temperature. (**b**) Atomic ratio of Cd/S in nanopowders as a function of oxidation temperature. ((**a**) Adapted with permission from Bootsma [12]. Copyright 1968: Fig. 3; (**b**) Adapted with permission from Trenczek-Zajaca [112]. Copyright 2019: RSC)

2.7 Chemical Properties

Chalcogenides are slightly soluble in water, chemically stable, and poorly soluble in dilute hydrochloric and sulfuric acids but decompose with concentrated hydrochloric and hydrochloric acids. Hydrogen peroxide, nitric acid, and other oxidizing agents convert them into the corresponding salts of sulfuric, selenic, and telluric acids.

As might be expected from the relative chemical stability of II-VI compounds, strong oxidants are typically needed to effect etching [102]. Solution conditions are commonly adjusted to obtain soluble products in reasonable periods of time. Two of the most widely used and studied etchants are bromine in methanol and alkaline peroxide. Treatment of surfaces of II-VI semiconductors with alcoholic solutions of bromine is a common method for preparing clean fresh surfaces. Main regularities revealed during etching of II-VI semiconductors with alcoholic solutions of bromine are shown in Fig. 2.8. It is seen that the etch rate depends on the crystal face being exposed and decreases as you move from tellurides and selenides to sulfides. In this case, the minimum etching rate is characteristic of ZnS, which fully corresponds to its physicochemical properties.

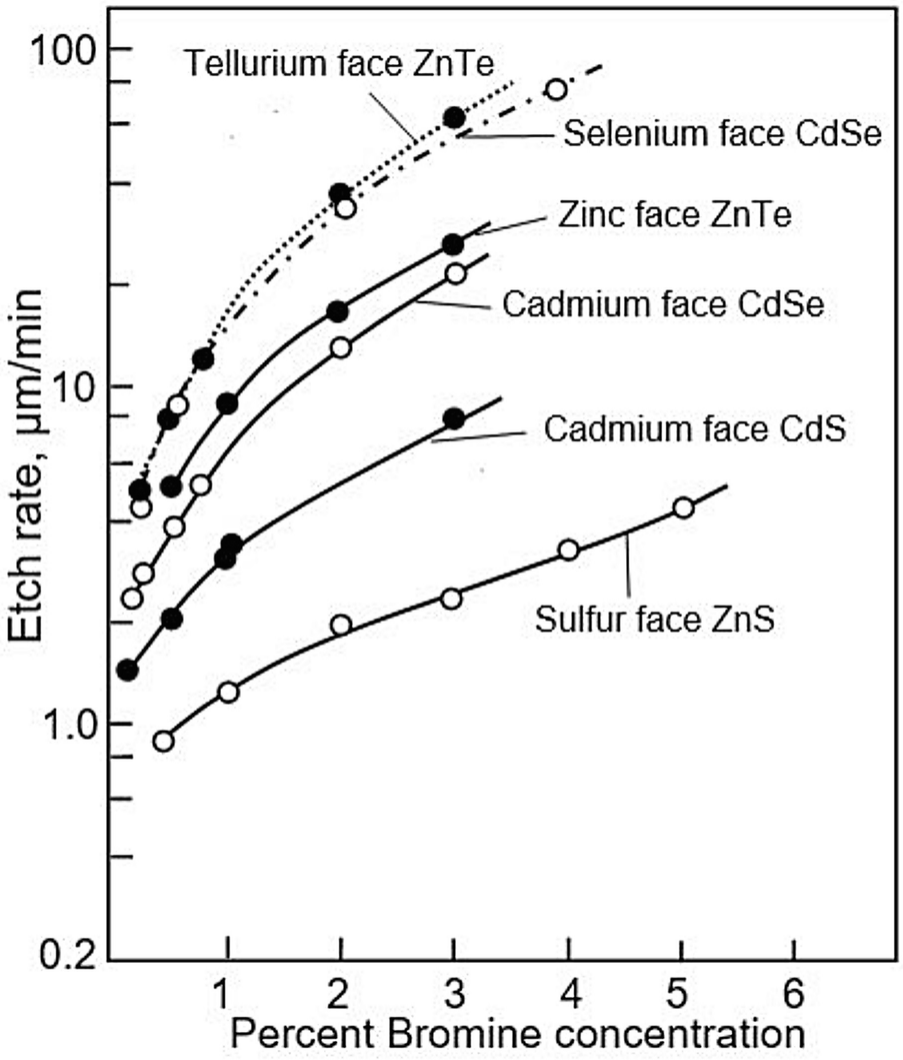

Fig. 2.8 Etch rate at room temperature for the anion faces of ZnO, ZnS, CdSe, ZnTe, and InSb and for the cation faces of CdS, CdSe, ZnTe, and InSb, versus bromine concentration in methanol. (Data extracted from Strehlow [107])

2.8 Material Technologies

2.8.1 Single Crystals

The technology for growing single crystals of II-VI semiconductor compounds is less developed than the technology for semiconductors of III-V group. Wide-gap II-VI semiconductors are technologically difficult objects, since they have high melting temperatures and high dissociation pressures at the melting point. The vapor pressures of the components above the melts of the compounds range from two to several tens of

atmospheres (Table 2.8); the melting point of most compounds exceeds 1200 °C [6].

Table 2.8 Melting points (T_m) and vapor pressures (P^0) over melts of II-VI compounds at these temperatures

II-VI	ZnS	ZnSe	ZnTe	CdS	CdSe	CdTe
T_m, K	1973–2038	1788–1799	1511–1578	1643–1748	1513–1537	1323–1371
P^o, MPA	0.19–0.37	0.053–0.18	0.064–0.19	0.15–0.38	0.027–0.055	0.023

The growth of single crystals of refractory compounds of II-VI group in most cases is carried out using the following approaches:

(a) Direct fusion of initial components (Zn, Cd, S, Se, Te) in an inert atmosphere of argon at a temperature 1000–1100 °C.

(b) Sublimation through the vapor phase of pre-synthesized powders of the appropriate composition, sealed in evacuated or argon-filled quartz ampoules, at a temperature of 1100–1200 °C. High vapor pressure determines their ability to easy sublimation.

(c) Zone recrystallization of a preliminarily synthesized compound.

The Bridgman method is also widely used for growing large single crystals. The methods used to grow single crystals of II-VI compounds are discussed in more detail in relation to CdTe in the chapter.

These methods are used to obtain single crystals of such semiconductor compounds as CdS, CdSe, CdTe, and ZnS, as well as solid solutions based on them with unlimited solubility in the CdS-CdSe and ZnS-CdS systems and with limited solubility in the CdS-CdTe system, etc.. CdTe and CdZnTe single crystals are widely used as substrates in the growth of HgCdTe epitaxial layers as well as in the manufacture of X-ray, gamma, and neutron radiation detectors.

2.8.2 Thin Films

Polycrystalline films of II-VI compounds are the main element on which the operation of thin-film photodetectors and sensors for various purposes depends. There are many ways to deposit films of II-VI compounds in order

to prepare layers with the required parameters: vacuum thermal deposition (PVD), high-frequency magnetron sputtering, electrochemical deposition, wet chemical deposition methods, spray pyrolysis, etc. [39, 88, 95, 104]. Each deposition method has its own advantages and disadvantages [65, 67, 68]. Let's take a look at the most common methods.

Wet chemical deposition is suitable for obtaining large-area thin films; the method is simple and relatively cheap. It is one of the most common methods for film deposition of II-VI compounds. In particular, this method is used as a way to obtain reproducible and homogeneous films at low temperatures. There are many variations of this method, such as the method of successive ionic layer adsorption and reaction (SILAR) and chemical bath deposition (CBD). They allow the formation of films of II-VI compounds with properties that vary over a wide range. The film properties are significantly affected by the synthesis temperature, the presence of impurities, the quality of the substrates used, etc. Polycrystalline sulfides and tellurides are most often obtained by precipitation from aqueous solutions of salts with sulfuric acid H_2S.

Vacuum thermal evaporation is a method in which the sublimation of the deposited material in vacuum and its subsequent condensation on the substrate take place. This is a well-established technique for preparing homogeneous films with a good degree of crystallinity. The physical properties of thin films obtained in this way depend on many factors such as film thickness, vapor pressure during evaporation, substrate temperature, and deposition rate. For example, CdS films are usually sputtered onto substrates heated to a temperature of 150–200 °C. The value of the substrate temperature and deposition rate is very important for obtaining certain electrical and structural properties of the film. For example, only a slight change in the substrate temperature can lead to a change in the resistivity of the CdS film from 0.1 Ω cm to 10^8 Ω cm. By increasing the substrate temperature and decreasing the deposition rate, films with high resistivity are obtained. When deposited on a heated substrate, the films have a columnar structure, when the crystallites forming the film have a predominant orientation perpendicular to the substrate. At the same time, when too low temperatures are used, the crystallinity of the formed films deteriorates.

Magnetron sputtering uses a sputtering technique in which a solid target of evaporating material is bombarded with gas ions generated by electric

and magnetic fields, causing the ejection of molecules and their subsequent deposition on the substrate. This method is well adapted to the deposition of II-VI compounds, since it is usually used in the formation of films of compounds that dissociate when heated in vacuum. Depending on the sputtering regimes, films of II-VI compounds obtained by magnetron sputtering at low temperatures usually have a dense amorphous or polycrystalline structure with a small crystallite size. Therefore, magnetron sputtering is usually accompanied by recrystallization annealing. In this case, the film composition is usually close to the stoichiometric composition.

Techniques such as chemical vapor deposition (CVD) [76], metal-organic chemical vapor deposition (MOCVD), molecular beam epitaxy (MBE) [76, 94], ion beam synthesis [22], electrochemical deposition [75, 76], and pulsed laser deposition [10, 76] can also be used to form films of II-VI compounds. However, the use of these methods requires large amounts of energy, sophisticated equipment, and expensive precursors. The presence of toxic gaseous wastes from some methods can also make them difficult to use. However, many of these methods have such important advantages as the possibility of precise control of film growth and the possibility of obtaining pure material. A description of all these methods can be found in Chap. 10 (Vol. 1).

2.8.3 Nanocrystals and Polycrystals

In the manufacture of photodetectors, sensors, and radiation sensors, along with thin-film technology, the principles of thick-film technology are widely used, when powders of already synthesized II-VI compounds are used to form layers of these compounds. In this case, the synthesized nano- or polycrystals are deposited on the substrate surface by various methods, such as dip coating, screen printing, spin coating, spray coating, and inkjet printing (read the Chap. 11, Vol. 1).

Synthesis of the powders and nanocrystals of II-VI compounds can be carried out using a variety of approaches [115, 124]. The most common methods are sol-gel technology, hydrothermal and solvothermal synthesis, microwave-assistant synthesis, precipitation, spray pyrolysis, aerosol flow synthesis, and wet chemical synthesis. The use of water as a solvent can significantly reduce the cost of the process of obtaining materials and reduce the negative impact on the environment [13]. Therefore, zinc sulfide

usually is precipitated from an aqueous solution of $ZnSO_4$ by passing hydrogen sulfide H_2S through it. For the manufacturing of powders with a low content of oxides, the synthesis is carried out by reacting the corresponding metals of group II with hydrogen sulfide and selenide. A more detailed description of the use of the previously mentioned methods for the synthesis of nano- and polycrystals of II-VI compounds can be found in Chaps. 11, 12, and 13 (Vol. 1).

2.9 Electrophysical Properties

2.9.1 Undoped Materials

Data on the electrophysical properties of II-VI compounds are given in Table 2.9. As can be seen from Table 2.9, the electrical properties of II-VI compounds vary over a very wide range. In particular, the electron mobility can vary from 70 $cm^2/V\ s$ in ZnS to 1200 $cm^2/V\ s$ in CdTe, increasing with decreasing band gap (Fig. 2.9a) and effective electron mass (Fig. 2.9b).

Table 2.9 Basic electrophysical properties of II-VI compounds (T = 300 K)

II-VI	Type of electro-conductivity	Electrical resistivity, ρ, Ohm· m	Charge carrier mobility, $cm^2/(V\ s)$ (300 K)		Effective mass of charge carriers	
			Electrons	Holes	Electrons	Holes
ZnS	*n*	10^6–10^{12}	70–140	5–72	0.20–0.4 m_0	0.5–1 m_0
ZnSe	*n*, *p*	10^2–10^{12}	260–700	15–250	0.1–0.15 m_0	0.6 m_0
ZnTe	*p*	10^2–10^4	530–1000	30–300	0.1–0.2 m_0	0.1–0.3 m_0
CdS	*n*	0.1–10^7	120–600	15–48	0.15–0.3 m_0	0.5–0.7 m_0
CdSe	*n*	1–10^{10}	580–900	50–75	0.13 m_0	0.45 m_0
CdTe	*n*, *p*	0.1–10^5	900–1200	60–600	0.09–0.14 m_0	0.35 m_0

m_0 free electron mass

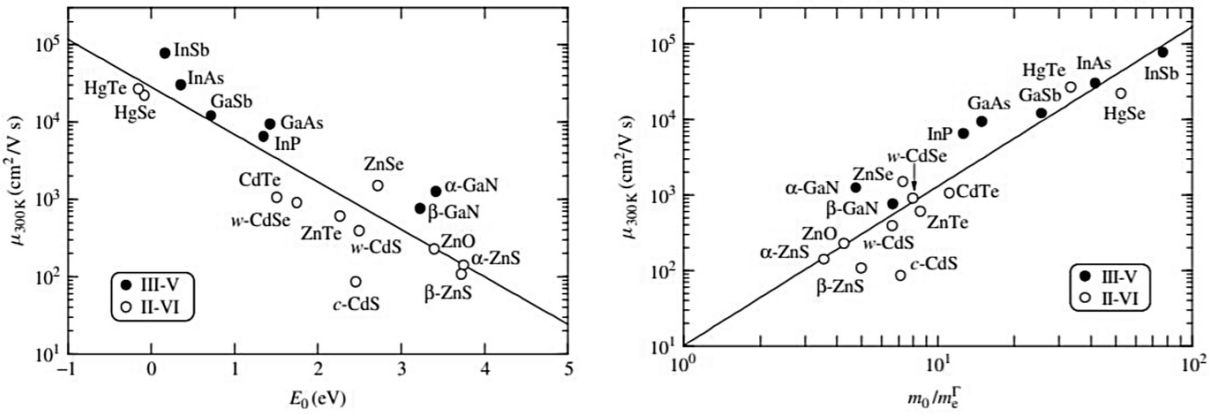

Fig. 2.9 (**a**) Electron Hall mobility at 300 K, μ_{300} K, versus E_0 for some III-V and II-VI semiconductors. (**b**) Electron Hall mobility at 300 K, versus inverse-valley electron conductivity mass m_0/m_e for some III-V and II-VI semiconductors. (Reprinted with permission from Adachi [2]. Copyright 2005: Wiley)

ZnS single crystals grown by the sublimation method in an atmosphere of hydrogen sulfide have a resistivity of ~10^6–10^8 Ohm m. It is also possible to obtain crystals with ρ up to 10^{12} Ohm·m. Undoped ZnS single crystals typically have an electron density of $6{\cdot}10^{16}$ cm^{-3} with a mobility of about 70–140 cm^2/V·s. At the same time, the concentration of free charge carriers in CdTe can vary within 10^{14}–10^{19} cm^{-3}. The purest CdTe has a high electron mobility, which at room temperature can reach 1200 cm^2/V·s. In undoped CdS, the electron mobility at room temperature is in the order of 240–400 cm^2/V·c.

Such a strong change in the electrical conductivity of II-VI semiconductors is due to violations of the stoichiometric composition of the compound. Since II-VI semiconductors are characterized by a significant proportion of ionic bonding, nonstoichiometric defects behave like electrically active centers, in particular, vacancies in the metalloid sublattice play the role of donors, and vacancies in the metal sublattice behave like acceptors. Then, proceeding from general principles, it should follow that, depending on the ratio of components, II-VI compounds should have electronic or hole conductivity: an excess of metal A^{II} should lead to the appearance of electronic electrical conductivity, and an excess of chalcogen B^{VI} to the appearance of hole electrical conductivity.

However, in fact, an important feature of semiconductors of II-VI groups is that many of them, regardless of the conditions of preparation and the nature of the doping of crystals, have only one type of electrical

conductivity. So, sulfides and selenides of zinc and cadmium are always n-type semiconductors. In contrast to them, zinc telluride has only hole electrical conductivity. And only CdTe can have both n- and p-type electrical conductivity, depending on the manufacturing conditions. Measurements of thermal emf and the Hall constant on crystals heated to 900 °C followed by quenching at various cadmium vapor pressures showed that CdTe has n-type conductivity at $P_{Cd} > 7 \cdot 10^4$ Pa. If the cadmium vapor pressure is less than this value, then cadmium telluride crystals have hole conductivity [6]. Thus, depending on the cadmium vapor pressure and temperature, CdTe can have both n- and p-type conductivity. Electronic conductivity is provided by cadmium atoms embedded in the lattice interstices and hole conductivity – by cadmium vacancies [17]. This difference in the behavior of CdTe is directly related to the peculiarity of the chemical bond in it, which, in contrast to Cd and Zn sulfides, is close to covalent. This is confirmed by the high mobility of electrons and the temperature dependence of the mobility of charge carriers. In addition, in CdTe, the thermal and optical band gaps almost coincide. For CdSe, a change in the type of conductivity was also observed after annealing of the n-type material in selenium vapor at 400 °C for 4–10 h. However, a change in the type of conductivity was observed only in the surface region of the crystal.

Thus, when obtaining crystals of II-VI compounds, it is necessary not only to monitor the chemical purity of the components used but also to control the degree of defectiveness of the crystal lattice, i.e., the concentration of vacancies. It was found that the self-compensation of sulfides, selenides, and tellurides by their own structural defects is the main reason that prevents the type of electrical conductivity from being reversed during their doping. There are currently two explanations for n-type conductivity in cadmium sulfide based on different types of defects. In one case, the dominant electroactive defects in cadmium sulfide are cadmium atoms embedded in interstices, which provide n-type conductivity, and cadmium vacancies responsible for p-type. The existence of such defects was found under conditions of high temperature and fixed during fast cooling. For such defects, cadmium in the interstices is a double donor, while cadmium vacancies are a double acceptor. In the second case, the n-type conductivity in cadmium sulfide at high temperatures is due to intrinsic donors, the role of which is played by sulfur vacancies. The latter

explanation finds wider application in explaining the properties of CdS. It is believed that, as in CdS, the intrinsic donor centers in CdSe are anion-forming vacancies. In other words, the electronic conductivity of CdS and CdSe is due to the lack of sulfur and selenium relative to the stoichiometric composition, i.e., the intrinsic donor centers in CdS and CdSe are sulfur and selenium vacancies. As for cadmium telluride, the main structural defects in CdTe are cadmium atoms embedded in lattice sites that have lost one electron, and cadmium vacancies with a unit effective negative charge [11, 73]. It should be added to this that acceptors have low solubility in II-VI semiconductors and, as a rule, form deep levels.

The importance of vacancies in II-VI compounds is well illustrated in Fig. 2.10, where the relative sizes of atoms (and hence the relative sizes of respective vacancies) for II-VI compounds are shown, together with experimentally observed tendency toward n- or p-type conductivity. Although relative size is only just one of the factors, it is indicative that in each case, larger metal atom (vacancy) corresponds to an inclination toward n-doping and spells difficulties for p-type doping, while compounds having larger halcogenide atoms (vacancies) show just the opposite tendency. Only CdTe, which has almost equally sized atoms, can be doped both types.

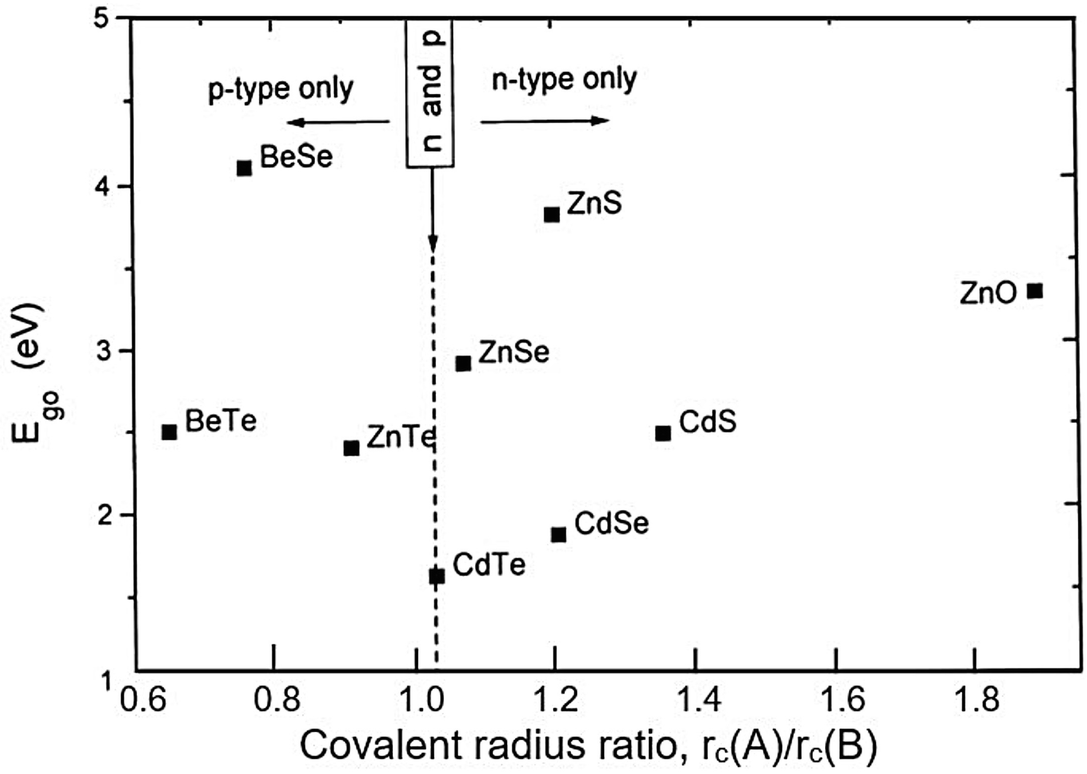

Fig. 2.10 Experimentally observed trends toward n- or p-type conductivity for II-VI compounds. (Reprinted with permission from Desnica [23]. Copyright 1998: Elsevier)

Another characteristic feature of II-VI compounds is the possibility of changing the conductivity over a very wide range (by several orders of magnitude) by heat treatment in vapors of one of its own components. For example, the specific conductivity of cadmium sulfide while maintaining the n-type conductivity under the influence of heat treatment in sulfur vapor can change by ten orders of magnitude. Annealing in an inert, reducing, or oxidizing atmosphere also gives a significant change in material properties. For example, Fig. 2.11 shows the effect of annealing at T = 250 and 400 °C on the Raman spectrum and electrical conductivity of CdS films [80]. It can be seen that if the changes are insignificant up to 250 °C, then annealing already at T = 400 °C is accompanied by both a significant change in the electrical conductivity and the structure of the films.

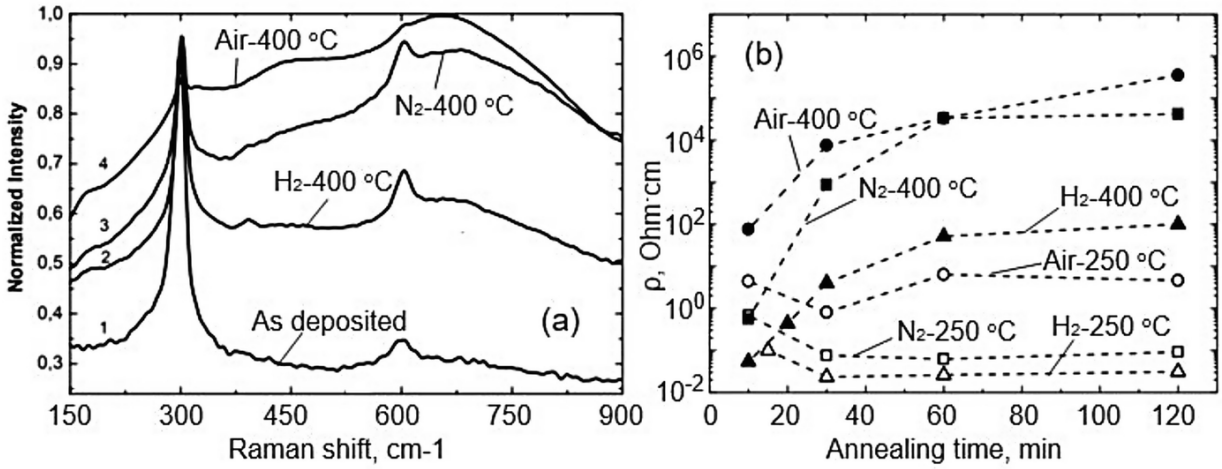

Fig. 2.11 (**a**) Raman spectra of CdS films annealed for 1 h in different ambient at 400 °C; (**b**) Electrical resistivity of CdS films at RT as a function of annealing time, temperature, and atmosphere. (Reprinted with permission from Maticiuc et al. [80]. Copyright 2014: Elsevier)

The experiment showed that the heat treatment of II-VI compounds predominantly gives rise to those defects whose formation energy is lower. In sulfides and selenides, vacancies in the anionic sublattice are the dominant type of defects. Vacancies in anionic sites are formed with a lack of sulfur and selenium. For example, sulfur can leave the crystal only in the form of neutral S^0 atoms, leaving excess electrons on vacancies. Each vacancy creates an energy level near the conduction band filled with electrons at low temperature. A small impact is enough to detach electrons from a structural defect, i.e., to transfer them to the conduction band. In

ZnTe crystals, vacancies are predominantly formed in the sublattice of the cation former. Zinc ions, leaving the crystal, take the missing electrons from the nearest tellurium ions, due to which hole electrical conductivity appears.

As for the possibility of changing the type of conductivity due to doping, such a possibility exists (read the following section). For example, when ZnS is doped with selenium, hole conductivity is observed, and after treatment in molten zinc, electronic conductivity is observed.

2.9.2 Doping of II-VI Compounds

The behavior of impurities in II-VI-type compounds basically obeys the same laws as in III-V-type semiconductors, i.e., substitutional impurities having a valency lower than the valency of the displaced atoms play the role of acceptors, and impurities with a higher valence are donors. The state of atomic impurities is more stable if their entry into the lattice is not accompanied by the formation of large local charges. For example, impurity atoms of group I elements (Cu, Ag, Au), replacing Zn or Cd in the crystal lattice of a semiconductor, exhibit acceptor properties. At the same time, as a rule, they form deep energy levels. Copper doping is commonly used in the development of phosphors based on ZnS and CdS. Copper-activated ZnS-based electroluminophores emit in the green and blue regions of the spectrum. To increase the solubility of the copper acceptor impurity, an equivalent amount of donors (halogens) is introduced into the phosphor composition, which acts as luminescence coactivators. Effective phosphors with radiation in the yellow region of the spectrum are obtained by activating zinc sulfide with manganese. ZnS doped with Ag has a luminescence in the blue region of the spectrum. The concentration of these impurities during doping does not exceed 3%. Group III element atoms (Al, Ga, In), which also replace cations, behave as donors with low ionization energies. Accordingly, acceptor and donor properties are exhibited by elements of groups V and VII of the periodic table, replacing chalcogen atoms in the II-VI semiconductor lattice [46]. Presently, identified levels of potential dopants in II-VI compounds are shown in Table 2.10, presenting ionization energies for donors, and Table 2.11, presenting ionization energies for acceptors.

Table 2.10 Ionization energies E_D (in meV) of various foreign donors in different Zn- and Cd-chalcogenides

Doping element	ZnS	ZnSe	ZnTe	CdS	CdSe	CdTe
B	–	25.6–26.0	–			
Al	74–100	25.6–26.3	18–18.5			14.05
Ga	400	27.0–27.9		33.1		13.9
In	400–600	28.1–28.9		31.3–33.8	19.5	14.1–14.5
F	13.7	28.2–29.3		35.1		
Cl	–	26.1–26.9	20.1	32.7		14.0–14.5
Br	–	26.8		32.5		
I	600	23.9–30.4		32.1		
Li_i	–	17–30.4		28		13.9
Na_i	–	20				
N_i	–	26–29.1				

Source: Data extracted from Desnica [24]

Table 2.11 Ionization energies E_A (in meV) of various foreign acceptors in different Zn and Cd-chalcogenides

Doping element	ZnS	ZnSe	ZnTe	CdS	CdSe	CdTe
Li_M	150	111–114	60.5–61	165	109	57.8–58
Na_M	190	126–128	62.8	196		58.7–58.8
Cu_M	1250	650	140–149	860–1100		140–147
Ag_M	113–720	113–430	121–123	260		92–123
Au_M		~550	277			263
N_X		100–111			21–31	56
O	110	80		116		46
P_X		85–85.6 550–700	63.5	120 600	83	50–68.2
As_X		110–113	78.5–79	750		92

Source: Data extracted from Desnica [24]

Impurities can also play a significant role in the mechanism of intrinsic photoconductivity of II-VI semiconductors, since the lifetime of nonequilibrium charge carriers depends on their nature and concentration,

and this, in turn, determines the photosensitivity and photoresponse rate. For example, the addition of excess zinc to ZnS makes it possible to obtain a very short afterglow time. In this case, it is not so much the donor or acceptor nature of impurity atoms that is important but rather their belonging to recombination centers or capture traps. By introducing special impurities, the so-called sensitization centers, it is possible to increase significantly the sensitivity of intrinsic photoresistors. In cadmium sulfide, the sensing centers are compensated acceptors, which can be cadmium vacancies. The concentration of the latter increases upon doping with donors. Accordingly, the intrinsic photoconductivity also increases. Samples of copper-doped cadmium sulfide also exhibit high photosensitivity. In the case of heavy doping with copper, the impurity photoconductivity begins to play a dominant role, which is reflected in a shift in the spectral characteristic. Zinc selenide is similar in properties to zinc sulfide in many ways, but its properties are easier to control.

It should be noted that the doping of II-VI compounds is not a simple process. Difficulties in achieving efficient doping of wide band gap II-VI compounds both p- and/or n-type are the main obstacle in their applications. For example, as noted earlier, not all II-VI compounds obtained can be p- and p-type. Zinc selenide can be produced with both types of conductivity, but n-ZnSe can be grown with difficulty [110]. It is believed that the doping limiting mechanism in II-VI semiconductors is primarily self-compensation by native defects or native defect-dopant pairs [23]. The results of the calculation carried out by Desnica [23] are shown in Fig. 2.12a. Desnica [23] calculated the minimal degree of self-compensation by ionized native vacancies for practically all II-VI compounds. The vacancy formation energies and enthalpies were calculated using Phillips-Van Vechten's two-band theory [117], and the chemical potentials were calculated from the dissociation pressures of the compounds and partial pressures of the constituents. Their thermodynamical calculations showed a considerable tendency toward self-compensation of acceptors in most II-VI compounds (CdS, CdSe, ZnSe, and CdSe), and donors in ZnTe, and no compensation in other cases. The results of vacancy self-compensation calculations, although obtained with an approximate theory of vacancy formation, exactly follow the trends observed experimentally for all these compounds, but in most cases, the calculated vacancy self-compensation is insufficient to explain the extent of observed doping problems. The same Fig. 2.12b shows a

summary of doping results of II-VI compounds and ternary II-VI alloys [24]. Figure 2.12b refers to free carrier concentrations obtained by doping with donors, n_{max}, and acceptors, p_{max}. Most successful doping obtained both under quasi-equilibrium conditions and under nonequilibrium conditions are presented. Cases of traditionally "difficult" doping, where p- or n-doping was practically impossible to obtain under quasi-equilibrium conditions, were included as well (full squares). The results are presented as a function of ratio R of atomic covalent radii of M and X constituents of each compound, just as in Fig. 2.12a.

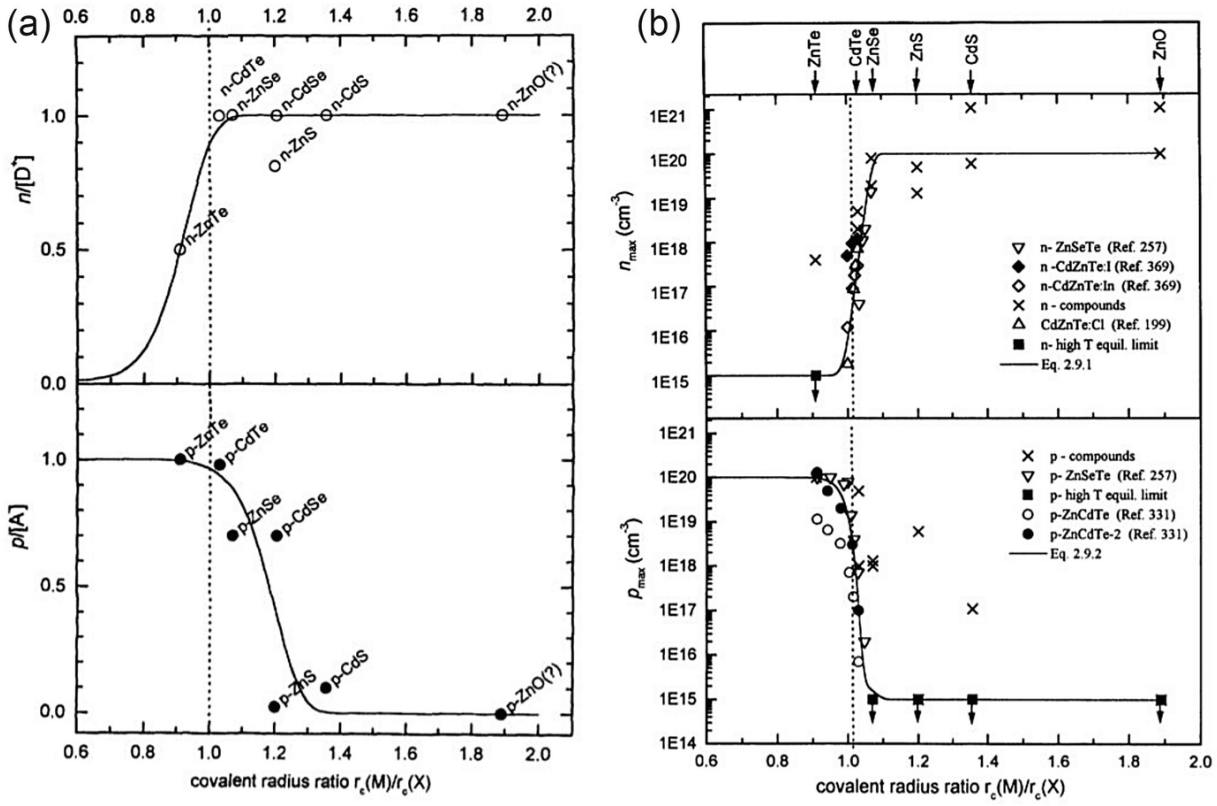

Fig. 2.12 (**a**) Maximum doping efficiency with donors, n/[D^+], and acceptors, p/[A], limited by self-compensation with native vacancy, calculated for conditions of thermodynamic equilibrium. The results are presented in dependence of relative atom (vacancy) size of each compound. (**b**) Maximum experimental free carrier concentrations achieved for doping with donors, n_{max}, and acceptors, p_{max}, in II-VI compounds and alloys obtained for growth/doping in the equilibrium and nonequilibrium conditions. The high T equilibrium limits (full squares with downward-pointed arrows) are also included in the Figure as 10^{15} cm^{-3} values of n- and p-type semiconductors. (Reprinted with permission from Desnica [24]. Copyright 1998: Elsevier)

One should note that the relative size of atoms plays a big role in doping processes, as predicted by Van Vechten [117] a long time ago, irrespective

of the particular mechanism that limits dopability. The importance of the sizes of M and X atom lies in the fact that their size determines the sizes of their respective vacancies [35]. Since the formation energy of a vacancy is proportional to its size [117], the ratio of M to X atom radii, actually, determines the ratio of the formation energies for vacancies at M and X sites. It means that, the larger the ratio $R = r_c(M)/r_c(X)$, the larger is the ratio of concentrations of the donor-like native vacancies V_X to the acceptor-like native vacancies V_M, $[V_x]/[V_M]$. Experimental results presented in Fig. 2.10b clearly demonstrate the importance of ratio R on dupability [24]. Above discussion shows that the ratio $[V_x]/[V_M]$ is the factor that predominantly influences the success of dopability in II-VI binary or ternary compounds.

Besides self-compensation by spontaneously generated native defects having opposite charge than dopants, particularly by making compensating pairs with dopants (A centers), Desnica [24] identifies several other mechanisms that create difficulties in doping II-VI compounds. These include:

- Auto-compensation by some dopants, in particular light dopants like Li, Na, N, etc..
- Deactivation of dopants due to lattice relaxation; strong lattice relaxation around some doping atoms leads to the breaking of bonds with host atoms and the formation of deep levels.
- Problems with insufficient solubility of dopants, leading to inadequately high concentrations of many additives and the formation of a second phase.
- Lack of appropriate shallow acceptors and donor; the insufficiently shallow level of some dopants makes them only partly ionized at RT.
- The relative size of atoms in II-VI compounds, which translates in preference to form relatively more vacancies in M or X sub-lattice.
- Insufficient rigidity of the lattice in II-VI's (as compared to III-V's), which results in higher self-diffusion of host atoms, dopants, and native defects, and a lower formation energy for both point defects and dislocations make most of the identified doping-limiting mechanisms more effective.

Although there is no consensus yet about the relative importance of these doping limiting mechanisms, it has become clear that the question of

successful doping of the II-VI compounds is indeed a very difficult one, since almost all of the potentially “good” dopants have one or several serious drawbacks. As a result, there are no general rules for optimal doping of these compounds, and the solutions to the doping problem depend on the type of semiconductor and the technology available. The most promising ways to solve the doping problems in II-VI compounds are nonequilibrium processes. Nonequilibrium processes like ion implantation and particularly low-temperature crystal growth, such as molecular beam epitaxy (MBE) and vapor phase epitaxy (VPE), are the best practical hope to transcend doping limits and to obtain material suitable for various applications [23, 24]. The advantages of a lower growth temperature are firstly in reducing the possibility of the thermodynamic restrains and surpassing their limitations and secondly in a lower concentration of compensating defects. Regarding ion implantation, one can say that dopant incorporation by ion implantation offers two major advantages over conventional doping methods. Since ion implantation is a nonequilibrium process, the amount of the introduced dopant depends only on the time-integrated current of the implanted ion beam. Furthermore, since the doping and subsequent annealing can be performed at relatively low temperatures (≤500 °C), the formation of compensating defect centers can be minimized. A positive example of indicated approach is a very high concentration of holes, up to p – 5×10^{19} см$^{-3}$ (the maximum value achieved up to now by any method), obtained in CdTe by implantation of P and pulsed electron beam annealing [44]. In [78], it was also reported that In can be incorporated in CdS up to very high concentrations into undisturbed In_{Cd} place by implantation and proper annealing procedure, without formation of compensating pairs predicted for thermodynamical equilibrium conditions. They obtained ~100% implanted In atoms in substitutional Cd place, In_{Cd}, in CdS for a very wide In dose range (10^{16} cm^{-3}–10^{19} cm^{-3}) after appropriate annealing under Cd pressure.

Co-doping with different sized atoms or co-doping into both lattice sites can also increase dupability. Such doping should reduce internal strains around doping atoms [24].

2.10 Surface Properties

The works [55, 57–59, 64] analyzed the results of a comprehensive study of the surface of II-VI compounds and the effect of impurities and the oxide phase on adsorption and surface charging processes. In particular, it was found that the surface of II-VI semiconductors is not shielded by oxide phases present on the surface of II-VI compounds. Ebina et al. [27, 28] studied the interaction of oxygen with the II-VI compound surfaces using low-energy electron-loss spectroscopy and 21 eV photoemission spectroscopy. They found that the oxygen uptake is very slow with exposures to molecular oxygen (the initial sticking coefficient of the oxygen on the vacuum cleaved surface is about 10^{-13}), and to accelerate this process, additional excitation is needed. Ebina et al. [27, 28] used for these purposes electron-beam irradiation technique. As a result of studying the surface properties of ZnSe, ZnTe, CdSe, and CdTe, they concluded that when oxidizing the II-VI compounds at room temperatures by means of an electron-beam technique, the following processes take place [25, 27, 28]:

- During the oxidation of CdTe, oxygen apparently adsorbs on the surface of Te atoms, breaking the back bonds already at the initial stage of oxidation, which leads to the formation of TeO_2. This result is very reasonable because TeO_2 is more stable than CdO. In addition, according to the thermodynamical data [81], the vapor pressure of TeO_2 is very low (less than 10^{-28} Pa) at room temperature.
- In case of ZnTe, TeO_2 dominates on the surface only at low oxygen coverage of the surface ($\theta \leq 0.5$ ML), while at high oxygen coverage ($\theta > 1$ ML), ZnO appears on the surface. According to generally accepted concepts, one monolayer of an oxygen coating corresponds to the condition – one oxygen atom for each of the atoms of the compound surface. According to Ebina et al. [26–28], the changes that occur in the process of oxygen adsorption are related to the fact that at low coverages, oxygen is adsorbed mainly on the surface Te atoms, and with further adsorption, oxygen is absorbed on the Zn atoms, in addition to the surface Te atoms. As a result, an overlayer on ZnTe under these conditions consists of TeO_2 and ZnO. With further oxidation, ZnO becomes the dominant phase in overlayer of ZnTe. This development of events differs significantly from what was observed on the CdTe surface. The absence of TeO_2 dominance in the overlayer was explained by the

fact that ZnO is more stable than TeO_2, and due to the reaction (Eq. 2.10), TeO_2 is reduced by Zn to a lower oxide, which sublimates from the surface, leaving ZnO on the surface [26].

$$TeO_2 + Zn \rightarrow TeO \uparrow + ZnO \tag{2.10}$$

- In the case of Se-based compounds, at the initial stages of oxidation ($\theta < 0.5$ ML), oxygen is adsorbed on the surface Se atoms without breaking the back bonds. At $\theta > 0.5$ ML, the back bonds are broken, which leads to the formation of a bulk-like cation oxide (CdO or ZnO) and, possibly, anion oxide, SeO_2. Due to its vapor pressure (~2 10^{-6} Torr), SeO_2 can sublimate from the surface of Se-based compounds, leaving a top layer rich in ZnO for ZnSe and rich in CdO for CdSe. It is important to note that due to the predominant interaction of oxygen with Se atoms, and the subsequent sublimation of SeO_2, the surface is enriched in metal atoms, Cd or Zn [26].
- Thus, for heavy oxidation, the following oxides were found: TeO_2 on CdTe, CdO on CdSe, ZnO on ZnSe, and ZnO + TeO_2 on ZnTe. For each II-VI compound, the single oxides listed above had the largest heat of formations.

Thus, the conducted studies show that on the surface of II-VI compounds, in contact with air, the presence of natural oxides is possible, the thickness of which will depend on the state of the surrounding atmosphere and the treatments to which these compounds have been subjected. In particular, it has been found that illumination, especially UV irradiation, stimulates the oxidation of II-VI semiconductors at room temperatures [43]. Moreover, this effect is most pronounced for small QDs, in which the region subjected to oxidation becomes commensurate with the diameter of these QDs. For example, according to Hu and Wu [43], a photo-corrosion effect reduced the CdSe QD size and caused blue shift of the band edge (BE) peak. At that, they observed that under the same UV irradiation, the PL spectrum of small QDs vary faster than that of large QDs. The shape and position of the PL spectrum for the large QDs under UV irradiation were relatively stable. Taking into account the different reactivity of different crystallographic planes of II-VI semiconductors, it was assumed that the effect of photooxidation tends to predominantly happen on the Se-

rich surface of QDs. The same effect was observed by Wang et al. [120]. These results are shown in Fig. 2.13. CdSe QDs samples ~4.5 nm in diameter were illuminated with laser radiation at a wavelength of 420 nm. It is important to note that irradiation of the 420 nm laser pulses had no obvious effect on the CdSe QDs when the sample was placed in vacuum. However, if the film sample was in ambient air, photoirradiation caused a blue shift in PL peak position and a significant change in PL intensity.

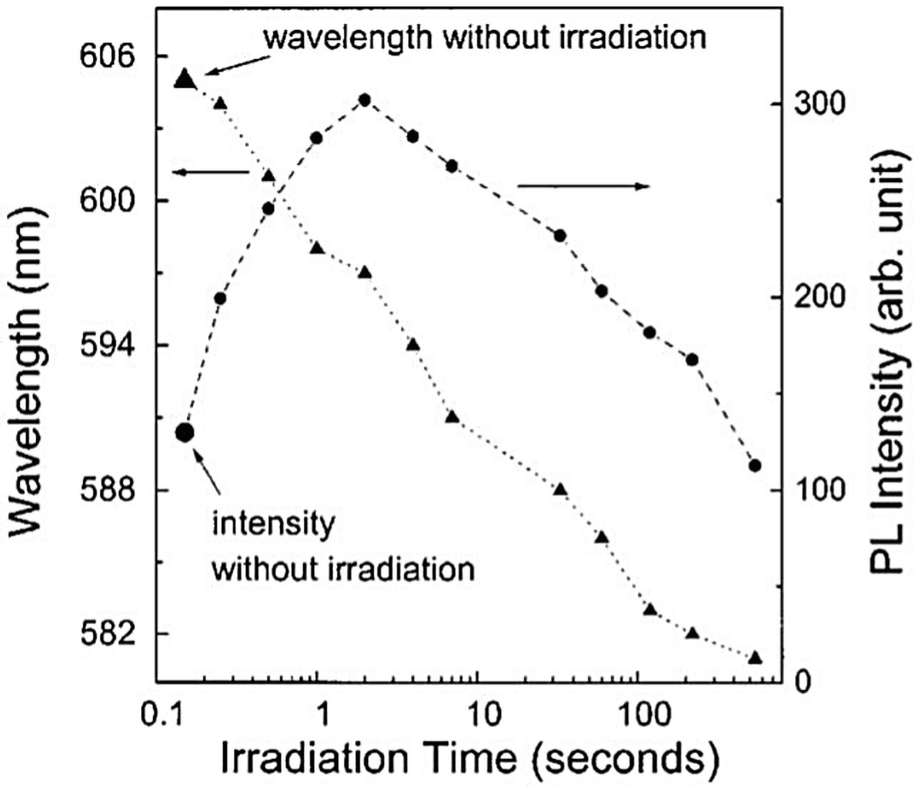

Fig. 2.13 Intensity and peak wavelength position of the PL spectra vs the photoirradiation time for the CdSe QDs. (Reprinted with permission from Wang et al. [120]. Copyright 2003: AIP Publishing)

It is usually assumed that photochemical modifications of nanocrystals, such as their photooxidation, are triggered by absorption of a photon in the QDs itself [120]. In particular, Wang et al. [120] believe that the electrons produced during photoirradiation contribute to the oxidation of CdSe QDs. However, Manner et al. [79], using the example of CdSe QDs, demonstrated that contrary to the generally accepted picture, the oxidation of nanocrystals can be initiated by photoexcitation of solvent-oxygen ion pairs that relax with the formation of singlet oxygen, which then reacts with nanocrystals. This agrees with the results of experiments previously carried out by Ebina et al. [27] and indicating the need for excitation of oxygen.

These data indicate that the properties of the environment have a significant impact on the stability of colloidal nanocrystals, and to improve their resistance to photooxidation, it may be necessary to control the properties of the surrounding atmosphere and solvent. No doubts, encapsulation of II-VI semiconductor QDs can prevent oxidation of QDs. However, this will exclude the possibility of using II-VI compounds in the development of gas sensors, photocatalysts, and biosensors.

However, in most early studies using single crystals and polycrystalline films of II-VI compounds, this factor, i.e., the presence of natural oxides, was not taken into account when analyzing the measured data. Therefore, based on the results obtained, it was concluded that the state of the unoxidized surface of II-VI semiconductors determines the characteristics of adsorption-catalytic processes. According to this model, the active centers involved in these processes are predominantly coordinatively unsaturated surface atoms and structural vacancy defects in II-VI compounds [37].

As shown by mass spectrometric studies, the main components of the desorbed phase from the surface of ZnSe, ZnTe, CdSe, and CdTe samples are H_2O, CO_2, CO, and O_2 [12]. In addition, hydrogen and reaction products are also found in small amounts. As the time of exposure to air increases, water, carbon dioxide, and oxygen accumulate predominantly on the surface of II-VI compounds. At the same time, at the early stages of adsorption, water takes the greatest part in the formation of surface properties. It also plays a decisive role in surface charging. The chemisorption of water molecule on the surface of CdS was established by Gupta and van Huis [34]. Figure 2.14 shows how the surface of II-VI semiconductors behaves when interacting with water. As can be seen from Fig. 2.14, water dissociates to form proton and hydroxide, the concentration of which depends on the surface stoichiometry; proton and hydroxide are balanced or one of them is dominating at the surfaces [119]. At that there are possibly three ways for water molecules to bind with II-VI semiconductor surfaces: (a) via formation of Zn(Cd)-O bonds; (b) via formation of S(Se, Te)-H bonds; and (c) via formation of both Zn(Cd)-O and S(Se, Te)-H bonds. And this means that the surface stoichiometry strongly affects the surface properties of II-VI semiconductors; either a zinc-rich (cadmium) or a sulfur-rich (selenium, tellurium) surface will have different acid-base properties, i.e., different surface acidity constants.

Jasieniak and Mulvaney [48] showed that a change in the stoichiometry of II-VI semiconductors is accompanied by a significant change in the luminescent properties. It was also determined that particles with different surface stoichiometries have quite different passivation requirements.

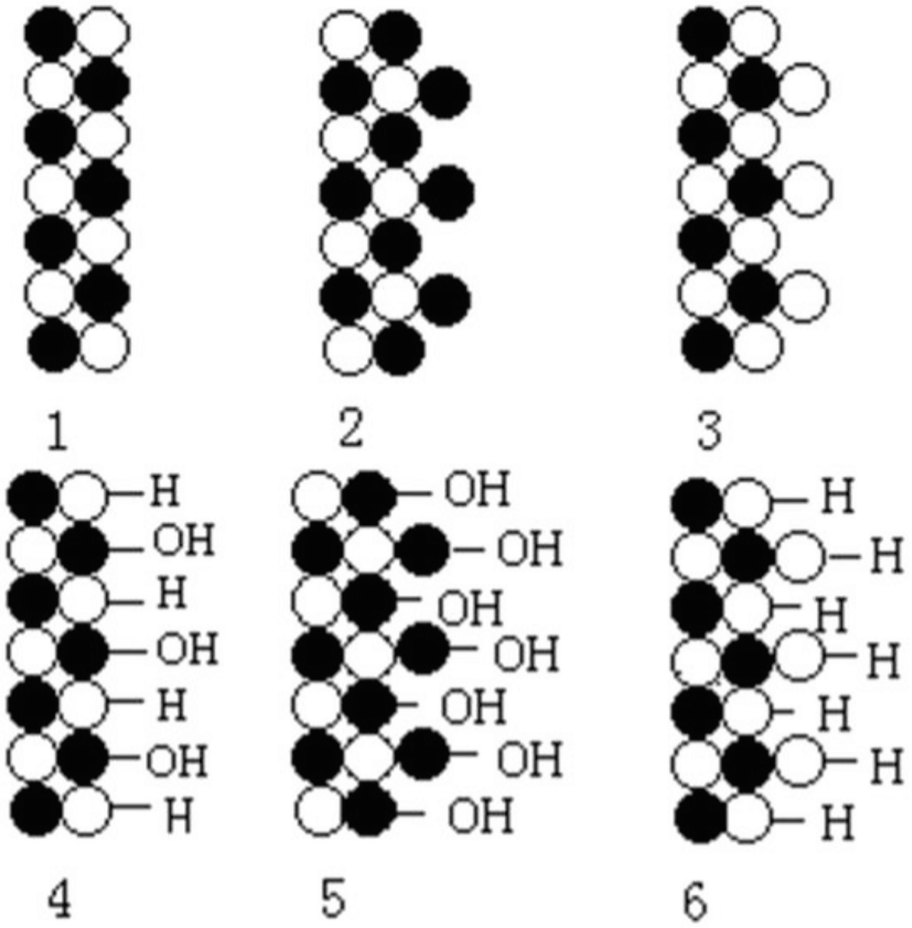

Fig. 2.14 Schematic illustration of the surface stoichiometry and hydration of II-VI semiconductor: (1) Non-hydrated stoichiometric II-VI surface; (2) non-hydrated zinc (cadmium) rich II-VI surface; (3) non-hydrated sulfur (selenium, tellurium) rich II-VI surface; (4) hydrated stoichiometric II-VI surface; (5) hydrated zinc (Cd) rich II-VI surface; (6) hydrated sulfur (Se, Te) rich II-VI surface. (Reprinted from Wang et al. [119]. Published 2011 by BMC as open access)

Ebina et al. [26] established another feature of II-VI compounds; the natural stoichiometry of the surface of these compounds depends on the ionicity of the bonds. They concluded that the polar surface of II-VI compounds, which have rather ionic bonds, is apparently non-stoichiometric, while the II-VI compound with rather covalent bonds has a polar surface of stoichiometric composition. Nosker et al. [83] made the same conclusion. Based on their calculations of electrostatic (Madelung

potential) surface energies, they also assumed that the polar surface has a stable structure with a nonstoichiometric composition.

It is important to note that at low temperatures, the adsorption of gases is usually not accompanied by chemical reactions that affect the semiconductor structure. In particular, Campbell and Farnsworth [16] found that adsorption of CO_2, H_2O, H_2, and CH_4 was not accompanied by changes in diffraction patterns of clean CdS surface. Although at the nanoscale, the influence of water is enhanced. So, Goodell et al. [32] observed structural transformation of zinc sulfide nanoparticles of 3 nm in diameter, caused by water adsorption. Zhang et al. [125] also found that the highly reduced particle size affects water adsorption. They found that firstly, ZnS (3 nm) nanoparticles can adsorb more water molecules per unit surface area, and secondly, the binding energy of water in nanoparticles is higher than in bulk crystals. Zhang et al. [125] believe that this conclusion can be extended to other nanoparticles interacting with other molecules, such as environmental species.

As the temperature rises, the concentration of adsorbed molecules naturally decreases. With an increase in temperature, a change in desorption activity is observed with maxima at 100–200 °C (for weakly bound oxygen and molecular water) and 300 °C (for chemisorbed water). Bootsma [12] studied the adsorption of oxygen and H_XA gases (H_2S, HBr, NH_3, PH_3) on the surface of CdS and found that the quantities adsorbed at a given pressure are for all the gases negligible at 400 °C. Hence it follows that the removal of these impurities during thermal vacuum treatment should include at least two stages: (1) heating the samples to 180–200 °C and keeping them at this temperature for several hours to more completely remove oxygen and molecular water weakly bound to the surface and (2) further heating to remove chemisorbed water. As a result of this treatment, a certain amount of chemisorbed oxygen remains on the surface. According to Campbell and Farnsworth [16], the chemisorbed oxygen could not be removed at room temperature. It was established that the rate of oxygen desorption of the CdS surface in vacuum depended exponentially on the reciprocal of the absolute temperature, so that the removal of the oxygen monolayer required 4 h at 350 °C or 5 min at 550 °C. In an argon atmosphere, chemisorbed oxygen was almost completely removed as a result of thermal treatment of single-crystal samples at T ~ 700 °C.

The results of mass-spectrometric studies presented earlier are confirmed and supplemented by the IR spectra of II-VI semiconductor films [37, 63]. In air, they contain bands of stretching (3570–3450 cm^{-1}) and bending (1650–1620 cm^{-1}) vibrations of adsorbed water, a small number of absorption bands in the regions of 2960–2860 cm^{-1} and 1460–1380 cm^{-1}, corresponding to the vibrations of the C–H, C–O groups, and the absorption bands around 1150 and 1205 cm^{-1}, for which hydrated metal oxides may be responsible. According to the IR spectra, thermal treatment of the samples at T = 420–473 K in a helium flow leads to a decrease in the intensity of all absorption bands and predominantly adsorbed water. At 250–400 °C, adsorbed impurities are almost completely removed. Figure 2.15 shows a typical spectrum of the purified zinc sulfide. The specific features observed are those of hydroxyl groups (3691 cm^{-1}), water (3410, 1640 cm^{-1}; some of which remains sorbed after evacuation at 400 °C), and sulfate groups (1086, 1132, 1191 cm^{-1}). On a pure ZnS surface, one would not expect to see ZnOH groups. This material is partially oxidized on the surface as shown by the presence of sulfate groups.

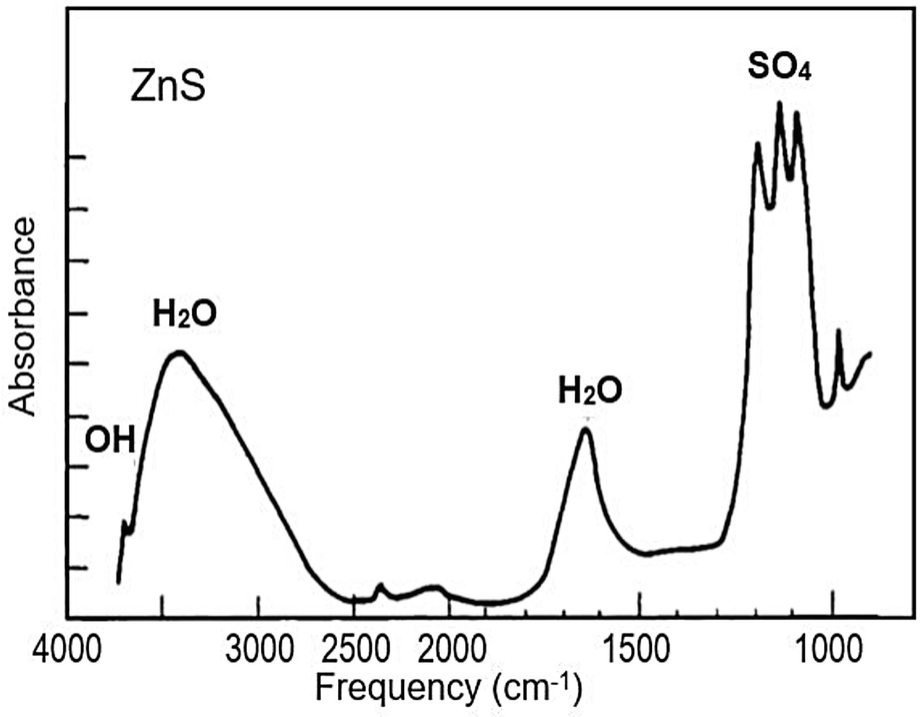

Fig. 2.15 FTIR spectrum of ZnS powders. (Adapted with permission from Herl [37]. Copyright 1988: Elsevier)

It is important to note that the surface properties of II-VI compounds are identical to those of metal oxides such as ZnO and CdO. Moreover, the desorption of impurities adsorbed on their surfaces occurs in the same temperature range. This is quite understandable, since II-VI compounds and metal oxides ZnO and CdO, in principle, belong to the same group of materials.

Another common regularity observed for II-VI compounds and metal oxides is the absence of a pinning of surface Fermi level. The absence of the pinning of surface Fermi level is due to the low density of surface states in these semiconductors (<10^{11} cm^{-2}). This feature of these compounds is especially important for gas sensors, where the sensor response is directly related to the range of changes in the position of the surface Fermi level during interaction with the detecting gas. Interestingly, the change in the sensitivity of the surface Fermi level to the gaseous environment (Fig. 2.16a) occurs in full accordance with the change in the ionicity of the semiconductor compound (Fig. 2.16b). The slope $S = \frac{d\Phi_{Bn}}{dX_M}$, shown in Fig. 2.16a, is inversely correlated to the extent of Fermi-level stabilization [71]. It was found that S = 1 (no Fermi-level stabilization) for “ionic” materials and S = 0.1 (nearly complete Fermi level stabilization) for “covalent” materials.

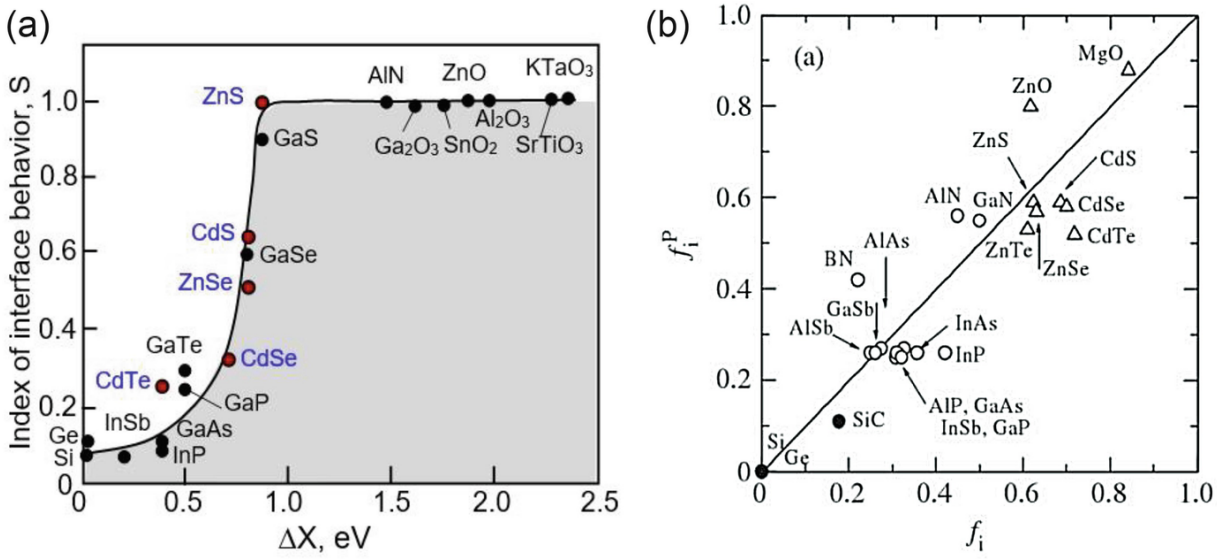

Fig. 2.16 (**a**) Influence of electronegativity (X) on the value of *S* in $\Phi_{Bn} = S\,\Delta X$. (Data extracted from Kurtin et al. [71]). (**b**) Phillips iconicity f_i versus Pauling iconicity for some group-IV, III-V, and

II-VI semiconductors. The solid line indicates the relation of f_i and f_i^P. (Reprinted with permission from Adachi [2]. Copyright 2005: Wiley)

In this case, just as for metal oxides, the surface Fermi level (E_F) shifts toward the midgap with adsorption of oxygen for II-VI semiconductors (ZnSe and ZnTe), which results in an upward band bend for n-type semiconductors (ZnSe) and a downward band bend for p-type semiconductors (ZnTe) [26]. Figure 2.17 shows changes in band bending (ΔqV), work function (Δϕ), and dipole potential (ΔX) as a function of oxygen coverage. The appearance of a potential barrier on the surface is explained by the capture of electrons from the conduction band by chemisorbed oxygen. According to generally accepted concepts, it is the change in the surface charge, captured by oxygen in the process of interaction with the detected gases, that determines the sensor response of conductometric gas sensors.

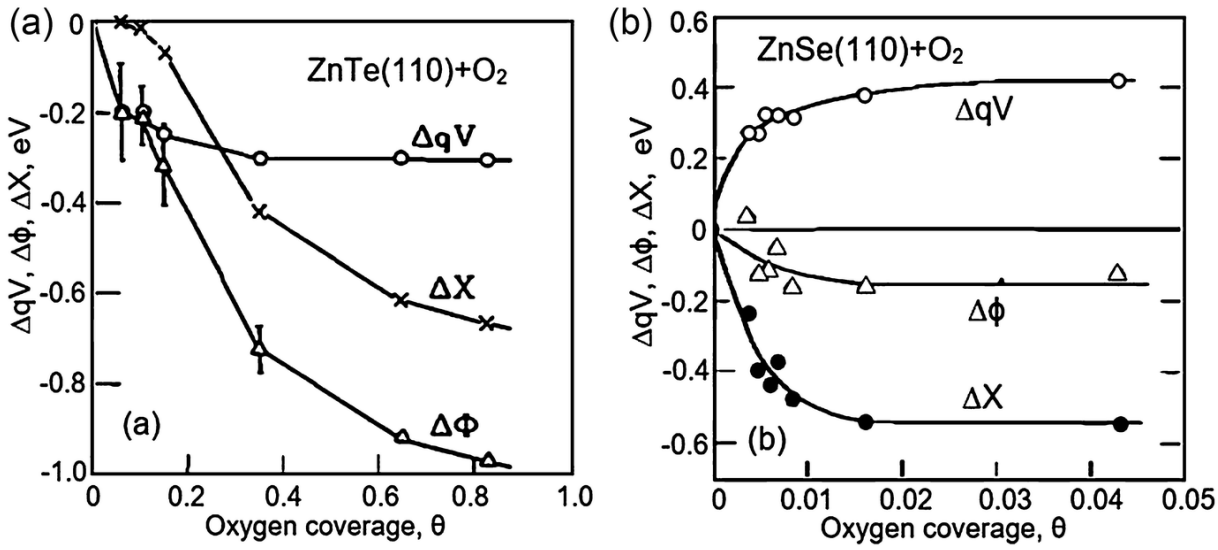

Fig. 2.17 Changes in band bending (ΔqV), work function (Δϕ), and dipole potential (ΔX) as a function of oxygen coverage (**a**) for p-type ZnTe and (**b**) for n-type ZnSe(110) in the region of small coverages where the changes are large. (Adapted with permission from Ebina et al. [26]. Copyright 1982: Taylor and Francis Ltd)

As is seen in Fig. 2.14, CdS and, especially, ZnS, which are characterized by the maximum proportion of ionic bonds, are the closest to metal oxides in their behavior. For this compound, $S = 1$ (see Fig. 2.16a). While for CdTe, which has the maximum contribution from the covalent bond, $S = 0.3$. This means that ZnS and CdS, in terms of their surface properties, are the most suitable II-VI compounds for the development of

gas sensors [122]. Experimental studies have shown the validity of these statements. Smyntyna et al. [105] and Golovanov et al. [31] reported an increase or decrease of the electrical conductivity of CdS-based sensors when exposed to O_2, CO, or SO_2 gases and showed the ability of these sensors to detect air pollutants. At that it was found that CdS-based adsorption-type gas sensors can be developed based on various sensor platforms. In addition to conductometric-type sensors, photoluminescence-based optical gas sensors [85, 102] and surface acoustic wave sensors based on CdS films can also be made. Urbanczyk et al. [116] showed that such sensors can be used for detections of NO_2, SO_2, NH_3, and H_2S gases.

As for the height of the potential barrier formed upon contact of the metal and the II-VI compound, these values for the contact formed by gold are given in Table 2.12.

Table 2.12 Schottky barrier heights φ_n and φ_p between Au/n-type and Au/p-type semiconductors, respectively, $\varphi_n + \varphi_p$ and semiconductor band gap energy E_g at 300 K

Semiconductor	φ_n, eV	φ_p, eV	$\varphi_n + \varphi_p$, eV	E_g, eV
α-ZnS	2.0–2.19			3.75
β-ZnS	2.0–2.19			3.726
ZnSe	1.36–1.55	1.2	2.56–2.75	2.721
ZnTe		0.51–0.64		2.27
CdS	0.68–0.84			2.501
CdSe	0.49–0.7			1.751
CdTe	0.59–1.0	0.6	1.19–1.6	1.51

Source: Data extracted from Adachi [2]

2.11 Catalytic Properties

As well as metal oxides, II-VI compounds exhibit pronounced catalytic and photocatalytic properties [14, 18, 103, 124]. It has been found that they can be catalysts in various redox reactions. Vacancy defects usually act as active centers in these reactions. For example, the work [62] presents the results of the catalytic activity of ZnSe and CdTe and their solid solutions in the reaction of hydrogen oxidation in the temperature range of 323–523 K with

an excess of oxygen. The reaction rate ϑ on all samples increased both with an increase in temperature (according to the Arrhenius law) and with an increase in the hydrogen concentration in the reaction mixture and did not depend on the grain size. These moments, as well as the absence of heating of the catalysts, indicate that the reaction proceeds in the kinetic region. Kirovskaya [62] also showed the possibility of using ZnSe-ZnTe and ZnSe-CdSe for carbon dioxide hydrogenation. These studies have shown that the hydrogenation of CO_2 on the studied samples passes at a noticeable rate at temperatures of 323–498 K and 473–613 K, respectively. A comparative analysis of the CO conversion curves on CdTe in the works Kirovskaya et al. [56, 60, 61] showed that, regardless of the carrier gas (argon, air), the CO oxidation reaction passes most intensively at 423 K. In [61], the reaction of CO hydrogenation on CdTe was studied: at room temperature, the degree of CO conversion was 87%, and at a temperature of 377 K, it was 91%. Compared to oxide catalysts, the hydrogenation reaction of CO on CdTe passes at lower temperatures. According to Kirovskaya [62], typical redox reactions pass predominantly by impact ion-radical or ionic and decomposition reactions by adsorption, donor-acceptor mechanisms. Tristao et al. [114] have prepared a coupled CdS/TiO_2 photocatalyst for degradation of an organic textile dye (azo dye; Drimaren red) in the presence of artificial UV light. Cheng et al. [18] have shown that CdS-based photocatalyst has attracted extensive attention due to its relatively narrow band gap for visible-light response and sufficiently negative potential of the conduction band edge for the reduction of protons. Studies have shown that CdS-based photocatalysts possess excellent photocatalytic performance in terms of solar-fuel generation and environmental purification. In addition, applications of CdS-based photocatalysts have been discussed, for example, for photocatalytic hydrogen production, reduction of CO_2 to hydrocarbon fuels, and degradation of pollutants. Figure 2.18 further illustrates the specific photocatalytic process of CdS photocatalysts for the degradation of pollutants. CdS photocatalyst can produce photogenerated electrons and holes under visible light irradiation, and these carriers are very chemically active and metastatic, and can react with oxygen or water molecules adsorbed on the surface of the CdS photocatalysts to form *OH or O_2^{*-}. Based on the oxidation of *OH, O_2^{*-} and holes, contaminants can be effectively degraded over the CdS photocatalysts. Hong et al. [41] have

used a simple monolithic film system (CdS/TiO_2) for H_2 production. The repeated unit CdS/TiO_2 structure generated large amount of H_2 without decreased efficiency. Research carried out by Kim et al. [54] showed that the CdS-based composite had an enhanced efficiency of the water splitting reaction under visible light. Qin et al. [93] found that CdS/TiO_2 composite exhibited high photocatalytic activity in the selective oxidation of a number of alcohols to the corresponding aldehydes under the action of visible light.

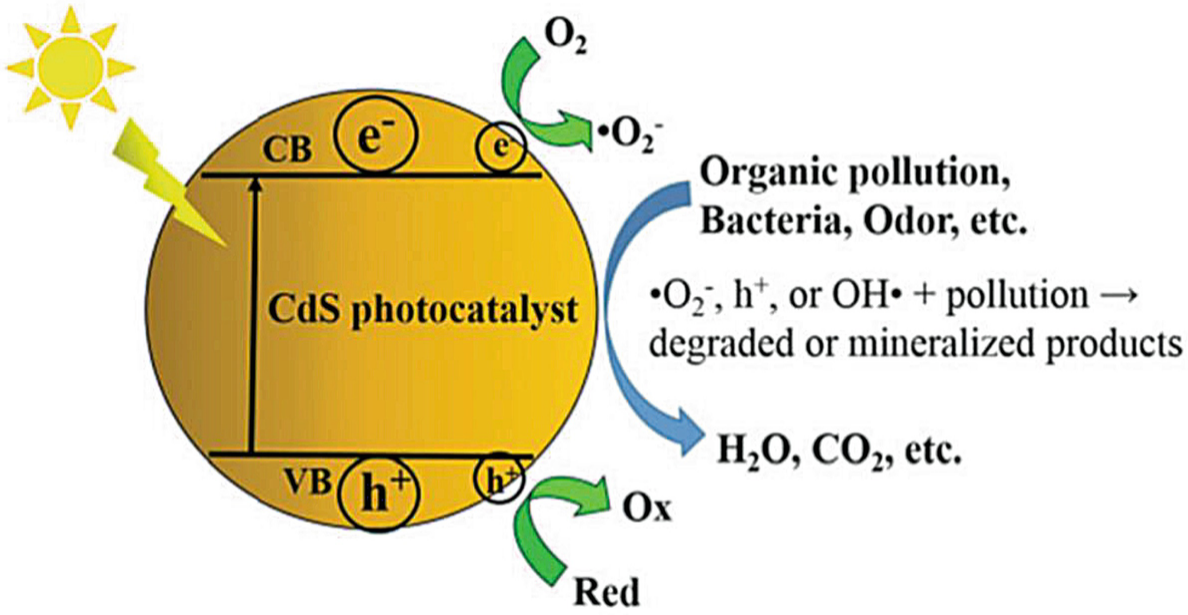

Fig. 2.18 Schematic illustration of the reaction process for degrading pollution over the CdS photocatalysts under visible light irradiation. (Reprinted with permission from Cheng et al. [18]. Copyright 2018: RSC)

Many studies have shown that the photocatalytic performance of CdS photocatalysts can be modified by changing the external conditions such as polytropic synthesis conditions, variety and quantity of reagents, structure, size, morphology, etc. [18, 103]. In particular, various strategies have been developed to increase photocatalytic H_2 production using CdS-based photocatalytic nanomaterials, such as creating multicomponent solid solutions, loading cocatalysts, creating Z-pattern heterojunctions, designing 2D nanosheets, and reducing photocorrosion [103]. While Hou et al. [42] and Shen et al. [103] believe that the use of 2D nanomaterials is the most promising approach, 2D nanomaterials possess many advantages, such as good chemical and physical stability, high interlayer adhesion, large surface area, high electron mobility, and rich surface-active sites, which facilitate

photocatalytic H_2 evolution. In addition, band gap tuning and heterojunction design can be conveniently designed by combining the strengths of different 2D nanomaterials in the form of 2D/2D-layered nanocomposites [42, 74]. Therefore, it is possible to obtain CdS photocatalysts with extended visible-light absorption and enhanced redox capacities, as well as better charge separation efficiencies. The construction of single-layer CdS nanosheets could minimize the charge migration distance from the bulk to the CdS surface.

However, there is still a gap in the fundamental identification of real active sites in CdS photocatalysts. The mechanisms of e-transfer between CdS heterojunctions and other components remain debatable. The durability and stability of photocatalysts also remain an urgent problem that needs to be addressed in the future [103].

2.12 Applications

Metal chalcogenides are semiconductors and one of the best photoconductors. All chalcogenides have a high sensitivity to radiation from infrared to X-ray spectrum, brightly showing photoresistive and luminescent properties [46]. Chalcogenides significantly expand the possibilities of semiconductor electronics due to their valuable electrophysical, photo- and piezoelectric properties (Fig. 2.19). Therefore, these materials are of interest from the point of view of their use in electronics and optoelectronics as a material for the creation of thin-film transistors, LEDs, semiconductor lasers, energy storage devices, and various types of photodetectors [40, 76, 90, 96].

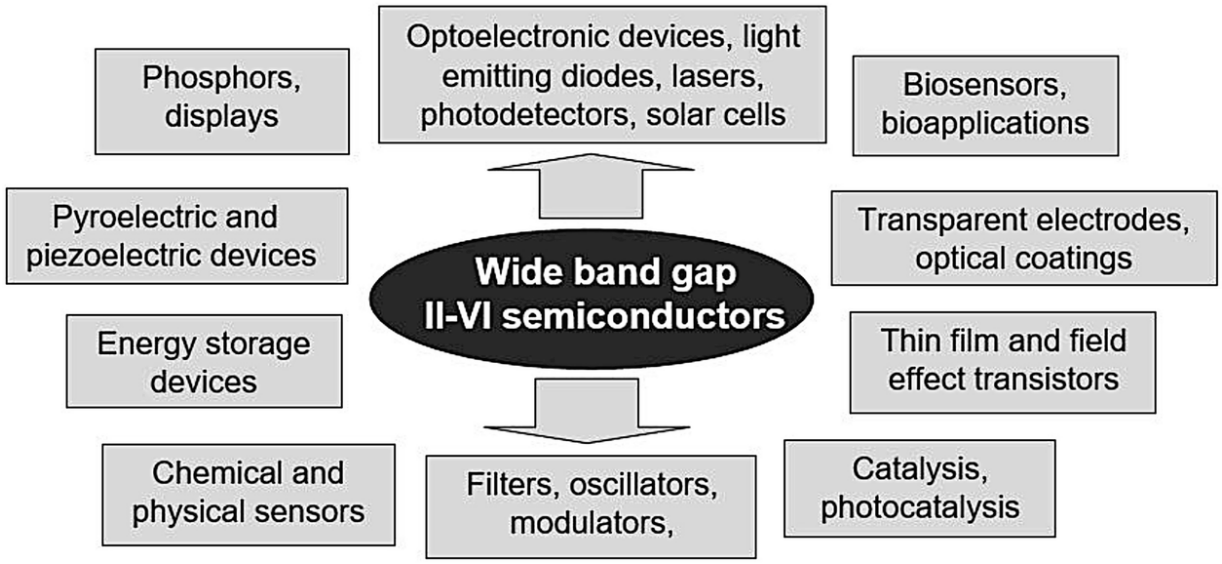
Phosphors, displays
Optoelectronic devices, light emitting diodes, lasers, photodetectors, solar cells
Biosensors, bioapplications
Pyroelectric and piezoelectric devices
Wide band gap II-VI semiconductors
Transparent electrodes, optical coatings
Energy storage devices
Thin film and field effect transistors
Chemical and physical sensors
Filters, oscillators, modulators,
Catalysis, photocatalysis

Fig. 2.19 Applications of II-VI semiconductors

The most common type of photodetectors is photoresistors. The main characteristics of these devices are the ratio of dark to light resistance, quantum efficiency or gain, photoresponse time, detectivity, and sensitivity. The best combination of properties with respect to visible light is possessed by polycrystalline CdS and CdSe films and especially solid solutions based on them, such as CdS_xSe_{1-x}. Their spectral sensitivity coincides almost perfectly with the spectrum of solar radiation, capturing even the near-IR region. Due to their sensitivity to visible light, II-VI compounds are used as materials for thin-film solar cells [19]. For example, cadmium selenide (CdSe) with a band gap of 1.74 eV absorbs visible radiation more efficiently than silicon [40]. CdTe has even more optimal properties for use in solar cells. Among II-VI compounds, CdTe has an optimal band gap $E \approx 1.45–1.5$ eV for direct conversion of sunlight into electricity. High absorption CdTe materials ($\alpha > 10^4$ cm^{-1}) [15] are more efficient for the production of photovoltaic converters than Si [30]. According to [3], a thin film of CdTe with thickness of 2 μm absorbs nearly 100% of incident solar radiation. This means that a thin layer of CdTe is enough to efficiently convert solar energy, which can significantly reduce material consumption and reduce the cost of manufacturing solar cells.

At the same time, ZnS and CdS are the basis for many industrial phosphors. Zinc-sulfide phosphors have high brightness, the glow of which under the action of an alternating electric field or an electron beam is activated by impurities of Cu, Cl, Al, Eu, and Mn. It is important to note

that ZnS electroluminophores (ELs) still outperform other materials in terms of intrinsic quantum efficiency. However, electroluminescent devices based on zinc sulfide have a significant disadvantage. They are characterized by a relatively high rate of degradation of devices (deterioration of their properties), due to the strengthening of the ionic nature of the chemical bond, which stimulates the processes of electrolysis.

ZnS is also an effective ultraviolet radiation sensor due to its large band gap. A promising direction for the use of ZnS and CdS is also the development of various chemical sensors (read Vol. 3) operating on the principles of chemical reactions, when an analytical signal arises due to the chemical or physical interaction of the detected gas with the sensitive layer [102, 122]. Sensors developed on these principles [66, 69] can be used for expressing detection and analysis of harmful components of gas emissions (CO, NO, NO_2, SO_2, NH_3, Cl2, etc.) from motor vehicles, chemical and petrochemical enterprises, and for monitoring the state of the environment. The development of electrochemical and biosensors is also a promising field of application for CdS, ZnS, ZnSe, and other II-VI compounds [45, 95].

As we mentioned earlier, CdS and CdSe films formed using thin-film and thick-film technologies are widely used to fabricate photoresistors with high sensitivity in the visible part of the spectrum. Films of CdS and CdSe compounds are also widely used as materials in photoelectric devices such as optocouplers, photopotentiometers, photocapacitors, photoelectrochemical cells, electroluminescent amplifiers, and radiation converters. Zinc sulfide single crystals are also used as an optical material that is transparent in the infrared region of the spectrum, as well as for piezoamplifiers of acoustic vibrations. CdS and CdSe are also suitable for use as a photocatalyst or material for building photocatalyst systems [18, 76], for photoelectrochemical splitting of water and organic substances, as well as for hydrogen production [103].

ZnSe and ZnSe-based compounds such as ZnCdSe, ZnCdMgSe, ZnSse, and ZnMgSSe are promising materials for infrared devices, opto-thermal devices, and light-emitting devices [49, 70]. Another area of application of ZnSe is the formation of a buffer layer both in thin-film solar cells and in thin absorbing elements. The use of ZnSe as a buffer layer material instead of CdS in Cu (In, Ga)Se_2 (CIGS)-based solar cells was reported [46]. The advantages of using ZnSe over CdS include its nontoxicity, its wider energy

band gap than CdS, and its ability to provide a better lattice matching with CIGS absorber layer [8]. ZnSe is a high refractive index material, so it can be used in multilayer film combinations and as a protective and antireflection coating for infrared-operating electro-chromic thermal-control surfaces [108]. ZnSe-based materials have also been found to be a promising candidate for scintillation applications [47, 92]. These scintillators show much-needed scintillation efficiency along with advantages such as high thermal and radiation stability, less toxicity, non-hygroscopicity, emissions in the visible range and small decay time, etc. Further, in quantum confinement regime, they show improvement in luminescent properties and size-dependent emissions. ZnSe-based scintillators have an additional advantage as its response wavelength matches well with silicon photodiode spectral sensitivity. The region of maximum spectral sensitivity of Si-p-i-n-PD and ZnSe crystal radioluminescence shows of about 80% overlap [72]. X-ray luminescence spectra of II-VI semiconductor scintillators and photosensitivity of Si-PD are given in Fig. 2.20. From the figure, it is evident that ZnSe-based scintillators are suitable to be used with silicon photodiode. ZnSe-based scintillators are highly efficient for detection of alpha, beta particles, low-energy gamma rays, and X-rays with high radiation stability. These scintillators also have a better light output and fast decay time [72, 92]. The response time of photodiode is of the order of 10^{-5} s, which is the same as that of scintillation flash duration of ZnSe doped scintillator [91]. Jagtapa et al. [47] believe that with optimized synthesis, these highly efficient quantum dot scintillators can have various extended scientific and industrial applications.

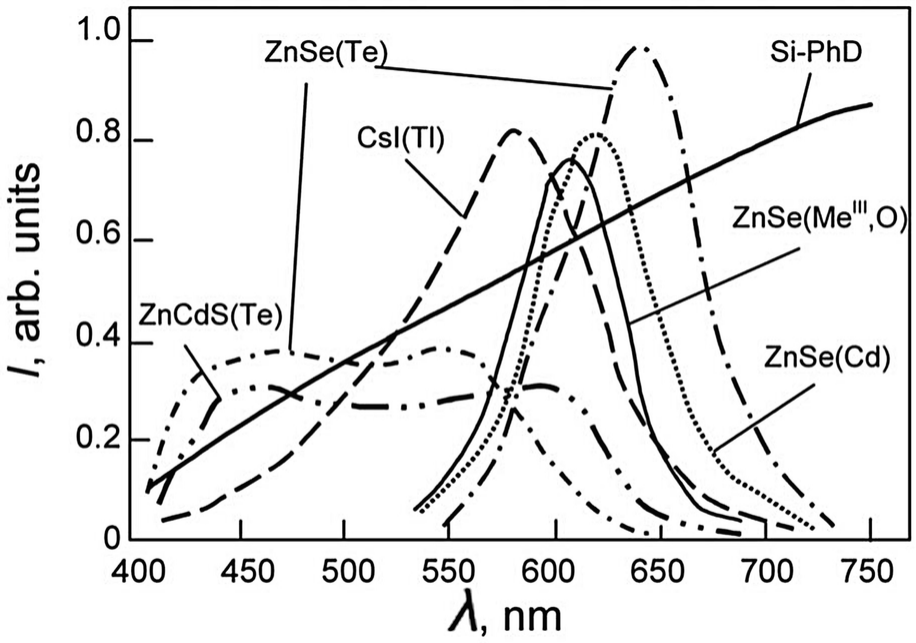

Fig. 2.20 Radioluminescence spectrum of AII-BVI scintillators and photosensitivity of Si-PD. (Reprinted with permission from Katrunov et al. [51]. Copyright 2013: Elsevier)

Zinc telluride (ZnTe), like other compounds II-VI, has potential applications in a variety of solid-state devices such as solar cells, photodetectors, and light-emitting diodes [126]. In solar cell applications, low resistive p-type ZnTe is required as a back contact for cadmium telluride (CdTe) solar cells, which is important for the functionality of these cells [46]. Heterostructures based on ZnTe and HgTe are used for infrared optics. When doped with vanadium, ZnTe becomes a photorefractive semiconducting material and has good potential applications for optical power limiting applications.

Owing to their direct-gap structure and high efficiency of radiative recombination, II-VI compounds are also used in quantum electronics [124]. Injection lasers in the IR range can only be made on compounds with both types of conductivity. However, it was found that unipolar sulfides and selenides are also suitable for lasers, but with a different type of excitation [106]. In particular, single crystals of these compounds can be used as the working body of semiconductor lasers excited by an electron beam.

Cadmium telluride (CdTe) is another member of the class of wide-gap semiconductors with unique parameters [118]. The tellurium and cadmium atoms that form CdTe have high atomic numbers of the components (z = 48 and 52, respectively), which make gamma radiation braking more efficient. This allows the use of smaller volumes of material when creating X-ray

detectors compared to other popular semiconductors: Si, Ge, and GaAs [87, 92, 109]. The high stopping power of the material makes it possible to create detectors for a wide energy range from 5 keV to 10 MeV, and the use of smaller volumes of elements contributes to an increase in spatial resolution and, accordingly, image quality. The band gap of CdTe (Eg ≈ 1.5 eV at 300 K) exceeds that of Si, Ge, and GaAs, because of which X-ray and gamma-ray detectors, based on CdTe, can operate effectively at room temperature or under conditions of weak cooling, implemented using thermoelectric refrigerators. It should be noted that the most high-quality spectrometric gamma ray detectors made of germanium operate only at liquid nitrogen temperature. The GaAs semiconductor closest in band gap is inferior in properties to CdTe detectors due to the presence of a deep level due to intrinsic point defects. Thus, CdTe crystals and solid solutions based on it $Cd_{1-x}Zn_xTe$ are currently one of the key materials for the manufacture of ionizing radiation detectors operating at room temperature. In the last two decades, great efforts have been made in the development of both technologies for growing these crystals and devices based on them. This makes it possible to create detector matrices based on CdTe and $Cd_{1-x}Zn_xTe$ with the possibility of single-photon registration, taking into account the resolution energy for color and spectroscopic radiography, which opens up new prospects for application in the fields of diagnostic medicine, as well as for equipping experimental stations on synchrotron radiation sources [4, 87].

Along with detector properties, CdTe has extraordinary optical properties. In particular, it is characterized by high transmission in the IR range of the emission spectrum (0.8–25 μm). The value of the electro-optical coefficient of CdTe is four times higher than that of GaAs. CdTe crystals doped with transition metals exhibit photorefractive properties. In this regard, CdTe is a promising material for infrared optics and electro-optics. CdTe is also used in laser switches (Q-switch) used in CO_2 lasers. Just like CdSe, CdTe is promising for biosensing and photocatalysis applications [77, 82].

CdTe crystals occupy also a special place as substrates for epitaxial layer growth of $Hg_xCd_{1-x}Te$, used as infrared detectors. Due to the chemical identity and the possibility of precise matching of the lattice parameters of the substrate (by introducing Zn) and the epitaxial layer, CdTe crystals are

the most preferred over Si, Ge, and GaAs substrates. Only the high prices for CdTe substrates and the complexity of the technology for their large-area fabrication limit the use of such substrates at present (read the Chap. 9, Vol. 1).

Acknowledgments

G.K. is grateful to the State Program of the Republic of Moldova (project 20.80009.5007.02) for supporting his research.

References

1. Adachi S (2004) Handbook of physical properties of semiconductors. Vol. 3. II-VI compounds semiconductors. Kluwer Academic Publishers, Boston
2. Adachi S (2005) Properties of group-IV, III-V and II-VI semiconductors. Wiley, Chichester
3. Afzaal M, O'Brien P (2006) Recent developments in II–VI and III–VI semiconductors and their applications in solar cells. J Mater Chem 16:1597–1602
4. Allahgholi A, Becker J, Delfs A, Delfs A, Dinapoli R, Gottlicher P et al (2019) Megapixels @ megahertz – the AGIPD high-speed cameras for the European XFEL. Nuclear Inst Methods Phys Res A 942:1–9
5. Al'fer SA, Skums VF (2001) Investigation of the electrical conductivity of CdSe and CdTe at elevated temperatures and pressures. Inorg Mater (Russia) 37(12):1449–1453. (in Russian)
6. Aven JS, Prender M (eds) (1967) Physics and chemistry of II-VI compounds. North-Holland Publishing Co, Amsterdam
7. Avetisov IK, Ivanov YM, Zorin AV (2001) The problem of polymorphic transitions in CdTe. Surface (Russia) 10:82–88. (in Russian)
8. Bacaksiz E, Aksu S, Polat I, Yılmaz S, Altunbaş M (2009) The influence of substrate temperature on the morphology, optical and electrical properties of thermal-evaporated ZnSe thin films. J Alloys Compd 487:280–285
9. Bai Z, Wang D (2012) Oxidation of CdTe thin film in air coated with and without a $CdCl_2$ layer. Phys Status Solidi A 209(10):1982–1987
10. Bao Z, Yang X, Li B, Luo R, Liu B, Tang P et al (2016) The study of CdSe thin film prepared by pulsed laser deposition for CdSe/CdTe solar cell. J Mater Sci Mater Electron 27(7):7233–7239
11. Berding MA (1999) Native defects in CdTe. Phys Rev B 70(12):8943–8950
12. Bootsma GA (1968) Gas adsorption on cadmium sulphide. Surf Sci 9:396–406

13. Bouroushian M (2010) Electrochemistry of metal chalcogenides: monographs in electrochemistry. Springer, Berlin/Heidelberg, p 349
14. Bukashkina T.L. (2018) Bulk and surface properties of adsorbent-catalysts based on CdSe-CdTe system. PhD thesis, Omsk State Technical University, Omsk (in Russian)
15. Caglar M, Zor M, Ilican S, Caglar Y (2006) Effect of indium incorporation on the optical properties of spray pyrolyzed $Cd_{0.22}Zn_{0.78}S$ thin films. Czechoslov J Phys 56(3):277–287
16. Campbell BD, Farnsworth HE (1968) Studies of structure and oxygen adsorption of (0001) CdS surfaces by LEED. Surf Sci 10:197–214
17. Chen Q, Hillert M, Sundman B (1998) Phase equilibria, defect chemistry and semiconducting properties of CdTe(S) – thermodynamic modeling. J Electron Mater 27(8):145–158
18. Cheng L, Xiang Q, Liao Y, Zhang H (2018) CdS-based photocatalysts. Energy Environ Sci 11(6):1362–1391
19. Chopra KL (1983) Thin film solar cells. Plenum Press, New York
20. Daweritz L (1971) Relative stability of zincblende and wurtzite structure in AIIBVI-compounds. Krist Tech 6(1):101–107
21. Dengo N, De Fazio AF, Weiss M, Marschall R, Dolcet P, Fanetti M, Gross S (2018) Thermal evolution of ZnS nanostructures: effect of oxidation phenomena on structural features and photocatalytical performances. Inorg Chem 57(21):13104–13114
22. Desnica-Frankovic ID, Dubcek P, Buljan M, Furic K, Desnica UV, Bernstorff S et al (2005) Influence of stoichiometry deviations on properties of ion-beam synthesized CdSe QDs. Nuclear Instr Meth Phys Res B 238:302–305
23. Desnica UV (1998a) Wide band-gap II–VI compounds – can efficient doping be achieved? Vacuum 50(3–4):463–471
24. Desnica UV (1998b) Doping limits in II-VI compounds-challenges, problems and solutions. Prog Cryst Growth Charact 36(4):291–357
25. Ebina A, Takahashi T (1982) Studies of clean and adatom treated surfaces of II-VI compounds. J Cryst Growth 59:51–64
26. Ebina A, Suda Y, Takahashi TT (1982) Oxidation of ZnSe (110) and ZnTe (110). Int J Electron 52(1):77–88
27. Ebina A, Asano K, Suda Y, Takahaski T (1980) Oxidation properties of II-VI compound surfaces studied by low-energy electron-loss spectroscopy and 21 eV photoemission spectroscopy. J Vac Sci Technol 17(5):1074–1079
28. Ebina A, Asano K, Takahashi T (1980) Surface properties of clean, and with adsorbed oxygen, surfaces of CdTe (110), (111), and (100) and of CdSe (0001) studied by electron-energy-loss spectroscopy and Auger-electron spectroscopy. Phys Rev B 22(4):1980–1991

29. Eom NSA, Kim T-S, Choa Y-H, Kim W-B, Kim BS (2014) Surface oxidation behaviors of cd-rich CdSe quantum dot phosphors at high temperature. J Nanosci Nanotechnol 14:8024–8027
30. Gloeckler M, Sankin I, Zhao Z (2013) CdTe solar cells at the threshold to 20% efficiency. IEEE J Photovolt 3(4):1389–1393
31. Golovanov V, Smyntyna V, Korotcenkov G, Brinzari V (2001) Cd_xS- and Sn_xWO_3-based gas sensors: the role of chemical composition in CO sensing. J Fotoelectron (Ukraine) 10:6–11
32. Goodell CM, Gilbert B, Weigand SJ, Banfield JF (2008) Kinetics of water adsorption-driven structural transformation of ZnS nanoparticles. J Phys Chem C 112:4791–4796
33. Gréboval C, Chu A, Goubet N, Livache C, Ithurria S, Lhuillier E (2021) Mercury chalcogenide quantum dots: material perspective for device integration. Chem Rev 121(7):3627–3700
34. Gupta SS, van Huis MA (2017) Adsorption study of a water molecule on vacancy-defected nonpolar CdS surfaces. J Phys Chem C 121:9815–9824
35. Friedl J (1967) Dislocations. Addison-Wesley, Reading, p 74
36. Han P, Bester G (2017) Force field potentials for the vibrational properties of II-VI semiconductor nanostructures. Phys Rev B 96:195436
37. Herl W (1988) Surface chemical properties of zinc sulfide. Langmuir 4(3):595–598
38. Hernández-Calderón I (2002) Optical properties and electronic structure of wide band gap II-VI semiconductors. In: II-VI semiconductor materials and their applications. Taylor and Francis, New York, pp 113–170
39. Ho SM, Olusola OI, Sharma DC, Mahmood W (2018) Zinc telluride thin films: a review. Asian J Chem 30(3):469–473
40. Hodes G, Manassen J, Cahen D (1976) Photoelectrochemical energy conversion and storage using polycrystalline chalcogenide electrodes. Nature 261:403–404
41. Hong E, Kim JH, Yu S, Kim JH (2011) Effect of CdS contents on H_2 production from Pt-(CdS/TiO_2) film-typed photocatalysts. Korean J Chem Eng 28:1684–1687
42. Hou Y, Laursen AB, Zhang J, Zhang G, Zhu Y, Wang X et al (2013) Layered nanojunctions for hydrogen-evolution catalysis. Angew Chem Int Ed 52:3621–3625
43. Hu L, Wu H (2016) Influence of size and surface state emission on photoluminescence of CdSe quantum dots under UV irradiation. J Lumin 177:307–313
44. Hwang HL, Hsu KYJ, Ueng HY (1996) Fundamental studies of p-type doping of CdTe. J Cryst Growth 161:73–81
45. Ibrahim I, Lim HN, Zawawi RM, Tajudin AA, Ng YH, Guo H, Huang NM (2018) A review on visible-light induced photoelectrochemical sensors based on CdS nanoparticles. J Mater Chem B 6:4551–4568

46. Ikhmayies SJ (ed) (2014) Advances in the II-VI compounds suitable for solar cell applications. Signpost Publisher
47. Jagtapa S, Chopade P, Tadepalli S, Bhalerao A, Gosavi S (2019) A review on the progress of ZnSe as inorganic scintillator. Opto-Electon Rev 27(1):90–103
48. Jasieniak J, Mulvaney P (2007) From cd-rich to se-rich: the manipulation of CdSe nanocrystal surface stoichiometry. J Am Chem Soc 129:2841–2848
49. Jia L, Kou H, Jiang Y, Yu S, Li J, Wang C (2013) Electrochemical deposition semiconductor ZnSe on a new substrate CNTs/PVA and its photoelectrical properties. Electrochim Acta 107:71–77
50. Kasap S, Capper P (eds) (2006) Handbook of electronic and photonic materials. Springer, New York
51. Katrunov K, Ryzhikov V, Gavrilyuk V, Naydenov S, ZnSe Lysetska O, Litichevsky V (2013) Optimum design calculations for detectors based (Te, O) scintillators. Nuclear Instrum Methods Phys Res A 712:126–129
52. Kendall EJM (1961) Structural peculiarities of zinc sulphide, cadmium sulphide, cadmium telluride and gallium phosphide. Phys Lett 8(4):237–238
53. Khlopochkina EL, Gaivoronskii PE, Gavrishchuk EM, Elliev YE, Yashina EV (2001) Oxidation of polycrystalline zinc selenide with atmospheric oxygen. Russ J Appl Chem 74(7):1079–1081
54. Kim JC, Choi J, Lee YB, Hong JH, Lee JI, Yang JW et al (2006) Enhanced photocatalytic activity in composites of TiO_2 nanotubes and CdS nanoparticles. Chem Commun 2006:5024–5026
55. Kirovskaya IA, Nor PE, Ushakov OV, Pogodin SN (2017) Surface-active state of semiconductor materials based on CdTe–$A^{II}S$ systems. AIP Conf Proc 1876:020068
56. Kirovskaya IA, Mironova EV (2015) Oxidation and hydrogenation of carbon monoxide (II) on semiconductors of the InSb–CdTe system. Russ J Phys Chem 89:1286–1292
57. Kirovskaya IA, Mironova EV (2014) Adsorbent surface. Semiconductor and oxide adsorbents. Publishing House of OmGTU, Omsk, 156 p (in Russian)
58. Kirovskaya IA, Nor PE (2013) Adsorption properties of CdS-CdTe system semiconductors. Russ J Phys Chem A 87(12):2077–2081
59. Kirovskaya IA (2012) Surface properties of binary diamond-like semiconductors. OmSTU Publishing House, Omsk, 416 p (in Russian)
60. Kirovskaya IA, Podgornyi SO (2012) New catalysts for the oxidation of carbon monoxide. Rus J Phys Chem A 86(1):14–18
61. Kirovskaya IA, Mironova EV, Rudko TL (2007) Catalytic properties of the InSb–CdTe system in the hydrogenation of carbon monoxide. J Phys Chem (Russia) 81(8):1385–1388

62. Kirovskaya IA (2004) Catalysis. Semiconductor catalysts. Publishing House of OmSTU, Omsk. (in Russian)
63. Kirovskaya IA, Murashko YA (2004) IR – spectroscopic studies of the surface of the components of the ZnTe – CdTe system. Omsk Sci Bull 1(26):66–67. (in Russian)
64. Kirovskaya IA (1989) Chemical state of the real surface of compounds of the A2B6 type. Izv Acad Sci USSR Ser Inorg Mater (Russia) 29(9):1472–1475. (in Russian)
65. Korotcenkov G (2020) Handbook of humidity measurement: methods, materials and technologies, Vol. 3: sensing materials and technologies. CRC Press, Boca Raton
66. Korotcenkov G (2019) Handbook of humidity measurement: methods, materials and technologies, Vol. 2: electronic and electrical humidity sensors. CRC Press, Boca Raton
67. Korotcenkov G (2014) Handbook of gas sensor materials. Vol. 2: new trends and technologies. Springer, New York
68. Korotcenkov G (2013) Handbook of gas sensor materials. Vol. 1: conventional approaches. Springer, New York
69. Korotcenkov G (ed) (2011) Chemical sensors: comprehensive sensor technologies. Vol. 6: sensors applications. Momentum Press, New York
70. Kovalenko AV, Korbutyak DV, Budzulyak SI (2011) Laser quntum-size structures based on II-VI compounds (review). Optoelectron Semicond Tech 46:7–27. (in Russian)
71. Kurtin S, McGill TC, Mead CA (1969) Fundamental transition in the electronic nature of solids. Phys Rev Lett 22(26):1433–1436
72. Lee WG, Kim YK, Kim JK, Seo HJ, Ryzhikov V, Starzhinskiy N et al (2006) Particularities of ZnSe-based scintillators for a spectrometry of charged particles and gamma quanta. J Korean Phys Soc 48(1):47–50
73. Li Y, Ma G, Jie W (2003) Point defects in CdTe. J Cryst Growth 256:266–275
74. Lin B, Li H, An H, Hao W, Wei J, Dai Y et al (2018) Preparation of 2D/2D g-C_3N_4 nanosheet@$ZnIn_2S_4$ nanoleaf heterojunctions with well-designed high-speed charge transfer nanochannels towards high-efficiency photocatalytic hydrogen evolution. Appl Catal B-Environ 220:542–552
75. Lincot D (2005) Electrodeposition of semiconductors. Thin Solid Films 487:40–48
76. Lu T, Dong S, Zhang C, Zhang L, Cui G (2017) Fabrication of transition metal selenides and their applications in energy storage. Coord Chem Rev 332:75–99
77. Ma Q, Wang X, Li Y, Su X, Jin Q (2007) The use of CdTe quantum dot fluorescent microspheres in fluoro-immunoassays and a microfluidic chip system. Luminescence 22(5):438–445

78. Magerle R, Deicher M, Desnica U, Keller R, Pfeiffer W, Pleiffter F et al (1991) Structural defect recovery in GaP after heavy ion implantation. Appl Surf Sci 50:169–172
79. Manner VW, Koposov AY, Szymanski P, Klimov VI, Sykora M (2012) Role of solvent-oxygen ion pairs in photooxidation of CdSe nanocrystal quantum dots. ACS Nano 6(3):2371–2377
80. Maticiuc N, Kukk M, Spalatu N, Potlog T, Krunks M, Valdna V, Hiie J (2014) Comparative study of CdS films annealed in neutral, oxidizing and reducing atmospheres. Energy Procedia 44:77–84
81. Mills KC (1974) Thermodynamic data for inorganic sulphides, selenides and tellurides. Butterworths, London
82. Mil'vidsky MG (1986) Semiconductor materials in modern electronics. Nauka, Moscow (in Russian)
83. Noskar RW, Mark P, Levine JD (1970) Polar surfaces of wurtzite and zincblende lattices. Surf Sci 19:291–317
84. Oda O (2007) Compound semiconductor bulk materials and characterizations. World Scientific Publishing Company, p 538
85. Oda M, Tsukamoto J, Hasegawa A, Iwami N, Nishiura K, Hagiwara I et al (2006) Photoluminescence of CdSe/ZnS/TOPO nanocrystals expanded on silica glass substrates: adsorption and desorption effects of polar molecules on nanocrystal surfaces. J Lumin 119–120:570–575
86. Osip'yan Yu A, Petrenko VF, Zaretski AV (1986) Properties of II-VI semiconductors associated with moving dislocations. Adv Phys 35(2):115–188
87. Owens A, Peacock A (2004) Compound semiconductor radiation detectors. Nuclear Instrum Methods Phys Res A 531:18–37
88. Palatnik LS, Sorokin VK (1973) Fundamentals of film materials science. Energy, Moscow
89. Park DH, Cho YH, Shin DH, Ahn BT (2013) Preparation of intrinsic ZnO films at low temperature using oxidation of ZnS precursor and characterization of the films. Curr Photovolt Res 1(2):115–121
90. Pautrat JL (1994) II-VI semiconductor microstructures: from physics to optoelectronics. J Phys III France 4:2413–2425
91. Ryzhikov V, Starzhinskiy N, Gal'chinetskii L, Gáshin P, Kozin D, Danshin E (2001) New semiconductor scintillators ZnSe (Te, O) and integrated radiation detectors based thereon. IEEE Trans Nucl Sci 48(3):356–359
92. Ryzhikov V, Chernikov V, Galochinetskii L, Galkin S, Lisetskaya E, Opolonin A, Volkov V (1999) The use of semiconductor scintillation crystal AII-BVI in radiation instruments. J Cryst Growth 197(3):655–658

93. Qin N, Liu Y, Wu W, Shen L, Chen X, Li Z, Wu L (2015) One-dimensional CdS/TiO_2 nanofiber composites as efficient visible-light-driven photocatalysts for selective organic transformation: synthesis, characterization, and performance. Langmuir 31(3):1203–1209
94. Yang Q, Zhao J, Guan M, Liu C, Cui L, Han D, Zeng Y (2011) Growth and annealing of zinc-blende CdSe thin films on GaAs (0 0 1) by molecular beam epitaxy. Appl Surf Sci 257(21):9038–9043
95. Sadovnikov SI (2019) Synthesis, properties and applications of semiconductor nanostructured zinc sulfide. Russ Chem Rev 88:571–593
96. Salas-Villasenor AL, Mejia I, Quevedo-Lopez MA (2014) Transparent and flexible thin film transistors with solution-based chalcogenide materials. ECS J Solid State Sci Technol 3(4):P107–P110
97. Samantilleke AP, Cerqueira MF, Heavens S, Warren P, Dharmadasa IM, Muftah GEA et al (2011) Characterisation of chemical bath deposited CdS thin films on different substrates using electrolyte contacts. Thin Solid Films 519(21):7583–7586
98. Sasaoka E, Hatori M, Sada N, Uddin MA (2000) Role of H_2O in oxidative regeneration of ZnS formed from high-temperature desulfurization ZnO sorbent. Ind Eng Chem Res 39(10):3844–3848
99. Schultze D, Steinike U, Kussin J, Kretzschma U (1995) Thermal oxidation of ZnS modifications Sphalerite and Wurtzite. Cryst Res Technol 30(4):553–558
100. Shanmugam N, Cholan S, Kannadasan N, Sathishkumar K, Viruthagiri G (2013) Effect of annealing on the ZnS nanocrystals prepared by chemical precipitation method. J Nanomater 2013:351798
101. Sbiojiri M, Suito E, Sella C, Suryanaryanan R, Paparoditis C (1968) Influence of stoichiometric deviations on the nucleation and structure of co-evaporated thin films of PbTe and CdTe. J Cryst Growth 3–4:206
102. Seker F, Meeker K, Kuech TF, Ellis AB (2000) Surface chemistry of prototypical bulk II−VI and III−V semiconductors and implications for chemical sensing. Chem Rev 100:2505–2536
103. Shen R, Ren D, Ding Y, Guan Y, Ng YH, Zhang P, Li X (2020) Nanostructured CdS for efficient photocatalytic H_2 evolution: a review. Sci China Mater 63(11):2153–2188
104. Singh H, Singh T, Sharma J (2018) Review on optical, structural and electrical properties of ZnTe thin films: effect of deposition techniques, annealing and doping. J Micro Smart Syst 7:123–143
105. Smyntyna V, Golovanov V, Kaciulis S, Mattogno G, Righini G (1995) Influence of chemical composition on sensitivity and signal reproducibility of CdS sensors of oxygen. Sens Actuators B Chem 25:628–630
106. Sorokina IT, Sorokin E (2015) Femtosecond Cr^{2+}-based lasers. IEEE J Sel Top Quantum Electron 21(1):1601519

107. Strehlow WH (1969) Chemical polishing of II-VI compounds. J Appl Phys 40:2928–2932
108. Su B, Choy KL (2000) Electrostatic assisted aerosol jet deposition of CdS, CdSe and ZnS thin films. Thin Solid Films 361–362:102–106
109. Takahashi T, Watanabe S (2001) Recent progress in CdTe and CdZnTe detectors. IEEE Trans Nucl Sci 48(4):950–959
110. Thiyagarajan R, Anusuya M, Mahaboob BM (2009) Study of structural and mechanical properties of zirconium doped cadmium sulphide thin film. J Am Sci 5(3):26–30
111. Tikhonova EL, Gaivoronskii PE, Elliev YE, Gavrisc EM (2003) Influence of conditions of zinc selenide oxidation with atmospheric oxygen on the composition of volatile products. Russ J Appl Chem 76(11):1724–1727
112. Trenczek-Zajaca A (2019) Thermally oxidized CdS as a photoactive material. New J Chem 43:8892–8902
113. Tripathy SK, Pattanaik A (2016) Optical and electronic properties of some binary semiconductors from energy gaps. Opt Mater 53:123–133
114. Tristao JC, Magalhaes F, Corio P, Sansiviero MTC (2006) Electronic characterization and photocatalytic properties of CdS/TiO_2 semiconductor composite. J Photochem Photobiol A Chem 181:152–157
115. Ummartyotin S, Infahsaeng Y (2016) A comprehensive review on ZnS: from synthesis to an approach on solar cell. Renew Sust Energ Rev 55:17–24
116. Urbańczyk M, Jakubik W, Maciak E (2005) Sensor properties of cadmium sulphide (Cds) thin films in surface acoustic wave system – preliminary results. Mol Quant Acoustics 26:273–281
117. Van Vechten JA (1975) Simple theoretical estimates of the Schottky constants and virtuaI-enthalpies of single vacancy formation in zinc-blende and Wurtzite type semiconductors. J Electrochem Soc 122:419–422
118. Wald FV (1977) Applications of CdTe. A review. Rev Phys Appl 12(2):277–290
119. Wang M, Zhang Q, Hao W, Sun Z-X (2011) Surface stoichiometry of zinc sulfide and its effect on the adsorption behaviors of xanthate. Chem Central J 5:73
120. Wang X, Zhang J, Nazzal A, Xiao M (2003) Photo-oxidation-enhanced coupling in densely packed CdSe quantum-dot films. Appl Phys Lett 83(1):162–164
121. Woods-Robinson R, Han Y, Zhang H, Ablekim T, Khan I, Persson KA, Zakutayev A (2020) Wide band gap chalcogenide semiconductors. Chem Mater 120(9):4007–4055
122. Yan Q, Gao L, Tang J, Liu H (2019) Flexible and stretchable photodetectors and gas sensors for wearable healthcare based on solution-processable metal chalcogenides. J Semicond 40:111604
123. Zakharov O, Rubio A, Blasé X, Cohen ML, Louie SG (1994) Quasiparticle band structures of six II-VI compounds: ZnS, ZnSe, ZnTe, CdS, CdSe, and CdTe. Phys Rev B 50(15):10780–

10787
124. Zhang Q, Li H, Ma Y, Zhai T (2016) ZnSe nanostructures: synthesis, properties and applications. Phys Mater Sci 83:472–535
125. Zhang H, Rustad JR, Banfield JF (2007) Interaction between water molecules and zinc sulfide nanoparticles studied by temperature-programmed desorption and molecular dynamics simulations. J Phys Chem A 111:5008–5014
126. Skhouni O, El Manouni A, Mari B, Ullah H (2016) Numerical study of the influence of ZnTe thickness on CdS/ZnTe solar cells performance. Eur Phys J Appl Phys 74:24602

OceanofPDF.com

© The Author(s), under exclusive license to Springer Nature Switzerland AG 2023
G. Korotcenkov (ed.), *Handbook of II-VI Semiconductor-Based Sensors and Radiation Detectors*
https://doi.org/10.1007/978-3-031-19531-0_3

3. Hg-Based Narrow Bandgap II-VI Semiconductors

Ghenadii Korotcenkov[1] ✉ and Denis L. Nika[1]
(1) Department of Physics and Engineering, Moldova State University, Chisinau, Moldova

Keywords Hg-based II-VI semiconductors – Band diagram – Chemical bond – Chemical properties – Doping – Acceptor – Donor – Electrophysical parameters – Chalcogen vacancies – Interstices – Mobility – HgS – HgSe – HgTe – Physical parameters – Stability – Stoichiometry – Synthesis – Hg-based II-VI semiconductors applications – IR detectors – GDs – Superlattices – Hall sensors – Limitations – Magnetoelectronics – Optoelectronics – Quantum electronics – Spintronics – Thermoelectric converters – Topological insulator – Natural minerals – Cinnabar – Coloradoite – Methacinnabarite – Timannite – Structural properties – Cubic – Lattice parameter – Trigonal – Hexagonal – Zincblende

3.1 Introduction

Hg-based II-VI compounds HgX, which include HgS, HgSe and HgTe, form a group of compounds with their own specific properties, which differ significantly from those of the compounds discussed in the previous chapter. Since mercury is located below cadmium and zinc in the periodic table, the switch from Cd and Zn to Hg is associated with an increased number of electrons and a reduced bandgap. The main parameters of the elements that form these compounds are given in the Table 3.1.

Table 3.1 Atomic number and relative electronegativity of elements forming Hg-based II-VI compounds

Element	S	Se	Te	Hg
Atomic number	16	34	52	80
Atomic weight	32.066	78.96	127.60	200.59
Covalent radii, nm	0.104	0.114	0.132	0.148
Ionic radii, nm	0.184	0.198	0.221	0.110
Electronegativity	2.5	2.4	2.1	1.9

3.2 Crystallography

In nature, mercury chalcogenides exist as natural minerals. HgS exists in two modifications: α-HgS (cinnabar, the main natural mineral of mercury) and β-HgS (methacinnabarite). Cinnabar/vermilion (α-HgS) is the hexagonal form of mercury sulfide; α-HgS, with the lattice parameters a = 4.149 Å and c = 9.495 Å [50], has a distorted NaCl structure (space group $P3_121$ or $P3_221$). Its coordination number is 6. Metacinnabar (β-HgS) is the cubic form of mercury sulfide (sphalerite or zincblende structure; a = 5.851 Å [50]), relating to F43m space group. The study of the relations between these two phases has shown that the conversion of α-HgS to β-HgS takes place in the temperature range of 345–381 °C [13].

Tiemannite is a mineral, mercury selenide, and formula HgSe. It occurs in hydrothermal veins associated with other selenides, or other mercury minerals such as cinnabar, and often with calcite. HgSe is discovered in 1855 in Germany, and it is named after C. W. Tiemann (1848–1899). Unlike the previously mentioned minerals, coloradoite (mercury telluride, HgTe) is a rare mineral. It is found in deposits of metals (especially gold and silver). Coloradoite was first found in 1877 in the USA, the state of Colorado, after which it was named. Coloradoite is formed under conditions of low-medium-temperature hydrothermal process of mineral formation in rocks bearing gold-sulfide mineralization. Mercury telluride as well as mercury selenide crystallize in the zincblende structure with space group F43m(216) [60]. The structural parameters of mercury chalcogenides are given in Table 3.2.

Table 3.2 Main structural parameters of mercury chalcogenides

Parameter	α-HgS	β-HgS	HgSe	HgTe
Crystal system	Trigonal	Zinc blende	Zinc blende	Zinc blende

Parameter	α-HgS	β-HgS	HgSe	HgTe
Unit cell	Hexagonal	Cubic	Cubic	Cubic
Lattice parameters at 300 K, nm				
a	0.4149	0.5851	0.6082	0.6460
c	0.9495	–	–	–
Nearest-neighbor distance, nm	0.375	0.253	0.263	0.280
Number of formula units in a cell, Z	6	4	4	4
Formula weight	232.65	232.65	279.55	328.19
Space group	$P3_121$	F43m	F43m	F43m

Source: Data extracted from Abrikosov et al. [1]

HgSe and HgTe behave similarly when compressed [35]. When compressed, their atmospheric (semimetallic) zincblende phases transform first into a semiconducting cinnabar-type structure, and upon further compression up to ~1–2 GPa, into the NaCl phase (α-HgS).

3.3 Synthesis

For the synthesis of mercury chalcogenides, one can use a variety of methods, such as various wet chemical methods; sonochemical [68], solvothermal [55], hydrothermal [57], and microwave-assisted synthesis [14]; and sol-gel technology [22]. They are described in detail in Chap. 11 (Vol. 1) for Cd- and Zn-based compounds. Mercury chalcogenides can be synthesized by reacting Hg and chalcogen by heating in sealed evacuated quartz ampoules. Single crystals can be grown by sublimation or growth from nonstoichiometric HgX melts in mercury [17]. The main difference in the synthesis of HgX-based compounds compared to that of their Cd- and Zn-based analogs is the use of lower synthesis temperatures, which indicates a significant difference in the reactivity of these compounds. α-HgS can also be obtained by triturating Hg with S. The compounds α-HgS, β-HgS, HgSe, and HgTe are also precipitated from aqueous solutions of Hg salts, such as $HgCl_2$, $HgBr_2$, mercury(II) acetate ($Hg(CH_3COO)_2$), and mercury(II) nitrate ($Hg(NO_3)_2$), using chemical bath deposition [27] and photochemical [53] and electrochemical [39, 50] methods. Epitaxial single-crystal HgX films can be obtained by the MOCVD method during the

decomposition of metalorganic compounds of chalcogen and mercury. Molecular beam epitaxy is also used to deposit epitaxial layers of mercury chalcogenides [16].

When interacting with Al, Ga, and In, mercury chalcogenides form semiconductor compounds of the type HgM_2X_4. On the basis of mercury chalcogenides, obtained are numerous solid solutions of the type $Hg_{1-x}M_xX$, $HgTe_{1-x}X_x$, and $HgSe_{1-x}X_x$, where M is Zn, Cd, and Mn, and x is the content of X or M in atomic fractions. Many of these solutions are gapless semiconductors. The main multicomponent compound based on mercury chalcogenides is $Hg_{1-x}Cd_xTe$, basic material of IR technology [54].

3.4 Chemical Properties

Mercury chalcogenides are practically insoluble in water and organic solvents and dilute mineral acids (H_2SO_4, HCl, HNO_3). They decompose in the Aqua Regia (HNO_3 + 3HCl). However, HgTe is easily etched even with dilute acids such as hydrobromic and hydroiodic acid (Eq. 3.1).

$$HgTe + 2HI \rightarrow HgI_2 + H_2Te \uparrow \tag{3.1}$$

The resulting hydrogen telluride is highly toxic, so HgTe is considered a toxic compound. Taking into account the abovementioned feature of HgX compounds for their polishing etching, etchants based on the solution Br_2 + CH_3OH were developed [8].

HgS also reacts with concentrated solutions of alkali metal sulfides to form M_2HgS_2 thiosalts, which are used to extract Hg from sulfide ores.

3.5 Stability

When heated in vacuum, mercury chalcogenides easily evaporate, dissociating into Hg and chalcogen (S, Se, Te). For example, when heating α-HgS in a closed vessel or in a sealed tube placed in an oven, at 380 °C, the sample was completely evaporated. The share of HgX molecules in a vapor did not exceed 10^{-4}. The same effect should also be observed for HgSe, since the HgSe components are also volatile. For HgTe, which contains Te with low vapor pressure, the situation is somewhat different.

Takita et al. [62] when studying HgTe have found that no changes in surface properties were observed when HgTe was heated in vacuum to temperatures of 160 °C. However, already at T above 180 °C, the backscattering spectra showed a significant change, which increased with increasing temperature and annealing time. It was found that these changes are associated with the dissociation of mercury from the surface of HgTe. At temperatures 230–250 °C, the Hg atoms are dissociated almost completely from the near-surface region and that the surface of the crystal is covered with Te atoms. The thickness of the surface Te layer increases with increasing temperature and annealing time. Figure 3.1 shows that already at temperatures of 180 °C, this thickness exceeds 100 nm.

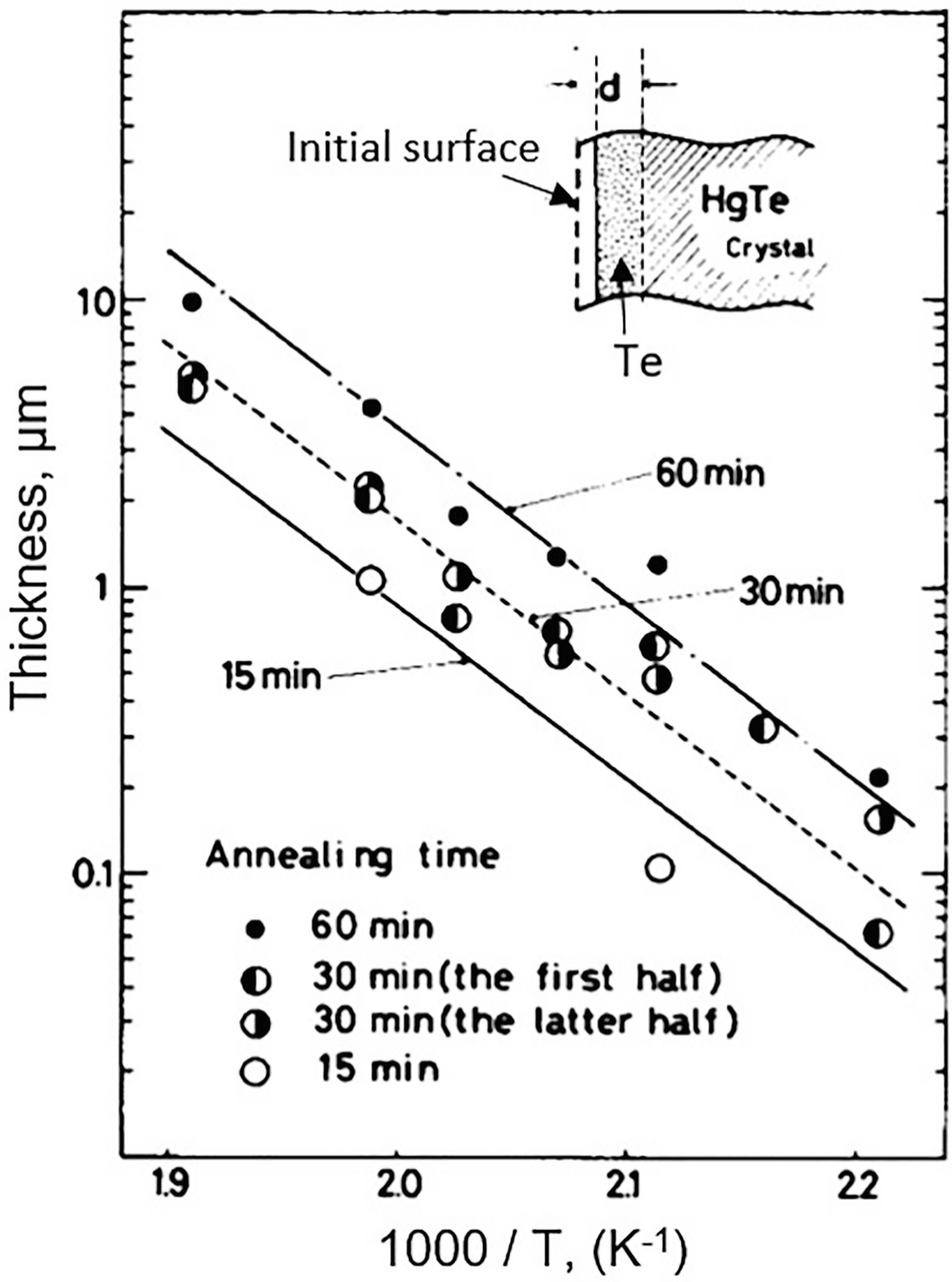

Fig. 3.1 Annealing temperature dependence of the depth d of the interface between the Te region and the HgTe crystal region; d is measured from the initial surface of the HgTe crystal as is schematically shown in the inset. (Reprinted with permission from Takita et al. [62]. Copyright 1980: AIP Publishing)

The equation for the temperature dependence of the HgX vapor pressure above the melt can be calculated using the expression (3.2) (Table 3.3):

Table 3.3 The value of the coefficients A and B

Compound	A	B	T, K	The main components of steam
α-HgS	6200	10.266	500–618	Hg, S_2-S_9
β-HgS	5814	9.633	774–924	Hg, S_2-S_9
HgSe	6445	9.610	613–1043	Hg, Se_2-Se_6
HgTe	5251	7.03	213–323	Hg, Te_2 (HgTe sublimates incongruently, p(Hg) >> p(Te_2))

$$\lg p\ (\mathrm{mmHg}) = -\mathrm{A}/\mathrm{T} + \mathrm{B} \tag{3.2}$$

When heated in air, mercury chalcogenides react with oxygen according to the reaction (Eq. 3.3)

$$\mathrm{HgX} + \mathrm{O_2} \rightarrow \mathrm{Hg} + \mathrm{XO_2}\ \ (\mathrm{SO_2}; \mathrm{SeO_2}) \tag{3.3}$$

Although as the studies reviewed in the previous chapter show, this process can be much more difficult.

3.6 Chemical Bond

In a simple chemical picture of Hg II–VI semiconductors, mercury contributes two *s* electrons to the bond, while chalcogen contributes two *s* electrons and four *p* electrons [58]. In Hg-based II–VI compounds, the bonds are rather covalent, and sp^3 hybrids predominate, as evidenced by tetrahedral coordination [66]. Compared to Ca, Sr, and Ba chalcogenides, the ionicity of Hg chalcogenides is reduced. The Hg *d* electrons are partially delocalized, and therefore the effective nuclear charge experienced by the valence electrons is increased. This results in the Hg valence electrons being more tightly bound. Therefore, it has a less ionic and more covalent bond. In this respect, these systems are very close to II-VI electronic semiconductors based on Cd and Zn, but with a larger proportion of covalent bonds. Their contribution is enhanced in the series HgS, HgSe, and HgTe. The delocalization of the *d*-shell in Hg is stronger than in Cd or Zn and is so strong that it causes the *s*-level to drop below the *p*-chalcogen level [11]. All of the above indicates that the bond in HgTe and HgSe is predominantly covalent.

3.7 Band Diagram

Figure 3.2 shows band structure of HgX compounds near the Γ-point from a hybrid quasi-particle self-consistent GW (QSGW) approach [61]. It should be noted that while switching from wide bandgap Cd- and Zn-based compounds to Hg-based II−VI semiconductors, the band ordering is considerably affected [19, 61].

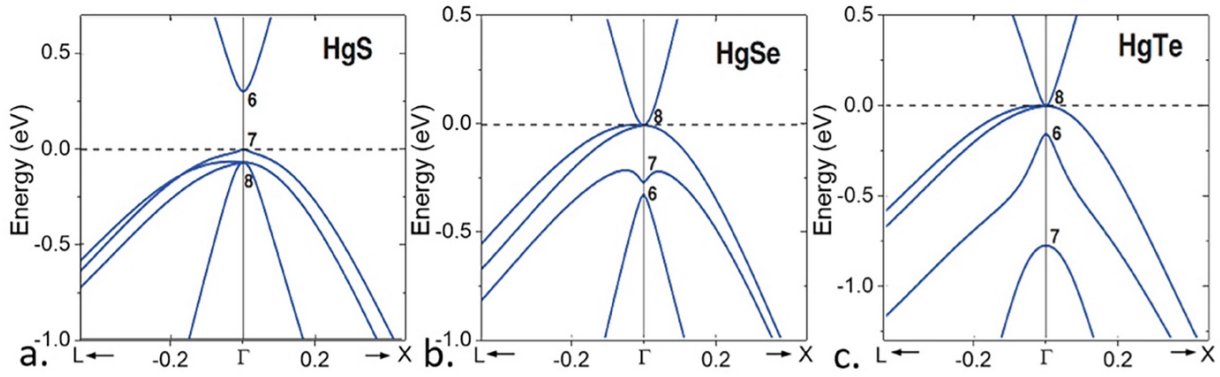

Fig. 3.2 (**a**) Band structure of HgS near the Γ-point from a hybrid QSGW approach. The unit along the x axis is 2π/*a*, with *a* = 0.584 nm. (**b**) Band structure of HgSe near the Γ point from a hybrid QSGW approach. The unit along the x axis is 2π/*a*, with *a* = 0.608 nm. (**c**) Band structure of HgTe near the Γ point from a hybrid QSGW approach. The unit along the x axis is 2π/*a*, with *a* = 0.647 nm. (Reproduced with permission from Svane et al. [61]. Copyright 2011 by the American Physical Society)

If we consider the usual definition of the bandgap, which is the difference between the top of the valence band Γ8 and the lowest conduction band Γ6, then these gaps for HgTe and HgSe turn out to be negative [19]. The Hg level *s*, the conduction band minimum (CBM), which forms the Γ6 symmetry state, falls below the p-like level Γ8, which is the valence band maximum (VBM). This is due to the large effective positive charge of the Hg nucleus. This inversion is generally formulated considering a negative bandgap value that describes the relative position of the Γ6 and Γ 8 bands. This value corresponds to a Γ6 value below the Fermi level. In HgTe, this negative bandgap is typically approximately −0.3 eV at 0 K [21], and it is reduced by approximately −0.15 eV at room temperature [42]. Because of the band ordering inversion, the conduction band in HgTe corresponds to the band with light hole symmetry in cadmium chalcogenides. This band is strongly dispersive and associated with a weak electron effective mass (typically 0.01–0.03 m_0) [42, 47]. This low value of the effective mass leads to the large carrier mobility (>10^3 $cm^2/V{\cdot}s$

and > 10^5 $cm^2/V{\cdot}s$ at room temperature and low temperature [5], respectively) observed in bulk HgTe.

In contrast, the valence band is almost flat, and the heavy hole mass is larger than 0.3 m_0 [42]. The Fermi level for the intrinsic HgTe lies between these two bands, which share the same energy at the Γ-point. This aspect is the second key characteristic of the bulk HgTe band structure: the degeneracy of the valence and conduction bands at the Γ-point causes HgTe to exhibit zero bandgap semiconductor characteristics, corresponding to a semimetal. This lack of a bulk bandgap is the reason for the ultrabroad tunability of the optical spectrum of HgTe NCs compared to that of the other semiconductors, for which the spectral tunability is limited by the material bulk bandgap [19]. In HgTe, the band edge energy can be designed to be arbitrarily narrow, thereby expanding the absorption of this material toward extremely large wavelengths in the infrared region. The optical absorption in HgTe occurs between the less dispersive valence band and conduction band. In this sense, the optical bandgap is always positive and should not be erroneously considered as the negative value mentioned previously, which only describes the band ordering. At the Γ-point, the two bands with Γ8 symmetry are mostly composed of *p* Te orbitals. Nevertheless, the strong band mixing in HgTe causes the wave functions to acquire the *s* nature from the Hg atoms as soon as the wave vector is moved away from the Γ-point.

HgSe presents a band structure similar to that of HgTe, although, quantitatively, the negative bandgap value is lower. HgSe can also be described as a zero bandgap semiconductor with an inverted band ordering. Nevertheless, the lower mass of Se compared to Te reduces the spin−orbit coupling, and the Γ7 band lies above the Γ6 band (see Fig. 3.2b). This means that HgSe like HgTe is a semimetal.

Among HgX materials, HgS appears to be an exception as a narrow bandgap semiconductor (212). The exact value of the bandgap is typically a few hundred meV [9, 41, 61]: a value of approximately 0.65 eV matches that reported in spectroscopy experiments with HgS NCs [9].

3.8 Specific Properties of Zero or Very Narrow Bandgap HgSe and HgTe

Wang et al. [67] note that only a few materials have a zero or very narrow bandgap with quadratic energy-momentum dispersion. Mercury telluride (HgTe) is one of the very few parent compounds of this class that have been extensively studied since the 1950s [65]. The energy gap of HgTe at 4.2 K is −0.30 eV. The intrinsic concentration of charge carriers (n) of the zero gap material depends on the temperature (T) according to the power law $n \propto T^{3/2}$. In an ordinary semiconductor with a discrete energy gap, n increases exponentially with temperature [65].

Because the edges of the conduction and valence bands intersect at the Fermi level, the transport and optical properties of zero-gap materials are extremely sensitive to physical perturbations. For example, a zero-gap band can be modified by electric and magnetic fields, as well as by pressure and chemical inhomogeneity. The electric fields act on the charge carriers, and the magnetic field changes the size of the gap, which in turn changes the density of the charge carriers. An increase in the average energy of electrons under the action of an external electric field leads to a nonlinear current–voltage curve. The energy gap can be opened by applying a magnetic field and external pressure, and the zero-gap state can be restored at a higher pressure, which leads to a change in resistivity by more than 4–6 orders of magnitude (see Fig. 3.3) [65].

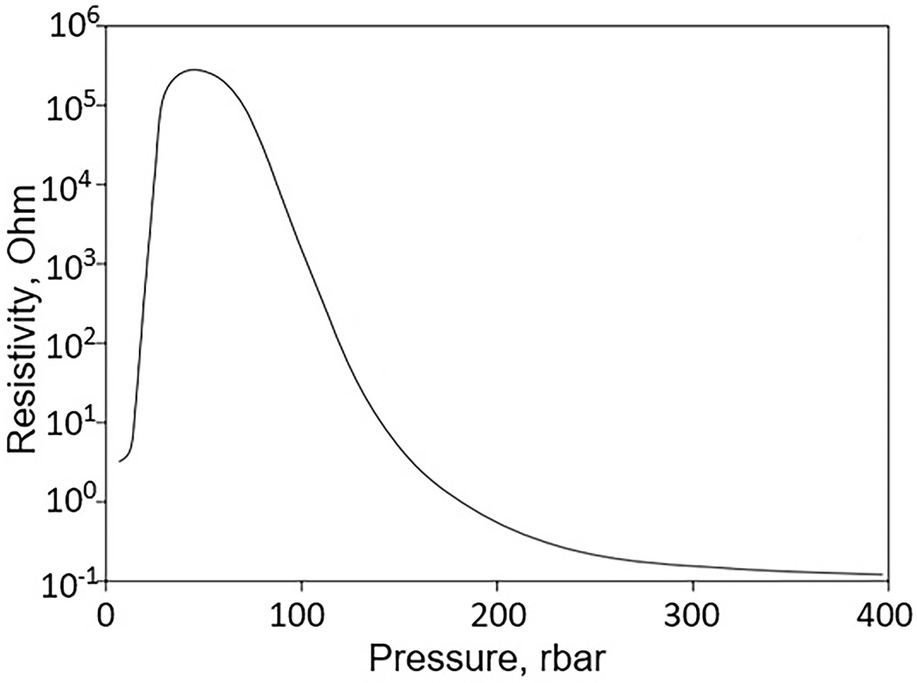

Fig. 3.3 Pressure dependence of resistivity of HgSe. (Inset) Inverted band model (reversed s and p bands) for HgTe. (Reprinted from Wang et al. [67]. Published 2010 by Springer Nature as open access)

In zero-gap mercury selenide (HgSe), another well-studied gapless material, the longitudinal magnetoresistance increases dramatically when the crystal is subjected to a magnetic field oriented parallel to the current direction. This component of the magnetoresistance increases exponentially with increasing magnetic field strength. Resistivity also depends markedly on pressure, as shown in Fig. 3.2. Pressure causes the transition of HgSe from a material with a zero bandgap to a semiconductor with a discrete energy gap and, ultimately, to a metal [65].

3.9 Physical Parameters

Tables 3.4 and 3.5 list the main physical parameters of Hg-based II-VI compounds. As we can see, just as for wide-gap II-VI compounds, the same regularities hold for narrow-gap II-VI compounds. Namely, as the ionicity of the bond in the compound increases, the lattice parameter decreases (Table 3.2) and the melting temperature and bandgap increase. At the same time, there is an increase in the effective mass and a decrease in the mobility of charge carriers (Table 3.6). A significant difference is observed only in the temperature behavior of the bandgap. In conventional wide bandgap semiconductors (CdTe, CdSe), the trend is to observe a redshift as the temperature increases, i.e., the bandgap decreases with increasing temperature. Bulk HgTe is an exception to this rule, exhibiting a positive value for dEg/dT.

Table 3.4 Main physical parameters of mercury chalcogenides

Parameter	α-HgS	β-HgS	HgSe	HgTe
Density, g/cm^3	8.19	7.71–7.73	8.24–8.26	8.08–8.42
Microhardness, MPa	–	30	230	350–370
Thermal expansion coefficient	$1.8\cdot10^{-6}$/K	$4.3\cdot10^{-6}$/K	$<2\cdot10^{-6}$/K	$5.2\cdot10^{-6}$/K
Thermal conductivity, W/cm·K	0.006	–	0.019	0.027
Thermopower coefficient, μV/grad	−120	–	−(40–95)	−(80–145)
Dielectric constant,				
ε (static)	30.7		25.2–25.6	20–48.0

Parameter	α-HgS	β-HgS	HgSe	HgTe
ε (dynamic)				14.4–15.1
Refractive index			5.06	3.79

Source: Data extracted from Abrikosov et al. [1]

Table 3.5 Main energy parameters of mercury chalcogenides

Parameter	α-HgS	β-HgS	HgSe	HgTe
Melting point, °C	583	825–1540	790–800	670
C_p^0, J/mol·K	48.41	48.5	54.5	55.30
ΔH^0, kJ/mol	−57.6	−49.4	−59.4	−32.17
S^0(298 K), J/mol·K	82.4	88.7	99.02	111.50
Heat of atomization, kcal/atom		47	42	37
Atomization energy, kJ/mol		393	352	310
Energy bandgap, eV	1.78–2.0	0.5–0.65	0–0.12	0.08 – (−0.261)
Electronegativity difference	0.6	0.6	0.5	0.2

Table 3.6 Main electrophysical parameters of mercury chalcogenides

Parameter	α-HgS	β-HgS	HgSe	HgTe
Conductivity type		*n*	*n*	*n*, *p*
Electron effective mass, m_e/m_o	–	–	0.04–0.05	0.02–0.04
Electron Hall mobility at 77 K, $cm^2/V{\cdot}s$	38	250–350	$(1.4–8){\cdot}10^4$	$(1.2–2.5){\cdot}10^5$
Electron Hall mobility at 300 K, $cm^2/V{\cdot}s$			$1.8{\cdot}10^4$	$2.5{\cdot}10^4$
Hole mobility, $cm^2/V{\cdot}s$ (300 K)		15	–	100
Resistivity, ρ, Ohm·cm	10^9–10^{12}	–	$7{\cdot}10^{-4}$	$5{\cdot}10^{-4}$

HgX bonds are weak. For example, the enthalpy of formation of HgTe, about −32 kJ/mol, is less than a third of that of the related compound, cadmium telluride.

Other physical parameters of mercury chalcogenides can be found in [4, 15].

3.10 Electrophysical Properties

Mercury chalcogenides are nonstoichiometric compounds. The homogeneity range of HgSe is 49.99–50.00 at.% Hg at 280 °C (according to other data, a deviation from stoichiometry towards a higher Hg content is observed). The homogeneity region of HgTe is 49.40–49.95 at.% Hg at 400 °C and 49.40–50.009 at.% Hg at 353 °C. This means that the composition of the HgX may have significant deviations from the stoichiometric composition. Therefore, the properties of HgX are largely determined by the degree of deviation from the stoichiometric composition and the concentration of point defects that affect the electrical properties as atoms of foreign impurities. For mercury chalcogenides, the predominant types of defects are Hg and chalcogen vacancies and Hg atoms in the interstitial space. Their concentration depends on the conditions of synthesis and subsequent heat treatments, and therefore the data of different researchers on the electrical parameters of HgX compounds are contradictory.

Table 3.6 shows the main electrophysical properties of mercury chalcogenides. As we can see, HgTe is a p- and n-type semiconductor. However, mostly HgTe has p-type conductivity. HgTe samples are p-type due to Hg vacancies. At the same time, HgSe and HgS are n-type semiconductors. The n-type conductivity of the HgSe and HgS compounds is explained by the incorporation of mercury atoms into interstices or by vacancies in the selenium and sulfur sublattices. For HgSe crystals with an electron concentration of at least $3.5 \cdot 10^{17}$ cm^{-3}, their mobility reaches 18,500 $cm^2/(V \cdot s)$ at 300 K. It is not possible to obtain p-type mercury selenide by doping. The study of thermo- and galvanomagnetic effects in mercury selenide showed that the mobility of electrons in it is limited by scattering by acoustic phonons. This serves as evidence for the predominant covalent interatomic bond in mercury selenide.

According to the electrical properties, HgTe and HgSe are semimetals, that is, at 0 K, the valence bands are in contact and even overlap. Therefore, unlike semiconductors, its conductivity is not equal to 0 at 0 K, but, like semiconductors, it increases with increasing temperature due to for the overlap of the valence and conduction bands.

3.11 Doping

Similarly, with wide-gap II-VI semiconductors, n-type doping in narrow gap II-VI compounds can be achieved with elements such as boron, aluminum, gallium, or indium. Iodine and iron will also dope the n-type. P-type doping can be achieved by introducing zinc, copper, silver, or gold. However, in practice, in narrow-gap compounds, changes in the concentration and type of carriers in undoped materials are associated largely with the features of the band structure of narrow bandgap compounds and the deviation of their composition from stoichiometric. Specifically, the high carrier density in HgX cannot be attributed to the introduction of extrinsic impurities. Lhuillier and co-workers [19, 37] believe that the high carrier density results from two processes. The first process is self-doping (i.e., doping that occurs without the introduction of extrinsic impurities), which can lead to degenerate doping. The Fermi level lies within the conduction band. The second process is observed in small HgX nanocrystals (NCs) (diameter less than 12 nm) and corresponds to thermal activation. In addition, thermal activation originates from material nonstoichiometry.

In addition, it has been found that the efficiency of dopants depends on the material to be doped [4]. For example, in the case of HgTe, copper turns out to be an acceptor impurity with a doping efficiency of about unit, while Al is an insufficiently effective donor impurity to transfer a p-type material to an n-type, although the concentration of free holes somewhat decreases in this case. If these data are compared with the results obtained during annealing in mercury vapor of samples doped with indium, then the inefficiency of alloying Al atoms in pure HgTe can be explained by the effect of their compensation by atomic point defects or lattice defects. In the case of HgSe, aluminum is a donor impurity, while copper does not affect the electrical properties. For HgSe-HgTe alloys, the efficiency of copper as an acceptor impurity, and aluminum as a donor impurity, varies smoothly depending on the composition between two extreme values characteristic of pure compounds. For example, in the $HgTe_{0.5}Se_{0.5}$ alloy, both elements are effective dopants [4].

It must be recognized that despite the notable progress that has been made to enhance the knowledge of doping of II-VI compounds and its

tenability [8], the amount of works dedicated to doping in HgX and especially in HgX-based NCs remains inadequate.

3.12 Applications

Taking into account the bandgap of mercury chalcogenides, these materials are primarily of interest for the creation of various IR photodetectors, since they provide effective absorption in the spectral region covering the short-, mid- and long-wavelength infrared spectral ranges. This is a very important area of application because active imaging, night glow imaging, and tissue imaging devices are being developed in this wavelength range [37]. Kovalenko et al. [30], Keuleyan et al. [28], and Green and Mirzai [20] showed that HgTe and HgSe represent huge opportunities for these applications.

In the mid-wavelength infrared (MWIR: 3–5 μm), HgTe and HgSe are of interest due to the tunable band-to-band IR transition; see Fig. 3.4d. Another strategy to achieve a low energy transition in MWIR is to use intraband transitions (see Fig. 3.4b, d) [12, 24, 29]. In this case, the transition occurs at the first levels of the conduction band, so doped semiconductors are needed [37]. Due to self-doping, mercury chalcogenides make it possible to realize this possibility as well [12, 24, 29].

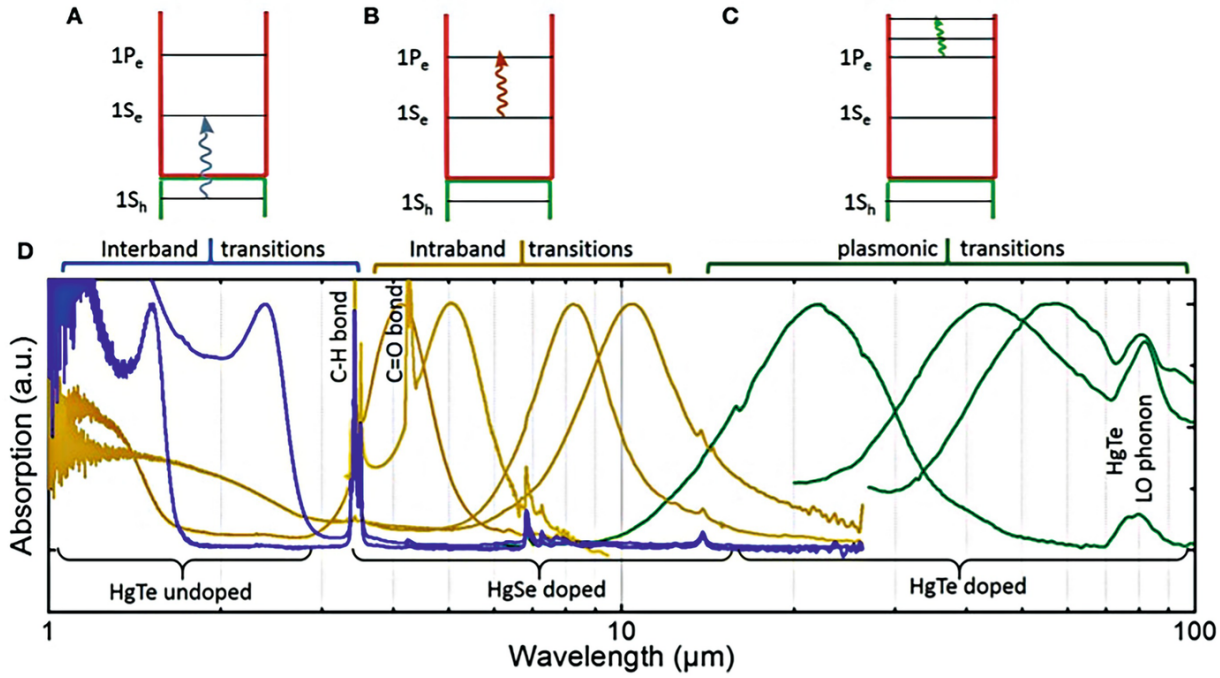

Fig. 3.4 (**A**–**C**) are, respectively, the scheme for interband, intraband, and plasmonic transitions in nanocrystals. (**D**) Absorption spectra for mercury chalcogenide (HgSe and HgTe) nanocrystals of various sizes. (Reprinted from Livache et al. [37]. Published 2018 by Frontiers Media as open access)

Long-wave infrared (LWIR: 5–30 μm) is the optimal range to perform thermal imaging of room-temperature objects since their blackbody emission maximum lies around 10 μm. Addressing such low energy with interband transitions is extremely challenging, since the confinement energy needs to be so small that the required size of nanocrystals becomes incompatible with colloidal stability or monodispersity. Studies have shown the intraband [49] and plasmonic transitions [2, 3, 10, 33, 38] in doped HgTe and HgSe nanocrystals, see Fig. 3.4c, d, are also interesting for such applications [37].

All of the above indicates that photodetectors based on HgTe and HgSe nanocrystals can cover the entire spectral range from 1 to 100 μm and further up to the THz range [37, 63]. In this case, the observed IR transition will be controlled by the degree of doping of mercury chalcogenides. When the size of particles is small, confinement reduces the doping, and this is mostly interband absorption that is observed. When confinement is reduced but is still present (typically in the 3–12 μm range), intraband absorption, which is the 0D analog of the intersubband absorption in quantum wells, is observed [25, 31, 38, 40]. When doping is vanishing or doping level is very high, the density of state becomes dense, and the optical feature acquires more and more a metallic nature, leading to the observation of plasmonic transitions [7, 18, 36]. This unique combination with various types of transitions and their tunability, thanks to doping and quantum confinement, make that mercury chalcogenides are the most tunable nanocrystals. The energy of the first excitonic feature can be tuned by almost two orders of magnitude. For the sake of comparison, in CdSe, quantum confinement offers not more than 30% of tunability for the energy of the excitonic feature.

Superlattices are another important application for mercury chalcogenides. The band structures of these superlattices exhibit unique features that are distinct from those found in either Hg-based alloys or in wide-gap superlattices [23]. In particular, Meyer et al. [46] found that HgTe/CdTe superlattice has yielded the highest p-type mobilities ever reported for a II-VI semiconductors ($>10^5$ cm^2/Vs at $T < 30$ K) (Fig. 3.5). The unique nature of narrow gap HgTe-CdTe superlattice band structures makes them attractive for a variety of electronic and electro-optical

applications. Indeed, promising infrared applications of these superlattices were discussed theoretically as early as 1979 [59]. Studies have shown that the same prospects in the field of IR technology have supperlattice based on HgTe/CdHgTe quantum wells heterostructures [32, 54].

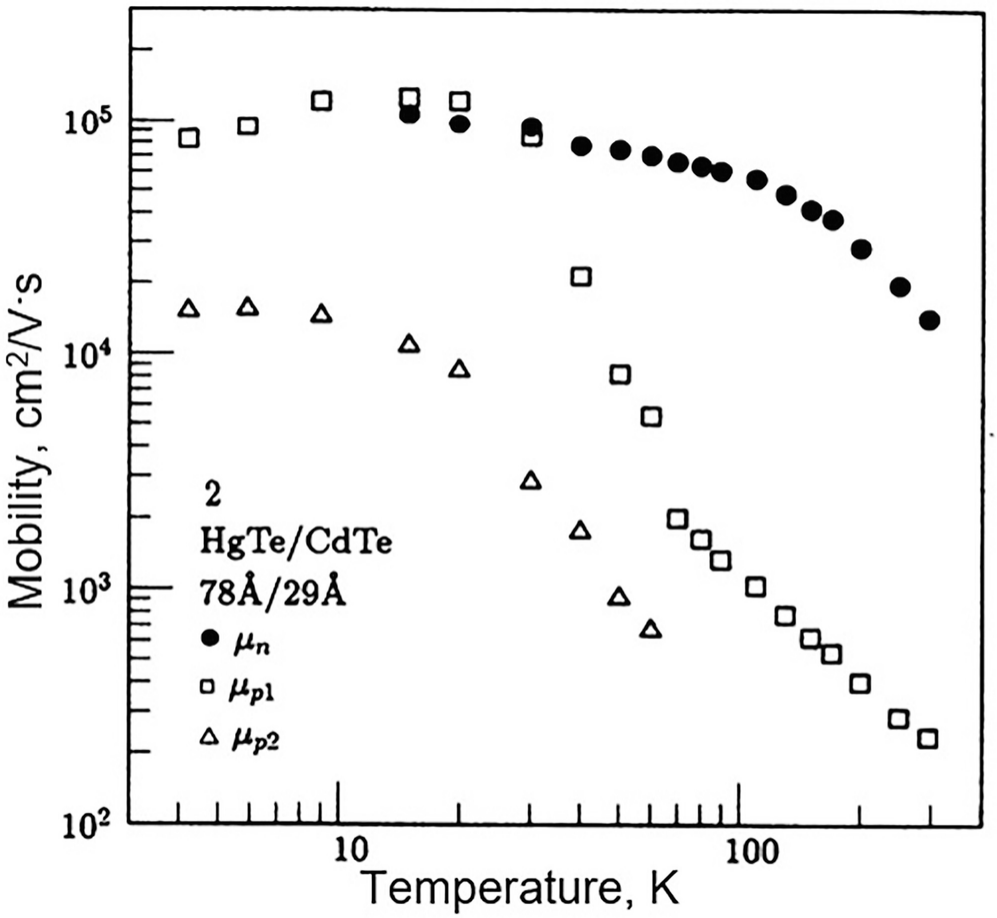

Fig. 3.5 Experimental electron and hole mobilities vs temperature for HgTe/CdTe supperlatice. The superlattice was grown by molecular-beam epitaxy. (Reprinted with permission from Meyer et al. [46]. Copyright 1988: Am. Phys. Soc.)

Lhuillier and co-workers [36] have shown that based on QDs of HgSe and HgTe, it is possible to develop IR photodetectors, which are similar in principle to photodetectors based on superlattice (see Fig. 3.6). They demonstrated that the energy landscape of infrared photodetectors with quantum wells and quantum dots can be simulated from a mixture of mercury selenide and mercury telluride nanocrystals. They also found that this metamaterial combines intraband absorption with improved transport properties (i.e., low dark current, fast time response, and high thermal activation energy). Photodiodes based on this material demonstrated the

highest infrared detection performance reported for intraband-based nanocrystal IR detectors.

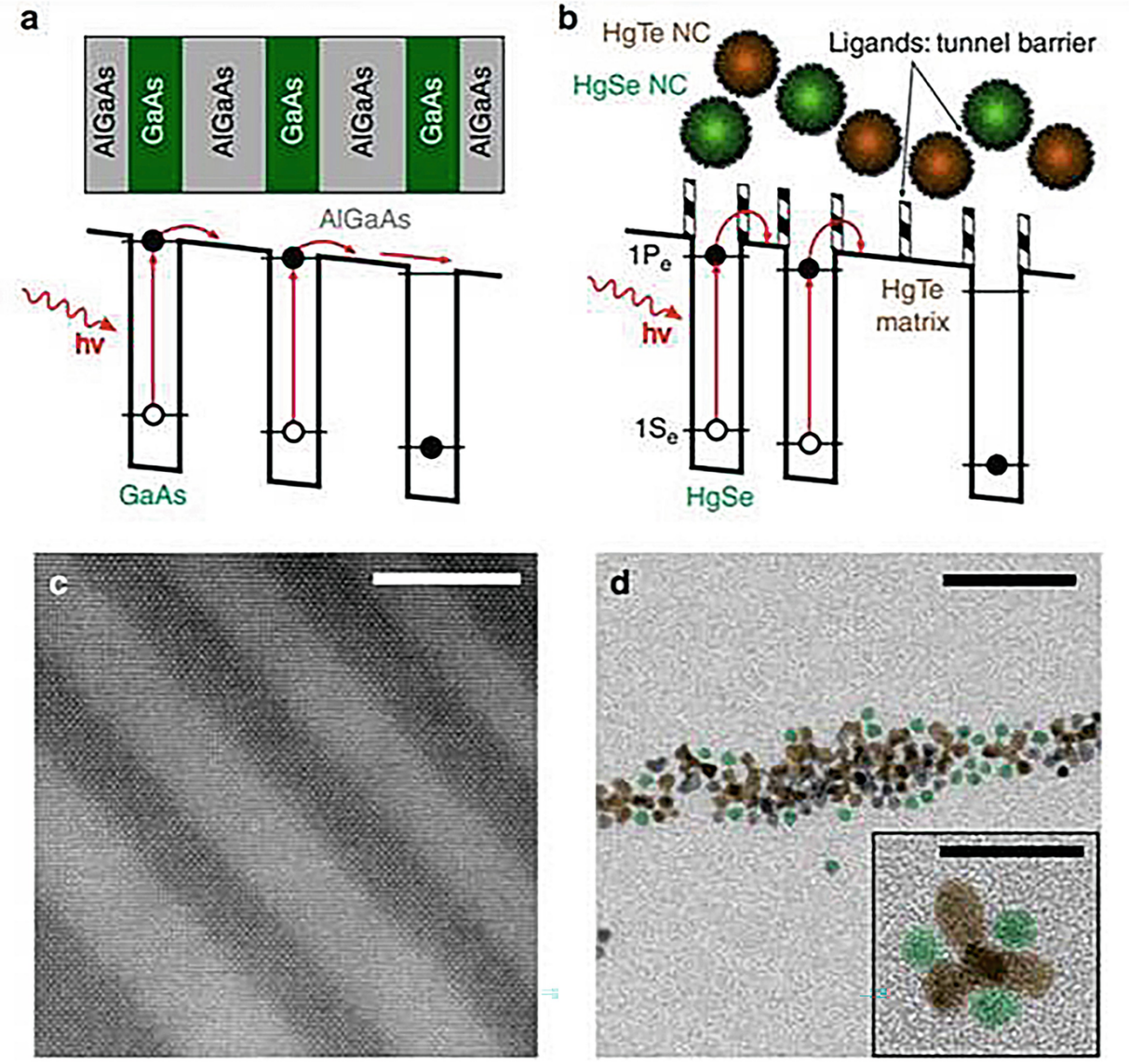

Fig. 3.6 Principle of operation for a random colloidal quantum dot infrared photodetector (CQDIP). (**a**) Scheme of a standard GaAs/AlGaAs quantum well infrared photodetector (QWIP) band structure under polarization. (**b**) Scheme of polarized band structure of a random CQDIP consisting of HgSe nanocrystals (NCs) as absorber material and HgTe NCs as barrier material. (**c**) Transmission electron microscopic (TEM) image of an epitaxially grown GaAs/AlGaAs QWIP structure. GaAs quantum wells are shown in dark. Scale bar is 20 nm. (**d**) TEM image of mixed HgSe and HgTe NCs for random CQDIP fabrication. Some HgSe (resp. HgTe) NCs have been colored in green (resp. brown). Scale bar is 50 nm. Inset: higher-resolution TEM image showing a HgTe tetrapod along with three HgSe spheres. Scale bar is 20 nm. (Reprinted from Livache et al. [36]. Published 2019 by Springer Nature as open access)

Narrow-gap selenides and tellurides have a very high electron mobility, which means large values of the Hall constant and magnetoresistance. Their high sensitivity to a magnetic field makes it possible to use these materials as Hall sensors – devices for measuring the intensity of constant and variable magnetic fields, wattmeters, generators of electrical oscillations, etc. Pool et al. [51] found that doping HgSe and HgTe with magnetic ions such as manganese or iron improves their magnetic properties. Liu and Guyot-Sionnest [34] also studied HgS nanoparticles doped with Mn (up to 15%) and observed an enhanced magnetoresistance with a higher Mn content. It was established that such doping can lead to giant magnetoresistance in HgTe or HgSe [51], making doped HgSe and HgTe a suitable material for magnetoelectronics and magnetic-field sensor applications, where extremely high sensitivity is required. In zero-gap HgMnTe, the transverse magnetoresistance first increases sharply with increasing magnetic field and then falls rather abruptly. The longitudinal magnetoresistance, however, decreases monotonically. This evolution in magnetoresistance with magnetic field strength is caused by magnetic field-induced band adjustments [65]. HgMnTe and HgMnSe change from a paramagnetic state to a spin-glass state at a critical temperature (T_s) as a result of the collapse of the antiferromagnetic interaction in the face-centered cubic lattice. Thus, in addition to their use in infrared photodetectors, zero-gap HgTe and HgSe are also useful as Hall and magnetoresistance sensors and as spin photoconductors [65]. The physics and applications of these classical zero-gap materials have been discussed in detail in [65].

Due to high mobility of the electrons, HgTe and HgSe are an ideal matrix to study additional quantization effects in low-dimensional structures and semimagnetic properties [60]. The cubic Hg II–VI systems β-HgS, HgSe, and HgTe are technologically interesting materials with application in quantum electronics [11]. They form part of several artificial nanostructured materials [11]. In particular, it was found that mercury chalcogenides have the properties of a topological insulator [6], several facets of them exhibit surface states with spin-momentum locking [64]. At the same time, it was established that spin-filtered surface conduction channels have been found to classify topological insulator (TI) materials into a class of their own and give them physical properties, suitable for discovering new quantum phenomena and advanced applications such as

topological quantum computing. A topological insulator is a material that behaves as an insulator in its interior but whose surface contains conducting states [48], meaning that electrons can only move along the surface of the material. Важно отметить, что temperature-driven topological phase transition was also observed in HgTe/CdHgTe quantum wells [26, 70].

In addition, natural cinnabar (HgS) is the main industrial raw material in the production of Hg. HgS can also be used as a material for photoresistors, catalysts, pigments, and light components for CdS-based phosphors.

There has also been a great interest in thin films of ternary alloys containing HgSe and HgTe as a base material in spintronic and optoeletronic devices such as IR emitters and tunable lasers [39]. In particular, Qu et al. [56] demonstrated a SWIR LED based on ITO/ZnO/HgTe-ZnO/PbS/gold stacked structure (Fig. 3.7a). The emitting layer consists of a mixture of ZnO and HgTe nanocrystals which enables the formation of a bulk heterojunction with ambipolar conduction and allows one to tune the hole injection within the emitted layer. This diode being based only on inorganic layers shows great promises to also address longer wavelengths in the future. The LED achieves sub-bandgap turn on voltage (30 h) and broad spectral tunability from 1250 to 1600 nm (see Fig. 3.7b). Even though the EQE remains modest (0.67%), the diode achieves high brightness (9 $W \cdot Sr^{-1} \cdot m^{-2}$) at relatively low current density due to a high onset of external quantum efficiency (EQE) droop.

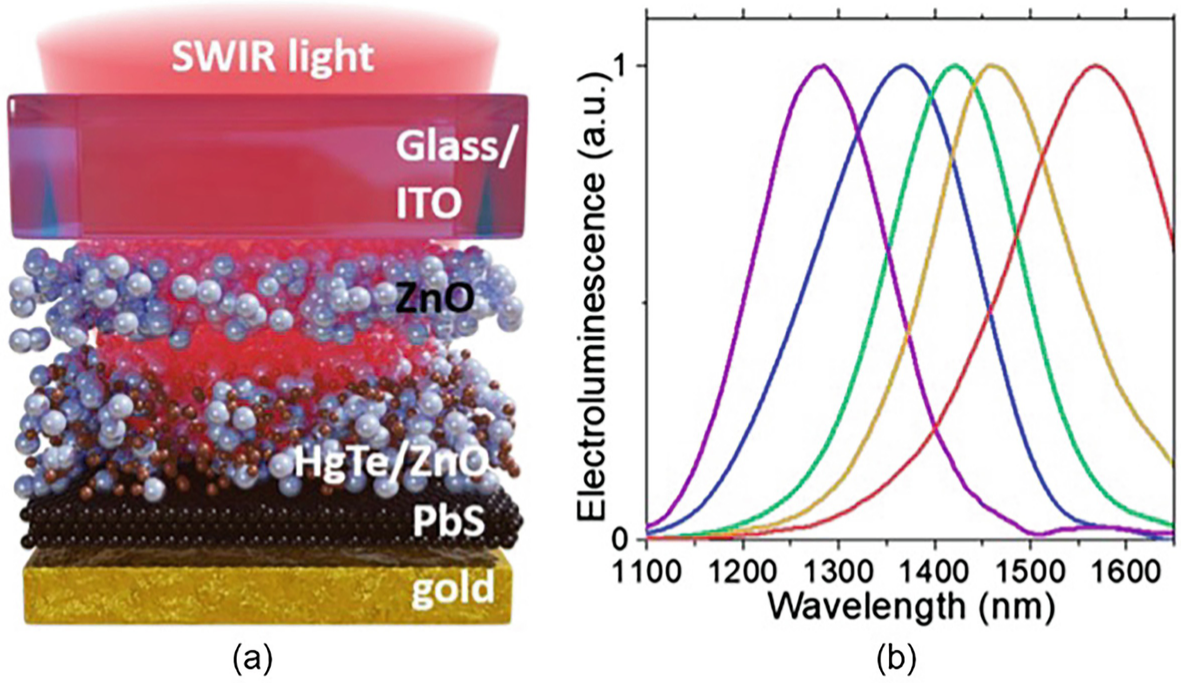

Fig. 3.7 (**a**) Scheme of a diode made of ITO/ZnO/ZnO-HgTe/PbS/Au-emitting SWIR light; (**b**) normalized electroluminescence spectra obtained from various HgTe NCs in the diode depicted in part (**a**). (Reprinted with permission from Qu et al. [56]. Copyright 2020: ACS)

Obtaining low-resistance ohmic contacts has been a major challenge in optical device technology based on ZnSe and CdTe. But recent studies have proven the possibility of the ohmic contact between HgSe and ZnSe and between HgTe and CdTe.

Thermoelectric converters [45] are another possible area of HgS, HgTe, and HgSe application. Markov et al. [44] studied the electronic transport properties of HgTe. They calculated the thermal conductivity of the lattice using first principles and estimated the overall figure of merit both theoretically and experimentally. They showed that heavily doped HgTe, a semimetal with a large difference in electron and hole masses, has a high thermoelectric power factor comparable to the best-known thermoelectric materials (Fig. 3.8). This means that semiconductors, such as semimetals with a large asymmetry between the conduction and valence bands, represent an alternative class of promising thermoelectric materials. Subsequent studies confirmed the hypothesis that materials with no bandgap but with a large mass ratio can have large Seebeck coefficient values comparable to those of heavily doped semiconductors [43]. This is in good agreement with previous results indicating that *a*-HgS and HgSe had Seebeck coefficient values exceed 100 μV/K [52, 69].

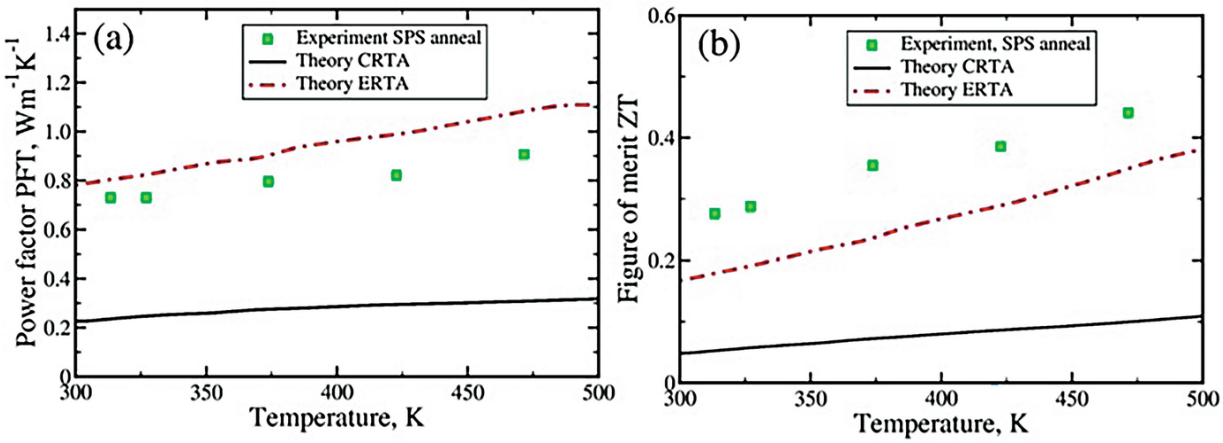

Fig. 3.8 Temperature variation of the power factor $P_F = S^2\sigma T$ (**a**) and thermoelectric figure of merit $zT = P_F/k$ (**b**), measured in the experiment (green squares) and calculated using various approaches (CRTA – black solid line, ERTA – red dashed-dotted line). S– Seebeck coefficient, σ is the electrical conductivity, κ is the thermal conductivity, and T is the absolute temperature. (Reprinted from Markov et al. [44]. Published 2018 by Springer Nature as open access)

3.13 Limitations

It should be noted that despite the undeniable advantages of mercury chalcogenides, their use in the development of various devices encounters some difficulties associated with the following problems [19, 37]:

- Long capping ligands are used to stabilize colloidal particles, which ensure the nanometer size growth and preserve the colloidal stability. However, this limits the interaction of QDs and, as a result, reduces carrier mobility. Therefore, a new surface chemistry is needed that would allow the removal of long capping ligands from the surface of HgSe and HgTe in order to reduce the inter QD tunnel barrier and obtain reasonable carrier mobility.
- Another major problem associated with the use of mercury chalcogenides is related to the softness of the material. As a result, any annealing step (to boost the mobility or as part of a lithography process) leads to sintering of the nanocrystal film. This induces an increase of the QD effective radius, which broadens the absorption cutoff and, even worse, dramatically increases the dark current (through a reduction of the effective bandgap). Thus, core-shell objects with an external material, which is able to sustain temperatures around 160 °C (i.e., typical baking

temperature of lithography resist such as polymethyl methacrylate) without aggregation will be of utmost interest.

- Long-term instability of QDs-based device is a problem which has been largely hushed up. It is convenient to admit that stability of QDs based on HgSe or HgTe is higher than the one of organic materials, but data on this issue are clearly insufficient. Therefore, stability is the main issue that needs to be addressed. The aim is that the material can be used without permanent damage at temperatures up to 60 °C and must be suitable for processing with limited damage up to 150 °C. Unfortunately, these goals have not yet been achieved.
- Thermal instability and oxidation of mercury chalcogenides also create certain difficulties in the manufacture of devices and ensuring their long-term operation.
- The toxicity of mercury chalcogenides, especially their aerosols and solutions, is another important limitation of the use of mercury chalcogenides.

Acknowledgments

G.K. and D.N. are grateful to the State Program of the Republic of Moldova (project 20.80009.5007.02) for supporting their research.

References

1. Abrikosov NK, Bankina VF, Poretskaya LV (1975) Semiconductor chalcogenides and alloys based on them. Nauka, Moscow, pp 48–82. (in Russian)
2. Agrawal A, Johns RW, Milliron DJ (2017) Control of localized surface plasmon resonances in metal oxide nanocrystals. Annu Rev Mater Res 47:1–31. https://doi.org/10.1146/annurev-matsci-070616-124259 [Crossref]
3. Askari S, Mariotti D, Stehr JE, Benedikt J, Keraudy J, Helmersson U (2018) Low-loss and tunable localized mid-infrared plasmons in nanocrystals of highly degenerate InN. Nano Lett 18:5681–5687. https://doi.org/10.1021/acs.nanolett.8b02260 [Crossref]
4. Baransky PI, Klochkov VP, Potykevich IV (1975) Semiconductor electronics. Handbook. Naukova Dumka, Kiev, p 581. (in Russian)
5. Bendias K, Shamim S, Herrmann O, Budewitz A, Shekhar P, Leubner P, Kleinlein J, Bocquillon E, Buhmann H, Molenkamp LW (2018) High mobility HgTe microstructures for quantum spin Hall studies. Nano Lett 18:4831–4836

6. Bernevig BA, Hughes TL, Zhang S-C (2006) Quantum spin Hall effect and topological phase transition in HgTe quantum wells. Science 314:1757–1761
7. Brown PR, Kim D, Lunt RR, Zhao N, Bawendi MG, Grossman JC, Bulović V (2014) Energy level modification in Lead Sulfide quantum dot thin films through ligand exchange. ACS Nano 8(6):5863–5872
8. Capper P (ed) (1997) Narrow-gap II-VI compounds for optoelectronic and electromagnetic applications. Chapman and Hall, London
9. Chen M, Guyot-Sionnest P (2017) Reversible electrochemistry of mercury chalcogenide colloidal quantum dot films. ACS Nano 11:4165–4173
10. Coughlan C, Ibáñez M, Dobrozhan O, Singh A, Cabot A, Ryan KM (2017) Compound copper chalcogenide nanocrystals. Chem Rev 117:5865–6109. https://doi.org/10.1021/acs.chemrev.6b00376
[Crossref]
11. Delin A, Kluner T (2002) Exitation spectra and ground-state properties from density-functional theory for the inverted bandstructure systems β-HgS, HgSe and HgTe. Phys Rev B 66:1–8
12. Deng Z, Jeong KS, Guyot-Sionnest P (2014) Colloidal quantum dots intraband photodetectors. ACS Nano 8:11707–11714. https://doi.org/10.1021/nn505092a
[Crossref]
13. Dickson FW, Tunell G (1959) The stability relations of cinnabar and metacinnabar. Am Mineral 44:471–487
14. Ding T, Zhu J (2003) Microwave heating synthesis of HgS and PbS nanocrystals in ethanol solvent. Mater Sci Eng B 100:307–313
15. Duz I, Erdem I, Ozdemir KS, Kuzucu V (2016) First principles investigations of HgX(X=S, Se, Te). Arch Mater Sci Eng 79(1):5–11
16. Einfeldt S, Heinke H, Behringer M, Becker CR, Kurtz E, Hommel D et al (1994) The growth of HgSe by molecular beam epitaxy for ohmic contacts to p-ZnSe. J Cryst Growth 138:471–476
17. Goubet N, Thomas M, Gréboval C, Chu A, Qu J, Rastogi P et al (2020) Near to long-wave infrared mercury chalcogenide nanocrystals from liquid mercury. J Phys Chem C 124(15):8423–8430
18. Goubet N, Jagtap A, Livache C, Martinez B, Portalès H, Xu XZ et al (2018) Terahertz HgTe nanocrystals: beyond confinement. J Am Chem Soc 140(15):5033–5036
19. Gréboval C, Chu A, Goubet N, Livache C, Ithurria S, Lhuillier E (2021) Mercury chalcogenide quantum dots: material perspective for device integration. Chem Rev 121(7):3627–3700
20. Green M, Mirzai H (2018) Synthetic routes to mercury chalcogenide quantum dots. J Mater Chem C 6:5097–5112. https://doi.org/10.1039/C8TC00910D
[Crossref]

21. Groves SH, Brown RN, Pidgeon CR (1967) Interband magnetoreflection and band structure of HgTe. Phys Rev 161:779–793
22. Guglielmi M, Martucci A, Fick J, Vitrant G (1998) Preparation and characterization of $Hg_xCd_{1-x}S$ and $Pb_xCd_{1-x}S$ quantum dots and doped thin films. J Sol-Gel Sci Technol 11:229–240
23. Hoffman CA, Meyer JR, Bartoli J (1989) Transport properties of narrow gap II-VI superlattices. MRS Proc 161:403–411
24. Jagtap A, Livache C, Martinez B, Qu J, Chu A, Gréboval C et al (2018) Emergence of intraband transitions in colloidal nanocrystals. Opt Mater Express 8:1174–1183. https://doi.org/10.1364/OME.8.001174
[Crossref]
25. Jeong KS, Deng Z, Keuleyan S, Liu H, Guyot-Sionnest P (2014) Air-stable n-doped colloidal HgS quantum dots. J Phys Chem Lett 5(7):1139–1143
26. Kadykov AM, Krishtopenko SS, Jouault B, Desrat W, Knap WM, Ruffenach S et al (2018) Temperature-induced topological phase transition in HgTe quantum wells. Phys Rev Lett 120:086401
27. Kale SS, Lokhande CD (1999) Preparation and characterization of HgS films by chemical deposition. Mater Chem Phys 59:242–246
28. Keuleyan S, Lhuillier E, Brajuskovic V, Guyot-Sionnest P (2011) Mid-infrared HgTe colloidal quantum dot photodetectors. Nat Photonics 5:489–493. https://doi.org/10.1038/nphoton.2011.142
[Crossref]
29. Kim J, Choi D, Jeong KS (2018) Self-doped colloidal semiconductor nanocrystals with intraband transitions in steady state. Chem Commun 54:8435–8445. https://doi.org/10.1039/C8CC02488J
[Crossref]
30. Kovalenko MV, Kaufmann E, Pachinger D, Roither J, Huber M, Stangl J et al (2006) Colloidal HgTe nanocrystals with widely tunable narrow band gap energies: from telecommunications to molecular vibrations. J Am Chem Soc 128:3516–3517. https://doi.org/10.1021/ja058440j
[Crossref]
31. Kroupa DM, Vörös M, Brawand NP, McNichols BW, Miller EM, Gu J, Nozik AJ, Sellinger A, Galli G, Beard MC (2017) Tuning colloidal quantum dot band edge positions through solution-phase surface chemistry modification. Nat Commun 8(1):15257
32. Kudryavtsev KE, Rumyantsev VV, Aleshkin VY, Dubinov AA, Utochkin VV, Fadeev MA et al (2020) Temperature limitations for stimulated emission in 3–4 lm range due to threshold and non-threshold Auger recombination in HgTe/CdHgTe quantum wells. Appl Phys Lett 117:083103
33. Liu Z, Janes LM, Saniepay M, Beaulac R (2018) Charge storage and quantum confinement resilience in colloidal indium nitride nanocrystals. Chem Mater 30:5435–5443. https://doi.org/10.1021/acs.chemmater.8b02340

[Crossref]
34. Liu H, Guyot-Sionnest P (2015) Magnetoresistance of manganese-doped colloidal quantum dot films. J Phys Chem 119(26):14797–14804
35. Livache C, Goubet N, Gréboval C, Martinez B, Ramade J, Qu J et al (2019a) Effect of pressure on interband and intraband transition of mercury chalcogenides quantum dots. J Phys Chem 123(20):13122–13130
36. Livache C, Martinez B, Greboval C, Lhuillier E (2019b) A colloidal quantum dot infrared photodetector and its use for intraband detection. Nat Commun 10(1):2125
37. Livache C, Martinez B, Goubet N, Ramade J, Lhuillier E (2018) Road map for nanocrystal based infrared photodetectors. Front Chem 6:575
38. Luther JM, Jain PK, Ewers T, Alivisatos AP (2011) Localized surface plasmon resonances arising from free carriers in doped quantum dots. Nat Mater 10:361–366. https://doi.org/10.1038/nmat3004
[Crossref]
39. Mahalingam T, Kathalingam A, Sanjeeviraja C, Chandramohan R, Chu JP, Kim YD, Velumani S (2007) Electrodeposition and characterization of HgSe thin films. J Mater Character 58:735–739
40. Martinez B, Livache C, Notemgnou Mouafo LD, Goubet N, Keuleyan S, Cruguel H et al (2017) HgSe self-doped nanocrystals as a platform to investigate the effects of vanishing confinement. ACS Appl Mater Interfaces 9(41):36173–36180
41. Madelung O (2012) Semiconductors: data handbook. Springer
42. Man P, Pan DS (1991) Infrared absorption in HgTe. Phys Rev B 44:8745–8758
43. Markov M, Rezaei E, Nayeb SS, Esfarjani K, Zebarjadi M (2019) Thermoelectric properties of semimetals. https://arxiv.org/abs/1905.08282
44. Markov M, Hu X, Liu H-C, Liu N, Poon SJ, Esfarjani K, Zebarjadi M (2018) Semi-metals as potential thermoelectric materials. Sci Rep 8:9876
45. Mathe MK, Cox SM, Venkatasamy V, Happek U, Stickney JL (2005) Formation of HgSe thin films using electrochemical atomic layer epitaxy. J Electrochem Soc 152(11):751–755
46. Meyer JR, Hoffman CA, Bartoli FJ, Han JW, Cook JW, Schetzina JF et al (1988) Ultrahigh electron and hole mobilities in zero-gal Hg-based superlattices. Phys Rev B 38(3):2204–2207
47. Moghaddam N, Gréboval C, Qu J, Chu A, Rastogi P, Livache C et al (2020) The strong confinement regime in HgTe two-dimentional nanoplatelets. J Phys Chem C 124:23460–23468
48. Moore JE (2010) The birth of topological insulators. Nature 464(7286):194–198
49. Park M, Choi D, Choi Y, Shin H, Jeong KS (2018) Mid-infrared intraband transition of metal excess colloidal Ag2Se nanocrystals. ACS Photon 5:1907–1911. https://doi.org/10.1021/acsphotonics.8b00291
[Crossref]

50. Patel BK, Rath S, Sarangi SN, Sahu SN (2007) HgS nanoparticles: structure and optical properties. Appl Phys A Mater Sci Process 86:447–450
51. Pool F, Kossut J, Debska U, Reifenberger R (1987) Reduction of charge-center scattering rate in $Hg_{1-x}Fe_xSe$. Phys Rev B 35:3900
52. Ramesh TG, Shubha V (1982) Transport properties under pressure in HgSe. J Phys C Solid State Phys 15:6193
53. Ren T, Xu S, Zhao W, Zhu J (2005) A surfactant-assisted photochemical route to single crystalline HgS nanotubes. J Photochem Photobiol A 173:93–98
54. Rogalski A (2005) HgCdTe infrared detector material: history, status and outlook. Rep Prog Phys 68:2267
55. Qin A, Fang Y, Zhao W, Liu H, Su C (2005) Directionally dendritic growth of metal chalcogenide crystals via mild template-free solvothermal method. J Cryst Growth 283:230–241
56. Qu J, Rastogi P, Greboval C, Lagarde D, Chu A, Dabard C et al (2020) Electroluminescence from HgTe nanocrystals and its use for active imaging. Nano Lett 20:6185–6190
57. Sadat SF, Salavati-Niasari M, Esmaeili-Zare M (2014) Synthesis and characterization of mercury telluride nanoparticles using a new precursor. J Ind Eng Chem 20(5):3415–3420
58. Salehi H, Hoseini FA (2019) First-principles study of structure, electronic and optical properties of HgSe in zinc blende (B3) phase. J Optoelectron Nanostruct 4(2):69–81
59. Schulman JN, McGillm TC (1979) The CdTe/HgTe superlattice: proposal for a new infrared material. Appl Phys Lett 34:663
60. Stolpe J, Portugal O, Puhlmann N, Mueller H-U (2001) Intra and inter-band transitions in HgSe in magagauss fields. J Phys B 294:459–462
61. Svane A, Christensen NE, Cardona M, Chantis AN, van Schilfgaarde M, Kotani T (2011) Quasiparticle band structures of β-HgS, HgSe, and HgTe. Phys Rev B 84:205205
62. Takita K, Masuda K, Kudo H, Seki S (1980) Observation of surface evaporation of Hg from HgTe crystals by means of energetic oxygen ion backscattering. Appl Phys Lett 37:460–462
63. Tang X, Tang X, Lai KWC (2016) Scalable fabrication of infrared detectors with multispectral photoresponse based on patterned colloidal quantum dot films. ACS Photon 3:2396–2404. https://doi.org/10.1021/acsphotonics.6b00620 [Crossref]
64. Torres DD, Jain PK (2020) Crystal symmetry, strain, and facet-dependent nature of topological surface states in mercury selenide. J Phys Chem C 124(46):25615–25620
65. Tsidilkovski IM (1996) Electron spectrum of gapless semiconductors, Springer series in solid-state sciences, vol 116. Springer, New York [zbMATH]

66. Villars P, Calvert LD (1985) Handbook of crystallographic data for inter metallic phases, 2nd edn. Asm International, Metals Park
67. Wang X-L, Dou SX, Zhang C (2010) Zero-gap materials for future spintronics, electronics and optics. NPG Asia Mater 2(1):31–38. https://doi.org/10.1038/asiamat.2010.7
68. Wang H, Zhu J (2004) A sonochemical method for the selective synthesis of alpha-HgS and beta HgS NPs. Ultrason Sonochem 11:293–300
69. Whitsett CR, Nelson DA (1972) Lattice thermal conductivity of p-type mercury telluride. Phys Rev B 5:3125–3138
70. Zholudev MS, Kadykov AM, Fadeev MA, Marcinkiewicz M, Ruffenach S, Consejo C et al (2019) Experimental observation of temperature-driven topological phase transition in HgTe/CdHgTe quantum wells. Condens Matter 4:27

OceanofPDF.com

© The Author(s), under exclusive license to Springer Nature Switzerland AG 2023
G. Korotcenkov (ed.), *Handbook of II-VI Semiconductor-Based Sensors and Radiation Detectors*
https://doi.org/10.1007/978-3-031-19531-0_4

4. Ternary II-VI Alloys Promising for Application in Photodetectors

Mustafa Kurban[1], Osman Barış Malcıoğlu[2] and Şakir Erkoç[2] ✉
(1) Department of Electrical and Electronics Engineering, Kırşehir Ahi Evran University, Kırşehir, Turkey
(2) Department of Physics, Middle East Technical University, Ankara, Turkey

✉ **Şakir Erkoç**
Email: erkoc@metu.edu.tr

Keywords II-VI alloys – Application – Displays – Lasers – Photodetectors – Photovoltaic devices – Binary semiconductors – Ternary II-VI semiconductors – CdHgTe – CdZnTe – HgZnTe – Bandgap engineering – Tunability of bandgaps – Dimensionality – Doping – Energy spectrum – Heterostructures – Lattice strain – Molecular beam epitaxy – Nanoparticles – Optical absorption – Quantum dots – Quantum size effect – Quantum wells – Semiconductors – Simulations – Superlattices – Thin films

4.1 Introduction

A chemical compound is a substance consisting of two or more chemical elements that are chemically combined in fixed proportions. The ratio of each element is usually expressed by a chemical formula. On the other hand, an alloy is a combination, either in solution or compound, of two or more elements. An alloy with two components is called a binary alloy; one with three is a ternary alloy. The resulting alloy substance generally has properties significantly different from those of its components. In other words, an alloy is formed from a physical mixture of two or more

substances, whereas a compound is formed from a chemical reaction. The reader is referred to the excellent book of Adachi about semiconductor alloys [1].

The subject of this chapter is ternary alloys, particularly the II-VI alloys. Special attention is focused on the IIb elements Zn, Cd, and Hg forming both compound and alloy with VIa element Te. Namely, CdZnTe, CdHgTe, and HgZnTe ternary alloys are the main objectives of this chapter.

The II-VI alloys are well known as very convenient materials for photodetectors, because they have large nonlinear optical properties [2–4]. On the other hand, they have favorable photoelectrical properties of high atomic number, sufficiently large bandgap for high resistivity and low leakage current, and high intrinsic mobility–lifetime product [5–10].

These ternaries are also known as good candidates for terahertz wave emitters and detectors [11]. Moreover, these ternaries have been the subject of intensive research for a variety of applications that are used in solar cells, optoelectronic devices, nano-field-effect transistors, X-ray as well as γ-ray detectors for medical, industrial imaging systems, and security fields, as well as space applications at room temperature covering the energy range from a few keV to the MeV region [12–17].

In the following sections, the structural and electronic properties of the ternary alloys mentioned will be reviewed.

4.2 Properties of Ternary II-VI Alloys

Some of the physical and chemical properties of alloys may not be measured and/or experimentally observed directly. This necessitates the use of some sort of interpolation scheme [1]. If the linear interpolation scheme is used, the ternary material parameter $T_|$ for an alloy of the form $A_xB_{1-x}C$ can be derived from binary parameters (B) using a linear equation:

$$T_|(x) = xB_{AC} + (1-x)\,B_{BC} = a + bx \tag{4.1}$$

where $a = B_{BC}$ and $b = B_{AC} - B_{BC}$. Some material parameters, however, deviate significantly from the linear relationship shown in Eq. (4.1) and exhibit an approximately quadratic dependence on x. The ternary material parameter T_q in such a case can be very efficiently approximated using a quadratic equation by the relationship

$$T_q(x) = xB_{AC} + (1-x)\,B_{BC} + (1-x)\,C_{AB} = a + bx + cx^2 \quad (4.2)$$

where $a = B_{BC}$, $b = B_{AC} - B_{BC} + C_{AB}$, and $c = -C_{AB}$. The parameter c is called a bowing parameter [1].

4.2.1 Structural Properties of Ternary II-VI Alloys

The crystal structures of II-VI binary compounds are either in zincblende (at room temperature) or wurtzite (at high temperature) structures [18, 19] in general. For ternary compounds, the empirical formula of zincblende-type ternary alloys is typically written in $A_{1-x}B_xC$ form (A = Cd or Hg, B = Zn or Hg, and C = Te). Here, the subscript indicates the combining fraction of ZnTe in CdTe for $Cd_{1-x}Zn_xTe$, HgTe in CdTe for $Cd_{1-x}Hg_xTe$, and HgTe in ZnTe for $Hg_{1-x}Zn_xTe$. The structures of binary ZnTe and ternary CdZnTe for zincblende structure, as an example, are shown in Fig. 4.1.

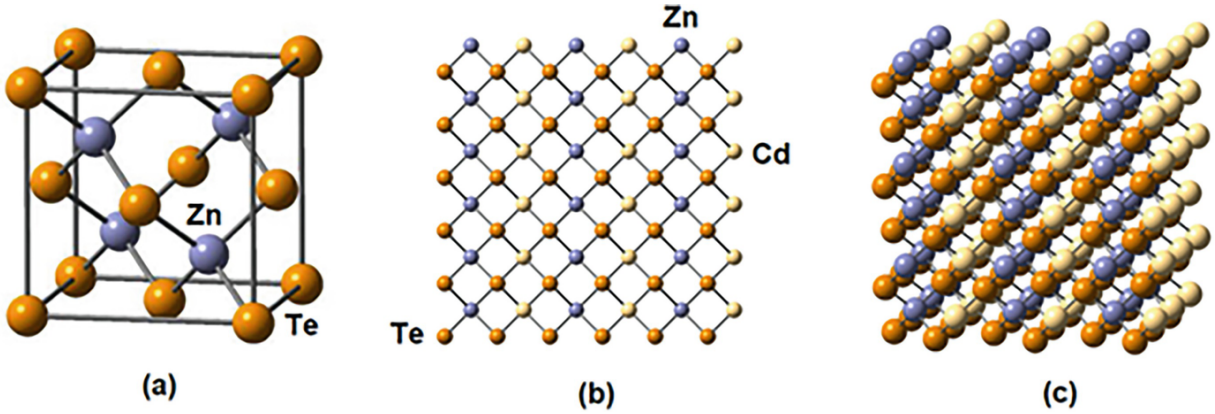

Fig. 4.1 (**a**) Unit cell of the zinc blende crystal structure of ZnTe binary. (**b**), (**c**) Different views of 3x3x3 lattice of zinc blende for $Cd_{0.50}Zn_{0.50}Te$ ternary

The experimental lattice parameters of CdTe and ZnTe are 6.482 Å and 6.104 Å, respectively [20]. The CdZnTe lattice constant can therefore be expressed using Vegard's Law [21]:

$$a(x) = a_1\,(1-x) + a_2 x \quad (4.3)$$

In Eq. (4.3), a_1 is the lattice parameter of CdTe and a_2 is the lattice parameter of ZnTe, respectively. The difference in the lattice parameters shows that Zn substitution of Cd atoms results in a small variation in the

average of the unit cell dimensions. Some lattice constants of CdZnTe alloy with different Zn concentrations are tabulated in Table 4.1.

Table 4.1 Lattice constants (*a*) of CdZnTe ternaries with various compositions

Compound	***a* (Å)**
$Cd_{0.95}Zn_{0.05}Te$	6.495
$Cd_{0.90}Zn_{0.10}Te$	6.441
$Cd_{0.70}Zn_{0.30}Te$	6.364
$Cd_{0.50}Zn_{0.50}Te$	6.287

Source: Data extracted from [22, 23]

The average lattice constant of the alloy $Cd_{1-x}Zn_xTe$ can also be found by Bragg's law:

$$n\lambda = 2d\mathrm{Sin}\,(\theta) \tag{4.4}$$

In Eq. (4.4), λ and d are the wavelength of the incident radiation and the distance between crystal planes, respectively, as well as θ and n are the angle of incidence and a positive integer, respectively. The lattice constant is proportional to distance d. Therefore, using the position of the diffraction peak, the composition of $Cd_{1-x}Zn_xTe$ ternary alloy can be determined.

The knowledge of the lattice constant is especially important in the infrared detector industry. Commercial infrared $Hg_{0.8}Cd_{0.2}Te$ detectors are mostly grown on $Cd_{0.96}Zn_{0.04}Te$ substrates due to matching of lattice constants, which suppresses the formation of interface stress.

4.2.2 Electronic Properties of Ternary II-VI Alloys

The interaction of light with the material is determined by the optical properties of that material. These optical properties depend on microscopic and macroscopic properties, such as surface properties and electronic structure. In this chapter, we will summarize archetypical electronic properties that influence the photodetection efficiency of an II-VI alloy.

The crystalline properties of II-VI alloys allow them to mix readily. The range of attainable bandgaps in doing so varies from near zero for the semimetal Hg compounds to more than 3.8 eV for ZnS [24]. This extensive

range combined with scalable alloying techniques makes the material favorable in the optoelectronics industry.

4.2.3 Optical Absorption

The absorption coefficient $\alpha(\lambda)$ is the attenuation coefficient of the light passing through a material. It captures all the absorption cross-sections due to various optical processes per unit volume of a material. The archetypal features observed in the absorption coefficient (α) of a crystalline semiconductor as a function of the photon energy (hv) are summarized in Fig. 4.2.

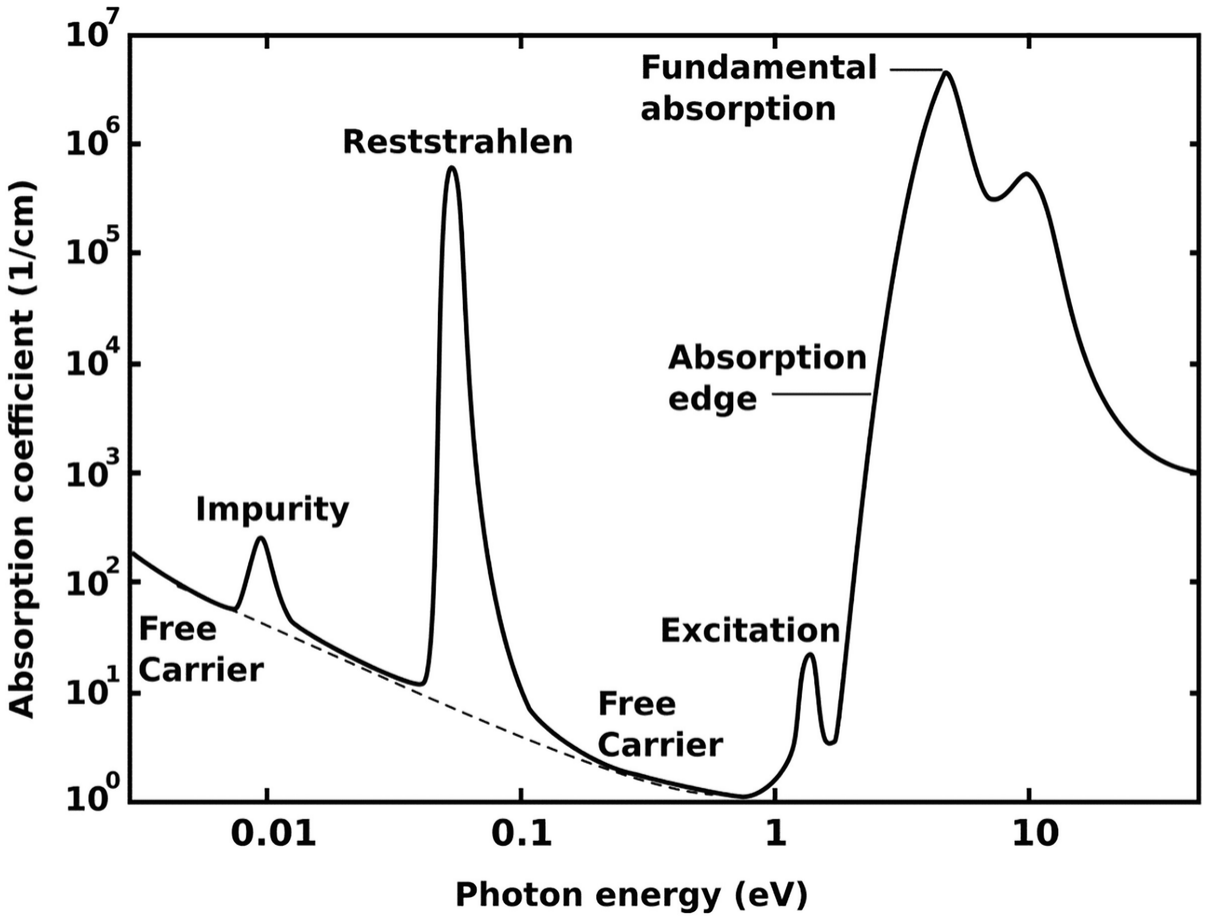

Fig. 4.2 Archetypal features in absorption coefficient in a typical crystalline semiconductor. Free-carrier absorption decreases with increasing photon energy. If present, an impurity absorption band due to the dopants (usually narrow) will also be present. The photon absorption due to crystal ions is called the Reststrahlen (lattice absorption) peak. Exciton absorption peaks (usually more apparent at lower temperatures) are observed close to fundamental absorption bands

II-VIs are more ionic in comparison to the III-Vs, and the corresponding Reststrahlen interaction is significantly larger. Exceptional mixing in II-VIs allows incorporating transition metal ions of the iron group resulting in diluted magnetic semiconductors (DMSs) with spectacular magneto-optical phenomena [25].

The absorption coefficient $\alpha(\lambda)$ is a function of the probability of transition from E (the occupied density of states at the valance band) to E' (the unoccupied conduction band states at $E + h\nu$). Near the band edges, the density of states can be approximated by a parabolic band, resulting in a behavior [26]:

$$\alpha h\nu = A(h\nu - E_g)^{1/2} \tag{4.5}$$

where

$$A \approx \left[\frac{e^2}{nch^2 m_e^*}\right](2\mu^*)^{3/2}$$

in which μ^* is a reduced electron and hole effective mass and n is the refractive index. This formula can be extrapolated to zero photon energy to estimate the direct bandgap E_g. The extrapolation is indeed very linear for CdTe giving an E_g= 1.49 eV.

When the photon energy is very close to the bandgap energy, the exciton absorption is highly likely, especially at low temperatures (see Fig. 4.3). The excitons due to electron-hole coupling can be effectively captured by the vertex function. The vertex function is the one-particle irreducible correlation function involving the fermion ψ, the antifermion $\overline{\psi}$, and the vector potential A. The absorbed optical energy remains held within the solid for the lifetime of the exciton. In nonmetallic solids, the common electron-hole excitonic states can be classified as Wannier–Mott excitons or Frenkel excitons [27]. In the Wannier–Mott excitons, the large overlap of interatomic electronic wave functions enables the electrons and holes to be far apart but bound in an excitonic state. Frenkel excitons are usually seen in organic or molecular crystals. In these materials, the overlap of intermolecular electronic wave functions is very small, and electrons remain tightly bound to individual sites. The resulting electronic energy bands are very narrow and closely related to individual molecular electronic energy levels. In the case of lower-dimensional materials, due to the higher

field intensity of the confined photon, more complex excitons are readily observed, such as plasmon-polaritons.

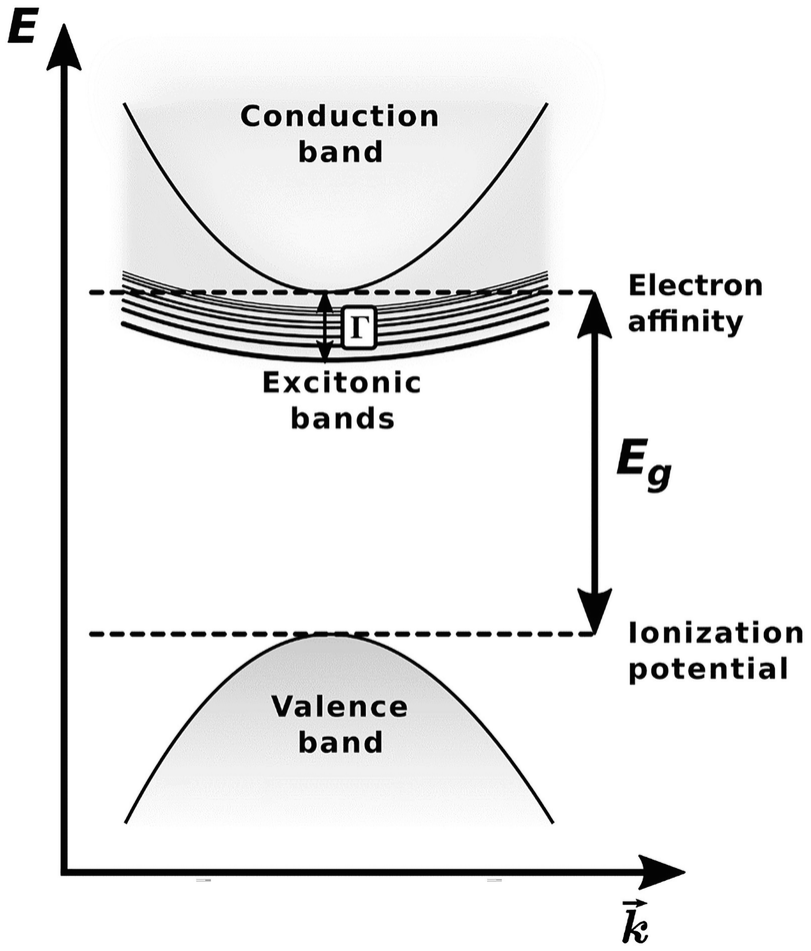

Fig. 4.3 Representation of the parabolic band structure in a semiconductor. In the typical convention, the valance band edge is defined as the ionization potential, and the conduction band edge is defined as the electron affinity. In pure optical excitations where the electron number is conserved, band energy gets renormalized (vertex corrections, indicated by Γ), forming what is conventionally referred to as the "excitonic bands" (Idea from [28])

The direct bandgaps of II-VI materials tend to exhibit a temperature dependence almost twice that of silicon. For example, ZnSe and ZnTe have direct bandgaps of 2.7 eV and 2.3 eV with a temperature dependence dE_g/dT of −0.50 and − 0.45 meV/K. On the other hand, due to the direct nature of the bandgap, the refractive index n may not be as much affected as silicon by temperature; for example, ZnSe has a refractive index of 2.3 near E_g, and dn/dT is 6.3 $10^{-5}K^{-1}$, almost a third of silicon.

In a crystalline solid, electron-hole coupling to excitonic states is possible both for direct and indirect semiconductors. This exciton can be

seen as a vertex normalization to the conduction band edge and hence can be modelled as an “optical band” appearing below the edge of the electronic conduction band in the single-particle picture. In this picture, the exciton-photon interaction operator and excited electron and hole pair and photon interaction operator depend only on their relative motion, mimicking the band-to-band and excitonic absorption. This approximation allows the calculation of the excitonic absorption coefficient using the same form of interaction as that used for band-to-band absorption. However, one must use the joint density of states to cast the many-body interaction to an effective single-particle picture. Using the joint density of states, the absorption coefficient associated with the excitonic states in crystalline semiconductors is obtained as [29]:

$$\alpha\hbar\omega = A_x(\hbar\omega - E_x)^{1/2} \tag{4.6}$$

where

$$A_x = \frac{4\sqrt{2}e^2|p_{xy}|^2}{nc\sqrt{\mu_x}\hbar^2}$$

and p_{xy} is the transition matrix element between the valance and excitonic bands. This form is very similar to the band-to-band transition mentioned above, E_g replaced by the vertex corrected E_x and renormalized. In pure crystalline solids, optical absorption below the excitonic ground state is forbidden. The excitonic energy level can be reached through either the excitation of electrons to higher energy levels in the conduction band and then nonradiative relaxation to the excitonic energy level or through the excitation of an electron directly to the exciton energy level.

4.3 Overview of Relevant Photovoltaic Device Physics

In this section, we examine the solid-state physics of a photovoltaic device to provide a foundation to explain various considerations of manufacturing an II-VI-based photodetector.

The optical absorption coefficient alone is not enough by itself to determine the prospect of a material as a photovoltaic device. When a photovoltaic device generates a charge due to an optical absorption process,

the charges must be separated and collected at the junction. Hence, loss mechanisms such as charge recombination processes and interface efficiencies are an important factor as optical absorption coefficient.

An ideal diffusion-limited diode exposed to a photon flux φ_λ is given by:

$$I_{\mathrm{d}} = I_{\mathrm{s}} \left[\left(\frac{qV_{\mathrm{d}}}{k_{\mathrm{B}}T} \right) - 1 \right] - I_{\mathrm{ph}} \tag{4.7}$$

where I_{d} and I_{s} are the diode and diffusion currents, $I_{\mathrm{ph}} = qA\eta\phi_\lambda$ is the photocurrent, and V_d is the diode bias voltage. The spectral responsivity of the device is η, and A is the detector area. The spectral responsivity η is a quantification combining all the electronic processes (including device-related macroscopic properties) for measuring the suitability of the material for a particular photovoltaic application.

$$\eta = (1 - R)\left[1 - \exp\left(-\alpha_\lambda t\right)\right] F \tag{4.8}$$

where R is the reflectivity of the front surface, α_λ is the wavelength-dependent absorption coefficient, t is the optical path length through the observer, and F is a geometry factor that captures the number of photogenerated carriers that can be captured before recombining.

High-performance detectors must be background limited. The detector is called background limited when the internal thermal generation is much less than the photon generation in the lowest flux case $I_s \ll I_{ph}$. Minimizing the above formula $I_s = k_B T/qR_0$ where R_0 is the zero-bias resistance. Then, the background limited condition can be written as

$$R_0 \gg k_B T/qI_{ph} \tag{4.9}$$

Hence, not only the bandgap but also the band curvature is an important factor determining the suitability of a material for use in photodetectors. An advantage of II-VI photodetectors is the scalable capacity to form photoconductor or photodiode arrays with embedded amplification electronics, which offer a number of device topology methods for optimizing the performance. The huge commercial success of HgCdTe infrared detectors can be seen as an example. A schematic illustration of a photodetector is shown in Fig. 4.4.

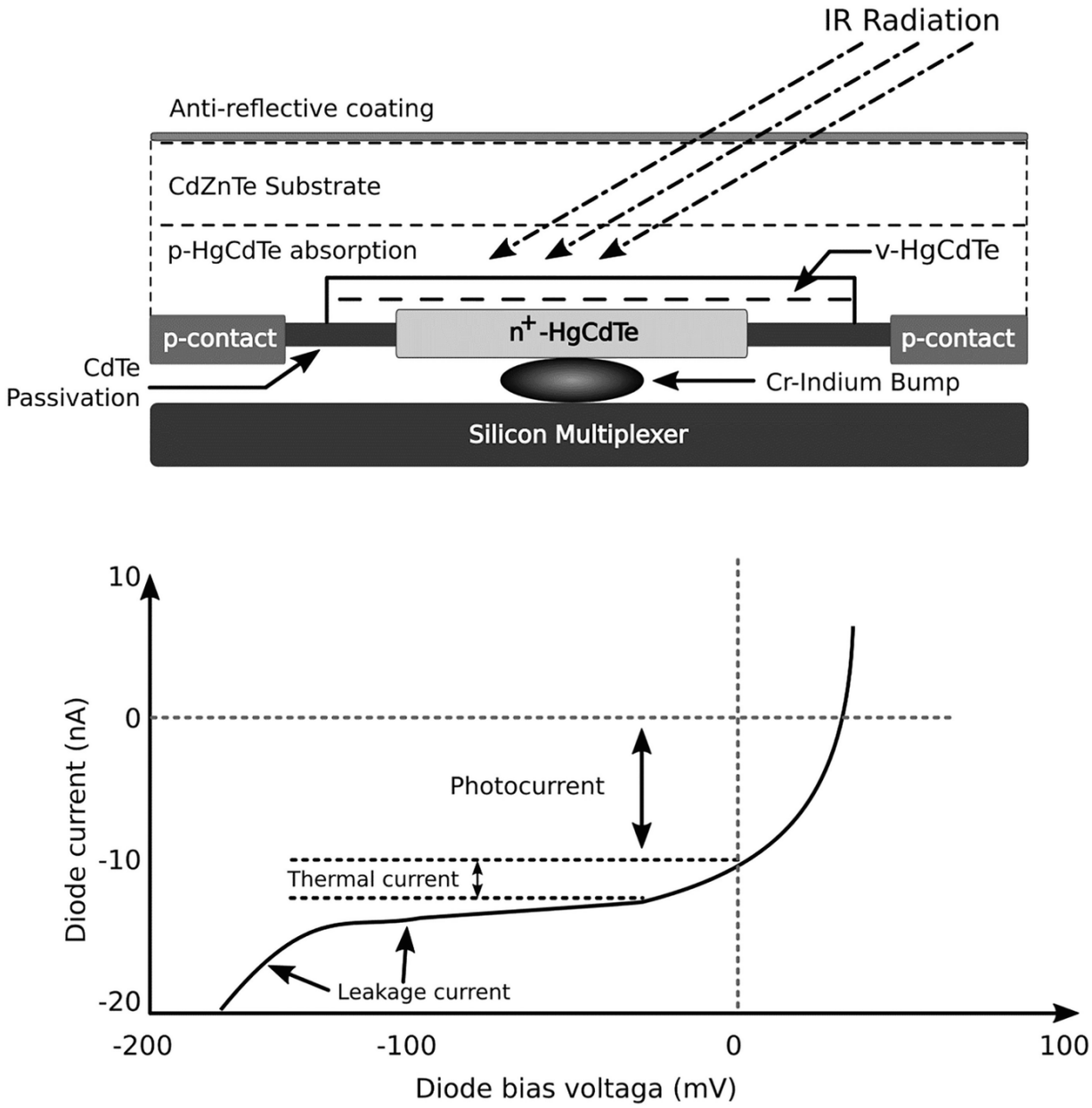

Fig. 4.4 An example photodetector device and typical I-V characteristics. The example is a back-illuminated indium-bumped HgCdTe-based IR detector. The silicon multiplexer is directly connected to the device for minimizing various losses and noise. Thermal noise can be controlled by carefully controlling the device architecture and the interface properties

4.4 Effects Relevant to Photodetector Applications in II-VI Semiconductor

The thermally generated current, shunt resistance, and breakdown currents at a high bias degrade the performance of a photodetector. Longer

wavelengths and/or higher operating temperatures are usually the most difficult regions for which a photodetector to operate.

The electronic properties of II-VI semiconductors are not the only components to consider in a photodetector application. The photocurrent must be injected into a silicon-integrated circuit for reading the signal. Direct injection where the photocurrent is directly injected into the source of a common gate MOSFET is the simplest method. A capacitor is attached to the drain for the integration. This means the II-VI semiconductor diode should have a dynamic resistance higher than the input impedance of the MOSFET. The background-limited case has an injection efficiency of $I_{\mathrm{ph}}R_v$ where R_v is the dynamic impedance of the diode. Hence a high dynamic resistance is often desired. See [30, 31] for a review. There are some other pixel design strategies for signal processing that is compatible with II-VI technology easing direct injection limitations, CMOS multiplexing being the contemporary preferred method [32, 33]. A thermal minority-carrier generation within the diffusion length from the p-n junction gives rise to a current that cannot be distinguished from the photocurrent being measured. The Auger process is the first dominant thermal diffusion current source in II-VIs. This process involves the interaction of three carriers. In n-type semiconductors, Auger generation is due to the interaction of two electrons and a hole, and it is called Auger 1. Auger 1 is dependent on the square of the carrier concentration. Hence a low-carrier concentration is preferred for an n-type photodetector. N-type II-VI semiconductors can be produced with low-carrier concentration with relative ease, i.e., ($<5 \times 10^{14}\mathrm{cm}^{-3}$) for HgCdTe. Furthermore, n-type II-VIs with low-carrier concentration nearly always have a long-carrier lifetime [34–36]. In p-type semiconductors, Auger recombination involves two holes and an electron. This process is called Auger 7. Lifetimes of this process are an order greater than Auger 1. At higher temperature, the lifetime will transition from Auger 7 to Auger 1. In p-type material, dark current generation through trap levels often dominates over Auger 7. Tennant et al. proposed an empirical relationship for the minimum Auger-generated dark current [37, 38].

The second dominant thermal current process in II-VIs is the Shockley–Read–Hall (SRH) process which is also called trap-assisted recombination [39]. SRH can be significant in direct bandgap materials when carrier densities are very low. In the SRH model, an electron in the conduction band can be trapped in an intragap state, an electron can be emitted into the

conduction band from a trap level, an electron hole in the valence band can be captured by a trap, and a captured hole can be released into the valence band. The use of extrinsic doping is an effective way to reduce thermal currents from the p-side in homojunction devices [40].

The action of traps in the depletion region is actually very complex. Another source of problem due to the increased number of localized traps is the trap-assisted tunneling which leads to leakage currents [41–46]. The origin of the intrinsic trap levels can also be complex, such as Zhang-Rice singlets and doublets when strong correlation effects are pronounced, and not always clearly understood.

Exposing only one side of the junction is enough to collect photocurrent. The other side can be tailored to minimize thermal current contribution, i.e., by using a wider bandgap material, making a heterostructure. It has been demonstrated that high-quality II-VI heterostructures can be fabricated even when the lattice mismatch between adjacent layers is large. For the best quantum efficiency, device engineers favor n-type absorbers with long lifetimes and low carrier concentrations and use a wide bandgap p-region in order to lower thermal leakage currents.

At low temperatures or for very long wavelength devices, interband tunneling can become dominant. When the effective mass of the charge carrier in II-VI semiconductors is very low (i.e., the electron in HgCdTe), direct band-to-band tunneling is significant [47]. This tunneling current increases very rapidly as the applied voltage or doping is increased, or the bandgap or temperature decreased. Low doping on one side of the junction can minimize interband tunneling under normal operating conditions.

In the following sections, we briefly focus on the applications of CdZnTe, HgCdTe, and HgZnTe ternary II-VI alloys as a photodetector.

4.5 Cadmium Zinc Telluride (CZT, CdZnTe)

The use of cadmium zinc telluride (CZT) has recently been an area of intense scrutiny in important detector applications because CZT crystals have a wide bandgap (~1.68 eV) which is a need to operate the detector at room temperature, a large photon absorption cross-section (~10^4 cm^2/g) converting efficiently optical energy to electrical energy that means high absorption efficiency and high resistivity (10^{10} Ω.cm) reducing level of noise [48–52]. These excellent features enable to use CZT in different areas

especially in detector technology [53–57] as the most promising material compared with the traditional semiconductors, such as silicon (Si), germanium (Ge), GaAs, etc. Herein, structural and electronic properties of CZT at 25 °C temperature are given in Table 4.2 to compare CZT with the semiconductors mentioned above because they have high detection efficiency and are suitable for the improving reliability of detection systems. From Table 4.2, CZT has the highest resistivity than the other semiconductors, which is desirable to prevent leakage currents and thus allows the detectors to work at high voltages. The difference between resistivities of CdTe and CZT results from the substitution of zinc (Zn) atoms into CdTe. On the other hand, a material with lower resistivity acts as a thinner detector due to its narrower depletion region and thus producing desired collection efficiencies [58]. In this context, the mobility–lifetime products ($\mu\tau$) for CZT are relatively lower than Si and Ge which can be seen as a disadvantage because the $\mu\tau$ is desirable for better charge collection efficiencies [59]. When it comes to the other features such as relatively high density, high atomic number, and the wide bandgap, CZT has an advantage for radiation detectors over traditional semiconductors like Si and Ge, so it has the capability to be used in visible photodetector technology [54].

Table 4.2 Structural and electronic properties of well-suited semiconductors for detector applications (μτ is mobility-lifetime products)

Property	**Si**	**Ge**	**GaAs**	**CdTe**	**$Cd_{09}Zn_{0.1}Te$**
Crystal structure	Cubic	Cubic	Cubic (ZB)	Cubic (ZB)	Cubic (ZB)
Atomic number	14	32	31, 33	48, 52	48, 30, 52
Resistivity (Ωcm)	10^4	50	10^7	10^9	10^{10}
μτ (cm^2/V)	>1	>1	10^{-5}	10^{-3}	10^{-3}–10^{-2}
Density (g/cm^3)	2.33	5.33	5.32	6.20	5.78
Bandgap (eV)	1.12	0.67	1.43	1.44	1.57

Source: Data extracted from [54]

To improve the radiation detector performance, some important properties such as the wide bandgap, high crystalline perfection, and resistivity are required for intrinsic material as mentioned above. Here, some examples are given from the literature to understand how to accomplish these requirements and what are the obstacles to get the CZT

detectors with desired properties. Figure 4.5 demonstrates the modulation of bandgap energy according to Zn concentrations [60]. The bandgap width of CZT can be tunable by the substitution of Zn atoms into CdTe. Therefore, the physical properties of CdTe as seen in this example may be improved by getting ternary CZT with the addition of Zn for detector applications. The increase in the bandgap with the presence of zinc atoms gives rise to low noise performance and then allows for use at either lower photon energies or higher temperatures.

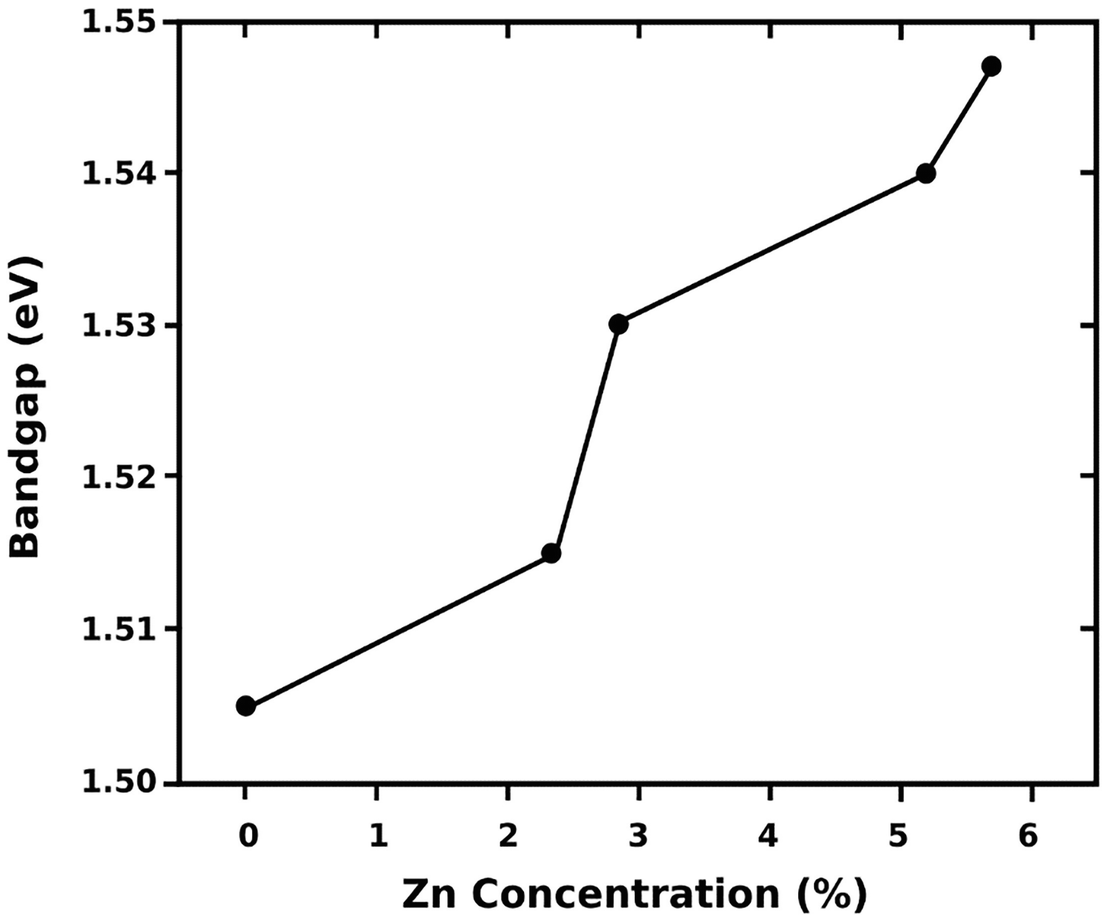

Fig. 4.5 The bandgap energy for CZT single crystal samples with different Zn concentrations (Data extracted from [60])

The substitution of Zn into CdTe helps to grow CZT with larger sizes and low cost in comparison with CdTe crystals. However, the increased content of Zn may induce a decrease in crystal quality because of lattice dislocation [61–63], even if the bandgap and resistivity of CZT alloys increase with the increase of the zinc mole fraction x. Thus, the concentration of Zn in most CZT detectors is used up to 20% in general

[54], although advantages of the use of CZT with higher Zn concentrations up to 80% have been shown in a theoretical calculation [64]. The main reason is the nonuniform distribution of Zn in the large volume CZT crystal [54, 64–66]. To overcome this problem, some studies show that CZT films and layers with the low-cost and large-area uniform can provide the use of CZT with the thickness of 20 and 30 μm [67, 68] and more [69–73] instead of bulk crystals. Besides, the compensation of Cd vacancies by indium (In) brings about a low concentration of free electrons and then the increase resistivity of CZT crystal [74]. The next chapter (Chap. 6) discusses bandgap in detail.

4.6 Mercury Cadmium Telluride (HCT, HgCdTe)

The ternary compound HgCdTe is a close to ideal IR detector material due to its key features such as adjustable bandgap in the range of 1–30 μm, high quantum efficiency, thanks to large optical coefficients, and favorable inherent recombination mechanisms that lead to high operating temperature [75]. Additionally, its direct bandgap, achieving both low and high carrier concentrations, high electron mobility (μ), and desirable dielectric constant, is the specific advantage of HgCdTe over the other ternary alloys. HgCdTe can be used as different types of devices such as photodetectors, photoconductors, and photodiodes and can be optimized for operation at a broad range of the IR spectrum and in a wide range of temperatures. Some properties of the $Hg_{1-x}Cd_xTe$ ternary alloy based on composition (x), which are important in photodetector applications [76], are given in Table 4.3. In the previous section, we have mentioned that replacing a small fraction of Cd with Zn can be a disadvantage for CZT detectors at higher Zn concentrations due to the residual lattice mismatch. When it comes to HgCdTe, composition independence of the lattice parameter of HgCdTe is a significant advantage over other materials. A very small variety of its lattice constant based on composition enables it to cover the whole IR spectral range and thus grow high-quality layers and heterostructures. In addition, the small bandgap of HgCdTe absorbs IR radiation, which can be encapsulated in a wider gap HgCdTe and prevents instabilities due to the weak Hg-Te bonds [77]. The composition-dependence especially with larger Hg content of HgCdTe also results in an increase in the μ; thus, increasing the conductivity of the HgCdTe can make a positive contribution

to the performance of the photodetector [78]. The increase in the carrier concentration leads to an increase in conductivity [79, 80]. Herein, HgCdTe with high Hg concentrations makes it possible to fabricate high-speed photodetectors with $Hg_{1-x}Cd_xTe$ ternary alloy.

Table 4.3 Some properties of the $Hg_{1-x}Cd_xTe$ ternary alloy which are important in photodetector applications

Parameter	**Properties**						
x	0	0.194	0.205	0.225	0.31	0.44	0.62
a (Å)	6.461	6.464	6.464	6.464	6.465	6.468	6.472
T (K)	77	77	77	77	140	200	300
μ_e ($cm^2/V^{-1}\ s^{-1}$)	–	4.5×10^5	3.0×10^5	1.0×10^5	–	–	–
Bandgap (eV)	0.261	0.073	0.091	0.123	0.272	0.474	0.749
n_i (cm^{-3})	–	1.9×10^{14}	5.8×10^{13}	6.3×10^{12}	3.7×10^{12}	7.1×10^{11}	3.1×10^{10}

Source: Data extracted from [76]
Abbreviations: a is lattice parameter, *T* is temperature, μ_e is the mobility of electrons, and n_i is carrier concentration

A recent study shows that it is possible to obtain a highly efficient bilayer graphene- HgCdTe (BLG/HgCdTe) heterojunction-based p^+-*n* photodetector for long-wavelength infrared (LWIR) absorbed in a lightly doped *n*-$Hg_{0.7783}Cd_{0.2217}Te$ active layer [81]. The schematic representation of BLG/HgCdTe photodetector is shown in Fig. 4.6. In the heterojunction device, p^+-doped graphene layers are deposited on *n*– $Hg_{0.7783}Cd_{0.2217}Te$ acting as an absorbing/active layer. The device shows highly efficient properties such as a better photocurrent of 1.9 nA and high external quantum efficiency of 88.38% [81].

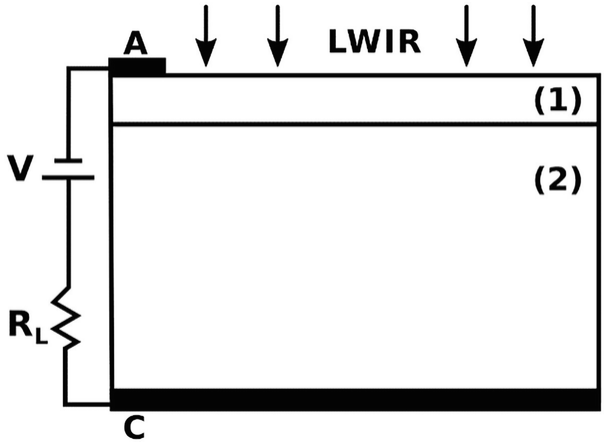

Fig. 4.6 The schematic representation of BLG/HgCdTe photodetector. The arrows near the anode show the long-wavelength infrared (LWIR) incident light with an intensity of 1 mW/cm^2. A, anode; C, cathode; (1): p^+-BLG; (2): *n*– $Hg_{0.7783}Cd_{0.2217}Te$, active layer, ~10.0 μm. (Idea from Ref. [81])

4.7 Mercury Zinc Telluride (HZT, HgZnTe)

HgZnTe is a ternary alloy of HgTe and ZnTe, and it has been considered as an alternative material to $Hg_{1-x}Cd_xTe$ which is commonly used in bulk or epitaxial form for the IR devices due to its broad range of bandgap from −0.15 for HgTe and 2.25 eV for ZnTe at ~300 K [82, 83]. HgZnTe has less surface segregation of Hg near its surface due to the higher bond strength when compared to HgCdTe, and thus, HgZnTe surfaces have a better stoichiometry than HgCdTe [84]. The carrier mobility and lifetime, accordingly, increase because of an increase in the bond strength, at least at low temperature. For example, $Hg_{1-x}Zn_xTe$ layers for $x = 0.248$ [85] growing on CZT substrates have relatively high lifetimes reaching 0.1 μs at 120 K. The μ is primarily limited by the scattering process such as optical phonon under 50 K in HgZnTe and HgCdTe compounds [86]. The μ is higher in Hg-rich HgZnTe than in HgCdTe with the same gap, especially when it comes to the optical longitudinal mode of the lowest frequency of Hg-Te type [87, 88]. The main reason is the higher frequency of the optical mode as compared to the same in HgCdTe. Although the oscillator strength of the high-frequency mode (of Cd-Te or Zn-Te type) in $Hg_{1-x}Zn_xTe$ or $Hg_{1-x}Cd_xTe$ is small, its contribution to the interaction with electrons rises gradually with x [89]. Additionally, the explicit difference of μ for HgZnTe and HgCdTe is lower than 1.5% at 300 K under the same conditions such as

the same gap and concentration. The difference continues to decrease at lower temperatures, which results from defect concentrations [89, 90]. The situation of approximately equal values of μ of HgZnTe and HgCdTe with the same gap remains up to almost 0.65 eV [91]. Besides, electron mobilities above 10^5 cm^2 V^{-1} s^{-1} have obtained for $Hg_{1-x}Zn_xTe$ (x = 0.15) in bulk form [86, 89] and on epitaxial layers [92].

In applications of IR detection of HgZnTe with rich Hg content, the type of carriers can be controlled in the same way as for HgCdTe [86, 93–95]. The most important difference, which is linked to the higher bond stability, is the lowest diffusion coefficient of cations in HgZnTe as compared to HgCdTe. This leads to a lower interdiffusion coefficient in HgZnTe [96] and to a lower diffusion of cation vacancies which control acceptor concentrations [94]. The higher bond strength of HgZnTe also gives rise to lower damage of the lattice when it is ion milled [97]. The low diffusion of native species or foreign dopants [93] is very important for practical applications such as detectors whose lifetime is considerably increased when they are elaborated with HgZnTe [98]. The Hg diffusion coefficient is slower in HgZnTe and strongly dependent on Te precipitates, extended defects, and acceptor residual impurities [93]. The better stability of bonds in HgZnTe can induce a smaller number of extended defects which are thought to enhance Hg diffusion.

4.8 Dimensionality

In any material, substantial variation of electrical and optical properties will be observed with reduced size dimensionality [99]. This effect is actively used in optical devices for some time [100, 101]. Some physical properties of materials show a dependence of dimensionality, as shown in Fig. 4.7.

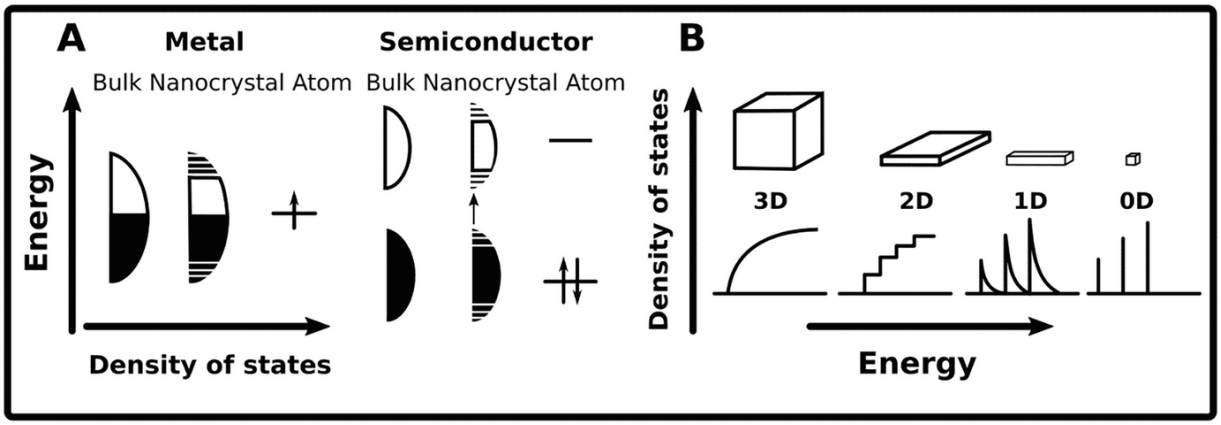

Fig. 4.7 (**a**) Density of states (DOS) for metal and semiconductor nanocrystals compared to those of the bulk and isolated atoms. (**b**) DOS vs. energy as a function of dimensionality (for bulk material, quantum well, quantum wire, and quantum dot)

In a 0D semiconductor quantum dot, the edges of the bands dominate the low-energy optical and electrical behavior. Electrical transport and charge separation capabilities depend strongly on the size. Often device-relevant quantum dots are nanocrystals with an identifiable crystalline interior [102]. When the size of a crystal is reduced, a ratio of atoms at the surface to atoms in a bulk environment increases. At the nanocrystal scale, the material is mostly surface; hence, surface trap states play a dominant role in optical and electronic properties. Furthermore, the reduced size introduces confinement effects. For example, the bandgap in CdSe can be tuned from 1.7 to 2.4 eV by reducing the nanocrystal diameter from 200 to 20 Å [103]. Both the confinement potential and surface states can be controlled by choosing different surface passivation strategies, providing controllable parameters for tuning carrier separation and absorption coefficient [104]. Furthermore, in a nanocrystal, the oscillator strength of the captured photon is compressed in a very narrow region in space, leading to strong nonlinear effects. This property is important in nonlinear optical detectors [105]. Among the colloidal nanocrystals, II-VIs stand out as the prototypical systems with well-established passivation and even network-forming protocols [106–108].

1D nanostructures of ternary alloys are an effective bandgap-engineering strategy [109, 110]. 1D nanostructures made out of II–VIs, especially cadmium and zinc chalcogenides, are investigated heavily in the literature due to their high quantum efficiency and light sensitivity [111]. Tunable photodetectors based on the CdS_xSe_{1-x} and ZnS_xSe_{1-x} nanonetworks offer high quantum efficiency and readout speed [112–116].

CdS_xSe_{1-x} nanoribbons with lateral heterostructures were demonstrated as high-performance photodetectors [117].

A thin film of CdTe with a thickness of ca. 2 μm will absorb nearly 100% of incident solar radiation [118]. Ternary cadmium zinc sulfide ($Cd_{1-x}Zn_xS$) in conjunction with CdS is a good candidate for wide bandgap window material for traditional CdTe/CdS contact. Its bandgap can be tuned between 2.42 eV (CdS) and 3.6 eV (ZnS). It improves the wavelength spectral response of the cell at the same time, without compromising the transport properties and the shunt resistances of the cell. $Cd_{1-x}Zn_xS$ is a suitable alternative window material to ZnS, because an efficient cell is only possible when ZnS is heavily n-doped which is difficult. As a result, $Cd_{1-x}Zn_xS$ is used as the doped form of ZnS.

References

1. Adachi S (2009) Properties of semiconductor alloys: group-IV, III–V and II–VI semiconductors. John Wiley & Sons, Ltd, Chichester
[Crossref]
2. Weil R, Joucla M, Loison JL, Mazilu M, Ohlmann D, Robino M, Schwalbach G (1998) Preparation of optical quality ZnCdTe thin films by vacuum evaporation. Appl Opt 37:2681–2686. https://doi.org/10.1364/AO.37.002681
[ADS][Crossref]
3. Ohlmann D, Crégut O, Pelant I, Granger R, Triboulet R, Hönerlage B (1993) Linear and nonlinear optical properties of ZnCdTe monocrystals. J Lumin 54:357–367. https://doi.org/10.1016/0022-2313(93)90004-7
[Crossref]
4. Netiksis V, Hönerlage B, Weil R, Loison JL, Grun JB, Levy R (1993) Picosecond dynamics of absorption bleaching in polycrystalline ZnCdTe films. J Appl Phys 74:5729–5736. https://doi.org/10.1063/1.354190
[ADS][Crossref]
5. Zhao XC, Ouyang XP, Xu YD, Han HT, Zhang ZC, Wang T, Zha GQ, Ouyang X (2012) Time response of Cd0.9Zn0.1Te crystals under transient and pulsed irradiation. AIP Adv 2:12162. https://doi.org/10.1063/1.3693970
[ADS][Crossref]
6. Bale DS, Soldner SA, Szeles C (2008) A mechanism for dynamic lateral polarization in CdZnTe under high flux X-ray irradiation. Appl Phys Lett 92:82101. https://doi.org/10.1063/1.2883924
[Crossref]

7. Koley G, Liu J, Mandal KC (2007) Investigation of CdZnTe crystal defects using scanning probe microscopy. Appl Phys Lett 90:102121. https://doi.org/10.1063/1.2712496 [ADS][Crossref]
8. McNeil WJ, McGregor DS, Bolotnikov AE, Wright GW, James RB (2004) Single-charge-carrier-type sensing with an insulated Frisch ring CdZnTe semiconductor radiation detector. Appl Phys Lett 84:1988–1990. https://doi.org/10.1063/1.1668332 [ADS][Crossref]
9. Chu M, Terterian S, Ting D, Wang CC, Gurgenian HK, Mesropian S (2001) Tellurium antisites in CdZnTe. Appl Phys Lett 79:2728–2730. https://doi.org/10.1063/1.1412588 [ADS][Crossref]
10. Schlesinger TE, Toney JE, Yoon H, Lee EY, Brunett BA, Franks L, James RB (2001) Cadmium zinc telluride and its use as a nuclear radiation detector material. Mater Sci Eng R Rep 32:103–189. https://doi.org/10.1016/S0927-796X(01)00027-4 [Crossref]
11. Liu K, Kang H-S, Kim T-K, Zhang X-C (2002) Study of ZnCdTe crystals as terahertz wave emitters and detectors. Appl Phys Lett 81:4115–4117. https://doi.org/10.1063/1.1524696 [ADS][Crossref]
12. Gupta A, Parikh V, Compaan AD (2006) High efficiency ultra-thin sputtered CdTe solar cells. Sol Energy Mater Sol Cells 90:2263–2271. https://doi.org/10.1016/j.solmat.2006.02.029 [Crossref]
13. Melnikov AA (1999) CdZnTe radiation detectors. J Cryst Growth 197:663–665. https://doi.org/10.1016/S0022-0248(98)00967-1 [ADS][Crossref]
14. Li S, Jiang Y, Wu D, Wang B, Li J, Zhang Y, Wang W, Lan X, Zhong H, Chen L (2011) Synthesis and nano-field-effect transistors of p-type Zn0.3Cd0.7Te nanoribbons. Mater Lett 65:1753–1755. https://doi.org/10.1016/j.matlet.2011.03.068 [Crossref]
15. Mandal K, Kang SH, Choi M, Mertiri A, Pabst GW, Noblitt C (2007) Crystal growth and characterization of CdTe and Cd0.9Zn0.1Te for nuclear radiation detectors. MRS Proc 1038:1038-O04–02. https://doi.org/10.1557/PROC-1038-O04-02 [Crossref]
16. Eisen Y, Shor A, Mardor I (1999) CdTe and CdZnTe gamma ray detectors for medical and industrial imaging systems. Nucl Instrum Methods Phys Res, Sect A 428:158–170. https://doi.org/10.1016/S0168-9002(99)00003-0 [ADS][Crossref]
17. Auricchio N, Marchini L, Caroli E, Zappettini A, Abbene L, Honkimaki V (2011) Charge transport properties in CdZnTe detectors grown by the vertical Bridgman technique. J Appl Phys 110:124502. https://doi.org/10.1063/1.3667201 [ADS][Crossref]

18. Ikhmayies SJ (2014) Introduction to II-VI compounds: in “advances in II-VI compounds suitable for solar cell applications”. Signpost publisher
19. Özgür Ü, Alivov YI, Liu C, Teke A, Reshchikov MA, Doğan S, Avrutin V, Cho S-J, Morkoç H (2005) A comprehensive review of ZnO materials and devices. J Appl Phys 98. https://doi.org/10.1063/1.1992666
20. Lide DR (2011) CRC handbook of chemistry and physics. CRC press
21. Wang Y, Kudo K, Inatomi Y, Ji R, Motegi T (2005) Growth interface of CdZnTe grown from Te solution with THM technique under static magnetic field. J Cryst Growth 284:406–411. https://doi.org/10.1016/j.jcrysgro.2005.02.076
[ADS][Crossref]
22. Sivaraman G (2003) Characterization of cadmium zinc telluride solar cells. USF Tampa Graduate Theses and Dissertations, United States
23. Bensalah H, Hortelano V, Plaza JL, Martínez O, Crocco J, Zheng Q, Carcelen V, Dieguez E (2012) Characterization of CdZnTe after argon ion beam bombardment. J Alloys Compd 543:233–238. https://doi.org/10.1016/j.jallcom.2012.07.109
[Crossref]
24. Gunshor RL (1991) Strained-layer superlattices: materials science and technology. Elsevier
25. Furdyna JK (1988) Diluted magnetic semiconductors. J Appl Phys 64:R29–R64. https://doi.org/10.1063/1.341700
[ADS][Crossref]
26. Simmons JH, Potter KS (2000) Optical materials. Elsevier
27. Singh J (1994) Excitation energy transfer processes in condensed matter. Springer, US
[Crossref]
28. Rakhshani AE (1997) Electrodeposited CdTe—optical properties. J Appl Phys 81:7988–7993. https://doi.org/10.1063/1.365402
[ADS][Crossref]
29. Singh J, Shimakawa K (2003) Advances in amorphous semiconductors. CRC Press
[Crossref]
30. Kozlowski LJ, Montroy JT, Vural K, Kleinhans WE (1998) Ultralow-noise infrared focal plane array status. In: Infrared technology and applications, vol XXIV, pp 162–171
[Crossref]
31. Kozlowski LJ (1996) Low-noise capacitive transimpedance amplifier performance versus alternative IR detector interface schemes in submicron CMOS. In: Infrared readout electronics III, pp 2–11
[Crossref]
32. Reine MB, Sood AK, Tredwell TJ (1981) Photovoltaic infrared detectors. In: Semiconductors and semimetals. Elsevier

33. Reine MB (2001) Photovoltaic detectors in MCT. In: Infrared detectors and emitters: materials and devices. Springer US, Boston, MA
34. Lacklison DE, Capper P (1987) Minority carrier lifetime in doped and undoped p-type Cdx Hg1-xTe. Semicond Sci Technol 2:33–43. https://doi.org/10.1088/0268-1242/2/1/005 [ADS][Crossref]
35. Polla DL, Aggarwal RL, Nelson DA, Shanley JF, Reine MB (1983) Hg vacancy related lifetime in Hg0.68Cd0.32Te by optical modulation spectroscopy. Appl Phys Lett 43:941–943. https://doi.org/10.1063/1.94189 [ADS][Crossref]
36. Lopes VC, Syllaios AJ, Chen MC (1993) Minority carrier lifetime in mercury cadmium telluride. Semicond Sci Technol 8:824–841. https://doi.org/10.1088/0268-1242/8/6s/005 [ADS][Crossref]
37. Tennant WE, Lee D, Zandian M, Piquette E, Carmody M (2008) MBE HgCdTe technology: a very general solution to IR detection, described by “rule 07”, a very convenient heuristic. J Electron Mater 37:1406–1410. https://doi.org/10.1007/s11664-008-0426-3 [ADS][Crossref]
38. Tennant WE (2010) “Rule 07” revisited: still a good heuristic predictor of p/n HgCdTe photodiode performance? J Electron Mater 39:1030–1035. https://doi.org/10.1007/s11664-010-1084-9 [ADS][Crossref]
39. Nisoli M (2016) Semiconductor photonics. Principles and applications. Societ’a Editrice Esculapio. Italy
40. Kinch MA (2007) Fundamentals of infrared detector materials. SPIE press [Crossref]
41. Wong JY (1980) Effect of trap tunneling on the performance of long-wavelength hg<inf>1-x</inf>cd<inf>x</inf>Te photodiodes. IEEE Trans Electron Devices 27:48–57. https://doi.org/10.1109/T-ED.1980.19818 [ADS][Crossref]
42. Anderson WW, Hoffman HJ (1982) Field ionization of deep levels in semiconductors with applications to Hg1−xCdxTe p-n junctions. J Appl Phys 53:9130–9145. https://doi.org/10.1063/1.330425 [ADS][Crossref]
43. Sah CT (1961) Electronic processes and excess currents in gold-doped narrow silicon junctions. Phys Rev 123:1594–1612. https://doi.org/10.1103/PhysRev.123.1594 [ADS][Crossref]
44. DeWames RE, Pasko JG, Yao ES, Vanderwyck AHB, Williams GM (1988) Dark current generation mechanisms and spectral noise current in long-wavelength infrared photodiodes. J Vac Sci Technol A 6:2655–2663. https://doi.org/10.1116/1.575526 [Crossref]

45. Nemirovsky Y, Rosenfeld D, Adar R, Kornfeld A (1989) Tunneling and dark currents in HgCdTe photodiodes. J Vac Sci Technol A 7:528–535. https://doi.org/10.1116/1.576215 [Crossref]
46. Rosenfeld D, Bahir G (1992) A model for the trap-assisted tunneling mechanism in diffused n-p and implanted n/sup +/−p HgCdTe photodiodes. IEEE Transactions on Electron Devices. 39:1638–1645. https://doi.org/10.1109/16.141229 [ADS][Crossref]
47. Anderson WW (1980) Absorption constant of Pb1−xSnxTe and Hg1−xCdxTe alloys. Infrared Phys 20:363–372. https://doi.org/10.1016/0020-0891(80)90053-6 [ADS][Crossref]
48. Carcelén V, Hidalgo P, Rodriguez-Fernández J, Dieguez E (2010) Growth of bi doped cadmium zinc telluride single crystals by Bridgman oscillation method and its structural, optical, and electrical analyses. J Appl Phys 107:93501 [Crossref]
49. Yang G, Jie W, Li Q, Wang T, Li G, Hua H (2005) Effects of in doping on the properties of CdZnTe single crystals. J Cryst Growth 283:431–437 [ADS][Crossref]
50. Foschini L (2009): Notes on the data analysis in high-energy astrophysicsar Xiv preprint ar Xiv: 0910.2156, Cornell University Library, Itaca, New York
51. Franc J, Höschl P, Belas E, Grill R, Hldek P, Moravec P, Bok J (1999) CdTe and CdZnTe crystals for room temperature gamma-ray detectors. Nucl Instrum Methods Phys Res, Sect A 434:146–151 [ADS][Crossref]
52. Rybka AV, Davydov LN, Shlyakhov IN, Kutny VE, Prokhoretz IM, Kutny DV, Orobinsky AN (2004) Gamma-radiation dosimetry with semiconductor CdTe and CdZnTe detectors. Nucl Instrum Methods Phys Res, Sect A 531:147–156 [ADS][Crossref]
53. Shkir M, Ganesh V, AlFaify S, Black A, Dieguez E, Maurya KK (2018) Large size crystal growth, photoluminescence, crystal excellence, and hardness properties of in-doped cadmium zinc telluride. Cryst Growth Des 18:2046–2054 [Crossref]
54. del Sordo S, Abbene L, Caroli E, Mancini AM, Zappettini A, Ubertini P (2009) Progress in the development of CdTe and CdZnTe semiconductor radiation detectors for astrophysical and medical applications. Sensors 9:3491–3526 [ADS][Crossref]
55. Owens A, Peacock A (2004) Compound semiconductor radiation detectors. Nucl Instrum Methods Phys Res, Sect A 531:18–37 [ADS][Crossref]
56. Szeles C, Soldner SA, Vydrin S, Graves J, Bale DS (2008) CdZnTe semiconductor detectors for spectroscopic x-ray imaging. IEEE Trans Nucl Sci 55:572–582

[ADS][Crossref]
57. Vadawale SV, Sreekumar P, Acharya YB, Shanmugam M, Banerjee D, Goswami JN, Bhandari N, Umapathy CN, Sharma MR, Tyagi A et al (2014) Hard X-ray continuum from lunar surface: results from high energy X-ray spectrometer (HEX) onboard Chandrayaan-1. Adv Space Res 54:2041–2049
[ADS][Crossref]
58. Nemirovsky Y, Ruzin A, Asa G, Gorelik J (1996) Study of the charge collection efficiency of CdZnTe radiation detectors. J Electron Mater 25:1221–1231. https://doi.org/10.1007/BF02655012
[ADS][Crossref]
59. Cho HY, Lee JH, Kwon YK, Moon JY, Lee CS (2011) Measurement of the drift mobilities and the mobility-lifetime products of charge carriers in a CdZnTe crystal by using a transient pulse technique. J Instrum 6:C01025–C01025. https://doi.org/10.1088/1748-0221/6/01/c01025
[Crossref]
60. Prías-Barragán JJ, Tirado-Mejía L, Ariza-Calderón H, Baños L, Perez-Bueno JJ, Rodríguez ME (2006) Band gap energy determination by photoacoustic absorption and optical analysis of Cd1−xZnxTe for low zinc concentrations. J Cryst Growth 286:279–283. https://doi.org/10.1016/j.jcrysgro.2005.09.022
[ADS][Crossref]
61. Rodriguez ME, Alvarado-Gil JJ, Delgadillo I, Zelaya O, Vargas H, Sánchez-Sinencio F, Tufiño-Velázquez M, Baños L (1996) On the Thermal and Structural Properties of Cd1- xZnxTe in the Range 0<< 0.3. Phys Status Solidi A 158:67–72
[ADS][Crossref]
62. Reno JL, Jones ED (1992) Determination of the dependence of the band-gap energy on composition for Cd 1- x Zn x Te. Phys Rev B 45:1440
[ADS][Crossref]
63. Stolyarova S, Edelman F, Chack A, Berner A, Werner P, Zakharov N, Vytrykhivsky M, Beserman R, Weil R, Nemirovsky Y (2008) Structure of CdZnTe films on glass. J Phys D Appl Phys 41:65402
[Crossref]
64. Toney JE, Schlesinger TE, James RB (1998) Modeling and simulation of uniformity effects in Cd/sub 1-x/Zn/sub x/Te gamma-ray spectrometers. IEEE Trans Nucl Sci 45:105–113. https://doi.org/10.1109/23.659560
[ADS][Crossref]
65. Fiederle M, Feltgen T, Meinhardt J, Rogalla M, Benz KW (1999) State of the art of (Cd, Zn) Te as gamma detector. J Cryst Growth 197:635–640
[ADS][Crossref]
66. Bueno JJP, Rodrguez ME, Zelaya-Angel O, Baquero R, Gonzalez-Hernández J, Baños L, Fitzpatrick BJ (2000) Growth and characterization of Cd1- xZnxTe crystals with high Zn concentrations. J Cryst Growth 209:701–708
[ADS][Crossref]

67. Kang S, Jung B, Noh S, Cho C, Yoon I, Park J (2012) Feasibility study of direct-conversion x-ray detection using cadmium zinc telluride films. J Instrum 7:C01010 [Crossref]
68. Niraula M, Yasuda K, Namba S, Kondo T, Muramatsu S, Wajima Y, Yamashita H, Agata Y (2013) MOVPE growth of thick single crystal CdZnTe epitaxial layers on Si substrates for nuclear radiation detector development. IEEE Trans Nucl Sci 60:2859–2863 [ADS][Crossref]
69. Sellin PJ (2006) Thick film compound semiconductors for X-ray imaging applications. Nucl Instrum Methods Phys Res, Sect A 563:1–8 [ADS][Crossref]
70. Takahashi J, Mochizuki K, Hitomi K, Shoji T (2004) Growth of Cd1- xZnxTe (x~ 0.04) films by hot-wall method and its evaluation. J Cryst Growth 269:419–424 [ADS][Crossref]
71. Kim K, Cho S, Seo J, Won J, Hong J, Kim S (2008) Type conversion of polycrystalline CdZnTe thick films by multiple compensation. Nucl Instrum Methods Phys Res, Sect A 584:191–195 [ADS][Crossref]
72. Tokuda S, Kishihara H, Adachi S, Sato T (2004) Preparation and characterization of polycrystalline CdZnTe films for large-area, high-sensitivity X-ray detectors. J Mater Sci Mater Electron 15:1–8 [Crossref]
73. Won JH, Kim KH, Suh JH, Cho SH, Cho PK, Hong JK, Kim SU (2008) The X-ray sensitivity of semi-insulating polycrystalline CdZnTe thick films. Nucl Instrum Methods Phys Res, Sect A 591:206–208 [ADS][Crossref]
74. Xu L, Jie W, Fu X, Bolotnikov AE, James RB, Feng T, Zha G, Wang T, Xu Y, Zaman Y (2015) Axial distribution of deep-level defects in as-grown CdZnTe: in ingots and their effects on the material′ s electrical properties. J Cryst Growth 409:71–74 [ADS][Crossref]
75. Reine MB (2004) Fundamental properties of mercury cadmium telluride. Encyclopedia of Modern Optics/Academic Press, London
76. Rogalski A (2005) HgCdTe infrared detector material: history, status and outlook. Rep Prog Phys 68:2267–2336. https://doi.org/10.1088/0034-4885/68/10/r01 [ADS][Crossref]
77. Rogalski A (2000) Infrared detectors at the beginning of the next millennium. Sens materials 12:233–288
78. Ruzgar S, Caglar Y, Polat O, Sobola D, Caglar M (2020) The tuning of electrical performance of Au/(CuO:La)/n-Si photodiode with La doping. Surf Interfaces 21:100750. https://doi.org/10.1016/j.surfin.2020.100750 [Crossref]

79. Kim J, Choi J-H, Chae H, Kim H (2014) Effect of indium doping on low-voltage ZnO nanocrystal field-effect transistors with ion-gel gate dielectric. Jpn J Appl Phys 53:71101. https://doi.org/10.7567/jjap.53.071101 [Crossref]
80. Lee JH, Jang BR, Lee JY, Kim HS, Jang NW, Kong BH, Cho HK, Bae KR, Lee WJ, Yun Y (2011) Effect of indium mole fraction on the diode characteristics of ZnO:in/p-Si (111) heterojunctions. Jpn J Appl Phys 50:31101. https://doi.org/10.1143/jjap.50.031101 [Crossref]
81. Bansal S, Jain P, Gupta N, Singh AK, Kumar N, Kumar S, Sardana N (2018) A highly efficient bilayer graphene-HgCdTe heterojunction based p^{+}−n photodetector for long wavelength infrared (LWIR). In: IEEE 13th nanotechnology materials and devices conference (NMDC). IEEE, pp 1–4
82. Rogalski A (1989) Hg1−xZnxTe as a potential infrared detector material. Prog Quantum 13:299–353. https://doi.org/10.1016/0079-6727(89)90008-6 [ADS][Crossref]
83. Toulouse B, Granger R, Rolland S, Triboulet R (1987) Band gap in Hg1-x Znx Te solid solutions. J Phys 48:247–251. https://doi.org/10.1051/jphys:01987004802024700 [Crossref]
84. Berding MA, Sher A, Chen A-B, Patrick R (1990) Vacancies and surface segregation in HgCdTe and HgZnTe. Semicond Sci Technol 5:S86–S89. https://doi.org/10.1088/0268-1242/5/3s/019 [Crossref]
85. Ravid A, Sher A, Zussman A (1990) Photoluminescence study of HgZnTe alloys. J Appl Phys 68:3592–3597. https://doi.org/10.1063/1.346319 [ADS][Crossref]
86. Granger R, Lasbley A, Rolland S, Pelletier CM, Triboulet R (1988) Carrier concentration and transport in Hg1−xZnxTe for x near 0.15. J Cryst Growth 86:682–688. https://doi.org/10.1016/0022-0248(90)90795-M [ADS][Crossref]
87. Baars J, Sorger F (1972) Reststrahlen spectra of HgTe and cdx Hg1-xTe. Solid State Commun 10:875–878. https://doi.org/10.1016/0038-1098(72)90211-6 [ADS][Crossref]
88. Nintz G (1982) in Landolt-Börstein numerical data. Springer, Verlag Berlin
89. Granger R, Pelletier CM (1992) Electron mobility evaluation in Hg1−xCdxTe and Hg1−xZnxTe with two-optical-mode dispersion. J Cryst Growth 117:203–207. https://doi.org/10.1016/0022-0248(92)90745-5 [ADS][Crossref]
90. Patterson JD, Gobba WA, Lehoczky SL (1992) Electron mobility in n-type Hg1−xCdxTe and Hg1−xZnx Te alloys. J Mater Res 7:2211–2218. https://doi.org/10.1557/JMR.1992.2211

[ADS][Crossref]
91. Granger R, Pelletier CM (1994) A prediction of the electron mobility in medium gap HgCdTe and HgZnTe solid solutions. J Cryst Growth 138:486–492. https://doi.org/10.1016/0022-0248(94)90855-9
[ADS][Crossref]
92. Sivananthan S, Chu X, Boukerche M, Faurie JP (1985) Growth of Hg1−xZnxTe by molecular beam epitaxy on a GaAs (100) substrate. Appl Phys Lett 47:1291–1293. https://doi.org/10.1063/1.96308
[ADS][Crossref]
93. Rolland S, Lasbley A, Seyni A, Granger R, Triboulet R (1989) Electrical characterization of as-grown, annealed and indium-doped Hg1-xZnxTe for x near 0.15. Revue de Physique Appliquée 24:795–802. https://doi.org/10.1051/rphysap:01989002408079500
[Crossref]
94. Granger R, Lasbley A, Seyni A, Rolland S, Triboulet R (1990) Study of p-to-n-type conversion in bulk Hg1-xZnxTe near x = 0.15. J Cryst Growth 101:241–245. https://doi.org/10.1016/0022-0248(90)90974-P
[ADS][Crossref]
95. Seyni A, Granger R, Triboulet R, Rolland S, Lasbley A (1991) Acceptor level in narrow gap Hg1−xZnx Te. Phys Status Solidi A 128:K27–K32. https://doi.org/10.1002/pssa.2211280135
[ADS][Crossref]
96. Granger R, Pobla C, Rolland S, Triboulet R (1990) Interdiffusion coefficient in Hg1-xZnxTe solid solutions. J Cryst Growth 101:261–265. https://doi.org/10.1016/0022-0248(90)90978-T
[ADS][Crossref]
97. Rolland S, Granger R, Triboulet R (1992) P-to-n conversion in Hg1−xZnxTe by ion beam milling effect. J Cryst Growth 117:208–212. https://doi.org/10.1016/0022-0248(92)90746-6
[ADS][Crossref]
98. Granger R, Triboulet R, Rolland SR (1996) Bond stability and electronic properties of Hg1-xZnxTe solid solutions. In: Longshore RE, Baars JW (eds) Infrared detectors for remote sensing: physics, materials, and devices. SPIE, pp 14–28
[Crossref]
99. Brus L (1991) Quantum crystallites and nonlinear optics. Applied Physics A 53:465–474. https://doi.org/10.1007/BF00331535
[Crossref]
100. Colvin VL, Schlamp MC, Alivisatos AP (1994) Light-emitting diodes made from cadmium selenide nanocrystals and a semiconducting polymer. Nature 370:354–357. https://doi.org/10.1038/370354a0
[ADS][Crossref]
101. Dabbousi BO, Bawendi MG, Onitsuka O, Rubner MF (1995) Electroluminescence from CdSe quantum-dot/polymer composites. Appl Phys Lett 66:1316–1318. https://doi.org/10.1063/1.113227
[ADS][Crossref]

102. Alivisatos AP (1996) Semiconductor clusters, nanocrystals, and quantum dots. Science 271:933–937. https://doi.org/10.1126/science.271.5251.933 [ADS][Crossref]
103. Weller H, Vossmeyer T, Eychmüller A, Mews A, Katsikas L, Reck G (1994) Nanocrystals of II-VI semiconductor materials. MRS Proc 358:213. https://doi.org/10.1557/PROC-358-213 [Crossref]
104. Malcıoğlu OB, Raty J-Y (2013) Dynamic effect of solvation on the optical properties of a CdTe nanocrystal. Adv Opt Mater 1:239–243. https://doi.org/10.1002/adom.201200037 [Crossref]
105. Schmitt-Rink S, Miller DAB, Chemla DS (1987) Theory of the linear and nonlinear optical properties of semiconductor microcrystallites. Phys Rev B 35:8113–8125. https://doi.org/10.1103/PhysRevB.35.8113 [ADS][Crossref]
106. Vossmeyer T, Katsikas L, Giersig M, Popovic IG, Diesner K, Chemseddine A, Eychmueller A, Weller H (1994) CdS nanoclusters: synthesis, characterization, size dependent oscillator strength, temperature shift of the excitonic transition energy, and reversible absorbance shift. J Phys Chem 98:7665–7673. https://doi.org/10.1021/j100082a044 [Crossref]
107. Murray CB, Norris DJ, Bawendi MG (1993) Synthesis and characterization of nearly monodisperse CdE (E = sulfur, selenium, tellurium) semiconductor nanocrystallites. J Am Chem Soc 115:8706–8715. https://doi.org/10.1021/ja00072a025 [Crossref]
108. Murray CB, Kagan CR, Bawendi MG (1995) Self-organization of CdSe Nanocrystallites into three-dimensional quantum dot Superlattices. Science 270:1335–1338. https://doi.org/10.1126/science.270.5240.1335 [ADS][Crossref]
109. Bailey RE, Nie S (2003) Alloyed semiconductor quantum dots: tuning the optical properties without changing the particle size. J Am Chem Soc 125:7100–7106. https://doi.org/10.1021/ja035000o [Crossref]
110. Xing X, Zhang Q, Huang Z, Lu Z, Zhang J, Li H, Zeng H, Zhai T (2016) Strain driven spectral broadening of Pb ion exchanged CdS nanowires. Small 12:874–881. https://doi.org/10.1002/smll.201503044 [ADS][Crossref]
111. Lu J, Liu H, Zhang X, Sow CH (2018) One-dimensional nanostructures of II–VI ternary alloys: synthesis, optical properties, and applications. Nanoscale 10:17456–17476. https://doi.org/10.1039/C8NR05019H [Crossref]
112. Junpeng L, Cheng S, Minrui Z, Mathews N, Hongwei L, Gin Seng C, Xinhai Z, Mhaisalkar SG, Chorng Haur S (2011) Facile one-step synthesis of CdSxSe1–x nanobelts with uniform and

controllable stoichiometry. J Phys Chem C 115:19538–19545. https://doi.org/10.1021/jp205760r
[Crossref]

113. Takahashi T, Nichols P, Takei K, Ford AC, Jamshidi A, Wu MC, Ning CZ, Javey A (2012) Contact printing of compositionally graded CdSxSe1-xnanowire parallel arrays for tunable photodetectors. Nanotechnology 23:45201. https://doi.org/10.1088/0957-4484/23/4/045201
[Crossref]

114. Lu J, Lim X, Zheng M, Mhaisalkar SG, Sow C-H (2012) Direct laser pruning of CdSxSe1–x nanobelts en route to a multicolored pattern with controlled functionalities. ACS Nano 6:8298–8307. https://doi.org/10.1021/nn303000j
[Crossref]

115. Wu D, Chang Y, Lou Z, Xu T, Xu J, Shi Z, Tian Y, Li X (2017) Controllable synthesis of ternary ZnSxSe1-x nanowires with tunable band-gaps for optoelectronic applications. J Alloys Compd 708:623–627. https://doi.org/10.1016/j.jallcom.2017.03.012
[Crossref]

116. Choi Y-J, Park K-S, Park J-G (2010) Network-bridge structure of CdSxSe1-xnanowire-based optical sensors. Nanotechnology 21:505605. https://doi.org/10.1088/0957-4484/21/50/505605
[Crossref]

117. Guo P, Hu W, Zhang Q, Zhuang X, Zhu X, Zhou H, Shan Z, Xu J, Pan A (2014) Semiconductor alloy nanoribbon lateral heterostructures for high-performance photodetectors. Adv Mater 26:2844–2849. https://doi.org/10.1002/adma.201304967
[Crossref]

118. Ferekides CS, Balasubramanian U, Mamazza R, Viswanathan V, Zhao H, Morel DL (2004) CdTe thin film solar cells: device and technology issues. Sol Energy 77:823–830. https://doi.org/10.1016/j.solener.2004.05.023
[ADS][Crossref]

OceanofPDF.com

© The Author(s), under exclusive license to Springer Nature Switzerland AG 2023
G. Korotcenkov (ed.), *Handbook of II-VI Semiconductor-Based Sensors and Radiation Detectors*
https://doi.org/10.1007/978-3-031-19531-0_5

5. II-VI Semiconductors Bandgap Engineering

Mustafa Kurban[1], Yusuf Şimşek[2] and Şakir Erkoç[3] ✉
(1) Department of Electrical and Electronics Engineering, Kırşehir Ahi Evran University, Kırşehir, Turkey
(2) Vocational School of Health Services, Gazi University, Gölbaşı/Ankara, Turkey
(3) Department of Physics, Middle East Technical University, Ankara, Turkey

✉ **Şakir Erkoç**
Email: erkoc@metu.edu.tr

Keywords 0D structures – 1D structures – 2D structures – II-VI compounds – II-VI semiconductors – Alloys – Bandgap – Bandgap engineering – Binary semiconductors – Detectors – Displays – Doping – Energy spectrum – Heterostructures – Lasers – Lattice strain – Molecular beam epitaxy – Nanoparticles – Optical materials – Photovoltaic cells – Quantum dots – Quantum size effect – Quantum wells – Semiconductors – Simulations – Solar cells – Superlattices – Ternary semiconductors – Thin films – Tunability of bandgaps

5.1 Introduction

The bandgap energy, E_g, determines many of the semiconductors' properties, and because of this, a great deal of interest has been given to bandgap engineering as a powerful technique in the development of new semiconductor materials. The bandgap of a semiconductor is a significant parameter for many applications such as solar photovoltaic cells, solid-state

lighting, detectors, displays, lasers, etc. Each application requires materials with a certain set of properties that are often not possessed by known double semiconductor compounds. As a result, the problem always arises to find a new semiconductor compound with the required bandgap and, through the optimization of the bandgap of the semiconductor material, to improve the efficiency of the devices under development [1, 2]. For example, the following tasks can be solved through bandgap engineering:

- Increasing the efficiency of solar cells – production of tandem solar cells covering the entire spectrum of solar radiation. In photovoltaic cells, the principal condition for solar energy conversion to electrical energy is the energies of phonon close to the bandgap where thermalization and phonon generation cause losing photons with higher energy, but photons with lower energy are simply transmitted by the photovoltaic cell. To get the photovoltaic cells with highly efficient, it is important to use multiple semiconductors with different bandgaps.
- Manufacturing of selective photodetectors, LEDs, and lasers for the required spectral region. For example, multicolor emission in displays is a desirable property to get a low cost highly efficient production and need bandgaps between 1.77 and 3.1 eV [3].
- Optimization of electronic and electrophysical properties of semiconductors required for specific applications. The electronic properties of crystalline condensed matter are determined by their electronic energy band structures.

There are various approaches in bandgap engineering. In the following sections, the details of the approaches have been discussed.

5.2 Approaches for Bandgap Engineering

Material design with bandgap engineering is a robust technique to obtain new semiconductor devices with profoundly different properties for the constituent materials. Particularly the wide gap II-VI compounds are widely investigated because of the attractive applications in fabricating blue-green and blue optoelectronic devices, such as light-emitting diodes and laser diodes [4, 5]. The applications include the use of II-VI compound-based materials as light sources, in full color displays, and for increasing the information density in optical recording [6]. The optical and electrical properties of the films, such as the bandgap energy range and resistance,

directly affect device performance. This allows the selection of films with suitable parameters for the device to be planned. One of the most important consequences of this process is the possibility of independently tuning electron and hole transport properties by using heterostructures [7], superlattices [8] strain [9] intercalation [10], alloying [2], doping [11], and size controlling of nanoparticles [12].

5.3 Bandgap Engineering via II-VI Solid Solutions Formation

II-VI semiconductors are distinguished by the fact that they form a continuous series of solid solutions among themselves, as a result of which any bandgap between the E_g of these compounds can be obtained. This is the most common and most effective method of II-VI semiconductors bandgap engineering. In addition, on the basis of II-VI semiconductors, both triple and quadruple compounds can be formed.

II-VI binary semiconductors have a direct bandgap and exhibit good photoluminescence (PL) properties. The PL emission peaks when it comes to ternary alloys can be gradually shifted under controlled stoichiometry, which results in the tunable bandgap. For example, Fig. 5.1 schematically shows the tuning ability of the ternary bandgap of CdS_xSe_{1-x}. The bandgap of CdS_xSe_{1-x} can be continuously decreased from CdS to CdSe as x decreases [13].

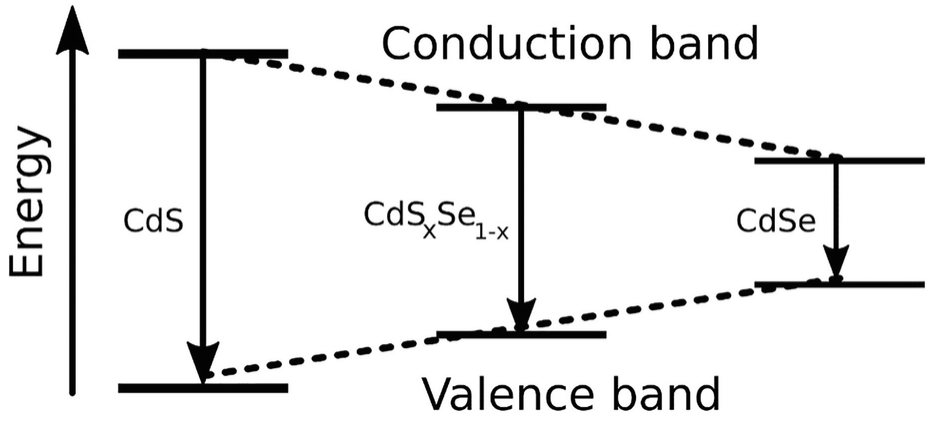

Fig. 5.1 Schematic representation of the tunability of bandgap of ternary and binary semiconductors (CdS, CdS_xSe_{1-x} and CdSe) based on S and Se content (x). (Idea from Ref. [13])

One of the advantages of the alloying process is the possibility to vary the bandgap of the studied materials with different concentrations [14]. For example, alloying CdTe with Zn gives rise to the increase of the bandgap based on the concentration of x in the $Cd_{1-x}Zn_xTe$ ternary alloy [15]. The electronic properties of $Cd_{1-x}Zn_x$ Te with $x = 0.1–0.15$ are very suitable for X-ray and Γ-ray radiation detectors [16] when compared to CdTe. On the other hand, alloying CdTe with CdS or CdSe forming $CdTe_{1-x}Se_x$ reduces the bandgap of CdTe effectively [17], and thus enhancing CdTe solar cell performance through $CdTe_{1-x}Se_x$ alloying [18].

The II-VI semiconductors cover the full solar spectrum due to their tunability of bandgaps. For example, the bandgap of quaternary ZnCdSSe nanowires can be tuned from 1.75 eV to 3.55 eV covering the entire visible spectral range [19, 20]. This facilitates them the excellent material platforms for solar cell design with full spectrum response.

The wide bandgap of CdTe quantum dots (QDs) can be tailored by alloying with the concentration x of Hg in the $Cd_{1-x}Hg_xTe$, which covers a wide range of the infrared (IR) region [21]. The possibility of changing the bandgap of $Cd_{1-x}Hg_xTe$ alloys by manipulating the Hg composition leads to a change from a semimetal to a semiconducting behavior, where the bandgap decreases with increasing Hg composition [22] (see Fig. 5.2). From the examples mentioned above, one can see that the electronic structures of II-VI compounds can be modified by alloying to make them available for a variety of applications.

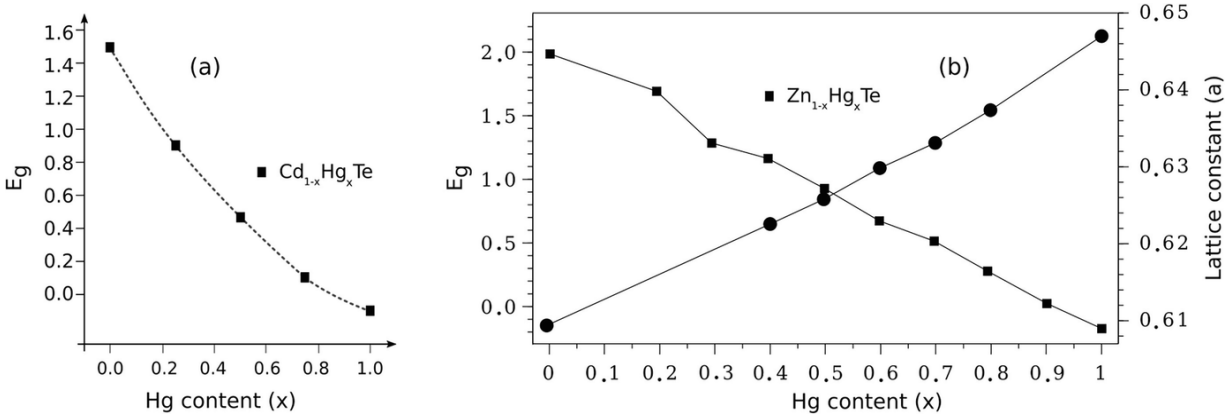

Fig. 5.2 (**a**) The variation of bandgap energy (in eV) with respect to Hg content (x) for $Cd_{1-x}Hg_xTe$ alloy. (**b**) The variation of bandgap energy (in eV, decreasing line) and lattice constant (in nm,

increasing line) with respect to Hg content (x) for $Zn_{1-x}Hg_xTe$ alloy. (Data extracted from Refs. [22, 23])

Lattice constant of $Zn_{1-x}Hg_xTe$ increases nonlinearly as the x composition number increases, and bandgap energy decreases nonlinearly as Hg composition ratio increases. The energy bandgap of $Hg_xZn_{1-x}Te$ varies between −0.140 and 2.25 eV at room temperature, and this range offers the possible usage of these alloys in electronics such as light-emitting diodes, tandem solar cells, and thermoelectric generators. El-Soud et al. [23] used an inter-diffusion process at high temperatures to produce $Zn_{1-x}Hg_xTe$ alloy from HgTe and ZnTe alloys in the form of compressed powder. This procedure provides homogeneity over the entire composition range.

To simulate the electronic and optical characteristics of $Zn_{1-x}Hg_xTe$ ternary alloys, first-principle calculations were employed by Laref et al. [24]. Modified Becke-Jhonson exchange-correlation potential as implemented in the full-potential linearized augmented plane-wave scheme was used to find bandgaps and optical spectra. A bandgap of 0.25 eV was obtained in $Zn_{0.25}Hg_{0.75}Te$ alloy and displays a semiconducting behavior with a small positive energy bandgap. Vegard's law was used to obtain lattice constant and energy bandgap of $Zn_{1-x}Hg_xTe$ ternary from binary alloys. Mathematical relation for lattice constant is as follows:

$$a\mathrm{Zn}_{1-x}\mathrm{Hg}_x = (1-x)\,a\mathrm{ZnTe} + x a\mathrm{HgTe} \tag{5.1}$$

Behavior of the lattice parameter with respect to x composition is shown in Fig. 5.3, and it obeys the nonlinear behavior of Vegard's law. aZnTe and aHgTe are lattice constants of the ZnTe (6.09 Å) and HgTe (6.47 Å), respectively. Lattice constant increases nonlinearly as the ratio increases from 0 to 1, whereas bandgap energy decreases nonlinearly. Analytical formulation of lattice parameter could be written as follows:

$$a\mathrm{Zn}_{1-x}\mathrm{Hg}_x\mathrm{Te} = 6.078 + 0.61x - 0.22x^2 \tag{5.2}$$

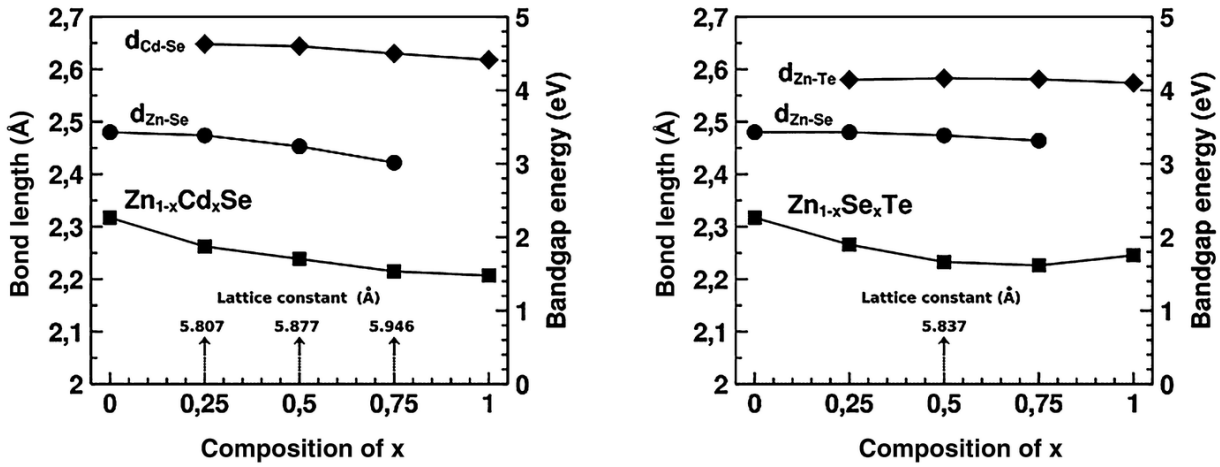

Fig. 5.3 Bond lengths of binary compounds in $Zn_{1-x}Cd_xSe$, $Zn_{1-x}Se_xTe$, and the bandgaps of the ternary alloys of $Zn_{1-x}Cd_xSe$, $Zn_{1-x}Se_xTe$ with respect to the composition of *x*. (Data extracted from Ref. [26])

Energy bandgap of $Zn_{1-x}Hg_xTe$ alloy was calculated with the following equation:

$$E_g(x) = (1-x)\,E_g,\mathrm{ZnTe} + xE_g,\mathrm{HgTe} - bx\,(1-x)\,, \tag{5.3}$$

where $E_g(x)$ represents the energy bandgap of $Zn_{1-x}Hg_x$ Te alloys and $E_{(g,\,ZnTe)}$ and $E_{(g,\,HgTe)}$ are energy bandgap of ZnTe and HgTe, respectively. b is the bowing parameter, and the average value of gap bowing is 1.2 for overall concentrations. Energy bandgap separation between conduction band maximum and valence band minimum of the $Zn_{1-x}Hg_x$ Te alloy decreases as *x* composition increases. That is, composition of Hg plays an important role in the transition from semiconductor to semimetal state (see Fig. 5.3). Besides, multiphoton absorption was achieved in a solar cell based on O-doped ZnTe [25].

In addition to structural properties of ternary alloys, the electronic properties, particularly the charge distribution on atoms in the material, also show interesting features. According to TB-calculation results [27] for $CdSe_xTe_{1-x}$ and $Cd_{1-x}Zn_xTe$ ternary alloys, the charges of cations (Cd and Zn) vary around two electrons, while the charges of anions (Se and Te) vary around six electrons. The variation of calculated excess charges on atoms as a function of alloy composition is displayed in Fig. 5.4.

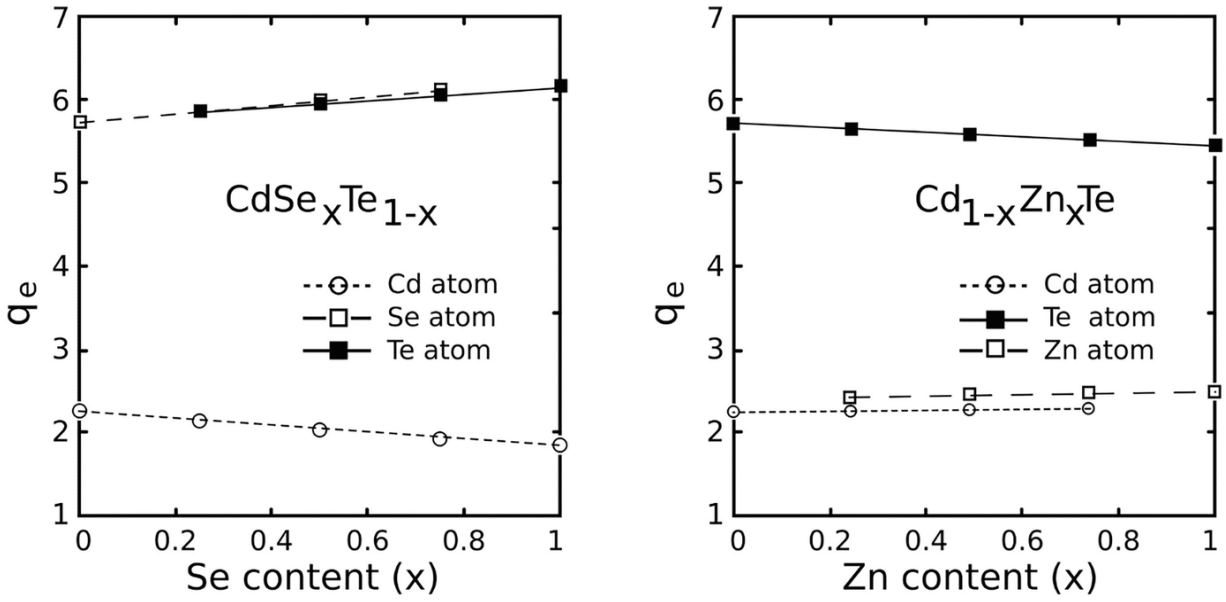

Fig. 5.4 Calculated excess charge q_e (in e/atom) on atoms with respect to the content of $CdSe_xTe_{1-x}$ and $Cd_{1-x}Zn_xTe$ compounds. (Data extracted from Ref. [27])

5.4 BandGap Engineering via Doping

Studies have shown that the bandgap can also be controlled by doping II-VI compounds with elements that do not belong to the II group. However, in this case, it is necessary to take into account the phase diagram and the limiting solubility of the alloying addition in the II-VI compound. At present, Be [26], B [28], S [29], Mn [30], Ag [31], and Cu [32] were used as dopants affecting the bandgap of II-VI compounds.

Electronic and structural properties of $Zn_{1-x}Be_xSe$ alloys were studied with real-space density-functional molecular-dynamics and conventional electronics-structure calculation methods [26]. Lattice constants and bond lengths of binary groups were obtained via energy minimization method with molecular dynamics, and lattice constants of ternary alloys were tested and/or computed using Vegards rule (see Fig. 5.5).

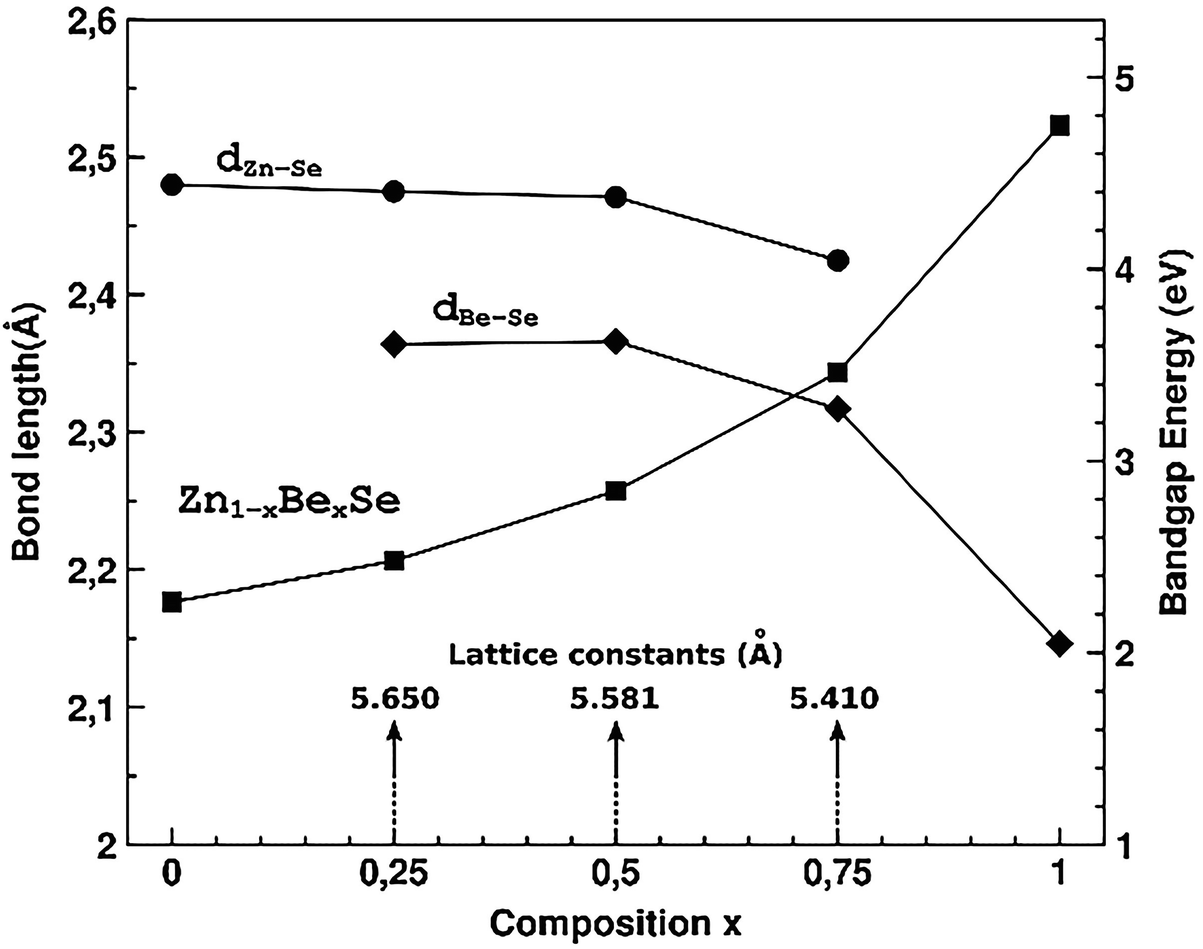

Fig. 5.5 Bond lengths of binary compounds in $Zn_{1-x}Be_xSe$ and the bandgaps of the ternary alloys of $Zn_{1-x}Be_xSe$ with respect to the composition of *x*. (Data extracted from Ref. [26])

XRD measurements on nominally ternary $Cd_{1-x}Mn_xS$ powders established that these materials have hexagonal crystal structure clearly distinct from that of the starting powders (CdS: cubic zinc blende; MnS: cubic rocksalt) [30]. Lattice constants vary substantially with the concentration of Mn in the system.

Refinement of the crystal structure has yielded reliable values of the lattice constants. The values for lattice constants for this hexagonal material are shown in Fig. 5.6. It combines data for the Cd-based compounds, with lattice constants for the corresponding Zn-based materials. The values for wurtzite CdS, MnS, and ZnS are also shown for comparison. For both *a* and *c*, an approximate linear relationship, following Vegards law, is observed with varying Mn fraction across the entire Cd-Mn-Zn system.

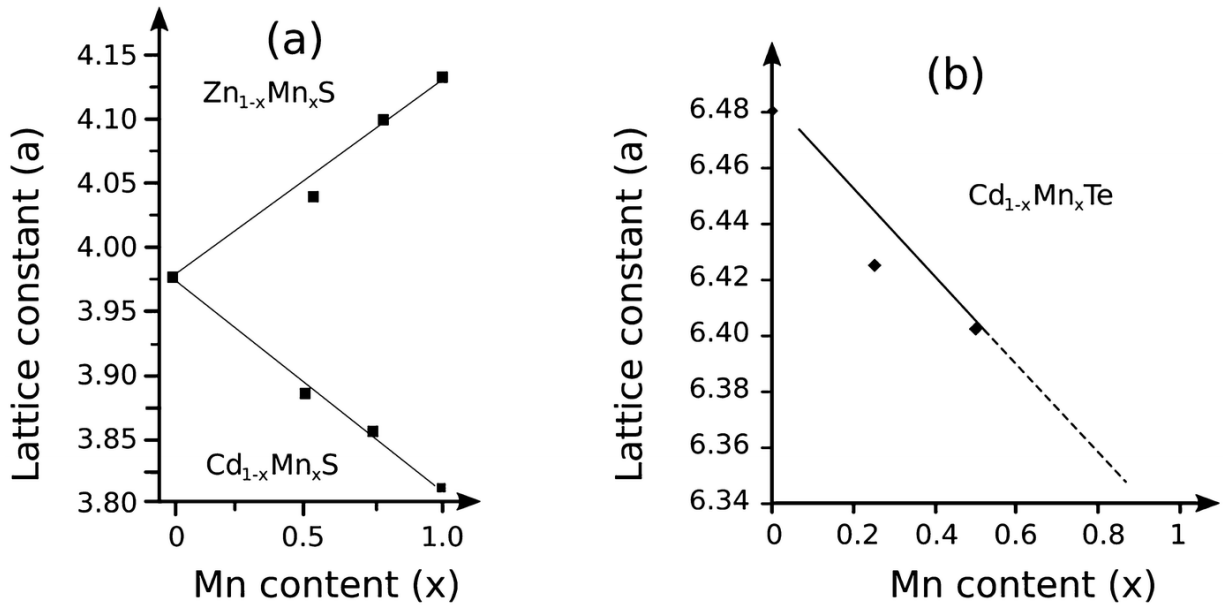

Fig. 5.6 (**a**) Effect of Mn content (*x*) on the lattice constant *a* (in Å) of the hexagonal structure of $Cd_{1-x}Mn_xS$ and $Zn_{1-x}Mn_xS$. (**b**) Effect of Mn content (*x*) on the lattice constant *a* (in Å) of the zinc blende structure of $Cd_{1-x}Mn_xTe$. Linear trend for $x > 0.5$ is shown as a dashed line. (Data extracted from Ref. [30])

In the $Zn_{1-x}Be_xSe$ alloys, the Zn-Se (d_{Zn-Se}) bond length decreases by not more than 2%, while the Be-Se (d_{Be-Se}) bond length increases by 10% compared to their binary compounds. This significant difference in dBe-Se is due to the softening of the Be-Se bonds. Be atom has a smaller electronegativity than the others. Thus, Be-Se bond is more ionic and less rigid than the Zn-Se bond. Theoretical lattice constants were reported as 5.728, 5.945, 4.955, and 6.045 Å for ZnSe, ZnTe, BeSe, and CdSe binaries, respectively. As seen in Fig. 5.5, when Be composition ratio increases, the lattice constant of $Zn_{1-x}Be_xSe$ decreases, and energy bandgap increases significantly. Similar characteristic in bandgap for $Cd_{1-x}Be_xSe$ appears and shows the following quadratic behavior [4].

$$E_g(x) = 0.466–0.088x + 3.99x^2 \tag{5.4}$$

ZnS thin films are widely used in solar cells as widow material. Optical and electrical properties of the films such as bandgap energy and resistivity directly affect device performance [28]. The bandgap energy values of 1, 5, 10, 15% boron-doped films vary between 3.37–3.82 eV. (See Table 5.1). This wide range makes doped ZnS thin films applicable for fabrication of

different optoelectronic devices such as sensors, solar cells, photodiodes, etc. with different bandgap requirements.

Table 5.1 Bandgap energy values (in eV) of ZnS films with Boron doping before and after annealing

Boron doping level	Before annealing	After annealing
Undoped	3.48	3.69
1%	3.62	3.68
5%	3.63	3.52
10%	3.73	3.48
15%	3.82	3.37

Data collected from Ref. [28]

It was found that beryllium-containing II-VI compounds have an improved ability to significantly reduce the propagation of defects, which is due to a greater prevalence of strong covalent bonds and lattice hardening in the materials [33, 34]. These compounds are promising candidate to fabricate full color visible optical devices because of the large range of bandgaps of the binary constituents from 1.74 eV (CdSe) to 5.5 eV (BeSe) [35]. Silver (Ag) can be incorporated as an acceptor in the II-VI semiconductors, as it affects the electrical and optical features of these materials [36]. With vanadium doping, ZnTe becomes a photorefractive material and is suitable for optical power-limiting applications [37]. Moreover, when doped with Ti, Mn, and Cr, the bandgap of ZnTe varies between 0.7 and 2.27 eV, making the resulting material very suitable for applications in the three main regions of the spectrum: visible, UV, and infrared. It is also possible to use the material as filter for certain wavelengths [38]. Ni-, Co-, and Fe-doped CdS NPs are more effective as catalyst than undoped CdS due to fast reduction of methylene blue [39].

Producing ternary II-VI materials with variable concentration of the second cation (Mn, Ca, Zn, Fe) causes interesting results. From these results, two important statements are concluded [30]: (1) It is possible to produce ternary and quaternary II-VI materials doped with TM ions by simple annealing of the commercially available binary powders omitting expensive and complicated crystal growth processes. (2) It is possible to effectively shift absorption and PL of TM in II-VI host materials towards shorter or longer wavelength by varying composition, type, and amount of

the second cation in ternary II-VI materials. Iron-doped $Zn_{1-x}Cd_xTe$ active powders are very attractive for tunable lasing with a wavelength longer than 6 μm [30].

The doping of CdS by Ag changed the structure of the cubic phase to the hexagonal phase [31]. The results showed that doping of Ag in CdS crystal lattice increases the photocatalytic properties. Doping also leads to a reduction of the bandgap, easy release of electrons, formation of hole and free radicals, and better degradation. The best efficiency was related to Ag/CdS irradiated under visible light. Kinetic studies showed that the highest correlation coefficient belongs to the Blanchard model, so this reaction followed pseudo-second-order kinetics [31].

Zinc oxide (ZnO) and zinc sulfide (ZnS) are among the most intensively investigated semiconductor materials. It is triggered by the broad spectrum of their physical characteristics being appropriate for designing various devices, such as ultraviolet (UV) light-emitting diodes (LEDs), electroluminescent displays, gas sensors, anti-reflection coatings, transparent electrodes, and windows in thin-film solar cells. The great interest into these materials is mainly driven by their wide bandgap energy (E_g 3.3–3.4 eV for ZnO and E_g 3.4–3.8 eV for ZnS), meaning a high transparency in visible and near-UV range [29]. It is quite interesting that the bandgap energy of $ZnO_{1-x}S_x$ varies nonlinearly with changing the sulfur content (see Fig. 5.7). Changing x from 1.0 to 0, i.e. reduction of S content and increase in O content, E_g initially decreases, reaching the minimum at $x = 0.32$ ($E_g = 2.7$ eV), and then increases to 3.30 eV (ZnO). Behavior of $ZnO_{1-x}S_x$ bandgap energy can be described as [40]:

$$E_g\mathrm{ZnOS}(x) = x_g\mathrm{ZnS} + (1-x)\,E_g\mathrm{ZnO} - b\,(1-x)\,x, \tag{5.5}$$

where $E_{g\mathrm{ZnS}}$ and $E_{g\mathrm{ZnO}}$ are bandgap energy of binary compounds at 300 K (3.62 eV and 3.30 eV, respectively), b is the bowing parameter. According to our data, its value is 3.5 eV. Nonlinear dependence of the bandgap energy is caused by difference in electronic properties of oxygen and sulfur anions in the zinc oxide lattice. Since oxygen electronegativity ($\chi = 3.44$) is higher than that of sulfur ($\chi = 2.58$), the density of charge around the oxygen atom is larger than that of sulfur atom [29].

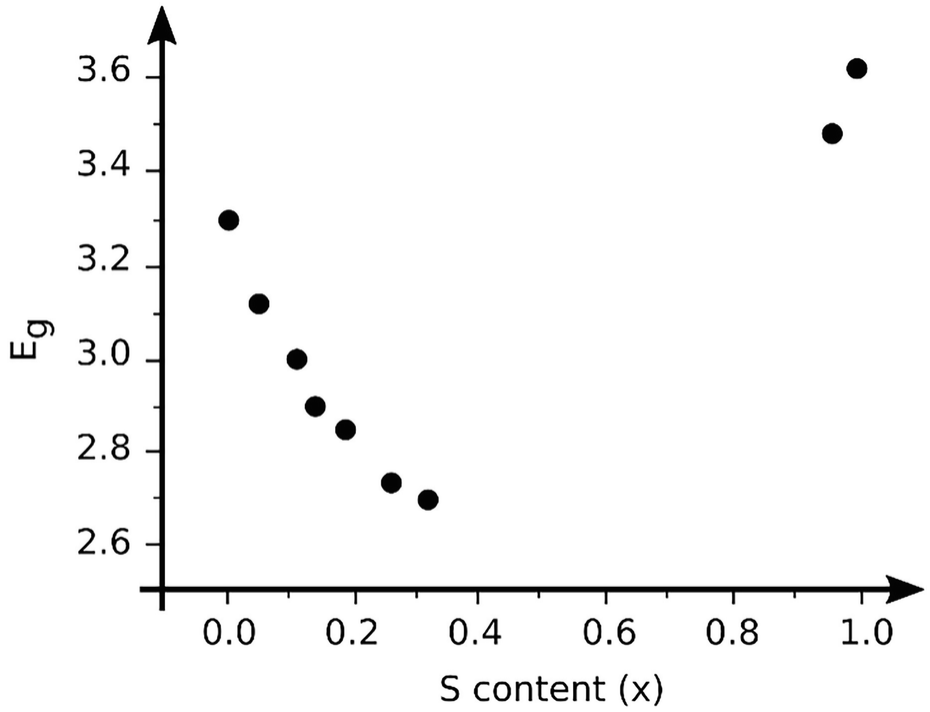

Fig. 5.7 Dependence of the bandgap energy E_g (in eV) on the S content in the $ZnO_{1-x}S_x$. (Data extracted from Ref. [29])

In a recent experimental work, Ca et al. [32] investigated the influence of precursor ratio and dopant concentration on the structure and optical properties of 0.5% Cu-doped ZnCdSe-alloyed QDs. The variation of the optical bandgap of ZnCdSe-alloyed QDs with respect to the Cd/Zn ratio is shown in Fig. 5.8. The experimental data were obtained at room temperature. The bandgap characteristic shows a linear dependence on the Cd/Zn ratio. The constituent ratio of the host and dopant concentration changes the crystal structure from ZB to WZ. The dopant concentration also influences the optical properties.

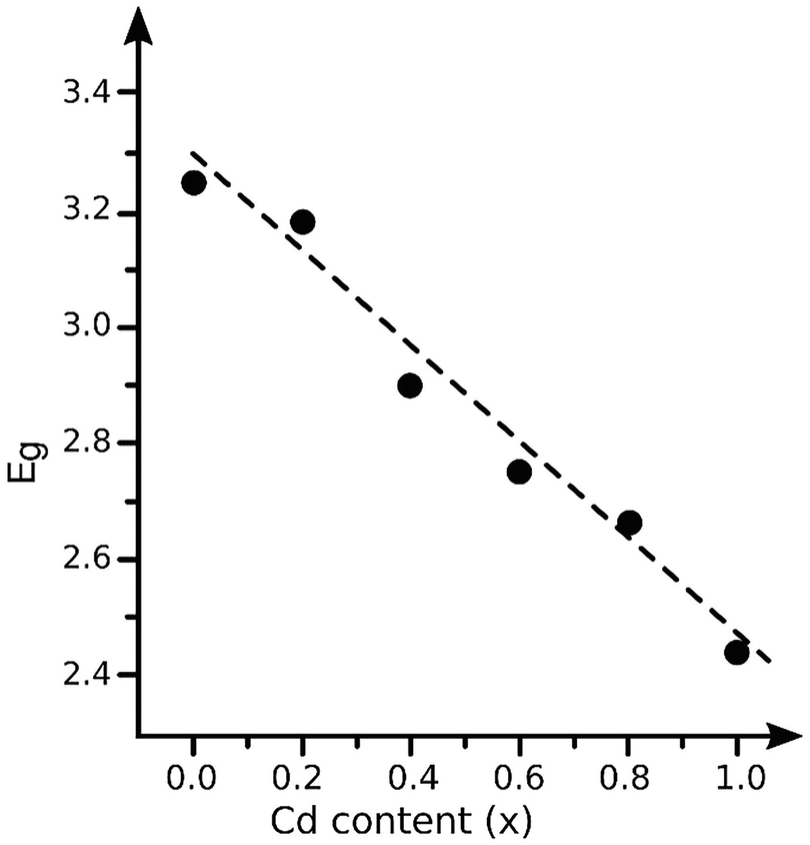

Fig. 5.8 The optical bandgap energy, E_g (in eV) of $Zn_{1-x}Cd_xSe$ with 0.5% Cu alloy quantum dots. The fitted dashed line corresponds to the equation $y = 3.43–0.162x$. (Data extracted from Ref. [32])

5.5 BandGap Engineering via Heterostructures Forming (Superlattices, Quantum Wells)

The fabrication of superlattices such as a heterostructures with quantum wells (QWs) and strained-layer superlattice (SLS) is one of the most interesting approaches to developing IR materials based on wide gap semiconductors. This approach is described in sufficient detail in [41, 42]. Superlattices are a periodic repetition of layers of two materials with dissimilar bandgaps. A material with a lower bandgap is usually called a well layer, and a material with a higher bandgap is called a barrier layer. The ability to vary the binding energy of electrons in superlattices to match the desired IR response by changing quantum well depth and width is an important advantage of such structures. Currently, these structures are manufactured based on III-V semiconductors such as GaAs/AlGaAs and InAs/GaSb. Photodetectors based on these superlattices, depending on the

width of the quantum wells, can have a high photosensitivity in the wavelength range from 3 to 15 μm, which corresponds to a bandgap of 0.4–0.08 eV. However, theoretical calculations have shown that effective superlattices can also be developed based on II-VI semiconductors. It was found that HgTe-CdTe superlattice should have unique properties, due to the inversion of the conduction and valence bands in the well materials. This system unites a direct-gap semiconductor with a symmetry-induced semimetal. Predictions by Schulman and McGill [43, 44] suggested that this new material would have a number of advantages over the HgCdTe compounds. For example, it was shown that the cut-off wavelength for HgTeCdTe superlattice would be easier to control than the HgCdTe alloy at longer wavelengths. In these structures, the cut-off wavelength depends on the HgTe width. According to theoretical simulations, an increase in thickness within 1–6 nm leads to an increase in the cut-off wavelength from 2 to 100 μm. The first HgTe-CdTe superlattice by MBE was grown in 1982 [45]. Subsequently, using MBE technology, fabricated HgTe-HgCdTe superlattice-based photodetectors with cut-off wavelength of about 30 μm at 4 K were obtained [46]. The superlattice consisted of 100 periods of 8 nm-thick HgTe wells alternating with 7.7 nm thick $Hg_{0.05}Cd_{0.95}Te$ barriers. However, it is not clear when it will be possible to fully realize the advantages of HgTe-CdTe superlattices, since due to intense diffusion at the interfaces, only very low-temperature processes can be used when growing these structures and fabricating devices. A schematic illustration of an intersubband HgTe-CdHgTe quantum-well infrared photodetector (QWIP) structure is shown in Fig. 5.9.

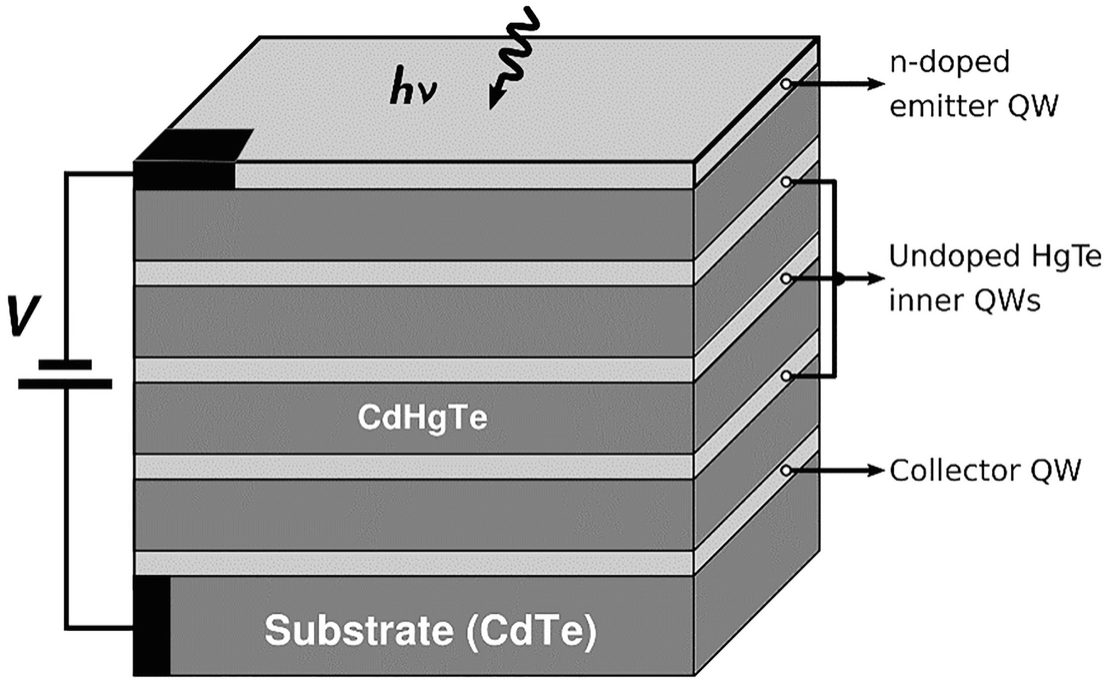

Fig. 5.9 Diagrammatic view of an interband HgTe-CdHgTe quantum well infrared photodetector structure. (Idea from Ref. [47])

The II-VI ZnCdSe/ZnCdMgSe lattice matched to InP system presents itself as an alternative to address challenges associated with conventional material systems by its large conduction band offset up to 1.1 eV [48] and the absence of scattering into satellite valleys [49]. The large conduction band offset of ZnCdSe/ZnCdMgSe permits covering a wide spectral range, essential for multi-band detectors, from 2 μm to 10 μm with a single material system [50]. For instance, CdS/CdTe heterostructures have a potential for higher device performance with over 20% conversion efficiency in photovoltaic devices [51]. HgTe/CdTe superlattices have proven to be new materials with enormous functionalities which are desirable for solar cells [22]. The bandgap of HgTe quantum wells (QW) significantly enhances via strain engineering of CdTe-$Cd_{0.5}Zn_{0.5}Te$ strained-layer superlattices on GaAs [52].

5.6 BandGap Engineering via Temperature Control

In a theoretical study related to temperature phase transitions in HgTe QW [53], it was shown that nonlocal band structure was affected by temperature

and can be used for the transitions between the band insulators, topological insulators, and the semimetal phases. Additionally, behavior of the bandgap was found to strongly depend on the QW width. When HgTe QW is wide enough, the system has an indirect bandgap, and temperature does not affect the bandgap up to a certain point. Further increasing temperature causes a linear increase in the bandgap. On the other hand, if the QW width is small, then the bandgap becomes strongly sensitive to temperature.

The bandgap of HgTe/CdHgTe QW heterostructures [54] produced via molecular beam epitaxy was found strong temperature-dependent, and effective wavelength can be tuned by changing the temperature. For example, emission wavelength at around 230 K ranges from 3.2 to 3.4 μm. Narrow HgTe/CdHgTe heterostructures reduce the Auger recombination and increase the operating temperature. Hence, bandgap energy increases almost linearly as the temperature increases. Temperature effects for stimulation emission spectra were studied in HgTe/CdHgTe QWs heterostructures grown via molecular beam epitaxy methods [55]. At 240 K, $Cd_{0.75}Hg_{0.25}Te$ barrier layers could produce stimulated emission at 3.65 μm, and the optical bandgap seemed to be broadened as the temperature increased.

Mynbaev et al. [56] studied acceptor states of $Cd_xHg_{1-x}Te$/GaAs heteroepitaxial films grown via molecular beam epitaxy in the temperature range 4.2 K < T < 300 K under excitation with a semiconductor laser at a wavelength of 1.03 or 0.81 μm. They showed photoluminescence spectra are temperature dependent, and acceptor levels are ionized above 180 K. Moreover, 18 and 27 meV acceptor states could be observed under certain growth conditions and post-growth procedures such as mercury deficiency and annealing procedures. The unusual property of the binary HgTe alloy is its inverted band structure or a zero bandgap. The inverted bandgap arises from the interaction between the 6s orbital of the Hg half nucleus and the sp band formed by the hybridization between the maximum of the 5p valence band and the minimum of the 7s conduction band of Te and Hg atoms, respectively. HgTe-based QWs are graphene-like 2D systems, and QW width d influences the bandgap. When d is smaller than the critical width dc, electron-like subband (E1) becomes larger than the hole-like subband (H1), and the semiconductor phase is obtained. If d is larger than the dc, then E1 subband drops below the H1 subband, and 2D topological insulator

phase occurs. Therefore, dc is an important parameter for phase transition, and bandgap is tuned by the QW width [57, 58].

The annealing of materials after synthesis or deposition can also cause a change in the bandgap. For example, Yesilkaya and Ulutas [28], studying ZnS films deposited by spray pyrolysis (T_{pyr} = 350 °C), found that annealing of undoped films (T_{an} = 350 °C) and films doped with boron (1–15%) can be accompanied by a change in the bandgap measured by optical transmission in the range 3.48–3.69 eV. In this case, annealing of undoped samples led to an increase in E_g from 3.48 to 3.69 eV, and annealing of samples doped with boron led to a decrease in E_g from 3.82 to 3.37 eV. Unfortunately, the authors do not explain the nature of the observed effect. However, the presence of such an effect requires more careful control of the temperature regimes of manufacturing and subsequent processing of fabricated devices. In the production stage of the thin films, the bandgap energy of the material shows a dependence on also annealing as well as doping. The effect of both doping and annealing on ZnS thin films is displayed in Table 5.1.

5.7 BandGap Engineering via Lattice Strain

The theoretical study has shown that lattice strain is also a factor that has a noticeable effect on the bandgap of II-VI compounds. For example, it was established that band structure of HgTe QWs is sensitive to hydrostatic pressure [59]. Hydrostatic pressure can cause the transition between the band insulators, topological insulators, and the semimetal phases. Additionally, behavior of the bandgap was found to strongly depend on the QW width. When HgTe QW is wide enough, the system has an indirect bandgap, and pressure does not affect the bandgap up to a certain point. On the other hand, if the QW width is small, then the bandgap becomes strongly sensitive to pressure.

The experiment showed that semimetallic states in HgTe can also appear due to the stress arising in heterostructures. Semimetallic states caused by strain had been reported for the 20 nm thick HgTe based QWs sandwiched between two CdHgTe layers [60]. Measurements were done at the temperature of 1–16 K. Calculation of the energy band structure showed that the key reason for the formation of semimetallic states was due to the

overlapping of the conduction band and valence band when lattice mismatch of the HgTe and CdTe occurred by the strain. Another theoretical study also reported that HgTe shows semimetallic property as the tensile strain was applied [61]. The bandgap of ZnTe nanowires can also be modulated using uniaxial strain [62]. In particular, it has been found that compression allows direct-to-indirect band transition in ZnTe at nanowire diameters larger than 1.4 nm. In nanowires, the bandgap energy value also shows a diameter-dependent characteristic. Figure 5.10 displays the dependence of E_g with respect to the diameter of the nanowires.

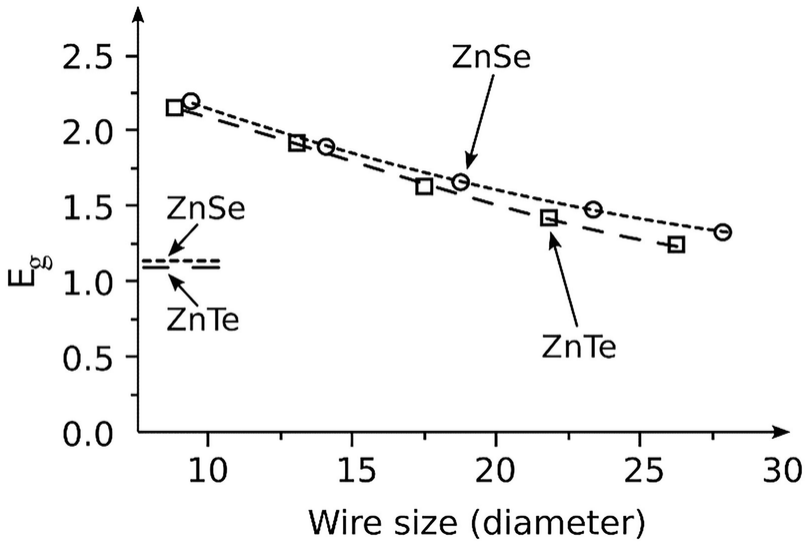

Fig. 5.10 The calculated bandgap energies, E_g (in eV) of ZnSe and ZnTe nanowires with respect to wire size (diameter, in Å). The corresponding bulk values are shown with horizontal lines. (Data extracted from Ref. [62])

Bandgap of the CdTe-$Cd_{0.5}Zn_{0.5}Te$(001) superlattices was also enhanced via strain engineering [52]. A significantly increased energy gap E_g (as high as 55 meV) was reported when the compressive strain was applied to the QWs. Shape of the valence band was affected with strain, and a transition from a semimetal-like system to a direct-band-gap semiconductor was observed. Additionally, thick QWs were transformed from semimetals to 2D topological insulator when the strain changed from tensile to compressive.

5.8 BandGap Engineering via Size Control of Nanoparticles (QDs) Size

Quantum dots (QDs), i.e., particles, containing conduction electrons, with characteristic sizes less than 100 nm in all three dimensions have recently become one of the most studied objects. Drastic changes in most material properties depend on the nanocrystal size, due to quantum confinement. Quantum dots can be obtained by two methods: using colloidal chemical synthesis and epitaxial technologies. Both methods provide many opportunities both in obtaining QDs based on various semiconductor materials and QDs with different geometries. This technology for II-VI compounds is described in Chapters 12 and 13 (Vol. 1). The most significant effect observed in quantum dots is the dependence of the energy spectrum on the size of nanoparticles. In the experiment, this manifests itself in an increase in the bandgap. A schematic illustration of electronic structure of QDs is displayed in Fig. 5.11.

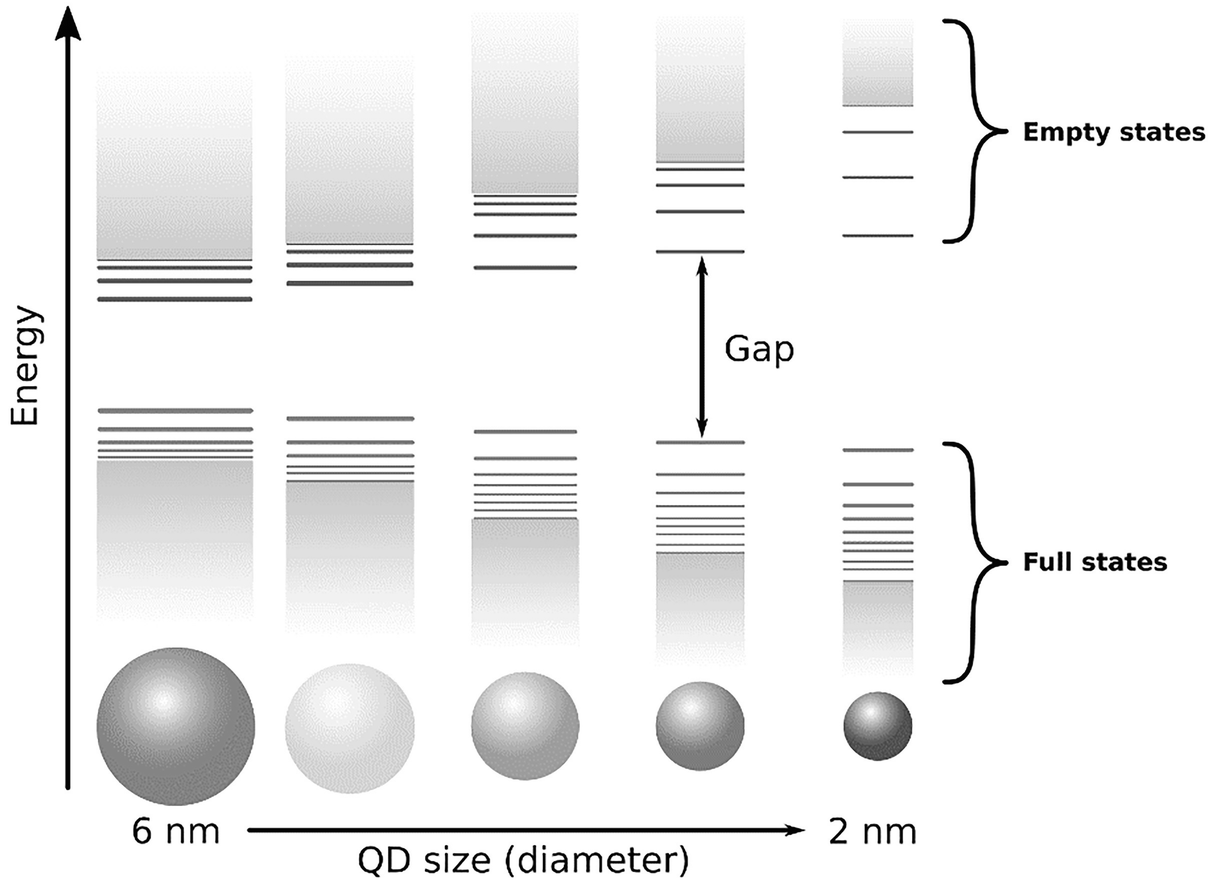

Fig. 5.11 Schematic illustration of electronic structure of quantum dots (nanocrystals) showing the dependence of gap with respect to size (diameter). (Idea from Ref. [63])

QDs are too sparse to create the continuous valence and conduct band. Generally, the smaller the particle size, the larger the bandgap. As the emission wavelength depends on the QDs' size, their fluorescence can be readily controlled by changing their size during the synthesis process. The emission wavelengths of QDs span from the ultraviolet (UV) to the infrared (IR). Other properties of QDs include high quantum yield, high photostability, and high molar extinction coefficients. Their emissions are also relatively narrow and symmetrical at specific wavelengths. In addition, it is reported that the fluorescence quantum yield of QDs can be improved through building a "shell" of a larger bandgap semiconductor material around them.

The bandgap energy is the minimal energy required to exit an electron from a highest occupied orbital to a lowest unoccupied orbital. As the electron relaxes and returns back to the initial orbital, before excitation, a photon gets emitted, leading to a visible fluorescence. Most of the electrons occupy energy levels below this bandgap in the area known as the valence band, and energy levels in the valence band are all occupied. If, however, an external stimulus is applied, an electron may move from the valence band to the conduction band, i.e., those energy levels above the bandgap. The electron in the conduction band and the hole it has left in the valence band are collectively known as an exciton. Energy is then released in the form of electromagnetic radiation as the electron falls back across the bandgap to the valence band. The wavelength of these photon emissions depends not on the material from which the dot is made but its size [64].

Organically capped ternary alloyed CdHgTe QDs with sizes varying from 2.5–4.2 nm were synthesized by a hydrothermal method, and their temperature-dependent PL spectra were studied between 15 K and 300 K. Synthesized QDs have elemental composition of $Cd_{0.8}Hg_{0.2}Te$ and do emission in the range of 650–855 nm. Increasing temperature leads to redshift in their emission peak, decreased PL intensity, and increased FWHM. Moreover, energy bandgap of CdHgTe QDs decreases with increasing temperature, and CdHgTe QDs show CdTe-like behavior. On the other hand, energy bandgap increases with decreasing QD size [65].

Nguyen et al. [66] synthesized ternary CdZnSe core QDs using embryonic nuclei-induced alloying procedures [67]. The core diameter of the QDs ranged from 4.2 nm to 5 nm. ZnSeS precursors were used for shelling CdZnSe QDs. Synthesis temperature and Cd/Zn ratio of the core

QDs changed the emission in the range of 530–607 nm. As the synthesis temperature increased from 285 °C to 310 °C, the Zn concentration decreased in the core QDs. Hence, strong luminescence had been obtained in the spectral range of 530–607 nm.

Theoretical modeling has shown that the observed increase in the bandgap is a consequence of the quantum size effect. The quantum size effect, which manifests itself in a change in the properties of a crystal, arises when at least one of its geometric dimensions falls below a certain threshold value. The experiment indicates that such effects appear when the average size of crystal grains (quantum dots) does not exceed 100 nm and is most pronounced when the grain size is less than 10 nm. For semiconductor materials, this usually occurs at sizes less than 4–5 nm. These values are comparable to the de Broglie wavelength for electrons. This effect is associated with the quantization of the energy of charge carriers, the movement of which is limited in one, two, or three directions. When an infinite crystal is limited by potential barriers or when boundaries are created, discrete quantization levels appear, which effectively shift the conduction band upward in energy.

The indicated properties of QDs offer great potential for their practical application. QDs based on II-VI compounds can be used in the development of light-emitting diodes, lasers, solar cells, and photodetectors for the entire spectral range from IR (Chapters 7 and 8, Vol. 2) to UV (Chapter 17, Vol. 2), chemical sensors of various types (Chapter 10, Vol. 3), biomarkers (Chapter 24, Vol. 3), and biosensors (Chapters 17–27, Vol. 3), i.e., wherever variable, wavelength-tunable optical properties are required.

5.9 BandGap Engineering via Modification of Core-Shell Structures

Core-shell structures are usually called as quasi-0D and 1D heterostructures in which a quantum dot or nanorod acts as a core. Covering a nanocrystal with a shell of another semiconductor material can form an efficient combination to increase the quantum yield of photoluminescence and the photostabibility of the crystal [68].

Heterostructures may be classified into three groups as type I, type II, and quasi-type II. In type I heterostructures, a wide bandgap semiconductor

is used as a shell and a narrow-bandgap semiconductor as a core. A wide bandgap semiconductor acts as a passivator of surface states and localizes an electron-hole pair inside the core. This approach is used to increase the efficiency of photoluminescence. In type II heterostructures, the widths of the bandgaps of the semiconductors are comparable, but the edges of the gaps are shifted relative to each other. It is energetically advantageous for photoexcited charge carriers to be in different parts of such a nanocrystal. In some type I heterostructures, a narrow bandgap can be strongly displaced and almost reach beyond the bandgap edge of a wide bandgap semiconductor. In this case, holes are still localized inside the core, while electrons are partially distributed over the entire volume of the nanostructure, which leads to a number of distinctive properties of type II heterostructures, such as the red shift of the absorption and luminescence bands. In this case, changing the relative sizes of the core and the shell makes it possible to control the degree of delocalization of electrons between the type I and quasi-type II regimes [69]. The energy structure variations of these three types of heterostructures are schematically displayed in Fig. 5.12.

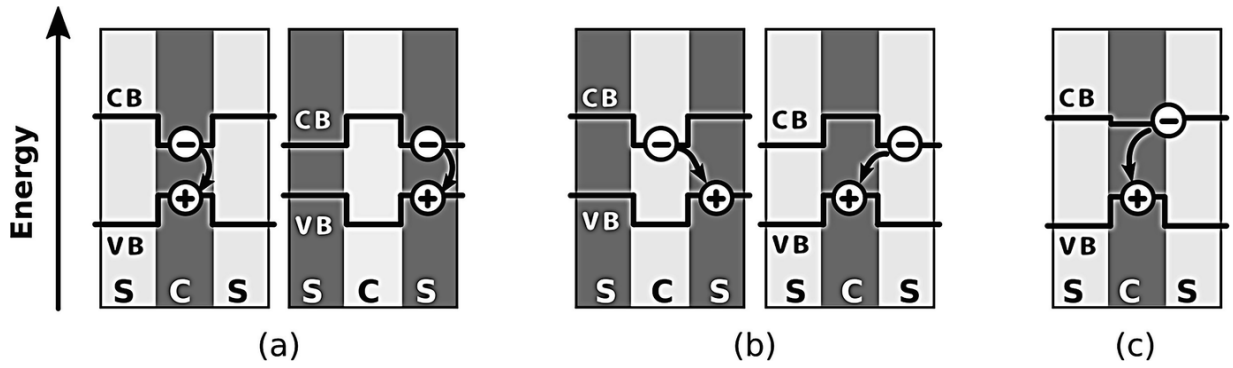

Fig. 5.12 The energy structures of various types of core (C) – shell (S)-like semiconductor heterostructures. (**a**) Type I, (**b**) type II, (**c**) quasi-type II. (Idea from Ref. [69])

Moreover, shelling QDs with ZnSeS increased the average PL QY by a factor of 2 up to 17. They claimed that non-emitting QDs became photoluminescent and did contribute to the average PL QY after shelling them with ZnSeS. Additionally, shelling the core QDs improved their blinking property [66].

Highly luminescent red-emitting CdZnSe/ZnSe quantum dots (QDs) were synthesized simply by a one-pot method [70]. Cd^{+2} and Zn^{+2} ions were obtained after mixing Cd and Zn precursors together. Ternary CdZnSe

particles were obtained after first injection of Se-TBP precursor into the solution, and ZnSe shell that covers the surface of CdZnSe core was produced after the second injection of the Se-TBP precursor. Emission from 620 nm to 690 nm with moderate absolute quantum yields (QYs) from 20% up to 50% was obtained from the alloyed CdZnSe/ZnSe QDs under UV light. Impurity and defect density were found to be dependent on the growing conditions of the QDs, and these conditions such as temperature and concentration of Se-TBP caused different photoluminescence (PL) QYs. PL peak positions shift from 688 to 618 nm as the temperature increased or Se-TBP decreased. Similar red shift was observed in the absorption peaks. Additionally, a narrower full width half maximum (FWHM) of the emission was reported as the temperature decreased. The highest PL QY (50%) was obtained at 672 nm emission with a narrowest FWHM (35 nm) when the temperature was 300 K, and the concentration of Se-TBP was 2.5 mmol. Their X-ray diffraction analysis showed that the core of the QDs with a highest PL QYs can be $Cd_3Zn_7Se_{10}$ with a cubic crystal structure capped with ZnSe shells and displays a spherical particle with a mean size of nearly 3.5 nm.

CdZnSeS/$ZnSe_{1.0}S_{1.3}$ QDs in a conjugated molecular beacon (MB) assay were used for detection of influenza virus RNA [71]. The alloyed QDs display bright emission when illuminated by UV light and have a remarkable PL QY range of 36–98%. Bandgap of the alloyed CdZnSeS/ZnSeS QDs was engineered via tuning and controlling the sulfur molar fraction. Mean particle size of QDs is 9 nm, and when it is shelled with ZnSeS, particle size increases to 10 nm. Nonlinear physical properties of the alloyed CdZnSeS/$ZnSe_{1.0}S_x$ QDs are tabulated in Table 5.2 with respect to the molar fraction of the sulfur. Covalent conjugation of the alloyed core/shell QDs with the MB probe triggers the fluorescence quenching of the former due to Förster resonance energy transfer. When H1N1 viral RNA nucleotide sequence hybridizes with the loop sequence of the QD-MB probe in the solution, the distance between the alloyed QD and the quencher molecule increases. Hence, an enhanced PL read-out signal is generated. Therefore, H1N1 RNA with a concentration as low as two copies per mL in human serum could be detected rapidly.

Table 5.2 Comparison of the properties of alloyed CdZnSeS/$ZnSe_{1.0}S_x$ QD-MB probe with respect to sulfur molar fraction

Parameter	S_X molar fraction					
	1.3	1.4	1.5	1.6	1.7	1.8
Lattice par. *c*(Å)	4.09	4.13	7.6	6.8	5.8	7.2
Bandgap (eV)	2.02	1.99	1.99	1.99	2	2
Wavelength (nm)	636	638	638	636	634	632
PL QY (%)	98	58	93	65	36	51
FWHM (nm)	40	35	40	38	38	36

Data collected from Ref. [71]

5.10 BandGap Engineering via Technology Control

Theoretical simulations have shown that quantum size effect can be realized not only in quantum dots and 1D structures but also in thin films with an appropriate thickness. In particular, Lamouri et al. [72], using first-principle calculations, found an increase in the bandgap energy in CdS, CdSe, and ZnSe thin films with decreasing the film thickness from 4 to 1.2 nm (Fig. 5.13). With a further increase in the thickness of the films, the value of the bandgap approached the value characteristic of a bulk material. At that, it was established that CdS, CdSe, and ZnSe thin films with indicated thickness exhibited a semiconductor character with a direct bandgap at the Γ-point like the bulk systems. Bandgap widening in doped ZnS thin films can be attributed to the Burstein-Moss effect. According to the Burstein-Moss effect, Fermi level moves upward with increasing donor concentration. This also causes the shift of unoccupied levels in the conduction band. Therefore, the energy gap between the valence band and the conduction band widens, and higher energies are needed for electrons to reach from the valence band to the shifted conduction band. Surface resistivity of the ZnS thin films was decreased with boron doping and also with thermal annealing which was a preferred result for increasing the performance of fabricated devices [28]. ZnS thin films were decreased with boron doping and also with thermal annealing which was a preferred result for increasing the performance of fabricated devices [28].

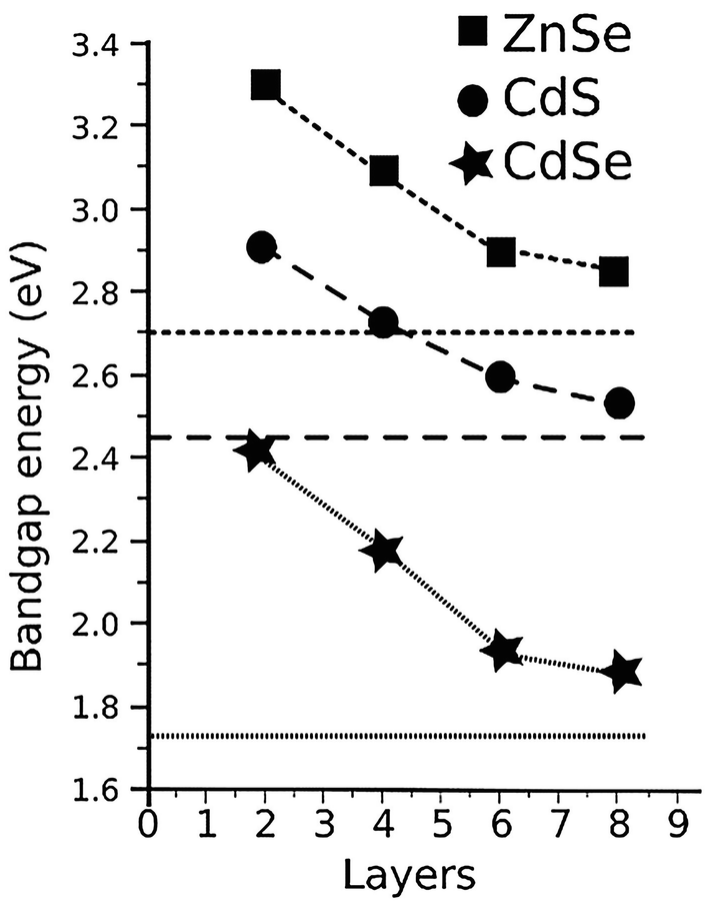

Fig. 5.13 The variation of the bandgap energy as function of the number of layers for CdS, CdSe, and ZnSe. Horizontal lines represent the corresponding bulk values. (Data extracted from Ref. [72])

Final Words

In R&D, both theoretical studies (for making reliable predictions) and experimental works (for designing efficient production and fabrication methods) are essential. They should go together!

References

1. Ge C-H, Li H-L, Zhu X-L, Pan A-L (2017) Band gap engineering of atomically thin two-dimensional semiconductors. Chin Phys B 26(3):034208. https://doi.org/10.1088/1674-1056/26/3/034208
[ADS][Crossref]
2. Ning C-Z, Dou L, Yang P (2017) Bandgap engineering in semiconductor alloy nanomaterials with widely tunable compositions. Nat Rev Mater 2(12). https://doi.org/10.1038/natrevmats.2017.70

3. Peidong Yang CZN, Dou L, Yang P (2017) Bandgap engineering in semiconductor alloy nanomaterials with widely tunable compositions. Nat Rev Mater 2:1–15. https://doi.org/10.1038/natrevmats.2017.70 [ADS][Crossref]
4. Bensaid D, Ameri M, Benseddik N, Mir A, Bouzouira NE, Benzoudji F (2014) Band gap engineering of CdBeSe alloys. Int J Met 2014:1–7. https://doi.org/10.1155/2014/286393 [Crossref]
5. Tamargo MC, Lin W, Guo SP, Guo Y, Luo Y, Chen YC (2000) Full-color light-emitting diodes from ZnCdMgSe/ZnCdSe quantum well structures grown on InP substrates. J Cryst Growth 214:1058–1063. https://doi.org/10.1016/s0022-0248(00)00274-8 [ADS][Crossref]
6. Vigue F, Tournie E, Faurie JP (2000) Zn(Mg)BeSe-based p-i-n photodiodes operating in the blue-violet and near-ultraviolet spectral range. Appl Phys Lett 76(2):242–244. https://doi.org/10.1063/1.125715 [ADS][Crossref]
7. Kroemer H (2001) Nobel lecture: quasielectric fields and band offsets: teaching electrons new tricks. Rev Mod Phys 73(3):783–793. https://doi.org/10.1103/revmodphys.73.783 [ADS][Crossref]
8. Esaki L, Tsu R (1970) Superlattice and negative differential conductivity in semiconductors. IBM J Res Dev 14(1):61–65. https://doi.org/10.1147/rd.141.0061 [Crossref]
9. Lee ML, Fitzgerald EA, Bulsara MT, Currie MT, Lochtefeld A (2005) Strained Si, SiGe, and ge channels for high-mobility metal-oxidesemiconductor field-effect transistors. J Appl Phys 97(1):011101. https://doi.org/10.1063/1.1819976 [ADS][Crossref]
10. Ghafari A, Janowitz C, Manzke R (2013) The effect of lithium intercalation on the electronic structure of the ternary compound semiconductors $ZrSe_{2-x}S_x$. J Phys Condens Matter 25(31):315502. https://doi.org/10.1088/0953-8984/25/31/315502 [Crossref]
11. Ulicna S, Isherwood PJM, Kaminski PM, Walls JM, Li J, Wolden CA (2017) Development of ZnTe as a back contact material for thin film cadmium telluride solar cells. Vacuum 139:159–163. https://doi.org/10.1016/j.vacuum.2017.01.001 [ADS][Crossref]
12. Singh M, Goyal M, Devlal K (2018) Size and shape effects on the bandgap of semiconductor compound nanomaterials. J Taibah Univ Sci 12(4):470–475. https://doi.org/10.1080/16583655.2018.1473946 [Crossref]
13. Lu J, Liu H, Zhang X, Sow CH (2018) One-dimensional nanostructures of II–VI ternary alloys: synthesis, optical properties, and applications. Nanoscale 10(37):17456–17476. https://doi.org/10.1039/c8nr05019h

[Crossref]
14. Wang Y, Xu J, Ren P, Zhuang X, Zhou H, Zhang Q, Zhu X, Pan A (2013) Complete composition tunability of $Cd_{1-x}Zn_xTe$ alloy nanostructures along a single substrate. Mater Lett 105:90–94. https://doi.org/10.1016/j.matlet.2013.04.054
[Crossref]
15. GoL acki Z, Gorska M, Makowski J, Szczerbakow A (1982) Vapour phase growth of CdTe. J Cryst Growth 56(1):213–214. https://doi.org/10.1016/0022-0248(82)90030-6
[ADS][Crossref]
16. Awadalla SA, Mackenzie J, Chen H, Redden B, Bindley G, Duff MC, Burger A, Groza M, Buliga V, Bradley JP, Dai ZR, Teslich N, Black DR (2010) Characterization of detector-grade CdZnTe crystals grown by traveling heater method (THM). J Cryst Growth 312(4):507–513. https://doi.org/10.1016/j.jcrysgro.2009.11.007
[ADS][Crossref]
17. Wei S-H, Zhang SB, Zunger A (2000) First-principles calculation of band offsets, optical bowings, and defects in CdS, CdSe, CdTe, and their alloys. J Appl Phys 87(3):1304–1311. https://doi.org/10.1063/1.372014
[ADS][Crossref]
18. Yang J, Wei S-H (2019) First-principles study of the bandgap tuning and doping control in $CdSe_xTe_{1-x}$ alloy for high efficiency solar cell. Chin Phys B 28(8):086106. https://doi.org/10.1088/1674-1056/28/8/086106
[ADS][Crossref]
19. Kwon SJ, Jeong H-M, Jung K, Ko D-H, Ko H, Han I-K, Kim GT, Park J-G (2015) Structural origin of the bandgap anomaly of quaternary alloy $Cd_xZn_{1-x}SySe_{1-y}$ nanowires, nanobelts, and nanosheets in the visible spectrum. ACS Nano 9(5):5486–5499. https://doi.org/10.1021/acsnano.5b01472
[Crossref]
20. Pan A, Liu R, Sun M, Ning C-Z (2010) Spatial composition grading of quaternary ZnCdSSe alloy nanowires with tunable light emission between 350 and 710 nm on a single substrate. ACS Nano 4(2):671–680. https://doi.org/10.1021/nn901699h
[Crossref]
21. Harrison MT, Kershaw SV, Burt MG, Eychmüller A, Weller H, Rogach AL (2000) Wet chemical synthesis and spectroscopic study of CdHgTe nanocrystals with strong near-infrared luminescence. Mater Sci Eng B 69–70:355–360. https://doi.org/10.1016/s0921-5107(99)00254-8
[Crossref]
22. Laref A, Alsagri M, Alahmed ZA, Laref S (2019) First-principles analysis for the modulation of energy bandgap and optical characteristics in HgTe/CdTe superlattices. RSC Adv 9(29):16390–16405. https://doi.org/10.1039/c8ra10101a
[ADS][Crossref]
23. El-Soud AMA, Akkad FE, Hammad S, Ali NA (1991) Properties of Hg_{1-x} Zn_x te solid solutions. J Mater Sci Mater Electron 2(3):171–173. https://doi.org/10.1007/bf00696294
[Crossref]

24. Lemoine D, Khelladi KH, Castaing O, Benhlal J, Quémerais A, Pollini I, Triboulet R, Granger R (1994) Effect of chemical treatments on the composition of HgZnTe surfaces. Mater Sci Eng B 28(1–3):39–42. https://doi.org/10.1016/0921-5107(94)90011-6 [Crossref]
25. Kim J, Yin W-J, Kang J, Yan Y, Wei S-H, Al-Jassim MM (2014) Creating intermediate bands in ZnTe via co-alloying approach. Appl Phys Express 7(12):121201. https://doi.org/10.7567/apex.7.121201 [ADS][Crossref]
26. Tsai M-H, Peiris FC, Lee S, Furdyna JK (2002) Electronic and structural properties of II–VI ternary alloys and superlattices. Phys Rev B 65(23). https://doi.org/10.1103/physrevb.65.235202
27. Tit N, Obaidat IM, Reshak AH, Alawadhi H (2010) Existence or absence of bandgap bowing in II–VI ternary alloys: comparison between commonanion and common-cation cases. J Phys Conf Ser 209. https://doi.org/10.1088/1742-6596/209/1/012024
28. Yeşilkaya SS, Ulutaş U (2020) Band gap modification of spray pyrolysed ZnS films by doping and thermal annealing. Res Eng Struct Mater 6(2):119–126. https://doi.org/10.17515/resm2019.104ma0130 [Crossref]
29. Khomyak V, Shtepliuk I, Khranovskyy V, Yakimova R (2015) Band-gap engineering of $ZnO_{1-x}S_x$ films grown by rf magnetron sputtering of ZnS target. Vacuum 121(121):120–124. https://doi.org/10.1016/j.vacuum.2015.08.008 [ADS][Crossref]
30. Martinez AD, Martyshkin DV, Camata RP, Fedorov VV, Mirov SB (2015) Crystal field engineering of transition metal doped II–VI ternary and quaternary semiconductors for mid-IR tunable laser applications. Opt Mater Express 5(9):2036. https://doi.org/10.1364/ome.5.002036 [ADS][Crossref]
31. Fard NE, Fazaeli R, Ghiasi R (2016) Band gap energies and photocatalytic properties of CdS and Ag/CdS nanoparticles for Azo Dye degradation. Chem Eng Technol 39(1):149–157. https://doi.org/10.1002/ceat.201500116 [Crossref]
32. Ca NX, Van HT, Do PV, Thanh LD, Tan PM, Truong NX, Oanh VTK, Binh NT, Hien NT (2020) Influence of precursor ratio and dopant concentration on the structure and optical properties of Cu-doped ZnCdSe-alloyed quantum dots. RSC Adv 10(43):25618–25628. https://doi.org/10.1039/d0ra04257a [ADS][Crossref]
33. Waag A, Fischer F, Schull K, Baron T, Lugauer H-J, Litz T, Zehnder U, Ossau W, Gerhard T, Keim M, Reuscher G, Landwehr G (1997) Laser diodes based on beryllium-chalcogenides. Appl Phys Lett 70(3):280–282. https://doi.org/10.1063/1.118422 [ADS][Crossref]
34. Zhang JY, Shen DZ, Fan XW, Yang BJ, Zheng ZH (2000) ZnBeSe epitaxy layers grown by photo-assisted metalorganic chemical vapor deposition. J Cryst Growth 214–215:100–103.

https://doi.org/10.1016/s0022-0248(00)00036-1
[ADS][Crossref]

35. Maksimov O, Guo SP, Tamargo MC (2002) Be-chalcogenide alloys for improved R-G-B LEDs: $Be_XZnyCd_{1-x-y}Se$ on InP. Physica Status Solidi (b) 229(2):1005–1009. https://doi.org/10.1002/1521-3951(200201)229:2<1005::aid-pssb1005>3.0.co;2-5
[ADS][Crossref]

36. Shah NA, Mahmood W (2013) Physical properties of sublimated zinc telluride thin films for solar cell applications. Thin Solid Films 544:307–312. https://doi.org/10.1016/j.tsf.2013.03.088
[ADS][Crossref]

37. Amutha R, Subbarayan A, Sathyamoorthy R, Natarajan K, Velumani S (2007) Conduction studies on znte thin films. J New Mater Electrochem Syst 10(1):27

38. Zaari H, Boujnah M, Hachimi AE, Benyoussef A, Kenz AE (2013) Optical properties of ZnTe doped with transition metals (ti, cr and mn). Opt Quant Electron 46(1):75–86. https://doi.org/10.1007/s11082-013-9708-y
[Crossref]

39. Rafiq A, Imran M, Aqeel M, Naz M, Ikram M, Ali S (2019) Study of transition metal ion doped CdS nanoparticles for removal of dye from textile wastewater. J Inorg Organomet Polym Mater 30(6):1915–1923. https://doi.org/10.1007/s10904-019-01343-5
[Crossref]

40. Rozale H, Beldi L, Bouhafs B, Ruterana P (2007) A theoretical investigation of ZnO_XS_{1-x} alloy band structure. Physica Status Solidi (B) Basic Res 244(5):1560–1566. https://doi.org/10.1002/pssb.200675147
[ADS][Crossref]

41. Rogalski A (2003) Infrared detectors: status and trends. Prog Quant Electron 27(2–3):59–210. https://doi.org/10.1016/s0079-6727(02)00024-1
[ADS][Crossref]

42. Downs C, Vandervelde TE (2013) Progress in infrared photodetectors since 2000. Sensors 13:5054–5098. https://doi.org/10.3390/s130405054
[ADS][Crossref]

43. Schulman JN, McGill TC (1979) The CdTe/HgTe superlattice: proposal for a new infrared material. Appl Phys Lett 34(10):663–665. https://doi.org/10.1063/1.90629
[ADS][Crossref]

44. McGill TC, Wu GY, Hetzler SR (1986) Superlattices: progress and prospects. J Vac Sci Technol A 4(4):2091–2095. https://doi.org/10.1116/1.574033
[Crossref]

45. Faurie JP, Million A, Piaguet J (1982) CdTe-HgTe multilayers grown by molecular beam epitaxy. Appl Phys Lett 41(8):713–715. https://doi.org/10.1063/1.93644
[ADS][Crossref]

46. Zhou YD, Becker CR, Selamet Y, Chang Y, Ashokan R, Boreiko RT, Aoki T, Smith DJ, Betz AL, Sivananthan S (2003) Farinfrared detector based on HgTe/HgCdTe superlattices. J Electron Mater 32:608–614. https://doi.org/10.1007/s11664-003-0040-3 [ADS][Crossref]
47. Aleshkin VY, Dubinov AA, Morozov SV, Ryzhii M, Otsuji T, Mitin V, Shur MS, Ryzhii V (2018) Interband infrared photodetectors based on HgTe–CdHgTe quantum-well heterostructures. Opt Mater Express 8(5):1349. https://doi.org/10.1364/ome.8.001349 [ADS][Crossref]
48. Sohel M, Zhou X, Lu H, Perez-Paz MN, Tamargo M, Munoz M (2005) Optical characterization and evaluation of the conduction band offset for ZnCdSe/ZnMgSe quantum wells grown on inp(001) by molecular-beam epitaxy. J Vac Sci Technol B Microelectron Nanometer Struct 23(3):1209. https://doi.org/10.1116/1.1878992 [ADS][Crossref]
49. Zakharov O, Rubio A, Blase X, Cohen ML, Louie SG (1994) Quasiparticle band structures of six II–VI compounds: ZnS, ZnSe, ZnTe, CdS, CdSe, and CdTe. Phys Rev B 50(15):10780–10787. https://doi.org/10.1103/PhysRevB.50.10780 [ADS][Crossref]
50. Kaya Y, Ravikumar A, Chen G, Tamargo MC, Shen A, Gmachl C (2018) Two-band ZnCdSe/ZnCdMgSe quantum well infrared photodetector. AIP Adv 8(7). https://doi.org/10.1063/1.5013607
51. Gessert TA, Wei S-H, Ma J, Albin DS, Dhere RG, Duenow JN, Kuciauskas D, Kanevce A, Barnes TM, Burst JM, Rance WL, Reese MO, Moutinho HR (2013) Research strategies toward improving thinfilm CdTe photovoltaic devices beyond 20% conversion efficiency. Solar Energy Mater Solar Cells 119:149–155. https://doi.org/10.1016/j.solmat.2013.05.055 [Crossref]
52. Leubner P, Lunczer L, Brune C, Buhmann H, Molenkamp LW (2016) Strain engineering of the bandgap of HgTe quantum wells using superlattice virtual substrates. Phys Rev Lett 117(8):1–5. https://doi.org/10.1103/PhysRevLett.117.086403 [Crossref]
53. Krishtopenko SS, Yahniuk I, But DB, Gavrilenko VI, Knap W, Teppe F (2016) Pressure- and temperature-driven phase transitions in HgTe quantum wells. Phys Rev B 94(24). https://doi.org/10.1103/physrevb.94.245402
54. Fadeev MA, Rumyantsev VV, Kadykov AM, Dubinov AA, Antonov AV, Kudryavtsev KE, Dvoretskii SA, Mikhailov NN, Gavrilenko VI, Morozov SV (2018) Stimulated emission in the 28–35 μm wavelength range from peltier cooled HgTe/CdHgTe quantum well heterostructures. Opt Express 26(10):12755. https://doi.org/10.1364/oe.26.012755 [ADS][Crossref]
55. Kudryavtsev KE, Rumyantsev VV, Aleshkin VY, Dubinov AA, Utochkin VV, Fadeev MA, Mikhailov NN, Alymov G, Svintsov D, Gavrilenko VI, Morozov SV (2020) Temperature limitations for stimulated emission in 3–4 μm range due to threshold and non-threshold auger recombination in HgTe/CdHgTe quantum wells. Appl Phys Lett 117(8):083103. https://doi.org/10.1063/5.0020218

[ADS][Crossref]
56. Mynbaev KD, Shilyaev AV, Bazhenov NL, Izhnin AI, Izhnin II, Mikhailov NN, Varavin VS, Dvoretsky SA (2015) Acceptor states in heteroepitaxial CdHgTe films grown by molecular-beam epitaxy. Semiconductors 49(3):367–372. https://doi.org/10.1134/s1063782615030148
[ADS][Crossref]
57. Bernevig BA, Hughes TL, Zhang S-C (2006) Quantum spin hall effect and topological phase transition in HgTe quantum wells. Science 314(5806):1757–1761. https://doi.org/10.1126/science.1133734
[ADS][Crossref]
58. Konig M, Wiedmann S, Brune C, Roth A, Buhmann H, Molenkamp LW, Qi X-L, Zhang S-C (2007) Quantum spin hall insulator state in HgTe quantum wells. Science 318(5851):766–770. https://doi.org/10.1126/science.1148047
[ADS][Crossref]
59. Krishtopenko SS, Yahniuk I, But DB, Gavrilenko VI, Knap W, Teppe F (2016) Pressure- and temperature-driven phase transitions in HgTe quantum wells. Phys Rev B 94(24):1–8. https://doi.org/10.1103/PhysRevB.94.245402
[Crossref]
60. Kvon ZD, Olshanetsky EB, Novik EG, Kozlov DA, Mikhailov NN, Parm IO, Dvoretsky SA (2011) Two-dimensional electron-hole system in HgTe-based quantum wells with surface orientation (112). Phys Rev B Condens Matter Mater Phys 83(19):6–9. https://doi.org/10.1103/PhysRevB.83.193304
[Crossref]
61. Zaheer S, Young SM, Cellucci D, Teo JCY, Kane CL, Mele EJ, Rappe AM (2013) Spin texture on the Fermi surface of tensile-strained HgTe. Phys Rev B Condens Matter Mater Phys 87(4):1–7. https://doi.org/10.1103/PhysRevB.87.045202
[Crossref]
62. Peköz R, Raty JY (2011) Band structure modulation of ZnSe/ZnTe nanowires under strain. Phys Rev B Condens Matter Mater Phys 84(16):1–8. https://doi.org/10.1103/PhysRevB.84.165444
[Crossref]
63. Rabouw FT, de Mello Donega C (2016) Excited-state dynamics in colloidal semiconductor nanocrystals. Top Curr Chem 374(5):1–30. https://doi.org/10.1007/s41061-016-0060-0
[Crossref]
64. Brkic S (2016) Optical properties of quantum dots. Eur Int J Sci Technol 5(9):98–107
65. Jagtap AM, Chatterjee A, Banerjee A, Pendyala NB, Rao KSRK (2016) Size and temperature dependence of the photoluminescence properties of NIR emitting ternary alloyed mercury cadmium telluride quantum dots. J Phys D Appl Phys 49(13):135302. https://doi.org/10.1088/0022-3727/49/13/135302
[ADS][Crossref]
66. Nguyen HY, de Marcillac WD, Lethiec C, Phan NH, Schwob C, Maître A, Nguyen QL, Le VV, Bénalloul P, Coolen L, Nga PT (2014) Synthesis and optical properties of core/shell

ternary/ternary CdZnSe/ZnSeS quantum dots. Opt Mater 36(9):1534–1541. https://doi.org/10.1016/j.optmat.2014.04.020
[ADS][Crossref]

67. Zhong X, Zhang Z, Liu S, Han M, Knoll W (2004) Embryonic nucleiinduced alloying process for the reproducible synthesis of blue-emitting $Zn_xCd_{1-x}Se$ nanocrystals with long-time thermal stability in size distribution and emission wavelength. J Phys Chem B 108(40):15552–15559. https://doi.org/10.1021/jp048071y
[Crossref]

68. Mahler B, Spinicelli P, Buil S, Quelin X, Hermier JP, Dubertret B (2008) Towards non-blinking colloidal quantum dots. Nat Mater 7(8):659–664. https://doi.org/10.1038/nmat2222
[ADS][Crossref]

69. Kormilina TK, Cherevkov SA, Fedorov AV, Baranov AV (2017) Cadmium chalcogenide nanoheteroplatelets: creating advanced nanostructured materials by shell growth, substitution, and attachment. Small 13(41):1–18. https://doi.org/10.1002/smll.201702300
[Crossref]

70. Zhang Q, Nie C, Chang C, Guo C, Jin X, Qin Y, Li F, Li Q (2017) Highly luminescent red emitting CdZnSe/ZnSe quantum dots synthesis and application for quantum dot light emitting diodes. Opt Mater Express 7(11):3875. https://doi.org/10.1364/ome.7.003875
[ADS][Crossref]

71. Adegoke O, Seo M-W, Kato T, Kawahito S, Park EY (2016) Gradient bandgap engineered alloyed quaternary/ternary CdZnSeS/ZnSeS quantum dots: an ultrasensitive fluorescence reporter in a conjugated molecular beacon system for the biosensing of influenza virus RNA. J Mater Chem B 4(8):1489–1498. https://doi.org/10.1039/c5tb02449h
[Crossref]

72. Lamouri R, Salmani EM, Ez-Zahraouy H, Benyoussef A (2017) Bandgap engineering of CdS, CdSe and ZnSe first-principles calculations. In: Proceedings of 2016 international renewable and sustainable energy conference. IRSEC, pp 120–123. https://doi.org/10.1109/irsec.2016.7983969
[Crossref]

OceanofPDF.com

© The Author(s), under exclusive license to Springer Nature Switzerland AG 2023
G. Korotcenkov (ed.), *Handbook of II-VI Semiconductor-Based Sensors and Radiation Detectors*
https://doi.org/10.1007/978-3-031-19531-0_6

6. Electronic Structure of Mercury Chalcogenides Nanocrystals

Emmanuel Lhuillier[1] ✉, Tung Huu Dang[1], Mariarosa Cavallo[1], Claire Abadie[1], Adrien Khalili[1] and Charlie Gréboval[1]
(1) Sorbonne Université, CNRS, Institut des NanoSciences de Paris, Paris, France

✉ **Emmanuel Lhuillier**
Email: el@insp.upmc.fr

Keywords Carrier dynamics – Mercury chalcogenides – Doping – Electronic structure – HgTe – HgSe – HgS – Infrared – Interband transition – Ligands – Light emission – Nanocrystals – Quantum confinement – THz

6.1 Introduction

This chapter will focus on mercury chalcogenides nanocrystals (NCs) [1, 2] (HgX: HgS, HgSe, and HgTe). The NC field started in the 1980s with pioneers such as Brus [3], Henglein, Itoh, and Ekimov [4]. At this stage, size-dependent optical features started to be observed in samples of nanocrystals, a feature previously only observed in quantum wells grown by molecular beam epitaxy. The field received a clear boost with the development of the so-called hot injection method by Bawendi's group [5] at MIT. During this procedure, a solution of metallic salts and chalcogenides precursors is injected into a solvent at an elevated temperature in the presence of surfactants (also called ligands). This leads to a much narrower size distribution, enabling higher-quality spectra (i.e., several clearly identified optical transitions which can be connected to the particle size, shape, and semiconductor electronic structure). In the early

1990s, efforts were focused on cadmium chalcogenides compounds. CdSe remains to date, the most investigated material in nanocrystal form. The interest in Hg-based materials came later, at the end of the 1990s.

The introduction of Hg was inspired by a commercial interest in infrared wavelengths during the telecom boom around the year 2000. HgTe NCs behave as narrow band gap semiconductors, and their use was initially motivated by the design of optical amplifiers at the telecom wavelength (1.3–1.5 μm) range [6, 7]. Though this could have been the first application for HgTe NCs, it remains unproven. More or less in the same period (the early 2000s), NC-based solar cells were demonstrated [8]. NCs, thanks to their quantum-confined tunable band gap, can easily display a band gap matching the *Queisser Shockley* criteria (around 1.2 eV). This tunable band gap and the low threshold multi-exciton generation (MEG) have been the first motivations to design NC-based solar cells. Though MEG [9–12] (i.e., the generation of more than one photocarrier per absorbed photon) was demonstrated, the efficiency of NC-based solar cells remained low, and it quickly became apparent that transport was the actual bottleneck to achieve a high efficiency in NC-based solar cells. Transport in a NC array occurs through hopping. At every step, carriers have to tunnel from one NC to the next one through the intermediate medium (vacuum or ligand). The macroscopic consequence of this hopping conduction is a low carrier mobility, around 10^{-6} $cm^2.V^{-1}$ s^{-1} after synthesis. Significant efforts were made to increase the local coupling while maintaining the electronic surface passivation, without introducing disorders at the mesoscopic scale. An important milestone is the use of a ligand exchange procedure, allowing for a higher carrier mobility in NC arrays. This technique opened up the use of NC films as photoconductive materials.

It then became of utmost interest to explore the potential of NCs for optoelectronics at longer wavelengths, beyond the one required for solar cells. Although lead chalcogenides are certainly the most mature material for wavelengths from 800 nm to 1.5 μm, their use at longer wavelengths is limited by the bulk band gap and confinement residues that are always present for colloidal nanoparticles. Therefore, semimetals such as HgTe or HgSe raised the possibility of exploring not only the near-infrared but also the mid- and far- infrared ranges.

We begin the discussion of HgX with an introduction to the NC synthesis by briefly reviewing the field’s history and the type of NCs that

can be grown. As discussed in Chap. 7 of the second volume of this book collection, the HgX NCs are highly promising for infrared sensing [13–15]. As understanding basic material properties is crucial for device integration, we therefore extensively discuss the electronic properties of HgX NC and their connection to the NC optical features. While quantum confinement is certainly the main driving parameter of HgX NCs spectra, we also discuss the effects of surface chemistry, temperature, pressure, as well as carrier relaxation mechanisms. We end this chapter with a short discussion on the light emission and complex optical index properties of HgTe NCs.

6.2 Synthesis

The purpose of this section is not to give an extensive description of HgX NCs synthesis but rather to provide basic insight on what can be obtained in terms of materials. Interested readers can refer to more complete reviews [1, 16] about HgX NC growth. The first report dedicated to Hg containing NCs is due to Eychmüller et al. [17]. They proposed to modify CdS NCs by exposing them to Hg ions (this procedure is now called cation exchange [18, 19]). Some of the surface Cd ions are then stripped off and replaced by Hg, leading to the formation of a few HgS layers. The author observed a significant redshift of the absorption and photoluminescence (PL) by doing so. A few years later, Rogach et al. [7] proposed the first direct growth of HgTe NCs and pushed the absorption and light emission up to the telecom wavelength. This first synthesis was conducted in an aqueous medium. Hg cations dissolved in water reacted with H_2Te gas bubbling in the solution. This method [7] and its later improvement [20, 21] are still used to date for device integration. Kovalenko et al. [22] proposed an interesting improvement to this method. They added an Ostwald ripening step to the HgTe growth enabling the particle band edge to reach 3 μm.

On the way toward longer wavelength absorption, Keuleyan et al. [26] proposed a change in the growth method based on the organic medium. They were the first to report an absorption edge reaching 5 μm, which was highly promising for mid-IR detector design. This first report for large HgTe nanocrystals led to strongly aggregated particles, and they later proposed an updated procedure [27, 28]. In this case, $HgCl_2$ is dissolved in a long chain amine (oleylamine) used both as a solvent and a ligand. At moderate temperature, the Te complexed with phosphine is injected, leading

to the formation of NCs. Their size and shape are mostly tuned by the synthesis temperature (60–120 °C range) and the duration (1–30 min typically). With most of these protocols, the particle tends to be nonspherical. The transmission electron microscopy (TEM) image shows that for a band edge at 2.5 μm, the particle shape is a tripod (Fig. 6.1b). This is better highlighted by electron tomography (Fig. 6.1c). Goubet et al. have proposed to synthesize even larger nanoparticles [25] (from 5 nm to 1 μm, see Fig. 6.1d) by simultaneously injecting the Te and Hg precursors into a hot solvent (up to 300 °C), leading to the first report of nanocrystals with an absorption edge reaching the THz range [25].

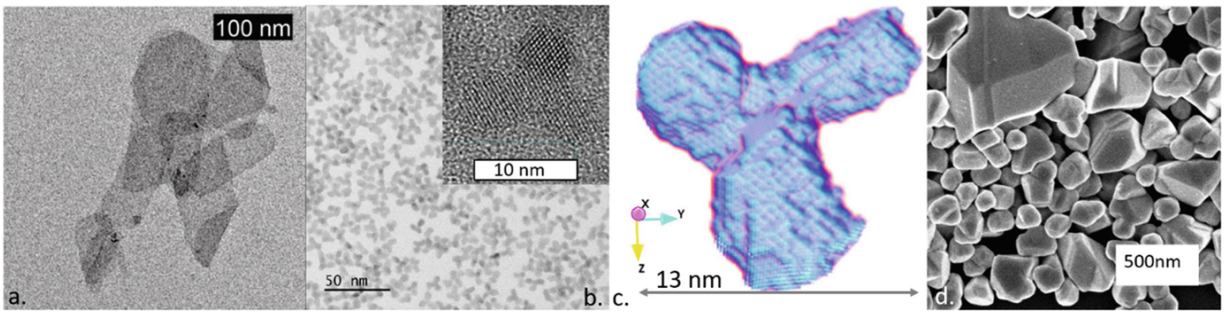

Fig. 6.1 Electron microscopy of HgTe NC. (**a**) TEM image of 2D nanoplatelets of HgTe (Part (**a**) is adapted with permission from ref. [23]. Copyright 2016, American Chemical Society). (**b**) TEM image of a HgTe tripod. The inset is a high-resolution image of one of this tripod. (**c**) 3D reconstruction of a HgTe tripod obtained by electron tomography (Parts (**b**, **c**) are adapted with permission from ref. [24]. Copyright (2021) American Chemical Society). (**d**) SEM image of very large HgTe NCs presenting THz absorption. (Part (**d**) is adapted with permission from ref. [25]. Copyright 2018, American Chemical Society)

More recently, the control of the particle shape has become a central interest, especially with the aim of forming denser films with higher NC packing and electronic coupling. Shen et al. [29] proposed to use a more reactive precursor of Te to achieve sphere shaped particles. Alternatively, Prado et al. [30] proposed a two-step growth where seeds are first formed by reacting Hg and Te at room temperature, and then the seeds are grown in a hot solvent.

Syntheses of 2D particles have also been reported by Izquierdo et al. [23, 31], see Fig. 6.1a. For CdSe, the growth of 2D nanoplatelets [32, 33] (NPLs) led to unique properties. Indeed NPL, thanks to a specific growth mechanism, do not present any inhomogeneous broadening. They consequently show the narrowest optical feature among NCs. In the case of HgX, the direct growth of NPLs remains unreported; thus, Izquierdo et al. [34] used an alternative process where CdTe NPL are first grown and then

cation exchanged [18, 19] to form HgTe NPLs, see Fig. 6.1a [23]. Final objects show a 1 nm thickness (only in the confined direction), while the lateral extension reaches several hundred nm. The photoluminescence (PL) linewidth of the HgTe NPL is the narrowest reported for NC in the near IR. However, the process is limited to thin objects [35], and the band edge of the NPL remains limited at 1.5 μm to date [36].

Heterostructures of HgX-based nanocrystals have also been reported. Motivations are multiple: (i) the PL signal enhancement to balance the inherent long radiative lifetime observed in the infrared; (ii) redshift of the absorption; (*iii*) reduction of the electrical noise associated with non-radiative processes; or (*iv*) enhanced thermal stability to avoid particle sintering. The direct growth of a shell remains a challenge because the usual process to grow shells requires a relatively high temperature (>200 °C), while HgTe NCs are completely sintered at this temperature. There are few reports for dedicated methods to grow shells at a moderate temperature [37, 38] (i.e., between room T and 150 °C typically). Most of the efforts to grow shells of HgX NCs are focused on cadmium chalcogenides shells. Thus, to prevent particle sintering, it is mainly through low-temperature approaches that heterostructures have been obtained. As already stated in the introduction, Eychmüller et al. [39–42] reported a CdS/HgS/CdS structure very early, described as a spherical quantum well of HgS. The latter is obtained using a cation exchange step by exposing a CdS core to Hg ions [43–45]. Later, the method was used on other HgX-based NCs to achieve heterostructure [45] and alloyed [44, 46] NCs. Several groups also reported the growth of shells on HgX NCs [47–49] using the colloidal atomic layer deposition (C-ALD) method [50]. This method consists in exposing a core nanocrystal successively to cations and anions at room temperature to grow a shell. The process is repeated as many times as the targeted number of layers. Even though some degree of PL enhancement and higher thermal stability [38] have been reported, the benefit of the shell to date remains not as striking as what has been obtained for wider band gap materials.

HgTe remains the most popular mercury chalcogenide for NC research. This is in contrast to cadmium chalcogenides, where the use of CdTe is often avoided due to its tendency to oxidize. The success of HgTe is likely connected to its vicinity with the well-known HgCdTe alloy that has been extensively studied in bulk material for infrared sensing. Nonetheless, it remains that HgS [49, 52–57] and HgSe [46, 51, 58–60] can also easily be

grown under NC form. Initially, they were grown under small NCs form to achieve PL in the near IR. Later, larger particles (>5 nm) have also been synthesized, and it appears that such particles display a second interesting feature: a narrow peak of absorption in the mid-IR; see Fig. 6.2. The latter results from the intraband absorption within the conduction band and can be seen as a sign of degenerate doping in these particles.

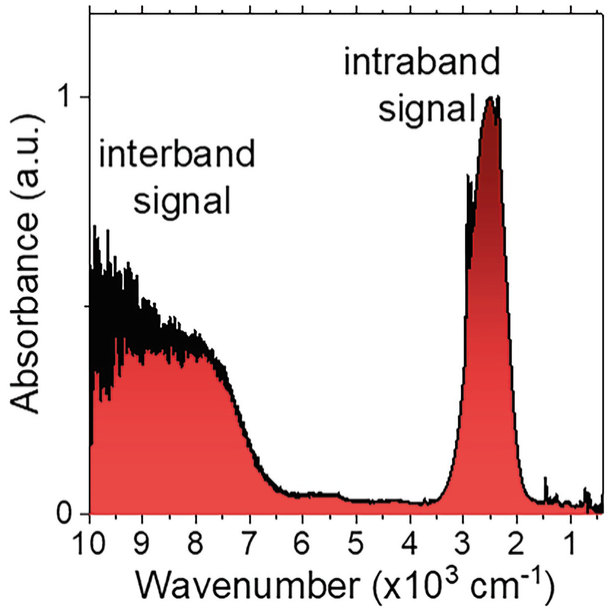

Fig. 6.2 Absorption spectrum of HgSe NCs showing two clear features. At high energy a broad interband feature, at low energy a narrow intraband absorption, used as a signature of the doped nature of the nanocrystals (figure is adapted with permission from Ref. [51]. Copyright 2016, American Chemical Society)

Now that the particle synthesis has been discussed, we can focus on NC electronic structure and its relation to bulk materials and quantum confinement.

6.3 Electronic Structure

6.3.1 Confined HgTe

Bulk HgTe presents a very peculiar band structure. Since HgTe is composed of heavy atoms, it subject to a strong spin-orbit coupling, leading to an inverted band ordering compared to cadmium chalcogenides. The band with Γ_6 symmetry, which plays the role of the conduction band in CdTe, is now within the valence band [61, 62]. The bands with Γ_8 symmetry, usually playing the role of the heavy hole and light hole bands, are now around the

Fermi level and act, respectively, as valence and conduction bands. The degeneracy of these two bands at the Γ point is preserved. As a result, HgTe is a zero band gap semiconductor; and a band structure obtained using a 14 band kp model [63] is provided in Fig. 6.3a. This property is of utmost interest to design IR tunable optical band gaps. Indeed, in HgTe NCs, absorption occurs between these two bands [64], and the band gap can be made vanishingly small by growing large HgTe NCs. Eventhough in HgTe the Bohr radius is quite large [65] (40 nm), it is possible to grow particles up to 1 μm (see Fig. 6.1d) where quantum confinement effects are minor. This property strongly contrasts with narrow band gap semiconductors, where bulk band gap values remain a limit beyond which no optical feature can be designed. The other striking feature of HgTe is a strong asymmetry for the hole and electron dispersion. The effective mass of the electron is small ($m_e^* = 0.03\ m_0$), while the heavy hole band is barely dispersive ($m_e^* = 0.5\ m_0$ [63]). This leads to strong consequences for the band edge energy of NCs. Usually, the band edge energy of NC is the sum of the bulk band gap, corrected by a confinement term and possibly by a Coulombic term. In HgTe there is no bulk band gap, and quantum confinement is weak for the holes and strong for the electrons. The Coulombic correction is generally small (a few tens of meV). As a result, even if the band edge is often called exciton, the electron-hole pair mostly behaves as a confined particle. The electron confinement term is the main contribution of the band edge energy and can be made extremely large (1.5 eV) when small particles such as 2D NPL are used [23, 63]. In HgSe, the conclusion drawn for HgTe (lack of bulk band gap, significant mass asymmetry) mostly remains valid. The main difference is that the presence of Se tends to increase the work function compared to Te. In other words, the bands are deeper with respect to the vacuum level. As a result, for a similar environment (i.e., the same Fermi level), HgSe is easier reduced and a degenerate electron doping gets achieved easier [66]. With S being a much lighter atom than Se and Te, the spin-orbit in HgS is strongly reduced, and a conventional band ordering is observed in bulk HgS (β-phase). This makes HgS a narrow band gap semiconductor (Eg = 0.6 eV [66]).

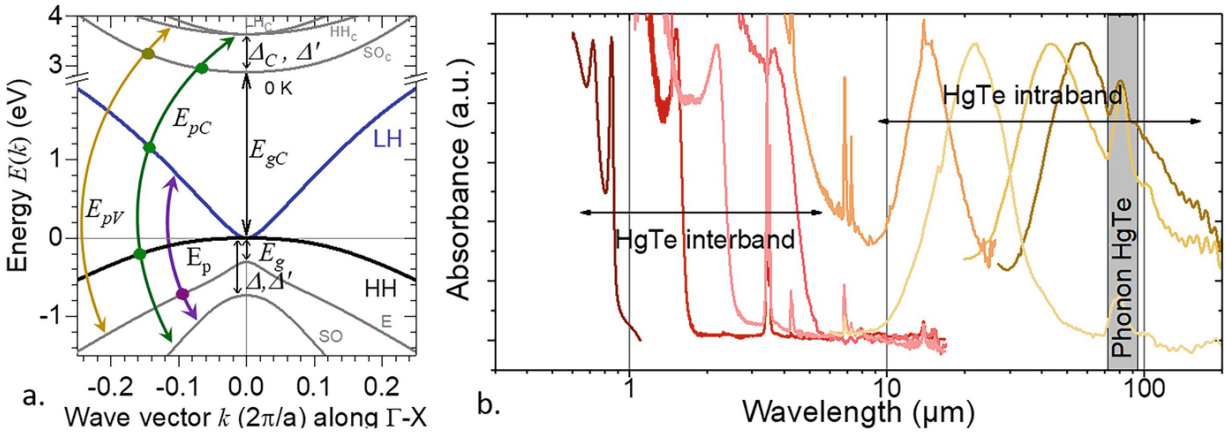

Fig. 6.3 HgTe electronic structure and spectroscopic properties. (**a**) Energy diagram of bulk HgTe described by a 14 bands kp model (Part (**a**) is adapted with permission from Ref. [63]. Copyright 2020, American Chemical Society). (**b**) Absorption spectra of HgTe NC with various sizes (Part (**b**) is adapted with permission from Ref. [1]. Copyright 2020, American Chemical Society)

Based on these considerations, we can analyze the absorption spectra of HgTe NCs with various sizes; see Figure 6.3b. For a strongly confined form of HgTe, the absorption spectrum shows no absorption at long wavelengths (beyond the ones resulting from ligands and, in particular, the strong absorption due to the C-H bond at around 2900 cm^{-1} or 3 μm), and an absorption edge at lower wavelengths. At shorter wavelengths than this edge, the particle keeps absorbing due to the high density of states. In particular, HgX NCs absorb all visible light, therefore, presenting a black color. This regime corresponds to particles with a size below 12 nm typically. For particles larger than 12 nm, the absorption presents a second peaky feature, similar to that observed for HgS and HgSe (see Fig. 6.2). It is now established that this corresponds to an intraband transition [29] (i.e., not a plasmon), even for the largest particles displaying THz absorption [67]. To further understand the nature of this intraband absorption, doping needs to be discussed.

6.3.2 Intraband Absorption and Doping

Doping in HgX NC occurs through a specific mechanism called self-doping (i.e. without introducing impurities but rather through a reduction by the environment). Carrier density control in NCs has been a challenge with the introduction of extrinsic impurities being thermodynamically unfavorable [68]. Even today, there is still no systematic strategy to transform a given population of NCs into its doped form. Nevertheless, significant progress has been made in this direction. Examples include the use of magnetic

impurities (Mn [69]) and non-isovalent atoms (*i.e.* Ag^+ [70] and Cu^+ [71] in a matrix of II-VI semiconductors). However, most of these doping strategies do not lead to electrically active doping (i.e., effect on transport). Often, the dopant only provides a trap state at constant energy with respect to the band edge [70]. In other words, in many cases, dopants are not leading to free carriers.

For device manufacturing, this is less of a problem for narrow band gap NCs. Even if the material is perfectly intrinsic, the thermally activated carrier density may be non-negligible, and so the conductivity is higher. The population of the 1S state is given by $n_{1S} = \frac{2 \text{ x } 0.64}{4/3\pi R^3} \exp\left(-\frac{E_G}{2k_BT}\right)$ with R the particle radius, k_BT the thermal energy (~25 meV at room temperature), and the factor 0.64 corresponding to the volume fraction of a randomly close-packed NC film. For the sake of illustration, thermally activated carrier density in 5 µm cutoff wavelength HgTe NC reaches one carrier per thousands of NC. This is 14 orders of magnitude larger than the value in CdSe NC with a similar size, making transport far easier to obtain in HgX NC array than for wider band gap NCs where achieving large mobility becomes even more critical.

In addition, the material can be nonstoichiometric. In this case, the Fermi level is no longer in the middle of the band gap; see Fig. 6.4a. In HgX NCs, natural degenerate doping can be achieved due to the narrow band gap. This process is responsible for the observation of intraband absorption in HgS [49] and HgSe [51, 60] NCs, as well as in the case of large HgTe NCs [25, 73]. Using photoemission measurements, a shift of the majority carrier from holes (Fermi level in the bottom part of the band gap) to electrons (Fermi level in the upper part of the band gap) has been observed as the particle size increases; see Fig. 6.4b. This trend is consistent with transport measurements probed in a field-effect transistor; see Fig. 6.4c. Small HgTe NCs present only p-type conduction, while the largest ones show mostly n-type conduction. In the intermediate range (for sizes between 6 and 12 nm typically), HgTe NCs present an ambipolar character with conduction from both electrons and holes. Empirically, this is also the range of size that leads to the highest performances for photodetection since the material is nearly intrinsic and so has presents an higher resistance. As it will be discussed in the next paragraph, the precise size for which the

material presents a Fermi level lying in the middle of the band gap appears to strongly depend on the surface chemistry.

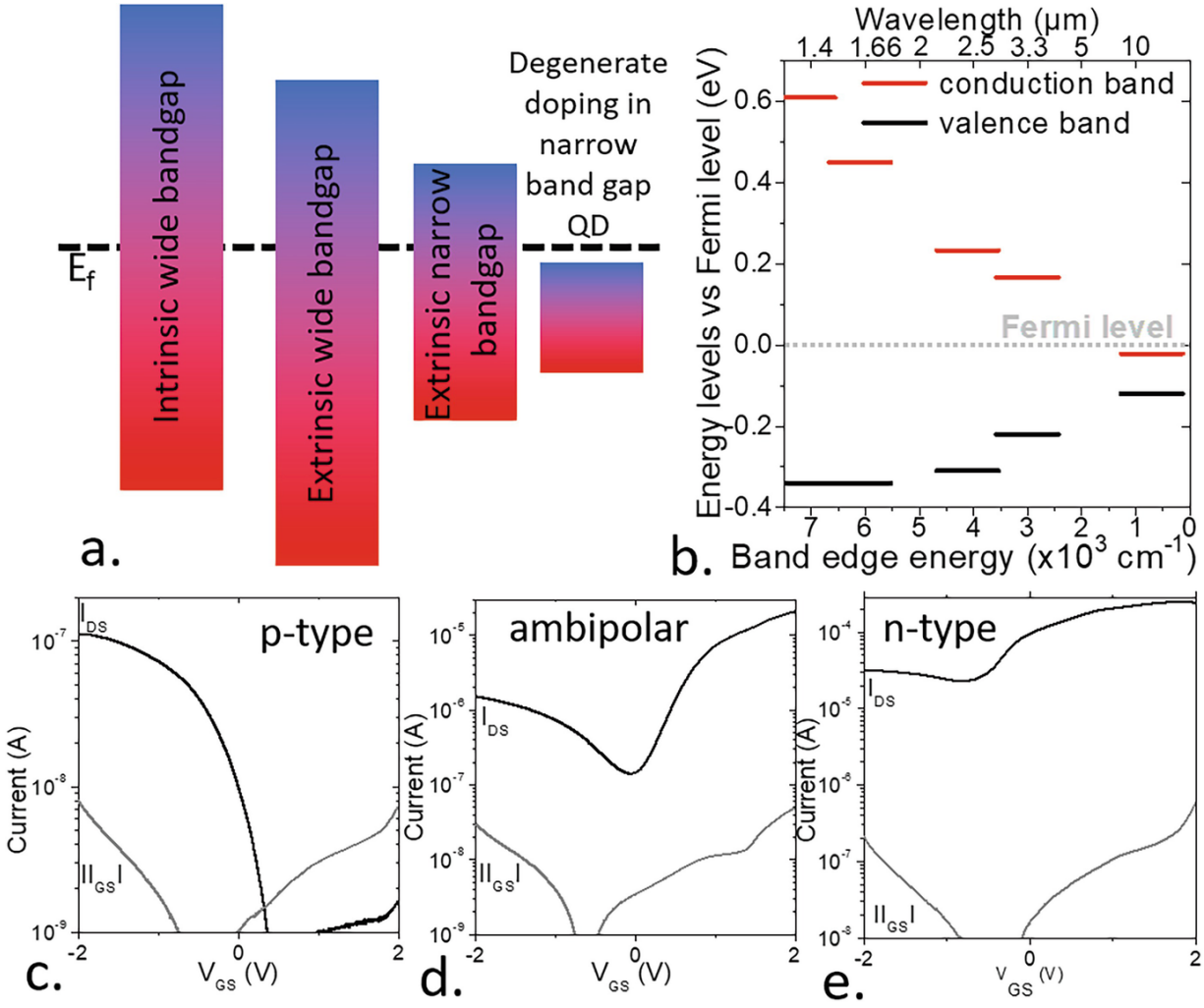

Fig. 6.4 Connection between quantum confinement, band alignment, and doping. (**a**) Scheme of the effect of the band gap value on the carrier density. The rectangle displays the band gap and the dashed line the Fermi level. (**b**) Conduction band (red) and valence band (black) for various sizes of HgTe NCs. (**c**) Field-effect transistor transfer curve (drain and gate current as a function of gate bias) for a channel made of small HgTe NCs (i.e., band gap above 700 meV). (**d**) Field-effect transistor transfer curve (drain and gate current as a function of gate bias) for a channel made of medium HgTe NCs (i.e., band gap around 500 meV). (**e**) Field effect transistor transfer curve (drain and gate current as a function of gate bias) for a channel made of large HgTe NCs (i.e., band gap below 300 meV) (Parts (**b**–**e**) are adapted with permission from Ref. [72]. Copyright 2018, American Chemical Society)

6.3.3 Doping and Surface Chemistry

Because of the high surface-to-volume ratio of NCs, their electronic properties strongly depend on surface chemistry in contrast to the bulk. The

motivation for introducing ligands during NC synthesis was first driven by size control and the achievement of monodisperse synthesis. The coupling of ligands to surface dangling bonds plays an important role in the formation of trap states within the band gaps. As a consequence, ligands drive the magnitude of the PL signal. Long ligands separate NCs from one another, limiting the electronic transport. The latter has also motivated the attempt to perform ligand exchange on colloidal nanocrystals. However, ligands also behave as a surface dipole [76]. This dipole induces an electric field and results in a NC surface gating. One can relate the energy shift of the band (ΔE_{vac}) to the magnitude μ of the dipole using the expression $\Delta E_{vac} = -N\frac{\mu_{\perp}(ligand)}{\varepsilon_0 \varepsilon_{ligand}}$ with N the surface density of dipoles and ε_{ligand} the dielectric constant of the ligands. This band shift with respect to the Fermi level resulting from ligand exchange was first used to design *pn* junctions based on PbS NCs. In the case of HgTe [74], a shift from *n* to *p* can be induced by changing the capping ligands; see Fig. 6.5a. It is worth pointing out that the expression of the shift does not depend on the NC size. As a result, the relative change of properties remains marginal for wide band gaps. However, the change can be significant for narrow band gaps since the dipole-induced shift can be as large as the band gap, resulting in the observation of degenerate doping or its suppression. In the case of HgSe NCs [48], this dipole-induced change in the carrier density can lead to the suppression of several carriers per NC [77, 78]; see Fig. 6.5c, d. Consequently, a drastic change in the absorption spectrum can also be seen; see Fig. 6.5b. Initial NCs are doped and include two electrons per NC, leading to a strong intraband signal and a bleached interband band edge. Once the HgSe NCs are coupled with S^{2-} ions, the intraband signal almost disappears, and the interband signal is recovered, meaning that the degenerate doping is lost.

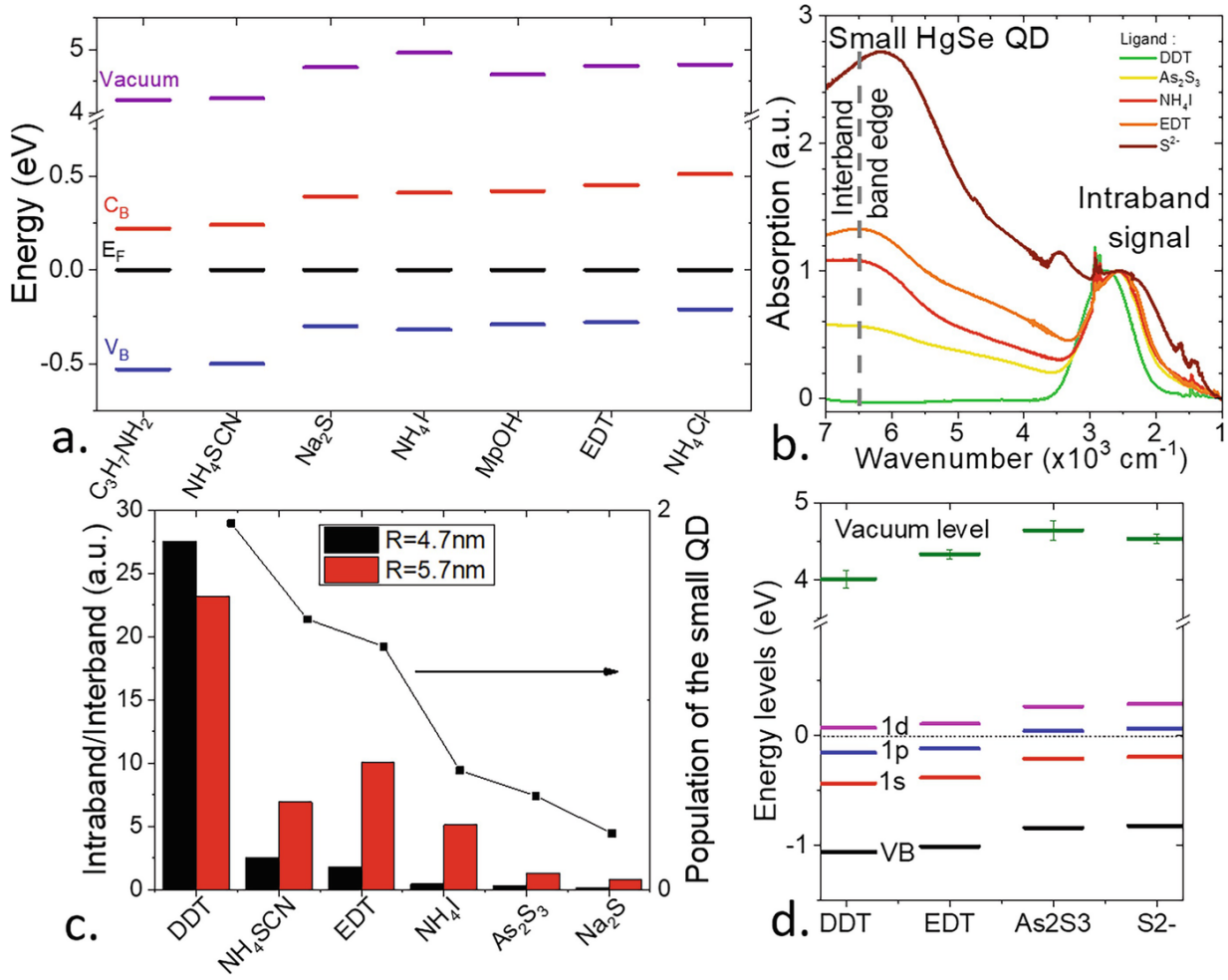

Fig. 6.5 Effect of surface chemistry on doping and band alignment. (**a**) Energy of the valence band, conduction band, and vacuum level for HgTe nanocrystals with a 1.7 μm cutoff wavelength and different capping ligands. The Fermi level is set as 0 eV (Part (**a**) is adapted with permission from Ref. [74] Copyright 2019, American Chemical Society). (**b**) Absorption spectra of small (4.7 nm) HgSe NCs capped with different ligands. (**c**) Plot of the ratio of the intraband signal divided by the fitted magnitude of the interband signal for two sizes of HgSe nanocrystals. The related population of the CQDs is given on the right scale for small CQDs (diameter of 4.7 nm) (Graphs (**b**) and (**c**) are adapted with permission from Ref. [48]. Copyright 2016, American Chemical Society). (**d**) Electronic spectrum (black, red, blue, pink, and green correspond to the valence band, $1S_e$ state, $1P_e$ state, $1D_e$ state, and vacuum level, respectively) for medium HgSe CQDs capped with four different ligands. Zero on the energy scale corresponds to the Fermi level (Part (**c**) is adapted with permission from ref. [75]. Copyright 2017, American Chemical Society)

6.3.4 Temperature and Pressure Effects on the Band Gap

The band gap of HgTe NCs also appears to be drastically affected by temperature [63, 79, 80] and pressure [63, 80]. Bulk HgTe presents an inverted band gap dependence on temperature with a positive value for dE_G/dT (i.e., band edge redshifts upon cooling). Large HgTe NCs present a

similar sign for dE_G/dT; see Fig. 6.6. This trend is the opposite of what was observed for cadmium chalcogenide NCs, though this behavior is not unique since lead halide perovskites [81] and large PbS NCs [82] also exhibit such behavior. However, the actual value of dE_G/dT appears to be strongly connected to the band gap value. As confinement increases, the value of dE_G/dT drops from 200 $\mu eV.K^{-1}$ to a smaller value. In HgTe nanoplatelets, dE_G/dT even changes sign and becomes negative; see Fig. 6.6b. However, this sign change does not seem connected to the 2D shape since 0D NCs and 2D NPLs, with similar band gaps, present similar dE_G/dT value. In the case of doped NCs, we also observe a shift of the intraband transition with temperature. In this case, only a blue shift is observed upon cooling ($dE_{intra}/dT = -80\ \mu eV.K^{-1} < 0$).

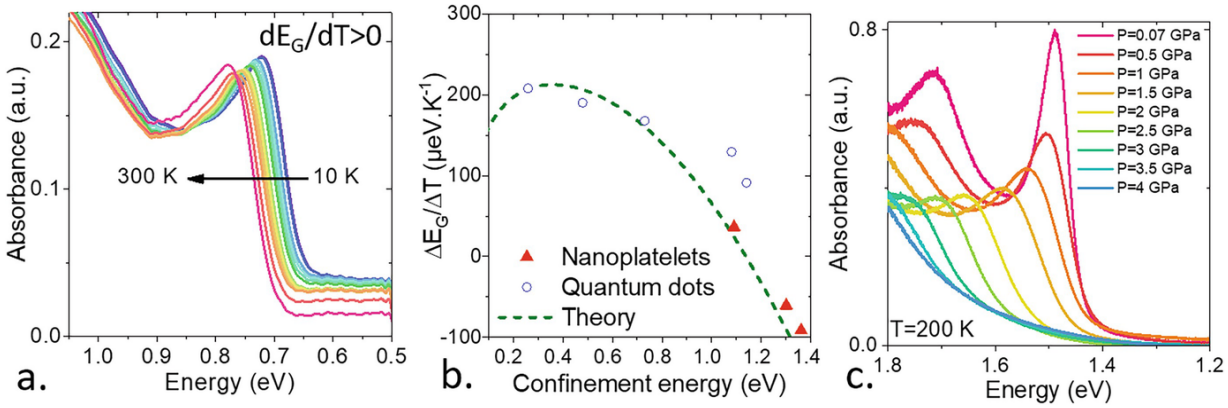

Fig. 6.6 Temperature and pressure dependence of the band gap. (**a**) Absorption spectra of HgTe NCs with a band edge at 6000 cm^{-1} for various temperatures between 10 K and 300 K, without external applied pressure. (**b**) dE_G/dT as a function of the confinement energy for the same set of samples. The simulated value of dE_G/dT extracted from the pseudo k.p modeling is plotted as the green dashed line. (**c**) Infrared spectrum of HgTe NPLs at 200 K under various pressures ranging from 0 to 4 GPa (Figures are adapted with permission from Ref. [63]. Copyright 2020, American Chemical Society)

Though the application of pressure appears less practical than cooling for an infrared material, the band gap change under the application of a few GPa pressure is larger than the one resulting from a 300 K cooling. Although the direct application of pressure in a diamond anvil cell is probably not a viable strategy to achieve spectroscopic tuning, one should always consider the effects of pressure when using heterostructures. In a non-lattice matched heterostructure, the strain induced by the shell growth on the core can easily reach several GPa and thus induce a drastic shift

beyond the one resulting from the band alignment. Bulk HgX experiences a series of structural phase changes under pressure application from zinc blende to cinnabar [83, 84] and then rock salt [85]. For bulk HgTe, the first transition is expected to occur at 1.4 GPa. NC form appears to stabilize the low-pressure zinc blende phase above 3 GPa. For pressures in the 0 to 10 GPa range, effects of pressure appear to be fully reversible though presenting a large hysteresis [80]. The application of pressure leads to a blue shift of the exciton; see Fig. 6.6c. Similar behavior is observed for weakly and strongly confined HgTe NCs. However, the exact value of dE_G/dP is slightly larger for strongly confined particles ($dE_G/dP = 100$ meV.GPa^{-1} for HgTe NPL), compared to $dE_G/dP = 60$ meV.GPa^{-1} for particles around 10 nm. Interestingly, the intraband transition is also affected by the pressure, but this time a redshift is observed ($dE_G/dP < 0$), and the absolute value of the shift is also smaller ($dE_G/dP = -8 \pm 2$ meV.GPa^{-1}).

6.3.5 Experimental Determination of the Electronic Structure: Results from Photoemission

While optical spectroscopy is a powerful tool to unveil the material band gap and the carrier dynamics, the method can only observe difference between energy states rather than the absolute energy of the electronic states. Identifying the absolute energy of the different states involved in the device is nevertheless of utmost interest for the device integration of HgX NCs, where it is used to minimize contact Schottky barriers or to design barriers for diodes. Two methods are typically used to obtain this absolute energy information: electrochemistry [66, 86], where the exact location of the state is obtained relatively to the potential of a reference electrode, and X-ray photoemission. Both methods have pros and cons. Photoemission is conducted under ultrahigh vacuum, which might not represent the actual device environment, while the electrolyte used for electrochemistry is neither representative of the final NC surroundings. Here, we choose to focus on photoemission because the method not only provides insight into the semiconductor (i.e., the relative position of the Fermi level with respect to the band: Fig. 6.7d, work function: Fig. 6.7c) but also enables a detailed analysis of the chemical environment of the atoms. Although the method is typically used for surface science, where samples are degassed at high

temperatures, a clean surface (i.e., with weak O and C contaminations) can be obtained simply from a moderately long vacuum pumping at room temperature.

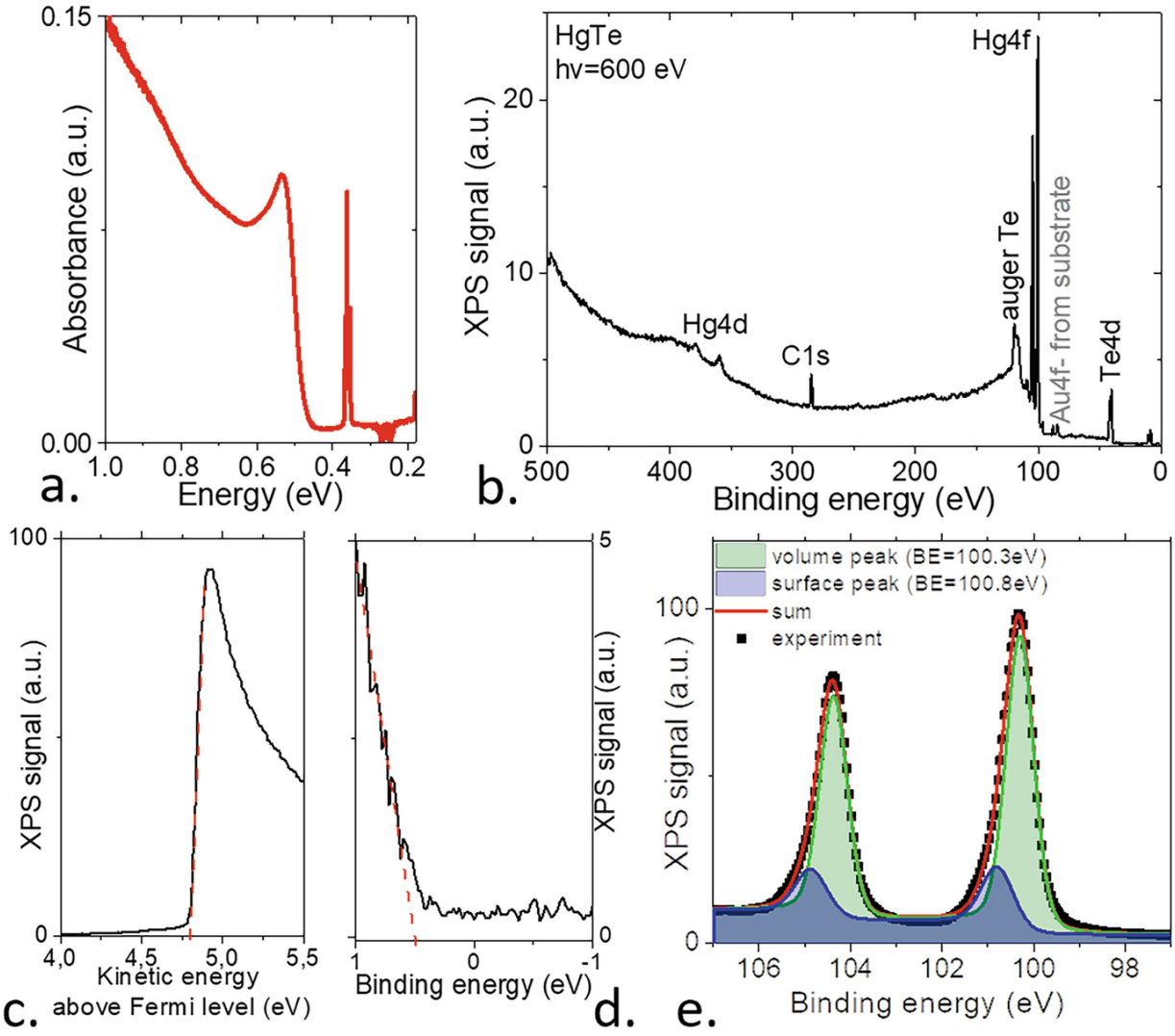

Fig. 6.7 Electronic structure of HgTe NC revealed by absorption and photoemission spectroscopy. (**a**) absorption spectrum of HgTe NCs. (**b**) X-ray photoemission overview spectrum of HgTe NC thin films. (**c**) X-ray photoemission spectrum of the secondary electron cutoff of HgTe NCs whose energy revealed the work function. (**d**) X-ray photoemission spectrum of the valence band of HgTe NCs. (**e**) X-ray photoemission spectrum of the Hg 4f state from HgTe NCs (Part **e** is adapted with permission from Ref. [31]. Copyright (2017), American Chemical Society)

A typical photoemission overview spectrum of HgTe NCs is given in Fig. 6.7b. The spectrum mostly shows the contributions of Hg and Te. A carbon contribution (C1s at 284 eV) is also present due to the presence of organic ligands. On the other hand, the contribution from the thiol (S2p is expected at 160 eV) is generally weak. The overview spectrum can also

show some Auger peaks, but the presence of those peaks is strongly connected to the choice of source used for the X-ray (synchrotron *vs*. conventional source). A zoom on the Hg 4f state (Fig. 6.7e) systematically reveals two contributions. The magnitude of the large binding energy contribution is typically reduced when the photon energy is increased, which suggests that this contribution is primarily a surface contribution [31]. We may thus attribute the weak large binding energy contribution to the surface mercury coupled to thiol ligands. The main contribution is then associated with the bulk Hg coupled with Te atoms. The weaker electronegativity of Te compared to S explains why that contribution appears at a reduced binding energy.

By combining the optical spectroscopy to reveal the band gap value and the photoemission, to obtain the work function and the valence band spectrum, it becomes possible to reconstruct an effective energy diagram, as presented in Fig. 6.5.

6.3.6 Carrier Dynamics from fs to ms

Using a series of time-resolved experiments: transient reflectivity [87], time-resolved PL [88, 89], time-resolved photoemission [31, 36], and transient photocurrent [90, 91], it is possible to depict the carrier dynamics in HgTe NCs from a few fs up to the ms range.

Transient reflectivity with ultrashort laser pulses (<50 fs) has been used to reveal the carrier relaxation at early time scale. In this experiment, Qu et al. [87] used a two-color pump-probe configuration where the pump is used to excite far above the band edge (800 nm or 1.55 eV), while the relaxation is probed at the band edge (2 μm in this case). Over a duration of 3 ps (Fig. 6.8a, b), the hot carriers generated by the pump relax down to the band edge. This corresponds to regimes I and II of Fig. 6.8f. A similar rise time has been observed while investigating HgTe THz NC with a much smaller band gap [67]. This suggests that the relaxation from the hot states to the band edge is poorly dependent on the detail of the density of states.

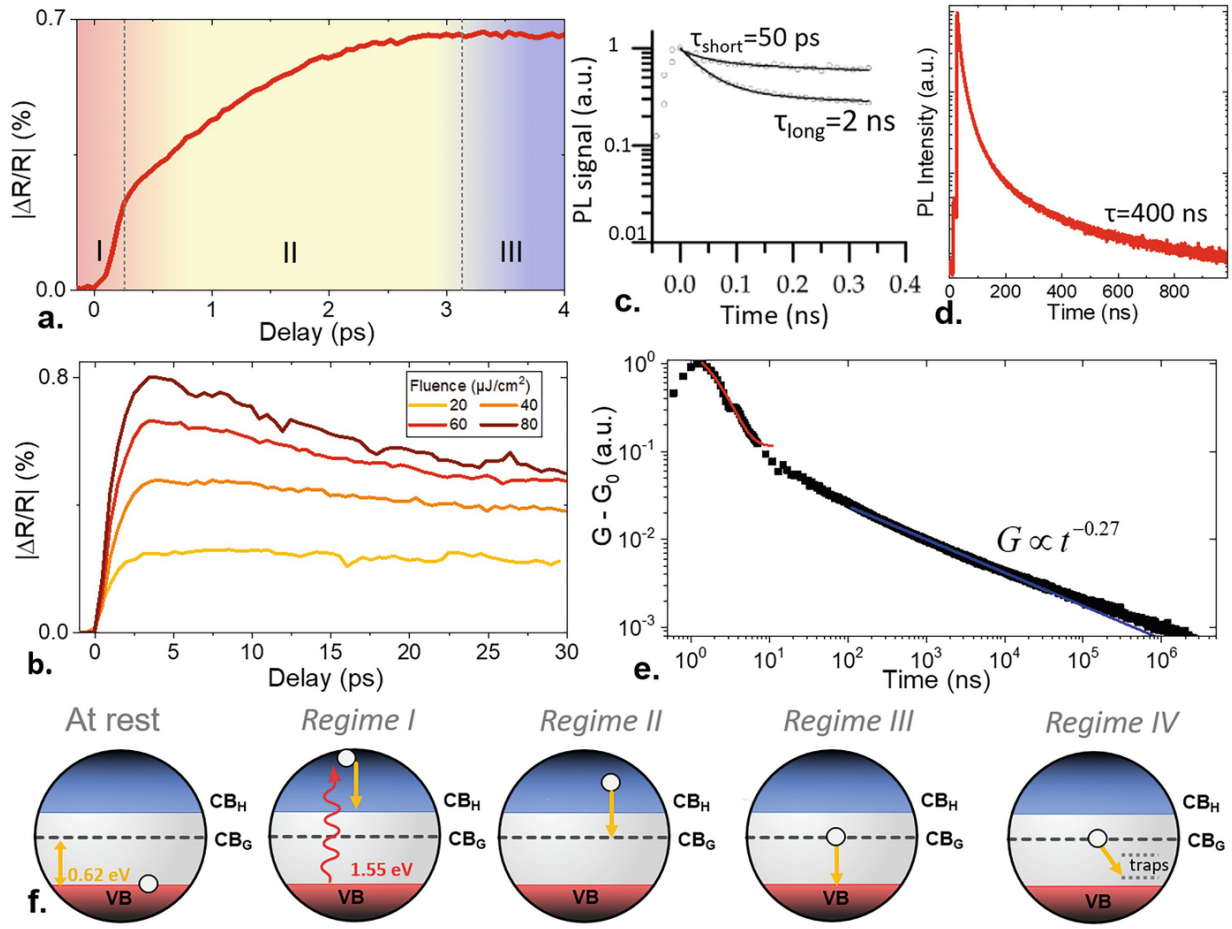

Fig. 6.8 Carrier dynamics in HgTe NCs. (**a**) Early time scale transient reflectivity signal as depicted in part b for a fluency of 60 μJ cm^{-2}. **(b**) Transient reflectivity measurements in a two-color pump/probe configuration for several pump fluences. A 800 nm pump pulse and a 2 μm probe pulse are used (Parts (**a**, **b**) are adapted with permission from Ref. [87] Copyright 2021). (**c**) PL decays for HgTe CQDs emitting at 2 μm. The open circles denote the measured intensity; the solid lines represent the biexponential fits with the time constants presented as labels. (Part (**c**) is adapted with permission from ref. [88]. Copyright 2014, American Chemical Society). (**d**) Photoluminescence intensity as a function of time after excitation with 1.5 ps laser pulses at 780 nm for a film of HgTe NCs. (Part (**d**) is adapted with permission from Ref. [92]. Copyright 2020, American Chemical Society). (**e**) Evolution of the conductance as a function of time after a 1 ns long pulse of light at 355 nm (Part (**e**) is adapted with permission from ref. [90]. Copyright 2017, American Chemical Society). (**f**) Simplified scheme of the transitions involved in the pump and probe processes. VB and CB stand for valence and conduction band, respectively, while H and G subscripts are used, respectively, for hot and ground

After this rise time in the transient reflectivity signal, a decay of the signal is observed. There is a first fast component (τ_{Auger} = 50 ps) that is observed in both transient reflectivity (Fig. 6.8b) and time-resolved PL (Fig. 6.8c). It is worth pointing out that Auger efficiency has been significantly reduced in HgX NCs compared to the bulk materials [67, 89, 93]. Ruppert

et al. [94] have determined a 0.36 eV.ps^{-1} cooling rate, which appears independent of the energy of the excitation.

This time scale is connected to the pump fluence, see Fig. 6.8b, and has been attributed to the Auger effect. Then the ns regime (τ_{rad} = few ns for an emission below 2 μm) corresponds to the radiative band edge emission; see Fig. 6.8c and regime III from Fig. 6.8f. This radiative decay rate tends to be slower when the cutoff wavelength increases to an energy corresponding to the resonance with organic ligands. This long radiative rate causes PL to quickly drop beyond telecom wavelengths. At even longer time scales (hundreds of ns range, see Fig. 6.8d and regime IV from Fig. 6.8f), the PL presents a long decay tail. This regime has been associated with the emission from the conduction band to shallow trap states in the vicinity of the valence band. Evidence for the involvement of trap states has also been observed using transient photocurrent [90, 95, 96]; see Fig. 6.8e. A trap state is often associated with multiexponential decay or even power-law decay. In this case, the exponent of the power law can be directly connected to the Urbach energy that describes the density of trap states within the band gap [90].

6.4 Optical Features

The last part of this chapter discusses the optical features of HgX films, a direct consequence of the previously described electronic structure.

6.4.1 Light Emission: Pholuminescence, Lasing, and Electroluminescence

Thanks to their narrow band gap HgX NCs can also be used for light emission. Light emission in the near IR range where the water presents a high degree of transparency, was one of the first targeted applications for HgX NCs. Very small HgS and HgSe or Cd containing HgCdTe alloyed NCs can match this criterion. PL in HgTe has been reported from 800 nm [6, 7] to 5 μm [27]; see Fig. 6.9a. In the near IR and even at telecom wavelength, PL QY above 25% has been reported by several groups even without a shell [20, 21, 30, 88]. However, when longer wavelengths are concerned, the PLQY drops very fast. This reflects the lengthening of the radiative decays as the band gap is reduced and the efficient energy transfer

to the ligands, which are also absorbing in this spectral range. A rough order of magnitude is 1% PL QY for 2 μm PL and 0.01% at 5 μm. This drop of the PL QY is associated with the inherent slower decay rate of the radiative recombination, while the band gap is reduced, and a very efficient near-field coupling between the exciton and the surface ligand tends to quench the radiative decay path. It is worth pointing out that PL is not limited to interband recombination, and that intraband PL can be observed in self-doped forms of HgX NCs [38, 97]. However, the emission being already deep in the infrared (5 μm and more), the PL QY is low, similar to the interband at the same wavelength.

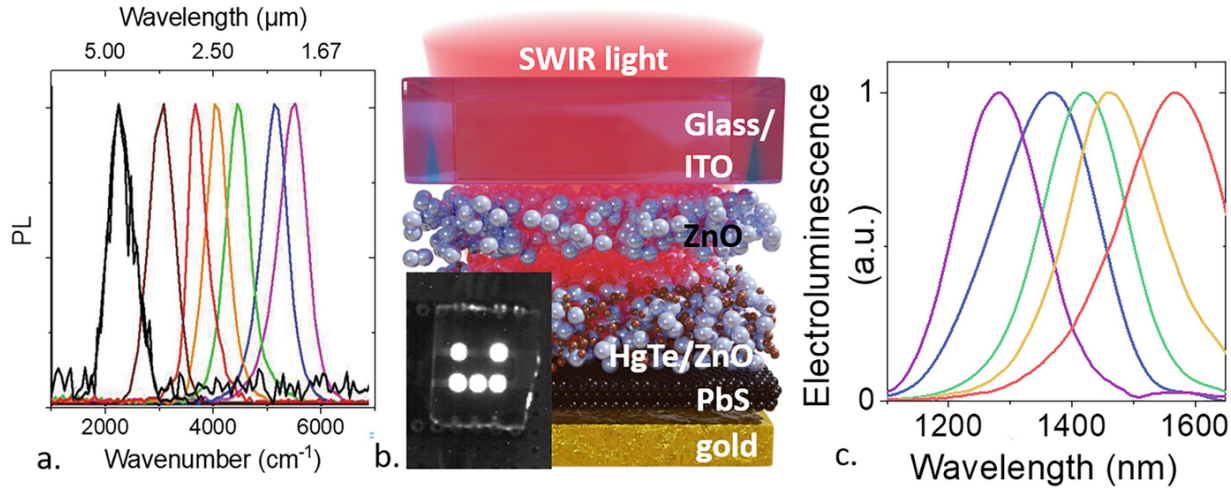

Fig. 6.9 Light emission from HgTe NCs. (**a**) PL spectra for HgTe NCs with various sizes (Part (**a**) is adapted with permission from Ref. [27] Copyright (2011), American Chemical Society). (**b**) Schematic of HgTe NC-based LED. The inset is an infrared image of five operating pixels. (**c**) Electroluminescence spectra of HgTe NC-based LED (Part **b**, **c** are adapted with permission from ref. [92]. Copyright (2011): American Chemical Society)

Coupling of HgTe NCs to a plasmonic cavity appears as a promising direction to tune the light emission while controlling the directionality or the decay rate. The first report in this direction was obtained by Sergeev et al. [98], where HgTe NCs are coated onto a laser fabricated grating. Coherent emission from HgTe NCs has also been reported [99, 100]. In particular, Geiregat et al. [101] have claimed that low threshold CW lasing should be observed in small HgTe NCs. Interestingly, in such HgTe NCs with Te surface excess, for once trap states appear to have a beneficial role and are used to form a three-level system.

Regarding electroluminescence, there are still only a few reports based on HgX NCs [30, 87, 92, 102–104]. Certainly, the toxicity of HgX has

hindered the exploration of the HgX NC for light-emitting diodes (LED). While this consideration is certainly justified at 1.5 μm where other materials [105, 106] present higher efficiencies, the recent report by Qu et al. [87] of electroluminescence above 2 μm may change this consideration, since no other material presents EL signal at such a long infrared wavelength. LED design based on HgTe relies on a solar cell stack [105, 107] based on ITO/ZnO/HgTe/PbS/gold, as shown in Fig. 6.9b. The best device presents an external quantum efficiency of around 2% [104], with a sub-band gap turn-on voltage at around 0.85 V for emission at 1.3 μm and tunable emission from 1200 [92] to 2300 nm [87]; see Fig. 6.9c.

6.4.2 Optical Index

To finish this chapter, we would like to discuss the complex optical index $\bar{n}(\omega) = n(\omega) + ik(\omega)$ of HgTe NC thin films. Here, ω is the angular frequency of the incident light. This is a critical input for the design of devices, especially to achieve by design light-matter coupling as discussed in Chap. 7 of the second volume of this book collection. Unlike quantum well systems in which light with only a particular polarization can be absorbed, NC films can be approximated as homogenous media, which allows optical features of the designed system to be simulated given the values of $\bar{n}(\omega)$. The power dissipated per unit volume in the NC film can be calculated from $P_{NC}(\omega) = \omega|E|^2\varepsilon_0 nk$, where E is the electric field, ε_0 is the permittivity of free space, and n and k are the real and the imaginary parts of the optical index, respectively. The overall absorption of the NC material is then calculated using

$$Abs_{NC}(\omega) = \frac{P_{NC}(\omega)}{P_{incidence}} = \frac{\iiint dV_{NC}\omega|E|^2\varepsilon_0 nk}{P_{incidence}} \tag{6.1}$$

where dV_{NC} is the infinitesimal volume of NC film and $P_{incidence}$ is the power of the incident light. In practice, this integral can be conveniently performed using numerical simulations.

Spectrally resolved ellipsometry measurements have been conducted by Rastogi et al. [108] on HgTe NC thin films with various sizes and surface chemistries. The spectral dependence of the extinction coefficient is somehow trivial and follows the absorption spectrum. A rough order of

magnitude reminds us that k = 0.1 is more or less independent of the size at the exciton; see Fig. 6.10b. Regarding the refractive index, it presents a much weaker spectral dependence. Rastogi et al. [108] have also shown that the error introduced when using the spectrally average value of n instead of its actual value with its full spectral dependence is acceptable for electromagnetic simulations. In practice, this means that for a new particle shape or surface chemistry, there is no need to conduct a fully spectrally resolved study of the film refractive index, and that measurement at a single wavelength can be used. The value for n is found to be between 2.2 and 2.5 depending on the particle size; see Fig. 6.10a. This is an intermediate value between the value of void (n = 1), the value of the organic capping ligand (n < 2), and the value of bulk HgTe [109–112] (3 < n < 4). Note that the trends with size are not trivial, and, in particular, the smallest particle here presents a larger value for n, while for sphere forms, the opposite trends would have been expected (i.e., small spheres have weaker volume fraction). This reflects the change of particle shape with size, which results in different packing densities.

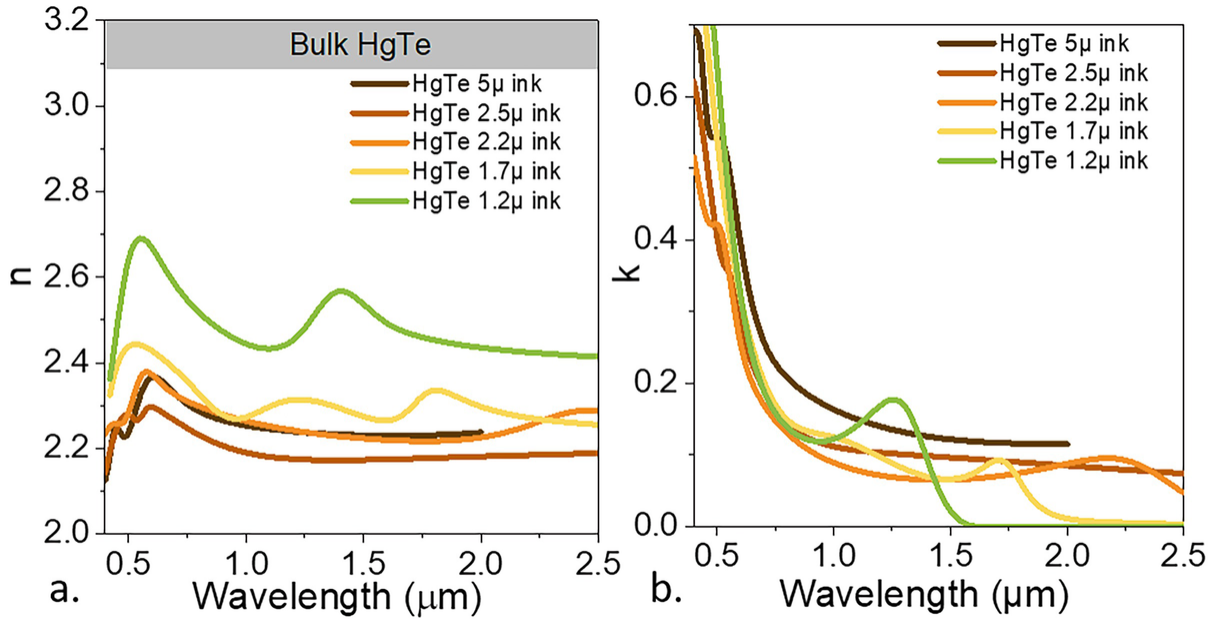

Fig. 6.10 Complex optical index from HgTe NC films. (**a**) Refractive index spectra for thin films of HgTe NCs with various band gaps. The legend Nµ means N µm cutoff wavelength. (**b**) Extinction coefficient spectra for thin films of HgTe NCs with various band gaps (the figure is adapted with permission from Ref. [108]. Copyright 2021: Wiley)

6.5 Conclusion

Thanks to their tunable narrow band gap, HgX NCs can cover the whole infrared spectrum from the visible to the THz range. Two main effects are at play to achieve such a broad tunability: quantum confinement and self-doping enabling intraband absorption. Over a few years time scale, the challenges for these NCs have been evolved from material growth to their integration into complex optoelectronic devices. In particular, they appear as a promising building block for the design of cost-effective infrared sensors. This aspect is the topic of Chap. 7 of the second volume of this book collection.

References

1. Gréboval C, Chu A, Goubet N, Livache C, Ithurria S, Lhuillier E (2021) Mercury chalcogenide quantum dots: material perspective for device integration. Chem Rev 121:3627–3700. https://doi.org/10.1021/acs.chemrev.0c01120 [Crossref]
2. Lhuillier E, Keuleyan S, Liu H, Guyot-Sionnest P (2013) Mid-IR colloidal nanocrystals. Chem Mater 25:1272–1282. https://doi.org/10.1021/cm303801s [Crossref]
3. Brus LE (1984) Electron–electron and electron-hole interactions in small semiconductor crystallites: the size dependence of the lowest excited electronic state. J Chem Phys 80:4403–4409. https://doi.org/10.1063/1.447218 [Crossref]
4. Chamarro M, Gourdon C, Lavallard P, Lublinskaya O, Ekimov AI (1996) Enhancement of electron-hole exchange interaction in CdSe nanocrystals: a quantum confinement effect. Phys Rev B 53:1336–1342. https://doi.org/10.1103/PhysRevB.53.1336 [Crossref]
5. Murray CB, Norris DJ, Bawendi MG (1993) Synthesis and characterization of nearly monodisperse CdE (E = sulfur, selenium, tellurium) semiconductor nanocrystallites. J Am Chem Soc 115:8706–8715. https://doi.org/10.1021/ja00072a025 [Crossref]
6. Kershaw SV, Rogach AL (2015) Infrared emitting HgTe quantum dots and their waveguide and optoelectronic devices. Z Für Phys Chem 229:23–64. https://doi.org/10.1515/zpch-2014-0590 [Crossref]
7. Rogach A, Kershaw SV, Burt M, Harrison MT, Kornowski A, Eychmüller A et al (1999) Colloidally prepared HgTe nanocrystals with strong room-temperature infrared luminescence. Adv Mater 11:552–555

[Crossref]
8. Nozik AJ (2002) Quantum dot solar cells. Phys E Low-Dimens Syst Nanostructures 14:115–120. https://doi.org/10.1016/S1386-9477(02)00374-0
[Crossref]
9. Semonin OE, Luther JM, Choi S, Chen H-Y, Gao J, Nozik AJ et al (2011) Peak external photocurrent quantum efficiency exceeding 100% via MEG in a quantum dot solar cell. Science 334:1530–1533. https://doi.org/10.1126/science.1209845
[Crossref]
10. Schaller RD, Klimov VI (2004) High efficiency carrier multiplication in PbSe nanocrystals: implications for solar energy conversion. Phys Rev Lett 92:186601. https://doi.org/10.1103/PhysRevLett.92.186601
[Crossref]
11. Pijpers JJH, Ulbricht R, Tielrooij KJ, Osherov A, Golan Y, Delerue C et al (2009) Assessment of carrier-multiplication efficiency in bulk PbSe and PbS. Nat Phys 5:811–814. https://doi.org/10.1038/nphys1393
[Crossref]
12. Melnychuk C, Guyot-Sionnest P (2021) Multicarrier dynamics in quantum dots. Chem Rev 121:2325–2372. https://doi.org/10.1021/acs.chemrev.0c00931
[Crossref]
13. Lhuillier E, Guyot-Sionnest P (2017) Recent progresses in mid infrared nanocrystal optoelectronics. IEEE J Sel Top Quantum Electron 23:1–8. https://doi.org/10.1109/JSTQE.2017.2690838
[Crossref]
14. Livache C, Martinez B, Goubet N, Ramade J, Lhuillier E (2018) Road map for nanocrystal based infrared photodetectors. Front Chem 6:575. https://doi.org/10.3389/fchem.2018.00575
[Crossref]
15. Hafiz SB, Scimeca M, Sahu A, Ko D-K (2019) Colloidal quantum dots for thermal infrared sensing and imaging. Nano Converg 6:7. https://doi.org/10.1186/s40580-019-0178-1
[Crossref]
16. Green M, Mirzai H (2018) Synthetic routes to mercury chalcogenide quantum dots. J Mater Chem C 6:5097–5112. https://doi.org/10.1039/C8TC00910D
[Crossref]
17. Eychmüller A, Mews A, Weller H (1993) A quantum dot quantum well: CdS/HgS/CdS. Chem Phys Lett 208:59–62. https://doi.org/10.1016/0009-2614(93)80076-2
[Crossref]
18. De Trizio L, Manna L (2016) Forging colloidal nanostructures via cation exchange reactions. Chem Rev 116:10852–10887. https://doi.org/10.1021/acs.chemrev.5b00739
[Crossref]
19. Son DH (2004) Cation exchange reactions in ionic nanocrystals. Science 306:1009–1012. https://doi.org/10.1126/science.1103755

[Crossref]
20. Kershaw SV, Yiu WK, Sergeev A, Rogach AL (2020) Development of synthetic methods to grow long-wavelength infrared-emitting HgTe quantum dots in Dimethylformamide. Chem Mater 32:3930–3943. https://doi.org/10.1021/acs.chemmater.0c00249
[Crossref]
21. Abdelazim NM, Zhu Q, Xiong Y, Zhu Y, Chen M, Zhao N et al (2017) Room temperature synthesis of HgTe quantum dots in an aprotic solvent realizing high photoluminescence quantum yields in the infrared. Chem Mater 29:7859–7867. https://doi.org/10.1021/acs.chemmater.7b02637
[Crossref]
22. Kovalenko MV, Kaufmann E, Pachinger D, Roither J, Huber M, Stangl J et al (2006) Colloidal HgTe nanocrystals with widely tunable narrow band gap energies: from telecommunications to molecular vibrations. J Am Chem Soc 128:3516–3517. https://doi.org/10.1021/ja058440j
[Crossref]
23. Izquierdo E, Robin A, Keuleyan S, Lequeux N, Lhuillier E, Ithurria S (2016) Strongly confined HgTe 2D nanoplatelets as narrow near-infrared emitters. J Am Chem Soc 138:10496–10501. https://doi.org/10.1021/jacs.6b04429
[Crossref]
24. Chee S-S, Gréboval C, Magalhaes DV, Ramade J, Chu A, Qu J et al (2021) Correlating structure and detection properties in HgTe nanocrystal films. Nano Lett 21:4145–4151. https://doi.org/10.1021/acs.nanolett.0c04346
[Crossref]
25. Goubet N, Jagtap A, Livache C, Martinez B, Portalès H, Xu XZ et al (2018) Terahertz HgTe nanocrystals: beyond confinement. J Am Chem Soc 140:5033–5036. https://doi.org/10.1021/jacs.8b02039
[Crossref]
26. Keuleyan S, Lhuillier E, Brajuskovic V, Guyot-Sionnest P (2011) Mid-infrared HgTe colloidal quantum dot photodetectors. Nat Photonics 5:489–493. https://doi.org/10.1038/nphoton.2011.142
[Crossref]
27. Keuleyan S, Lhuillier E, Guyot-Sionnest P (2011) Synthesis of colloidal HgTe quantum dots for narrow mid-IR emission and detection. J Am Chem Soc 133:16422–16424. https://doi.org/10.1021/ja2079509
[Crossref]
28. Keuleyan SE, Guyot-Sionnest P, Delerue C, Allan G (2014) Mercury telluride colloidal quantum dots: electronic structure, size-dependent spectra, and photocurrent detection up to 12 μm. ACS Nano 8:8676–8682. https://doi.org/10.1021/nn503805h
[Crossref]
29. Shen G, Chen M, Guyot-Sionnest P (2017) Synthesis of nonaggregating HgTe colloidal quantum dots and the emergence of air-stable n-doping. J Phys Chem Lett 8:2224–2228. https://doi.org/10.1021/acs.jpclett.7b00775
[Crossref]

30. Prado Y, Qu J, Gréboval C, Dabard C, Rastogi P, Chu A et al (2021) Seeded growth of HgTe nanocrystals for shape control and their use in narrow infrared electroluminescence. Chem Mater 33:2054–2061. https://doi.org/10.1021/acs.chemmater.0c04526 [Crossref]
31. Livache C, Izquierdo E, Martinez B, Dufour M, Pierucci D, Keuleyan S et al (2017) Charge dynamics and optolectronic properties in HgTe colloidal quantum wells. Nano Lett 17:4067–4074. https://doi.org/10.1021/acs.nanolett.7b00683 [Crossref]
32. Nasilowski M, Mahler B, Lhuillier E, Ithurria S, Dubertret B (2016) Two-dimensional colloidal nanocrystals. Chem Rev 116:10934–10982. https://doi.org/10.1021/acs.chemrev.6b00164 [Crossref]
33. Lhuillier E, Pedetti S, Ithurria S, Nadal B, Heuclin H, Dubertret B (2015) Two-dimensional colloidal metal chalcogenides semiconductors: synthesis, spectroscopy, and applications. Acc Chem Res 48:22–30. https://doi.org/10.1021/ar500326c [Crossref]
34. Pedetti S, Nadal B, Lhuillier E, Mahler B, Bouet C, Abécassis B et al (2013) Optimized synthesis of CdTe nanoplatelets and photoresponse of CdTe Nanoplatelets films. Chem Mater 25:2455–2462. https://doi.org/10.1021/cm4006844 [Crossref]
35. Izquierdo E, Dufour M, Chu A, Livache C, Martinez B, Amelot D et al (2018) Coupled HgSe colloidal quantum wells through a tunable barrier: a strategy to uncouple optical and transport band gap. Chem Mater 30:4065–4072. https://doi.org/10.1021/acs.chemmater.8b01028 [Crossref]
36. Gréboval C, Izquierdo E, Livache C, Martinez B, Dufour M, Goubet N et al (2019) Impact of dimensionality and confinement on the electronic properties of mercury chalcogenide nanocrystals. Nanoscale 11:3905–3915. https://doi.org/10.1039/C8NR09644A [Crossref]
37. Goubet N, Livache C, Martinez B, Xu XZ, Ithurria S, Royer S et al (2018) Wave-function engineering in HgSe/HgTe colloidal heterostructures to enhance mid-infrared photoconductive properties. Nano Lett 18:4590–4597. https://doi.org/10.1021/acs.nanolett.8b01861 [Crossref]
38. Shen G, Guyot-Sionnest P (2019) HgTe/CdTe and HgSe/CdX (X = S, se, and Te) core/shell mid-infrared quantum dots. Chem Mater 31:286–293. https://doi.org/10.1021/acs.chemmater.8b04727 [Crossref]
39. Schooss D, Mews A, Eychmüller A, Weller H (1994) Quantum-dot quantum well CdS/HgS/CdS: theory and experiment. Phys Rev B 49:17072–17078. https://doi.org/10.1103/PhysRevB.49.17072 [Crossref]
40. Kamalov VF, Little R, Logunov SL, El-Sayed MA (1996) Picosecond electronic relaxation in CdS/HgS/CdS quantum dot quantum well semiconductor nanoparticles. J Phys Chem

100:6381–6384. https://doi.org/10.1021/jp953708m
[Crossref]

41. Mews A, Kadavanich AV, Banin U, Alivisatos AP (1996) Structural and spectroscopic investigations of CdS/HgS/CdS quantum-dot quantum wells. Phys Rev B 53:R13242–R13245. https://doi.org/10.1103/PhysRevB.53.R13242
[Crossref]

42. Dorfs D, Henschel H, Kolny J, Eychmüller A (2004) Multilayered nanoheterostructures: theory and experiment. J Phys Chem B 108:1578–1583. https://doi.org/10.1021/jp036643t
[Crossref]

43. Smith AM, Lane LA, Nie S (2014) Mapping the spatial distribution of charge carriers in quantum-confined heterostructures. Nat Commun 5:4506. https://doi.org/10.1038/ncomms5506
[Crossref]

44. Smith AM, Nie S (2011) Bright and compact alloyed quantum dots with broadly tunable near-infrared absorption and fluorescence spectra through mercury cation exchange. J Am Chem Soc 133:24–26. https://doi.org/10.1021/ja108482a
[Crossref]

45. Kershaw SV, Burt M, Harrison M, Rogach A, Weller H, Eychmüller A (1999) Colloidal CdTe/HgTe quantum dots with high photoluminescence quantum efficiency at room temperature. Appl Phys Lett 75:1694–1696. https://doi.org/10.1063/1.124792
[Crossref]

46. Choi D, Yoon B, Kim D-K, Baik H, Choi J-H, Jeong KS (2017) Major electronic transition shift from bandgap to localized surface plasmon resonance in $Cd_xHg_{1-x}Se$ alloy nanocrystals. Chem Mater 29:8548–8554. https://doi.org/10.1021/acs.chemmater.7b03813
[Crossref]

47. Sagar LK, Walravens W, Maes J, Geiregat P, Hens Z (2017) HgSe/CdE (E = S, Se) Core/Shell nanocrystals by colloidal atomic layer deposition. J Phys Chem C 121:13816–13822. https://doi.org/10.1021/acs.jpcc.7b02803
[Crossref]

48. Robin A, Livache C, Ithurria S, Lacaze E, Dubertret B, Lhuillier E (2016) Surface control of doping in self-doped nanocrystals. ACS Appl Mater Interfaces 8:27122–27128. https://doi.org/10.1021/acsami.6b09530
[Crossref]

49. Jeong KS, Deng Z, Keuleyan S, Liu H, Guyot-Sionnest P (2014) Air-stable n-doped colloidal HgS quantum dots. J Phys Chem Lett 5:1139–1143. https://doi.org/10.1021/jz500436x
[Crossref]

50. Ithurria S, Talapin DV (2012) Colloidal atomic layer deposition (c-ALD) using self-limiting reactions at nanocrystal surface coupled to phase transfer between polar and nonpolar media. J Am Chem Soc 134:18585–18590. https://doi.org/10.1021/ja308088d
[Crossref]

51. Lhuillier E, Scarafagio M, Hease P, Nadal B, Aubin H, Xu XZ et al (2016) Infrared photodetection based on colloidal quantum-dot films with high mobility and optical absorption up to THz. Nano Lett 16:1282–1286. https://doi.org/10.1021/acs.nanolett.5b04616 [Crossref]
52. Wichiansee W, Nordin MN, Green M, Curry RJ (2011) Synthesis and optical characterization of infra-red emitting mercury sulfide (HgS) quantum dots. J Mater Chem 21:7331. https://doi.org/10.1039/c1jm10363f [Crossref]
53. Yang J, Zhang W-H, Hu Y-P, Yu J-S (2012) Aqueous synthesis and characterization of glutathione-stabilized β-HgS nanocrystals with near-infrared photoluminescence. J Colloid Interface Sci 379:8–13. https://doi.org/10.1016/j.jcis.2012.04.057 [Crossref]
54. Zhang L, Yang G, He G, Wang L, Liu Q, Zhang Q et al (2012) Synthesis of HgS nanocrystals in the Lysozyme aqueous solution through biomimetic method. Appl Surf Sci 258:8185–8191. https://doi.org/10.1016/j.apsusc.2012.05.018 [Crossref]
55. Goswami N, Giri A, Kar S, Bootharaju MS, John R, Xavier PL et al (2012) Protein-directed synthesis of NIR-emitting, tunable HgS quantum dots and their applications in metal-ion sensing. Small 8:3175–3184. https://doi.org/10.1002/smll.201200760 [Crossref]
56. Han L, Hou P, Feng Y, Liu H, Li J, Peng Z et al (2014) Phase transfer-based synthesis of HgS nanocrystals. Dalton Trans 43:11981–11987. https://doi.org/10.1039/C4DT00998C [Crossref]
57. Shen G, Guyot-Sionnest P (2016) HgS and HgS/CdS colloidal quantum dots with infrared intraband transitions and emergence of a surface Plasmon. J Phys Chem C 120:11744–11753. https://doi.org/10.1021/acs.jpcc.6b04014 [Crossref]
58. Kuno M, Higginson KA, Qadri SB, Yousuf M, Lee SH, Davis BL et al (2003) Molecular clusters of binary and ternary mercury chalcogenides: colloidal synthesis, characterization, and optical spectra. J Phys Chem B 107:5758–5767. https://doi.org/10.1021/jp0274684 [Crossref]
59. Howes P, Green M, Johnston C, Crossley A (2008) Synthesis and shape control of mercury selenide (HgSe) quantum dots. J Mater Chem 18:3474. https://doi.org/10.1039/b804158j [Crossref]
60. Deng Z, Jeong KS, Guyot-Sionnest P (2014) Colloidal quantum dots intraband photodetectors. ACS Nano 8:11707–11714. https://doi.org/10.1021/nn505092a [Crossref]
61. Delin A, Klüner T (2002) Excitation spectra and ground-state properties from density-functional theory for the inverted band-structure systems β -HgS, HgSe, and HgTe. Phys Rev B 66:035117. https://doi.org/10.1103/PhysRevB.66.035117 [Crossref]

62. Svane A, Christensen NE, Cardona M, Chantis AN, van Schilfgaarde M, Kotani T (2011) Quasiparticle band structures of β-HgS, HgSe, and HgTe. Phys Rev B 84:205205. https://doi.org/10.1103/PhysRevB.84.205205 [Crossref]
63. Moghaddam N, Gréboval C, Qu J, Chu A, Rastogi P, Livache C et al (2020) The strong confinement regime in HgTe two-dimensional nanoplatelets. J Phys Chem C 124:23460–23468. https://doi.org/10.1021/acs.jpcc.0c07533 [Crossref]
64. Allan G, Delerue C (2012) Tight-binding calculations of the optical properties of HgTe nanocrystals. Phys Rev B 86:165437. https://doi.org/10.1103/PhysRevB.86.165437 [Crossref]
65. Rinnerbauer V, Hingerl K, Kovalenko M, Heiss W (2006) Effect of quantum confinement on higher transitions in HgTe nanocrystals. Appl Phys Lett 89:193114. https://doi.org/10.1063/1.2387110 [Crossref]
66. Chen M, Guyot-Sionnest P (2017) Reversible electrochemistry of mercury chalcogenide colloidal quantum dot films. ACS Nano 11:4165–4173. https://doi.org/10.1021/acsnano.7b01014 [Crossref]
67. Apretna T, Massabeau S, Gréboval C, Goubet N, Tignon J, Dhillon S et al (2021) Few picosecond dynamics of intraband transitions in THz HgTe nanocrystals. Nano 10:249. https://doi.org/10.1515/nanoph-2021-0249 [Crossref]
68. Dalpian GM, Chelikowsky JR (2006) Self-purification in semiconductor nanocrystals. Phys Rev Lett 96:226802. https://doi.org/10.1103/PhysRevLett.96.226802 [Crossref]
69. Nag A, Chakraborty S, Sarma DD (2008) To dope Mn^{2+} in a semiconducting nanocrystal. J Am Chem Soc 130:10605–10611. https://doi.org/10.1021/ja801249z [Crossref]
70. Dufour M, Izquierdo E, Livache C, Martinez B, Silly MG, Pons T et al (2019) Doping as a strategy to tune color of 2D colloidal Nanoplatelets. ACS Appl Mater Interfaces 11:10128–10134. https://doi.org/10.1021/acsami.8b18650 [Crossref]
71. Knowles KE, Hartstein KH, Kilburn TB, Marchioro A, Nelson HD, Whitham PJ et al (2016) Luminescent colloidal semiconductor nanocrystals containing copper: synthesis, photophysics, and applications. Chem Rev 116:10820–10851. https://doi.org/10.1021/acs.chemrev.6b00048 [Crossref]
72. Jagtap A, Martinez B, Goubet N, Chu A, Livache C, Gréboval C et al (2018) Design of a unipolar barrier for a nanocrystal-based short-wave infrared photodiode. ACS Photonics 5:4569–4576. https://doi.org/10.1021/acsphotonics.8b01032

[Crossref]
73. Hudson MH, Chen M, Kamysbayev V, Janke EM, Lan X, Allan G et al (2018) Conduction band fine structure in colloidal HgTe quantum dots. ACS Nano 12:9397–9404. https://doi.org/10.1021/acsnano.8b04539
[Crossref]
74. Chu A, Martinez B, Ferré S, Noguier V, Gréboval C, Livache C et al (2019) HgTe nanocrystals for SWIR detection and their integration up to the focal plane array. ACS Appl Mater Interfaces 11:33116–33123. https://doi.org/10.1021/acsami.9b09954
[Crossref]
75. Martinez B, Livache C, Notemgnou Mouafo LD, Goubet N, Keuleyan S, Cruguel H et al (2017) HgSe self-doped nanocrystals as a platform to investigate the effects of vanishing confinement. ACS Appl Mater Interfaces 9:36173–36180. https://doi.org/10.1021/acsami.7b10665
[Crossref]
76. Brown PR, Kim D, Lunt RR, Zhao N, Bawendi MG, Grossman JC et al (2014) Energy level modification in lead sulfide quantum dot thin films through ligand exchange. ACS Nano 8:5863–5872. https://doi.org/10.1021/nn500897c
[Crossref]
77. Martinez B, Plamont R, Gréboval C, Rastogi P, Prado Y, Qu J et al (2019) Azobenzenes as light-Activable carrier density switches in nanocrystals. J Phys Chem C 123:27257–27263. https://doi.org/10.1021/acs.jpcc.9b08597
[Crossref]
78. Martinez B, Livache C, Meriggio E, Xu XZ, Cruguel H, Lacaze E et al (2018) Polyoxometalate as control agent for the doping in HgSe self-doped nanocrystals. J Phys Chem C 122:26680–26685. https://doi.org/10.1021/acs.jpcc.8b07190
[Crossref]
79. Lhuillier E, Keuleyan S, Guyot-Sionnest P (2014) Corrigendum: optical properties of HgTe colloidal quantum dots (2012 *nanotechnology* 23 175705). Nanotechnology 25:189501. https://doi.org/10.1088/0957-4484/25/18/189501
[Crossref]
80. Livache C, Goubet N, Gréboval C, Martinez B, Ramade J, Qu J et al (2019) Effect of pressure on interband and intraband transition of mercury chalcogenide quantum dots. J Phys Chem C 123:13122–13130. https://doi.org/10.1021/acs.jpcc.9b01695
[Crossref]
81. Ramade J, Andriambariarijaona LM, Steinmetz V, Goubet N, Legrand L, Barisien T et al (2018) Exciton-phonon coupling in a $CsPbBr_3$ single nanocrystal. Appl Phys Lett 112:072104. https://doi.org/10.1063/1.5018413
[Crossref]
82. Olkhovets A, Hsu R-C, Lipovskii A, Wise FW (1998) Size-dependent temperature variation of the energy gap in lead-salt quantum dots. Phys Rev Lett 81:3539–3542. https://doi.org/10.1103/PhysRevLett.81.3539

[Crossref]
83. Wright NG, McMahon MI, Nelmes RJ, San-Miguel A (1993) Crystal structure of the cinnabar phase of HgTe. Phys Rev B 48:13111–13114. https://doi.org/10.1103/PhysRevB.48.13111 [Crossref]
84. San-Miguel A, Wright NG, McMahon MI, Nelmes RJ (1995) Pressure evolution of the cinnabar phase of HgTe. Phys Rev B 51:8731–8736. https://doi.org/10.1103/PhysRevB.51.8731 [Crossref]
85. Werner A, Hochheimer HD, Strössner K, Jayaraman A (1983) High-pressure x-ray diffraction studies on HgTe and HgS to 20 GPa. Phys Rev B 28:3330–3334. https://doi.org/10.1103/PhysRevB.28.3330 [Crossref]
86. Liu H, Keuleyan S, Guyot-Sionnest P (2012) *n*- and *p*-type HgTe quantum dot films. J Phys Chem C 116:1344–1349. https://doi.org/10.1021/jp2109169 [Crossref]
87. Qu J, Weis M, Izquiedro E, Mizrahi SG, Chu A, Dabard C et al (2021) Electroluminescence from nanocrystals above 2 μm. Nat Photonics 16:38–44. https://doi.org/10.1038/s41566-021-00902-y [Crossref]
88. Keuleyan S, Kohler J, Guyot-Sionnest P (2014) Photoluminescence of mid-infrared HgTe colloidal quantum dots. J Phys Chem C 118:2749–2753. https://doi.org/10.1021/jp409061g [Crossref]
89. Melnychuk C, Guyot-Sionnest P (2018) Slow auger relaxation in HgTe colloidal quantum dots. J Phys Chem Lett 9:2208–2211. https://doi.org/10.1021/acs.jpclett.8b00750 [Crossref]
90. Martinez B, Livache C, Goubet N, Jagtap A, Cruguel H, Ouerghi A et al (2018) Probing charge carrier dynamics to unveil the role of surface ligands in HgTe narrow band gap nanocrystals. J Phys Chem C 122:859–865. https://doi.org/10.1021/acs.jpcc.7b09972 [Crossref]
91. Livache C, Goubet N, Martinez B, Jagtap A, Qu J, Ithurria S et al (2018) Band edge dynamics and multiexciton generation in narrow band gap HgTe nanocrystals. ACS Appl Mater Interfaces 10:11880–11887. https://doi.org/10.1021/acsami.8b00153 [Crossref]
92. Qu J, Rastogi P, Gréboval C, Lagarde D, Chu A, Dabard C et al (2020) Electroluminescence from HgTe nanocrystals and its use for active imaging. Nano Lett 20:6185–6190. https://doi.org/10.1021/acs.nanolett.0c02557 [Crossref]
93. Melnychuk C, Guyot-Sionnest P (2019) Auger suppression in n-type HgSe colloidal quantum dots. ACS Nano 13:10512–10519. https://doi.org/10.1021/acsnano.9b04608 [Crossref]

94. Ruppert M, Bui H, Sagar LK, Geiregat P, Hens Z, Bester G et al (2021) Intraband dynamics of mid-infrared HgTe quantum dots. Nanoscale. https://doi.org/10.1039/D1NR07007J
95. Chen M, Yu H, Kershaw SV, Xu H, Gupta S, Hetsch F et al (2014) Fast, air-stable infrared photodetectors based on spray-deposited aqueous HgTe quantum dots. Adv Funct Mater 24:53–59. https://doi.org/10.1002/adfm.201301006
[Crossref]
96. Cryer ME, Fiedler H, Halpert JE (2018) Photo-electrosensitive memristor using oxygen doping in HgTe nanocrystal films. ACS Appl Mater Interfaces 10:18927–18934. https://doi.org/10.1021/acsami.8b05429
[Crossref]
97. Bera R, Kim G, Choi D, Kim J, Jeong KS (2021) Beyond the bandgap photoluminescence of colloidal semiconductor nanocrystals. J Phys Chem Lett 12:2562–2569. https://doi.org/10.1021/acs.jpclett.1c00142
[Crossref]
98. Sergeev AA, Pavlov DV, Kuchmizhak AA, Lapine MV, Yiu WK, Dong Y et al (2020) Tailoring spontaneous infrared emission of HgTe quantum dots with laser-printed plasmonic arrays. Light Sci Appl 9:16. https://doi.org/10.1038/s41377-020-0247-6
[Crossref]
99. Olk P, Buchler BC, Sandoghdar V, Gaponik N, Eychmüller A, Rogach AL (2004) Subwavelength emitters in the near-infrared based on mercury telluride nanocrystals. Appl Phys Lett 84:4732–4734. https://doi.org/10.1063/1.1759386
[Crossref]
100. Shopova SI, Farca G, Rosenberger AT, Wickramanayake WMS, Kotov NA (2004) Microsphere whispering-gallery-mode laser using HgTe quantum dots. Appl Phys Lett 85:6101–6103. https://doi.org/10.1063/1.1841459
[Crossref]
101. Geiregat P, Houtepen AJ, Sagar LK, Infante I, Zapata F, Grigel V et al (2018) Continuous-wave infrared optical gain and amplified spontaneous emission at ultralow threshold by colloidal HgTe quantum dots. Nat Mater 17:35–42. https://doi.org/10.1038/nmat5000
[Crossref]
102. Koktysh DS, Gaponik N, Reufer M, Crewett J, Scherf U, Eychmüller A et al (2004) Near-infrared electroluminescence from HgTe nanocrystals. ChemPhysChem 5:1435–1438. https://doi.org/10.1002/cphc.200400178
[Crossref]
103. O'Connor É, O'Riordan A, Doyle H, Moynihan S, Cuddihy A, Redmond G (2005) Near-infrared electroluminescent devices based on colloidal HgTe quantum dot arrays. Appl Phys Lett 86:201114. https://doi.org/10.1063/1.1928321
[Crossref]
104. Bossavit E, Qu J, Abadie C, Dabard C, Dang TH, Izquierdo E et al (2021) Optimized infrared LED and its use in an all-HgTe nanocrystal-based active imaging setup. Adv Opt Mater 2101755. https://doi.org/10.1002/adom.202101755

105. Pradhan S, Di Stasio F, Bi Y, Gupta S, Christodoulou S, Stavrinadis A et al (2019) High-efficiency colloidal quantum dot infrared light-emitting diodes via engineering at the supra-nanocrystalline level. Nat Nanotechnol 14:72–79. https://doi.org/10.1038/s41565-018-0312-y [Crossref]
106. Vasilopoulou M, Kim HP, Kim BS, Papadakis M, Ximim Gavim AE, Macedo AG et al (2020) Efficient colloidal quantum dot light-emitting diodes operating in the second near-infrared biological window. Nat Photonics 14:50–56. https://doi.org/10.1038/s41566-019-0526-z [Crossref]
107. Chuang C-HM, Brown PR, Bulović V, Bawendi MG (2014) Improved performance and stability in quantum dot solar cells through band alignment engineering. Nat Mater 13:796–801. https://doi.org/10.1038/nmat3984 [Crossref]
108. Rastogi P, Chu A, Dang TH, Prado Y, Gréboval C, Qu J et al (2021) Complex optical index of HgTe nanocrystal infrared thin films and its use for short wave infrared photodiode design. Adv Opt Mater 9:2002066. https://doi.org/10.1002/adom.202002066 [Crossref]
109. Szuszkiewicz W, Witowski AM, Grynberg M (1978) The dynamic dielectric function in HgSe and HgTe. Phys Status Solidi B 87:637–645. https://doi.org/10.1002/pssb.2220870229 [Crossref]
110. Secuk MN, Aycibin M, Erdinc B, Gulebaglan SE, Dogan EK, Akkus H (2014) Ab-initio calculations of structural, electronic, optical, dynamic and thermodynamic properties of HgTe and HgSe. Am J Condens Matter Phys 4:13–19
111. El-Nahass MM, Abd El-Salam F, Seyam MAM (2006) Optical and structural properties of flash evaporated HgTe thin films. J Mater Sci 41:3573–3580. https://doi.org/10.1007/s10853-005-5621-5 [Crossref]
112. Moritani A, Sekiya H, Taniguchi K, Hamaguchi C, Nakai J, Makabe R (1971) Optical constants of HgTe and HgSe. Jpn J Appl Phys 10:1410–1414. https://doi.org/10.1143/JJAP.10.1410 [Crossref]

OceanofPDF.com

© The Author(s), under exclusive license to Springer Nature Switzerland AG 2023
G. Korotcenkov (ed.), *Handbook of II-VI Semiconductor-Based Sensors and Radiation Detectors*
https://doi.org/10.1007/978-3-031-19531-0_7

7. Colloidal Nanoparticles of II-VI Semiconductor Compounds and Their Participation in Photosensitization of Metal Oxides

Roman B. Vasiliev[1] ✉, Artem S. Chizhov[1] and Marina N. Rumyantseva[1]
(1) Chemistry Department, Moscow State University, Moscow, Russia

✉ **Roman B. Vasiliev**
Email: romvas@inorg.chem.msu.ru

Keywords Cadmium selenide – Cadmium sulfide – Cadmium telluride – Charge transfer – Colloidal synthesis – Colloidal quantum dots – Hybrid nanoparticles – Light activation – Metal oxides – Nanocomposite – Nanocrystal heterostructures – Nanoparticles – Photoexcited charges – Seeded growth – Semiconductor heterojunction – Surface passivation – Successive ionic layer adsorption and reaction – Zinc selenide – Zinc sulfide – Zinc telluride

7.1 Introduction

Colloidal semiconductor crystalline nanoparticles (nanocrystals or quantum dots) have become in recent years an important class of materials with great potential for applications. Easy and efficient control of the electronic properties and adjustment of the spectral position of the absorption bands, extinction coefficients, etc. by simply changing the size of the nanoparticles is a great advantage. The colloidal method for the synthesis of such nanoparticles makes it possible to obtain a wide range of nanoparticles,

control their size and shape of particles, and minimize the polydispersity of particles. Semiconductor nanoparticles synthesized in colloidal systems and stabilized with surfactants (ligands) have become an important class of materials with a wide range of practical applications, including light-emitting devices and lasers, optoelectronic converters, photovoltaic devices, and microelectronic components [1–3]. Synthesis in colloidal systems in nonpolar organic solvents turned out to be effective; modification of this method made it possible to achieve a quantum yield of more than 99% for nanoparticles based on cadmium chalcogenides [4]. The most popular semiconductor material is binary compounds of the II-VI group, which have either already found application or are promising for use in solar energy, photocatalysis, photoconverters, light filters, light-emitting devices, etc. The fundamental characteristics of these compounds, namely, the direct-gap nature of the band structure, the large radius of the Bohr exciton, and the band gap corresponding to the visible spectral range make size effects pronounced in nanostructures based on them.

One of the important applications of colloidal semiconductor nanoparticles is the creation of photosensitive nanocomposites, the operation of which is based on the effect of spatial separation of photoexcited charges between nanoparticles, and the matrix. The use of nanocrystalline wide-gap oxides as porous matrices for creating nanocomposites has a number of advantages: wide-gap oxide transparency in the visible light range, high stability, ease of obtaining porous systems, and high specific surface area. The difference in the energy position of the electronic levels is accompanied by efficient charge transfer between the nanoparticles and the oxide matrix upon photoexcitation, which leads to the modulation of the oxide matrix conductivity due to the injected nonequilibrium charge carriers. Such systems find application in photodetectors, solar cells, photocatalysts, and light-activated gas sensors.

This review considers modern approaches to the colloidal method for the preparation of nanoparticles and nanostructures of II-VI semiconductor compounds, the electronic properties of II-VI nanoparticles, as well as methods for the preparation and optical and electronic properties of nanocomposites II-VI nanoparticles/wide-gap metal oxides.

7.2 Recent Approaches to the Colloidal Synthesis of Nanocrystals and Nanocrystal Heterostructures Based on II-VI Semiconductors

Modern methods for obtaining nanoparticles in colloidal systems follow the idea of the formation of colloids by the rapid reaction of two or more reagents. This approach has come to be known as the “hot injection” method, involving rapid reaction of reactants at high temperatures and using an organic medium to carry out the reaction. Prior to the advent of this approach, diffusion-controlled growth in silicate or borosilicate glass matrices was used for the synthesis of nanoparticles, presented in the works of Efros and Efros [5] and Ekimov and Onushchenko [6], which made it possible to observe the effect of quantum confinement. Growth in glass matrices is important for the commercial production of optical filters but does not provide a narrow size distribution of nanoparticles.

The hot injection method arose on the basis of the pioneering work of scientific groups led by Henglein and co-workers [7–10] and Brus and co-workers [11–13] on the synthesis of CdS nanoparticles in the medium of organic compounds of tributylphosphine and tributylphosphine oxide. The synthesis using these compounds as a solvent makes it possible to control the growth of nanoparticles at high temperatures of ~300 °C. Carrying out the synthesis at high temperatures in organic media significantly reduces the number of defects and increases the crystallinity of nanocrystals. Subsequently, the method was further modified for the synthesis of the entire series of cadmium chalcogenides in the works of Murray et al. [14]. The successful choice of the combination of precursors, stabilizers, and reaction medium presented in this work made it possible to reproducibly obtain high-quality nanoparticles with a narrow size distribution and stimulated explosive growth in the number of works on colloidal quantum dots.

Typical protocols for syntheses by the hot injection method, as a rule, include rapid injection of anionic and cationic precursors into a nonpolar solvent heated to high temperatures and containing a nanoparticle stabilizer [15]. Rapid injection and high temperatures lead to intense interaction of precursors, rapid achievement of high supersaturation, and subsequent rapid nucleation; therefore, the hot injection method is otherwise called the

“explosive nucleation” method; the occurring processes follow the La Mer diagram [16]: the first stage corresponds to the formation of a monomer; then when the critical supersaturation level is exceeded, the nucleation stage occurs; then, when the supersaturation drops below the threshold value, the growth stage occurs. The short duration of the second stage, nucleation (“explosive” nucleation) and its temporal separation from the growth stage, ensures a narrow particle size distribution (Fig. 7.1a). The main approaches to controlling the size distribution of nanoparticles are considered in [17]. During growth at a retained high supersaturation, a mechanism for reducing polydispersity is possible – “focusing” of sizes [18, 19]. At high monomer concentration, the critical size is small, which causes smaller particles to grow faster than larger ones, and as a result, the size distribution can be focused close to monodisperse. If the monomer concentration is below the critical threshold, small nanoparticles dissolve as larger ones grow, and the size distribution becomes defocused – this is Ostwald ripening regime (Fig. 7.1b). Obtaining almost monodisperse spherical particles can be achieved by stopping the reaction, while it is still in “focusing” regime with a high monomer concentration, or by adding additional portions of precursors, which restores a high monomer concentration.

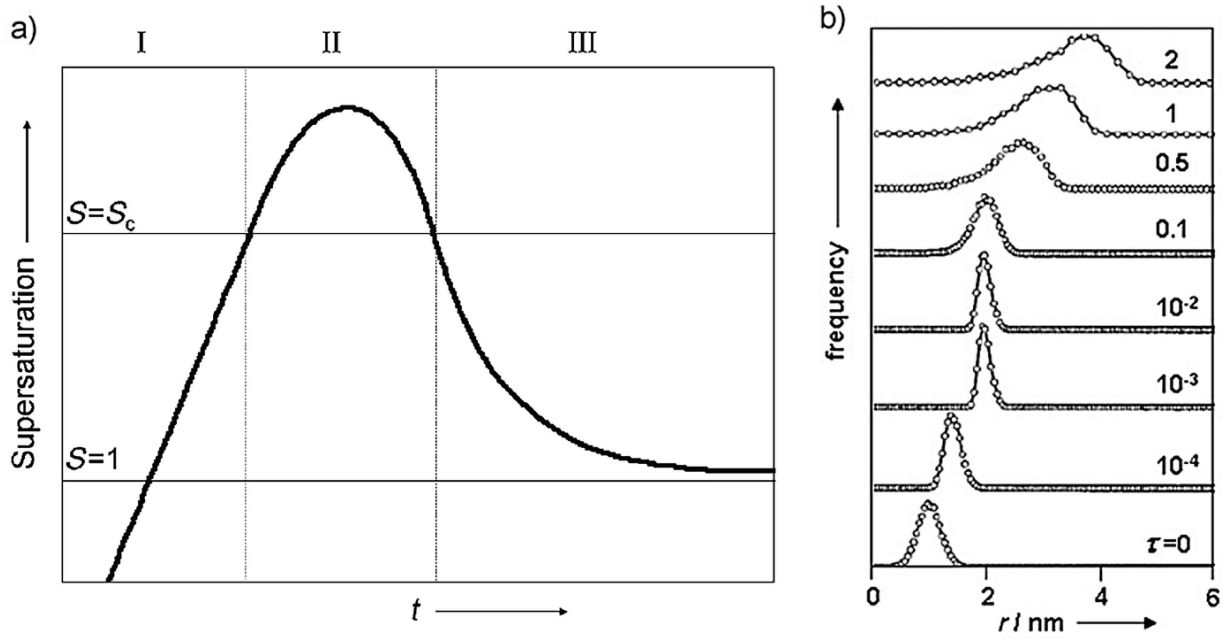

Fig. 7.1 (**a**) LaMer plot: Change of degree of supersaturation as a function of time t. (**b**) Time evolution of the size distribution of the ensemble of particles. (Reprinted with permission from Ref. [17]. Copyright 2007: Wiley)

For the colloidal synthesis of nanoparticles of semiconductor compounds of the AIIBVI type, alkyl derivatives of cadmium or zinc, oxides of these elements, and their organic salts are described as cationic precursors. CdO [20–28], $Cd(Ac)_2$ [29, 30], Me_2Cd [31–36], and others have been described as cadmium precursors. Phosphine chalcogenides [24–36] or trimethylsilylchalcogenides [14] act as anionic precursors of Group VI elements. Another convenient and highly effective variant of anionic chalcogen precursors is solutions of elemental chalcogens (sulfur or selenium) in octadecene [37, 38]. In the case of a solution of sulfur as a precursor, the mechanism of interaction with the cationic precursor proceeds through the formation of hydrogen sulfide; for selenium, the activity is associated with the formation of dialkyl selenide as an intermediate. In the case of a solution of elemental sulfur in octadecene, the threshold temperature for the start of interaction with cadmium salts is about 180 °C; to activate the interaction and lower the temperature to almost 100 °C, it was proposed to add primary amines [37]. Similarly, activation of the interaction of anionic precursors with zinc carboxylates or diethylzinc by primary amines in the preparation of ZnSe nanoparticles was shown in [39–42], which made it possible to obtain high-quality nanoparticles at temperatures of 300–320 °C; in the absence of amines, the reaction was inefficient. The use of a solution of elemental sulfur in aliphatic amines as an anionic precursor turned out to be very effective; for example, a solution of sulfur in oleylamine was proposed in [43] as an effective anionic precursor for the synthesis of CuS covellite nanoparticles. At the same time, elemental selenium has the worst solubility in aliphatic amines and can be activated only by adding strong reducing agents [44, 45].

The mechanisms of chemical reactions that occur during the interaction of cationic and anionic precursors based on metal carboxylates and phosphine derivatives during the formation of cadmium chalcogenide nanoparticles are considered in detail in [46, 47]. The proposed interaction scheme includes the formation of a transition state between cadmium carboxylate and trioctylphosphine chalcogenide [48–50]. This leads to the formation of a metal-chalcogen bond and the formation of a metal-chalcogen monomer, which transforms into nanoparticles. In turn, organic groups form trioctylphosphine carboxylate, which is transformed into carboxylic anhydride and trioctylphosphine oxide. A similar scheme is shown for the case of obtaining PbSe nanoparticles [51]. Another variant of

the interaction is the formation of metallic cadmium as an intermediate state as a result of the reduction of carboxylate, which is especially pronounced in the presence of secondary phosphines [52]. It is necessary to note the role of amines, which activate the interaction of metal carboxylates and the anionic precursor, which plays an important role in the synthesis of zinc chalcogenides [39–42]. Activation proceeds through the coordination of two amine molecules through a nitrogen atom and a metal atom in the carboxylate [53].

In addition to the hot injection method, non-injection methods have been proposed [54], which exclude the stage of fast injection and, as a rule, consist in heating a solution containing both anionic and cationic precursors. The emergence of such methods is associated with synthesis scaling, which is difficult for the hot injection method due to restrictions on the mixing time of the reagents. For non-injection methods, supersaturation control is achieved by increasing the temperature of the system at a given rate, which activates the chemical reactions of precursors, increasing the monomer concentration and leading to high supersaturation and rapid nucleation and then growth of nanoparticles (Fig. 7.2). After the first publication of the Y.C. Cao group [55], high-quality nanoparticles of CdS, CdSe, and CdTe [56–59], as well as ZnS, ZnSe, and ZnTe [60–62], were obtained by this method. Cadmium carboxylates are used as the cationic precursor, and solutions of elemental chalcogens in octadecene are used as the anionic precursor. The choice of the latter is due to the simplicity of the synthesis, which consists in adding chalcogen powder to a solution of a cationic precursor at the beginning of the synthesis and subsequent heating, the chalcogen being dissolved in octadecene as it is heated. Thiols are also used as an anionic precursor for the synthesis of sulfides [63, 64].

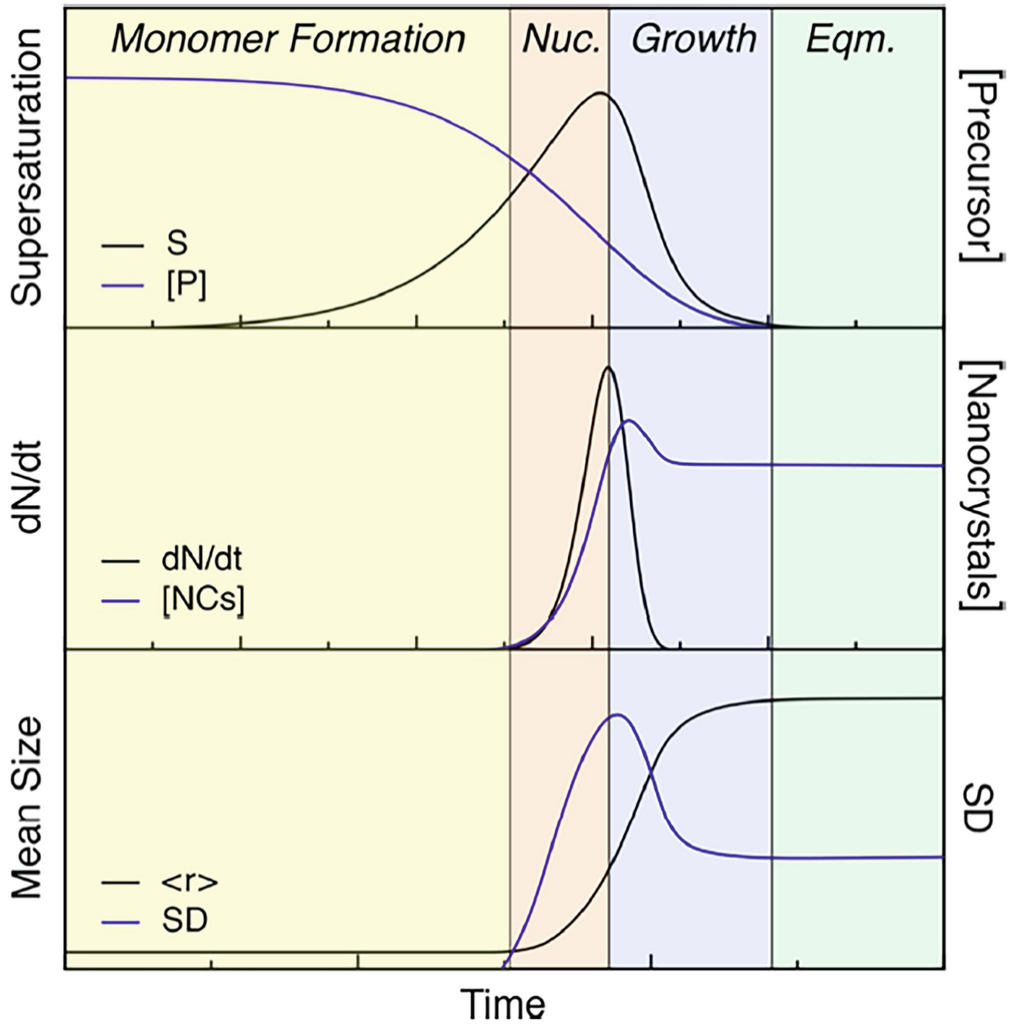

Fig. 7.2 Simulated evolution of the prominent reaction parameters: supersaturation S, precursor [P], and nanocrystal [NCs] concentration during the heating of a precursor solution during a typical heat-up synthesis. (Reprinted from Ref. [54]. Published 2015 by ACS according to Creative Commons public use license)

The approaches considered above lead to the growth of spherical nanoparticles, while changing the shape of a nanoparticle requires other growth regimes. The mechanism of oriented attachment can be mentioned [65]. Another option is to control the growth rate of faces with different energies. Compared to “equilibrium” nanoparticles with an almost “round” shape, nanoparticles with a highly anisotropic shape have a large surface area and, accordingly, a large energy, which makes them metastable high-energy forms. Thus, the growth of nanoparticles of complex morphology occurs in the kinetic growth regime, while equilibrium nanoparticles with a shape close to spherical are obtained in the limit of slow growth under the thermodynamic regime [18]. At a low growth rate, almost round

nanoparticles with a wide size distribution are formed. At higher growth rates, size focusing is observed. A further increase in the growth rate leads to the formation of metastable nanoparticles with different morphologies. At high growth rates in a kinetically controlled growth regime, high-energy faces grow faster than low-energy faces, causing the faceted crystal with slower-growing faces. Another important factor promoting the formation of highly anisotropic nanoparticles is specific ligands, which also change the facet growth rate as a result of specific adsorption [66]. As a rule, such ligands are alkylphosphonic acids, which promote the formation of rods and branched nanoparticles [67, 68]. With their use, a number of high-quality nanoparticles of cadmium chalcogenides with an anisotropic shape of nanorods and its derivatives have been obtained [69–72]. The effect is based on the change in the growth rate of facets, which is determined by the strength of the bond between ligands and surface atoms (ions) of the crystal lattice, which should be related to face affinity and selectivity [73, 74, 75] and the density of surface coverage with ligands.

A separate issue is the production of branched nanoparticles. Branched nanoparticles with four arms – tetrapods – are described for II-VI materials: CdS [76], CdSe [77–80], CdTe [27], ZnO [81], ZnS [82], and ZnSe [83]. An important parameter that determines the possibility of forming tetrapods is the polytype of this material and the difference in the energies of the modifications of wurtzite and zinc blende. For predominantly ionic and covalent materials, the energy difference between polytypes reaches 10 meV/atom. The formation of different polytypes during growth is difficult in this case. For partially ionic cadmium and zinc chalcogenides, the energies of wurtzite and zinc blende modifications are close to ~1 meV/atom. For cadmium chalcogenides, the coexistence and transformation of these crystalline modifications into each other becomes possible, which makes it easy to form tetrapods. To explain the structure of tetrapods (Fig. 7.3), the multiple twinning model [81] and the polytype model [27] have been proposed. Thus, strategies for the colloidal synthesis of tetrapods are based on the coexistence of zinc blende and wurtzite modifications for II-VI nanoparticles. While the formation of nanoparticle nuclei occurs in the zinc blende modification, under conditions of high supersaturation, tetrapod rays grow in the wurtzite modification. That is, the growth scheme is similar to the growth of nanorods, only the selection of conditions for the initial formation of nanoparticles in the zinc blende

modification is required, which, however, is a separate problem. The data described in the literature are reduced to the use of alkylphosphonic acids, which promote the growth of anisotropic rays in the wurtzite modification, although CdTe tetrapods were obtained using oleic acid [68, 84]. In addition to cadmium chalcogenide tetrapods, octapods [85] and hyperbranched nanoparticles [86] have also been synthesized. The detailed state of current research in the field of tetrapod-shaped nanocrystals obtained in colloidal systems is given in [87].

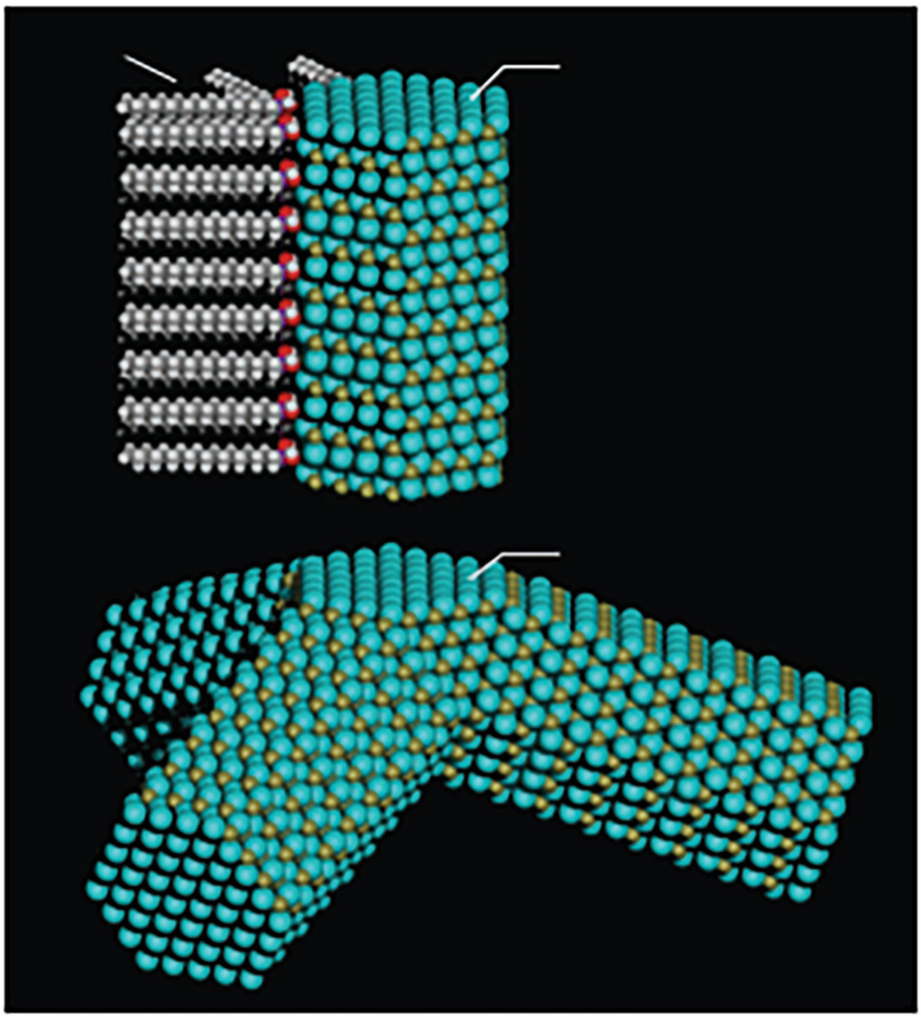

Fig. 7.3 Model of a CdTe tetrapod. The exploded view of one arm illustrates the identical nature of the (111) zinc blende (ZB) and (0001) wurtzite (WZ) facets of the nucleus and the arms, respectively (Cd atoms are yellow, Te atoms are blue). (Reprinted with permission from Ref. [27]. Copyright 2003: Springer)

The formation of nanoparticles consisting of domains of dissimilar materials is associated with the formation of an interface between materials that differ in chemical nature and crystal structure. Such nanoparticles

(nanocrystal heterostructures) have two or more semiconductor parts of different composition, epitaxially bonded along certain crystallographic planes. The growth of such nanoparticles requires the heterogeneous nucleation of a new phase, which differs from the homogeneous nucleation considered above. The synthesis strategy using heterogeneous nucleation is reduced to the growth of the second component on preformed nuclei of the first material, the so-called seeded growth [88]. Various types of nanocrystal heterostructures are considered in reviews [89–94]. In addition to obtaining nanocrystals of multicomponent composition, the method of “seeded growth” makes it possible to obtain anisotropic nanocrystal heterostructures with a given shape. For example, the formation of nanoparticles with a tetrapod morphology due to the growth of arms with a wurtzite structure on seed nanoparticles of cadmium chalcogenides with a zinc blende structure was demonstrated [95]. The authors of [26] showed that the rapid anisotropic growth of CdS arms on seed CdSe nanoparticles with a wurtzite structure leads to the formation of nanorods, while in the case of CdSe nanoparticles with a sphalerite structure, tetrapods are formed. Another example is growth of CdSe domains selectively at the end faces of CdTe tetrapod arms or at lateral faces (Fig. 7.4) depending on the concentration of oleic acid [96, 97]. From the point of view of optical properties, the difference between anisotropic and spherically symmetric nanoparticles is the presence of an internal field due to the spatial separation of charge carriers [98]. This leads to a significant dependence of the optical properties of such nanoparticles on external influences, for example, an electric field [99, 100] or environmental conditions, for example, on the permittivity of a solvent [101].

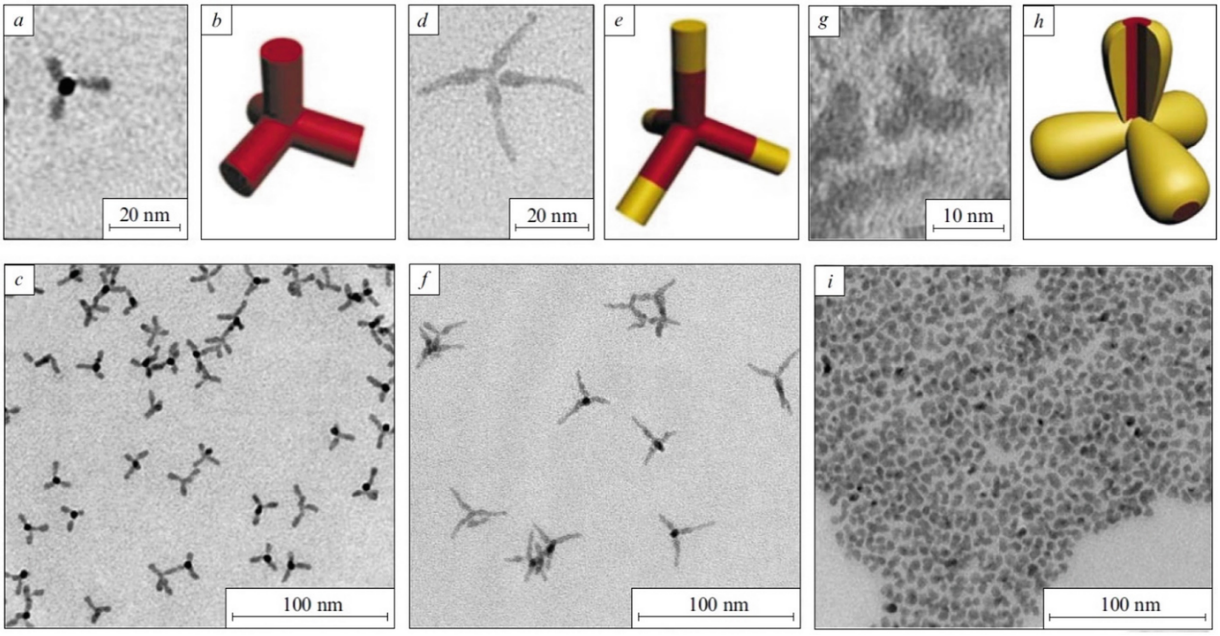

Fig. 7.4 Tetrapod-shaped CdTe nanoparticles (**a**–**c**); CdTe/CdSe nanoparticles based on CdTe tetrapods, obtained at [Cd]: [oleic acid] = 1:2 (**d**–**f**); and CdTe/CdSe nanoparticles based on tetrapods CdTe, obtained at [Cd]: [oleic acid] = 1:3 (**g**–**i**). (Reprinted with permission from Ref. [94]. Copyright 2011: Turpion-Moscow Ltd.)

Another variant of the strategy for the synthesis of multicomponent core/shell nanoparticles is the sequential adsorption and reaction of cationic and anionic layers (Successive Ionic Layer Adsorption and Reaction, SILAR) [102, 103]. This method involves the layer-by-layer formation of the shell, making it possible to achieve precision with an accuracy of one monolayer thickness of the formed layers.

7.3 Electronic Properties of Nanoparticles of II-VI Semiconductors

Quantum size effects in semiconductor nanoparticles were first demonstrated and explained in the early 1980s by Efros and Efros [5] and Ekimov and Onushchenko [6] using the example of nanoparticles in a glass matrix and by Rossetti et al. [13] for nanoparticles in sols. By that time, quantum size effects in semiconductors were known for quasi-two-dimensional structures (quantum wells) consisting of a thin epitaxial semiconductor film enclosed between layers of a wider-gap material [104]. In such quantum wells, the motion of charge carriers is limited by the boundaries of the film. Similarly, in quantum wires, the movement of

charge carriers is possible only in one direction [105]. In the case of quantum dots, the implementation of which is semiconductor nanoparticles, the motion of charge carriers is limited in all three dimensions [106]. This leads to the degeneration of the continuous energy spectrum into discrete atom-like levels. As the size of the nanoparticle and, accordingly, the number of atoms that form such levels increase, the energy gaps between the highest occupied ("HOMO") and the lowest unoccupied ("LUMO") levels decrease. Thus, the energy of the HOMO-LUMO transition, being an analogue of the effective band gap of a nanocrystal, depends on its size, decreasing with increasing size up to the band gap of a bulk semiconductor. As a conditional threshold size of a nanoparticle, at which size effects arise, it is customary to consider the Bohr radius of an exciton in a given material:

$$a_B = a_0 \frac{\varepsilon m_0}{\mu}, \tag{7.1}$$

where a_0 is the first Bohr radius of the hydrogen atom, ε is the permittivity of the semiconductor, m_0 is the rest mass of an electron, and μ is the reduced effective exciton mass. For a nanoparticle radius $R < a_B$, the exciton energy is greater than the energy of a free exciton in a bulk material [106].

Table 7.1 shows the Bohr radii for II-VI semiconductors. As can be seen, for most of the given substances, the Bohr radius of the exciton is in the range of nanoparticle sizes (up to 10 nm). In practice, this means that nanoparticles with a pronounced quantum size effect can be obtained for all these materials. For anisotropic nanoparticles, the size-dependent properties are affected by the smaller size of the nanoparticle. Thus, for CdSe nanorods, it was shown that, at a length greater than ~10–15 nm, length variation has little effect on the effective band gap E_g, while variation in the nanorod diameter can change E_g significantly [70].

Table 7.1 Crystal structure of II-VI semiconductors stable at room temperature, corresponding lattice parameters and exciton Bohr radii calculated from the data given in [107] and formula (1)

Semiconductor	**Structure**	***a* (Å)**	***c* (Å)**	**a_B (nm)**
ZnO	Wurtzite	3.2495	5.2069	2.6
ZnS	Wurtzite	3.8226	6.2605	2.5
ZnSe	Zinc blende	5.6692	–	4.0

Semiconductor	Structure	a (Å)	c (Å)	a_B (nm)
ZnTe	Zinc blende	6.009	–	5.0
CdS	Wurtzite	4.1367	6.7161	4.1
CdSe	Wurtzite	4.2999	7.0109	5.2
CdTe	Zinc blende	6.481	–	6.8

Source: Reprinted with permission from Ref. [94]. Copyright 2011: Turpion-Moscow Ltd.

As already noted, as the size of the nanoparticle decreases, the energy gaps between the size quantization levels of the electron and hole increase. Upon resonant excitation (e.g., absorption of a photon of suitable energy), the electron passes from the upper filled level (valence band) to the lower free level (conduction bands). The nomenclature of optical transitions is described in detail in [108, 109]. For example, in spherical CdSe nanoparticles, the observed optical transitions are lower in energy: $1S_{3/2}(h)-1S(e)$, $2S_{3/2}(h)-1S(e)$, $1S_{1/2}(h)-1S(e)$, $2S_{1/2}(h)-1S(e)$, and $1P_{3/2}(h)-1P(e)$ [109]. In some cases, the order of transitions may be different. The complication of the morphology or composition of nanoparticles entails a change in the symmetry of the electron–hole states and the order of the corresponding transitions [70]. Such electronic transitions between size-quantization levels are quite often called exciton in the literature, although the meaning is different from the concept of an exciton in a solid.

The lower-energy exciton maximum in the absorption spectra of nanoparticles, located near the absorption edge, is detected most clearly and can serve as a source of a large amount of information both on the electronic structure of nanoparticles and on the statistical characteristics of their ensemble [110]. The energy of the first exciton maximum (the effective band gap, E_g[QD]) is primarily determined by the material and size d of the nanoparticle and, without taking into account small electrostatic corrections, can be estimated as

$$E_g\,[QD] = E_g\,[bulk] + \frac{2\pi^2\hbar^2}{\mu d^2}, \tag{7.2}$$

where E_g[bulk] is the band gap of the bulk semiconductor and μ is the reduced effective mass $1/\mu = 1/m_e + 1/m_h$. Thus, the effective band gap

increases with decreasing nanoparticle size approximately as d^{-2}. The use of various materials and size variation potentially makes it possible to obtain nanoparticles with an effective band gap in the range from ~0.5 eV to 3.5–4 eV. This allows you to cover the wavelength range from IR to near UV.

An important optical characteristic is the absorption coefficient. In practice, the decrease in the intensity of radiation transmitted through the sample is the sum of absorption and scattering. Since the size of nanoparticles is much smaller than the wavelength of the incident radiation, scattering is much smaller than absorption, and scattering can be neglected [111]. The absorption of nanoparticles at the wavelength of the electronic transition is related to the oscillator strength f of the corresponding electronic transition and the number of structural units:

$$\varepsilon \sim \sigma \sim \mu V \tag{7.3}$$

where ε is the extinction coefficient of nanoparticles, σ is its effective absorption cross section, μ is the effective capture cross section of one semiconductor structural unit ($\mu \sim f$), and V is the volume of nanoparticles [110, 111]. The extinction coefficient at the first exciton maximum of cadmium chalcogenide nanoparticles depends on their size, which is primarily associated with an increase in the effective capture cross section with an increase in the nanoparticle size [112]. The relationship between the molar extinction coefficient of spherical nanoparticles and their size is described by a power law of the form $\varepsilon \sim D^n$, where D is the linear size of the nanoparticle.

A significant modification of the electronic and optical properties of nanocrystals of II-VI semiconductors can be carried out by creating nanoparticles of the “core-shell” type containing a semiconductor/semiconductor heterojunction. It is believed that a sharp transition from one semiconductor to another occurs at no more than a few lattice parameters, so that when considering semiconductor heterostructures, the band structure at the boundary changes abruptly in the first approximation. The following types of heterojunctions can be classified according to the sign and magnitude of the band gap [113]: (i) type I heterojunction is a female heterojunction formed by wide-gap and narrow-gap semiconductors, with the conduction and valence band gaps having different signs. In this case, it is energetically favorable for an

electron and a hole to be localized in one part of the heterostructure, i.e., in a narrow-gap semiconductor; (ii) type II heterojunction – a stepped heterojunction formed by semiconductors with a comparable band gap, and band gaps have the same sign. Energetically favorable is the spatial separation of charge carriers – an electron in one part of the heterostructure, a hole in another. The properties of nanoparticles with heterojunctions are considered in the review [94].

7.4 Photosensitive Properties of II-VI Semiconductors/Metal Oxides Nanocomposites

The creation of photosensitive nanocomposites based on the spatial separation of photoexcited charges between nanoparticles and a matrix consists in the immobilization of sensitizer particles on the surface of semiconductor oxides that satisfies the following conditions: (i) high absorption coefficient of visible light and (ii) the ability to transfer a photoexcited charge carrier into the oxide matrix, due to the mutual arrangement of the energy levels of the sensitizer and the matrix. A similar scenario is realized, in particular, when n-type semiconductor oxides are sensitized by quantum dot of II-VI semiconductors (Fig. 7.5).

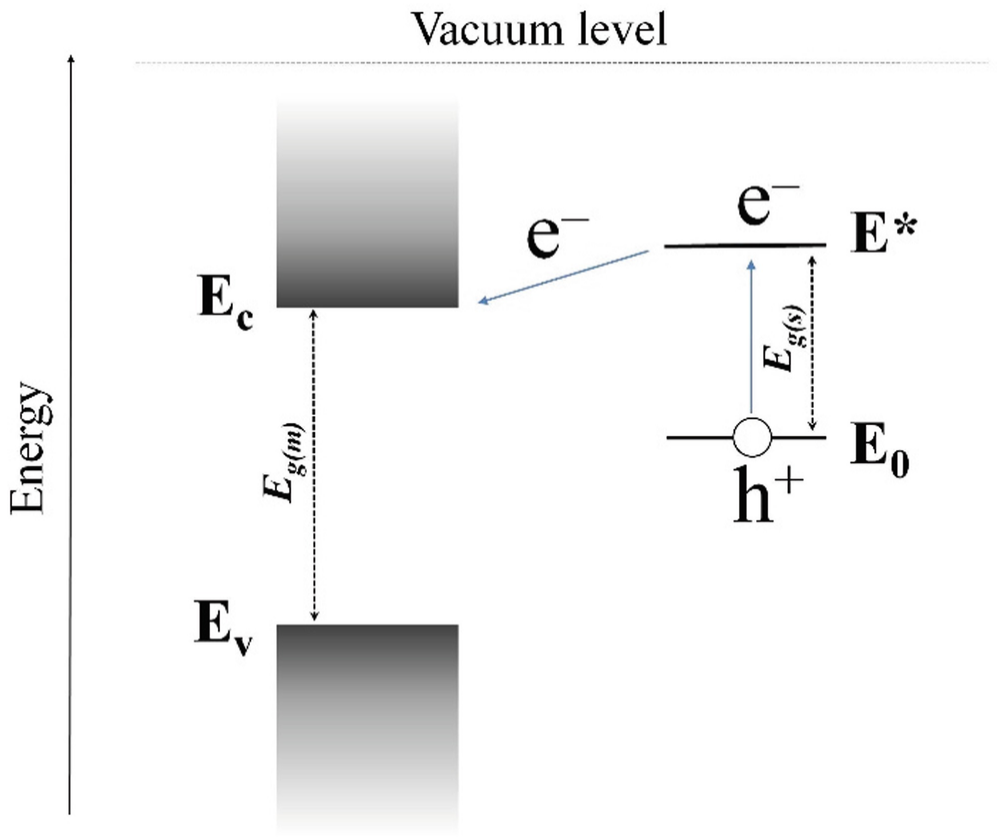

Fig. 7.5 Photoinduced electron transfer between a quantum dot and a wide-band gap metal oxide matrix. E_C and E_V – bottom of conduction band and top of valence band of metal oxide semiconductor, E_0 and E^* – lowest and highest energy level of quantum dot, respectively. Photoexcited electron transfers from quantum dot into metal oxide matrix

To obtain nanocomposites based on II-VI nanoparticles of semiconductors and metal oxides, two fundamentally different methods can be distinguished. According to the first method, the formation of semiconductor quantum dots occurs directly on the surface of a semiconductor oxide, in the second method, quantum dots are synthesized and isolated in a separate chemical process, then immobilized on the surface of metal oxide crystallites.

Let us consider the main techniques that make it possible to obtain quantum dots directly on the surface of a metal oxide matrix. In the first method, known as SILAR (successive ionic layer adsorption and reaction), a metal oxide substrate is immersed alternately in a solution containing a metal ion source and in a solution containing a chalcogenide ion source. Between immersions, the substrate is washed with distilled water to remove excess precursors from the surface and leave a monolayer of adsorbed ions. Thus, the reaction of formation of metal chalcogenide occurs in the layer of

adsorbed ions, and after several cycles of immersion, flat island particles several nanometers in size appear on the surface of the metal oxide [114, 115]. In another method, CBD (chemical bath deposition), the source of metal ions, and chalcogenide ions are in the same solution, in which a metal oxide substrate is also placed. During the isolation of metal chalcogenide in the form of a precipitate, part of it is deposited on the surface of the metal oxide substrate in the form of nanosized particles [116]. Their soluble salts are used as a source of metal ions, and Na_2S, $(NH_2)_2CS$, Na_2SeSO_3, and $(NH_2)_2CSe$ are used as a source of chalcogenide ions. Although the in situ sensitization of metal oxides by quantum dots can significantly simplify synthetic work due to the absence of the stages of isolation and purification of nanocrystals, the nanocrystals obtained in this process usually have a very wide size distribution, and therefore it is difficult to control their morphology and optical properties. The advantage of these methods is that the resulting quantum dots are in close contact with the metal oxide matrix, which provides conditions for efficient electron injection.

The sensitization of metal oxides by preliminarily synthesized quantum dots can be carried out by various methods. In the direct adsorption method, a metal oxide matrix is immersed in a quantum dot sol and kept for some time. In this case, quantum dots are adsorbed on the metal oxide surface [117]. On the metal surface, two processes occur in parallel – the formation of a submonolayer of quantum dots, the kinetics of which is described by the pseudo-first order Langmuir equation, and the formation of aggregates of quantum dots. Another way is to “attach” quantum dots to the metal oxide surface using bifunctional molecules (linkers), one functional group of which has a pronounced affinity for the quantum dot material, the other – to the metal oxide surface, for example, 2-mercaptopropionic acid. Treatment of the metal oxide surface with an MPA solution under certain conditions leads to the formation of a chemical bond between the carboxyl groups of the MPA molecules and the surface of the metal oxide. Subsequent treatment of this surface with quantum dot sol leads to binding of quantum dots to linker molecules by interaction with the HS-group. When using this method of sensitization, it is possible to achieve a stronger bond of quantum dots with the surface and a higher surface concentration compared to the method of directed adsorption.

The main mechanism of photoexcitation transfer from quantum dots to metal oxide is the injection of photoexcited charge carriers. When wide-gap

metal oxides such as SnO_2, ZnO, In_2O_3, WO_3, etc. are sensitized by II-VI semiconductor quantum dots, the main process is electron injection (Fig. 7.1). The injection of photoexcited holes occurs much less frequently and was observed, for example, in the case of NiO sensitization by CdSe quantum dots [118]. From the thermodynamic point of view, the possibility of injection of photoexcited charge carriers is determined by the change in the free energy of the system as a result of this process. At present, to describe the process of photoinduced electron transfer between a semiconductor oxide and a sensitizer, a model based on the Marcus theory [119] is proposed, which establishes a relationship between the electron injection rate constant and the total change in the Gibbs free energy in this process. It was shown in [120] that the total change in free energy upon injection of an electron from a quantum dot into the conduction band of a metal oxide is determined by three main contributions: the energy of formation of the charged state of the donor and acceptor $\Delta G_{\text{charging}}$; the energy of the electron-electron interaction, including the energy required for spatial separation electron-hole pair $\Delta G_{\text{coloumb}}$; and the difference in energy levels of the initial and final state of the electron $\Delta G_{\text{electronic}}$:

$$\Delta G = \Delta G_{\text{charging}} + \Delta G_{\text{coloumb}} + \Delta G_{\text{electronic}} \tag{7.4}$$

Only the $\Delta G_{\text{electronic}}$ contribution, which is the difference in energy between the level of the quantum dot from which the electron is transferred, and the bottom of the metal oxide conduction, can be experimentally determined. The contributions $\Delta G_{\text{coloumb}}$ and $\Delta G_{\text{electronic}}$ can be estimated theoretically. Taking into account a number of assumptions, it can be shown that, according to the model developed in [120], the growth of the electron injection rate constant k_{ET} occurs in proportion to the square root of $-\Delta G$:

$$k_{\text{ET}} = C(-\Delta G - E_s)^{1/2} \tag{7.5}$$

where C is a constant and E_s is the energy of system reorganization (a parameter following from the Marcus model). Experimental confirmation of the above dependence was also obtained in [120] when studying the electron injection rate by transient absorption spectroscopy on nanocrystalline SnO_2, ZnO, and TiO_2 sensitized by CdSe quantum dots of various sizes.

An alternative way to transfer the photoexcitation energy is the transfer by the resonance mechanism (Förster mechanism) [121], due to the dipole-dipole interaction between the donor and acceptor. This process occurs according to a nonradiative mechanism and has a specific dependence of the injection rate constant k_F on the distance r between the donor and acceptor (k_F decreases proportionally to r^{-6}). Experimentally, the transfer of photoexcitation energy by the resonance mechanism was observed in close-packed layers of CdSe quantum dots of various sizes [122], but there is no evidence of such a mechanism for the transfer of photoexcitation energy between quantum dots and an oxide matrix.

It should be taken into account that in the photoexcitation of a quantum dot, in addition to the injection of charge carriers, other processes are also possible – radiative recombination (luminescence) and nonradiative recombination, in which the photoexcitation energy is converted into thermal energy. Each of the ongoing processes can be characterized by the rate constant k, which is equal to the number of corresponding acts occurring in 1 second. Accordingly, the value $\tau = 1/k$ gives the average time for which one act occurs. The probability of an individual process can be expressed as the ratio of its rate constant to the sum of the rate constants of all ongoing processes. It has been established that electron injection occurs on time scales on the order of 10^{-12} s [120], while the lifetime of the excited state during radiative recombination is on the order of 10^{-9} s. Thus, electron injection is a more probable process that suppresses luminescence. The lifetime of the excited state with the resonant energy transfer mechanism is also about 10^{-9} s, which causes the suppression of this process by the electron injection process. On the other hand, nonradiative recombination in quantum dots has characteristic times of the order of 10^{-11} – 10^{-12} s; therefore, it is the main competing process with the process of electron injection. For effective injection of electrons, the channel of nonradiative recombination should be suppressed, for example, by surface passivation and “healing” of surface defects of quantum dots.

The photoconductive properties of nanocomposites based on nanocrystalline SnO_2 sensitized by CdSe quantum dots of various sizes were studied in [123]. CdSe quantum dots were synthesized by high-temperature colloidal synthesis using oleic acid as a steric stabilizer, and nanocomposites were synthesized by dropping a CdSe dispersion onto

preliminarily formed porous SnO_2 layers. The presence of adsorbed CdSe QDs incorporated into the porous SnO_2 matrix was proved by HAADF-STEM analysis of the SnO_2–CdSe sample (Fig. 7.6a). The smaller CdSe nanoparticles (marked with arrows) are seen directly attached to the larger crystalline SnO_2 grains. It is shown that this approach is successful for sensitizing the photoconductivity of wide-gap oxides in the visible region of the spectrum (Fig. 7.6b), while the spectral dependence of the photoconductivity of the obtained nanocomposites correlates with their optical absorption spectra as shown in Fig. 7.6b for SnO_2 sensitized with CdSe nanocrystals of 2.7, 3.8, and 4.7 nm sizes, which exhibit absorption in the visible spectral range with a sharp low-energy excitonic transition at wavelength of 525, 575, and 600 nm, respectively. Maxima of photoresponse curves for each SnO_2-CdSe composite matches well corresponding maxima in absorption spectrum of the CdSe nanocrystals that shows a causal relationship between the processes of light absorption and the generation of photoexcited charge carriers. The photoresponse of the sensitized SnO_2 thick films reaches more than two orders of magnitude under illumination with the wavelength of excitonic transition of the quantum dots. Long-term photoconductivity kinetics and photoresponse dependence on illumination intensity reveal power-law behavior inherent to disordered SnO_2 matrix nature. Photoconductivity of the samples rises with the coarsening of the granular structure of the SnO_2 matrix. At the saturation region photoresponse amplitude keeps stable under 10^4 pulses of illumination switching, demonstrating a remarkably high stability (Fig. 7.6c).

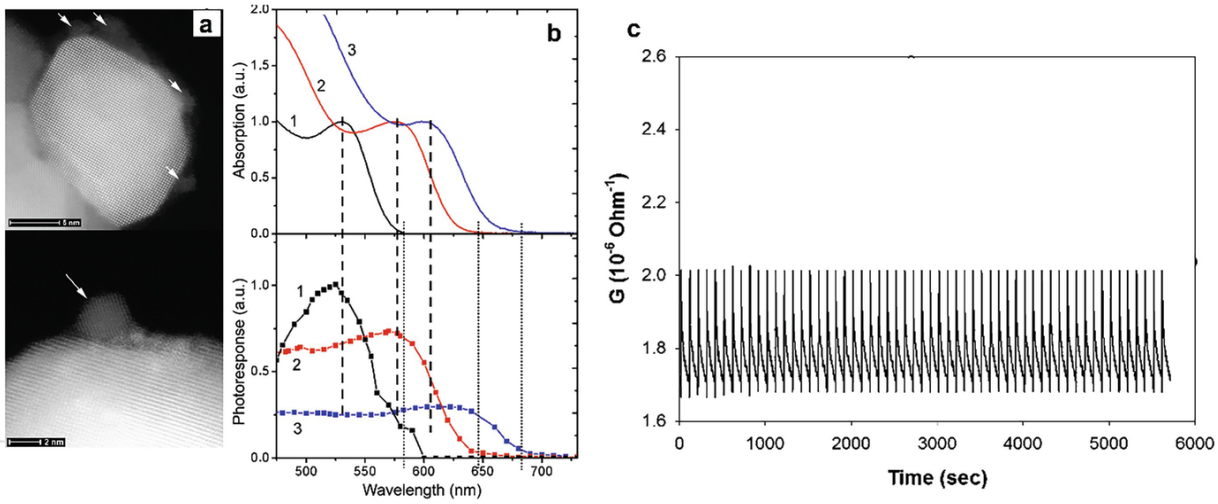

Fig. 7.6 (**a**) HAADF-STEM images of the SnO_2–CdSe sample. The smaller CdSe nanoparticles (marked with arrows) are seen attached to the larger SnO_2 grains. (**b**) Absorption spectra of CdSe QD with 2.7, 3.8, and 4.7 nm sizes (line 1, 2, and 3, respectively) and corresponding dependences of photoconductivity of SnO_2–CdSe samples. (**c**) Conductivity transient for the SnO_2–CdSe sample recorded under periodic illumination switching. Illumination pulses of 2 s duration pass with a frequency of 0.01 Hz. (Reprinted with permission from Ref. [123]. Copyright 2013: RSC)

Quantum dots of the “core-shell” type (CdSe core with a CdS shell of various thicknesses) also demonstrated the ability to sensitize the photoconductivity of the same matrix in the visible range, while the highest photoresponse was demonstrated by a sample sensitized by CdSe QDs with three CdS monolayers, which can be attributed to the effective passivation of traps [124]. Thus, the use of core-shell nanoparticles is an additional tool for controlling the processes of charge injection into a matrix due to control of charge localization in quantum dots and opens up possibilities for a number of applications [125].

7.5 Conclusions

An analysis of the literature shows that the creation of photosensitive nanocomposites based on oxide matrices sensitized with II-VI semiconductor nanoparticles is an actively developing area. Prospects for practical application are associated with the possibility of creating spectrally adjustable devices and the high stability of the resulting systems. These nanocomposites include a heterointerface between a wide-gap semiconductor like SnO_2, ZnO, In_2O_3, WO_3, etc. with a continuous density of states and II-VI nanoparticles having a system of discrete size levels.

Photoexcited electrons are injected into the oxide matrix, while holes remain trapped in the nanoparticle. Efficient charge separation between nanoparticles/nanostructures and a wide-gap oxide semiconductor are achieved by selecting the energy position of the top of the oxide conduction band and the lower energy level of the nanoparticles. This opens up wide possibilities for controlling the injection efficiency simply by changing the size of II-VI nanoparticles. Additional possibilities are related to the use of core-shell nanoparticles due to defect suppression and control of charge localization in nanoparticles. Design of photosensitive nanocomposites based on oxide matrices sensitized with II-VI semiconductor nanoparticles opens up new possibilities for practical applications such as photodetectors, gas sensors, etc.

Acknowledgments

This work was supported by Russian Science Foundation grant No. 22-13-00101.

References

1. Kovalenko MV, Manna L, Cabot A, Hens Z, Talapin DV, Kagan CR, Klimov VI, Rogach AL, Reiss P, Milliron DJ, Guyot-Sionnnest P, Konstantatos G, Parak WJ, Hyeon T, Korgel BA, Murray CB, Heiss W (2015) Prospects of nanoscience with nanocrystals. ACS Nano 9:1012–1057. https://doi.org/10.1021/nn506223h
[Crossref]
2. Talapin DV, Lee J-S, Kovalenko MV, Shevchenko EV (2010) Prospects of colloidal nanocrystals for electronic and optoelectronic applications. Chem Rev 110:389–458. https://doi.org/10.1021/cr900137k
[Crossref]
3. Brichkin SB, Razumov VF (2016) Colloidal quantum dots: synthesis, properties and applications. Russ Chem Rev 85(12):1297–1312. https://doi.org/10.1070/RCR4656
[ADS][Crossref]
4. Hanifi DA, Bronstein ND, Koscher BA, Nett Z, Swabeck JK, Takano K, Schwartzberg AM, Maserati L, Vandewal K, van de Burgt Y, Salleo A, Alivisatos AP (2019) Redefining near-unity luminescence in quantum dots with photothermal threshold quantum yield. Science 363:1199–1202. https://doi.org/10.1126/science.aat3803
[ADS][Crossref]
5. Efros AL, Efros Al.L. (1982) Interband absorption of light in a semiconductor sphere. Sov Phys Semicond 16:772–775

6. Ekimov AI, Onushchenko AA (1982) Quantum size effect in the optical spectra of semiconductor microcrystals. Sov Phys Semicond 16:775–778
7. Henglein A (1982) Photochemistry of colloidal cadmium sulfide. 2. Effects of adsorbed methyl viologen and of colloidal platinum. J Phys Chem 86:2291–2293 [Crossref]
8. Spanhel L, Haase M, Weller H, Henglein A (1987) Photochemistry of colloidal semiconductors. 20. Surface modification and stability of strong luminescing CdS particles. J Am Chem Soc 109:5649–5655. https://doi.org/10.1021/j100210a010 [Crossref]
9. Spanhel L, Weller H, Fojtik A, Henglein A (1987) Photochemistry of semiconductor colloids. 17. Strong luminescing CdS and CdS-Ag2S particles. Ber Bunsenges Phys Chem 91:88–94. https://doi.org/10.1002/bbpc.19870910204 [Crossref]
10. Haase M, Weller H, Henglein A (1988) Photochemistry of colloidal semiconductors. 26. Photoelectron emission from cadmium sulfide particles and related chemical effects. J Phys Chem 92:4706–4712. https://doi.org/10.1021/j100327a030 [Crossref]
11. Rossetti R, Brus LJ (1982) Electron-hole recombination emission as a probe of surface chemistry in aqueous cadmium sulfide colloids. Phys Chem 86:4470–4472. https://doi.org/10.1021/j100220a003 [Crossref]
12. Rossetti R, Ellison JL, Gibson JM, Brus LE (1984) Size effects in the excited electronic states of small colloidal CdS crystallites. J Chem Phys 80:4464−4469.м. https://doi.org/10.1063/1.447228 [Crossref]
13. Rossetti R, Nakahara S, Brus LE (1983) Quantum size effects in the redox potentials, resonance Raman spectra, and electronic spectra of CdS crystallites in aqueous solution. J Chem Phys 79:1086–1088. https://doi.org/10.1063/1.445834 [ADS][Crossref]
14. Murray CB, Norris DJ, Bawendi MG (1993) Synthesis and characterization of nearly monodisperse CdE (E = sulfur, selenium, tellurium) semiconductor nanocrystallites. J Am Chem Soc 115:8706–8715. https://doi.org/10.1021/ja00072a025 [Crossref]
15. Hühn J, Carrillo-Carrion C, Soliman MG, Pfeiffer C, Valdeperez D, Masood A, Chakraborty I, Zhu L, Gallego M, Yue Z, Carril M, Feliu N, Escudero A, Alkilany AM, Pelaz B, del Pino Orcid P, Parak WJ (2017) Selected standard protocols for the synthesis, phase transfer, and characterization of inorganic colloidal nanoparticles. Chem Mater 29:399–461. https://doi.org/10.1021/acs.chemmater.6b04738 [Crossref]
16. LaMer VK, Dinegar RH (1950) Theory, production and mechanism of formation of monodispersed hydrosols. J Am Chem Soc 72:4847–4854. https://doi.org/10.1021/ja01167a001

[Crossref]
17. Park J, Joo J, Kwon SG, Jang Y, Hyeon T (2007) Synthesis of monodisperse spherical nanocrystals. Angew Chem Int Ed Engl 46:4630–4660. https://doi.org/10.1002/anie.200603148 [Crossref]
18. Yin Y, Alivisatos AP (2005) Colloidal nanocrystal synthesis and the organic-inorganic interface. Nature 437:664–670. https://doi.org/10.1038/nature04165 [ADS][Crossref]
19. Peng X, Wickham J, Alivisatos AP (1998) Kinetics of II-VI and III-V colloidal semiconductor nanocrystal growth: “focusing” of size distributions. J Am Chem Soc 120:5343–5344. https://doi.org/10.1021/ja9805425 [Crossref]
20. Jones M, Kumar S, Lo SS, Scholes GD (2008) Exciton trapping and recombination in type II CdSe/CdTe nanorod heterostructures. J Phys Chem C 112:5423–5431. https://doi.org/10.1021/jp711009h [Crossref]
21. Dooley CJ, Dimitrov SD, Fiebig T (2008) Ultrafast electron transfer dynamics in CdSe/CdTe donor−acceptor nanorods. J Phys Chem C 112:12074–12076. https://doi.org/10.1021/jp804040r [Crossref]
22. Shieh F, Saunders AE, Korgel BA (2005) General shape control of colloidal CdS, CdSe, CdTe quantum rods and quantum rod heterostructures. J Phys Chem B 109:8538–8542. https://doi.org/10.1021/jp0509008 [Crossref]
23. Sun ZH, Oyanagi H, Uehara M, Nakamura H, Yamashita K, Fukano A, Maeda H (2009) Study on initial kinetics of CdSe nanocrystals by a combination of in situ X-ray absorption fine structure and microfluidic reactor. J Phys Chem C 113:18608–18613. https://doi.org/10.1021/jp907481q [Crossref]
24. Park J, Lee KH, Galloway JF, Searson PC (2008) Synthesis of cadmium selenide quantum dots from a non-coordinating solvent: growth kinetics and particle size distribution. J Phys Chem C 112:17849–17854. https://doi.org/10.1021/jp803746b [Crossref]
25. Crouch DJ, O’Brien P, Malik MA, Skabara PJ, Wright SP (2003) A one-step synthesis of cadmium selenide quantum dots from a novel single source precursor. Chem Commun 12:1454–1455. https://doi.org/10.1039/B301096A [Crossref]
26. Milliron DJ, Hughes SM, Cui Y, Manna L, Li J, Wang L-W, Alivisatos AP (2004) Colloidal nanocrystal heterostructures with linear and branched topology. Nature 430:190–195. https://doi.org/10.1038/nature02695 [ADS][Crossref]
27. Manna L, Milliron DJ, Meisel A, Scher EC, Alivisatos AP (2003) Controlled growth of tetrapod-branched inorganic nanocrystals. Nat Mater 2:382–385. https://doi.org/10.1038/

nmat902
[ADS][Crossref]
28. Talapin DV, Nelson JH, Shevchenko EV, Aloni S, Sadtler B, Alivisatos AP (2007) Seeded growth of highly luminescent CdSe/CdS nanoheterostructures with rod and tetrapod morphologies. Nano Lett 7:2951–2959. https://doi.org/10.1021/nl072003g
[ADS][Crossref]
29. Vasiliev RB, Dorofeev SG, Dirin DN, Belov DA, Kuznetsova TA (2004) Synthesis and optical properties of PbSe and CdSe colloidal quantum dots capped with oleic acid. Mendeleev Commun 14:169–171. https://doi.org/10.1070/MC2004v014n04ABEH001970
[Crossref]
30. Qu LH, Peng ZA, Peng XG (2001) Alternative routes toward high quality CdSe nanocrystals. Nano Lett 1:333–337. https://doi.org/10.1021/nl0155532
[ADS][Crossref]
31. Talapin DV, Koeppe R, Gotzinger S, Kornowski A, Lupton JM, Rogach AL, Benson O, Feldman J, Weller H (2003) Highly emissive colloidal CdSe/CdS heterostructures of mixed dimensionality. Nano Lett 3:1677–1681. https://doi.org/10.1021/nl034815s
[ADS][Crossref]
32. Peng ZA, Peng X (2001) Formation of high-quality CdTe, CdSe, and CdS nanocrystals using CdO as precursor. J Am Chem Soc 123:183–184. https://doi.org/10.1021/ja003633m
[Crossref]
33. Manna L, Scher EC, Alivisatos AP (2000) Synthesis of soluble and processable rod-, arrow-, teardrop-, and tetrapod-shaped CdSe nanocrystals. J Am Chem Soc 122:12700–12706. https://doi.org/10.1021/ja003055+
[Crossref]
34. Talapin DV, Haubold S, Rogach AL, Kornowski A, Haase M, Weller H (2001) A novel organometallic synthesis of highly luminescent CdTe nanocrystals. J Phys Chem B 105:2260–2263. https://doi.org/10.1021/jp003177o
[Crossref]
35. Manna L, Scher EC, Li L-S, Alivisatos AP (2002) Epitaxial growth and photochemical annealing of graded CdS/ZnS shells on colloidal CdSe nanorods. J Am Chem Soc 124:7136–7145. https://doi.org/10.1021/ja025946i
[Crossref]
36. Brennan JG, Siegrist T, Carroll PJ, Stuczynski SM, Reynders P, Brus LE, Steigerwald ML (1990) Bulk and nanostructure group II-VI compounds from molecular organometallic precursors. Chem Mater 2:403–409. https://doi.org/10.1021/cm00010a017
[Crossref]
37. Li Z, Ji Y, Xie R, Grisham SY, Peng X (2011) Correlation of CdS nanocrystal formation with elemental sulfur activation and its implication in synthetic development. J Am Chem Soc 133:17248–17256. https://doi.org/10.1021/ja204538f
[Crossref]

38. Bullen C, van Embden J, Jasieniak J, Cosgriff JE, Mulder RJ, Rizzardo E, Gu M, Raston CL (2010) High activity phosphine-free selenium precursor solution for semiconductor nanocrystal growth. Chem Mater 22:4135–4143. https://doi.org/10.1021/cm903813r
[Crossref]
39. Li LS, Pradhan N, Wang Y, Peng X (2004) High quality ZnSe and ZnS nanocrystals formed by activating zinc carboxylate precursors. Nano Lett 4:2261–2264. https://doi.org/10.1021/nl048650e
[ADS][Crossref]
40. Pradhan N, Peng X (2007) Efficient and color-tunable Mn-doped ZnSe nanocrystal emitters: control of optical performance via greener synthetic chemistry. J Am Chem Soc 129:3339–3347. https://doi.org/10.1021/ja068360v
[Crossref]
41. Pradhan N, Goorskey D, Thessing J, Peng X (2005) An alternative of CdSe nanocrystal emitters: pure and tunable impurity emissions in ZnSe nanocrystals. J Am Chem Soc 127:17586–17587. https://doi.org/10.1021/ja055557z
[Crossref]
42. Hines MA, Guyot-Sionnest P (1998) Bright UV-blue luminescent colloidal ZnSe nanocrystals. J Phys Chem B 102:3655–3657. https://doi.org/10.1021/jp9810217
[Crossref]
43. Xie Y, Carbone L, Nobile C, Grillo V, D'Agostino S, Della SF, Giannini C, Altamura D, Oelsner C, Kryschi C, Cozzoli PD (2013) Metallic-like stoichiometric copper sulfide nanocrystals: phase- and shape-selective synthesis, near-infrared surface plasmon resonance properties, and their modeling. ACS Nano 7:7352–7369. https://doi.org/10.1021/nn403035s
[Crossref]
44. Wei Y, Yang J, Lin AWH, Ying JY (2010) Highly reactive se precursor for the phosphine-free synthesis of metal selenide nanocrystals. Chem Mater 22:5672–5677. https://doi.org/10.1021/cm101308f
[Crossref]
45. Liu Y, Yao D, Shen L, Zhang H, Zhang X, Yang B (2012) Alkylthiol-enabled Se powder dissolution in oleylamine at room temperature for the phosphine-free synthesis of copper-based quaternary selenide nanocrystals. J Am Chem Soc 134:7207–7210. https://doi.org/10.1021/ja300064t
[Crossref]
46. Sowers KL, Swartz B, Krauss TD (2013) Chemical mechanisms of semiconductor nanocrystal synthesis. Chem Mater 25:1351–1362. https://doi.org/10.1021/cm400005c
[Crossref]
47. García-Rodríguez R, Hendricks MP, Cossairt BM, Liu H, Owen JS (2013) Conversion reactions of cadmium chalcogenide nanocrystal precursors. Chem Mater 25:1233–1249. https://doi.org/10.1021/cm3035642
[Crossref]

48. Liu HT, Owen JS, Alivisatos AP (2007) Mechanistic study of precursor evolution in colloidal group II−VI semiconductor nanocrystal synthesis. J Am Chem Soc 129:305–312. https://doi.org/10.1021/ja0656696
[Crossref]
49. Owen JS, Park J, Trudeau P-E, Alivisatos AP (2008) Reaction chemistry and ligand exchange at cadmium−selenide nanocrystal surfaces. J Am Chem Soc 130:12279–12281. https://doi.org/10.1021/ja804414f
[Crossref]
50. Owen JS, Chan EM, Liu H, Alivisatos AP (2010) Precursor conversion kinetics and the nucleation of cadmium selenide nanocrystals. J Am Chem Soc 132:18206–18213. https://doi.org/10.1021/ja106777j
[Crossref]
51. Steckel JS, Yen BKH, Oertel DC, Bawendi MG (2006) On the mechanism of lead chalcogenide nanocrystal formation. J Am Chem Soc 128:13032–13033. https://doi.org/10.1021/ja062626g
[Crossref]
52. Evans CM, Evans ME, Krauss TD (2010) Mysteries of TOPSe revealed: insights into quantum dot nucleation. J Am Chem Soc 132:10973–10975. https://doi.org/10.1021/ja103805s
[Crossref]
53. Guo YJ, Marchuk K, Sampat S, Abraham R, Fang N, Malko AV, Vela J (2012) Unique challenges accompany thick-shell CdSe/nCdS (n > 10) nanocrystal synthesis. J Phys Chem C 116:2791–2800. https://doi.org/10.1021/jp210949v
[Crossref]
54. van Embden J, Chesman ASR, Jasieniak JJ (2015) The heat-up synthesis of colloidal nanocrystals. Chem Mater 27:2246–2285. https://doi.org/10.1021/cm5028964
[Crossref]
55. Yang YA, Wu H, Williams KR, Cao YC (2005) Synthesis of CdSe and CdTe nanocrystals without precursor injection. Angew Chem Int Ed 44:6712–6715. https://doi.org/10.1002/anie.200502279
[Crossref]
56. Ouyang J, Vincent M, Kingston D, Descours P, Boivineau T, Zaman MB, Wu X, Yu K (2009) Noninjection, one-pot synthesis of photoluminescent colloidal homogeneously alloyed CdSeS quantum dots. J Phys Chem C 113:5193–5200. https://doi.org/10.1021/jp8110138
[Crossref]
57. Jia J, Tian J, Mi W, Tian W, Liu X, Dai J, Wang X (2013) Growth kinetics of CdSe nanocrystals synthesized in liquid paraffin via one-pot method. J Nanopart Res 15:1724. https://doi.org/10.1007/s11051-013-1724-0
[Crossref]
58. Park E, Ryu J, Choi Y, Hwang K-J, Song R (2013) Photochemical properties and shape evolution of CdSe QDs in a non-injection reaction. Nanotechnology 24:145601. https://doi.org/10.1088/0957-4484/24/14/145601
[ADS][Crossref]

59. Zhu C-Q, Wang P, Wang X, Li Y (2008) Facile phosphine-free synthesis of CdSe/ZnS Core/Shell nanocrystals without precursor injection. Nanoscale Res Lett 3:213. https://doi.org/10.1007/s11671-008-9139-z
[ADS][Crossref]

60. Zhuang Z, Lu X, Peng Q, Li Y (2011) A facile “dispersion–decomposition” route to metal sulfide nanocrystals. Chem Eur J 17:10445–10452. https://doi.org/10.1002/chem.201101145
[Crossref]

61. Liu Y, Tang Y, Ning Y, Li M, Zhang H, Yanga B (2010) “One-pot” synthesis and shape control of ZnSe semiconductor nanocrystals in liquid paraffin. J Mater Chem 20:4451–4458. https://doi.org/10.1039/C0JM00115E
[Crossref]

62. Zhang J, Sun K, Kumbhar A, Fang J (2008) Shape-control of ZnTe nanocrystal growth in organic solution. J Phys Chem C 112:5454–5458. https://doi.org/10.1021/jp711778u
[Crossref]

63. Zhong H, Zhou Y, Ye M, He Y, Ye J, He C, Yang C, Li Y (2008) Controlled synthesis and optical properties of colloidal ternary chalcogenide $CuInS_2$ nanocrystals. Chem Mater 20:6434–6443. https://doi.org/10.1021/cm8006827
[Crossref]

64. Liao H-C, Jao M-H, Shyue J-J, Chenc Y-F, Su W-F (2013) Facile synthesis of wurtzite copper–zinc–tin sulfide nanocrystals from plasmonic djurleite nuclei. J Mater Chem A 1:337–341. https://doi.org/10.1039/C2TA00151A
[Crossref]

65. Ivanov VK, Fedorov PP, Baranchikov AE, Osiko VV (2014) Oriented attachment of particles: 100 years of investigations of non-classical crystal growth Russ. Chem Rev 83(12):1204–1222. https://doi.org/10.1070/RCR4453
[Crossref]

66. Choi CL, Alivisatos AP (2010) From artificial atoms to nanocrystal molecules: preparation and properties of more complex nanostructures. Annu Rev Phys Chem 61:369–389. https://doi.org/10.1146/annurev.physchem.012809.103311
[Crossref]

67. Carbone L, Kudera S, Carlino E, Parak WJ, Giannini C, Cingolani R, Manna L (2005) Multiple wurtzite twinning in CdTe nanocrystals indicued by methylphosphonic acid. J Am Chem Soc 128:748–755. https://doi.org/10.1021/ja054893c
[Crossref]

68. Yu WW, Wang YA, Peng X (2003) Formation and stability of size-, shape-, and structure-controlled CdTe nanocrystals: ligand effects on monomers and nanocrystals. Chem Mater 15:4300–4308. https://doi.org/10.1021/cm034729t
[Crossref]

69. Li L, Hu J, Yang W, Alivisatos AP (2001) Band gap variation of size- and shape-controlled colloidal CdSe quantum rods. Nano Lett 1:349–351. https://doi.org/10.1021/nl015559r

[ADS][Crossref]

70. Katz D, Wizansky T, Millo O, Rothenberg E, Mokari T, Banin U (2002) Size-dependent tunneling and optical spectroscopy of CdSe quantum rods. Phys Rev Lett 89:086801. https://doi.org/10.1103/PhysRevLett.89.086801
[ADS][Crossref]

71. Li H, Kanaras AG, Manna L (2013) Colloidal branched semiconductor nanocrystals: state of the art and perspectives. Acc Chem Res 46(7):1387–1396. https://doi.org/10.1021/ar3002409
[Crossref]

72. Enders F, Sutter S, Fischli D, Köser R, Monter S, Cardinal S, Boldt K (2020) Regioselective growth mechanism of single semiconductor tips on CdS nanorods. Chem Mater 32(24):10566–10574. https://doi.org/10.1021/acs.chemmater.0c03636
[Crossref]

73. Rempel JY, Trout BL, Bawendi MG, Jensen KF (2006) Density functional theory study of ligand binding on CdSe (0001), (000-1), and (1120) single crystal relaxed and reconstructed surfaces: implications for nanocrystalline growth. J Phys Chem B 110:18007–18016. https://doi.org/10.1021/jp064051f
[Crossref]

74. Puzder A, Williamson AJ, Zaitseva N, Galli G, Manna L, Alivisatos AP (2004) The effect of organic ligand binding on the growth of CdSe nanoparticles probed by ab initio calculations. Nano Lett 4:2361–2365. https://doi.org/10.1021/nl0485861
[ADS][Crossref]

75. Rempel JY, Trout BL, Bawendi MG, Jensen KF (2005) Properties of the CdSe(0001), (0001), and (1120) single crystal surfaces: relaxation, reconstruction, and adatom and admolecule adsorption. J Phys Chem B 109:19320–19328. https://doi.org/10.1021/jp053560z
[Crossref]

76. Peng ZA, Peng X (2001) Mechanisms of the shape evolution of CdSe nanocrystals. J Am Chem Soc 123:1389–1395. https://doi.org/10.1021/ja0027766
[Crossref]

77. Peng ZA, Peng X (2002) Nearly monodisperse and shape-controlled CdSe nanocrystals via alternative routes: nucleation and growth. J Am Chem Soc 124:3343–3353. https://doi.org/10.1021/ja0173167
[Crossref]

78. Jun Y-W, Lee S-M, Kang N-J, Cheon J (2001) Controlled synthesis of multi-armed CdS nanorod architectures using monosurfactant system. J Am Chem Soc 123:5150–5151. https://doi.org/10.1021/ja0157595
[Crossref]

79. Pang Q, Zhao LJ, Cai Y, Nguyen DP, Regnault N, Wang N, Yang SH, Ge WK, Ferreira R, Bastard G, Wang JN (2005) CdSe nano-tetrapods: controllable synthesis, structure analysis, and electronic and optical properties. Chem Mater 17:5263–5267. https://doi.org/10.1021/cm050774k
[Crossref]

80. Asokan S, Krueger KM, Colvin VL, Wong MS (2007) Shape controlled synthesis of CdSe tetrapods using cationic surfactant ligands. Small 3:1164–1169. https://doi.org/10.1002/smll.200700120 [Crossref]
81. Nishio K, Isshiki T, Kitano M, Shiojiri M (1997) Structure and growth mechanism of tetrapod-like ZnO particles. Philos Mag A 76:889–904. https://doi.org/10.1080/01418619708214216 [ADS][Crossref]
82. Zhu Y-C, Yo B, Xue D-F, Golberg D (2003) Nanocable aligned ZnS tetrapod nanocrystals. J Am Chem Soc 125:16196–16197. https://doi.org/10.1021/ja037965d [Crossref]
83. Hu J, Yo B, Golberg D (2005) Sn-catalyzed thermal evaporation synthesis of tetrapod-branched ZnSe nanorod architectures. Small 1:95–99. https://doi.org/10.1002/smll.200400013 [Crossref]
84. Vasiliev RB, Dirin DN, Gaskov AM (2009) Temperature effect on the growth of colloidal CdTe nanotetrapods. Mendeleev Commun 19:126–127. https://doi.org/10.1016/j.mencom.2009.05.003 [Crossref]
85. Miszta K, Dorfs D, Genovese A, Kim MR, Manna L (2011) Cation exchange reactions in colloidal branched nanocrystals. ACS Nano 5:7176–7183. https://doi.org/10.1021/nn201988w [Crossref]
86. Kanaras AG, Sonnichsen C, Liu H, Alivisatos AP (2005) Controlled synthesis of hyperbranched inorganic nanocrystals with rich three-dimensional structures. Nano Lett 5:2164–2167. https://doi.org/10.1021/nl0518728 [ADS][Crossref]
87. Mishra N, Vasavi Dutt VG, Arciniegas MP (2019) Recent progress on metal chalcogenide semiconductor tetrapod-shaped colloidal nanocrystals and their applications in optoelectronics. Chem Mater 31:9216–9242. https://doi.org/10.1021/acs.chemmater.8b05363 [Crossref]
88. Carbone L, Cozzoli PD (2010) Colloidal heterostructured nanocrystals: synthesis and growth mechanisms. Nano Today 5:449–493. https://doi.org/10.1016/j.nantod.2010.08.006 [Crossref]
89. Kundu P, Anumol EA, Nethravathi C, Ravishankar N (2011) Existing and emerging strategies for the synthesis of nanoscale heterostructures. Phys Chem Chem Phys 13:19256–19269. https://doi.org/10.1039/C1CP22343G [Crossref]
90. Costi R, Saunders AE, Banin U (2010) Colloidal hybrid nanostructures: a new type of functional materials. Angew Chem Int Ed 49:4878–4897. https://doi.org/10.1002/anie.200906010 [Crossref]

91. Schartl W (2010) Current directions in core–shell nanoparticle design. Nanoscale 2:829–843. https://doi.org/10.1039/C0NR00028K [ADS][Crossref]
92. Reiss P, Protiere M, Li L (2009) Core/shell semiconductor nanocrystals. Small 5:154–168. https://doi.org/10.1002/smll.200800841 [Crossref]
93. Donega CM (2011) Synthesis and properties of colloidal heteronanocrystals. Chem Soc Rev 40:1512–1546. https://doi.org/10.1039/C0CS00055H [Crossref]
94. Vasiliev RB, Dirin DN, Gaskov AM (2011) Semiconductor nanoparticles with spatial separation of charge carriers: synthesis and optical properties. Russ Chem Rev 80(12):1190–1210. https://doi.org/10.1070/RC2011v080n12ABEH004240 [Crossref]
95. Fiore A, Mastria R, Lupo MG, Lanzani G, Giannini C, Carlino E, Morello G, De Giorgi M, Li Y, Cingolani R, Manna L (2009) Tetrapod-shaped colloidal nanocrystals of II-VI semiconductors prepared by seeded growth. J Am Chem Soc 131:2274–2282. https://doi.org/10.1021/ja807874e [Crossref]
96. Vasiliev RB, Dirin DN, Sokolikova MS, Roddatis VV, Vasiliev AL, Vitukhnovsky AG, Gaskov AM (2011) Facet-selective growth and optical properties of CdTe/CdSe tetrapod-shaped nanocrystal heterostructures. J Mater Res 26:1621–1626. https://doi.org/10.1557/jmr.2011.207 [ADS][Crossref]
97. Vasiliev RB, Dirin DN, Sokolikova MS, Dorofeev SG, Vitukhnovsky AG, Gaskov AM (2009) Growth of near-IR luminescent colloidal CdTe/CdS nanoheterostructures based on CdTe tetrapods. Mendeleev Commun 19:128–130. https://doi.org/10.1016/j.mencom.2009.05.004 [Crossref]
98. Morello G, Sala FD, Carbone L, Manna L, Maruccio G, Cingolani R, De Giorgi M (2008) Intrinsic optical nonlinearity in colloidal seeded grown CdSe/CdS nanostructures: photoinduced screening of the internal electric field. Phys Rev B 78:195313. https://doi.org/10.1103/PhysRevB.78.195313 [ADS][Crossref]
99. Kraus RM, Lagoudakis PG, Rogach AL, Talapin DV, Weller H, Lupton JM, Feldmann J (2007) Room-temperature exciton storage in elongated semiconductor nanocrystals. Phys Rev Lett 98:017401. https://doi.org/10.1103/PhysRevLett.98.017401 [ADS][Crossref]
100. Müller J, Lupton JM, Lagoudakis PG, Schindler F, Koeppe R, Rogach AL, Feldmann J, Talapin DV, Weller H (2005) Wave function engineering in elongated semiconductor nanocrystals with heterogeneous carrier confinement. Nano Lett 5:2044–2049. https://doi.org/10.1021/nl051596x [ADS][Crossref]
101. Lo SS, Khan Y, Jones M, Scholes GD (2009) Temperature and solvent dependence of CdSe/CdTe heterostructure nanorod spectra. J Chem Phys 131:084714. https://doi.org/10.1063/

1.3212693
[ADS][Crossref]
102. Li JJ, Tsay JM, Michalet X, Weiss S (2005) Wavefunction engineering: from quantum wells to near-infrared type-II colloidal quantum dots synthesized by layer-by-layer colloidal epitaxy. Chem Phys 318:82–90. https://doi.org/10.1016/j.chemphys.2005.04.029
[Crossref]
103. Li JJ, Wang YA, Guo W, Keay JC, Mishima TD, Johnson MB, Peng X (2003) Large-scale synthesis of nearly monodisperse CdSe/CdS core/shell nanocrystals using air-stable reagents via successive ion layer adsorption and reaction. J Am Chem Soc 125:12567–12575. https://doi.org/10.1021/ja0363563
[Crossref]
104. Esaki L (1986) A bird's-eye view on the evolution of semiconductor superlattices and quantum wells. IEEE J Quantum Electron 22:1611. https://doi.org/10.1109/JQE.1986.1073162
[ADS][Crossref]
105. Xia Y, Yang P, Sun Y, Wu Y, Mayers B, Gates B, Yin Y, Kim F, Yan H (2003) One-dimensional nanostructures: synthesis, characterization, and applications. Adv Mater 15:353. https://doi.org/10.1002/adma.200390087
[Crossref]
106. Alivisatos AP (1996) Semiconductor clusters, nanocrystals, and quantum dots. Science 271:933. https://doi.org/10.1126/science.271.5251.933
[ADS][Crossref]
107. Adachi S (2005) Properties of group-IV, III-V and II-VI semiconductors. Willey, Chichester
[Crossref]
108. Burda C, Chen X, Narayanan R, El-Sayed MA (2005) Chemistry and properties of nanocrystals of different shapes. Chem Rev 105:1025–1102. https://doi.org/10.1021/cr030063a
[Crossref]
109. Ekimov AI, Hache F, Schanne-Klein MC, Ricard D, Flytzanis C, Kudryavtsev IA, Yazeva TV, Rodina AV, Efros Al L (1993) Absorption and intensity-dependent photoluminescence measurements on CdSe quantum dots: assignment of the first electronic transitions. J Opt Soc Am B 10:100. https://doi.org/10.1364/JOSAB.10.000100
[ADS][Crossref]
110. Klimov VI (2000) Optical nonlinearities and ultrafast carrier dynamics in semiconductor nanocrystals. J Phys Chem B 104:6112. https://doi.org/10.1021/jp9944132
[Crossref]
111. Leatherdale CA, Woo W-K, Mikulec FV, Bawendi MG (2002) On the absorption cross section of CdSe nanocrystal quantum dots. J Phys Chem B 106:7619–7622. https://doi.org/10.1021/jp025698c
[Crossref]
112. Yu WW, Qu L, Guo W, Peng X (2003) Experimental determination of the extinction coefficient of CdTe, CdSe, and CdS nanocrystals. Chem Mater 15:2854–2860. https://doi.org/10.1021/cm034081k

[Crossref]
113. Vasko FT, Kuznetsov AV (1999) Electronic states and optical transitions in semiconductor heterostructures. Springer, New York
[Crossref][zbMATH]
114. Larramona G, Choné C, Jacob A, Sakakura D, Delatouche B, Péré D, Cieren X, Nagino M, Bayón R (2006) Nanostructured photovoltaic cell of the type titanium dioxide, cadmium sulfide thin coating, and copper thiocyanate showing high quantum efficiency. Chem Mater 18:1688–1696. https://doi.org/10.1021/cm052819n
[Crossref]
115. Guijarro N, Lana-Villarreal T, Shen Q, Toyod T, Gómez R (2010) Sensitization of titanium dioxide photoanodes with cadmium selenide quantum dots prepared by SILAR: photoelectrochemical and carrier dynamics studies. J Phys Chem C 114:21928–21937. https://doi.org/10.1021/jp105890x
[Crossref]
116. Lee W, Min SK, Dhas V, Ogale SB, Han S-H (2009) Chemical bath deposition of CdS quantum dots on vertically aligned ZnO nanorods for quantum dots-sensitized solar cells. Electrochem Commun 11:103–106. https://doi.org/10.1016/j.elecom.2008.10.042
[Crossref]
117. Pernik DR, Tvrdy K, Radich JG, Kamat PV (2011) Tracking the adsorption and electron injection rates of CdSe quantum dots on TiO_2: linked versus direct attachment. J Phys Chem C 115:13511–13519. https://doi.org/10.1021/jp203055d
[Crossref]
118. Zheng K, Žídek K, Abdellah M, Zhang W, Chábera P, Lenngren N, Yartsev A, Pullerits T (2014) Ultrafast charge transfer from CdSe quantum dots to p-type NiO: hole injection vs hole trapping. J Phys Chem C 118:18462–18471. https://doi.org/10.1021/jp506963q
[Crossref]
119. Marcus R (1964) Chemical and electrochemical electron-transfer theory. Ann Rev Phys Chem 15:155–196. https://doi.org/10.1146/annurev.pc.15.100164.001103
[ADS][Crossref]
120. Tvrdy K, Frantsuzov PA, Kamat PV (2011) Photoinduced electron transfer from semiconductor quantum dots to metal oxide nanoparticles. Proc Natl Acad Sci 108:29–34. https://doi.org/10.1073/pnas.1011972107
[ADS][Crossref]
121. Förster T (1948) Zwischenmolekulare Energiewanderung und Fluoreszenz Annalen der Physik. WILEY-VCH Verlag 437:55–75
[zbMATH]
122. Kagan CR, Murray CB, Nirmal M, Bawendi MG (1996) Electronic energy transfer in CdSe quantum dot solids. Phys Rev Lett 76:1517–1520. https://doi.org/10.1103/PhysRevLett.76.1517
[ADS][Crossref]

123. Vasiliev RB, Babynina AV, Maslova OA, Rumyantseva MN, Ryabova LI, Dobrovolsky AA, Drozdov KA, Khokhlov DR, Abakumov AM, Gaskov AM (2013) Photoconductivity of nanocrystalline SnO_2 sensitized with colloidal CdSe quantum dots. J Mater Chem C 1:1005–1010. https://doi.org/10.1039/C2TC00236A [Crossref]

124. Drozdov KA, Kochnev VI, Dobrovolsky AA, Popelo AV, Rumyantseva MN, Gaskov AM, Ryabova LI, Khokhlov DR, Vasiliev RB (2013) Photoconductivity of structures based on the SnO_2 porous matrix coupled with core-shell CdSe/CdS quantum dots. Appl Phys Lett 103:133115. https://doi.org/10.1063/1.4823549 [ADS][Crossref]

125. Chizhov A, Vasiliev R, Rumyantseva M, Krylov I, Drozdov K, Batuk M, Hadermann J, Abakumov A, Gaskov A (2019) Light-activated sub-ppm NO2 detection by hybrid ZnO/QD nanomaterials vs. charge localization in core-shell QD. Front Mater 6(231). https://doi.org/10.3389/fmats.2019.00231

OceanofPDF.com

© The Author(s), under exclusive license to Springer Nature Switzerland AG 2023
G. Korotcenkov (ed.), *Handbook of II-VI Semiconductor-Based Sensors and Radiation Detectors*
https://doi.org/10.1007/978-3-031-19531-0_8

8. Quantum Dot (QD)-Induced Toxicity and Biocompatibility

Karishma Niveria[1], Priyanka Singh[1], Monika Yadav[1] and Anita K. Verma[1, 2] ✉
(1) Nanobiotech Lab, Kirori Mal College, University of Delhi, Delhi, India
(2) Fellow, Delhi School of Public Health, Institution of Eminence, University of Delhi, Delhi, India

✉ **Anita K. Verma**
Email: akverma@kmc.du.ac.in

Keywords Alloy QDs – Artificial atoms – Biocompatibility – Capping agents – Comet assay – Core/shell Quantum dots – Cytotoxicity – Endocytosis – Fluorescence imaging – Genotoxicity – Macropinocytosis – Clathrin/caveolin pathway – Nanosensor – Nanotechnology – Oxidative stress – Phagocytosis – Photodynamic therapy – Photo-induced toxicity – Polymer coating – Quantum dots – Reactive oxygen species – Semiconductors – Surface modifications – Silanization – Toxicity

8.1 Introduction

The foundation for quantum nanotechnology in form of quantum nanomaterials was laid much earlier with the discovery of semiconductor nanocrystalline solution, which was later on termed as Quantum dots (QDs). They are most commonly referred as “artificial atoms.” QDs are nanocrystals belonging to group II–VI semiconductors with unique optical properties, like sharp emission bands and broad absorption along with size-tunable photoluminescence present in the visible spectral range [1–3]. Presently, QDs are not only composed of CdSe or CdS but of various semiconducting materials that are derived from II–VI elemental groups (e.g., zinc selenide [ZnSe], zinc sulfide [ZnS], and cadmium telluride [CdTe]), or the semiconductors from III to V elemental groups (e.g., indium arsenate [InAs] and indium phosphide [InP]), or the IV–VI elemental groups (e.g., lead sulfide [PbS] and lead selenide [PbSe]) (Table 8.1). Additionally, due to the advances in synthesis of semiconductors, novel QDs such as core/shell of CdTe/CdSe, CdSe/ZnTe core/shell, cadmium-free QDs, and Mn-doped ZnSe have been developed as well. Due to the adverse effects of II–IV binary nanocrystals, some nontoxic I–III–VI ternary QDs are also beginning to find use in bioapplications (Table 8.1).

Table 8.1 Bioapplications of various groups of QDs

Element category	Example of interest	Application
Group II–VI elements	CdS, CdSe, CdTe, ZnSe, ZnS, ZnTe	Analysis through sensor
Group III–V elements	InP or InAs	Limited biological applications; analysis through sensor
Group I–III–VI2 elements	$CuInS_2$ or $AgInS_2$	Used for biological applications and light-emitting diodes
Group IV–VI elements	PbS, PbSe, PbTe	Important for contrast imaging
Group IV elements	C, Si, Ge	Sensor applications; biological applications

QDs attracted prodigious attention as alternatives. The effortless designing of fluorescent semiconductor-based electrochemical or biosensor using quantum dots can be one such self-sustained integrated device/system which can be employed for sensitive and specific analytical information processing in biologics, where recognition of desired biological element can be accomplished with the direct spatial contact of it with electrochemical transduction element. Such uniqueness can also render distinct advantages over conventional luminous dyes in terms of tunable spectral range (excitation and emission spectra), detection of signal intensity or as an amplifier, quantum yield, electrocatalytic activity, electron transport properties, and photon-based stability, etc. [4, 5]. These features have enabled researchers to proceed with QDs in diverse research applications for fluorescence imaging [6] biosensing [7] in research areas such as medicines, clinical research, etc.; further it can also aid in development of personalized detection care also known as “point-of-care” (POC) QDs nanosensors. In non-biogenic research areas such as engineering, it has also enabled researchers to fabricate improved light-emitting diodes (LEDs) with diverse emission spectra [8], designing of solar cells with enhanced photovoltaic power conversion efficiency [9]. In this chapter, we have briefly discussed QDs structures, physiochemical properties, processing and biocompatible performance of QDs, and toxicity related to it in multimodal applications in diverse research fields.

8.2 Properties of Quantum Dots (QDs)

Semiconductor nanocrystals (NCs) or QDs are tiny nanoscale particles with the size ranging from a few nanometers to tensor even hundreds of nanometers. In the case of bulk materials, the optical, chemical, and physical properties are not influenced by the size. Conversely, the NCs have characteristics that are greatly determined by their morphology, size, and shape. Once the radius or size of NCs becomes smaller or equivalent to related bulk Bohr radius, then the electrons undergo “quantum confinement” in all three spatial dimensions. During this condition, the KBT value (KB is Boltzmann constant) becomes lower than the energy disparity between two levels of QDs, which results in a restricted hole and the electron mobility in the crystal dimension. Also, according to the radius of NCs, the QDs show absorption and emission based on size coupled with distinct electronic shifts [10, 11]. This effect is known as *quantum confinement*. This effect can influence various characteristics of QDs such as

conductivity, magnetic properties, and the size and shape-reliant optoelectronic characteristics. The reduction in size of NCs results in their free energy boost that makes them more reactive and dynamic than their bulk equivalents. It alters the various properties of NCs and makes them easily soluble in solvents that will further assist to functionalize their surface. This is the utmost attractive characteristic of NCs that can be utilized to create targeted bio-drugs and optoelectronic tools. So, the foremost physical characteristic that is desired to understand is the crystalline assembly. Analogous to their bulk equivalents, the class II–VI semiconductor QDs generally possess zinc blende or wurtzite constructs. However, occasionally, based on the conditions employed to assemble the particles, ligand-particle interaction, and impurities, many materials can possess both the crystalline assemblies [12]. The next is the matrix disparity between sowed core matter and the deposited shell matter during epitaxial development. The matrix disparity has a major role in the fabrication of core-shell structures and also can significantly influence the shell conditions and the optical characteristics [13] (Fig. 8.1). The third is morphology and shape of the semiconductor QDs. Mostly, the relatively low-temperature conditions will create nanocarriers with low dimensionality such as nano-plates or nano-disks. The intermediate temperature with weak or moderate directing ligands will generate spherical QDs, whereas the high-temperature conditions with durable directing ligands will create rod-like QDs. However, with the support of robust binding ligands such as phosphonic acid, the shell on zinc blende and wurtzite tend to fabricate dot-tetrapod and dot-rod morphologies, respectively [14, 15].

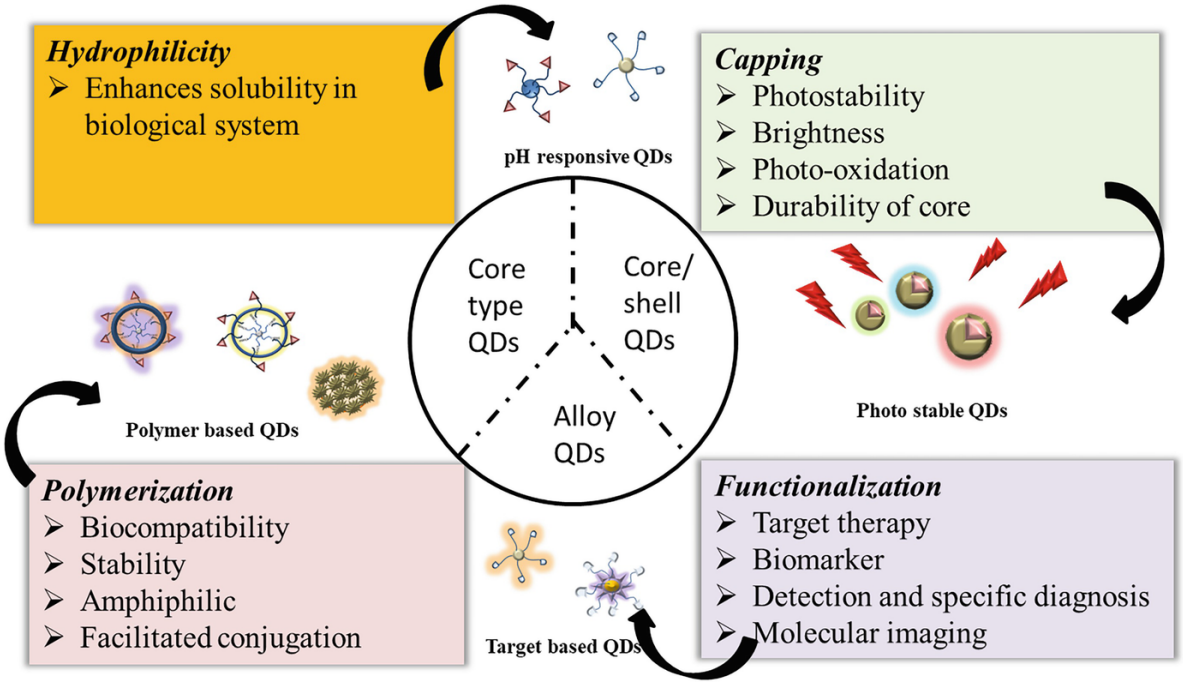

Fig. 8.1 The structure and classification based on physiochemical properties of quantum dots (QDs). They can be classified based on the core of QDs, core having a shell or alloy type

8.3 Core/Shell Nanostructures

Depending on the core material, they can be roughly divided into cadmium, silver, indium, carbon, and silicon QDs. They are different types of core/shell QDs as depicted in Fig. 8.2 based on edge alignment of conduction and balance bands [16].

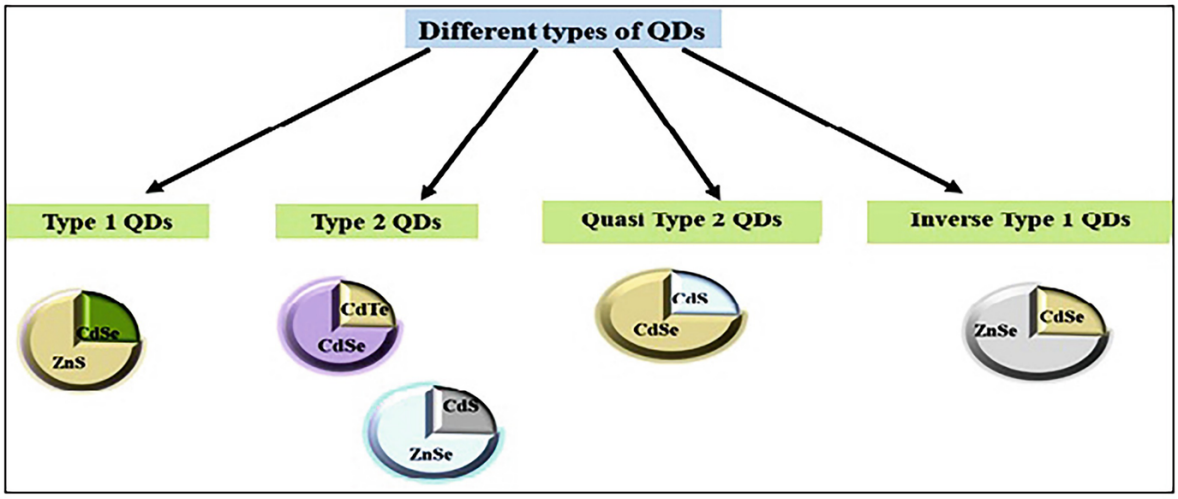

Fig. 8.2 A schematic representation of different types of QDs

From biological applications, the most frequently synthesized QDs are the core/shell nanocrystals, wherein the core nanocrystal is over-shelled by another semiconductor material to fortify and enhance its optical properties. Undeniably, CdSe/ZnS cores/shells are the “flagship” QD material, but the common representatives of Group II–VI QDs are CdSe, CdTe and other core/shell analogues such as CdSe/ZnS and CdTe/ZnS [17]. Basically, these core/shell QDs are like the earth structure that consists of a core with multiple layers surrounding it, called a shell. The core of QDs regulates the inclusive characteristics of the QDs and also refines the lights that illuminate through the QDs. The most frequently used cores are indium phosphide (InP) or cadmium selenide (CdSe) cores, which have multiple properties that make them more suitable than other materials. Although CdSe QDs are more competent and bear high quantum yield, the reported acute toxicity makes them unusable for biological purposes [18]. In the succeeding section, we discuss the cytotoxicity associated with QDs II–IV groups.

8.4 Surface Modifications

Given that the QDs are composed of toxic heavy-metal ions, the surface coating becomes a crucial parameter to ensure their biocompatibility. Owing to their non-dissolubility, photoluminescence instability, and metallic toxicity in water, QDs are usually required to be modified by passivation process, wherein additional hydrophilic coating materials coordinate or bind to the surface of QDs, to render them biocompatible and biostable. The chemically prepared QDs generally have the outermost surface containing an

organic ligand, as the nonpolar capping agent that facilitates its solubility is only in organic solvent, which restricts their direct application in biological fluids. Therefore, it is imperative to select an appropriate strategy for stabilization and solubilization of QDs in aqueous solutions to be used in physiological conditions. Two key approaches are used to achieve surface modifications of QDs (i) hydrophobic interaction of amphiphilic molecules with QDs and (ii) interaction of the polar groups of the coating moieties with the surface of QDs (the ligand exchange/modifiers) [19]. Among the bifunctional molecules, thiols (–SH) are used as anchoring groups to bind to the QDs surface, while carboxyl (–COOH) groups are used as the hydrophilic ends. The suitability of a specific strategy is determined by the chemical properties of QDs that depend on their process of synthesis.

8.4.1 Polymer Coating

Polymers with exceptional biocompatibility and reduced toxicity are widely and effectively used to engineer biocompatible QDs composites for varied medical and biological applications. Existing synthetic strategies of biocompatible QDs for in vivo applications typically involve high-temperature organometallic approaches [16] and subsequent solubilization in aqueous solution using amphiphilic polymers [20, 21] or phospholipid micelles [22]. Different polymer coatings are reported to enhance the water solubility and to provide multifunctionality for targeted delivery or for use as biosensors to detect low concentration of molecules (Fig. 8.3).

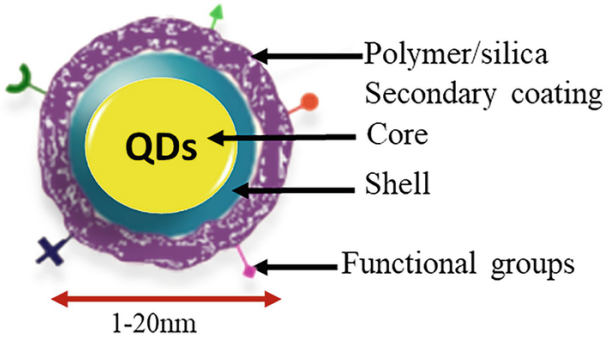

Fig. 8.3 Illustration of a generic QD that is coated with a polymer to reduce toxicity and functionalized for targeted delivery

Generally, QDs are coated with the amphiphilic graft and block copolymers [23, 24]. When a solution of QDs that are coated with hydrophobic surfactants like tri-octyl phosphine (TOP) and tri-n-octyl phosphine oxide (TOPO) is mixed with polymers, the polymeric hydrophobic chains tend to intercalate in between the surfactant moieties, making the hydrophilic groups visible on the surface, helping the QDs to stabilize in aqueous milieu (Fig. 8.4). Further, the polymers present on the QDs surface can be additionally cross-linked to enhance their stability. Generally, while solubilizing, the nonpolar solvent such as chloroform is dissolved with the amphiphilic polymer along with the QDs. Then the organic solvent is evaporated from the mixture, and an aqueous buffer solution is added [25]. To maintain the colloidal stability of polymer-coated QDs,

few parameters are critical, and they influence (i) the molecular weight of the polymer, (ii) the QD to polymer ratio, (iii) the ratio between the hydrophilic and hydrophobic molecules of the polymer and the number of hydrophobic chains per polymer moiety and the length of the polymer, and (iv) the number of charged groups that are exposed in the QD coating of polymer. Innumerable methodical investigations on QD-polymer interactions are necessary for each specific experiment, to optimize and regulate the optimal conditions for solubilization of QDs [26, 27].

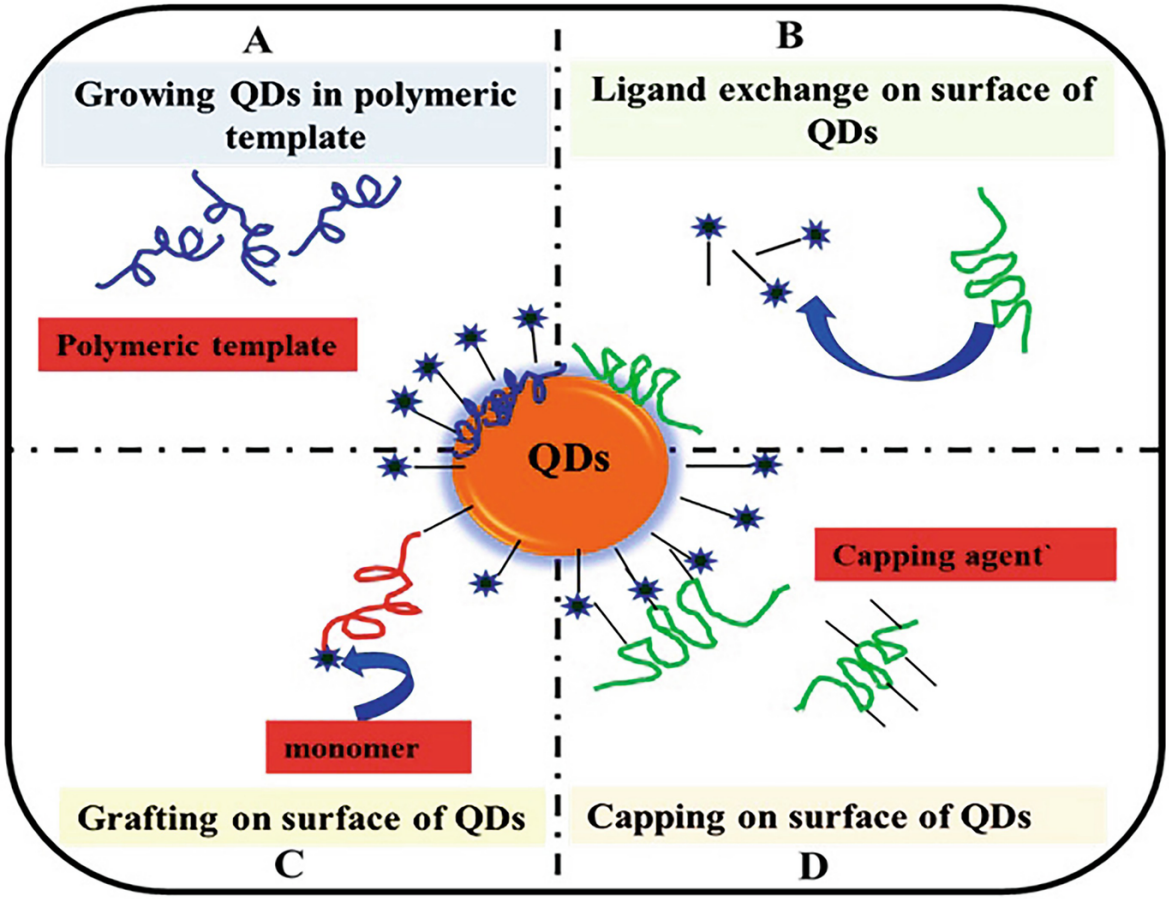

Fig. 8.4 Strategies for surface modifications of QDs. (**a**) Grafting QDs to polymer template; (**b**) ligand exchange on surface of QDs; (**c**) grafting polymer on surface of QDsl (**d**) capping on surface of QDs

Introducing polyethylene glycol (PEG) to QDs enhances the circulation time, which is important in biodistribution studies using QDs as contrast agents [28] or for drug delivery. QDs may be coated with amphiphilic molecules where the coating happens via the hydrophobic exchanges of the nonpolar parts of the amphiphilic molecules with TOPO present on the QDs surface. The ligand exchange approach differs as the QDs are directly bound with the coating molecules, typically a thiol- or amine-containing compound. Both the strategies have advantages and disadvantages. The direct addition of the thiol-containing moieties to QDs, rather than the bulky TOPO/polymer coating, produces ultrasmall nanoparticles. This is vital for various in vivo applications; the size of QDs may drastically alter the pharmacokinetics, and biodistribution [29, 30] may affect the efficacy of FRET-based assays that are extremely sensitive to the donor-

acceptor distance [31]. Innumerable methodical investigations on QD-polymer interactions are necessary for each specific experiment so as to optimize and regulate the optimal conditions for solubilization of QDs [26, 27].

8.4.2 Silanization

Silanization is an effective, low-cost covalent coating process that helps modify the surface that may be rich in hydroxyl groups, like titanium, metal oxide surfaces, and hydroxyapatites. The silica shell on QDs is chemically inert, optically transparent, safe, and innocuous. The silica surface can easily be modified to form silica-coated QDs that are ideal for conjugating various biomolecules such as antibody, antigen, aptamer, etc. Additionally, the monodispersed silica QDs confirmed high fluorescence intensity and are less likely to induce aggregation [32]. The surface of QDs is covered by a protective silica coating that prevents its exposure to the biological milieu, thereby enhancing the biocompatibility of QDs for in vivo applications. Therefore, silanization becomes a critical parameter to reduce the toxicity of QDs.

The initial step of silanization is to interchange the surface ligand with a thiol-derived silane, i.e., mercaptopropyltris (methyloxy) silane (MPS) (Fig. 8.5). This silica shell can be further modified with a variety of silicon to endow multifunctionality, and the most commonly used ones are aminopropylsilanes (APS), phosphosilanes, and polyethylene glycol (PEG) silane. Initially, Chen et al. synthesized silica-coated CdTe QDs and functionalized covalently with α-fetoprotein antibody, anti-AFP (secondary antibodies denoted Ab_2) to establish a novel technique for the ultrasensitive detection of biomarkers based on CdTe quantum dots [33]. The cytotoxicity of PbSe QDs that were functionalized with silica was verified on two different cell lines and showed that the silica-coated PbSe QDs were much less cytotoxic than the polymer-coated PbSe QDs [34]. Because the silica shells are exceedingly cross-linked, the silanized QDs are very stable. Therefore, silanization is favored as it is less toxic when compared to other ligands. Even though numerous groups have successfully reported silica-coated core-shell QDs, different types of surface-silanized QDs can be categorized into three classes, like core-shell QDs, single QDs, and multiple-layered QDs being coated by silica shell.

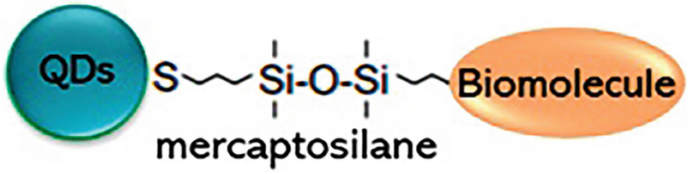

Fig. 8.5 Silanization of QDs and bioconjugation using a mercaptosilane compound

8.5 Biocompatibility

Biocompatibility is an important aspect for the success of biological and biomedical applications of QDs and is based on its solubility, stability, and toxicity. It is extremely crucial to understand and address the increasing biological complexity keeping in mind

the progress toward clinical translation of QDs. Further to evaluate whether the surface-modified QDs are biocompatible, their intracellular fate, mechanism of internalization, and toxicity caused by them that may depend on the core material, surface modification, size, shape, and surface charge need to be understood (Fig. 8.6).

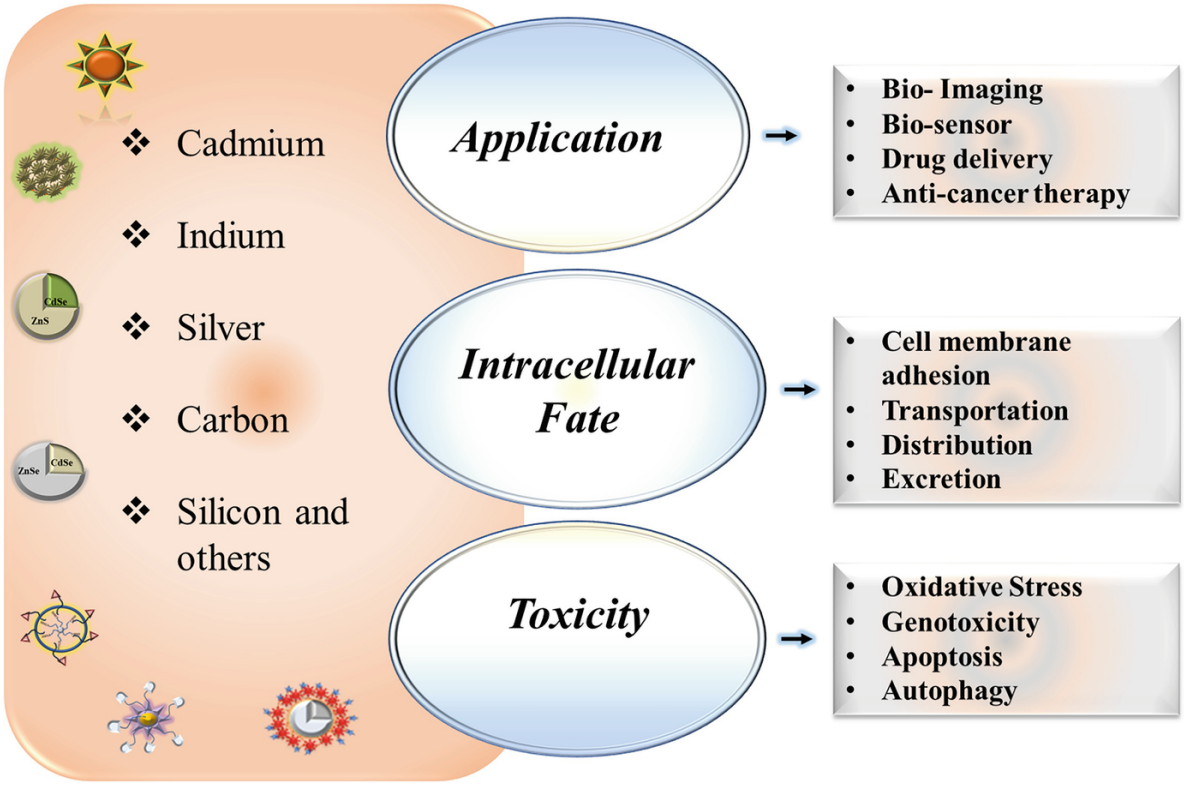

Fig. 8.6 Overview of the biological interaction of QDs

8.5.1 Intracellular Fate of QDs in Cells

The extracellular environment is separated from the intracellular milieu by the cell membrane that acts as a natural barrier. The process of QDs adhering to the cell surface may be internalized by transmembrane, cell membrane, transporters, distribution patterns, mean residence time, and elimination, all of which are closely linked to their application and subsequently associated toxicities. Alternately, for therapeutics, the adverse effects induced by QDs can be correlated with the therapeutic regimen, dosage, or the internalized concentrations [35].

8.5.1.1 Cellular Uptake of QDs

The factors that determine the cellular uptake of QDs depend on the cell type, morphology, size, and surface coating (independent of the core) of QDs. Therefore, for the given QDs, there may be one size and concentration parameter of the highest cell internalization efficiency.

Direct penetration of QDs via the cell membrane is possible Fig. 8.7 [36, 37]; but mostly QDs are internalized by endocytosis. Endocytosis includes phagocytosis by

specialized cells, such as neutrophils, monocytes, and macrophages; Pinocytosis involves the uptake of fluids containing solutes and particles by vesicles of smaller size than those generated during phagocytosis. This endocytic mechanism can be classified in macropinocytosis and receptor-mediated endocytosis. Figure 8.8 elucidates the various pathways for internalization of QDs.

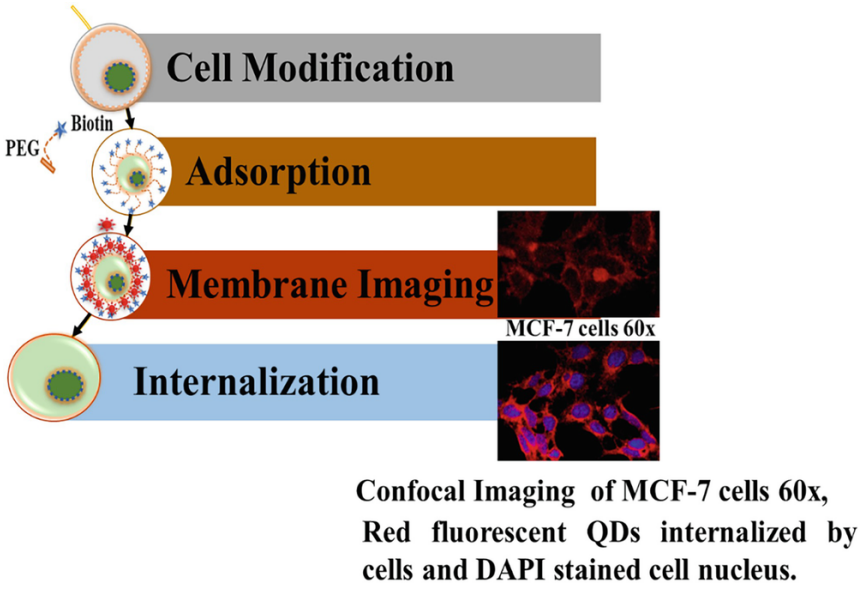

Fig. 8.7 Cellular uptake of QDs

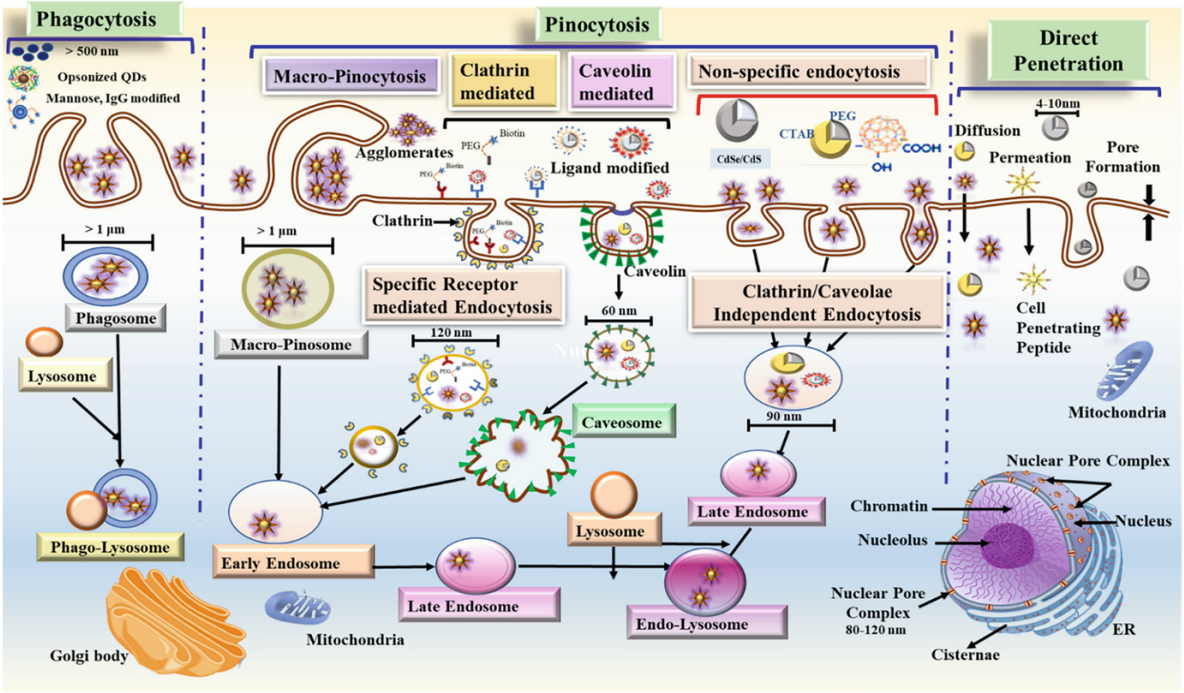

Fig. 8.8 Intracellular trafficking of QDs by distinct pathways by cells

Following steps for endocytosis are observed: initially, QDs bind to the plasma membrane receptors, which causes formation of coated pits, but mostly QDs are

internalized by endocytosis. Macropinocytosis is observed in almost all cell types. It generates large macropinosomes that contain the extracellular fluid and soluble protein, which eventually fuse with lysosomes or recycle its content to the surface; clathrin/caveolin further makes intracellular buds to create endosomes or endocytic vesicles. Clathrin-dependent endocytosis comprises the assembly of clathrin and adaptor proteins on a region of the plasma membrane where specific receptors are clustered to form a budding vesicle ordained for internalization. Caveolin-dependent endocytosis includes the assembly of caveolin coats on portions of plasma membrane that are rich in lipid rafts to form the budding vesicle to be internalized. Later, the QDs are transported to the subcellular targets like the late endosomes/lysosomes or eliminated from the cytosol. Both macropinocytosis and phagocytosis are dependent on remodeling of the actin cytoskeleton and clathrin-independent processes [38].

Hence, for any given QDs, there may be a uniform parameter of both size and concentration that indicates the maximum internalization efficiency in a particular cell type. A widely used method for studying the uptake mechanism is to observe the changes of cell uptake efficiency by pretreating the cells with specific inhibitors. Since QDs emit fluorescence, they can be directly tracked in biological systems when compared to other nanomaterials. Therefore, it is feasible to observe the mechanism of cellular internalization of QDs using various endocytic inhibitors (Table 8.2) and cell transfection techniques, and quantitative and qualitative analysis of sub-localization of QDs can also be assessed.

Table 8.2 A list of inhibitors that are generally used by researchers

Endocytosis	Description	QDs	Localization	Inhibitor	Ref.
Phagocytosis	Plasma membrane forms a pseudopod to entrap the particles into the cells.	Graphene QDs (GQDs)	Cytoplasm, mitochondria, lysosome and ER, nucleus	Colchicine Nocodazole Cytochalasin D Cytochalasin B	[39]
Macropinocytosis	Macropinosomes that are irregular endocytic vesicles are formed by the folds of the cell membrane. Large vesicle with a diameter of 0.5 μm–2 μm sometimes 5 μm with caveolin coating.	Eu^{3+}/Mn^{2+}-co-doped ZnSe@ZnS core/shell QDs	Cytoplasm Endosome	Ly294002 (LY); Wortmannin (WMN); 5-(N,N-dimethyl)-amiloride (DMA)	[40]
Clathrin-mediated endocytosis	Involvement of the membrane-associated protein clathrin in forming membrane vesicles that become internalized into the cell.	Streptavidin-conjugated QDs	Early to late endosomes (lysosomes)	Chlorpromazine Nocodazole Cytochalasin D Bafilomycin A1 Nystatin	[41]
Caveolin-mediated endocytosis	Bulb-shaped, 50–60 nm plasma membrane invaginations called caveolae (or “little caves”). Caveolae formation is driven by integral membrane proteins called	QDs-labeled GCRV particles	Cytoplasm Caveolin-1	Methyl-β-cyclodextrin Nystatin Genistein	[42]

Endocytosis	Description	QDs	Localization	Inhibitor	Ref.
	caveolins as well as peripheral membrane proteins called cavins.				

8.5.1.2 Dynamic Process of Uptake and Elimination of QDs

Biological systems are dynamic, and the mechanism of QDs uptake and removal is continuous. Therefore, different QDs will behave differently. Based on the material of the core, QDs can be roughly categorized as cadmium, indium, silver, silicon, and carbon QDs and have been briefly discussed in terms of internalization and toxicity observed.

8.5.1.2.1 Cadmium-Based QDs

The amount of QDs internalized by cells largely depends on the surface modifications and surface charge [43]. Reports suggested that D-penicillamine-coated CdSe/ZnS QDs adhere to the plasma membrane of cells [44], and only when the concentration of QDs exceed the threshold, the process of internalization is triggered in human cervical cancer cells-HeLa cells. For example, the negatively charged (–COOH) CdSe [36, 45] and CdTe QDs [46, 47] were greater than the internalization of PEG-modified QDs that were neutral in charge as well as the positively charged ($–NH_2$) ones. Some surface modifications weaken the internalization process such as N-acetylL-cysteine (NAC) [47] and Gum arabic (GA)/TOPO [48]. But, reports also reveal that the amount of internalized QDs was equal [49] in all QDs irrespective of surface charge such as positively charged (polydially-dimethyl ammonium chloride (PDDA)), negatively charged carboxylic acid (CA), and the neutrally charged PEG QDs.

Different cells have varied internalization mechanisms of QDs. Macrophages can internalize by phagocytosis and significantly higher amount of CdSe/ZnS QDs than epithelial cells [50]. But higher internalization of CdSe/ZnS QDs was observed by epithelial cells when compared to lymphoblastoid (TK6) and fibroblasts (HFF-1) cells [51]. Additionally, more uptake of CdTe/CdS lipids QDs was observed by HepG2 cells when compared to normal hepatocytes HL-7702 [42]. Generally, CdTe and CdSe QDs have been reported to be internalized by macropinocytosis [52], caveolae/lipid raft-dependent pathway [53], and clathrin-mediated endocytosis [47, 54, 55]. Likewise, human embryonic kidney (HEK) cells were observed to uptake of CdSe/ZnS-COOH without caveolin, clathrin, macropinocytosis, melanosome-transfer, and F-actin pathway but by lipid rafts that could be associated with G-protein-coupled receptor (GPCR) and low-density lipoprotein receptor/scavenger receptor (LDLR/SR). Also, the distribution and uptake of QDs by cells are time-dependent and dynamic processes [56]. Based on reports, cysteine (Cys)-CdTe QDs primarily remain adhered to the cell membrane in the first 5 min, and most of the QDs were found in cytoplasm within the next 40 min [57].

Similarly, after 6 h, the crystalline core (Cd/Se/Te QDs) with shell of ZnS (QD705) was sited at the lysosome, endosome, and endoplasmic reticulum (ER) of mouse renal adenocarcinoma and transported to mitochondria at 24 h [58]. Usually, CdSe and CdTe QDs were localized in cytoplasm and organelles, especially in the perinuclear region [52], rather than the nucleus [56–60]. More specifically, when compared to ER, mitochondrion, [50] and Golgi apparatus, QDs were localized in the lysosomes [54, 61].

Further, the subcellular localization of CdTe QDs was based on their size, the red QDs (~5 nm) were dispersed throughout the cytosol of microglia (N9 cells), and the 2 nm, green QDs were predominantly localized in the nuclear compartment [62].

Remarkably, irrespective of the different surface coatings (–COOH, –PEG, and –NH_2) affected the efficiency of uptake of CdSe/CdTe/ZnS QDs by J774.A1 macrophage cell line and did not govern the localization [63]. The QDs only partially entered the cells and were eliminated via exocytosis, and maximum were retained within the cells [54]. It is important to mention that exocytosis of QDs from cell was energy dependent and was again dependent on the size, shape, surface charge, dose [64], coating group, [65], and cell type [66].

8.5.1.2.2 Indium-Based QDs

The cellular uptake of InP/ZnS was observed to be dependent on type of cell, its surface modification, and its concentration (optimal range ~20–100 nM) [67]. Enhanced uptake of –NH_2- and –COOH-coated InP/ZnS QDs was observed in human lung cancer cells (HCC-15) after being incubated for 4 h with alveolar type II epithelial cells (RLE-6TN), when compared to InP/ZnS-OH at a concentration of 2 μg/mL. Further, HCC-15 cells had significantly improved uptake of QDs than RLE-6TN cells [68]. Also, InP/ZnS QDs were predominantly localized in the cytosol and the perinuclear region in human neuroblastoma cells SH-SY5Y, lung adenocarcinoma A549, RLE-6TN, and HCC-15 cells [69]. There is insufficient data on the mechanism of cellular uptake of In-based QDs.

8.5.1.2.3 Silver-Based QDs

Cellular uptake of Ag-based QDs has been sparsely reported. The cellular uptake of Ag_2S QDs was dependent on various cell types. The highest internalization of QDs was observed in A549 and BEAS-2B cells, while the least uptake of QDs was observed in HeLa cells. Moreover, with increase in the concentration of dose and incubation time, enhanced internalization of Ag2Se QDs was observed in BV2 cells [70].

8.5.1.2.4 Silicon-Based QDs

Exposure to SiQDs at suboptimal concentration indicated substantial time-dependent intracellular accumulation in human embryonic hepatocyte HepG2, mouse embryo fibroblast 3T3-L1 [71], HUVECs [72], and HeLa cells [66]. But then again, the amount of internalized SiQDs is progressively stabilized leading to a gradual decrease in the concentration of the intracellular QDs, although maximum SiQDs were localized within the cells [68]. Prior report specified that HeLa cells internalized the alkyl-SiQDs via a cholesterol-dependent endocytosis or a caveolin- and lipid rafts-mediated endocytosis. The intracellular accumulation of alkyl-capped SiQDs was significantly higher in HuH7 and HepG2 cells and considerably reduced in HeLa cells and human colorectal adenocarcinoma CACO-2. Also, SiQDs get internalized in HeLa cells through endocytosis and eliminated via exocytosis, localizing the QDs in the lysosomes and getting trapped in the exocytic vesicles [73].

8.5.1.2.5 Carbon-Based QDs

C-based QDs preferentially locate in the nucleus, unlike all the Cd- and In-based QDs discussed so far that are normally localized in the cytosol. Aminated CQDs were mainly internalized by rat alveolar macrophages (NR8383), initially by phagocytosis, and then by caveolin-mediated endocytosis [43]. Besides, size-dependent variation in the mechanism of internalization was observed in dendritic cells (DCs), wherein small graphene GQDs (24 nm) exhibit increased accumulation and larger sized GQDs (66 nm) show reduced internalization; the larger GQDs were internalized by the dynamin-dependent process, whereas the smaller GQDs via dynamin-independent but cholesterol-dependent pathways [74]. The cellular internalization of GQDs is a dynamic process and changes over time. When NR8383 cells were incubated with GQDs for ~12 h, the GQDs were dispersed in the cytoplasm, ER, mitochondria, and endo-lysosomes; but when the incubation was for 24 h, the GQDs were localized in the nucleus much more than the cytosol of the NR8383 cells. Post 48 h of exposure, the intracellular GQDs was drastically reduced by ~35%. Incidentally, ample amount of GQDs persisted in the nucleus and cytosol. Also, expression of the two main genes of nuclear pore complex (NPC): Nucleoporin 98 (Nup98) and karyopherin β2 (Kapβ2) have an important role in the nuclear uptake of GQDs. Surprisingly, the intracellular amount of GQDs did not vary with time, especially between 24 and 48 h, signifying that primarily GQDs internalization occurred earlier, i.e., before 24 h.

8.6 Elucidation of Potential Toxicity

QD toxicity is a complicated issue as it relies on its intrinsic properties including size, charge, surface chemistry, and chemical composition of QDs. Group III and IV quantum dots show reduced toxic effects; hence, they are widely used as optical probes and biosensors. Toxicity severely limits the potential for clinical translation of II–VI semiconductor QDs, such as CdSe and CdTe QDs as they easily disintegrate in the biological systems if their surfaces are not coated carefully with protective shells, biocompatible polymers, and biomolecules that are inert.

An ideal solubilization strategy should reduce the undesirable nonspecific uptake of QDs by living tissues and scavenging by the reticuloendothelial system. Literature suggests that few QDs have shown direct cytotoxicity, particularly after oxidative and/or photolytic deterioration of their core coatings. QDs are efficient energy donors and can easily transfer energy to nearby oxygen molecules that induce generation of reactive oxygen species (ROS), which in turn causes cell damage and eventually leads to cell death. Figure 8.9 gives a schematic view of the recent in vitro and in vivo experimental design that can be undertaken to assess the potential toxicity of QDs based on their characteristics in the biological environment.

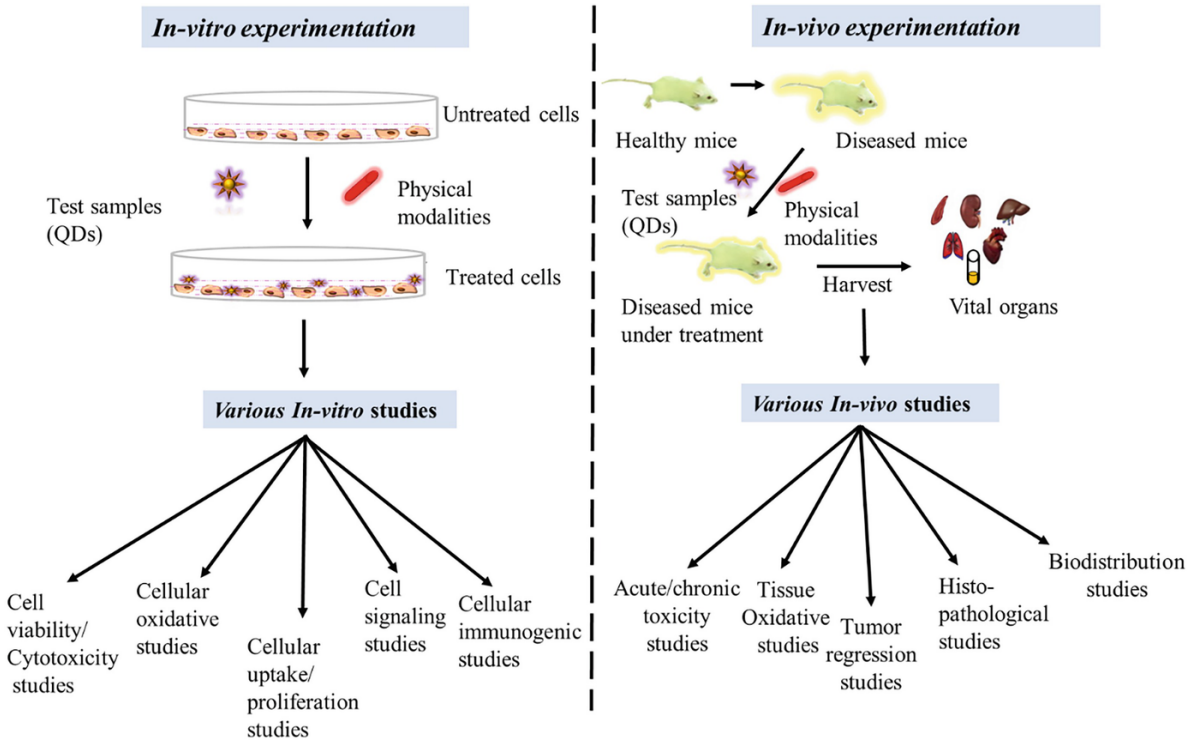

Fig. 8.9 Schematic illustration of experimental design for in vitro and in vivo studies

8.6.1 Genotoxicity

Genotoxicity is the damage to DNA – the genetic material, often caused by interaction of innumerable agents that alter the cellular genetic information leading to mutations. The extent, type, and persistence of damage compromise the DNA integrity by various mechanisms. Absence of an inflammatory response induces primary genotoxicity, while activation of the proinflammatory cells such as macrophages and neutrophils mediates the secondary genotoxicity, which further generates significant quantities of reactive species [75]. Moreover, physical perturbations caused by interaction of particulate material with DNA can cause direct genotoxicity, and indirect genotoxicity may be a consequence of increased generation of ROS after interaction with cellular organelles such as cell membrane, mitochondria, etc., resulting in elimination of intracellular antioxidants [76]. In this way, ROS, generated by the cellular pathways, may accrue and induce DNA damage. This alteration could have a direct or an indirect effect on the DNA: the event activation that is mistimed, induction of mutations, and direct DNA damage that may also cause mutations. Known DNA mutations include mutations of the key loci in the genetic code that are characteristic molecular hallmarks of cancer. Proto-oncogenes can stimulate the cellular proliferation and growth (e.g., K-ras), and inhibition of proliferation involves the tumor suppressor genes that may also do DNA repair (e.g., p53). Apart from causing carcinogenesis, DNA mutations are responsible for causing numerous pathological conditions that can modify susceptibility to the disease. Mutations can involve relatively small sequences, involving single genes, or can occur on a larger scale. Point mutations are small-scale mutations such as transversion or

transition, wherein a nucleotide is substituted by another; deletions that remove the nucleotides from DNA; and insertions, where nucleotides are added to the genetic code. The chromosomal structure may get affected by mutations that may cause genotoxicity. Clastogenic chemicals induce chromosomal aberrations that can either be numerical (aneugenic) or structural (clastogenic). Micronucleus (MN) assay is a reliable and sensitive tool to estimate the chromosomal damage caused by DNA breakage (clastogenic) or by abnormal segregation (aneugenic) methods. The alkaline comet assay helps in identification of single and double DNA strand breaks (DSBs) [77, 78]. DSBs damage the integrity of chromosomes and subsequently affect cell viability. Mis-repaired or unrepaired DSBs induce chromosome rearrangements inducing mutations leading to cell death and cancer [78–82]. Therefore, evaluation of genotoxicity is marked as an important tool to study the potential carcinogenic risk, i.e., damages to genetic material caused by exposure to QDs. Banerjee et al. observed remarkable dose-dependent genotoxic effects by CdSe QDs along with oxidative stress in *Allium cepa* plant using the DNA comet assay [83]. Another study showed that genotoxicity induced by QDs was based on the intrinsic surface chemistry and charge. Manshian et al. assessed various surface coatings of QDs such as neutral (hexadecyl amine; negative (carboxyl), HDA) or positive (amine) polymer and evaluated their effects on human lymphoblastoid TK6 cells. Genotoxicity was analyzed using the micronucleus assay (gross chromosomal damage) and the hypoxanthine phosphoribosyltransferase (HPRT) forward mutation assay (point mutagenicity). This study concluded that HAD-QDs induced the greatest genotoxicity and cytotoxicity in comparison to carboxyl and amine-coated QDs. The possibility of this genotoxicity was caused by release of free cadmium ion [84]. Moreover, PCR (polymerase chain reaction) evaluation is used to show the upregulation of DNA damage, the responsive gene, as well as proinflammatory cytokine genes. In addition, transcriptome sequencing demonstrated the upregulation of metallothionein family of genes in cells treated with mercaptopropionic acid (MPA)-coated CdSe (MPA-CdSe) QDs in comparison to cysteamine (Cyst) CdSe (Cyst-CdSe) QDs [85]. Similarly, preparation of MPA-CdSe QDs (water soluble) was evaluated in *Escherichia coli* DH5α (gram-negative) and *Staphylococcus aureus* (gram-positive bacteria) based on agar disc, and cytotoxicity was determined by measuring ROS level in QD-treated cells. *S. aureus* was highly sensitive when compared to *E. coli*; size- and dose-dependent elevation of generation of reactive oxygen species (ROS) as well as enhanced zone of inhibition was observed in agar-disc diffusion assay. The oxidative stress analysis (glutathione (GSH), lactate dehydrogenase (LDH)) and ROS-induced DNA damage caused genotoxicity in *S. aureus* [86]. *Drosophila melanogaster* is also frequently used as a genotoxic model organism, wherein the comet assay was used to demonstrate the genotoxicity of Cd QDs and $CdCl_2$ QDs. Cd QDs exhibited both dose- and time-dependent genotoxicities in larvae by penetrating the intestinal barrier, passing to the hemolymph and interacting with the hemocytes [87].

8.6.2 Cytotoxicity

Despite numerous preclinical studies on QDs, the key question that remains unresolved is their potential cytotoxicity. It has been reported that core of QDs (Se/Cd) exhibited inherent toxicity to cell cultures and to live animals. Recently, Derfus et al. evaluated the cytotoxicity of QDs based on certain conditions such as synthesis, UV exposure, and surface functionalization as observed in primary rat hepatocytes cells and in in vivo model. This study concluded that coated Cd/Se QDs exhibited low cytotoxicity as compared to uncoated QDs, which release free cadmium ions in cells [88]. In addition, cytotoxic analysis of InP/ZnS QDs modified with three different groups ($–NH_2$, –COOH, –OH) was studied in two lung-derived cell lines. The results suggested that InP/ZnS-COOH QDs and InP/ZnS-NH_2 QDs exerted more cytotoxicity than InP/ZnS-OH QDs based on the concentration and surface functionality. All these QDs promoted cell apoptosis and intracellular ROS generation [67]. Similarly, it has been reported that MPA- and cysteamine-coated (Cyst) CdTe QDs were cytotoxic at 10 μg/mL, when exposed to rat pheochromocytoma (PC12) cells, while uncoated showed cytotoxicity at 1 μg/mL. This cytotoxicity was determined by chromatin condensation and membrane blebbing, the characteristic traits of apoptosis. Although positively small-sized QDs impart higher toxicity than neutral-charged large-sized QDs, because of their subcellular biodistribution, smaller QDs localized to the nuclear compartment while larger ones in the cytosol compartment. Therefore, cell death may be considered due to the release of free Cd, which leads to ROS production and ultimately causes loss of function [62]. Dussert et al. reported the cytotoxicity of the single-shelled InZnP/Zn(Se,S) core/gradient shell as well as the double-shelled InZnP/Zn(Se,S)/ZnS core/shell/shell QDs, using both the pristine form and the aging form that give a real-time conservational weathering of QDs. This concluded that aged QDs evinced significant cytotoxic and genotoxic activity, thereby regulating gene expression that is responsible for zinc homeostasis, cell redox response, and inflammation in human primary keratinocytes, whereas pristine QDs showed insignificant toxicity. Furthermore, this study focuses on the end product of InP-based QDs, which is pernicious to skin cells as observed by accidental exposure that caused oxidative stress, inflammation, and imbalance of cell metal homeostasis, specifically Zn homeostasis [89, 90]. In addition, Bhanoth et al. synthesized different combinations of core-shell QDs using ZnSe, CdS, and CdSe (CdS/CdSe, ZnSe/CdS, and ZnSe/CdSe) were analyzed in subjected to cytotoxicity and therapeutic efficacy. From these different combinations, the ZnSe/CdS QDs possessed excellent optical properties; therefore, this formulation was further used for in vitro and in vivo study for the assessment of cytotoxicity and therapeutic efficacy. Hence, ZnSe/CdS QDs displayed 65% cytotoxicity against MCF-7 cells (breast cancer) and also imparted negligible hemolysis. ZnSe/CdS QD-treated mice model represented that 34% tumor regression in comparison to mitomycin C (positive control) observed 93% with respect to PBS [91].

8.6.3 Photo-Induced Toxicity

QDs stability/toxicity is the most important aspect to be considered during synthesis, storage and in biological studies. It has been reported that maximum cytotoxicity is

induced by photolysis and oxidation. Under the influence of photolytic and oxidative environments, QD core-shell coatings are known to be labile and prone to degradation, thereby exposing the inherently toxic “capping” matter or the entire core metalloid compound or releasing the core metals ions (e.g., Cd, Se, Zn). Pathakoti et al. studied photo-induced toxicity of CdSe/ZnS QDs with multiple surface coating at three different wavelengths (530, 580, and 620 nm) to *E. coli* under solar irradiation. This study concluded PEI (polyethylene imine)-coated QDs exhibited maximum phototoxicity to *E. coli*, QSA (polyethylene glycol)-coated QDs and QSH QDs with amphiphilic polymer coating had negligible phototoxicity. The phototoxic activity triggered due to the oxidative stress via production of hydroxyl radicals caused lipid peroxidation and consequently a drop in the reduced glutathione level. Therefore, PEI-coated CdSe/ZnS QD was highly toxic, while non-cadmium-based QDs have remarkable biocompatibility [92].

Similarly, the effect of photo-induced ROS evaluated in differently functionalized ZnO QDs demonstrated that the highest ROS generator QDs (ZnO-GLYMO) were most deleterious toward DNA. This study showed photo-induced damages caused by various factors, not only based on ROS generation but also biomolecule interactions [93]. In another study, primary rat hepatocytes treated with 62.5 μg/mL MAA–CdSe QDs promoted cell toxicity, accounted to photodegradation and oxidation of the QD coating. Likewise, under UV light exposure, MAA–TOPO-capped CdSe QDs undergo dose-dependent cytotoxicity, and prolonged exposure enhanced toxicity by almost 91%. It was deduced that long-lasting exposure of QDs to oxidative and photolytic conditions endows degradation of MAA–TOPO-capped CdSe QDs nanocrystals [94].

8.7 Molecular Mechanisms Induced by QDs

Currently, the underlying mechanisms of toxicity caused by QDs remain unpredictable. Hyperactivation and increased oxidative stress, sudden elevation of intracellular Ca^{2+} levels, QDs, and Cd^{2+} ions released from Cd-carrying QDs were reported to be main source of toxicity (Fig. 8.10 and Table 8.3).

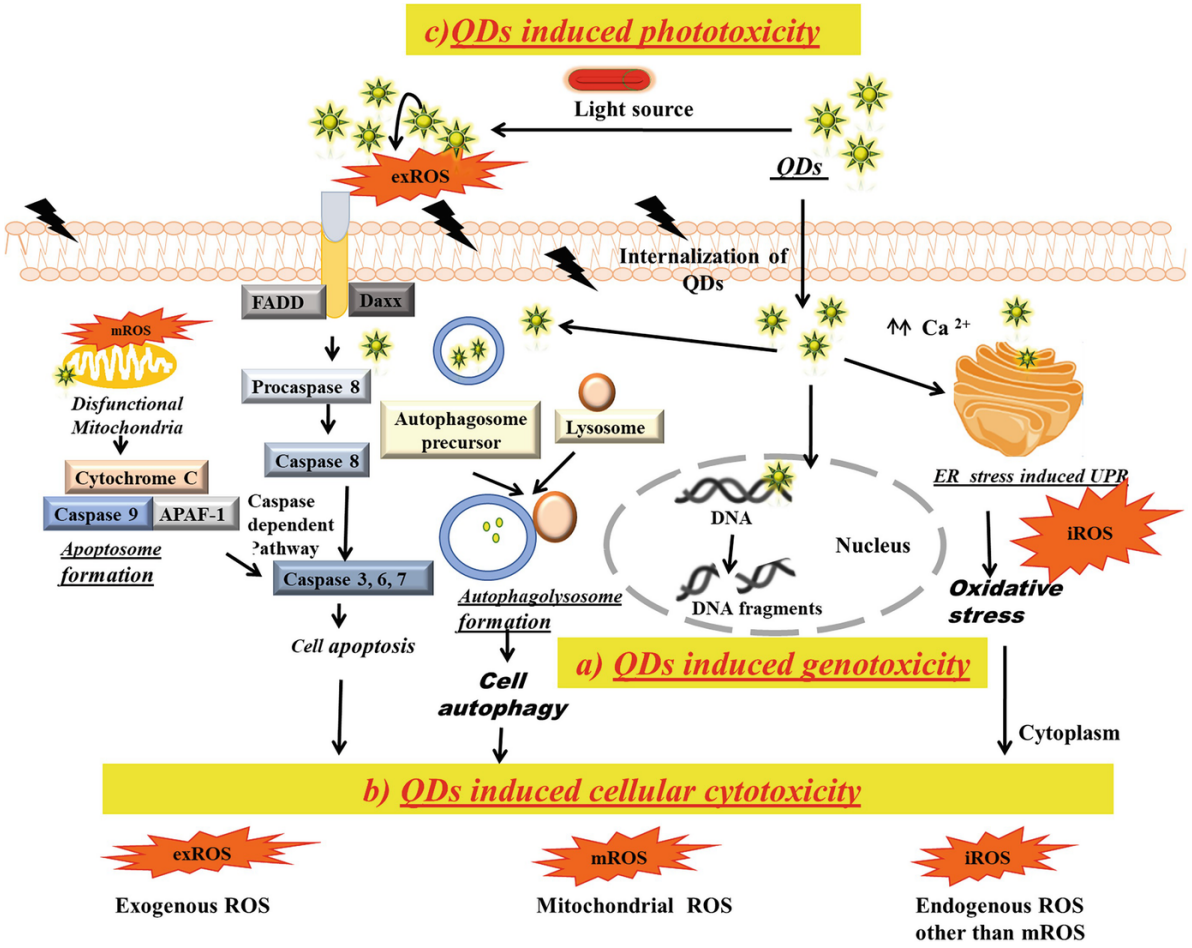

Fig. 8.10 QD-induced toxicity mechanisms. (**a**) QD-induced genotoxicity. (**b**) QD-induced cellular cytotoxicity. (**c**) QD-induced phototoxicity

Table 8.3 Tabular representation of mechanisms of action of QDs

QDs	Functionalization	Experimental model	Exposure time	Assay	Cell fate (toxicity)	Mechanisms	Ref.
ZnSe/CdSe QDs	PVP & oleic acid	Cancer cell line (EAC, MCF-7) and HEK-293	24–48 h	MTT	Dose- and time-dependent cytotoxicity	Release of free Cd^{2+} & Se^{2+} ions	[97]
CdSe QDs	MAA	In vivo study in male Balb/c mice	2–7 days	DNA fragmentation and micronucleus assay	Genotoxicity (DNA damage, formation of micronuclei, and DNA adduct)	Induction of oxidative stress	[98]
ZnSe/CdSe	Oleic acid	Human hepatocellular carcinoma (Hep3B and HepG2)	24–48 h	MTT, DNA fragmentation, ROS assay, and intracellular Ca^{2+} level	Apoptosis induced cytotoxicity and also exhibited genotoxicity	Cytotoxicity via ROS generation by ER stress and mitochondrial disruption. Elevated level	[99]

QDs	Functionalization	Experimental model	Exposure time	Assay	Cell fate (toxicity)	Mechanisms	Ref.
						of Ca^{2+} level and genotoxicity induced by DNA fragmentation.	
CdTe QDs	Glutathione	Bacterial strain (*E. coli* BW25113)	24 days	Growth inhibition assay and intracellular ROS-level assay	Photo-induced toxicity	Photon induced the transfer electrons and generated ROS level and caused oxidative stress inside cells.	[100]
In-based water-soluble QDs	–	Wistar rat model	90 days	Histological assessments, hematological and biochemical markers	Less toxic	Accumulation of QDs was observed maximum in liver, and spleen-indicated indium QDs are degraded by liver.	[101]
CdTe QDs	–	Human hepatic carcinoma (HuH-7 cells)	48 h	MTS and LDH assay, comet assay, oxidative stress	Dose and time exposure cytotoxicity and genotoxicity	Induction of apoptosis facilitated via ROS generation, GSH reduction, and oxidative stress.	[102]
CdSe/ZnSe QDs	Streptavidin	pDNA	1 h	Agarose gel electrophoresis AFM imaging and DNA damage assays	Photo-induced toxicity	DNA strand breakages and nucleobase damages in pDNA are correlated with photo-induced production of ROI.	[103]
Gradient-alloyed QDs	MPA and PEG	Cervical cancer cell (HeLa-cells)	24 h	MTT, oxidative stress, lysosomal and autophagy markers	Autophagy-mediated cytotoxicity	MPA-QDs induced autophagy by decreasing ROS generation while PEG-QDs induced elevate ROS	[104]

QDs	Functionalization	Experimental model	Exposure time	Assay	Cell fate (toxicity)	Mechanisms	Ref.
						generation and autophagy blockage via lysosomal impairment.	
$CuInS_2$/ZnS QDs	PEGylated	In vivo model of Balb/c mice	1–90 days	Histology, ICP-MS, serum analyses	Low cytotoxicity	PEG modification can be $CuInS_2$ QDs in order to achieve low toxicity.	[105]
CdS/ZnS	mAbs (trastuzumab)	Human breast cancer cell line (SK-BR-3 and BT-474)	24–72 h	MTT assay	Exhibited low cytotoxicity and high biocompatibility	Provide targeted delivery to HER2 overexpressing cancer cells.	[106]

DNA, deoxyribonucleic acid; *EAC*, Ehrlich-Lettre ascites carcinoma; *ER*, endoplasmic reticulum; *ICP-MS* inductively coupled plasma mass spectrometry; *LDH*, lactate dehydrogenase; *MAA*, mercaptoacetic acid; *MPA*, mercaptopropionic acid; *MTT*, 3-[4,5-dimethylthiazole-2-yl]-2,5-diphenyltetrazolium bromide; *PEG*, polyethylene glycol; *PVP*, polyvinylpyrrolidone; *ROS*, reactive oxygen species.

8.7.1 Reactive Oxygen Species and Oxidative Stress

Enhanced ROS production is considered a key mechanism for nanomaterial toxicity. The ROS molecules interact with macromolecules such as proteins, DNA, lipids, etc., affecting their structural and functional integrity causing severe oxidative damage to the cells. Tang et al. demonstrated that CdTe QDs and $CdCl_2$ administered in zebrafish liver cells significantly increased ROS levels that cleave the DNA strand, upregulating the expression of antioxidant genes and inhibited DNA repair [95]. Similarly, CdTe QDs were observed to activate the apoptotic pathway too. QDs damage the mitochondria causing mitochondrial swelling, loss of cristae, thus facilitating the loss of mitochondrial membrane potential (MMP) and mitochondrial permeability transition (MPT). This ultimately results in the release of cytochrome c into the cytosol thereby, stimulating the downstream cascade resulting in apoptosis. Further, its pernicious effect shown on mitochondrial electron transfer chain (ETC) results in decreased activity of ETC complex (I, II, and IV). Lai et al. demonstrated that reduced GSH-Cd-QDs bind with the pore-forming proteins of mitochondrial membrane in human embryonic kidney cells (HEK-293), which hyperactivates the mobility of transmembrane protein. This enhances the MPT formation, which eventually elevates the intracellular ROS levels [96].

8.7.2 Release of Cadmium from Cadmium-Containing Quantum Dots

Release of Cd^{2+} ions from QDs is one of the proposed mechanisms of toxicity induced by QDs. Once QDs are internalized in the cell, they are degraded by the acidic environment of lysosomes, the Cd^{2+} ions so released can attach to the thiol groups of the intracellular proteins that can disrupt their structure and function [107]. Wang et al. analyzed the histopathological changes that occurred in mice liver and kidney based upon time-dependent toxicity of CdTe QDs. The toxicity was possibly induced by the elevated levels of Cd^{2+} ions and OH^{-} ions, and they used metallothionein (MT) as a biomarker to measure the increased Cd^{2+} ions in the tissues. This study concluded that elevated MT levels can interact with Cd in the cytosol and reduce its bioavailability to vital organelles [108]. In addition to this, QDs also have tendency to destroy the structure and function of macromolecular substances. One such study performed by Sun et al. found that QDs can bind to Cu/Zn superoxide dismutase (SOD) under the influence of hydrophobic forces, which causes alteration in the tyrosine kinase and secondary structure of the protein. The activity of SOD is inhibited causing oxidative damage to the cell [108, 109].

8.7.3 Elevated Intracellular Ca^{2+} Levels

Apart from the above-mentioned mechanisms, dysregulation of cellular calcium homeostasis also plays a pivotal role in QDs toxicity. Ca^{2+} are the most significant second messenger molecules in eukaryotic cells which are responsible for the regulation of cellular function by activating different protein kinases involved in biological processes such as ROS generation, cellular proliferation, differentiation, and apoptosis [109]. It was reported that CdSe QDs triggered elevation of cytoplasmic calcium levels in primary cultured hippocampal neurons, which impaired the function of voltage-gated sodium ion channels that ultimately disrupted the electrical activity and augmented neuro-toxicological damage [110]. Richter et al. showed that increase in intracellular calcium levels impaired mitochondrial membrane permeability (MMP), caused the release of free cytochrome c, and initiated apoptosis [109]. Moreover, it has been studied that CdTe QDs induced a 7.4-fold elevation in Ca^{2+} levels that was facilitated by ROS generation. Meantime, high concentration of calcium further boosts ROS production and depletes oxidative stress [111]. Analogously, CdSe/ZnS QDs led to increased calcium levels in L02 cells, which mediated mitochondrial ROS generation and triggered formation of NLRP3 inflammasomes [112].

8.8 Absorption, Distribution, Metabolism, and Excretion of QDs In Vivo

Pharmacokinetics helps to assess the disposition of the drug within an organism by the four phases it traverses: absorption, distribution, metabolism, and excretion (ADME). Literature suggests that QDs can be systemically circulated and may accumulate in the tissues and organs. The ADME of QDs is highly variable owing to the extensive variation in their physicochemical properties. The stability, size, surface charge,

concentration, and the shell/outer coating and its bioactivity, each contributes to the possible toxicity of the QDs and also to their ADME characteristics. Physicochemical properties in conjunction with microenvironmental factors and QD stability (oxidative and photolytic lability) together make a paradigm shift in the way ADME characteristics of QDs behave as it can be highly variable and extremely difficult to predict.

Elimination of QDs from the system largely depends on the excretory mechanisms and the metabolic processes involved, along with the in vivo bioactivity, all of which are poorly understood and need to be evaluated. In vivo data suggests that, irrespective of the specificity of QDs, they are recognized as foreign by the vertebrate system and are eliminated via the primary excretory organs/systems: mainly liver, lymphatic systems, and spleen. However, this is a gross generalization, and plenty of inconsistencies exist in the published literature, such as subcutaneous injection of CdSe/ZnS-PEG-coated QDs in mice showed clearance of the QDs from the site of injection, with accumulation of QDs in lymph nodes [113]. Distribution kinetics of QDs can be significantly affected by size alone, and the surface coating can further influence the serum half-life and the pattern of accumulation. Since studies are limited, the tissue/organ distribution of QDs appears to be multifactorial, depending on size, core-shell components, and the bioactivity of conjugated or other incorporated functional groups. Nonspecific QDs, especially without specific functionalized groups, are internalized via the endocytic mechanisms by various types of cells, both in vivo and in vitro. Paradoxically, QDs with natural ligands that are specific for certain cell surface receptors and membrane proteins are specific only for that given cell membrane proteins or type of receptor. Nonspecific QDs tend to adhere to cell surfaces, probably via interactions of QD with glycolipids and glycoproteins present in cell membranes. The exact mechanism of toxicity needs elucidation, although innumerable reports indicate the intracellular vesicular trafficking and accumulation of QDs. Variable subcellular localization and systemic distribution exist based on the unique physicochemical properties' dependent on type of QDs. This will definitely prove extremely relevant for developing screening protocols for evaluating QD toxicity based on their characterization, including the size nonuniformity, biofunctional coatings, core-shell conjugates, and surface coating oxidative and photolytic stability [76, 114–116].

8.9 Conclusion and Future Perspectives

Over the last 20 years, emergence of nanotoxicology has attracted attention to address the main issues and to intricately understand the mechanisms of nanomaterials toxicity. The prevalence of QD-related products is increasing rapidly in the market; these products also require further evaluation of toxicity under toxicity standards with safer range for sustainable application. It is essential to thoroughly characterize the QDs with respect to size, activity, and cross-reactivity with various biological biomolecules. The physiochemical properties of QDs such as shape, size, composition, and surface coating after solubilized in suitable biological buffer must be well understood during biocompatibility evaluation. In addition, there is first step to select appropriate test model system, period of exposure, and relevant assay that are also important factors in order to

study the engineered QDs. Therefore, all the toxicity protocols should be validated by alternative methods to assess the accuracy of the experimental outcomes.

The major finding reported in literature described in this chapter highlights concerns toward the genotoxicity, cytotoxicity, and photo-induced toxicity, but this is not limited to QDs size, charge, morphology, and dissolution. There is a need to study the intrusion between QDs and experimental components that may affect the actual toxicity. The key points to summarize are that all QDs are not alike and engineered QDs cannot be considered as a uniform group of nanomaterials. The ADME and toxicity of QDs depend on multiple factors resulting from both the inherent physicochemical properties and the microenvironment. The size, surface charge, concentration, surface coating bioactivity (capping material and functional groups), and mechanical, oxidative, and photolytic stability have been implicated as the critical factors in QD toxicity. Therefore, it is likely that QDs may be grouped or classified as per their possible toxicities depending on the size or other physicochemical properties. We conclude that under certain conditions, QDs may pose hazardous to human health as observed in rodent animal models as well as in in vitro cell cultures.

A few techniques based on predictive computational models, mechanism-centered high-throughput testing, genome arrays, and high-throughput screening are being extensively explored but have not been established in toxicity assay approval. Therefore, in order to prevent and challenge the hazard and risks associated with experiments and associated activities, the regulatory and safety precautions must be implemented. The researchers should harness the full potential of nanotechnology by bridging the gap of nanomedicine, medical science, biomedical engineering, and toxicology for betterment of human beings.

References

1. Reed MA, Randall JN, Aggarwal RJ, Matyi RJ, Moore TM, Wetsel AE (1988) Observation of discrete electronic states in a zero-dimensional semiconductor nanostructure. Phys Rev Lett 60(6):535–537
2. Mukherjee A, Shim Y, Myong Song J (2016) Quantum dot as probe for disease diagnosis and monitoring. Biotechnol J 11(1):31–42
3. Fang M, Peng CW, Pang DW, Li Y (2012) Quantum dots for cancer research: current status, remaining issues, and future perspectives. Cancer Biol Med 9(3):151–163
4. Ehzari H, Safari M, Shahlaei M (2019) A signal amplification by QDs used for ferrocene-labeled sandwich aptasensor for determination of Hg^{2+} in water samples. J Iran Chem Soc 16(12):2555–2564
5. Ehzari H, Safari M, Shahlaei M (2019) A new sensing strategy based on thymine bases– Hg^{2+} Hg^{2+}–methylene blue coordination on the electrospun PES–QDs platform for detection of Hg^{2+} in fruit juice samples. J Iran Chem Soc 16(10):2269–2279
6. Kashani HM, Madrakian T, Afkhami A, Mahjoubi F, Moosavi MA (2019) Bottom-up and green-synthesis route of amino functionalized graphene quantum dot as a novel biocompatible and label-free fluorescence probe for in vitro cellular imaging of human ACHN cell lines. Mater Sci Eng B 251:114452

7. Hoan BT, Thanh TT, Tam PD, Trung NN, Cho S, Pham VH (2019) A green luminescence of lemon derived carbon quantum dots and their applications for sensing of V^{5+} ions. Mater Sci Eng B 251:114455
8. Shen H, Gao Q, Zhang Y, Lin Y, Lin Q, Li Z, Zhang Z (2019) Visible quantum dot light-emitting diodes with simultaneous high brightness and efficiency. Nat Photonics 13(3):192–197
9. Shen X, Jia J, Lin Y, Zhou X (2015) Enhanced performance of CdTe quantum dot sensitized solar cell via anion exchanges. J Power Sources 277:215–221
10. Babentsov V, Sizov F (2008) Defects in quantum dots of IIB–VI semiconductors. Opto-Electron Rev 16(3):208–225
11. Yoffe AD (2001) Semiconductor quantum dots and related systems: electronic, optical, luminescence and related properties of low dimensional systems. Adv Phys 50(1):1–208
12. Nan W, Niu Y, Qin H, Cui F, Yang Y, Lai R et al (2012) Crystal structure control of zinc-blende CdSe/CdS core/shell nanocrystals: synthesis and structure-dependent optical properties. J Am Chem Soc 134(48):19685–19693
13. Cai X, Mirafzal H, Nguyen K, Leppert V, Kelley DF (2012) Spectroscopy of CdTe/CdSe type-II nanostructures: morphology, lattice mismatch, and band-bowing effects. J Phys Chem C 116(14):8118–8127
14. Crooker SA, Barrick T, Hollingsworth JA, Klimov VI (2003) Multiple temperature regimes of radiative decay in CdSe nanocrystal quantum dots: intrinsic limits to the dark-exciton lifetime. Appl Phys Lett 82(17):2793–2795
15. Chin PT, de Mello Donegá C, van Bavel SS, Meskers SC, Sommerdijk NA, Janssen RA (2007) Highly luminescent CdTe/CdSe colloidal heteronanocrystals with temperature-dependent emission color. J Am Chem Soc 129(48):14880–14886
16. Rosenthal SJ, Chang JC, Kovtun O, McBride JR, Tomlinson ID (2011) Biocompatible quantum dots for biological applications. Chem Biol 18(1):10–24
17. Pathak S, Choi S-K, Arnheim N, Thompson ME (2001) Hydroxylated quantum dots as luminescent probes for in situ hybridization. J Am Chem Soc 123:4103–4104. [PubMed: 11457171]
18. Bruchez M Jr, Moronne M, Gin P, Weiss S, Alivisatos AP (1998) Semiconductor nanocrystals as fluorescent biological labels. Science 281:2013–2016. [PubMed: 9748157]
19. Jańczewski D, Tomczak N, Han MY, Vancso GJ (2011) Synthesis of functionalized amphiphilic polymers for coating quantum dots. Nat Protoc 6(10):1546–1553
20. Potapova I, Mruk R, Hübner C, Zentel R, Basché T, Mews A (2005) CdSe/ZnS nanocrystals with dye-functionalized polymer ligands containing many anchor groups. Angew Chem Int Ed 44(16):2437–2440
21. Nikolic MS, Krack M, Aleksandrovic V, Kornowski A, Förster S, Weller H (2006) Tailor-made ligands for biocompatible nanoparticles. Angew Chem Int Ed 45(39):6577–6580
22. Dubertret B, Skourides P, Norris DJ, Noireaux V, Brivanlou AH, Libchaber A (2002) In vivo imaging of quantum dots encapsulated in phospholipid micelles. Science 298(5599):1759–1762
23. Qian J, Gao X (2013) Triblock copolymer-encapsulated nanoparticles with outstanding colloidal stability for siRNA delivery. ACS Appl Mater Interfaces 5(8):2845–2852
24. Schmidtke C, Pöselt E, Ostermann J, Pietsch A, Kloust H, Tran H, Weller H (2013) Amphiphilic, cross-linkable diblock copolymers for multifunctionalized nanoparticles as biological probes. Nanoscale 5(16):7433–7444
25. Anderson RE, Chan WC (2008) Systematic investigation of preparing biocompatible, single, and small ZnS-capped CdSe quantum dots with amphiphilic polymers. ACS Nano 2(7):1341–1352

26. Geidel C, Schmachtel S, Riedinger A, Pfeiffer C, Müllen K, Klapper M, Parak WJ (2011) A general synthetic approach for obtaining cationic and anionic inorganic nanoparticles via encapsulation in amphiphilic copolymers. Small 7(20):2929–2934
27. Luccardini C, Tribet C, Vial F, Marchi-Artzner V, Dahan M (2006) Size, charge, and interactions with giant lipid vesicles of quantum dots coated with an amphiphilic macromolecule. Langmuir 22(5):2304–2310
28. Papagiannaros A, Levchenko T, Hartner W, Mongayt D, Torchilin V (2009) Quantum dots encapsulated in phospholipid micelles for imaging and quantification of tumors in the near-infrared region. Nanomed Nanotechnol Biol Med 5(2):216–224
29. Balasubramanian SK, Poh KW, Ong CN, Kreyling WG, Ong WY, Liya EY (2013) The effect of primary particle size on biodistribution of inhaled gold nano-agglomerates. Biomaterials 34(22):5439–5452
30. Kulkarni SA, Feng SS (2013) Effects of particle size and surface modification on cellular uptake and biodistribution of polymeric nanoparticles for drug delivery. Pharm Res 30(10):2512–2522
31. Duan H, Kuang M, Wang YA (2010) Quantum dots with multivalent and compact polymer coatings for efficient fluorescence resonance energy transfer and self-assembled biotagging. Chem Mater 22(15):4372–4378
32. Drozd D, Zhang H, Goryacheva I, De Saeger S, Beloglazova NV (2019) Silanization of quantum dots: challenges and perspectives. Talanta 205:120164
33. Chen L, Chen C, Li R, Li Y, Liu S (2009) CdTe quantum dot functionalized silica nanosphere labels for ultrasensitive detection of biomarker. ChemComm 19:2670–2672
34. Tan TT, Selvan ST, Zhao L, Gao S, Ying JY (2007) Size control, shape evolution, and silica coating of near-infrared-emitting PbSe quantum dots. Chem Mater 19(13):3112–3117
35. Manshian BB, Abdelmonem AM, Kantner K, Pelaz B, Klapper M, Nardi Tironi C et al (2016) Evaluation of quantum dot cytotoxicity: interpretation of nanoparticle concentrations versus intracellular nanoparticle numbers. Nanotoxicology 10(9):1318–1328
36. Zhang LW, Monteiro-Riviere NA (2009) Mechanisms of quantum dot nanoparticle cellular uptake. Toxicol Sci 110(1):138–155
37. Dubavik A, Sezgin E, Lesnyak V, Gaponik N, Schwille P, Eychmüller A (2012) Penetration of amphiphilic quantum dots through model and cellular plasma membranes. ACS Nano 6(3):2150–2156
38. Liu N, Tang M (2020) Toxic effects and involved molecular pathways of nanoparticles on cells and subcellular organelles. J Appl Toxicol 40(1):16–36
39. Xu L, Dai Y, Wang Z, Zhao J, Li F, White JC, Xing B (2018) Graphene quantum dots in alveolar macrophage: uptake-exocytosis, accumulation in nuclei, nuclear responses and DNA cleavage. Part Fibre Toxicol 15(1):1–17
40. Khan ZU, Uchiyama MK, Khan LU, Araki K, Goto H, Felinto MCFC, Gidlund M (2022) Wide visible-range activatable fluorescence ZnSe: Eu^{3+}/Mn^{2+}@ ZnS quantum dots: local atomic structure order and application as a nanoprobe for bioimaging. J Mater Chem B 10:247–261
41. Liu H, Liu Y, Liu S, Pang DW, Xiao G (2011) Clathrin-mediated endocytosis in living host cells visualized through quantum dot labeling of infectious hematopoietic necrosis virus. J Virol 85(13):6252–6262
42. Zhang F, Guo H, Zhang J, Chen Q, Fang Q (2018) Identification of the caveolae/raft-mediated endocytosis as the primary entry pathway for aquareovirus. Virology 513:195–207
43. Martynenko IV, Kuznetsova VA, Litvinov IK, Orlova AO, Maslov VG, Fedorov AV, Baranov AV (2016) Enantioselective cellular uptake of chiral semiconductor nanocrystals. Nanotechnology 27(7):075102
44. Jiang X, Rocker C, Hafner M, Brandholt S, Dorlich RM, Nienhaus GU (2010) Endo-and exocytosis of zwitterionic quantum dot nanoparticles by live HeLa cells. ACS Nano 4(11):6787–6797

45. Kuo TR, Lee CF, Lin SJ, Dong CY, Chen CC, Tan HY (2011) Studies of intracorneal distribution and cytotoxicity of quantum dots: risk assessment of eye exposure. Chem Res Toxicol 24(2):253–261
46. Tu M, Sun S, Wang K, Peng X, Wang R, Li L et al (2013) Organic cation transporter 1 mediates the uptake of monocrotaline and plays an important role in its hepatotoxicity. Toxicology 311(3):225–230
47. Clift MJ, Brandenberger C, Rothen-Rutishauser B, Brown DM, Stone V (2011) The uptake and intracellular fate of a series of different surface coated quantum dots in vitro. Toxicology 286(1–3):58–68
48. Mahto SK, Park C, Yoon TH, Rhee SW (2010) Assessment of cytocompatibility of surface-modified CdSe/ZnSe quantum dots for BALB/3T3 fibroblast cells. Toxicol In Vitro 24(4):1070–1077
49. Liu Q, Li H, Xia Q, Liu Y, Xiao K (2015) Role of surface charge in determining the biological effects of CdSe/ZnS quantum dots. Int J Nanomedicine 10:7073
50. Lee V, McMahan RS, Hu X, Gao X, Faustman EM, Griffith WC et al (2015) Amphiphilic polymer-coated CdSe/ZnS quantum dots induce pro-inflammatory cytokine expression in mouse lung epithelial cells and macrophages. Nanotoxicology 9(3):336–343
51. Manshian BB, Soenen SJ, Al-Ali A, Brown A, Hondow N, Wills J, Doak SH (2015) Cell type-dependent changes in CdSe/ZnS quantum dot uptake and toxic endpoints. Toxicol Sci 144(2):246–258
52. Ruan G, Agrawal A, Marcus AI, Nie S (2007) Imaging and tracking of tat peptide-conjugated quantum dots in living cells: new insights into nanoparticle uptake, intracellular transport, and vesicle shedding. J Am Chem Soc 129(47):14759–14766
53. Yan M, Zhang Y, Qin H, Liu K, Guo M, Ge Y, Zheng X (2016) Cytotoxicity of CdTe quantum dots in human umbilical vein endothelial cells: the involvement of cellular uptake and induction of pro-apoptotic endoplasmic reticulum stress. Int J Nanomedicine 11:529
54. Jiang S, Lin Y, Yao H, Yang C, Zhang L, Luo B, He C (2018) The role of unfolded protein response and ER-phagy in quantum dots-induced nephrotoxicity: an in vitro and in vivo study. Arch Toxicol 92(4):1421–1434
55. Fan J, Wang S, Zhang X, Chen W, Li Y, Yang P, Ju D (2018) Quantum dots elicit hepatotoxicity through lysosome-dependent autophagy activation and reactive oxygen species production. ACS Biomater Sci Eng 4(4):1418–1427
56. Peng L, He M, Chen B, Wu Q, Zhang Z, Pang D, Hu B (2013) Cellular uptake, elimination and toxicity of CdSe/ZnS quantum dots in HepG2 cells. Biomaterials 34(37):9545–9558
57. Wu C, Shi L, Li Q, Jiang H, Selke M, Ba L, Wang X (2010) Probing the dynamic effect of cys-CdTe quantum dots toward cancer cells in vitro. Chem Res 23(1):82–88
58. Luo YH, Wu SB, Wei YH, Chen YC, Tsai MH, Ho CC, Lin P (2013) Cadmium-based quantum dot induced autophagy formation for cell survival via oxidative stress. Chem Res Toxicol 26(5):662–673
59. Chen N, He Y, Su Y, Li X, Huang Q, Wang H, Fan C (2012) The cytotoxicity of cadmium-based quantum dots. Biomaterials 33(5):1238–1244
60. Dai T, Li N, Liu L, Liu Q, Zhang Y (2015) AMP-conjugated quantum dots: low immunotoxicity both in vitro and in vivo. Nanoscale Res Lett 10(1):1–9
61. McConnachie LA, White CC, Botta D, Zadworny ME, Cox DP, Beyer RP, Kavanagh TJ (2013) Heme oxygenase expression as a biomarker of exposure to amphiphilic polymer-coated CdSe/ZnS quantum dots. Nanotoxicology 7(2):181–191
62. Lovrić J, Bazzi HS, Cuie Y, Fortin GR, Winnik FM, Maysinger D (2005) Differences in subcellular distribution and toxicity of green and red emitting CdTe quantum dots. J Mol Med 83(5):377–385

63. Kendall M, Ding P, Mackay RM, Deb R, McKenzie Z, Kendall K, Clark H (2013) Surfactant protein D (SP-D) alters cellular uptake of particles and nanoparticles. Nanotoxicology 7(5):963–973
64. Chen L, Miao Y, Chen L, Jin P, Zha Y, Chai Y, Wang M (2013) The role of elevated autophagy on the synaptic plasticity impairment caused by CdSe/ZnS quantum dots. Biomaterials 34(38):10172–10181
65. Li Y, Zheng Y, Zhang K, Ying JY, Zink D (2012) Effects of quantum dots on different renal proximal tubule cell models and on gel-free renal tubules generated in vitro. Nanotoxicology 6(2):121–133
66. Soenen SJ, Manshian BB, Aubert T, Himmelreich U, Demeester J, De Smedt SC, Braeckmans K (2014) Cytotoxicity of cadmium-free quantum dots and their use in cell bioimaging. Chem Res Toxicol 27(6):1050–1059
67. Chen T, Li L, Xu G, Wang X, Wang J, Chen Y, Lin G (2018) Cytotoxicity of InP/ZnS quantum dots with different surface functional groups toward two lung-derived cell lines. Front Pharmacol 9:763
68. Brunetti V, Chibli H, Fiammengo R, Galeone A, Malvindi MA, Vecchio G, Pompa PP (2013) InP/ZnS as a safer alternative to CdSe/ZnS core/shell quantum dots: in vitro and in vivo toxicity assessment. Nanoscale 5(1):307–317
69. Buz PT, Duman FD, Erkisa M, Demirci G, Ari F, Ulukaya E, Acar HY (2019) Development of near-infrared region luminescent N-acetyl-L-cysteine-coated Ag_2S quantum dots with differential therapeutic effect. Nanomedicine 14(8):969–987
70. Wu T, Liang X, He K, Wei T, Wang Y, Zou L, Tang M (2019) The role of NLRP3 inflammasome activation in the neuroinflammatory responses to Ag_2Se quantum dots in microglia. Nanoscale 11(43):20820–20836
71. Wang Q, Bao Y, Zhang X, Coxon PR, Jayasooriya UA, Chao Y (2012) Uptake and toxicity studies of poly-acrylic acid functionalized silicon nanoparticles in cultured mammalian cells. Adv Healthc Mater 1(2):189–198
72. Ohta S, Inasawa S, Yamaguchi Y (2012) Real time observation and kinetic modeling of the cellular uptake and removal of silicon quantum dots. Biomaterials 33(18):4639–4645
73. Cao Z, Peng F, Hu Z, Chu B, Zhong Y, Su Y et al (2017) In vitro cellular behaviors and toxicity assays of small-sized fluorescent silicon nanoparticles. Nanoscale 9(22):7602–7611
74. Tomić S, Janjetović K, Mihajlović D, Milenković M, Kravić-Stevović T, Marković Z, Trajković V (2017) Graphene quantum dots suppress proinflammatory T cell responses via autophagy-dependent induction of tolerogenic dendritic cells. Biomaterials 146:13–28
75. Mansur AA, Mansur HS, De Carvalho SM, Lobato ZI, Guedes MI, Leite MF (2016) Surface biofunctionalized CdS and ZnS quantum dot nanoconjugates for nanomedicine and oncology: to be or not to be nanotoxic? Int J Nanomedicine 11:4669–4690
76. Zhang Y, Zhang Y, Hong G, He W, Zhou K, Yang K, Wang Q (2013) Biodistribution, pharmacokinetics and toxicology of Ag_2S near-infrared quantum dots in mice. Biomaterials 34(14):3639–3646
77. Lin CH, Yang MH, Chang LW, Yang CS, Chang H, Chang WH, Lin P (2011) Cd/Se/Te-based quantum dot 705 modulated redox homeostasis with hepatotoxicity in mice. Nanotoxicology 5(4):650–663
78. Roberts JR, Antonini JM, Porter DW, Chapman RS, Scabilloni JF, Young SH, Mercer RR (2013) Lung toxicity and biodistribution of Cd/Se-ZnS quantum dots with different surface functional groups after pulmonary exposure in rats. Part Fibre Toxicol 10(1):1–17
79. Ho CC, Chang H, Tsai HT, Tsai MH, Yang CS, Ling YC, Lin P (2013) Quantum dot 705, a cadmium-based nanoparticle, induces persistent inflammation and granuloma formation in the mouse lung. Nanotoxicology 7(1):105–115

80. Kermanizadeh A, Balharry D, Wallin H, Loft S, Møller P (2015) Nanomaterial translocation–the biokinetics, tissue accumulation, toxicity and fate of materials in secondary organs–a review. Crit Rev Toxicol 45(10):837–872
81. Ye L, Yong KT, Liu L, Roy I, Hu R, Zhu J, Prasad PN (2012) A pilot study in non-human primates shows no adverse response to intravenous injection of quantum dots. Nat Nanotechnol 7(7):453–458
82. Tang H, Yang ST, Yang YF, Ke DM, Liu JH, Chen X, Liu Y (2016) Blood clearance, distribution, transformation, excretion, and toxicity of near-infrared quantum dots Ag2Se in mice. ACS Appl Mater Interfaces 8(28):17859–17869
83. Banerjee R, Goswami P, Chakrabarti M, Chakraborty D, Mukherjee A, Mukherjee A (2021) Cadmium selenide (CdSe) quantum dots cause genotoxicity and oxidative stress in Allium cepa plants. Mutat Res Genet Toxicol Environ Mutagen 865:503338
84. Manshian BB, Soenen SJ, Brown A, Hondow N, Wills J, Jenkins GJ, Doak SH (2016) Genotoxic capacity of Cd/Se semiconductor quantum dots with differing surface chemistries. Mutagenesis 31(1):97–106
85. Nagy A, Hollingsworth JA, Hu B, Steinbruck A, Stark PC, Rios Valdez C, Iyer R (2013) Functionalization-dependent induction of cellular survival pathways by CdSe quantum dots in primary normal human bronchial epithelial cells. ACS Nano 7(10):8397–8411
86. Tyagi A, Rawat K, Verma AK, Bohidar HB (2016) Mechanistic evaluation of the size dependent antimicrobial activity of water soluble QDs. Anal Methods 8(5):1060–1068
87. Alaraby M, Demir E, Hernández A, Marcos R (2015) Assessing potential harmful effects of CdSe quantum dots by using Drosophila melanogaster as in vivo model. Sci Total Environ 530:66–75
88. Derfus AM, Chan WC, Bhatia SN (2004) Probing the cytotoxicity of semiconductor quantum dots. Nano Lett 4(1):11–18
89. Dussert F, Wegner KD, Moriscot C, Gallet B, Jouneau PH, Reiss P, Carriere M (2021) Evaluation of the dermal toxicity of InZnP quantum dots before and after accelerated weathering: toward a safer-by-design strategy. Front Toxicol 3:6
90. Cai M, Ding C, Cao X, Wang F, Zhang C, Xian Y (2019) Label-free fluorometric assay for cytochrome c in apoptotic cells based on near infrared Ag_2S quantum dots. Anal Chim Acta 1056:153–160
91. Bhanoth S, Kshirsagar A, Khanna PK, Tyagi A, Leekha A, Kumar V, Verma A (2017) Synthesis, characterization and bio-evaluation of core-shell QDs with ZnSe, CdS and CdSe combinations. Adv Mater Lett 8(4):352–361
92. Pathakoti K, Hwang HM, Wang X, Aker WG (2013) Photoinduced toxicity of CdSe/ZnS quantum dots with different surface coatings to Escherichia coli. Int J Nanotechnol 10(12):1093–1108
93. Bellanger X, Schneider R, Dezanet C, Arroua B, Balan L, Billard P, Merlin C (2020) Zn^{2+} leakage and photo-induced reactive oxidative species do not explain the full toxicity of ZnO core quantum dots. J Hazard Mater 396:122616
94. Tang S, Allagadda V, Chibli H, Nadeau JL, Mayer GD (2013) Comparison of cytotoxicity and expression of metal regulatory genes in zebrafish (Danio rerio) liver cells exposed to cadmium sulfate, zinc sulfate and quantum dots. Metallomics 5(10):1411–1422
95. Nguyen KC, Rippstein P, Tayabali AF, Willmore WG (2015) Mitochondrial toxicity of cadmium telluride quantum dot nanoparticles in mammalian hepatocytes. Toxicol Sci 146(1):31–42
96. Lai L, Li YP, Mei P, Chen W, Jiang FL, Liu Y (2016) Size effects on the interaction of QDs with the mitochondrial membrane in vitro. Mol Membr Biol 249(6):757–767

97. Khalil WKB, Girgis E, Emam AN, Mohamed MB, Rao KV (2011) Genotoxicity evaluation of nanomaterials: DNA damage, micronuclei, and 8-hydroxy-2-deoxyguanosine induced by magnetic doped CdSe quantum dots in male mice. Chem Res Toxicol 24(5):640–650
98. Tyagi A, Kumari N, Leekha A, Mittal D, Verma AK (2019) Core shell quantum dots induced apoptosis in human hepatocellular carcinoma cells via reactive oxygen species-mediated mitochondrial-dependent pathway. Int J Life Sci Res 7:518–530
99. Oetiker N, Muñoz-Villagrán C, Vásquez CC, Bravo D, Pérez-Donoso JM (2021) Bacterial phototoxicity of biomimetic CdTe-GSH quantum dots. J Appl Microbiol 131(1):155–168
100. Yaghini E, Turner H, Pilling A, Naasani I, MacRobert AJ (2018) In vivo biodistribution and toxicology studies of cadmium-free indium-based quantum dot nanoparticles in a rat model. Nanomed Nanotechnol Biol Med 14(8):2644–2655
101. Katubi KM, Alzahrani FM, Ali D, Alarifi S (2019) Dose-and duration-dependent cytotoxicity and genotoxicity in human hepato carcinoma cells due to CdTe QDs exposure. Hum Exp Toxicol 38(8):914–926
102. Anas A, Akita H, Harashima H, Itoh T, Ishikawa M, Biju V (2008) Photosensitized breakage and damage of DNA by CdSe− ZnS quantum dots. J Phys Chem 112(32):10005–10011
103. Peynshaert K, Soenen SJ, Manshian BB, Doak SH, Braeckmans K, De Smedt SC, Remaut K (2017) Coating of quantum dots strongly defines their effect on lysosomal health and autophagy. Acta Biomater 48:195–205
104. Zou W, Li L, Chen Y, Chen T, Yang Z, Wang J, Wang X (2019) In vivo toxicity evaluation of PEGylated $CuInS_2$/ZnS quantum dots in BALB/c mice. Front Pharmacol 10:437
105. Nifontova G, Ramos-Gomes F, Baryshnikova M, Alves F, Nabiev I, Sukhanova A (2019) Cancer cell targeting with functionalized quantum dot-encoded polyelectrolyte microcapsules. Front Chem 7:34
106. Wang M, Wang J, Sun H, Han S, Feng S, Shi L, Sun Z (2016) Time-dependent toxicity of cadmium telluride quantum dots on liver and kidneys in mice: histopathological changes with elevated free cadmium ions and hydroxyl radicals. Int J Nanomedicine 11:2319
107. Mo D, Hu L, Zeng G, Chen G, Wan J, Yu Z, Cheng M (2017) Cadmium-containing quantum dots: properties, applications, and toxicity. Appl Microbiol Biotechnol 101:2713–2733
108. Sun H, Cui E, Liu R (2015) Molecular mechanism of copper-zinc superoxide dismutase activity change exposed to N-acetyl-L-cysteine- capped CdTe quantum dots-induced oxidative damage in mouse primary hepatocytes and nephrocytes. Environ Sci Pollut Res Int 22:18267–18277
109. Richter M, Vidovic N, Honrath B, Mahavadi P, Dodel R, Dolga AM, Culmsee C (2016) Activation of SK2 channels preserves ER Ca^{2+} homeostasis and protects against ER stress-induced cell death. Cell Death Differ 23(5):814–827
110. Tang M, Xing T, Zeng J, Wang H, Li C, Yin S, Ruan DY (2008) Unmodified CdSe quantum dots induce elevation of cytoplasmic calcium levels and impairment of functional properties of sodium channels in rat primary cultured hippocampal neurons. Environ Health Perspect 116(7):915–922
111. Lu Y, Xu S, Chen H, He M, Deng Y, Cao Z, Zhou Z (2016) CdSe/ZnS quantum dots induce hepatocyte pyroptosis and liver inflammation via NLRP3 inflammasome activation. Biomaterials 90:27–39
112. Bhanoth S, Tyagi A, Verma AK, Khanna PK (2017) Cytotoxicity studies of II-VI semiconductor quantum dots on various cancer cell lines, vol 8, pp 368–376
113. Gopee NV, Roberts DW, Webb P, Cozart CR, Siitonen PH, Warbritton AR, Howard PC (2007) Migration of intradermally injected quantum dots to sentinel organs in mice. Toxicol Sci 98(1):249–257

114. Zhang T, Wang Y, Kong L, Xue Y, Tang M (2015) Threshold dose of three types of quantum dots (QDs) induces oxidative stress triggers DNA damage and apoptosis in mouse fibroblast L929 cells. Int J Environ Res Public Health 12(10):13435–13454
115. Tang H, Yang ST, Ke DM, Yang YF, Liu JH, Chen X, Liu Y (2017) Biological behaviors and chemical fates of Ag2Se quantum dots in vivo: the effect of surface chemistry. Toxicol Res 6(5):693–704
116. Zhou Y, Zhang Y, Zhong Y, Fu R, Wu S, Wang Q et al (2018) The in vivo targeted molecular imaging of fluorescent silicon nanoparticles in Caenorhabditis elegans. Nano Res 11(5):2336–2346

OceanofPDF.com

Part II
Material Technology

OceanofPDF.com

© The Author(s), under exclusive license to Springer Nature Switzerland AG 2023
G. Korotcenkov (ed.), *Handbook of II-VI Semiconductor-Based Sensors and Radiation Detectors*
https://doi.org/10.1007/978-3-031-19531-0_9

9. Features of Single-Crystal Growth of CdTe and $Cd_{1-x}Zn_xTe$ Compounds Designed for Radiation Detectors

Ghenadii Korotcenkov[1] ✉ and Sergiu Vatavu[1]
(1) Department of Physics and Engineering, Moldova State University, Chisinau, Moldova

Keywords Annealing – Recrystallization – Purification – CdTe – CdZnTe (CZT) – Doping – Indium – Chlorine – Compensation – Segregation – Ingots – Single crystals – Polycrystals – Block crystals – Diameter – Producers of CdZnTe (CdTe) – 5NPlus – Acrorad – CEA-Leti – eV Products – Eurorad – Giredmet

9.1 Introduction

As shown earlier, CdTe and solid solutions based on it $Cd_{1-x}Zn_xTe$ (mainly with $x \approx 0,1$), on the one hand, are one of the key materials for the manufacture of ionizing radiation detectors (Chap. 2, Vol. 3), on the other hand, they are widely used as substrates for growing epitaxial HgCdTe layers for the development of various IR detectors, including photodetector arrays (Chaps. 1–8, Vol. 2). It is important to note that in both cases, the size of the grown single crystals of these compounds is of great importance, since this size determines the number of elements in the matrix of radiation detectors and IR photodetectors and therefore determines many operational characteristics of devices developed on the basis of these matrices.

9.2 Problems of Growing Large Single Crystals

Unfortunately, the problem of growing large high-quality single crystals of the indicated compounds with uniform and reproducible parameters turned out to be a difficult task. According to the authors of [34], the production of single-crystal cadmium telluride even with a crystal diameter of 5–10 mm is already causing serious growth problems. In most attempts to grow large single crystals, block crystals with an increased density of dislocations precipitate, and inclusions were obtained (see Fig. 9.1a). Such polycrystals are unsuitable for the manufacture of radiation detectors intended for practical applications such as various types of tomography described in the Chap. 5 (Vol. 3). For the development of such devices, it is necessary to determine and separate single-crystal blocks from a polycrystal, which can constitute a smaller part of the crystal and from them to manufacture substrates and active elements of radiation detectors. Therefore, in many cases, to obtain monocrystalline blocks of the required size, for example, 20–30 cm^3, one has to follow the path of increasing the mass of grown crystals up to 8–25 kg [39, 44, 47]. Single-crystal blocks used by Kromek to fabricate radiation detectors are shown in Fig. 9.1b. This naturally complicates the manufacturing process of the devices and makes the process more expensive.

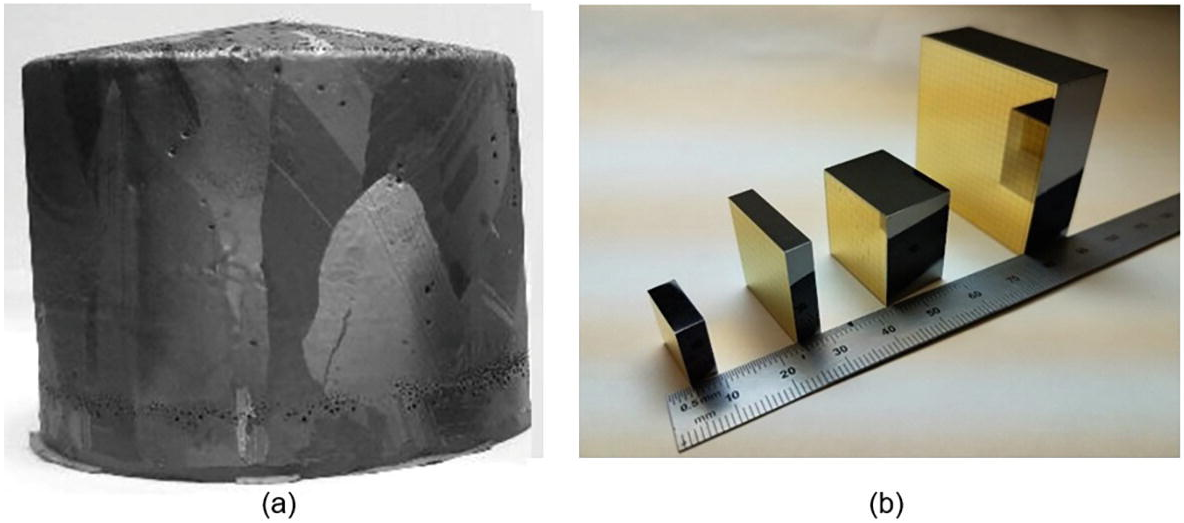

Fig. 9.1 (**a**) Typical 8 in. (~24 kg) CZT ingot grown by the HPB technique at eV Products, Inc. (2011) (reprinted with permission from [39]). Copyright 2018: AIP. (**b**) Kromek monolithic spectroscopic CZT detectors, from left to right: 1 cm × 1 cm × 0.5 cm; 2.2 cm × 2.2 cm × 0.5 cm, 2.2 cm × 2.2 cm × 1.5 cm and 4 cm × 4 cm × 1.5 cm (https://www.kromek.com/cadmium-zinc-telluride-czt/)

The above difficulties are due to the following reasons [2, 35]:

1. Low thermal conductivity of CdTe и $Cd_{1-x}Zn_xTe$, which causes difficulties in controlling the shape of the crystallization front due to heat dissipation during the solidification of the melt [49].

2. High melting point of CdTe и $Cd_{1-x}Zn_xTe$. Therefore, softening quartz tubes become a source of contamination and hinder obtaining the crystals of large diameter [35].

3. Low critical resolved shear stress [36, 49]. As a result, dislocations are easily generated due to the stress from the container and the thermal stress during crystal growth. For this reason, dislocation densities exceeding 10^6 cm^{-2} are usually observed in CdTe and $Cd_{1-x}Zn_xTe$ crystals.

4. The tendency to twinning due to low stacking fault energy [51]. Therefore, twinning may take place easily due to the temperature fluctuation during crystal growth.

5. Segregation of Cd, Zn, and especially Te at block boundaries and the presence of Te inclusions [42, 54]. Precipitation of the excess component occurs in crystal areas where the solubility limit is exceeded. The density of Te inclusions in CdZnTe crystals can vary depending on the synthesis conditions from ≈20 cm^{-3} [13] to $1 \cdot 10^3$–$8 \cdot 10^3$ cm^{-3} in CZT crystals grown by the Bridgman method [54].

Strict requirements for the electrical properties of single crystals create additional problems during their growth [35]. The main characteristic that indirectly indicates the good detector quality of CdTe and CZT is the value, equal to the multiplication of the carrier mobility by the lifetime, $\mu \cdot \tau$. In zinc and cadmium tellurides, the mobility of electrons is significantly higher than that of holes; therefore, for radiation detectors of spectrometric quality with an energy resolution of ≈1%, crystals with n-type conductivity and $\mu_e \cdot \tau$ equal $\approx 1.3 \cdot 10^{-2}$ cm^2/V are required [13]. Nevertheless, the problem of obtaining such materials has not been completely solved. The requirement for high electrophysical characteristics can be met only on

perfect twin-free single-crystal samples [13]. In addition, the twin boundary distorts the electric field distribution in CdZnTe detectors [14]. In block materials, mechanical strains also arise due to the difference in the specific volumes of coexisting phases. These strains in the two-phase region stimulate the migration of atoms and, thus, contribute to the polygonization of dislocations and the formation of a cellular microstructure [21]. In addition, the material used in radiation detectors must be high resistance. Typically, a resistance of the order of 10^{10} Ohm·cm is required. To achieve the required parameters of the radiation detectors, it is necessary to maintain a very low concentration of free charge carriers (10^5–10^6 cm^3), charge carrier traps, recombination centers in the grown single crystals, and impurities, responsible for shallow levels. Compensation with the opposite type of impurity is not very good, since it reduces the mobility of charge carriers. Therefore, achieving these parameters requires very good control over the purity and stoichiometry of the material. For example, for the manufacture of high-quality detectors, the contamination level of the initial components Cd, Zn, and Te should not exceed a few ppm. The concentration of radioactive elements should also be kept as low as possible to reduce the background of the detector. Therefore, for the synthesis of crystals, high-purity components Cd, Zn, and Te with a purity of 6 N – 7 N (99,9999–99,99,999%) are required. The presence of phase transitions that worsen the microstructure of crystals also contributes to the instability and non-reproducibility of the electrophysical properties. In addition, one should not forget that very often detector crystals or detector arrays are rather large. For obvious reasons, the properties of the crystal should be the same throughout the volume. When using a ternary crystal, a homogeneous composition is also required [35]. In addition, the issue of mechanical processing of these materials to obtain sensitive elements of the detector has not been resolved. Due to the low hardness and high brittleness of the CdTe and CdZnTe, large losses occur during machining processing, including cutting, grinding, and polishing of a single crystal. In view of the above problems, the prices for these crystals of detector quality were very high, which naturally hindered their widespread use. Therefore, in the last two decades, tremendous efforts have been made in the development of technologies for the growth of these crystals. Because of numerous studies, the quality of CdTe and CZT crystals has been undoubtedly improved: Crystals of larger diameter, lower cost, with less inclusions and greater

homogeneity were grown, which made it possible to manufacture monolithic spectroscopic CZT radiation detectors of larger and larger sizes. eV Products reported that their technology allows the production of spectrometric quality CdZnTe samples with a size of 80 × 80 mm^2 and a thickness of 5 mm. At smaller sizes, the thickness of single-crystal CZT reaches 15 mm. With the growing market for medical imaging applications and increased productivity, crystal prices have dropped significantly over the past decade, and we hope prices will continue to fall and CdTe- and CZT-based radiation detectors will become more popular. Currently, the average CZT price reaches $250 for wafers with the size 10 × 10 × 1 mm and more than $2000 for 1 cm^3 (https://www.mtixtl.com/cztsubstrates.aspx). However, even at these prices, the use of CdTe and CZT is often worth the cost.

9.3 Features of Growing Single Crystals of CdTe and $Cd_{1-x}Zn_xTe$

Currently, several technologies have been developed that make it possible to grow CdTe и $Cd_{1-x}Zn_xTe$ single crystals of an acceptable size [12, 35, 50]. These are as follows:

1. Growing from the vapor phase either by sublimation or by chemical vapor transport
2. Growing from off-stoichiometric melt or growing from tellurium solution – melt; and
3. Growing from “stoichiometric” melt (melt-growth)

9.3.1 Vapor-Phase Growing Method

Vapor-phase growing methods can be roughly divided into non-seeding methods, the Piper-Polich’s method [38], and seeding methods, the Markov-Davydov’s method [30, 31]. The advantage of this method is the elimination of the influence of the container walls on the growth of the single crystal. Besides, this technology can be applied to any compound that readily sublimates below its melting point. This method was used to obtain

CdTe crystals 50 mm in diameter, 250–300 g in weight and with a dislocation density of $7 \cdot 10^4$ cm^2 [8], as well as CdZnTe crystals with a diameter of 50 mm with a resistance of $8 \cdot 10^{10}$ Ohm·cm [32]. The advantage of all vapor-phase methods of growing II–VI compounds is the low temperature, which is usually 250–400°C below the melting point. Thus, the tendency towards twinning and fouling is greatly reduced. Another good thing about these methods is the "self-purification" effect. The impurities, which are less volatile than the crystallizing compound, remain at the place of the source material [35]. At present, the method of growing CdZnTe crystals from the vapor phase (CVD, chemical vapor deposition) is used in Kromek (Great Britain) and NII Materialovedeniya (Zelenograd, Russia).

The disadvantage of this method is the use of monocrystalline large-diameter seed plates such as CdZnTe, which are expensive and scarce. An attempt to use more affordable and cheaper GaAs seed plates leads to contamination of CdTe with gallium to a level of $2 \cdot 10^{15}$ cm^{-3} [34], the appearance of electron traps, and a reduction in the carrier lifetime. Such crystal parameters limit their application in the development of radiation detectors.

In [11, 23], the method of growing CdTe single crystals on germanium single-crystal seed plates 100 mm in diameter was applied. Single crystals were characterized by a resistance of over 10^9 Ohm·cm. However, germanium creates a deep level in the band gap of CdTe; therefore, a good quantum efficiency of the material was achieved only at energies up to 40 keV and with a layer thickness not exceeding several hundred microns.

In addition, the method of growing from the vapor phase leads to obtaining strained crystals, with the presence of tellurium inclusions in them [41]. Low growth rates lead also to problems of dislocation equilibrium and the formation of grain boundaries, which is the main disadvantage of this growth method. For example, Mullins et al. [34] reported that the growth of monocrystalline CdTe on 50 mm diameter GaAs seed plates was carried out with growth rates of ∼120 μm/h. There are also significant limitations to growing thick monocrystals. According to Cantwell et al. [11], the maximum CdTe thickness did not exceed 1–4 mm.

9.3.2 Growing from Tellurium Solution-Melt

In this group, the main method is the traveling heater method (THM), which is a vertical version of the zone melting method in a temperature

gradient [12, 13]. The zone of hot liquid travels slowly (a few millimeters per day) along a batch of previously synthesized polycrystalline material. The use of low temperatures during growth has a positive effect on the structural perfection and purity of crystals. That is why the first high-quality single crystals of cadmium telluride with a low concentration of free carriers, high values of mobility, and lifetime of charge carriers were obtained from a solution-melt [16, 22]. The high purity of crystals grown with THM is the result of the purification effect of the moving zone of melt. However, for a long time, it was not possible to obtain a crystal with a diameter greater than 10–32 mm. Only in 2008 in Japan [43], using the crystallization of CdTe from a tellurium solution-melt by the THM method, single crystals with a diameter of 100 mm, a length of 300 mm, and a mass of 15 kg were obtained. These developments were carried out at Acrorad (Japan, www.acrorad.co.jp). The obtained single crystals had the value $\mu \cdot \tau$ (multiplication of mobility to lifetime of charge carriers, transport characteristic) for electrons ~$2 \cdot 10^{-3}$ cm^2/V and for the holes ~$2 \cdot 10^{-4}$ cm^2/V. These are good parameters indicating a high degree of macrohomogeneity and a high level of material purity. Redlen (Canada) also reported on the success of growing CZT crystals using the THM method [13]. By modifying the THM method, they grew a CZT crystal with a diameter of 75 mm (Fig. 9.2a) of which 80% was a single crystal. They have also successfully produced near 100% single-crystal ingots (see Fig. 9.2b). In addition, they have also increased the thickness of sliced CZT wafers from 6 to 12 mm, allowing the production of 10-mm-thick detectors. The obtained $\mu \cdot \tau_e$ value for these crystals was $1.3 \cdot 10^{-2}$ cm^2/V. THM method is also used in 5NPlus (Canada, www.5nplus.com/) [3].

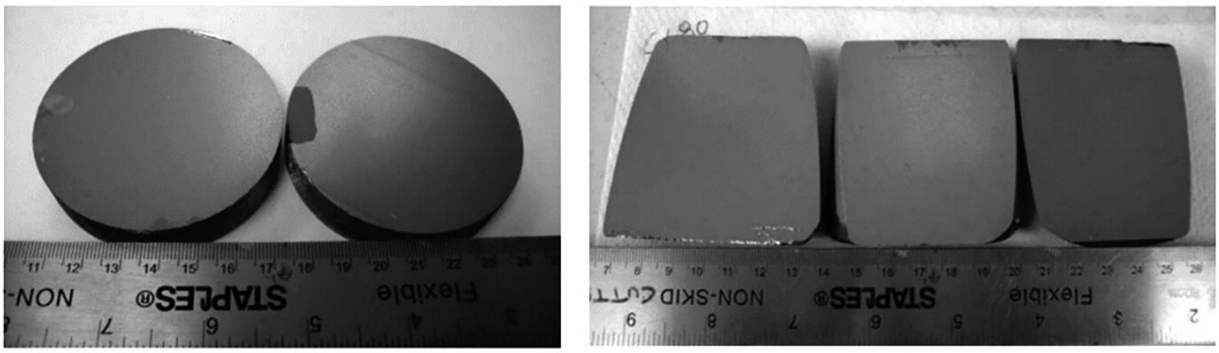

(a) (b)

Fig. 9.2 (**a**) Typical singularity (~80%) in the current Redlen 75 mm diameter THM CZT ingots. (**b**) 100% single crystals cut from a 75 mm diameter CZT ingot along the direction of their growth (reprinted with permission from [13]. Copyright 2008: AIP)

With regard to earlier reports such as [37], where it was reported about the growth of crystals with a diameter of up to 300 mm, these crystals were polycrystals. They were grown from a tellurium solution-melt by evaporation of Te. In this method, CdTe and CdZnTe were doped with both chlorine and aluminum, and the growth itself was carried out in open crucibles with a diameter of 65–300 mm. The resulting large polycrystal was characterized by good transport characteristics: $\mu\tau_e = 3 \cdot 10^{-3}$ cm^2/V and $\mu_e = 1020$ cm^2/V·s, high resistance (10^9–10^{10} Ohm·cm), and an insignificant amount of tellurium inclusions in crystals with a size of 20–25 μm [37]. The authors themselves note that the above method requires many refinements and optimizations, due to the fact that the thickness of the ingot is on average ~5 mm, and although the crystal has a diameter of 300 mm (see Fig. 9.3), this crystal is a polycrystal, not a single crystal. However, the same studies have shown that even such materials, with a corresponding improvement in the growing technology and optimization of the modes of subsequent heat treatment, can be used for the manufacture of radiation sensors. These works were conducted at CEA-Leti (France) [6, 52]. The CEA-Leti method for growing CdTe and CdZnTe crystals has been named “Process by Solvent Evaporation” (PBSE). The authors believe this method is scalable to large sizes. Its advantages include the ability of this method to produce a single-crystal wafer that matches the thickness required for device applications.

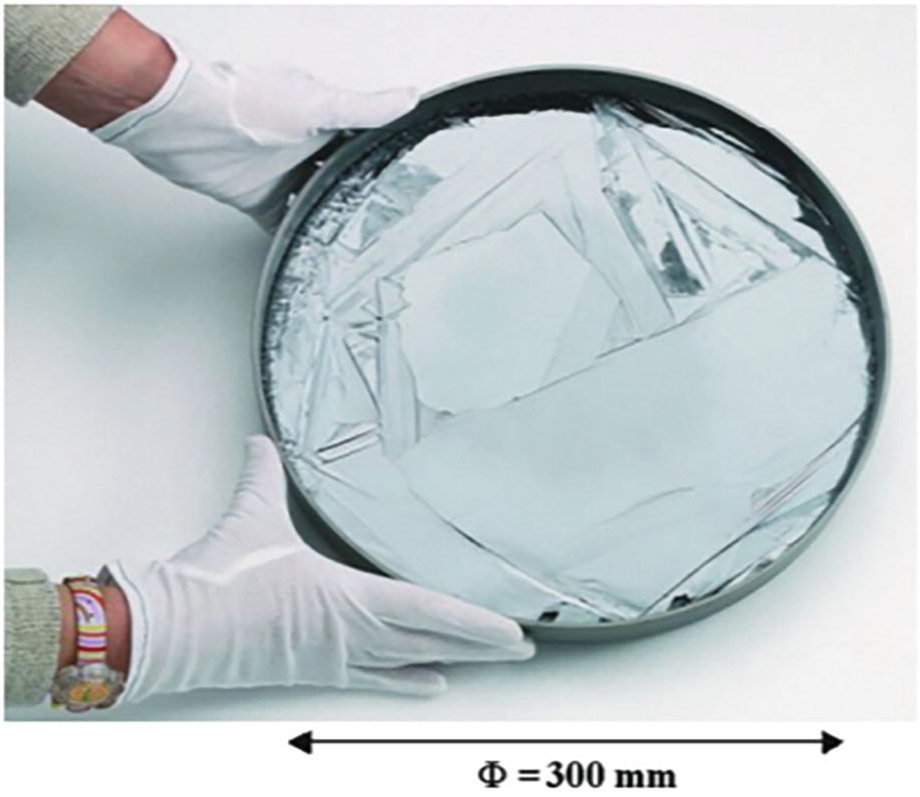

Fig. 9.3 A 300 mm diameter as-grown PBSE CdTe plate (thickness 1–10 mm) (Reprinted with permission from [52]. Copyright 2007: Elsevier)

It should be noted that CdTe and CdZnTe crystals grown using the conventional solution-melt method are usually characterized by a large number of tellurium precipitates and inclusions caused by the release of excess Te in the solid phase during cooling [57]. CdZnTe also suffers from compositional inhomogeneity due to the higher segregation coefficient of Zn. Serious problems caused by the presence of extended defects in CdZnTe crystals grown from a solution-melt are also noted by the authors of the work [7]. Low growth rate is a disadvantage of the tellurium solution-melt growth method as well. The need for additional annealing of the wafers to prevent the formation of large inclusions in crystals grown from solution is another disadvantage of this method [55]. This additional processing further increases the growth time. However, adding as low as 2% (atomic) Se into CdZnTe matrix during crystal growth was found to successfully mitigate many performance-limiting defects and provide improved compositional homogeneity [40].

9.3.3 Melt Growing

The most common method for growing CdTe and CdZnTe single crystals is a growth from a stoichiometric melt [50]. This method has the largest number of options. To obtain large single crystals of CdTe and CdZnTe, the Bridgman method in vertical (VB) and horizontal (HB) versions and the Obreimov-Shubnikov method are used. The difference between the Bridgman method and the Obreimov-Shubnikov method is that in Bridgman, the ampoule with the melt moves in a temperature gradient, while in the Obreimov-Shubnikov method, the melt is cooled in a temperature gradient. Therefore, this method is called the vertical gradient freezing (VGF) method [1, 2]. The zone melting (ZM) method used to obtain CdTe and CdZnTe crystals also refers to the processes of growing single crystals from a melt.

As for the classical Czochralski method, which makes it possible to grow large dislocation-free silicon and germanium single crystals from a melt, it turned out that this method is fundamentally inapplicable to cadmium telluride crystals and solid solutions based on it [50]. Due to the reasons stated earlier, the high volatility and incongruent evaporation in CdTe and $Cd_{1-x}Zn_xTe$, when growing these crystals by the Czochralski method at high axial temperature gradients (150–450°C/cm), it is not possible to achieve a convex crystallization front [49]. The result is a polycrystal with many grain boundaries and twins [20].

It is important to note that all of these methods are varieties of the directional crystallization technique. Such crystallization is defined by exterior factors: by the motion of container with crystal and melt concerning the furnace (usually with constant velocity V) and by the temperature distribution. With directional crystallization, the front slowly moves along the molten system, and a single crystal grows behind the front. Because of the predominant removal of heat in one direction, directional crystallization of the melt occurs. The directional crystallization process is usually described in terms of diffusion supercooling or concentration supercooling. The process can be carried out in vertical and horizontal versions and belongs to the group of methods, which are characterized by the presence of only one interface between the liquid and solid phases during the crystallization process. The growth of CdTe and $Cd_{1-x}Zn_xTe$ single crystals from the melt by the directed crystallization method takes significantly less time compared to the growth from the solution-melt method.

9.3.3.1 Bridgman Method

The Bridgman method is the most common method for growing CdTe and $Cd_{1-x}Zn_xTe$ crystals. It can be realized both vertically and horizontally [12, 50]. In both cases, the crystal grows out of the melt, moving it along a region with a temperature gradient that extends from top to bottom from the melting point. It is believed that higher-quality single crystals can be obtained with horizontal growth. However, the vertical version makes it possible to grow a crystal with a shape more suitable for further use in the manufacture of large-diameter substrates and large-volume radiation sensor elements. The vertical version of this technique is shown in Fig. 9.4a.

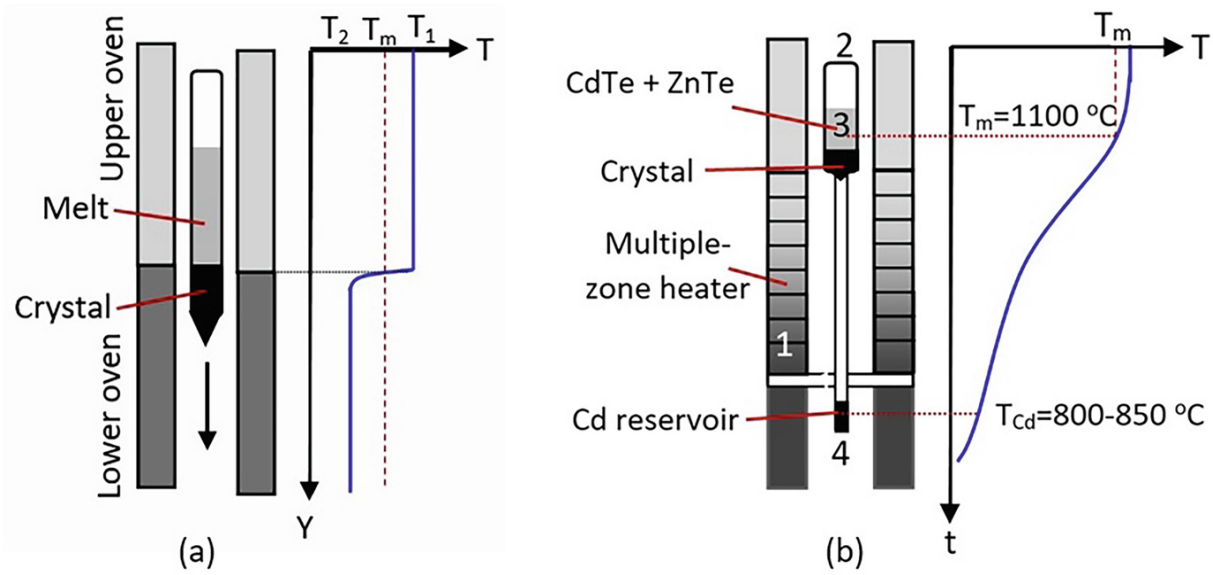

Fig. 9.4 (**a**) CdTe crystal growth by vertical and horizontal Bridgman with cadmium vapor pressure control. Constant vapor pressure keeps constant liquid composition and balanced amounts of cadmium and tellurium within the crystal. (**b**) Schematic diagram of the vertical gradient freezing furnace used by Asahi et al. [2] for synthesis of CZT by VGF method (modified Bridgman method). Section 1, multiple-zone heater. The temperature distribution during crystal growth was precisely controlled; 2, quartz ampoule. The sealed ampoules were set in the furnace, and the source materials were heated up at a higher temperature than the melting point; 3, CdTe+ZnTe; 4, Cd reservoir. The temperature of the Cd reservoir was controlled at 785–850°C. The ampoule was loaded with pre-synthesized polycrystalline CdTe and ZnTe. The axial temperature gradient near the crucible was controlled to lower than 10°C/cm, and the cooling rate was lower than l°C/h during crystal growth. After solidification, the ampoules were cooled with a rate of about 100°C/h (idea from Asahi et al. [2])

The growth can take place by mechanically moving the ampoule or moving a heating furnace. However, the introduction into the process of moving the ampoule leads to an undesirable effect, which can lead to a

violation of the stability of growth and, as a consequence, to the appearance of microinhomogeneity and a decrease in the percentage of the single-crystal yield. Therefore, in modern systems, as it is shown in Fig. 9.4b, the furnace consists of many heating zones [56], and the temperature profile is controlled by a computer. The computer changes the profile electronically, and there are no mechanically moving parts inside the furnace [10]. The presence of many heating zones with separately controlled heaters makes it possible to maintain a constant temperature gradient at the crystallization front, reduce overheating of the melt, and provide a more uniform thermal field in the cooling zone of the grown crystal.

Unlike the method of horizontal directional crystallization, the use of a seed in the vertical Bridgman method is difficult due to the lack of visual control of the seed and further growth of the ingot. Therefore, the growing process is usually carried out under conditions of spontaneous nucleation of a solid phase. In this case, the quartz ampoule in which the growth takes place has a pointed end to exclude the formation of a large number of nuclei. Another embodiment of the construction is an ampoule with a “constriction” through which only an embryo of one crystallographic direction grows. However, crystals grown in this way contain, as a rule, several blocks of different sizes, having a random orientation, twins, and other structural defects caused by a high growth rate in the initial period of crystallization of the melt. Plates cut from such crystals, as a rule, at an angle to the growth direction, have a significant degree of inhomogeneity in the distribution of the concentration of zinc telluride over the area.

The use of seeding in the growth of CdTe and $Cd_{1-x}Zn_xTe$ crystals increases the yield of single-crystal ingots [17, 53]. In addition, the implementation of the growth process using a seed allows one to obtain oriented single crystals and to fabricate from their plates, perpendicular to the growth direction with a more perfect structure and less inhomogeneity in composition. However, the use of the method in this version is accompanied by experimental difficulties associated with the choice of the seed, the implementation of the exact orientation of the seed in the ampoule, and the choice of optimal temperature conditions [17]. In addition, there is a risk of complete melting of the seed. This necessitates an increase in the axial temperature gradient, which adversely affects the structural characteristics of the grown crystal. Sun et al. [45] and Grishechkin et al. [17] showed that when optimizing the growth process, it

becomes possible to obtain $Cd_{1-x}Zn_xTe$ crystals with a diameter of up to 100 mm and more, and the volume fraction of a single crystal above 90%.

9.3.3.1.1 Bridgman-Stockbarger Method

The Stockbarger method is an enhanced Bridgman method. Therefore, very often this method is called the Bridgman-Stockbarger method. Stockbarger's technique differs slightly from Bridgman's technique. Both methods use a temperature gradient and a moving crucible. However, the Bridgman method uses a relatively uncontrollable gradient that occurs at the exit of the furnace, while the Stockbarger method introduces in the construction of the furnace a baffle, or shelf, separating two coupled furnaces with temperatures above and below the freezing point of the melt. Stockbarger's modification of the Bridgman technique allows for better control of the temperature gradient at the melt/crystal interface.

9.3.3.1.2 High-Pressure Bridgman Method

Historically, the first commercial technology for growing CdZnTe single crystals is the method of vertical directional crystallization (Bridgman's method) under high pressure of inert gas (HPVB, high-pressure vertical Bridgman; or HPB , high-pressure Bridgman). This method is now widely used by eV Products (USA). Using this method, most of the CdZnTe crystals produced in the world are obtained. Saint-Gobain crystals (USA), Eurorad (France), and Giredmet (Russia) use also this method.

When developing this method, it was assumed that during the growth of CdZnTe crystals at a high pressure of an inert gas, the processes of sublimation and evaporation are suppressed, and therefore, to obtain a single crystal of stoichiometric composition, it is sufficient to accurately weigh the components of the compound in the equiatomic ratio. However, in the process of growing crystals, there is a loss of mass of the melt and depletion of the crystal with cadmium and, as a consequence, the formation of precipitates in it. In addition, it turned out that high pressure stimulates structural imperfection arising in the process of crystal growth. The emerging defects develop in the process of crystal growth, and the resulting ingot has a block structure, i.e., consists of several single-crystal blocks.

As a result, the standard version of the Bridgman method, as a rule, does not provide a consistently high yield of a single-crystal material of spectrometric quality [53]. Only a few works are known where the authors,

using the vertical Bridgman method, obtained the yield of single crystals of large diameter and spectrometric quality of more than 50% [27]. In addition, they reported that grown crystals had a resistivity in the range $(2–9)\cdot10^{10}$ Ohm·cm and a high value of transport characteristic (μ·τ) up to 1×10^{-2} cm^2/V. In Yinnel Tech, Inc. [27], such result was achieved by optimizing the conditions for crystal growth and adding impurities during the growth, which significantly increase the electron lifetime due to the conversion of electrically charged defects into neutral ones. It should be noted that in most works, transport characteristics are on the order of 10^{-3} cm^2/V [53]. However, this method has one very interesting feature. Without using chlorine compensation for defects, this method can be used to obtain semi-insulating single crystals.

9.3.3.1.3 Low-Pressure Bridgman Method

Another technology for obtaining single crystals of solid solutions CdZnTe is the same Bridgman method in a modification with low pressure (Bridgman LP or LPB). When using HPB, the vapor pressure of cadmium at the melting point of CdTe (1092°C) exceeds 10 atm; therefore, the ampoule explosion is highly probable upon direct fusion of the components forming the compound. In addition, the higher the process temperature, the higher the rate of diffusion of impurities from the ampoule and technological equipment. Therefore, an original synthesis method was developed, which allows carrying out the process at a temperature of 300–400°C below the melting point of CdTe. This avoids depressurization of the ampoule and minimizes contamination of the material with impurities from the walls of the container. In this way, it is possible to obtain crystals of higher quality. This technology is developed in Orbotech (Israel), YinneTech (USA), and Letti (France).

When growing large single crystals from a melt, one of the problems is the control of their composition. The growth of a single crystal at a temperature below the melting point leads to concentration overcooling of the melt, which reduces the probability of its nucleation. The presence of precipitates and inclusions (both Cd and Te) in the crystal is also a negative factor associated with a change in the composition of the melt during growth. The most common method for fixing the composition of the melt is by regulating the temperature of the cadmium reservoir located at the “cold” end of the ampoule (see Fig. 9.4b). By changing this temperature,

we get the opportunity to control the required partial pressure of cadmium vapors in the ampoule [1, 2]. To achieve the desired results, the temperature of the cadmium reservoir was usually kept constant throughout the crystal growth process. As a rule, the temperature was chosen in the range from 800 to 850°C. A detailed analysis of the effect of the temperature of the cadmium reservoir on the composition and properties of CdZnTe crystals is given in the work [48]. However, the application of this method is possible only when using complex multi-zone furnaces. When using short single zone large-diameter furnaces [46], the regulation of the composition of the melt in them is not reliable. It should be noted that with an increase in the diameter of the grown crystals, regardless of the design of the devices, the energy consumption increases significantly, which leads to an increase in the cost of the crystals.

9.3.3.2 Vertical Gradient Freezing (VGF) Method or Modified Bridgman Method

A growth method called “vertical gradient freezing method” (VGF) has been described by Asahi et al. [1, 2], as applied to CdZnTe. VGF is a Bridgman method modified so that neither the furnace nor the ampoule containing the crystal moves, and the furnace temperature profile is continuously shifted by proper electronic temperature control depending on position and time in the multi-zone furnace. The absence of the relative movement of the ampoule and furnace ensures more stable conditions at the crystallization front. The second modification was the use of a Cd reservoir outside the crucible made of pyrolytic boron nitride, in which the crystal was growing [4]. Both the crucible and cadmium reservoir were sealed in 1 quartz ampoule, and the pressure of cadmium vapors in the crucible was controlled by the temperature of the cadmium reservoir (the temperature of the appropriate zone of the furnace) in order to regulate the stoichiometry of the melt. It was possible to achieve low concentration of cadmium vacancies. The VGF method minimizes thermal stress on dislocations by using low-temperature gradients, lower growth rates, and post-set cooling rate control to keep thermal stress below the material’s yield strength. Due to the very low thermal conductivity, a low growth rate of 1 mm/h was used.

Using this method, Franc et al. [18] as well as Asahi et al. [1, 2] grew 4-inch (100 mm) diameter CZT single-crystal wafers (see Fig. 9.5a). The

temperature of the Cd source was held at approximately 830°C in order to match the partial pressure of Cd in CZT. A slender space was used in the lower part of the quartz ampoule to provide sufficient distance between the seed and element source. Resistivity in the range of 10^9–10^{10} Ohm·cm was achieved in both not intentionally doped and In-doped crystals. To remove Te inclusions, it was suggested two-step annealing during 24 h.

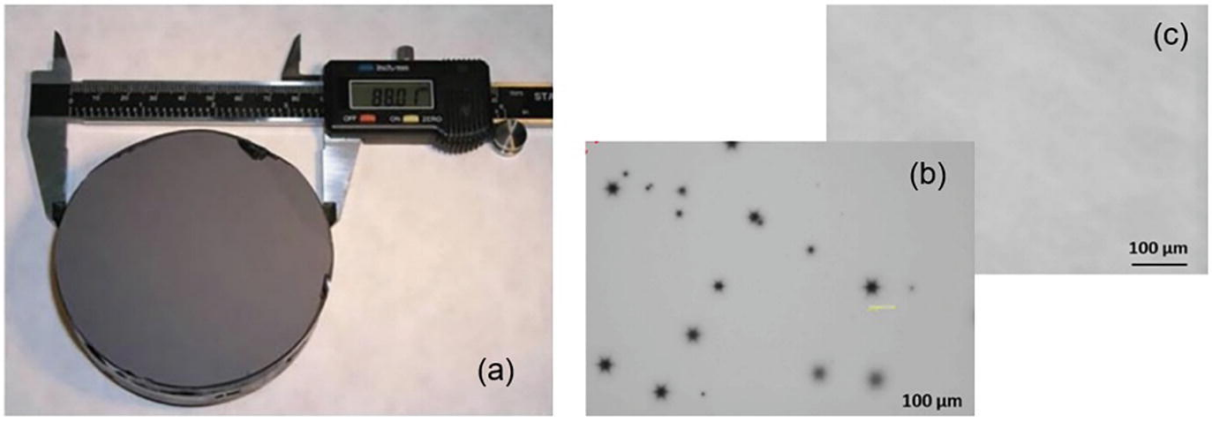

Fig. 9.5 (**a**) CdZnTe crystal (4 inch [100 mm] diameter) prepared in the Institute of Physics, Charles University in Prague by Vertical Gradient Freeze method. (Reprinted with permission from [18]. Copyright 2013: Wiley). (**b**, **c**) IR-microscopy images obtained in transmission mode through CdZnTe wafers: (**b**) without P_{Cd} control, (**c**) with P_{Cd} control. (Reprinted with permission from [9]. Copyright 2014: Springer)

CEA-Leti (www.leti-cea.com) also reported significant progress in growing CZT crystals by VGF [9]. Using accurate determination of the beginning and end of the crystallization stage by carefully monitoring the thermal cycle, single-crystal CZT ingots with a diameter of 80 mm without grain boundary or twin were grown. Subsequently, the size of the CdZnTe ingots was increased to 115 mm in diameter, which made it possible to fabricate large substrates suitable for infrared detector arrays and megapixel-resolution radiation detectors. They also showed that controlling the cadmium partial pressure (P_{Cd}) throughout the thermal cycle is very effective in reducing the size of the second phase particles in the bulk of the material (see Fig. 9.5b).

9.3.3.3 Zone Felting Method

Zone melting is sequential melting. In this process, a narrow melt zone is formed, which then crystallizes when the sample or heater moves relative to each other. The method allows for multiple recrystallization in order to

purify it. As in the case of the Bridgman method, both horizontal (HZM - horizontal zone melting) and vertical zone meltings are possible (VZM). It should be noted that the zone melting principle is used when implementing the THM method described earlier in Sect. 9.3.2. By using the growth of crystals from enriched (Te) melts, the growth temperature in the THM process can be significantly reduced.

Currently, several companies use the zone melting method for growing CdZnTe crystals. In particular, the Institute of Solid State Physics RAS (Chernogolovka, Russia) (www.issp.ac.ru) uses the high-pressure vertical zone melting (HPVZM) method for these purposes [24]. They offer 38 mm diameter CdZnTe crystals with resistivity ~10^{10} Ohm·cm. As a result of research, it was found that any II–VI compound crystal, grown from the melt, has some bubbles due to the permanent melt dissociation. The "bubbles" are in fact voids in the shape of formed or semi-formed negative crystals (in the case of selenides and sulfides) or tellurium inclusions (in case of tellurides). They arise in a molten state in the form of bubbles filled with the vapors of free components (liquid and vapor in the case of Te) and then are captured by the growing crystal. However, the closer the composition is to stoichiometry, the lower the bubble content. In this regard, the HPVZM has an advantage over other methods of growing crystals from the melt.

9.4 Market of CdTe and CdZnTe Crystals

Many manufacturing companies are working on the development of technology for growing CdTe and CdZnTe single crystals. These companies can be conditionally divided into three groups:

1. Manufacturers of a wide range of different materials: MaTeck GmbH (Germany, https://mateck.com/), MTI Corporation (USA, www.mtixtl.com/), NII Materialovedeniya (Zelenograd, Russia, www.niimv.ru/), CEA Leti (France, www.leti-cea.com/); PAM-Xiamen (China, www.powerwaywafer.com)

2. Companies, specializing in the production of ultrapure materials: 5NPlus (Canada, www.5nplus.com) and AO Giredmet (Russia, https://giredmet.ru/)

3. Companies, highly specialized in production technologies of CdTe, ZnTe и CdZnTe: Eurorad (France, www.eurorad.org), Orbotech (Imarad, Israel, www.orbotech.com/), Kromek (GB, www.kromek.com/), eV Products (division of a corporation II-VI, USA, www.evproducts.com), Acrorad (Japan, www.acrorad.co.jp), Redlen (Canada, https://redlen.com)

At the same time, the largest producer of CdZnTe (CdTe) is eV Product. In addition to the previously mentioned firms and institutes, top key players in CdZnTe crystal market are Kunming Physics Institute, Imdetek Co Ltd., Henan Guoxi Ultrapure New Materials Co., Ltd., Northwestern Polytechnical University, Suzhou U King Photoelectric Technology Co., Ltd., and Aselsan.

It is important to note that at present, almost all participants in the CdTe and CdZnTe crystal market have mastered the technology of growing CdTe and CdZnTe crystals with ingot diameters from 50 to 100 mm with parameters acceptable for the production of radiation detectors for various purposes [15, 25, 26]. You can learn more about the achievements of these companies on their websites and in the publications of their employees. The most important achievements have been summarized in this chapter.

9.5 Electrical Conductivity Control

Currently, information on the quality of the manufactured CdTe and CdZnTe crystals and their electrophysical properties is contradictory. CdTe and CdZnTe crystals grown by the same method can have different properties. It turned out that these parameters are significantly affected not only by the preparation method but also by the subsequent processing of the samples. Therefore, let us highlight the most general principles of controlling the parameters of CdTe and CdZnTe crystals.

As noted earlier, CdTe and CdZnTe crystals grown by different methods often had structural imperfections that affect their electrical properties. In addition, CdTe and CdZnTe crystals can deviate from stoichiometry with a corresponding consequence for their properties. As is known, chalcogenes are acceptor impurities in compounds II–VI, and zinc and cadmium are donor impurities [29, 33]. Thus, the deviation of the crystal composition from stoichiometry can lead to the appearance of inclusions and a change in

the electrophysical and optical characteristics of these materials. For example, cadmium excess in pure CdTe transforms it into a medium resistivity, 10^5–10^6 Ohm·cm, n-type material. Tellurium excess transforms it to 10^3–10^5 Ohm·cm p-type material. It should be noted that materials with noticeable deviations from stoichiometry are in all cases partially compensated, and their properties largely depend on the manufacturing conditions. Therefore, as a rule, after the main synthesis process, additional treatments are carried out, which make it possible to significantly improve the structural properties of crystals and remove most of the inclusions from the bulk [18, 50]. Such treatments include:

- Rerecrystallization by the method of zone melting, carried out at a certain pressure of cadmium vapor.
- Heat treatment at temperatures below the melting point in an atmosphere of cadmium vapor under a certain pressure [19]. The change in the properties of the material because of heat treatment is provided by the diffusion of cadmium atoms from the vapor phase into the crystal or from the crystal into the vapor phase (depending on the crystal composition and on the value of the cadmium vapor pressure). In addition, during such heat treatments, abnormal grain growth or secondary recrystallization can also occur, which can improve the single crystallinity of the crystal. However, to achieve such a result, it is necessary to carry out extremely long heat treatments [18]. The lower the heat treatment temperature, the longer the process itself. Sometimes, in order for the crystal to recrystallize and homogenize, annealing for several weeks is required.

In most cases, the processes of synthesis, recrystallization, and subsequent heat treatment are combined in one ampoule, which makes it possible to fast and with minimal costs obtain material of spectrometric quality [53]. Interestingly, the vertical Bridgman method is very often used to improve the properties of crystals obtained by the main competing THM method by repeated recrystallization in a vertical furnace. It is important that the high resistance material can be produced in a single-crystal growth process by appropriately reducing the cadmium vapor pressure during the cooling step. However, the best detectors are obtained by dividing the process into separate growth and annealing stages, tuned for optimal crystal quality and electron characteristics.

Another way to improve the electrophysical parameters of CdTe and CdZnTe crystals is their doping during synthesis. For example, dopants such as Cl, P, As, and In are used to increase the lifetime of electrons and holes created by ionizing radiation [5]. Trivalent atoms, indium or aluminum, act as donors, replacing cadmium atoms in the crystal lattice, while halide atoms act as acceptors, replacing tellurium. It is believed that indium is the best dopant in CZT for compensation of the deep and shallow acceptor trapping centers in CZT materials. Chlorine doping is also a very common procedure [18]. It was shown that doping with chlorine makes it possible to obtain semi-insulating large single crystals of cadmium telluride, suitable for the creation of spectrometric detectors of gamma radiation. This effect takes place due to acceptor complexe formation, self-compensation, and self-purification [28]. However, the studies carried out have shown that chlorine-compensated CdZnTe crystals are insufficiently stable in strong electric fields. This makes it difficult to use them as gamma radiation sensors. Obviously, an increase in the resistivity of crystals should nevertheless be achieved not by chlorine compensation but by a higher degree of material purification from residual impurities and a decrease in the concentration of intrinsic defects. It should also be borne in mind that the introduction of a dopant is accompanied by the appearance of an opposite charged defect, and the carrier concentration should depend on the deviations from stoichiometry.

It should also be taken into account that in the CdTe and CdZnTe crystals grown by the modified Bridgman method, the amounts of cadmium and tellurium are balanced; therefore, the addition of donor impurities such as indium will increase their conductivity. Crystals with uncompensated donors are highly conductive. Annealing of crystals in saturated tellurium vapor at a sufficiently low temperature makes it possible to transfer dopants to a compensated state due to the diffusion of cadmium and tellurium atoms. Moreover, such annealing will not deteriorate the single crystallinity of the material. However, the crystal transforms into a state with high electrical resistance and high sensitivity to gamma radiation. Taking into account that diffusion processes are rather slow at low temperatures, it is recommended to cut the crystal into plates of the required thickness before starting annealing. During annealing, one end of the ampoule should be at a lower temperature in order to avoid condensation of tellurium vapor on the plates during cooling.

Acknowledgments

G.K. and S.V. are grateful to the State Program of the Republic of Moldova (projects 20.80009.5007.02 and 20.80009.5007.12) for supporting their research.

References

1. Asahi T, Oda O, Taniguchi Y, Koyama A (1996) Growth and characterization of 100 mm diameter CdZnTe single crystals by the vertical gradient freezing method. J Crystal Growth 161:20–27
2. Asahi T, Oda O, Taniguchi Y, Koyama A (1995) Characterization of 100 mm diameter CdZnTe single crystals grown by the vertical gradient freezing method. J Crystal Growth 149:23–29
3. Audet N, Guskov VN, Greenberg JH (2005) Traveling heater method preparation and composition analysis of CdTe ingots. J Electron Mater 34(6):687–992
4. Azoulay M, Zilber R, Shusterman S, Goldgirsh A, Zontag I (2003) Growth and csssssssscharacterization of CdTe and CdZnTe crystals for substrate application. Proc SPIE 4820:790–808
5. Belas E, Grill R, Toth AL, Franc J, Moravec P, Horodysky P et al (2005) Electrical and optical properties of in-doped CdTe after CdRich annealing. IEEE Trans Nucl Sci 52(5):1932–1936
6. Bisotto S, Abergel J, Dupont B, Ferron A, Mailliart O, Nicolas JA (2019) 7.5 μm and 5 μm pitch IRFPA developments in MWIR at CEA-Leti. Proc SPIE 11002:110021C
7. Bolotnikov AE, Babalola S, Camarda GS, Chen H, Awadalla S, Cui Y et al (2009) Extended defects in CdZnTe radiation detectors. IEEE Trans Nuclear Sci 56(4):1775–1783
8. Boone J, Cantwell G, Harsch W, Thomas J, Foreman B (1994) Electrical and crystallographic characterization of CdTe grown by the vapor transport method. J Crystal Growth 139:27–36
9. Brellier D, Gout E, Gaude G, Pelenc D, Ballet P, Miguet T, Mamzato MC (2014) Bulk growth of CdZnTe: quality improvement and size increase. J Electron Mater 43:2901–2907
10. Brunet P, Katty A, Schneider D, Tromsoncarli A, Triboulet R (1993) Horizontal Bridgman growth of large high quality $Cd_{1-y}Zn_yTe$ crystals. Mat Sci Eng B 16:44–47
11. Cantwell BJ, Dierre F., Ayoub M, Mullins JT, Pym ITG, Scott PD, et al (2008) Growth of high crystalline quality CdTe layers on 100 mm diameter Ge substrates for room temperature radiation detection. IEEE nuclear science symposium conference record, 19–25 Oct. 2008. Dresden, Germany, pp 146–149
12. Capper P (2011) Bulk growth of Mercury Cadmium Telluride (MCT). In: Capper P, Garland J (eds) Mercury cadmium telluride: growth, properties and applications. Wiley, pp 1–20

13. Chen H, Awadalla SA, Iniewski K, Lu PH, Harris F, Mackenzie J et al (2008) Characterization of large cadmium zinc telluride crystals grown by traveling heater method. J Appl Phys 103:014903
14. Dong J, Jie W, Yu J, Guo R, Teichert C, Gradwohl K-P et al (2018) Twin boundary dominated electric field distribution in CdZnTe detectors. Chinese Phys B 27(11):117202
15. Gasanov A, Naumov A, Kouznetsov M (2018) Domestic crystals manufacturing for devices used in photonics. Part 2 – semicoductor ionizing radiation detectors. Photonics (Russia) 12(5):514–519. (in Russian)
16. Gonzalez R (2005) Spectrometric response of large volume CdZnTe coplanar detectors. IEEE Trans Nucl Sci 52(5):2076–2084
17. Grishechkin MB, Denisov IA, Silina AA, Smirnova NA, Shmatov NI (2014) Investigation of growing conditions of $Cd_{1-x}Zn_xTe$ single crystals ($x \leq 0{,}04$) by the vertical directed crystallization (Bridgman) method. Prikladnaya Fizika 5:72–75 (in Russian)
18. Franc J, Sedivy L, Belas E, Bugar M, Zazvorka J, Pekarek J, Uxa S, Hoschl P, Fesh R (2013) Mealt growth and post-grown annealing of semiinsulating (CdZn)Te by vertical gradient freeze method. Cryst Res Technol 48:214–220
19. Hassani S, Lusson A, Tromson-Carli A, Triboulet R (2003) Seed-free growth of (111) oriented CdTe and CdZnTe crystals by solid-state recrystallization. J Crystal Growth 249:121–127
20. Hobgood HM, Swanson BW, Thomas RN (1987) Czochralski growth of CdTe and CdMnTe from liquid encapsulated melts. J Crystal Growth 85:510–520
21. Ivanov YM, Artemov VV, Kanevsky VM, Polyakov AN, Chudakov VS, Pashaev EM, Senin RA (2004) Production of structurally perfect single crystals of CdTe and CdZnTe. Eur Phys J Appl Phys 27:371–374
22. Ivanov YM (1996) Growth and homogeneity region of CdTe. J Cryst Growth 161:12–15
23. Jiang Q, Haliday DP, Tanner BK, Brinkman AW, Cantwell BJ, Mullins JT, Basu A (2009) Thick epitaxial CdTe films grown by close space sublimation on Ge substrates. J Phys D Appl Phys 42:012004
24. Kolesnikov NN, James RB, Berzigiarova NS, Kulakov MP (2002) HPVB and HPVZM shaped growth of CdZnTe, CdSe and ZnSe crystals. Proc SPIE 4787:93–104
25. Kulchitsky NA, Melnikov AA (2011) Current state of production of CdTe, ZnTe, $Cd_{1-x}Zn_xTe$ and devices based on them. Nano- and Microsystemnaya Technika 6:9–16. (in Russian)
26. Kulchitsky NA, Naumov AV (2010) Review of world markets for cadmium, tellurium and compounds based on them. Tcvetnaya Metalurgia 2:31–44. (in Russian)
27. Li L, Lu F, Shah K, Squillante M, Cirignano L, Yao W et al (2001) A new method for growing detectorgrade cadmium zinc telluride crystals. IEEE Nuclear Science Symposium Conference Record 4(4–10):2396–2400

28. Lindström A, Klintenberg M, Sanyal B, Mirbt S (2015) Cl-doping of Te-rich CdTe: complex formation, self-compensation and self-purification from first principles. AIP Adv 5:087101
29. Marfaing Y (1996) Fundamental studies on compensation mechanisms in II-VI compounds. J Cryst Growth 161(1–4):205–213
30. Markov EV, Davydov AA (1971) Sublimation of CdS crystals. Inorg Mater 7:503–506
31. Markov EV, Davydov AA (1975) Growing of oriented monocrystals of cadmium sulfides from vapor phase. Inorg Mater 11(10):1755–1758
32. Melnikov A, Sigov A, Vorotilov K, Davydov A, Topalova L (1999) Growth of CdZnTe single crystals for radiation detectors. J Cryst Growth 197:666–669
33. Meyer BK, Stadler W (1996) Native defect identification in II-VI materials. J Cryst Growth 161(1–4):119–127
34. Mullins JT, Cantwell BJ, Basu A, Jiang O, Choibey A, Brinkman A (2008) Crystal growth of large-diameter bulk CdTe on GaAs wafer seed plates. J Cryst Growth 310:2058–2061
35. Mycielski A, Szadkowski A, Kaliszek W, Witkowsk B (2021) Very high quality crystals of wide-gap 11-Vt semiconductors: what for? *Proc*. SPIE 4412:38–45
36. Parfeniuk C, Weineberg F, Samarasekera IV, Schvezov C, Li L (1992) Measured critical resolved shear stress and calculated temperature and stress fields during growth of CdZnTe. J Crystal Growth 119:261–270
37. Pelliciari B, Dierre F, Brellier D, Verger L, Glasser F, Schoab B (2005) A new growth method for CdTe: a breakthrough toward large areas. J Electron Mater 34(6):693–698
38. Piper WW, Polich SJ (1961) Vapor-phase growth of single crystals of II-VI compounds. J Appl Phys 32(7):1278–1279
39. Prokesch M, Soldner SA, Sundaram AG (2018) CdZnTe detectors for gamma spectroscopy and x-ray photon counting at 50×10^6 photons/(mm^2 s). J Appl Phys 124:044503
40. Roy UN, Camarda GS, Cui Y, Yang G, James RB (2021) Impact of selenium addition to the cadmium-zinc-telluride matrix for producing high energy resolution X-and gamma-ray detectors. Sci Rep 11:10338
41. Schlesinger TE, Toney JE, Yoon H, Lee EY, Brunett BA, Franks L, James RB (2001) Cadmium zinc telluride and its use as a nuclear radiation detector material. Mater Sci Eng 32:103–189
42. Shin SH, Bajaj J, Mondy LA, Cheng DT (1983) Characterization of Te precipitates in CdTe crystals. Appl Phys Lett 43(1):68–70
43. Shiraki H, Funaki M, Ando Y, Tachibana A, Kominami S, Amemiya K, Ohno R (2010) Improvement of the productivity in the THM growth of CdTe single crystal as nuclear radiation detector. IEEE Trans Nuclear Sci 57(1):395–399

44. Sudharsanan B, Parnham KB, Karam NH (1996) Cadmium zinc telluride detects gamma rays. Laser Focus World 6:199–203
45. Sun S-W, Zhou C-H, Yu H-X, Xu C, Sheng F-F, Sui S-Y et al (2013) Progress in the CdZnTe single crystal growth and substrates fabrication. Proc SPIE 8907:890704
46. Suzuki K, Seto S, Tanaka A, Kawashima M (1990) Carrier drift mobilities and PL spectra of high resistivity cadmium telluride. J Crystal Growth 101(1–4):859–863
47. Szeles C, Bale D, Grosholz J Jr, Smith GL, Blostein M, Eger J (2006) Fabrication of high performance CdZnTe quasi-hemispherical gamma-ray CAPture™ plus detectors. Proc SPIE 6319:191–198
48. Szeles C, Cameron SE, Ndap J-O, Chalmers WC (2002) Advances in the crystal growth of semi-insulating CdZnTe for radiation detector applications. IEEE Trans Nucl Sci 49(5):2535–2540
49. Thomas RN, Hobgood HM, Ravishnkar PS, Braggins TT (1990) Meeting device needs through melt growth of large-diameter elemental and compound semiconductors. J Crystal Growth 99:643–653
50. Triboulet R, Siffert P (2010) CdTe and related compounds; physics, defects, hetero- and nano-structures, crystal growth, surfaces and applications. Amsterdam, the Netherlands, Elsevier
51. Vere AW, Cole S, Williams DJ (1983) The origins of twinning in CdTe. J Electron Mater 12(3):551–561
52. Verger L, Aillon EGD, Monnet O, Montemont G, Pelliciari B (2007) New trends in γ-ray imaging with CdZnTe/CdTe at CEA-Leti. Nucl Instr Meth A 571:33–43
53. Yang F, Jie W, Wang M, Sun X, Jia N, Yin L et al (2020) Growth of single-crystal $Cd_{0.9}Zn_{0.1}Te$ ingots using pressure controlled Bridgman method. Crystals 10:261
54. Xu Y, Jie W, He Y, Guo R, Wang T, Zha G (2011) Size and distribution of Te inclusions in detector-grade CdZnTe ingots. Progr Natural Sci Mater Intern 21:66–72
55. Zappettini A, Zambelli N, Benassi G, Calestani D, Pavesi M (2014) Live-monitoring of Te inclusion laser-induced thermo-diffusion and annealing in CdZnTe crystal. Appl Phys Lett 104:252105
56. Zelenina NK, Karpenko VP, Matveev OA, Sedov VE, Terentyev AI, Thomas AA (2009) Growth and annealing of CdZnTe: Cl crystals with different zinc content for nuclear radiation detectors. Fizika and Technika Poluprovodnikov 43(10):1419–1425. (in Russian)
57. Zou J, Fauler A, Senchenkov AS, Kolesnikov NN, Fiederle M (2021) Analysis of Te inclusion striations in (Cd,Zn)Te crystals grown by traveling heater method. Crystals 11:649

OceanofPDF.com

© The Author(s), under exclusive license to Springer Nature Switzerland AG 2023
G. Korotcenkov (ed.), *Handbook of II-VI Semiconductor-Based Sensors and Radiation Detectors*
https://doi.org/10.1007/978-3-031-19531-0_10

10. Thin Films of Wide Band Gap II-VI Semiconductor Compounds: Features of Preparation

Vyacheslav F. Markov[1] ✉, Ghenadii Korotcenkov[2] and Larisa N. Maskaeva[1]
(1) Ural Federal University, Yekaterinburg, Russia
(2) Department of Physics and Engineering, Moldova State University, Chisinau, Moldova

✉ **Vyacheslav F. Markov**
Email: v.f.markov@urfu.ru

Keywords II-VI semiconductors – Cadmium selenide – Cadmium sulfide – Cadmium telluride – Zinc selenide – Zinc sulfide – Zinc telluride – Chemical sensors – Methods of deposition – Aerosol spray pyrolysis – Atomic layer deposition – Arc-PVD – Chemical bath deposition – Chemical vapor deposition – Electrochemical deposition – Electron beam vacuum evaporation – Ion beam sputtering – Magnetron sputtering – Metalorganic vapor phase epitaxy – Molecular-beam epitaxy – Physical vapor deposition| – Pulsed laser deposition technique – Successive ionic layer adsorption and reaction – Vacuum thermal sputtering – Methods of synthesis – Hydrothermal synthesis – Sol-gel synthesis – Photodetectors – Photonics – Thin films

10.1 Introduction

The formation of thin films of II-VI compounds with specified parameters is one of the most critical operations in the manufacturing process of

various optoelectronic, photonics, and sensory devices. The experiment showed that films of II-VI compounds on the surface of substrates can be formed using a variety of approaches. The most commonly used methods of film formation used in the manufacture of photodetectors and gas sensors are listed in Table 10.1. It should be noted that the data given in Table 10.1 were obtained without taking into account approaches based on the use of 1D nanostructures and the principles of thick-film technology, when pre-synthesized nanocrystals are deposited on the substrate surface in various ways. In the methods presented in Table 10.1, nanocrystals are synthesized directly on the substrate surface. It can be seen that the most commonly used methods include vacuum thermal evaporation and some of its varieties, deposition from the gas or vapor phase, sputtering, spray pyrolysis, deposition in a chemical bath, electrochemical deposition, and some other methods that have been actively developed in recent years. Given the above, consider these methods in more detail.

Table 10.1 The number of articles, in percentage terms, in which certain methods of film deposition are used in the development of film devices based on wide-gap II-VI semiconductors

Method of film forming	**Application**	
	Photodetectors	**Gas sensors**
Wet chemical methods (bath, etc.)	18%	29%
Successive ionic layer adsorption and reaction (SILAR, SILD)	4%	7%
Spray pyrolysis	19%	15%
Thermal evaporation	24%	36%
DC and HF sputtering	8%	11%
Electrodeposition	5%	
Chemical vapor deposition (CVD) and metal-organic CVD (MOCVD)	7%	
Molecular-beam epitaxy (MBE)	13%	
Pulse laser deposition (PLD)	1%	
Other	1%	2%

10.2 Vacuum Thermal Evaporation

In general, vacuum deposition is a set of processes used to deposit films with a thickness from one monolayer to hundreds of micrometers in negative pressure conditions. The principle of vacuum thermal sputtering (vacuum evaporation) is the transfer of original substances into the vapor phase due to heating by the direct deposition of vapors on a specially prepared substrate (see Fig. 10.1). Historically, this method is one of the first used to produce thin films of II-VI compounds. Any vacuum deposition unit includes an energy source, which provides the evaporation of the deposited material. There are many designs of evaporators implementing resistance, radiation, induction, laser impulse, and other heating techniques.

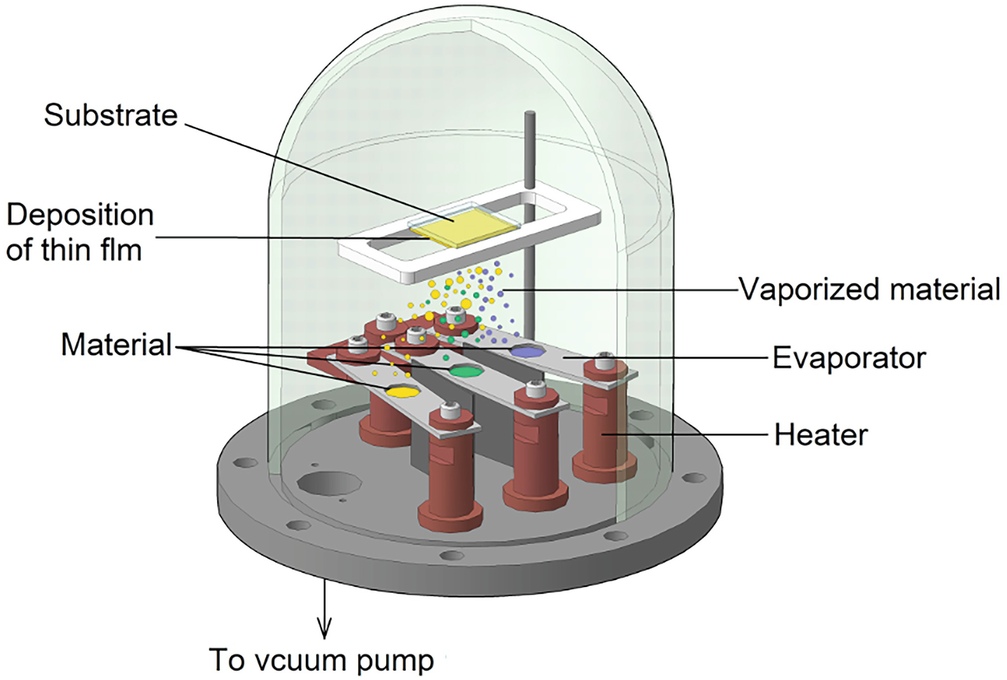

Fig. 10.1 Working chamber for film application by vacuum thermal evaporation

Film deposition process is carried out at temperatures that provide the necessary pressure of vapors of evaporating substances. The rate of vapor condensation and film growth, in turn, depends on the relative position of the evaporator and the substrate as well as substrate temperature [51]. Thus, the optimal choice of the distance from the evaporator to the substrate is important taking into account the mean free path of molecule in the residual gas atmosphere, which is evaluated experimentally. Three main processes simultaneously occur while applying thin films in vacuum: Reaching a

certain concentration of particles of the evaporating substance, their transit in vacuum to the substrate, and vapor condensation on the substrate surface. The purity of the deposited film depends on the vacuum level and the purity of the precursor used. It will be higher as the deposition rate increases since this reduces the inclusion of gaseous impurities in its composition. The film thickness can also vary depending on the geometry of the evaporation chamber. Collisions of particles with molecules and residual gas atoms increase the irregularity of the thickness.

At thermal vacuum deposition of films, the evaporation temperature is nominally taken as its value at which vapor pressure of the substance above its surface is 0.01 mm of mercury. The standard evaporation rate by weight at this pressure for most II-VI semiconductor compounds is about 10^{-4}g·cm^{-2}·s^{-1}. According to kinetic studies to avoid significant contamination of films with atmospheric gases at average growth rate of the layer up to 1 nm·s^{-1}, deposition should be carried out at residual pressure of not more than 10^{-3} Pa.

Vacuum thermal-furnace evaporated deposition of II-VI compounds has several advantages in that the physical and electrical properties of the films can be easily controlled by the various processing conditions such as deposition temperature, annealing temperature, and deposition pressure. In addition, thermal evaporation technique under certain conditions provides high crystalline quality and uniform films with excellent adherence due to the use of vacuum conditions.

When depositing films by thermal sputtering, various scenarios can be used. For example, when forming ZnTe and CdS films, high-purity zinc and telluride powders or elements Cd and S can be used as a source, which, mixed in a certain weight ratio, are placed on a molybdenum or tungsten boat, heated to temperatures of 400–600°C [60, 99]. Elemental S, Se, and Te are mainly evaporated in the form of polyatomic clusters. CdTe and CdS powders can also be used as a source. During the spraying process, the chamber is usually evacuated to a low-pressure situation (10^{-3}–10^{-6} Pa). The chamber can also be filled with argon or an Ar/H_2 [5] mixture to inhibit oxidation processes.

Evaporation of binary II-VI compounds is usually accomplished by dissociation during their thermal decomposition. Due to both significant difference in the volatility of the compound components and difference in

the chemical potential of each of them in vapor and solid states, the vapor composition in the vacuum chamber and the film on the substrate can differ from the starting material. In particular, during CdSe deposition, it was found that the stoichiometry of CdSe films improves with an increase in the substrate temperature up to 550 K. At 550 K, the CdSe films were exactly stoichiometric (atomic ratio Cd/Se = 1) (see Fig. 10.2). Above 550 K substrate temperature, the films were nonstoichiometric and showed deficiency of selenium [99]. This may be due to reevaporation of highly volatile selenium from the substrate. An increase in the Cd/Se ratio, due to depletion of the source, can also be observed with an increase in the thickness of the deposited film. In this case, separate evaporators with different temperatures must be used to provide stoichiometric composition of the deposited layer. For example, to form CdS films, two separate sources of CdS and S can be used to produce Cd and S vapors. This approach allows to grow the films of II-VI compounds with a required composition at appropriate temperature control.

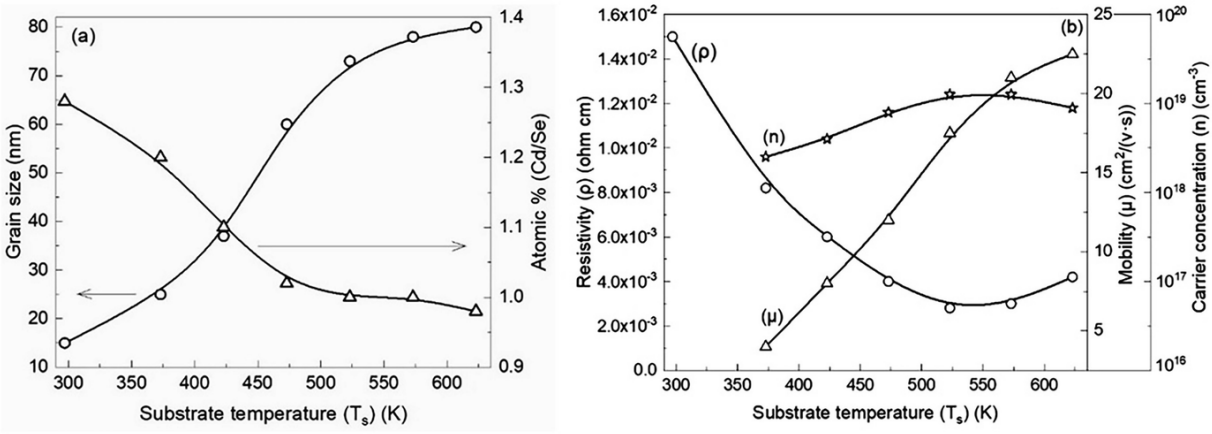

Fig. 10.2 The variation of grain size and elemental atomic ratio Cd/Se of the CdSe thin films deposited at different substrate temperatures keeping constant a thickness of 100 nm (**a**). Variation of resistivity, carrier mobility, carrier concentration in CdSe thin films with different substrate temperatures at a constant thickness of 100 nm (**b**). (Adapted with permission from Patel et al. [99]. Copyright 1994: Wiley)

Numerous experiments have shown that the substrate temperature during film deposition is indeed one of the main parameters affecting film parameters. For example, Fig. 10.2 shows the influence of the substrate temperature on the electrophysical properties of CdSe films, and Table 10.2 shows typical results of the effect of substrate temperature on the parameters of ZnS films. These results were reported by Patel et al. [99] and

Vishwakarma [121]. Nanocrystalline semiconductor ZnS films 500 nm thick were deposited on a glass substrate at various substrate temperatures. It can be seen that with an increase in the deposition temperature from 300 to 400 K, the grain size increases, while the dislocation density, the electrical resistance of the film, and the band gap decrease. At the same time, when the dislocation density decreases by 1.5 times in this temperature range, the electrical resistance decreases by 2.4 times. As the substrate temperature range increases, the changes in film properties become even greater. As is known, the temperature of the thermal evaporation substrate can vary over a very wide range from RT to 600°C [5, 69, 70, 121]. The argon pressure in the deposition chamber also has a significant effect on the film parameters. For example, Lin et al. [60] found that the relative concentration of carriers in ZnTe films increased with decreasing argon pressure and increasing deposition temperature.

Table 10.2 Influence of substrate temperature on grain size, dislocation density, electrical resistance, and band gap of ZnS films obtained by vacuum thermal deposition

Substrate temperature, K	**Grain size, nm**	**Dislocation density $\times 10^{15}$, line/m^2**	**Resistivity $\times 10^6$, Ω cm**	**Band gap, eV**
300	36.12	0.76	0.36	3.52
323	39.64	0.63	0.28	3.47
350	42.17	0.56	0.19	3.44
373	43.56	0.52	0.16	3.43
400	43.82	0.52	0.15	3.43

Source: Reprinted from Vishwakarma [121] Published 2015 by Springer as open access

It is important to note that films of ternary compounds can also be obtained using the thermal evaporation method. For example, in [87], 300-nm-thick CdS_xSe_{1-x} ternary films with composition, x, varying from 0 to 1 were obtained by this method. High-purity CdS and CdSe materials were used as a source. $Zn_xCd_{1-x}S$ films (x = 0, 0.15, 0.30, and 0.45) and $Cd_xZn_{1-x}Te$ ($0.2 \leq x \leq 1.0$) were obtained by the same method. High-purity CdS and ZnS or CdTe and ZnTe powders were used to deposit these films [6].

Thermal evaporation also makes it possible to deposit doped films of II-VI compounds. In work [5] CdS nanostructures undoped and doped with

zinc were grown on Si/SiO_2 substrates in the pipe furnace under the Ar/H_2 atmosphere. The results of the studies showed the combination of ribbon and rod forms of nanoparticles for undoped layers, whereas the CdS sample doped with Zn had morphology of nanorod with hexagonal crystal structure. Mahdi et al. [70] synthesized nanostructured films doped with aluminum using thermal evaporation in a vacuum. The undoped and Al-doped ZnTe thin films were deposited on glass and Si substrates to produce heterojunction detectors [74]. Doping with aluminum was accompanied by a significant change in the film morphology and crystallite size.

As for the disadvantages of this method, as it is mentioned above, there is a problem with the sputtering of the materials with complex composition due to the difference of vapor pressure of the compound components. In some cases, another problem is the poor crystallinity of the films when deposited on low-temperature substrates and their poor adhesion observed when using relatively low temperatures of the substrate and also due to contamination with atmospheric gases under poor vacuum. For example, Kalita et al. [42] performed a detailed analysis of the structural parameters of ZnSe thin films deposited by thermal evaporation on a substrate heated to a temperature varying in the range of 30–350°C during deposition. It was found that the peak intensities on the X-ray diffraction pattern, indicating the crystallinity of the deposited material, increase noticeably only at a substrate temperature above 300 °C. See [8, 14, 18, 41, 71, 78, 122] for more details on vacuum thermal evaporation of II-VI films, and we strongly recommend to refer to these works.

10.3 Magnetron Sputtering

Magnetron sputtering is a technique of applying thin films on the substrate using cathode sputtering of the target in crossed electric and magnetic fields [7, 51]. Magnetic field is applied perpendicular to electric field and oriented parallel to the cathode. When negative potential is applied to the cathode, electric lines of force appearing near it are crossed with magnetic lines of force. In the unit with a flat cathode, magnetic field prevents the releasing of electrons from the cathode region directing them along a closed path (see Fig. 10.3). This prevents electron bombardment of the deposited film and increases the ionization efficiency of the working gas atoms due to a series of sequential collisions with them. Thus, most of the electron energy is used

for ionization and excitation before it reaches the anode. Positive ions in turn bombarding the cathode surface cause its sputter. Increasing sputtering rate due to plasma localization at the cathode surface and simultaneously decreasing working pressure to 0.1 Pa and lower allow to reduce film contamination with gaseous occlusions significantly. Decreasing the bombardment intensity of the substrate also reduces temperature and radiation effects in deposited materials.

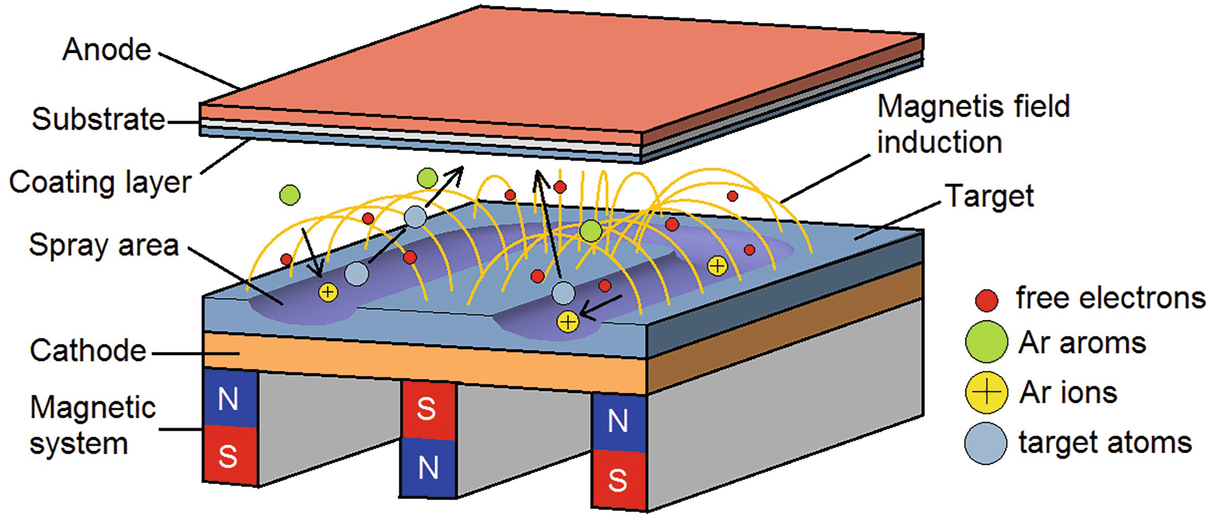

Fig. 10.3 Scheme of magnetron sputtering system with a flat cathode

However, the main advantages of magnetron sputtering are relatively high sputtering rate and the possibility to obtain the films uniform in thickness on the substrates of a large area, which allows to consider this technique as a very perspective low-temperature technique. The use of magnetron sputtering for II-VI compounds allows to increase the deposition film rate by one order more compared to thermal deposition. If it is necessary to apply films having high ohmic resistance, such as compounds of cadmium and zinc sulfides, high-frequency magnetron sputtering is used for their synthesis. In this case, the target is bombarded with ions only in the negative half-period of the supply voltage.

In work [109] CdS thin films were deposited at room temperature by high-frequency magnetron sputtering at different deposition times. The formation of solid and dense layers without any significant defects such as cracks, pores, and protrusions has been established. Their element analysis showed that films have almost stoichiometric composition. Photodetectors made using the deposited CdS film demonstrated a high value of the photoconductive response to optical radiation. At the same time, some

disadvantages of magnetron sputtering technique at the formation of CdS layers were noted in work [49]: relatively small grain size and high surface roughness, which can negatively affect their photovoltaic characteristics. Magnetron deposition was successfully used for the deposition of ZnS films [39, 126] and CdTe and CdS films [57]. Moreover, Li et al. [57] established for deposited CdS and CdTe films the relationships between the physical and optical properties of these films, including how their semiconductor and physical properties are affected by the void fraction, grain size, and developing deformations. Highly conductive polycrystalline ZnSe thin films can also be deposited using reactive d.c. magnetron sputtering of zinc in an Ar + H_2Se atmosphere [16]. The composition of the deposited films can be controlled by the zinc deposition power, the substrate temperature, and the partial pressure of H_2Se. Shallow donors can be introduced by co-sputtering of Al, Ga, or In or by incorporating In into a zinc target. As a result of such doping, ZnSe films with a resistivity of up to 20 Ohm·cm can be obtained even when ZnSe is deposited on a substrate at a temperature of up to 120 °C.

As a rule, films of II-VI compounds deposited using magnetron sputtering at low temperatures are amorphous or nanocrystalline with a crystallite size from 2–3 nm to 15 nm, increasing with increasing film thickness. Postdeposition heat treatments make it possible to increase the size of nanocrystals [73]. Changing the sputtering conditions and HF power is also accompanied by a change in the degree of orientation of the films and the size of the nanoparticles [126]. An increase in the substrate temperature during deposition also leads to a significant increase in the crystallinity and the size of the crystallites forming the films. As can be seen from Fig. 10.4, clear peaks appear on the X-ray diffraction patterns only at a substrate temperature above 100 °C. With a further increase in the substrate temperature from 100 to 400 °C, the diffraction patterns of films of a nanostructural nature are enhanced [39]. Table 10.3 shows the variation of the structural characteristics in the ZnS film: full width at half maximum (FWHM), the sizes of crystallites according to both X-ray diffraction (XRD) and field emission scanning electron microscopy (FESEM), as well as the Zn/S ratio in the layer when the substrate temperature increases to 400 °C. It can be seen that its growth within the studied limits increases the crystallinity of the films and brings the content of the main elements closer to the stoichiometric ratio.

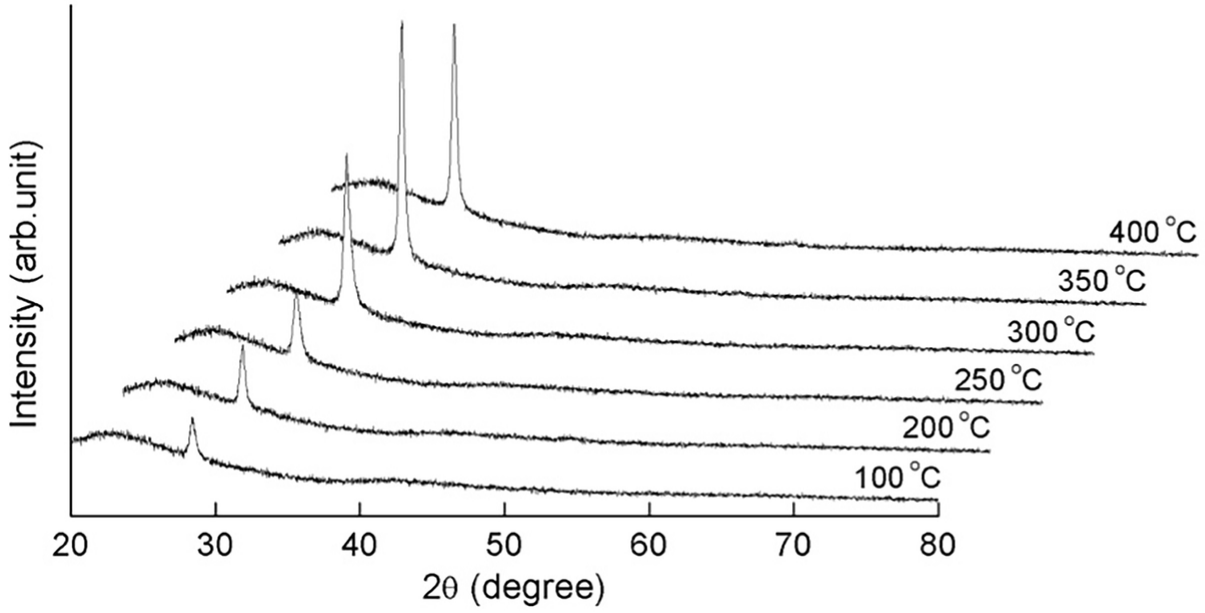

Fig. 10.4 XRD patterns of ZnS films grown at various substrate temperatures from 100 to 400 °C. (Reprinted from Ref. [39]. Published 2012 by Springer as open access)

Table 10.3 The structural parameters and the ratio of the main elements in the ZnS film at the substrate temperature variations during the magnetron sputtering process

Substrate temperature, °C	FWHM values, degrees	Crystallite size by XRD, nm	Grain size by FESEM, nm	Zn/S ratio
100	0.384	22.3	27.2	1.19
200	0.314	25.5	30.1	1.17
250	0.288	29.8	36.5	1.16
300	0.199	43.1	50.3	1.13
350	0.141	60.8	69.4	0.99
400	0.154	55.6	66.2	1.04

Source: Adapted from Hwang et al. [39] Published 2012 by Springer as open access

10.4 Pulsed Laser Deposition Technique

Pulsed laser deposition (PLD) is a physical vapor deposition technique that uses a powerful pulsed laser as an evaporator [65]. For these purposes, the CO_2 lasers (λ = 10.6 μm) and Nd:YAG lasers (λ = 355 nm) are usually used [55, 65]. But other lasers such as krypton fluoride laser (Kr:F laser) (λ =

248 nm) can also be used [83]. Parameters of these lasers are listed in Table 10.4. Its beam is focused inside the vacuum chamber on a target made of the deposited material. As a target for sputtering, single-crystal plates or polycrystalline films formed by various methods can be used. The pulse lasts about 10–40 μs, depending on the parameters of the laser.

Table 10.4 Lasers used for PLD

Laser	Wavelength	Pulse duration on target	Maximum energy	Maximum frequency
Excimer	193; 248; 308 nm	6–50 ns	400 mJ	20–50 Hz
Q-switched Nd:YAG	266; 248; 532; 1064 nm	5–20 ns	300–600 mJ	20 Hz
Free-running ND:YAG	1064 nm	0.1–0.6 ms	9000 mJ	1 Hz
TEA-CO_2	10.6 μm	80 ns (3μs)	900 mJ	20 Hz

As a rule, the process of PLD takes place in ultrahigh vacuum [34]. A typical installation configuration used for PLD is shown in Fig. 10.5. The particles that have left the target are extremely diverse. These are atoms, molecules, electrons, ions, clusters, and melt particles. The parameters of the working laser, the laser radiation flux density, the time and duration of the pulse, and the degree of ionization of the deposited material will affect the quality of the film during deposition and its stoichiometry.

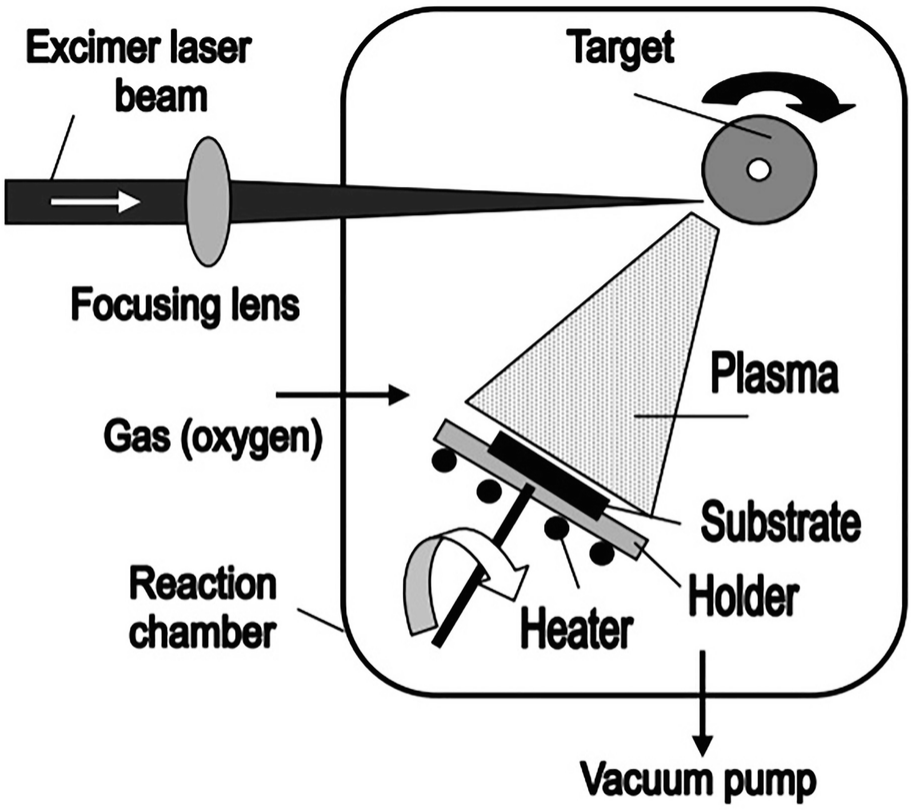

Fig. 10.5 Schematic off-axis configuration of the apparatus for laser ablation

As a rule, the method of PLD consists of several important parts [65]. Each of them will greatly affect the quality of thin films. According to many researchers, these stages include the interaction of laser radiation with the target, the dynamics of ablative materials, the deposition of ablative materials on a substrate, and the growth of thin films on a substrate. In other words, this deposition method depends on the interaction of photons to create an ejected plume of material from the target. Then the vapor is collected on a substrate located at a small distance from the target. The PLD method during film deposition is characterized by significant supersaturation, which leads to a more intense process of nucleation on the substrate surface compared to thermal vacuum deposition. This increases the uniformity of the film in terms of microrelief and the size of the particles forming the film. According to Zhang et al. [127], PLD makes it possible to control the size and crystalline phase by varying the laser parameters and growth conditions. In addition, this method maintains stoichiometry when materials are transferred from the target to the substrate and exhibits good crystallinity of the films as described by Xin et al. [123].

Thus, the development of laser technologies makes the PLD method very competitive for growing thin homogeneous films of complex stoichiometry.

Experiments have shown that in addition to vacuum, an inert or active gas atmosphere can be used for PLD. Chalana et al. [11] studied the effect of an argon atmosphere (0, 5, 10, 15, and 20 Pa) on the parameters of ZnS films and found that an increase in the argon pressure from 0 to 15 Pa is accompanied by an increase in the crystallinity of the ZnS films. However, the crystallinity decreases as the argon pressure is beyond 15 Pa. Therefore, they concluded that 15 Pa is the best argon pressure for PLD of ZnS films. In addition, these films show the highest photoluminescence intensity for excitation wavelength 325 nm and the best crystallinity. Similar studies with respect to CdS films were carried out by Kumar et al. [55]. They found that at a pressure of 100 mTorr in a vacuum chamber, a cardinal change occurs in the electrophysical, optical, and luminescent properties of the grown films. In this case, the crystallite size decreases from 38.5 nm to 11.5 nm as the argon pressure increases from 0 to 100 mTorr.

The temperature of the substrate during the PLD process can vary over a very wide range. Tong et al. [118] changed the substrate temperature from 100 to 600 °C during the deposition of CdS films and studied the effect of this parameter on the film properties. They found that the crystallinity, optical properties, and surface quality of the films could be improved by increasing the temperature up to 450 °C. However, degradation of the quality of the films could be observed as the temperature was increased to 600 °C. Ming et al. [85] also analyzed the effect of substrate temperature on the properties of ZnS films. However, they were limited to the region of low temperatures of 150–200 °C, which did not allow to determine the truly optimal deposition parameters. They only found that the intensity of (111) peak increased and the surface was more homogenous with the increasing of the substrate.

In principle, given the low deposition rates, PLD technology is most suitable for the formation of thin films (d<100 nm). However, as shown by Zhang et al. [127], thick films can also be formed. Using PLD, Zhang et al. [127] grew uniform stoichiometric ZnS films with a thickness of 3 μm. With an increase in the thickness of the films, a regular process of an increase in the size of the crystallites forming the films is observed. For example, Alias et al. [3] reported that the crystallite size was observed to increase from 12.1 to 51.9 nm as the thickness of CdS film was increased

from 130 to 780 nm. In the XRD studies, the grown CdS films were polycrystalline, and the peaks appear sharper when the film thickness increases.

It was shown that in addition to depositing films of binary II-VI compounds, the PLD method can be used to deposit multicomponent II-VI semiconductors such as Cu_2ZnSnS_4 [88, 89], and others.

Other research results related to film formation of II-VI compounds using the PLD method can be found in other published articles [83, 124]. In work [36], a brief overview of the deposition of thin films applied with a pulsed laser is presented. In [83] a study of manganese-doped luminescent ZnS, thin films obtained using Kr:F-laser demonstrate a good stoichiometric quality of the layers at a high process rate. Moreover, the comparison of the characteristics of the films with the samples obtained by magnetron sputtering technique was made. The results received in [26] at the deposition of CdS thin films by pulsed laser chemical deposition technique in a bath (PLACBD) are of great interest. The results show that irradiation of a chemical bath with a laser during the deposition of films leads to their accelerated growth.

In spite of the mentioned benefits of the pulsed laser deposition method, some shortcomings have been identified by many researchers [51]. A laser beam with sufficient energy density for coating processes has a limited size. Therefore, a laser-applied coating technique is less efficient than other conventional methods like thermal evaporation, spraying, in terms of coverage rate. This means that this method has low productivity. In addition, coverage of large area components by laser-applied coatings requires overlapping of individual tracks. Other disadvantages of PLD include (i) relatively high investment costs; (ii) the composition and thickness depend on many deposition conditions. The processing parameters, such as wavelength, energy, and shape of the laser pulse, focusing geometry, process atmosphere, and substrate temperature, all greatly influence the parameters of the ablative particle fluxes and, hence, the properties of the deposited films and the efficiency of the deposition process; (iii) difficulties in the deposition of thick layers; (iv) difficulties in attaining the necessary stoichiometry of materials containing volatile components, (v) difficulties in scaling up to large wafers; and (vi) as a result of repeated interaction of the laser beam with the target, structural changes occur on the surface with craters forming. Therefore, the composition and

properties of the deposited material will depend on the duration of the deposition process.

Given the above, it becomes quite reasonable that this technique has been scarcely employed for the development of sensors and photodetectors aimed for the market.

10.5 Ion Beam Sputtering (IBS)

The main feature of ion beam sputtering technique (IBS) during film deposition, in contrast to the ion plasma (cathode) methods, is the absence of the necessity to supply an electrical potential to the sputtering target. In ion beam spraying devices the functions of working gas ionization units and material sputtering source are separated. The target is sputtered by beam of ions of certain energy directed from an independent source.

Typically, a beam of inert gas ions, usually argon, is directed to the target as a concentrated flow. Sputtering particles are predominantly neutral atoms, or their conglomerates (clusters), as well as ions. With an increase of the energy of bombarding ions over 100 eV, the sputtering yield increases dramatically, and it comes up to saturation at 5–10 keV. The inert gas ions make the structure of the applied film be more robust and resistant to various effects, ensuring good quality and reproducibility of the applied layers.

One variety of ion beam sputtering is a reactive film application, which involves dosed introduction of so-called reactive gases capable of interacting with the material of the sputtered target. Use of sulfur, selenium, tellurium, or their hydrogen compounds as vapors at varying partial pressure, process parameters, and geometry of sputtering devices allows to obtain and control composition of deposited films of II-VI chalcogenides. The synthesis is usually carried out at moderate deposition rates and substrate temperatures of 300–500 K. In order to obtain ultraclean films, it is necessary, in particular, to use an ultrahigh vacuum. The ion beam technique has a number of significant advantages over the magnetron and other ion plasma methods. These include relatively low process temperatures allowing coatings to be applied to thermally sensitive materials (plastics), possibility to transfer stoichiometric composition of the target material onto the substrate, and possibility of controlling ionic beam

energy and target sputtering rate due to its bombardment at an angle to the surface.

In [59], the deposition of a thin film of cadmium sulfide (CdS) demonstrates the absence of impurity elements and good transfer of the target material with an initial Cd/S ratio close to stoichiometric. In work [120] ion beam sputtering was used for nonreactive deposition of adhesive ZnS films of high quality. In [45], using the example of deposition of ZnS thin films, it was concluded that the ion beam sputtering method can be used to adjust the optical band gap of zinc sulfide when used in optoelectronic devices.

10.6 Chemical Vapor Deposition (CVD)

Chemical vapor deposition method (CVD) is a classic method and allows to obtain layers of high quality from different materials [15, 51]. The substrate is usually placed into the vapors of one or several substances which form a required compound on its surface while reacting and/or decomposing. All of them follow the same basic principles depending on the process conditions and the transferring of precursor materials into the gaseous phase (heating, plasma simulation, laser irradiation). Unlike physical deposition methods, vapor phase and film compositions can vary significantly. The film is formed as a result of a chemical reaction both near and on the surface of the substrate. This greatly complicates the deposition but makes it much more universally valid. The main chemical reactions at the vapor deposition of II-VI compounds are reduction and thermal decomposition processes.

The CVD process can be carried out both at atmospheric pressure (atmospheric pressure chemical vapor deposition (APCVD)) and at its reduced value (low-pressure chemical vapor deposition (LPCVD)). Low pressure reduces the probability of undesirable reactions in the system and leads to more homogeneous film deposition on the substrate. In some cases, a vacuum variant of the process is also used, when the pressure in the chamber is 10^{-6} Pa and lower (ultrahigh vacuum chemical vapor deposition (UHVCVD)) [15]. Chemical deposition, in which precursors are transported to the substrate as an aerosol stream, is called “aerosol-assisted chemical vapor deposition” (AACVD) [97]. The aerosol can be produced in various ways. If plasma is used to decompose precursors, then the method is called “plasma-enhanced chemical vapor deposition” (PECVD). Unlike

PECVD, at the “remote plasma-enhanced CVD” method (RPECVD), due to the spatial separation of the decomposition regions of precursor compounds and film deposition, the substrate is not exposed to high temperatures, which excludes radiation damage in it. At flaming decomposition, i.e., at combustion of precursors in an open atmosphere, the method is called “combination chemical vapor deposition” (CCVD), and if organometallic precursors are used, the method is called “metalorganic chemical vapor deposition” (MOCVD). In addition to the abovementioned methods, a number of CVD methods have been developed with their own characteristics. According to literature data, AACVD and MOCVD processes are most widely used methods to form thin films for optoelectronic devices.

In the classic version of the CVD process, two precursors are used as independent sources of elements of II and VI groups for growing II-VI films (Table 10.5). However, as a rule, such precursors are very toxic with different vapor pressures, which significantly complicates the process of film growth [15]. Therefore, in recent decades, great interest has been shown in the search for single-molecule precursors in which the elements of a binary semiconductor are juxtaposed within a single molecule [1, 27, 97]. Typical single-molecule precursors are listed in Table 10.6. The single-molecule precursor has some distinct advantages over such conventional dual precursors. MOCVD with single-molecule precursor is a one-step synthesis featuring improved air/moisture stability, stoichiometric control, limited pre-reactions, and no need for harmful gases such as H_2S.

Table 10.5 Typical precursors used for CVD of II-VI compounds

Material	Precursors, metal source	Precursors, chalcogen source
CdTe	$Cd(CH_3)_2$	$C_6H_{14}Te$
CdS	$Cd(CH_3)_2$	H_2S
CdSe	$Cd(CH_3)_2$	H_2Se
ZnS	$Zn(CH_3)_2$ or $Zn(C_2H_5)_2$	H_2S
ZnSe	$Zn(CH_3)_2$ or $Zn(C_2H_5)_2$	H_2Se

Table 10.6 Single-molecule precursors used for MOCVD of II-VI compounds

Material	Single-molecule precursors
CdTe	$Cd((^{t}Bu)_2\text{-}P(Te)NR)_2$
	$Cd(TeSi(SiMe_3)_3)_2$ or $Cd(TeC(SiMe_3)_3)_2$
	$Cd((TePi\ Pr_2)_2N)_2$
CdSe	$Cd((SePi\ Pr_2)_2N)_2$
CdS	$Cd(S_2COEt)_2$
ZnTe	$Zn(TeSi(SiMe_3)_3)_2$ or $Zn(TeC(SiMe_3)_3)_2$
ZnS	$Zn(S_2COCHMe_2)_2$
	$Zn(cinnamtscz)_2$ or $Zn(4\text{-}Clbenztscz)_2$
	$ZnCl_2(cinnamtsczH)_2$, $ZnCl_2(4\text{-}ClbenztsczH)_2$ or $ZnCl_2(thioptsczH)_2$

Source: Data extracted from Afzaal et al. [1]; Garje et al. [27]; Palve [97]

Detailed conditions of CVD synthesis of nanostructured films of II-VI cadmium-containing compounds can be found in monograph [73]. In work [13], ZnS thin films were deposited under vacuum conditions using $Zn(S_2COCHMe_2)_2$ as a precursor; its decomposition was carried out by a controlled laser during the MOCVD process. Zinc sulfide thin films were deposited by Palve [97] using the aerosol-assisted chemical vapor deposition (AACVD) method. The precursors, Zn(II) thiosemicarbazone complexes, were dissolved in methanol. The deposition was carried out on a substrate with a temperature of 400–500 °C. It was shown that the deposition at 450 °C was reproducible with good adhesion with a glass substrate. At this temperature, ZnS films were stoichiometric with the ratio 1:1 of zinc to sulfur. Below 400 °C the films were very poorly deposited on a glass substrate. The same approach was used by Ketchemen et al. [47] and Buckingham et al. [10]. In [47], cadmium (II) dithiocarbamate and cadmium xanthate complexes in tetrahydrofuran and its mixture with chloroform were used for producing CdS films. In [10], cadmium ethylxanthate complexes $Cd(S_2COEt)_2$ decomposing at 225–350 °C were used as precursor materials. Decomposition of various metalorganic compounds was also carried out at low operating pressure in work [125] for obtaining ZnS, ZnSe high-quality films with the thickness of 3 and 1 microns, respectively. In work [107], the influence of the temperature of modified MOCVD synthesis on the photoluminescent properties of CdTe

nanocrystallites was studied. As it can be seen from Table 10.7 in the range 130–250 °C, the wavelength photoluminescence (PL) dependence is extreme. The disadvantages of the method of chemical vapor deposition of II-VI films are its comparatively low productivity and the relatively weak adhesion of the films to the substrate.

Table 10.7 Influence of temperature of modified MOCVD synthesis of CdTe nanocrystallites on the position of wavelength photoluminescence PL maximum

Temperature, °C	130	160	190	220	250
Wavelength PL, nm	572	595	640	635	623

Source: Data extracted from Qi et al. [107]

10.7 Epitaxial Deposition

In recent years, vapor phase epitaxy methods such as Molecular Beam Epitaxy (MBE) have been widely used to produce functional films of II-VI semiconductors [25, 33, 35]. Figure 10.6 shows a rough schematic representation of MBE system using the low-temperature, low-fux, and UHV conditions typical of most single-crystal epitaxial processes. MBE allows growing films of a given thickness with clear interfacial boundaries and with a given doping profile. In MBE installations, due to the high process control, it is possible to evaluate the thickness and quality of the layers in situ, that is, directly during their growth. The MBE process is based on the interaction of one or more molecular beams of different chemical compositions, produced using effusion cells with a heated substrate. The evaporation and condensation processes take place in an ultrahigh vacuum (10^{-8} Pa or less). Selecting the temperatures of the substrate and cells, epitaxial films of the desired chemical composition are obtained. The quality of films largely depends on the matching of the parameters of the crystal lattice of the material and the substrate. Thus, the greater the differences in these parameters, the smaller thickness of the grown defect-free film can be.

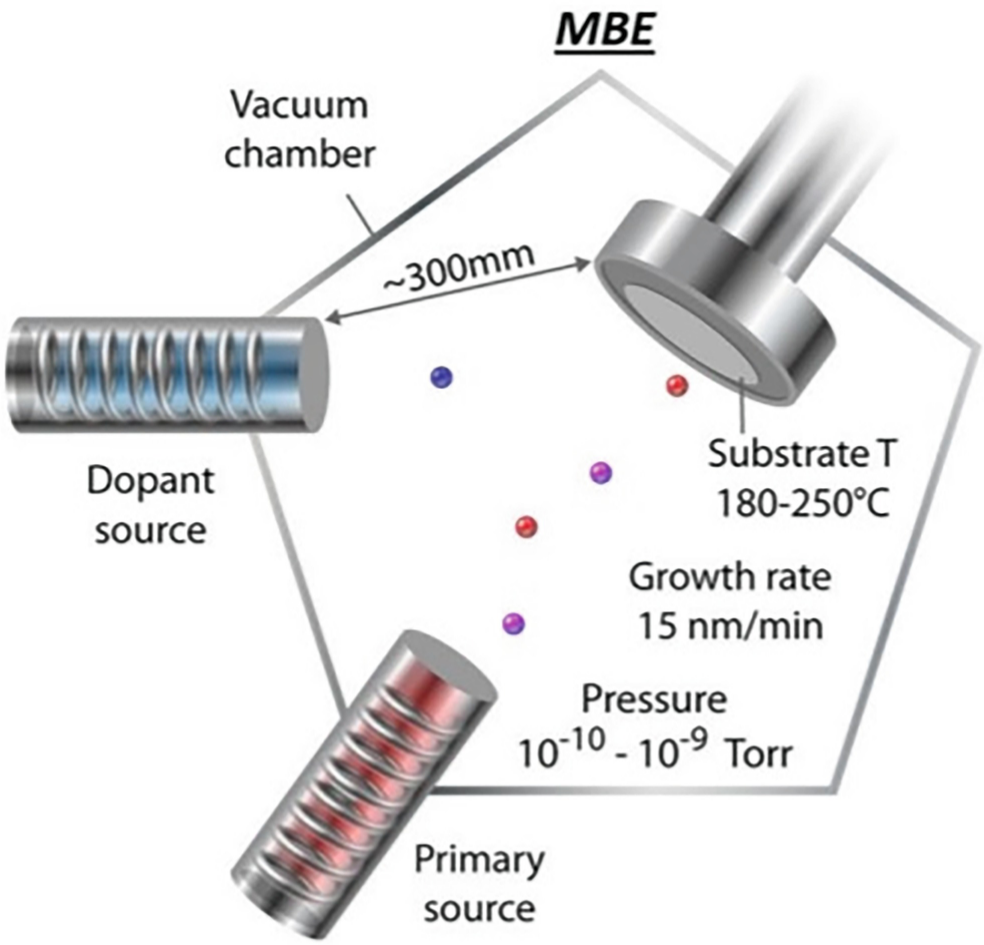

Fig. 10.6 Schematics of MBE and parameters used in film deposition. (Reprinted from Ref. [17]. Published 2020 by Nature as open access)

The advantage of the MBE method is the relatively low temperature of the process, which reduces the diffusion of impurities from the substrate. The use of inertia-free doping, in its turn, allows to control the process of film growth at the atomic level. The disadvantages of the MBE method include the complexity of the equipment, as well as the low growth rate of the films. A number of fundamental physical mechanisms leads to the slow rates and high costs associated with single-crystal deposition, including the need for [17] (1) sufficient time for atoms to bind at appropriate lattice sites within chemoadsorption, surface transport, and flow rates; (2) single-crystal substrates and careful surface preparation to ensure crystal structure and a clean surface for nucleation; (3) high-purity raw materials to eliminate unintentional impurities that cause improper bonding and structural defects; and (4) ultrahigh vacuum (UHV) and/or ultrahigh-purity (UHP) gases to

prevent impurities that cause poor nucleation and/or degrade electro-optical properties.

It should be noted that MBE growth of binary II-VI compounds can be carried out using a single effusion cell containing the compound or, more conveniently, using two cells loaded with the appropriate elements. When using a single effusion cell, it is heated to a congruent sublimation temperature. When using two effusion cells, the ratio of anion and cation fluxes, depending on the vapor pressure of each element (Table 10.8), is adjusted for a given growth temperature in order to obtain the required growth rate with the correct stoichiometry and optimal crystal quality. The smoothness of the surface often depends on this flow ratio, and faceted thick-film surfaces can be obtained if the individual flow values and flow ratios are not properly adjusted [35].

Table 10.8 Vapor pressure of elements used for the MBE growth of II-VI compounds

Pressure (Torr)	**Temperatures (°C) for specified vapor pressure**		
	10^{-7}	**10^{-6}**	**10^{-5}**
Zn	148	177	209
Cd	94	117	145
Te	199	225	255
Se	84	107	134
S	6	21	38

Source: Data extracted from Hernandez-Calderon [35]

As an example of the implementation of the MBE method in the deposition of epitaxial layers of II-VI compounds, we describe the process used in the formation of CdTe films by Colegrove et al. [17]. For deposition of quality layers, state-of-the-art vacuum equipment is required to maintain the background ambient pressure to 10^{-9}–10^{-10} torr; this provides excellent impurity control to avoid both nucleation defects and carrier compensation. It also makes it possible to extremely reduce the flow of atoms from the primary source, usually from the CdTe effusion cell. Too much flux can result in Cd and Te atoms on the surface not having enough time to bond at their appropriate locations, resulting in a higher defect density and possibly a polycrystalline material. If the substrate temperature rises too high, then

the atoms on the crystal surface sublimate at a dangerous rate, resulting in film loss instead of crystal growth. The dopant atoms are introduced from a separate source and the dopant flow rate is varied according to target concentration levels. Because of these physical limitations, CdTe MBE is usually carried out at a substrate temperature of 180–250 °C. The temperature of the effusion cells, depending on the source used, can reach several hundred degrees. The pressure generated by the flow of Cd and Te molecules, represented by the red and purple spheres in Fig. 10.5, known as the beam equivalent pressure, is about 10^{-6} Torr, resulting in a deposition rate of about 15 nm/min. Similar modes are also used in the deposition of epitaxial films of other II-VI compounds [33, 35].

One of the variants of MBE method is a method of vapor phase epitaxy using metalorganic compounds (metalorganic vapor phase epitaxy (MOVPE)) [106]. Another abbreviation for this method is metalorganic chemical vapor deposition (MOCVD) [25]. MOVPE is a method of epitaxial films chemical deposition, when the initial gaseous reagents pyrolytically decompose at the surface of the substrate, releasing film-forming components. The process is carried out in a flow reactor at vapor pressure of 10^{-3}–10^{-1} Pa. Pressure reduction allows to obtain more homogeneous films with thickness control up to several angstroms. MOVPE method, successfully competing in its simplicity and productivity with MBE, has a relatively worse reproductivity of film composition and properties. This is due to the use of both higher temperatures and longer deposition time. Optimization of the process even when obtaining films of binary II-VI compounds: CdS, CdSe, ZnS, and ZnSe, is a rather laborious and costly process [53, 54, 56]. Precursors are usually methyl, ethyl, and isobutyl metal compounds, as well as their hydrides. For example, for the deposition of II-VI binary compounds, such as CdS and CdSe, diethyl sulfide $(C_2H_5)_2S$ and dimethyl selenide $(CH_3)_2Se$, as well as metal methylates and ethylates, are used as initial components. The results of the study [82] demonstrated good photoluminescent properties in ZnS polycrystalline films grown by the MBE method by congruent sublimation from one Knudsen cell. Figure 10.7 shows the variation of the growth time of zinc sulfide films with a thickness of 200 nm doped with manganese and the intensity of their photoluminescence at 580 nm depending on the temperature of the Knudsen cell. As found in the work, at the given

wavelength, the intensity of irradiation is maximum and differs in a pronounced dependence on the cell temperature.

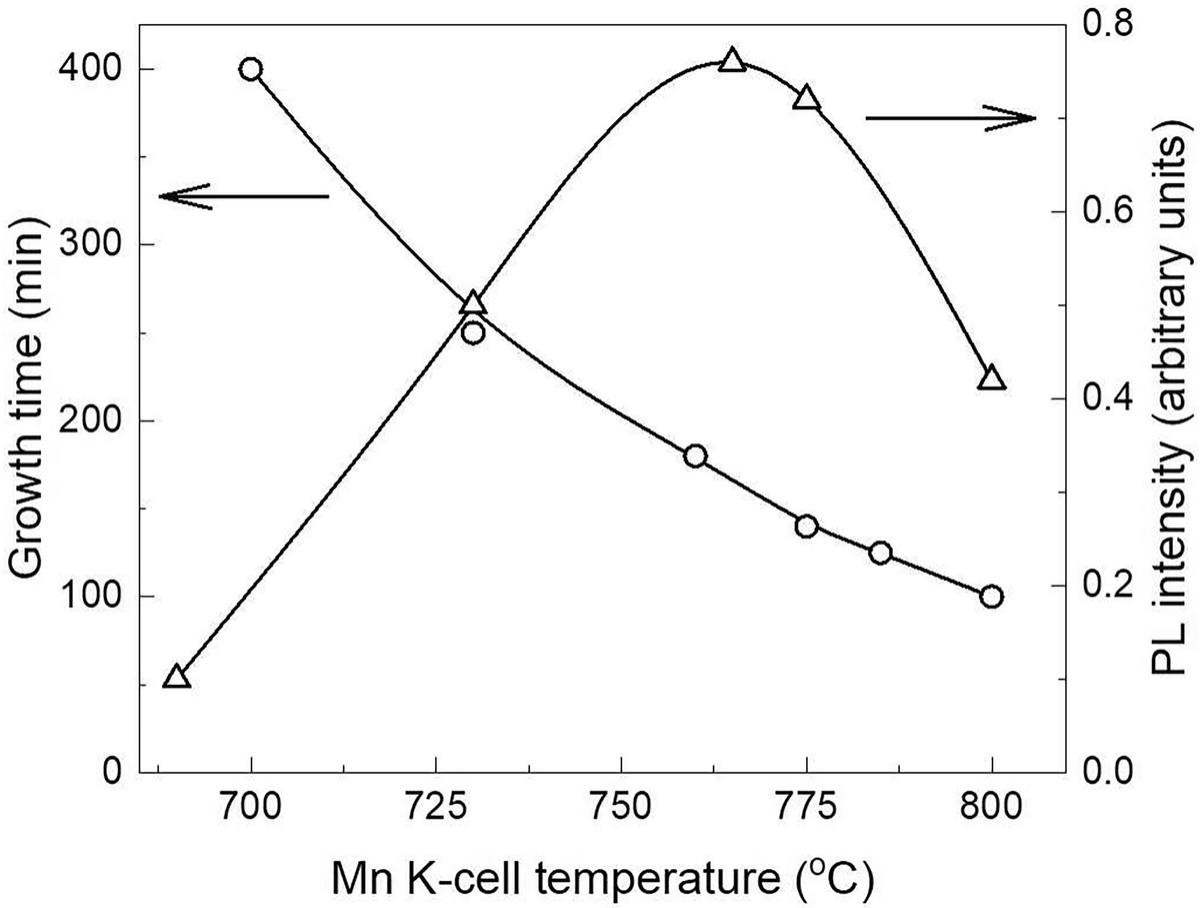

Fig. 10.7 Variation of the growth time of ZnS:Mn films with a thickness of 200 nm and the intensity of their photoluminescent radiation at 580 nm depending on the temperature of Knudsen cell. (Data extracted from Ref. [82])

Atomic layer deposition (ALD) or atomic layer epitaxy (ALE) is an epitaxial film deposition technology that is based on a cycle of consequent chemical reactions on the gas-solid interfacial boundary [35]. This technique is based on a self-regulated layer-by-layer growth mode. Precursors from the gaseous phase alternately react with the surface layer of the film and gradually grow it. The growth of layers consists of specific four stages, which are cyclically repeated:

1. The action of the first precursor. At this stage the substrate is exposed alternately to the vapor beam of effusion cells loaded with the elements (anion and cation) that constitute the compound to be deposited: One cell shutter is open while the other is closed.

2. Exposure and removal of unreacted residues from the reactor. The exposure time is chosen so that the exposed surface is saturated, and the chemisorption process leads to the deposition of a complete or partial monolayer (ML) of one of the elements. Excess atoms adsorbed on atoms of the same type are physisorbed and easily reevaporate after closing the appropriate shutter.

3. The action of the second precursor.

4. Exposure and removal of reagent residues from the reactor.

The process is repeated as many times as necessary in order to reach the expected thickness. For example, the formation and growth of the zinc sulfide film are due to cyclic reactions between sulfur and zinc vapors in the adsorbed layer. Thus, it is important to have a monomolecular adsorption of the particles that is provided by the substrate temperature. During ALD chemical reactions usually take place in the temperature range of 200–400 °C and at an operating pressure range of 0.1–10 kPa. The film is doped by adding an impurity into the gaseous phase. The final thickness of the layer is determined only by the number of treatment cycles of the substrate with precursors.

A description of several processes of epitaxial growth of several II-VI semiconductors can be found in [43, 50]. For example, Konagai et al. [50] using ALD method deposited epitaxial layer of ZnSe and ZnTe. Nitrogen gas was introduced into the chamber. The shutters of zinc and chalcogen were alternately opened and closed for 7 s with an interval of 1 s. In total, 1000 cycles were used for the ALD of ZnSe and ZnTe during the entire experiment. Figure 10.8 shows the change in the growth rate of ZnSe and ZnTe films depending on the growth temperature. This clearly shows that ideal ALD growth was achieved in the substrate temperature range of 250–350 °C for ZnSe and around 220–250 °C for ZnTe.

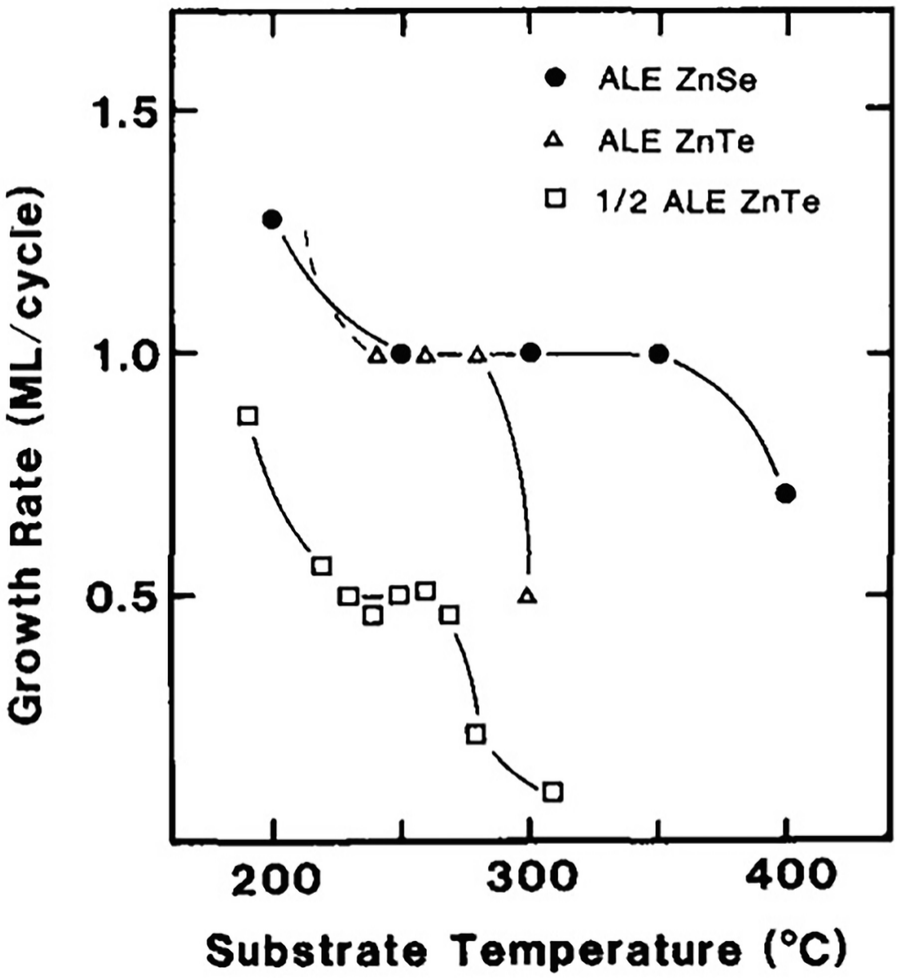

Fig. 10.8 Growth rates of ZnSe and ZnTe grown at various substrate temperatures by ALD. (Reprinted with permission from Konagai et al. [50]. Copyright 1993: Elsevier)

The ALD method offers several advantages over MBE growth modes for the deposition of high-quality epitaxial films of II-VI compounds. In particular, the ALD method is very promising for obtaining homogeneous films necessary for further miniaturization of optoelectronic elements. ALD is also of great interest for the development of quantum structures, in particular for quantum wells, where a small number of layers are used and precise control of thickness and composition is required. It is important to note that the method is a simplified version of MBE, since it does not require ultrahigh vacuum. However, ALD growth of thick films takes much longer and requires intensive use of shutters.

10.8 Successive Ionic Layer Adsorption and Reaction (SILAR)

Successive ionic layer adsorption and reaction (SILAR) is a widely used method for the layer-by-layer synthesis of thin films, including films of II-VI compounds [92, 93]. The method has several names: in addition to SILAR, this method is referred to in various articles as layer-by-layer (LbL) synthesis or SILD (successive ionic layer deposition) [117]. The SILAR method consists of successive, multiple processes of adsorption of cations and anions with the formation of a poorly soluble compound on the substrate (see Fig. 10.9) [20, 117].

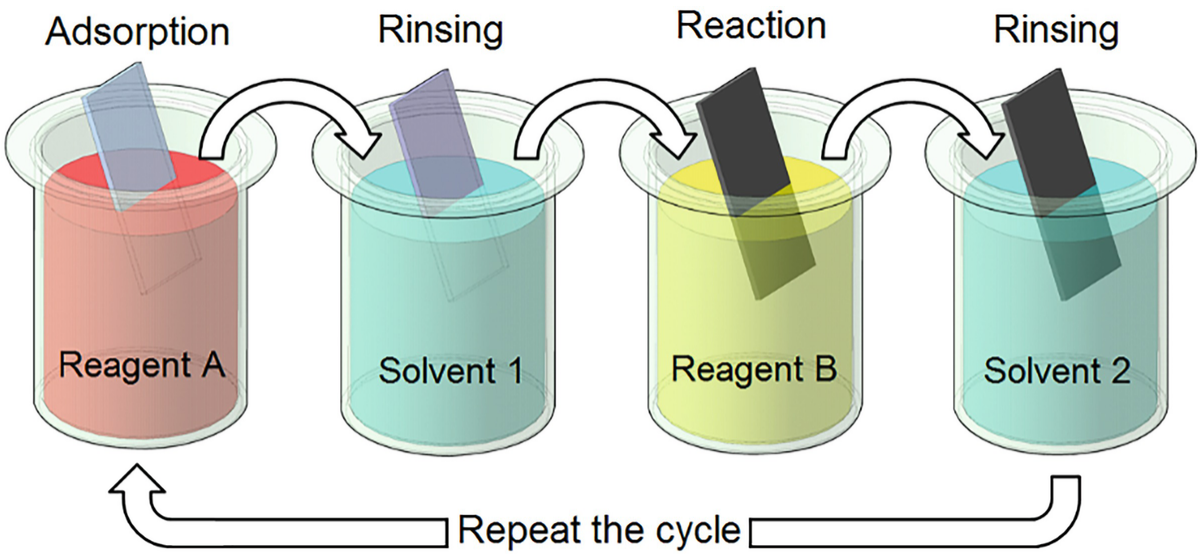

Fig. 10.9 Schematic diagram of the film deposition by successive ionic layer deposition

In the pioneering works of Nicolau – one of the founders of the method [92, 93] – it was shown that alternate dipping of the substrate into the solution containing cadmium and zinc soluble salts and then into the solution containing sulfur-anions followed by washing-up in deionized water allows to form polycrystalline epitaxial ZnS and CdS layers. Precursors used during these processes are listed in Table 10.9. According to Nicolau [92], the growth mechanism involves three most important steps: (i) specific adsorption of the most strongly adsorbed ions of the compound to be grown by substrate immersion in a solution of one of its salts, (ii) water rinsing of the excess solution still adhering to the substrate, and (iii)

chemical reaction between the most strongly specifically adsorbed ions and the less strongly adsorbed ones by the subsequent substrate immersion in a solution containing the latter, entailing the growth. The application of this method for fabricating thin films for solar converters, photodetectors, LEDs, etc. is described in [117].

Table 10.9 Precursors used for deposition of II-VI semiconductor films using SILAR method

Material	Cationic precursors	Anionic precursor
CdTe	$CdSO_4$	TeO_2
	$Cd(NO_3)_2$	
	$CdCl_2$	
CdSe	$CdCl_2$	SeO_2 or H_2SeO_3
	$CdSO_4$	Na_2SeO_3 or Na_2SeSO_3
	$CdAc_2$	Na_2SeSO_3
	$Cd(CH_3COO)_2$	Na_2SeSO_3
CdS	$CdCl_2$	$Na_2S_2O_3$ or $NH_4S_2O_3$ or NH_2CSNH_2 or Na_2S
	$Cd(NO_3)_2$	$(CH_3)_2SO$ or Na_2S
	$CdAc_2$	Na_2S or $S(NH_4)_2$
ZnTe	$ZnSO_4$	TeO_2
ZnSe	$ZnSO_4$	SeO_2
	$Zn(CH_3COO)_2$	Na_2SeSO_3
ZnS	$ZnSO_4$	$(NH_4)_2S_2O_3$
	$ZnCl_2$	Na_2S
HgS	$Hg(CH_3COO)_2$	Na_2S

Source: Data extracted from Chaudhari et al. [12]; Geethanjali et al. [28]; Majid and Bibi [72, 73]; Pawar et al. [102]; Tolstoy [116, 117]

Numerous reactions at ionic layer deposition can be divided into different subgroups according to the basic types of interaction of cations and anions in the solutions [116, 117]. The main group involves the reactions that proceed without changing of the oxidation state of the ions. Such reactions include, for example, the reaction between adsorbed Cd^{2+},

Zn^{2+} cations and HS^{-} anions. The result of this interaction is the formation of sulfide layer on the substrate. The essential condition of the targeted SILAR synthesis is the washing-up of the grown layer from the remaining reagents of the previous stage. It is obvious that the compounds for which the best synthesis conditions of ionic layer deposition are satisfied involve those, which have the lowest solubility product values in the range of used pH values. They are cadmium and zinc sulfides and selenides: CdS, CdSe, ZnS, and ZnSe. When the substrate is washed in distilled water, some of the zinc ions are removed from the surface, but the pH at the surface is changed to 7 by the water, causing hydrolysis of the Zn and Cd ions which opposes the desorption.

If the substrate is c of Na_2S, the S^{2-} and HS^{-} ions react on the surface, giving a layer of CdS or ZnS:

$$\mathrm{Zn}^{2+}_{ads} + \mathrm{S}^{2-}_{aq} \rightarrow \mathrm{ZnS} \tag{10.1}$$

$$\mathrm{ZnOH}^{+}{}_{ads} + \mathrm{HS}^{-} \rightarrow \mathrm{ZnS} + \mathrm{H_2O} \tag{10.2}$$

Despite the simplicity of the process, the synthesis due to its multistage nature is preferably carried out using special installations that operate in the automated mode according to the pre-defined program. As noted in review [100], the SILAR method has proven to be an inexpensive and convenient process for applying metal chalcogenides films on large regions. It is possible to use the substrates made of organic materials because the deposition takes place at or near room temperature. The main condition for obtaining the high-quality films is optimization of process parameters, selection of reagent concentrations, pH, and improvement of washing-up quality.

The concentration of the salt solutions should be high enough in order to promote the specific adsorption, but at the same, time the rinsing time must be sufficient to entail ion diffusion from the diffusion layer. Optimum magnitudes for the solution concentration-rinsing time parameters should be experimentally determined. The pH of solutions plays an important role. OH- may interfere with the specific anion adsorption entailing the contamination of the sulfide with hydroxide, may change the substrate surface state, especially for oxides, and may change the sulfide and substrate solubility. For example, the optimal parameters of ZnS films (homogeneous, adherent, compact, specularly reflecting) when deposited

from $ZnSO_4$ and Na_2S reagents were obtained using $ZnSO_4$ (0.005M, pH = 3.9) and Na_2S (0.005M, pH = 11.6) solutions [92]. The growth rate in one cycle is usually in the range of 0.1–0.8 nm (Table 10.10). This means that more than 100 deposition cycles are needed to obtain a film with a thickness of 100–200 nm. One cycle usually takes 1–3 min. This means that the SILAR method is characterized by a very low deposition rate. However, in some studies, higher growth rates were also achieved due to the use of highly concentrated solutions. For example, in work [12] the average growth rate of the CdSe film was about 6–8 nm (see Fig. 10.10).

Table 10.10 Synthesis of nanolayers of II-VI semiconductors by SILAR method

Materials	Reagents	Note
CdSe	0.2 M $CdSO_4$ and 0.1 M Na_2SeSO_3	Δd_1 = 0.8 nm.
ZnS	5 M $ZnCl_2$ and 2.8 M Na_2S	Δd_1 = 0.3 nm
	0.1 M $ZnSO_4$ and Na_2S	Δd_1 = 0.29 nm
CdS	5 M $CdCl_2$ and 2.8 M Na_2S	Δd_1 = 0.13 nm
	0.1 M $Cd(NO_3)_2$ and Na_2S	Δd_1 = 0.32 nm

Source: Data extracted from [12, 28, 116, 117]
Note. Here Δd_1 is the thickness of the deposited layer per one cycle of deposition

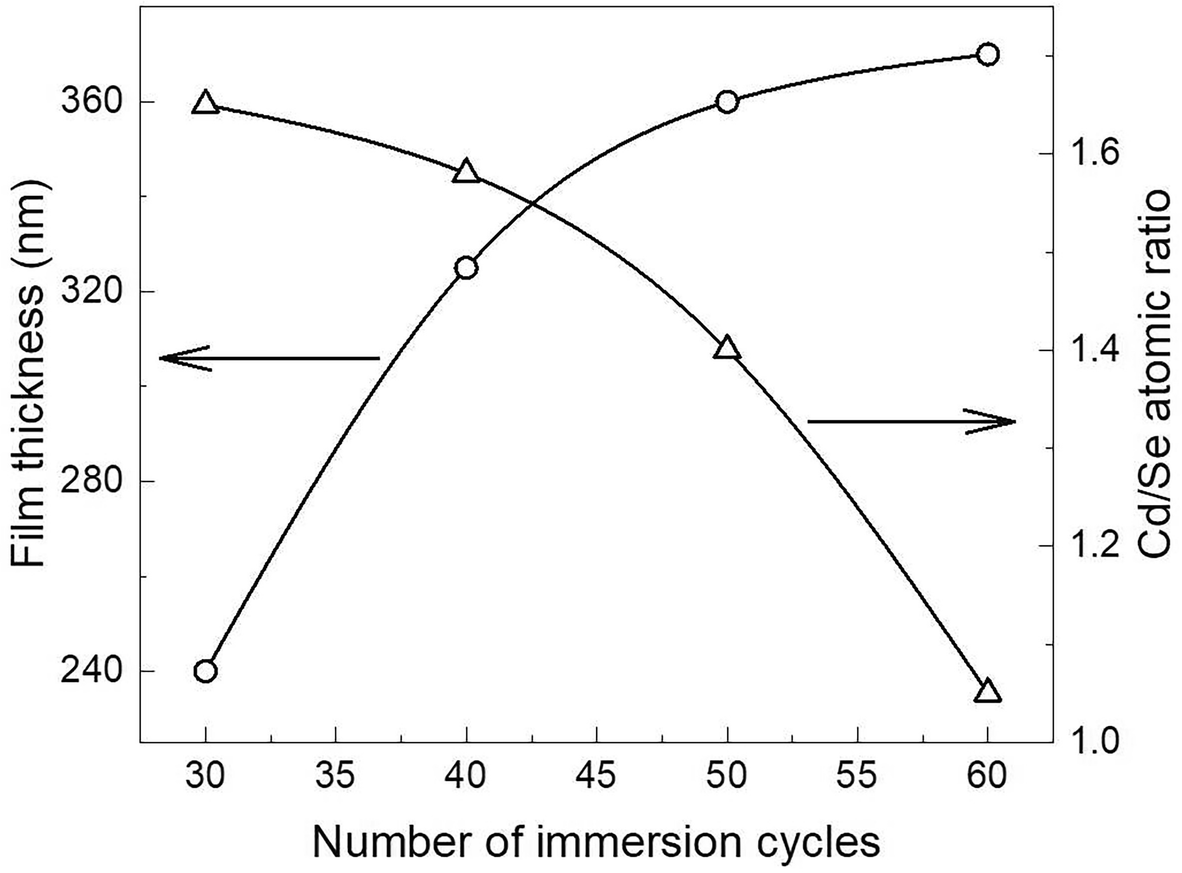

Fig. 10.10 Variation of CdSe film thickness and cadmium and selenium ratio depending on number of immersion cycles under SILAR synthesis method. (Data extracted from Chaudhari et al. [12])

The experiment showed that the deposited ZnS and CdS films had good adhesion. It was also found that the synthesized films can be doped during the synthesis. There are many publications where the SILAR method is used to form cadmium and zinc sulfide films from aqueous and nonaqueous solutions with various dopants (Mn, Ni, Ti, Zn, et al.) [63, 64, 67, 90]. It should be noted that the complete coating of the substrate in the case of CdS occurs after about 50 synthesis cycles and the crystallinity of ZnS layers appears for the films with a thickness of about 250 nm. It is also shown that the composition of the deposited films, as well as microstrains and dislocation density, depends on the number of deposition cycles. As can be seen from Fig. 10.10, as the number of cycles increases, the composition of the CdSe film gradually approaches the stoichiometric ratio. Using ZnSe as an example, it was shown in [28] that, with an increase in the number of cycles, the number of defects and microstrains in the film decreases, while the band gap increases.

10.9 Chemical Bath Deposition (CBD)

Chemical bath deposition method (CBD) is an analogue of chemical vapor deposition method but carried out in a liquid medium. The method has proved to be one of the most available for obtaining II-VI films with high photovoltaic and sensor properties. It is most effectively used for deposition of CdS, CdSe, CdTe, ZnS, and ZnSe layers. In CBD, deposition of thin films takes place from aqueous solutions at low temperatures by a chemical reaction between dissolved precursors, with the help of a complexing agent. Among the advantages of the CDB method are the simplicity of its technological process (see Fig. 10.11), the use of temperatures up to 100°C, the ease of film doping, and high efficiency. CBD is suitable for growing nanofilms over large areas at low temperature. This method can also be used to synthesize multicomponent nanofilms. In addition, the CBD method allows the use of a wide range of substrates (in terms of material and geometry). The deposition of layers on the substrate is usually carried out without the risk of the substrate dissolving in the chemical bath.

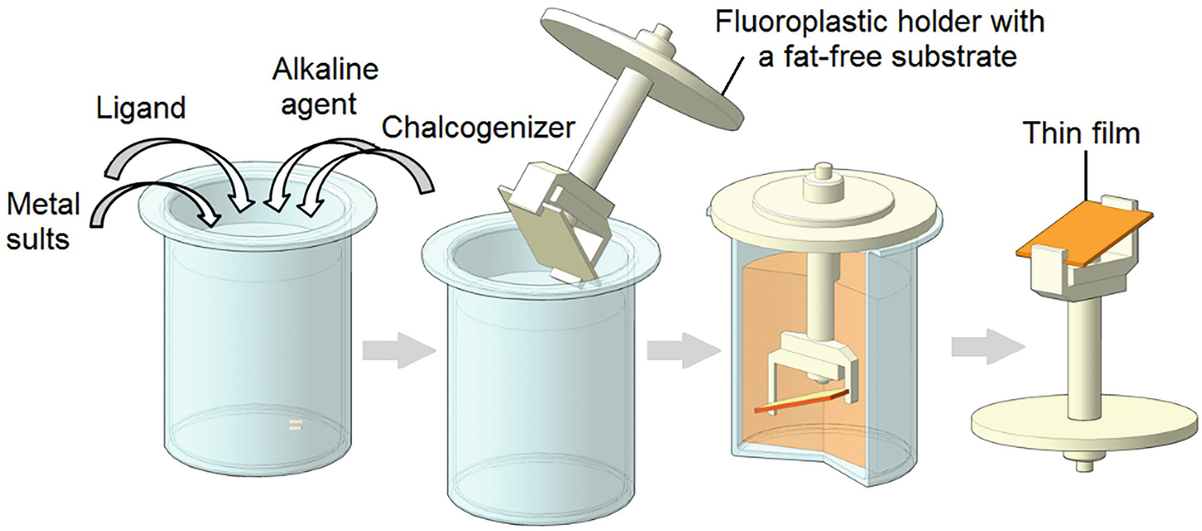

Fig. 10.11 Scheme of film application by chemical bath deposition method

A great number of reviews on CBD method are published nowadays [14, 37, 51, 62, 66, 91, 110]. In reviews [62, 66] the results of the CBD synthesis of metal sulfide, selenide, and telluride films with the analysis of their nucleation and growth processes are presented. The data of chemical

synthesis of II-VI compound films in nanocrystalline form for photonics as well as cadmium and zinc sulfides are given in [37, 52, 91, 110].

It is believed that chemical bath deposition is based on the following steps [94]:

1. Equilibrium between the complexing agent and water
2. Formation/dissociation of ionic metal-ligand complexes $(M(L)_i)^{2-ik}$, where L^{k-} denotes one or more ligands
3. Hydrolysis of the source of chalcogenides
4. Formation of a solid body

In this process, the hydrolysis of the chalcogenide source (step 3) is critical because it provides the desired nonmetal particles that draw metal cations out of solution to form a solid film. This step is very sensitive to the pH and temperature of the solution.

At the CDB method of II-VI compounds, the reaction mixture is typically a mixture of an aqueous solution of M^{n+} metal salt, a chalcogenizer (a source of chalcogenide-ions S^{2-}, Se^{2-}, Te^{2-}), and complexing agents. Thiourea $CS(NH_2)_2$, hydrogen sulfide H_2S, thiosulfate $S_2O_3^{2-}$, or thioacetamide CH_3CSNH_2 are used as a chalcogenizers in the production of sulfides: selenium hydrogen H_2Se, selenourea $C(NH_2)_2Se$, and selenosulfate Na_2SeSO_3 – in the production of selenides, metal tellurides – in the production of H_2Te telluride films. As a rule, aqueous ammonia or KOH is used as complexing agents. Some deposition modes for Cd-based compounds are shown in Table 10.11.

Table 10.11 Cd-containing II-VI semiconductor nanostructured films prepared through the CBD method

Material	Precursors	Deposition temp./dep. time	pH
CdS	$Cd(NO_3)_2$ + $(NH_2)_2CS$,	80 °C/20–50 min	10
	$CdCl_2$ + $SC(NH_2)_2$ and NH_4Cl	80 °C/ 6 h	9
	$CdCl_2$ + CH_4N_2S	85 °C	10
	$CdCl_2$ and $CdAc_2$	90 °C/6 h	N/A
	$CdAc_2$ + $SC(NH_2)_2$	60 °C/8 h	5.6–9.5
	$Cd(CH_3COO)_2$ + $CS(NH_2)_2$	60 °C/20–80 min	>7
	$CdSO_4$ + $CS(NH_2)_2$	55–85 °C/30 min	>7
CdSe	$CdAc_2$, $C_4H_6O_6$ + Na_2SeSO_3	80 °C/6 h	N/A
	$CdSO_4$ + Na_2SeSO_3	70 °C/–	N/A
	$CdH_8N_2O_{10}$, $SeC(NH_2)_2$ / $C_2H_5NO_2$	60 °C/0.5 h	10
	$CdAc_2$, Na_2SeSO_3, $C_6H_{15}NO_3$	60 °C/1 h	N/A
	$CdCl_2$ + $CSe(NH_2)_2$	75 °C/-	>7
	$Cd(CH_3COO)_2$ + Na_2SeSO_3	25 °C/5 h	>7
	$Cd(NO_3)_2$ + Na_2SeSO_3	60/30–90 min	10
CdS, CdSe and CdSSe	$CdAc_2$ + Na_2SeSO_3 / $SC(NH_2)_2$	RT	N/A
ZnS	$ZnCl_2$ + $CS(NH_2)_2$	90 °C/3 h	10–11.5
	$ZnSO_4$ + $CS(NH_2)_2$	80 °C/80 min	>7
	$Zn(CH_3COO)_2$ + $CS(NH_2)_2$	80–85 °C/250 min	9.5–10.5
	$Zn(NO_3)_2$ + $CS(NH_2)_2$	80 °C/2 h	10–10.6
ZnSe	$ZnSO_4$ + Na_2SeO_3	25 °C/–	<7
	$ZnSO_4$ + $CSe(NH_2)_2$	50 °C/1 h	11.5
	$Zn(CH_3COO)_2$ + Na_2SeO_3	70 °C/5 h	11
CdZnSe	$CdSO_4$ + $ZnSO_4$ + Na_2SeSO_3	70 °C/3 h	10
	$Cd(CH_3COO)_2$ + $Zn(CH_3COO)_2$ + Na_2SeSO_3	70 °C/4 h	>7

Material	Precursors	Deposition temp./dep. time	pH
CdZnS	$Cd(CH_3COO)_2$ + $Zn(CH_3COO)_2$ + $CS(NH_2)_2$	90–95 °C/15 min	>7
	$CdSO_4$ + $ZnSO_4$ + $CS(NH_2)_2$	80 °C/–	11.4
HgS	$Hg(CH_3COO)_2$ + $CS(NH_2)_2$	25 °C/3 h	8
	$HgCl_2$ + Na_2SO_3	0–85 °C/45 min–75 h	2–3
CdHgSe	$CdSO_4$ +$Hg(NO_3)_2$ + Na_2SeSO_3	20 °C/3 h	–

Source: Data extracted from Majid and Bibi [72, 73] and Pawar et al. [102]

The ways of prediction of boundary conditions of solid phase deposition by analysis of ion equilibrium in the reaction system are suggested in [76]. The necessary condition of its formation is the supersaturation in the deposited compound. The use of such ligands for cadmium and zinc as chloride ions, tartrate ions, citrate ions, ammonia, ethylenediamine, triethanolamine, hydrazine, etc. in the reaction bath provides the control of phase formation. The strength of obtaining metal complex forms and the nature of ligands influence both the nucleation rate and its growth and due to the spatial structure the interaction between initial particles defining microstructure and morphology of the synthesized films [68, 79].

The ways of prediction of boundary conditions of solid phase deposition by analysis of ion equilibrium in the reaction system are suggested in [76]. The necessary condition of its formation is the supersaturation in the deposited compound. The use of such ligands for cadmium and zinc as chloride ions, tartrate ions, citrate ions, ammonia, ethylenediamine, triethanolamine, hydrazine, etc. in the reaction bath provides the control of phase formation. The strength of obtaining metal complex forms and the nature of ligands influence both the nucleation rate and its growth and due to the spatial structure the interaction between initial particles defining microstructure and morphology of the synthesized films [68, 79].

Work [79] provides comparative data on the influence of three different reaction baths varying in complexing agent composition: citrate, ammonia, and citrate-ammonia on activation energy of the cadmium sulfide synthesis process, thickness, average particle size, roughness, and elemental composition of deposited CdS films (see Table 10.12).

Table 10.12 Influence of the nature of a ligand background on activation energy of chemical deposition process, thickness, average size of particles, roughness, and element composition of CdS films

Complexing agent and its concentration	Synthesis activation energy, kJ/mol	Thickness, nm	Average grain size, nm	Roughness, nm	Ratio, Cd/S
$Na_3C_6H_5O_7$ (0.3 M)	39.16	430	20	8.7	1.2
NH_3 (2.0 M)	55.25	490	80	17.8	1.1
$Na_3C_6H_5O_7$ (0.3 M) NH_3 (2.0 M)	63.34	100	55	22.6	1.1

Source: Data extracted from Maskaeva et al. [79]

The concentration of complexing agents and the type of chalcogenizer allow to regulate the crystallographic orientation of the particles, which can vary from several nanometers to several microns. In addition, ligands are necessary for prevention of the formation of impurity phases (hydroxides, hydroxide salts, cyanamides) in the system. At the same time, as it is noted in [14, 80], the main role of nucleation and adhesive contact of the film with the substrate belongs to the hydroxide phase which activates the substrate surface. Thiourea $C(NH_2)_2S$, which is sulfocarbonate diamide, is most frequently used in the synthesis of CdS and ZnS films for photodetectors and other optoelectronic devices. A detailed review of its chemical properties and decomposition was made by the authors in [80, 84]. According to Markov and Maskaeva [76, 80], thiourea is susceptible to reversible hydrolytic decomposition in an alkaline solution with the formation of hydrogen sulfide and cyanamide. But there are fewer studies of the cadmium and zinc telluride deposition by the CBD method. The film deposition in this case is carried out using sodium telluride or TeO_2 in the presence of strong reducing agents capable of converting tellurium (IV) into Te^{2-} [21].

The CDB method usually produces stable, uniform in thickness, and almost stoichiometric in composition II-VI semiconductor films, which results in high dark resistivity and high photosensitivity of these films. The thickness of the deposited films is usually in the range from 0.02 μm to 1 μm for various materials. However, the quality of the films is higher in the lower thickness range of 0.02–0.05 μm. It is important that complete

coverage of the substrate surface is observed even at a very small film thickness.

The main control over the CBD process is the selection and regulation of metal salt concentration, chalcogenizer, complexing agents, temperature, and pH of the reaction mixture [40, 77, 80]. In work [40] the complex study of the influence of deposition conditions (thiourea concentration, additives of ammonium sulfate and time of process) on thickness, element composition, and electrical resistance of chemically deposited CdS films was carried out (see Table 10.13).

Table 10.13 Variation of thickness of CdS films, element composition, and conductivity depending on thiourea concentration in reaction mixture, additives of ammonium sulfate, and time of deposition

Thiourea, M	Ammonium sulfate, M	Deposition time, min	Thickness, nm	Ratio (Cd/S)	Conductivity, 1/Ω cm
0.3	0.3	45	190	0.87	2.27×10^{-5}
0.3	0.6	45	170	0.83	1.30×10^{-5}
0.3	0.9	45	75	0.76	4.84×10^{-4}
0.5	0.3	45	200	0.86	1.45×10^{-5}
0.7	0.3	45	205	0.84	2.51×10^{-5}
0.5	0.3	30	100	0.84	1.37×10^{-5}
0.5	0.3	60	280	0.86	1.44×10^{-5}

Source: Data extracted from Islam et al. [40]

Analysis of Table 10.13 shows that the thickness of the CdS films naturally increases with increasing thiourea concentration and the time of deposition and rather dramatically decreases at the introduction of ammonium sulfate into the reaction mixture. The used additive also decreases the Cd/S ratio, which is probably a consequence of the formation of impurity phases.

An important factor of the increasing film thickness is also the optimization of conditions and the correct choice of chalcogenizer. It is shown in work [80], providing data on deposition ZnSe films with a thickness of more than 1000 nanometers when using the sodium

selenosulfate Na_2SeSO_3. Figure 10.12 shows the influence of temperature and synthesis time on the thickness of zinc selenide films.

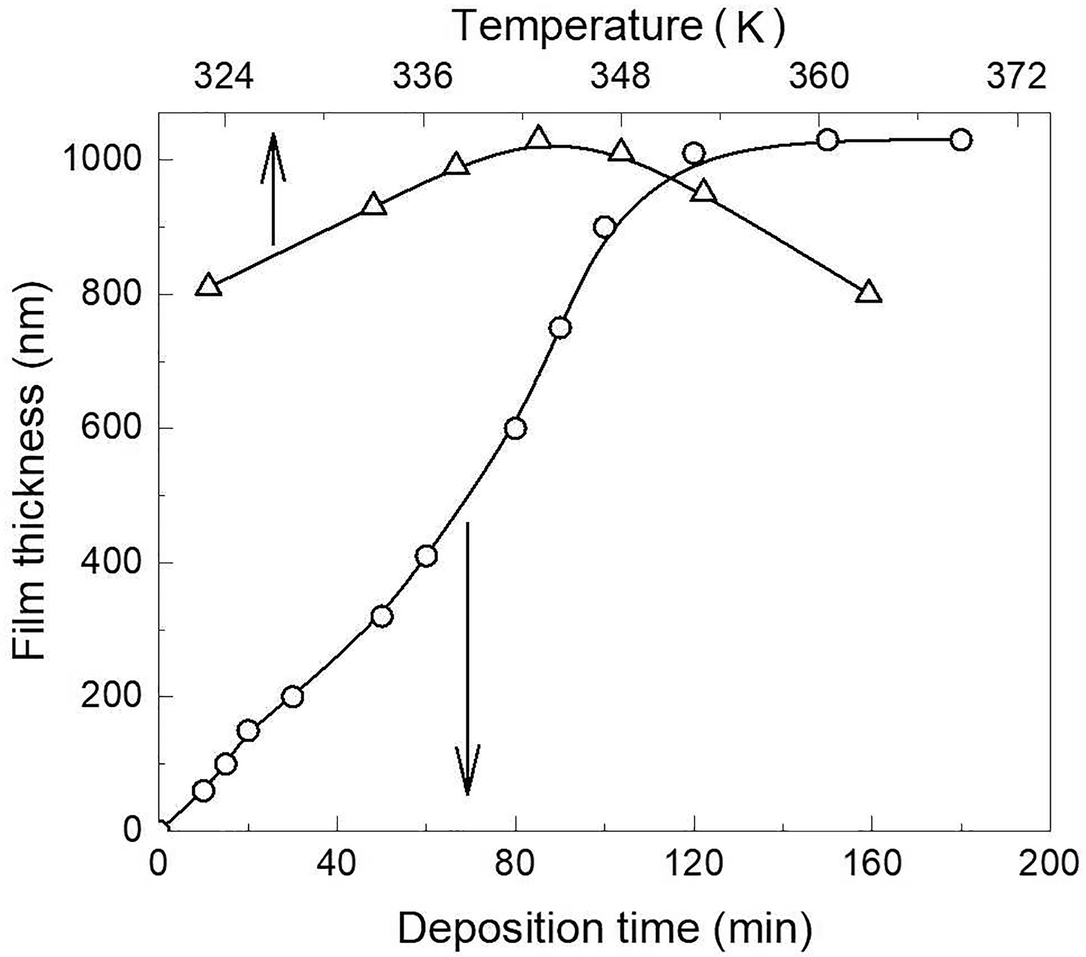

Fig. 10.12 Dependence of ZnSe film thicknesses on temperature and time of the CDB process with a sodium selenosulfate chalcogenizer. (Data extracted from Ref. [80])

Subsequent annealing of deposited films of II-VI compounds also has a significant effect on the electrical and structural properties of the films. As a rule, after annealing, the crystallinity of the films improves, the size of the crystallites increases, and the dislocation density decreases. As for the concentration of charge carriers, its value largely depends on the atmosphere used in the annealing process. It was also found that doping and microwave radiation are effective ways of film property modification in obtaining high-functioning II-VI films for photonics [38, 81].

10.10 Aerosol Spray Pyrolysis (ASP)

Aerosol spray pyrolysis (ASP) is a film production method based on thermal decomposition of aerosol obtained by sputtering the reaction mixture. The method is attractive in terms of its simplicity. Aerosol pyrolysis is a low-cost method in its use, and it is a preferable method for production of II-IV compounds nowadays. It allows to synthesize highly functional films with a large surface area, a high package density, and homogeneousness of particles in their size.

The method is characterized by a relatively high rate of film growth up to 100 nm/s and an ease of doping process [51]. The technology of this method consists of sputtering an aqueous solution containing metal salt, a chalcogenizer, and various functional additives on the substrate heated up to 100–500 °C in order to obtain metal chalcogenide films [31, 103].

The basic elements of technological installation for spray pyrolysis are the chamber where a substrate with a heating system is installed and the sputtering system. Pneumatic, electrostatic, and ultrasonic sputtering methods are commonly used for aerosol production. The wide review on influence of sputtering parameters on film quality to demonstrate the importance of optimization process is given in [103].

At pneumatic sputtering method, the flow rate of the gas carrier, typically air or nitrogen [51], is about 50–300 m/s, and the average size of droplets is in the range of 100–200 μm. The method is characterized by low-energy efficiency and relatively large droplet size. In the electrostatic sputtering method, the energy is supplied to a thin layer of disperse liquid by electrostatic charge. Coulomb forces applied to a film of liquid make it break down into droplets of 0.1–10 μm. The electrostatic sputtering method is influenced by the value of surface tension, viscosity, liquid conductivity, and electric field intensity. The main disadvantages of the method are the high energy costs and complexity of the equipment. The use of ultrasonic sputtering method converts liquid into aerosol state due to application of mechanical oscillations of ultrasonic frequency. The method is quite economical but has a relatively low sputtering rate (less than 2 cm^3/min). The aerosol particles, depending on the specified conditions, have a diameter from 0.1 to 10 μm and are characterized by high monodispersity.

The properties of the synthesized films primarily depend on the choice of aerosol precursors (molecular solutions, sols, colloid dispersions), the bulk sputtering rate, the size of the aerosol droplets, and the substrate temperature. The use of aqueous solutions is associated with a large range

of water-soluble metal salts, as well as safety conditions. For the deposition of cadmium and zinc sulfide films, solutions containing chlorides or organometallic metal compounds and thiourea are most commonly used. Precursors usually used for deposition of Cd-based compounds are listed in Table 10.14.

Table 10.14 Growth parameters used for growth on the glass substrate of Cd-based films by employing ASP process

Material deposited	Substrate temperature °C	Precursors	Spray rate ml/min
CdS	400	$CdCl_2{\cdot}5H_2O$, $(NH_2)_2CS$	2.5
CdS	275–350	$CdCl_2 \cdot H_2O$, H_2NCSNH_2	3
CdS	250	$CdCl_2$ and Thiourea	3
CdS	400	$CdAc_2$, $(NH_2)_2CS$, (NH_4) Ac	
CdS:Al	300	$Cd(COOCH_3)_2$, (NH_2CSNH_2) and $Al(CH_3COO)_3{\cdot}2H_2O$	-
CdS:Pb	400	$CdCl_2$, $(SC(NH)_2$, Pb (NO_3)	-
CdSe	275–350	$CdCl_2{\cdot}H_2O$, H_2NC (Se)NH_2	3
p-CdTe	225–300	$CdCl_2$, TeO_2	1.5
p-CdTe	350	$CdCl_2{\cdot}H_2O$, TeO_2	5

Source: Data extracted from Majid and Bibi [73]

The mechanism of film formation in the application of spray pyrolysis is very complex and has been poorly studied so far [51]. In order to obtain a homogeneous solid layer, it is important that the droplet appears at the substrate immediately after evaporation of the solvent from it. However, during movement, the aerosol droplets gradually dry out and a solid crust is formed on their surface. When completely dried, hollow solid particles are formed, which deposition on the substrate leads to a deterioration of the film properties. To prevent this phenomenon, optimization of process parameters such as solution concentration, aerosol flow rate, substrate temperature, particle size, and distance to the substrate is necessary. It has been found that at low temperatures of the substrate, the deposited film is often cracked, and a loose low-adhesion coating is formed at considerable heating due to the rapid removal of the solvent. It should also be considered

that the different volatility of the solution components can cause deviation of the film composition from the stoichiometric one while forming. A large number of works on synthesis of II-VI films for photodetectors and chemical sensors by spray pyrolysis method have been published [4, 22–24, 44, 114, 115, 119]. In addition to the evaluation of the influence of substrate temperature on their morphology, semiconductor and photoelectric properties [22], spray gas pressure [44], solution concentration [23], and optimization of synthesis conditions [114], a significant number of publications relate to film doping with various chemical elements: Al, La, Sm, Pb, F, Br, Fe, etc. ([4, 24, 115]; 89–91). In most cases, the basic functional properties of the deposited films are improved with the introduction of the dopant of 5–6% by weight into the film.

The crystallinity and the size of crystallites in deposited II-VI films depend on the time of deposition and the temperature of substrate. For example, it was established for CdS films, an increase in crystal quality was observed when substrate temperature was raised to 300 °C. At this temperature the grown CdS films were stoichiometric, polycrystalline in nature, having a hexagonal structure and containing uniformly distributed, and uneven spherical grains of size about 120 nm. The films deposited at 300 °C were n-type semiconducting with direct band gap of 2.44 eV and have minimum resistivity [73]. The effect of deposition time on film parameters is shown in Fig. 10.13 and Table 10.15. They refer to ZnS films obtained by spray pyrolysis at 450 °C [22]. As it can be seen from these results, after 10 minutes, the thickness of the layer reaches 1750 nm with an increase in crystallite sizes to 102 nm. The average film growth rate also increases to 205 nm/min by the 8th minute of the process. It also should be noted that as the deposition time increases, the crystallinity of the ZnS films increases with a decrease in dislocation density and microstrains in them.

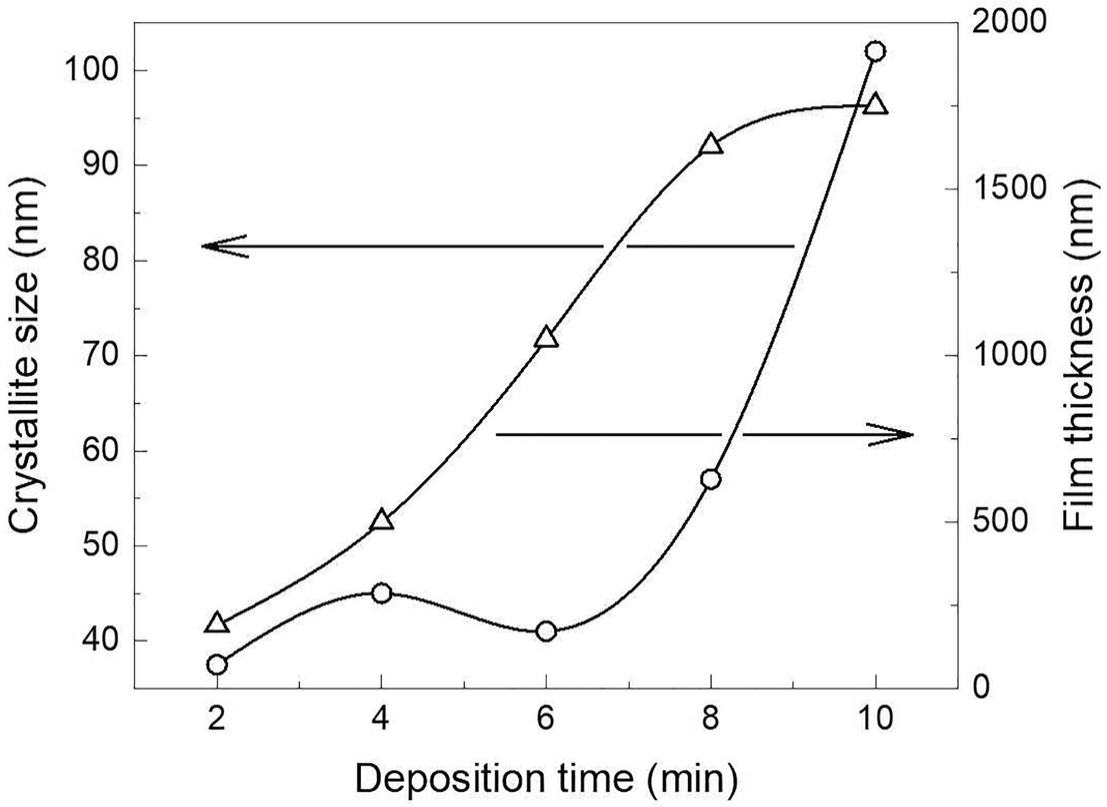

Fig. 10.13 Dependence of the thickness and average grain size of the ZnS films on the time of the spray pyrolysis process at a substrate temperature of 450 °C. (Data extracted from Ref. [22])

Table 10.15 Full width at half maximum (FWHM), growth rate, dislocation density, microstrain, conductivity of the ZnS films produced by the spray pyrolysis process at a substrate temperature of 450 °C

Deposition time, min	**2θ, degree**	**FWHM, degree**	**Growth rate, nm/min**	**Dislocation density $\times 10^{14}$, lines/m^2**	**Microstrain $\times 10^{-4}$**	**Conductivity $\times 10^{-6}$, $\Omega^{-1}\cdot cm^{-1}$**
2	28.7488	0.216	95	6.93	9.13	0.50
4	28.7358	0.18	132	4.81	7.6	0.55
6	28.806	0.2	176	5.94	8.45	0.93
8	28.7785	0.144	205	3.08	6.08	2.35
10	28.6966	0.08	180	0.95	3.38	6.60

Source: Data extracted from Derbali et al. [22]

Thermal annealing of as-deposited films also strongly affects the properties of II-VI films. The lattice constant and grain size increased consistently with increase in annealing temperature of the films. Another

factor affecting the crystallite size is film doping during deposition. It has been observed that, as a rule, crystallite size consistently decreases with an increase in metal doping concentration in the spray solution.

Since SPD is a solution-based chemical deposition method, the nature of the solution also plays an important role in determining the quality of the grown materials. Recently, Kerimova et al. [46] deposited nanocrystalline CdS films at different solution pH values using the SPD method. The films grown at pH 6.7 and 9.5 had a wurtzite crystal structure, while the film grown at pH = 10.2 was almost amorphous. Based on the structural and optical characteristics, it was concluded that the crystallinity and grain size of films deposited with SP decrease with increasing pH of the solution used.

10.11 Electrochemical Deposition

Electrodeposition is the process of depositing metals or semiconductors onto a conductive substrate by passing an electric current through an ionic electrolyte containing metal or semiconductor ions. It should be noted that the electroplating technique in the deposition of II-VI semiconductor materials dates back to the 1970s [30, 98]. A typical two-electrode configuration electrodeposition setup consists of a deposition vessel with an electrolyte, a magnetic stirrer, a hotplate, a power supply, a working electrode (conductive substrate), a counter electrode, and an additional reference electrode in the case of a three-electrode configuration. The use of a potentiostatic power supply is necessary due to the influence of the deposition voltage on the atomic percentage composition of the elements in the electroplated layer, which is one of the factors that determine the type of conduction of II-VI compounds [96, 111].

Both cathodic and anodic methods can be used to precipitate II-VI compounds in an aqueous medium, the first of which includes the joint precipitation of higher-valence metal ions and chalcogenide ions, and the second is based on metal corrosion in a chalcogenide medium. For example, for the deposition of CdTe layers, the component processes can be represented by Eqs. (10.3, 10.4, 10.5, 10.6 and 10.7) [108, 111]:

Cathodic

$$\mathrm{Cd}^{2+} + 2\mathrm{e}^{-} = \mathrm{Cd}^{0} \tag{10.3}$$

$$HTeO_2^+ + 4\ e^- + 3H^+ = Te^o + 2H_2O \tag{10.4}$$

$$Cd^o + Te^o = CdTe \tag{10.5}$$

Anodic

$$Cd^o = Cd^{2+} + 2e^- \tag{10.6}$$

$$Cd^{2+} + Te^{2-} = CdTe \tag{10.7}$$

It must be emphasized, however, that the actual electrodeposition chemistry that is involved is much more complex than that indicated by Eqs. (10.3, 10.4, 10.5, 10.6, and 10.7). It should be noted that in indicated above reactions the solution pH plays an important role. Cathodic electrodeposition is routinely carried out in acidic media; anodization on the other hand is facilitated at alkaline pHs by the stability of low-oxidation state chalcogen species in this range. The main disadvantage of anodic chemical synthesis is that thin film growth is self-limiting. Thus, films thicker than a few tens of nanometers are difficult to achieve. At the same time, much thicker films (several μm) can be realized through the cathodic strategy [108]. As a rule, cathodic deposition is mainly utilized due to its ability to produce stoichiometric thin films with good adherence to the substrate as compared to anodic deposition [96].

The precipitation of Cd-based compounds (CdSe, CdTe, CdS) can be carried out in both acidic and basic solutions [111]. The particle size depends on the anions used in the bath (chloride or perchlorate). For zinc compounds (ZnTe, ZnSe, ZnS), electrodeposition from standard acidic aqueous solutions is more difficult [61]. The films often contain an excess of Se or Te, which indicates that the self-regulation mechanism predicted by the Kroger theory is less effective. This may be due to the fact that the zinc potential is more negative than the cadmium potential by 0.36 V, and it is known that deposition close to the metal potential is favorable. Increasing the negative precipitation potential leads to new problems due to hydrogen evolution and further reduction of chalcogenide elements by parallel reactions. These parasitic reactions disrupt film growth. Examples of precursors that can be used for electrodeposition of II-VI semiconductors are listed in Table 10.16.

Table 10.16 Electrodeposition of II-VI compounds from aqueous solutions

Material	Precursors used	Comments
CdTe	$CdSO_4$ or $Cd(NO_3)_2$ or $CdCl_2$ for Cd ions and TeO_2 for Te ions	Ability to grow both p- and n-type CdTe using Cd-sulfate, nitrate, and chloride precursors
CdSe	$CdCl_2$ for Cd ions and SeO_2 or H_2SeO_3 for Se ions	Ability to grow both p- and n-type material
	$CdSO_4$ for Cd ions and Na_2SeO_3 for Se ions	
CdS	$CdCl_2$ for Cd ions and $Na_2S_2O_3$, $NH_4S_2O_3$ or NH_2CSNH_2 for S ions	Conductivity type is always n-type
	$Cd(NO_3)_2$ for Cd ions and $(CH_3)_2SO$ for S ions	
ZnTe	$ZnSO_4$ for Zn ions and TeO_2 for Te ions	Ability to grow both p- and n-type material
ZnSe	$ZnSO_4$ for Zn ions and SeO_2 for Se ions	Ability to grow both p- and n-type material
ZnS	$ZnSO_4$ for Zn and $(NH_4)_2S_2O_3$ for S ions	Ability to grow both p- and n-type material

Source: Adapted from Ref. [96]. Published in 2018 by MDPI as open access

The deposition temperature depends on the electrolyte used. For electroplated semiconductor materials from aqueous solution, there is a limitation on the growth temperature due to the boiling temperature of water at 100 °C under standard atmospheric pressure, while the electroplating from other electrolytic baths can go as high as 160 °C. The electrolytic bath temperature increases the transport of species participated in reactions, which results in an increase in the deposition current density and rate of deposition of constituent elements or compounds. It was also shown that an increase in the crystallinity of as-deposited semiconductor material is achievable at higher growth temperature. Deposition of materials at a higher temperature provides the energy needed for the ions/atoms to move and deposit in a regular crystal structure. Current dc density during deposition process can vary over a very wide range from 0.8 to 200 mA/cm^2. Platinum is usually used as the cathode.

Poor adhesion and nonuniform films are common problems when depositing films of II-VI compounds onto a smooth surface, as the

contaminated surface provides nucleation sites facilitating the growth, which results in nonuniform film growth. Therefore, during the deposition of thin film, substrate cleaning is very important.

Ternary II-VI compounds can also be deposited using electrodeposition techniques. Thus, thin films of Cd_xSe_{1-x}, Cd_xTe_{1-x}, and $Hg_{1-x}Cd_xTe$ were formed using these methods [108, 111]. However, due to the presence of a greater number of active species in the solution, the choice of operational parameters for the electrosynthesis of semiconductor alloys in this case becomes more laborious.

Electroplating is a simple and cheap method for depositing II-VI semiconductor compounds. However, this method also has disadvantages. According to Ojo and Dharmadasa [96], the disadvantages of this method include:

- Instability of current density during deposition
- Difficulties with control and regulation of ions within the electrolytic bath
- Extrinsic doping of electrolytic bath by the electrodes
- Nonuniformity of electrodeposited semiconductor layers
- Need for post-growth treatment

Despite intensive development, electrochemical methods have not yet found a wide practical application for the production of photonics materials and chemical sensors. There is a high degree of dependence of the properties of the deposited films on the deposition mode and electrolyte composition [29]. Using ZnS as an example, Table 10.17 and Fig. 10.13 show how strong the influence of deposition modes on the parameters of films deposited by this method can be. It can be seen that a change in the potential applied to the electrode from -1.0 to -1.3 V is accompanied by a doubling of the growth rate and film thickness, a threefold decrease in the dislocation density, a significant increase in the roughness and microstress in the layer, and a decrease in the size of crystallites (see Fig. 10.14).

Table 10.17 Parameters of ZnS obtained by electrodeposition at various values of the electrode potential

Applied potential, V	**Lattice constant, nm**	**Thickness, nm**	**Growth rate, nm/s**	**Roughness, nm**	**Dislocation density $\times 10^{10}$, lines/cm^2**
–1.0	0.54299	202.60	0.675	8.7	2.3047

Applied potential, V	Lattice constant, nm	Thickness, nm	Growth rate, nm/s	Roughness, nm	Dislocation density $\times 10^{10}$, lines/cm^2
–1.1	0.54161	229.92	0.766	13.2	1.0760
–1.2	0.54336	365.50	1.218	12.8	0.7554
–1.3	0.54351	401.54	1.338	33.1	0.7455

Source: Adapted with permission from Ghezali et al. [29] Copyright 2017: Elsevier

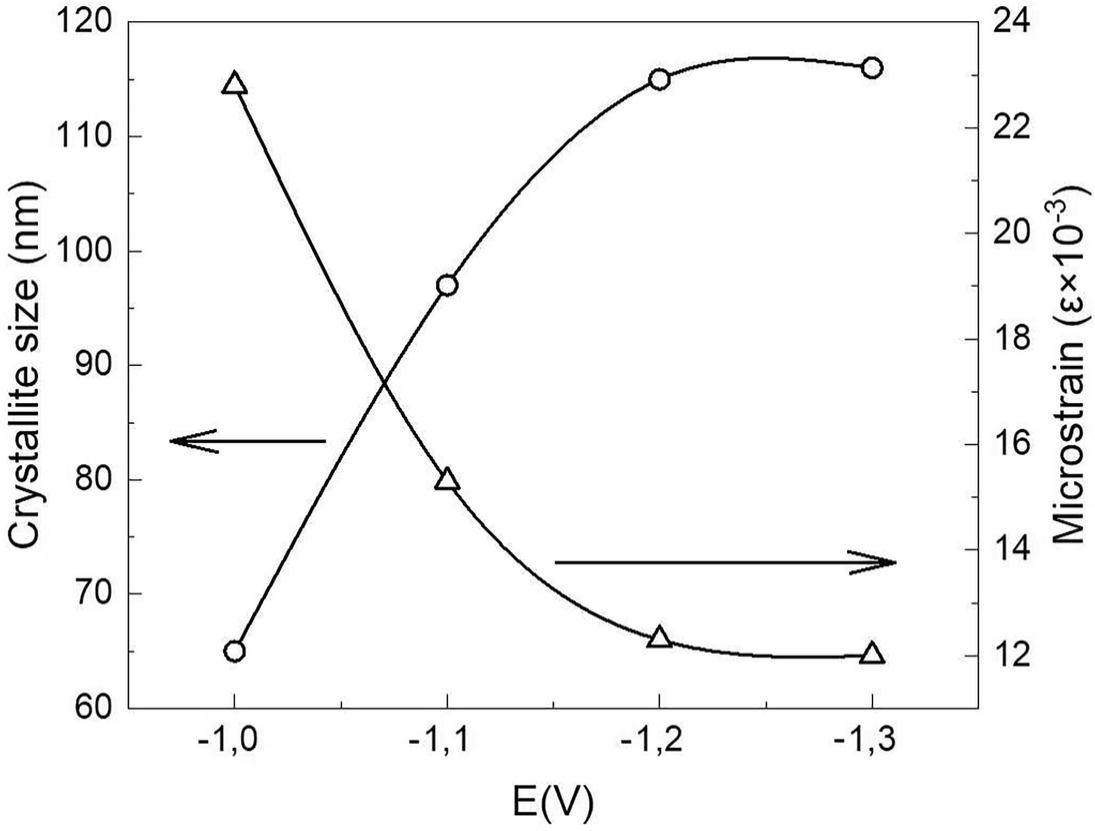

Fig. 10.14 Dependence of the average size of crystallites and microstrains in electrodeposited ZnS films on the magnitude of the potential at the electrode. (Adapted with permission from Ref. [29]. Copyright 2017: Elsevier)

Recently, much attention has been paid to the development of pulsed electrodeposition of II-VI compounds, which allows to increase the deposition rate significantly and obtain films with improved morphological and structural properties due to the effect of short high-voltage pulses (10^{-4}–10^{-5} s) of polarizing voltage on the electrode-solution phase boundary [75].

There is also an electrophoretic deposition of II-VI semiconductors, which is based on the phenomenon of electrophoresis in colloid systems [30]. An overview of electrophoretic film deposition is published in [9]. The deposited layers are loose and weakly bonded to the substrate. Thus, their heat treatment is required.

As regards the structure of the deposited films of the II-VI compounds, in most cases the deposited samples consist of an amorphous phase. Therefore, to transfer them to the crystalline state, additional heat treatment after deposition is required. For example, Ohta and Ohgai [95] used annealing at 653–683 K for 5 h to crystallize electrodeposited ZnTe films. They found that the electrodeposited thin films of zinc telluride crystallized at an annealing temperature above 653 K. The electrodeposited thin films of zinc telluride, post-annealed at 653–673 K, consisted of binary phases (ZnTe and Te). On the contrary, the electrodeposited thin film after annealing at 683 K consisted of single-phase zinc telluride. Crystallization was also accompanied by an increase in the optical band gap and a decrease in resistivity.

10.12 Close-Space Sublimation Method

Close-space sublimation (CSS) method is inherently a form of thermal evaporation. The CSS technique is one of the most economical and cheap. The CSS process offers the advantages of a simple deposition apparatus and high transport efficiency under low vacuum conditions at moderate temperatures. This simplifies the scaling of the process, which is necessary for the organization of large-scale production. Films and crystals of II-VI semiconductors such as CdS [104], CdTe [48, 113], CdSe [58], CdTe/CdS [104], ZnTe [105], ZnSe [119], and others were obtained by this method.

The CSS method is based on the thermal-heating-induced sublimation of a material followed by vapor condensation onto a closely spaced substrate [112]. Figure 10.15 shows the schematic diagram of the CSS system and substrate sandwiched in the growth chamber. The source and substrate are separated by spacers enclosed in a reaction chamber and held between two graphite susceptors inside a quartz reactor. The cross dimensions of the source and the substrate greatly exceed the distance between them. The distance between the source material and the substrate usually does not exceed 4 mm. The source of heating is usually from visible

or infrared lamps outside the reactor facing the blocks of graphite, used to reduce the temperature gradient in the chamber. Other heaters may also be used. In particular, Plaza et al. [104] used the SiC electrical heating elements for these purposes. A set of thermocouples monitored the temperature of the graphite blocks for both the source and the substrate temperatures. A diffusion-controlled transport mechanism takes place during the temperature difference between the source and substrate. The material to be deposited is placed on a boat heated to temperatures above the substrate temperature. Polycrystals of II-VI compounds, synthesized by various methods, are usually used as a source. You can also use single-crystal or polycrystalline wafers, powders, pellets or pieces, and a thick II-VI film deposited onto glass or molybdenum substrate. Due to the temperature difference, the material sublimating from the source transfers to the substrate. The deposition rate depends upon the source, spacing, substrate temperature, and ambient gas nature.

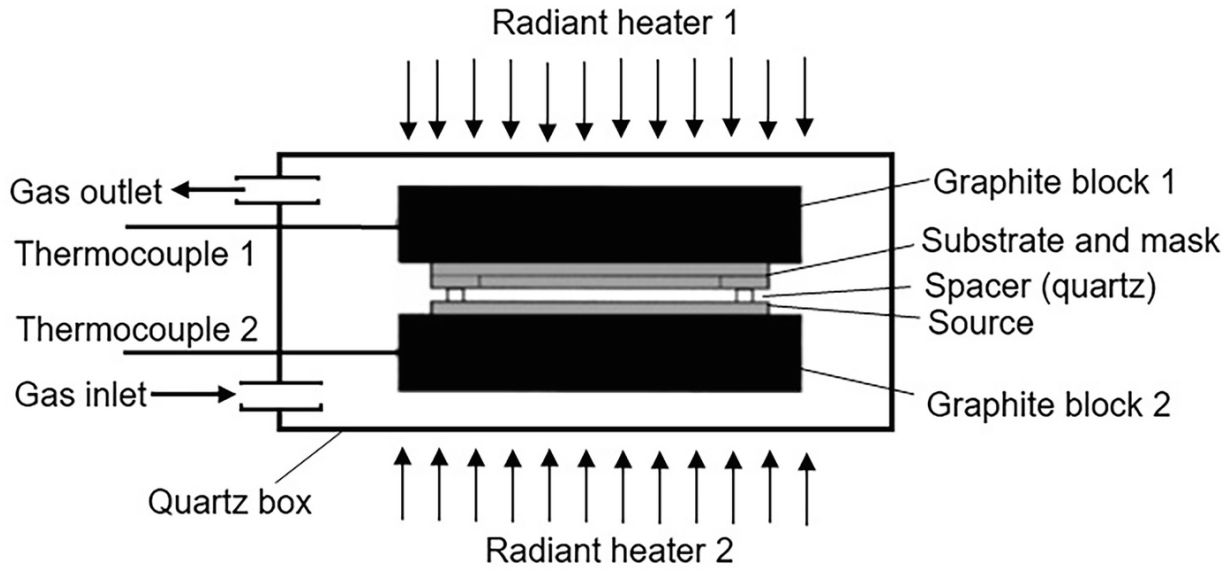

Fig. 10.15 (**a**) Schematic showing (**a**) the CSS system, and (**b**) the source and the substrate sandwiched in the growth chamber

In “classic” CSS, the substrate to be coated and the source material are both placed in a vacuum chamber, which is pumped out [104, 113]. In particular, in [113] the chamber for CSS was evacuated down to 10^{-3} mbar. Plaza et al. [104] deposited films at pressures below 1 mbar. However, it has been shown that the precipitation of II-VI compounds can be carried out without the use of vacuum [48]. It has been found that a hydrogen or inert gas atmosphere is also suitable for this process [86]. For example, Cruz et

al. [19] for deposition of CdS/CdTe films used the atmosphere of argon, nitrogen, or a mixture of oxygen/argon with a pressure between 5 and 15 Torr.

The temperature of the source material and the substrate depends on the deposited material. For example, during the deposition of CdS films, the source temperature was 680 °C, and substrate was kept at 520 °C [32]. The film growth rate was ~7–8 nm/min. Cruz et al. [19] deposited CdS films, using for the source and substrate the temperatures 660 °C and 540 °C, respectively. The rate of deposition varied in the range from 50 to 150 nm/min. The size of crystallites in CdS films increased with increasing temperature and film thickness (Fig. 10.16). Typically, film thickness increases linearly with deposition time. According to Plaza et al. [104], the best source temperature for the homogeneous deposition of CdS films was 800 °C. Deposited films were quite compact, with microcrystals close to 30 μm in size. For higher-source temperatures, the structure of the crystals was distorted. Shah et al. [113] for deposition of CdTe films used source and substrate heated to 450 °C and 300 °C, respectively. Similar parameters for deposition of CdTe films were used by Potlog et al. [105]. CdTe thin films were deposited at a temperature of the source and substrate of 340 °C and 590 °C, respectively. At the same time, Plaza et al. [104] believe that the source and the substrate during CdTe deposition should have temperatures 700 °C and 590 °C, respectively. It was established that the grain size in CdTe films was much smaller (typically in the range between 2 and 3 μm) than in the case of the CdS films. For the deposition of ZnTe films, Potlog et al. [105] used source and substrate heated to temperatures of 660 °C and 430 °C. Undoped ZnTe layers had a resistivity of (10^6–10^8) Ω·cm. The resistivity of ZnTe thin films grown from ZnTe crystals doped with As reached a value of (10^2–10^3) Ω·cm.

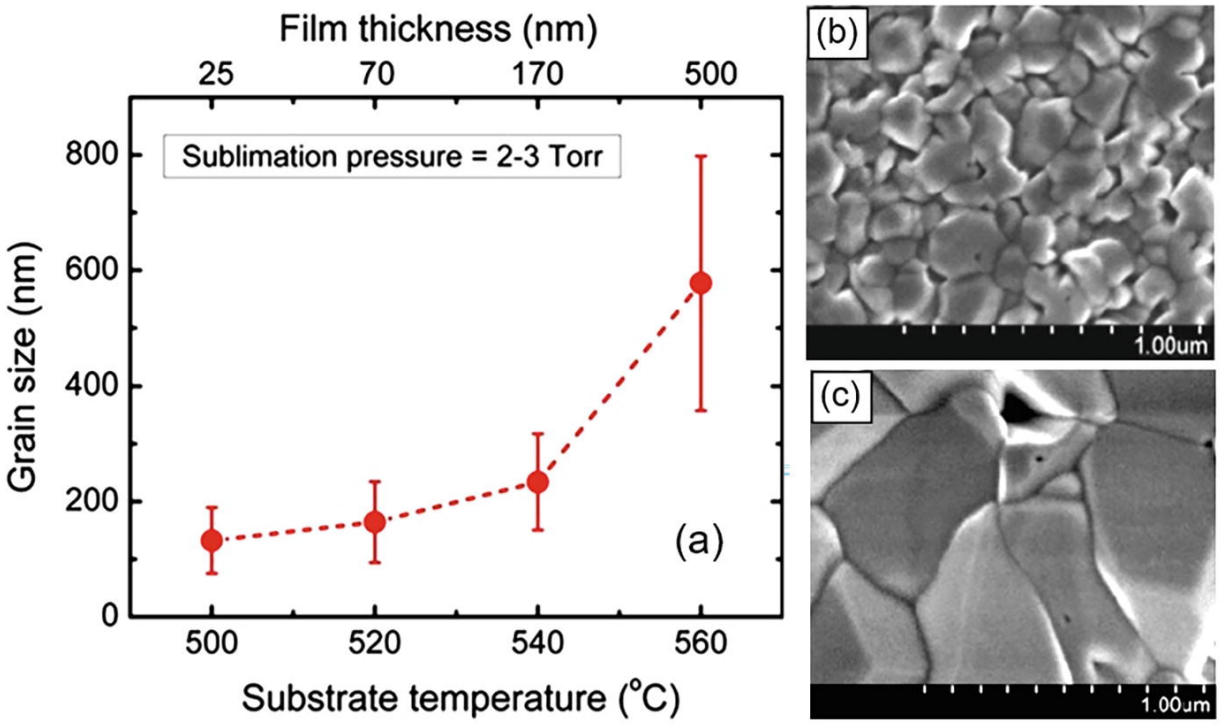

Fig. 10.16 (**a**) Average grain sizes of CSS CdS layers deposited at different temperature. (**b**, **c**) Plan-view SEM images of CSS CdS films grown at (**b**) 500 °C (*d* = 25 nm) and (**c**) 560 °C (*d* = 500 nm). (Reprinted with permission from Paudel et al. [101]. Copyright 2014: Springer)

Depending on the conditions, the film growth process can be described using the following mechanisms [2]: (a) Diffusion-limited transport: The deposited materials migrate to the substrate through the ambient gas and collide several times with gas molecules before condensing on the substrate. (b) Langmuir's theory: The deposited materials are moved directly to the substrate without any gas phase collision.

If we compare CSS deposition technology with sputtering and chemical bath deposition (CBD) methods, often used in the formation of II-VI compound films, then due to the high substrate temperatures, grain size and roughness in CSS films are larger than in CBD and sputtered films [19]. CBD and sputtering have also much lower deposition rate than CSS method. In addition, CBD is a wet process; therefore, in terms of manufacture compatibility, CSS technology is the most preferred growth method. However, as CSS is a high-rate deposition technique, it is difficult to get very thin films (d<100 nm) with nanosize crystallites using this process. In this case, the control of some parameters, such as pressure and source/substrate temperatures, is essential for obtaining thin continuous films. In addition, Paudel et al. [101] believe that a significant disadvantage

of CSS films is also the formation of voids (holes) in the films, caused by the large grain size due to growth at high temperature. It is these shortcomings of CSS deposition technology that significantly limit its use in the development of gas sensors and photodetectors.

Acknowledgments

G. Korotcenkov is grateful to the State Program of the Republic of Moldova, project 20.80009.5007.02, for supporting his research.

References

1. Afzaal M, Crouch D, O'Brien P, Park J-H (2002) Metal-organic chemical vapour deposition of II-VI semiconductor thin films using single-source approach. MRS Proc 730:V3.5.1–V3.5.6
2. Alamri SN (2003) The growth of CdTe thin film by close space sublimation system. Phys Status Solidi 200(2):352–360
3. Alias MFA, Salman M, Al-Douri AAJ (2014) The role of thickness on structural properties of thin CdS films prepared by pulse laser deposition. Int J Adv Sci Tech Res 4:620–626
4. Attaf A, Derbali A, Saidi H, Benamra H, Aida MS, Attaf N et al (2020) Physical properties of Pb doped ZnS thin films prepared by ultrasonic spray technique. Phys Lett A 384:126199
5. Baghchesara MA, Yousefi R, Cheraghizade M, Jamali-Sheini F, Sáaedi A (2016) Photocurrent application of Zn-doped CdS nanostructures grown by thermal evaporation method. Ceram Int 42(1):1891–1896
6. Barman B, Bangera KV, Shivakumar GK (2019) ZnxCd1-xS thin films: A study towards its application as a reliable photodetector. Superlattice Microst 137:106349
7. Berlin EV, Seidman LA (2014) Obtaining Thin films by Reactive Magnetron Sputtering. Technosphere, Moscow. (in Russian)
8. Berlin EV, Dvinin SA, Seidman LA (2007) Vacuum technology and equipment for the applying and etching thin films. Technosphere, Moscow, p 176. (in Russian)
9. Besra L, Liu M (2007) A review on fundamentals and applications of electrophoretic deposition (EPD). Progr Mater Sci 52:1–61
10. Buckingham MA, Catherall AL, Hill MS, Johnson AL, Parish JD (2017) Aerosol-assisted chemical vapor deposition of CdS from xanthate single source precursors. Cryst Growth Des 17(2):907–912
11. Chalana SR, Vinodkumar R, Navas I, Ganesan V, Pillai VPM (2012) Influence of argon ambience on the structural, morphological and optical properties of pulsed laser ablated zinc sulfide thin films. J Lumin 132:944–952

12. Chaudhari KB, Gosavi NM, Deshpande NG, Gosavi SR (2016) Chemical synthesis and characterization of CdSe thin films deposited by SILAR technique for optoelectronic applications. J Sci Adv Mater Dev 1(4):476–481
13. Cheon JW, Talaga DS, Zink JI (1997) Photochemical deposition of ZnS from the gas phase and simultaneous luminescence detection of photofragments from a single-source precursor, Zn (S2COCHMe2)2. J Am Chem Soc 119(1):163–168
14. Chopra KL, Das SR (1983) Thin Film solar cells. Plenum Press, New York–London
15. Choy KL (2003) Chemical vapour deposition. Progr Mater Sci 48:57–170
16. Chu TL, Chu SS (1995) Thin film II-VI photovoltaics. Solid State Electron 38(3):533–549
17. Colegrove E, Albin DS, Moutinho HR, Amarasinghe M, Burst JM, Metzger WK (2020) Scalable ultrafast epitaxy of large-grain and single-crystal II-VI semiconductors. Sci Rep 10:2426
18. Coutts TJ (ed) (1978) Active and Passive Thin Film Devices. Academic Press, London, p 858
19. Cruz LR, Sousa Fernandes JA, Ferreira CL, Pinheir WA (2014) Microstructural and optical properties of CSS and CBD-CdS thin films for photovoltaic solar cells. Revista Mater 19(3):228–234
20. Decher G, Schlenoff JB (eds) (2003) Multilayer thin films: Sequential assembly of nanocomposite materials. Wiley-VCH, New York, p 511
21. Deivanayaki S, Jayamurugan P, Mariappan R, Ponnuswamy V (2010) Optical and structural characterization of CdTe thin films by chemical bath deposition technique. Chalcogenide Lett 7:159–163
22. Derbali A, Attaf A, Saidi H, Benamra H, Nouadji M, Aida MS et al (2018a) Investigation of structural, optical and electrical properties of ZnS thin films prepared by ultrasonic spray technique for photovoltaic applications. Optik 154:286–293
23. Derbali A, Saidi H, Attaf A, Benamra H, Bouhdjer A, Attaf N et al (2018b) Solution flow rate influence on ZnS thin films properties grown by ultrasonic spray for optoelectronic application. J Semicond 39:093001
24. Derbali A, Attaf A, Saidi H, Aida MS, Benamra H, Attaf R et al (2021) Br doping effect on structural, optical and electrical properties of ZnS thin films deposited by ultrasonic spray. Mater Sci Eng A 268:115135
25. Doering R, Nishi Y (eds) (2008) Handbook of Semiconductor Manufacturing Technology. CRC press, New York
26. Garcia LV, Loredo SL, Shaji S, Aguilar Martinez JA, Krishnan B (2016) Structure and properties of CdS thin films prepared by pulsed laser assisted chemical bath deposition. Mater Res Bull 83:495–467

27. Garje SS, Ritch JS, Eisler DJ, Afzaal M, O'Brien P, Chivers T (2006) Chemical vapour deposition of II-VI semiconductor thin films using $M[(TePiPr_2)_2N]_2$ (M = Cd, Hg) as single-source precursors. J Mater Chem 16:966–969
28. Geethanjali PM, Deepa K, Remadevi TL (2021) Effect of number of cycles on SILAR deposited ZnSe thin films. AIP Conf Proc 2352:020011
29. Ghezali K, Mentar L, Boudine B, Azizi A (2017) Electrochemical deposition of ZnS thin films and their structural, morphological and optical properties. J Electroanal Chem 794:212
30. Glasstone S (1960) The fundamentals of electrochemistry and electrodeposition. American Electroplaters Society/ Franklin Pub Co, p 90
31. Gurav A, Kodas T, Pluym T, Yun X (1993) Aerosol processing of materials. Aerosol Sci Technol 19:411–452
32. Han J, Liao C, Jiang T, Spanheimer C, Haindl G, Fu G et al (2011) An optimized multilayer structure of CdS layer for CdTe solar cells. J Alloys Compounds 509(17):5285–5289
33. Hartmann H. (1975) Vapour phase epitaxy of II-VI compounds: a review, In: Vapour growth and epitaxy, proceedings of the third international conference on vapour growth and epitaxy, Amsterdam, The Netherlands, 18–21 August 1975, pp 323–332
34. Hendi AA (2014) Optical characterizations of CdS thin films grown by pulsed laser deposition technique. J Nano Electron Optoelectron 9:596–600
35. Hernandez-Calderon I (2013) Epitaxial growth of thin films and quantum structures of II-VI visible-bandgap semiconductors. In: Henini M (ed) Molecular Beam Epitaxy. Elsevier, pp 311–346
36. Ho S (2016) A brief review of the growth of pulsed laser deposited thin films. J Appl Sci Technol 14(6):1–6
37. Hodes G (2002) Chemical Solution Deposition of Semiconductor Films. Marcel Dekker Inc., New York, p 388
38. Husham M, Hassan Z, Selman A (2016) Synthesis and characterization of nanocrystalline CdS thin films for highly photosensitive self-powered photodetector. Eur Phys J Appl Phys 74:10101
39. Hwang DH, Ahn JH, Hui KN, Hui KS, Son YG (2012) Structural and optical properties of ZnS thin films deposited by RF magnetron sputtering. Nanoscale Res Lett 7:26
40. Islam S, Hossain T, Sarwar H, Junaebur RM (2020) A systematic study on chemically deposited cadmium sulfide (CdS) thin film. J Theor Appl Phys 14(3):265–274
41. Jaeger RC (2002) Film Deposition: Introduction to Microelectronic Fabrication. Prentice Hall Upper Saddle River, New Jersey, p 303
42. Kalita PKR, Sarma BK, Das HL (2000) Structural characterization of vacuum evaporated ZnSe thin films. Bull Mater Sci 23:313–317

43. Karam NH, Wolfson RG, Bhat IB, Ehsani H, Ghandhi SK (1993) Growth and characterization of CdTe, HgTe and HgCdTe by atomic layer epitaxy. Thin Solid Films 225:261–264
44. Kathalingam A, Valanarasu S, Ahamad T, Alshehri SM, Kim H (2020) Spray pressure variation effect on the properties of CdS thin films for photodetector applications. Ceram Int 47:7608–7616
45. Kennedy J, Murmu PP, Gupta PS, Carder DA, Chong SV, Leveneur J, Rubanov S (2014) Effects of annealing on the structural and optical properties of zinc sulfide thin films deposited by ion beam sputtering. Mater Sci Semicond Process 26:567–566
46. Kerimova A, Bagiyev E, Aliyeva E, Bayramov A (2017) Nanostructured CdS thin films deposited by spray pyrolysis method. Phys Status Solidi C 14(6):1600144
47. Ketchemen KIY, Mlowe S, Nyamen LD, Ndifon PT, Revaprasadu N, O'Brien P (2018) CdS thin films deposition by AACVD: effect of precursor type, decomposition temperature and solvent. J Mater Sci Mater Electron 29(17):14462–14470
48. Khomchenko VS, Sopinskyy MV, Dan'ko VA, Olkhovik GP (2020) Doping the thin films by using the original close space sublimation method. Semicond Phys Quant Electron Optoelectron (SPQEO) 23(1):5–28
49. Kim D, Park Y, Kim M, Choi Y, Park YS, Lee J (2015) Optical and structural properties of sputtered CdS films for thin film solar cell applications. Mater Res Bull 69:78–83
50. Konagai M, Takemura Y, Yamasaki K, Takahashi K (1993) Self-limiting growth of zinc chalcogenides and their superlattices. Thin Solid Films 225:256–260
51. Korotcenkov G, Cho BK (2010) Synthesis and deposition of sensor materials. In: Korotcenkov G (ed) Chemical Sensors: Fundamentals of Sensing Materials, General Approaches, vol 1. Momentum Press, New York, USA, pp 215–304
52. Kozhevnikova NS, Vorokh AS, Uritskaya AA (2015) Cadmium sulfide nanoparticles obtained by chemical bath deposition. Russ Chem Rev 84:225–250
53. Kozlovsky VI, Martovitsky VP, Sannikov DA, Kuznetsov PI, Yakushcheva GG, Jitov VA (2003) MOVPE growth and characterization of hexagonal CdS epilayers and CdS-based QW structures on CdS and ZnCdS substrates. J Cryst Growth 248:62–66
54. Kumar P, Saxena N, Gupta V (2018) Ion beam assisted fortification of photoconduction and photosensitivity. Sens Actuators A 279:343–350
55. Kumar P, Saxena N, Gupta V (2020) Vital role of Ar ambient pressure in controlled properties of nanocrystalline CdS thin films. J Mater Sci - Mater Electron 31:6755–6763
56. Kuznetsov PI, Yakushcheva GG, Jitov VA, Zakharov LY, Shchamkhalova BS, Kozlovsky VI et al (2006) MOVPE growth and study of ZnCdSe/ZnSSe MQW structures for green VCSELs. Phys Status Solidi 3:771–775
57. Li J, Chen J, Sestak MN, Thornberry C, Collins RW (2009) Spectroscopic ellipsometry studies of thin film CdTe and CdS: From dielectric functions to solar cell structures. In: Proceeding of

34th IEEE photovoltaic specialists conference (PVSC). 11152208

58. Li K, Lin X, Song B, Kondrotas R, Wang C, Lu Y et al (2021) Rapid thermal evaporation for cadmium selenide thin-film solar cells. Fron Optoelectron 14(4):482–490

59. Liang G-X, Fan P, Zheng Z-H, Luo J-T, Zhang D-P, Chen C-M, Cao P-J (2013) Room-temperature preparation and properties of cadmium sulfide thin films by ion-beam sputtering deposition. Appl Surf Sci 273:491–495

60. Lin J-S, Wei S-S, Yu Y-T, Hsu C-H, Kao W-H, Chen W-S et al (2013) Synthesis and characterization of ZnTe thin films on silicon by thermal-furnace evaporation. Proc SPIE 8913:89130K

61. Lincot D (2005) Electrodeposition of semiconductors. Thin Solid Films 487:40–48

62. Lincot D, Froment M, Cachet H (1999) Advances in Electrochemical Science and Engineering. Wiley-VCH, Weinheim, p 165

63. Lindroos S, Kanniainen T, Leskela M, Rauhala E (1995) Deposition of manganese-doped zinc sulfide thin films by the successive ionic layer adsorption and reaction (SILAR) method. Thin Solid Films 263:79–84

64. Lindroos S, Kanniainen T, Leskelä M (1997) Growth of zinc sulfide thin films by the successive ionic layer adsorption and reaction (Silar) method on polyester substrates. Mater Res Bull 32(12):1631–1636

65. Liu Z (2010) Laser applied coatings. In: Materials Science and Materials Engineering Materials Science and Materials Engineering, Shreir's Corrosion, vol 4. Elsevier, pp 2622–2635

66. Lokhande CD (1991) Chemical deposition of metal chalcogenide thin films. Mater Chem Phys 27:1–43

67. Lokhande CD, Sankapal BR, Pathan HM, Muller M, Giersig M, Tributsch H (2001) Structural studies on successive ionic layer adsorption (SILAR)-deposited CdS thin films. Appl Surf Sci 181:277–282

68. Londhe PU, Rohom AB, Bhand GR, Jadhav S, Lakhe MG, Chaure NB (2017) Effect of complexing agent on the chemically deposited ZnS thin film. J Mater Sci Mater Electron 28(7):5207–5214

69. Mahdi MA, Hassan JJ, Ng SS, Hassan Z, Ahmed NM (2012) Synthesis and characterization of single-crystal CdS nanosheet for high-speed photodetection. Physica E Low Dimens Syst Nanostruct 44(7-8):1716–1721

70. Mahdi MA, Hassan JJ, Ahmed NM, Ng SS, Hassan Z (2013) Growth and characterization of CdS single-crystalline micro-rod photodetector. Superlattice Microst 54:137–145

71. Maissel LI, Glang R (eds) (1970) Handbook of Thin Film Technology. McGraw-Hill Book Company, New York

72. Majid A, Bibi M (2018a) Wet chemical synthesis methods. In: Cadmium based II-VI Semiconducting Nanomaterials, Topics in Mining, Metallurgy and Materials Engineering.

Springer, Cham, Switzerland, pp 43–101

73. Majid A, Bibi M (2018b) Vapor deposition synthesis. In: Cadmium based II-VI Semiconducting Nanomaterials, Topics in Mining. Metallurgy and Materials Engineering. Springer, Cham, Switzerland, pp 103–144

74. Maki SA, Hassun HK (2018) Effect of Aluminum on characterization of ZnTe/n-Si heterojunction photo detector. J Phys Conf Ser 1003:012085

75. Maliy L, Mamaev A, Mamaeva V (2017) Electrochemical high-energy deposition of CdSe nanostructures: modelling, synthesis and characterization. J Appl Electrochem 47(9):1073–1082

76. Markov VF, Maskaeva LN (2010) Calculating the boundary conditions of the formation of solid-phase metal sulfides and selenides by deposition with thio- and selenourea. Russ J Phys Chem A 84:1288–1293

77. Markov VF, Maskaeva LN, Ivanov PN (2006) Chemical bath deposition of metal sulfide films: modeling and experiment. Ural Branch of RAS, Ekaterinburg, p 218

78. Martin PM (2009) Handbook of Deposition Technologies for Films and Coatings: Science, Applications and Technology. William Andrew, p 936

79. Maskaeva LN, Markov VF, Forostyanaya NA, Kutyavina AD, Mokrousova OA (2016) Kinetic aspects of hydrochemical deposition of cadmium sulfide from solutions with diverse ligand backgrounds. Russ J Gen Chem 86(10):2273–2281

80. Maskaeva LN, Markov VF, Fedorova EA, Kuznetsov MV (2018) Influence of the conditions of the chemical bath deposition of thin ZnSe films on their morphology and internal mechanical stresses. Russ J Appl Chem 91(9):1528–1537

81. Maskaeva LN, Markov VF, Lipina OA, Pozdin AV, Anokhina LA (2020) Morphology, structure and optical properties of nanocrystalline CdSe films doped with copper. Russ J Phys Chem A 94(12):2441–2449

82. McClean IP, Thomas CB (1992) Photoluminescence study of MBE-grown films on ZnS. Semicond Sci Technol 7(11):1394

83. McLaughlin M, Sakeek H, Maguire PD, Graham WG, Molloy J, Morrow T, Laverty S (1993) Properties of ZnS thin films prepared by 248-nm pulsed laser deposition. Appl Phys Lett 63(14):1865–1867

84. Mertschenk B, Beck F, Bauer W (2005) Thiourea and Thiourea Derivatives. Wiley-VCH Verlag Gmb H and Co, KGaA, Weinheim, p 15

85. Ming Z, Ding C, Li B, Zhang J, Li W, Wu L, Feng L, Wu J (2013) Properties study of ZnS thin films fabricated at different substrate temperatures by pulsed laser deposition. Adv Mater Res 821-822:835–840

86. Mirsagatov SA, Uteniyazov AK (2012) Injection photodiode based on p-CdTe film. Tech Phys Lett 38(1):34–37

87. Moger SN, Mahesha MG (2020) Colour tunable co-evaporated CdS_xSe_{1-x} ($0 < x < 1$) ternary chalcogenide thin films for photodetector applications. Mater Sci Semicond Proc 120:105288
88. Moholkar AV, Shinde SS, Babar AR, Sim K, Lee HK, Rajpure KY, Patil PS (2011) Synthesis and characterization of Cu2ZnSnS4 thin films grown by PLD: Solar cells. J Alloys Compd 509:7439–7446
89. Moholkar AV, Shinde SS, Agawane GL, Jo SH, Rajpure KY, Patil PS, Bhosale CH, Kim JH (2012) Studies of compositional dependent CZTS thin film solar cells by pulsed laser deposition technique: An attempt to improve the efficiency. J Alloys Compd 544:145–151
90. Munusamy G, Peruma S (2020) Structural and optical properties of Silar deposited CdS and Ni, Ti & Zn doped CdS thin films. Int J Thin Film Sci Tec 9(3):169–174
91. Nair PK, Nair MTS, Garcia VM, Arenas OL, Pena Y, Castillo A et al (1998) Semiconductor thin films by chemical bath deposition for solar energy related applications. Sol Energy Mater Sol Cells 52:313–344
92. Nicolau YF (1985) Solution deposition of thin solid compound films by a successive ionic-layer adsorption and reaction process. Appl Surf Sci 22:1061–1074
93. Nicolau YF, Dupuy M, Brunel M (1990) ZnS, CdS, and $Zn_{1-x}Cd_xS$ thin films deposited by the successive ionic layer adsorption and reaction process. J Electrochem Soc 137:2915
94. Niesen TP, De Guire MR (2001) Review: Deposition of ceramic thin films at low temperatures from aqueous solutions. J Electroceramics 6:169–207
95. Ohta J, Ohgai T (2021) Post-annealing effects on the structure and semiconductor performance of nanocrystalline ZnTe thin films electrodeposited from an aqueous solution containing citric acid. Appl Sci 11:10632
96. Ojo AA, Dharmadasa IM (2018) Electroplating of semiconductor materials for applications in large area electronics: A review. CoatingsTech 8:262
97. Palve AM (2019) Deposition of Zinc Sulfide thin films from Zinc(II) Thiosemicarbazones as single molecular precursors using aerosol assisted chemical vapor deposition technique. Front Mater 6:46
98. Pandey RK, Sahu SN, Chandra S (1996) Handbook of Semiconductor Electrodeposition. Marcel Dekker, New York, NY
99. Patel NG, Panchal CJ, Makhija KK (1994) Use of Cadmium Selenide thin films as a Carbon dioxide gas sensor. Cryst Res Technol 29:1013–1020
100. Pathan HM, Lokhande CD (2004) Deposition of metal chalcogenide thin films by successive ionic layer adsorption and reaction (SILAR) method. Bull Mater Sci 27(2):85–111
101. Paudel JL, Xiao C, Yan Y (2014) Close-space sublimation grown CdS window layers for CdS/CdTe thin-film solar cells. J Mater Sci Mater Electron 25:1991–1998

102. Pawar SM, Pawar BS, Kim JH, Joo O-S, Lokhande CD (2011) Recent status of chemical bath deposited metal chalcogenide and metal oxide films. Current Appl Phys 11:117–161
103. Perednis D, Gauckler LJ (2005) Thin film deposition using spray pyrolysis. J Electroceramics 14:103–111
104. Plaza JL, Martinez O, Rubio S, Hortelano V, Diegueza E (2013) CdS and CdTe films by close space vapour sublimation by using SiC resistive elements. Cryst Eng Comm 15:2314–2318
105. Potlog T, Spalatu N, Fedorov V, Maticiuc N, Antoniuc C, Botnariuc V, et al (2011) The performance of thin film solar cells employing photovoltaic ZnSe/CdTe, CdS/CdTe and ZnTe/CdTe heterojunctions, In: Proceedings of 37th IEEE Photovoltaic Specialists Conference. 19–24 June 2011, Seattle, WA, US, 12710867
106. Putkonen M, Niinistö L (2005) Organometallic precursors for atomic layer deposition. Top Organomet Com 9:125–145
107. Qi X-Y, Pu K-Y, Fang C, Fan Q-L, Tang D-F, Wen G-A et al (2008) Cadmium telluride nanocrystals: synthesis, growth mode and effect of reaction temperature on crystal structures. NANO Brief Reports and Reviews 3(2):109–115
108. Rajeshwar K (1992) Electrosynthesized thin films of group II-VI compound semiconductors, alloys and superstructures. Adv Mater 4(1):23–29
109. Rondiya S, Rokade A, Funde A, Karthab M, Pathanb H, Jadkar S (2017) Synthesis of CdS thin films at room temperature by RF-magnetron sputtering and study of its structural, electrical, optical and morphology properties. Thin Solid Films 631:41–49
110. Sadovnikov I (2019) Synthesis, properties and applications of semiconductor nanostructured zinc sulfide. Russ Chem Rev 88:571–593
111. Saha S, Johnson M, Altayaran F, Wang Y, Wang D, Zhang Q (2020) Electrodeposition fabrication of chalcogenide thin films for photovoltaic applications. Electrochemistry 1:286–321
112. Seth A, Lush GB, McChue JC, Singh VP, Flood D (1999) Growth and characterisation of CdTe by CSS on metal substrates. Sol Energy Mater Sol Cells 59:35–41
113. Shah NA, Ali A, Aqili AKS, Maqsood A (2006) Physical properties of Ag-doped cadmium telluride thin films fabricated by closed–space sublimation technique. J Cryst Growth 290(2):452–458
114. Shelke NT, Karle SC, Karche BR (2020) Photoresponse properties of CdSe thin film photodetector. J Mater Sci Mater Electron 31:15061–15069
115. Shkir M, Khan ZR, Alshammari AS, Gandouzi M, Ashraf IM, AlFaify S (2021) A comprehensive experimental investigation of La@CdS nanostructured thin films: Structural, opto-nonlinear and photodetection properties. Surf Interfaces 24:101063
116. Tolstoi VP (1993) Synthesis of thin-layer structures by the ionic layer deposition method. Russ Chem Rev 62(3):237–242

117. Tolstoy VP (2006) Successive ionic layer deposition. The use in nanotechnology. Russ Chem Rev 75(2):161–175
118. Tong XL, Jiang DS, Li Y, Liu ZM, Luo MZ (2006) Femtosecond pulsed laser deposition of CdS thin films onto quartz substrates. Phys Status Solidi A 203:1992–1998
119. Triboulet R, N'tep JM, Barbe M, Lemasson P, Mora-Sero I, Munoz V (1999) Some fundamentals of the vapor and solution growth of ZnSe and ZnO. J Cryst Growth 198(199):968–974
120. Varitimos TE, Tustison RW (1987) Ion beam sputtering of ZnS thin films. Thin Solid Films 151(1):27–33
121. Vishwakarma R (2015) Effect of substrate temperature on ZnS films prepared by thermal evaporation technique. J Theor Appl Phys 9:185–192
122. Vossen JL, Kern W (eds) (1978) Thin Film Processes. Academic, New York, p 564
123. Xin ZJ, Peaty RJ, Rutt HN, Eason RW (1999) Epitaxial growth of high quality ZnS films on sapphire and silicon by pulsed laser deposition. Semicond Sci Technol 14:695–698
124. Yano S, Schroeder R, Ullrich B, Sakai H (2003) Absorption and photocurrent properties of thin ZnS films formed by pulsed laser deposition on quartz. Thin Solid Films 423:273–276
125. Yoshikawa A, Yamaga S, Tanaka K, Kasai H (1985) Growth of low-resistivity high-quality ZnSe, ZnS films by low-pressure metalorganic chemical vapour deposition. J Cryst Growth 72(1–2):13–16
126. Zhang R, Wang B, Wei L (2008) Influence of RF power on the structure of ZnS thin films grown by sulfurizing RF sputter deposited ZnO. Mater Chem Phys 112:557–561
127. Zhang W, Zeng X, Lu J, Chen L (2013) Phase controlled synthesis and optical properties of ZnS thin films by pulsed laser deposition. Mater Res Bull 48:3843–3846

OceanofPDF.com

© The Author(s), under exclusive license to Springer Nature Switzerland AG 2023
G. Korotcenkov (ed.), *Handbook of II-VI Semiconductor-Based Sensors and Radiation Detectors*
https://doi.org/10.1007/978-3-031-19531-0_11

11. Synthesis of II-VI Semiconductor Nanocrystals

Ghenadii Korotcenkov[1] ✉ and Igor A. Pronin[2]
(1) Department of Physics and Engineering, Moldova State University, Chisinau, Moldova
(2) Department of Nano- and Microelectronics, Penza State University, Penza, Russia

Keywords II-VI semiconductor – CdS – CdSe – CdTe – Hgcds – HgS – HgTe – ZnS – ZnSe – ZnTe – Technology – Thick film – Thin film – Nanocrystals synthesis – Co-precipitation methods – Advantages – Disadvantages – Doping – Precursors – Supersaturation – Green synthesis – Advantages – Microorganisms – Plant extractions – Hot-injection method – Capping agent – Limitations – Solvents – Temperature – Hydrothermal technique – Autoclave – Pressure – Water – Mechanochemical method – Advantages – Ball milling – Disadvantages – Microemulsion technique – Disadvantages – Micelles – Microemulsion scheme – Oil – Surfactant – Microwave-assisted method – Advantages – Limitations – Microwave irradiation – One-step colloidal method – Advantages – Photochemical synthesis

11.1 Introduction

As is known, devices based on II-VI compounds can be manufactured using both thin-film and thick-film technologies. As a rule, thin-film technology is based on the principles of synthesis of semiconductor compounds directly on the surface of substrates during their deposition or transfer of a semiconductor compound formed by various methods from a source to a substrate. For this purpose, various technologies for the deposition of

semiconductor compounds are used, such as thermal evaporation, sputtering, laser ablation, chemical deposition, chemical vapor phase deposition, electrochemical deposition, etc. These methods are described in Chap. 10 (Vol. 1). In this case, the parameters of the semiconductors in the formed films, such as the crystallite size, orientation, and morphology of the films, are determined by the conditions used to deposit these films. In the case of thick-film technology, we may have a completely different situation. For the manufacture of devices based on II-VI compounds using thick-film technologies, such as screen printing (Fig. 11.1), spin coating (Fig. 11.2a), inkjet printing, drop, spray (Fig. 11.2b), and dip coating (Fig. 11.2c), etc., it is possible to use already synthesized powders of these compounds. In this case, the structural parameters of semiconductor-forming films will not depend on the conditions of film formation but will be determined by the conditions of synthesis of their powders. For the formation of films, one can also use pre-synthesized sol and gel of II-VI semiconductors and carry out their crystallization on the surface of the substrates. Each of these methods has its own advantages and disadvantages. They are discussed in detail in [100, 101].

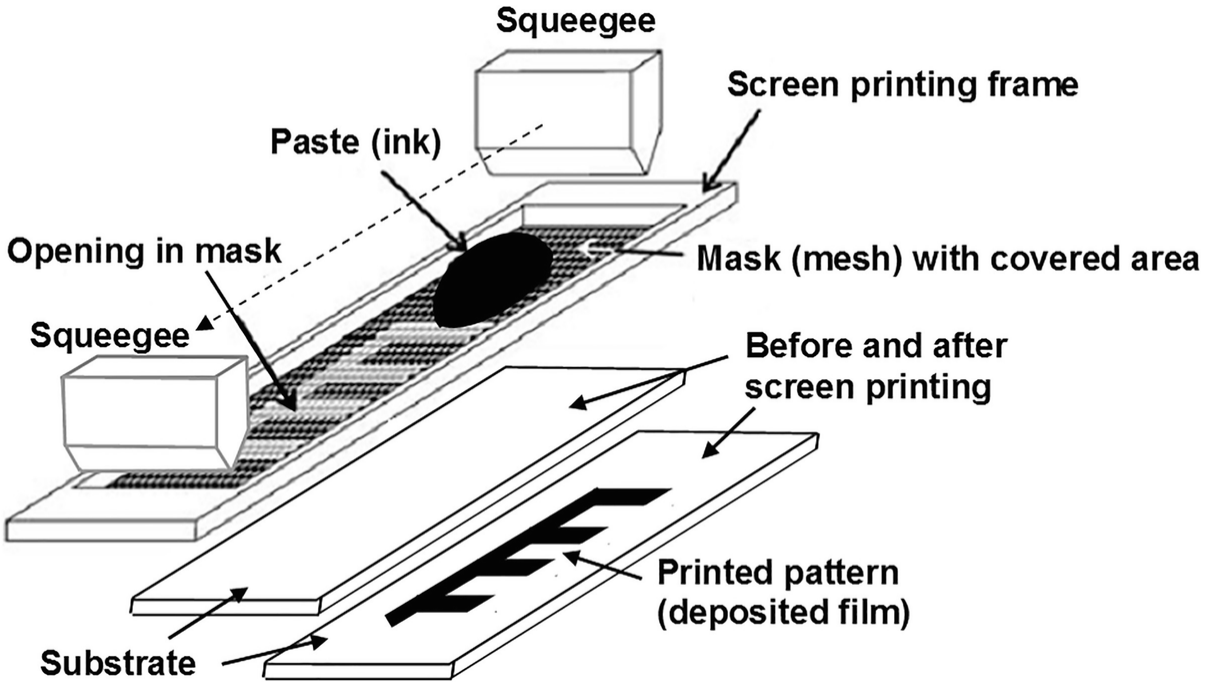

Fig. 11.1 Manufacture of thick-film structures by screen printing. (Idea from Ref. [56])

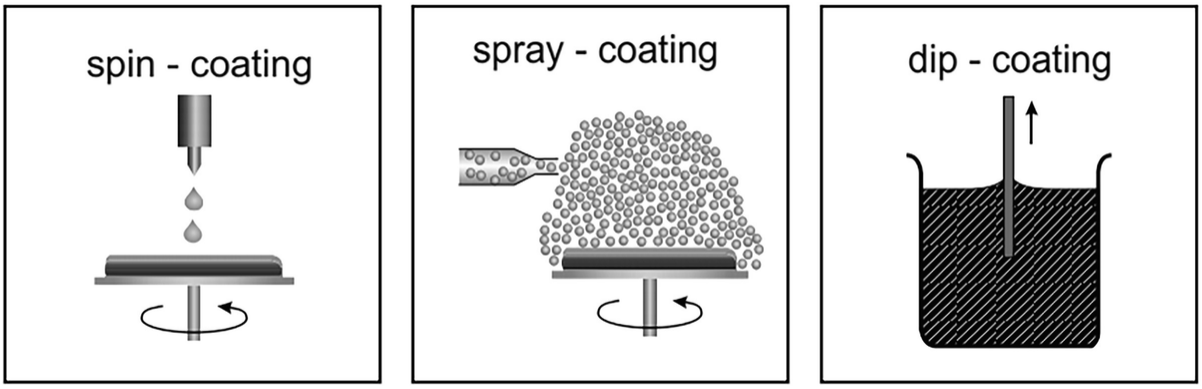

Fig. 11.2 Illustration of the commonly used coating techniques. (Reprinted with permission from Ref. [170]. Copyright 2004: Elsevier)

As we indicated earlier, the technologies for film deposition of II-VI compounds are already described earlier in Chap. 10. Therefore, in this chapter, we focus on the consideration of methods for the synthesis of nanocrystallites (powders) of II-VI compounds used in thick-film technology.

11.2 Mechanochemical Method

Grinding is one of the oldest methods for the synthesis of fine particles from solid precursors. In this method, mechanical energy is used to break the atomic bonds of the precursor and form new materials [146]. The mechanochemical method is a combination of mechanical and chemical phenomena on a solid material at the nanoscale. This method makes extensive use of the ball mill, in which a powder mixture is placed in a ball mill and subjected to a high-energy impact from the balls. Mechanochemical processing is characterized by repeated welding, deformation, and destruction of the mixture of reagents. Chemical reactions take place at nanometer-sized grain boundaries, which are continuously regenerated during the grinding process [98]. Therefore, chemical reactions that normally require high temperatures due to separation of reaction phases into product phases can take place at low temperatures in a ball mill without the need for external heating [215]. In addition, it is very easy to introduce impurities in this method with less effort, high uniformity, and high yield [88].

The rotation speed of the balls collision determines the efficiency of the grinding mechanism. The grinding capability also depends on the number of balls and ball diameter, as the ball diameter is inversely proportional to

the frequency of the balls collisions. The structure, shape, and morphology of nanomaterials strongly depend on the parameters of bill milling strategy. For example, it was found that the energy of the mill is not critical for the final microstructure, but the kinetics of the process depends on the energy. The time required to reach the same microstructure can be several orders of magnitude longer in low-energy mills than in high-energy mills. It has also been suggested that the total strain introduced by milling is responsible for determining the nanocrystalline grain size [97]. With an appropriate choice of milling parameters and growth conditions, it is possible to produce nanomaterials in the form of diverse shapes like particles, rods, cubes, fibers, etc.

During this high-energy ball milling process, there is a choice to add a surfactant. Without a surfactant, the aggregation process takes place because of high surface energy of the particles, which results in the formation of larger NPs during mechanical grinding. If the surfactant is added, then the surfactant molecules form an organic layer on the surface of particles. The adsorption of these molecules lowers the surface energy of particles, and consequently no agglomeration takes place and NPs are produced with smaller size range and desired surface properties.

Examples of the implementation of the mechanochemical synthesis method as applied to II-VI compounds are given in Table 11.1. It can be seen that the simplest precursors such as Zn, Cd, Te, S, and Se powders can be used to synthesize nanoparticles of II-VI compounds.

Table 11.1 Cd containing II-VI semiconductor nanomaterials prepared using different mechanochemical synthesis conditions

II-VI	Precursors	Loading conditions of mills	Milling rate	Atmosphere	Ref.
CdS	Cd and S powders	2–12 mm diameter		Inert gas	[193]
	Na_2S, $CdCl_2$, and NaCl	4.8–12.6 mm diameter	n/a	Inert gas	[198]
	Cadmium acetates and sodium sulfide	50 balls of 10 mm diameter	500 rpm	Argon	[11, 36]
		3 mm diameter	350 rpm	Air	[197]
CdSe	Cd and Se powders	2–12 mm diameter	n/a	Inert gas	[192]
CdTe	Cd and Te powders	2–12 mm diameter	n/a	Inert gas	[194]

II-VI	Precursors	Loading conditions of mills	Milling rate	Atmosphere	Ref.
CdS, CdSe, CdTe	Cd, S, Se, and Te powders	n/a	n/a	Air	[103]

It was established that the mechanochemical method makes it possible to synthesize nanoparticles of II-VI compounds of small size. For example, Godočíková et al. [52] reported that using this method they synthesized CdS NPs with average size of 9 nm. According to Kristl et al. [103], their CdS NPs had the size of ~8 nm.

Tsuzuki and McCormick [198] studied CdS nanoparticles synthesized by mechanochemical process and found the presence of mixed cubic and hexagonal phases in CdS NPs, prepared by using balls of diameter of 12.6 mm. However, when the ball size was reduced to 4.8 mm, the samples turned out to be completely in the cubic crystal structure. Furthermore, it was found that particle size of the product decreased in direct proportion to the size of milling balls. This means that this method appears to be an appropriate route for optimizing crystalline structure by suitable selection of milling conditions.

Another important process parameter is the milling time. In particular, Tan et al. [193] studied the process of CdS NCs synthesis with capping agent trioctylphosphine oxide/trioctylphosphine/nitric acid (TOPO/TOP/NA). They found that the CdS-related XRD peak was not detected during the first 30 min of milling, while milling for 10 h appeared to completely convert the element precursors into CdS NPs. Tolia et al. [197] obtained similar results. It was observed that phase transformation of CdS NPs takes place after 6 h milling time. In addition to structural changes, there is also a change in the size of nanoparticles. Tan et al. [194] reported that the size of CdTe NPs was decreased from 23 to 3.5 nm when milling time was increased from 4.5 to 50 h.

The top-down method, such as mechanochemical synthesis, is an inexpensive, well-established, and traditional method for obtaining large-scale nanomaterials [167]. Moreover, this method is applicable to almost all classes of materials. However, the synthesized nanomaterials are often irregular in shapes and have defects. As a result of mechanical milling, additional mechanical tensions appear in the material. The appearance of mechanical tensions and structural defects can be an important factor that influences properties of synthesized materials. Therefore, these factors

should be taken into account when designing technology of device fabrication. These tensions are only removed by thermal treatment. Thus, an additional thermal treatment after mechanical milling may be required.

Contamination, long processing time, no control on particle morphology, agglomerates, and residual strain in the crystallized phase are other disadvantages of high-energy ball milling process. In fact, the contamination problem is often presented as a reason to dismiss this method, at least for some materials. If steel balls and containers are used, iron contamination becomes a problem. This is the most serious problem for the highly energetic mills, and it depends on the mechanical behavior of the powder being milled as well as its chemical affinity for the milling media. Lower-energy mills result in much less, often negligible, iron contamination. Other milling media, such as tungsten carbide or ceramics, may be used, but contamination is also possible from such media [97]. Surfactants (process control agents) may also be used to minimize contamination.

11.3 Co-precipitation Methods

Co-precipitation from solution is one of the oldest methods for preparing metal–chalcogenides with good compositional control. This process involves dissolving a salt precursor, usually sulfates, nitrates, etc., in some appropriate medium to form a uniform solution containing ion clusters. In this method, a basic precursor’s solution is prepared by dropwise mixing in solvents, such as de-ionized water, ethanol, methanol, and acidic solutions, to better control the pH value [231]. Then, at room temperature, these prepared solutions are mixed and stirred for hours to fully react.

Figure 11.3 shows a schematic representation of the mechanism proposed to explain the formation of uniform particles during co-precipitation synthesis. In a homogeneous precipitation, a short single burst of nucleation occurs when the concentration of the constituent species reaches critical supersaturation. The nucleation continues until the monomer concentration drops below a critical threshold value, resulting in the quenching of the nucleation process. The nuclei thus obtained are then allowed to grow uniformly by diffusion of the solutes from the solution onto their surface until the final size is reached. To achieve monodispersity, it is necessary to separate these two stages and avoid nucleation during the

growth time. This is the classical model first proposed by Lamer and Dinegar [108] to explain the mechanism of formation of sulfur colloids.

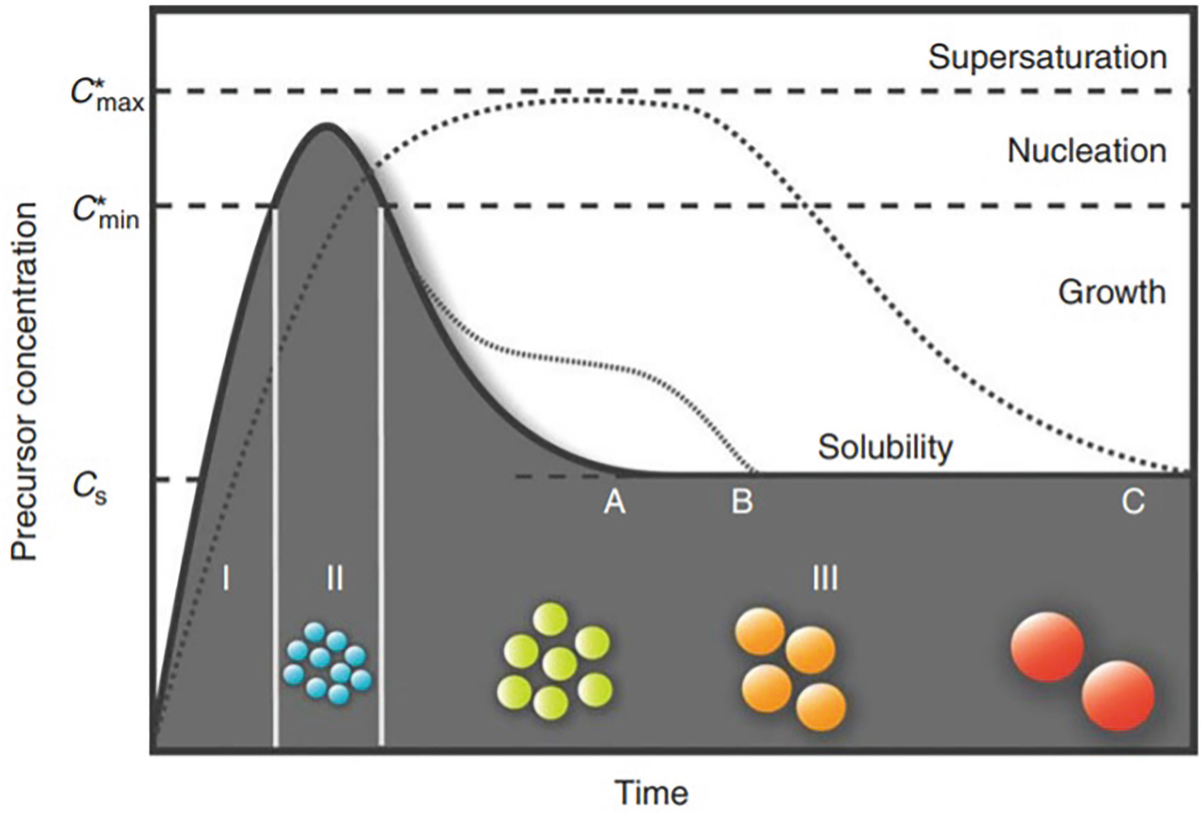

Fig. 11.3 Mechanisms of monodisperse colloid formation. (Reprinted with permission from Ref. [232]. Copyright 2011: Elsevier)

Thus, the precipitation includes several processes that occur simultaneously including initial nucleation (formation of small crystallites), growth (aggregation), coarsening, and agglomeration. In chemical precipitation, the reactants precipitate as precursors after the completion of the reaction due to their low solubility. The solubility of precursors depends on the pH value. Metal salts often require an alkaline/weak acidic environment for this process, so a well-organized pH is needed for the reaction. Chemical composition is an essential feature influencing the structures and properties of nanomaterials. Therefore, it is necessary to accurately organize the stoichiometric ratio of precursors. Solution pH, mixing rates, temperature, and concentration of precursors have to be also controlled to obtain satisfactory results [161]. For example, the addition of NaOH to the Se precursor during the synthesis of CdSe NPs accelerated nucleation and increased the concentration of CdSe QDs [46]. According to

Lee et al. [122], with an increase in the content of $CdCl_2$ in the solution for synthesis of CdS NPs, a transformation of the crystalline phase from cubic to hexagonal is observed.

Finally, the precipitated product with low solubility in the solvent is separated from the liquid by filtration. Different stages involved in the synthesis of nanomaterials using co-precipitation are presented in Fig. 11.4. As is seen, the calcination at elevated temperature for several hours is the final operation in the co-precipitation method. Thus, co-precipitation comprises two main steps: (1) a chemical synthesis in the liquid phase that determines the chemical composition and (2) a thermal treatment that determines the crystal structure and morphology [134]. However, in the case of II-VI compounds, the annealing temperature usually does not exceed 130–200 °C, and the annealing itself is carried out in an inert or reducing atmosphere. In some cases, no heat treatment is used at all.

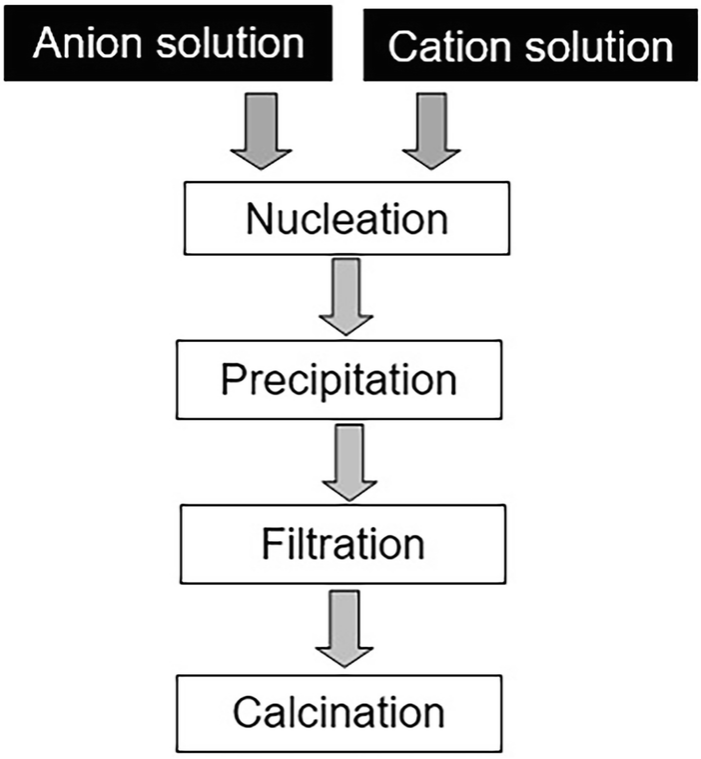

Fig. 11.4 Schematic presentation of co-precipitation method

The experiment has shown that the co-precipitation method applied to II-VI compounds makes it possible to synthesize stoichiometric nanocrystals with sizes ranging from a few nm to 80 nm. For example, Rao

et al. [159] synthesized very well-structured CdS nanoparticles with a size of 13 nm. Devi et al. [31] using $CdCl_2$, Na_2S, tetrabutylammonium bromide, and water as a solvent prepared stoichiometric CdS NPs with cubic structure and their size varying in the range of 15–80 nm. Raj and Rajendran [158] by reaction of cadmium acetate and sodium sulfide in aqueous environment synthesized CdS NPs with an average particle size of 7 nm. The temperature of the solution during the synthesis, depending on the solvent used, can vary within 40–160 °C. As a rule, with increasing temperature, the size of nanocrystallites formed in the process of co-precipitation increases [46]. Temperature conditions in relation to synthesis of ZnS NPs in ethylene glycol (EG)-based solution are given in Fig. 11.5.

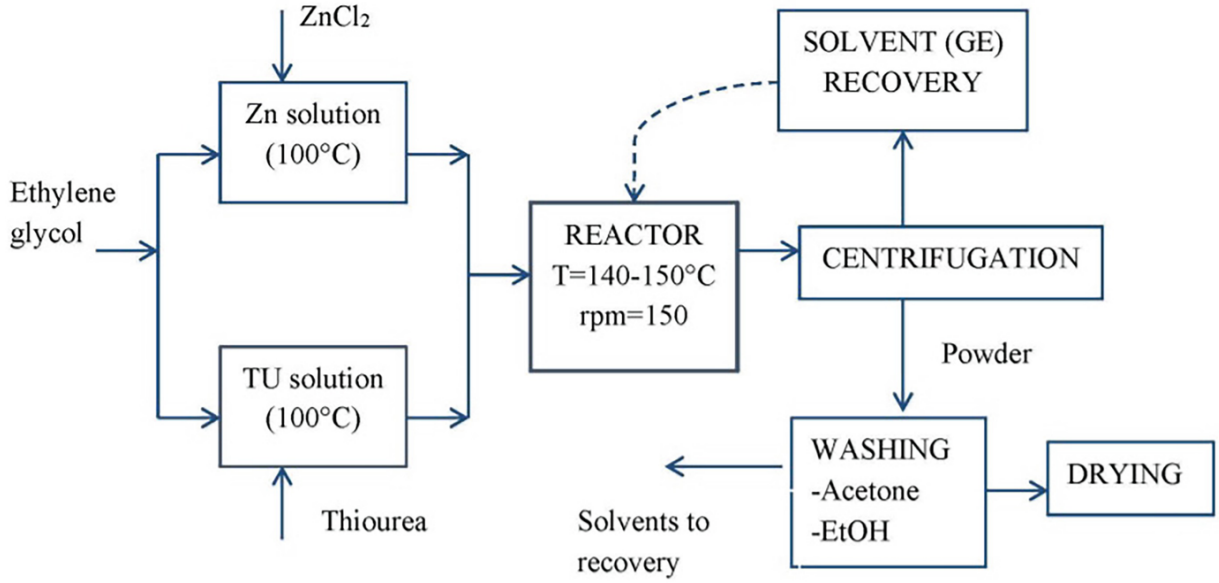

Fig. 11.5 The schematic representation of the ZnS nanopowder synthesis. (Reprinted from Ref. [210]. Published 2021 by MDPI as open access)

Nanocrystals of other II-VI compounds, such as CdTe [53], CdSe [46], ZnS [81], ZnTe [139], and various heterostructures such as CdTe/CdS [204] have also been successfully synthesized using the co-precipitation method. For example, Mntungwa et al. [139] for the synthesis of ZnTe NPs suggested using the following reactions:

$$2\ \mathrm{Te} + 4\ \mathrm{NaBH_4} + 7\ \mathrm{H_2O} \rightarrow 2\ \mathrm{NaHTe} + \mathrm{Na_2B_4O_7} + 14\ \mathrm{H_2}\uparrow \quad (11.1)$$

$$\mathrm{NaHTe} + \mathrm{ZnCl_2} \rightarrow \mathrm{ZnTe} + \mathrm{NaCl} + \mathrm{HCl} \quad (11.2)$$

$$2\ \mathrm{NaHTe} + 2\ \mathrm{ZnSO_4 \cdot 7H_2O} \rightarrow 2\ \mathrm{ZnTe} + \mathrm{Na_2SO_4} + \mathrm{H_2SO_4} + 14\ \mathrm{H_2O} \quad (11.3)$$

$$NaHTe + Zn(NO_3)_2 \cdot 6H_2O \rightarrow ZnTe + NaNO_3 + HNO_3 + 6H_2O \quad (11.4)$$

Iranmanesh et al. [81] using zinc acetate ($Zn(Ace)_2 \cdot 2H_2O$) and sodium sulfide (Na_2S) and ethylenediaminetetraacetic acid (EDTA) as a stabilizer and capping agent synthesized ZnS nanocrystals with average particle size of 50 nm.

It is shown that the co-precipitation method also makes it possible to dope II-VI compounds. In particular, cerium-doped CdS NPs have been prepared by using co-precipitation technique [166]. The doping of Ce atom was carried out at concentrations of 1, 2, and 3 mol%. Both the doped and undoped NPs were found having wurtzite structure with particle size of 3 nm. The co-precipitation synthesis and characterization of Mn-doped CdS NPs have been reported by Gupta and Kripal [60]. The grown material had a wurtzite structure and a crystallite size of 2–4 nm. Elavarthi et al. [40] reported the preparation of pure and Cr-doped CdS NPs using chemical co-precipitation process. The doping at 3–5% Cr concentration appeared to change the structure of the NPs. Muruganandam et al. [142] carried out the preparation of polyvinylpyrrolidone (PVP)-capped CdS NPs and doping with Cu and Mn using chemical precipitation technique. Co-precipitation technique was also used to synthesize the Cr-doped CdSe NPs [127]. With increasing the chromium doping concentration, the lattice parameters showed a consistent decrease in such a way that for 4, 5, and 6% doping concentration, the size of NPs was 3.02, 2.48, and 2.11 nm, respectively.

The advantage of co-precipitation method is its low-cost and simple equipment, simple water-based reaction, flexibility, mild reaction conditions, comparatively low temperature, and size control. The composition control and purity of the resulting product are good. One disadvantage of this method is the difficulty to control the particle size and size distribution. In addition, this method is not suitable for the reactants, which have dissimilar solubility and precipitate rate. Different rates of precipitation of each individual compound may lead to microscopic inhomogeneity. Moreover, very often, fast (uncontrolled) precipitation takes place resulting in large particles. In addition, aggregates are generally formed, as with other solution techniques. Therefore, the use of surfactants is a common practice to prevent agglomeration, which also affects the particle size of the composites obtained by this technique [83].

11.4 The Sol–Gel Processing

Sol–gel techniques for the preparations of various materials have long been known and described in several books and reviews [28, 57]. A *sol* is a dispersion of colloidal solid particles (~0.01–1 μm) in a liquid in which only Brownian motion suspends the particles. In a *gel*, liquid and solid are dispersed within each other, presenting a solid network, containing liquid components. In this method, a liquid (sol) is chemically converted into gel state followed by condensation in the form of solid nanostructures.

It was established that through sol–gel process, homogeneous inorganic materials with desirable properties of hardness, optical transparency, chemical durability, tailored porosity, and thermal resistance can be produced at room temperatures [18, 76, 99, 115]. The surfactant-free process involves the simple wet chemical reaction based on hydrolysis of metal reactive precursors, usually metal chlorides, metal nitrates, and alkoxides in an alcoholic solution, and condensation, leading to formation of sol, which through the process of aging results in formation of an integrated network of metal hydroxide as gel. The gel is a polymer of three-dimensional skeleton surrounding interconnected pores. Different reactions can create the cross-linkages that result in the gelation of the solution [18, 28].

According to Brinker and Scherer [18], sol–gel polymerization occurs in three stages. First, the monomers are polymerized to form particles, followed by the growth of particles, and finally, the particles are linked into chains. Networks then extend throughout the liquid medium, thickening into a gel. The characteristics and properties of a sol–gel inorganic network are related to a number of factors that affect the rate of hydrolysis and condensation reactions: the pH level, the temperature and time of the reaction, the reagent concentrations, the nature and concentration of the catalyst, the H_2O/M molar ratio (R), the aging temperature, and the drying time. Among these factors, the pH level, the nature and concentration of the catalyst, the H_2O/M molar ratio (R), and the temperature were identified as the most important [18]. Although hydrolysis can occur without the addition of an external catalyst, it is more rapid and complete when a catalyst is employed. Mineral acids (HCl) and ammonia are used most often; however,

other catalysts may be used as well, including acetic acid, KOH, amines, KF, HF, and H_2O_2.

Removal of the solvents and appropriate drying of the gel is an important step in the sol–gel process. When the sol is cast into a mold, a wet gel forms. With further drying, the gel is converted into dense particles. If the liquid in a wet gel is removed under a supercritical condition, a highly porous and extremely low-density material, called an aerogel, is obtained. Heat treatment of the gel is a final step that leads to the forming of ultrafine powders. Nanoparticles in the gel are often amorphous, and the thermal treatment imparts the desired crystalline structure to the particles, although it also leads to some agglomeration [28]. Depending on the heat treatment procedure, the final product may end up in the form of a nanometer-scale powder or bulk material. The size, shape, and structure of the final product are greatly influenced by the reaction parameters.

Thus, the sol–gel process has seven steps: (1) preparing of required solution, (2) formation of a stable metal precursor solution (sol), (3) formation of a gel by a polycondensation reaction (gel), (4) aging the gel for hours to days resulting in the expulsion of solvent, Ostwald ripening and formation of a solid mass, (5) drying the gel of any liquids, (6) dehydration and surface stabilization, and (7) heat treatment of the gels to generate crystalline nanoparticles. Details of the sol–gel process are discussed more extensively in several excellent review articles [18, 28, 57, 99].

Up to now, most publications related to the sol–gel synthesis have been confined to the preparation of ultrafine metal oxide powders or thin films. Reports on the sol–gel synthesis of nanosized sulfides, selenides, or tellurides are relatively much scarcer. However, despite this, when using sol–gel processing, a lot of different II-VI compounds such as CdS [47, 140, 160, 186], CdTe [116], CdSe [5, 49], ZnS [19, 188], ZnTe [172], various nanocomposites [58], and doped II-VI semiconductors [116, 172] were synthesized. It is important to note that studies by Starnic et al. [188] during the sol–gel synthesis of ZnS showed that the gel formed during this process is indeed a ZnS gel. The following reaction mechanism can be proposed for the formation of ZnS gel:

$$\mathrm{Zn-OR + H_2S \rightarrow \quad --Zn-SH + ROH} \tag{11.5}$$

$$\mathrm{Zn-SH + RO-Zn--\rightarrow \quad --Zn-S-Zn-+ROH} \tag{11.6}$$

$$Zn-SH+HS--Zn---\rightarrow\quad--Zn-S-Zn---+H_2S\uparrow \quad (11.7)$$

Currently, there are two sol–gel routes that are used most commonly in the preparation of metal chalcogenides. The first one involves a modified sol–gel route in which the conventional alcohol sol is exposed to a stream of H_2S or some other source of chalcogens. The other one is the use of thiols instead of alcohol for the formation of sulfides or selenides by a modification of the first sol–gel route. It should be noted that, in addition to inorganic precursors, metal-organic precursors may also be used in the sol–gel process. Taurino et al. [195] believe that the choice between these two classes should be based on a number of factors. First, metallorganic precursors are more expensive, and the sol preparation requires sometimes the use of organic solvents [143], such as 2-methoxyethanol, that require careful handling and disposal due to their combined toxicity and high vapor pressure [28]. At the same time, handling of inorganic precursors does not generally require any special equipment such as a glovebox. Their chemistry is also more extensively known and more easily manipulated than that of metal-organic precursors, and the spin coating of their solutions does not require any special conditions such as low moisture. Additionally, the solutions have long-term stability against the increase of viscosity. On the other hand, films prepared from solutions based on metal-organic precursors are much more uniform than those when using inorganic precursors, and they can be easily deposited onto various substrates, including silicon. The organometallic precursors also do not contain possible contaminants such as chlorine or sulfur.

As an example, we describe several processes of sol–gel synthesis of CdS NPs. In a process developed by Munirah et al. [140], cadmium acetate $(CH_3COO)_2Cd{\cdot}2H_2O$ and thiourea (NH_2CSNH_2) dissolved in 2-methoxyethanol separately and kept for constant stirrer for 2 h were used as Cd and S sources, respectively. After then, these solutions were mixed together. The cadmium acetate and thiourea concentration was 1.0 M. Monoethanolamine (MEA: $H_2N(CH_2)_2OH$) was added to obtain the desired sols. To gain the thermal stability, solution was aged for 3 h. Fresh solution was applied to the substrate. Finally, the samples were annealed at a temperature of 200 °C for 2 h. The grain size of CdS NPs from SEM estimations was ∼10–12 nm.

Rathinama et al. [160] prepared CdS sol–gel using the following two solutions. Solution I was prepared by mixing 0.6 ml polyethylene glycol, 0.5 ml acetic acid, and 8.9 ml ethanol and stirred for 1 h. Solution II was prepared by mixing 0.1 M cadmium nitrate and 0.2 M thiourea in 100 ml ethanol, and it was also stirred for 1 h. Solutions I and II were mixed and stirred again for 4 h to obtain the final sol – gel used for preparing the film. Continuous film was formed onto the substrates by spin deposition of CdS sol–gel. The films were subjected to subsequent annealing in air at 473 K, 573 K, and 673 K. The measurements showed that synthesized CdS nanocrystallites had hexagonal crystal phase and the size increased from 7 to 14 nm with an increase in the annealing temperature from 473 to 673°C.

It was found that, as for other wet chemical methods of II-VI compound synthesis, the result of the sol–gel process strongly depends on the composition of the solution and the presence in it of such components as capping agents or stabilizers, catalyst, and mineralizers. For example, by synthesizing CdS without surface coating agents, Guglielmi et al. [59] obtained CdS nanoparticles that crystallize into a zinc blende cubic structure with an average crystal size of about 3 nm. Instead, CdS particles prepared using (3-mercaptopropyl)trimethoxysilane (MPTMS) had a hexagonal wurtzite-type structure and were significantly smaller in size.

Arachchige and Brock [5] used standard room temperature inverse micellar strategies to prepare CdSe nanoparticles. These nanoparticles were complexed with the thiolate ligands, 4-fluorobenzenethiol (inverse micellar route), and dispersed in acetone or methanol, respectively, to make orange-red colored CdSe sols. They established that if the natural process of photooxidation is used, then gel formation occurs within 4–5 weeks. On the other hand, the use of chemical oxidant (tetranitromethane or H_2O_2) leads to gelation within 1–2 h.

However, it should be recognized that the sol–gel process is not the dominant method for the synthesis of II-VI semiconductor nanoparticles. It turned out that the sol–gel technology is more efficient in the synthesis of SiO_2 or metal oxide matrices incorporated with nanoparticles of II-VI compounds. Currently, there are reports of synthesis SiO_2:$Hg_xCd_{1-x}S$ [58], SiO_2:CdSe [120], (SiO_2-P_2O_5):CdSe [45], SiO_2:CdS [48, 86], SiO_2:CdTe [112, 145], SiO_2:ZnSe [63, 77], SiO_2:ZnS [13], ZrO_2:CdTe [222], and ($95SiO_2$–$5B_2O_3$):ZnSe [118] структур. The sol–gel matrices doped with

semiconductor nanoparticles can be made by synthesis of the semiconductor particles directly in a sol containing functionalized alkoxides [86, 145]. For example, Nogami et al. [145] synthesized CdTe NCs-doped silica glasses using the following stages: $Si(OC_2H_5)_4$ was hydrolyzed by adding it dropwise to a mixed solution of H_2O, HCl, and C_2H_sOH in the molar ratio 1:0.0027: 1 per mole of $Si(OC_2H_5)_4$. After the solution was stirred for 1 h, $Cd(CH_3COO)_2{\cdot}2H_2O$ and Te or $CdTeO_4$ (dissolved in concentrated HNO_3) were added, followed by 1 h of stirring at room temperature. The resultant homogeneous solution was hydrolyzed by adding a mixed solution of H_2O and C_2H_5OH. In this second hydrolysis reaction, a molar ratio of 4:1 per mole of $Si(OC_2H_5)_4$ was maintained. After the solution had been stirred for 1 h, it was poured into a polystyrene container and left for about 1 week until it formed a stiff gel. The gel was then further dried (uncovered) for 1 week at room temperature. This dried gel was heated at 150°C in the atmosphere of H_2-N_2. The crystalline morphology of CdTe NPs in SiO_2 matrix was nearly spherical, and average diameters were determined as 5.0 and 8.0 nm for samples heated for 5 h at 400 and 500 °C in H_2-N_2 gas, respectively. Hao et al. [63] also used direct synthesis of ZnSe nanoparticles in a sol of alkoxides. This sol–gel process is shown in Fig. 11.6. The final treatment to promote the formation of the ZnSe/silica nanocomposite was annealing at a temperature of 500 °C (3 h) in a CO-reducing gas atmosphere. ZnSe nanocrystals were spherical with the average radius of about 4–10 nm. The size of doped ZnSe nanocrystals depended on the annealing time, annealing temperature, and the molar ratio of $ZnSeO_4$ in sol–gel glass.

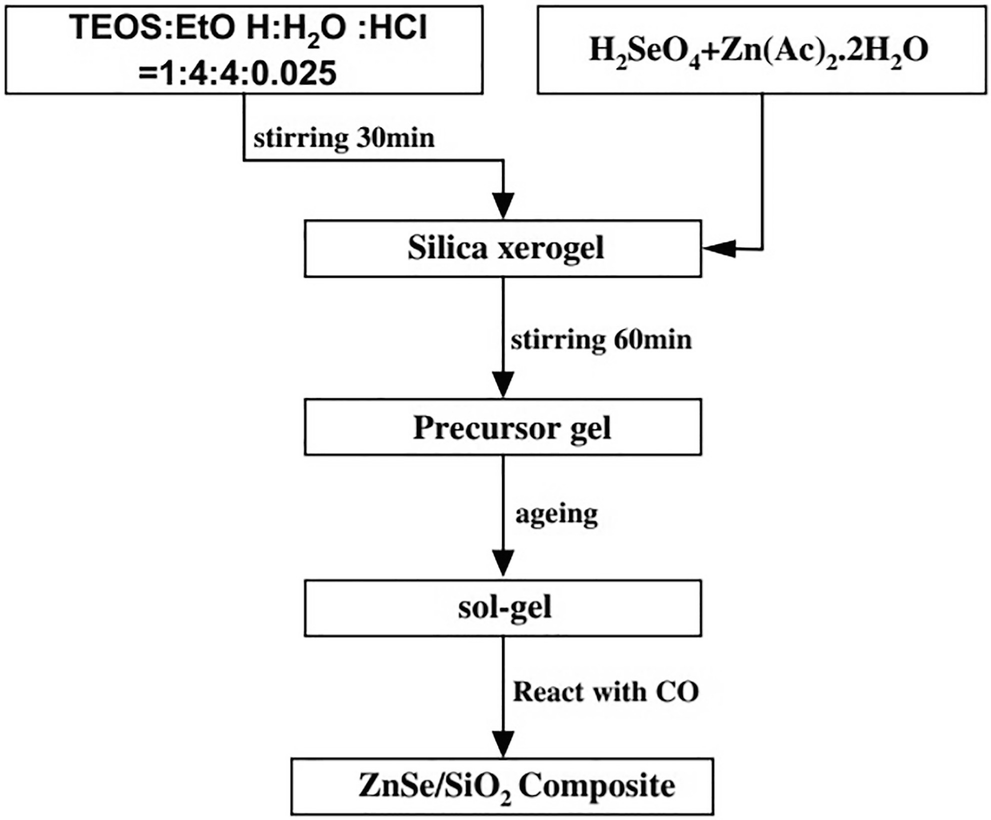

Fig. 11.6 Flow chart of preparation of $ZnSe/SiO_2$ nanocomposites. (Reprinted with permission from Ref. [63]. Copyright 2007: Elsevier)

However, the experiment showed that the synthesis of the nanoparticles separately from the sol–gel medium is more optimal [48]. This makes it possible to use various techniques developed in colloid chemistry to more effectively control parameters that directly affect the properties of final composite materials, such as chemical composition, average size and particle size distribution, electronic state of the surface, and the concentration of the particles in the matrix. That is why in most cases a two-step process is used. For example, Guglielmi et al. [58] first synthesized sulfide sol through a simple chemical method and silica sol via sol–gel process, which were then mixed in the right proportion, and after the completion of the process, the gel synthesized and dried at $T = 60$ °C was annealed at a temperature up to 300 °C. Gacoin et al. [48] used a similar strategy. The incorporation of the CdS particles in the sol was directly achieved by adding the CdS colloidal solution to the silica sol. Colloidal CdS nanoparticles were synthesized by precipitation method. In order to prevent the irreversible flocculation of CdS colloidal particles in the silica sol, they used a functionalized alkoxide $F\text{-}RSi(OEt)_3$. This

alkoxide allows the stabilization of the CdS particles through their grafting to the silica network. Lifshitz et al. [120] used a slightly different sequence for the synthesis of SiO_2:CdSe structures. They first synthesized selenium-doped silica sol via the sol–gel process and Cd-containing sol, which were deposited in layers on the surface of the substrate and, after drying, were annealed at 400 °C (1.5–2 h). During the indicated thermal treatments, the SeO_2 sublimed through the upper layer and reacted with the cadmium acetate to form CdSe. CdSe nanoparticles with a size of 4–6 nm, embedded in a silica sol–gel matrix, had high crystallinity with bulk cubic crystallographic structure. Feraru et al. [45] proposed a very simple way to make a (SiO_2-P_2O_5):CdSe. To incorporate CdSe into a silicophosphate film, they suggested using pre-synthesized CdSe NPs, which were directly added to the silicophosphate solution. The CdSe-doped silicophosphate solution was kept at room temperature. The gelification occurred on the ninth day. The gel was dried at room temperature in air and then thermally treated at temperatures from 200 to 550 °C for 2 h. Li and Qu [112] used the same approach in the synthesis of SiO_2:CdTe composite. However, instead of CdTe powders, they used CdTe QDs.

Sol–gel method has various advantages. First, the mixing of starting reagents at the atomic/molecular level leads to faster reaction times at lower temperatures, which helps to reduce the interdiffusion from one phase into another and the formation of parasitic phases. Since the process starts with a relatively homogeneous mixture, the final product is a uniform ultrafine porous powder. In addition, it allows you to adjust the particle size by simply changing the gelation time. Sol–gel processing also has the advantage that it can be expanded for industrial-scale production. In addition, the sol–gel process also allows the coating of substrates with complex shapes on the nanometer to micrometer scale, which cannot be achieved with some commonly used coating processes. Moreover, sol–gel is suitable the manufacture of thick porous ceramics required for various sensor applications, since the reaction proceeds with the coexisting solvent phase in which evaporation leaves numerous cavities.

On the other hand, sol–gel process can have some disadvantages. These disadvantages include the following:

The cost of the raw materials (the chemicals) can be high:

- Long process duration

- Shrinkage of a wet gel upon drying, which often leads to fracture due to the generation of large capillary stresses and, consequently, makes difficult the attainment of large monolithic pieces
- Difficulties in the process chemistry with respect to properties control and reproducibility
- Difficult to avoid residual OH groups

11.5 Hydrothermal Technique

Hydrothermal synthesis is a potentially superior method for low-cost production of II-VI semiconductors, including advanced multicomponent materials and nanocomposites for various applications, since powders of complex II-VI semiconductor can be synthesized directly. Its main feature is the use of water as the solvent [109]. Since water is an exceptional solvent, it is possible to dissolve even nonionic compounds at high-pressure and high-temperature conditions involved in the hydrothermal process. In high-temperature and high-pressure hydrothermal systems, the properties of water will produce the following changes [213]: (1) the ionic product increases, and the ionic product of water rapidly increases with the increase in pressure and temperature. Under high-temperature and high-pressure hydrothermal conditions, the hydrolysis reaction and ion reaction rates will naturally increase with water as the medium. (2) The viscosity and surface tension of water decrease as the temperature increases. In hydrothermal systems, the viscosity of water decreases, and the mobility of molecules and ions in solution greatly increases, such that crystals grow under hydrothermal conditions faster than under other conditions. (3) The dielectric constant of the water solution is often low, and the dielectric constant generally decreases with increasing temperature and increases with increasing pressure. Under hydrothermal conditions, the reaction is mainly affected by temperature, and the dielectric constant of water is significantly reduced. (4) The density decreases, and properties, such as the viscosity, dielectric constant, and solubility of the material, increase with increasing density while the diffusion coefficient decreases with increasing density. (5) The vapor pressure increases and accelerates the reaction by increasing the chance of collision among molecules.

To create such conditions, the precursor with water is placed in an autoclave (see Fig. 11.7). Thus, this chemical process in solution can be

easily distinguished from other processes such as sol–gel and co-precipitation by temperature and especially pressure [21]. The temperatures during hydrothermal synthesis are in the range between the boiling point of water (100 °C) and its critical temperature (374 °C), whereas pressures can increase up to 15 MPa. The chemical reaction takes place within a few hours (typically 6–48), leading to the nucleation and growth of nanoparticles. Currently, the production of various particles of II-VI compounds such as CdS [2, 125], CdSe [123, 124], CdTe [20, 228], ZnS [72], ZnSe [144], and ZnTe [228], using hydrothermal process, has been demonstrated. Narrowed band gap II-VI compounds, such as HgTe [164], have also been synthesized hydrothermally.

Fig. 11.7 Tefon-lined stainless steel autoclave used for solvothermal and hydrothermal methods of synthesis. Here, the metal precursors and solvents are premixed and introduced. The steel container is then asserted to a minimum range temperature and pressure. The solutions after treating with temperature and pressure are filtered, washed, and dried to get powdered composites. (Reprinted with permission from Ref. [211]. Copyright 2021: Springer)

As an example, we will describe the technological process for the synthesis of CdS microspheres used by Al Balushi et al. [2]. In a typical synthesis process, cadmium acetate dehydrate, ($Cd(CH_3COO)_2 \cdot 2H_2O$), and

thiourea, ($SC(NH_2)_2$) were dissolved in deionized water (75 ml) and stirred continuously for 30 min to form a homogeneous solution. Thereafter, the resulting solution was transferred into a Teflon vessel and heated at 160 °C for 12 h in an oven. After the heating process, the Teflon vessel was cooled down up to room temperature, and the deep-yellow powder was collected after centrifugation for 5 min at 5000 rpm. The resulting powder was repeatedly washed with deionized (DI) water and absolute ethanol. Finally, the CdS powder was dried at 80 °C in an oven for 12 h. The average size of CdS crystallites was 26–32 nm. As a rule, the rate of crystal growth is faster at higher temperature. Longer reaction time leads to a larger crystal size. In contrast, higher reactant concentration promotes nucleation and produces smaller crystals [117, 228].

As in other wet chemical methods, the parameters of the synthesized II-VI semiconductors are significantly affected by the composition of the solution and, in particular, the presence of capping agents or stabilizers and mineralizers in it. An appropriate capping agent or stabilizer can be added to the reaction contents at an appropriate time to inhibit particle growth and thus ensure that they are stabilized against agglomeration. The steric or electrostatic stabilization of the reactive molecules affects the nucleation and growth steps, which in turn control the particle size, shape, composition, and crystal structure of the particles. Stabilizers also help dissolve particles in various solvents. As capping agents in the synthesis of II-VI compounds, a long-chain amine, thiol, and trioctylphospine oxide [TOPO], and tri-n-octylphosphine (TOP) can be used. In particular, Schneider and Balan [169] systematized the influence of various capping agents such as ethylene diamine, pyridine, triethanolamine (TEA), cetyltrimethylammonium bromide (CTAB), triethylenetetramine (TETA), trisodium citrate ligand, thiol, and carboxylic acid on the properties of CdSe NPs. They showed that capping agent can determine the structure of synthesized NPs. For example, it was found that hydrothermal synthesis (100 °C, for 10 h) of CdSe QDs from $CdCl_2$ and sodium selenosulfate, Na_2SeSO_3, in the presence of ethylene diamine produce a cubic zinc blende CdSe nanoparticles with an average diameter of 12 nm. High-quality CdSe nanorods and fractals can be prepared from Na_2SeO_3 and $Cd(NO_3)_2$ at temperatures varying from 100 to 180 °C when using hydrazine N_2H_4 as reductant. Close results were obtained using cetyltrimethylammonium

bromide (CTAB) as surfactant during hydrothermal synthesis at 180 °C for 10 h. Dendritic structures and nanoparticles are produced in the absence or at low CTAB concentration, while high CTAB concentration favored the production of nanorods with wurtzite structure (diameter of 40–60 nm and lengths between 200 and 500 nm). Four different morphologies (taper microrods, nanotetrapods, fringy nanostructures, and fasciculate nanostructures) were recently prepared from $Cd(NO_3)_2$, Na_2SeO_3, and ethylene diamine tetraacetic acid tetrasodium salt (EDTA) as both a chelating agent and a reductant. Amino acids and small peptides containing a thiol group like cysteine (Cys) and its derivatives and glutathione GSH can also be used to stabilize CdSe QDs in aqueous solution [124]. One can also judge from SEM images for HgTe NPs synthesized under different conditions how strong the influence of solution composition on the structure of the material can be. HgTe nanostructures were synthesized via hydrothermal route by employing Hg(salen) (H_2salen = *N*,*N*′-bis-salicylidene-1,2-ethylenediamine) as a mercury source, $TeCl_4$ and $N_2H_4H_2O$ as the starting reactants at 180 °C for 12 h [164]. Ethylenediaminetetraacetic acid (EDTA) and polyvinylpyrrolidone (PVP) were used as capping agents. $N_2H_4{\cdot}H_2O$ was used as a reductant.

The addition of mineralizers also helps to reduce the size of crystallites [213]. Typical mineralizers are hydroxides (NaOH, KOH, LiOH), carbonates (Na_2CO_3), and halides (NaF, KF, NaCl, KCl, LiCl). Different mineralizers result in crystals of different sizes and shapes. For example, Liu and Xue [123] demonstrated that the important factors that influence the morphology of CdSe crystals are the concentration of NaOH, the reaction temperature, and to lesser extent, the concentration of SeO_3^{2-}. At low NaOH concentration, the formation of Se^{2-} is slow, which favors the anisotropic nucleation and growth of the CdSe structure along the c-axis (formation of rods). With an increased quantity of NaOH, the concentration of Se^{2-} becomes higher, providing more CdSe building units that grow on nanorods. Sangsefidi et al. [164] also pointed to a strong influence of mineralizers. They found that with variation base from NaOH (Fig. 11.8a) to NH_3 (Fig. 11.8d) with keeping the other experimental conditions constant, the morphology of HgTe nanostructure exchanged from rod-shape to agglomeration nanoparticles.

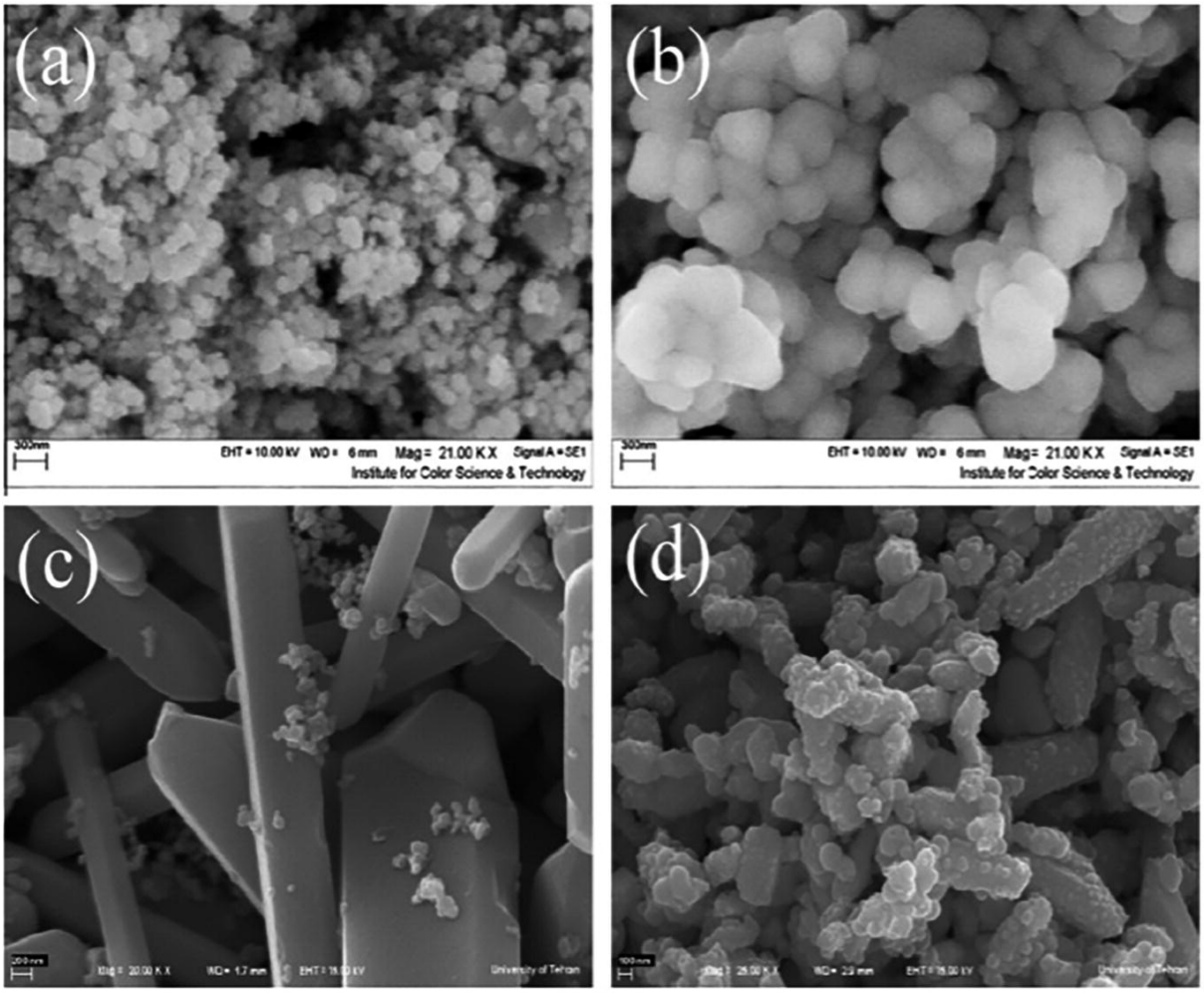

Fig. 11.8 SEM images of HgTe in presence of (**a**) EDTA and (**b**) PVP as capping agent, N_2H_4 as reductant, NaOH as Alkaline agent, (**c**) EDTA as capping agent, Zn as reductant, NaOH as alkaline source, and (**d**) EDTA as capping agent, N_2H_4 as reductant, NH_3 as alkaline source. (Reprinted with permission from Ref. [164]. Copyright 2013: Elsevier)

Thus, hydrothermal synthesis is an inexpensive, controllable, reproducible deposition strategy with better nucleation control, so it is considered as an attractive technique to prepare the nanostructures (Aliofkhazraei, 2016). By simply changing the temperature, time, and pressure of the reaction, you can control the particle size, composition, stoichiometry, and particle shape [66, 136]. Moreover, since the properties of the solvent mixture as well as those of the reactants differ intrinsically under high-temperature and high-pressure conditions from their corresponding properties under ambient conditions, the overall result is that this type of processing allows more manipulation of a large set of

experimental variables in the synthesis of high-quality nanomaterials [130, 136].

One should also note that the calcination step required by earlier discussed techniques can be eliminated in the case of hydrothermal synthesis [21]. However, many of the other steps employed in the previous wet methods can be used in hydrothermal synthesis. Therefore, hydrothermal synthesis with the exception of heat treatment contains the same steps as the sol–gel process. Hydrothermal synthesis generally produces nanoparticles with crystalline structure that are relatively uncontaminated and thus do not require purification or post-treatment annealing but may have a wider size distribution if special treatment for size control is not applied. Other advantages are the use of inexpensive raw materials such as chlorides, nitrates, and organometallic complex. Elimination of impurities, associated with milling and achievement of very fine crystalline powders, is also an advantage of this method.

However, there are also some difficulties connected with hydrothermal synthesis, such as (i) requirement of costly autoclaves, (ii) necessity for high-quality seeds, (iii) high temperature, and (iv) unfeasibility to observe the process during growth. The long duration of the process is also a disadvantage of this method. Insufficient knowledge for a detailed understanding of the chemistry of complex solutions also creates certain difficulties in the development of hydrothermal synthesis of new materials [136]. To eliminate some of the shortcomings of hydrothermal technique, it was suggested to use this technique in combination with microwave [132, 213] and sol–gel [114]. It was found that indicated approaches allow not only varying the physiochemical and structural properties of the materials but, in addition to that, may lead to the formation of the single-phased materials with improved properties [114].

11.6 Solvothermal Technique

The solvothermal process, in which interest has increased significantly in recent years, is an analogue of the hydrothermal process. The main difference between this process and hydrothermal synthesis is the use of organic solvents instead of water as the reaction medium. There are several reasons to stimulate research in this area [216]:

- Firstly, there is a need for technological processes capable to form solid phases with desired properties at intermediate temperatures (100–600 °C). In this regard, the solvothermal method is an appropriate method, as it is a low-temperature process that eliminates diffusion control by using a suitable solvent and limits the reaction to one or more functional groups and leaves most of the chemical bonds intact [176].
- Secondly, the traditional hydrothermal method is limited by the conditions under which some reagents will decompose in the presence of water, or precursors are very sensitive to water, or some reactions will not proceed in the presence of water, which will lead to a failure in the synthesis of the desired compounds. Therefore, it is difficult to obtain many kinds of powders such as carbonides, nitrides, phosphides, silicides, chalcogenides, etc. by a conventional hydrothermal process. The solvothermal process, in which water is replaced by nonaqueous solvents (both polar and polar) such as alcohols, C_3H_6, polyamines, NH_2NH_2, and liquid NH_3, solves this problem and allows the synthesis of compounds that cannot be obtained using hydrothermal synthesis [216]. This means that the so-called solvothermal process can be widely used to obtain various kinds of non-oxide nanocrystalline materials the precursors of which are very sensitive to water. In addition, solvents with a high boiling point are used in solvothermal synthesis, which makes it possible to carry out the growth process without involving high pressures.

As mentioned earlier, in the solvothermal process, one or more types of precursors are dissolved in nonaqueous solvents. The reagents are dispersed in the solution and become more active. The reactions proceed in the liquid phase or in the supercritical state [216]. The solvothermal process is relatively simple and easily controlled by several variable parameters such as solvents, temperature, and reaction time. The sealed system can effectively prevent the contamination of air-sensitive precursors.

Currently, great efforts have been made to synthesize II-VI semiconductors using the solvothermal process [217, 218]. In particular, the group of Yu [216] proposed and investigated several variants of solvothermal reactions for the synthesis of powders of II-VI semiconductors (Eqs. 11.8, 11.9, and 11.10):

$$\mathrm{CdC_2O_4} + \mathrm{E}\ \ (\mathrm{Se}, \mathrm{Se}, \mathrm{Te}) + \mathrm{solvent} \rightarrow \mathrm{CdS}\,(\mathrm{Se}, \mathrm{Te}) + 2\mathrm{CO_2}\uparrow \quad (11.8)$$

$$Cd^{2+} + NH_2CSNH_2 + \text{solvent} \rightarrow CdS \tag{11.9}$$

$$Na_2S_3 + CdSO_4 + \text{Solvent} \rightarrow CdS + Na_2SO_4 + 2S \tag{11.10}$$

As a solvent they used ethylenediamine (en) and pyridine (py). It was shown that using the proposed solvothermal reactions, it is possible to synthesize nanoparticles of Cd-based compounds with different morphology, particle sizes, and phases. Table 11.2 lists the detained experimental conditions for synthesis of various metal chalcogenides materials by solvothermal reaction between metal oxalates and chalcogens and the characterization of the powders. Examples of other modes of solvothermal synthesis of II-VI compounds are presented in Table 11.3.

Table 11.2 Summary of Cd-based chalcogenides synthesized by the solvothermal process

Compound	Reactants (M/E ratio)	Solvent	Reaction conditions	Symmetry	Shape
CdS	CdC_2O_4+S (2:1)	Ethylenediamine	120–180 °C, 12 h	Hexagonal	Rod-like
	CdC_2O_4+S (2:1)	Pyridine	120–180 °C, 12 h	Hexagonal	Spherical
	CdC_2O_4+S (2:1)	Ethylene glycol	160–180 °C, 12 h	Hexagonal	Spherical
CdSe	CdC_2O_4+Se (2:1)	Ethylenediamine	140 °C, 12 h	Hexagonal	Rod-like
	CdC_2O_4+Se (2:1)	Pyridine	160 °C, 12 h	Hexagonal	Spherical
CdTe	CdC_2O_4+Te (2:1)	Ethylenediamine	180 °C, 12 h	Cubic	Rod-like

Source: Data extracted from [216]

Table 11.3 Examples of solvothermal synthesis of II-VI compound nanoparticles

II-VI	Precursors		Solvent	T, °C/t, h	Ref.
	Metal	Chalcogen			
ZnS	$Zn(NCS)_2(C_5H_5N)_2$		Ethylene glycol	160–180/12	[85]
	$C_{10}H_{20}N_2S_4Zn$		Ethanol	150–200/12–72	[226]
ZnS:Mn	$ZnCl_2$ + $MnCl_2$	S powders	Oleic acid	180/60	[225]
ZnSe	$ZnSO_4$	Se elemental	Triethylamine		[74]
	$Zn(Ac)_2$	Na_2SeO_3	Hydrazine hydrate	180/1–5	[242]

II-VI	Precursors		Solvent	T, °C/t, h	Ref.
	Metal	Chalcogen			
ZnTe	Zn foils	TeO_2	Hydrazine hydrate	80/12; annealing 520 °C (N_2)	[203]
	Zn powders	Te powders	Ethylenediamine + Hydrazine hydrate	180/6; annealing 290 °C (N_2)	[34]
CdS	$Cd(NO_3)_2$	CH_4N_2S	Ethylene glycol	140/0.1–1	[113]
	$CdSO_4$	Na_2S_3	Benzene	80–120	[218]
	$CdCl_2$	CH_4N_2S	Diethylenetriamine	220/48	[33]
CdSe	$Cd(NO_3)_2$	$Se[HNaO_3]$	Ethylenediamine	180/12–24	[201]
	$Cd(NO_3)_2$	Se powders	Polyethylene glycol	200/72	[155]
CdTe	$CdCl_2$	K_2TeO_3	Ethylene glycol	150/12	[230]
	$Cd(NO_3)_2$	Te powders	Ethylenediamine	200/72	[189]

It was found that both solvent and temperature play key roles in the reaction, shapes, sizes, and phases (see Fig. 11.9). However, especially solvent has a significant effect on the morphology of the particles. At the same time, it was established that polyamines such as ethylenediamine (en), diethylenetriamine (dien), and triethylenetetramine (trien), which have more than two N-chelating atoms, can be used as “shape-controller” of nanoparticles. For example, it was found that CdS nanocrystallites synthesized by a reaction of CdC_2O_4 with S in ethylenediamine at 160–C are uniform nanorods with diameters of 20–50 nm and lengths of 200–1300 nm. In contrast, the particles obtained in pyridine under the same conditions display spherical disc-like shape with a size of 40 nm. It was also found that increasing the temperature and using a solvent with low dielectric constant are beneficial for producing nanocrystalline CdS in hexagonal phase [218]. The water content in the system not only induces the presence of cubic phase CdS nanocrystalline but also leads to a particle size increase. At the same time, Vaquero et al. [200] studied different solvents and found that ethylenediamine is an optimal solvent to control the growth, morphology, and crystal structure of the CdS.

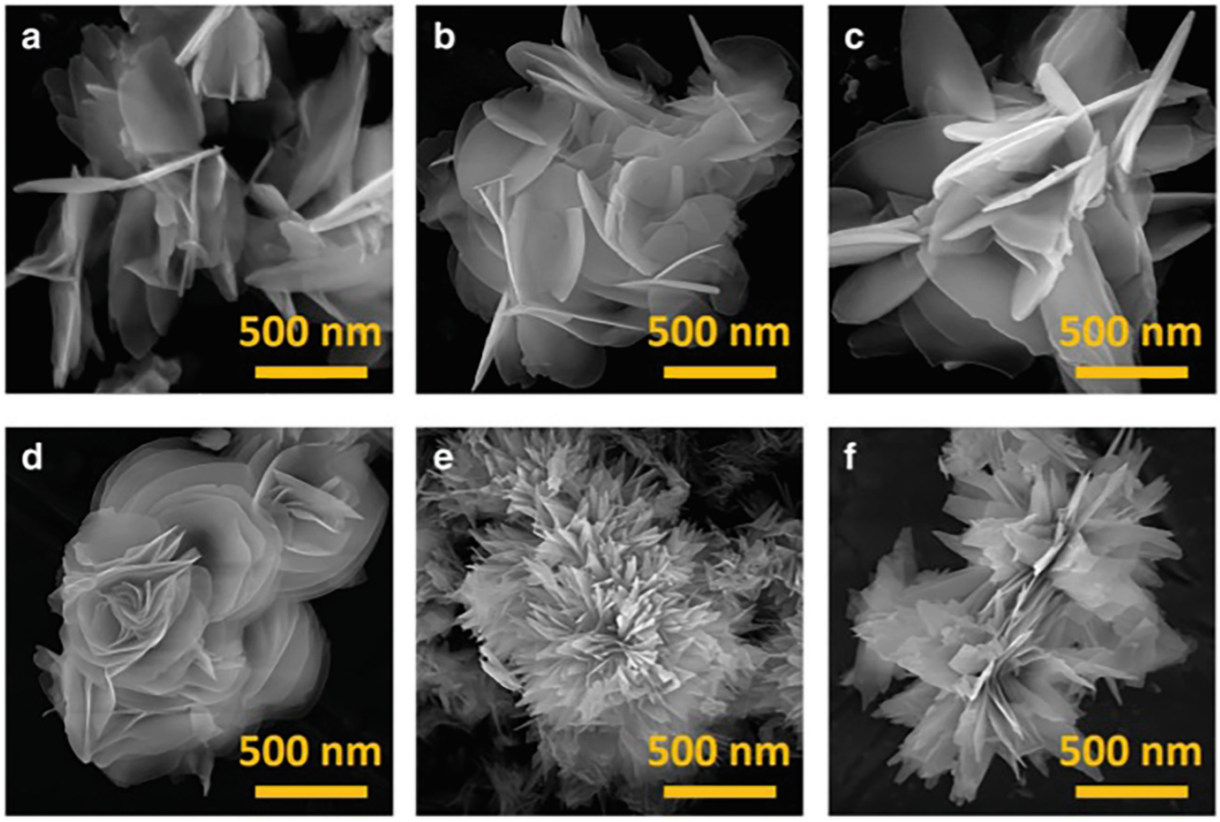

Fig. 11.9 FESEM images of ZnS nanoflowers prepared by solvothermal synthesis ($Zn(NO_3)_2$ + thiourea + $C_2H_4(NH_2)_2$) + water) during the reaction time of 6 h at the different growth temperatures: (**a**) 100 °C, (**b**) 110 °C, (**c**) 120 °C, (**d**) 130 °C, (**e**) 140 °C, and (**f**) 180 °C. (Reprinted with permission from Ref. [38]. Copyright 2009: Springer)

Generally, the size of the particles synthesized during the solvothermal process increases with increasing process temperature. For example, Jiang et al. [85] observed that nanospheres increase in size with increasing reaction temperature, reaching sizes of 200, 350, and 450 nm over a 12 h reaction period at 160 °C, 180 °C, and 200 °C, respectively. Such nanospheres are usually aggregates of many tiny nanocrystals, the size of which can be at the level of 10 nm or less [227]. An increase in the concentration of precursors is also accompanied by the growth of nanoparticles. Wang et al. [206] found that initial precursor concentrations are also key factors in controlling the shape of the resulting CdSe and CdTe nanocrystals, and different shapes such as dot shape, rod shape, and branched shape can be controlled by only changing initial precursor concentrations. The process time also has a significant effect on the parameters of the synthesized nanoparticles. According to Venci et al. [201], an increase in the time of the synthesis of CdSe nanoparticles from 12 to

24 h was accompanied by an increase in the crystallite size from 12 mm to 28 nm. To better control the size and shape of nanocrystals, reducing agent KBH_4 [74] and polyvinylpyrrolidone (PVP) as a capping agent [113, 230] can be added to the solution. For example, the addition of PVP helps to reduce the size of nanoparticles [113].

In some cases, annealing in an inert atmosphere is necessary to complete the reaction. Thus, in the synthesis of ZnTe powders, at the final stage after solvothermal synthesis at a low temperature and washing of the synthesized samples, annealing was carried out in a nitrogen atmosphere at a temperature of 290 °C [34] and 520 °C [203].

Thereby, the solvothermal synthesis method is an efficient and facile method for preparing NPs of II-VI compounds. Nanocrystallite of these materials with high crystallinity and good orientation could be obtained by this method. Despite the fact that the method has several advantages, the particle size distribution, purity of nanophase, and morphology variation still remain a challenge to overcome. In addition, as with hydrothermal synthesis, there are some safety issues with this process due to the very high pressure generated in the reactor. Hence, care must be taken when filling the autoclave, which should not exceed 85% by volume (usually 80%). Moreover, the reaction process is unobservable because the reactions take place in a closed reactor and the progress of the reaction is not controlled. Therefore, it is difficult to investigate the mechanism of formation of synthesized nanostructures.

11.7 Sonochemical Method

Sonochemistry provides a simple and resourceful method for the chemical preparation of nanomaterials. In sonochemical methods, solution of the starting material (e.g., metallic salts) is subjected to a stream of intensified ultrasonic vibrations (between 20 kHz and 15 MHz), which breaks the chemical bonds of the compounds [190, 221]. The physical phenomenon responsible for the sonochemical process is acoustic cavitation. The ultrasound waves pass through the solution, causing alternate compression and relaxation. This leads to acoustic cavitation, i.e., formation, growth, and implosive collapse of bubbles in the liquid. In addition, the change in pressure creates microscopic bubbles that implode violently, leading to emergence of shock waves within the gas phase of the collapsing bubbles.

These bubbles are in the nanometer-size range. Cumulatively, the effect of the collapse of millions of bubbles leads to an excess amount of energy released in solution, which creates the conditions for chemical reactions. Transition temperatures of ~5000 K, pressures of ~1800 atm, and cooling rates above 1010 K/s have been recorded in localized hot spots of cavitation implosion [190]. Studies have shown that ultrasonic irradiation of aqueous liquids leads to the formation of free radicals. The primary products of sonolysis in water are H• and OH• radicals. These radicals can recombine to return to their original form, or combine to produce H_2 and H_2O_2. They can also produce HO_2 in combination with O_2. It is these strong oxidizing and reducing agents that are involved in various sonochemical reactions occurring in aqueous solutions.

A typical apparatus that permits easy control over ambient temperature and atmosphere during sonochemical synthesis is shown in Fig. 11.10. Sonochemical decomposition rates for volatile organometallic compounds depend on a variety of experimental parameters such as vapor pressure of precursors, solvent vapor pressure, and ambient gas. In order to achieve high sonochemical yields, the precursors should be highly volatile since the primary sonochemical reaction site is the vapor inside the cavitating bubbles [190]. So that decomposition takes place only during cavitation, thermal stability is also important. In addition, the solvent vapor pressure should be low at the sonication temperature, because significant solvent vapor inside the bubble reduces the bubble collapse efficiency. The excessively high rate of cooling process is found to affect the formation and crystallization of the obtained products [51]. The products could be either amorphous or crystalline depending on the temperature in the ring region of the bubble. Time, energy, and pressure conditions make sonochemistry a distinct process as compared to other conventional methods.

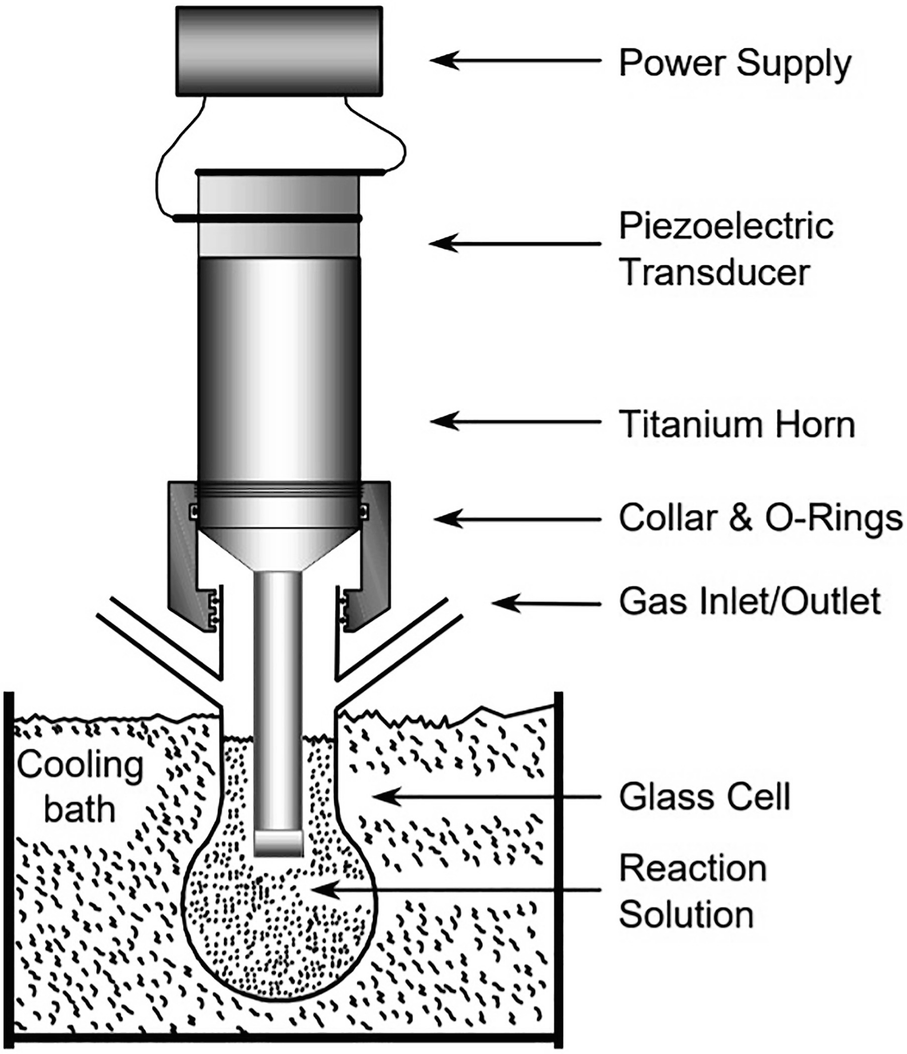

Fig. 11.10 A typical sonochemical apparatus with direct immersion ultrasonic horn. Ultrasound can be easily introduced into a chemical reaction with good control of temperature and ambient atmosphere. The usual piezoelectric ceramic is PZT, a lead zirconate titanate ceramic. Similar designs for sealed stainless steel cells can operate at pressures above 10 bar. (Reprinted with permission from Ref. [190]. Copyright 1999: Springer)

It was shown that the sonochemical synthesis is appropriate and well-organized method for the preparation of metal chalcogenide with controlled nanostructures. In particular, Zhou et al. [234] synthesized CdS nanostructures using sonochemical method with Cd (EDTA) and $Na_2S_2O_3$ in deionized water solution. They found that concentration of ethylenediaminetetraacetic acid (EDTA) greatly affects the process. Concentration of EDTA below 7% produced spherical-shaped CdS NPs, while with 8.5–10.5% concentration, mostly CdS NRs were developed. Semiconductor CdS with nanoporous hollow structure has been prepared utilizing the sonochemical method with the help of *Escherichia coli*

bacteria as template [177]. The structure of CdS showed a change from cubic to hexagonal form. The hexagonal-structured CdS nanoporous hollow microrods showed unique improvements in photoconversion performance.

Importantly, sonochemical synthesis has been successfully used to synthesize a wide range of II-VI semiconductors. Examples of reported II-VI semiconductors synthesized by this method, besides CdS [6, 17, 61, 177, 187, 207, 234], include CdSe [104, 174], CdTe [78, 111, 131, 163], ZnS [27], ZnSe [237, 239], ZnTe [80], and HgS [238].

The advantages associated with sonochemical methods include uniform size distribution of synthesized nanoparticles, a higher surface area, and faster reaction time. However, problems associated with process scaling, inefficient use of energy, and low yield limit the application of this method.

11.8 Microemulsion Technique

Microemulsions or micelles (including reverse micelles) represent an approach based on the formation of micro-/nano-reaction vessels for the preparation of nanoparticles, and they have received considerable interest in recent years [22, 37, 129]. This technique uses an inorganic phase in water-in-oil (w/o) microemulsions, which are isotropic liquid media with nanosized water droplets that are dispersed in a continuous oil phase. In general, microemulsions consist of, at least, a ternary mixture of water, a surfactant, or a mixture of surface-active agents and oil. The classic examples for emulsifiers are sodium dodecyl sulfate (SDC) and aerosol sodium bis(2-ethylhexyl)sulfosuccinate (AOT). Surfactants such as pentadecaoxyethylene nonylphenylether (TNP-35), decaoxyethylene nonylphenyl ether (TNT-10), polyoxyethylene(5)nonylphenolether (NP5), polyoxyethylene(10)nonylphenol ether (NP10), cetyltrimethylammonium bromide (CTAB), polyoxyethylene tert-octylphenyl ether (Triton X-100), octylphenoxy poly(ethyleneoxy)ethanol (IGEPAL), and many others, that are commercially available, can also be used in these processes. The surfactant (emulsifier) molecule stabilizes the water droplets, which have polar heads and nonpolar organic tails. The organic (hydrophobic) portion faces toward the oil phase, and the polar (hydrophilic) group toward water. In diluted water (or oil) solutions, the emulsifier dissolves and exists as a monomer. However, when its concentration exceeds a certain limit, called the critical micell concentration (CMC), the molecules of emulsifier

associate spontaneously to form aggregates called micelles. These micro-water droplets then form nanoreactors for the formation of nanoparticles. Some examples of surfactants and oils used in the synthesis of II–VI nanoparticles are listed in Table 11.4.

Table 11.4 Examples of Cd-based nanostructures synthesized by microemulsion technique

Material	Surfactant	Oil	Microemulsion scheme with w/o system	Ref.
CdS/PMMA nanocomposite	AOT	Methyl methacrylate	Two microemulsion scheme	[116]
CdS/PANI nanocomposites	NP5 and NP10	Cyclohexane		[96]
CdS NRs	TX-100 + hexanol	Cyclohexane		[226]
	IGEPAL			[202]
CdTe@SiO_2 nanospheres	Triton X-100 + n-hexanol	Cyclohexane	One microemulsion scheme	[214]
CdSe NRs	AOT + n-hexanol	Hydrazine hydrate		[219]
CdSe nanospheres	CTAB + isobutanol	Cyclohexane	Two microemulsion scheme	[32]

A typical method for preparing II-VI semiconductor nanoparticles in micelles is to form two microemulsions, one with the metal salt of interest and the other with the chalcogen precursor, and mix them together [129]. Various metal salts can be used as a source of metal ions, such as $CdSO_4$, $Cd[NH_3]_4SO_4$, $ZnCl_2$, $Cd(CH_3COO)_2$, $CdCl_2$, $Cd(NO_3)_2$ $Cd(ClO_4)_2$, etc., and both elemental Zn, Cd, S, Se, and Te, as well as salts containing chalcogen, such as Na_2SeSO_3, Na_2SO_3, NaHSe, Na_2S, H_2Te, $(NH_4)_2S$, Na_2TeO_3, and Na_2SeO_3, etc., can be used as a chalcogen precursor. The microemulsion reaction can easily be carried out at room temperature, and no aggregation occurs between the NPs due to the presence of surfactant material. A schematic diagram is shown in Fig. 11.11. When two different reactants mix, the interchange of the reactants takes place due to the collision of water microdroplets. Once a nucleus forms with the minimum number of atoms, the growth process starts. Nanoparticle synthesis inside the micelles can be achieved by different methods, including hydrolysis of reactive precursors, such as alkoxides, and precipitation reactions of metal salts [129]. The reaction (reduction, nucleation, and growth) takes place

inside the droplet, which controls the final size of the particles. The interchange of the reactant is very fast, so for the most commonly used microemulsions, it occurs just during the mixing process. The reactant concentration has a major influence on the reduction rate. The interchange of nuclei between two microdroplets does not take place due to the special restrictions from the emulsifier. Once the particle inside the droplets attains its full size, the surfactant molecules attach to the metal surface, thus stabilizing and preventing further growth. Solvent removal and subsequent calcination lead to the final product.

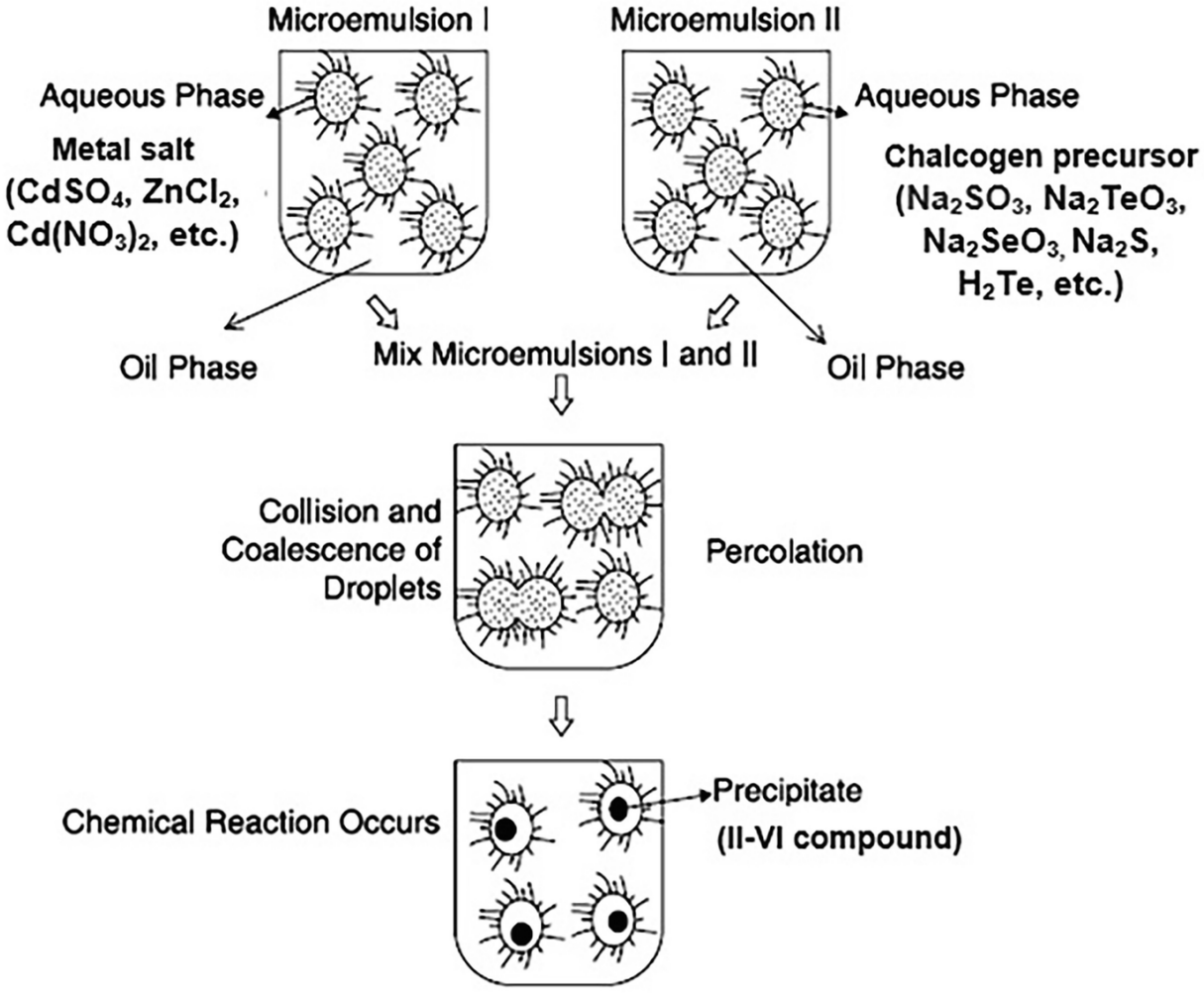

Fig. 11.11 Proposed mechanism for the formation of metal particles by the microemulsion approach using two microemulsion scheme. (Adapted with permission from Capek [22]. Copyright 2004: Elsevier)

The experiment showed that the microemulsion method provides the ability to manipulate the size and shape of nanoparticles by adjusting parameters, such as concentration and type of surfactant, the type of

continuous phase, the concentration of precursors, and molar ratio of water to surfactant [129, 184]. This means that this method allows the preparation of various morphologies and intricate nanostructures. Therefore, the microemulsion technique is very useful for the preparation of the nanomaterials with required properties including the geometry of the particles, the surface area, and most importantly the homogeneity of the obtained material. For example, Holmes et al. [73] demonstrated size control of CdS NPs by varying the ratio of water to surfactant. Zhang et al. [226] have shown the possibility of forming nanorods (NRs) and nanofibers by microemulsion synthesis method. The size of the NRs has been dependent on the concentration of the reagents used and defined the limit of concentration. In general, a higher water content provided a wider dispersion of NRs. It has also been shown that using the microemulsions method nanocomposites can be formed. For example, Li et al. [116] synthesized a CdS/PMMA nanocomposite using this method, and Khiew et al. [96] synthesized PANI/CdS nanocomposite.

The microemulsion method also allows the synthesis of core/shell structures. In particular, Hao et al. [65] synthesized CdSe/CdS nanomaterials, and Song et al. [185] and Aubert et al. [7] synthesized CdTe/CdS and CdTe/CdS/SiO_2 core/shell structures. The resulting core/shell QDs (with diameter 64 nm) were found inert and chemically established even in insensitive environments as a consequence of the silica layer. CdTe NCs encapsulated in silica spheres (CdTe@SiO_2) as core-shell-structured spheres have been synthesized by hydrolysis and microemulsion by Yang and Gao [214]. There are also reports indicating the synthesis of CdS/ZnS [71], CdS/HgS [87], Ag_2S/CdS [62], and CdSe/ZnS structures [154]. The ability to control the formation of different kinds of core-shell structures with sub-nanometric resolution is considered to be the main advantage of this method. A literature survey depicts that the ultrafine nanoparticles in the size range between 2 and 50 nm can be easily prepared by this method [129, 184]. Hollow-structured CdSe NPs have been also prepared via microemulsion technique [32].

Disadvantages include low production yields and the need to use a large amount of solvents and surfactants: this method requires several washing processes and further stabilization treatment due to the aggregation of the obtained nanoparticles [22, 129]. Modifications have been made to overcome these shortcomings. For instance, reverse microemulsion

technique has been developed [37]. The synthesis of II-VI compounds from reverse micelles is similar in most aspects to the synthesis of these materials in aqueous phase by the precipitation process.

In order to solve some of the problems of the microemulsion method, the combination of microemulsion with some other synthetic methods has been reported in recent decades. For example, it has been shown that the combination of sonochemistry and microemulsions or micelles can be an effective method for the synthesis of various types of nanostructures. The cavitation behavior of ultrasonic radiation can lead to extraction, mixed-phase reactions, and emulsification in a heterogeneous liquid-liquid system. Thus, under ultrasonic irradiation, it is possible to emulsify liquid-liquid heterogeneous systems with the formation of microemulsions. Using this approach, Huang et al. [75] synthesized spherical assemblies of nanocrystalline CdS particles.

11.9 Microwave-Assisted Method

Microwave irradiation is electromagnetic irradiation in the frequency range of 0.3–300 GHz, (wavelengths of 1 mm to 1 m). Therefore, the microwave region of the electromagnetic spectrum lies between infrared and radio frequencies. The microwave method is gaining more and more interest because it requires relatively little energy and time [8, 107, 134]. In this synthesis method, a definite quantity of precursors mixed solution enclosed in a special vessel and heated up in a microwave absorption oven by means of microwave irradiation. As it stated above, in spite of benefits of wet chemical routes for synthesis of II-VI semiconductor NPs, as a rule, they need a long time for synthesis. Microwave processing has attracted a lot of attention due to its advantages of providing faster synthesis rate, resulting superior to traditional heating. Indeed, since microwaves can penetrate the material and supply energy, heat can be generated throughout the volume of the material, resulting in volumetric heating. Microwave-assisted methods involve rapid and uniform heating of the reaction medium with no temperature gradients through two mechanisms: dipolar polarization and ionic conduction. The ability to elevate the temperature of a reaction well above the boiling point of the solvent increases the speed of reactions by a factor of 10–1000. As a result, the reaction times are reduced from a few hours to several minutes or even seconds without compromising the purity

or particle size [162]. The effect of microwave irradiation on the synthesis process has not yet been studied. Quick changes due to electric and magnetic forces directions, friction, and collisions of molecules are observed [110]. Thermal effects of microwave irradiations include consistent heating and superheating, while nonthermal effects have not been properly understood. It is considered that microwave irradiation reduces the activation energy of the materials and consequently provides a quick growth mechanism. Faster reaction rates favor rapid nucleation and formation of small, highly monodisperse particles. Yields are also generally higher, and the technique may provide a means of synthesizing compounds that are not available conventionally [168]. Additionally, the method can lead to the synthesis of materials with smaller particle size, narrow particle size distribution, high purity, and enhanced physicochemical properties [138]. Furthermore, microwave methods are unique in providing scaled-up processes without suffering thermal gradient effects, thus leading to a potentially industrially important advancement in the large-scale synthesis of nanomaterials [151]. Therefore, it is not surprising that microwave processes have been used to synthesize different highly crystalline nanoparticles of pure and doped II-VI compounds. Examples of microwave-assisted synthesis modes of Cd-based II-VI compounds are listed in Table 11.5. Other II-VI semiconductors, such as wide bandgap compounds ZnS [93], ZnSe [183], ZnTe [178], and narrow gap HgS [119, 208], have also been synthesized using a microwave-assisted process.

Table 11.5 Cd containing II-VI semiconductor nanomaterials prepared through microwave-assisted method using different synthesis conditions

Material	Power/frequency	Precursors	Irradiation time	pH	Ref.
CdS NTs	10 W/2450 MHz	Na_2S and $CdSO_4$	–	–	[175, 177]
CdS NPs	1300 W/2.4 GHz	Thioacetamide (CH_3CSNH_2) and $CdCl_2$	60 s	8	[171]
CdS and CdS:Cu NPs	720 W/2.45 GHz	$CdCl_2{\cdot}5H_2O$, CH_2CSNH_2 and $Cu(CH_3COO){\cdot}2H_2O$	1–15 min	–	[165]
CdSe NCs	900 W/2.43 GHz	$CdSO_4$, potassium nitriloacetate, and Na_2SeSO_3	30–60 min	–	[237, 239]

Material	Power/frequency	Precursors	Irradiation time	pH	Ref.
CdTe QDs	400 W/2450 MHz	$CdCl_2$, Na_2TeO_3, $NaBH_4$, and 3-mercaptopropionic acid (MPA)	10–40 min	–	[35]
CdSe–CdS QDs	0– 1000 W/2450 MHz	$CdCl_2$, NaHSe, and MPA	5–60 min	9	[150]
CdTe/CdS CShs	0– 300 W/2450 MHz	$CdCl_2$, Na_2S, NaHTe, and MPA	–	8.4	[69]
CdS/CdSe QDs	0– 1000 W/2450 MHz	$CdCl_2$, NaHSe, and MPA	30 min	9	[223]
ZnS/CdSe	880 W/2.44 GHz	$Cd(stearate)_2$, Se, stearic acid, $Zn(Un)_2$, CySCN, octylamine	30–120 s 30 s	–	[240]
(PVP)-capped CdS NPs	1000 W/2450 MHz	$Cd(Ac)_2$ and thiourea in N,N-dimethylformamide (DMF)	30 s with cycles	–	[70]

Source: Data extracted from Majid and Bibi [126]

As in all wet chemical methods of NPs synthesis, the parameters of the synthesized materials are highly dependent on temperature, time, and reagents molar ratio [67, 68]. The value of pH of the solution is also an important parameter to be considered; the optimal value of pH for this method is 8–10 [110].

At present, microwave heating seems to be the most promising way to achieve short synthesis times. Microwave energy is precisely controllable and can be turned on and off instantly, eliminating the need for warm-up and cool-down. In addition, automation allows control over the reaction conditions and hence facilitates control of particle size, morphology, and crystallinity [14]. The choice of starting metal oxide precursors (as acetates, chlorides, isopropyls) and solvents (as ethylene glycol, benzene) can govern reaction success, particle size, and crystal structure [15].

Limitations of the microwave-assisted processes are associated with the instrumental apparatus itself. The possibility of varying the reaction conditions by finely tuning/controlling the irradiation power and the temperature are the main drawbacks that, in some cases, may hinder reproducibility, especially when not laboratory-designed microwave ovens are used [134]. Finally, it should be noted that the articles published so far in the literature on semiconductors of the II-VI group synthesized using a microwave process indicate a lack of comprehensive studies. Many

researchers have simply synthesized materials using microwave irradiation and have not focused on understanding the effect of microwave irradiation parameters such as irradiation time, microwave power, etc. on their final properties.

11.10 Hot-Injection and One-Step Colloidal Method

The hot-injection method pioneered by Murray et al. [141] to obtain CdSe nanocrystals is an efficient method for the synthesis of high-quality nanocrystals with good crystallinity and narrow size distribution. This simple method only requires the rapid introduction of hot, highly reactive precursors into a hot organic solvent to induce a short burst of nucleation and then subsequent growth into nanocrystals of varying morphology and conditions. However, if we want to achieve better control over the growth of nanocrystals, it is desirable to separate the stages of nucleation and growth [153]. As well as hydrothermal and solvothermal methods, this method has good controllability and reproducibility, but unlike them, it is much faster and much safer, since it is carried out under ambient pressure. However, this method also has disadvantages. They are the following:

(i) Usually, in hot-injection synthesis, the solvents are organic compounds, and the capping agents are often chain organic compounds containing phosphine (such as trioctylphosphine and tributylphosphine). However, these organic compounds are often toxic, unstable at high temperature, and expensive. Thus, solvents which are less toxic, more stable at high temperature, and relatively cheaper are desired.

(ii) Capping ligands are always present on the surface of the product, which may interfere with their use.

(iii) Sometimes a low concentration of precursors is needed to obtain monodisperse nanostructures, which means a low yield.

(iv) Purging of protection gas or Schlink line is necessary to prevent oxidation or water absorption, which complicates operation.

(v) The main drawback with it is the requirements of rapid injection and subsequently fast cooling. It is not easy to realize in industrial production. Consequently, hot-injection synthesis is not suitable for large-scale production. In addition, it performs poorly in synthesis reproducibility [149].

Nevertheless, using hot-injection method, the size and morphology of the synthesized nanocrystals can be effectively controlled by adjusting several experimental parameters, such as the type and ratio of starting reagents, temperature and time of reaction, solvent, blocking ligands, etc. Synthesis usually starts at the temperature 250–300 °C. The process takes 1–4 min. As an example, consider the synthesis of CdSe NPs [24]. The solution of cadmium carboxylate, hexadecylamine (HAD), and 2-octadecene (ODE) was degassed for 1 h at room temperature and 1 h at 100 °C under a nitrogen flow. Under a nitrogen atmosphere, the temperature was raised to the injection temperature, and TOPSe solution was injected. The injection temperature was set to 245 °C, and the growth temperature was adjusted at 230 °C. The reaction was stopped by the injection of a solvent at 20 °C. Cadmium carboxylate was prepared by mixing CdO and the stearic or carboxylic acid in a 1:3 molar ratio, degassing for 1 h at 100 °C under a nitrogen flow, and dissolving the cadmium oxide under a nitrogen atmosphere at about 250 °C. The TOPSe solution was prepared by selenium dissolving in trioctylphospine (TOP). Because of this process, CdSe NPs with the size ~1.5–2.5 nm were synthesized. A more detailed description of this method and its use can be found in the Chaps. 12 and 13 (Vol. 1) and reviews [110].

An important advance over the hot-injection method is the development of a non-injection or one-step colloidal method that does not use the rapid introduction of precursors into solution at high temperature [23, 149, 220, 241]. The precursors are mixed at room temperature and then heated to the reaction temperature. For example, for synthesis of ZnS nanocrystals, 3 mmol of $Zn(acac)_2$ was added into 5 ml of n-dodecanethiol (DDT; $CH_3(CH_2)_{11}SH$) and 25 ml of ODE in a three-necked flask, and then the mixture was heated to 240 °C and kept for 180 min. For synthesis of CdS nanocrystals, 5 mmol of $Cd(acac)_2$ and 30 ml of DDT were added into a three-necked flask, and then the mixture was heated to 200 °C and kept for

23 h [220]. The synthesized ZnS and CdS nanocrystals with cubic zinc blende structure were ~5 nm in size.

Compared to the traditional hot-injection method, processing is simplified while maintaining good control over product properties. Another important notable thing is the selection of precursor. As the precursors are mixed at the first beginning, the reactivity of precursors should be much weaker at room temperature (otherwise the reaction procedure would be out of control), such as the combination of insoluble solid precursors, which are less expensive than high activity precursors. Thus, it is possible to further reduce the cost compared to the hot-injection method.

11.11 Photochemical Synthesis

It is known that irradiation with light, especially from the UV region, can change the structure of molecules and cause various photochemical reactions, including photochemical synthesis [41, 182]. A central feature of all light-promoted transformations is the involvement of electronically excited states, generated upon absorption of photons. This produces transient reactive intermediates and significantly alters the reactivity of a chemical compound [92, 182].

In recent years, photochemical synthesis has become widespread in the synthesis of nanostructures of metal chalcogenides of various morphologies [55, 229, 235]. This method has the advantages of mild reaction conditions, and the equipment used is quite simple and cheap, since the well-known low-pressure mercury pillar lamp (λ = 253.7 nm) and high-pressure indium column-like lamp (λ = 420–450 nm) can be used for these purposes. The processes occurring during the synthesis under the action of UV irradiation in relation to CdSe can be described by the following reactions [236]:

$$\mathrm{SeSO_3^{2-} + e \rightarrow Se^- + SO_3^{2-}} \tag{11.11}$$

$$\mathrm{Se^- + e \rightarrow Se^{2-}} \tag{11.12}$$

$$\mathrm{Cd^{2+} + Se^{2-} \rightarrow CdSe} \tag{11.13}$$

Thus, the formation of CdSe nanoparticles under the action of photoirradiation includes the above three stages: First, $\mathrm{SeSO_3^{2-}}$ is reduced to $\mathrm{Se^-}$; then $\mathrm{Se^-}$ is further reduced to $\mathrm{Se^{2-}}$; finally, $\mathrm{Se^{2-}}$ reacts with metal

cations to form metal selenide nanoparticles. The first reaction may be a slow reaction and the second reaction may be a fast reaction. Using indicated approach Zhu et al. [236] synthesized 7 nm CdSe spherical nanoparticles. For doing this, they irradiated aqueous solution containing $CdCl_2$ and Na_2SeSO_3 in the presence of complexing agents for several hours at room temperature. A high-pressure indium lamp was used as the visible photoirradiation source. They have shown that both light intensity and irradiation time have influence on the size of the final products. The complexing agents also play an important role: they can retard the rate of the reactions and cause the particle size to be small. The reactions conducted without complexing agents were unsuccessful.

Studies have shown that this method, in addition to the synthesis of CdSe NPs [212, 229], can be used to synthesize binary CdS [148, 205, 209, 224], CdTe [50, 121], ZnS [54], ZnSe [94, 106], doped QDs [94], ternary compounds [50, 79], and composites [42, 224]. In particular, Wang et al. [209] synthesized CdS nanocrystallites with a cubic or hexagonal phase structure using ultraviolet irradiation. Synthesis proceeded at room temperature by precipitation of Cd^{2+} ions with homogeneously released S^{2-} ions formed during the decomposition of thioacetamide by ultraviolet irradiation. Irradiation time can reach several hours. Usually, the solution is deaerated by continuous N_2 bubbling during the whole period of UV irradiation. It has been found that the concentrations of Cd^{2+} and thioacetamide, as well as the solvent, have a great effect on the phase structure, product composition, and average size of CdS nanocrystals. For example, Hao et al. [64] prepared CdS nanocrystals in C_2H_5OH and H_2O solvents using sodium dodecyl sulfate (SDS) as capping agent by ultraviolet irradiation technique. They established that SDS as capping agent in the solvents with different C_2H_5OH and H_2O volume ratios has a great effect on the morphology of the synthesized CdS nanocrystals. At solvent with a C_2H_5OH/H_2O = 9:1 volume ratio containing 0.2 mol/L, SDS was a favorite medium for the formation of CdS nanorods. While the C_2H_5OH/H_2O volume ratio was changed up to 9.5:1, the dendritic supermolecular CdS nanostructures were obtained. When the C_2H_5OH/H_2O volume ratio was down to 6:1, only CdS nanocrystals with irregular morphologies could be formed. Hao et al. [64] believed that the composition of the solution, i.e.,

the C_2H_5OH/H_2O volume ratio, influenced such physicochemical properties of the solution as polarity (dielectric constant) and softness, which can affect the dissolution and transport of ions in solution, and thus may lead to the different cap structures of SDS in the formation of CdS nanocrystals. As a result, SDS in different solvents can produce patterns of the different structures. These different patterns can act as suitable nucleation sites or interact with the special crystal planes of the growing CdS nanocrystals, resulting in the formation of CdS nanorods and dendritic CdS nanostructures. Mo et al. [135] observed the same significant effect on the morphologies of CdS NPs (2001). They established a morphology-controlled synthesis of CdS nanocrystallites by introducing poly(vinyl alcohol) (PVA) as the protecting agent, which self-assemble into desirable shapes. CdS spherical nanoparticles, nanodisks, and nanowires were obtained conveniently, and there were some CdS nanotubes that appeared in the CdS nanodisk sample.

Gao et al. [50] and Zhao et al. [229] have shown that the intensity of UV light, UV irradiation time, pH value of solution, solution temperature, and concentration of anions in solution also play important roles in properties of the photochemically prepared NCs. In Zhao et al. [229], the optimal value of pH for the synthesis of CdSe NPs should be in the range of 10–11. Increasing the irradiation intensity shortens the reaction time, required for the synthesis of nanoparticles of a given size. An increase in the irradiation time and temperature was accompanied by an increase in the size of QDs [94]. Depending on the irradiation time, the size of nanoparticles can vary from 1–2 nm after 10–20 min of irradiation [94] to 25 nm after 48 h of irradiation [212]. In principle, the main conclusions drawn from the study of the photochemical synthesis of CdS and CdSe nanocrystallites can also be applied to other chalcogenides.

11.12 Green Synthesis

“Green” synthesis involves the use of a set of green chemistry principles originally defined by Anastas and Warner [3]. Green synthesis developments can be divided into three categories: namely, safety, environment, and efficiency [29]. Safety developments include the development of safer materials and safer processes, i.e., development of less hazardous chemical synthesis using safer chemicals and solvents.

Development for the environment includes the development of processes that produce less waste to reduce environmental impact and do not use substances that pose a risk to human health and the environment. As for efficiency, the main thing here is the material and energy efficiency of the processes used, aimed at reducing material and energy costs in the synthesis of the necessary materials. In this regard, the use of aqueous solutions for the synthesis of II-VI compounds, ball milling, and sonochemical and microwave-assisted syntheses can be considered as elements of a “green” technology [95, 157].

However, there is another direction in the synthesis of II-VI compounds, which can literally be attributed to the “green” technology This is the synthesis of II-VI compounds using natural components such as microorganisms (algae, bacteria, fungus, viruses, yeast), and extractions of plants. At present, the combination of nanotechnologies and biotechnologies has formed a promising area for the synthesis of nanomaterials [44, 126]. It has been found that microorganisms and plant extracts are able to use their internal biochemical processes to convert inorganic metal salts into the required NPs [10]. In particular, in 2004, Sweeney et al. found that when Cd^{2+} is added to *E. coli* cultures, *E. coli* binds toxic Cd^{2+} into a Cd-thiolate complex, thereby neutralizing Cd toxicity. Then, if sulfide ions (Na_2S) are added, the Cd complex reacts with the added sulfide ions and forms intracellular CdS NPs. The biosynthetic method for obtaining NPs turned out to be harmless compared to all other (physical and chemical) methods. Moreover, it turned out that using this approach, it is possible to synthesize nanoparticles with small size. For example, using this approach were synthesized CdS NPs with the size ~1 nm [30], 1–2 nm [102], 1.5 nm [233], and 2–5 nm [89, 90].

In a microorganism-based approach, microorganisms such as bacteria [90, 156, 181, 191], fungi [25, 105], and yeasts [4, 26] are cultured in favorable conditions (light, nutrients, pH, temperature, stirring speed). Optimizing all of these culture conditions can significantly increase enzyme activity. Then, a metal salt solution is added to the resulting material and incubated. Synthesis of nanomaterials is observed by visual examination of changes in the color of the culture medium. Microorganisms used in the synthesis of NPs of II-VI compounds are listed in Table 11.6. The mechanisms by which different, natural bacterial strains affect metal chalcogenide NPs precipitation are still largely unclear. However, recent

studies on bacterial CdS biosynthesis [199] showed that it is critical to select the correct bacterial strain to precipitate CdS NPs at appreciable yields. Here, synthetic biology provides an exciting means to increase NPs yield and to exert control over the precipitation reaction. For example, in [90], Kang et al. inserted the phytochelatin synthase (SpPCS) gene from the yeast *S. pombe* into *E. coli* to promote $CdCl_2$ precursor intake and thus, increase NP yield.

Table 11.6 Microorganisms and plant extracts used for biosynthesis of II-VI semiconductor NPs

Compound	Microorganisn	Name	Location	NPs size, nm
CdS	Bacteria	*Escherichia coli*; *A. ferrooxidans*; *A. caldus*; *Stenotrophomonas maltophilia*; *Klebsiella pneumoniae*; *Desulfovibrio alaskensis*; *Thermoanaerobacter*;	Ext.	2–50
		Escherichia coli; *Pseudomonas*; *Acidithiobacillus thiooxidans*	Int.	2–20
	Fungi	*Phanerochaete crysosporium*; *Rhizopus stolonifer*; *Pleurotus ostreatus*	Ext.	2–9
	Algae	*Chlamydomonas reinhardtii*;	Ext.	2–7
		Arthrospira platensis; *C. reinhardtii*; *C. merolae*	Int	~8
	Yeast	*Schizosaccharomyces pombe*	Ext., Int.	2–6
		Candidas;	Int.	MCs
	Enzymes	Cystathionine gamma-lyases;	Cell-free	~3
	Virus virus	Bacteriophage	Int.	~40
	Plant extracts	Tomato hairy root extract; *N. tabacum* L. cv.; Fenugreek seed extract; Pomegranate peel extract; Banana peel extract; Hairy root culture of *Linaria maroccana* L; *S. lycopersicum*	n/a	3–10
CdSe	Bacteria	*Veillonella atypica*; *Bacillus licheniformis*	Int.	2–4
	Fungi	Helminthosporium solani	Ext.	3–7
	Enzyme	*Nitrate reductase*	Cell-free	4–9
CdTe	Bacteria	*Escherichia coli*	Ext., Int.	2–5
	Fungi	*Rhizopus stolonifer*; *Fusarium oxysporum*	Ext.	3–20
	Earthworm	*Lumbricus rubellus*	n/a	~2.5

Compound	Microorganisn	Name	Location	NPs size, nm
ZnS	Bacteria	*Klebsiella pneumonia*; *Desulfovibrio desulfuricans*; *R. sphaeroides*; *S. nematodiphila*	Ext.	18–40
	Fungi	*Fusarium oxysporum*; *Aspergillus flavus*; *S. cerevisiae*	Ext.	15–60
	Yeast	*Saccharomyces cerevisiae*	Int.	30–40
	Plant extract	Moringa oleifera leaf extract	n/a	~30

Source: Data extracted from [44]
Int Intracellular, *Ext.* Extracellular, *MC* mycrocrystals

There are two types of biosynthetic strategies after incubation period: intracellular and extracellular synthesis processes, when the processes occur inside and outside the cell. In extracellular synthesis, centrifugation at various speeds and a washing process are used to get rid of biomass. In an intracellular process, media components and large particles are separated using repeated cycles of sonication, washing, and centrifugation. An extracellular process is preferred over an intracellular one due to the ease of post-processing. It is also more suitable for industrial applications [91]. Finally, after washing with water/solvent (ethanol/methanol), the particles are obtained as bottom granules. A schematic illustration of this method is shown in Fig. 11.12.

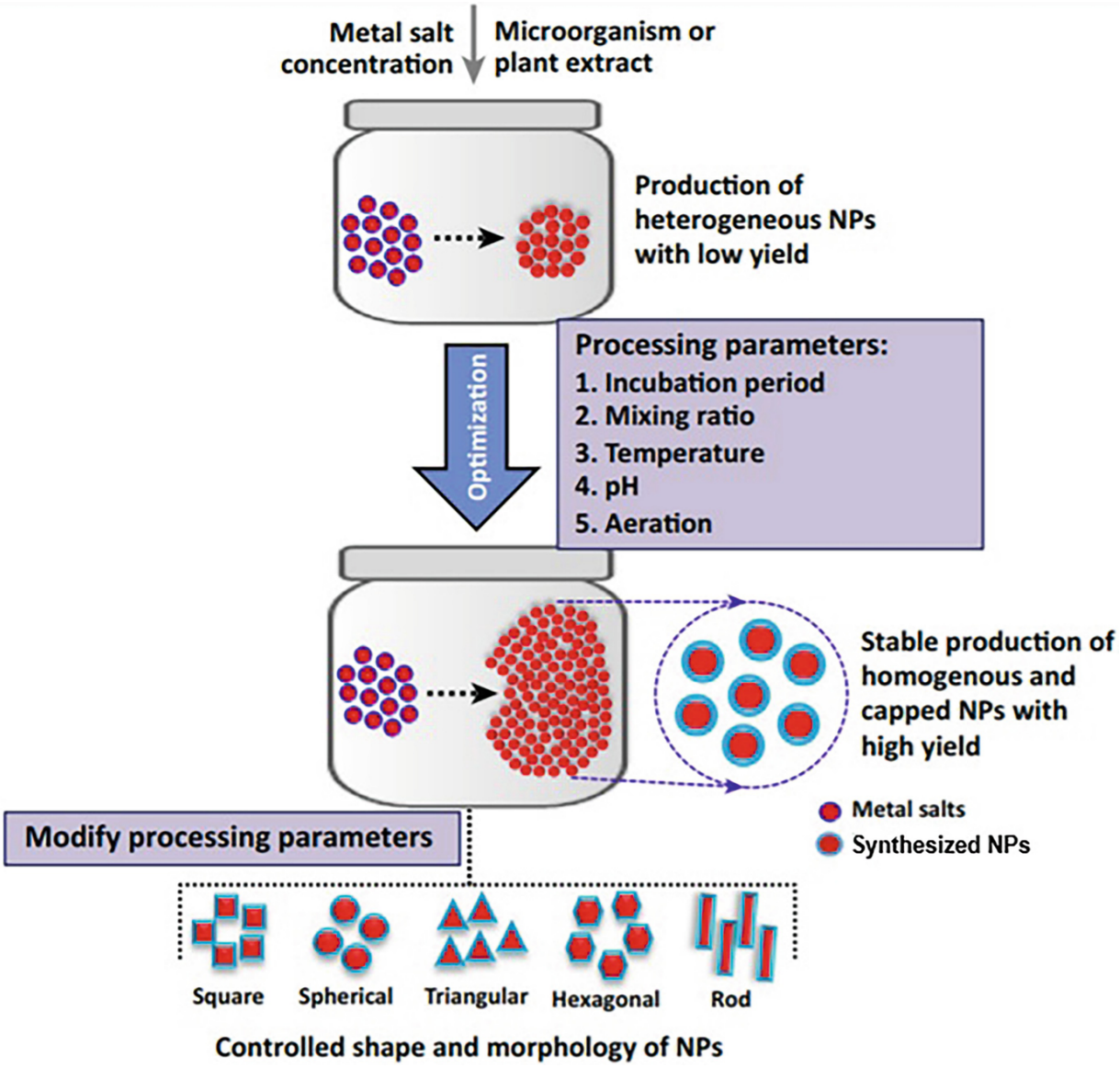

Fig. 11.12 Parameters of biological synthesis. Synthesis of homogeneous nanoparticles of the same size and shape requires optimization of control parameters, such as salt concentration, mixing ratio of biological extract and metal salt, pH value, temperature, incubation time, and aeration. Biological synthesis can also provide an additional coating layer on the synthesized nanoparticles with the addition of several biologically active groups, which can increase the efficiency of synthesized nanoparticles. (Reprinted with permission from Ref. [180]. Copyright 2016: Elsevier)

With the emergence of a broad range of biosynthetic NP precipitation approaches, there also has been a growing interest in controlling these approaches to affect NP properties. Most strategies to date focus on controlling the particle size, which has large impact on the photoelectronic properties of TM NPs. Already in 1989, when Dameron et al. [30] first precipitated CdS with yeast, they influenced particle size by using different peptide-Cd complexes as precursors, which effectively limited CdS

crystallite growth. However, perhaps the simplest way to influence NP size is to control precipitation or incubation time. In particular, Bai et al. [9] found that by changing the culture time, the size of the nanoparticles can be controlled. Cadmium ions were transferred into a living cell from a solution after its incubation at 30 °C in the dark and in an aerobic environment. Testing of the synthesized material showed that the average particle size of CdS was 2.3 nm, 6.8 nm, and 36.8 nm at culture times of 36, 42, and 48 h, respectively. In 2010, Bao et al. [12] showed that the size of extracellularly precipitated CdTe NPs increased predictably with increasing incubation time. Fellowes et al. [43] showed a similar behavior for CdSe NPs when prolonging the refluxing time. There are also studies that show that using biosynthesis can also influence the particle size distribution [89, 90] and NP crystal structure [137].

In the plant-based approach, components, i.e., leaves [84], fruits [39, 233], flowers [133], seeds [196], roots [16, 179], skins (Sasidharan et al., 2014), or other bio entities [152], are extracted through a purification, filtration, and centrifugation. For the synthesis process, a suitable amount of water, a metal salt solution, and various fractions of plant extracts are used. In the process of incubation (3–48 h), simultaneously with a decrease in the concentration of metal salts, the assembly of nanoparticles begins, similar to that observed with the help of microorganisms. In plant-based biosynthesis, there are no requirements for well-conditioned culture, expensive isolation methods, or any special, complex, and multistep processes. Several examples of the biosynthesis of compounds II-VI are given in [44, 82, 173, 233]. Zhou et al. [233], synthesizing CdS NPs using banana peel extract as a suitable, harmless, environmentally friendly closure agent, showed that as in all wet chemical processes reaction parameters like quantity of banana peel extract, pH, concentration, and temperature played significant role in NPs formation.

The experiment showed that biosynthesis is really a low-cost technique acceptable for nanoparticle synthesis. It is an environment-friendly technique which provides an extensive variety of environmentally suitable synthesis process. In addition, it is completely free of the poisonous chemical agents and high-energy requirement as in physiochemical methods. As it was shown before, NPs of II-VI compounds can be synthesized both in bacteria and fungi. However, Jacob et al. [82] believe that fungal-based systems have the advantage of ease of handling and

extracellular synthesis. Although bacterial synthesis has an advantage of involving directed evolution or genetic manipulation, fungi have a niche with respect to the cost factor on scale-up and large-scale synthesis. At the same time, Shah et al. [173] believe that in contrast to microorganism, plants approach provides more benefits because it is faster, more cost-effective, and straightforward. This method is more supportive for the synthesis of metal chalcogenide NPs. However, to move to the next stage of development, it is needed to improve the control over size, shape, and complete monodispersivity of the nanostructures. In addition, biosynthetic methods are typically slow and produce particles of low purity, compared with chemical bath deposition methods. While the purity of TM chalcogenide NPs is crucial for some applications, biosynthetic NPs can outperform their pure, chemically synthesized counterparts in other applications. For example, due to the natural presence of organic capping ligands, biosynthetic NPs can bind dye molecules or can bind to other materials, including cells and graphene. This makes them useful as efficient photocatalysts, as natural bioimaging tracers, and as photoabsorbers in energy devices. A more accurate mechanism of biosynthesis is also required for manufacturing of nanomaterials for technological applications. More details on the problems of the synthesis of nanoparticles of II-VI compounds by biosynthetic methods can be found in the reviews [1, 44, 82, 95, 128, 147].

Acknowledgments

G. Korotcenkov is grateful to the State Program of the Republic of Moldova, project 20.80009.5007.02, for supporting his research.

References

1. Aguayo OPY, Mouheb L, Revelo KV, Vásquez-Ucho PA, Pawar PP, Rahman A et al (2022) Biogenic sulfur-based chalcogenide nanocrystals: methods of fabrication, mechanistic aspects, and bio-applications. Molecules 27:458
2. Al Balushi BSM, Al MF, Al WB, Kuvarega AT, Al Kindy SMZ, Kim Y, Selvaraj R (2018) Hydrothermal synthesis of CdS sub-microspheres for photocatalytic degradation of pharmaceuticals. Appl Surf Sci 457:559–565
3. Anastas P, Warner J (1998) Green chemistry: theory and practice. Oxford University Press, New York

4. Apte M, Sambre D, Gaikawad S, Joshi S, Bankar A, Kumar AR et al (2013) Psychrotrophic yeast Yarrowia lipolytica NCYC 789 mediates the synthesis of antimicrobial silver NPs via cell-associated melanin. AMB Express 3(1):32
5. Arachchige IU, Brock SL (2006) Sol-gel assembly of CdSe nanoparticles to form porous aerogel networks. J Am Chem Soc 128:7964–7971
6. Arul Dhas N, Gedanken A (1998) A sonochemical approach to the surface synthesis of cadmium sulfide NPs on submicron silica. Appl Phys Lett 72(20):2514–2516
7. Aubert T, Soenen SJ, Wassmuth D, Cirillo M, Van Deun R, Braeckmans K et al (2014) Bright and stable CdSe/CdS@ SiO_2 NPs suitable for long-term cell labeling. ACS Appl Mater Interfaces 6(14):11714–11723
8. Baghbanzadeh M, Carbone L, Cozzoli PD, Kappe CO (2011) Microwave assisted synthesis of colloidal inorganic nanocrystals. Angew Chem 50:11312–11359
9. Bai H, Zhang Z, Guo Y, Jia W (2009) Biological synthesis of size-controlled cadmium sulfide NPs using immobilized Rhodobacter sphaeroides. Nanoscale Res Lett 4(7):717
10. Baker S, Harini BP, Rakshith D, Satish S (2013) Marine microbes: invisible nanofactories. J Pharm Res 6(3):383–388
11. Baláž P, Boldižárová E, Godočí E., Briančin J. (2003) Mechanochemical route for sulphide NPs preparation. Mater Lett 57(9):1585–1589
12. Bao H, Lu Z, Cui X, Qiao Y, Guo J, Anderson JM et al (2010) Extracellular microbial synthesis of biocompatible CdTe quantum dots. Acta Biomater 6:3534–3541
13. Bhattacharjee B, Ganguli D, Iakoubovskii K, Sesmans A, Chaughuri S (2002) Synthesis and characterization of sol–gel derived ZnS:Mn^{2+} nanocrystallites embedded in a silica matrix. Bull Mater Sci 25(3):175–180
14. Bilecka I, Niederberger M (2010) Microwave chemistry for inorganic nanomaterials synthesis. Nanoscale 2:1358–1374
15. Bilecka I, Djerdj I, Niederberger M (2008) One-minute synthesis of crystalline binary and ternary metal oxide nanoparticles. Chem Commun 7:886–888
16. Borovaya MN, Naumenko AP, Matvieieva NA, Blume YB, Yemets AI (2014) Biosynthesis of luminescent CdS QDs using plant hairy root culture. Nanoscale Res Lett 9(1):686
17. Bozkurt PA, Derkuş B (2016) Synthesis and characterization of CdS NRs by combined sonochemical-solvothermal method. Mater Sci Poland 34(3):684–690
18. Brinker CJ, Scherer GW (1990) Sol-gel science: the physics and chemistry of sol-gel processing. Academic, San Diego
19. Bu IYY (2013) Sol–gel synthesis of ZnS (O,OH) thin films: Influence of precursor and process temperature on its optoelectronic properties. J Lumin 134, 423–428

20. Bu H-B, Kikunaga H, Shimura K, Takahasi K, Taniguchi T, Kim DG (2013) Hydrothermal synthesis of thiol-capped CdTe nanoparticles and their optical properties. Phys Chem Chem Phys 15:2903
21. Byrappa K, Yoshimura M (2012) Handbook of hydrothermal technology. Elsevier, New York
22. Capek I (2004) Preparation of metal nanoparticles in water-in-oil (w/o) microemulsions. Adv Colloidal Interface Sci 110(1–2):49–74
23. Cao YC, Wang JH (2004) One-pot synthesis of high-quality zinc-blende CdS nanocrystals. J Am Chem Soc 126(44):14336–14337
24. Capek RK, Lambert K, Dorfs D, Frederic P, Smet PF, Poelman D et al (2009) Synthesis of extremely small CdSe and bright blue luminescent CdSe/ZnS nanoparticles by a prefocused hot-injection approach. Chem Mater 21:1743–1749
25. Castro-Longoria E, Vilchis-Nestor AR, Avalos-Borja M (2011) Biosynthesis of silver, gold and bimetallic NPs using the filamentous fungus *Neurospora crassa*. Colloids Surf B: Biointerfaces 83(1):42–48
26. Chen G, Yi B, Zeng G, Niu Q, Yan M, Chen A et al (2014) Facile green extracellular biosynthesis of CdS QDs by white rot fungus *Phanerochaete chrysosporium*. Colloids Surf B: Biointerfaces 117:199–205
27. Cheon SY, Yoon J-S, Oh KH, Jang KY, Seo JH, Park JY et al (2017) Sonochemical synthesis of ZnO-ZnS core-shell nanorods for enhanced photoelectrochemical water oxidation. J Am Ceram Soc 100(9):3825–3834
28. Corriu R, Anh NT (2009) Molecular chemistry of sol-gel derived nanomaterials. Wiley, Chichester
29. Dahl JA, Maddux BLS, Hutchison JE (2007) Toward greener nanosynthesis. Chem Rev 107:2228–2269
30. Dameron CT, Reese RN, Mehra RK, Kortan AR, Carroll PJ, Steigerwald ML et al (1989) Biosynthesis of cadmium sulphide quantum semiconductor crystallites. Nature 338(6216):596–597
31. Devi RA, Latha M, Velumani S, Oza G, Reyes-Figueroa P, Rohini M, Yi J (2015) Synthesis and characterization of cadmium sulfide NPs by chemical precipitation method. J Nanosci Nanotechnol 15(11):8434–8439
32. Dong CZ, Zhang LF, Chen S, Zhang MX, Feng L, Cui ZM, Zhang QJ (2013) Hollow structure of CdSe by W/O microemulsion method. In: Advanced materials research, vol 652. Trans Tech Publications, Zürich, pp 215–218
33. Du Y, Zeng F (2013) Solvothermal route to CdS nanocrystals. J Experim Nanosci 8(7–8):965–970
34. Du J, Xu L, Zou G, Chai L, Qian Y (2006) Solvothermal synthesis of single crystalline ZnTe nanorod bundles in a mixed solvent of ethylenediamine and hydrazine hydrate. J Crystal

Growth 291:183–186
35. Duan J, Song L, Zhan J (2009) One-pot synthesis of highly luminescent CdTe QDs by microwave irradiation reduction and their Hg^{2+} −sensitive properties. Nano Res 2(1):61–68
36. Dutková E, Balaz P, Pourghahramani P (2009) CdS NPs mechanochemically synthesized in a high-energy mill. J Optoelectron Adv Mater 11(12):2102–2107
37. Eastoe J, Hollamby MJ, Hudson L (2006) Recent advances in nanoparticle synthesis with reversed micelles. Adv Colloid Interf Sci 128–130:5–15
38. Ebrahimi S, Yarmand B (2019) Morphology engineering and growth mechanism of ZnS nanostructures synthesized by solvothermal process. J Nanopart Res 21:264
39. Edison TJI, Sethuraman MG (2012) Instant green synthesis of silver NPs using Terminalia chebula fruit extract and evaluation of their catalytic activity on reduction of methylene blue. Process Biochem 47(9):1351–1357
40. Elavarthi P, Kumar AA, Murali G, Reddy DA, Gunasekhar KR (2016) Room temperature ferromagnetism and white light emissive CdS: Cr NPs synthesized by chemical co-precipitation method. J Alloys Comp 656:510–517
41. Esser P, Pohlmann B, Scharf H-D (1994) The photochemical synthesis of fine chemicals with sunlight. Angew Chem Int Ed Engl 33:2009–2023
42. Fang Z, Fan Y, Liu Y (2011) Photochemical synthesis and photocatalysis application of ZnS/amorphous carbon nanotubes composites. Front Optoel China 4(1):121–127
43. Fellowes JW, Pattrick RAD, Lloyd JR, Charnock JM, Coker VS, Mosselmans JFW et al (2013) Ex situ formation of metal selenide quantum dots using bacterially derived selenide precursors. Nanotechnology 24:145603
44. Feng Y, Marusak KE, You L, Zauscher S (2018) Biosynthetic transition metal chalcogenide semiconductor nanoparticles: progress in synthesis, property control and applications. Curr Opin Colloid Interface Sci 38:190–203
45. Feraru I, Vasiliu IC, Iordanescu R, Elisa M, Bartha C (2013) Structural characterization of CdSe-doped sol-gel silicophosphate films. Electron Mater Process 49(6):50–56
46. Gao B, Shen C, Yuan S, Yang Y, Chen G (2013) Synthesis of highly emissive CdSe quantum dots by aqueous precipitation method. J Nanomater 2013:138526
47. Gacoin T, Malier L, Boilot J-P (1997) Sol–gel transition in CdS colloids. J Mater Chem 7(6):859–860
48. Gacoin T, Malier L, Counio G, Boilot J-P (1997) CdS nanoparticles and the sol-gel process. Proc SPIE 3136:358–365
49. Gaeeni MR, Tohidian M, Majles-Ara M (2014) Green synthesis of CdSe colloidal nanocrystals with strong green emission by the sol−gel method. Ind Eng Chem Res 53:7598–7603

50. Gao X, Wu J, Wei X, He C, Wang X, Guangsheng GG, Qiaosheng PQ (2012) Facile one-step photochemical synthesis of water soluble CdTe(S) nanocrystals with high quantum yields. J Mater Chem 22:6367–6373
51. Gendanken A (2003) Sonpchemistry and its applications in nanochemistry. Curr Sci 85:1720–1722
52. Godočíková E, Baláž P, Gock E, Choi WS, Kim BS (2006) Mechanochemical synthesis of the nanocrystalline semiconductors in an industrial mill. Powder Technol 164(3):147–152
53. Golsefidi MA, Ramandi MF, Shahkooie MAK (2016) Facile synthesis of CdTe nanoparticles and photo-degradation of Rhodamine B and methyl orange. J Mater Sci Mater Electron 27:12100–12105
54. Gonzalez CM, Wu W-C, Tracy J, Martin B (2015) Photochemical synthesis of size-tailored hexagonal ZnS quantum dots. Chem Commun 51:3087–3090
55. Goto F, Ichimura M, Arai E (1997) A new technique of compound semiconductor deposition from an aqueous solution by photochemical reactions. Jpn J Appl Phys 36(9A):L1146
56. Grundler P (2007) Chemical sensors: an introduction for scientists and engineers. Springer, Berlin
57. Guglielmi M, Kickelbic G, Martucci A (eds) (2014) Sol-gel nanocomposites. Springer, New York
58. Guglielmi M, Martucci A, Fick J, Vitrant G (1998) Preparation and characterization of HgxCd1-xS and PbxCd1-xS quantum dots and doped thin films. J Sol–Gel Sci Technol 11:229–240
59. Guglielmi M, Martucci A, Menegazzo E, Righini GC, Pelli S, Fick J, Vitrant G (1997) Control of semiconductor particle size in sol-gel thin films. J Sol-Gel Sci Techn 1–3:1017–1021
60. Gupta AK, Kripal R (2012) EPR and photoluminescence properties of Mn^{2+} doped CdS NPs synthesized via co-precipitation method. Spectrochim Acta A 96:626–631
61. Hanifehpour Y, Hamnabard N, Mirtamizdoust B, Joo SW (2016) Sonochemical synthesis, characterization and sonocatalytic performance of terbium-doped CdS NPs. J Inorg Org Polymers Mater 3(26):623–631
62. Han MY, Huang W, Chew CH, Gan LM, Zhang XJ, Ji W (1998) Large nonlinear absorption in coated Ag_2S/CdS nanoparticles by inverse microemulsion. J Phys Chem B 102:1884–1887
63. Hao H, Yao X, Wang M (2007) Preparation and optical characteristics of ZnSe nanocrystals doped glass by sol–gel in situ crystallization method. Opt Mater 29:573–577
64. Hao LY, Mo X, Wang CY, Wu Y, Huang DW, Zhu YR et al (2001) Fabrication of CdS nanocrystals with various morphologies in selective solvents via a convenient ultraviolet irradiation technique. Mater Res Bull 36:1005–1009

65. Hao E, Sun H, Zhou Z, Liu J, Yang B, Shen J (1999) Synthesis and optical properties of CdSe and CdSe/CdS NPs. Chem Mater 11(11):3096–3102
66. Hayashi H, Hakuta Y (2010) Hydrothermal synthesis of metal oxide nanoparticles in supercritical water. Materials 3:3794–3817
67. He Z, Zhu H, Zhou P (2012) Microwave-assisted aqueous synthesis of highly luminescent carboxymethyl chitosan-coated CdTe/CdS QDs as fluorescent probe for live cell imaging. J Fluoresc 22(1):193–199
68. He Y, Sai LM, Lu HT, Hu M, Lai WY, Fan QL et al (2007) Microwave-assisted synthesis of water-dispersed CdTe NCs with high luminescent efficiency and narrow size distribution. Chem Mater 19(3):359–365
69. He Y, Lu HT, Sai LM, Lai WY, Fan QL, Wang LH et al (2006) Microwave-assisted growth and characterization of water-dispersed CdTe/CdS core—shell NCs with high photoluminescence. J Phys Chem B 110(27):13370–13374
70. He R, Qian XF, Yin J, Xi HA, Bian LJ, Zhu ZK (2003) Formation of monodispersed PVP-capped ZnS and CdS NCs under microwave irradiation. Colloids Surf A Physicochem Eng Aspects 220(1):151–157
71. Hirai T, Shiojiri S, Komasawa I (1994) Preparation of metal sulfide composite ultrafine particles in reverse micellar systems and their photocatalytic property. J Chem Eng Jpn 27:590–597
72. Hoa TTQ, Vu LV, Canh TD, Long NN (2009) Preparation of ZnS nanoparticles by hydrothermal method. J Phys Conf Series 187:012081
73. Holmes JD, Bhargava PA, Korgel BA, Johnston KP (1999) Synthesis of cadmium sulfide Q particles in water-in-CO_2 microemulsions. Langmuir 15(20):6613–6615
74. Huang S (2006) The study of optical characteristic of ZnSe nanocrystal. Appl Phys B Lasers Opt 84:323–326
75. Huang J, Xie Y, Li B, Liu Y, Lu J, Qian Y (2001) Ultrasound-induced formation of CdS nanostructures in oil-in-water microemulsions. J Colloid Interface Sci 236:382–384
76. Hullavarad NV, Hullavarad SS (2007) Synthesis and characterization of monodispersed CdS NPs in SiO_2 fibers by sol–gel method. Photon Nanostr-Fundam Appl 5(4):156–163
77. Hutagalung SD, Loo SC (2007) Zinc selenide (ZnSe) nanoparticles prepared by sol-gel method. In: Proceedings of the 7th IEEE International Conference on Nanotechnology, August, vol 2–5, Hong Kong, pp 930–933
78. Hwang CH, Park JP, Song MY, Lee JH, Shim IW (2011) Syntheses of CdTe QDs and NPs through simple sonochemical method under multibubble sonoluminescence conditions. Bull Korean Chem Soc 32(7):2207–2211
79. Ichimura M, Maeda Y (2015) Conduction type of nonstoichiometric alloy semiconductor CuxZnyS deposited by the photochemical deposition method. Thin Solid Films 594:277–281

80. Ilanchezhiyan P, Mohan KG, Xiao F, Poongothai S, Madhan KA, Siva C et al (2017) Ultrasonic-assisted synthesis of ZnTe nanostructures and their structural, electrochemical and photoelectrical properties. Ultrason Sonochem 39:414–419
81. Iranmanesh P, Saeedni S, Nourzpoor M (2015) Characterization of ZnS nanoparticles synthesized by co-precipitation methodCharacterization of ZnS nanoparticles synthesized by co-precipitation method. Chin Phys B 24(4):046104
82. Jacob JM, Lens PNL, Balakrishnan RM (2016) Microbial synthesis of chalcogenide semiconductor nanoparticles: a review. Microbial Biotechnol 9(1):11–21
83. Jadhav AP, Kim CW, Cha HG, Pawar AU, Jadhav NA, Pal U et al (2009) Effect of different surfactants on the size control and optical properties of Y_2O_3:Eu^{3+} nanoparticles prepared by co-precipitation methods. J Phys Chem C 113(31):13600–13604
84. Jemal K, Sandeep BV, Pola S (2017) Synthesis, characterization, and evaluation of the antibacterial activity of allophylus serratus leaf and leaf derived callus extracts mediated silver NPs. J Nanomater 2017:4213275
85. Jiang L, Yang M, Zhu S, Pang G, Feng S (2008) Phase evolution and morphology control of ZnS in a solvothermal system with a single precursor. J Phys Chem C 112:15281
86. Julián B, Planelles J, Cordoncillo E, Escribano P, Sanchez C, Aschehoug P et al (2007) Gel elaboration and optical features of Eu3+-doped CdS nanocrystals in SiO_2. Mater Sci Forum 555:389–393
87. Kamalov VF, Little R, Logunov SL, El-Sayed MA (1996) Picosecond electronic relaxation in CdS/HgS/CdS quantum dot quantum well semiconductor nanoparticles. J Phys Chem 100:6381–6384
88. Kanatzia A, Papageorgiou CH, Lioutas CH, Kyratsi TH (2013) Design of ball-milling experiments on Bi2Te3 thermoelectric material. J Electron Mater 42(7):1652–1660
89. Kang B, Chang SQ, Dai YD, Chen D (2008a) Synthesis of green CdSe/chitosan QDs using a polymer-assisted c-radiation route. Rad Phys Chem 77(7):859–863
90. Kang SH, Bozhilov KN, Myung NV, Mulchandani A, Chen W (2008b) Microbial synthesis of CdS NCs in genetically engineered *E. coli*. Angew Chem Int Ed 47(28):5186–5189. https://doi.org/10.1002/anie.200705806
[Crossref]
91. Karimi JA, Mohsenzadeh S (2012) Phytosynthesis of cadmium oxide NPs from Achillea wilhelmsii flowers. J Chem 2013:147613
92. Karkas MD, Porco JA Jr, Stephenson CRJ (2016) Photochemical approaches to complex chemotypes: applications in natural product synthesis. Chem Rev 116(17):9683–9747
93. Kashinath L, Namratha K, Srikantaswamy S, Vinu A, Byrappa K (2017) Microwave treated sol–gel synthesis and characterization of hybrid ZnS–RGO composites for efficient photodegradation of dyes. New J Chem 41:1723–1735

94. Khafajeh R, Molaei M, Karimipour M (2017) Synthesis of ZnSe and ZnSe:Cu quantum dots by a room temperature photochemical (UV-assisted) approach using Na_2SeO_3 as Se source and investigating optical properties. Luminescence 32(4):581–587
95. Kharissova OV, Kharisov BI, González CMO, Méndez YP, López I (2019) Greener synthesis of chemical compounds and materials. R Soc Open Sci 6:191378
96. Khiew PS, Huang NM, Radiman S, Ahmad MS (2004) Synthesis and characterization of conducting polyaniline-coated cadmium sulphide nanocomposites in reverse microemulsion. Mater Lett 58(3):516–521
97. Koch CC (1997) Synthesis of nanostructured materials by mechanical milling: problems and opportunities. Nanostruct Mater 9:13–22
98. Koch CC (1991) Mechanical milling and alloying. In: Cahn RW, Haasen P, Kramer EJ (eds) Materials science and technology, vol 15. VCH Verlagsgesellschaft GmbH, Weinheim, pp 193–245
99. Komarneni S, Sakka S, Phule PP, Laine RM (eds) (1998) Sol-gel synthesis and Processisng, Ceramic transactions, vol 95. Wiley, New York
100. Korotcenkov G (2020) Handbook of humidity measurement: methods, materials and technologies, Sensing Materials and Technologies, vol 3. CRC Press, Boca Raton
101. Korotcenkov G (ed) (2010) Chemical sensors: fundamentals of sensing materials. Vol. 1: General approaches. Momentum Press, New York
102. Kowshik M, Deshmukh N, Vogel W, Urban J, Kulkarni SK, Paknikar KM (2002) Microbial synthesis of semiconductor CdS NPs, their characterization, and their use in the fabrication of an ideal diode. Biotechnol Bioeng 78(5):583–588
103. Kristl M, Ban I, Gyergyek S (2013) Preparation of nanosized copper and cadmium chalcogenides by mechanochemical synthesis. Mater Manufact Proces 28(9):1009–1013
104. Kristl M, Ban I, Danč A, Danč V, Drofenik M (2010) A sonochemical method for the preparation of cadmium sulfide and cadmium selenide NPs in aqueous solutions. Ultrason Sonochem 17(5):916–922
105. Kumar SA, Ansary AA, Ahmad A, Khan MI (2007) Extracellular biosynthesis of CdSe QDs by the fungus, Fusarium oxysporum. J Biomed Nanotechnol 3(2):190–194
106. Kumaresan R, Ichimura M, Arai E (2002) Photochemical deposition of ZnSe polycrystalline thin films and their characterization. Thin Solid Films 414:25–30
107. Lagashettya A, Havanoor V, Basavaraja S, Balaji SD, Venkataraman A (2007) Microwave-assisted route for synthesis of nanosized metal oxides. Sci Technol Adv Mater 8:484–493
108. Lamer VK, Dinegar RH (1950) Theory, production and mechanism of formation of monodispersed hydrosols. J Am Chem Soc 72:4847–4854

109. Li J, Wu Q, Wu J (2016) Synthesis of nanoparticles via solvothermal and hydrothermal methods. In: Aliofkhazraei M (ed) Handbook of nanoparticles. Springer, New York, pp 295–328
110. Li H, Wang C, Peng Z, Fu X (2015) A review on the synthesis methods of CdSeS-based nanostructures. J Nanomater 2015:519385
111. Li D, Wang S, Wang J, Zhang X, Liu S (2013) Synthesis of CdTe/TiO2 nanoparticles and their photocatalytic activity. Mater Res Bull 48(10):4283–4286
112. Li H, Qu F (2007) Synthesis of CdTe quantum dots in sol-gel-derived composite silica spheres coated with calix[4]arene as luminescent probes for pesticides. Chem Mater 19:4148–4154
113. Li X-H, Li J-X, Li G-D, Liu D-P, Chen J-S (2007) Controlled synthesis, growth mechanism, and properties of monodisperse CdS colloidal spheres. Eur J Chem A 13:8754–8761
114. Li Z, Hou B, Xu Y, Wu D, Sun Y, Hu W et al (2005) Comparative study of sol–gel-hydrothermal and sol–gel synthesis of titania–silica composite nanoparticles. J Solid State Chem 178(5):1395–1405
115. Li C, Murase N (2004) Synthesis of highly luminescent glasses incorporating CdTe NCs through Sol–Gel processing. Langmuir 20(1):1–4
116. Li Z, Zhang J, Du J, Mu T, Liu Z, Chen J et al (2004) Preparation of cadmium sulfide/poly (methyl methacrylate) composites by precipitation with compressed CO_2. J Appl Polym Sci 94(4):1643–1648
117. Li Y, Ding Y, Wang Z (1999) A novel chemical route to ZnTe semiconductor nanorods. Adv Mater 11:847–850
118. Li G, Nogami M (1994) Preparation and optical properties of solgel derived ZnSe crystallites doped in glass films. J Appl Phys 75:4276
119. Liao X-H, Zhu J-J, Chen H-J (2001) Microwave synthesis of nanocrystalline metal sulfides in formaldehyde solution. Mater Sci Eng B 85:85–91
120. Lifshitz E, Dag I, Litvin I, Hodes G, Gorer S, Reisfeld R et al (1998) Optical properties of CdSe nanoparticle films prepared by chemical deposition and sol–gel methods. Chem Phys Lett 288:188–196
121. Liu M, Zhao H, Chen S, Wang H, Quan X (2012) Photochemical synthesis of highly fluorescent CdTe quantum dots for “on–off–on” detection of Cu(II) ions. Inorg Chim Acta 392:236–240
122. Lee HL, Issam AM, Belmahi M, Assouar MB, Rinnert H, Alnot M (2009) Synthesis and characterizations of bare CdS nanocrystals using chemical precipitation method for photoluminescence application. J Nanomater 2009:914501
123. Liu J, Xue D (2010) Morphology-controlled synthesis of CdSe semiconductor through a low-temperature hydrothermal method. Phys Scr T139:014075

124. Liu P, Wang Q, Li X (2009) Studies on CdSe/L-cysteine quantum dots synthesized in aqueous solution for biological labelling. J Phys Chem C 113:7670–7676
125. Loudhaief N, Labiadh H, Hannachi E, Zouaoui M, Ben SM (2018) Synthesis of CdS nanoparticles by hydrothermal method and their effects on the electrical properties of bi-based superconductors. J Superconduct Novel Magnet 31:2305–2312
126. Majid A, Bibi M (2018) Cadmium based II-VI semiconducting nanomaterials. Springer Nature, Cham
127. Majid A, Arshad H, Murtaza S (2015) Synthesis and characterization of Cr doped CdSe NPs. Superlatt Microstr 85:620–623
128. Mal J, Nancharaiah YV, van Hullebusch ED, Lens PNL (2016) Metal chalcogenide quantum dots: biotechnological synthesis and applications. RSC Adv 6:41477–41495
129. Malik MA, Wani MY, Hashim MA (2012) Microemulsion method: a novel route to synthesize organic and inorganic nanomaterials: 1st nano update. Arab J Chem 5(4):397–417
130. Mao Y, Park T-J, Zhang F, Zhou H, Wong SS (2007) Environmentally friendly methodologies of nanostructure synthesis. Small 3(7):1122–1139
131. Menezes FD, Galembeck A, Junior SA (2011) New methodology for obtaining CdTe QDs by using ultrasound. Ultrason Sonochem 18(5):1008–1011
132. Meng L-Y, Wang B, Ma M-G, Lin K-L (2016) The progress of microwave-assisted hydrothermal method in the synthesis of functional nanomaterials. Mater Today Chem 1–2:63–83
133. Mittal AK, Kaler A, Banerjee UC (2012) Free radical scavenging and antioxidant activity of silver NPs synthesized from flower extract of rhododendron dauricum. Nano Biomed Eng 4(3):118–124
134. Mirzaei A, Neri G (2016) Microwave-assisted synthesis of metal oxide nanostructures for gas sensing application. A review Sens Actuators B 237:749–775
135. Mo X, Wang CY, You M, Zhu YR, Chen ZY, Hu Y (2001) A novel ultraviolet-irradiation route to CdS nanocrystallites with different morphologies. Mater Res Bull 36:2277–2282
136. Modeshia DR, Walton RI (2010) Solvothermal synthesis of perovskites and pyrochlores: crystallization of functional oxides under mild conditions. Chem Soc Rev 39:4303–4325
137. Moon J-W, Ivanov IN, Duty CE, Love LJ, Rondinone AJ, Wang W et al (2013) Scalable economic extracellular synthesis of CdS nanostructured particles by a non-pathogenic thermophile. J Industr Microbiol Biotechnol 40:1263–1271
138. Motshekga SC, Pillai SK, Ray SS, Jalama K, Krause RWM (2012) Recent trends in the microwave-assisted synthesis of metal oxide nanoparticles supported on carbon nanotubes and their applications. J Nanomater 2:1–12

139. Mntungwa N, Puilabhotla VSR, Revaprasadu N (2012) The synthesis of core-shell metal-semiconductor nanomaterials. Mater Lett 81:108–111
140. Munirah KMS, Aziz A, Rahman SA, Khan ZR (2013) Spectroscopic studies of sol–gel grown CdS nanocrystalline thin films for optoelectronic devices. Mater Sci Semicond Proc 16:1894–1898
141. Murray CB, Norris DJ, Bawendi MG (1993) Synthesis and characterization of nearly monodisperse CdE (E = sulfur, selenium, tellurium) semiconductor nanocrystallites. J Am Chem Soc 115:8706–8715
142. Muruganandam S, Anbalagan G, Murugadoss G (2017) Structural, electrochemical and magnetic properties of codoped (Cu, Mn) CdS NPs with surfactant PVP. Opt-Intern J Light Electron Opt 131:826–837
143. Niederberger M (2007) Nonaqueous sol-gel routes to metal oxide nanoparticles. Acc Chem Res 40:793–800
144. Nishimura H, Lin Y, Hizume M, Taniguchi T, Shigekawa N, Takagi T et al (2019) Hydrothermal synthesis of ZnSe:Mn quantum dots and their optical properties. AIP Adv 9:025223
145. Nogami M, Nagasaka K, Suzuki T (1992) Sol-gel synthesis of cadmium telluride-microcrystal-doped silica glasses. J Am Ceram Soc 75(1):220–223
146. Nogi K, Hosokawa M, Naito M, Yokoyama T (eds) (2012) Nanoparticle technology handbook. Elsevier, Oxford
147. Omran BA, Whitehead KA, Baek K-H (2021) One-pot bioinspired synthesis of fluorescent metal chalcogenide and carbon quantum dots: applications and potential biotoxicity. Colloid Surf Biointerfaces 200:111578
148. Onwudiwe DC, Krüger TP, Oluwatobi OS, Strydom CA (2014) Nanosecond laser irradiation synthesis of CdS NPs in a PVA system. Appl Surf Sci 290:18–26
149. Ouyang JY, Vincent M, Kingston D, Descours P, Boivineau T, Zaman B et al (2009) Noninjection, onepot synthesis of photoluminescent colloidal homogeneously alloyed CdSeS quantum dots. J Phys Chem C 113(13):5193–5200
150. Qian H, Li L, Ren J (2005) One-step and rapid synthesis of high quality alloyed QDs (CdSe–CdS) in aqueous phase by microwave irradiation with controllable temperature. Mater Res Bull 40(10):1726–1736
151. Panda AB, Glaspell G, El-Shall MS (2006) Microwave synthesis of highly aligned ultra-narrow semiconductor rods and wires. J Am Chem Soc 128:2790–2791
152. Pandian SRK, Deepak V, Kalishwaralal K, Gurunathan S (2011) Biologically synthesized fluorescent CdS NPs encapsulated by PHB. Enzym Microb Technol 48(4):319–325
153. Park J, Joo J, Kwon SG, Jang Y, Hyeon T (2007) Synthesis of monodisperse spherical nanocrystals. Angew Chem Intern Ed 46:4630–4660

154. Peng X, Sclamp MC, Kadavanich AV, Alivisatos AP, Epitaxial AP (1997) Growth of highly luminescent CdSe/CdS core/shell nanocrystals with photostability and electronic accessibility. J Am Chem Soc 119:7019–7029
155. Phuruangrat A, Thongtem T, Sinaim H, Thongtem S (2013) Synthesis of cadmium selenide nanorods by polyethylene glycol-assisted solvothermal process. J Experimen Nanosci 8(6):654–660
156. Plaza DO, Gallardo C, Straub YD, Bravo D, Pérez-Donoso JM (2016) Biological synthesis of fluorescent NPs by cadmium and tellurite resistant Antarctic bacteria: exploring novel natural nanofactories. Microb Cell Factor 15(1):76
157. Rabinal MHK, Gunnagol RM, Hodlur RM (2016) Recent developments in the green syntheses of chalcogenide based semi-conductor nanoparticles. Curr Nanomater 1:12–60
158. Raj FM, Rajendran AJ (2015) Synthesis and characterization of cadmium sulfide NPs for the applications of dye sensitized solar cell. Intern J Innov Res Sci Eng Technol 4(1):56–60
159. Rao BS, Kumar BR, Reddy VR, Rao TS, Chalapathi GV (2011) Preparation and characterization of CdS NPs by chemical co-precipitation technique. Chalcogenide Lett 8(3):177–185
160. Rathinama I, Parvathi AA, Pandiarajan J, Jeyakumaran N, Prithivikumaran N (2013) Influence of annealing temperature on structural and optical properties of CdS thin films prepared by sol-gel spin coating method. In: Proceedings of the “International Conference on Advanced Nanomaterials & Emerging Engineering Technologies” (ICANMEET-20J3), Chennai, India, 24–26 July, 2013, pp 713–717
161. Reddy CV, Vattikuti SP, Shim J (2016) Synthesis, structural and optical properties of CdS NPs with enhanced photocatalytic activities by photodegradation of organic dye molecules. J Mater Sci Mater Electron 27(8):7799–7808
162. Roberts BA, Strauss CR (2005) Toward rapid “green” predictable microwave-assisted synthesis. Acc Chem Res 38:653–661
163. Salavati-Niasari M, Bazarganipour M, Ghasemi-Kooch M (2015) Facile sonochemical synthesis and characterization of CdTe NPs. Synth React Inorg Metal-Org Nano-Metal Chem 45(10):1558–1564
164. Sangsefidi FS, Salavati-Niasari M, Esmaeili-Zare M (2013) Hydrothermal method for synthesis of HgTe nanorods in presence of a novel precursor. Supperlatt Microstructur 62:1–11
165. Saraji, M., Dizajib, H. R., Fallaha, M. (2012). An efficient method for synthesis and characterization of CdS and CdS:Cu NPs by microwave irradiation. In: Proceedings of the 4th international conference on nanostructures, pp. 1495–1497
166. Saravanan L, Pandurangan A, Jayavel R (2012) Synthesis and luminescence enhancement of cerium doped CdS NPs. Mater Lett 66(1):343–345
167. Saravanan P, Gopalan R, Chandrasekaran V (2008) Synthesis and characterisation of nanomaterials. Defence Sci J 58(4):504–516

168. Schanche JS (2003) Microwave synthesis solutions from personal chemistry. Mol Divers 7:293–300
169. Schneider R, Balan L (2012) Hydrothermal routes for the synthesis of CdSe Core quantum dots. In: Al-Ahmadi A (ed) Nanotechnology and nanomaterials: state of the art of quantum dot systems fabrications. Intech, pp 119–140
170. Schwartz RW, Schneller T, Waser R (2004) Chemical solution deposition of electronic oxide films. C R Chim 7:433–461
171. Serrano T, Gómez I, Colás R, Cavazos J (2009) Synthesis of CdS NCs stabilized with sodium citrate. Colloids Surf A: Physicochem Eng Aspects 338(1):20–24
172. Shafiee S, Akhavan O, Hatami H, Hoseinkhani P (2015) Sol-gel synthesis of thermoluminescent Cd-doped ZnTe nanoparticles. Indian J Pure Appl Phys 53:804–807
173. Shah M, Fawcett D, Sharma S, Tripathy SK, Poinern GEJ (2015) Green synthesis of metallic NPs via biological entities. Materials 8(11):7278–7308
174. Sharma K, Kumar A (2014) Synthesis and characterization of pure and Zn doped CdSe NPs by ultrasonication technique. Am Intern J Res Sci Technol Eng Math 8:75–79
175. Shao M, Xu F, Peng Y, Wu J, Li Q, Zhang S et al (2002) Microwave-templated synthesis of CdS NTs in aqueous solution at room temperature. New J Chem 26(10):1440–1442
176. Sheldrick WS, Wachhold M (1997) Solventothermal synthesis of solid-state chalcogenidometalates. Angew Chem Int Ed Engl 36:206–224
177. Shen L, Bao N, Prevelige PE, Gupta A (2010) *Escherichia coli* bacteria-templated synthesis of nanoporous cadmium sulfide hollow microrods for efficient photocatalytic hydrogen production. J Phys Chem C 114(6):2551–2559
178. Shkir M, Aarya S, Singh R, Arora M, Bhagavannarayana G, Senguttuvan TD (2012) Synthesis of ZnTe nanoparticles by microwave irradiation technique, and their characterization. Nanosci Nanotechnol Lett 4:405–408
179. Singh P, Kim YJ, Wang C, Mathiyalagan R, El-Agamy Farh M, Yang DC (2016) Biogenic silver and gold NPs synthesized using red ginseng root extract, and their applications. Artif Cells Nanomed Biotechnol 44(3):811–816
180. Singh P, Kim YJ, Zhang D, Yang DC (2016) Biological synthesis of NPs from plants and microorganisms. Trends Biotechnol 34(7):588–599
181. Singh BR, Dwivedi S, Al-Khedhairy AA, Musarrat J (2011) Synthesis of stable cadmium sulfide NPs using surfactin produced by *Bacillus amyloliquefaciens* strain KSU-109. Colloids Surf B: Biointerfaces 85(2):207–213
182. Skubi KL, Blum TR, Yoon TP (2016) Dual catalysis strategies in photochemical synthesis. Chem Rev 116(17):10035–10074

183. Sofronov DS, Sofronova EM, Starikov VV, Baumer VN, Matejchenko PV, Galkin SN et al (2013) Microwave synthesis of ZnSe. J Mater Eng Perform 22:1637–1641
184. Solans C, Izquierdo P, Nolla J, Azemar N, Garcia-Celma MJ (2005) Nanoemulsions. Curr Opin Colloid Interface Sci 10:102–110
185. Song J, Dai Z, Guo W, Li Y, Wang W, Li N et al (2013) Preparation of CdTe/CdS/SiO_2 core/multishell structured composite NPs. J Nanosci Nanotechnol 13(10):6924–6927
186. Sonker RK, Yadav BC, Gupta V, Tomar M (2020) Synthesis of CdS nanoparticle by sol-gel method as low temperature NO_2 sensor. Mater Chem Phys 239:121975
187. Sostaric JZ, Caruso-Hobson RA, Mulvaney P, Grieser F (1997) Ultrasound-induced formation and dissolution of colloidal CdS. J Chem Soc Faraday Trans 93(9):1791–1795
188. Starnic V, Etsell TH, Pierre AC, Mikula RJ (1997) Sol-gel processing of ZnS. Mater Lett 31:35–38
189. Suriwong T, Phuruangrat A, Thongtem S, Thongtem T (2015) Synthesis, characterization and photoluminescence properties of CdTe nanocrystals. J Ovonic Res 11(6):257–261
190. Suslick KS, Fang MM, Hyeon T, Mdleleni MM (1999) Applications of sonochemistry to materials synthesis. In: Crum LA, Mason TJ, Reisse JL, Suslick KS (eds) Sonochemistry and Sonoluminescence. Springer, Netherlands, pp 291–320
191. Sweeney RY, Mao C, Gao X, Burt JL, Belcher AM, Georgiou G et al (2004) Bacterial biosynthesis of cadmium sulfide NCs. Chem Biol 11(11):1553–1559
192. Tan GL, Yu XF (2009) Capping the ball-milled CdSe nanocrystals for light excitation. J Phys Chem C 113(20):8724–8729
193. Tan GL, Zhang L, Yu XF (2009) Preparation and optical properties of CdS NCs prepared by a mechanical alloying process. J Phys Chem C 114(1):290–293
194. Tan GL, Hömmerich U, Temple D, Wu NQ, Zheng JG, Loutts G (2003) Synthesis and optical characterization of CdTe NCs prepared by ball milling process. Scripta Mater 48(10):1469–1474
195. Taurino AM, Epifani M, Taccoli T, Iannotta S, Siciliano P (2003) Innovative aspects in thin film technologies for nanostructured materials in gas sensor devices. Thin Solid Films 436:52–63
196. Tho NTM, An TNM, Tri MD, Sreekanth TVM, Lee JS, Nagajyothi PC et al (2013) Green synthesis of silver NPs using Nelumbo nucifera seed extract and its antibacterial activity. Acta Chim Slovenica 60(3):673–678
197. Tolia JV, Chakraborty M, Murthy ZVP (2012) Mechanochemical synthesis and characterization of group II-VI semiconductor NPs. Partic Sci Technol 30(6):533–542
198. Tsuzuki T, McCormick PG (1997) Synthesis of CdS QDs by mechanochemical reaction. Appl Phys A: Mater Sci Proces 65(6):607–609

199. Ulloa G, Collao B, Araneda M, Escobar B, Álvarez S, Bravo D et al (2016) Use of acidophilic bacteria of the genus Acidithiobacillus to biosynthesize CdS fluorescent nanoparticles (quantum dots) with high tolerance to acidic pH. Enzyme Microbiol Technol 95:217–224
200. Vaquero F, Navarro RM, Fierro JLG (2017) Influence of the solvent on the structure, morphology and performance for H2 evolution of CdS photocatalysts prepared by solvothermal method. Appl Catal B Environ 203:753–767
201. Venci X, Gerge A, Raj AD, Irudayaraj AA, Raj DMA, Jayakumar G, Sundaram SJ (2021) Tuning the morphology and band gap of CdSe nanoparticles via solvothermal method. Mater Today 36(2):459–463
202. Veeranarayanan S, Poulose AC, Mohamed MS, Nagaoka Y, Iwai S, Nakagame Y et al (2012) Synthesis and application of luminescent single CdS quantum dot encapsulated silica NPs directed for precision optical bioimaging. Intern J Nanomed 7:3769
203. Wan B, Hu C, Feng B, Xu J, Zhang Y, Tian Y (2010) Optical properties of ZnTe nanorods synthesized via a facile low-temperature solvothermal route. Mater Sci Eng B 171:11–15
204. Wang J, Liu S, Mu Y, Liu L, Runa A, Su P et al (2017) Synthesis of uniform cadmium sulphide thin film by the homogeneous precipitation method on cadmium telluride nanorods and its application in three-dimensional heterojunction flexible solar cells. J Colloid Interface Sci 505:59–66
205. Wang Q, Li J, Bai Y, Lian J, Huang H, Li Z et al (2014) Photochemical preparation of Cd/CdS photocatalysts and their efficient photocatalytic hydrogen production under visible light irradiation. Green Chem 16(5):2728–2735
206. Wang Q, Pan D, Jiang S, Ji X, An L, Jiang B (2006) A solvothermal route to size- and shape-controlled CdSe and CdTe nanocrystals. J Crystal Growth 286:83–90
207. Wang GZ, Chen W, Liang CH, Wang YW, Meng GW, Zhang LD (2001) Preparation and characterization of CdS nanoparticles by ultrasonic irradiation. Inorg Chem Commun 4(4):208–210
208. Wang H, Zhang J-R, Zhu J-J (2001b) A microwave assisted heating method for the rapid synthesis of sphalrite-type mercury sulfide nanocrystals with different sizes. J Cryst Growth 233:829–836
209. Wang CY, Mo X, Zhou Y, Zhu YR, Liu HT, Chen ZY (2000) A convenient ultraviolet irradiation technique for in situ synthesis of CdS nanocrystallites at room temperature. J Mater Chem 10:607–608
210. Whiffen RK, Montone A, Pietrelli L, Pilloni L (2021) On tailoring co-precipitation synthesis to maximize production yield of nanocrystalline wurtzite ZnS. Nano 11:715
211. Yadav S, Yashas SR, Shivaraju HP (2021) Transitional metal chalcogenide nanostructures for remediation and energy: a review. Environ Chem Lett 19:683–3700
212. Yan YL, Li Y, Qian XF, Yin J, Zhu ZK (2003) Preparation and characterization of CdSe NCs via Na_2SO_3-assisted photochemical route. Mater Sci Eng B 103(2):202–206

213. Yang G, Park S-J (2019) Conventional and microwave hydrothermal synthesis and application of functional materials: a review. Materials 12:1177
214. Yang Y, Gao MY (2005) Preparation of fluorescent SiO_2 particles with single CdTe nanocrystal cores by the reverse microemulsion method. Adv Mater 17(19):2354–2357
215. Yang H, McCormick PG (1998) Mechanically activated reduction of nickel oxide with graphite. Metall Mater Trans B Process Metall Mater Process Sci 29:449–455
216. Yu S-H (2001) Hydrothermal/solvothermal processing of advanced ceramic materials. J Ceram Soc Jpn 109(5):S65–S75
217. Yu SH, Wu YS, Yang J, Han ZH, Xie Y, Qian YT, Liu XM (1998) A novel solventothermal synthetic route to nanocrystalline CdE (E = S, Se, Te) and morphological control. Chem Mater 10:2309–2312
218. Yu SH, Shu L, Wu YS, Tang KB, Xie Y, Qian YT, Zhang YH (1998) Benzene-thermal synthesis and optical properties of CdS nanocrystalline. Nanostruct Mater 10:1307–1316
219. Xi LF, Lam YM (2007) Synthesis and characterization of CdSe NRs using a novel microemulsion method at moderate temperature. J Colloid Interface Sci 316(2):771–778
220. Xiong C, Liu M, Zhu X, Tang A (2019) A general one-pot approach to synthesize binary and ternary metal sulfide nanocrystals. Nanoscale Res Lett 14:19
221. Xu H, Zeiger BW, Suslick KS (2013) Sonochemical synthesis of nanomaterials. Chem Soc Rev 42(7):2555–2567
222. Zelner M, Minti H, Reisfeld R, Cohen H, Feldman Y, Cohen SR, Tenne R (2001) Preparation and characterization of CdTe nanoparticles in zirconia films prepared by the sol gel method. J Sol-Gel Sci Technol 20:153–160
223. Zhan HJ, Zhou PJ, Ma R, Liu XJ, He YN, Zhou CY (2014) Enhanced oxidation stability of quasi core-shell alloyed CdSeS QDs prepared through aqueous microwave synthesis technique. J Fluoresc 24(1):57–65
224. Zhang R, Li G, Zhang Y (2017) Photochemical synthesis of CdS-MIL-125 (Ti) with enhanced visible light photocatalytic performance for the selective oxidation of benzyl alcohol to benzaldehyde. Photochem Photobiol Sci 16(6):996–1002
225. Zhang YC, Wang GY, Hu XY, Shi QF, Qiao T, Yang Y (2005) Phase-controlled synthesis of ZnS nanocrystallites by mild solvothermal decomposition of an air-stable single-source molecular precursor. J Crystal Growth 284:554–560
226. Zhang Q, Huang F, Li Y (2005) Cadmium sulfide NRs formed in microemulsions. Colloids Surf A Physicochem Eng Asp 257:497–501
227. Zhang Y, Li Y (2004) Synthesis and characterization of monodisperse doped ZnS nanospheres with enhanced thermal stability. J Phys Chem B 108:17805

228. Zhang H, Wang L, Xiong H, Hu L, Yang B, Li W (2003) Hydrothermal synthesis for high-quality CdTe nanocrystals. Adv Mater 15:1712
229. Zhao WB, Zhu JJ, Chen HY (2003) Photochemical preparation of rectangular PbSe and CdSe NPs. J Crystal Growth 252(4):587–592
230. Zhong B, Kang W, Zhang Z, Zhang L, Ma B (2020) Facile one-pot solvothermal synthesis of CdTe nanorods and their photoelectrical properties. CrystEngComm 22:3927–3393
231. Zhong WH (2012) Nanoscience and nanomaterials: synthesis, Manufacturing and Industry Impacts. DEStech Publications, Inc, Lancaster
232. Zhong H, Mirkovic T, Scholes GD (2011) Nanocrystal synthesis. In: Andrews DL, Scholes GD, Wiederrecht GP (eds) Comprehensive nanoscience and technology, vol 5. Elsevier, New York, pp 153–201
233. Zhou GJ, Li SH, Zhang YC, Fu YZ (2014) Biosynthesis of CdS NPs in banana peel extract. J Nanosci Nanotechnol 14(6):4437–4442
234. Zhou SM, Feng YS, Zhang LD (2003) Sonochemical synthesis of large-scale single crystal CdS NRs. Mater Lett 57(19):2936–2939
235. Zhu J-J, Wang H (2004) Synthesis of metal chalcogenide nanoparticles synthesis of metal chalcogenide nanoparticles. In: Nalwa HS (ed) Encyclopedia of nanoscience and nanotechnology, vol 10. American Scientific Publishers, pp 347–367
236. Zhu J, Liao X, Zhao X, Wang J (2001) Photochemical synthesis and characterization of CdSe NPs. Mater Lett 47(6):339–343
237. Zhu J, Koltypin Y, Gedanken A (2000) General sonochemical method for the preparation of nanophasic selenides: synthesis of ZnSe nanoparticles. Chem Mater 12:73–78
238. Zhu J, Liu S, Palchik O, Koltypin Y, Gedanken A (2000) A novel sonochemical method for the preparation of nanophasic sulfides: synthesis of HgS and PbS nanoparticles. J Solid State Chem 153:342–350
239. Zhu J, Palchik O, Chen S, Gedanken A (2000) Microwave assisted preparation of CdSe, PbSe, and $Cu_{2-x}Se$ NPs. J Phys Chem B 104(31):7344–7347
240. Ziegler J, Merkulov A, Grabolle M, Resch-Genger U, Nann T (2007) High-quality ZnS shells for CdSe nanoparticles: rapid microwave synthesis. Langmuir 23:7751–7759
241. Zou Y, Li DS, Yang D (2010) Noninjection synthesis of CdS and alloyed CdS_xSe_{1-x} nanocrystals without nucleation initiators. Nanoscale Res Lett 5(6):966–971
242. Zuala L, Agarwal P (2020) Growth and characterization of ZnSe nanocrystals synthesized using solvothermal process. J Mater Sci Mater Electron 31:14756–14766

OceanofPDF.com

© The Author(s), under exclusive license to Springer Nature Switzerland AG 2023
G. Korotcenkov (ed.), *Handbook of II-VI Semiconductor-Based Sensors and Radiation Detectors*
https://doi.org/10.1007/978-3-031-19531-0_12

12. II–VI Semiconductor-Based Nanomaterials

Yuliana Lukan[1, 2], Andrii Hotynchan[2], Yuliia Andriichuk[2], Sergii Vojtovych[3], Yulia Seti[2] and Yuriy Khalavka[2] ✉
(1) Bukovinian State Medical University, Chernivtsi, Ukraine
(2) Yuriy Fedkovych Chernivtsi National University, Chernivtsi, Ukraine
(3) Ivano-Frankivsk National Medical University, Galytska Str. 2, Ivano-Frankivsk, Ukraine

✉ **Yuriy Khalavka**
Email: y.khalavka@chnu.edu.ua

Keywords Nanomaterials – Core-shell nanoparticles – Hollow nanostructures – Nanoparticles – Nanosheets – Nanowires – Nanobelts – Quantum dot – Synthesis – PVD – Solvothermal synthesis – Ion exchange – Semiconductors – Selenide – Sulfides – Telluride – Catalysis – Colloidal stability – Closed heterostructures – Photosensors – Photoelectrochemistry – Open heterostructures – Zone diagram

12.1 Introduction

Nanometer-sized binary chalcogenides representing groups II–VI of the periodic table of elements, namely, ZnO, CdS, ZnS, HgS, ZnSe, CdSe, PbSe, CdTe, HgTe, and their alloys, attract considerable attention due to their unique quantum-dimensional properties [4, 28, 34]. Among these compounds, Cd compounds are the most intensively studied due to the possibility of their use in optoelectronics and biosensors and as an alternative to widely used organic dyes due to high photostability and

resistance to photobleaching. Over the past years, a high level of control over morphology was achieved in the chemical synthesis of II–VI semiconductor-based nanomaterials by manipulating the growth kinetics of various crystal phases [16, 49]. The popularity of II–VI nanomaterials can be assessed from Fig. 12.1, where search results from the Scopus database are provided for the different compounds.

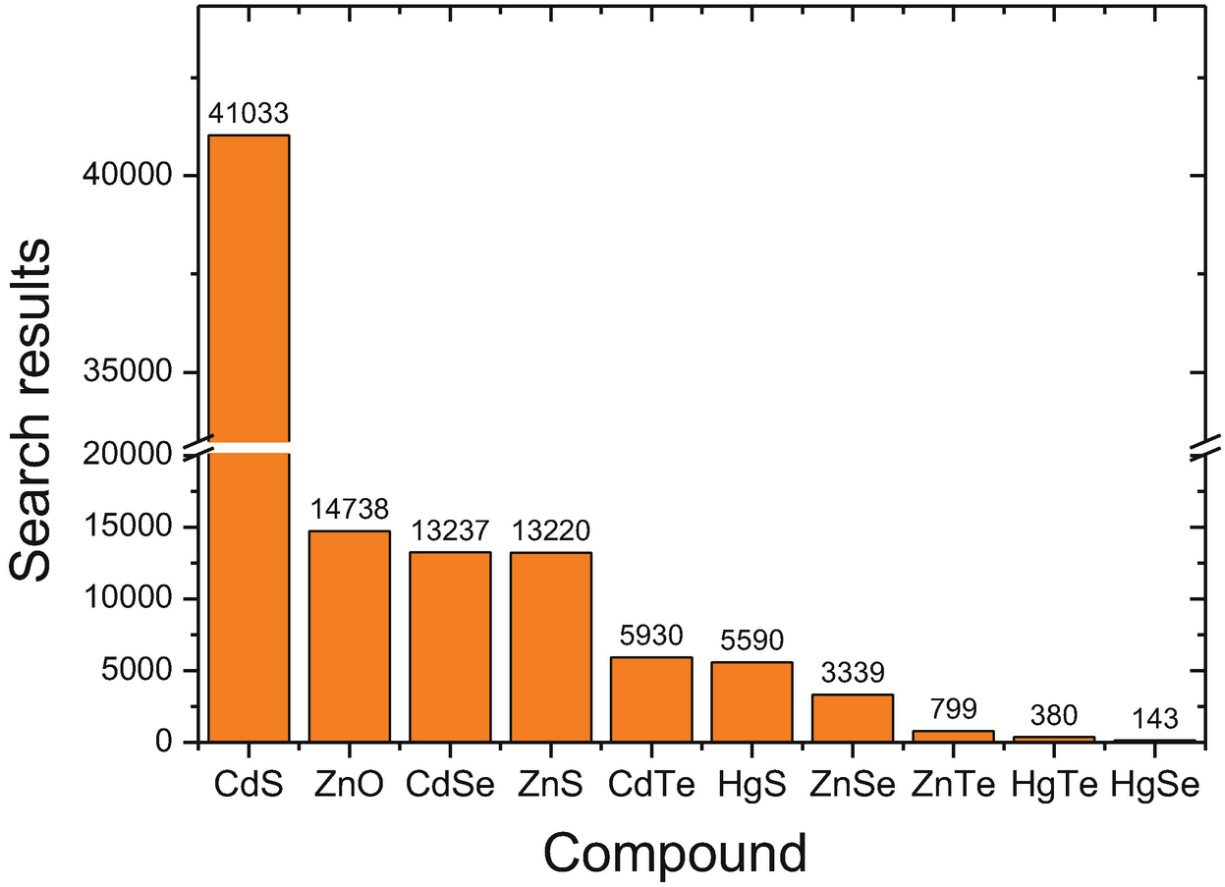

Fig. 12.1 Search results retrieved for the search query “compound” AND “nano*” in the Scopus database (July 2022)

An essential step toward more complex structures was the introduction of branching by switching between two crystal structures within one nanocrystal. Another development is related to the creation of core-shell materials and hollow forms. It is now possible to produce II–VI semiconductor nanostructures of a large variety of different shapes and different chemical compositions: spheres, rods, tetrapods, tripods, stars, and more elaborate forms of particles [24, 36, 69].

12.2 Colloidal Nanoparticles

There are two basic approaches to the synthesis of nanoparticles: “top-down,” mechanical or other fragmentation of larger particles (dispersion method); and “bottom-up” assembly of individual atoms and molecules, mainly by chemical reactions (condensation method).

The group of top-down or dispersion synthesis methods is based on microcrystalline or bulk material grinding processes. During the grinding, two opposite processes compete: dispersion and aggregation of emerging particles. The rate ratio of these processes depends on the duration of the grinding, temperature, the nature of the liquid phase in which grinding is carried out, the presence of stabilizers, etc. The size distribution of such particles is often quite broad [12, 97]. Mechanical dispersion to obtain nanoparticles has not become widespread due to ball mills’ very high-energy consumption and the poor quality of the obtained crystals.

Condensation methods (“bottom-up”) are divided into physical (deposition of nanoparticles from the gas phase) and chemical (synthesis in colloidal solution). If the deposition from the gas phase occurs with a change in the composition of the substance, it is called chemical (CVD, chemical vapor deposition). If there is no chemical reaction during precipitation, it is called physical (PVD, physical vapor deposition).

Semiconductor nanoparticles are obtained by chemical methods in homogeneous solutions, direct and reverse micelles, in Langmuir-Blodgett films, polymers, glasses, and zeolites [34].

The simplest and most common way to obtain II–VI semiconductor nanoparticles is to synthesize from starting reagents (precursors) in solution by interrupting the reaction at a specific time. Metal sulfide nanoparticles are synthesized by the reaction of a water-soluble metal salt and H_2S or Na_2S in the presence of a suitable stabilizer. For example, CdS nanoparticles can be synthesized by mixing solutions of $Cd(ClO_4)_2$ and Na_2S according to the equation:

$$Cd(ClO_4)_2 + Na_2S = CdS + 2NaClO_4 \tag{12.1}$$

CdS nanoparticles’ growth during the reaction is interrupted by abruptly increasing the pH of the solution or the depletion of reactants. Variety of

colloidal synthetic approaches are discussed in detail in Chaps. 11 and 13 (Vol. 1).

Unfortunately, most colloidal nanoparticle solutions have little stability to aggregation and coagulation. So passivation of the particle surface using macromolecular compounds is often used to prevent coagulation. The second way to stabilize colloidal solutions of nanoparticles is to cover their surface with covalently bound charged molecules like phosphates or thiols [94]. As a result, a stable colloidal solution can be obtained, nanoparticles in powder form can be isolated from it, and then a colloidal solution can be obtained again by dispersing the powder in a solvent. The nanocrystals stabilized in this way can be transferred from the aqueous phase to the organic phase and vice versa by phase transfer.

12.3 Synthesis of 1D Nanostructures

Methods of synthesis of 1D nanoparticles can be divided into two types: synthesis from the gas phase and the solution. A typical method of II–VI semiconductors synthesis from the gas phase includes evaporation of starting materials with subsequent vapors condensation on a suitable substrate containing sprayed nanoparticles of metal (most often gold), providing catalytic and selective actions on nanowires formation [22, 59].

The synthesis is usually carried out in the setup shown in Fig. 12.2, which consists of a horizontal tubular furnace, an alumina tube, a rotary pump system with a gas supply, and a control system. The source material is loaded into a special shuttle and located in the center of the tube, where the temperature is highest. The substrate is placed downstream for collecting growth products. Depending on the starting materials and substrate high-quality control over the final product can be achieved [47, 93].

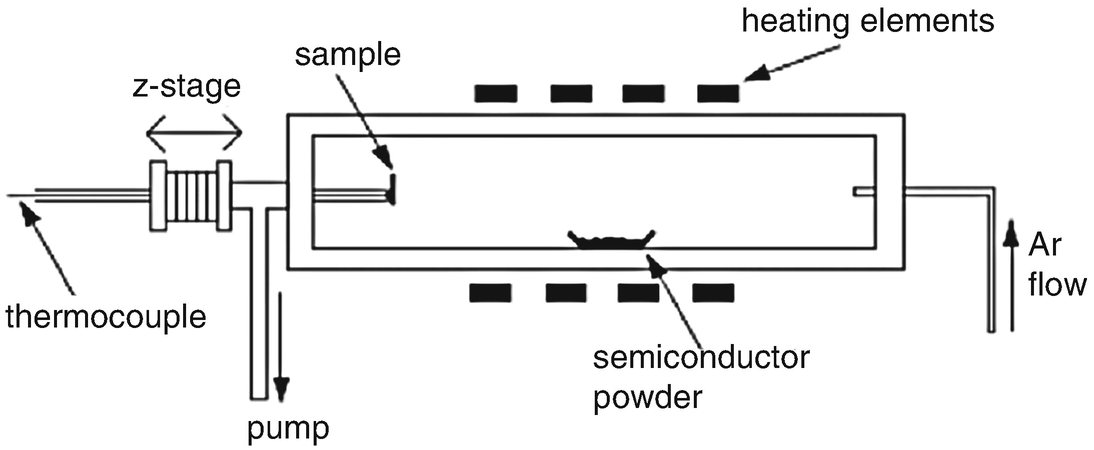

Fig. 12.2 A typical setup for the ZnTe and CdTe nanowires synthesis from the gas phase. (Reprinted with permission from (Fasoli et al., [21]). Copyright 2006: Wiley)

Depending on the type of starting material, the method of synthesis from the gas phase could be classified as physical vapor deposition (PVD), which consists of evaporation of the semiconductor material followed by spraying on the substrate, and chemical vapour deposition method (CVD), which differs from PVD in that during evaporation and condensation, chemical reactions occur to form the desired compound [93].

The 1D nanostructures synthesized by the PVD method are characterized mainly by the formation of a pure crystallographic form and the absence of impurities (Fig. 12.3a). The SEM image of the synthesized ZnS reflects the formation of 1D nanostructures with a diameter of 50–100 nm and a length of several hundred micrometers (Fig. 12.3b, c). The photoluminescence (PL) spectrum of ZnS nanowires is characterized by a photoluminescence peak position of approximately 575 nm (Fig. 12.3d), which is attributed to the following factors: self-activated centers, vacancies, and the presence of elemental sulfur on the ZnS surface [81].

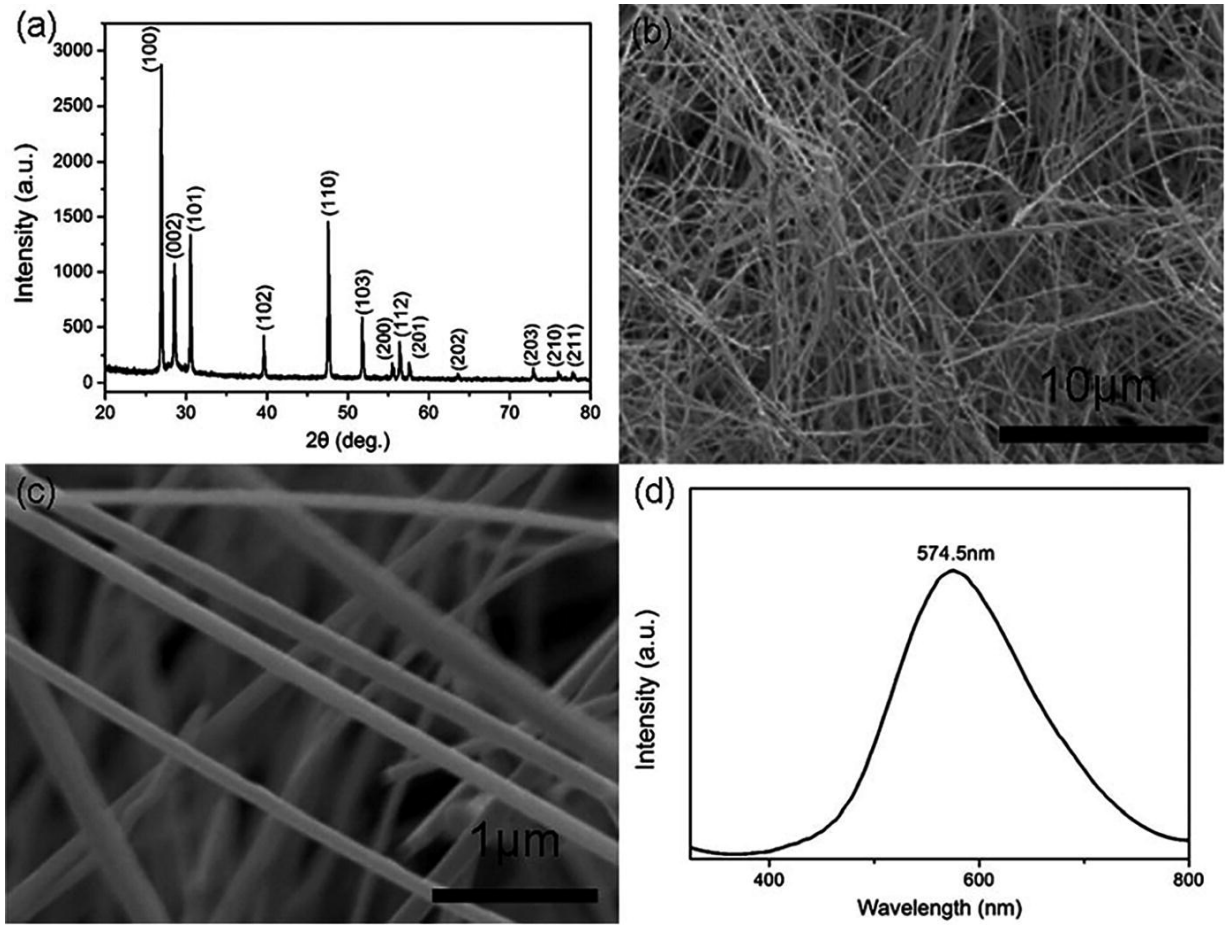

Fig. 12.3 (**a**) XRD pattern of the as-prepared ZnS products. (**b**) Low and (**c**) high magnification SEM images of the ZnS nanowires. (**d**) Room temperature photoluminescence spectrum of the as-synthesized ZnS nanowires (Reprinted with permission from [81]. Copyright 2012: Royal Society of Chemistry)

Additives (simple substances, salts) in PVD and CVD methods allow for synthesizing various heterostructures and doped 1D nanoparticles, for example, ZnSSe/ZnS [54], ZnSe/Sb [55], ZnO/Ga [95], ZnS/Ga [95], CdS/Er [19], ZnS/ZnO [30], $Zn_xCd_{1-x}Se$ [92], CdS/Cl [83], CdS_xSe_{1-x} [68], etc.

The change of the carrier gas can contribute to the formation of the structure of nanowires. For example, if typical carrier gases, such as argon, hydrogen, etc., are replaced with phosphine (PH_3) in the synthesis of ZnSe nanowires, it leads to the formation of a semiconductor doped with phosphorus [100].

Another method that can be considered as a variant of synthesis from the gas phase is the method of pulsed laser deposition (PLD), which includes the interaction of the source material with the laser pulse with

subsequent evaporation and vapor condensation that leads to the formation of the desired product. Compared to CVD and PVD, the advantages of this method are better nucleation and improved stoichiometry of the obtained compounds due to less contamination with tube materials. This method produces high-quality doped semiconductor 1D nanostructures, such as CdS_xSe_{1-x} [15].

Varying the nature of the substrate on which the formation of nanowires occurs allows not only to change the physical characteristics of the material but also to crystallize substances in different crystalline modifications [65].

In contrast to gas-phase deposition methods, solution deposition methods have the main advantage: The use of relatively lower temperatures and organic solvents prevents unwanted oxidation reactions during synthesis, so more and more studies are focused on improving known methods of obtaining 1D nanostructures from solutions. These methods can be divided into two types: a synthesis with nucleation (solvothermal method, electrochemical deposition method) and without nucleation (Van der Waals epitaxy method) [53].

Typically, the hydrothermal method is based on the heating of precursors in organic solvents. A typical method of synthesis of ZnO nanowires by hydrothermal method includes the decomposition of the complex $[Zn(OH)_4]^{2-}$ at a temperature of 180–200°C for 20 h in ethylenediamine. The formed ZnO nanowires are characterized by a 100% yield of the crystalline phase [43]. The size of the formed nanoparticles can be controlled by changing the acidity of the reaction or by changing the temperature: the higher the pH value, the faster the process of nanowire formation occurs, and the lower the temperature, the smaller the nanoobjects are obtained [53]. ZnSe and even ZnSe/Mn are synthesized by a similar method: zinc salt, selenium, and manganese salts are used, and the synthesis is carried out in oleynamine [41].

The method of electrochemical deposition is often combined with the utility of auxiliary templates – compounds, mainly porous or hollow structures (both organic and inorganic), in which the formation of the desired nanowires takes place [66]. The template substance is often an aluminum electrode with nanopores immersed in an electrolyte with appropriate precursors. This method could be used to qualitatively synthesize nanowires CdS [17], CdSe [32], CdTe [74], and ZnO [53]. Aluminum matrix can be etched to obtain isolated wires.

The main method of seedless 1D nanostructures synthesis from solution is the Van der Waals epitaxy method, which consists of the formation of chemical bonds between molecules of nanowires and substrate. To date, the use of this method of synthesis is under improvement because so far, high-quality and defect-free structures can be obtained only when the substrate and nanowires are of the same nature [53].

12.4 2D Nanomaterials (Nanosheets)

2D nanostructure synthesis methods are classified similarly to 1D, but the approaches and methodology are slightly different.

The standard PVD method of the typical II–VI semiconductor nanosheet synthesis is focused on the same approach as for synthesizing nanowires. However, in the case of nanosheets, the substrate is covered not with metal nanoparticles (usually gold) but with metal nanofilms that catalyze the formation of nanosheets. This method can be used to synthesize several semiconductors 2D nanostructures of different thicknesses of ZnTe [74] and CdS [25].

Methods of solvothermal synthesis are more widely used in obtaining 2D nanostructures compared to 1D because this method involves the use of relatively low temperatures (100–250°C), and control of the size of the material can be achieved by changing the synthesis conditions: temperature, solvent, precursors, etc. [79], which is clearly shown in Fig. 12.4. By controlling the synthesis conditions and, as a consequence, the thickness of the obtained material, it is possible to adjust the optical properties of 2D nanostructures (with increasing thickness, a bathochromic shift of the photoluminescence peak position is observed) [59]. Each solvothermal synthesis technique includes the use of solvents (water, ethylenediamine, 1-octadecene, etc.) and precursors based on the atoms of the A^{II} and B^{VI} elements. Salts of the corresponding metals and other precursors that serve as sources of chalcogens, such as tributylphosphine telluride, are used to obtain nanosheets and nanoplates of zinc and cadmium chalcogenides [77], sodium selenite [51], selenium [10, 11, 23, 57], thiourea [7, 24], sulfur [56], etc.

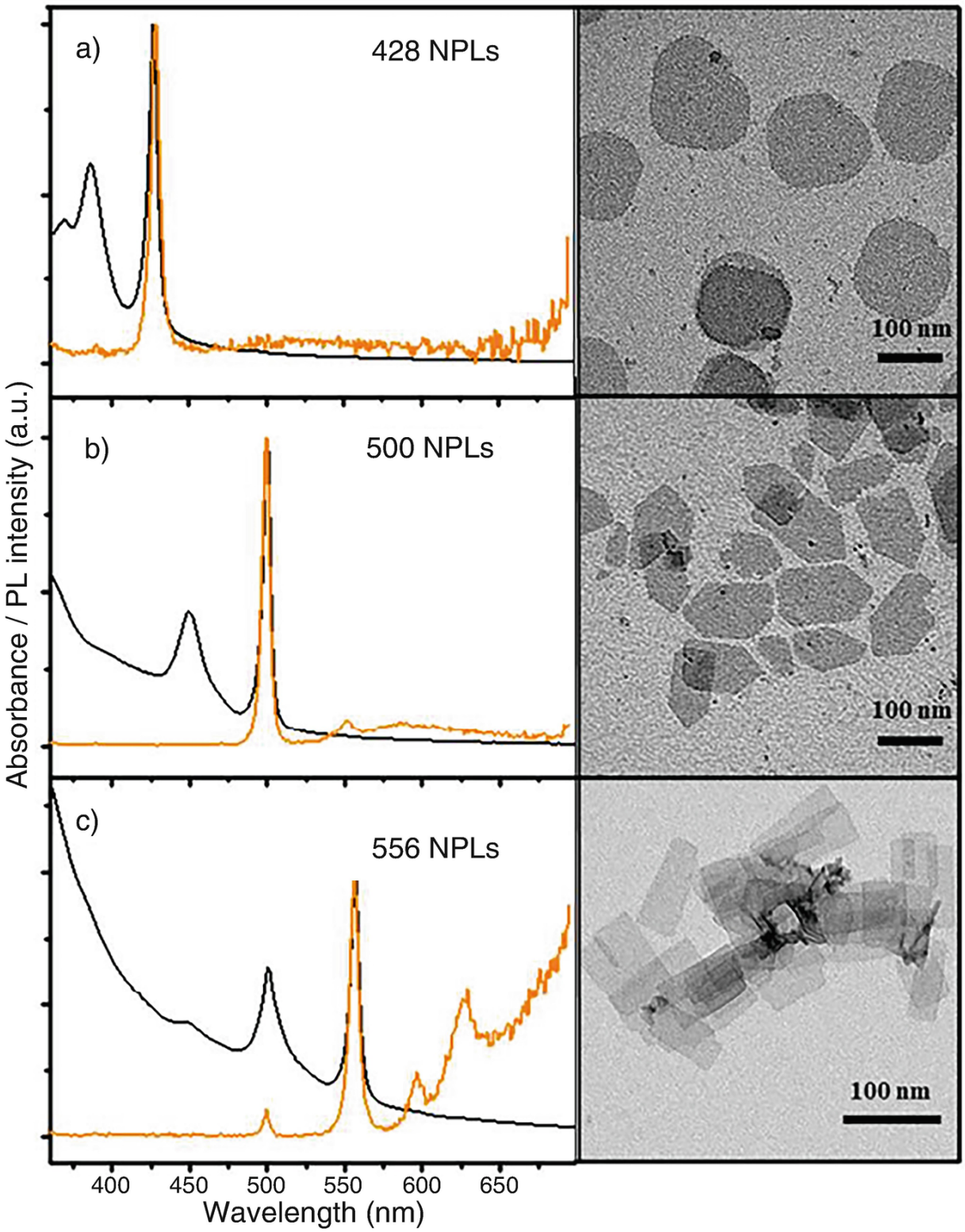

Fig. 12.4 CdTe NPLs of three different thicknesses. Left: absorption (black) and photoluminescence (orange) spectra of NPLs with different thicknesses. Right: TEM images of the corresponding samples. (**a**) NPLs with the first excitonic peak at 428 nm, (**b**) NPLs with the first excitonic peak at

500 nm, and (**c**) NPLs with the first excitonic peak at 556 nm (Reprinted with permission from [59]. Copyright 2013: American Chemical Society)

Using solvothermal methods, it is possible to cover the surface of nanosheets with different nanoparticles, such as carbon dots (CDs), platinum (Pt-NPs), etc., and obtain heterostructures, such as CdS@CDs or CdS@CDs/Pt-NPs [61]. Two-layer nanosheets of different materials, for example, ZnSe/ZnS [44], doped semiconductor nanosheets with the formation of solid solutions, such as ZnSe/Mn [51] or ZnS: Cu [9]. All the modifications mentioned above improve the photocatalytic properties of these nanostructures in their interaction with organic dyes.

The method of ultrasonic exfoliation could be regarded as a relatively different method of nanosheet synthesis, which includes using ultrasound to overcome the Van der Waals forces between each nanosheet (Fig. 12.5), followed by stabilization of the nanosystem with different stabilizers [56]. It is shown that CdS nanosheets synthesized by this method show better photocatalytic efficiency [87].

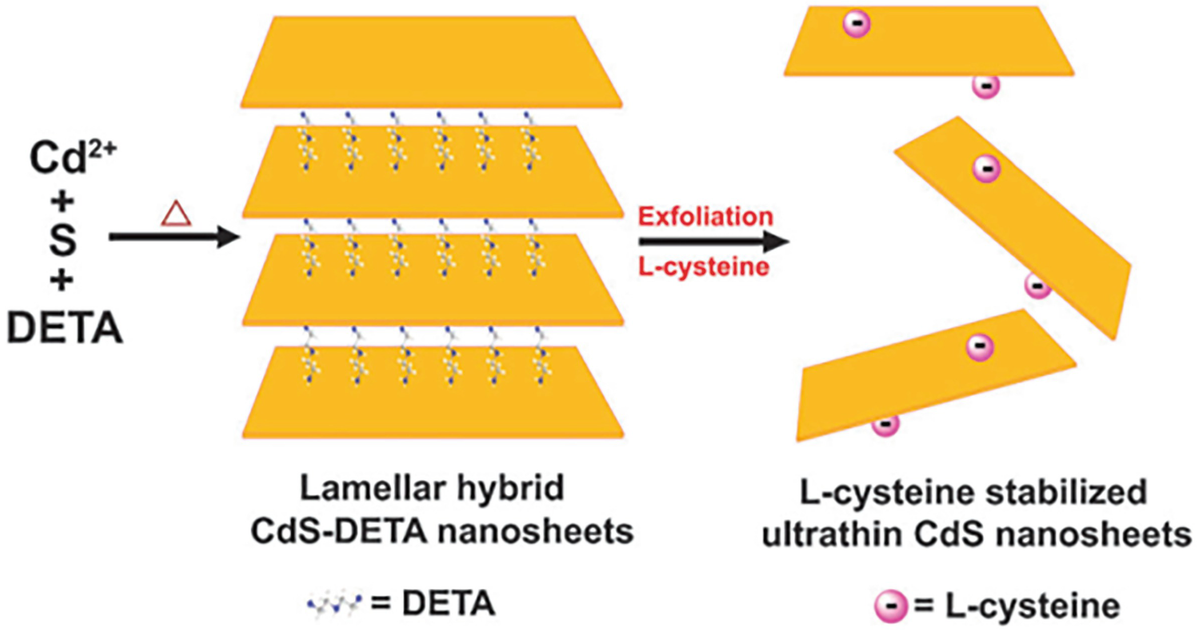

Fig. 12.5 Illustrative scheme of synthesis of CdS nanosheets by ultrasonic exfoliation (Reprinted with permission from [87]. Copyright Royal Society of Chemistry)

There are also methods of synthesizing semiconductor 2D nanostructures by laser ablation: the gradual removal of a semiconductor from a surface by a laser pulse with the subsequent formation of the desired nanosheets. In [91], it was noted that the use of a femtosecond laser pulse

allows for obtaining ultrathin ZnSe nanosheets, which show excellent photocatalytic activity in the discoloration of methylene orange.

12.5 Core-Shell Structures

Modern nanotechnologies allow the creation of multilayer nanostructures with various geometric and energy designs. It allows the use of various semiconductors to manipulate the behavior of electrons and holes to optimize the optical characteristics of nanostructures [1, 45, 50, 82, 84]. In general, the main reasons to synthesize core-shell nanostructures are either coating the particle surface with chemically stable layers to screen toxic or reactive core from the environment or creation of heterostructures that will affect electronic states within it – this includes surface passivation (removing defects) and growth of the materials that have different relative band alignments than the core. It may cause localization of the excited charge carriers in specific parts of the particles, or contrary, separate them in core and shell, respectively. Close lattice parameters of II–VI materials allow epitaxial growth of the materials, leading to various structures. In particular, using semiconductors with different values of band gaps, it is possible to form heterojunctions with properties that differ significantly. In such heterostructures, the conduction bands of the contacting semiconductors do not coincide, due to which a discontinuity of conduction band (ΔE_c) is formed. For similar reasons, there is a discontinuity of the valence band (ΔE_v). The nature of the discontinuities determines the type of heterojunction and, accordingly, the type of nanostructure.

Zone diagrams (Fig. 12.6) showing the levels of the conduction band and the valence band are used to represent the band structure of heterojunction materials.

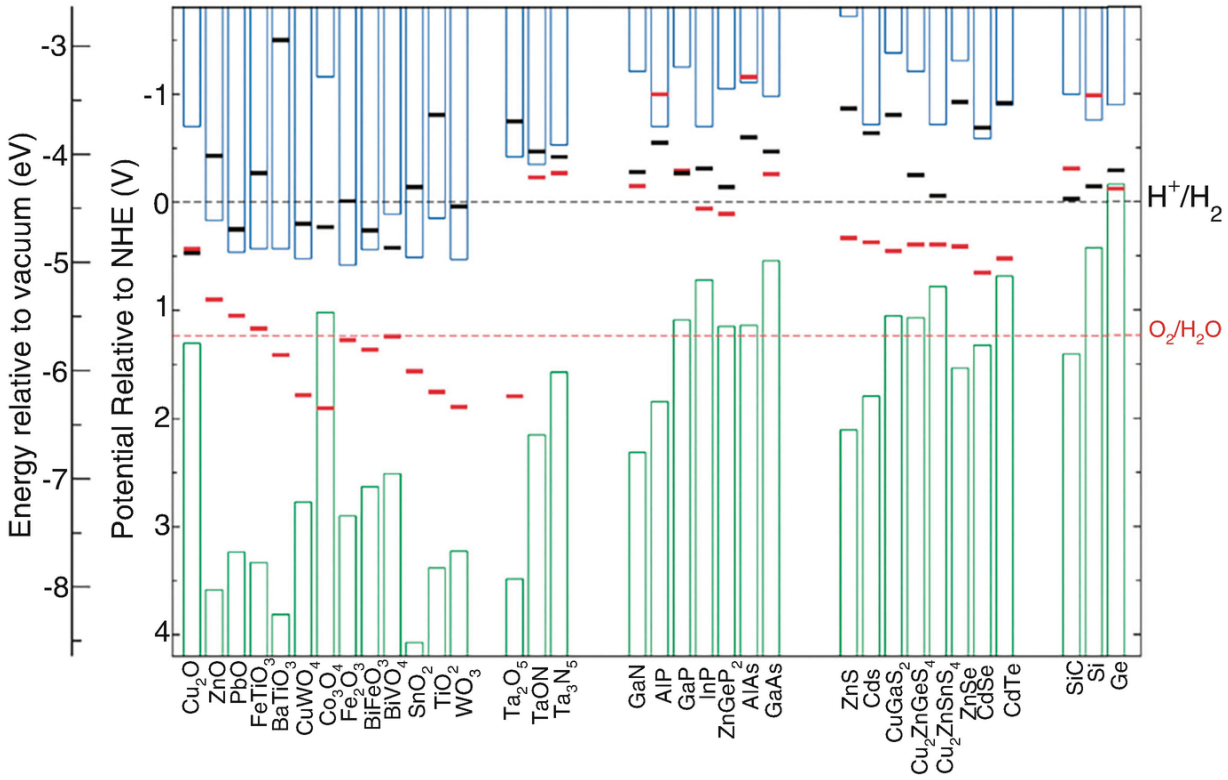

Fig. 12.6 Summary of the semiconductor conduction band (blue) and valence band (green) positions at pH = 0 relative to the O_2/H_2O and H^+/H_2 redox potentials (Reprinted with permission from ref. [14]. Copyright 2012: American Chemical Society)

Of course, the exact energies of the levels depend on many factors, and in reality, heterostructures may differ from the idealized situation, but the band diagram can reveal the fundamental features of heterojunctions. Particularly not only bulk parameters of the core and shell materials but also quantum size effects should always be taken into account.

Consider a heterojunction between two materials: A and B, with band gap E_{gA} and E_{gB}, respectively. A simple Anderson rule [29] is used to calculate the bands discontinuity (ΔE_c, ΔE_v), according to which the discontinuity of the conduction band is equal to the difference in electronic affinity of two materials $\Delta E_c = \chi_B - \chi_A$. The discontinuity of the valence band is obtained as:

$$\Delta E_v = (\chi_B + E_{gB}) - (\chi_A + E_{gA}) \tag{12.2}$$

The affinity for the electron is almost independent of the Fermi level and accordingly does not depend on the temperature and doping of materials. However, even for binary compounds, the values of χ are not

always reliable because the surface of the semiconductor is almost always contaminated. Therefore, usually seek to determine the band's discontinuity, rather than electronic affinity experimentally.

Band discontinuities ΔE_c and ΔE_v can be both positive and negative. Depending on it, there are three types of heterojunctions.

The most common case is a type-I heterojunction when a narrow band gap is inside a wider band gap, then ΔE_c and ΔE_v have opposite signs (Fig. 12.7a). It is implemented, for example, in CdSe/ZnS, CdS/ZnS, CdSe/CdS, and CdS/HgS heterojunctions [2]. A/B/A sandwich with type-I heterojunctions creates a potential well for both the electron and the hole, in which radiative recombination (direct optical transition) with an energy greater than E_{gB} can occur.

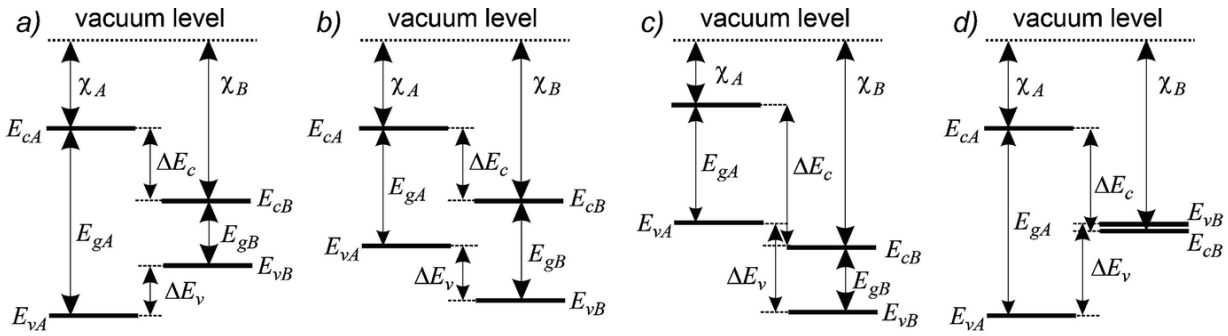

Fig. 12.7 Zone diagrams of heterojunctions of the first (**a**), second (**b**, **c**), and third (**d**) types

In another case of semiconductor pairs, the heterointerface between which ΔE_c and ΔE_v have the same sign implements a type-II heterojunction (Fig. 12.7b, c). In this type, band gaps either overlap only partially (step type, Fig. 12.7b) or do not overlap at all (discontinuous type II, Fig. 12.7c). This case is realized, for example, in the heterojunctions CdTe/CdSe, CdS/ZnSe, and CdSe/ZnTe [2]. A type-II heterostructure creates a potential well for electrons and a barrier for holes. Thus, the regions of electron and hole localization are spatially distributed. Nevertheless, radiative recombination (indirect optical transition) becomes possible with sufficient overlap of their wave functions. An important practical consequence is that the radiation energy may be less than the band gap of one or both semiconductors.

Type-III heterojunction is formed by an ordinary semiconductor and a material with an inverted band structure (Fig. 12.7d). This case is

infrequent, which is realized, for example, in the heterojunction CdTe/HgTe [2].

Multilayer quantum dots can also be classified by the type of potential of the quasiparticle (electron or hole) in the external environment [72, 73].

Closed systems are formed (Fig. 12.8a), in the structures in which the potential of the quasiparticle in the external environment is the highest. States with energies less than the barrier height are stationary, and the energy spectrum is discrete. In the region above the barrier, the energy spectrum is continuous.

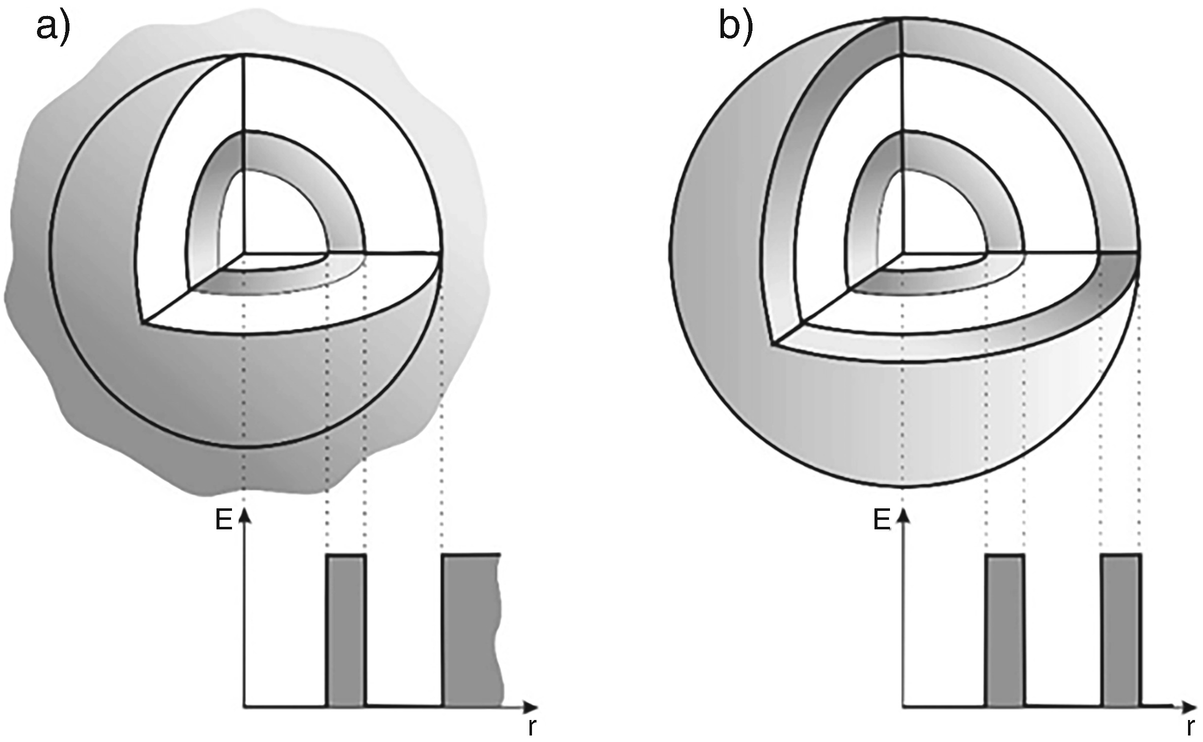

Fig. 12.8 Potential electron profile at closed (**a**) and open (**b**) quantum dots

In open systems (Fig. 12.8b), the potential of the quasiparticle in the external environment is the smallest. In such systems, the states of quasiparticles are quasi-stationary and are characterized by decays due to finite lifetimes. Through open systems, quasiparticles can tunnel into the outer medium, creating a current.

12.5.1 Core-Shell QDs

A typical synthesis of a colloid is designed so that the concentration of precursors increases rapidly above the threshold value when a short burst of

nucleation (discussed above) occurs with the formation of a large number of nuclei in a short period. These particles grow rapidly and lower the monomer concentration below the nucleation threshold, allowing the further growth of these particles.

When a new phase is formed on the surface of the other material, the process is called heterogeneous nucleation. Such an approach where “seeds” of the nanoparticles are synthesized separately became an advancement in bottom-up nanoparticle synthesis. When the same material is used as a seed, and growing phase, highly monodisperse colloidal nanoparticles can be grown. When materials are different, core-shell structures are produced. However, core-shell heterostructure encounters inherent limitations; building a thick shell beyond the critical thickness results in the creation of misfit defects near the core-shell interface that decreases the PL quantum yield of QDs. A less productive but very controllable approach of successive ionic layer adsorption and reaction (SILAR), also sometimes called colloid atomic layer deposition (c-ALD), allows practically ultimate resolution (one ionic layer) of the shell growth.

Synthesis of highly luminescent CdSe/ZnS type-I composite quantum dots with CdSe cores ranging in diameter from 2,3 to 5,5 nm was reported as early as 1997. The narrow photoluminescence (fwhm ≤40 nm) from these composite dots due to the effect of ZnS passivation on the electronic structure of the dots covers most of the visible spectrum from blue through red with high quantum yields of 30%–50% at room temperature [18]. Since then, different chemical approaches have been applied to produce core-shell particles. For example, in [67], CdSe nuclei were synthesized by mixing cadmium and selenium precursors without creating an inert atmosphere. The cadmium complex with sulphanilamide was used as a cadmium precursor and simultaneously as a stabilizing ligand [5]. To grow the shell, zinc stearate and thiourea were gradually added to the solution of cadmium selenide nuclei in octadecene at 200°C. TEM studies show that the obtained CdSe/ZnS nanoparticles have a shape close to tetrahedral with an effective diameter of up to 10 nm. The thickness of the ZnS shell was about 3–4 nm.

Type-II band-engineered quantum dots (CdTe/CdSe [core-shell] and CdSe/ZnTe [core-shell] heterostructures) are described in [37]. The distinctive peaks in the absorption spectra of the initial cores (Fig. 12.9) are replaced in the overcoated type-II structures with a featureless absorption tail into the red and near-infrared. Photoemission from CdTe/CdSe and

CdSe/ZnTe QDs was observed at longer wavelengths than the corresponding cores. Type-II emission originates from the radiative recombination of the electron-hole pair across the core-shell interface. The spatial separation of carriers and the long radiative lifetimes implies that nonradiative decay channels can dominate; therefore, the type-II QDs have PL much lower yield than type I.

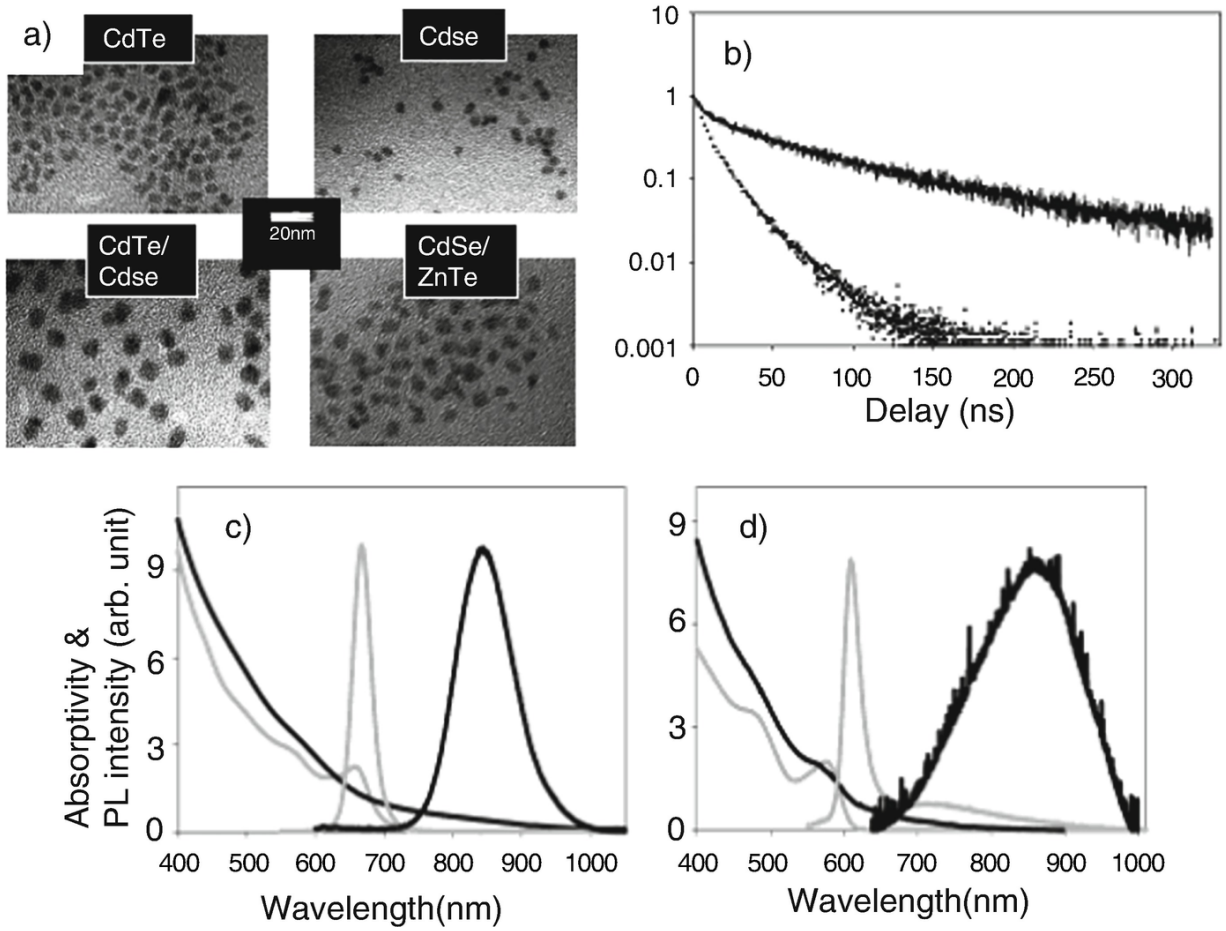

Fig. 12.9 (**a**) Bright field TEM images of the samples used for absorption and photoluminescence spectra measurements. (**b**) Normalized photoluminescence intensity decays of CdTe/CdSe (3,2 nm radius core/thickness of 1,1 nm radius) CdTe QD (dotted line, quantum yield 40%). Spectra of 3,2 nm radius CdTe QD (gray lines on (**c**)), CdTe/CdSe (32 Å radius core/thickness of 1,1 nm shell) QD (black lines on (**c**)), 22 Å radius CdSe QD (gray lines on (**d**)), and CdSe/ZnTe (2,2 nm radius core/thickness of 1,8 nm shell) OD (black lines on (**c)**) (Reprinted with permission from [37] Copyright 2003: American Chemical Society)

For many II–VI compounds, core-shell structures can be synthesized via the ion-exchange route – a versatile tool to transform colloidal nanocrystals (NCs) directly in a solution or deposited as NC films. Through these reactions, either a fraction or all of the “host” metal cations (or anions) of

presynthesized NCs are replaced with other ions while preserving both the NC size and shape and, in many cases, the crystal structure. Depending on the miscibility of the reactant and of the product materials, solubility products, and the kinetics of the exchange reaction, different types of nanostructures can be accessed: core-shell or core/graded-shell heterostructures, quantum wells, etc.

Metastable CdTe@HgTe core-shell nanostructures (Fig. 12.10) are formed when CdTe NCs are exposed to different Hg/Cd feed molar ratios, employing a slowly reacting Hg precursor dissolved in methanol [63].

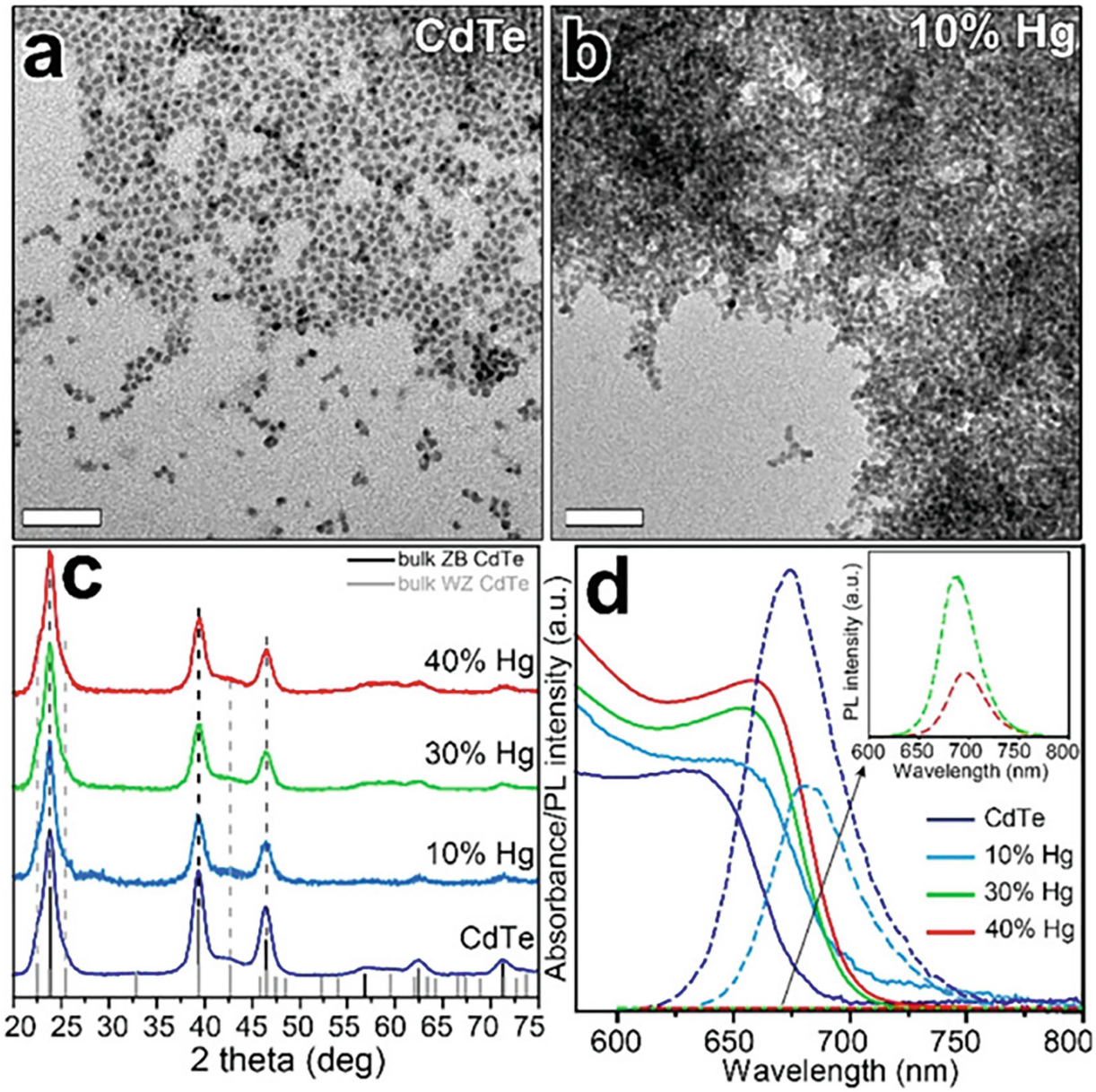

Fig. 12.10 TEM images of (**a**) CdTe and (**b**) CdTe-Hg 10% NCs. (**c**) XRD patterns of CdTe and CdTe-Hg samples together with the bulk reflections of WZ (ICSD numbers 620518) and ZB (ICSD number 43712) CdTe structures. (**d**) Absorption and PL spectra of CdTe NCs before and after partial CE with Hg (λex = 450 nm). The inset shows a magnification of the PL spectra of CdTe-Hg 30 and 40% samples (Reprinted with permission from [63]. Copyright 2020: American Chemical Society)

PbS/CdS core-shell QDs were synthesized starting from PbS core QDs by means of a cation exchange reaction with an excess of cadmium oleate added to a PbS QD suspension in toluene heated to between 100 and 150°C (between 10 and 300 min). The reaction was quenched after reaching the desired reaction time using a mixture of methanol and butanol (1:2). Given the correspondence between both the energy and the oscillator strength of the band gap transition of PbS/CdS core-shell and PbS QDs with the same core diameter, it follows that the room-temperature properties of this transition are not affected by CdS shell growth. This indicates that PbS/CdS core-shell QDs have a type-1 band alignment, in which the bands of the PbS core are contained within those of the CdS shell [35].

12.5.2 Core-Shell 1D Structures

If the nanoparticle core is nucleated in anisotropic modification or suitable ligands are used, 1D rod-like structures can be made at a high yield. One of the most impressive results of such structures is the synthesis of the CdSe/CdS structure developed independently by groups in Europe and the USA [13, 69]. They reported the synthesis of asymmetric core-shell CdSe/CdS nanorods with regular shapes and narrow distributions of rod diameters and lengths, the latter being easily tunable up to 150 nm (Fig. 12.11). These rods are highly fluorescent and show linearly polarized emission, whereby the emission energy depends mainly on the core diameter (Fig. 12.12).

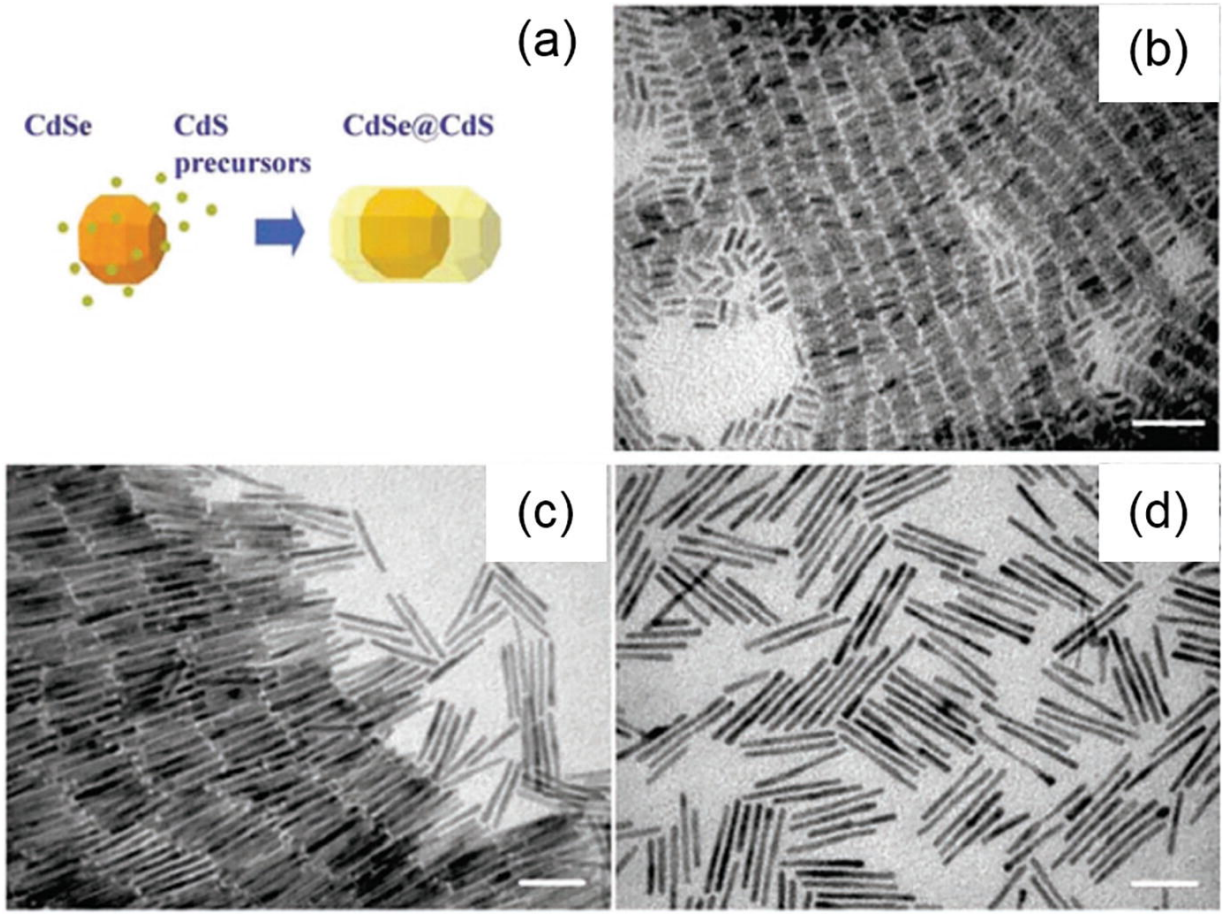

Fig. 12.11 Transmission electron micrographs of self-assembled CdSe/CdS nanorods average rod diameter and length, as determined by HRTEM, are respectively: (**a**) reaction scheme; (**b**) 4.9 ± 0.7 nm and 19 ± 1 nm; (**c**) 3.9 ± 0.2 nm and 53 ± 4 nm; (**d**) 3.8 ± 0.3 nm and 70 ± 4 nm (Reprinted with permission from [13]. Copyright 2007: American Chemical Society)

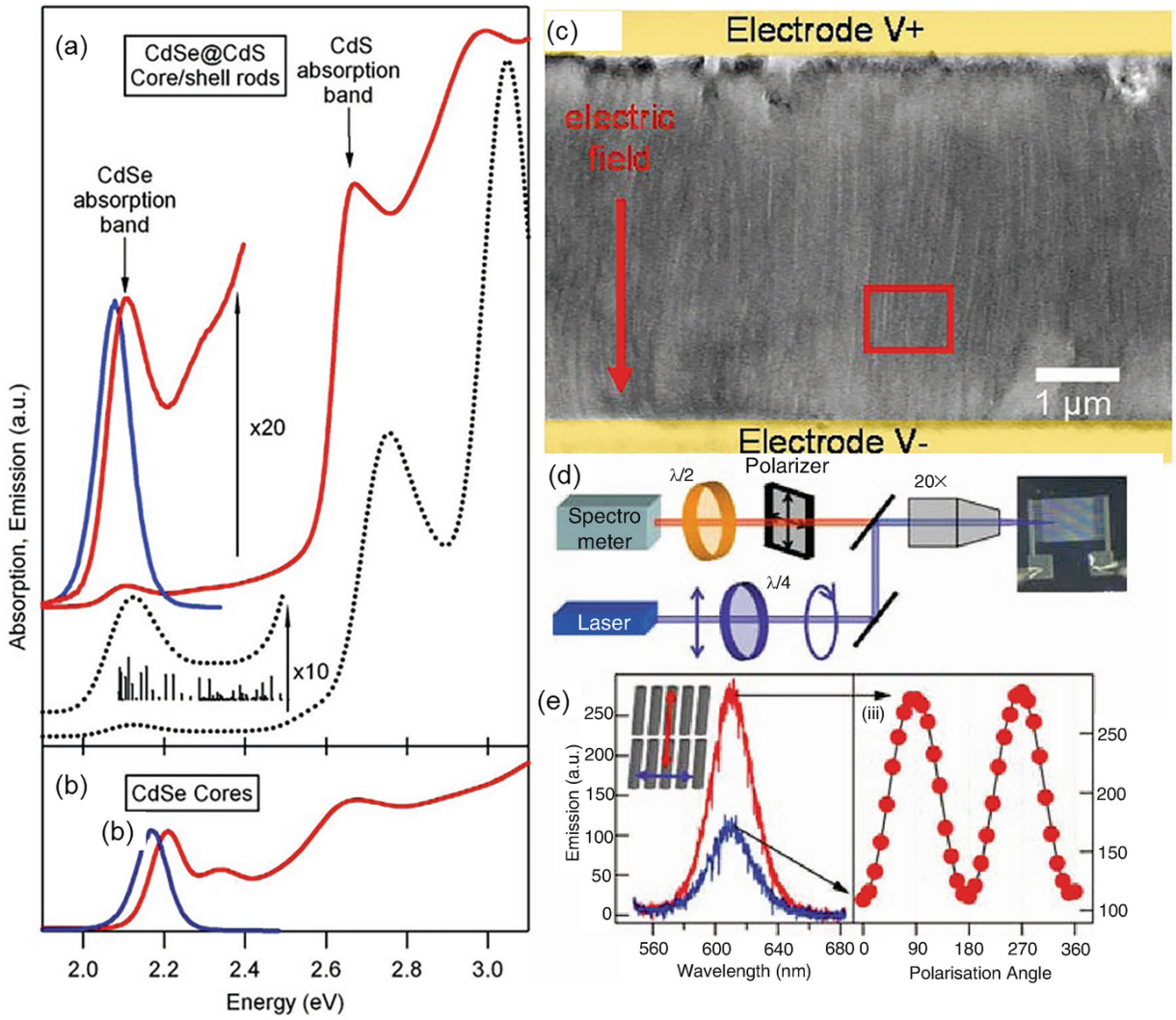

Fig. 12.12 (**a**) Optical absorption and photoluminescence (PL) spectra of a typical sample of CdSe/CdS nanorods dissolved in toluene (continuous lines). The rods have an average length of 51 nm and an average diameter of 3.9 nm. They were prepared from CdSe seeds with a diameter of 3.2 nm. The corresponding theoretical absorption spectrum is shown in dotted lines. Vertical bars in the ×10 magnification of the low-energy side of the calculated spectrum indicate the energy position and oscillator strength of the first few exciton levels, which represent transitions from the hole 1S level of the CdSe sphere to the electron nS levels of the CdS rod. The absorption and PL spectra of the starting spherical CdSe nanocrystal sample are shown in (**b**). Spectra of core-shell samples always show a considerable redshift with respect to the corresponding spectra of the starting CdSe seeds. Lateral alignment of nanorods with electric fields and polarized emission from aligned nanorods. (**c**) SEM images showing aligned arrays of nanorods with an aspect ratio of 10. (**d**) Schematic illustration of the experimental setup. (**e**) Nanorod emission spectra, recorded from the micrometer size regions of aligned nanorods under ambient conditions, polarized parallel (red) and perpendicular (blue) to the long axis of the nanorods, as illustrated by the schematic inset. (iii) Red dots show the PL intensity dependence on the polarization angle and can be fitted to a cos2 function (black line). From the data, a polarization ratio of 45% can be calculated as (Ijj−I⊥)/(Ijj + I⊥). Here, Ijj and I⊥ are the emission intensities parallel and perpendicular to the long axis of the rods, respectively (Reprinted with permission from [13]. Copyright 2007: American Chemical Society)

The use of starting ZnTe or ZnSe seeds in such synthesis creates tetrapod-shaped ZnTe/CdS and ZnSe/CdS nanocrystals [69]. In this case, seeds have a cubic zincblende structure, which leads to the concerted growth of four CdS arms on top of such seeds. In particular, for the case of ZnTe seeds, the resulting ZnTe/CdS tetrapods too have a narrow distribution of arm lengths and diameters.

Lin et al. [42] applied a combination of chemical bath deposition and SILAR method to obtain ZnO/ZnS core-shell nanorod arrays. In this case, fluorine-doped tin oxide (FTO) substrates were spin-coated with 0.6 M zinc acetate in a mixed solution of ethanolamine and 2-methoxyethanol to acquire a seed layer of ZnO, followed by thermal treatment. The seeded substrates were placed in aqueous growth solution containing zinc nitrate and hexamethylenetetramine, kept at 90°C for 12 h twice, and then annealed in air at 450°C to improve crystallinity and remove impurities. ZnS nanoparticle shells were prepared by a successive ionic layer adsorption and reaction (SILAR) method. A substrate with ZnO nanorod arrays was dipped alternately into zinc nitrate for 1 min, rinsed with deionized water, then dipped into Na_2S aqueous solution for another 1 min. This process was repeated for 2, 7, 10, and 15 cycles to achieve a different thickness of ZnS nanoparticles. Figure 12.13 demonstrates that ZnO/ZnS core-shell nanorod arrays can be used as an active photoanode for high-performance photoelectrochemical cell-type self-powered ultraviolet photodetectors.

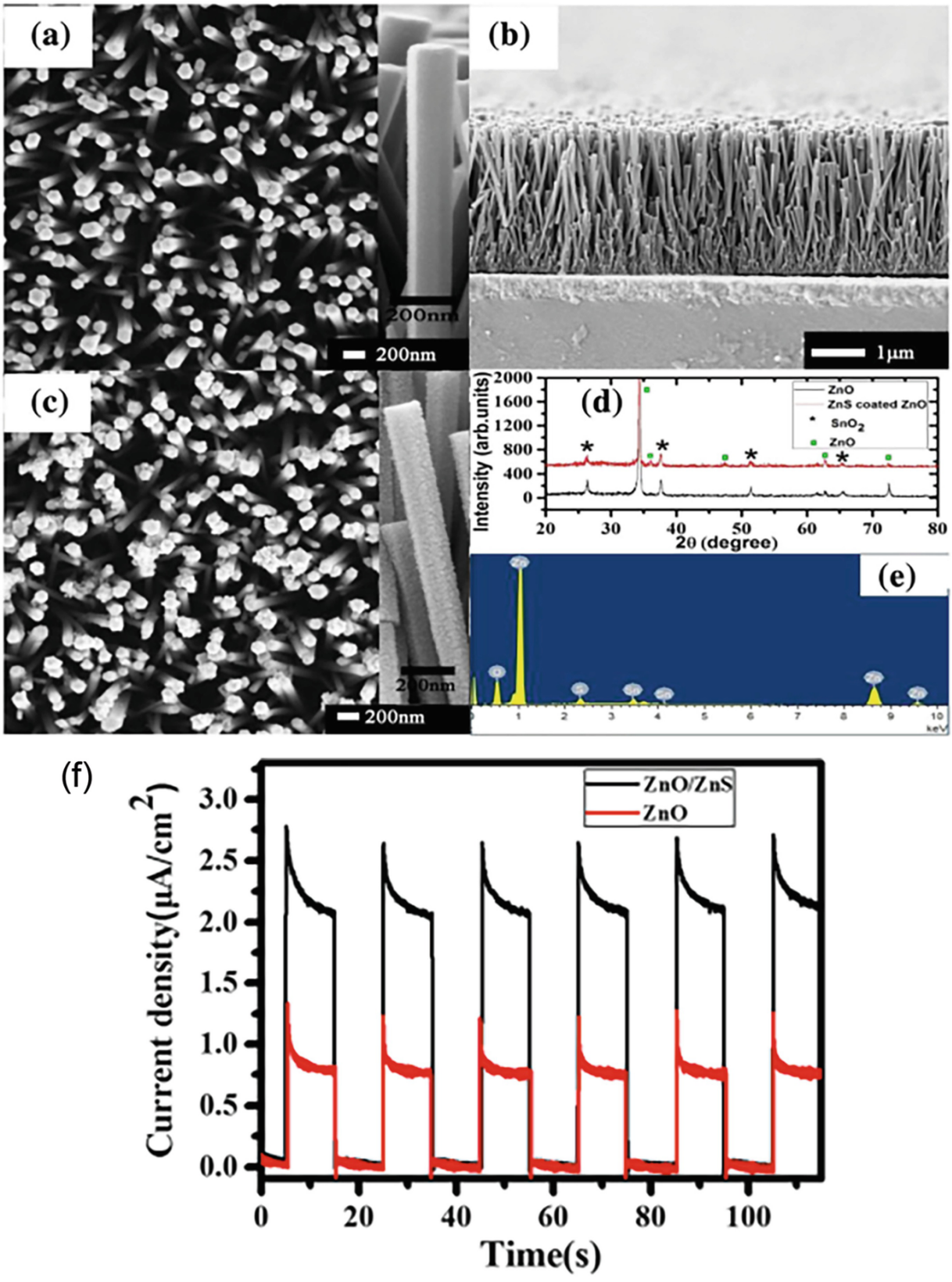

Fig. 12.13 FESEM images and XRD patterns of ZnO and ZnO/ZnS core-shell nanorod arrays (**a**–**e**). The real-time photocurrent response of the ZnO/ZnS core-shell nanorod array-based UV

photodetector with seven SILAR cycles under on/off UV light radiation with the illumination wavelength of 365 nm (**f**) (Reprinted with permission from [42]. Copyright 2016: Springer)

Similar semiconductor heterostructures: heterocrystalline-ZnS/single-crystalline-ZnO biaxial nanobelts and side-to-side single-crystalline ZnS/ZnO biaxial nanobelts via a simple vapor-liquid-solid approach – thermal evaporation method in which metal nanoparticles are used as catalysts for the growth of one-dimensional semiconductor nanomaterial from the vapor phase [88]. The performance of the photodetector based on ZnS/ZnO biaxial nanobelt is significantly enhanced compared with that of pure ZnS or ZnO nanostructures by combining the high UV-A light sensitivity and fast response speed, justifying the effective utilization of the present ZnS/ZnO biaxial nanobelt as the building blocks of UV photodetectors [30].

To study the possible applications of the thermally grown 1D ZnS/CdS heterostructure in flexible electronics, photodetectors based on 1D ZnS/CdS heterostructure (Fig. 12.14) were prepared on a flexible PET substrate [46].

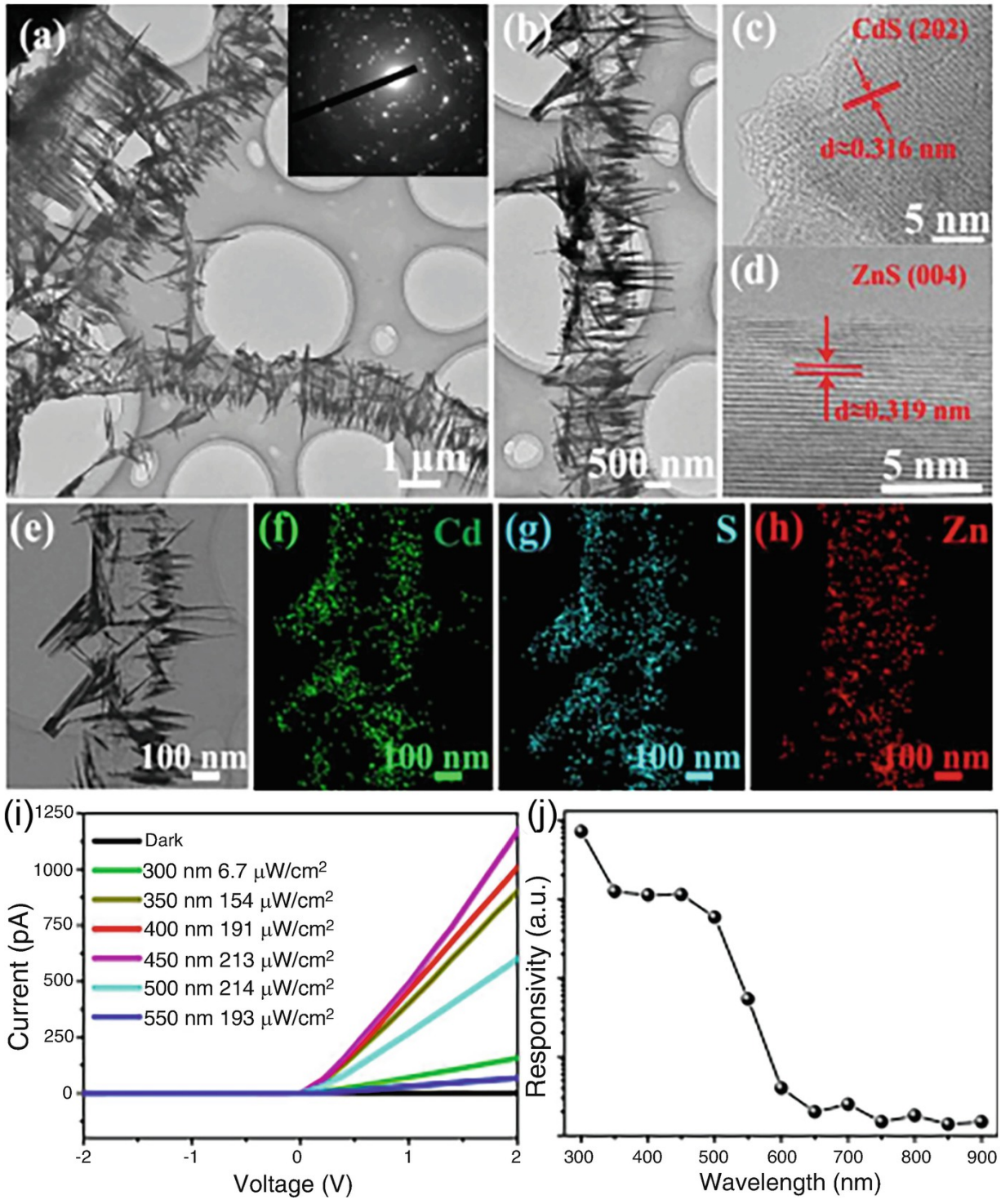

Fig. 12.14 (**a**) and (**b**) TEM image of 1D ZnS/CdS heterostructures. The inset of (**a**) is the SAED pattern; HRTEM image of (**c**) CdS nanorod and (**d**) ZnS nanobelt; (**e**) the STEM image of 1D ZnS/CdS heterostructures; (**f**–**h**) elemental distribution of Cd, S, Zn element in 1D ZnS/CdS heterostructures. (**i**) I–V test result of the ZnS/CdS device under 300 nm UV light with different power intensities and in the dark. (**j**) Photoresponse properties of the photodetector. The light

intensity was 6.7 μW/cm. (Reprinted with permission from [46]. Copyright 2016: Royal Society of Chemistry)

Authors attribute the high photoresponse performance of the 1D ZnS/CdS heterostructures to the following factors: a large surface area-to-volume ratio can adsorb more oxygen molecules on the surface, resulting in a thicker charge depletion layer, thus lowing the dark current; the multiple light scattering heightens the light absorption, which highly the photocurrent; dark current decrease due to the existence of ZnS-CdS interface results in junction barrier, the optimized band energy alignment of the 1D ZnS/CdS heterostructure.

A power conversion efficiency of 1.24% and a large open-circuit voltage of 0.87 V were realized in the doped coaxial 1D ZnSe-ZnO p–n junction under UV light. Bi-doped p-type ZnSe 1D nanostructures were first synthesized via a thermal evaporation method. Coaxial ZnSe-ZnO nanostructures were then fabricated by coating an n-type ZnO thin film on the surface of ZnSe 1D nanostructures by sputtering [99].

To synthesize CdS-CdS_xTe_{1-x}CdTe core-shell nanobelts, a two-step thermal deposition method was adopted using a source/substrate-movable chemical vapor deposition (CVD) system. The alloyed photodetector also demonstrates excellent sensing capability covering the whole visible spectrum (Fig. 12.15). The improved performance is ascribed to the heterostructure in CdS-CdS_xTe_{1-x}-CdTe [70].

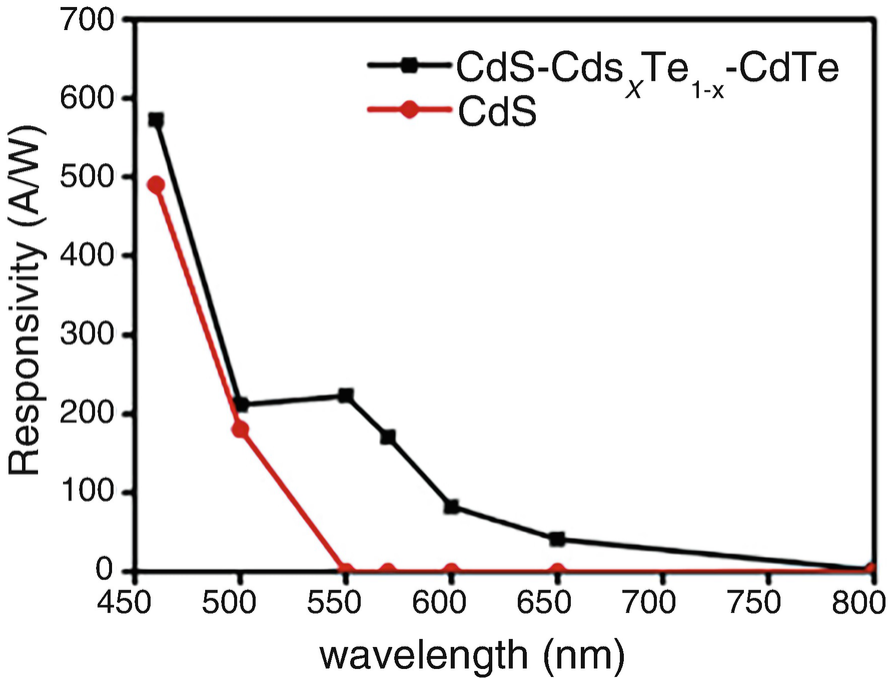

Fig. 12.15 The spectral response of the CdS-CdS$_x$Te$_{1-x}$-CdTe core-shell nanobelt and CdS nanobelt photodetectors (Reprinted with permission from [70]. Copyright 2018: Elsevier)

High-quality CdSe/ZnTe core-shell nanowires synthesized on silicon substrate by combining the techniques of thermal evaporation and pulsed laser deposition. The CdSe/ZnTe core-shell nanowire exhibited a sharp, core-shell interface with a WZ structure. The photovoltaic device based on such a single CdSe/ZnTe core-shell nanowire was fabricated, yielding an energy-conversion efficiency of ~1.7% [80]. An array of similar CdSe/ZnTe core-shell (Fig. 12.16) was implemented in the broadband photodetector, whose performance was greatly enhanced by the piezo-phototronic effect. The resulting (%) responsivity changed by four orders of magnitude. The significant increase in responsivity is believed to arise from (1) the piezo-phototronic effect induced by a change in the Schottky barrier height at the Ag contact–ZnTe junction, and in the type-II band alignment at the CdSe–ZnTe interfaces, in conjugation with (2) a minor lattice mismatch between the CdSe and ZnTe epitaxial layers, which lead to reduced charge carrier recombination [62].

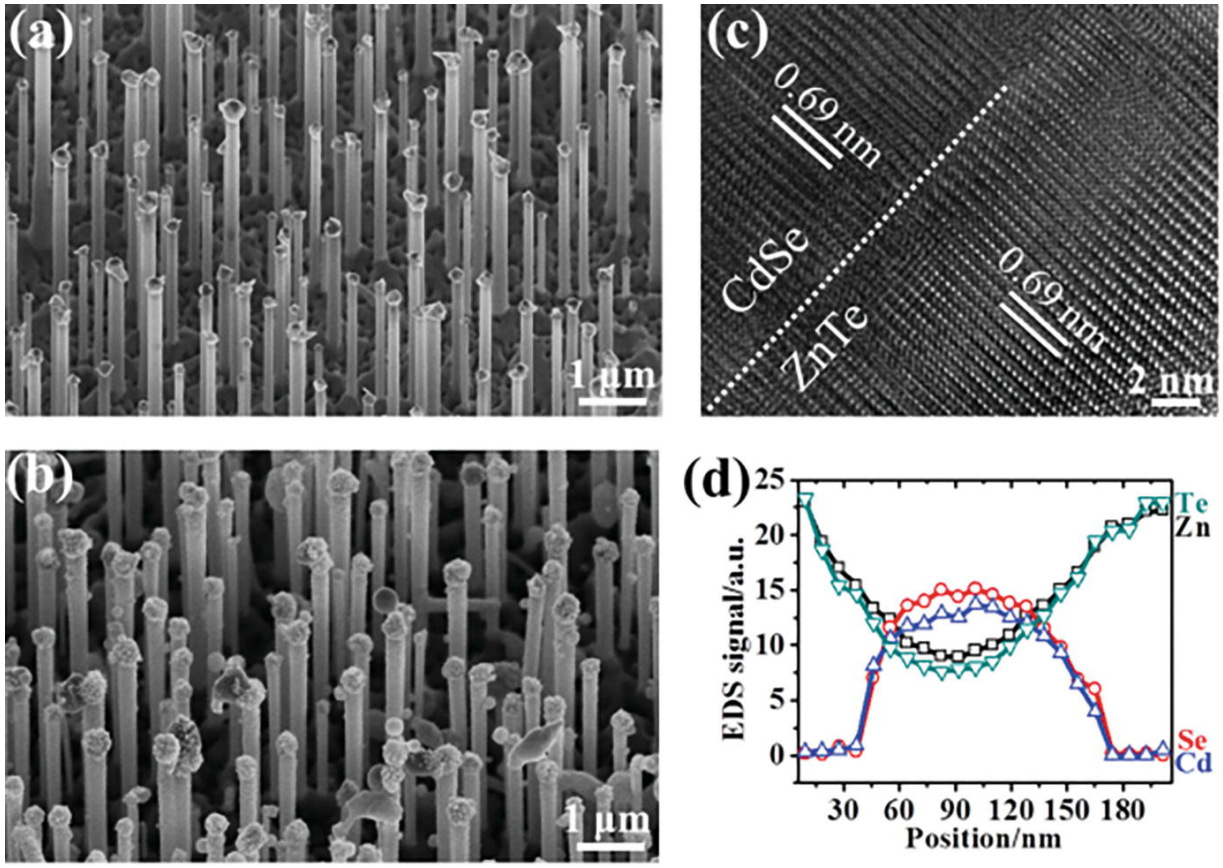

Fig. 12.16 Morphology and structural analysis of CdSe and CdSe/ZnTe core-shell nanowire arrays. (**a**) Low-magnification SEM image of a CdSe nanowire array. (**b**) Low-magnification SEM image of a CdSe/ZnTe core-shell nanowire array. (**c**) HRTEM image of a single CdSe/ZnTe core-shell nanowire. (**d**) A lateral energy dispersive (EDS) line scan across a CdSe/ZnTe core-shell nanowire demonstrates characteristic core-shell elemental peaks (Reprinted with permission from [62]. Copyright 2015: Wiley)

Core-shell morphology is not limited to quantum dots and 1D structures. Interesting, atomically flat, CdSe/CdTe core/crown nanoplatelets with thicknesses of a few monolayers were synthesized by Pedetti et al. [58]. After synthesizing CdSe sheets, they were used as seeds for the growth of CdTe flat structures – “crowns” (Fig. 12.17).

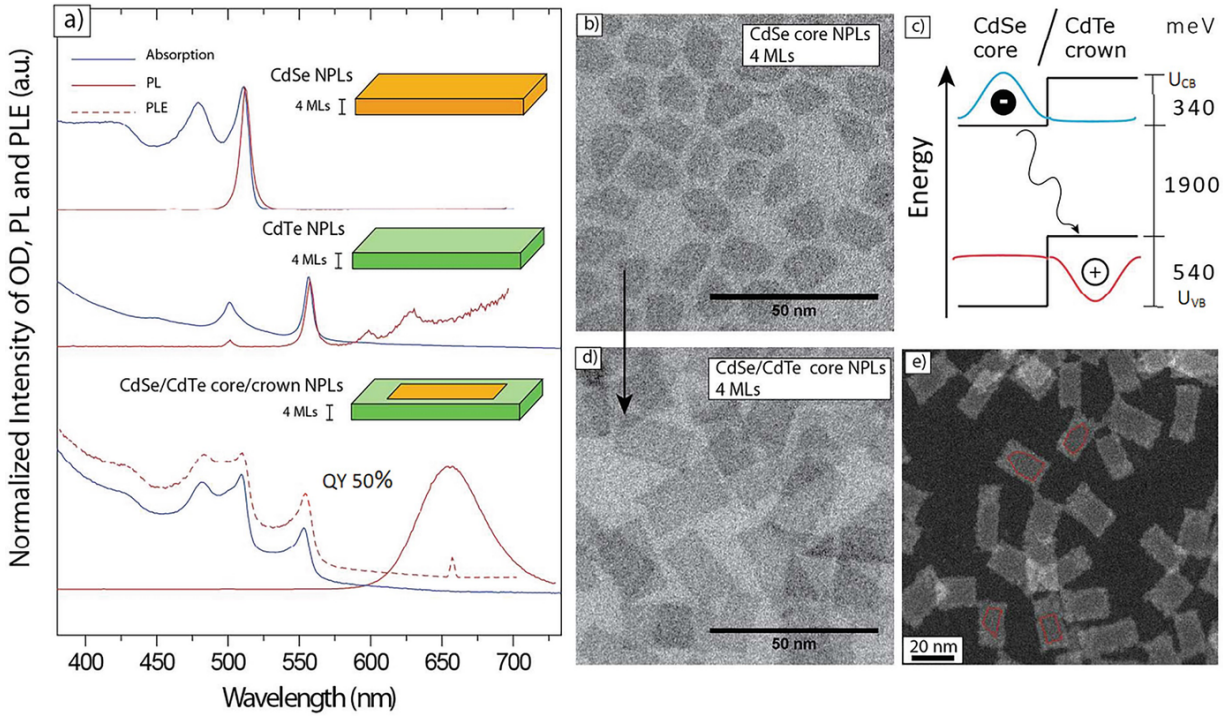

Fig. 12.17 (**a**) Absorption, fluorescence (PL), and excitation spectra (PLE) normalized at the first exciton peak and the maximum of the emission of CdTe NPLs (top), CdSe NPLs (medium), and CdSe/CdTe core/crown NPLs (bottom) 4 MLs thick. (**b**, **d**) TEM images of 4 MLs thick CdSe NPLs core 4 MLs CdSe/CdTe core/crown NPLs. (**c**) Schematic representation of band alignment in CdSe/CdTe semiconductors showing the indirect charges recombination. Energy values refer to 4 MLs thick CdSe/CdTe core/crown NPLs. (**e**) HAADF image of CdSe/CdTe core/crown NPLs, guidelines for the eyes correspond to the core region (Reprinted with permission from [58]. Copyright 2007: American Chemical Society)

In these type-II nanostructures, the charges separate spatially, and the electron wave function is localized in the CdSe core while the hole wave function is confined in the CdTe crown (Fig. 12.17c). The exciton's recombination occurs across the heterointerface, and as a result of their spatially indirect band gap, emission redshift up to the near-infrared region is observed with long fluorescence lifetimes up to 860 ns. Reported type-II nanoplatelets have a high quantum yield of 50% that can be further improved.

12.6 Hollow Nanostructures

Hollow semiconductor nanostructures are an exciting class of materials that combines the advantages of high surface area with semiconductor properties. They are beneficial for charge carrier separation for photovoltaic and various catalytic applications. A common approach to create hollow

nanostructures is to use a sacrificial template as a core on which target material is deposited. The next step is core removal by chemical etching leads to a hollow structure with defined inner space.

Miao et al. [52] demonstrated that hollow structures of CdX (X = Te, Se, S) could be successfully prepared by using Cd(OH)Cl precursors as a sacrificial template. The hollow structures can be hollow spheres or tubes by controlling the shape of the sacrificial template (Fig. 12.18). This is a general method for the synthesis of cadmium chalcogenide hollow structures, and the method is simpler and more practical than direct synthesis.

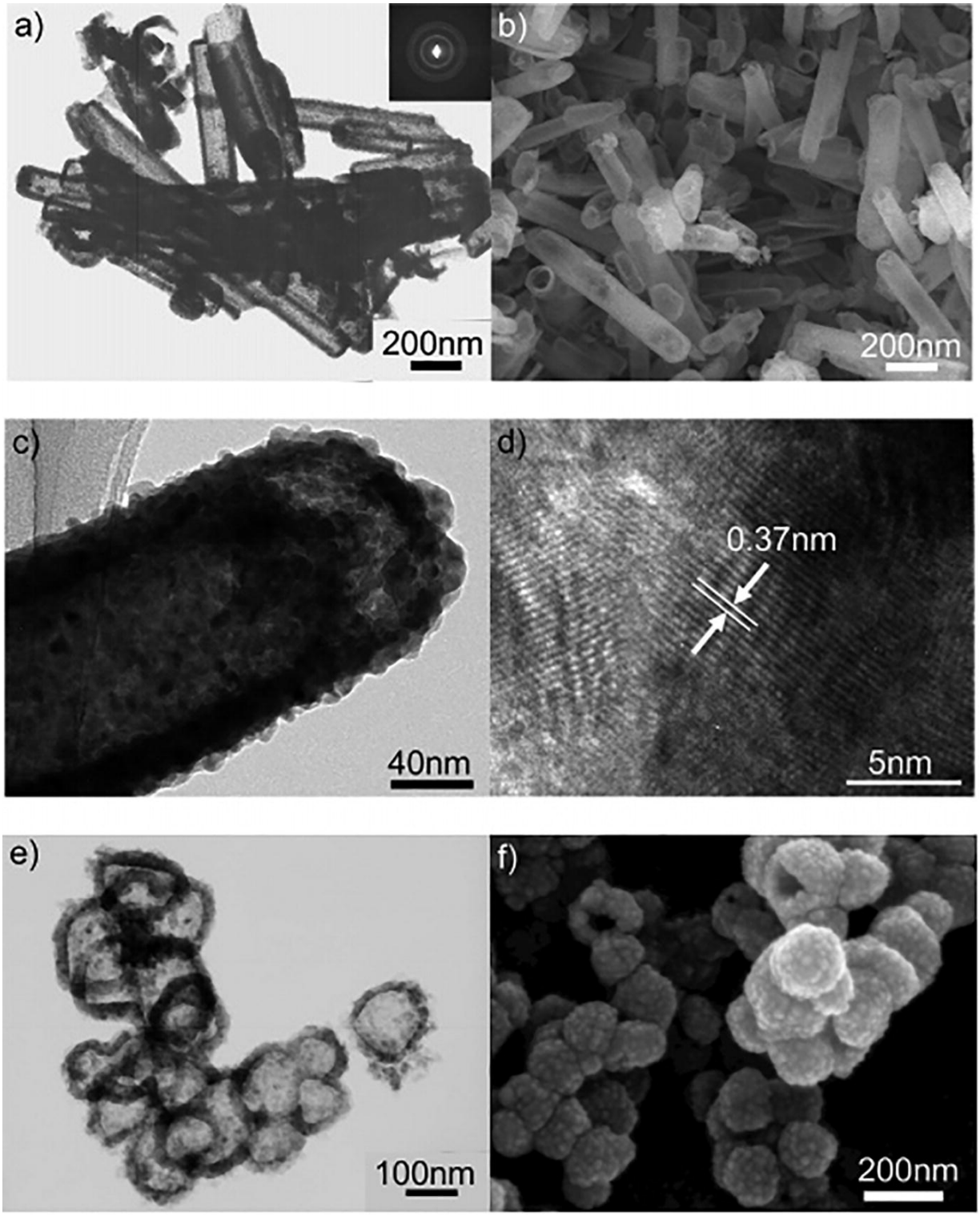

Fig. 12.18 TEM and SEM images of the CdTe nanotubes (**a** and **b**) and hollow spheres (**e** and **f**) and HRTEM images (**c** and **d**) of a single CdTe nanotube (Reprinted with permission from [52]. Copyright 2007: American Chemical Society)

A second way to obtain porous nanomaterials emerges from an interesting phenomenon that occurs when heterogeneous growth occurs under conditions when atoms of each phase can interdiffuse fast, particularly when metal nanoparticles react with oxygen or another chalcogen. This phenomenon is named in tribute to Kirkendall [38], who found in his interdiffusion experiment with contacting Cu and alpha-brass plates that displacement of one part of the diffusion couple relative to another one was accompanied by a pore formation, which was reliable evidence of the vacancy diffusion mechanism. If the temperature is high enough for vacancies injected into the core region to sample a fraction of the core volume, a significant fraction of the vacancies should end up coalescing into a single large void. Hollow nanostructures can also be assembled from individual nanoclusters or nanoparticles. Uniform ZnSe hollow nanospheres were synthesized via a post-synthetic chemical transformation reaction from solid $Cu_{2-x}Se$ nanocrystals with the help of tributylphosphine at room temperature under an ambient atmosphere. The formation of the ZnSe hollow structure was based on the synergetic effect of isotropic cation exchange from $Cu_{2-x}Se$ to ZnSe and concurrent selective etching of $Cu_{2-x}Se$ templates through anion extraction [31].

The hollow and mesoporous ZnTe microspheres (Fig. 12.19) have been successfully synthesized via the hydrothermal approach using NaOH as the structure-directing agent [20]. Reaction parameters like the reaction temperature and time are found to play an essential role in the formation of such microstructures. At a low temperature of 120°C, the temperature was not high enough for complete reduction and the inward diffusion of tellurium-based rod-like structures. Thus, both the structures of spheres and rods were visible (Fig. 12.19b). As the temperature increased to 140°C, the yield of the microspheres increased (Fig. 12.19b). Homogeneous and uniform hollow and mesoporous microspheres were formed at a reaction temperature of 160°C (Fig. 12.19c). As the temperature increased further to 180°C, it resulted in the nucleation of relatively large ZnTe crystals along with the microspheres (Fig. 12.19d, e) due to agglomeration at such an elevated temperature. The as-synthesized ZnTe microspheres exhibit relatively high photocatalytic activity for the photoconversion of CO_2 into CH_4 under visible-light irradiation (>420 nm) [20]. Applying a similar

method, the gelatin-assisted hydrothermal reaction of zinc acetate and thiourea was developed for the synthesis of ZnS hollow nanospheres [89].

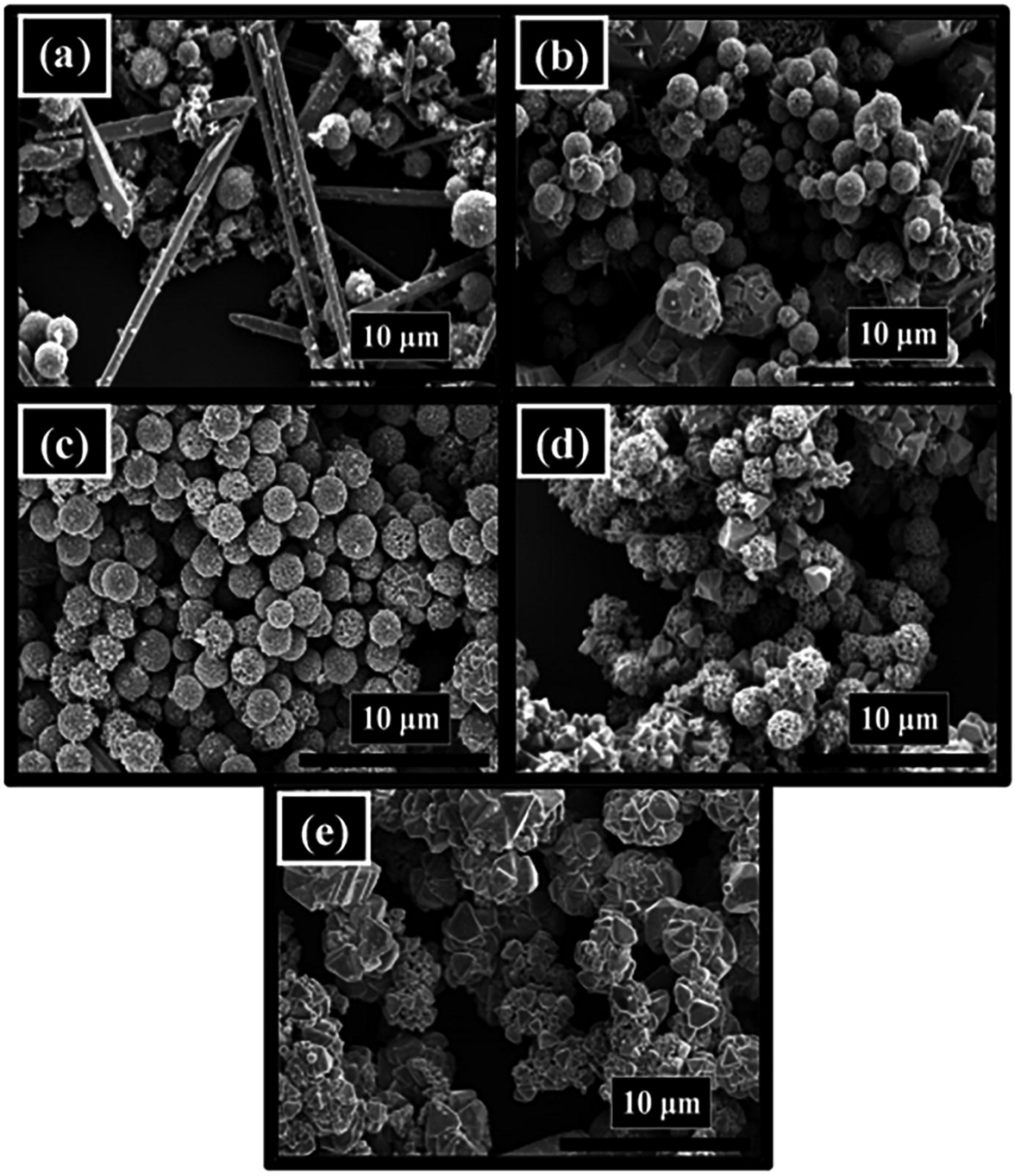

Fig. 12.19 Field-emission SEM images of ZnTe microspheres synthesized at different reaction temperatures: (**a**) 120, (**b**) 140, (**c**) 160, (**d**) 180, and (**e**) 200°C (Reprinted with permission from [20]. Copyright 2015: Royal Society of Chemistry)

Hollow nanospheres of $Cd_xZn_{1-x}S$ solid solutions were synthesized through a template-free process. $Cd(CH_3COO)_2 \cdot 2H_2O$, $Zn(CH_3COO)_2 \cdot 2H_2O$, and thiourea were used as the starting materials and dissolved in ethylene glycol, which works as a coordinating solvent. The results show that the range of Cd^{2+} molar ratios between 0.7 and 0.5 is suitable for obtaining information on the uniform volvox-like nanospheres. $Cd_{0.57}Zn_{0.43}S$ nanospheres showed the best photocatalytic activity with a hydrogen generation rate of 1766.4 mmol/h^{-1} g^{-1}. Remarkable photocatalytic water-splitting properties of these solid solutions are attributed to the synergetic effect of the tunable band gap, crystalline structure, and large surface area [102].

A couple of recent studies explored the synthesis and properties of two-dimensional porous sheets made of II–VI materials. Usually, a cation-exchange reaction leading to the Kirkendall effect is employed to obtain such structures [27, 85, 96]. Guo et al. [27] have successfully demonstrated a strategy to prepare porous CdSe nanobelts from ZnSe – hydrazine hybrid nanobelts through a cation-exchange reaction. The native photoelectric properties of such structures implemented in the devices fabricated with a single nanobelt and assembled nanobelt array indicate that they present a rapid, stable, and repeatable photoelectric response. Nanobelts also exhibited highly selective photoelectric sensing toward Cu^{2+} with a low detection limit down to 0.1 ppm (Fig. 12.20).

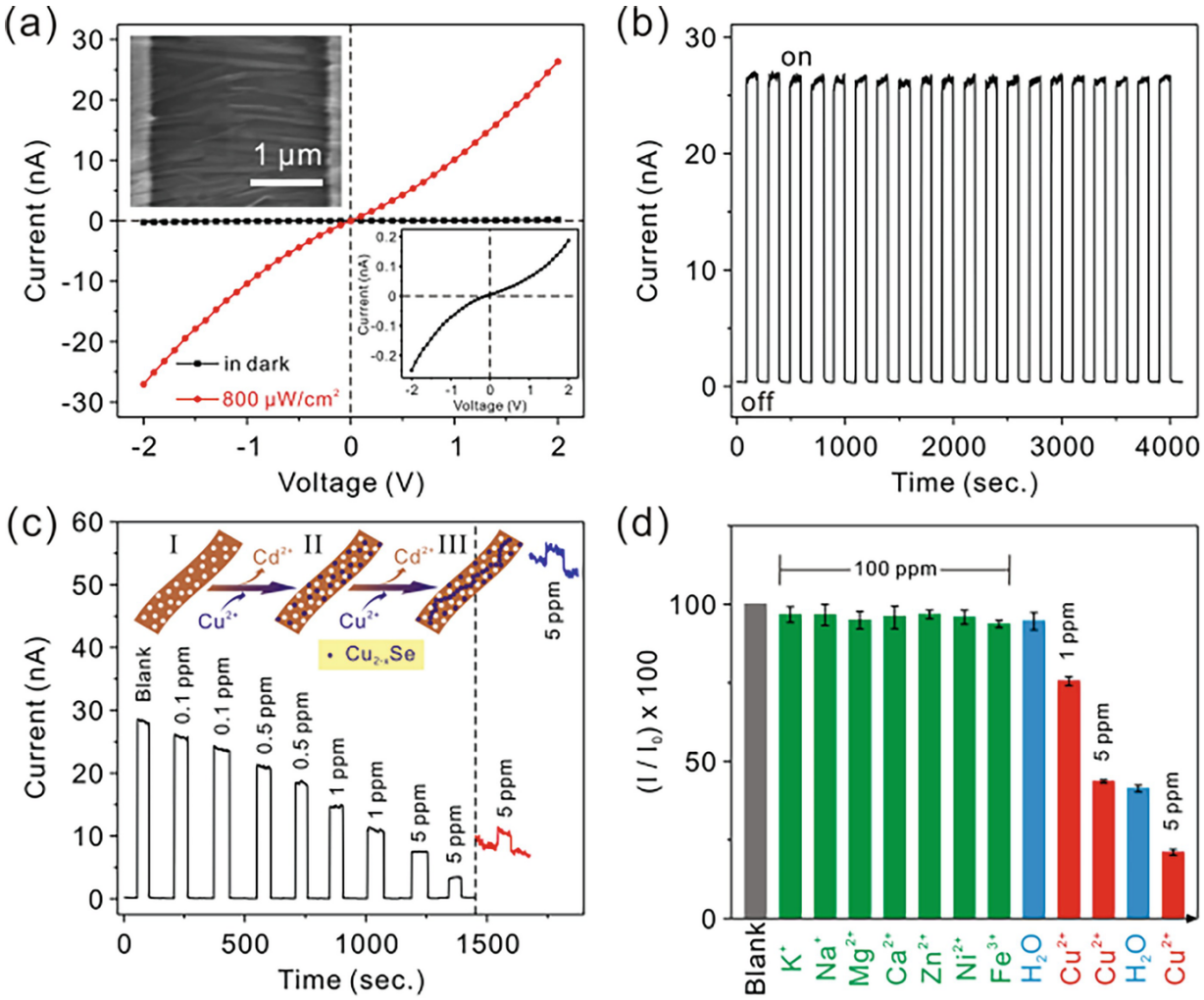

Fig. 12.20 (**a**) I–V curves at 800 μW/cm^2 with a light intensity of 480 nm or in the dark, the bottom right inset corresponds to I–V curve in the dark (the top-left inset is an SEM image of the fabricated device with assembled nanobelt array); (**b**) I–t curve of the fabricated device at 800 μW/cm^2 with incident light of 480 nm for a period of about 100 s at an applied voltage of 2 V; (**c**) photoelectric sensing performances of the nanodevice fabricated with the assembled nanobelt array toward different Cu^{2+} concentration, wherein the inset corresponds to the scheme of the cation-exchange formation of the $Cu_{2-x}Se$-doped CdSe nanobelts; and (**d**) relative responses (sensing photoelectric current (I) versus initial photoelectric current (I 0)) of the fabricated device toward different low concentrations of Cu^{2+} and 100 ppm of the other metal ions, wherein the responses were continuously measured from left to right (Reprinted with permission from [27]. Copyright 2018: Wiley)

12.7 Stability Issues of Sensors Based on II–VI Nanoparticles

High reactivity and developed surface of nanoparticles also raise a considerable challenge to their stability. It has several aspects – colloidal stability during the synthesis, storage, and processing, preservation of desired properties in the assembled active components of the sensor, stability, and reproducibility of the generated signal during the exploitation, issues related to component leakage, and, ultimately, utilization of the nanostructured device.

Since they are widely used as biomarkers, colloidal stability has been extensively studied for the CdSe-core-based core-shell QDs (like CdSe/ZnS). Usually synthesized in the organic phase and transferred to aqueous media, their stability strongly depends on the pH value that can influence the formation of agglomerates [8]. Low nanoparticle concentration in solution often facilitates ligands' detachment from their surface. On the other hand, if their concentration is too high, the formation of agglomerates is accelerated. However, it is possible to obtain colloidal solutions of these QDs that are stable for a long time without any noticeable aggregate formation. The content of ionic species in the solution also affects the colloidal stability, as they can remove ligands from the QDs surface or affect the particles' zeta potential. The stability is not only related to the medium in which the QDs are dispersed but is also strongly linked to the choice of ligands. Thiol ligands have been shown to form direct covalent bonds to the surface of two to six semiconductors, but desorption of such molecules during processing steps was also described as leading to agglomeration [60, 71, 76, 98].

While the PL intensity can even be initially boosted upon exposure to sunlight due to the surface passivation, since nanoparticles may undergo some structural and compositional changes under prolonged illumination, their PL intensity and the PL peak positions may change with time. It is important in which (inert or not) atmosphere the QDs are kept, as the presence of oxygen can play a major role in the degradation dynamics, as it can promote the formation of oxides on the surface of QDs. Extended storage of their solutions in the air may lead to the complete oxidation of their surface atoms. The PL peak of QD solutions illuminated in the air for a continuous period of time may undergo a blueshift caused by an effective size reduction of the QD core due to photooxidation, thus enhancing the effects of electron confinement and photobleaching due to the formation of nonradiative defects at the surface. Once the QD surface is fully oxidized,

the PL signal can vanish completely. Both effects could lead to the broadening of the PL spectra because of the gradual loss of ligands and the subsequent particle agglomeration. Exposure to heat could also reduce the PL intensity of such QDs, which is partly related to the removal of surface ligands at elevated temperatures [101].

A comparison of core-only and core-shell QDs with different shell thicknesses reveals that the particles without shell experience faster photobleaching. In contrast, core-shell QDs with moderate thicknesses show a relatively stable PL, but for very thick shells, the interface strain increases, thus resulting in more defects and the acceleration of degradation. Other II–VI QD materials such as CdSe and CdTe also show decreased PL signal due to agglomeration or photooxidation, with CdTe QDs being the most fragile [40, 48].

The degradation processes of semiconductor nanoparticles assembled in films are different from those in colloidal solutions. Various approaches have been developed to protect nanoparticles in films from degradation by controlling the composition of their shells and ligands. QDs and other II–VI nanostructures have been protected by bulky ligands, physical incorporation in polymer matrices, and covalent bonding with them. The ligands are not so easily removed from the surface in a solvent-free environment, and the dot packing is dense, enhancing interactive effects such as energy and charge transfer inside the film, thus altering the degradation pathways. The degradation of films in an aqueous environment will be affected by the penetration of water molecules to the core–ligand interface and will result in luminescence losses. This kinetic process can be especially damaging if the ligand density is low or the bond strength is not sufficiently high. The stability of nanoparticles in electroluminescent devices also can be enhanced by using inorganic charge transport layers and by improving charge balance.

The majority of sensing applications based on II–VI nanoparticles are based on chemical interaction with analytes (ions or biomolecules). Typically, ion exchange reaction or covalent bonding occurs in this case, which leads to changes in the intensity or chromaticity of the photoluminescence of the nanoparticles. Such interactions are usually irreversible, which makes them single-use sensors [6, 86, 90]. A similar approach is based on the photoelectrochemical properties of the QDs or their composites [33]. In Fig. 12.21, basic principle of this sensor is shown.

Composite electrode consisting of ITO, reduced graphene oxide, and CdS nanoparticles demonstrates lower photocurrent response in the presence of Copper ions. Such photoelectrode response for Cu^{2+} ion detection had a linear range of 0.5–120 μM, with a limit of detection of 16 nM. However, remarkable irreversibility can be seen after a few cycles.

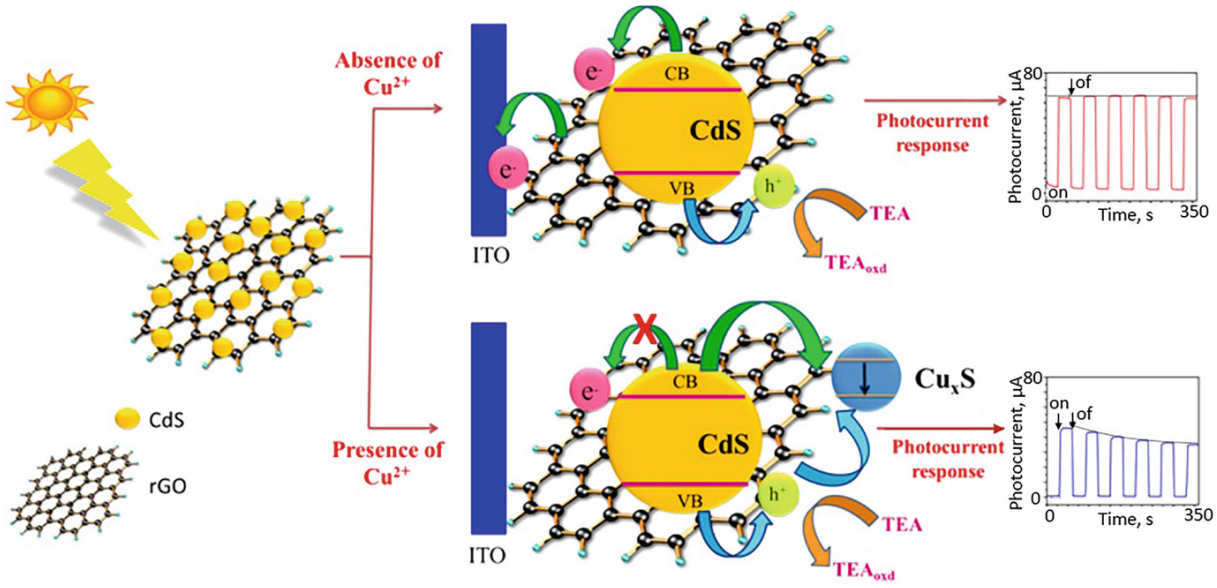

Fig. 12.21 The mechanism for sensing Cu^{2+} ions based on ITO/CdS-rGO nanocomposites (TEA, triethanolamine) (Reprinted from [33]. Published by PLOS as open access)

Based on the selective quenching by Cu^{2+} of the near-infrared electrochemiluminescence emission from the 3-mercaptopropionic acid (MPA)-capped CdTe/CdS core-shell quantum dots deposited at the ITO anode, a simple and sensitive method for the determination of Cu^{2+} was developed. Authors reported high reversibility of the sensor, with recoveries of the PL intensity varying from 93.3% to 104.6% [78].

Further increase of the stability and reproducibility of the nanoparticle-based sensors is the functionalization of nanoparticles with biomolecules that allows their safe and green use in the detection of compounds. Functionalization allows achieving the most crucial property of biosensors – its selectivity. Even so, an extra coating may hinder interaction between analyte and particles, decreasing sensitivity [64, 75].

Strong covalent bonding between the polymer matrix and the nanoparticles is the ideal approach to enhance their oxygen and moisture stability, photostability, and thermal stability when direct interaction with the nanoparticle surface is not critical for sensing [39]. For devices based on

electrochemical interactions, lifetimes can be enhanced by replacing unstable and reactive organic materials with stable inorganic charge transport materials [3]. As understanding of the degradation mechanisms of II–VI nanoparticles increases, more stable structures and sensing concepts are to be developed.

References

1. Ackerman M, Tang X, Guyot-Sionnest P (2018) Fast and sensitive colloidal quantum dot mid-wave infrared photodetectors. ACS Nano 12:7264–7271. https://doi.org/10.1021/acsnano.8b03425
[Crossref]
2. Adachi S (2005) Properties of Group-IV, III-V and II-VI semiconductors. Wiley, Hoboken
[Crossref]
3. Albaladejo-Siguan M, Baird E, Becker-Koch D, Li Y, Rogach A, Vaynzof Y (2021) Stability of quantum dot solar cells: a matter of (life)time. Adv Energy Mater 11:2003457. https://doi.org/10.1002/aenm.202003457
[Crossref]
4. Alivisatos AP (1996) Perspectives on the physical chemistry of semiconductor nanocrystals. J Phys Chem 100(31):13226–13239
[Crossref]
5. Andriichuk YM, Liavynets OS, Khalavka YB (2018) Influence of the synthesis temperature on the growth and optical properties of the cadmium selenide nanoparticles synthesized using the cadmium complex with 4-Aminobenzenesulfamide. Nanosistemi, Nanomater Nanotehnologii 16:693–700. https://doi.org/10.15407/nnn.16.04.693
6. Bian W, Wang F, Zhang H, Zhang L, Wang L, Shuang S (2015) Fluorescent probe for detection of Cu^{2+} using core-shell CdTe/ZnS quantum dots. Luminescence 30:1064–1070. https://doi.org/10.1002/bio.2859
[Crossref]
7. Bie C, Fu J, Cheng B, Zhang L (2018) Ultrathin CdS nanosheets with tunable thickness and efficient photocatalytic hydrogen generation. Appl Surf Sci 462:606–614. https://doi.org/10.1016/j.apsusc.2018.08.130
[Crossref]
8. Boldt K, Bruns OT, Gaponik N, Eychmüller A (2006) Comparative examination of the stability of semiconductor quantum dots in various biochemical buffers. J Phys Chem B 110:1959–1963. https://doi.org/10.1021/jp056371p
[Crossref]
9. Bodo B, Kalita PK (2010) Chemical synthesis of ZnS:Cu nanosheets. AIP Conf Proc 1276:31–36

[Crossref]

10. Bouet C, Mahler B, Nadal B, Abecassis B, Tessier M, Ithurria S, Xu X, Dubertret B (2013) Two-dimensional growth of CdSe nanocrystals, from nanoplatelets to nanosheets. Chem Mater 25:639–645. https://doi.org/10.1021/cm304080q
[Crossref]

11. Cao X, Cai X, Feng Q, Jia S, Wang N (2012) Ultrathin CdSe nanosheets: synthesis and application in simultaneous determination of catechol and hydroquinone. Anal Chim Acta 752:101–105. https://doi.org/10.1016/j.aca.2012.09.034
[Crossref]

12. Carbone L, Cozzoli PD (2010) Colloidal heterostructured nanocrystals: synthesis and growth mechanisms. Nano Today 5:449–493. https://doi.org/10.1016/j.nantod.2010.08.006
[Crossref]

13. Carbone L, Nobile C, De Giorgi M, Della Sala F, Morello G, Pompa P et al (2007) Synthesis and micrometer-scale assembly of colloidal CdSe/CdS nanorods prepared by a seeded growth approach. Nano Lett 7:2942–2950. https://doi.org/10.1021/nl0717661
[Crossref]

14. Chen S, Wang L-W (2012) Thermodynamic oxidation and reduction potentials of photocatalytic semiconductors in aqueous solution. Chem Mater 24:3659–3666. https://doi.org/10.1021/cm302533s
[Crossref]

15. Choi Y-J, Park K-S, Park J-G (2010) Network-bridge structure of CdS_xSe_{1-x} nanowire-based optical sensors. Nanotechnology 21:505605. https://doi.org/10.1088/0957-4484/21/50/505605
[Crossref]

16. Costi R, Saunders AE, Banin U (2010) Colloidal hybrid nanostructures: a new type of functional materials. Angew Chemie Int Ed 49:4878–4897. https://doi.org/10.1002/anie.200906010
[Crossref]

17. Crouse MM, James TL, Crouse D (2008) Fabrication, characterization of II-VI semiconductor nanowires and applications in infrared focal plane arrays. Proc. SPIE 7095, Nanophotonics and Macrophotonics for Space Environments II, 70950J. https://doi.org/10.1117/12.795399

18. Dabbousi BO, Rodriguez-Viejo J, Mikulec FV, Heine JR, Mattoussi H, Ober R et al (1997) (CdSe)ZnS core−shell quantum dots: synthesis and characterization of a size series of highly luminescent nanocrystallites. J Phys Chem B 101:9463–9475. https://doi.org/10.1021/jp971091y
[Crossref]

19. Dedong H, Ying-Kai L, Yu D-P (2015) Multicolor photodetector of a single Er^{3+}-doped CdS nanoribbon. Nanoscale Res Lett 10:285. https://doi.org/10.1186/s11671-015-0975-3
[Crossref]

20. Ehsan MF, Ashiq MN, He T (2015) Hollow and mesoporous ZnTe microspheres: synthesis and visible-light photocatalytic reduction of carbon dioxide into methane. RSC Adv 5:6186–6194.

https://doi.org/10.1039/C4RA13593H

21. Fasoli A, Colli A, Hofmann S, Ducati C, Robertson J, Ferrari AC (2006). Shape-selective synthesis of II–VI semiconductor nanowires. Physica Status Solidi (b), 243(13), 3301–3305. https://doi.org/10.1002/pssb.200669142

22. Fasoli A, Colli A, Kudera S, Manna L, Hofmann S, Ducati C et al (2007) Catalytic and seeded shape-selective synthesis of II–VI semiconductor nanowires. Phys E Low-Dimens Syst Nanostruct 37:138–141. https://doi.org/10.1016/j.physe.2006.06.010

23. Feng B, Yang J, Cao J, Yang L, Gao M, Wei M, Zhai H, Sun Y, Song H (2013) Growth mechanism, optical and photocatalytic properties of the ZnSe nanosheets constructed by the nanoparticles. J Alloys Compd 555:241–245. https://doi.org/10.1016/j.jallcom.2012.12.074 [Crossref]

24. Feng W, Yuan J, Zhang L, Hu W, Wu Z, Wang X et al (2020) Atomically thin ZnS nanosheets: facile synthesis and superior piezocatalytic H_2 production from pure H_2O. Appl Catal B Environ 277:119250. https://doi.org/10.1016/j.apcatb.2020.119250 [Crossref]

25. Gao T, Wang T (2010) Two-dimensional single crystal CdS nanosheets: synthesis and properties. Cryst Growth Des 10:4995–5000. https://doi.org/10.1021/cg1010852 [Crossref]

26. Gaponik N, Talapin DV, Rogach AL, Hoppe K, Shevchenko EV, Kornowski A et al (2002) Thiol-capping of CdTe nanocrystals: an alternative to organometallic synthetic routes. J Phys Chem B 106:7177–7185. https://doi.org/10.1021/jp025541k [Crossref]

27. Guo Z, Su Y, Li Y-X, Li G, Huang X-J (2018) Porous single-crystalline CdSe nanobelts: cation-exchange synthesis and highly selective photoelectric sensing toward Cu^{2+}. Chem Eur J 24:9877–9883. https://doi.org/10.1002/chem.201801215 [Crossref]

28. Harrison MT, Kershaw SV, Burt MG, Rogach AL, Kornowski A, Eychmüller A, Weller H (2000) Colloidal nanocrystals for telecommunications. Complete coverage of the low-loss fiber windows by mercury telluride quantum dot. Pure Appl Chem 72:295–307. https://doi.org/10.1351/pac200072010295 [Crossref]

29. Harrison P, Valavanis A (2016) Quantum wells, wires and dots. Wiley, Haboken [Crossref]

30. Hu L, Yan J, Liao M, Xiang H, Gong X, Zhang L, Fang X (2012) An optimized ultraviolet-a light photodetector with wide-range photoresponse based on ZnS/ZnO biaxial nanobelt. Adv Mater 24:2305–2309. https://doi.org/10.1002/adma.201200512 [Crossref]

31. Huang X, Zou Y, Hao J, Jiang J (2018) Synthesis of hollow ZnSe nanospheres with high photocatalytic activity: synergetic effect of cation exchange and selective Cu2−xSe template etching. CrystEngComm 20:4020–4024. https://doi.org/10.1039/C8CE00649K

[Crossref]
32. Hussain RA, Hussain I (2020) Cadmium selenide nanowires from growth to applications. Mater Res Express 6:122007. https://doi.org/10.1088/2053-1591/ab69be
[Crossref]
33. Ibrahim I, Lim HN, Huang NM, Pandikumar A (2016) Cadmium sulphide-reduced graphene oxide-modified photoelectrode-based photoelectrochemical sensing platform for copper(II) ions. PLoS One 11:e0154557. https://doi.org/10.1371/journal.pone.0154557
[Crossref]
34. Jing L, Kershaw SV, Li Y, Huang X, Li Y, Rogach AL, Gao M (2016) Aqueous based semiconductor nanocrystals. Chem Rev 116:10623–10730. https://doi.org/10.1021/acs.chemrev.6b00041
[Crossref]
35. Justo Y, Geiregat P, van Hoecke K, Vanhaecke F, De Mello DC, Hens Z (2013) Optical properties of PbS/CdS core/shell quantum dots. J Phys Chem C 117:20171–20177. https://doi.org/10.1021/jp406774p
[Crossref]
36. Kanaras AG, Sönnichsen C, Liu H, Alivisatos AP (2005) Controlled synthesis of hyperbranched inorganic nanocrystals with rich three-dimensional structures. Nano Lett 5:2164–2167. https://doi.org/10.1021/nl0518728
[Crossref]
37. Kim S, Fisher B, Eisler H-J, Bawendi M (2003) Type-II quantum dots: CdTe/CdSe(Core/Shell) and CdSe/ZnTe(Core/Shell) heterostructures. J Am Chem Soc 125:11466–11467. https://doi.org/10.1021/ja0361749
[Crossref]
38. Kirkendall E (1942) Diffusion of zinc in alpha brass. Trans Metall Soc AIME 147:104–110
39. Ko J, Jeong BG, Chang JH, Joung JF, Yoon S-Y, Lee DC et al (2020) Chemically resistant and thermally stable quantum dots prepared by shell encapsulation with cross-linkable block copolymer ligands. NPG Asia Mater 12:19. https://doi.org/10.1038/s41427-020-0200-4
[Crossref]
40. Landes CF, Braun M, El-Sayed MA (2001) On the nanoparticle to molecular size transition: fluorescence quenching studies. J Phys Chem B 105:10554–10558. https://doi.org/10.1021/jp0118726
[Crossref]
41. Li D, Xing G, Tang S, Li X, Fan L, Li Y (2017) Ultrathin ZnSe nanowires: one-pot synthesis via a heat-triggered precursor slow releasing route, controllable Mn doping and application in UV and near-visible light detection. Nanoscale 9:15044–15055. https://doi.org/10.1039/c7nr03547k
[Crossref]
42. Lin H, Wei L, Wu C, Chen Y, Yan S, Mei L, Jiao J (2016) High-performance self-powered photodetectors based on ZnO/ZnS core-shell nanorod arrays. Nanoscale Res Lett 11:420. https://doi.org/10.1186/s11671-016-1639-7

[Crossref]
43. Liu B, Zeng HC (2003) Hydrothermal synthesis of ZnO nanorods in the diameter regime of 50 nm. J Am Chem Soc 125:4430–4431. https://doi.org/10.1021/ja0299452
[Crossref]
44. Liu D, Li X, Shi Z, Zhu B, Chen X, Yang J (2018) Synthesis of porous ZnS/ZnSe nanosheets for enhanced visible light photocatalytic activity. J Mater Sci Mater Electron 29:11605–11612. https://doi.org/10.1007/s10854-018-9258-y
[Crossref]
45. Livache C, Martinez B, Goubet N, Gréboval C, Qu J, Chu A et al (2019) A colloidal quantum dot infrared photodetector and its use for intraband detection. Nat Commun 10:2125. https://doi.org/10.1038/s41467-019-10170-8
[Crossref]
46. Lou Z, Li L, Shen G (2016) Ultraviolet/visible photodetectors with ultrafast, high photosensitivity based on 1D ZnS/CdS heterostructures. Nanoscale 8:5219–5225. https://doi.org/10.1039/C5NR08792A
[Crossref]
47. Ma C, Moore D, Ding Y, Li J, Wang ZL (2004) Nanobelt and nanosaw structures of II-VI semiconductors. Int J Nanotechnol 1:431. https://doi.org/10.1504/ijnt.2004.005978
[Crossref]
48. Ma J, Chen J-Y, Zhang Y, Wang P-N, Guo J, Yang W-L, Wang C-C (2007) Photochemical instability of thiol-capped CdTe quantum dots in aqueous solution and living cells: process and mechanism. J Phys Chem B 111:12012–12016. https://doi.org/10.1021/jp073351+
[Crossref]
49. Manna L, Milliron DJ, Meisel A, Scher EC, Alivisatos AP (2003) Controlled growth of tetrapod-branched inorganic nanocrystals. Nat Mater 2:382–385. https://doi.org/10.1038/nmat902
[Crossref]
50. Mashford BS, Stevenson M, Popovic Z, Hamilton C, Zhou Z, Breen C et al (2013) High-efficiency quantum-dot light-emitting devices with enhanced charge injection. Nat Photonics 7:407–412. https://doi.org/10.1038/nphoton.2013.70
[Crossref]
51. Matras-Postołek K, Sovinska S, Węgrzynowicz A (2019) Synthesis and characterization of ZnSe and ZnSe:Mn nanosheets and microflowers with high photoactive properties by microwave-assisted method. Chem Eng Process Process Intensif 135:204–216. https://doi.org/10.1016/j.cep.2018.11.022
[Crossref]
52. Miao J-J, Jiang L-P, Liu C, Zhu J-MJ-J, Zhu J-MJ-J (2007) General sacrificial template method for the synthesis of cadmium chalcogenide hollow structures. Inorg Chem 46:5673–5677. https://doi.org/10.1021/ic700404n
[Crossref]

53. Miao J, Liu B (2015) II–VI semiconductor nanowires: ZnO. In: Arbiol J, Xiong Q (eds) Semiconductor nanowires. Woodhead Publishing, Sawston, pp 3–28
[Crossref]
54. Mu Z, Zheng Q, Liu R, Malik MWI, Tang D, Zhou W, Wan Q (2019) 1D ZnSSe-ZnSe axial heterostructure and its application for photodetectors. Adv Electron Mater 5:1800770. https://doi.org/10.1002/aelm.201800770
[Crossref]
55. Nie B, Luo L-B, Chen J-J, Hu J-G, Wu C-Y, Wang L et al (2013) Fabrication of p-type ZnSe:Sb nanowires for high-performance ultraviolet light photodetector application. Nanotechnology 24:95603. https://doi.org/10.1088/0957-4484/24/9/095603
[Crossref]
56. Pan Z, Li J, Zhou K (2018) Wrinkle-free atomically thin CdS nanosheets for photocatalytic hydrogen evolution. Nanotechnology 29:215402. https://doi.org/10.1088/1361-6528/aab4d5
[Crossref]
57. Park H, Chung H, Kim W (2013) Synthesis of ultrathin wurtzite ZnSe nanosheets. Mater Lett 99:172–175. https://doi.org/10.1016/j.matlet.2013.03.038
[Crossref]
58. Pedetti S, Ithurria S, Heuclin H, Patriarche G, Dubertret B (2014) Type-II CdSe/CdTe core/crown semiconductor nanoplatelets. J Am Chem Soc 136:16430–16438. https://doi.org/10.1021/ja509307m
[Crossref]
59. Pedetti S, Nadal B, Lhuillier E, Mahler B, Bouet C, Abécassis B, Xu X, Dubertret B (2013) Optimized synthesis of CdTe nanoplatelets and photoresponse of CdTe nanoplatelets films. Chem Mater 25:2455–2462. https://doi.org/10.1021/cm4006844
[Crossref]
60. Pons T, Uyeda HT, Medintz IL, Mattoussi H (2006) Hydrodynamic dimensions, electrophoretic mobility, and stability of hydrophilic quantum dots. J Phys Chem B 110:20308–20316. https://doi.org/10.1021/jp065041h
[Crossref]
61. Qiu S, Shen Y, Wei G, Yao S, Xi W, Shu M et al (2019) Carbon dots decorated ultrathin CdS nanosheets enabling in-situ anchored Pt single atoms: a highly efficient solar-driven photocatalyst for hydrogen evolution. Appl Catal B Environ 259:118036. https://doi.org/10.1016/j.apcatb.2019.118036
[Crossref]
62. Rai SC, Wang K, Chen J, Marmon JK, Bhatt M, Wozny S et al (2015) Enhanced broad band photodetection through piezo-phototronic effect in CdSe/ZnTe Core/shell nanowire array. Adv Electron Mater 1:1400050. https://doi.org/10.1002/aelm.201400050
[Crossref]
63. Rosina I, Martín-García B, Spirito D, Dang Z, Gariano G, Marras S et al (2020) Metastable CdTe@HgTe Core@Shell nanostructures obtained by partial cation exchange evolve into

sintered CdTe films upon annealing. Chem Mater 32:2978–2985. https://doi.org/10.1021/acs.chemmater.9b05281
[Crossref]

64. Sabzehmeidani MM, Kazemzad M (2022) Quantum dots based sensitive nanosensors for detection of antibiotics in natural products: a review. Sci Total Environ 810:151997. https://doi.org/10.1016/j.scitotenv.2021.151997
[Crossref]

65. Seo K, Bong J, Kim J-W, Song Y-H, Shin YH, Kim Y, Ju S (2015) Substrate-dependent differences in the crystal structures and optical properties of ZnSe nanowires. J Nanomater 2015:1–6. https://doi.org/10.1155/2015/201420
[Crossref]

66. She G, Mu L, Shi W (2009) Electrodeposition of one-dimensional nanostructures. Recent Pat Nanotechnol 3:182–191. https://doi.org/10.2174/187221009789177777
[Crossref]

67. Sliusariak T, Andriichuk Y, Vojtovych S, Zhukovskyi M, Khalavka Y (2020) Synthesis of CdSe/ZnS nanoparticles with multiple photoluminescence. Phys Chem Solid State 21:105–112. https://doi.org/10.15330/pcss.21.1.105-112

68. Takahashi T, Nichols P, Takei K, Ford AC, Jamshidi A, Wu MC et al (2012) Contact printing of compositionally graded CdS_xSe_{1-x}nanowire parallel arrays for tunable photodetectors. Nanotechnology 23:45201. https://doi.org/10.1088/0957-4484/23/4/045201
[Crossref]

69. Talapin DV, Nelson JH, Shevchenko EV, Aloni S, Sadtler B, Alivisatos AP (2007) Seeded growth of highly luminescent CdSe/CdS nanoheterostructures with rod and tetrapod morphologies. Nano Lett 7:2951–2959. https://doi.org/10.1021/nl072003g
[Crossref]

70. Tang M, Xu P, Wen Z, Chen X, Pang C, Xu X et al (2018) Fast response CdS-CdSxTe1−x-CdTe core-shell nanobelt photodetector. Sci Bull 63:1118–1124. https://doi.org/10.1016/j.scib.2018.08.003
[Crossref]

71. Tang Z, Zhang Z, Wang Y, Glotzer SC, Kotov NA (2006) Self-assembly of CdTe nanocrystals into free-floating sheets. Science 314:274–278. https://doi.org/10.1126/science.1128045
[Crossref]

72. Tkach, Seti (2007) Exciton in closed and opened quantum dot. Condens Matter Phys 10:23. https://doi.org/10.5488/cmp.10.1.23
[Crossref]

73. Tkach MV, Seti JO, Voitsekhivska OM (2012) Electron and exciton quasi-stationary s-states in open spherical quantum dots. Acta Phys Pol A 122:207–211. https://doi.org/10.12693/aphyspola.122.207
[Crossref]

74. Utama MIB, de la Mata M, Zhang Q, Magen C, Arbiol J, Xiong Q (2013) The growth of ultralong ZnTe micro/nanostructures: the influence of polarity and twin direction on the morphogenesis of nanobelts and nanosheets. Cryst Growth Des 13:2590–2596. https://doi.org/10.1021/cg4003498
[Crossref]
75. Valenti G, Rampazzo E, Kesarkar S, Genovese D, Fiorani A, Zanut A et al (2018) Electrogenerated chemiluminescence from metal complexes-based nanoparticles for highly sensitive sensors applications. Coord Chem Rev 367:65–81. https://doi.org/10.1016/j.ccr.2018.04.011
[Crossref]
76. Vasiliev RB, Lazareva EP, Karlova DA, Garshev AV, Yao Y, Kuroda T et al (2018) Spontaneous folding of CdTe nanosheets induced by ligand exchange. Chem Mater 30:1710–1717. https://doi.org/10.1021/acs.chemmater.7b05324
[Crossref]
77. Wang F, Zhang M, Chen W, Javaid S, Yang H, Wang S et al (2020) Atomically thin heavy-metal-free ZnTe nanoplatelets formed from magic-size nanoclusters. Nanoscale Adv 2:3316–3322. https://doi.org/10.1039/d0na00409j
[Crossref]
78. Wang J, Jiang X (2015) Anodic near-infrared electrochemiluminescence from CdTe/CdS coresmall/shellthick quantum dots and their sensing ability of Cu^{2+}. Sensors Actuators B Chem 207:552–555. https://doi.org/10.1016/j.snb.2014.10.112
[Crossref]
79. Wang J, Li G, Li L (2016) Synthesis strategies about 2D materials. In: Nayak PK (ed) Two-dimensional materials. IntechOpen, London, pp 1–20. https://doi.org/10.5772/63918
80. Wang K, Rai SC, Marmon J, Chen J, Yao K, Wozny S et al (2014) Nearly lattice matched all wurtzite CdSe/ZnTe type II core–shell nanowires with epitaxial interfaces for photovoltaics. Nanoscale 6:3679–3685. https://doi.org/10.1039/C3NR06137J
[Crossref]
81. Wang X, Xie Z, Huang H, Liu Z, Chen D, Shen G (2012) Gas sensors, thermistor and photodetector based on ZnS nanowires. J Mater Chem 22:6845. https://doi.org/10.1039/c2jm16523f
[Crossref]
82. Wood V, Bulović V (2010) Colloidal quantum dot light-emitting devices. Nano Rev 1:5202. https://doi.org/10.3402/nano.v1i0.5202
[Crossref]
83. Wu C, Jie J, Wang L, Yu Y, Peng Q, Zhang X et al (2010) Chlorine-doped n-type CdS nanowires with enhanced photoconductivity. Nanotechnology 21:505203. https://doi.org/10.1088/0957-4484/21/50/505203
[Crossref]

84. Wu J, Chen S, Seeds A, Liu H (2015) Quantum dot optoelectronic devices: lasers, photodetectors and solar cells. J Phys D Appl Phys 48:363001. https://doi.org/10.1088/0022-3727/48/36/363001
[Crossref]

85. Wu X, Yu Y, Liu Y, Xu Y, Liu C, Zhang B (2012) Synthesis of hollow $Cd_xZn_{1-x}Se$ nanoframes through the selective cation exchange of inorganic–organic hybrid ZnSe–amine nanoflakes with cadmium ions. Angew Chemie Int Ed 51:3211–3215. https://doi.org/10.1002/anie.201108098
[Crossref]

86. Xia Y-S, Zhu C-Q (2008) Use of surface-modified CdTe quantum dots as fluorescent probes in sensing mercury (II). Talanta 75:215–221. https://doi.org/10.1016/j.talanta.2007.11.008
[Crossref]

87. Xu Y, Zhao W, Xu R, Shi Y, Zhang B (2013) Synthesis of ultrathin CdS nanosheets as efficient visible-light-driven water splitting photocatalysts for hydrogen evolution. Chem Commun 49:9803–9805. https://doi.org/10.1039/c3cc46342g
[Crossref]

88. Yan J, Fang X, Zhang L, Bando Y, Gautam UK, Dierre B et al (2008) Structure and cathodoluminescence of individual ZnS/ZnO biaxial nanobelt heterostructures. Nano Lett 8:2794–2799. https://doi.org/10.1021/nl801353c
[Crossref]

89. Yan Q, Wu A, Yan H, Dong Y, Tian C, Jiang B, Fu H (2017) Gelatin-assisted synthesis of ZnS hollow nanospheres: the microstructure tuning, formation mechanism and application for Pt-free photocatalytic hydrogen production. CrystEngComm 19:461–468. https://doi.org/10.1039/C6CE02127A
[Crossref]

90. Yang P, Zhao Y, Lu Y, Xu Q-Z, Xu X-W, Dong L, Yu S-H (2011) Phenol formaldehyde resin nanoparticles loaded with CdTe quantum dots: a fluorescence resonance energy transfer probe for optical visual detection of copper(II) ions. ACS Nano 5:2147–2154. https://doi.org/10.1021/nn103352b
[Crossref]

91. Yin J, Feng G, Zhou S (2015) Fabrication and photocatalytic property of ZnSe nanosheets. Optoelectron Adv Mater Rapid Commun 9:682–687

92. Yoon Y-J, Park K-S, Heo J-H, Park J-G, Nahm S, Choi KJ (2010) Synthesis of ZnxCd1−xSe (0 ≤x≤ 1) alloyed nanowires for variable-wavelength photodetectors. J Mater Chem 20:2386. https://doi.org/10.1039/b917531h
[Crossref]

93. Yu H, Xin C, Zhang Q, Utama MIB, Tong L, Xiong QH (2015) II–VI compound semiconductor nanowires: optical properties and nanophotonics. In: Arbiol J, Xiong Q (eds) Semiconductor nanowires. Woodhead Publishing, Sawston, pp 29–69
[Crossref]

94. Yu WW, Peng X (2002) Formation of high-quality CdS and other II-VI semiconductor nanocrystals in noncoordinating solvents: tunable reactivity of monomers. Angew Chemie Int Ed 41:2368–2371. https://doi.org/10.1002/1521-3773(20020703)41:13<2368::aid-anie2368>3.0.co;2-g
[Crossref]
95. Yu Y, Jiang Y, Zheng K, Zhu Z, Lan X, Zhang YY, Zhang YY, Xuan X (2014) Ultralow-voltage and high gain photoconductor based on ZnS:Ga nanoribbons for the detection of low-intensity ultraviolet light. J Mater Chem C 2:3583. https://doi.org/10.1039/c3tc32310b
[Crossref]
96. Yu Y, Zhang J, Wu X, Zhao W, Zhang B (2012) Nanoporous single-crystal-like $Cd_xZn_{1-x}S$ nanosheets fabricated by the cation-exchange reaction of inorganic–organic hybrid ZnS–amine with cadmium ions. Angew Chemie Int Ed 51:897–900. https://doi.org/10.1002/anie.201105786
[Crossref]
97. Zeng H, Du X-W, Singh SC, Kulinich SA, Yang S, He J, Cai W (2012) Nanomaterials via laser ablation/irradiation in liquid: a review. Adv Funct Mater 22:1333–1353. https://doi.org/10.1002/adfm.201102295
[Crossref]
98. Zhang T, Kotov NA, Glotzer SC (2007) Simulations and analysis of self-assembly of CdTe nanoparticles into wires and sheets. Nano Lett 7:1670–1675. https://doi.org/10.1021/nl0706300
[Crossref]
99. Zhang X, Meng D, Hu D, Tang Z, Niu X, Yu F, Ju L (2016a) Construction of coaxial ZnSe/ZnO p–n junctions and their photovoltaic applications. Appl Phys Express 9:25201. https://doi.org/10.7567/apex.9.025201
[Crossref]
100. Zhang X, Tang Z, Hu D, Meng D, Jia S (2016b) Nanoscale p–n junctions based on p-type ZnSe nanowires and their optoelectronic applications. Mater Lett 168:121–124. https://doi.org/10.1016/j.matlet.2016.01.044
[Crossref]
101. Zhao Y, Riemersma C, Pietra F, Koole R, de Mello DC, Meijerink A (2012) High-temperature luminescence quenching of colloidal quantum dots. ACS Nano 6:9058–9067. https://doi.org/10.1021/nn303217q
[Crossref]
102. Zhou H, Liu Q, Liu W, Ge J, Lan M, Wang C, Geng J, Wang P (2014) Template-free preparation of volvox-like $Cd_xZn_{1-x}S$ nanospheres with cubic phase for efficient photocatalytic hydrogen production. Chem Asian J 9:811–818. https://doi.org/10.1002/asia.201301428
[Crossref]

OceanofPDF.com

© The Author(s), under exclusive license to Springer Nature Switzerland AG 2023
G. Korotcenkov (ed.), *Handbook of II-VI Semiconductor-Based Sensors and Radiation Detectors*
https://doi.org/10.1007/978-3-031-19531-0_13

13. CdTe-Based Nanoparticles Synthesized in Solutions

Galyna Okrepka[1], Olena Tynkevych[2], Nataliia Doskaliuk[2], Ghenadii Korotcenkov[3] and Yuriy Khalavka[2] ✉

(1) Department of Medical and Pharmaceutical Chemistry, Bukovinian State Medical University, Chernivtsi, Ukraine
(2) Department of General Chemistry and Chemistry of Materials, Yuriy Fedkovych Chernivtsi National University, Chernivtsi, Ukraine
(3) Department of Physics and Engineering, Moldova State University, Chisinau, Moldova

✉ **Yuriy Khalavka**
Email: y.khalavka@chnu.edu.ua

Keywords II-VI compounds – CdS – CdTe – Application – Luminescence – Quantum yield – CdTe-based alloys – CdHgTe – CdMnTe – CdSTe – CdSeTe – Homogeneous – Graduated – CdZnTe – Core-shell structures – CdTe/$Cd_{1-x}Hg_xTe$ – CdTe/CdMnTe – CdTe/CdS/ZnS – CdTe/CdS – CdTe/CdSe – CdTe/HgTe – CdTe/HgTe/CdTe – CdTe/ZnS – CdTe/ZnTe – Core – Shell – Core-shell synthesis – Hybrid – Microwave-assisted – SILAR – NC synthesis – Aqueous – Colloidal NPs – Organic synthesis – Organometallic – Precursors – Ostwald ripening – Shape – Solvents – Stabilizers – Surfactants – Thiol capping ligands

13.1 Introduction

In recent years, interest in nanomaterials and, especially, nanoparticles, related in size to quantum dots (QDs), has increased significantly. Due to the specific properties of such nanoparticles, their use can significantly

improve the parameters of gas sensors, phosphors, photocatalysts, and photodetectors. This optimizing effect becomes especially noticeable when the specific properties of nanoparticles are combined with the physical and optical properties of the materials that form these nanomaterials. In this regard, nanoparticles of II-VI compounds are especially distinguished, which, along with a high radiation absorption coefficient in a wide spectral range, have excellent luminescent properties. That is why there is such a high interest in the study and use of quantum dots based on these materials. For example, there are a number of studies, indicating that II-VI semiconductor nanocrystals (NCs) can be effectively used to detect the content of Hg^{2+} [12, 80], Zn^{2+} [8], Cu^{2+} [8], Ag^{+} [18], and Pb^{2+} ions [42] in various solutions.

Among II-VI compounds, CdTe and ternary alloys based on it are among the most widely used materials. Among nanomaterials, CdTe QDs are very important for the development of novel optoelectronic devices. The tunable luminescence and the high extinction coefficients of CdTe NCs determine their potential applicability in the fields of light-emitting diodes (LEDs), color conversion, solar cells, lasers, radiation detectors, and photodetectors for IR, visible, and UV spectral range (read Chaps. 9 and 17, Vol. 2). There is also a demand for water-compatible light emitters that give CdTe quantum dots prospective in biolabeling and bioimaging (Chap. 24, Vol. 3). That is why, in this chapter, we will consider the features of the synthesis of CdTe-based nanoparticles.

13.2 Synthesis of CdTe-Based Nanoparticles

Various methods are developed to prepare II-VI semiconductor NPs by a soft solution approach using reagents in different solvents. In particular, single-material colloidal NPs can be synthesized upon the reaction of molecular precursors in a liquid phase that may contain coordinating solvents and some stabilizing agents, such as ligands, polymers, surfactants, or soft templates (e.g., micelles). At a suitable temperature, the highly reactive species that are generated or injected, commonly called “monomers” or precursors, induce the nucleation of NCs and sustain their subsequent enlargement. The organic ligands, surfactants, or coordinating agents play several key roles along the course of NC formation. They can regulate the solution supersaturation degree upon forming complexes with

the monomers and participate in an adsorption-desorption equilibrium at the surface of the growing clusters, preventing irreversible aggregation and ensuring steady growth. The most popular routes for the synthesis of CdTe nanoparticles of various shape are summarized in Table 13.1. Depending on the solvent used, these methods are divided into organic synthetic methods and methods using aqueous media.

Table 13.1 Precursors and stabilizers that are used for the synthesis of CdTe NCs

Precursors and stabilizers	Solvent	Shape	References
Alkyl cadmium, silyl chalcogenides, phosphines, and phosphine chalcogenides	TOPO	Dots	Murray et al. [43]
CdO, TDPA, TOP-Te	TOPO	Dots	Yu et al. [69]
$CdMe_2$, TOP-Te	DDA/TOP	Dots	Talapin et al. [57]
CdO, TBP-Te/ODE or TOP-Te/ODE, OA	ODE	Dots, tetrapods	Yu et al. [69] and Kloper et al. [28]
CdO, TBP-Te, ODPA	ODE	Dots	Yang et al. [67]
TDPA, CdO, $Cd(OAc)_2$, Te, TOP, anhydrous toluene, $S(SiMe_3)_2$	TOPO	Nanorods, tetrapods, and spheres	Bunge et al. [6]
$CdCl_2$, TGA, other thiols (thioglycolic acid, 2-mercaptopropanoic acid, L-cysteine, 3-mercaptopropanoic acid, 2-mercaptobutanedioic acid, 1-thioglycerol, 2-mercaptoethylamine.)	Water	Dots	Rogach et al. [49]
ZnTe NRs in $CdCl_2$ vapor	Thermal transformation	Nanoribbons	Xie et al. [70]
Cadmium stearate, Te, TOP	TOPO	Wires	Kumar et al. [31]
CdO, TOP, Te, ODPA, methylphosphonic acid (MPA)	TOPO	Tetrapods	Carbone et al. [7]
CdO, Te, TOP, TDPA, 2-carboxyethyl phosphonic acid (CEPA), propylphosphonic acid (PPA), 1,2-ethylenediphosphonic acid (EDPA)	TOPO	Hyperbranched structures	Khalavka and Sönnichsen [26]
CdO, TOP-Te	TOPO, HDA	Dots	Bailey and Nie [3]

Precursors and stabilizers	Solvent	Shape	References
TDPA, CdO, $Cd(OAc)_2$, TOP, anhydrous toluene, $S(SiMe_3)_2$, Se, and Te	TOPO	Tetrapods	Li et al. [38]

Abbreviations: *CdO* cadmium oxide, *ODA* octadecylamine, *ODE* 1-octadecene, *ODPA* octadecylphosphonic acid, *HAD* hexadecylamine, *TBP* tributylphosphine, *TDPA* tetradecylphosphonic acid, *Te* tellurium powders, *TGA* thioglycolic acid, *TOP* tri-n-octylphosphine, *TOPO* tri-n-octylphosphine oxide, *CEPA* carboxyethyl phosphonic acid

It is important to note that by changing both the composition of the solution used for the synthesis of nanoparticles and the synthesis conditions, one can influence the shape of the synthesized nanoparticles. For example, the addition of small amounts of TDPA stabilizer, which contains a long carbon chain, which serves as a steric barrier to particle aggregation, allows obtaining monodisperse particles of CdTe with a diameter of 8 nm, which are well isolated from each other (Fig. 13.1). The optical properties of the latter are characterized by the absorption edge at 750 nm. This value corresponds to the bandgap of 1.65 eV and is close but higher than the energy gap of the bulk cadmium telluride (1.5 eV). In the same time, the combined use of these reagents in the ratio [TDPA]:[CEPA] = 10:1 leads to the formation of branched structures with a high degree of branching. Figure 13.2 shows the effect of different concentrations of stabilizers on the degree of branching of nanoparticles. The molar ratio [Cd]:[Te]:[TDPA]:[CEPA] varied according to needs and ranged from 1.1:0.117:1.8:0.16 (baseline synthesis) to 1.1:0.117:0.9:0.08.

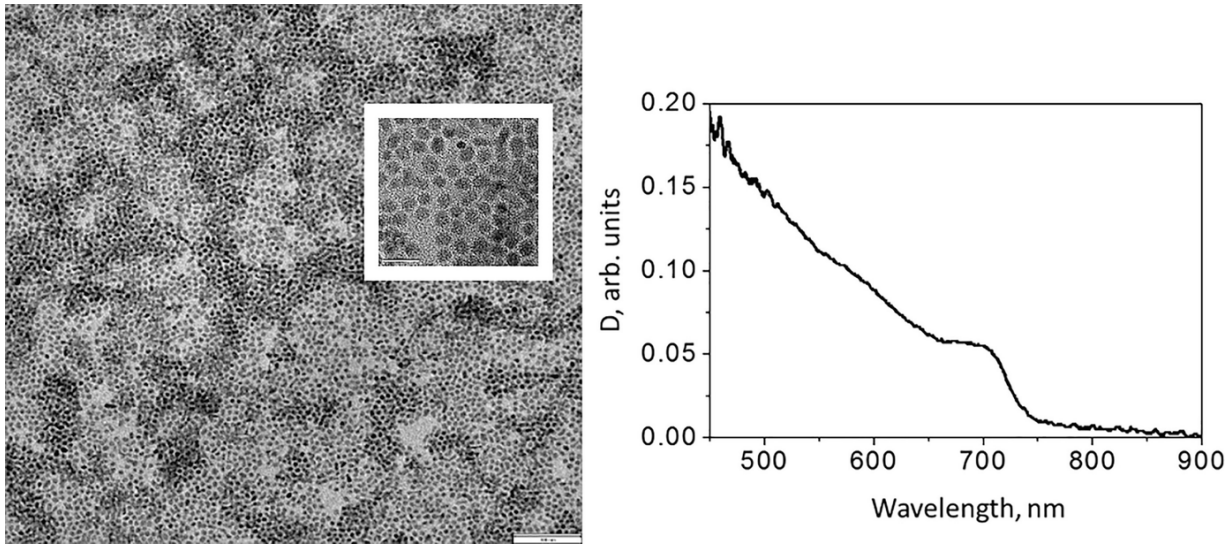

Fig. 13.1 Representative TEM image of spherical CdTe nanoparticles stabilized with a mixture of CEPA and TDPA. Absorption spectrum of spherical CdTe nanoparticles shown

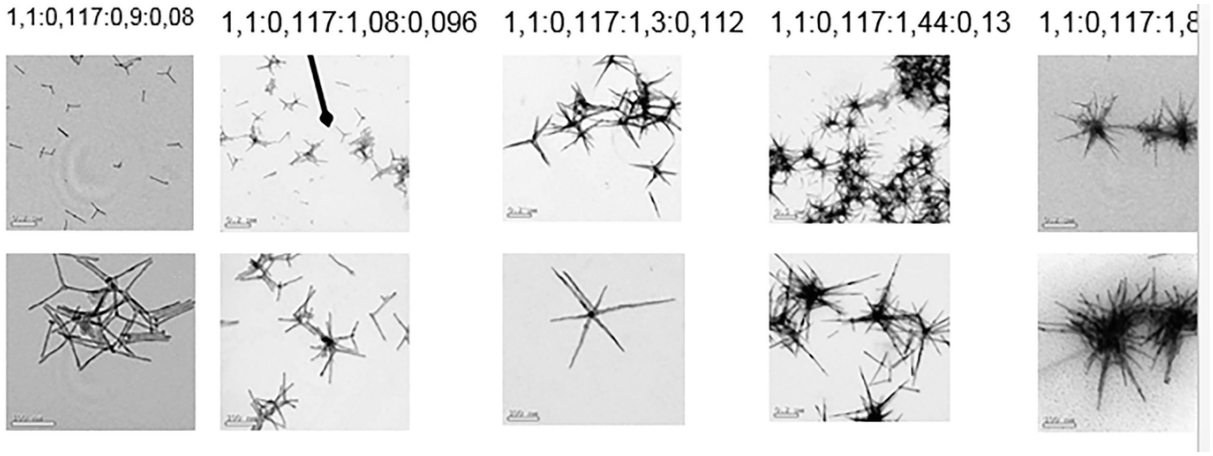

Fig. 13.2 Changes in the morphology of CdTe at different ratios of stabilizers

At that in Fig. 13.3, it is seen that reducing the amount of CEPA leads to the formation of structures with fewer branches. There are two main causes of branching in II-VI nanoparticles. The first is a slight difference in the energy of the transition from hexagonal to sphalerite modification. As a result, at high temperatures at which the synthesis is carried out, both phases can coexist in one particle. Indeed, Kumar and Nann [32] found that one-dimensional structures at a temperature of 300 °C contain about 10% of the sphalerite phase. This leads to the creation of additional growth planes and, accordingly, branching (see Fig. 13.3). According to another theory, the cause of branching can also be the coexistence of two-dimensional twinning defects, which theoretically can also lead to a similar result.

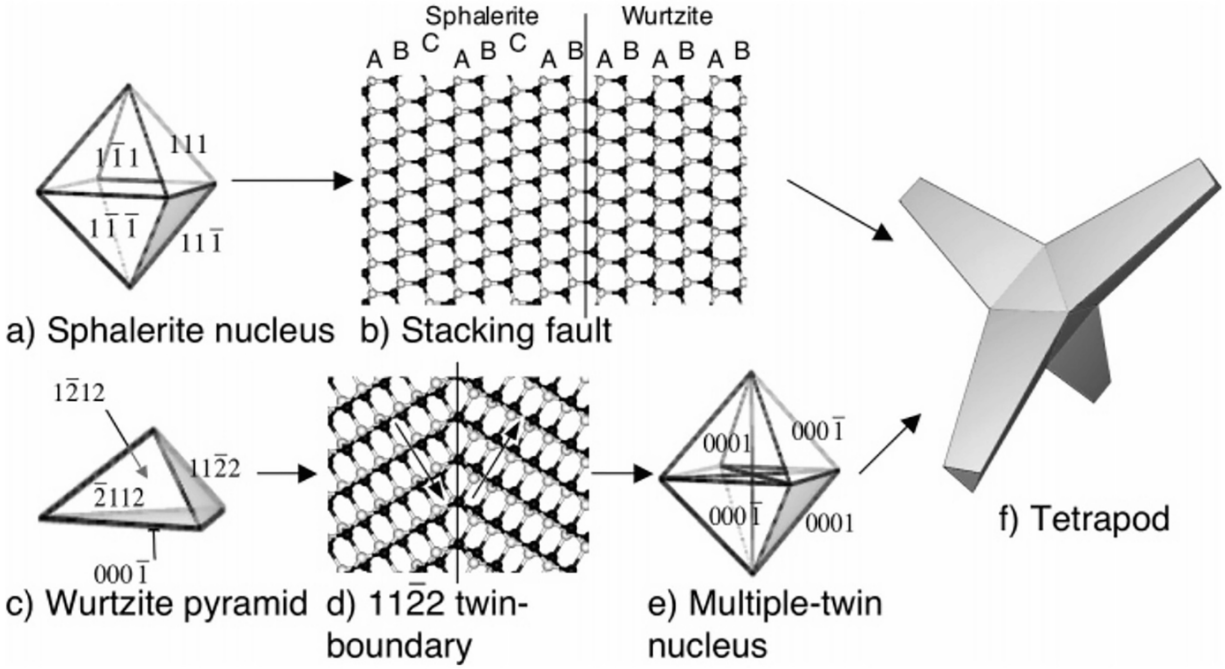

Fig. 13.3 Two different models rationalize the tetrapod shape. (**a**) A sphalerite nucleus with four equivalent {111} facets and four equivalent {111} facets. (**b**) By generation of stacking faults on the four fast-growing facets, the growth on these facets would continue in the hexagonal phase, leading to a tetrapod shape (**f**). (**e**) A multiple-twin nucleus formed by eight pyramid-shaped wurtzite crystals (**c**). (**d**) Structural details of the (1122) twin boundary present in this type of nucleus. The lattice boundary is observed from the (1010) zone axis. The arrows in (**d**) indicate the direction of the polarity in the two wurtzite domains. (Reprinted with permission from Ref. [7]. Copyright 2006: ACS)

The nature of the surfactant also plays an important role in determining the shape of nanoparticles. Nann and coworkers [31, 32] have found that depending upon the type and nature of the surfactant (TOPO or hexadecylamine (HDA)), various morphologies of CdTe nanoparticles can be prepared. A possible model for nanoparticle growth in various solution is shown in Fig. 13.4. In monosurfactant systems, it is possible that surfactant molecules build molecular templates within which the nanoparticles grow, a scenario similar to that where nanoparticles are formed in micellar systems.

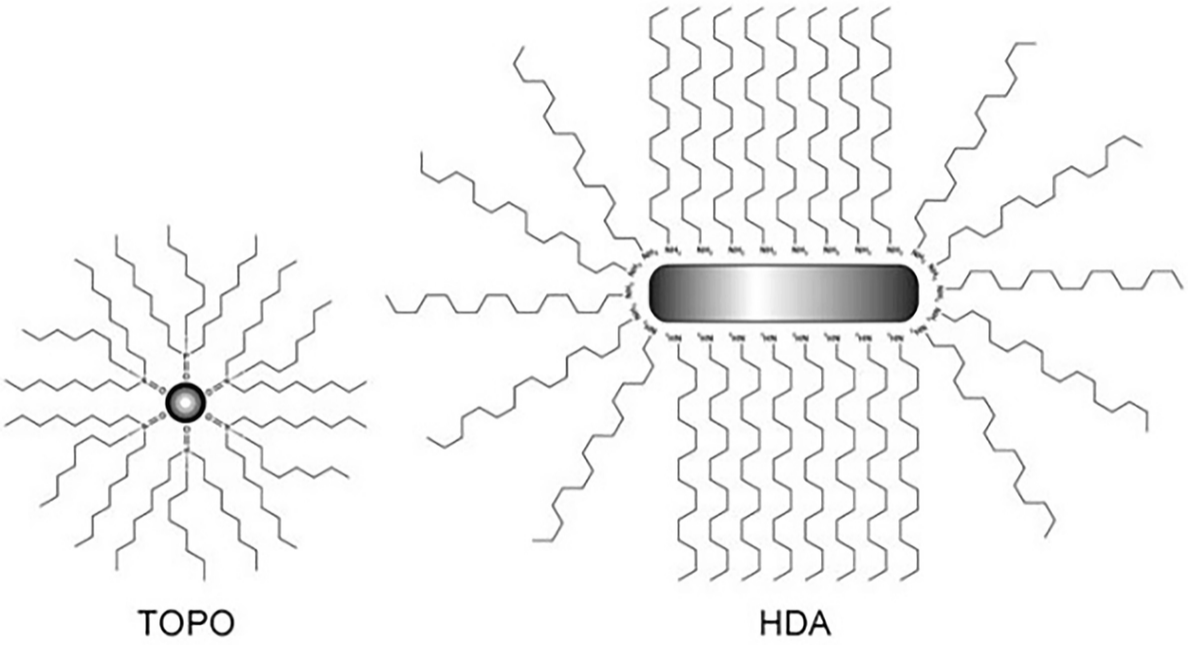

Fig. 13.4 A possible template mechanism for the growth of nanoparticles in monosurfactant systems, namely, TOPO and HDA. (Reprinted with permission from Ref. [30]. Copyright 2006: Wiley)

If we compare the parameters of nanoparticles synthesized in aqueous and organic solvents, we can conclude that nanoparticles obtained in an organic medium have a higher quantum yield of luminescence and monodispersity. For cadmium telluride, in particular, the use of phosphonic acids alone or in various combinations allows to obtain particles of various shapes: spherical, linear, and branched. However, these syntheses are very sensitive to the purity of the reagents, require significant time and energy, and often use expensive and toxic reagents. In addition, the nanocrystals obtained in the organic medium for further use as sensors in the aqueous medium must be further transferred into the aqueous phase. Therefore, in the last two decades, an active search for alternative methods for the synthesis of nanoparticles, in particular in aqueous solutions, has begun. Obtaining aqueous colloids of CdTe NCs significantly simplifies their application. It was also established that CdTe NCs synthesized using aqueous methods have increased stability in ambient conditions when compared to the extremely air-sensitive particles prepared by the organometallic route.

The first approaches to the synthesis of nanoparticles of II-VI compounds in aqueous solutions included reactions of Cd and Zn salts with sulfides known in analytical chemistry. Structural stabilization with

polymers or charge stabilization with thiols was successfully used to obtain inverse micelles of nanoparticles [29]. Chemical structures of thiols used for synthesis of II-VI semiconductor NCs are shown in Fig. 13.5. A comprehensive review of CdS nanoparticles was written by Hullavarad et al. [22]. While the focus is on CdS, the review provides an excellent overview of materials, methods, processes, and promising solutions that are emerging for various II-VI nanomaterials.

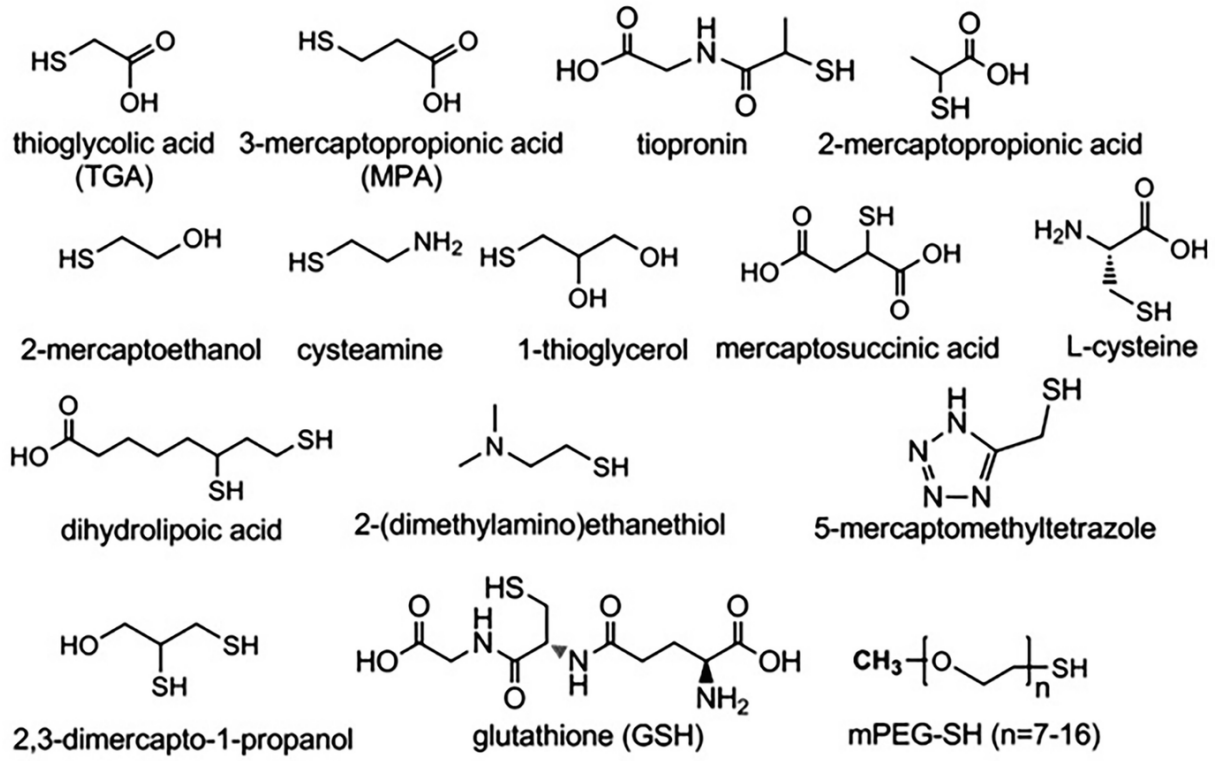

Fig. 13.5 Chemical structures of typical thiol capping ligands employed in the aqueous synthesis of NCs

As for CdTe, CdTe NCs had been obtained directly in water first by Langmuir [34] through the reaction of cadmium perchlorate with sodium telluride in the presence of sodium hexametaphosphate as stabilizer. Rajh et al. [47] employed a mixed stabilizer system containing hexametaphosphate and 3-mercapto-1,2-propanediol (thioglycerol (TG)) for successful synthesis of CdTe NCs. Later, optimization by Rogach et al. [51] led to a synthesis of stable NCs with sizes from 1.3 to 2.4 nm in the sole presence of thiols, viz., 2-mercaptoethanol and 1-thioglycerol. Currently, traditional synthesis of CdTe NCs includes the reactions of Cd salts (usually $Cd(ClO_4)_2$ or $CdCl_2$) with hydrogen telluride (gas) or NaHTe (Fig. 13.6).

The conditions used for the aqueous synthesis of CdTe nanocrystals are listed in Table 13.2. Hydrogen telluride is produced either by interaction of Al_2Te_3 with sulfuric acid or electrochemical generation [25]. Typically, hydrogen telluride is blown through a deaerated solution of cadmium thiolates using nitrogen as a carrier. The nucleation and growth of NCs usually occur by heating (usually by boiling in open air) [25] or under the influence of microwave irradiation. In particular, Khavalka et al. [25] showed that the synthesis of cadmium telluride colloid solutions at room temperature followed by an HT at 50 °C led to the formation of highly monodispersive NCs with an average size of about 7 nm. Khavalka et al. [25] also found that heating a solution after low-temperature synthesis at a temperature in the range of 50–100 °C can cause several effects: (1) intensification of the partial dissolution of small CdTe NPs as a source of growth of larger particles (Ostwald ripening). Ostwald ripening is the growth mechanism that is caused by the change in solubility of nanoparticles of different sizes. The high solubility and surface area of smaller nanoparticles lead to them breaking down and redissolving back into solution, leading to increased precursor concentration which results in further growth of the larger nanoparticles; 2) polymorphic transformation of the particle structure from sphalerite (S) to wurtzite (W); and/or (3) surface modification of CdTe NPs. In particular, thiol-capped CdTe nanocrystals represent a kind of core-shell system with a naturally sulfur-capped surface (CdS shell) created by mercapto groups covalently attached to the surface cadmium atoms [16]. Importantly, the synthesis of such kind of core-shell nanocrystals naturally occurs in one step, as the sulfur originates from the stabilizing thiol molecules during the particle growth. Thermal decomposition of sulfur-containing stabilizing ligands during heating speeds up the formation of CdS shell on the CdTe core [54]. Therefore, the thickness of the CdS shell can be controlled by variation of heat treatment process duration. It was shown that during the heat treatment for 6 hours at T = 100 °C occurs formation of a CdS shell that completely covers the CdTe QD core [11].

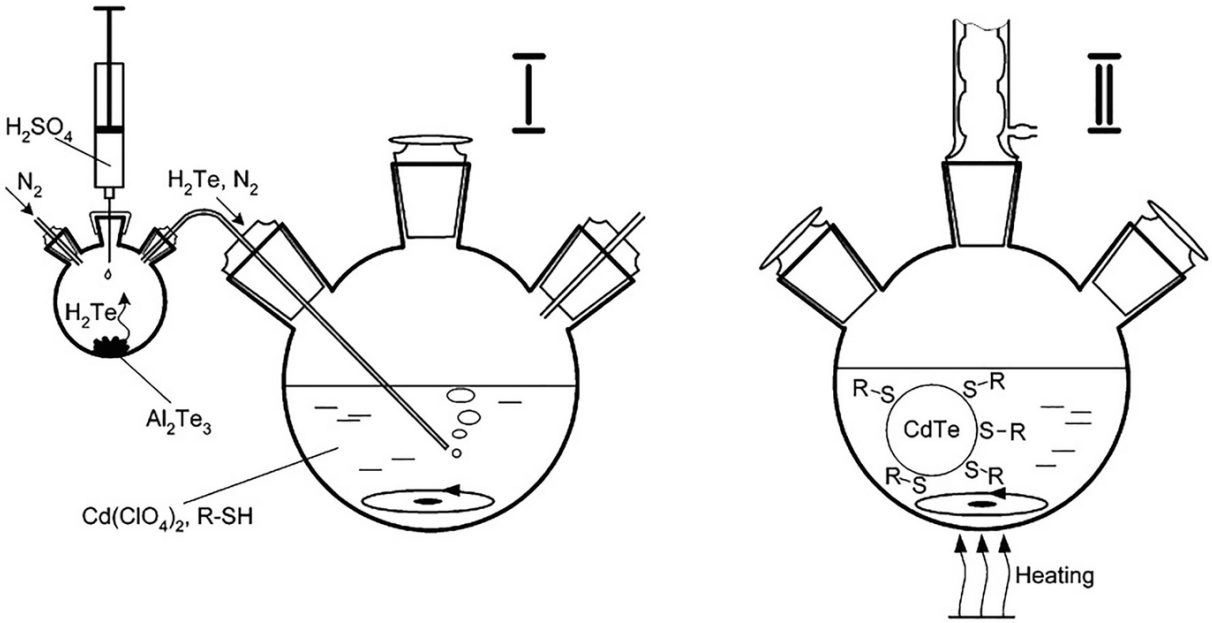

Fig. 13.6 Schematic presentation of the synthesis of thiol-capped CdTe QDs. First stage: formation of CdTe precursors by introducing H_2Te gas. Second stage: formation and growth of CdTe nanocrystals promoted by reflux. (Reprinted with permission from Ref. [17]. Copyright 2002: ACS)

Table 13.2 Typical conditions used for the aqueous synthesis of CdTe nanocrystals

Stabilizer	pH used for the synthesis	Stability of CdTe QDs	Surface charge of CdTe QDs	Typical PL QE of as-prepared CdTe QDs
2-Mercaptoethanol	11.2–11.8	Stable	Slightly negative in alkaline	<1%
1-Thioglycerol	11.2–11.8	Stable	Slightly negative in alkaline	3%
Mixture (1:1) of 1-thioglycerol and 2,3-dimercapto-1-propanol	11.2–11.8	Moderate	Slightly negative in alkaline	6%
Thioglycolic acid (TGA)	11.2–11.8	Stable	Negative	10%
2-Mercaptoethylamine (MA)	5.6–5.9	Moderate	Positive	10%
L-cysteine	11.2–11.8	Moderate	Negative or positive depending on the pH	10%
2-(Dimethylamino)ethanethiol	5.0–6.0	Moderate	Positive	30%

Source: Reprinted with permission from Ref. [17]. Copyright 2002: ACS
"Stable" means here that colloidal solutions of CdTe QDs are stable for months and even years being stored under air in the dark at room temperature. "Moderate" means that colloidal solutions coagulate occasionally during the storage; however, they are generally stable for months as well. Independent of the stabilizer nature, CdTe QDs are generally stable (no oxidation, no or only very minor changes of the optical properties) for years in powder form and in closely packed or nanocrystal/polymer films being kept in the dark under air

Another way to obtain cadmium telluride is to use sodium borohydride and elemental tellurium [14]. The formation of cadmium telluride nuclei is indicated by the appearance of a color that depends on the stabilizer used. It ranged from yellow (1-thioglycerol, 2-mercaptoethanol) or orange (thioglycolic acid) to dark red [49]. High-resolution TEM images of CdTe nanocrystals obtained by aqueous method are shown in Fig. 13.7.

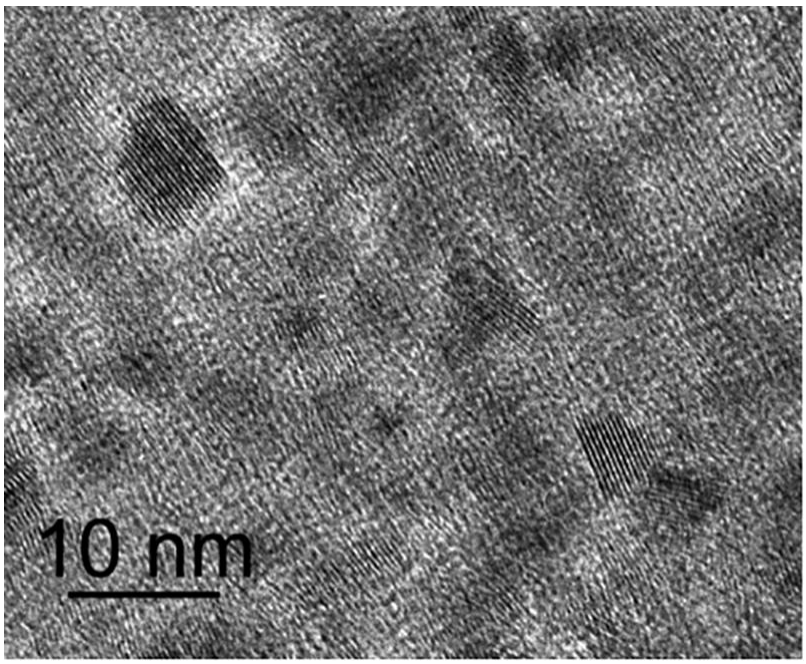

Fig. 13.7 HR TEM image of CdTe nanocrystals stabilized by the thioglycolic acid. (Reprinted with permission from Ref. [25]. Copyright 2010: Wiley)

These results indicate that the easy synthesis of CdTe NPs in aqueous solutions makes it possible to control their sizes. Nevertheless, we have to admit that the aqueous method usually does not permit direct efficient shape control of nanoparticles during their growth due to temperature limitations:

temperature of around 100 °C is not sufficient to overcome the energy barrier of transforming zinc blende to wurtzite structure. Thus, NCs synthesized exhibit as a rule an isotropic zinc blende cubic crystal structure and mainly spherical or quasi-spherical shape, since this shape is thermodynamically the most stable. Therefore, shaped CdTe nanostructures, such as 1D nanowires and nanoribbons, 2D sheets, and 3D structures, are achievable as a rule via postpreparative self-organization of preformed QDs.

In addition, mild synthetic conditions used in an aqueous synthesis often disable perfect structural localization of atoms in the crystal lattice of nanoparticles, normally achievable through the hot injection method. Therefore, in order to improve the crystal structure, size distribution, and correspondingly optical properties of CdTe QDs, we need to use additional treatments. For example, microwave irradiation has been successfully applied for these purposes [55]. Silva-Vidaurri et al. [55] have found that microwave irradiation promotes the formation of high-quality nanocrystals, with a well-defined crystal structure and an effective surface protection, since microwave irradiation guarantees the direct heating of nanocrystals.

State-of-the-art preparation techniques make it possible to easily synthesize in an aqueous medium CdTe QDs coated with various thiols, having a diameter of up to 6 nm and a PL covering most of the visible range up to the near infrared (NIR) with quantum yields (QYs) up to 60–80% [4, 68], which can compete with the best organometallic-prepared materials. We have to note that very high QYs reported should be considered very carefully, since the QY value is very dependent on the method of determination, standards used, instrument conditions, etc. [19]. The high quantum yields of the luminescence of CdTe nanoparticles make CdTe NCs a promising material for applications in the fabrication of light-emitting diodes (LEDs) [5], color conversion [40], solar cells [39], optical ion sensing [33], and bioimaging [63, 68].

It is important that the solubility of thiol-capped CdTe NCs is not limited to aqueous solutions. CdTe NCs synthesized in water can be transferred into nonpolar organic solvents, such as toluene and chloroform, via an exchange of stabilizer to long-chain thiols [16], by utilizing polymerizable surfactants [77] or by employing amphiphilic molecules for the stabilization [13]. After being converted into organic solutions, NRs can be used to fabricate functional polymer-NR composites [77].

More information about CdTe quantum dots, their synthesis, assembly, optical properties, and applications in biology and medicine can be found in the book edited by Donegan and Rakovich [10] and in reviews [17, 35].

13.3 Doping, Alloying, and Ion-Sensing via Incorporation of Transition Metals

As it was indicated before, nanocrystals (NCs) of II-VI semiconductors exhibit unique size-dependent optical properties in a wide spectral range from IR to UV, which make them promising materials for a wide range of applications. However, it turned out that pristine binary II-VI compounds could not always satisfy one or another requirement that arises in the development of a particular device. At the same time, the experiment showed that the incorporation of transition metals (Me) in the II-VI compounds, including CdTe NCs, significantly modifies their electrophysical and optical properties, contributing to the expansion of their functionality. An analysis of the advantages of CdTe-based multicomponent alloys for the development of photodetectors can be found in Vol. 2 of this issue. Such alloys are CdHgTe, on the basis of which IR photodetectors are developed (Chaps. 1–8, Vol. 2), and CdZnTe and CdMnTe, used in photodetectors for the visible and UV spectral regions (Chap. 15, Vol. 2). CdZnTe is also a material widely used in the development of radiation sensors (Chap. 2, Vol. 3).

13.3.1 Incorporation of Hg^{2+} Ions into the Structure of CdTe Nanocrystals

Rogach et al. [50], exploring the properties of colloidal composite CdHgTe nanocrystals and quantum dots synthesized in aqueous solutions, have established that the synthesis of Cd(Hg)Te NCs by addition of the precursor Hg^{2+} (X) to pre-synthesized CdTe NCs leads to a bathochromic shift of the absorption spectrum maxima from 510 nm (for pure CdTe) to 710 nm (for CdHg(X)Te nanocomposites with the highest Hg^{2+} content). At that the maximum of the PL spectrum for CdHg(X)Te nanocomposites with the highest content of Hg^{2+} ions was observed at 825 nm. The quantum yield of PL for this sample was 15% [50]. Mentioned above results are presented in

Fig. 13.8 for thioglycerol-stabilized NCs. Hg^{2+} ions have been added to CdTe colloidal solutions in amounts corresponding to 20%, 40%, 80%, and 120% of the cadmium content of the aliquots. These numbers (20, 40, 80, and 120) are used below in brackets in the formulas for CdHg(X)Te compounds. According to Rogach et al. [50], these changes in optical properties are due to two factors: an increase in the size of the NCs and an increase in the relative content of Hg^{2+} ions in CdHg(X)Te nanocomposite.

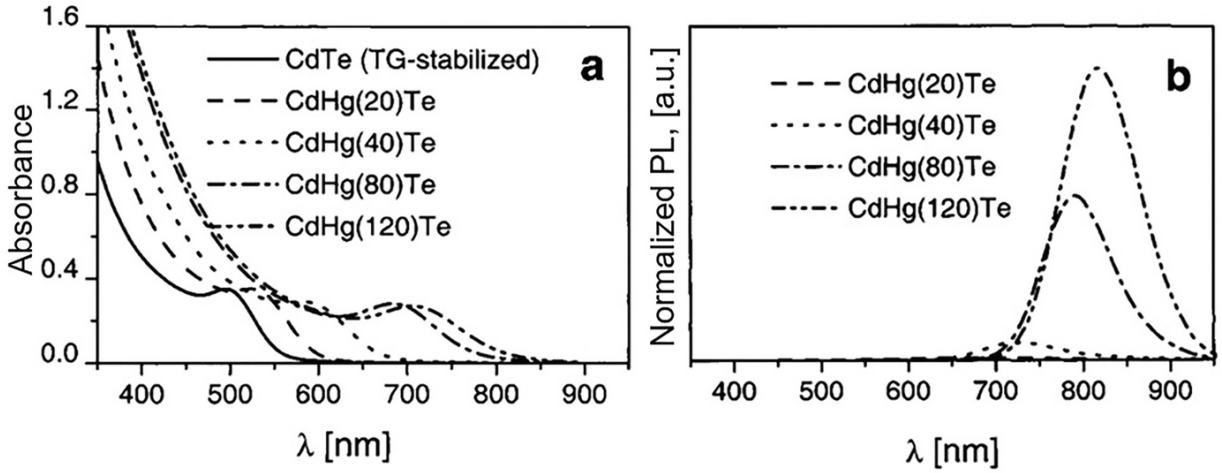

Fig. 13.8 Optical absorption (**a**) and PL (**b**) spectra of thioglycerol-stabilized CdHg(X)Te NCs. A similar effect was observed for NCs stabilized with mercaptoethanol. (Reprinted with permission from Ref. [50]. Copyright 2001: Wiley)

Rogach et al. [50] also found that the addition of a new portion of a precursors mixture (Hg^{2+} ions, Cd^{2+} ions, and a stabilizer) to the freshly prepared CdHg(X)Te NCs leads to the further shift to the infrared region of PL spectrum maxima. In this case, an additional expressive peak appears on the PL spectrum (see Fig. 13.9). Figure 13.9 shows the results related to mercaptoethanol-stabilized CdHg(X)Te nanocrystals. This approach, based on changing the composition of precursors during synthesis, makes it possible to form multilayer CdTe-based core-shell structures. The authors in the scheme (13.1) describe the mechanism of such a transformation:

$$\begin{aligned}&\mathrm{CdTe} \underset{-\mathrm{Cd}^{2+}}{\overset{\mathrm{Hg}^{2+}}{\rightarrow}} \mathrm{CdHgTe} \overset{\mathrm{Cd}^{2+},\ \mathrm{Te}^{-2}}{\rightarrow} \mathrm{CdHgTe/CdTe} \underset{-\mathrm{Cd}^{2+}}{\overset{\mathrm{Hg}^{2+}}{\rightarrow}} \\ &\underset{-\mathrm{Cd}^{2+}}{\overset{\mathrm{Hg}^{2+}}{\rightarrow}} \mathrm{CdHg\,(X)\,Hg\,(Y)\,Te} \overset{\mathrm{Cd}^{2+},\ \mathrm{Te}^{2-}}{\rightarrow} \mathrm{CdHg\,(X)\,Hg\,(Y)\,Te/CdTe} \overset{\mathrm{Hg}^{2+}}{\rightarrow} \ldots\ .\end{aligned} \tag{13.1}$$

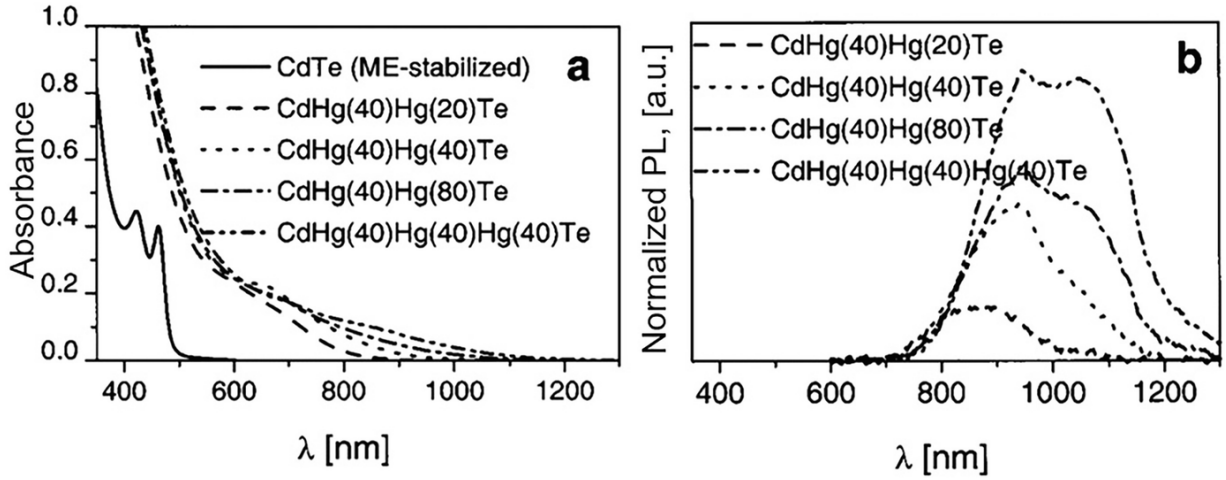

Fig. 13.9 Optical absorption (**a**) and PL (**b**) spectra of mercaptoethanol-stabilized CdTe nanocrystals and the nanocrystalline CdHg(X)Hg(Y)Te and CdHg(X)Hg(Y)Hg(Z)Te composites. (Reprinted with permission from Ref. [50]. Copyright 2001: Wiley)

Harrison et al. [20] described the formation of CdHgTe nanocomposites obtained by a similar method according the scheme shown in Fig. 13.10.

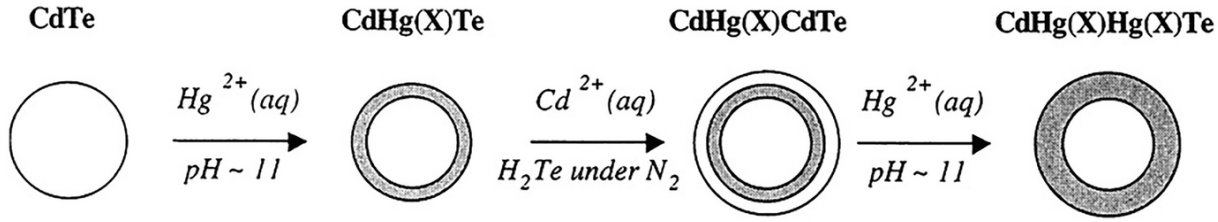

Fig. 13.10 Schematic diagram of the idealized route of CdHg(X)Te nanocomposite synthesis. (Reprinted from Ref. [20]. Published 2000 by De Gruyter as open access)

According to Harrison et al. [20], the HgTe shell is formed on the surface of the CdTe NCs by replacing the surface atoms of Cd^{2+} with Hg^{2+}. Subsequent addition of the Cd^{2+} and Te^{2-} precursors to the solution leads to the growth of the CdTe shell on the CdHgTe NCs' surface and the formation of a CdTe/HgTe/CdTe-type structure, which upon subsequent addition of the Hg^{2+} precursor undergoes ion exchange process and the formation of CdTe core/HgTe thick shell structure. The process of introducing the impurity into the NC structure by this mechanism occurs with the increase of the shell on top of NCs. This explains the increase in the size of the NCs. It should be noted that the optical properties of such nanocomposites are very similar to those described in [50]. The appearance of a double peak is observed on the PL spectra.

Smith et al. [56] and Kershaw et al. [24] also suggested that the synthesis in aqueous solutions of Cd(Hg)Te nanocrystals stabilized by TGA or MPA can lead to the formation of two different types of nanocrystals: the $Cd_{1-x}Hg_xTe$ alloy or the CdTe/HgTe core-shell structures. In the early stages of the ion exchange process, the formation of nanocomposites of the core-shell type takes place. The next step is a gradual transition to the formation of solid solution structures. The formation of a certain type of nanocomposite is influenced by the concentration of incorporated Hg^{2+} ions, the pH of the solution, and the bond strength between Hg^{2+} and stabilizing ligands. All these factors also affect the rate of Hg^{2+} incorporation into the NC structure. The ion exchange process with a gradual increase of Hg^{2+} ion concentration allows obtaining $Cd_{1-x}Hg_xTe$ NCs, while the synthesis, which proceeds with a sharp increase of Hg^{2+} concentrations, leads to the formation of NCs with Hg^{2+} ion-rich surface layers [24].

At the same time, Tynkevych et al. [62] have shown that the incorporation of Hg^{2+} ions at the stage of formation of CdTe nanoclusters with the subsequent heat treatment leads to the incorporation of Hg^{2+} ions into the structure of the CdTe nanocrystal with the formation of Cd(Hg)Te NCs. On the absorption spectra of a series of $Cd_{1-x}Hg_xTe$ samples with different content of Hg^{2+} ions obtained by this method, the absorption maximum shifts to the long-wavelength region, and the peak disappears. As a result of the influence of Hg^{2+} ions on the band structure of CdTe NCs, the bathochromic shift of PL peaks from 538 nm (for CdTe NCs) to 902 nm (for $Cd_{0.05}Hg_{0.95}Te$ NCs) is observed (Fig. 13.11). It was established that the high-temperature synthesis route results in a firm binding of mercury atoms within the Cd_{1-x}HgxTe responsible for a stable single-peak emission, while the low-temperature approach allows for both loosely (probably via interstitial incorporation) and firmly (substitutional) bound mercury atoms. The first causes stable single-peak emission, whereas the second creates two radiative recombination pathways of lower and higher energy [62]. Since loosely bound Hg atoms change their location/surrounding over time, becoming firmly incorporated into the lattice, the contribution of the higher-energy pathway decreases upon storage.

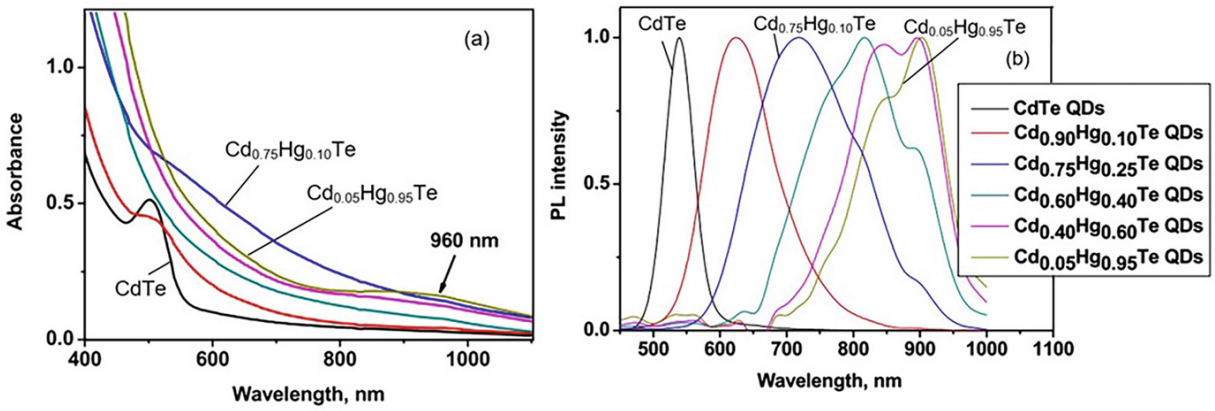

Fig. 13.11 Absorption (**a**) and normalized PL (**b**) spectra of TGA-stabilized CdTe and series of $Cd_{1-x}Hg_xTe$ QDs with different Hg^{2+} ion content. (Reprinted with permission from Ref. [62]. Copyright 2016: IOP Publishing)

It should be noted that the observed changes in the optical properties of the synthesized Cd_{1-x}HgxTe nanoparticles occur in full accordance with the decrease in the bandgap observed upon the replacement of Cd^{2+} by Hg^{2+} in CdTe NCs. At the same time, the change of quantum-dimensional effect caused by the significant difference between the bandgap energies and electron-hole masses of CdTe and HgTe is also observed [56]. If the bandgap of bulk $Cd_{1-x}Hg_xTe$ alloy varies linearly with composition from +1.6 eV (pure CdTe) to −0.3 eV (pure HgTe) [50] or − 0.15 eV [61], then the bandgap energy of Cd(Hg)Te NCs varies with composition from 2.21 eV (pure CdTe NCs, d = 3 nm) to 1.4 eV (HgTe NCs) [14].

Tynkevych et al. [62] analyzed the data of cyclic voltammograms (CVs) and found that the transformation of CdTe NCs into the $Cd_{1-x}Hg_xTe$ NCs with increasing Hg^{2+} ion content (x = 0.10–0.95) is accompanied by the appearance of additional energy levels in the bandgap of the NC (Fig. 13.12a). At x = 0.10–0.25 at. %, the appearance of an additional energy level below the conduction band of pure CdTe NCs was detected. Further replacement from 0.40 to 0.60 at. % of Cd^{2+} ions into the Hg^{2+} ions led to the formation of another energy level above the bottom level of the valence band of pure CdTe. When the impurity concentration reaches 0.95 at. %, the Cd^{2+} ions of the surface layers of the NC are completely replaced by Hg^{2+} ions. In this case, only two energy levels corresponding to the HgTe shell were recorded. The results obtained indicate that the gradual increase of Hg^{2+} ion concentration in the solution is accompanied by the formation of

three types of NCs: CdTe/$Cd_{1-x}Hg_xTe$, CdTe/$Cd_{1-x}Hg_xTe$/HgTe, and $Cd_{1-x}Hg_xTe$/HgTe without changing the average size of the NCs (Fig. 13.12b), which is a consequence of the gradual replacement of Cd^{2+} ions by Hg^{2+} ions in the direction from the surface layers into the depth in the layer of NCs.

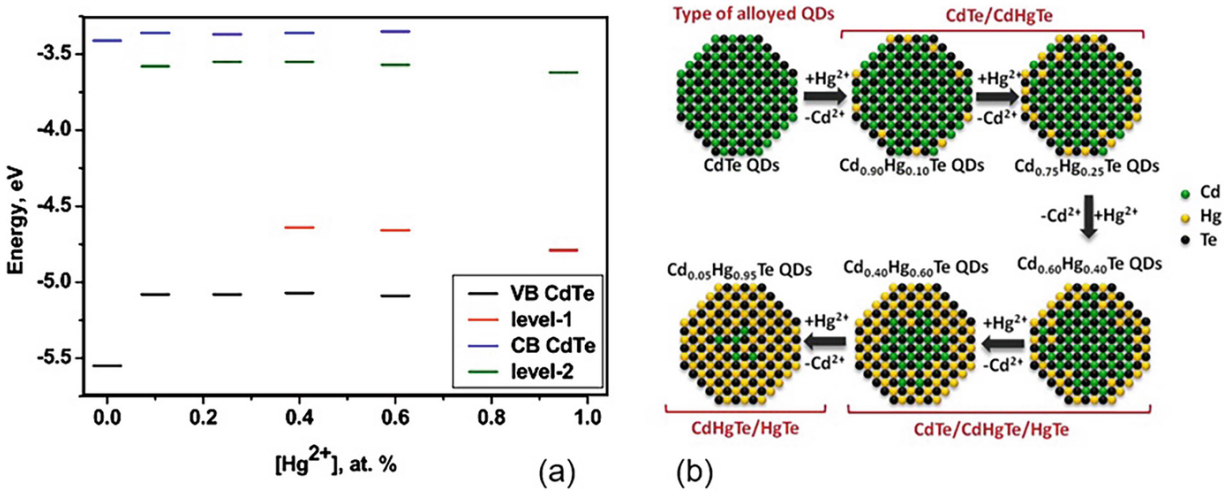

Fig. 13.12 (**a**) Plot of the valence band (VB) and conduction band (CB) edge positions for CdTe and the series of $Cd_{1-x}Hg_xTe$ NCs, obtained from the respective anodic (A) and cathodic (C) peaks of CVs; (**b**) scheme of the CdTe NC gradual doping with Hg^{2+} ion impurities. (Reprinted with permission from Ref. [62]. Copyright 2016: IOP Publishing)

13.3.2 Incorporation of Mn^{2+} and Zn^{2+} Ions into the Structure of CdTe Nanocrystals

It is known that the possibility of doping CdTe NCs with manganese and zinc ions is strongly limited by the fact that all aqueous colloids of NCs are obtained at alkaline pH values. Under such conditions, instead of the ion exchange process, insoluble manganese and zinc hydroxides are formed, which leads to the formation of a manganese or zinc oxide shell on the surface of semiconductor NCs [9, 64, 72].

13.3.2.1 CdTe:Mn

In general, there are two main methods for the synthesis of doped semiconductor NCs. The first method of synthesis is based on the addition of metal ions to pre-synthesized CdTe NPs. The authors [74] described such doping of CdTe NCs with manganese. Different amounts of manganese salt

were added to aliquots of pre-synthesized thioglycolic acid-stabilized CdTe NCs with followed heat treatment at 60 °C for 5 h. An increase in the impurity concentration led to a bathochromic shift of the PL spectrum (Fig. 13.13), which is explained by the formation of an optically active impurity level formed by the Mn^{2+} ion inside the bandgap of CdTe NC (see Fig. 13.14b).

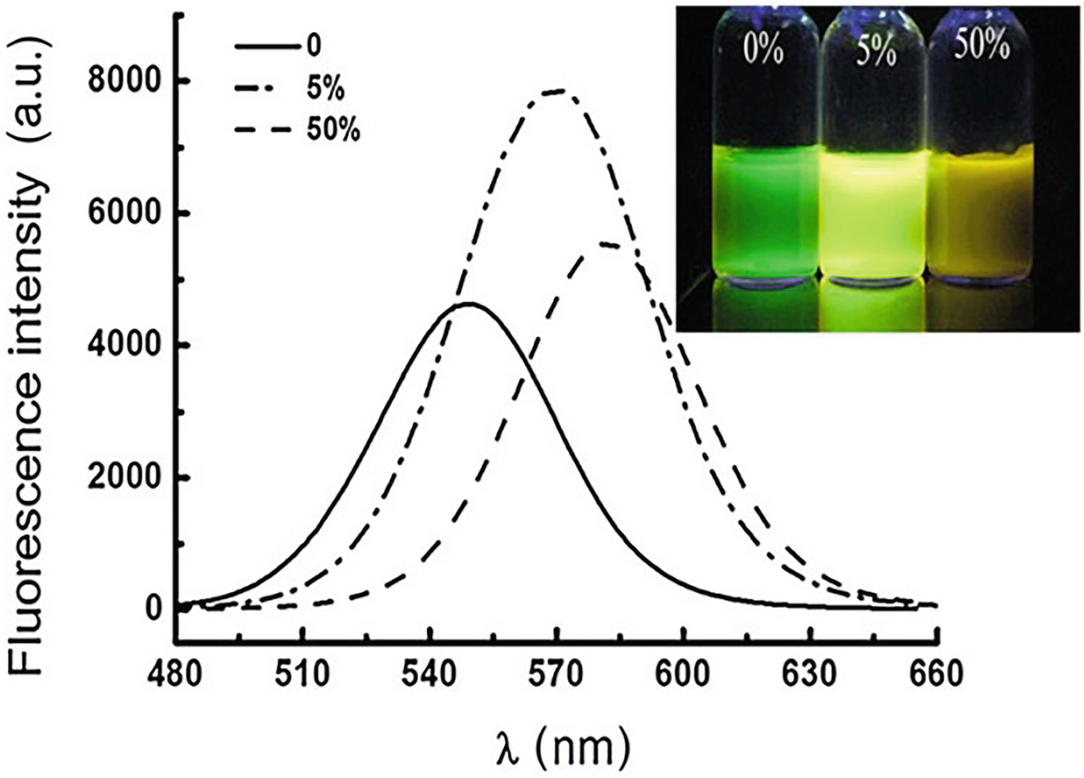

Fig. 13.13 PL spectra of CdTe NCs and manganese-doped CdTe NCs with the addition of 5 and 50% Mn^{2+} ions relative to the concentration of Cd^{2+} ions in CdTe NCs. *Insert* Luminescence of manganese-doped CdTe NCs. (Reprinted with permission from Ref. [74]. Copyright 2014: John Wiley & Sons, Ltd.)

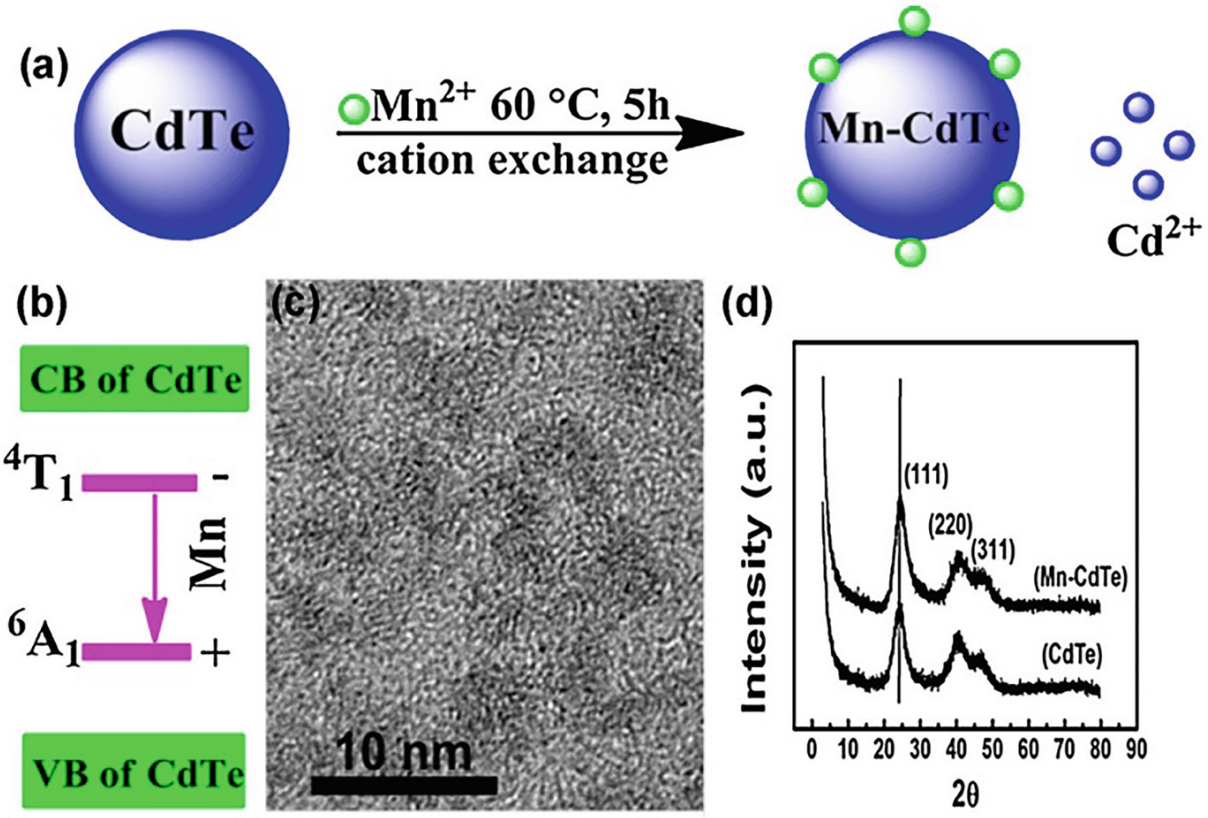

Fig. 13.14 (**a**) Scheme of the synthesis of the Mn^{2+}-doped CdTe quantum dots (QDs). (**b**) Luminescence mechanism of the Mn^{2+}-doped CdTe QDs, where "CB" and "VB" are the conduction band and valance band, respectively. (**c**) Transmission electron microscopy image of the Mn^{2+}-doped CdTe QDs. (**d**) X-ray diffraction pattern of the Mn^{2+}-doped CdTe QDs and CdTe. (Reprinted with permission from Ref. [74]. Copyright 2014: John Wiley & Sons, Ltd.)

According to TEM analysis, the average size of NCs was 3.7 nm (Fig. 13.14c), and the doping process did not affect the NC size. According to X-ray diffraction data (Fig. 13.14d), such doping had practically no effect on the change in the crystal structure of NCs as well. Zhang et al. [74] concluded that the formation of Mn^{2+}-doped CdTe NCs takes place via ion exchange mechanism with the replacement of surface Cd^{2+} atoms by Mn^{2+} atoms. During such doping with Mn, only a small amount of Mn^{2+} ions incorporate in the lattice of CdTe NCs. As a result, such surface doping affects the change in optical properties and does not lead to a change in the size and crystal structure of CdTe NCs.

The second method of synthesis of manganese-doped CdTe NCs is based on the addition of precursor impurities at the stage of synthesis of NCs [15]. As a result of such synthesis, Cd(Mn)Te NCs are obtained with

completely different properties than those of CdTe(Mn) NCs, obtained by the previously described method [74]. Increasing the molar ratio of Mn/Cd from 0.2 to 1.5 led to a hypsochromic shift of the maxima of the PL spectra from 578 to 553 nm (Fig. 13.15). This change in optical properties can be explained by an increase in the bandgap of the obtained NCs with increasing manganese content [15].

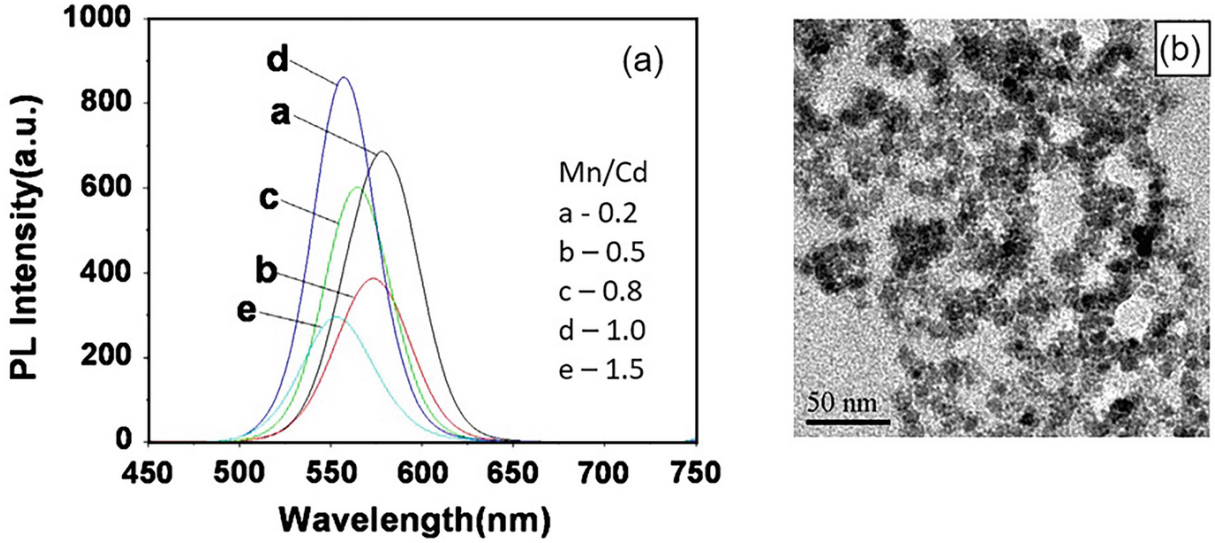

Fig. 13.15 (**a**) PL spectra of Mn^{2+}-doped CdTe NCs with different ratios of Mn to Cd in solution. (**b**) TEM image of Mn^{2+}-doped CdTe NCs (sample e). (Reprinted with permission from Ref. [15]. Copyright 2015: Elsevier)

Gao et al. [15], when studying CdTe NC morphology through TEM, and XPS analysis indicated that Mn atoms have been successfully incorporated into the NCs. The NC size obtained by this method was ~8.5 nm. Without the addition of a manganese precursor to the control solution, CdTe NCs with an average size of 2.3 nm were formed. It was assumed that due to the significant difference between the solubility products of CdTe (~10^{-35}) and MnTe (~10^{-15}), when using a mixture of manganese and cadmium precursors, the CdTe core is first formed in the synthesis process, followed by the growth of the Cd(Mn)Te shell with high manganese content around the CdTe core.

Tynkevych et al. [61] also synthesized $Cd_{1-x}Mn_xTe$ NCs by the ion exchange modification method. NCs with average size ~2.3 nm had PL in the blue region of the visible spectrum. As the Mn concentration increased, the PL peak shifted from 542 to 496 nm (Fig. 13.16). The successful

incorporation of manganese into the CdTe NC structure was confirmed by atomic emission spectroscopic analysis.

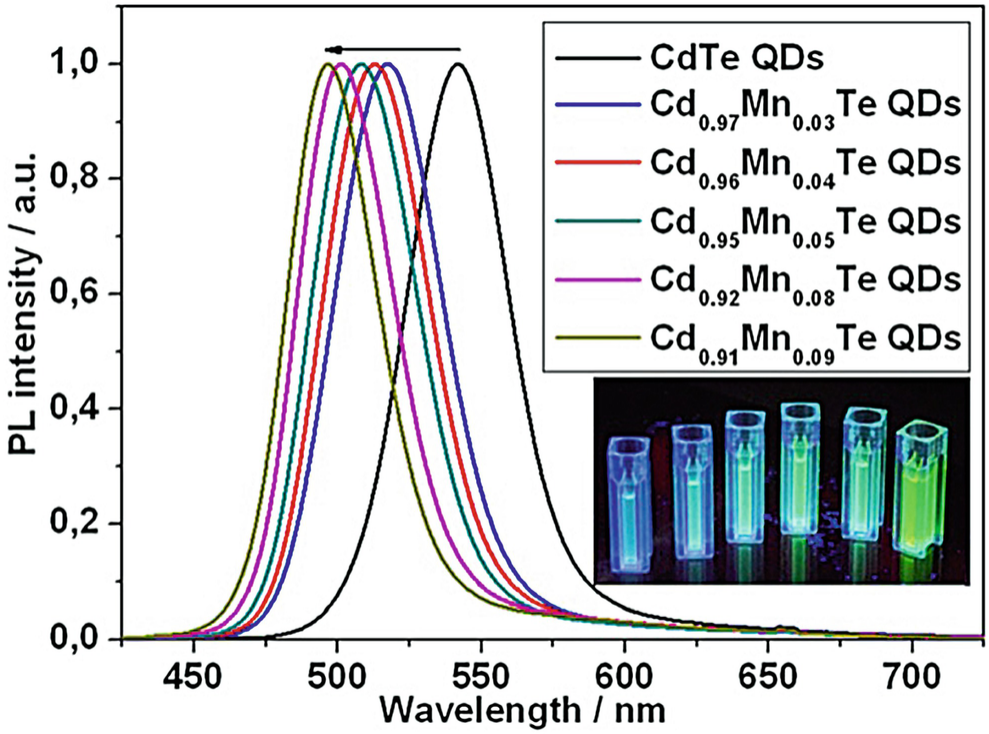

Fig. 13.16 Normalized PL spectra of CdTe NCs and a series of $Cd_{1-x}Mn_xTe$ NC samples with different manganese content. (Reprinted with permission from Ref. [61]. Copyright 2018: Elsevier)

13.3.2.2 CdTe:Zn

The most common method for the synthesis of Cd(Zn)Te NCs is based on mixing cadmium and zinc precursors with their subsequent interaction with the tellurium precursor in the presence of a stabilizer [41]. Cheng et al. [9] noted that the introduction of zinc into the structure of CdTe NCs in aqueous solutions at alkaline pH is almost impossible, since there is a process of formation of $Zn(OH)_2$, which covers the surface of CdTe NCs and leads to the formation of ZnO on the top of the NC surface. However, Matos et al. [41] showed that the synthesis of Cd(Zn)Te NCs at alkaline pH is significantly influenced by the type of stabilizer. Thus, it was found that the formation of Cd(Zn)Te NCs stabilized by glutathione strongly depends on pH (Fig. 13.17a), while mercaptopropionic acid-stabilized NCs revealed only a slight effect of pH (Fig. 13.17b). The shift of the PL spectra to the long-wavelength region for glutathione-stabilized NCs synthesized at higher pH (pH > 9) (Fig. 13.17a) is probably caused by the incorporation of

a smaller amount of Zn^{2+} ions into CdTe lattice, which is confirmed by atomic absorption spectrometry. The molar fraction of Zn^{2+} relative to Cd^{2+} in $Cd_{1-x}Zn_xTe$ decreased from 0.19 to 0.11 with increasing pH from 10 to 11.5. Similar assumptions were also made by the authors of Ref. [9, 36, 65, 78]. It was assumed that such pH influence is connected with different structure of stabilizers. Glutathione contains different groups that can coordinate Zn^{2+} cations in different pH ranges: thiol groups (mainly at pH 6.5–8.3), amino group (pH 8.3–10.3), and amide functional group (pH > 10.3) [75], whereas mercaptopropionic (MPA) and thioglycolic (TGA) have only thiol groups. This fact explains the less successful incorporation of Zn^{2+} ions into the structure of glutathione-stabilized NCs. In addition, Matos et al. [41] found that MPA-stabilized NCs are slightly smaller than glutathione-stabilized NCs, and their size decreased with increasing pH.

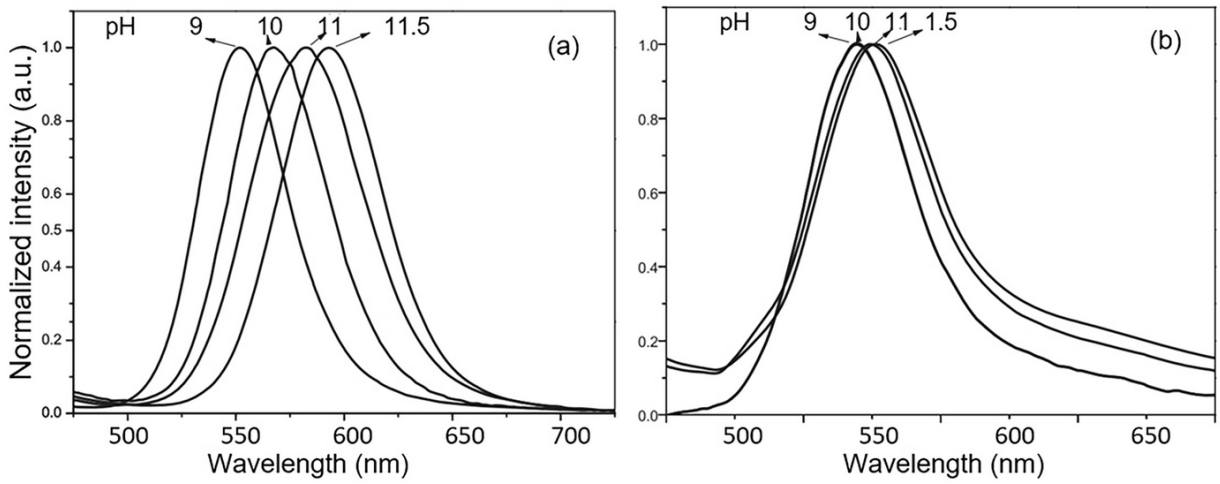

Fig. 13.17 (**a**) Normalized PL spectra of (**a**) glutathione-stabilized CdZnTe NCs and (**b**) MPA-stabilized CdZnTe NCs, which were synthesized at different pH values. (Reprinted with permission from Ref. [41]. Copyright 2016: Elsevier)

Studies have shown that various precursors can be used to dope CdTe with zinc. However, it should be kept in mind that changes in the properties of synthesized nanoparticles can also occur when the precursor is changed. Tynkevych and Khalavka [61] found that the use of $ZnSO_4$ as a precursor of the Zn^{2+} impurity for doping CdTe NCs leads to a hypsochromic shift in the PL spectrum of the nanocrystals (Fig. 13.18), which may indicate the successful completion of the ion exchange process and the formation of $Cd_{1-x}Zn_xTe$ by analogy with the synthesis of $Cd_{1-x}Mn_xTe$ and $Cd_{1-x}Hg_xTe$

NCs [61, 62]. According to atomic emission spectroscopic analysis, the composition of the formed nanocomposite was $Cd_{0.93}Zn_{0.07}Te$.

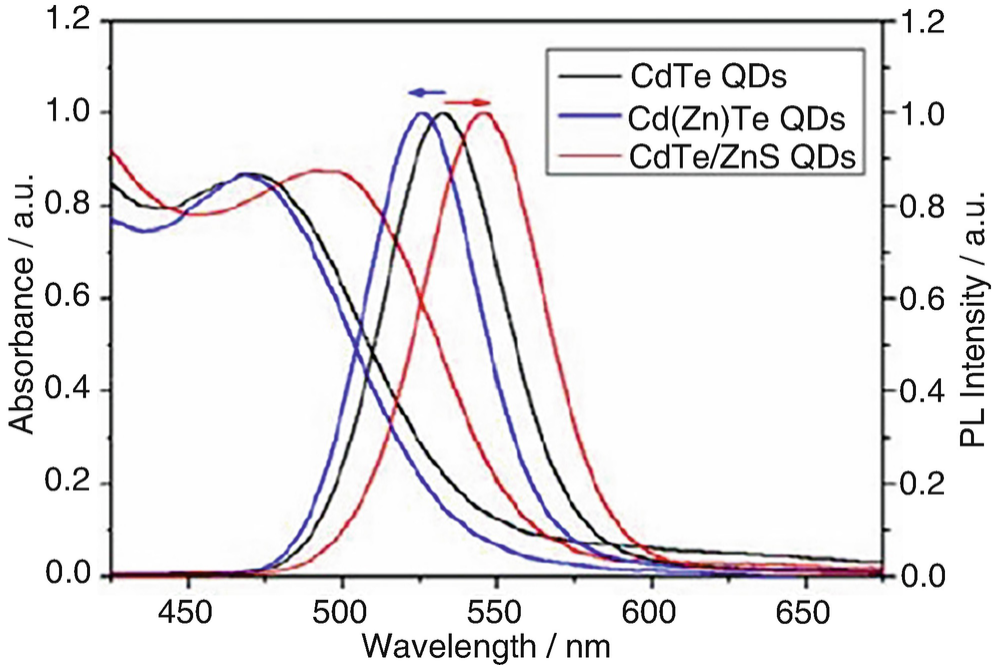

Fig. 13.18 Normalized absorption and PL spectra of CdTe, CdZnTe, and CdTe/ZnS NCs. (Reprinted with permission from Ref. [61]. Copyright 2018: Elsevier)

When zinc thioglycolate was used as a precursor, a bathochromic shift of the PL spectrum was observed (see Fig. 13.18). The signal of CdTe NCs disappeared at the cyclic voltammograms, and only one reduction peak at −1.20 V was detected. It can be assumed that a thin ZnS shell is formed on the CdTe surface upon the introduction of zinc thioglycolate, which is also a source of S^{2-} ions. A similar effect was reported in [9, 52, 72]. It was observed during the formation of the ZnS shell over the CdTe core during the synthesis of CdTe/ZnS core-shell structures.

13.4 Other CdTe-Based Alloys

In addition to the above $Cd_{1-x}Hg_xTe$, $Cd_{1-x}Mn_xTe$, and $Cd_{1-x}Zn_xTe$ alloys, other CdTe-based alloys, such as CdSeTe and CdSTe NCs, were also synthesized using the proposed approaches.

For the synthesis of CdSeTe NCs, a simple combination of precursors such as TOP-Se, TOP-Te, and CdO, thermalyzed in TOPO and had, was used [2, 3]. It was found that, under the described growth conditions,

tellurium is more reactive with cadmium than with selenium, which, under appropriate conditions, makes it possible to obtain two types of alloy with different compositions. Bailey and Nie [3] have shown that by varying the amount of cadmium, either a homogeneous or graduated structure of NCs can be synthesized. The former is achieved under cadmium-limited conditions and the latter under cadmium-high conditions. Under conditions of a limited content of cadmium, the particle composition was determined by the relative growth rate of CdSe and CdTe, but not by the concentration of cadmium, since cadmium was common for both species and was excluded from the kinetic equations. Therefore, the composition remained constant. In the case of the cadmium-rich reaction, a tellurium-rich nucleus was formed during nucleation due to the higher reaction rate of tellurium compared to selenium. When tellurium has been removed from the reactant mixture due to its high activity, selenium becomes the predominant substance in the subsequent growth step. As soon as all the reagents are used up, growth stops, and a structure with a variable composition is formed. The amount of tellurium or selenium in solution can be precisely controlled by the amount of any precursor used.

CdSTe alloy can also be synthesized using an aqueous solution. Rivera-Rodriguez et al. [48] used for this an aqueous telluride solution (produced by reducing metallic Te with $NaBH_4$), cadmium sulfate ($CdSO_4$), and thioglycolic acid (TGA), which were mixed together in an oxygen-free atmosphere to prevent oxidation of the telluride species. One can also use $CdNO_3$ instead of $CdSO_4$ [1]. The reaction temperature varied from 60 °C to 180 °C and was controlled by using a microwave reactor. As a result, water-stable S-rich CdSTe quantum dots were synthesized, the bandgap and the maximum emission peaks of which depended on reaction temperatures. As the reaction temperature increased from 60 °C to 180 °C, the bandgap decreased from 2.4 to 1.86 eV, and the emission maximum shifted from 506 to 640 nm (λ_{ex} = 380 nm). The highest quantum yield (14–16%) was observed for CdSTe QDs synthesized at temperature 120–150 °C. It was assumed that observed changes are connected with increase in the QD size from 1.4–2.0 nm to 3.2–7.0 nm.

Similar approach was used to synthesize $CdSe_xTe_{1-x}$ NCs stabilized with thioglycolic acid by simultaneous use of selenium NaHSe and tellurium NaHTe precursors. The spectral tunability of the absorption onset

between 550 and 690 nm depends on size and the composition of $CdSe_xTe_{1-x}$ nanocrystals. Such alloyed nanocrystals showed band-edge emission with an intensity reduced by an order of magnitude as compared to the bare CdTe nanoparticles. The growth of alloyed nanocrystals was faster than that for the bare CdSe and CdTe particles, leading to formation of bigger nanocrystals at given reaction times. The reactivity of NaHSe was higher than that for NaHTe at the reaction conditions employed, resulting in a sufficiently increased amount of Se incorporated into alloyed nanocrystals, as compared to the ratios of Se/Te precursor used [46].

13.5 CdTe-Based Core-Shell Structures

As shown earlier, core-shell structures in aqueous solutions are usually formed using a two-step process, since one-pot aqueous core-shell synthesis of NCs, in which both core and shell precursors are added and reacted simultaneously, in most cases results in the formation of fused structures rather than the classic core-shell structure. One should note that obtaining different core-shell and core-shell-shell structures, such as CdTe/CdS [79], CdTe/ZnTe [71], CdSe/CdTe [27], CdTe/CdSe [45], CdHgTe/CdS [44], CdSeTe/CdS [58], CdTe/CdSe/ZnS [53], and CdTe/CdS/ZnS [21], directly in water, reported during the last decade, is a great step forward toward a superior quality of NCs. However, the experiment showed that in some cases higher-quality NCs can be achieved using hybrid approaches for the synthesis of core-shell particles, combining aqueous and organometallic techniques. Depending on the accessibility of the corresponding core and shell materials, cores being synthesized in water (organics) have been transferred into organics (water) for subsequent shell formation [37, 59]. In particular [59], CdTe and CdHgTe cores transferred from water were coated by ZnS shell via the hot injection technique. Nanocrystals synthesized using the hybrid approach were highly luminescent, stable for months in butanol, and have a higher resistance to photobleaching compared to cores. The high quantum yield (over 50%) of these NCs is among the highest reported for the far-red region (670–700 nm). Quantum yields are also high (20–50%) in the near-IR region (>700 nm). This wavelength region is attractive for various biological applications because of reduced autofluorescence background, improved penetration into scattering tissue, and enhanced photostability.

He et al. [21] used another approach for synthesis of core-shell structures. They have shown that microwave irradiation is also an advantageous technique for synthesis of core-shell particles. By using this approach for synthesis in water of core-shell-shell MPA-capped CdTe/CdS/ZnS NCs. Process used is shown in Fig. 13.19. The resulting core-shell QDs were found to be very stable in biological media and noncytotoxic, which makes them promising candidates for biolabeling.

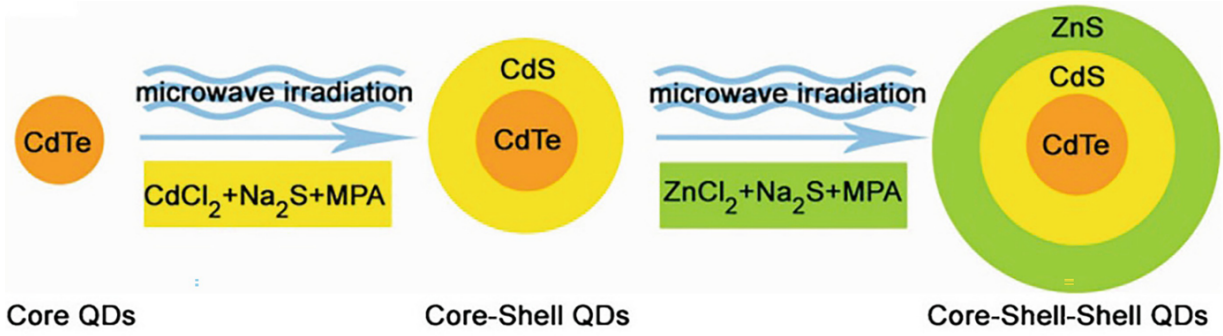

Fig. 13.19 Schematic illustration of the microwave-assisted three-step synthesis of aqueous CdTe/CdS/ZnS core-shell-shell QDs. (Reproduced with permission from Ref. [21]. Copyright 2008: WILEY-VCH Verlag GmbH & Co. KgaA)

Zhang et al. [76] have found that CdTe/CdSe core-shell QDs with NIR fluorescence can be prepared by applying a successive ionic layer adsorption and reaction (SILAR) technique. In this method, L-cysteine-stabilized CdTe cores are covered with 1–6 CdSe layers by sequential injection of Cd^{2+}/cysteine and KHSe solutions. The SILAR technique ensures very efficient control of the shell thickness, tuning the behavior of core-shell CdTe/CdS QDs by gradual deposition of several shell layers [73]. Wang et al. [66] have shown that ultrasonic treatment can also be used for CdS shell formation on CdTe NCs. In this case, acoustic cavitation facilitates the decomposition of thiourea which releases S^{2-} ions to react with Cd^{2+} present in solution with the subsequent creation of a gradated shell.

Jing et al. [23] tuned optical properties and band alignments of aqueous CdTe/CdS QDs by coating different-sized CdTe QD cores with CdS shells upon the thermal decomposition of glutathione under reflux as a sulfur source. Due to the lattice mismatch, CdTe and CdS represent a typical strain system where CdTe core and CdS shell are subjected to compressive and tensile strains, respectively. Strain exhibits remarkable effects on the optical

properties of mismatched core-shell QDs by altering the electronic structure of the system. The growth of thicker CdS shell substantially prolongs the PL lifetime of the QDs by forming a type II band alignment structure.

Acknowledgments

Yuriy Khalavka is supported by MESU grant № 122 U000932. G. Korotcenkov is grateful to the State Program of the Republic of Moldova, project 20.80009.5007.02, for supporting his research.

References

1. Aviles-Martin C, Alamo-Nole L (2017) Photogeneration of organic dyes using CdSTe quantum dots. TechConnect Briefs 1:141–144
2. Bailey RE, Smith AM, Nie SM (2004) Quantum dots in biology and medicine. Physical E 25(1):1–12
3. Bailey RE, Nie S (2003) Alloyed semiconductor quantum dots: tuning the optical properties without changing the particle size. J Am Chem Soc 125:7100–7106
4. Bao HB, Gong YJ, Li Z, Gao MY (2004) Enhancement effect of illumination on the photoluminescence of water-soluble CdTe nanocrystals: toward highly fluorescent CdTe/CdS core-shell structure. Chem Mater 16:3853–3859
5. Baruah L, Nath SS (2013) Oleic acid–capped CdTe quantum dots and their applications as nano-LED. Emerg Mater Res 2:186–190
6. Bunge SD, Krueger KM, Boyle TJ, Rodriguez MA, Headley TJ, Colvin VL (2003) Growth and morphology of cadmium chalcogenides: the synthesis of nanorods, tetrapods, and spheres from CdO and $Cd(O_2CCH_3)_2$. J Mater Chem 13:1705
7. Carbone L, Kudera S, Carlino E, Parak WJ, Giannini C, Cingolani R, Manna L (2006) Multiple wurtzite twinning in CdTe nanocrystals induced by methylphosphonic acid. J Am Chem Soc 128:748–755
8. Chen Y, Rosenzweig Z (2002) Luminescent CdS quantum Dots as selective ion probes. Anal Chem 74:5132–5138
9. Cheng J, Li D, Cheng T, Ren B, Wang G, Li J (2014) Aqueous synthesis of high-fluorescence CdZnTe alloyed quantum dots. J Alloys Compd 589:539–544
10. Donegan J, Rakovich Y (2013) Cadmium telluride quantum dots advances and applications. Jenny Stanford Publishing
11. Doskaliuk N, Khalavka Y, Fochuk P (2016) Influence of the shell thickness and ratio between core elements on photostability of the CdTe/CdS core/shell quantum dots embedded in a polymer matrix. Nanoscale Res Lett 11(1):216

12. Duan J, Song L, Zhan J (2009) One-pot synthesis of highly luminescent CdTe quantum dots by microwave irradiation reduction and their Hg^{2+-}sensitive properties. Nano Res 2:61–68
13. Dubavik A, Lesnyak V, Thiessen W, Gaponik N, Wolff T, Eychmuller A (2009) Synthesis of amphiphilic CdTe nanocrystals. J Phys Chem C 113:4748–4750
14. Feteha M, Ebrahim S, Soliman M, Ramdan W, Raoof M (2012) Effects of mercaptopropionic acid as a stabilizing agent and Cd:Te ion ratio on CdTe and CdHgTe quantum dots properties. J Mater Sci Mater Electron 23:1938–1943
15. Gao F, Li J, Wang F, Yang T, Zhao D (2015) Synthesis and characterization of high-quality water-soluble CdMnTe quantum dots capped by N-acetyl-L-cysteine through hydrothermal method. J Lumin 159:32–37
16. Gaponik N, Talapin DV, Rogach AL (2002) A. Eychmuller, H. Weller, Efficient phase transfer ¨ of luminescent thiol-capped nanocrystals: from water to nonpolar organic solvents. Nano Lett 2:803–806
17. Gaponik N, Talapin DV, Rogach AL (2002b) Thiol-capping of CdTe nanocrystals: an alternative to organometallic synthetic routes. J Phys Chem B 106(29):7177–7185
18. Gattás-Asfura KM, Leblanc RM (2003) Peptide-coated CdS quantum dots for the optical detection of copper(ii) and silver(i). Chem Commun:2684–2685
19. Grabolle M, Spieles M, Lesnyak V, Gaponik N, Eychmuller A, Resch-Genger U (2009) Determination of the fluorescence quantum yield of quantum dots: suitable procedures and achievable uncertainties. Anal Chem 81:6285–6294
20. Harrison MT, Kershaw SV, Burt MG, Rogach AL, Kornowski A, Eychmuller A, Weller H (2000) Colloidal nanocrystals for telecommunications. Complete coverage of the low-loss fiber windows by mercury telluride quantum dot. Pure Appl Chem 72:295–307
21. He Y, Lu HT, Sai LM, Su Y-Y, Hu M, Fan C-H, Huang W, Wang L-H (2008) Microwave synthesis of water-dispersed CdTe/CdS/ZnS core–shell–shell quantum dots with excellent photostability and biocompatibility. Adv Mater 20:3416–3421
22. Hullavarad NV, Hullavarad SS, Karulkar PC (2008) Cadmium sulphide (CdS) nanotechnology: synthesis and applications. J Nanosci Nanotechnol 8:3272–3299
23. Jing L, Kershaw SV, Kipp T, Kalytchuk S, Ding K, Zeng J, et al. (2015) Insight into strain effects on band alignment shifts, carrier localization and recombination kinetics in CdTe/CdS core/shell quantum dots. J Am Chem Soc 137:2073–2084. https://doi.org/10.1021/ja5127352
24. Kershaw SV, Abdelazim NM, Zhao Y, Susha AS, Zhovtiuk O, Teoh WY, Rogach AL (2017) Investigation of the exchange kinetics and surface recovery of $Cd_xHg_{1-x}Te$ quantum dots during cation exchange using a microfluidic flow reactor. Chem Mater 29:2756–2768
25. Khalavka Y, Mingler B, Friedbacher G, Okfepka G, Shcherbak L, Panchuk O (2010) Influence of temperature on the synthesis of thiol-stabilized CdTe nanoparticles in aqueous solutions. Phys Status Solidi (a) 207:370–374

26. Khalavka Y, Sönnichsen C (2008) Growth of gold tips onto hyperbranched CdTe nanostructures. Adv Mater 20:588–591
27. Kim S, Fisher B, Eisler H-J, Bawendi M (2003) Type-II quantum dots: CdTe/CdSe (Core/Shell) and CdSe/ZnTe (core/shell) heterostructures. J Am Chem Soc 2003(125):11466–11467
28. Kloper V, Osovsky R, Kolny-Olesiak J, Sachchiuk A, Lifshitz E (2007) The growth of colloidal cadmium telluride nanocrystal quantum dots in the presence of CdO nanoparticles. J Phys Chem C 111:10336–10341
29. Krupko OV, Khalavka YB, Shcherbak LP (2014) Synthesis of CdS/L-cys nanoparticles colloid solutions with predetermined optical properties. Mater Res Bull 60:264–269
30. Kumar S, Nann T (2006) Shape control of II–VI semiconductor nanomaterials. Small 2(3):316–329
31. Kumar S, Ade M, Nann T (2005) Synthesis and structural metastability of CdTe nanowires. Chem Eur J 2005(11):2220–2224
32. Kumar S, Nann T (2003) Hexagonal CdTe nanoparticles of various morphologies. Chem Commun 2003:2478–2479
33. Labeb M, Sakr A-H, Soliman M, Abdel-Fettah TM, Ebrahim S (2018) Effect of capping agent on selectivity and sensitivity of CdTe quantum dots optical sensor for detection of mercury ions. Opt Mater 79:331–335
34. Resch U, Weller H, Henglein A (1989) Photochemistry and radiation chemistry of colloidal semiconductors. 33. Chemical changes and fluorescence in CdTe and ZnTe. Langmuir 5:4, 1015–1020. https://doi.org/10.1021/la00088a023
35. Lesnyak V, Gaponik N (2013) Aqueous based colloidal quantum dots for optoelectronics. In: Sargent EH (ed) Konstantatos G. Cambridge University Press, Colloidal Quantum Dot Optoelectronics and Photonics, pp 30–58
36. Li W, Liu J, Sun K, Dou H, Tao K (2010) Highly fluorescent water soluble $Cd_xZn_{1-x}Te$ alloyed quantum dots prepared in aqueous solution: one-step synthesis and the alloy effect of Zn. J Mater Chem 20:133
37. Li C, Ando M, Enomoto H, Murase N (2008) Highly luminescent water-soluble InP/ZnS nanocrystals prepared via reactive phase transfer and photochemical processing. J Phys Chem C 112:20190–20199
38. Li Y, Zhong H, Li R, Zhou Y, Chunhe Y, Li Y (2006) High-yield fabrication and electrochemical characterization of tetrapodal CdSe, CdTe, and $CdSe_xTe_{1-x}$ nanocrystals. Adv Funct Mater 16:1705–1716
39. Liyanage GK, Phillips AB, Alfadhili FK, Ellingson RJ, Heben MJ (2019) The role of back buffer layers and absorber properties for >25% efficient CdTe solar cells. ACS Appl Energy Mater 2(8):5419–5426

40. Mao L-H, Zhang Q-H, Zhang Y, Wang C-F, Chen S (2014) Construction of highly luminescent CdTe/CdS@ZnS−SiO_2 quantum dots as conversion materials toward excellent color-rendering white-light-emitting diodes. Ind Eng Chem Res 53(43):16763–16770
41. Matos CRS, Candido LPM, Souza HO, Da Costa LP, Sussuchi EM, Gimenez IF (2016) Study of the aqueous synthesis, optical and electrochemical characterization of alloyed $Zn_xCd_{1-x}Te$ nanocrystals. Mater Chem Phys 178:104–111
42. Mohamed AE, Zheng Y, Yu H, Ying JY (2007) Ultrasensitive Pb^{2+} detection by glutathione-capped quantum dots. Anal Chem 79:9452–9458
43. Murray CB, Norris DJ, Bawendi MG (1993) Synthesis and characterization of nearly monodisperse CdE (E = sulfur, selenium, tellurium) semiconductor nanocrystallites. J Am Chem Soc 115:8706–8715
44. Qian H, Dong C, Peng J, Qiu X, Xu Y, Ren J (2007) High-quality and water-soluble near-infrared photoluminescent CdHgTe/CdS quantum dots prepared by adjusting size and composition. J Phys Chem C 111:16852–16857
45. Pan HC, Cui RJ, Zhu JJ (2008) CdTe quantum dots as probes for near-infrared fluorescence biosensing using biocatalytic growth of Au nanoparticles. J Phys Chem B 112(51):16895–16901
46. Piven N (2008) Aqueous synthesis of alloyed $CdSe_xTe_{1-x}$ nanocrystals. J Phys Chem C 112(39):15253–15259
47. Rajh T, Micic OI, Nozik AJ (1993) Synthesis and characterization of surface-modified 987 colloidal cadmium telluride quantum dots. J Phys Chem 97(46):11999–12003
48. Rivera-Rodriguez G, Peralez-Perez O, Su Y-F, Alamo-Nole L (2016) Effect of the reaction temperature on the optical properties of CdSTe quantum dots synthesized under microwave irradiation. MRS Adv 1:2207–2212
49. Rogach AL, Franzl T, Klar TA, Feldman J, Gaponik N, Lesnyak V et al (2007) Aqueous synthesis of thiol-capped CdTe nanocrystals: state-of-the-art. J Phys Chem C 111:14628–14637
50. Rogach AL, Harrison MT, Kershaw SV, Kornowski A, Burt MG, Eychmuller A, Weller H (2001) Colloidally prepared CdHgTe and HgTe quantum dots with strong near-infrared luminescence. Phys Status Solidi 224:153–158
51. Rogach AL, Katsikas L, Kornowski A, Su D, Eychmüller A, Weller H (1996) Synthesis and characterization of thiol-stabilized CdTe nanocrystals. Ber Bunsenges Phys Chem 100:1772–1778
52. Saikia D, Chakravarty S, Sarma NS, Bhattacharjee S, Datta P, Adhikary NC (2016) Aqueous synthesis of highly stable CdTe/ZnS core/shell quantum dots for bioimaging. Luminescence 32:401–408
53. Samanta A, Deng Z, Liu Y (2012) Aqueous synthesis of glutathione-capped CdTe/CdS/ZnS and CdTe/CdSe/ZnS core/shell/shell nanocrystal heterostructures. Langmuir 28:8205–8215

54. Silva FO, Carvalho MS, Mendonça R, Macedo WA, Balzuweit K, Reiss P, Schiavon MA (2012) Effect of surface ligands on the optical properties of aqueous soluble CdTe quantum dots. Nanoscale Res Lett 7(1):536–546
55. Silva-Vidaurri G, Ruiz-Robles MA, Gutierrez-Lazos CD, Solis-Pomar F, Fundora A, Melendrez MF, Perez-Tijerina E (2019) Study of the influence of microwave irradiation under controlled conditions on the optical and structural properties of CdTe quantum dots synthesized by one-pot synthesis. Chalcogen Lett 16(5):241–248
56. Smith AM, Lane LA, Nie S (2014) Mapping the spatial distribution of charge carriers in quantum-confined heterostructures. Nat Commun 5:4506
57. Talapin D-V, Haubold S, Rogach AL, Kornowski A, Haase M, Weller H (2001) A novel organometallic synthesis of highly luminescent CdTe nanocrystals. J Phys Chem B 105:2260–2263
58. Tohgha U, Varga K, Balaz M (2013) Achiral CdSe quantum dots exhibit optical activity in the visible region upon post-synthetic ligand exchange with D- or L-cysteine. Chem Commun 49(18):1844–1846
59. Tsay JM, Pflughoefft M, Bentolila LA, Weiss S (2004) Hybrid approach to the synthesis of highly luminescent CdTe/ZnS and CdHgTe/ZnS nanocrystals. J Am Chem Soc 126:1926–1927
60. Tynkevych O, Khalavka Y (2018) Influence of transition metal alloying and surface modification of the CdTe quantum dots on their optical properties, band structure and electrochemical activity. Appl Surf Sci 448:237–240
61. Tynkevych O, Karavan V, Vorona I, Filonenko S, Khalavka Y (2018) Synthesis and properties of water-soluble blue-emitting Mn-alloyed CdTe quantum dots. Nanoscale Res Lett 13:132
62. Tynkevych OO, Ranoszek-Soliwoda K, Grobelny J, Selyshchev OV, Khalavka YB (2016) Spectroscopic and electrochemical monitoring of band structure changes during the alloying of CdTe QDs by Hg^{2+} ions. Mater Res Express 3:105046
63. Venkatachalam V, Ganapathy S, Subramani T, Perumal I (2021) Aqueous CdTe colloidal quantum dots for bio-imaging of Artemia *sp*. Inorg Chem Commun 128:108510
64. Vlaskin VA, Barrows CJ, Erickson CS, Gamelin DR (2013) Nanocrystal diffusion doping. J Am Chem Soc 135:14380–14389
65. Wang Y, Hou Y, Tang A, Feng B, Li Y, Liu J, Teng F (2007) Synthesis and optical properties of composition-tunable and water-soluble $Zn_xCd_{1-x}Te$ alloyed nanocrystals. J Cryst Growth 308:19–25
66. Wang CL, Zhang H, Zhang JH, Li M, Sun HZ, Yang B (2007) Application of ultrasonic irradiation in aqueous synthesis of highly fluorescent CdTe/CdS core–shell nanocrystals. J Phys Chem C 111:2465–2469
67. Yang YA, Wu H, Williams KR, Cao YC (2005) Synthesis of CdSe and CdTe nanocrystals without precursor injection. Angew Chem Int Ed 44:6712–6715

68. Ying E, Li D, Guo S, Dong S, Wang J (2008) Synthesis and bio-imaging application of highly luminescent mercaptosuccinic acid-coated CdTe nanocrystals. PLoS One 3(5):e2222
69. Yu WW, Wang YA, Peng X (2003) Formation and stability of size-, shape-, and structure-controlled CdTe nanocrystals: ligand effects on monomers and nanocrystals. Chem Mater 15:4300–4308
70. Xie X, Kwok S-Y, Lu Z, Liu Y, Luo L, Zapien JA et al (2012) Visible–NIR photodetectors based on CdTe nanoribbons. Nanoscale 4:2914–2919
71. Xie R, Zhong X, Basché T (2005) Synthesis, characterization, and spectroscopy of type-II core/shell semiconductor nanocrystals with ZnTe cores. Adv Mater 17:2741–2745
72. Xu SC, Yao CC, Zhang JM, Dai Z, Zheng G, Sun B et al (2009) Synthesis and characterization of the core-shell CdTe/ZnS quantum dots. Adv Mater Res 60–61:165–169
73. Zeng Q, Kong X, Sun Y, Zhang Y, Tu L, Zhao J, Zhang H (2008) Synthesis and optical properties of type II CdTe/CdS core/shell quantum dots in aqueous solution via successive ion layer adsorption and reaction. J Phys Chem C 112:8587–8593
74. Zhang F, He F, He X-W, Li W-Y, Zhang Y-K (2014) Aqueous synthesis of highly luminescent surface Mn^{2+}-doped CdTe quantum dots as a potential multimodal agent. Luminescence 29:1059–1065
75. Zhang J, Li J, Zhang J, Xie R, Yang W (2010) Aqueous synthesis of ZnSe nanocrystals by using glutathione as ligand: the pH-mediated coordination of Zn^{2+} with glutathione. J Phys Chem C 114:11087–11091
76. Zhang Y, Li Y, Yan XP (2009) Aqueous layer-by-layer epitaxy of type-II CdTe/CdSe quantum dots with near-infrared fluorescence for bioimaging applications. Small 5:185–189
77. Zhang H, Wang CL, Li MJ, Ji XL, Zhang JH, Yang B (2005) Fluorescent nanocrystal-polymer composites from aqueous nanocrystals: methods without ligand exchange. Chem Mater 17:4783–4788
78. Zhao D, Fang Y, Wang H, He Z (2011) Synthesis and characterization of high-quality water-soluble CdTe: Zn^{2+} quantum dots capped by N-acetyl-l-cysteine via hydrothermal method. J Mater Chem 21:3365
79. Zhao D, He Z, Chan WH, Choi MMF (2008) Synthesis and characterization of high-quality water-soluble near-infrared-emitting CdTe/CdS quantum dots capped by N-acetyll-cysteine via hydrothermal method. J Phys Chem C 113:1293–1300
80. Zhu J, Zhao Z-J, Li J-J, Zhao J-W (2017) CdTe quantum dot-based fluorescent probes for selective detection of Hg (II): the effect of particle size. Spectrochim Acta A Mol Biomol Spectrosc 177:140–146

OceanofPDF.com

© The Author(s), under exclusive license to Springer Nature Switzerland AG 2023
G. Korotcenkov (ed.), *Handbook of II-VI Semiconductor-Based Sensors and Radiation Detectors*
https://doi.org/10.1007/978-3-031-19531-0_14

14. II-VI Quantum Dots and Their Surface Functionalization

Faheem Amin[1] ✉, Zulqurnain Ali[2] ✉ and Ghenadii Korotcenkov[3]
(1) Department of Physics, School of Natural Sciences, National University of Sciences and Technology, Islamabad, Pakistan
(2) Department of Physics, Air University, Islamabad, Pakistan
(3) Department of Physics and Engineering, Moldova State University, Chisinau, Moldova

✉ **Faheem Amin (Corresponding author)**
Email: faheemamin@sns.nust.edu.pk

✉ **Zulqurnain Ali**
Email: zulqurnain.ali@mail.au.edu.pk

Keywords II-VI QDs – Advantages – Biocompatibility – CdSe – CdSe/ZnS – Colloidal stability – Photostability – Functionalization of II-VI QDs – Application – Biolabeling – Biology – Biosensors – Drug delivery – Medicine – Bioconjugation – Covalent linkage – Electrostatic – Non-covalent linkage – Biofunctionalization – Biomolecules – Biotin – DNA – Peptides – Proteins – RNA – Functional groups – Amines – Carboxylic acids – Hydrocarbon chain – Polyethylene glycol (PEG) – Thiol groups – Phase transfer QDs – Encapsulation – Ligand bilayer – Ligand exchange – Ligand modification – Polymer coating – Quantum dots – Molecular orbital (MO) theory – Synthesis – Size-quantization

14.1 Introduction

II-VI nanocrystals (NCs) aka quantum dots (QDs) are important class of materials due to their size- and composition-dependent optical properties (broad absorption and narrow emission), large optical absorption coefficient, excellent photostability, superior quantum efficiency, and wide range of material choice. It is important to note that II-VI QDs such as CdSe have higher luminescence and quantum yield compared to conventional fluorophores under appropriate conditions (Table 14.1).

Table 14.1 Comparison of CdSe quantum dots and organic dyes

Parameter	Comparison of CdSe/ZnS QDs with fluorophores
Brightness emission	10–100 times better than organic fluorophores
Fluorescent lifetimes	10–40 ns unlike conventional organic dyes with few ns
Molar extinction coefficient	10–100 fold higher than most organic dyes
Stokes shift	Large separation between the excitation and emission wavelength maximum
Autofluorescence contribution	Quantum dots reduce the contribution of autofluorescence
Light source	Single QD light source for various-sized QDs
Emission spectra	QDs have narrow and symmetrical spectra
Photostability	Inorganic nature of QDs contributes to their photostability
Photobleaching	QDs have 100 times better stability against bleaching
Quantum yield	Up to 90% with ZnS shell

Source: Reprinted from Ref. [13]. Published 2017 by Springer as open access

14.1.1 Quantum Dots

Since their inception in 1981, inorganic semiconductor crystals have gained manifold progress due to their unique offering of quantum size effect. The pioneering works of Ekimov and Onushchenko [29, 30] and Brus [15] have been carried on by many groups even after four decades. In particular, the possibility of suspending small clusters in solution has paved the way for their applications in biological labeling of cells

The size quantization of electrons and holes in a semiconductor sphere results in the shifting of optical lines as a function of sphere radius. This can be explained on the basis of a model presented by Ekimov and

Onushchenko [30] to allow for the influence of size quantization on interband transition. Based on the orthogonality of the wave functions of electrons and holes in a spherically symmetric well with infinitely high walls, the absorption coefficient can be calculated and is given as follows [11]:

$$K = A \sum_{l,n} (2l+1)\, \delta \left(\Delta - \frac{\hbar^2}{2\mu} k_{ln}^2 \right) \tag{14.1}$$

Therefore, a series of interband transitions should occur with a threshold:

$$\hbar\omega_{01} = E_g + \frac{\hbar^2 \pi^2}{2\mu a^2}, \tag{14.2}$$

where E_g is the bulk bandgap and $\Delta = \hbar\omega - E_g$.

It follows that, for very small spherical crystals, the effective bandgap increases on decreasing the radius of the sphere. The understanding about development of band structures in semiconductor crystallites can be adopted from the description of polymeric systems having strong chemical bonding. This description is based upon molecular orbital (MO) theory presented by Huckel for conjugated linear polyene chain. The model π MOs are modeled as a linear chain of *N* one-electron, one-orbital atoms separated by a distance *a*. The energy eigenvalues for this system are given by the following:

$$\begin{aligned} E(N,m) &= e + 2\beta \cos\left(\tfrac{m\pi}{N+1}\right) & m &= 1, 2, \ldots\ldots..N \\ &= e + 2\beta \cos(k_m a) & k_m &= \tfrac{m\pi}{(N+1)a} \end{aligned} \tag{14.3}$$

Here *e* is orbital energy while *β* is the resonance integral. As N ➔ ∞, k becomes continuous from 0 to π/*a* and E(k) runs between *e* + 2*β* and *e* − 2*β*. The dispersion relation is plotted in Fig. 14.1a. For $k_m a << 1$:

$$E(k_m) = (e + 2\beta) + \frac{2\beta k_m^2 a^2}{2} = E_0 + \left(\frac{\pi^2}{2L^2}\right) 2\beta a^2 m^2 L = (N+1)\, a \tag{14.4}$$

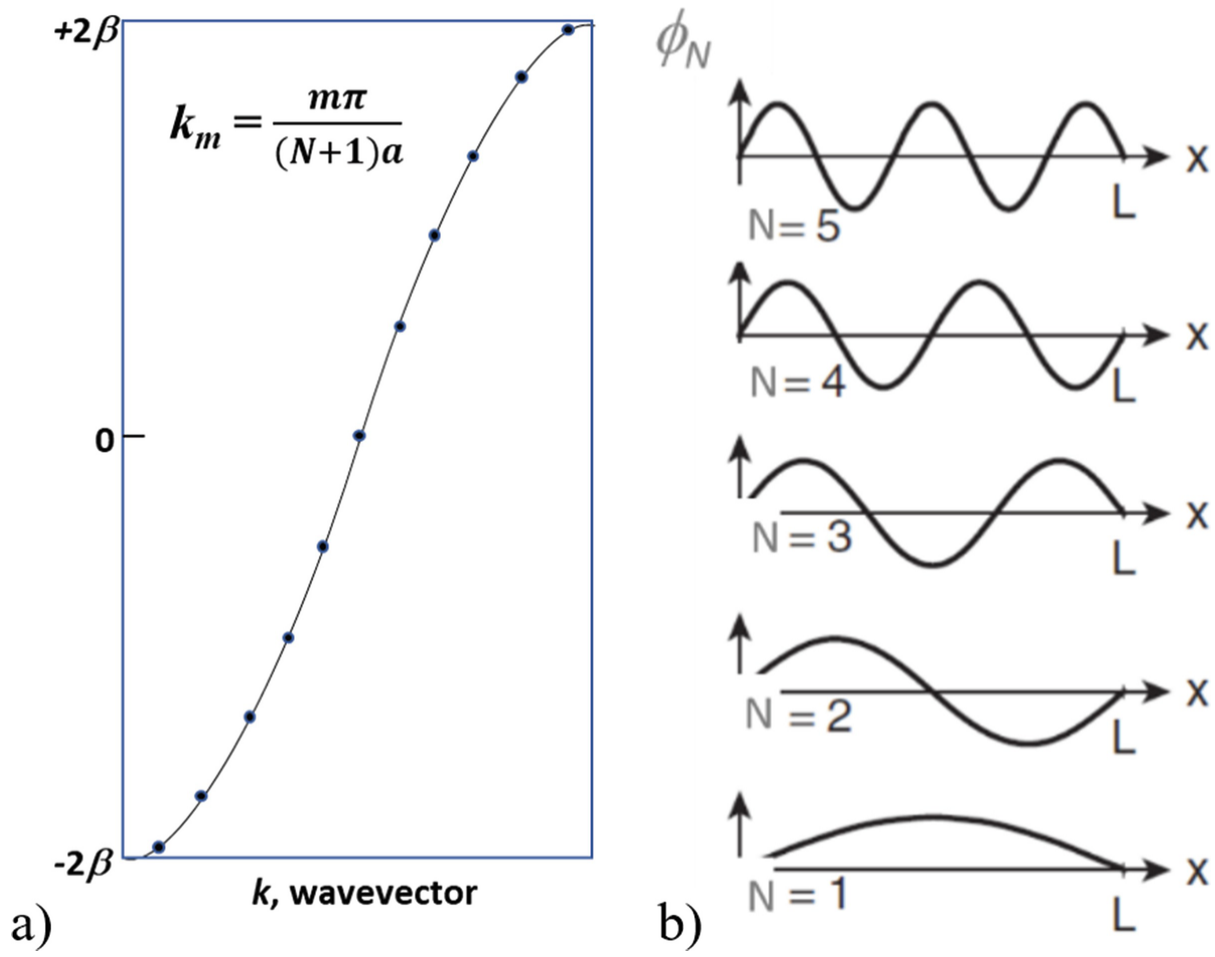

Fig. 14.1 (**a**) Dispersion relation of a polyene chain band structure. (**b**) MO within the linear *N* one-electron chain with increasing number of atoms

It shows that the MO eigenspectrum of an *N* atom chain, over a limited range of energy near the lower band edge, is the same as that of a particle of mass $m^* = \hbar^2/(2\beta a^2)$ in a potential well of length L. The lowest MO has no additional nodes within the chain. As N increases the lowest level becomes more stable, asymptotically approaching the lower band edge energy e + 2β. However, since this MO has nodes on the chain ends, its energy is shifted higher than the band edge: this is in essence the "quantum size effect" (see Fig. 14.1b).

Based upon the above MO description, we can now describe the band structure of a II-VI zinc blende structure. The orbitals in this case are bonding (σ) and antibonding (σ*) orbitals extended over the 3D crystallite as it grows (Fig. 14.2). The band edges are designated by HOMO (highest occupied MO in valence band) and LUMO (lowest unoccupied MO in conduction band). The bonding configuration is based upon the

tetrahedrally surrounded Cd atom by S atom on the corners of a tetrahedron. With a minimal basis of three *P* and one *S* atomic orbitals contributed by each cation and anion, there will be four occupied and four unoccupied electronic bands. These HOMO and LUMO bands are principally formed in the region $|K| \leq \pi/D$, and therefore the band structure depends upon the crystallite size. If *D* is much larger than a unit cell, then the region of BZ involved is small, and effective mass approximation can be used.

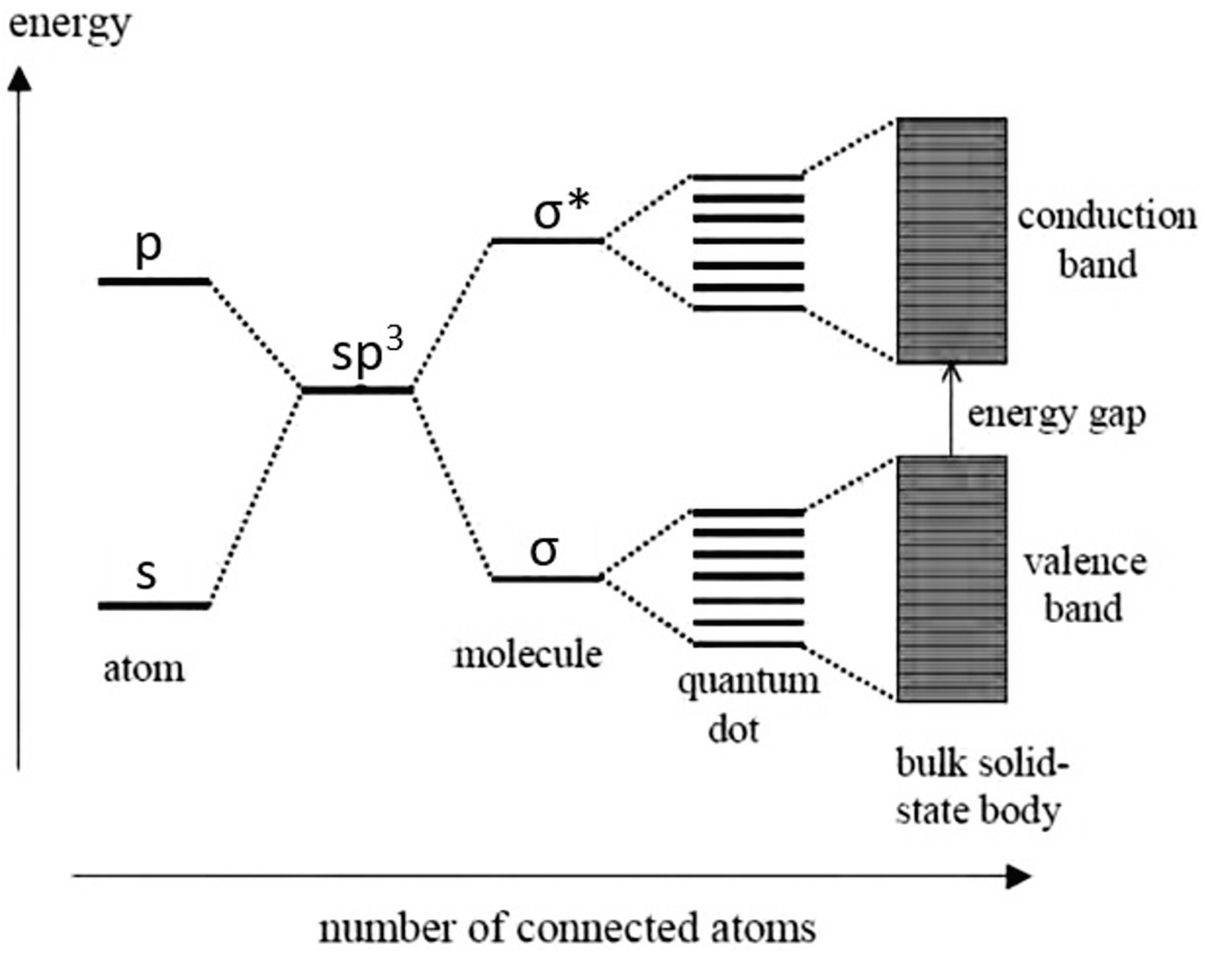

Fig. 14.2 Model for evolution of discrete MOs into continuous bands. By binding more and more atoms together, the discrete energy levels of the atomic orbitals merge into energy bands. (Adapted with permission from Ref. [4]. Copyright 1997: Elsevier)

The cluster size also has a definite impact on the bandgap of semiconductor as described in terms of quantum confinement (Fig. 14.3). This can be understood by the following plot of lowest allowed electronic transition energy as a function of size. The smaller the cluster size the larger the region in k space required for confinement of electron inside the cluster. The size-dependent expectation value of energy is as follows:

$$E_i = \left|\left\langle \psi_i \left| \hat{H} \right| \psi_i \right\rangle\right| \simeq E_c + \frac{\pi^2}{2R^2} \sum_{i=x,y,z} \left[\frac{\partial^2 E}{\partial {k_i}^2}\right] \tag{14.5}$$

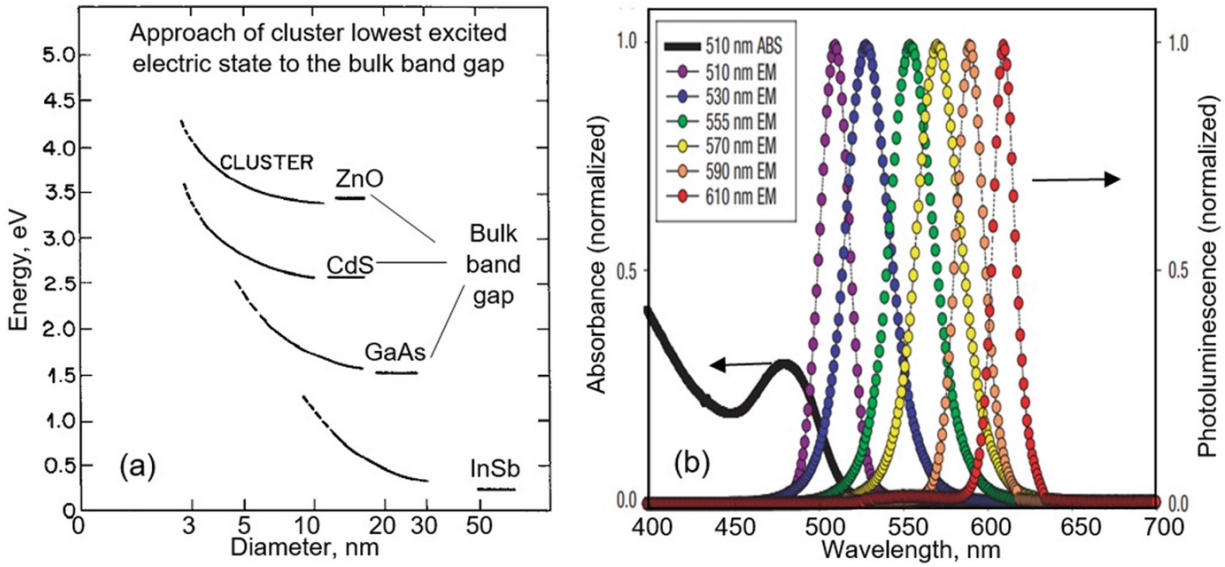

Fig. 14.3 (**a**) Calculated energy of the cluster lowest excited electronic state in relation to the bulk bandgap (Reprinted with permission from Ref. [15]. Copyright 1986: ACS). (**b**) Absorption and emission of six different dispersions of CdSe QD (λ_{max} (nm)) versus CdSe core size (r_{core} (nm)): 510–(1.35), 530–(1.45), 555–(1.75), 570–(1.90), 590–(2.15), and 610–(2.40). The black line shows the absorption of the 510 nm emitting QDs. (Reprinted with permission from Ref. [71]. Copyright 2005: Springer Nature)

The curvature term in this expression, near the k = 0 for conduction band, is isotropic. Therefore:

$$E_i \simeq E_c + \frac{\pi^2 \hbar^2}{2 m_e R^2} \tag{14.6}$$

If we also include holes, then:

$$E^* \simeq E_{g,bulk} + \frac{\pi^2 \hbar^2}{2R^2}\left[\frac{1}{m_e} + \frac{1}{m_h}\right] - \frac{1.8e^2}{\epsilon R}, \tag{14.7}$$

where $E_{g,bulk}$ is the optical bandgap. R/1.8 is the average separation between the charges. This is the so-called Brus equation which relates the transition energy with the bandgap and effective masses of the carriers m_e and m_h [15]. The third term is included to account for the coulomb interaction between electrons and holes. The transition energy is simply the

solution of Schrodinger wave equation and can be easily achieved for an electron-hole system like a standard particle in a box approach [52].

Due to the reasons explained above, the spatial confinement of excitons within these extremely small crystals results in emission at discrete wavelengths. In quantum dots, also sometimes called artificial atoms, the spacing of the energy levels can be precisely controlled through size variation. This allows one to excite several molecular readers with a single excitation and spatially resolvable readouts.

14.1.2 Synthesis of Semiconductor Quantum Dots

Synthesis of semiconductor quantum dots is an important area of semiconductor material technology. The earlier works on colloidally stable quantum dots include the organometallic synthesis by rapid pyrolysis of injected liquid precursors in coordinating solvents. The earlier work by Murray et al. [76, 77] has opened the way for basic research in colloidal chemistry to achieve highly stable monodispersed nanocrystals of metal chalcogenides. Especially nanocrystallites of CdSe attracted an epic attention of researchers due to their munificent offering toward tunable fluorescence. To obtain these nanocrystals, highly coordinating mixture of solvents trioctylphosphine oxide (TOPO) and a phosphine (trioctyl or butyl) is heated to a temperature of 300 °C under inert atmosphere. The precursors of metal as well as chalcogenide are then introduced into the hot liquid to provide free ions by thermal decomposition of precursors. Bawendi and coworkers [76, 77, 81] have worked tremendously on the study of colloidally stable CdSe quantum dots. In a series of studies during the early 1990s, they determined the excited electronic states [76, 77], size-dependent hole spectrum [81], and narrow emission attributed to surface localization of photogenerated excitons [80]. Other types of quantum dots made up of CdS, CdTe, and doped CdHgTe have also been reported [10, 91, 94]. Especially sequential discontinuous growth of magic-sized clusters is reported which resembles more to molecular behavior than small nanocrystals [55, 56, 123]. The features of the processes for the synthesis of QD of II-VI compounds using various approaches are considered in sufficient detail in the Chaps. 11–13, Vol. 1.

14.2 Stability and Biocompatibility of II-VI QDs

14.2.1 Stability of II-VI Colloidal Nanoparticles

Colloidal stability is one of the key requirement for biofunctionalization and subsequent application in labeling, sensing, and targeting. However, nanoparticles in suspension are known to be prone to aggregation, the rate of which depends upon physiological conditions such as pH, temperature, and the presence of other analytes. In principle, the stability of a colloidal suspension is determined by sum of the van der Waals attraction and repulsion between the colloidal particles. When the van der Waals attraction is stronger than repulsion, then the colloidal particles will aggregate, and therefore the state of the suspension will be unstable. If the repulsion is strong enough to overcome the van der Waals force, then the system will be stable. This means that in order to increase the stability of a colloidal suspension, it is necessary to increase the repulsion between nanoparticles. Currently, there are two mechanisms of colloidal stability based on steric repulsion and electrostatic repulsion. In practice, the most popular way to achieve colloidal stability is to add an additional component, such as a surfactant or polymer, which adsorbs onto the colloidal particles and changes their surface properties [116]. For example, the layering of polyethylene glycols on the surface of nanoparticles contributes to an increase in steric repulsion due to the surface charge. With some polymers [34], a combination of electrostatic and steric stabilization is also possible.

Figure 14.4 shows some hydrophobic ligand molecules commonly used to stabilize colloidal particles. They are drawn to scale corresponding to the particle diameter (5 nm). It was found that CdSe and CdSe/ZnS QDs can be stabilized by trioctylphosphine (TOP) or its oxide (trioctylphosphine; TOPO) by binding preferentially to Cd or Zn atoms of nanocrystals [3]. Besides TOP and/or TOPO, hexadecylamine or other amines are also commonly used ligands for CdSe quantum dots [44], which can also be replaced by stronger binding molecules, e.g., with one or more thiol groups [27].

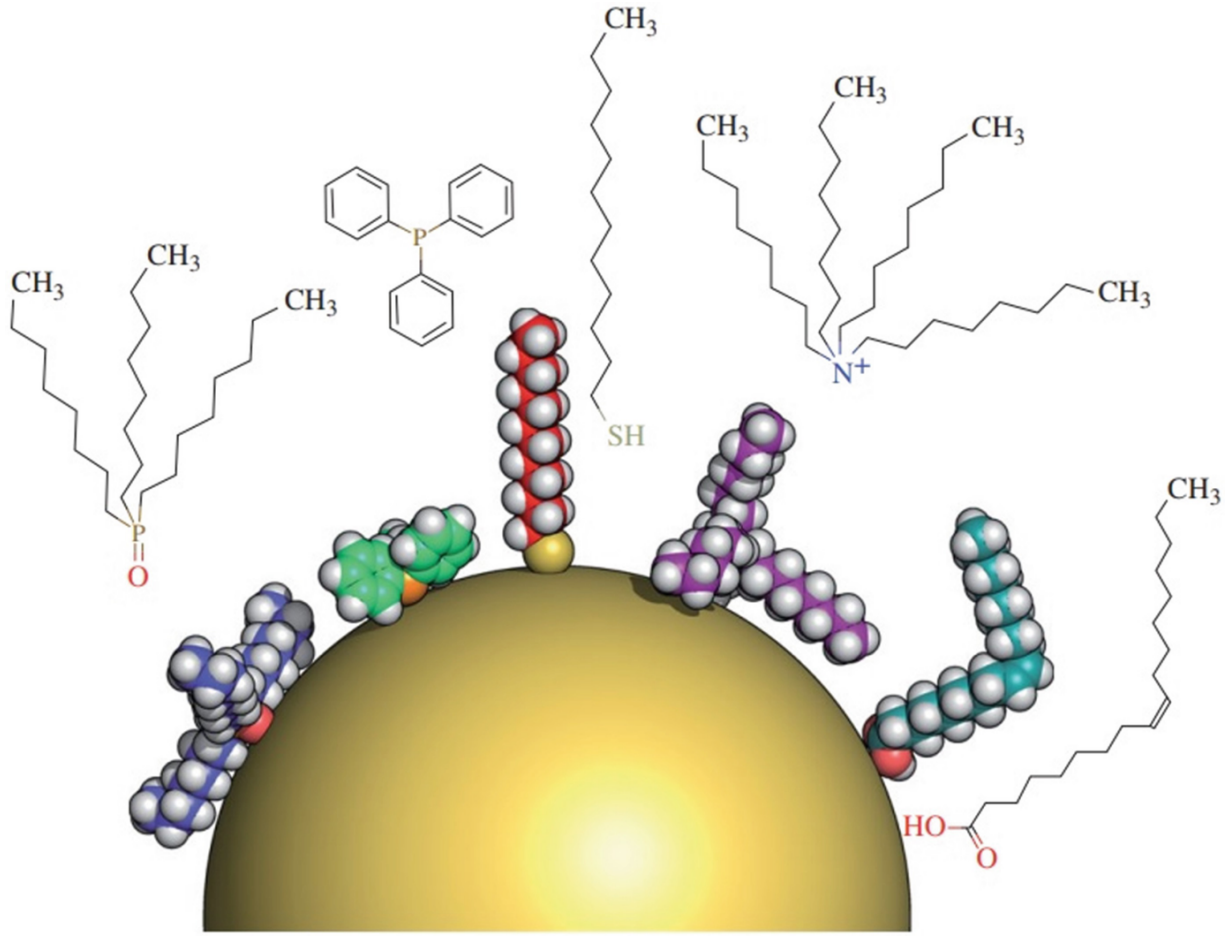

Fig. 14.4 A nanoparticle of 5 nm core diameter with different hydrophobic ligand molecules both drawn to scale. The particle is idealized as a smooth sphere; the schematic molecule structures above are not drawn to scale. Left to right: trioctylphosphine oxide (TOPO), triphenylphosphine (TPP), dodecanethiol (DDT), tetraoctylammonium bromide (TOAB), and oleic acid (OA). The spatial conformation of the molecules is only shown schematically as derived from their chemical structure and space-filling models. (Reprinted with permission from Ref. [101]. Copyright 2010: Royal Society)

The possible choice of ligand molecules depends on the material of the nanoparticle core, particle size, and solvent [101]. For example, it has been found that strongly binding molecules forming a dense layer stabilize particles better than weakly binding ones. In aqueous solutions, strongly charged ligand molecules containing, for example, carboxylic or sulfonic acid groups stabilize the particles for a longer time even at higher salt concentrations. Finally, sterically stabilized ligand molecules have been shown to be much more resistant to high salt concentrations than electrostatically stabilized nanoparticles [95], provided they are strongly bound to the surface of nanoparticles.

14.2.2 Surface Modification and Photostability

Surface modification, i.e., the formation of ligand shell, can also improve the photostability of colloidal II-VI nanoparticles [100, 115]. Bare quantum dots, suffer from the nonradiative relaxation of photogenerated charge carriers through the surface trap states [54]. This leads to a decrease in quantum yield [16], which limits the use of QDs in applications based on excitation. The surface modification makes it possible to passivate these surface trap states [100]. It should also be taken into account that in case of fluorescent quantum dots, light irradiation can also enhance oxidation of the surface of inorganic particles, which ultimately leads to their aggregation caused by desorption of stabilizing ligands [1, 19].

Experiment has shown that the best way to solve the problem of photostability is to grow an additional layer (shell) of another material on top of the stabilized inorganic core [22, 61, 92]. Improved photochemical stability is achieved by eliminating or blocking nonradiative recombination pathways. The use of core-shell assembly leads to high quantum yields at room temperature (>50%) [31]. Linkov et al. [61] have reported that careful engineering of multilayer shell around CdSe core may result in 100% quantum yield (QY) in organic solvents. However giant shell consisting of multilayers diminishes the QY of these QDs substantially [117]. The modified surface not only serves for the passivation of trap states but also provide a physical barrier between optically active core and surrounding medium, thus making the nanocrystal less sensitive to the environmental changes. Various materials can be used as shell including CdS, ZnS, ZnSe, silica, etc. At that, silanized CdSe/ZnS core-shell structures demonstrated the maximum photostability [35]. Hydrophobic CdSe/ZnS core-shell nanocrystals with a core size between 2 and 5 nm were embedded in a siloxane shell with thickness ~ 1–5 nm and functionalized with thiol and/or amine groups. It was found that silanized CdSe/ZnS nanocrystals exhibited enhanced photochemical stability over organic fluorophores. They also display high stability in buffers at physiological conditions (>150 mM NaCl) (see Fig. 14.5).

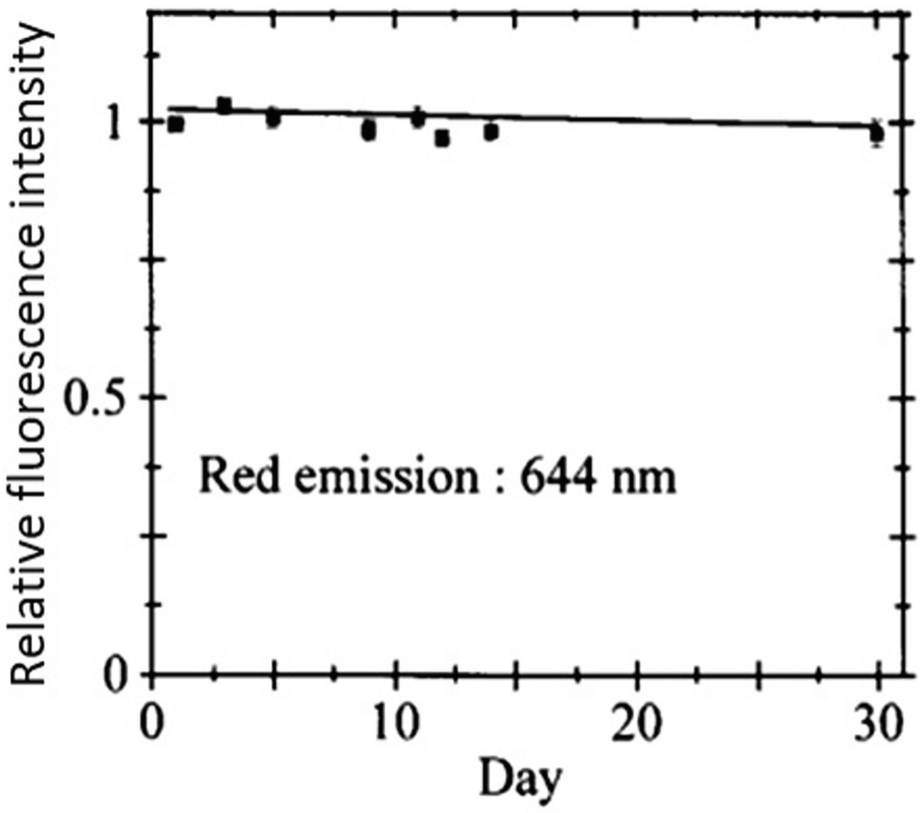

Fig. 14.5 Time dependence of fluorescence intensity of red silanized nanocrystals over time. The particles in the 10 mM PB buffer solution are excited each day and do not show an appreciable decrease of the luminescence over 1 month. (Reprinted with permission from Ref. [35]. Copyright 2001: ACS)

Besides this, incorporation of transition metals (Cu, Mn, Co) in the host core-shell has been done effectively to control the nonradiative decay from metal-excited state [12, 117, 118]. This helps in increasing the fluorescence lifetime of nearby fluorophore to milliseconds by resonance energy transfer action from quantum dot to fluorophore [49]. Depending upon the band alignment and relative positions of valence and conduction bands, the core-shell structures can be classified in two groups, i.e., type I and type II materials (see Fig. 14.6). In type I materials, the conduction band of shell is higher than the core material, while valence band is lower than the core material, whereas in case of type II materials, both the bands of core are higher than the corresponding bands of shell [43]. Features of the formation of core-shell structures based on II-VI compounds are discussed in detail in the Chap. 12 (Vol. 1).

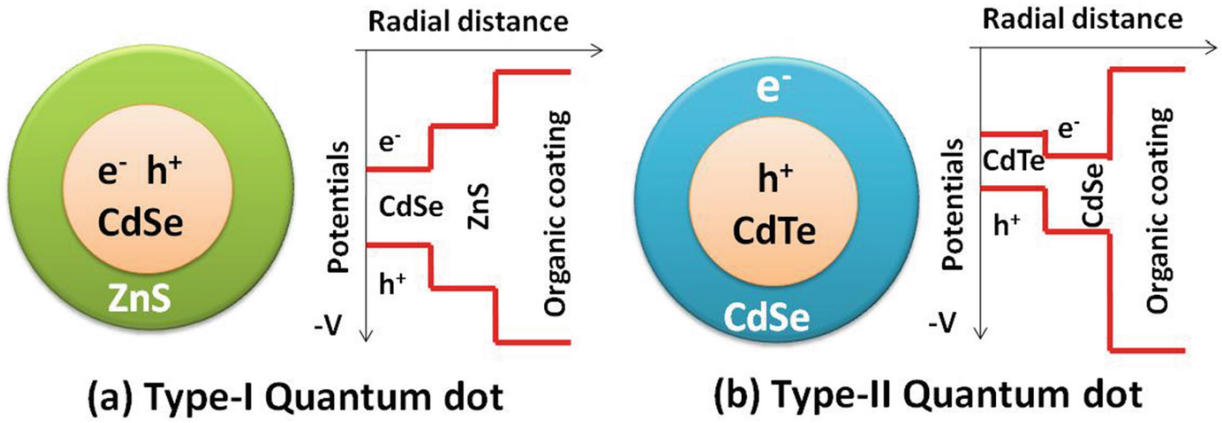

Fig. 14.6 Illustration of type I (**a**) and type II (**b**) quantum dots. (Reprinted from Ref. [43]. Published by Intechopen as open access)

14.2.3 Biocompatibility

The biocompatibility of materials is another issue that needs to be addressed in their biomedical use. Currently, there are many definitions of biocompatibility. However, taking into account the specifics of the field of application of II-VI compounds, in our case, the most correct definition, from our point of view, is that it is "the absence of toxic or harmful effects on biological systems, both during its testing and in the course of medical therapy."

Since the pioneering works by Alivisatos and coworkers [14] and Chan and Nie [17], a number of efforts have been made to develop biocompatible quantum dots that can be used for cellular labeling, tracing, physiological mapping, cell mobility, deep-tissue tomography, and sensing purposes. Nevertheless, biocompatibility of quantum dots has remained a challenge in their commendable use for biolabeling and sensing. For II-VI compounds involving Cd, the problem of biocompatibility is especially acute, since Cd compounds are toxic to the human body. The leaching of Cd ions from QD core has been demonstrated by Ipe et al. [42] where the authors irradiated the CdS and CdSe core structure. Quantum dot cores were found to generate ROS species (hydroxyl and superoxides) which were mitigated by the introduction of shell on the surface. CdTe quantum dot cores were also reported to produce ROS that lead to DNA damage and ultimately cause cell death [64]. A large number of studies have been carried out to date to ascertain the possible reasons of cytotoxicity. Therefore, in many cases, despite the high fluorescence efficiency of II-VI compounds, especially their quantum dots, there are limitations on their biomedical application.

To reduce the toxic effects of Cd compounds, the same approaches that were used to improve the stability of colloidal nanoparticles can be used. It was reported that the cytotoxicity of QDs can be modulated by processing parameters during synthesis, exposure to UV light, and surface coatings [25]. For example, Bakalova et al. [7] utilized the photosensitization of CdSe QDs through UV irradiation to sensitize leukemia cell upon antibody-specific interaction. It has been demonstrated that not only Cd ions but also the surface chemistry and thus particle stability against aggregation play a vital role for cytotoxic effects [25, 53]. Nagy et al. [78] synthesized 3 nm CdSe QDs functionalized with mercaptopropionic acid (MPA) or cysteamine (CYST). CYST QDs have been found to cause significant cytotoxicity accompanied by DNA strand breakage. MPA QDs do not cause cytotoxicity and the formation of reactive oxygen species. However, even in this case, MPA QDs induced a large number of DNA strand breaks. Apropos to this, Yildiz et al. [121] prepared a number of polythiol-coated QD systems containing poly(methacrylate) backbone decorated with polyethylene glycols and polythiols. However, although the use of thiols as coating agents has facilitated the application of CdTe QDs, the levels of biocompatibility of these QDs remain insufficient, and the harm they cause in various organisms, organs, or cells needs to be studied. Tan et al. [106] have reported the synthesis of QD-chitosan nanocomposites for biodetection of nitric oxide. However, the size of nanocomposites is much larger than QDs only. Perez-Donoso et al. [84] prepared glutathione (GSH)-capped CdTe QDs. These CdTe-GSH NPs had the same size, chemical composition, absorbance, fluorescence spectra, and quantum yields as in the case of QD synthesis by more complex and expensive methods. At the same time, the toxicity of these CdTe QDs was lower than that of QDs obtained by other chemical methods, probably as a result of a lower level of Cd^{+2} and a higher amount of GSH.

But, the experiment showed that the most effective approach to reduce the toxicity of Cd compounds is still the approach described earlier and based on the formation of core-shell structures, in which Cd compounds form the core and the shell is formed by a biocompatible compound, for example, Zn compounds, which are less toxic [67, 71]. Thus the shell serves as a barrier to leaching of toxic Cd ions from the core and helps in reducing the cytotoxicity effects of nanoparticles [105]. It should be noted that the best available QD fluorophores for biological applications are made from

ZnS-coated CdSe cores, as their lattices match pretty well and are compatible to each other [71]. The ZnS layer passivates the surface of the core, protects it from oxidation, prevents Cd/Se from seeping into the surrounding solution, and also provides a significant improvement in the photoluminescence yield. Although thin ZnS shells (1–2 monolayers) often give the highest PL yields, thicker ZnS shells (4–6 monolayers) provide greater core protection from oxidation and the harsher conditions presented by biological media (e.g., acidic buffers and cellular organelles). However, studies show extracellular cytotoxicity even of water-soluble CdSe/ZnS QDs, since Cd^{2+} can be released from nanoparticles in case of poor purification or incomplete coverage of the surface of the CdSe core by the ZnS shell [53].

The formation of a polymer shell on the surface of II-VI semiconductor core can also be adopted for passivation of Cd^{+2} poisoning. For example, Kumari et al. [58] found that all synthesized CdSe QD samples which have been coated with PVA and PEG were highly biocompatible. To this end, PEG-CdSe QDs were the best in terms of biocompatibility and photoluminescence intensity, which makes them promising as luminescent probes for bioimaging applications.

Nanoparticles of different core II-VI materials can also be modified with a silica shell, which can be considered as an inorganic polymer, by the so-called Stöber method [37]. The method comprises first a ligand exchange procedure in which a layer of silanes is first bound to the nanoparticle surface. Then, using this layer, a polymeric, cross-linked inorganic silica shell is deposited on the particles, which can be further derivatized. A number of reports on silica shell coating of fluorescent quantum dots have been reported [24, 35, 79]. It is important to note that QDs encapsulated by some simple molecules, such as mercaptoacetic acid, mercaptopropionic acid, 11-mercaptoundecanoic acid, and 2-aminoethanethiol, are more toxic than the ones coated with silica. The silica layer can be very thick (up to several micrometers), which reduces the possible leaking of interior toxic cadmium under physiological conditions. There is no clear toxic effect observed even if additional PEG molecules were attached to the silica exterior surface [21].

14.3 Surface Functionalization of Quantum Dots

To use a colloidally stable suspension of nanoparticles for biological applications, post-modification of the nanoparticle surface is always required. Post-modification of the surface of particles is mainly required with purpose to functionalize the surface and improve the stability and solubility of QDs in water, as well as the functionality of linking biomolecules (see Fig. 14.7). This is typically termed as functionalization or biofunctionalization of II-VI QDs. (Bio)functionalization of quantum dots can be done in various ways such as ligand (molecular) exchange, ligand modification, and surface coating or encapsulation [96, 124]. Among these ligand exchange and surface coating are more widely used techniques for surface modification. While ligand exchange provides an easy approach for surface functionalization, surface coating offers the perk of single system for a variety of surfaces. Below we discuss the advantages and shortcomings of both the approaches.

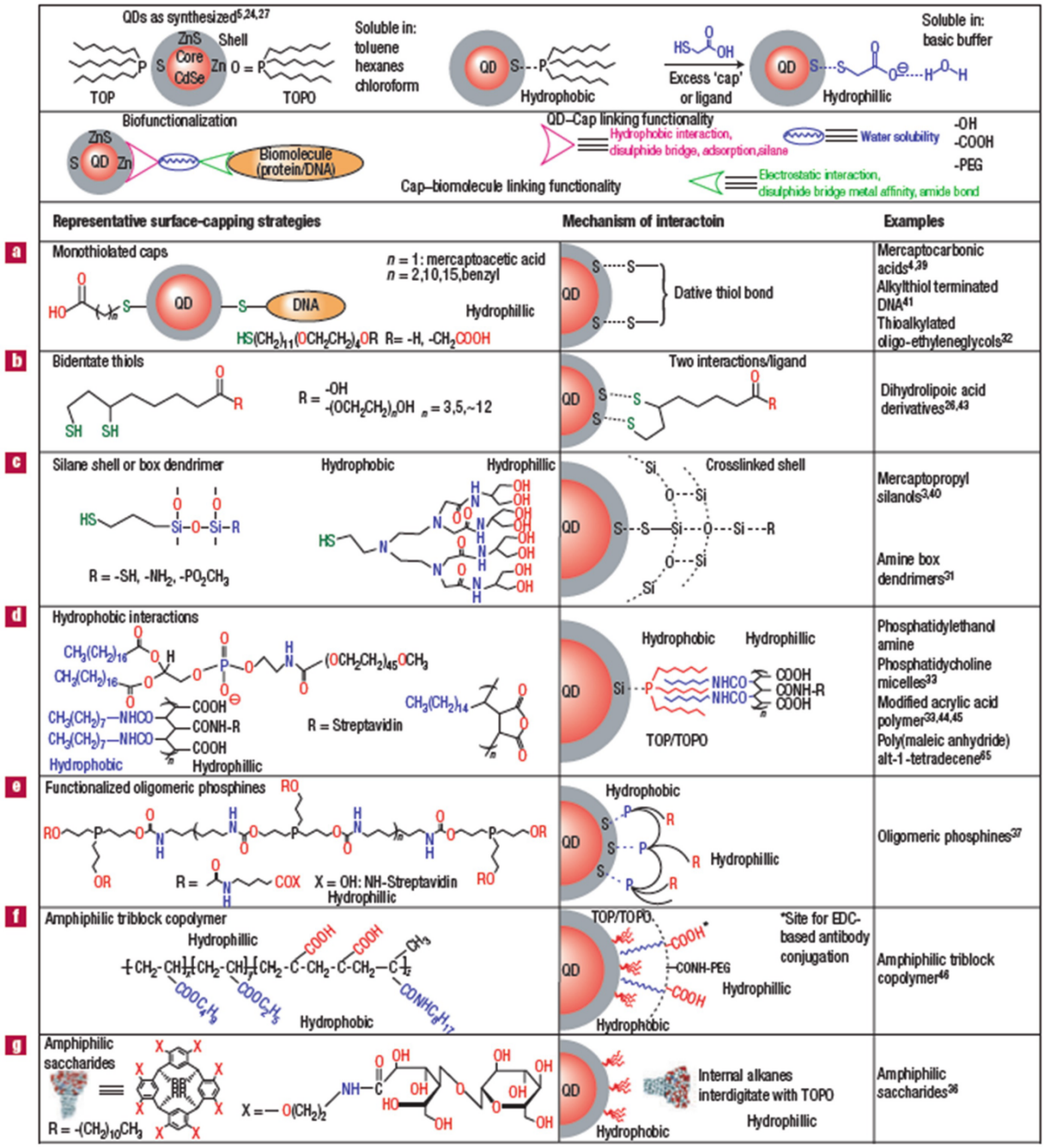

Fig. 14.7 Schematic of generic QD solubilization and biofunctionalization (**a**–**g**). Biofunctionalization (second panel from top) uses caps/ligands to provide three functions. Linkage to the QD (pink), water solubility (blue), and a biomolecule linking functionality (green). Examples of surface-capping strategies and the mechanism of interaction with the QD and the aqueous environment. For the cap exchange (top right), excess thiolated cap displaces the original TOP/TOPO organic coating by binding the ZnS surface with the thiol group and imparting hydrophilicity with the charged carboxyl (or other functionalities) yielding water-soluble colloidal QD dispersions. (Reprinted with permission from Ref. [71]. Copyright 2005: Springer Nature)

14.3.1 Phase Transfer of Nanoparticles

Monodispersed colloidal nanocrystals are usually obtained in organic solvents and therefore have hydrophobic alkyl chains on the surface. Such nanocrystals can dissolve only in nonpolar and aprotic polar solvents where they can be stable for a long time. Once these nanocrystals are transferred to an aqueous medium, which is required for most biomedical-related applications, they may lose their colloidal stability. Therefore, it is essential to develop methods which can retain colloidal stability of water-soluble QDs so that they can be used in biological applications. This is a rather difficult task, since the ligand chosen to change the surface properties of QDs must retain the excellent optical properties of QDs and also stabilize them in an aqueous solution. In addition, the phenomenon of transferring the particles from one solvent to another depends upon the parameters such as polarity, pH, and surface charge to name a few. Based upon numerous studies, it has been established that these requirements can be achieved by ligand exchange, ligand modification, or encapsulation in microspheres (such as silica nanoparticles), liposomes or hydrogel (see Fig. 14.8).

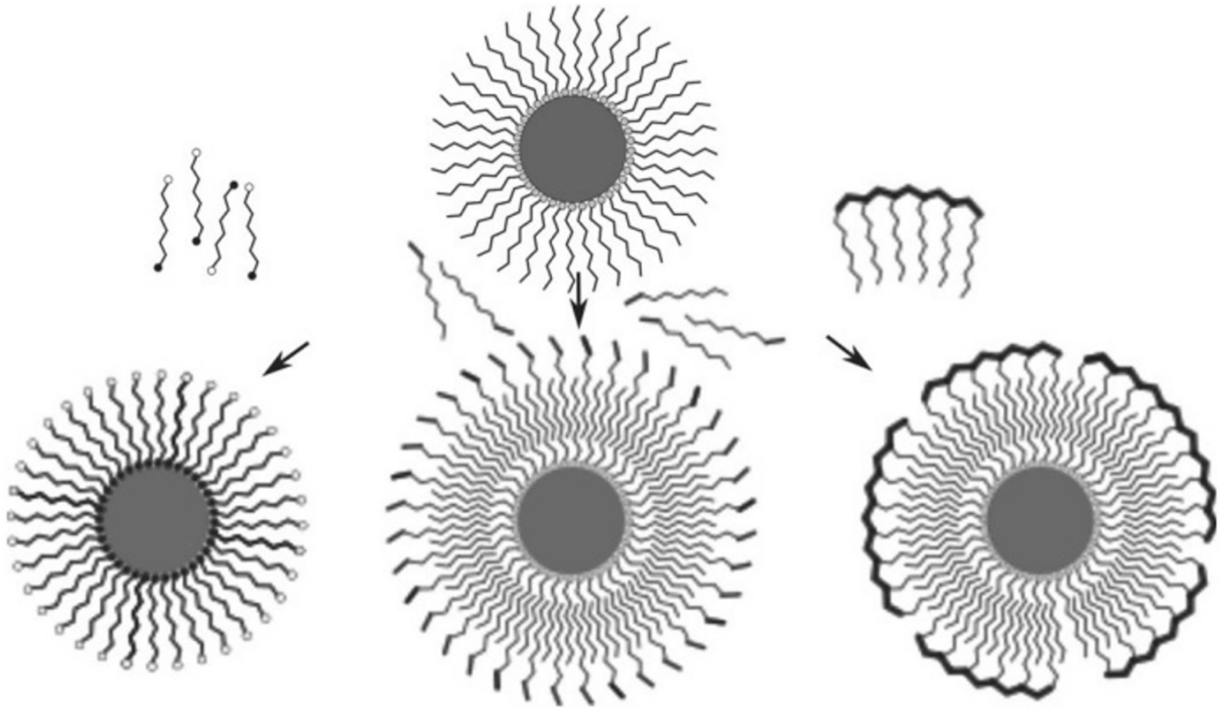

Fig. 14.8 Different strategies for phase transfer of nanoparticles. Left: ligand exchange, the incoming ligand has one head group binding to the nanoparticle surface (filled circles); the other end (empty circles) is, e.g., hydrophilic. Center: additional layer of ligand molecules adsorbing, e.g., by hydrophobic interaction. Right: amphiphilic polymer with hydrophobic side chains and a hydrophilic backbone (strong black). (Reprinted with permission from Ref. [101]. Copyright 2010: Royal Society)

14.3.1.1 Ligand Exchange

In the ligand exchange strategy, molecules that stabilize particles in the initial phase (e.g., after synthesis) are replaced by other, more strongly binding ligands, which allow the transfer to the second phase and provide colloidal stability there [101]. As a rule, this occurs by replacing hydrophobic ligands with hydrophilic ones. In general, the surface ligands used for this purpose can be divided into three groups, viz., X-, L-, and Z-type, based upon the number of donated electrons [63]. In general ligand exchange may alter the optical properties of the particles in the form of damaging or passivation of the surface states. Furthermore, it was found that ligand-ligand interactions had a great influence on the shape ligand exchange isotherm as suggested by ^{1}H NMR, FTIR, and XPS data [74]. The events of ligand exchange can be followed by studying the thermodynamic parameters such as K_a, ΔH, ΔS, and ΔG. This has been demonstrated for alkyl amines replacing the cadmium oleate in the form of $Cd(OA)_2$-$(C_xAm)_2$ complexes where the decrease in bound fraction of $Cd(OA)_2$ relates to the equilibrium between the two species. In addition, the equilibrium constant was found to decrease with increase in chain length of the alkyl group.

Experiment has shown that colloidal nanocrystals can be transferred to water-based medium by appropriate exchange of more loosely bound surface ligands, which nanoparticles usually have after synthesis, with water-soluble moieties (see Fig. 14.9). This is typically achieved by using PEG-polyethylenimine moieties where polyethylenimine performs the anchorage to the particle surface and provide strong bonding to inorganic surfaces of II-VI nanoparticles. Another way to achieve this is through mercapto-carbonic acid molecules (e.g., mercaptoacetic acid) where thiol (mercapto) moiety serves for anchoring on the particle surface while carboxylate (carbonic acid) moiety renders water solubility [71]. One example of the ligand exchange is the transfer of TOP/TOPO-coated CdSe/ZnS quantum dots into an aqueous solution by replacing hydrophobic phosphine-based ligands with a hydrophilic thiol-based molecule, often mercaptocarboxylic acids (e.g., MPA, MUA, etc.)

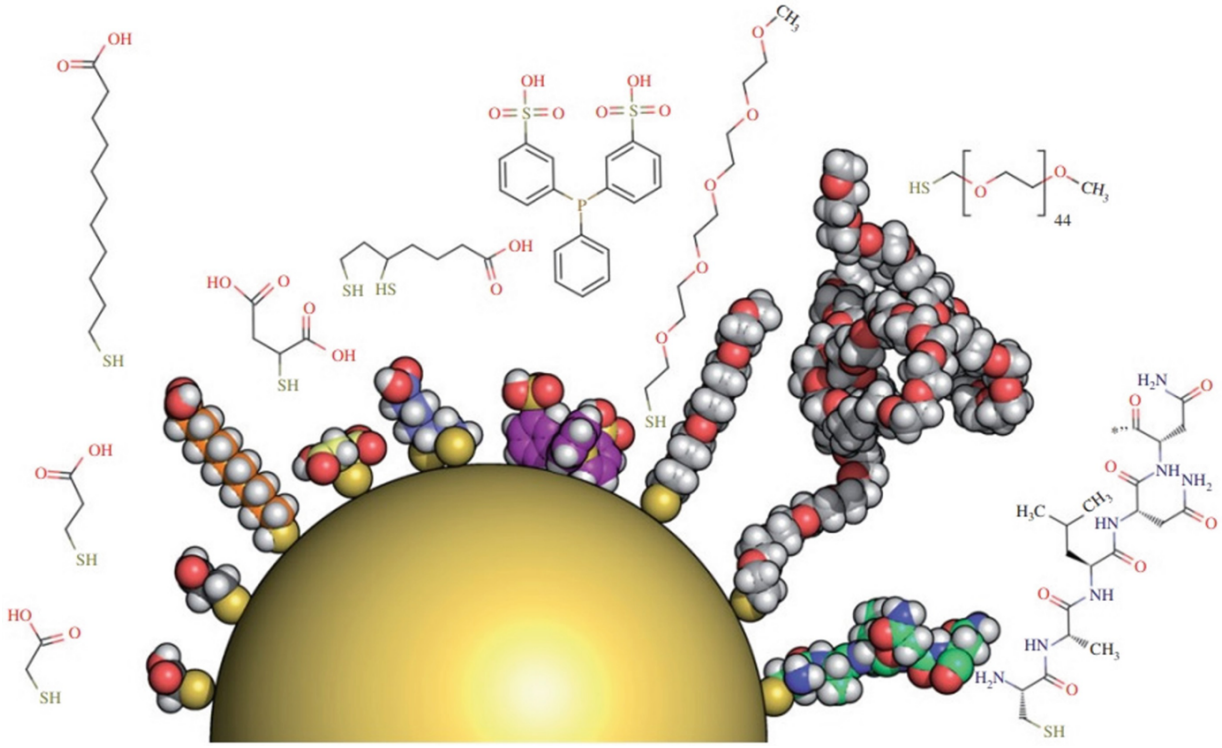

Fig. 14.9. A nanoparticle of 5 nm core diameter with different hydrophilic ligand molecules drawn to scale. The particle is idealized as a smooth sphere; the schematic structures of the molecules above are not drawn to scale. Left to right: mercaptoacetic acid (MAA), mercaptopropionic acid (MPA), mercaptoundecanoic acid (MUA), mercaptosuccinic acid (MSA), dihydrolipoic acid (DHLA), bis-sulfonated triphenylphosphine, mPEG5-SH, mPEG45-SH (2000 g mol^{-1}), and a short peptide of the sequence CALNN. (Reprinted with permission from Ref. [101]. Copyright 2010: Royal Society)

The ligand exchange is completed on the interface between two solvents in the presence of a biphasic layer usually ethanol. These short-chain-length ligands form a compact shell on nanoparticle surface and are suitable for FRET-based applications. However, this approach has certain pitfalls particularly diminishing quantum yield and poor colloidal stability. The reduced colloidal stability is acceptable for labeling purposes but becomes very crucial in case of sensing applications. This is because the nanoparticles lying deep inside the aggregate are inaccessible for receptors. In any case the weakly adsorbed ligand trioctylphosphine oxide can be displaced by the mercapto-containing ligands. However, the thiol group needs to be dehydrogenated for successful binding of sulfur moiety on the ZnS surface. Also, the thiol moieties are more susceptible toward oxidation. This drawback can however be overcome by using carbodithioate legends which may improve the resistance of nanocrystals against photooxidation [28]. The bond strengths calculated through first-principle approach for these systems revealed that the bond formation is carried out between Zn

and S_{thiol} and the corresponding energy is 46.5 kcal/mol [87]. Further to this, the sorbate (mercaptopropionic acid) was found to lie almost parallel to the ZnS surface putting a limitation on the number of sorbate molecules that can occupy the surface. The ligands can occupy the surface in three different ways, i.e., through chemisorption, physisorption, and free-standing ligands. Nevertheless, the presence of ligands or a combination of them may lead to the passivation of surface defect states. This on the other hand leads to enhancement in the fluorescence readout and hence a better optical label [36]. Polythiol-based ligands containing polyethylene copolymer can also be used to transfer the impervious nanoparticles into aqueous solutions [124].

Although ligand exchange is an efficient way for phase transfer of nanoparticles into aqueous solutions, it also has some shortcomings. This includes the fact that no single functional group can be universally used for exchange from different materials including metallic, semiconducting, and dielectric materials. Furthermore, the possibility of functionalizing the transferred nanoparticles is limited, and, in each case, a specific and adaptive strategy is needed to be applied. For more deeper insight on different strategies and role of ligand, the readers are directed to a detailed review on the topic [40].

14.3.1.2 Ligand Modification

Ligand modification is an alternative approach to phase transfer [101]. As a result of using this approach, the ligand molecule, which stabilizes colloidal nanoparticles in the initial first phase, becomes hydrophilic or hydrophobic for the transfer and stabilization of particles in the second phase. For example, hydrophilic nanoparticles stabilized with mercaptocarboxylic acid can be modified (*i*) by a hydrophobic molecule that is chemically bonded to its terminal carboxyl groups [70], (*ii*) by modification with a compound that can change its polarity through the removal of a blocking agent [59], (*iii*) by complexing the cyclodextrin with oleic acid present on the surface of the nanoparticles [108], or (*iv*) by covalently attaching an amphiphilic V-shaped ligand [127]. The experiment showed that the concept of ligand modification can provide efficient phase transfer, since the nanoparticles are modified with a new ligand in the same phase they are already in. The most detailed studies in this area have been carried out for colloidal gold

nanoparticles. But the conclusions made during these studies are also valid for colloidal particles of II-VI compounds.

14.3.1.3 Additional Coating Layers

The third phase transfer strategy is to form an additional molecular layer on the particles [101], which is adsorbed on the original ligand molecules and changes the surface properties accordingly. Thus, a ligand bilayer is formed, which allows the transfer of hydrophilic particles from the aqueous phase into organic solvents [62, 68], as well as hydrophobic nanoparticles into water [98, 113]. Molecules acting as interfacial transfer agents must be amphiphilic, containing hydrophobic and hydrophilic moieties, usually one or more aliphatic chains, and a polar, often charged, end group. Quaternary ammonium salts are one of the most common classes of such surfactants capable of providing interfacial transfer, in particular the transfer of hydrophilic nanoparticles into the organic phase. In these compounds, four hydrocarbon chains are linked to the nitrogen atom, which is thus positively charged, and the counter ions are usually chloride or bromide.

It is important to note that the additional layer conserves the native environment of the inorganic nanoparticles because the original ligand molecules are not replaced. This may be beneficial, e.g., to prevent sensitive core materials from oxidation.

14.3.2 Surface Functional Groups

Ligand particles stabilizing the nanoparticles against aggregation can simply consist of an inert molecular chain (hydrocarbon chain or PEG) or have functional groups that are terminating linear molecules. In case of polymer-coated water-soluble nanoparticles, these functional groups are often carboxylic acids stabilizing the nanoparticles by electrostatic repulsion and can be exploited for the conjugation of other molecules to the particles. These functional groups present on the nanoparticle surface can be converted to other functional groups by using bifunctional molecules [39]. This can be achieved by reacting carboxylic groups with primary amines by means of a condensation reaction to yield amide bonds. For this, a water-soluble carbodiimide (e.g., EDC) is commonly used (see Fig. 14.10a). After forming an intermediate compound with the carboxylic moiety, the activated group is reactive toward primary amines. In the event of primary amines present on the particle surface, active ester compounds

(N-hydroxy-succinimide; NHS) can be used to form amide bonds where NHS group reacts with primary amines, converting them to maleimides that are reactive toward thiols [57], as sketched in Fig. 14.10b. The negatively charged carboxylic groups can also be converted to hydroxyl groups [47] or tertiary amines [120]. In essence, the physicochemical properties of all nanoparticles predominantly depend on the ligand shell or surface coating and not on the actual inorganic core material.

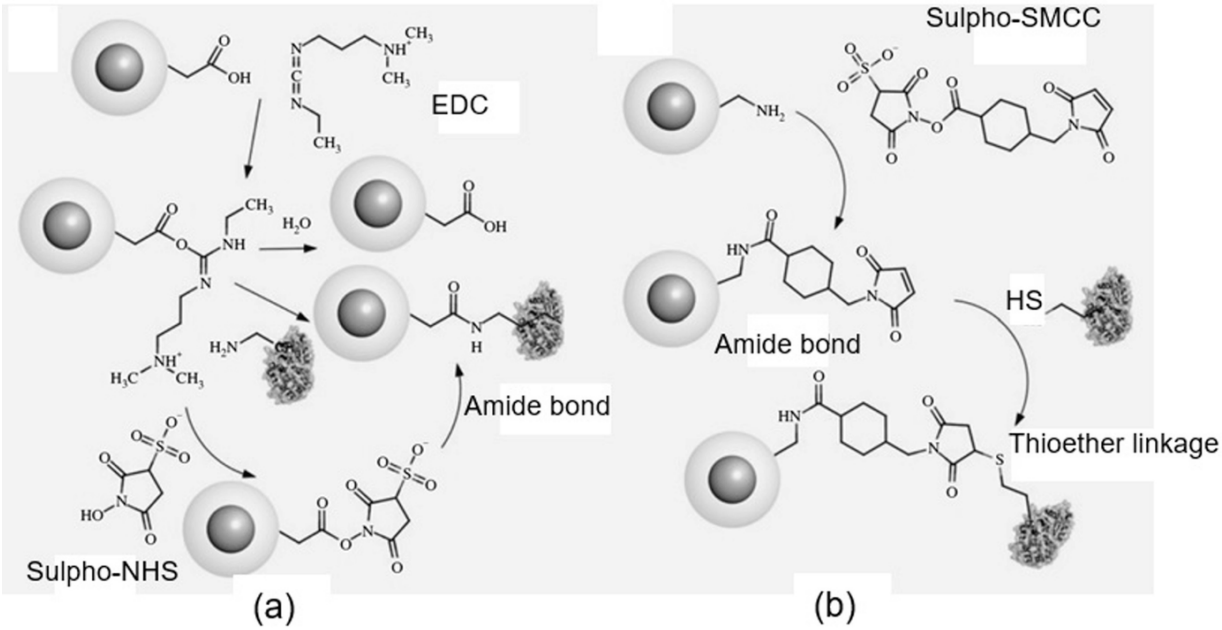

Fig. 14.10 (**a**) Common conjugation reaction for particles with carboxylic acid function: the water-soluble carbodiimide EDC forms an unstable intermediate, a so-called "activated" carboxylic group. This can either hydrolyze or react with a primary amino group under formation of a stable amide bond. Optionally, it can be reacted with NHS or sulfo-NHS. The active ester has an extended half-life and reacts also with primary amines. (**b**) Particles with primary amino groups can be reacted with active ester compounds to form amide bonds. Sulfo-SMCC is a heterobifunctional cross-linker with a sulfo-NHS group and a maleimide function on the other end that is reactive toward thiol groups. (Reprinted with permission from Ref. [101]. Copyright 2010: Royal Society)

14.3.3 Surface Modification with Polyethylene Glycol

Polyethylene glycol (PEG) is a linear biocompatible polymer consisting of repeated units of $–CH_2–CH_2–O–$; depending on the molecular weight, the same molecular structure is also termed as polyethylene oxide or polyoxyethylene. The inertness and nontoxic properties of PEG give rise to a number of applications in medicine, chemistry, or biotechnology. It is well soluble in a number of organic polar and apolar solvents, as well as in water where it is heavily hydrated, forming random coils with diameters much

larger than proteins of the corresponding molecular weight. PEG is used for nonionic surfactants and as an additive in cosmetics, pharmaceuticals, and food. When bound to surfaces, PEG repels other molecules by steric effects; the incoming molecule is not attracted by, e.g., electrostatic force and cannot penetrate the hydrated PEG layer, thereby warranting reduced "stickiness." This helps in promoting the stability of nanoparticles in ionic solutions by mitigating the Debye-Hückel effect and Stern double-layer phenomenon [86]. PEG-modified nanoparticles are more stable in biological environments; they show less nonspecific binding to proteins and cells [23, 107].

The modification of other molecules with PEG is often referred to as "PEGylation." A variety of mono-, homo-, and heterobifunctional PEG reagents are commercially available, with different functional groups and molecular weights. While monofunctional PEG molecules, e.g., with a methoxy group at the free end, yield basically more stable and inert particles, bifunctional PEG molecules can be used to introduce new functional groups on the surface, like with bifunctional cross-linkers in conjugation chemistry.

Apart from the post-modification approach by covalent chemistry, PEG-modified nanoparticles can also be obtained by ligand molecules that contain a block of PEG or that consist entirely of PEG with a functional group that can bind to the nanoparticle surface. Again, particle synthesis can already be carried out in the presence of these ligands; new PEG-containing ligands can be introduced by place exchange reactions or added as additional molecules such as lipids or polymers that have been modified with PEG before used for the coating process [60]. As already discussed, such PEG-containing ligands can be used for phase transfer of nanoparticles, and owing to the solubility of PEG itself, PEG-coated nanoparticles can also be dispersed in polar organic solvents such as chloroform, methanol, dimethyl sulfoxide, and dimethylformamide.

As for any additional shell, the overall particle diameter is increased by PEG modification. Increasing grafting density and molecular weight of the employed PEG molecules yields thicker shells that can be found to be of the order of a few to tens of nanometers [103], the thickness of about the order of the hydrodynamic diameter of a free PEG molecule forming a random coil.

When the PEG had a molecular weight more than or equal to 5000 g mol^{-1}, discrete bands could be separated by gel electrophoresis [102], and by employing bifunctional PEG, nanoparticles with a defined number of chemical reactive groups could be prepared [60]. Based on the same principle, quantum dots with a defined number of maltose binding protein [88] and a single monovalent streptavidin molecule have been demonstrated [41], which allowed the preparation of quantum dots conjugated with single antibodies.

14.3.4 Polymer Coating

As shown earlier, ligand exchange is a well-established method allowing the transfer of nanoparticles from organic to aqueous phase. However, this approach suffers from several drawbacks such as instability issues due to small ligands with one head group binding to the nanoparticle surface that can easily desorb from surface especially in solutions free of excess unbound ligands. Moreover, despite the fact that thiol-containing ligands bind relatively strongly to various metal particles and quantum dots, the ligand molecule has to be carefully chosen to the given core material, which is reflected in the large variety of reported protocols.

In contrast, an additional amphiphilic polymer coating layer that adsorbs by hydrophobic interaction to the hydrophobic ligand molecules of the nanoparticles has the advantage that it does not depend on the inorganic core material since the interaction is predominantly based on hydrophobic interaction of hydrocarbon chains and van der Waals forces between the molecules. Moreover, due to many anchoring sites between the ligand molecules and the polymer, facile desorption of the polymer molecule from the particle, e.g., by thermal fluctuations, is less probable. Finally, the coated particles have the same physical and chemical surface properties independent of their core material.

As the structure presented in Fig. 14.11, polymers provide surface passivation for QDs and protect them as a stable interface between QDs and biological networks. At the same time, polymers decrease the toxicity of QDs. In addition, polymers can introduce functional groups for QDs to fulfill their end-use application, such as receptor targeting and cell attachment. Although the mixing of polymer and nanoparticles is not a novel scientific project, the development of better polymer/QD materials

that exhibit advantageous biocompatible and optical properties has nowadays been an emerging research field [97].

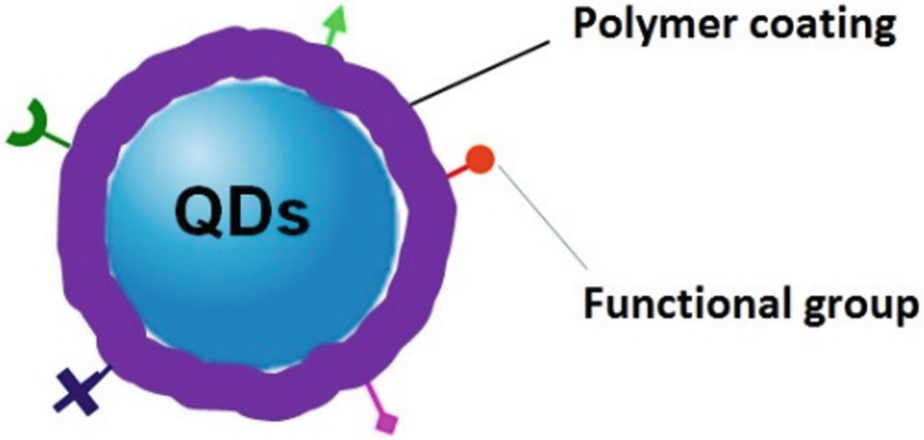

Fig. 14.11 A schematic depiction of polymer/QD hybrids. Biocompatible polymers protect QDs as shells providing biocompatibility and biostability and, at the same time, introduce functional groups for targeting cell and biomolecules. (Reprinted from Ref. [97]. Published 2011 by MDPI as open access)

Over the past decades, five major synthetic strategies have been developed to create biocompatible polymer/QD hybrid materials. As shown in Fig. 14.12, they include (A) ligand exchange between polymer and quantum dots, (B) grafting polymer to QD, (C) grafting polymer from CT, (D) polymer closure at CT, and (E) growth of QDs in a polymer matrix [97].

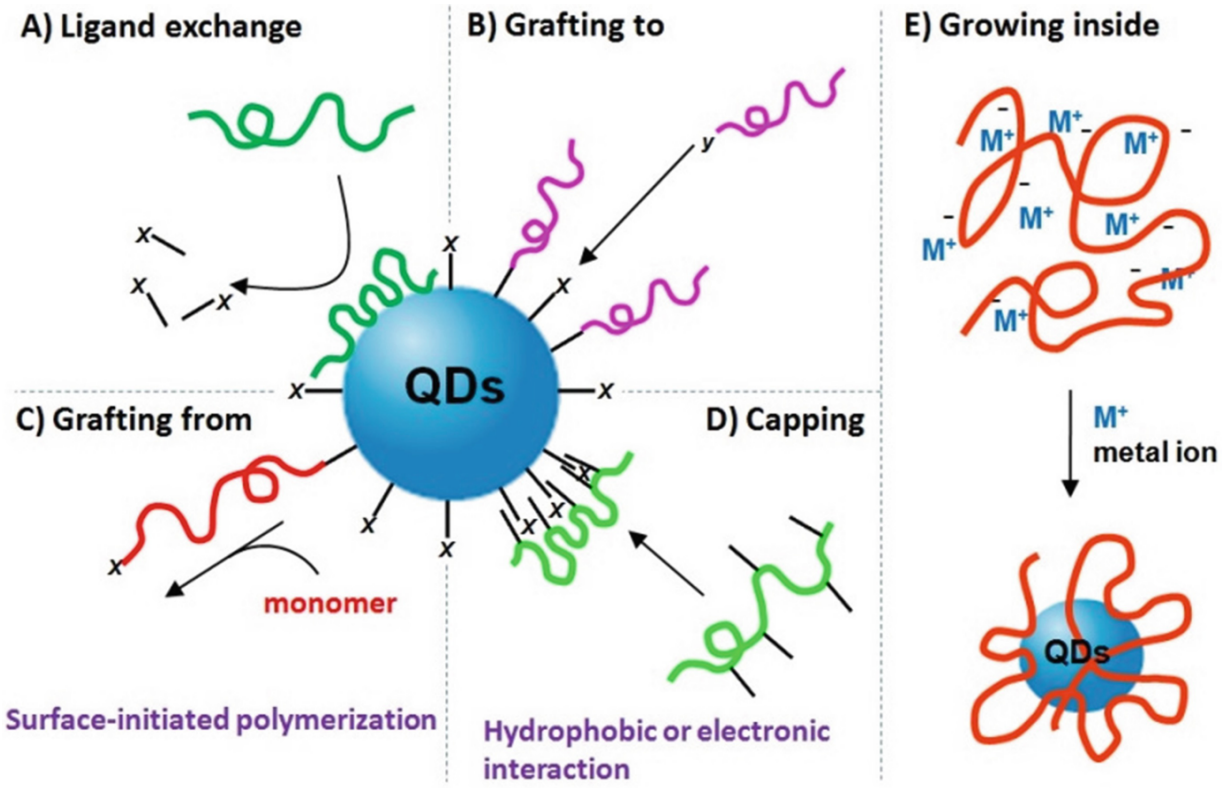

Fig. 14.12 Schematic summary of synthetic strategies for fabricating biocompatible polymer/QD hybrid materials, which can be categorized into (A) ligand exchange between polymer and QDs, (B) grafting polymer to QDs, (C) grafting polymer from QDs, (D) capping polymer onto QDs, and (E) growing QDs within polymeric template. (Reprinted from Ref. [97]. Published 2011 by MDPI as open access)

To date, a large number of different biocompatible polymers have been tested for surface modification of QDs [51, 97]. The most common example is polyacrylic acid-based polymer with hydrophobic side chains. Polyacrylic acid (mol. wt. 2000 g mol^{-1}) is a highly charged linear polyelectrolyte whose partial carboxylic groups (typically 40%) can be modified with aliphatic amines via an amide bond [114]. The resulting comblike polymer is soluble in organic solvent and can be added to hydrophobic nanoparticles, e.g., quantum dots with TOP/TOPO ligands. Optionally a cross-linker such as lysine or diaminopropanol can be used to cross-link the polymer for better stability using 1-ethyl-3-(3-dimethylaminopropyl)carbodiimide (EDC) as an activating agent [46]. The resulting polymer-coated nanoparticles can be suspended in different solvents such as ethanol [85]. The impact of grafting density and length of the hydrophobic side chains on the stability has been studied in great detail [65]. An alternative one-step approach is that the nanoparticles can be synthesized in the presence of polyacrylic acid, which yield polymer-coated

nanoparticles which can be suspended in various solvents including water [46] or other weakly adsorbing species like polyvinylpyrrolidone [38].

A different class of amphiphilic polymers is based on poly(maleic anhydride) copolymers that are synthesized by copolymerization of maleic anhydride with olefins, resulting in alternating copolymers. When exposed to water, these maleic anhydride rings hydrolyze providing carboxylic groups. The density of carboxylic groups is higher in case of poly(maleic anhydride) copolymers compared with modified polyacrylic acid. The maleic anhydride moieties also owe spontaneous reactivity toward primary amines (and to alcohols under acidic conditions), which lends the possibility of premodification of the polymer before it is used for particle coating. Another custom-made maleic anhydride-based polymer modified with hydrophobic sidechains has been developed by Lin et al. [60]. Hydrophobic side chains consisting of dodecylamine are grafted to a poly(maleic anhydride)-based backbone, leaving a part of the anhydride rings intact. If desired, additional functional molecules like fluorescent dyes, sugars, biotin, or PEG can be covalently grafted to the polymer provided they exhibit an amine function [5, 122]. This comblike amphiphilic polymer is made up of either an alternating or random sequence of building blocks that consist commonly of aliphatic chains as hydrophobic element and charged groups as hydrophilic part. The side chains intercalate hydrophobic ligands on the surface of nanoparticles, while the hydrophilic backbone is exposed to the aqueous environment. Even though the attraction between the polymer and the particle is due to rather weak van der Waals forces between the aliphatic chains, the large number of contact points by several side chains of polymer result in a very stable coating.

Other comblike polymers contain a mixture of simple aliphatic side chains with primary amines at their ends. The polymer can bind to the nanoparticle surface via the amino groups. Additionally, it was modified by fluorescent dye molecules [90]. A similar polymer was used to transfer negatively charged quantum dots to organic solution, after electrostatic adsorption of the polymer by its amino groups [89]. Also a polymer with tertiary amines and pyrene as a fluorescence marker [109] has been shown to stabilize quantum dots in organic solution. In addition, polyacrylic acid modified with free thiol and amino groups at the ends of the side chains has been demonstrated as coating for quantum dots, resulting in a relatively thin

shell with apparently little effect on the quantum yield of the particles after transfer to the aqueous phase [99]. Yet another substitute for obtaining nanoparticles with a polymer shell is by lateral cross-linking or polymerization of the small molecules forming the ligand shell [45, 125] or alternatively by growing a polymer off the particle surface from the attached ligands [111]. A detailed review for polymer-coated inorganic nanoparticles can be found [101].

Recently molecular imprinted polymer (MIP)-coated quantum dots of various II-VI semiconductors have been reported for fluorescence-based detection of pesticides [93, 119], bioaccumulating water contaminants [110, 126], and antibiotics and analgesics [18, 73]. The method is based upon the template-assisted copolymerization of functional monomers (usually aminotriethoxysilane) and cross-linker (tetraethyl orthosilicate) both of which make complexes with the template prior to polymerization.

14.4 Biofunctionalization and Bioconjugation of II-VI QDs for Biomedical and Biosensing Applications

14.4.1 Introduction in Bioconjugation

Bioconjugation of colloidal nanoparticles is one of the approaches to the biofunctionalization of quantum dots [6, 83]. Conjugation of nanoparticles and biomolecules combines the unique properties and functionality of both materials, i.e., fluorescence of inorganic particles such as QDs of II-VI compounds and, for example, the ability of biomolecules to bind highly specifically by molecular recognition. Currently, in nature, there is a wide variety of organic molecules of various composition, size, and complexity, which provide the structure and function of biological processes and organisms. Examples include, on the one hand, small molecules such as lipids, vitamins, peptides, and sugars and larger ones such as natural polymers, including proteins, enzymes, DNA, and RNA. This means that bioconjugation makes it possible to create hybrid materials that can be used to interact nanoparticles with biological systems. Some examples of bioconjugation are shown in Fig. 14.13.

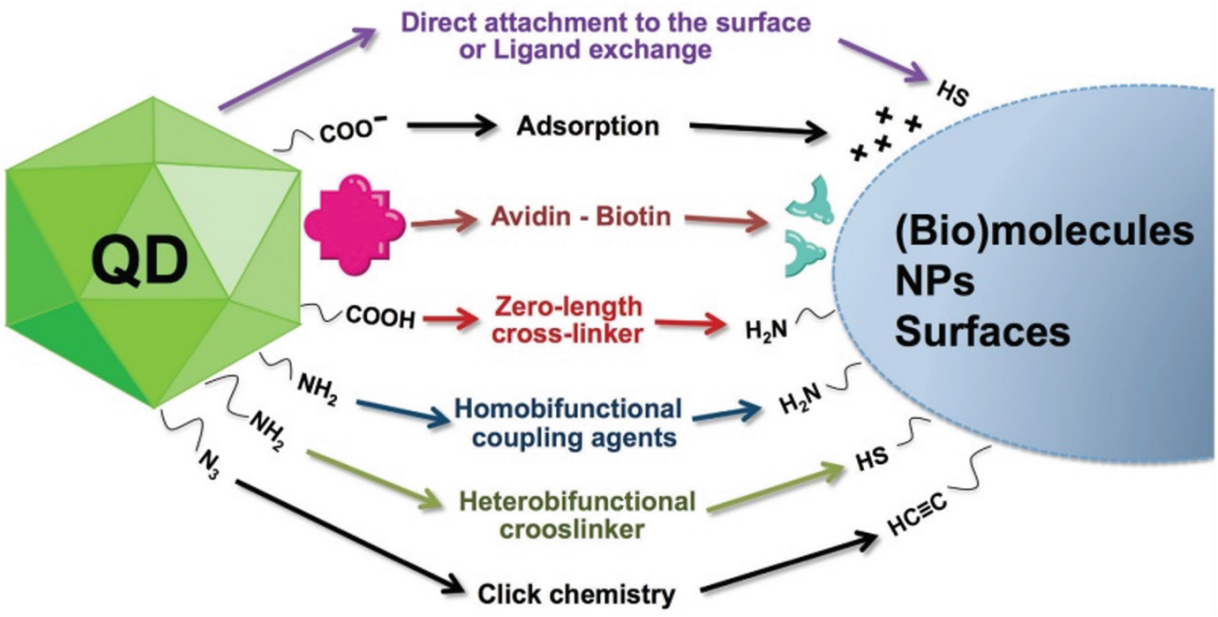

Fig. 14.13 Main strategies currently applied for QDs' conjugation to either (bio)molecules, nanoparticles (NPs), or surfaces. (Reprinted from Ref. [83]. Published 2019 by Sociedade Brasileira de Química as open access)

However, it must be recognized that the functionalization of nanoparticles with the help of biomolecules faces a number of obstacles [20, 83]. In particular, surface modification can have a significant impact on the physicochemical properties of QDs and their therapeutic efficacy, since biofunctionalization can change the surface charge, size, hydrophobicity, and targeting ability of QDs. Another important issue is that QDs must remain stable in solution while conjugation occurs. However, many NPs can precipitate upon activation, as their stability depends on a delicate balance between attractive and repulsive forces, which can be disturbed by various chemicals used during the biofunctionalization process. Moreover, due to huge number of different NPs and biomolecules, there are no standardized protocols for QD functionalization. Therefore, the choice of binding strategy depends on the stability of the QDs, functional groups, physiological conditions (pH, temperature, ionic strength, solvent choice, surfactant structure), and the nature of biomolecule to be attached. Finally, care must be taken to ensure that the biomolecule remain active after conjugation with QDs.

The strategy for coupling of indicated biomolecules to nanoparticles is usually divided into four classes [6, 101]:

- Ligand-like binding to the surface of the core of an inorganic particle, usually by chemisorption, for example, thiol groups

- Electrostatic adsorption of positively charged biomolecules onto negatively charged nanoparticles or vice versa

- Covalent bonding via conjugation chemistry using functional groups on both particles and biomolecules

- Non-covalent binding of the receptor-ligand system based on affinity

In recent years, the greatest interest has been in affinity-based systems found in nature. Streptavidin/biotin affinity-based conjugation is the best example of non-covalent linkage [112]. This system consists of a ligand, a small molecule of biotin (vitamin H), and a receptor, the protein avidin, which is present, for example, in egg white. Other non-covalent link strategies include electrostatic interaction, often referred as self-assembly, between the nanoparticle surface and functional molecule. For covalent linkage, lysine and cysteine residues can be utilized. Lysine and cysteine contain amino and thiol groups, respectively, which allow them to undergo modification with a wide variety of reagents. Table 14.2 and Table 14.3 summarize the advantages and drawbacks of covalent coupling procedures and non-covalent and dative conjugation strategies.

Table 14.2 Summary: advantages and drawbacks of non-covalent and dative conjugation strategies

Conjugation strategy	Advantages	Drawbacks	No preference applications (reason)
Electrostatic			
	Easy; fast; no need for cross-linkers; less aggregation and cross-linking QDs	Chance activity biomolecules compromised; no control orientation; no biomolecule/QD ratio control; less stable interaction; nonspecific interactions	Cellular research (stability)
High-affinity secondary interactions			
SA-biotin	Stable interaction; biotinylated monomer for polymer-coated QDs; QDs-SA commercially available	Large-sized bioconjugates; variety orientations; chance over biotinylation	FRET (size); cellular research (size); in vivo applications (biotin common in mammalian tissue)
NTA-Ni^{2+}-His	Control orientation; low cost; compact size	Less stable interaction	Immunochemical staining (stability)
Barnase-barstar	Small proteins; no covalent modification protein;		

Conjugation strategy	Advantages	Drawbacks	No preference applications (reason)
interaction	monomeric protein		
Ig-ligand	No modification biomolecule; ease of purification; no nonspecific and null combinations; control orientation; stable interaction	Large-sized bioconjugates; engineered proteins; heterogeneous protein/QD ratio	
Dave chemistry			
Metal affinity coordination	Little or no aggregation and cross-linking; control valence; control orientation; ease of purification; applicable on coated QDs (small molecules); stable interaction (in case of poly-His)	Less stable interaction; engineered proteins	Tissue imaging (stability – competition); drug delivery (stability – competition, unless it is intentional)
Thiol interactions	Thiolated proteins can act as solubilizing ligands	Less stable interaction; nonspecific interaction; biomolecule should contain thiol group; direct access QD surface; sometimes extra passivation QD necessary	

Source: Reprinted with permission from Ref. [6]. Copyright 2016: Elsevier
Abbreviations: FRET fluorescence resonance energy transfer, *His* histidine, *Ig* immunoglobulin, *Ni-NTA* nickel nitrilotriacetic acid, *SA* streptavidin, *QD* quantum dot

Table 14.3 Summary advantages and drawbacks of covalent conjugation procedures

Functionalized QD/attached biomolecule	Advantages	Drawbacks
QDs-COOH/biomolecule-NH_2	Simple; easy; small-sized bioconjugates; low yield (EDC alone); glutaraldehyde: higher QY	Activation carboxyl group; EDC: low QY (pH reasons); high amount EDC needed (hydrolysis); no control valence; no control orientation; aggregation and cross-linking
QDs-COOH/carbohydrate hydroxyls	Built in spacer; away from binding site	Activation by another compound; side/cross-reactions

Functionalized QD/attached biomolecule	Advantages	Drawbacks
QDs-NH_2/biomolecule-SH	Heterobifunctional cross-linkers; more selective; less cross-linking; homogeneous orientation	Hydrolysis; Ig reduction
QDs-NH_2/carbohydrate hydroxyls	More selective	Uncontrollability; aggregation
QDs-NH_2/biomolecule-NH_2		Cross-linking (nonspecific interaction); not reproducible
QDs-SH	More selective; direct solubilization of QDs possible; more stable in cellular media (vs disulfide bond); spectrophotometric follow-up	Molecule should contain thiol group; large-sized bioconjugates; side reactions (pH dependent); aggregation; instability of QD solution by reducing agents (e.g., TCEP)
QDs-epoxide	Small-sized bioconjugates; no cross-linker; reacts with different functional groups; strong emission of QD after conjugation	Aggregation; hydrolysis
QDs-OH	Stable bioconjugates; less aggregation; less nonspecific binding; photostability; strong emission	Slow coupling (CDI); alkaline conditions (CDI)
QDs-aldehyde	No cross-reaction; efficient coupling; chemoselective; biomolecule/QD ratio control; use of UV traceable markers	Catalyst necessary

Source: Reprinted with permission from Ref. [6]. Copyright 2016: Elsevier
Abbreviations: CDI N,N′-carbonyldiimidazole, *EDC* 1-ethyl-3-(3-dimethylaminopropyl)carbodiimide hydrochloride, *QY* quantum yield, *TCEP* tris(2-carboxyethyl)phosphine hydrochloride

It is experimentally observed that the ability to surface coat the quantum dots with amphiphilic polymer helps in utilizing the carboxylic groups on surface for bioconjugation. A large variety of commercial COOH-functionalized QDs are available. This allows one to link amine-containing proteins to the QD surface by using a cross-linker. A typical cross-linker carbodiimide, commonly known as EDC, is often used to accomplish this task. However, EDC alone may suffer a low yield due to the formation of

an intermediate compound O-acylisourea which tends to hydrolyze rapidly. This problem can be overcome by adding EDC in excess but is not advisable in cases where discrete number of molecules are required to be bound to the QD surface. It is customary to use water-soluble sulfo-NHS along with EDC which then converts it into a stable ester in water and avoid the risk of hydrolysis. EDC is a very short-length cross-linker and can be used in multistep development of complex bioconjugates. For example, in some cases, it is required to keep the functional molecule away from the surface of QD. This can be achieved by first linking a bi(tri)-functional homo/hetero cross-linker (usually linear PEGs) through EDC and then in the second step linking the functional molecule to the free end of PEG. Such multifunctional PEGs are commercially available, for example, from Rapp Polymere GmbH. In this way, as many procedural steps can be included as required. However, the final yield of bioconjugate is usually very low. Moreover, the intermediate purification steps can deteriorate the quality of conjugate. Nevertheless, such strategies are being preferentially used as they offer specificity as well as controlled orientation of the molecules on the underlying substrate for further application.

14.4.2 Applications of Bioconjugation

Currently, fluorescent probes have been found widespread and are used in countless applications [69]. All these applications are possible due to the versatile surface chemistry of QDs and bioconjugation [6, 20], which allow functionalization of QDs by one or more biomolecules (Fig. 14.14), such as DNA/RNA, oligonucleotides (i.e., ssDNA/RNA dsDNA/RNA), peptides and antibodies, fluorescent dyes, polymers (e.g., PEG), drugs, tumor markers, enzymes, and other proteins. This treatment gives QDs the necessary biofunctional properties required for the biological application of these NPs. Table 14.4 represents the bioconjugation of QD with different biolinkers and biomolecules necessary for different sensing applications.

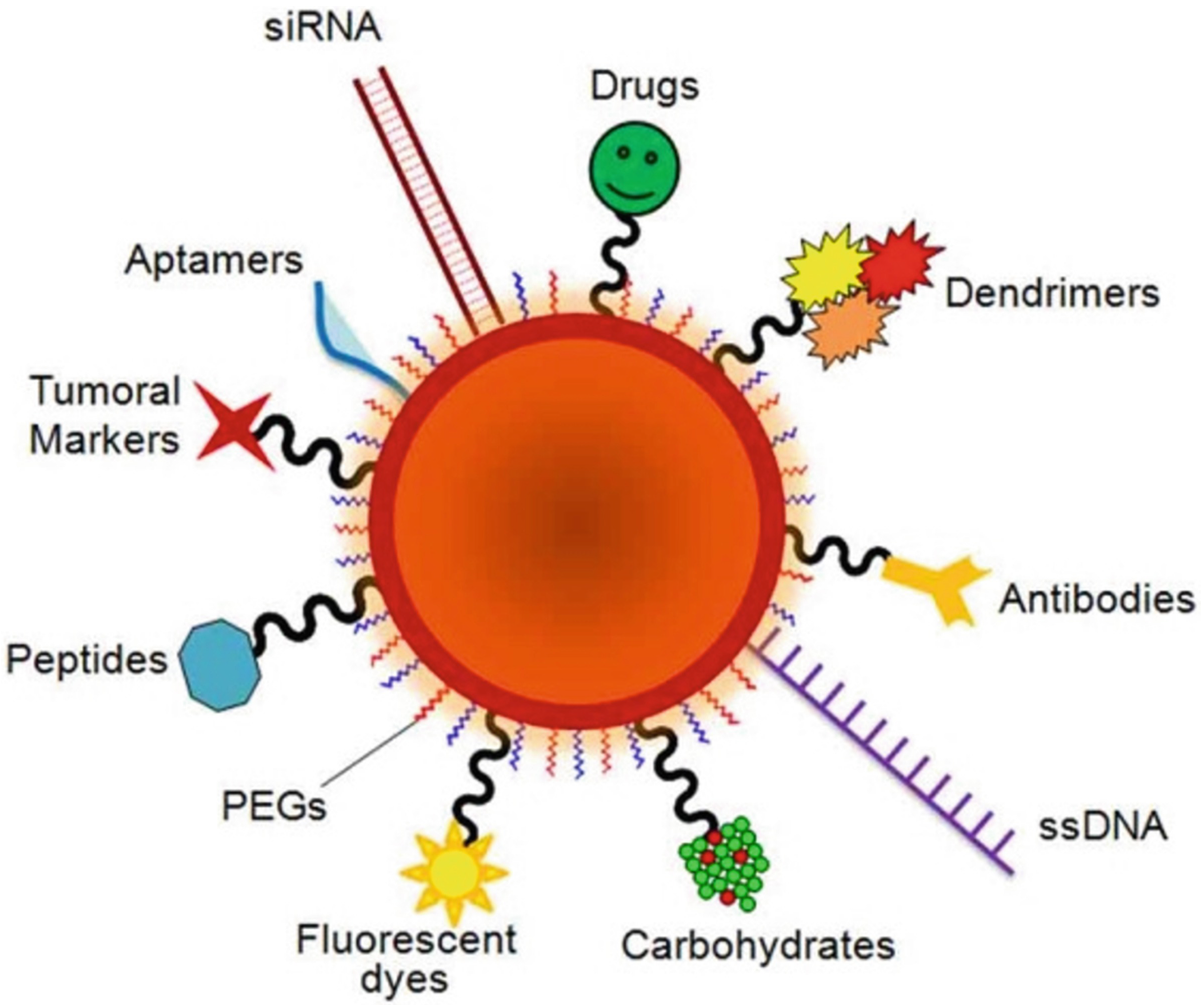

Fig. 14.14 Schematic representation of a multifunctional nanocarrier. These innovative NPs comprise nucleic acids such as RNA and DNA used for gene silencing approaches and in colorimetric assays, respectively. Aptamers and anticancer drug molecules are also used for delivery to the target tissue. Carbohydrates may be useful as sensitive colorimetric probes. PEG is used to improve solubility and decrease immunogenicity. Responsive nanocarriers can also trigger reaction upon external stimuli through the functionality of valuable tumor markers, peptides, carbohydrates, polymers, and antibodies that can be used to improve nanocarrier circulation, effectiveness, and selectivity. Multifunctional systems can also carry fluorescent dyes that are used as reporter molecules tethered to the particle surface and employed as tracking and/or contrast agents. (Reprinted from Ref. [20]. Published 2014 by Frontiers as open access)

Table 14.4 Examples of applications of biofunctionalized quantum dots of II-VI compounds in biology and medicine

Quantum dots	Biolinkers	Biomolecules attached	Applications as biosensor
CdSe	TOPO along with MAA	Glycoproteins	Label microorganisms and label specific cell type and lineages in in vitro system
	TOPO	Transferrin	Identifying bacteria and biochemical process of bacteria iron acquisition
	TOPO along with MES		Determination of free cyanide in aqueous solution with high sensitivity
	RGD peptide		Labeling and imaging of human mesenchymal stem cells
	Streptavidin	Actinomyosin	Cargo detection and filament tracking
CdTe	Thioglycolic acid	Cy3-DNA	Detection of DNA hybridization
	Polystyrene microspheres	Rabbit IgG	Detection of fluoromicrospheres in laser-induced fluorescent systems
CdS		DNA	DNA labeling
ZnS:Mn	Chitosan polymer		Detection of bacillus bacteria

Quantum dots	Biolinkers	Biomolecules attached	Applications as biosensor
CdSe/ZnS	Suitable amphiphilic polymer	Streptavidin	Detection of *E. coli* O157:H7 cells
	PEG polymer	GFE, F3, Lyp-1 peptide	In vivo targeting; blood vessel and tumor in mice
	Protein transferrin	HeLa cells	Ultrasensitive non-isotopic detection
	AFP antibody	Tumor tissue	Hepatic cancer detection
	Avidin	Antibody	Detection of cholera toxin and SEB
	Streptavidin	α-Tubulin antibody	Immunolabeling of mouse embryo fibroblast cells
		Biotinylated MAb	*C. parvum* oocyst detection Waterborne pathogen
			Human metaphase chromosomes
	Peptide	Angiotensin	Image angiotensin I-expressing CHO cells in vitro
	Phytochelatin peptides	Streptavidin	Cell imaging
	OPA copolymer by EDAC coupling reagent	Deltorphin-II	Labeling GPCRs (G-protein coupling receptors)
	Teflon-AF LCWs	Alexa Fluor 546-labeled IgG antibody	Detection of cTnI in PBS and human plasma
CdSe/CdSe-ZnS	Primary amine-containing molecules using the activator EDC	Adenine and AMP	Labeling bacteria by purine-dependent mechanisms

Source: Reprinted from Ref. [69]. Published 2009 by Hindawi Publishing Corporation as open access
Abbreviations: AFP alpha-fetoprotein, *CHO* Chinese hamster ovary, *EDAC* 1-(3-dimethylaminopropyl)-3-ethylcarbodiimide, *EDC* 1-ethyl-3-(3-dimethylaminopropyl)carbodiimide hydrochloride, *LCWs* liquid core waveguides, *MAA* mercaptoacetic acid, *MES* mercaptoethane sulfonate, *OPA* oligomer of amine-terminated polyaniline, *PBS* phosphate-buffered saline, *TOPO* trioctylphosphine oxide

14.4.2.1 Semiconductor Quantum Dots as Biological Labels

Optical imaging of living cells is a powerful diagnostic tool (Chap. 24, Vol. 3). The ability to observe cellular compartments with powerful microscopic techniques has enabled significant progress in this area. The pioneering works on the concept of biolabeling, as afforded by their photochemical stability and size tunable emission wavelength, were first demonstrated in 1998 by Alivisatos and coworkers [14] and Chan and Nie [17] (1998) separately. In particular Bruchez et al. [14] reported the potential application and limitation of semiconductor quantum dots in biological context. Subsequent studies have shown that the use of inorganic semiconductor nanocrystals as fluorescent probes has opened up new possibilities in diagnostic studies. For example, the wide absorption and narrow emission characteristics of QDs allow multicolor imaging with a single excitation source [82]. As a result, it becomes possible to study cellular compartments and subcellular structures, as well as to control signal transmission by labeling the corresponding molecules with fluorescent tags. Also included in this is DNA sequencing where each of the dideoxynucleotide is labeled with a fluorescent molecule having different emission profiles. For example, Fig. 14.15 shows the images of *N. benthamiana* live cells labeled with methionine-capped CdS/ZnS quantum dots. Consistent with the literature, *N. benthamiana* was able to uptake QDs through membrane transporters which further assist QDs' entry through the hydrophobic lipid bilayer. Figure 14.15 also shows that QDs uniformly bind to the cell wall and QD fluorescence remains stable inside the cell.

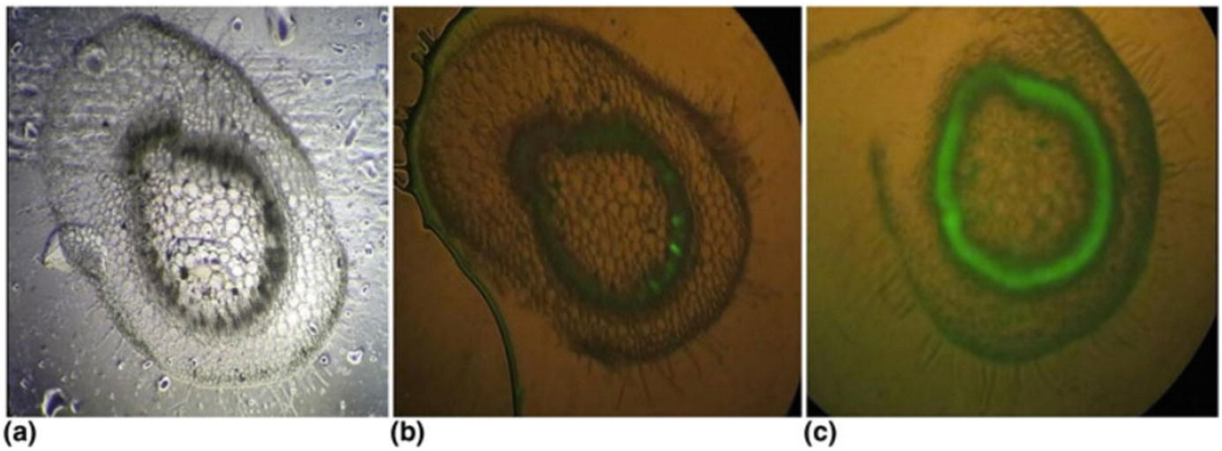

Fig. 14.15. *N. benthamiana* live cell images (**a**) under bright field (cross section of the shoot), (**b**) control, and (**c**) uptake QDs in the xylem region and its green fluorescence. (Reprinted with permission from Ref. [50]. Copyright 2019: Springer)

However conventional methods to fluorescently label proteins and their in vivo/in vitro imaging are laborious and require intricate controlled microinjection within the cells [72]. In addition, fluorescent proteins are relatively large in size (~27 kDa in monomeric form). However, a huge variety of organic fluorophores, such as fluorescein and rhodamine and their derivatives, are available having affinity for as many molecular machineries inside cell as desired offering reduced steric hinderance problems. Another important feature of fluorophore-labeled proteins is that their site-specific attachment can be exploited for Forster resonance energy transfer (FRET) studies. For instance, FRET visualization of epidermal growth factor receptor (EGFR) surprisingly revealed ligand-independent lateral propagation of receptor activation in plasma membrane which was once assumed to be a ligand-dependent phenomenon. Typical fluorophores face challenges of photobleaching, limited options for simultaneous excitation of multiple probes at different locations, and cross talk between the optical readout. Furthermore, organic fluorophores are also quite sensitive to the surrounding environment, such as thermal fluctuation of solvent and the so-called blinking due to conformational changes. Semiconductor nanocrystals have largely got the capability of circumventing all these challenges provided they are biofriendly in nature. This means that the prepared materials should be colloidally stable in an aqueous environment. Researchers in the field of chemistry, physics, and material sciences have made epic progress in the development of particles of various sizes, shapes, and compositions, whereas the necessary interface between materials and biological objects has been provided by the researchers in life sciences.

14.4.2.2 Biosensors

The superior luminescence characteristics of II-VI QDs are highly dependent on the state of the QD surface. It is known that any surface modification leads to abrupt changes in the luminescence intensity. Moreover, the fluorescence signal can be completely quenched in the presence of foreign molecules on the surface. The level of luminescence quenching is determined by the nature of the foreign molecule and the degree of its interaction with the surface states responsible for QD fluorescence. This behavior of QDs makes it possible to use this effect for

the determination/detection of an analyte and the development of biosensors [66].

Furthermore, bioconjugation makes it possible to provide selectivity to such biosensors. In particular, Chan and Nie [17] used the core-shell CdSe-ZnS quantum dots for ultrasensitive non-isotopic detection at single-molecule level. The quantum dot surface was passivated through mercaptoacetic acid coating and attachment with proteins. The prepared quantum dots were found to be well dispersed and were tested for their biocompatibility against HeLa cells. The quantum dots were also tested for photochemical stability and compared with R6G molecule.

It is clear that in order to achieve high selectivity of biosensors, it is necessary to synthesize nanoparticles with a certain set and number of functional groups. This is a difficult task that requires strict control of synthesis conditions and development of separation methods for nanoparticles with desired function, which could subsequently react to a specific molecule. Techniques for the mild and site-specific derivatization of proteins, DNA, RNA, and carboxylic acid have already been developed for such applications, including ligand recognition and disease diagnosis. For example, fluorescent or affinity-based molecules such as biotin can be added for ligand recognition, which can serve as reporters [6]. It has also been shown that fractions of particles having a certain number of functional groups (DNA or PEG molecules) can be separated using affinity chromatography [32, 122].

To date, there are several site-specific binding strategies using thiolates, amide bonds, carbon-nitrogen double bond, and cycloaddition. The most common linking strategies are based on the use of thiolates and amide bonds. In particular, the Biophotonik AG group (Parak group) has widely used the amide bond to bind ligands containing primary amines, such as fluorophores, polyethylene glycols, DNA, proteins, etc. However, their strategy suffers from multivalence and large hydrodynamic radii of the resulting conjugates. For a better understanding of the various advantages and disadvantages of these strategies, readers are encouraged to review [6]. A more detailed description of biosensors based on QDs of II-VI compounds can be found in Vol. 3 (Chaps. 17, 18, 19, 20, 21, 22, 23, 24, 25, 26, and 27) of this issue.

14.4.2.3 Quantum Dots for Drug Delivery and Therapeutics

QDs can be conjugated with DNA through various methods, notable among them are amine to carboxylic linkage via cross-linker, amine to thiol linkage, and click chemistry [8]. These conjugates can be used to develop highly complex, tunable, and reconfigurable macromolecular scaffolds [69]. These scaffolds can be used for intracellular delivery of biologically active materials, such as genes, and therapeutic purposes (Fig. 14.16). The trafficking of the QD-DNA conjugate with active payload enables both gene regulation and gene therapy. Srinivasan et al. [104] showed intracellular gene regulation by tracking and delivery of plasmid using QD-DNA conjugates. In terms of therapeutic applications, the use of QD-DNA conjugates for siRNA-mediated gene silencing was first demonstrated by Derfus et al. [26]. QDs were labeled with siRNA against EGFP and transfected in stable cell lines. The concomitant silencing of EGFP gene was observed by comparison of EGFP signal in trypsinized cells. However, several reports suggest that different nanoparticles can often get trapped in the endo-lysosomal pathway and get degraded. This impedes their full potential in therapeutics. Further details regarding QD-DNA bioconjugate preparation and therapeutic applications can be found here [9].

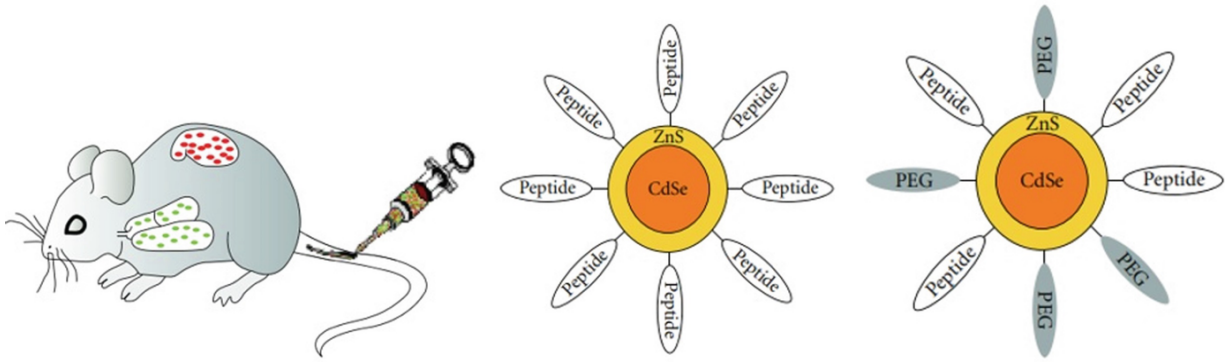

Fig. 14.16 Schematic representation of QD targeting. Intravenous delivery of QD into specific tissues of the mouse. (Left) Design of peptide-coated QD. (Center and right) QD were coated with either peptides only or with peptides and PEG. PEG helps the QD to maintain solubility in aqueous solvents and minimize nonspecific binding. (Reprinted from Ref. [69]. Published 2009 by Hindawi Publishing Corporation as open access)

14.4.2.4 Fluorescent Dyes and Other Functions, Multifunctional Particles

Apart from chemical functional groups or biomolecules, nanoparticles have also been modified with a number of other functionalities [69]. Common examples include fluorescent dyes [33, 48] or fluorescent proteins [101]

that can be used for fluorescence labeling of nonfluorescent particles or to generate systems exhibiting energy transfer. Common examples include fluorescent dyes that are quenched by gold nanoparticles or that can be excited by fluorescence resonant energy transfer via a quantum dot serving as donor, for instance, for biosensors. Other functions include paramagnetic ligand molecules [75] or chelator molecules for radionuclides [2].

14.5 Summary

In summary, quantum dots are superior over traditional organic fluorophores due to their relatively stable fluorescence lifetime. The emission wavelength can be controlled by controlling the size of QDs. However, colloidal stability is warranted in organic phase. Therefore, post-synthesis phase transfer protocols are important and have been thoroughly discussed. The functionalization and bioconjugation can be done by chemical as well as physical means. In general all these steps have some common aspects and overlap, e.g., with regard to the binding of organic ligand molecules to the inorganic particle surface, and often there, they depend on each other. The motivation for particle modification is the control over the interaction of the particles with their environment, which is naturally taking place at nanoparticle surface. By appropriate modification and phase transfer, specific and nonspecific binding to target molecules, surfaces, biomolecules, or cells can be achieved, e.g., for the controlled targeting or assembly of nanoparticles. Furthermore, amphiphilic polymer coating offers additional functionality to the QDs along with inherent characteristics coming from its core material. Analyte-sensitive fluorophore can also be incorporated into the polymer shell and provide extra control in tracing the site of nanoparticles within cells. Such systems can be used in a variety of applications including biolabeling, biosensing, drug and gene delivery, as well as affinity-based FRET for DNA sensing.

Acknowledgments

G.K. is grateful to the State Program of the Republic of Moldova, project 20.80009.5007.02, for supporting his research. F. A. is grateful to Higher Education Commission, Pakistan, HEC-NRPU grant # 10653 for supporting his research.

References

1. Aldana J, Wang YA, Peng X (2001) Photochemical instability of CdSe nanocrystals coated by hydrophilic thiols. J Am Chem Soc 123:8844–8850. https://doi.org/10.1021/ja016424q [Crossref]
2. Ali Z, Abbasi A, Zhang F, Arosio P, Lascialfari A, Casula MF et al (2011) Multifunctional nanoparticles for dual imaging. Anal Chem 83(8):2877–2882
3. Alivisatos AP (1996) Perspectives on the physical chemistry of semiconductor nanocrystals. J Phys Chem A 100:226–239. https://doi.org/10.1021/jp9535506 [Crossref]
4. Alivisatos AP (1997) Nanocrystals: building blocks for modern materials design. Endeavour 21:56–60
5. Amin F, Yushchenko DA, Montenegro JM, Parak WJ (2012) Integration of organic fluorophores in the surface of polymer-coated colloidal nanoparticles for sensing the local polarity of the environment. Chem Phys Chem 13(4):1030–1035
6. Astrid F, Beloglazova N, Rajkovic A, Sas B, Madder A, Goryacheva IY, De Saeger S, S. (2016) Bioconjugation of quantum dots: review and impact on future application. Trac-Trends Anal Chem 83:31–48
7. Bakalova R, Ohba H, Zhelev Z, Nagase T, Jose R, Ishikawa M et al (2004) Quantum dot anti-CD conjugates: are they potential photosensitizers or potentiators of classical photosensitizing agents in photodynamic therapy of cancer? Nano Lett 4(9):1567–1573
8. Banerjee A, Grazon C, Nadal B, Pons T, Krishnan Y, Dubertret B (2015) Fast, efficient and stable conjugation of multiple DNA strands on colloidal quantum dots. Bioconjug Chem 26:1582–1589
9. Banerjee A, Pons T, Lequeux N, Dubertret B (2016) Quantum dots–DNA bioconjugates: synthesis to applications. Interface Focus 6(6):0064
10. Bansal AK, Antolini F, Zhang S, Stroea L, Ortolani L, Lanzi M et al (2016) Highly luminescent colloidal CdS quantum dots with efficient near-infrared electroluminescence in light-emitting diodes. J Phys Chem C 120(3):1871–1880
11. Bawendi MG, Steigerwald ML, Brus LE (1990) The quantum mechanics of larger semiconductor clusters (" quantum dots"). Ann Rev Phys Chem 41(1):477–496
12. Bear JC, Hollingsworth N, McNaughter PD, Mayes AG, Ward MB, Nann T et al (2014) Copper-doped CdSe/ZnS quantum dots: controllable photoactivated copper (I) cation storage and release vectors for catalysis. Angew Chem Intern Ed 53(6):1598–1601
13. Brkić S (2017) Biocompatibility of Cadmium-selenide quantum dots. Eur Intern J Sci Technol 6(4):6–17

14. Bruchez Jr.M., Moronne M., Gin P., Weiss S., Alivisatos A.P. (1998) Semiconductor nanocrystals as fluorescent biological labels. Science 281(5385):2013–2016
15. Brus L (1986) Electronic wave functions in semiconductor clusters: experiment and theory. J Phys Chem 90(12):2555–2560
16. Bullen C, Mulvaney P (2006) The effects of chemisorption on the luminescence of CdSe quantum dots. Langmuir 22:3007–3013. https://doi.org/10.1021/la051898e [Crossref]
17. Chan WC, Nie S (1998) Quantum dot bioconjugates for ultrasensitive nonisotopic detection. Science 281(5385):2016–2018
18. Chen S, Li Y, Wu S, Jiang X, Yang H, Su X et al (2020) A phosphorescent probe for cephalexin consisting of mesoporous thioglycolic acid-modified Mn: ZnS quantum dots coated with a molecularly imprinted polymer. Microchim Acta 187(1):1–10
19. Clarke SJ, Hollmann CA, Zhang Z, Suffern D, Bradforth SE, Dimitrijevic N et al (2006) Photophysics of dopamine-modified quantum dots and effects on biological systems. Nat Mater 5:409–417. https://doi.org/10.1038/nmat1631 [Crossref]
20. Conde J, Dias JT, Grazú V, Moros M, Baptista PV, de la Fuente JM (2014) Revisiting 30 years of biofunctionalization and surface chemistry of inorganic nanoparticles for nanomedicine. Frontiers Chem 2:48
21. Correa-Duarte MA, Giersig M, Liz-Marzan LM (1998) Stabilization of CdS semiconductor nanoparticles against photodegradation by a silica coating procedure. Chem Phys Lett 286(5–6):497–501
22. Dabbousi BO, Rodriguez-Viejo J, Mikulec FV, Heine JR, Mattoussi H, Ober R et al (1997) (CdSe) ZnS core− shell quantum dots: synthesis and characterization of a size series of highly luminescent nanocrystallites. J Phys Chem B 101(46):9463–9475
23. Daou TJ, Li L, Reiss P, Josserand V, Texier I (2009) Effect of poly (ethylene glycol) length on the in vivo behavior of coated quantum dots. Langmuir 25(5):3040–3044
24. Darbandi M, Thomann R, Nann T (2005) Single quantum dots in silica spheres by microemulsion synthesis. Chem Mater 17(23):5720–5725
25. Derfus AM, Chan WC, Bhatia SN (2004) Probing the cytotoxicity of semiconductor quantum dots. Nano Lett 4(1):11–18
26. Derfus AM, Chen AA, Min D, Ruoslahti E, Bhatia SN (2007) Targeted quantum dot conjugates for siRNA delivery. Bioconjug Chem 18:1391–1396
27. Döllefeld H, Hoppe K, Kolny J, Schilling K, Weller H, Eychmüller A (2002) Investigations on the stability of thiol stabilized semiconductor nanoparticles. Phys Chem Chem Phys 4:4747–4753. https://doi.org/10.1039/b202101c [Crossref]

28. Dubois F, Mahler B, Dubertret B, Doris E, Mioskowski C (2007) A versatile strategy for quantum dot ligand exchange. J Am Chem Soc 129(3):482–483
29. Ekimov AI, Onushchenko AA (1981) Quantum size effect in three-dimensional microscopic semiconductor crystals. ZhETF Pisma Redaktsiiu 34:363. (in Russian)
30. Ekimov AI, Onushchenko AA (1984) Size quantization of the electron energy spectrum in semiconductor microcrystals. JETP Lett 40:1136–1139
31. Eychmüller A, Mews A, Weller H (1993) A quantum dot quantum well: CdS/HgS/CdS. Chem Phys Lett 208(1–2):59–62
32. Farlow J, Seo D, Broaders KE, Taylor MJ, Gartner ZJ, Jun Y-W (2013) Formation of targeted monovalent quantum dots by steric exclusion. Nat Methods 10(12):1203–1205
33. Fernandez-Argüelles MT, Yakovlev A, Sperling RA, Luccardini C, Gaillard S, Sanz MA et al (2007) Synthesis and characterization of polymer-coated quantum dots with integrated acceptor dyes as FRET-based nanoprobes. Nano Lett 7(9):2613–2617
34. Fritz G., Schadler V., Willenbacher N., Wagner N.J. (2002) Electrosteric stabilization of colloidal dispersions. Langmuir 18, 6381–6390. (doi:10.1021/la015734j).
35. Gerion D, Pinaud F, Williams SC, Parak WJ, Zanchet D, Weiss S, Alivisatos AP (2001) Synthesis and properties of biocompatible water-soluble silica-coated CdSe/ZnS semiconductor quantum dot. J Phys Chem B 105:8861–8871
36. Grandhi GK, Viswanatha R (2016) Understanding the role of surface capping ligands in passivating the quantum dots using copper dopants as internal sensor. J Phys Chem C 120(35):19785–19795
37. Guerrero-Martínez A, Pérez-Juste J, Liz-Marzán LM (2010) Recent progress on silica coating of nanoparticles and related nanomaterials. Adv Mater 22(11):1182–1195
38. Guo L, Yang S, Yang C, Yu P, Wang J, Ge W et al (2000) Highly monodisperse polymer-capped ZnO nanoparticles: preparation and optical properties. Appl Phys Lett 76(20):2901–2903
39. Hermanson GT (2013) Bioconjugate Techniques. Academic, Cambridge, USA
40. Heuer-Jungemann A, Feliu N, Bakaimi I, Hamaly M, Alkilany A, Chakraborty I et al (2019) The role of ligands in the chemical synthesis and applications of inorganic nanoparticles. Chem Rev 119(8):4819–4880
41. Howarth M, Ting AY (2008) Imaging proteins in live mammalian cells with biotin ligase and monovalent streptavidin. Nat Protoc 3(3):534–545
42. Ipe BI, Lehnig M, Niemeyer CM (2005) On the generation of free radical species from quantum dots. Small 1(7):706–709
43. Jasim KE (2015) Quantum dots solar cells. In: Kosyachenko LA (ed) Solar cells – new approaches and reviews. Intech, pp 303–331

44. Ji X, Copenhaver D, Sichmeller C, Peng X (2008) Ligand bonding and dynamics on colloidal nanocrystals at room temperature: the case of alkylamines on CdSe nanocrystals. J Am Chem Soc 130:5726–5735. https://doi.org/10.1021/ja710909f [Crossref]
45. Jiang W, Mardyani S, Fischer H, Chan WC (2006) Design and characterization of lysine cross-linked mercapto-acid biocompatible quantum dots. Chem Mater 18(4):872–878
46. Kairdolf BA, Smith AM, Nie S (2008a) One-pot synthesis, encapsulation, and solubilization of size-tuned quantum dots with amphiphilic multidentate ligands. J Am Chem Soc 130(39):12866–12867
47. Kairdolf BA, Mancini MC, Smith AM, Nie S (2008b) Minimizing nonspecific cellular binding of quantum dots with hydroxyl-derivatized surface coatings. Anal Chem 80(8):3029–3034
48. Kaiser U, Jimenez de Aberasturi D, Malinowski R, Amin F, Parak W, Heimbrodt W (2014) Multiplexed measurements by time resolved spectroscopy using colloidal CdSe/ZnS quantum dots. Appl Phys Lett 104(4):041901
49. Kaiser U, Sabir N, Carrillo-Carrion C, Del Pino P, Bossi M, Heimbrodt W et al (2015) Förster resonance energy transfer mediated enhancement of the fluorescence lifetime of organic fluorophores to the millisecond range by coupling to Mn-doped CdS/ZnS quantum dots. Nanotechnology 27(5):055101
50. Kanagasubbulakshmi S, Gowtham I, Kadirvelu K, Archana K (2019) Biocompatible methionine-capped CdS/ZnS quantum dots for live cell nucleus imaging. MRS Commun 9:344–351
51. Khanna PK, Dhanabalan K, More P, Viswanathan S, Renugopalakrishnan V (2012) Biocompatible hydrophilic CdSe quantum dots: Single-Step synthesis. Intern J Green Nanotechnol 4(1):62–70
52. Kippeny T, Swafford LA, Rosenthal SJ (2002) Semiconductor nanocrystals: a powerful visual aid for introducing the particle in a box. J Chem Educ 79(9):1094
53. Kirchner C, Liedl T, Kudera S, Pellegrino T, Muñoz JA, Gaub HE et al (2005) Cytotoxicity of colloidal CdSe and CdSe/ZnS nanoparticles. Nano Lett 5(2):331–338
54. Kortan A, Hull R, Opila RL, Bawendi MG, Steigerwald ML, Carroll P et al (1990) Nucleation and growth of CdSe on ZnS quantum crystallite seeds, and vice versa, in inverse micelle media. J Am Chem Soc 112(4):1327–1332
55. Kuçur E, Ziegler J, Nann T (2008) Synthesis and spectroscopic characterization of fluorescent blue-emitting ultrastable CdSe clusters. Small 4(7):883–887
56. Kudera S, Zanella M, Giannini C, Rizzo A, Li Y, Gigli G et al (2007) Sequential growth of magic-size CdSe nanocrystals. Adv Mater 19(4):548–552
57. Kuhn SJ, Finch SK, Hallahan DE, Giorgio TD (2007) Facile production of multivalent enzyme-nanoparticle conjugates. J Magnetism Magnetic Mater 311(1):68–72

58. Kumari A, Sharma A, Malairaman U, Singh RR (2018) Proficient surface modification of CdSe quantum dots for highly luminescent and biocompatible probes for bioimaging: A comparative experimental investigation. J Lumin 199:174–182
59. Lala N, Lalbegi SP, Adyanthaya SD, Sastry M (2001) Phase transfer of aqueous gold colloidal particles capped with inclusion complexes of cyclodextrin and alkanethiol molecules into chloroform. Langmuir 17:3766–3768. https://doi.org/10.1021/la0015765 [Crossref]
60. Lin CAJ, Sperling RA, Li JK, Yang TY, Li PY, Zanella M et al (2008) Design of an amphiphilic polymer for nanoparticle coating and functionalization. Small 4(3):334–341
61. Linkov P, Krivenkov V, Nabiev I, Samokhvalov P (2016) High quantum yield CdSe/ZnS/CdS/ZnS multishell quantum dots for biosensing and optoelectronic applications. Mater Today: Proc 3(2):104–108
62. Liu J, Alvarez J, Ong W, Román E, Kaifer AE (2001) Phase transfer of hydrophilic, cyclodextrin-modified gold nanoparticles to chloroform solutions. J Am Chem Soc 123:11148–11154. https://doi.org/10.1021/ja003957a [Crossref]
63. Liu M, Wang Y-Y, Liu Y, Jiang F-L (2020) Thermodynamic implications of the ligand exchange with alkylamines on the surface of CdSe quantum dots: the importance of ligand–ligand interactions. J Phys Chem C 124(8):4613–4625
64. Lovrić J, Cho SJ, Winnik FM, Maysinger D (2005) Unmodified cadmium telluride quantum dots induce reactive oxygen species formation leading to multiple organelle damage and cell death. Chem Biol 12(11):1227–1234
65. Luccardini C, Tribet C, Vial F, Marchi-Artzner V, Dahan M (2006) Size, charge, and interactions with giant lipid vesicles of quantum dots coated with an amphiphilic macromolecule. Langmuir 22(5):2304–2310
66. Ma W, Qin L-X, Liu F-T, Gu Z, Wang J, Zhi Gang Pan ZG et al (2013) Ubiquinone-quantum dot bioconjugates for in vitro and intracellular complex I sensing. Sci Rep 3:1537
67. Mansur AP, Mansur HS, de Carvalho SM, Lobato ZI, Guedes M, Leite MF (2016) Surface biofunctionalized CdS and ZnS quantum dot nanoconjugates for nanomedicine and oncology: to be or not to be nanotoxic? Intern J Nanomed 11:4669–4690
68. Mayya KS, Caruso F (2003) Phase transfer of surface-modified gold nanoparticles by hydrophobization with alkylamines. Langmuir 19:6987–6993. https://doi.org/10.1021/la034018+ [Crossref]
69. Mazumder S, Dey R, Mitra MK, Mukherjee S, Das GC (2009) Review: biofunctionalized quantum dots in biology and medicine. J. Nanomaterials 2009:815734
70. McMahon JM, Emory SR (2007) Phase transfer of large gold nanoparticles to organic solvents with increased stability. Langmuir 23:1414–1418. https://doi.org/10.1021/la0617560 [Crossref]

71. Medintz IL, Uyeda HT, Goldman ER, Mattoussi H (2005) Quantum dot bioconjugates for imaging, labelling and sensing. Nature Mater 4:435–446
72. Miyawaki A, Sawano A, Kogure T (2003) Lighting up cells: labelling proteins with fluorophores. Nat Cell Biol Suppl:S1–S7
73. Montaseri H, Abrahamse H, Forbes PBC (2021) Fluorescence sensing with molecularly imprinted polymer-capped quantum dots. In: Martín-Esteban A (ed) Molecularly imprinted polymers. Methods in molecular biology, vol 2359. Humana, New York, pp 183–194
74. Moreels I, Martins JC, Hens Z (2006) Ligand adsorption/desorption on sterically stabilized InP colloidal nanocrystals: observation and thermodynamic analysis. Chem Phys Chem 7(5):1028–1031
75. Mulder WJ, Koole R, Brandwijk RJ, Storm G, Chin PT, Strijkers GJ et al (2006) Quantum dots with a paramagnetic coating as a bimodal molecular imaging probe. Nano Lett 6(1):1–6
76. Murray C, Norris DJ, Bawendi MG (1993a) Synthesis and characterization of nearly monodisperse CdE (E=sulfur, selenium, tellurium) semiconductor nanocrystallites. J Am Chem Soc 115(19):8706–8715
77. Murray C, Nirmal M, Norris DJ, Bawendi M (1993b) Synthesis and structural characterization of II–VI semiconductor nanocrystallites (quantum dots). Zeitschrift für Physik D Atoms, Molecules Clusters 26(1):231–233
78. Nagy A, Hollingsworth JA, Hu B, Steinbrück A, Stark PC, Rios VC et al (2013) Functionalization-dependent induction of cellular survival pathways by CdSe quantum dots in primary normal human bronchial epithelial cells. ACS Nano 7(10):8397–8411
79. Nann T, Mulvaney P (2004) Single quantum dots in spherical silica particles. Angew Chem Intern Ed 43(40):5393–5396
80. Nirmal M, Murray C, Bawendi M (1994) Fluorescence-line narrowing in CdSe quantum dots: surface localization of the photogenerated exciton. Phys Rev B 50(4):2293
81. Norris DJ, Sacra A, Murray C, Bawendi M (1994) Measurement of the size dependent hole spectrum in CdSe quantum dots. Phys Rev Lett 72(16):2612
82. Parak WJ, Pellegrino T, Plank C (2005) Labelling of cells with quantum dots. Nanotechnology 16:R9–R25
83. Pereira G, Monteiro CAP, Albuquerque GM, Pereira MIA, Cabrera MP, Cabral Filho PE (2019) (Bio)conjugation strategies applied to fluorescent semiconductor quantum dots. J Braz Chem Soc 30(12):2536–2560
84. Perez-Donoso JM, Monras JP, Bravo D, Aquirre A, Quest AF, Osorio-Roman IO et al (2012) Biomimetic, mild chemical synthesis of CdTe-GSH quantum dots with improved biocompatibility. PLoS One 7(1):e30741
85. Petruska MA, Bartko AP, Klimov VI (2004) An amphiphilic approach to nanocrystal quantum dot− titania nanocomposites. J Am Chem Soc 126(3):714–715

86. Pfeiffer C, Rehbock C, Hühn D, Carrillo-Carrion C, de Aberasturi DJ, Merk V et al (2014) Interaction of colloidal nanoparticles with their local environment: the (ionic) nanoenvironment around nanoparticles is different from bulk and determines the physico-chemical properties of the nanoparticles. J Royal Soc Interface 11(96):20130931
87. Pong B-K, Trout BL, Lee J-Y (2008) Modified ligand-exchange for efficient solubilization of CdSe/ZnS quantum dots in water: a procedure guided by computational studies. Langmuir 24(10):5270–5276
88. Pons T, Uyeda HT, Medintz IL, Mattoussi H (2006) Hydrodynamic dimensions, electrophoretic mobility, and stability of hydrophilic quantum dots. J Phys Chem B 110(41):20308–20316
89. Potapova I, Mruk R, Prehl S, Zentel R, Basché T, Mews A (2003) Semiconductor nanocrystals with multifunctional polymer ligands. J Am Chem Soc 125(2):320–321
90. Potapova I, Mruk R, Hübner C, Zentel R, Basché T, Mews A (2005) CdSe/ZnS nanocrystals with dye-functionalized polymer ligands containing many anchor groups. Angew Chem Intern Ed 44(16):2437–2440
91. Rajh T, Micic OI, Nozik AJ (1993) Synthesis and characterization of surface-modified colloidal cadmium telluride quantum dots. J Phys Chem 97(46):11999–12003
92. Reiss P, Protiere M, Li L (2009) Core/shell semiconductor nanocrystals. Small 5(2):154–168
93. Ren X, Chen L (2015) Quantum dots coated with molecularly imprinted polymer as fluorescence probe for detection of cyphenothrin. Biosens Bioelectron 64:182–188
94. Rogach A, Harrison M, Kershaw S, Kornowski A, Burt M, Eychmüller A et al (2001) Colloidally prepared CdHgTe and HgTe quantum dots with strong near-infrared luminescence. Phys Status Solidi (b) 224(1):153–158
95. Sakura T, Takahashi T, Kataoka K, Nagasaki Y (2005) One-pot preparation of monodispersed and physiologically stabilized gold colloid. Colloid Polym Sci 284:97–101. https://doi.org/10.1007/s00396-005-1339-9 [Crossref]
96. Sapsford KE, Pons T, Medintz IL, Mattoussi H (2006) Biosensing with luminescent semiconductor quantum dots. Sensors 6(8):925–953
97. Shen L (2011) Biocompatible polymer/quantum dots hybrid materials: current status and future developments. J Funct Biomater 2:355–372
98. Shen L, Laibinis PE, Hatton TA (1999) Bilayer surfactant stabilized magnetic fluids: synthesis and interactions at interfaces. Langmuir 15:447–453. https://doi.org/10.1021/la9807661 [Crossref]
99. Smith AM, Nie S (2008) Minimizing the hydrodynamic size of quantum dots with multifunctional multidentate polymer ligands. J Am Chem Soc 130(34):11278–11279
100. Smith AM, Duan H, Rhyner MN, Ruan G, Nie S (2006) A systematic examination of surface coatings on the optical and chemical properties of semiconductor quantum dots. Phys Chem

Chem Phys 8:3895–3903. https://doi.org/10.1039/b606572b
[Crossref]

101. Sperling RA, Parak WJ (2010) Surface modification, functionalization and bioconjugation of colloidal inorganic nanoparticles. Phil Trans R Soc A 368:1333–1383

102. Sperling RA, Pellegrino T, Li JK, Chang WH, Parak WJ (2006) Electrophoretic separation of nanoparticles with a discrete number of functional groups. Adv Functional Mater 16(7):943–948

103. Sperling R, Liedl T, Duhr S, Kudera S, Zanella M, Lin C-A et al (2007) Size determination of (bio) conjugated water-soluble colloidal nanoparticles: a comparison of different techniques. J Phys Che C 111(31):11552–11559

104. Srinivasan C, Lee J, Papadimitrakopoulos F, Silbart LK, Zhao M, Burgess DJ (2006) Labeling and intracellular tracking of functionally active plasmid DNA with semiconductor quantum dots. Mol Ther 14(2):192–201

105. Su Y, He Y, Lu H, Sai L, Li Q, Li W et al (2009) The cytotoxicity of cadmium based, aqueous phase–synthesized, quantum dots and its modulation by surface coating. Biomaterials 30(1):19–25

106. Tan L, Wan A, Li H, Zhang H, Lu Q (2012) Biocompatible quantum dots–chitosan nanocomposites for fluorescence detection of nitric oxide. Mater Chem Phys 134(2–3):562–566

107. Van Vlerken LE, Vyas TK, Amiji MM (2007) Poly (ethylene glycol)-modified nanocarriers for tumor-targeted and intracellular delivery. Pharm Res 24(8):1405–1414

108. Wang Y, Wong JF, Teng X, Lin XZ, Yang H (2003) Pulling nanoparticles into water: phase transfer of oleic acid stabilized monodisperse nanoparticles into aqueous solutions of a-cyclodextrin. Nano 3:1555–1559. https://doi.org/10.1021/nl034731j
[Crossref]

109. Wang M, Dykstra TE, Lou X, Salvador MR, Scholes GD, Winnik MA (2006) Colloidal CdSe nanocrystals passivated by a dye-labeled multidentate polymer: quantitative analysis by size-exclusion chromatography. Angew Chem Intern Ed 45(14):2221–2224

110. Wang X, Ding H, Yu X, Shi X, Sun A, Li D et al (2019) Characterization and application of molecularly imprinted polymer-coated quantum dots for sensitive fluorescent determination of diethylstilbestrol in water samples. Talanta 197:98–104

111. Watson KJ, Zhu J, Nguyen ST, Mirkin CA (1999) Hybrid nanoparticles with block copolymer shell structures. J Am Chem Soc 121(2):462–463

112. Wilchek M, Bayer EA (1988) The avidin–biotin complex in bioanalytical applications. Anal Biochem 171:1–32. https://doi.org/10.1016/0003-2697(88)90120-0
[Crossref]

113. Wooding A, Kilner M, Lambrick DB (1991) Studies of the double surfactant layer stabilization of water-based magnetic fluids. J Colloid Interf Sci 144:236–242. https://doi.org/10.1016/0021-9797(91)90254-6
[Crossref]

114. Wu X, Liu H, Liu J, Haley KN, Treadway JA, Larson JP et al (2003) Immunofluorescent labeling of cancer marker Her 2 and other cellular targets with semiconductor quantum dots. Nature Biotechnol 21(1):41–46
115. Wuister SF, Swart I, van Driel F, Hickey SG, de Donega CM (2003) Highly luminescent water-soluble CdTe quantum dots. Nano 3:503–507. https://doi.org/10.1021/nl034054t [Crossref]
116. Xie H, Yu W (2012) A review on nanofluids: preparation, stability mechanisms and applications. J Nanomater 2012:435873. https://doi.org/10.1155/2012/435873 [Crossref]
117. Yang Y, Chen O, Angerhofer A, Cao YC (2006) Radial-position-controlled doping in CdS/ZnS core/shell nanocrystals. J Am Chem Soc 128(38):12428–12429
118. Yang Y, Chen O, Angerhofer A, Cao YC (2008) On doping CdS/ZnS core/shell nanocrystals with Mn. J Am Chem Soc 130(46):15649–15661
119. Yang Y, Chang Y, Guo Y, Yu L, Zhang G, Zhai D et al (2019) Fluorometric microplate-based dimethoate assay using CdSe/ZnS quantum dots coated with a molecularly imprinted polymer. Microchim Acta 186(8):1–10
120. Yezhelyev MV, Qi L, O'Regan RM, Nie S, Gao X (2008) Proton-sponge coated quantum dots for siRNA delivery and intracellular imaging. J Am Chem Soc 130(28):9006–9012
121. Yildiz I, McCaughan B, Cruickshank SF, Callan JF, Raymo FM (2009) Biocompatible CdSe−ZnS core−shell quantum dots coated with hydrophilic polythiols. Langmuir 25(12):7090–7096
122. Yu X, Lei DY, Amin F, Hartmann R, Acuna GP, Guerrero-Martínez A et al (2013) Distance control in-between plasmonic nanoparticles via biological and polymeric spacers. Nano Today 8(5):480–493
123. Zanella M, Abbasi AZ, Schaper AK, Parak WJ (2010) Discontinuous growth of II−VI semiconductor nanocrystals from different materials. J Phys Chem C 114(14):6205–6215
124. Zhang Y, Clapp A (2011) Overview of stabilizing ligands for biocompatible quantum dot nanocrystals. Sensors 11(12):11036–11055
125. Zheng Y, Yang Z, Li Y, Ying JY (2008) From glutathione capping to a crosslinked, phytochelatin-like coating of quantum dots. Adv Mater 20(18):3410–3415
126. Zheng L, Zheng Y, Liu Y, Long S, Du L, Liang J et al (2019) Core-shell quantum dots coated with molecularly imprinted polymer for selective photoluminescence sensing of perfluorooctanoic acid. Talanta 194:1–6
127. Zubarev ER, Xu J, Sayyad A, Gibson JD (2006) Amphiphilic gold nanoparticles with V-shaped arms. J Am Chem Soc 128(15):4958–4959

OceanofPDF.com

© The Author(s), under exclusive license to Springer Nature Switzerland AG 2023
G. Korotcenkov (ed.), *Handbook of II-VI Semiconductor-Based Sensors and Radiation Detectors*
https://doi.org/10.1007/978-3-031-19531-0_15

15. HgCdTe Device Technology

Sergey Alekseevich Dvoretsky[1] ✉, Vladimir Vasilievich Vasiliev[1] ✉, George Yurievich Sidorov[1] ✉ and Dmitriy Vitalievich Gorshkov[1] ✉
(1) Rzhanov Institute of Semiconductor Physics, Novosibirsk, Russia

✉ **Sergey Alekseevich Dvoretsky (Corresponding author)**
Email: dvor@isp.nsc.ru

✉ **Vladimir Vasilievich Vasiliev**
Email: vas@isp.nsc.ru

✉ **George Yurievich Sidorov**
Email: george@isp.nsc.ru

✉ **Dmitriy Vitalievich Gorshkov**
Email: gorshkovdv@isp.nsc.ru

Keywords Photodetector – C-V characteristic – FPAs – Junction – n-on-p – p-n – p-on-n – HgCdTe – Conductivity – Growth – Impurity – Layer – n-type – p-type – Technology – Device technology – Doping – In – As – Contact – Au – Ohmic contacts – Etching – Dry etching – Schottky barrier – Surface passivation – Anodic oxide – Al_2O_3 – SiN_x – SiO_2 – ZnS – HgCdTe material technology – Bulk crystal – Bridgman method – Recrystallization – Traveling heater method – HgCdTe epilayer technologies – Epitaxy – LPE – MBE – MOCVD – Temperature – P-n junction technology – Ion etching – Ion implantation – Ion – As – B – Mercury diffusion – Reactive ion etching – Spectral range – Infrared – LWIR – MWIR – Substrate – CdTe – CdZnTe – GaAs – Orientation – Si

15.1 Introduction

Over the past few decades, solid solution of ternary mercury cadmium telluride (MCT, HgCdTe) has demonstrated its excellent photoelectric performance for numerous infrared (IR) applications in “technical vision” systems. HgCdTe ranks first among a variety of solid-state photosensitive materials for the design and manufacture of IR detectors due to its unique physical properties, such as bandgap change over a wide spectral range, high absorption coefficient, high mobility, and carrier life. High-quality HgCdTe IR detectors successfully operated in three important atmospheric transparency windows: SWIR (1–3 μm), MWIR (3–5 μm), and LWIR (8–14 μm), as well as in VLWIR (over 14 μm) and THz spectral ranges.

Scientific research of technological processes was carried out to implement high-quality parameters of various HgCdTe IR detectors, determined by the background-limited performance (BLIP). The developed technologies represent a database of the developer companies, which is used for the development of specific focal plane arrays (FPA) for the infrared range and subsequent optimization of their performances. The scientific basis of technological processes of various manufacturers of IR HgCdTe detectors does not differ greatly. However, the application of this knowledge in the development of a specific version of technological processes for the manufacture of IR FPA requires many additional experiments to obtain the parameters of specific technological operations and their sequence to ensure the optimal technology. The choice of chemicals, required temperatures for technological processes, equipment, etc. determines the uniqueness of HgCdTe IR detector technology of each developer and generates its know-how. This, in turn, provides such technologies with the competition in the market. The rapid growth of the market of HgCdTe IR detectors is associated with the expansion of their field of application, which requires single or small-format FPAs with a number of pixels up to tens of thousands, up to unique megapixel matrices up to 17,000,000 pixels, and, as a consequence, a large number of technologies.

Nevertheless, given the uniqueness and compliance with the know-how of the parameters of technological processes, the enormous information about the studies of HgCdTe IR FPAs in the articles does not give detailed ideas about the technology of their fabrication, let alone reproduction. There

is only a general idea of how to develop an HgCdTe technology that satisfies such requirements as (1) the possibility of forming the required architecture of the photodetector, (2) creating conditions that ensure the manufacture of photosensitive pixels with the required size and spectral range of sensitivity, (3) the possibility of manufacturing photodetector matrices of the required format, (4) the possibility of passivating pixels and ensuring the stability of their parameters, and (5) creating ohmic low-resistance electrical contacts for outputting a signal from a pixel, etc.

The main modes of operation of IR photodetectors based on HgCdTe, which is a direct gap semiconductor, are photoconductive and photoelectric modes. The latter approach, using the formation of p-n junctions or heterojunctions, is currently the main direction in the development of infrared detector technologies based on HgCdTe. In this chapter the technologies for the manufacture of a photovoltaic matrix photosensitive element based on HgCdTe will be considered. We will discuss the HgCdTe material technology, p-n junction formation technologies, wet and dry etching technologies used for the matrix photosensitive element formation, passivation technologies by a deposition of dielectric layers, and the requirement for electric contacts used in photodetectors.

15.2 HgCdTe Material Technology

The HgCdTe material technology has gone through a consistent path of development from the bulk crystals to various epitaxial technologies. The evolution of the technology of photosensitive HgCdTe material, considered in [1, 2], is shown in Fig. 15.1. According to this figure, published in 2009, bulk crystal technology has not yet been developed. But it should be noted that the interest in bulk crystals has not been lost, and now single crystals of HgCdTe are produced in the required quantities.

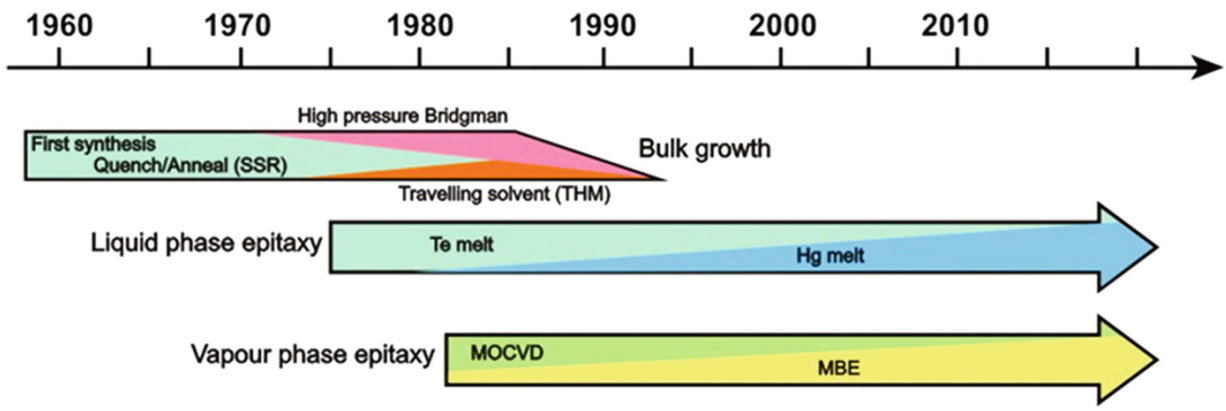

Fig. 15.1 Evolution of the technology of photosensitive HgCdTe material. (Data extracted from Refs. [1, 2])

15.2.1 HgCdTe Bulk Crystal Technology

The photosensitive HgCdTe material for IR detectors appeared in 1959. Lawson [3] and Schneider [4] synthesized the first HgCdTe bulk crystals. This research led to a real revolution in infrared photoelectronics. It was shown that in the CdTe/HgTe system, both compounds have infinite solubility with respect to each other and form a continuous series of solid solutions with a change in the bandgap in a wide range of the IR spectrum. Since the 1960s, with such impressive results, HgCdTe bulk crystal technology has been expanded through the development of various growth methods. The common requirements for obtaining the high-quality HgCdTe bulk crystal are the following:

- High purity of initial materials Cd, Te, and Hg, which will provide a low residual impurity level and controlled intentional impurity doping to stabilize a low level of electron photoconductor-based detectors and required hole concentration for photodiodes.
- Equipment to ensure the growth processes taking into account a high pressure of mercury during the crystallization of HgCdTe bulk crystals.
- Crucible materials and equipment must ensure minimal interaction with the initial materials and their compounds at high temperatures.

Bulk crystal technologies associated with HgCdTe are summarized by Capper in [5–8] based on data in [6–11] and are based on three basic methods: solid-state recrystallization (SSR), traveling heater method (THM), and Bridgman methods.

15.2.1.1 Solid-State Recrystallization Method

In the solid-state recrystallization (SSR) method developed in the United States, pure elements Hg, Cd, and Te are loaded into an etched silica ampoule and mixed in the melt at elevated temperature [9]. Then the homogeneous melt of Hg, Cd, and Te is rapidly quenched into air or oil up to room temperature. As a result of this process, a dendritic structure is formed. To obtain single-crystal grains, subsequent recrystallization of the synthesized material is required, carried out at temperatures below the solidus line for a long time. Various methods have been proposed for reducing the density of defects or eliminating the causes of their appearance in the synthesized material in SSR processes. For preparing n-type HgCdTe, the grown p-type material is converted to n-type material by thermal annealing in an Hg atmosphere. The precipitation of second phase formed in the ingot of HgCdTe can be minimized by increasing the partial pressure of Hg and slowing down the cooling process after reheating the slices, while encapsulating in another ampoule of silica. In this case, the dislocation density can be decreased to two orders of magnitude.

15.2.1.2 Traveling Heater Method

Traveling heater method (THM) developed in France was presented by Triboulet in [10]. In this method, the molten zone slowly moves through the solid homogeneous source material (polycrystalline HgCdTe) as the ampoule moves through the heater. During this process, dissolution of the material in the hot state and crystallization of HgCdTe of the same composition at cold interfaces are observed in the temperature gradient under steady-state conditions. The melt zone partially purifies the material during the TMH process. THM makes it possible to grow longer and larger bulk HgCdTe crystals up to 40 mm in diameter.

15.2.1.3 Bridgman Method

In the Bridgman process developed in the United Kingdom [8], pure elements Cd, Hg, and Te are loaded into a purified silica ampoule and then are homogenized, while heating to the melting state. Upon cooling, starting from the end of the ampoule of a certain configuration, a large-grained ingot was grown. To reduce radial temperature fluctuations, a slow rotation around the vertical axis was used. To prevent accidental explosions, which can be caused by a pressure of 70 atm arising in the ampoule upon rapid

heating, the ampoule for the growth of HgCdTe crystals was placed in an additional semi-hermetic cell. The accelerated crucible rotation technique (ACRT) is used to maintain the composition uniformity. The largest crystal up to 70 mm in diameter was grown by the Bridgman method (see Fig. 15.2). It is seen that the crystal structures degenerate with increasing diameter.

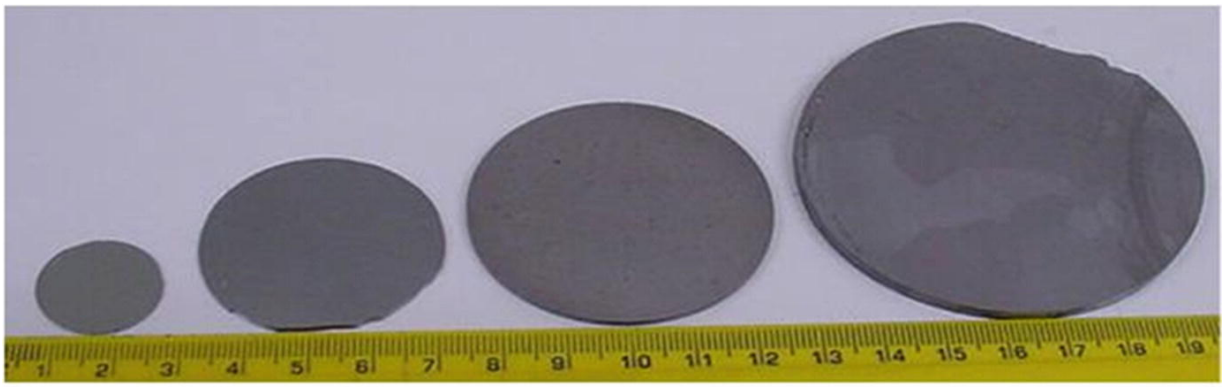

Fig. 15.2 HgCdTe wafers of different diameter grown by Bridgman process. (Reproduced with permission from Capper [8]. Copyright 2017 Springer)

In the former USSR (now in Ukraine), a HgCdTe bulk crystal, 50 mm in diameter, was grown by the method of melt crystallization of HgCdTe solid solution [12]. The composition of homogeneous HgCdTe solid solution corresponded to the solidus temperature. The HgCdTe bulk crystal was doped with In with concentration of (2–4) × 10^{14} cm^{-3} to a stabilized donor level. The dislocation density was ~3 × 10^{5} cm^{-2} for HgCdTe doped with In and ~10^{4} cm^{-2} for isovalent doping with Se. After the growth of a bulk HgCdTe crystal, a concentration of Hg vacancies of (1–10) × 10^{17} cm^{-3} and Te precipitations is observed. After thermal annealing at ~400 °C and further annealing at 250–280 °C in a saturated atmosphere of Hg, a homogeneous HgCdTe bulk crystal can have p-type or n-type conductivity with a carrier concentration of (5–20) × 10^{15} cm^{3} and (2–4) × 10^{14} cm^{-3}, respectively.

15.2.2 HgCdTe Epilayer Technologies

Bulk crystal technology of HgCdTe with n-type and p-type conductivity makes it possible to create single-crystal substrates for fabrication of small-sized photoconductors and photovoltaic infrared detectors aimed for application in thermal imaging systems. To increase the visibility range and

more accurate spatial resolution, which can be achieved through the use of large-format IR photodetector arrays, epitaxial technologies for growing HgCdTe layers on various large-diameter substrates have been developed. Epitaxial layers have an optimal thickness for absorption of radiation, the required electrophysical parameters, and a minimum number of defects. Heteroepitaxial structures (HES) made of HgCdTe grown on various substrates are a “semi-finished product” that significantly improves and simplifies the technology for fabricating devices based on HgCdTe. The first technology for growing epitaxial layers of HgCdTe was liquid-phase epitaxy (LPE), which was the simplest method suitable for this purpose. However, to carry out LPE processes, it was necessary to use only isovalent single-crystal substrates, such as CdTe, which was used at the initial stage and was subsequently replaced by CdZnTe.

15.2.2.1 Liquid-Phase Epitaxy

At present time, LPE is the most developed epitaxial technology for growing high-quality homogeneous HgCdTe epitaxial layers. Due to the relative simplicity and high manufacturability of LPE, the HgCdTe technology has been introduced in the industrial production. The main advantages of LPE technology are the following:

- Relatively low cost and high performance of the equipment
- Relatively low growth temperatures of 450–550 °C
- Uniform distribution of the composition over the area
- High crystal perfection
- Required electrophysical parameters

The analysis of the Cd-Hg-Te-phase diagram determined the main directions of the LPE technology development based on the use of Te- or Hg-rich melts. In connection with the use of various solvents, the development of LPE technology was carried out by various methods, such as:

- Horizontal open-tube slider method
- Vertical dipping method
- Tipping method in a closed sealed quartz ampoule

The important key problems of the LPE method are associated with removing a residual melt from the epitaxial layer surface (decantation) and

maintaining a given liquid-phase composition [13]. The scheme of decantation at different LPE techniques is shown in Fig. 15.3. In a horizontal slider-type LPE, the decantation is carried out by shifting the melt from the epitaxial layer surface by moving the parts of the graphite boat relative to each other. In a vertical dipping-type LPE, the melt flows free down from the surface under the gravity force. In a tipping-type LPE, the revolute architecture is used to free the melt removal or in combination with a slide. In [14, 15] it was shown that there are difficulties at the decantation of Te-rich melt because of its viscosity and the low surface tension value. Thus, the existence of residual melt drops is possible on the surface. It was proposed to carry out centrifugation to completely remove the Te-rich melt from the surface of the epitaxial layer surface at the growth in a sealed ampoule. An important problem of LPE is associated with the uniformity of the HgCdTe composition over the thickness of the epitaxial layer. Hg evaporates from the melt during epitaxial processes, resulting in uncontrolled composition of the growing HgCdTe layer. In a slider-type LPE with a Te-rich melt, the loss of Hg is replenished by adding Hg vapor to the hydrogen flow [14, 16] or HgTe to the melt [15, 17, 18].

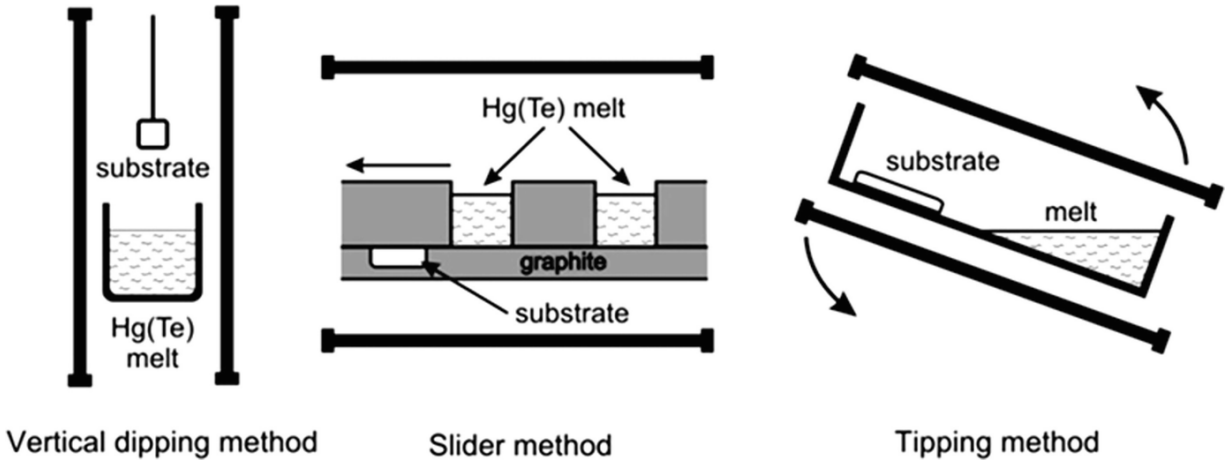

Fig. 15.3 The scheme of decantation in dipping (*left*), slider (*in the center*), and tipping (*on right*) types of LPE technologies

Various designs of quasi-hermetic boats based on high-purity and dense graphite have been developed [19, 20]. In the dipping-type LPE technology based on the Hg-rich and Te-rich melt [16, 21], the growth of large-area homogeneous HgCdTe layers is carried out from a very large melt volume called as “infinite melt” method [22]. It was shown that the HgCdTe layers of high composition reproducibility x = 0.223 ± 0.001 (further x means

CdTe mol. fr. in $Hg_{1-x}Cd_xTe$) over 54 cm^2 area in 200 LPE runs were grown from a 4–4.5 kg Te-rich melt [23]. For Hg-rich melts, the growth processes were carried out using a large mass of melt, up to 10 kg, with a decrease in temperature in the range of 200–245 °C [24–26]. The problem of changing the composition in the epitaxial layer during the growth in the closed tipping-type method is absent due to the constancy of the melt composition The Te-rich melt decantation using the revolute architecture and centrifugation was applied in [27–29]. When growing in a sealed ampoule, it was proposed to replace the CdTe substrate and to use two temperature zones of the furnace to enrich the Te-rich melt with Hg [30].

The characteristics of the HgCdTe HES material grown by the LPE method on (111) A, (111) B, (100) and misoriented from single-crystal CdZnTe substrates were studied by various physical methods. The presence of threaded and screw dislocations, as well as micron and submicron Te precipitates in epitaxial layers of HgCdTe grown from a Te-rich melt of sliding type [17, 31], dipping type [16, 32] and Hg-rich melt dipping type [26], and closed system tipping type [27], regardless of the growth method, was found. The dislocation density decreased from the interface to the surface throughout the entire thickness and reached a constant value (5–50) × 10^4 cm^{-2}. Thus, it was found that the dislocation densities on the surface are determined by the dislocation density in the substrate and are practically independent of the substrate/layer-matching conditions in the LPE method [33, 34]. Te precipitates in LPE epitaxial layers are localized, as a rule, near the interface and at the surface. The dependence of precipitate value on the growth conditions and the substrate misorientation from the (111) plane was found [32]. The specific feature of the surface morphology of the HgCdTe LPE epitaxial layer grown from a Te-rich melt is the presence of terraces, which is determined by the misorientation from optimal orientation (111) [16, 17, 32]. It is shown that the number of terraces decreases and a smoother surface is observed for misoriented substrates on 1.2–2 degrees from (111) A and (111) B. In addition, the smoothest and crystal-perfect layers are obtained at a minimum interval and cooling rate [16, 18]. The undoped LPE epitaxial layers, grown from Te-rich melts at 450–550 °C, have the p-type conductivity with the hole concentration and mobility (0.5–2.0) × 10^{17} cm^{-3} and (150–300) cm^2V^{-1} s^{-1} at 77 K, respectively. It is necessary to provide a low-

temperature thermal annealing in the Hg vapor in order to reduce the concentration of holes or convert the material from p-type to n-type conductivity. The highlighting of experimental results was presented in [35–39]. The following two types of annealing are used: (a) under Hg vapor pressure control and (b) under Hg saturated vapor pressure. It was found that the concentration of holes decreased to optimal values (0.5–2.0) × 10^{15} cm^{-3}, and the mobility was at least 300 cm^2V^{-1} s^{-1} at 77 K when the thermal annealing temperature decreased. At a certain temperature of thermal annealing, the p-type conductivity was converted to n-type. This temperature depended on the growing conditions for HgCdTe LPE epitaxial layers and varied in the range of 230–330 °C. In this case, the electron concentration differs in different samples by an order of magnitude. In the purest HgCdTe LPE epitaxial layers, after the thermal annealing at 260 °C during 100 hours, the electron concentration of 5 × 10^{13} cm^{-3} at 77 K was reported in [27]. The intentional HgCdTe doping during LPE growth makes it possible to significantly increase the reproducibility of the required electrophysical properties. A detailed analysis of the doping technology is presented in [40]. Very efficient doping was carried out with In, which provided ~100% degree of ionization and controlled electron concentration in the range (1.0–50) × 10^{14} cm^{-3} [22, 24, 27].

15.2.2.2 Metal-Organic Vapor-Phase Epitaxy

The results on growing HgCdTe layers using a metal-organic compound (MOVPE, MOCVD) by direct HgCdTe growth were first published in 1981 [41]. However, the method of direct growth of the HgCdTe layers did not allow obtaining the required quality of these layers, which is determined by the growth conditions during deposition process. Significant progress has been achieved only with the application of the MOCVD method, which is called the interdiffusion multilayer process (IMP) [42]. When using IMP method for HgCdTe layer growth, thin double layers of CdTe/HgTe, each 0.1–0.2 μm thick, are deposited with repetition and interdiffusion at the growth temperature. The composition of HgCdTe layer is changed by changing the ratio of CdTe and HgTe layers' thicknesses. Schematic cross section of the Aixtron AIX-200 reactor for the MOCVD HgCdTe growth is shown in Fig. 15.4 [43].

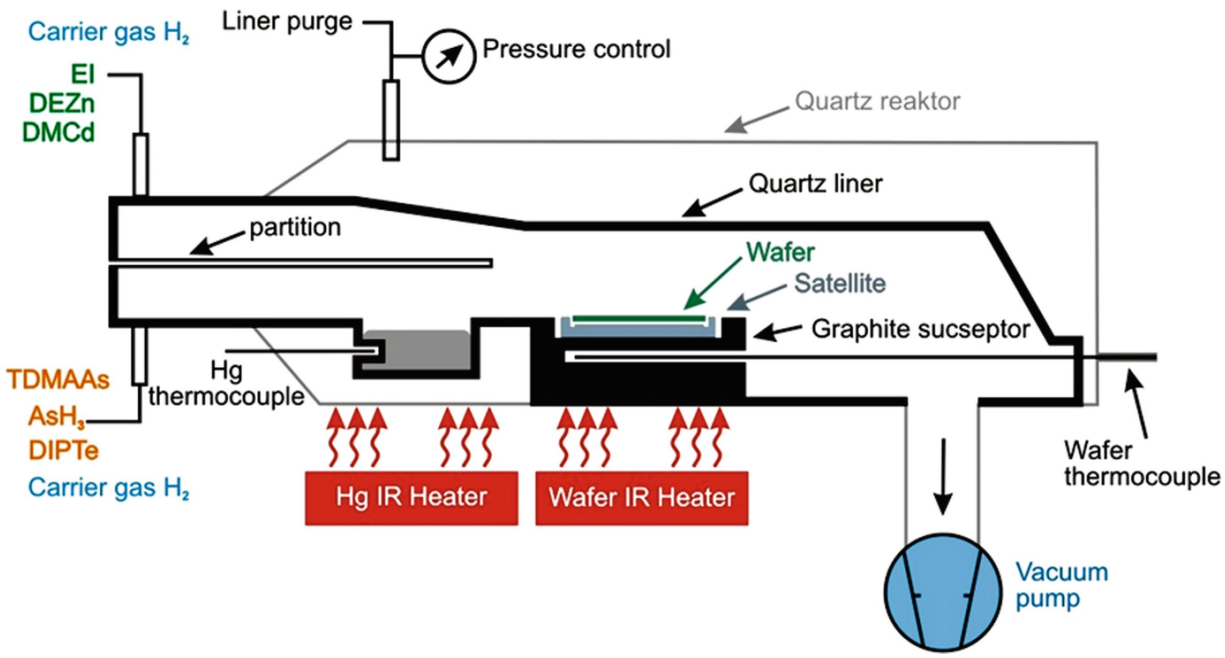

Fig. 15.4 Schematic cross section of the Aixtron AIX-200 reactor. (Reproduced with permission from Piotrowski et al. [43]. Copyright 2007 Springer)

The HgCdTe layers were grown on 2 inch epiready, oriented 2° off (100) GaAs substrates to (110) in horizontal MOCVD reactor with H_2 carrier gas by the IMP process, using the following precursors: diisopropyl telluride (DiPTe), dimethyl cadmium (DMCd), and elemental mercury. A tris-dimethylamino arsenic (TDMAAs, $As[N(CH_3)_2]_3$) was used to control acceptor doping in the 10^{14}–5×10^{17} cm^{-3} range. An ethyl iodide (EI) was used for control donor doping in the 10^{14} cm^{-3}–1×10^{18} cm^{-3} range. The substrate temperature was kept at 350 °C and mercury zone at 210 °C. Tellurium flush during nucleation process provided (111) CdTe growth. Surface morphology of (111) HgCdTe was improved by thermal annealing of GaAs substrate at 600 °C in hydrogen flow before Te nucleation [44]. The II/VI mole ratio was kept in the range from 1.5 to 5 during CdTe cycles of the IMP process. Typically, 3–4-μm-thick CdTe layer was used as a buffer layer, reducing stress caused by crystal lattice misfit between GaAs substrate and HgCdTe epitaxial layer structure. The given MOCVD setup (scheme in Fig. 15.4) and the technological process describe the MOCVD technology.

However, there are differences in MOCVD technology developed by other researchers and manufacturers. Various MOCVD settings, precursor materials, specific cultivation processes, substrates, etc. determine these

differences. GaAs substrates have proven to be the preferred substrates for growing high-quality MOCVD HgCdTe layers over large areas. The Si substrate is more attractive than the GaAs substrate. However, it is very difficult to implement the MOCVD HgCdTe technology on Si substrates due to the problem of in situ removal of thermal oxides. The optimal thickness of the CdTe buffer layer on the GaAs substrate for achieving high crystal quality and reducing the gallium doping level was determined in [44, 45]. This makes it possible to reduce the defect density and improve the quality of the HgCdTe epitaxial layers [46]. The orientation of the substrate should provide HgCdTe layers with a mirror-smooth surface, a minimum number of macrodefects, and the required doping level.

In Great Britain and Poland, the preferred orientation for MOVPE growth of HgCdTe is still misoriented (100) GaAs [44]. In the United States, (211)B CdZnTe substrates are the preferred orientation for MOCVD. In Russia, GaAs substrates with orientation (100) and (310) are used [47]. Surface roughness depends on the orientation of the substrate, surface preparation, and the nucleation process at the initial stage of growth. Although the surface roughness for (211)B HgCdTe is about half that for (111)B HgCdTe, the latter orientation gives the progress in improving the parameters of the IR detector. Growth temperatures for the IMP method range from 230 to 410 °C and are determined by the initial choice of metal-organic compounds (MOCs) [48–50].

The use of photostimulated and plasma-stimulated decomposition of MOCs in the gas phase allows the growth temperature to be reduced to 150 °C and 135 °C, respectively [51]. The IMP method makes it possible to obtain multilayer heterostructures with different designs of composition and doping distribution over the thickness, mirror-like surface morphology, and uniformity of HgCdTe composition over the surface area. This makes it possible to provide the processes of thermal annealing and deposition of a passivation coating in one growth cycle. In MOCVD, as in MBE, layer thickness and precursor concentration can be monitored using ellipsometry and in situ laser reflectometry [43, 52]. All this makes it possible to manufacture large-area IR focal plane photodetector arrays (FPAs) based on MOCVD HgCdTe layers with high operating parameters [5, 53]. The main disadvantage of the MOCVD HgCdTe technology is the toxicity of original precursors used during this process.

Studies of the behavior of impurities in epitaxial HgCdTe MOCVD epitaxial layers are presented in [54–57]. It was found that Ga, In, Al, and I exhibit donor properties, while P, As, and Sb exhibit acceptor properties. The most widely used impurities for obtaining n-type and p-type conductivities are I [43] and As [57, 58]. In the IMP, the doping with As is carried out during the growth of the CdTe layer and, as a rule, with an excess of Cd in the gas phase [58, 59]. The arsenic precursor AsH_3 provides almost 100% electric activities of As. However, due to its toxicity, other arsenic precursors have been considered. In the case of the precursors, such as trimethylarsine ($(CH_3)_3As$) and diethylarsine ($(C_2H_5)_2AsH$), doping with As led to its concentrations below 10^{16} cm^{-3} and low electrical activation [60] or to the formation Shockley-Read-Hall (SRH) recombination centers [3]. The most promising precursor for doping HgCdTe with arsenic is TDMAA, which, upon decomposition with the formation of atomic As, makes it possible to obtain 100% electrical activation of arsenic [43, 61].

The lifetime of minority carriers in HgCdTe doped with As from TDMAAs is an order of magnitude higher than lifetime in HgCdTe doped with other metal-organic precursors and is limited only by fundamental recombination processes [62]. It is important that the composition of the grown HgCdTe layers depends on the precursor used for doping. For example, a decrease or an increase (10% ($x \sim 0.2$)) was observed in the composition of the HgCdTe layers upon doping with As from AsH_3 or TDMAA, respectively. A significant increase in the composition of HgCdTe was also observed upon HgCdTe doping with $InMe_3$ and $AsMe_3$, and a decrease in the case of $SbMe_3$ [63].

15.2.2.3 Molecular Beam Epitaxy

Significant possibilities to realize the unique properties of HgCdTe for different applications, both in the traditional direction in the development of IR technology devices and in the direction of development of devices based on quantum phenomena, are associated with the technology of growing HgCdTe structures by molecular beam epitaxy (MBE). MBE is a very modern flexible technology and is widely developed due to the following advantages:

- Minimal low growth temperature (160–200 °C), which provides sharp interfaces between layers, a low background impurity doping level below

10^{11} cm^{-3}, and a low impurity diffusion from the substrate
- Absence of an aggressive medium, which allows using alternating Si, GaAs, and Ge substrates large in diameter
- Monitoring of growth processes by different electron and optical tools in situ
- Growth processes of multilayer HgCdTe HES with a required composition design and doping throughout the entire thickness, including CdTe/HgTe superlattices, HgCdTe/HgTe/HgCdTe quantum wells, and other nanostructures.

Ultrahigh vacuum (UHV) MBE setups have been developed for growing Hg-containing compounds and, first of all, HgCdTe HES using MBE technology. The latest generation of UHV MBE setups allows growing HgCdTe HES on 1 × 150 (200) mm (6″(8″)), 4 × 100 mm, or 5 × 76.2 mm substrates, such as MBE 49, RIBER 412, Veeco 20, and VG Semicon V-100, which advance the HgCdTe growth. In the Rzhanov Institute of Semiconductor Physics, Siberian Branch of Russian Academy of Sciences (ISP SB RAS), a multiple-chamber UHV MBE setup "Ob'-M" was developed for the growth of HgCdTe HES without rotation of 100 mm in diameter substrates [64]. All UHV MBE setups are equipped with oil-free pumps to obtain a residual gas pressure of less than 10^{-9} Pa. Technological chambers are equipped with molecular beam sources, usually Knudsen type, for basic and doping materials, a manipulator with heaters, and analytical equipment for monitoring the growth processes, such as reflection high-energy electron diffraction (RHEED), spectral ellipsometry and single-wavelength ellipsometry in situ, and vacuum and temperature gauges. The ellipsometry monitoring does not affect the growth processes over RHEED, especially in case of HgCdTe, and provides a high-accuracy monitoring in situ of the substrate temperature, composition, growth rate, thickness, and surface roughness [65–67]. To obtain a high uniformity of HgCdTe layer's composition, thickness, and doping level over the surface area during growth on large-diameter substrates, it is necessary to rotate the substrate, which limits the application of monitoring in situ. Large volume ring-type Cd and Zn, Knudsen-type Te molecular beam sources, and a ring-type Hg flux former coaxially designed together provide high composition uniformity over the surface without substrate rotation (Fig. 15.5) [68].

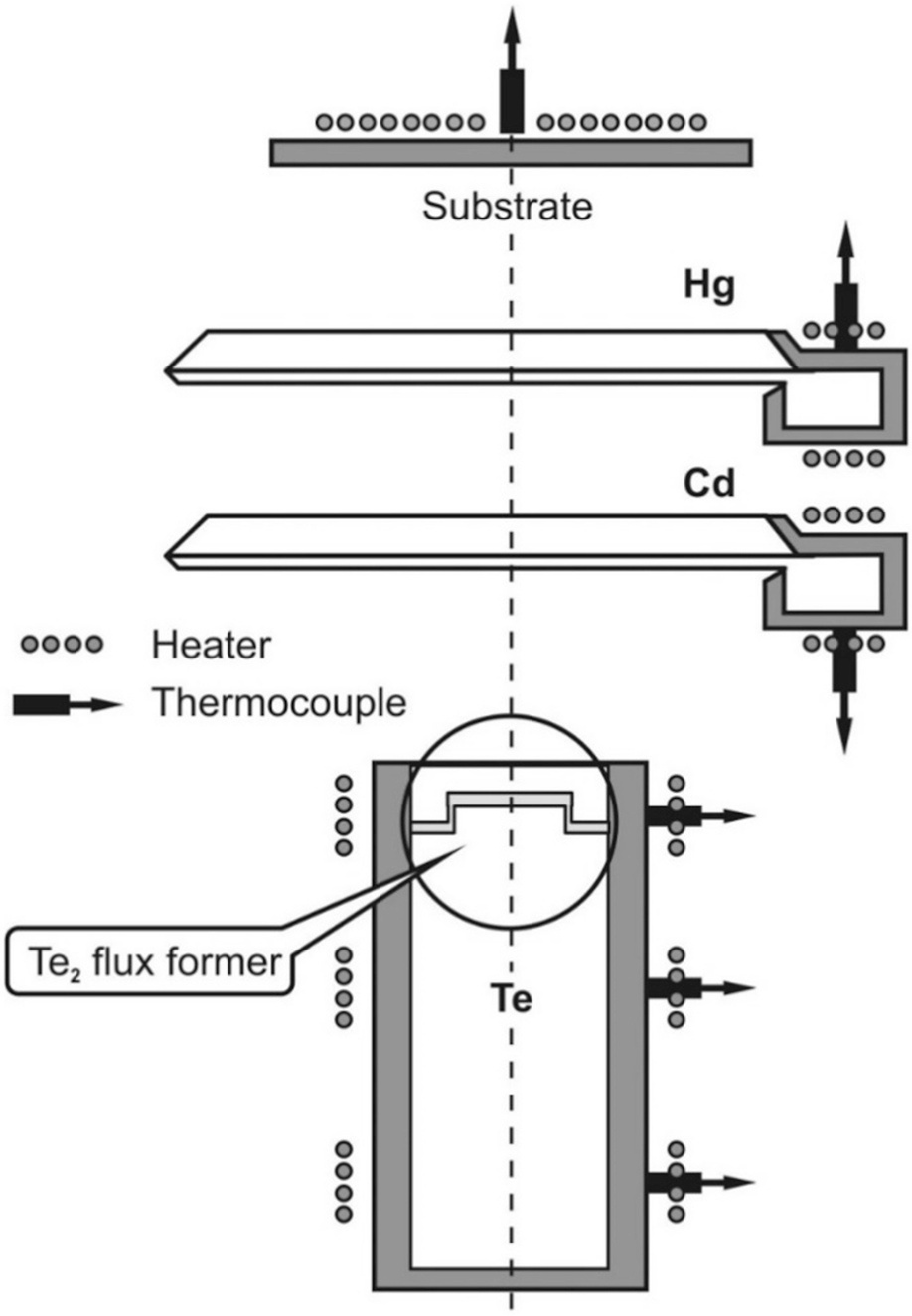

Fig. 15.5 The scheme of Cd and Zn ring-type and Te Knudsen-type molecular beam sources and Hg flux former location in HgCdTe deposition chamber

The Te molecular beam source has a low-temperature evaporation zone and a high-temperature zone of flux formation at the outlet. Cd and Zn molecular beam sources and Hg flux former have a narrow aperture outlet [69]. The proposed design of the technological unit allows obtaining the HgCdTe composition uniformity over the substrate area without substrate rotation, compared with the best-published data. CdZnTe, GaAs, Ge, and Si

are used as the basic substrates for the growth of HgCdTe HES by MBE. CdZnTe substrates provide the growth of high-quality HgCdTe HES for IR FPAs operated in important spectral ranges, such as 1–3 μm (SWIR), 3–5 μm (MWIR), 8–14 μm (LWIR), and over 14 μm (VLWIR). But at present, preference is given to larger-area GaAs, Ge, and Si substrates from the point of view of a significant reduction in material cost and subsequent costs for MFP. Despite the high mismatch of crystal lattices between HgCdTe and GaAs, Ge, and Si, numerical studies make it possible to develop MBE technologies for high-quality growth of large-area HgCdTe HES on such substrates. The low growth temperatures of HgCdTe and the strong dependence of the mercury sticking coefficient [70] require the choice of orientation to obtain high-quality layers [71]. Studies of the growth of HgCdTe on (100), (111)B, (211)A, (211)B, and (013) substrate orientations showed that better surface morphology, the absence of twins, and higher sticking coefficients are achieved through the use of (211)B and (013) orientations [72, 73]. To maintain the initial substrate orientation and eliminate a large lattice mismatch between Si, GaAs, Ge, and HgCdTe, it is necessary to grow, sequentially, a buffer layer of ZnTe and CdTe for creating alternative CdTe/ZnTe/Si (GaAs, Ge) substrates [74–76].

Before growing, the surface substrates were prepared by liquid chemical etching (no need for epiready) and thermal cleaning in a vacuum. All substrates were cleaned in an organic solvent. This is followed by chemical etching of CdZnTe in 0.5–1 vol. % Br/methanol [5], Ge in the H_3PO_4:H_2O_2:H_2O solution [76], GaAs in the H_2SO_4/H_2O_2/H_2O [77] with the following treatment in the HCl:isopropanol solution, and Si – in RCA, based on HF. Thermal annealing of CdZnTe substrates in ultrahigh vacuum was carried out at 220 °C to remove the passivating layer of Te, Ge annealing at ~650 °C to remove oxides in As flux, annealing of GaAs substrates at ~580 °C to remove oxides (in case of epiready) [78] or the As passivation layer, and Si annealing at 550–600 °C to remove the hydrogen passivation layer. The last technological procedure for creating an atomically clean and smooth substrate surface before growing HgCdTe is necessary for growing at 200–320 °C a thin CdTe layer on a CdZnTe substrate, as well as a thin ZnTe and a thick CdTe buffer layer on Ge, GaAs, and Si substrates [5, 77, 78].

The (211)B HgCdTe/CdZnTe HES technology on a (8x8) cm^2 CdZnTe substrate was developed in Teledyne [79] and Raytheon [80]. The growth of

the HgCdTe layer is carried out at T ~ 180–190 °C from the sources of Te, CdTe, Hg, In, and As. The obtained HgCdTe HES had the following parameters: x = 0.2072 ± 0.0021 (cutoff wavelength λ_c = 11.0 ± 0.1 μm at 78 K), thickness 13.26 ± 0.06 μm; the electron concentration ranged from 10^{14} to 10^{16} cm^{-3}, and the density of macrodefects was less than 10 cm^{-2} for sizes exceeding 10 microns, less than 10^3 cm^{-2} for sizes 4–10 μm, and less than 10^4 cm^{-2} for sizes less than 4 μm. The dislocation density was less than 5×10^5 cm^{-2}. In Sofradir, the technology (211)B HgCdTe/Ge HES was developed on Ge substrates with a diameter of 100 and 125 mm with spectral ellipsometry control [84, 85]. The temperature distribution over the substrate was no worse than 3 °C and was kept in the process no worse than 0.25 °C. The following parameters of HgCdTe HES were obtained: mirror-smooth surface, density of macrodefects from 200 to 300 cm^{-2}, and density of dislocations from 5×10^6 to 2×10^7 cm^{-2}. 1280 × 1024 IR FPAs with a pixel size of 15 μm were manufactured with the following parameters: wavelength cutoff, 5.20 ± 0.04 μm; sensitivities, 7.7×10^9 V/W and 2.75 A/W; quantum efficiency, 70%; NETD, 19 mK; and operability, more than 99.8%. These results lead to the conclusion that HgCdTe/Ge HES technology provides a high quality of megapixel MWIR FPAs.

The (211)B HgCdTe/GaAs HES technology on 100 mm in diameter GaAs substrates was developed in AIM Infrarot [81]. The resulting MCT layers had the following parameters: the homogeneity of the composition of HgCdTe for the MWIR and LWIR spectral ranges was ±1% in area, the dislocation density was (2–3) × 10^7 cm^{-2}, and the density of macrodefects was 50 cm^{-2} with their size <10 μm and 4 cm^{-2} at a size >10 μm. The improvement of the technology was associated with the introduction of wide-gap passivation layers, which led to an improvement in the performance of IR 640x512 FPAs [81]. The Rzhanov Institute of Semiconductor Physics SB RAS has developed the (013)HgCdTe/GaAs HES technology on GaAs 3 inch substrates without rotation using the growth process control by single-wave ellipsometry [75, 82, 83]. The popular “semifinal” HgCdTe HES has wide-gap gradient layers (x = 0.18–0.32) at the absorber interface and the surface to simplify the technology of manufacturing IR detectors and improve their parameters (see Fig. 15.6). The concentration and mobility of electrons varied in the ranges 10^{14}–10^{15} cm^{-3} and (0.5–1.5) × 10^5 cm^2V^{-1} s^{-1}, respectively. The lifetime of

minor charge carriers varied from 1 to 10 μs. The dislocation density was about 5×10^6 cm^{-2}. The p-type HgCdTe HES with hole concentrations (5–20) $\times 10^{16}$ cm^{-3} was obtained during the thermal annealing at 200–220 °C for 24 hours. The (211)HgCdTe/GaAs HES technology on Si 6 inch substrates was developed at Raytheon [86]. Growth temperature and molecular fluxes of Hg, Cd, and Te have been optimized to grow high-quality HgCdTe HES. The p+-n detectors, based on the double-layer heterojunction structures (DLHJ), were grown for single-spectral IR FPAs.

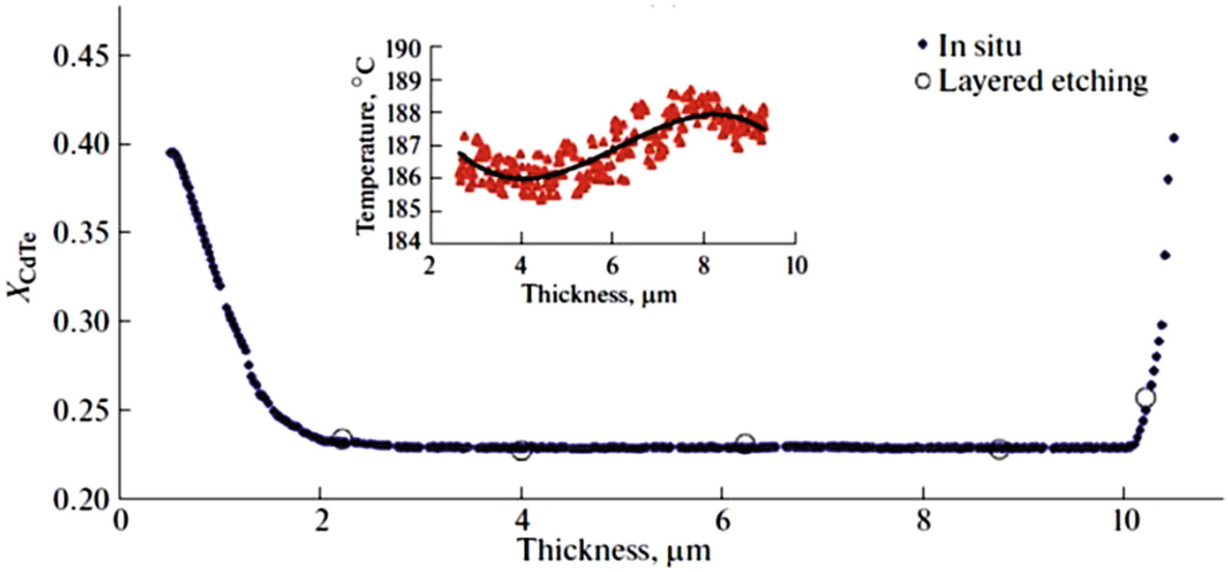

Fig. 15.6 The HgCdTe composition distribution throughout the thickness in HgCdTe layer with graded wide-gap layers on absorber interface and surface. Inset showed the temperature during the HgCdTe growth. The points are HgCdTe composition measured by transmission spectra with layer-by-layer etching. (Data extracted from Ref. [83])

For MWIR HgCdTe HES, the composition uniformity was ~0.1% (the cutoff wavelength – ±0.2 μm); dislocation density, 5×10^6 cm^{-2}; and macrodefects density, less than 100 cm^{-2}. For 640 × 480 IR FPAs, the following high-sensitivity values were obtained: NETD 19 mK, operability 99.7% for MWIR, and NETD 22 mK, operability 99.3% for LWIR. Thus, it was shown that HgCdTe/Si layers provide IR FPAs a quality comparable to that based on HgCdTe/CdZnTe layers. Recently [87] reported impressive results of growing HgCdTe HESs on Si substrates 200 μm in diameter. Twin-free high-quality HgCdTe layers were obtained with the following HgCdTe HES parameters: composition, x = 0.2903 ± 2.2% (the cutoff wavelength – 5.26 ± 5%); thickness, (9–10) ± 0.33 μm; and macrodefects density, 22–170 cm^{-2}. The As concentration varied in range (1.5–

3.5) × 10^{18} over a length of 100 mm from the center to the edge. A photograph of HgCdTe/Si structures grown on 6 and 8 inch Si substrates is shown in Fig. 15.7a.

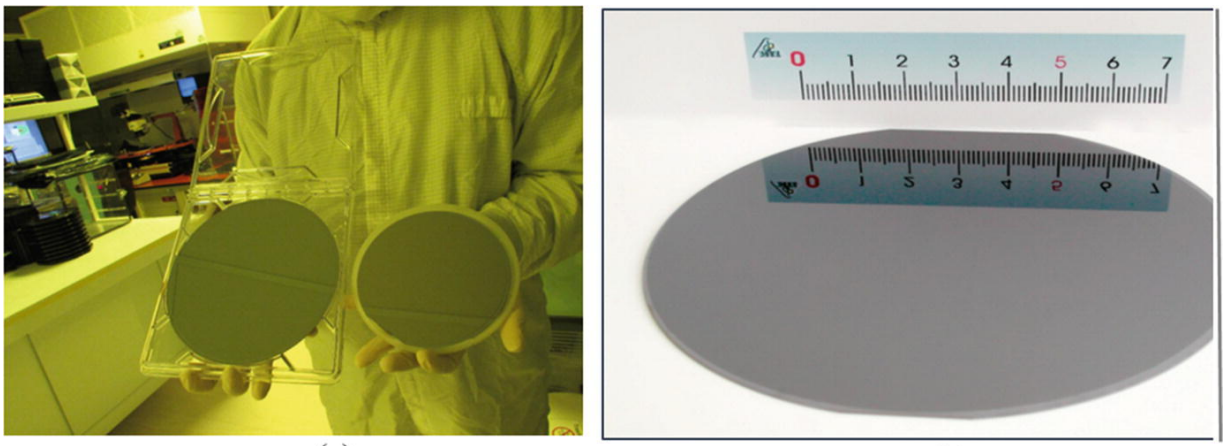

Fig. 15.7 The photograph of HgCdTe/Si structures: (**a**) 8″ in diameter and 6″ in diameter; (**b**) 4″ in diameter. ((**a**) Reproduced with permission from Reddy et al. [87]. Copyright 2019 Springer; and (**b**) from Yakushev et al. [88]. Copyright 2011 Springer)

The (013) HgCdTe/Si HES technology on Si substrates up to 4 inches in diameter was developed in Rzhanov Institute of Semiconductor Physics SB RAS for MWIR IR FPA [88, 89]. A photo of HgCdTe/Si structures grown on 4 inch Si substrates is shown in Fig. 15.7b. The HgCdTe HES had the following parameters: mirror-smooth surface; the density of macrodefects, less than 500 cm^{-2}; and thickness ~5 μm, x = (0.3–0.35) ± 0.002 (cutoff wavelength ~0.1 μm) at 77 K. As-grown undoped HgCdTe layers had n-type conductivity with electron concentration, mobility, and lifetime (5–10) × 10^{14} cm^{-3}, (15000–25,000) $cm^2V^{-1}c^{-1}$, and 5–15 μs, respectively. After thermal annealing HgCdTe layers had p-type conductivity with hole concentration, mobility, and lifetime (1–15) × 10^{15} cm^{-3}, (200–400) $cm^2V^{-1}c^{-1}$, and 3–50 ns, respectively. In P+-n DLHJ n-HgCdTe In-doped absorber had the following parameters: thickness ~5 μm, x = 0.29–0.31, and n = (1–10) × 10^{15} cm^{-3}. The p+-HgCdTe layers doped with As ions and two-step thermal annealing, first at 360 °C and then at 225 °C, had the following parameters: x = 0.35–0.6 and p = (1–10) × 10^{17} cm^{-3}. DLHJ structures are used for the manufacturing of large-format IR FPAs operating at elevated temperatures. It was shown that HgCdTe layers with a dislocation density of less than 5 × 10^5 cm^{-2} do not affect the photoelectric

parameters of IR FPAs. HgCdTe/CdZnTe HES technology has low dislocation density and allows obtaining high-quality IR FPAs in wide spectral range. HgCdTe/Si(Ge, GaAs) HES technology has high dislocation density exceeding 5×10^6 cm^{-2}. Nevertheless, SWIR, MWIR, and LWIR IR FPAs based on HgCdTe/Si(GaAs, Ge) HES have sensitivity which is comparable to those based on HgCdTe/CdZnTe. For VLWIR IR FPAs, the sensitivity is an order of magnitude lower [90]. It was shown earlier that the dislocation density in the (211)HgCdTe/Si HES was decreased to 10^6 cm^{-2} by a fast thermal cycling during 1 min in the range 290–350 °C without a composition change [91]. Macrodefects on the surface in the form of hillocks or pits (voids, V-defects) determine the quality of HgCdTe HES and the performance of IR photodiodes [92]. V-defects inside p-n junctions are called “killers.” It was found that the presence of V-defects near the p-n junction is the reason for the increase in the dark current. The reasons for the formation of V-defects are the crystallization of elemental tellurium during growth in places of deficiency of mercury and high temperatures [93–95].

It was shown that well-controlled n-HgCdTe in MBE technology is easily achieved by the intentional In doping in a wide range of 10^{14}–10^{19} cm^{-3} [96]. The introduction of Hg vacancies provides the obtaining of p-HgCdTe with the hole concentration in the range $(5–20) \times 10^{15}$ cm^{-3}. However, they are unstable to diffusion processes, reduce the hole mobility, and act as SRH recombination centers [97]. Group I elements show up to 100% activation upon doping during growth and exhibit excellent transport properties. However, such impurities quickly diffuse, both during growth and during thermal annealing, which does not allow the use of these impurities for obtaining a stable p-type and their application in the device technology. The low diffusion coefficient of As atoms allows the growth of stable, well-controlled p-type layers and p-n junctions. After growing, As-doped HgCdTe layers show their n-type conductivity [98]. For the conversion to p-type conductivity, it is necessary to activate As for the insertion into Te vacancies. Several activation methods have been proposed. The standard activation method consists of a two-stage thermal annealing, first for 10 min at 425 °C and then for 24 hours at 250 °C, which leads to almost complete activation of As to a hole concentration of $\geq 10^{18}$ cm^{-3}.

15.3 Etching Technology

The HgCdTe etching material technologies are used in the mesa technology of manufacturing IR detector. It is necessary to divide pixels for cross-talking elimination that leads to the deterioration in the frequency-contrast characteristic. The etching technology can be carried out by using liquid-phase (wet) or gas-phase (dry) etchings.

In wet etching the solution of Br in HBr [99] or Br in methanol (Br/Me) [100] is used as a liquid etchant. The etching rate is determined with high precision by accurately controlling the concentration of the liquid etchant and the temperature. It was shown that the temperature affects the etching rate during technological process using a Br solution in HBr [101]. The linear dependence of the groove depth on the etching temperature is shown in Fig. 15.8. It was shown that the etching temperature in the range from −18 °C to +15 °C does not change the surface morphology.

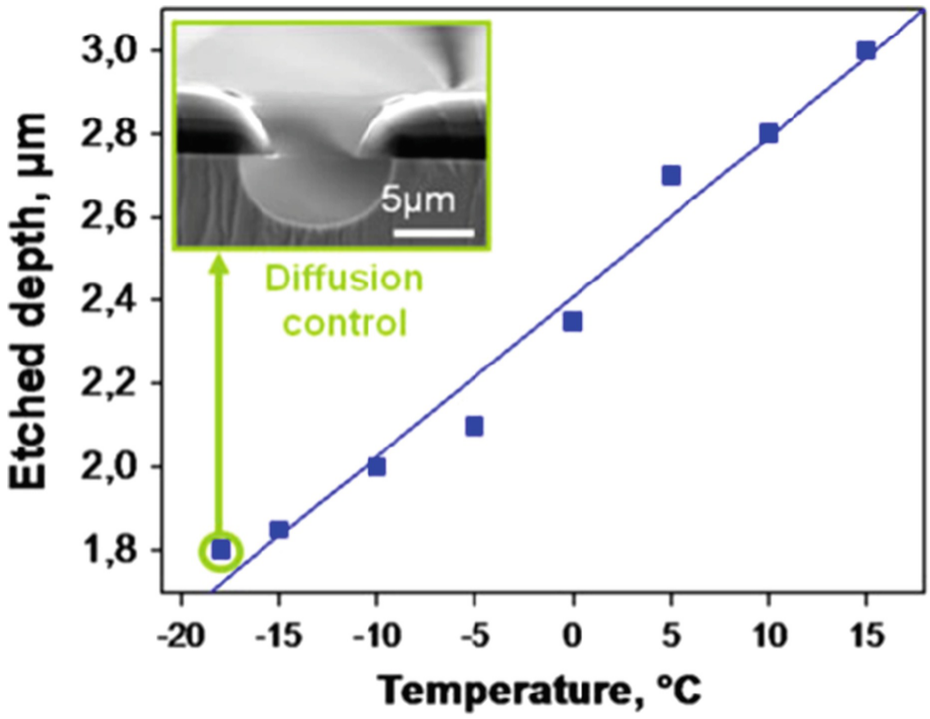

Fig. 15.8 The etched depth of HgCdTe vs. temperature. The inset shows a scanning electron micrograph of the groove etched at −18 ° C. (Reproduced with permission from Causier et al. [101]. Copyright 2011 Springer)

It was shown that an etching rate of ~10 nm/min makes it possible to provide a groove depth of 50 ± 5 nm in HgCdTe with good accuracy. The

disadvantages of wet etching include the following:

- Formation of an excess Cd layer on the surface of the HgCdTe grooves after both Br/HBr and Br/Me with cadmium oxide as the last etchant
- Anisotropic nature of groove etching (see inset in Fig. 15.8)
- Reduction of pixel sizes at large groove depth

Dry etching technological processes, using ionic and plasma-chemical modes have been intensively developed. In the ionic mode, Ar gas is used to create ions for the etching process [102, 103]. In the plasma-chemical mode, the following gas mixtures are used: Ar + H_2 [99, 104], CH_4 + H_2 [99], CH_4 + Ar [99], CH_4 + H_2 + Ar [99, 104], H_2 + Ar + N_2 [99], and CH_4 + H_2 + N_2 + Ar [104]. In the case of the CH_4 + H_2 + Ar gas mixture, $Te(CH_3)_2$, TeH_2, $Cd(CH_3)$, and Hg were formed as etching products [105, 106]. However, in the case of the H_2 + Ar gas mixture, etching products TeH_2 and Hg were formed [105]. This means that for etching Cd, a CH_3 radical is required. The SIMS studies show that the addition of N_2 to the CH_4 + H_2 gas mixture leads to the formation of NH_3 and HCN [106]. The addition of N_2 to the CH_4 + H_2 + Ar gas mixture leads to a decreasing H concentration and an increasing in the CH_3 radical density [99, 107, 108]. The SEM photos of HgCdTe top (a) and cleaved (b) views after the dry etching of HgCdTe in inductively coupled plasma (ICP) [109] are shown in Fig. 15.9.

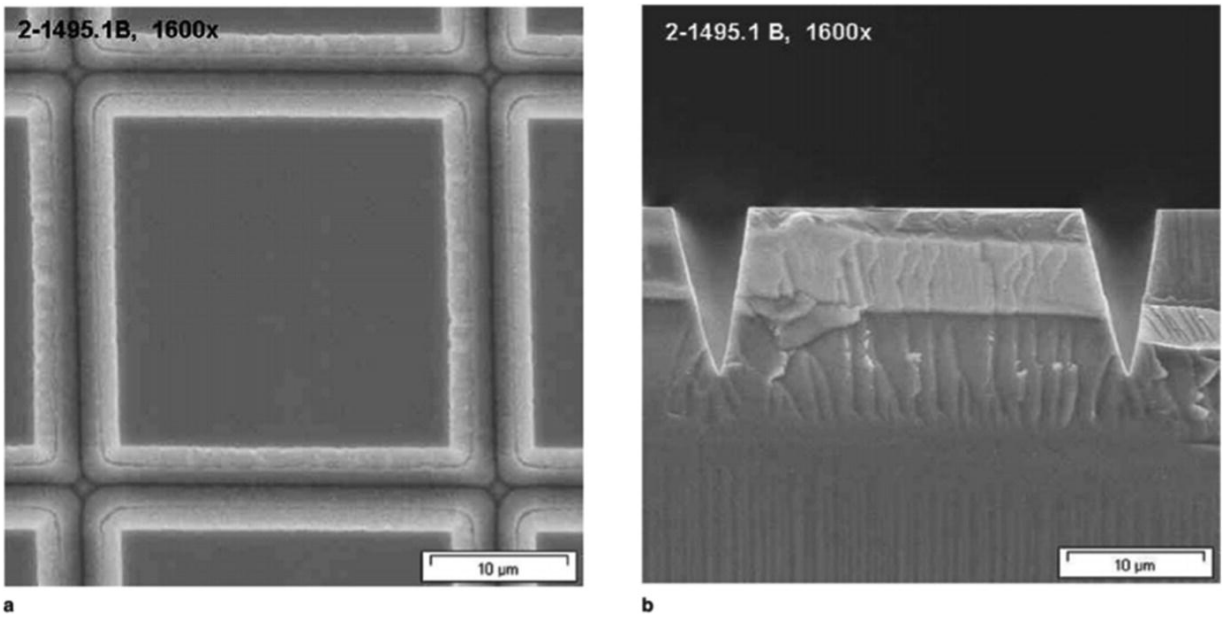

a b

Fig. 15.9 The SEM photo of 30 × 30 μm diode area after dry etching using inductively coupled plasma (ICP): (**a**) top view; (**b**) cleaved lateral face. The mesa depth is approximately 15 μm. The photoresist is used at etching process and then removed. (Reproduced with permission from Cmith et al. 2003. Copyright 2003 Springer)

The advantage of dry etching technology is associated with anisotropic etching (see Fig. 15.9). The disadvantage of dry etching is the formation of a damaged layer on the surface after etching. Donor complexes are usually formed in the damaged layer. The formation of a donor complex in a damaged layer has been studied in detail during ion beam etching with argon [102, 103]. It was found that the donor complexes are based on interstitial Hg atoms captured by a defect formed during etching. In the damaged layer, the conductivity is converted from p- to n-type. The concentration of charge carriers over the thickness after ion etching of p-HgCdTe [111] is shown in Fig. 15.10. It is clear that the thickness of n-type conductivity at the conversion process exceeds 7 μm. After dry etching of In-doped n-HgCdTe, a thin n+-type layer is formed on the surface. It should be noted that the concentration of electrons in the damaged layer depends on the storage time. Numerous studies showed that the thickness and electron concentration in the damaged layer depend on the ion energy, ion flux, and the temperature of etching. It was also found that the thickness of the damaged layer and etch depth are represented by the square root and linear dependences on time [112]. The Hg interstitial atom migration energy was determined as 120 ± 30 meV. To minimize the influence of the damaged layer on the characteristics of the diodes, it is proposed to remove the damaged layer by liquid etching followed by annealing [104].

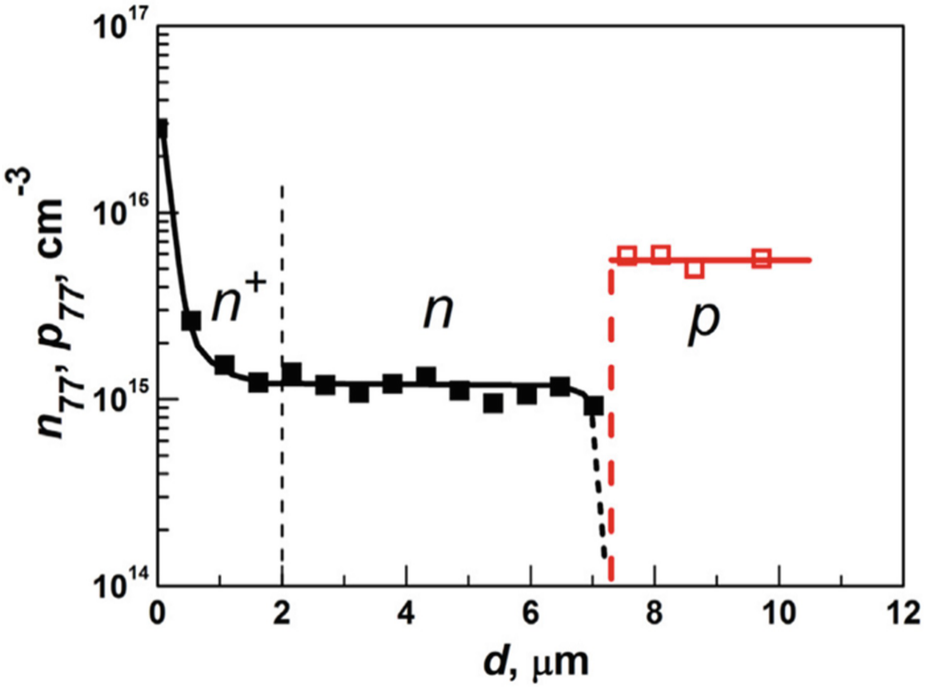

Fig. 15.10 The charge carrier concentration profile in ion-etched HgCdTe: solid squares corresponded to electrons, open squares corresponded to holes. (Reproduced with permission from Izhnin et al. [103]. Copyright 2017 Elsevier)

The study [113] showed the possibility of plasma-chemical etching without the formation of a damaged layer. This method is very promising, since the technological process of removing the damaged layer formed during other dry etching processes is excluded.

15.4 HgCdTe Surface Passivation Technology

The HgCdTe surface passivation technology plays a key role in reducing or eliminating surface leakage currents. These currents lead to a significant increase in the dark current of photoconductor and photovoltaic detectors and a decrease in their sensitivity. The requirements for the HgCdTe surface passivation technology are the following [114, 115]:

- Good adhesion of the passivation layer
- Stability of the interface between the HgCdTe surface and the passivating layer during temperature cycling in the range of 78–300 K
- A small built-in charge

The most developed passivation of the n-p diodes, fabricated on the basis of Hg vacancy-doped p-HgCdTe by CdTe and ZnS [115], is shown in

Fig. 15.11.

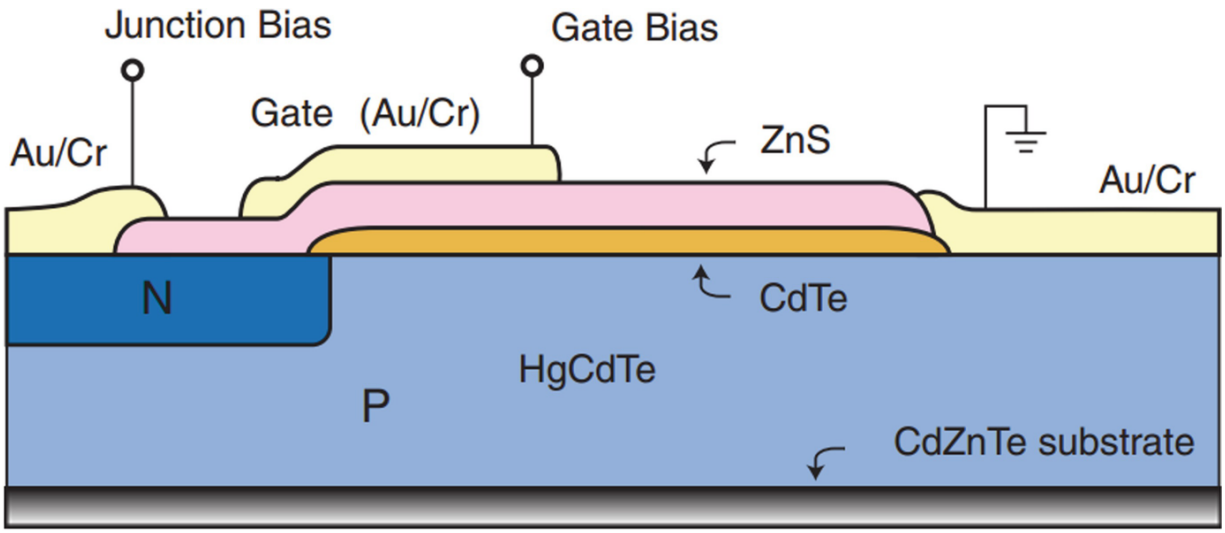

Fig. 15.11 The scheme of cross section of fabricated diodes on the base of Hg vacancy-doped p-type MWIR material from Fermionics Corporation grown by LPE. The CdTe is used as both a passivant and a mask for the plasma-based type conversion. The diodes were passivated with 200 nm of ZnS and contacts were formed with Au/Cr. (Reproduced with permission from Smith et. al., [110]. Copyright 2007 Springer)

The deposition temperature of the passivating layer is very important, since Hg begins to evaporate from the HgCdTe surface already at temperatures above 80 °C [116]. It should also be noted that for the passivation of p-HgCdTe, it is necessary to exclude the conversion of the conductivity type during the deposition of the passivation coating [117]. The built-in charge in the dielectric coating can significantly affect the quality of the photodiodes. It has been shown that the surface potential affects both the differential resistance diode (R_d) and the noise spectrum [115]. The noise spectrum of an n-p diode is shown in Fig. 15.12. It is clear that the noise is decreased with an increase of frequencies and depends on the gate voltage that should be explained by the influence of the built-in charge at the interface (passivation coating (CdTe+ZnS)/HgCdTe). It should be noted that there is a difficulty in identifying the density of surface states at the passivation coating/semiconductor interface. The most common Terman method for calculating the density of surface states requires an ideal capacitance-voltage (C-V) characteristic. The difficulties in the calculations of an ideal C-V characteristic are associated with the nonparabolicity of the HgCdTe band structure and the effects of quantization of charge carriers. The most complete consideration of all HgCdTe features when calculating

the C-V characteristic was carried out in [118]. The authors used different approximations when calculating the ideal C-V characteristic. Therefore, it is impossible to statistically compare the density of surface states obtained in different studies.

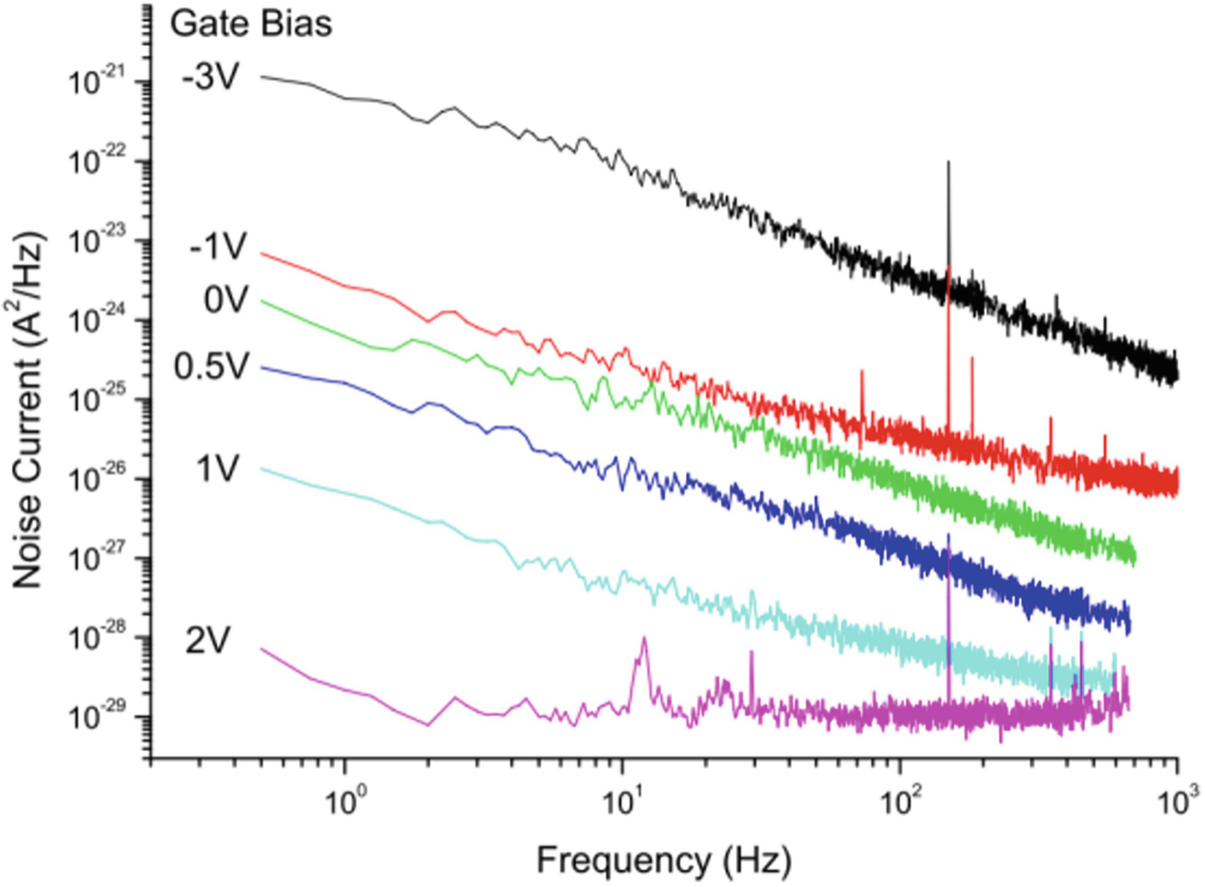

Fig. 15.12 The noise spectrum of a gated 300 μm in diameter photodiode at 77 K for various gate biases. (Reproduced with permission from Smith et. al., [110]. Copyright 2007 Springer)

The HgCdTe passivation technology can be conditionally divided into four types, taking into account the nature of coating layer, for example:

- Anodic and plasma oxides
- Sulfides
- Deposited layers with dielectric properties (SiOx, SiNx, Al_2O_3)
- Wide bandgap semiconductors (HgCdTe, CdTe, ZnS)

Anodic oxide (AO) effectively passivates the surface of n-HgCdTe and therefore can be used in the manufacture of IR photoconductive detectors. Wet anodizing is carried out at room temperature in a solution of 0.1 M KOH in 90% ethylene glycol/10% water at a current density of 0.1–

0.3 mA·cm^{-2} [119]. However, upon passivation of p-HgCdTe with anodic oxide, a large positive fixed charge is formed on the surface of the n-type inversion layer. The density of fixed anodic oxide/HgCdTe surface charge varies within (5–20) × 10^{11} cm^{-2}. The fast surface states are U-shaped and have a minimum located at the center of bandgap. Slow surface traps cause small hysteresis in the C-V characteristics. Therefore, the anodic oxide is not used as a passivation coating for the HgCdTe surface in the manufacture of IR photodetectors [117].

Plasma oxides also have passivating properties. They are grown on the HgCdTe surface using a commercial gas mixture of oxygen and trifluoroethane in a commercially available plasma stripper system (LFE Corporation, model PDS/PDE-301). Low-pressure cold oxygen plasma (0.2–0.4 Torr) is formed by RF power supply (10–50 W, 13.5 MHz). The HgCdTe sample has a positively biased voltage (20–100 V) relative to ground. The fixed surface charge (plasma oxide)/HgCdTe interface is 1 × 10^{11} cm^{-2} which is an order of magnitude lower than in the case of anodic oxide. The fast surface states are located at the center of bandgap with a minimum of 2 × 10^{11} cm^{-2}eV^{-1}. The absence of hysteresis in the C-V characteristics indicates the absence of slow traps. Plasma oxides have shown excellent thermal stability. The flat band structure and fixed surface charge density are constant up to 90–95 °C. Nemirovsky and Bakhir [119] believe that this effect is probably due to the presence of fluorine in the oxide.

Anodic sulfides are very stable compounds. However, in several cases, anodic sulfides dissolve preferably in polysulfide solutions with an appropriate pH. The technological process of obtaining CdS on the HgCdTe surface by the anodic method was shown in [120]. Anodic sulfide films were grown in an electrochemical cell with a carbon counter electrode without using aqueous basic sulfide solutions in ethylene glycol at current density of 60–140 μA·cm^{-2} and growth rate of ~10 A/min. The stable state of native sulfides on the $Hg_{0.78}Cd_{0.22}Te$ surface was shown at the thermal surface heating in vacuum up to 95 °C [121].

The excellent surface passivating properties of the silicon oxide could not be maintained during prolonged heating of the device in a vacuum [1]. In addition, there are problems with SiO_2 layer adhesion [121]. It is interesting to note that the best results are obtained with SiO_2 when several

layers of native or anodic oxide are present on the HgCdTe surface before the deposition of SiO_2. An extremely thin native oxide (5–10 nm) protects the crystal from damage and possibly improves the adhesion of the SiO_2 layer [122]. The passivation properties of $SiO_2/Hg_{0.7}Cd_{0.3}Te$ interface were studied in [123]. Interfacial trap density (D_{it}) was evaluated by measuring the difference between high- and low-frequency C-V curves [124]. The surface-state densities (4–5) × 10^{11} cm^{-2} eV^{-1} in the bandgap center and (2–4) × 10^{13} cm^{-2} eV^{-1} near the valence band were found. The density built-in charge was 10^{10} cm^{-2}.

The ZnS antireflection coating for HgCdTe photoconductors has been used with varying success and was not stable during vacuum baking [1, 125]. The properties of $ZnS/Hg_{0.8}Cd_{0.2}Te$ interface were investigated by measuring the C-V characteristics of MIS structures [126]. The density of surface states in the range (1–6) × 10^{11} cm^{-2} eV^{-1} was obtained by measuring the C-V characteristics at a frequency of 1 MHz in the parabolic band approximation using the formulas given in [127]. ZnS thin films were prepared by vacuum evaporation using conventional evaporation systems from a quartz boat slowly heated in a resistance furnace or with an electron gun.

The SiN_x layers were robust and chemically resistant with good passivation quality and thermal stability. In [128] the authors described the SiN_x layer deposition in ICPECVD system with SiH_4 + N_2 gas mixtures in the temperature range of 80–100 °C. The interface trap density (D_{it}) was determined by the C-V measurement at 1 kHz and 1 MHz using MIS structure on $Hg_{0.68}Cd_{0.32}Te$ [129]. The minimum density of fast traps D_{it} was 4 × 10^{10} cm^{-2} eV^{-1}.

The good passivation properties of the Al_2O_3 layer grown by the plasma-enhanced ALD (PEALD) method on the HgCdTe surface were demonstrated in [118, 130, 131]. The trimethylaluminum (TMA) was as a source of Al. Oxygen plasma plays the role of an oxidizing agent. The Al_2O_3 coating layers were deposited on side surfaces of mesa structures [132]. In addition, it was shown that the lifetime of minority carriers in HgCdTe increased after ALD deposition at room temperature [132]. It has been found that the optimal Al_2O_3 deposition is observed in the range 120–

160 °C [130]. Wide-gap II-VI compounds were also studied as a surface passivation coating for HgCdTe. CdTe is now considered the most advantageous material for this purpose due to its high resistivity and crystal lattice close to that of HgCdTe [133–135]. CdTe is chemically stable, more robust than HgCdTe, and transparent to IR radiation. As a result, CdTe has become the most important and widely used passivation coating in HgCdTe technology for the production of IR photoelectric detectors [136]. The deposition of a CdTe layer on the HgCdTe surface requires a low temperature to prevent mercury depletion. Kumar et al. [135] compared the passivating properties of CdTe and AO deposited on the n-n-$Hg_{0.786}Cd_{0.214}Te$ surface. A 100 nm in thickness CdTe layer was deposited using thermal evaporation. The n-HgCdTe surface passivated with CdTe had a surface recombination rate approximately five times lower than the AO-passivated surface. The activation energy of the surface trap for CdTe- and AO-passivated HgCdTe surface, estimated from the data analysis, was in the range of 6–8 meV. This trap level is associated with Hg vacancies at the HgCdTe surface. The fixed charge density for the CdTe/HgCdTe interface measured by the C-V method was (5–9) × 10^{10} cm^{-2}.

15.5 Electric Contact Technology

Metal contacts to semiconductors play a key role in the manufacture of the device, affecting its long-term performance and reliability. The basic characteristics of metallic contacts are contact resistance value, recombination at the interface with the contact, 1/f noise, and long-term and thermal stability [137, 138]. Ideal ohmic contacts are obtained when the work function of the metal is less than the electron affinity of the n-type semiconductor. However, the surface properties of II-VI semiconductors are often poorly understood. Therefore, in practice, ohmic contacts are usually made according to empirical recipes. In this regard, in order to reduce the influence of the surface on the contact resistance, a heavily doped region is often formed on the surface. In this case, the thickness of space charge region is greatly reduced, allowing the electrons to tunnel, resulting in a low resistance. As a rule, contacts consist of several layers of various metals, which are necessary to improve adhesion and reduce solid-state reactions.

In Ref. [139] it is performed a theoretical analysis of the position of the Fermi level at the metal/$Hg_{1-x}Cd_xTe$ interface. For extrapolation from CdTe to $Hg_{1-x}Cd_xTe$, three models of the pinning of the Fermi level at the metal-semiconductor interface were used [140]. Two models of Schottky barrier pinning were considered: Spicer defect model [141, 142] and the metal-induced gap-state model (MIGS) [143]), as well as the third model based on the effective work function [144]. The consideration of these models gives the same overall result showing the formation of ohmic contacts to n-type HgCdTe with a composition less than a certain value and nonohmic-rectifying contacts to all p-type HgCdTe. Results of these considerations are shown in Fig. 15.13. These results show that ohmic contacts are to be expected to n-type HgCdTe at $x < 0.4$, in contrast to p-type HgCdTe where a Schottky barrier should form regardless of composition.

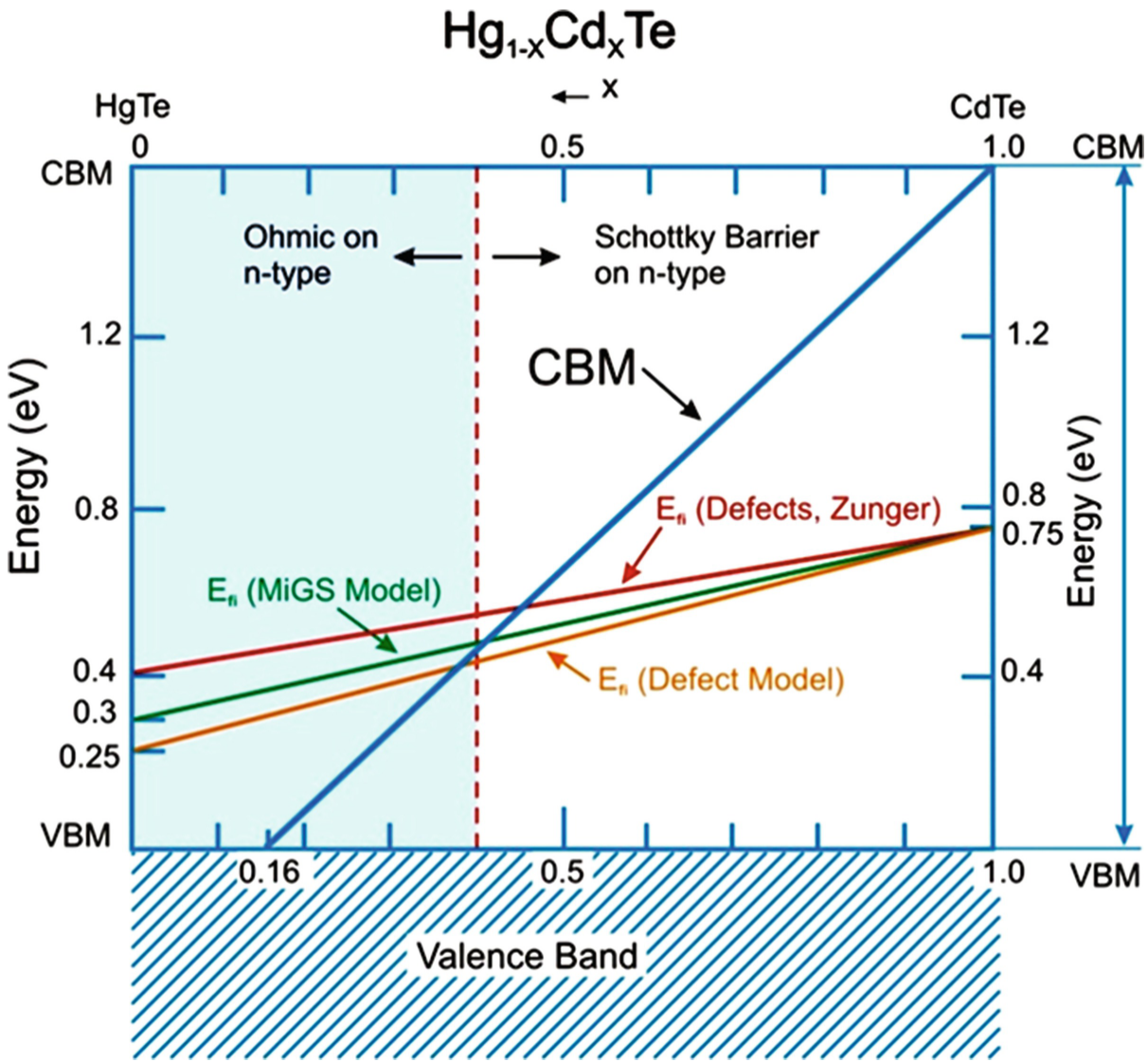

Fig. 15.13 The energy of Fermi-level position (E_{fi}) at the interface on HgCdTe composition. For this extrapolation, two models (MIGS and defects) were used. Near x = 0.4, E_{fi} moves into the conduction band, providing its own ohmic contacts on the n-type material. (Data extracted from Freeouf et al. [144])

The most commonly used metal for n-$Hg_{1-x}Cd_xTe$ is indium [145–147], which has a low work function. Leech and Reeves investigated In/n-HgCdTe contacts, which exhibited an ohmic nature in the composition range x = 0.30–0.68 [148]. The charge carrier transport in these contacts was attributed to the process of field effect thermal emission. This behavior was explained by the formation of the n^+-region under the contact upon rapid diffusion of In, which is a donor impurity in HgCdTe. The specific contact resistance ranged from 2.6×10^{-5} ohm cm^2 at x = 0.68 to 2.0×10^{-5} ohm cm^2 at x = 0.30, which correlates with the change in the resistivity of

the HgCdTe layer. In the general case, an ohmic contact with p-type HgCdTe is more difficult to implement, since a large work function of the contact metal is required. Au, Cr/Au, and Ti/Au were most commonly used for p-type HgCdTe. Beck et al. [149] showed that Au and Al contacts with p-type $Hg_{0.79}Cd_{0.21}Te$ are ohmic with specific contact resistance from 9×10^{-4} to 3×10^{-4} Ω cm^2 at room temperature. The dependences of the 1/f noise implied that the noise in the Au contact originated at the Au/HgCdTe interface or near it, while the noise in the Al contacts originated from the surface conduction layer near the contact.

The metal contacts of Pt, Cu, and Au with p-HgCdTe were studied in [150]. For this purpose, depth profiles were measured using SNMS, SIMS, AES, and XPS methods. I-V characteristics were measured and then compared with both the distribution profile of metal concentration throughout the thickness of interface and chemical state at the metal/HgCdTe interface. It was found that Pt does not form an ohmic contact with HgCdTe, while Cu forms unstable ohmic contacts. Au forms ohmic contacts by diffusion at elevated temperatures and exhibit long-term stability. Therefore, Au is currently the preferred metal for making ohmic contacts to p-HgCdTe. In [151], the authors proposed a method for manufacturing ohmic contacts to n- and p-type HgCdTe layers in a single technological cycle. The ohmic behavior of Cr, Mo, and Ti with HgCdTe ($x \approx 0.3$) does not depend on the metal used for both n- and p-type MCT layers and indicates that the Fermi level is pinned. The ohmic or close to ohmic behavior of Cr, Mo, and Ti contacts can be explained by the reactive nature of metals. The contact resistance R_c is significantly less than the resistance of the p-n junction HgCdTe ($x \approx 0.3$) R_0 at zero bias at 80 K ($R_cA < 10^{-2}$ ohm cm^2 and $R_0A > 10^3$ ohm cm^2, where A is p-n junction area). Thus, such contacts are suitable for manufacturing HgCdTe photovoltaic detectors. Cr, Mo, and Ti were chosen for the deposition at room temperature, since, as a rule, they provide a high adhesion to HgCdTe layers. Au and In were used as bonding spacers to which gold contact wires were attached by ultrasonic welding or micro-soldering. It was shown that under the used deposition conditions, gold has low adhesion to HgCdTe epitaxial layers. However, for light-doped p-type $Hg_{1-x}Cd_xTe$, there are no good contacts, and all metals tend to form Schottky barriers. This problem is especially difficult for HgCdTe with a high HgCdTe composition. This

problem can be solved by using a highly doped region near the metal contact to increase the tunneling current. However, in practice, it is difficult to achieve the required high p-type doping. One of the practical solutions is the use of HgCdTe growth with a narrowing bandgap at the metal/HgCdTe interface [152]. An analogous decision was used for manufacturing the ohmic contact to CdTe and for the $Cd_{0,7}Hg_{0,3}Te$ p-type conductivity [153]. It was proposed to use HgTe, the work function of the metal contact which corresponds to p-CdTe. The HgTe contacts were deposited by the vapor-phase epitaxy on a CdTe surface etched in Br_2/methanol (CH_30H). The interdiffusion zone formed a graded junction between the bandgaps of HgTe and CdTe without rectifying. This allows suppression of barrier at interface. The CdTe/HgTe/Au energy band diagram is shown in Fig. 15.14.

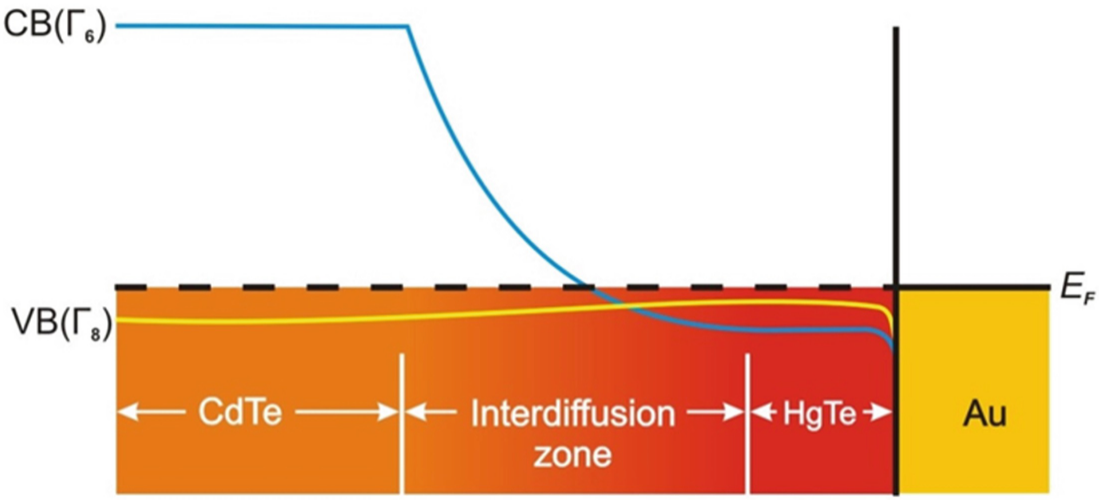

Fig. 15.14 The equilibrium energy band diagram at room temperature in CdTe/HgTe/Au: *CB* conduction band, *VB* valence band. (Data extracted from Janik et al. [153])

The measured specific contact resistances are ten times lower than the best results obtained so far.

15.6 p-n Junction Technology

The p-n junction in HgCdTe is formed by numerous methods, including in and out diffusion of Hg and impurity diffusion, ion implantation, electron bombardment-induced conduction, plasma-induced-type transformation, and doping during growth from the vapor or liquid phase [5, 117, 154–156]. A brief description of the main methods of p-n junction formation in HgCdTe layers is presented in [138]. Low binding energies of ionic bonds

in HgCdTe influenced the technological processes of the formation of p-n-junctions. Free Hg atoms were formed in the processes of ion implantation and ion beam etching. This creates much deeper transitions than it would be expected only from ion implantation. The dislocations play a certain role in the elimination of Hg vacancies. The role of Hg, impurities, dislocations, and ion implantation in the formation of p-n junction is very complex and insufficiently studied. Nevertheless, producers have obtained a good phenomenological control of the transition depths and dopant profile through various p-n junction formation processes. Recently, the epitaxial methods with doping in the growth process have been used to obtain p-n junctions. MBE and MOCVD were successfully implemented by doping with In and As during growth, as shown earlier (see Sect. 15.2.2).

15.6.1 Mercury Diffusion

It is relatively easy to achieve the conversion of p-HgCdTe to the n-type due to vacancy annihilation during free diffusion of Hg atoms. The n-type conductivity layer is determined by the background donor impurity. Dutton et al. [157] summarized the knowledge about the mercury diffusion process. The mercury diffusion accompanied with the vacancy diffusion created the p-n junction at 200–250 °C in p-HgCdTe ($p \sim 10^{16}$ cm^{-3}) in 10–15 min. This corresponds to a diffusion coefficient ~10^{-10} cm^2s^{-1}. The presence of dislocations can increase the mobility of vacancies. The presence of Te precipitates can decrease the Hg motion in the lattice. Jenner and Blackman reported about the free Hg diffusion from the AO [158]. Anodic oxidation results in the formation of a mercury-rich layer at the interface. Hg diffuses into the substrate during the thermal annealing resulting in the formation of an n-type HgCdTe. In addition, the anodic oxide layer acts as a diffusion mask to prevent the loss of mercury in vacuum upon contact with the surrounding atmosphere. This method is especially suitable for high-speed devices where the low and uniform doping of n-type regions is required.

15.6.2 Ion Etching

The low-energy ion bombardment is used to fabricate p-n junctions by conversion of the vacancies doped with p-HgCdTe into n-type [159, 160]. The ion beam introduces a small fraction of free Hg atoms (approximately 0.02% of ion gas atoms) into the lattice. Then Hg atoms fill Hg vacancies, creating weakly doped n-type background atoms, limited by donor atoms.

The ion energy and dose are usually less than 1 keV and range from 10^{16} to 10^{19} cm^{-2}, respectively. Blackman showed that the p-n junction depth depends on the ion dose and can extend for several hundred microns from the surface [159]. The Hg diffusion during ion etching is very fast, even in comparison with experiments on thermal annealing of HgCdTe at 500 °C. The deeper p-n junctions are created by using higher ion beam current, longer etching time, lower beam voltage, and higher ion mass. The whole process is carried out at low temperatures that do not change the initial HgCdTe electrophysical properties and the quality of passivation. The p-type material conversion using an ion beam have been commercially used by GEC-Marconi Infrared Ltd. for FPAs based on HgCdTe since the late 1970s [161].

15.6.3 Reactive Ion Etching

Reactive ion etching is a method of reactive chemical plasma etching of a substrate surface, often used in microelectronics to remove material from a surface. Plasma is created at low discharge gas pressure. Ions are accelerated by the applied voltage between the plasma and the substrate. The combined physical processes involve ion sputtering and chemical reactions on the surface, resulting in the formation of volatiles and their desorption. This plasma-induced method is also used as a technology for the formation of p-n junctions [99, 162]. It is important to note that if postimplantation thermal annealing is required when using ion implantation to create p-n junctions in the process of manufacturing high-quality photodiodes, then when reactive ion etching is used for these purposes, such annealing is not required. The conductivity conversion of p-HgCdTe in reactive ion etching technology occurs due to the formation of a source of free Hg atoms. Hg atoms quickly diffuse into the bulk of HgCdTe, decreasing the concentration of Hg vacancies occupying their crystal lattice points. Residual donor impurities become dominant in conductivity and participate in the formation of p-n junctions.

15.6.4 Ion Implantation

The ion implantation in HgCdTe is a widely and well-proven technology applied to fabricate photovoltaic HgCdTe FPAs [163–167]. N^{+}-p junctions are formed by the implantation of Al, Be, In, and B ions into the vacancy-doped p-type HgCdTe material. Usually, the ion implantation technology

uses light ions, such as B or Be, to form the n-region. The ion flux with doses 10^{12}–10^{15} cm^{-2} and an energy range of 30–200 keV are usually used. Regardless of the nature of the ion atoms used, the n-type layer is associated with a material damage, as Voith first noted [168]. In the case of the ion implantation in p-type or n-type HgCdTe, the junction has N^+-p or N^+-n-p types. The N^+-n-p junction is the most desirable case because it is located far from the region of radiation defects. It is not necessary to use postimplantation thermal annealing to achieve high performance of SWIR and MWIR devices, especially at lower ion doses during implantation. However, many researchers have now concluded that the photodiode characteristics can be improved by the thermal annealing after ion implantation to eliminate radiation damages [169]. The annealing temperature depends on the nature of the ions and the conditions of the implantation process. At low radiation fluxes, the dark current noise can lead to a deterioration in the parameters of the diode. In this case, deliberate doping of the p-type absorber layer can be used to make n-p diodes. This makes it possible to increase the parameter R_0A by almost an order of magnitude for long-wavelength IR FPAs with a cutoff wavelength up to 20 μm [170].

The main trend and the most promising direction in the development of research and technology is the creation of photovoltaic IR FPAs based on the P^+-n junction [171, 172]. The motivation for the study is associated with the expansion of the spectral range of sensitivity in the long-wavelength region of 8–14 microns and/or operating at elevated temperatures. Au, Ag, Cu, and P ions were used as implants to convert n-type HgCdTe with a subsequent thermal annealing. As a rule, p-n junctions are located in a depth of 1–3 μm from the HgCdTe surface, which is significantly larger than the area of implanted ions less than 30 nm [173]. Based on long-term studies of the technology of ion implantation with various chemical elements, As was chosen as the only impurity, which showed the high-quality p-on-n-type IR FPA detectors and determined the main development for industrial production. To create the P^+-n junction, In and As are used as base donor and acceptor impurities, respectively. The main problem is associated with the need to carry out the As activation using thermal annealing at high temperatures (more than 300 °C), which creates great problems for further technological processes. However, the design of the P+-n-type photodiode

can significantly reduce the dark current and the resistance spreading over the base layer due to long-living minority carriers (holes) and highly mobile majority carriers (electrons), respectively. Nowadays, many companies conduct intensive research and development of IR FPAs based on the P+-n junction technology using HgCdTe HES grown by LPE, MOCVD, and promising MBE [174–177].

15.6.5 p-on-n Versus n-on-p HgCdTe Diodes

Among the technologies for the formation of p-n junctions, the most widely used methods are the ion implantation and doping during growth [178]. The doping-during-growth method is mainly used to create multispectral IR FPAs, using mesa etching technology. Ion implantation methods are used to create both single-color and multicolor IR FPAs, created by planar and mesa topologies, respectively [179]. A photograph of a pseudoplanar topology of 256 × 256 dual-band IR FPAs fabricated using ion implantation technology to form n-p junctions in the wide-gap (MWIR) and narrow-gap (LWIR) HgCdTe layers is shown in Fig. 15.15 [179].

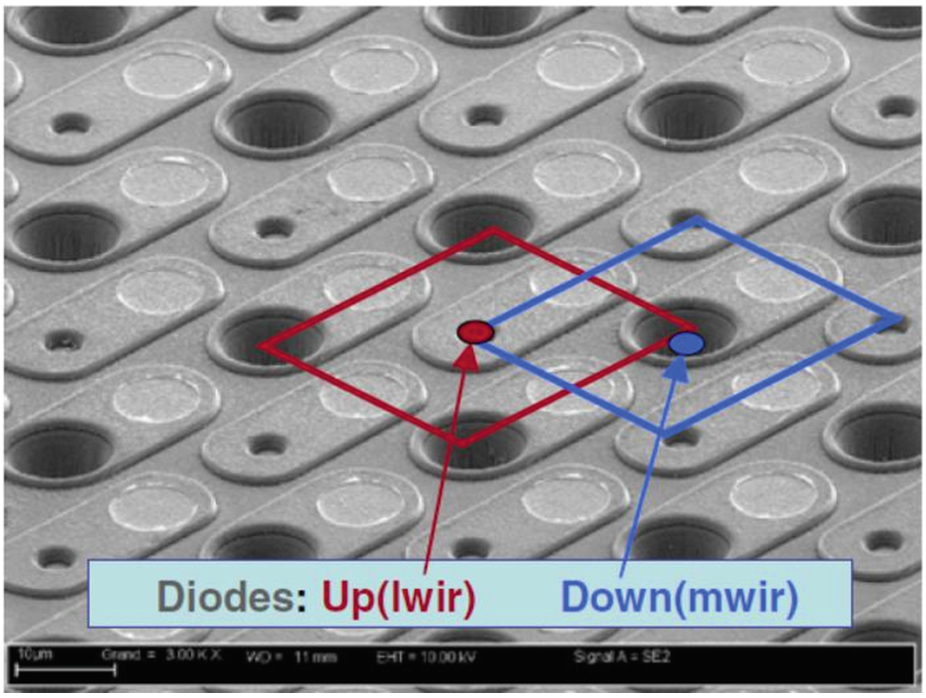

Fig. 15.15 The top and cross-section view of scheme (up) and photo (down) two-color 256 × 256 MWIR and LWIR IR FPA. (Reproduced with permission from Destefanis et al. [179]. Copyright 2007 Springer)

Dark current is the fundamental parameter of a photon photodiode and is determined by the thermal charge carrier generation [180]. The generated thermal dark current is calculated on the basis of the following expression $G_{th} = n_{maj}/2\alpha\tau_{Ai}$, where G_{th} is thermal generation rate, n_{maj} is concentration of the majority carriers, α is absorption coefficient, and τ_{Ai} is Auger lifetime of minority carriers. In n-HgCdTe layers, the minority carrier lifetime is determined by the Auger 1 process, including two electrons and a heavy hole. Thermally generated normalized dark current density for MWIR and LWIR, based on n-HgCdTe for two cutoff wavelengths of 5 μm and 10 μm, and the background flux for F/2 optics are shown in Fig. 15.16. The electron concentration and the layer thickness were 10^{15} cm^{-3} and 10 μm (~1/α), respectively. It is clear that BLIP regime can be reached at temperatures <120 K for LWIR and at <180 K for MWIR. The similar representation of thermal dark current should be used for a p-type material, taking into account the Auger 7 recombination mechanism, including two heavy holes and one electron, as shown in [181]. The minority lifetime τ_{Ai7} in p-HgCdTe is longer than in n-HgCdTe (τ_{Ai7} = (6–20) τ_{Ai1}). It means that the thermally generated dark current in the p-HgCdTe layers will be 6–20 times less than in the n-HgCdTe layer. The calculations of dark current, limited by Auger and S-R carrier recombination for the HgCdTe HOT IR detector (P+-ν-N+ architecture), made by Kinch [180] for the p-HgCdTe layer with a low acceptor concentration in Na = 5×10^{14} cm^{-3}, are shown in Fig. 15.17.

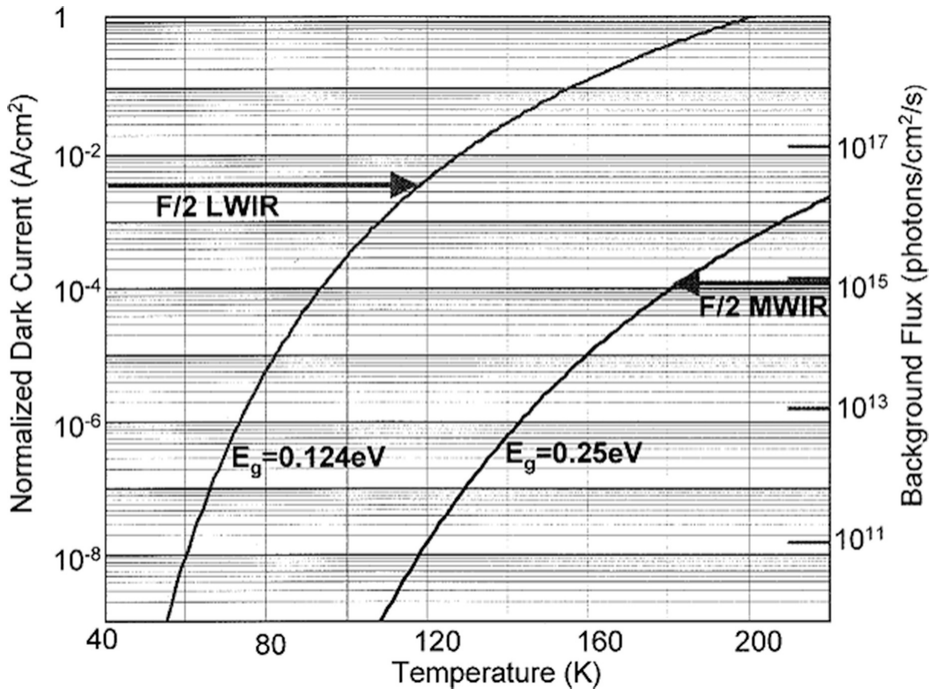

Fig. 15.16 The normalized dark current density vs. temperature for MWIR and LWIR based on n-HgCdTe. (Reproduced with permission from Kinch [180]. Copyright 2000 Springer)

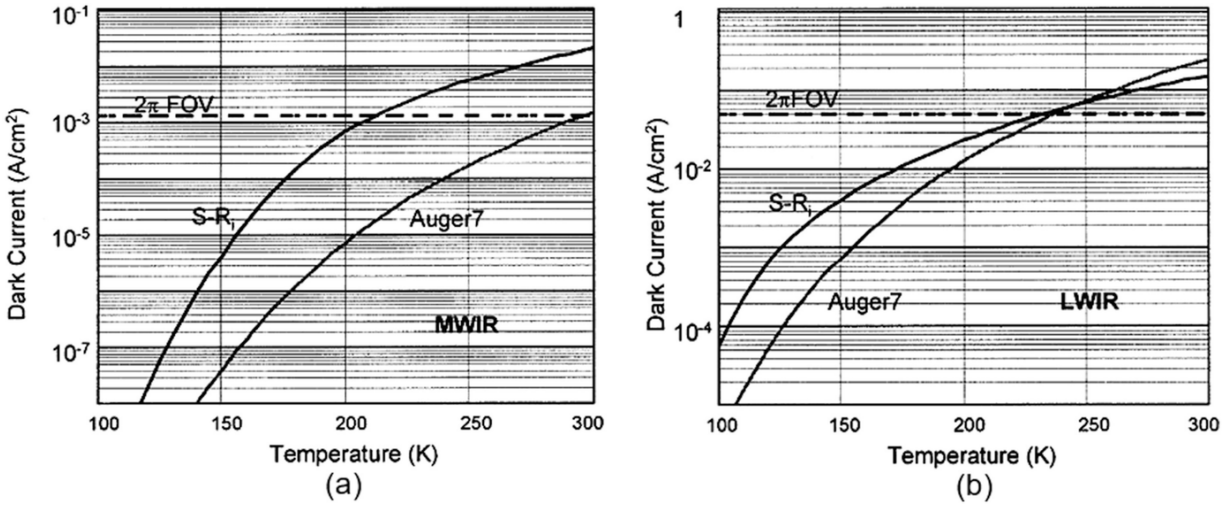

Fig. 15.17 Shockley-Read (S-R) and Auger 7 dark current vs. temperature for P^{+}-π-N^{+} HOT MWIR (**a**) and LWIR (**b**) detector with Na = 5×10^{14} cm^{-3}. (Reproduced with permission from Kinch [180]. Copyright 2000 Springer)

It is clear that in the case of Auger carrier recombination, it is possible to achieve operation with the background-limited performance (BLIP) for MWIR detectors at room temperature. In the case of LWIR detectors, BLIP operation is possible at temperature up to 220–230 K.

Usually, for n-on-p-type HgCdTe detectors, p-type absorber layer is doped with Hg vacancies with a concentration of ~10^{16} cm^{-3}. In this case, the dark current of IR detectors (intrinsic) is being determined by S-R center parameters. The essential improvement of the photovoltaic characteristics of IR detectors is achieved by doping the absorber layer with intentional acceptor impurities.

Doping of the HgCdTe absorber layer with Au to a hole concentration of $<5 \times 10^{15}$ cm^{-3} was made in AIM (https://www.aim-ir.com/de/home.html) [182, 183]. A comparison of the characteristics of p-on-n and n-on-p LWIR and VLWIR detectors, manufactured by AIM technology, is presented in [184]. P-n junctions were formed by ion implantation of As and B into n-type and p-type absorbing layers doped with In and Au, respectively. The HgCdTe absorber layers were grown by LPE on CdZnTe substrates. The temperature dependences of the dark current density for LWIR and VLWIR FPAs and photodiodes for the n-on-p technology with cutoff wavelengths 11.4 μm, 11.5 μm, and 12.2 μm, measured at 80 K, are shown in Fig. 15.18. For comparison, the dependences according to Tennant's Rule 07 for p-on-n diodes and for AIM n-on-p diodes on HgCdTe layers doped with external impurities according to the standard LWIR technology are also shown in this figure. It is clear that the fabrication of an IR FPA with an n-on-p junction based on p-HgCdTe doped with intentional impurity (Au in AIM) shows results comparable to those obtained for the p-on-n junction, providing the operation of IR FPA in the background-limited (BLIP) mode at elevated temperatures. This opens up a new trend in the development of SWaP (size, weight, and power) technology of IR detector.

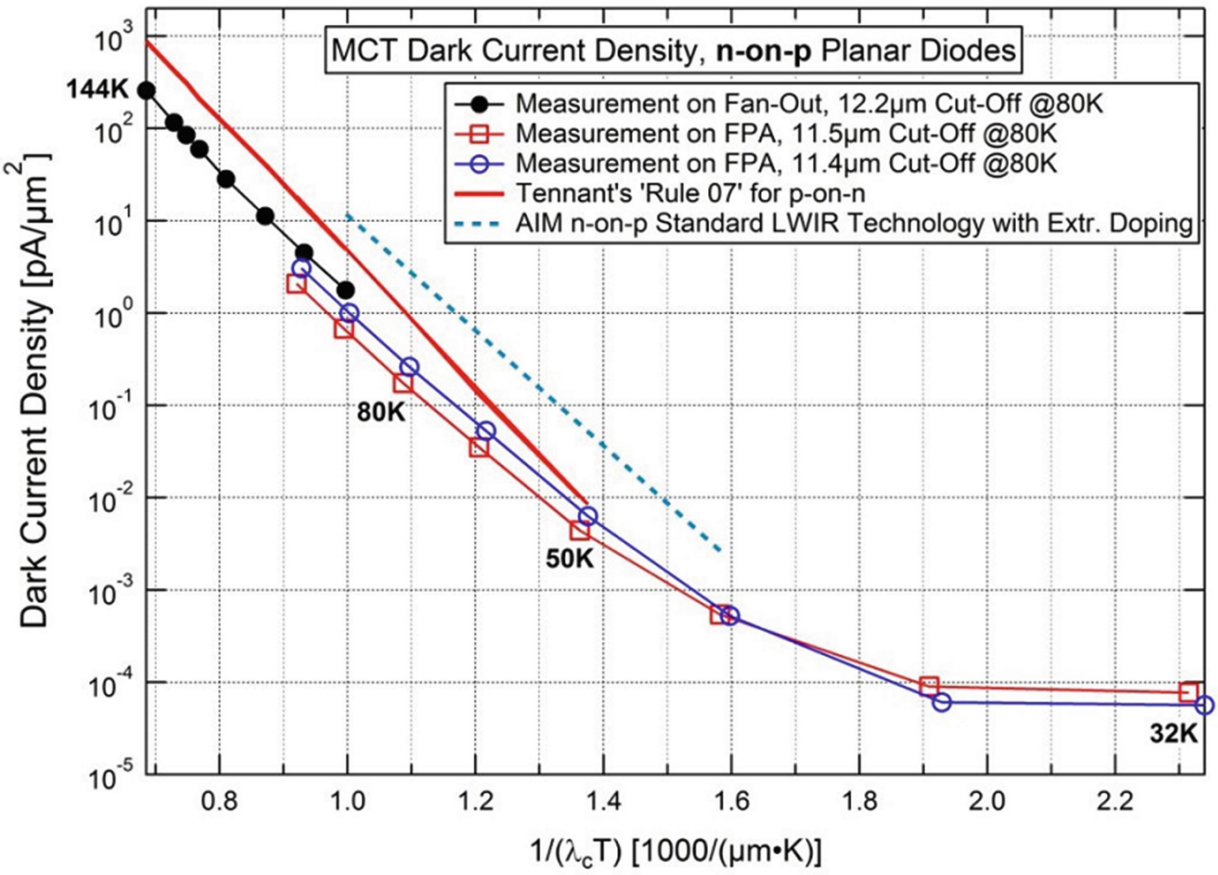
MCT Dark Current Density, n-on-p Planar Diodes
Measurement on Fan-Out, 12.2μm Cut-Off @80K
Measurement on FPA, 11.5μm Cut-Off @80K
Measurement on FPA, 11.4μm Cut-Off @80K
Tennant's 'Rule 07' for p-on-n
AIM n-on-p Standard LWIR Technology with Extr. Doping
144K
80K
50K
32K
Dark Current Density [pA/μm²]
1/(λcT) [1000/(μm•K)]

Fig. 15.18 Thermal dark current density versus detector operating temperature for p-on-n (a) and n-on-p LWIR and VLWIR HgCdTe detectors with cutoff wavelengths at 80 K (see in insert). (Reproduced with permission from Hanna et al. [184]. Copyright 2016 Springer)

15.7 Conclusion

Since the 1960s, HgCdTe device technology has been developed in many countries. Most of the research has focused on infrared detectors and focal plane arrays, mainly operating in photoconduction or photovoltaic modes. Due to its unique physical properties, the solid solution compounds of HgCdTe alloys have taken a leading position among light-sensitive IR materials and made it possible to fabricate IR FPAs that are sensitive in a wide spectral range and, first of all, in “atmospheric windows.” The technologies of HgCdTe materials, starting from a bulk crystal, have gone through the development of epitaxial growth by various methods. The simplest LPE technique ensured the development of technology on CdZnTe substrates and reached the modern level as an industrial technology for obtaining very high-quality HgCdTe epilayers. The existing limitations in

the properties of CdZnTe substrates, difficulties of their preparing, and, finally, their high cost lead to the development of vapor-phase epitaxy on a large-diameter GaAs and Si substrate by MOCVD and MBE technologies. Now MOCVD technology provides high-quality HgCdTe on GaAs substrate. MBE is a very flexible technology which allows growing both HgCdTe hetero- and nanostructures with a high-accuracy control of the composition and thickness of the layer at the nanometer level. Currently, MBE HgCdTe technology on large substrates provides a high-quality, inexpensive photosensitive material for large-format IR FPAs. It is shown that MBE HgCdTe/Si HES provides the possibility of industrial production of IR detectors for SWIR and MWIR spectral ranges. The study of etching mesotechnology showed that dry etching has practically no effect on the size of pixels when they are separated even at great depths, which is required in the manufacture of large-format IR MFPs. Passivation technology is necessary to protect the pixel surface and prevent the appearance of leakage current. The best passivation materials are CdTe and/or dielectric layers. The conducted study of electrical contacts identified metals such as In and Au, which provide ohmic contacts with the n-type and p-type HgCdTe material. The considered versions of p-n junction technologies show that the p-on-n type formed by the implantation of As ions into an n-HgCdTe absorber or growing DLHJ gives a significant decrease in the dark current. The developed n-on-p type based on intentional doping of the p-HgCdTe absorber with acceptor impurities has parameters similar to the p-on-n type. These two types provide the ability to operate IR detectors at elevated temperatures, which allows the development of SWaP technologies.

References

1. Norton P (2002) HgCdTe infrared detectors. Opto-Electron Rev 10(3):159–174
2. Rogalski A, Antoszewski J, Faraone L (2009) Third-generation infrared photodetector arrays. J Appl Phys 105:091101. https://doi.org/10.1063/1.3099572 [Crossref]
3. Lawson WD, Nielsen S, Putley EH, Young AS (1959) Preparation and properties of HgTe and mixed crystals of HgTe-CdTe. J Phys Chem Solids 9:325–329 [Crossref]

4. Shneider AD, Gavrishchak IV (1960) The structure and properties HgTe-CdTe. Phisica Tverdogo Tela 2:2079–2081. (in Russian)
5. Capper P, Garland J (eds) (2011) Mercury cadmium telluride. Growth, properties and applications. Wiley, Chichester, p 556
6. Capper P (ed) (1994) Properties of narrow gap cadmium-based compounds. IEE, INSPEC, London, p 620
7. Capper P (1994) The role of accelerated crucible rotation on the growth of HgCdTe and CdTe/CdZnTe. Prog Cryst Growth Charact 28(1–2):1–55. https://doi.org/10.1016/0960-6974(94)90012-4 [Crossref]
8. Capper P (2017) A UK retrospective- reminiscence of crystal grower. J Electron Mater 46(9):5430–5441. https://doi.org/10.1007/s11664-0175563-0 [Crossref]
9. Tregilgas JH (1994) Development of recrystallized bulk HgCdTe. Prog Cryst Growth Charact 28(1–2):57–83. https://doi.org/10.1016/0960-6974(94)90013-2 [Crossref]
10. Triboulet R (1994) The Traveling Heater Method (THM) for HgCdTe and related materials. Prog Cryst Growth Charact 28(1–2):85–144. https://doi.org/10.1016/0960-6974(94)90014-0 [Crossref]
11. Ponomarenko VP (2003) Cadmium mercury telluride and the new generation of photoelectronic devices. Physics-Uspekhi 46(6):629–635. https://doi.org/10.1070/PU2003v046n06ABEH001372 [Crossref]
12. Bogoboyashchiy VV, Kurbanov KR, Oksanich AP (2000) Industrial production of GaAs and $Hg_{1-x}Cd_xTe$ based crystals and epitaxial structures in Ukraine: actuality and development outlook. Funct Mater 7(3):546–551
13. Castro CA, Tregilgas JN (1988) Recent developments in HgCdTe and HgZnTe growth from Te solution. J Cryst Growth 86:138–145. https://doi.org/10.1016/0022-0248(90)90711-S [Crossref]
14. Astles M, Blackmore G, Steward V, Rodway DC, Kirton P (1987) The use of in-situ wash melts in the LPE growth of (CdHg)Te. J Cryst Growth 80:1–8. https://doi.org/10.1016/0022-0248(87)90516-1 [Crossref]
15. Radhakrishnan LK, Sitharaman S, Gupta SC (2003) Liquid phase epitaxial growth of HgCdTe using a modified horizontal slider. J Cryst Growth 252(1–30):79–86. https://doi.org/10.1016/S0022-0248(02)02530-7 [Crossref]
16. Parker SG, Weirauch DF, Chandra D (1988) Terracing in HgCdTe LPE films grown from Te solution. J Cryst Growth 86(1–4):173–182. https://doi.org/10.1016/0022-0248(90)90714-V

[Crossref]
17. Edwall DD, Gertner ER, Tennant WE (1984) Liquid phase epitaxial growth of large area $Hg_{1-x}Cd_xTe$ epitaxial layers. J Appl Phys 55(6):1453–1460. https://doi.org/10.1063/1.333400 [Crossref]
18. Gupta SC, Sitharaman S, Nagpal A, Gautam M, Berlouis LEA (1996) Growth and characterization $Hg_{1-x}Cd_xTe$ ($0.21<x<0.36$) epilayers grown from Te – rich solution by the dipping technique. J Cryst Growth 165(1–2):19–24. https://doi.org/10.1016/0022-0248(95)00993-0 [Crossref]
19. Bowers JE, Schmit JL (1982) Mercury containment for liquid phase growth of mercury cadmium telluride from tellurium-rich solution. US Patent 4,317,689, 2 March 1982
20. Hager RJ (1987) Wipe-off apparatus of liquid phase epitaxy of mercury cadmium telluride. US Patent. 4,706,604, 17 Nov., 1987
21. Biao L, Chen XQ, Chu JH, Cao JY, Zhu JQ, Tang DY (1996) Growth and characterization of liquid – phase epitaxial $Hg_{1-x}Cd_xTe$ films. Thin Solid Films 278:1–5. https://doi.org/10.1016/0040-6090(95)08122-4 [Crossref]
22. Tung T (1988) Infinite – melt vertical liquid – phase epitaxy of HgCdTe from Hg solution: status and prospects. J Cryst Growth 86(1–4):161–172. https://doi.org/10.1016/0022-0248(90)90713-U [Crossref]
23. Colombo L, Westphal GH, Liao PK, Chen VC, Schaake HF (1992) Producibility of (Hg,Cd)Te by dipping liquid phase epitaxy. Proc SPIE 1683:33–39. https://doi.org/10.1117/12.137777 [Crossref]
24. Kalisher MH (1984) The behavior of doped $Hg_{1-x}Cd_xTe$ epitaxial layers grown from Hg-rich melts. J Cryst Growth 70(1–2):365–372. https://doi.org/10.1016/0022-0248(84)90288-4 [Crossref]
25. Tung T, DeArmoud LV, Herald RF, Herning PE, Kalisher MH, Olson DA et al (1992) State of the art of Hg – melt LPE HgCdTe at Santa Barbara research center. Proc SPIE 1735:109–134. https://doi.org/10.1117/12.138616 [Crossref]
26. Sangha SPS, Medland JD, Berry JA, Rinn LM (1987) Low temperature epitaxial growth of cadmium telluride from mercury solvent. J Cryst Growth 83(1):127–136. https://doi.org/10.1016/0022-0248(87)90513-6 [Crossref]
27. Yoshikawa M, Ueda S, Takigawa H (1985) High – purity HgCdTe with low dislocation density, grown by LPE. Fujitsu Sci Tech J 25(5):494–503
28. Janik E, Ferah M, Legros R, Triboulet R, Brossat T, Riant Y (1985) LPE growth and characterization of 1.3 μm (Hg,Cd)Te layers. J Cryst Growth 72(1–2):133–138. https://doi.org/

10.1016/0022-0248(85)90131-9
[Crossref]

29. Sydorchuk P, Khlyap G, Andrukhiv A (2001) Growth and some properties of heterostructures based on new narrow-gap semiconductor ZnCdHgTe. Cryst Res Technol 36(4–5):361–369. https://doi.org/10.1002/1521-4079(200106)36:4/53.0.CO;2-5
[Crossref]

30. Ruda H, Jedral L, Lagowski J, Gatos HC (1984) Mercury – pressure – induced epitaxy of HgCdTe. J Electrochem Soc 131(5):1159–1163. https://doi.org/10.1149/1.2115770
[Crossref]

31. Belogorokhov AI, Denisov IA, Smirnova NA, Belogorokhova LI (2004) The investigation of structural perfection of CdHgTe/CdZnTe epitaxial layers by Raman scattering method. Semiconductors 38(1):82–90. https://doi.org/10.1134/1.1641138
[Crossref]

32. Li B, Chu JH, Zhu JQ, Chen XQ, Cao JY, Tang DY (1996) Growth of $Hg_{1-x}Cd_xTe$ liquid phase epitaxial films on vicinal planes. J Cryst Growth 169:480–484. https://doi.org/10.1016/0022-0248(96)00418-6
[Crossref]

33. Takigawa H, Yoshikawa M, Maekawa T (1988) Dislocation in HgCdTe – CdTe and HgCdTe – CdZnTe heterojunction. J Cryst Growth 86(1–4):446–451. https://doi.org/10.1016/0022-0248(90)90757-C
[Crossref]

34. Yoshikawa M, Maruyama K, Saito T, Maekawa T, Takigawa H (1987) Dislocation in HgCdTe/CdTe and HgCdTe/CdZnTe heterojunctions. J Vac Sci Technol A 5(5):3052–3054. https://doi.org/10.1116/1.574214
[Crossref]

35. Vydyanath HR (1996) Incorporation of dopants and native defects in bulk $Hg_{1-x}Cd_xTe$ crystals and epitaxial layers. J Cryst Growth 161(1–4):64–72. https://doi.org/10.1016/0022-0248(95)00613-3
[Crossref]

36. Vydyanath HR (1981) Lattice defects in semiconducting $Hg_{1-x}Cd_xTe$ alloys. I. Defect structure of undoped and copper doped $Hg_{0.8}Cd_{0.2}Te$. J Electrochem Soc 128(12):2609–2619. https://doi.org/10.1149/1.2127314
[Crossref]

37. Vydyanath HR (1981) Lattice defects in semiconducting $Hg_{1-x}Cd_xTe$ alloys. II. Defect structure of indium – doped $Hg_{0.8}Cd_{0.2}Te$. J Electrochem Soc 128(12):2619–2625. https://doi.org/10.1149/1.2127315

38. Vydyanath HR, Donovan JC and Nelson DA (1981) Lattice defects in semiconducting $Hg_{1-x}Cd_xTe$ alloys. III. Defect structure of undoped $Hg_{0.6}Cd_{0.4}Te$. J Electrochem Soc 128(12):2625–2629. https://doi.org/10.1149/1.2127316

39. Chandra D, Schaake HF, Tregilgas JH, Aqariden F, Kinch MA, Syllaios AJ (2000) Vacancies in $Hg_{1-x}Cd_xTe$. J Electron Mater 29(6):729–731. https://doi.org/10.1007/s11664-000-0215-0 [Crossref]
40. Mynbaev KD, Ivanov-Omskii VI (2006) Doping of epitaxial and heterostructures based on HgCdTe. Semiconductors 40(1):1–21. https://doi.org/10.1134/S1063782606010015 [Crossref]
41. Irvine SJC, Mullin JB (1981) The growth by MOVPE and characterization of CdxHg1−xTe. J Cryst Growth 55(1):107–115. https://doi.org/10.1016/0022-0248(81)90277-3 [Crossref]
42. Tunnicliffe J, Irvine SJC, Dosser OD, Mullin JB (1984) A new MOVPE technique for growth of highly uniform CMT. J Cryst Growth 68(1):245–253. https://doi.org/10.1016/0022-0248(84)90423-8 [Crossref]
43. Piotrowski A, Klos K (2007) Metal-Organic vapor deposition of Hg1-xCdxTe fully doped heterostructures without postgrowth anneal for uncooled MWIR and LWIR detectors. J Electron Mater 36(8):1052–1058. https://doi.org/10.1007/s11664-007-0171-z [Crossref]
44. Madejczyk P, Piotrowski A, Kłos K, Gawron W, Rogalski A, Rutkowski J, Mroz W (2009) Surface smoothness improvement of HgCdTe layers grown by MOCVD. Bull Pol Acad Sci Tech Sci 57(2):139–146. https://doi.org/10.2478/V10175-010-0114-3 [Crossref]
45. Nishino H, Murakami S, Saito T, Nishijima Y, Takigawa H (1995) Dislocation profiles in MCT (100) on GaAs (100) grown by metalorganic chemical vapor deposition. J Electron Mater 24(5):533–537. https://doi.org/10.1007/BF02657959 [Crossref]
46. Maxey CD, Fitzmaurice JC, Lau HW, Hipwood LG, Shaw CS, Jones CL, Capper P (2006) Current status of large-area MOVPE growth of MCT device heterostructures for infrared focal plane arrays. J Electron Mater 35(6):1275–1282. https://doi.org/10.1007/s11664-006-0254-2 [Crossref]
47. Chilyasov AV, Moiseev AN, Evstigneev VS, Stepanov BS, Drozdov MN (2016) Growth of Arsenic-doped cadmium telluride epilayers by metalorganic chemical vapor deposition. Inorg Mater 52(12):1210–1214. https://doi.org/10.1134/S0020168516120037 [Crossref]
48. Hoke WE, Lemonias PJ (1985) Metalorganic growth of CdTe and HgCdTe epitaxial films at a reduced substrate temperature using diisopropyl telluride. Appl Phys Let 46(4):398–400. https://doi.org/10.1063/1.95591 [Crossref]
49. Hoke WE, Lemonias PJ (1986) Low-temperature metalorganic growth of CdTe and HgTe films. Appl Phys Let 48(24):1669–1671. https://doi.org/10.1063/1.96850 [Crossref]

50. Ghandhi SK, Bhat IB, Ehsani H, Nucciarone D, Miller G (1989) Low temperature growth of HgTe and HgCdTe using methylallyltelluride. Appl Phys Let 55(2):137–139. https://doi.org/10.1063/1.102124
[Crossref]
51. Morris BJ (1986) Photochemical organometallic vapor phase epitaxy of mercury cadmium telluride. Appl Phys Let 48(13):867–869. https://doi.org/10.1063/1.96694
[Crossref]
52. Irvine SJC, Bajaj J (1993) In situ characterization techniques for monitoring and control of VPE growth of $Hg_{1-x}Cd_xTe$. Semicond Sci Technol 8(6S):860–871. https://doi.org/10.1088/0268-1242/8/6S/007
[Crossref]
53. Irvine S, Capper P (eds) (2020) Metalorganic Vapor Phase Epitaxy (MOVPE): growth, materials properties and applications. Wiley, Chichester, p 558
54. Korenstein R, Hallock P, MacLeod B, Hoke W, Oguz S (1990) The influence of crystallographic orientation on gallium incorporation in HgCdTe grown by metalorganic chemical vapor deposition on GaAs. J Vac Sci Technol A 8(2):1039–1044. https://doi.org/10.1116/1.576958
[Crossref]
55. Capper PAC, Whiffin BC, Easton CD, Maxey IK (1988) Group V acceptor doping of $Cd_xHg_{1-x}Te$ layers grown by metalorganic vapour phase epitaxy. Mater Let 6(10):365–368. https://doi.org/10.1016/0167-577X(88)90125-5
[Crossref]
56. Easton BC, Maxey CD, Whiffin PAC, Roberts JA, Gale IG, Grainger F, Capper P (1991) Impurities and metal organic chemical-vapor deposition growth of mercury cadmium telluride. J Vac Sci Technol B 9(3):1682–1686. https://doi.org/10.1116/1/585399
[Crossref]
57. Maxey CD, Whiffin PAC, Easton BC (1991) MOVPE growth and characterization of doped $Cd_xHg_{1-x}Te$ structures. Semicond Sci Technol 6(12C):C26–C30. https://doi.org/10.1088/0268-1242/6/12C/006
[Crossref]
58. Madejczyk P, Piotrowski A, Kłos K, Gawron W, Rutkowski J, Rogalski A (2010) Control of acceptor doping in MOCVD HgCdTe epilayers. Opto-Electron Rev 18(3):271–275. https://doi.org/10.2478/s11772-010-1023-x
[Crossref]
59. Capper P, Maxey CD, Whiffin PAC, Easton BC (1989) Incorporation and activation of group V elements in MOVPE-grown $Cd_xHg_{1-x}Te$. J Cryst Growth 97(3–4):833–844. https://doi.org/10.1016/0022-0248(89)90585-X
[Crossref]

60. Clerjaud B, Gôte D, Svob L, Marfaing Y, Druilhe R (1993) Hydrogen-acceptor pairing in CdTe epitaxial layers grown by OMVPE. Solid State Comm 85(2):167–170. https://doi.org/10.1016/0038-1098(93)90368-W [Crossref]

61. Mitra P, Tyan YL, Case FC, Starr R, Reine MB (1996) Improved arsenic doping in metalorganic chemical vapor deposition of HgCdTe and in situ growth of high performance long wavelength infrared photodiodes. J Electron Mater 25(8):1328–1335. https://doi.org/10.1007/BF02655028 [Crossref]

62. Madejczyk P, Piotrowski A, Gawron W, Kłos K, Pawluczyk J, Rutkowski J, Piotrowski J, Rogalski A (2005) Growth and properties of MOCVD HgCdTe epilayers on GaAs substrates. Opto-Electron Rev 13(3):239–251

63. Whiteley JS, Koppel P, Conger VL, Owens KE (1988) Annealing and electrical properties of organometallic vapor phase epitaxy-interdiffused multilayer process grown HgCdTe. J Vac Sci Technol A 6(4):2804–2807. https://doi.org/10.1116/1.575511 [Crossref]

64. Sidorov YG, Dvoretski SA, Mikhailov NN, Yakushev MV, Varavin VS, Antsiferov AP (2000) Molecular-beam epitaxy of narrow-band CdHgTe. Equipment and technology. J Opt Technol 67(1):31–37. https://doi.org/10.1364/JOT.67.000031 [Crossref]

65. Svitashev KK, Dvoretsky SA, Sidorov YG, Shvets VA, Mardezhov AS, Nis IE et al (1994) The growth of high-quality MCT films by MBE using in situ ellipsometry. Cryst Res Tech 29(7):931–937. https://doi.org/10.1002/crat.2170290703 [Crossref]

66. Vilela MF, Buell AA, Newton MD, Venzor GM, Childs AC, Peterson JM et al (2005) Control and growth of middle wave infrared (MWIR) $Hg_{1-x}Cd_xTe$ on Si by molecular beam epitaxy. J Electron Mater 34(6):898–904. https://doi.org/10.1007/s11664-005-0039-z [Crossref]

67. Shvets VA, Mikhailov NN, Dvoretskii SA (2011) Growing of HgCdTe heterostructures with in situ elipsometric control. Optoelectron Instrument Proc 47(5):426–435. https://doi.org/10.3103/S8756699011050220 [Crossref]

68. Mikhailov NN (2005) PhD Thesis, Moleculyarno-luchevaya epitaksiya geterostructur CdxHg1-xTe na podlazhrfh GaAs dlya infrakrasnyh fotopriemnikov, Institute of Semiconductor Physics, Novosibirsk. (in Russian)

69. Blinov VV, Goryaev EP, Dvoretsky SA, Mikhailov NN, Myasnikov VN, Sidorov YG, Stenin SI (1998) Usroystvo dlya moleculyarno-luchevoy epitaxii. RU Patent 2111291. May 20 1998 (in Russian)

70. Sivananthan S, Chu X, Reno J, Faurie JP (1986) Relation between crystallographic orientation and the condensation coefficients of Hg, Cd and Te during molecular beam epitaxial growth of

$Hg_{1-x}Cd_xTe$ and CdTe. J Appl Phys 60(4):1359–1363. https://doi.org/10.1063/1.337310
[Crossref]

71. Almeida LA, Groenert M, Markunas J, Dinan JH (2006) Influence of substrate orientation on the growth of HgCdTe by molecular beam epitaxy. J Electron Mater 35(6):1214–1218. https://doi.org/10.1007/s11664-006-0243-5
[Crossref]

72. Koestner RJ, Schaake HF (1988) Kinetics of molecular beam epitaxial HgCdTe growth. J Vac Sci Technol A 6:2834–2839. https://doi.org/10.1116/1.575611
[Crossref]

73. Varavin VS, Dvoretsky SA, Liberman VI, Mikhailov NN, Sidorov YG (1996) Molecular beam epitaxy of high quality Hg1−xCdxTe films with control of the composition distribution. J Cryst Growth 159:1161–1166. https://doi.org/10.1016/0022-0248(95)00845-4
[Crossref]

74. Rujirawat S, Almeida LA, Chen YP, Sivananthan S, Smith DJ (1997) High quality large-area CdTe(211)B on Si(211) grown by molecular beam epitaxy. Appl Phys Lett 71:1810–1812. https://doi.org/10.1063/1.119406
[Crossref]

75. Sidorov YG, Dvoretskii SA, Varavin VS, Mikhailov NN, Yakushev MV, Sabinina IV (2001) Molecular-beam epitaxy of Mercury–Cadmium–Telluride solid solutions on alternative substrates. Semiconductors 35(9):1045–1053. https://doi.org/10.1134/1.14035694
[Crossref]

76. Zanatta JP, Ferret P, Theret G, Million A, Wolny M, Chamonal JP, Destefanis G (1998) Heteroepitaxy of HgCdTe (211)B on Ge substrates by molecular beam epitaxy for infrared detectors. J Electron Mater 27:542–545. https://doi.org/10.1007/s11664-998-0012-8
[Crossref]

77. Dvoretsky SA, Mikhailov NN, Ikusov DG, Kartashev VA, Kolesnikov AV, Sabinina IV, Sidorov YG, Shvets VA (2020) The growth of CdTe on GaAs substrate by MBE. In: Nanai L, Samantara A, Ratha S (eds) Method for film synthesis and coating procedures. INTECH, p 704. https://doi.org/10.5772/intechopen.73994

78. Wenisch J, Eich D, Lutz H, Schallenberg T, Wollrab R, Ziegler J (2012) MBE growth of MCT on GaAs substrates at AIM. J Electron Mater 41:2828–2832. https://doi.org/10.1007/s11664-012-2113-7
[Crossref]

79. Erdem Arkun F, Edwall DD, Ellsworth J, Douglas S, Zandian M, Carmody M (2017) Characterization of HgCdTe films grown on large-area CdZnTe substrates by molecular beam epitaxy. J Electron Mater 46:5374–5378. https://doi.org/10.1007/s11664-017-5441-9
[Crossref]

80. Reddy M, Peterson JM, Vang T, Franklin JA, Vilela MF, Olsson K et al (2011) Molecular beam epitaxy growth of HgCdTe on large-area Si and CdZnTe substrates. J Electron Mater 40:1706–1716. https://doi.org/10.1007/s11664-011-1665-2
[Crossref]

81. Ziegler J, Wenisch R, Breiter D, Eich H, Figgemeier P, Fries HL, Wollrab R (2014) Improvements of MCT MBE growth on GaAs improvements of MCT MBE growth on GaAs. J Electron Mater 43:2935–2940. https://doi.org/10.1007/s11664-014-3149-7 [Crossref]
82. Varavin VS, Vasilyev VV, Dvoretskii SA, Mikhailov NN, Ovsyuk VN, Sidorov YG et al (2003) HgCdTe epilayers on GaAs: growth and devices. Opto-Electron Rev 11(2):99–111; *Proc. SPIE*, 5136, 381 (2003). https://doi.org/10.1117/12.519761 [Crossref]
83. Sidorov YG, Anciferov AP, Varavin VS, Dvoretsky SA, Mikhailov NN, Yakushev MV et al (2016) Molecular beam epitaxy of $Cd_xHg_{1-x}Te$. In: Latyshev AV, Dvurechenskii AV, Aseev AL (eds) Advances in semiconductor nanostructures. Growth, characterization, properties and applications. Elsevier, p 297. https://doi.org/10.1016/B978-0-12-810512-2.00012-3 [Crossref]
84. Zanatta JP, Badano G, Ballet P, Largeron C, Baylet J, Gravrand O et al (2006) Molecular beam epitaxy growth of HgCdTe on Ge for third-generation infrared detectors. J Electron Mater 35:1231–1236. https://doi.org/10.1007/s11664-006-0246-2 [Crossref]
85. Vilela MF, Lofgreen DD, Smith EPG, Newton MD, Venzor GM, Peteson JM et al (2008) LWIR HgCDTe detectors grown on Ge substrates. J Electron Mater 37(9):1465–1470. https://doi.org/10.1007/s11664-008-0443-2 [Crossref]
86. Reddy M, Peterson JM, Vang T, Franklin JA, Vilela MF, Olsson K et al (2011) Molecular beam epitaxy growth of HgCdTe on large-area Si and CdZnTe substrates. J Electron Mater 40(8):1706–1716. https://doi.org/10.1007/s11664-011-1665-2 [Crossref]
87. Reddy M, Jin X, Lofgreen DD, Franklin JA, Peterson JM, Vang T et al (2019) Demonstration of high-quality MBE HgCdTe on 8-inch wafers. J Electron Mater 48(10):6040–6044. https://doi.org/10.1007/s11664-019-07246-y [Crossref]
88. Yakushev MV, Brunev DV, Varavin VS, Vasilyev VV, Dvoretskii SA, Marchishin IV et al (2011) HgCdTe heterostructures on Si (310) substrates for mid infrared focal plane arrays. Semiconductors 45(3):385–391. https://doi.org/10.1134/S1063782611030250 [Crossref]
89. Varavin VS, Vasilyev VV, Guzev AA, Dvoretsky SA, Kovchavtsev AP, Marin DV et al (2016) CdHgTe heterostructures for new generation IR photodetectors operating at elevated temperatures. Semiconductors 50(12):1626–1629. https://doi.org/10.1134/S1063782616120265 [Crossref]
90. Johnson SM, Buell AA, Vilela MF, Peterson JM, Varesi JB, Newton MD et al (2004) HgCdTe/Si materials for long wavelength infrared detectors. J Electron Mater 33(6):526–530. https://doi.org/10.1007/s11664-004-0041-x [Crossref]

91. Simingalam S, Brill G, Wijewarnasuriya P, Rao MV (2015) Low temperature, rapid thermal cycle annealing of HgCdTe grown on CdTe/Si. J Electron Mater 44(9):1321–1326. https://doi.org/10.1007/s11664-014-3542-2 [Crossref]
92. Wijewarnasuriya PS, Zandian M, Young DB, Waldrop J, Edwall DD, Mclevige WV et al (1999) Microscopic defects on MBE grown LWIR $Hg_{1-x}Cd_xTe$ material and their impact on device performance. J Electron Mater 28(6):649–653. https://doi.org/10.1007/s11664-999-0048-4 [Crossref]
93. Sabinina IV, Gutakovsky AK, Sidorov YG, Dvoretsky SA, Kuzmin VD (1992) Defect formation during growth of CdTe (111) and HgCdTe films by molecular beam epitaxy. J Cryst Growth 117:238–243. https://doi.org/10.1016/0022-0248(92)90752-5 [Crossref]
94. Aoki T, Chang Y, Badano G, Zhao J, Grein C, Sivananthan S, Smith DJ (2003) Electron microscopy of surface-crater defects on HgCdTe/CdZnTe(211)B epilayers grown by molecular beam epitaxy. J Electron Mater 32(7):703–709. https://doi.org/10.1007/s11664-003-0056-8 [Crossref]
95. Sabinina IV, Gutakovsky AK, Sidorov YG, Latyshev AV (2005) Nature of V-shaped defects in HgCdTe epilayers grown by molecular beam epitaxy. J Cryst Growth 274:339–346. https://doi.org/10.1016/j.jcrysgro.2004.10.053 [Crossref]
96. Wijewarnasuriya PS, Lange MD, Sivananthan S, Faurie JP (1994) Carrier recombination in indium doped HgCdTe(211)B epitaxial layers grown by molecular beam epitaxy. J Appl Phys 75:1005–1009. https://doi.org/10.1063/1.356506 [Crossref]
97. Bakhtin PA, Dvoretskii SA, Varavin VS, Korobkin AP, Mikhailov NN, Sabinina IV, Sidorov YG (2004) Effect of low-temperature annealing on electrical properties of n-HgCdTe. Semiconductors 38(10):1172–1175. https://doi.org/10.1134/1.1808823 [Crossref]
98. Sidorov GY, Mikhailov NN, Varavin VS, Sidorov YG, Dvoretskii SA (2008) Effect of the arsenic cracking zone temperature on the efficiency of arsenic incorporation in CdHgTe films in molecular-beam epitaxy. Semiconductors 42(6):651–654. https://doi.org/10.1134/S1063782608060043 [Crossref]
99. Srivastav V, Pal R, Vyas HP (2005) Overview of etching technologies used for HgCdTe. Opto-Electron Rev 13(3):197–211
100. Kotina IM, Tukhkonen LM, Patsekina GV, Shchukarev AV, Gusinskii GM (1998) Study of CdTe etching process in alcoholic solutions of bromine. Semicond Sci Technol 13(8):890–894. https://doi.org/10.1088/0268-1242/13/8/011 [Crossref]

101. Causier A, Gerard I, Bouttemy M, Etchberry A, Pautet C, Baylet J, Mollard L (2011) Wet etching of HgCdTe in aqueous bromine solution. J Electron Mater 40(8):1823–1829. https://doi.org/10.1007/s11664-011-1660-7 [Crossref]
102. Belas E, Grill R, Franc J, Toth A, Höschl P, Sitter H, Moravec P (1996) Determination of the migration energy of Hg interstitials in (HgCd)Te from ion milling experiments. J Cryst Growth 159(1):1117–1122. https://doi.org/10.1016/0022-0248(95)00696-6 [Crossref]
103. Izhnin II, Mynbaev KD, Voitsekhovskii AV, Korotaev AG, Fitsych OI, Pociask-Bialy M (2017) Ion etching of HgCdTe: properties, patterns and use as a method for defect studies. Opto-Electron Rev 25(2):148–170. https://doi.org/10.1016/j.opelre.2017.03.007
104. Liu L, Chen Y, Ye Z, Ding R (2018) A review on plasma-etch-process induced damage of HgCdTe. Infrared Phys Technol 90:175–185. https://doi.org/10.1016/j.infrared.2018.03.009 [Crossref]
105. Keller RC, Seelmann-Eggerbert M, Richter HJ (1995) Reaction chemistry and resulting surface structure of HgCdTe etched in CH_4/H_2 and H_2 ECR plasmas. J Electron Mater 24(9):1155–1160. https://doi.org/10.1007/BF02653068 [Crossref]
106. Eddy CR, Leonhardt JD, Shamamiam VA, Holm RT, Glembocki OJ, Meyer JR, Hogman CA, Butler JE (1996) Characterization of CH_4/H_2 /Ar high density plasma etch process for HgCdTe. MRS Online Proc Library 450:275. https://doi.org/10.1557/PROC-450-275 [Crossref]
107. Boulard E, Cardinaud C, Baylet JJ (2009) Effect of Ar and N_2 addition on CH_4-H_2 based chemistry inductively coupled plasma etching of HgCdTe. J Vac Sci Technol A 27(4):855–861. https://doi.org/10.1116/1.3147219 [Crossref]
108. Keller RC, Seelmann-Egelbert M, Richter JH (1995) Addition of N_2 as a polymer deposition inhibitor in CH_4/H_2 electron cyclotron plasma etching of $Hg_{1-x}Cd_xTe$. Appl Phys Let 67:3750–3752. https://doi.org/10.1063/1.115372 [Crossref]
109. Smith EGP, Gleason JK, Pham LT, Patten EA, Welkowsky MS (2003) Inductivity coupled plasma etching of HgCdTe. J Electron Mater 32(7):816–820. https://doi.org/10.1007/s11664-003-0076-4 [Crossref]
110. Smith EGP et. al., (2007) J Electron Mater 36(8):884
111. Izhnin II, Mynbaev KD, Voitsechovskii AV, Korotaev AG, Fitsych OI, Pociask-Bialy M (2017) Ion etching of HgCdTe: properties, pattern and use as a method for defect studies. Opto-Electron Rev 25(2):148–170. https://doi.org/10.1016/j.opelre.2017.03.007 [Crossref]

112. Belas E, Franc J, Toth A, Moravec P, Grill R, Sitter H, Höschl P (1996) Type conversion of p-(HgCd)Te using and Ar reactive ion etching. Semicond Sci Technol 11(7):1116–1120. https://doi.org/10.1088/0268-1242/11/7/024 [Crossref]
113. Gorshkov DV, Sidorov GY, Varavin VS, Sabinina IV, Yakushev MV (2020) Reconversion of the CdHgTe conductivity type after plasma etching process at low temperature. Appl Phys Let 116(8):082102. https://doi.org/10.1063/1.5136265 [Crossref]
114. Sidorov GY, Gorshkov DV, Sidorov YG, Sabinina IV, Varavin VS (2020) Effect of surface treatment on the charge density at the interface between CdHgTe epitaxial films and Al_2O_3 grown by atomic layer deposition. Optoelectron Instrument Proc 56(5):492–497. https://doi.org/10.3103/S875669902005012X [Crossref]
115. Westerhout R, Musca C, Antoszewski J, Dell JM, Faraone L (2007) Investigation of 1/f noise mechanisms in midwave infrared HgCdTe gated photodiodes. J Elecrtron Mater 36(8):884–889. https://doi.org/10.1007/s11664-007-0120-x [Crossref]
116. Zakirov ER, Kesler VG, Sidorov GY, Prosvirin IP, Gutakovsky AK, Vdovin VI (2019) XPS investigation of the ALD Al_2O_3/HgCdTe heterointerface. Semicond Sci Technol 34(6):065007. https://doi.org/10.1088/1361-6641/ab1961 [Crossref]
117. Rogalski A, Adamiec K, Rutkowski J (eds) (2000) Narrow-gap semiconductor photodiodes. SPIE Press, Bellingham
118. Kovchavtsev AP, Sidorov GY, Nastovjak AE, Tsarenko AV, Sabinina IV, Vasilyev VV (2017) Mercury cadmium telluride surface passivation by the thin alumina film atomic-layer deposition. J App Phys 121(12):125304. https://doi.org/10.1063/1.4978967 [Crossref]
119. Nemirovsky Y, Bahir G (1989) Passivation of mercury cadmium telluride surfaces. J Vac Sci Technol A 7(2):450–459. https://doi.org/10.1116/1.576202 [Crossref]
120. Nemirovsky Y, Burstein L (1984) Anodic sulfide films on $Hg_{1-x}Cd_xTe$. AppI Phys Lett 44:443. https://doi.org/10.1063/1.94760 [Crossref]
121. Nemirovsky Y, Burstein L (1985) Interface of p-type $Hg_{1-x}Cd_xTe$ passivated with native sulfides. J Appl Phys 58:366. https://doi.org/10.1063/1.335686 [Crossref]
122. Spicer WE, Silberman JA, Lindau I, Chen A-B, Sher A, Wilson JA (1983) Band gap variation and lattice, surface, and interface “instabilities” in $Hg_{1-x}Cd_xTe$ and related compounds. J Vac Sci Technol A 1(3):1735–1743. https://doi.org/10.1116/1.572206

[Crossref]
123. Wilson JA, Cotton VA (1985) Electrical properties of the SiO_2:HgCdTe interface. J Vac Sci Technol A 3(1):199–202. https://doi.org/10.1116/1.573200 [Crossref]
124. Castagne R, Vapaille A (1970) Effet des fluctuations spatiales du potential a l'interface SiO2/Si sur les courbes capacite-tension d'une structure MOS. C R Acad Sci (Paris) 270:1347
125. Bhan RK, Srivastava V, Saxena RS, Sareen L, Pal R, Sharma RK (2010) Improved high resistivity ZnS films on HgCdTe for passivation of infrared devices. Infrared Phys Technol 53(I.5):404–409. https://doi.org/10.1016/j.infrared.2010.07.008 [Crossref]
126. Biryulin PV, Dudko SA, Konovalov SA, Pelevin YA, Turinov VI (2003) Investigation of the ZnS-CdHgTe interface. Semiconductors 37(12):1383–1386. https://doi.org/10.1134/1.1634658 [Crossref]
127. Whelan MV (1965) Graphical relation between surface parameters of silicon, to be used in connection with MOS-capacitance measurement. Philips Res Rep 20:620–632
128. Zhang J, Umana-Membreno GA, Gu R, Lei W, Antoszewski J, Dell JM, Faraone L (2015) Investigation of ICPECVD silicon nitride films for HgCdTe surface passivation. J Electron Mater 44(9):2990–3001. https://doi.org/10.1007/s11664-015-3703-y [Crossref]
129. Castagné R, Vapaille A (1971) Description of the SiO2-Si interface properties by means of very low frequency MOS capacitance measurements. Surf Sci 28(1):157–193. https://doi.org/10.1016/0039-6028(71)90092-6 [Crossref]
130. Gorshkov DV, Sidorov GY, Sabinina IV, Sidorov Y, Marin DV, Yakushev MV (2020) The effect of the growth temperature on the passivating properties of the Al_2O_3 films formed by atomic layer deposition on the CdHgTe surface. Technical Phys Let 46(8):741–744. https://doi.org/10.1134/S1063785020080064 [Crossref]
131. Voitsekhovskii AV, Nesmelov SN, Dzyadukh SM (2017) Admittance measurements in the temperature range (8−77) K for characterization of MIS structures based on MBE n-$Hg_{0.78}Cd_{0.22}Te$ with and without graded-gap layers. J Phys Chem Sol 102:42–48. https://doi.org/10.1016/j.jpcs.2016.10.015 [Crossref]
132. Fu R, Pattison J, Chen A, Nayfeh O (2012) Mercury cadmium telluride (HgCdTe) passivation by advanced thin conformal Al_2O_3 films. Proc SPIE 8353:885–891. https://doi.org/10.1117/12.918605 [Crossref]
133. Banerjee S, Su P, Dahal R, Bhat IB, Bergeson JD, Blissett C, Aqariden F, Hanyaloglu B (2014) Surface passivation of HgCdTe using low-pressure chemical vapor deposition of CdTe. J Electron Mater 43:3012–3017. https://doi.org/10.1007/s11664-014-3178-2

[Crossref]
134. Nemirovsky Y, Mainzer N, Weiss E (1994) Passivation of HgCdTe. In: Capper P (ed) Properties of narrow gap cadmium based compounds. INSPEC, IEE, London, p 284
135. Kumar V, Pal R, Chaudhury PK, Sharma BL, Gopal V (2005) A CdTe passivation process for long wavelength infrared HgCdTe photodetectors. J Electron Mater 34(9):1225–1229. https://doi.org/10.1007/s11664-005-0267-2
[Crossref]
136. Tennant WE, Cockrum CA, Gilpin JB, Kinch MA, Reine MB, Ruth RP (1992) Key issues in HgCdTe based focal plane arrays: an industry perspective. J Vac Sci Technol B 10:1359. https://doi.org/10.1116/1.585869
[Crossref]
137. Rogalski A (2020) HgCdTe photodetectors. In: Tournir E, Gerutti L (eds) Mid-infrared optoelectronics. Materials, devices and applications. Elsevier Duxford, p 235
[Crossref]
138. Nemirovsky Y, Amir N (1997) Surfaces/interfaces of narrow-gap II-VI compounds. In: Capper P (ed) *Narrow-Gap II-VI compounds for optoelectronic and electromagnetic applications*. Chapman & Hall, London, p 291
139. Spicer WE, Friedman DJ, Carey GP (1988) The electrical properties of metallic contacts on $Hg_{1-x}Cd_xTe$. J Vac Sci Technol A 6(4):2746–2751. https://doi.org/10.1116/1.575499
[Crossref]
140. Flores F, Tejidor C (1987) On the formation of semiconductor interface. J Phys C Solid State Phys 20(2):145–176. https://doi.org/10.1088/0022-3719/20/2/001
[Crossref]
141. Spicer WE, Chye PW, Skeath PR, Su CY, Lindau I (1979) New and unified model for Shottky barrier and III-V insulator interface state formation. J Vac Sci Technol 16(5):1422–1433. https://doi.org/10.1116/1.57015
[Crossref]
142. Spicer WE, Lindau I, Skeath PR, Chye PW, Su CY (1980) Unified defect model and beyond. J Vac Sci Technol 17(5):1019–1027. https://doi.org/10.1116/1.570583
[Crossref]
143. Heine V (1965) Theory of surface states. Phys Rev 138(6A0):A1689–A1698. https://doi.org/10.1103/Phys.Rev.138.A1689
[Crossref][zbMATH]
144. Freeouf JL, Woodall JM (1981) Schottky barrier: an effective work function model. Appl Phys Lett 39:727. https://doi.org/10.1063/1.92863
[Crossref]
145. Long D, Schmit JL (1970) In: Willardson RK, Beer AC (eds) Semiconductors and semimetals, vol 5. Academic, New York, p 175

146. Rogalski A, Piotrowski J (1988) Intrinsic infrared detectors. Prog Quant Electron 12:87–289. https://doi.org/10.1016/0079-6727(88)90001-8 [Crossref]
147. Reine MB (2001) Photovoltaic detectors in MCT. In: Capper P, Elliott CT (eds) Infrared detectors and emitters: materials and devices. Kluwer Academic Publishers, Boston, p 313 [Crossref]
148. Leech PW, Reeves GK (1992) Specific contact resistance of indium ohmic contacts to n-type $Hg_{1-x}Cd_xTe$. J Vac Sci Technol A 10(1):105–109. https://doi.org/10.1116/1.578121 [Crossref]
149. Beck WA, Davis GD, Goldberg AC (1990) Resistance and 1/f noise of Au, Al, and Ge contacts to (Hg,Cd)Te. J Appl Phys 67:6340–6346. https://doi.org/10.1063/1.345154 [Crossref]
150. Storm W, Altebockwinkel M, Wiedmann L, Benninghoven A, Ziegler J, Bauer A (1991) Depth profile analysis of Pt, Cu, and Au overlayers on p-$Hg_{1-x}Cd_xTe$. J Vac Sci Technol A 9(1):14–20. https://doi.org/10.1116/1.577115 [Crossref]
151. Sizov F, Tsybrii Z, Apats'ka M, Dmytruk N, Slipokurov V, Bunchuk S et al (2020) Ohmic metal/ $Hg_{1-x}Cd_xTe$ ($x \approx 0.3$) contacts. Semicond Sci Technol 35:125030. https://doi.org/10.1088/1361-6641/abc0f7 [Crossref]
152. Piotrowski A, Madejczyk P, Gawron W, Kłos K, Romanis M, Grudzień M, Rogalski A, Piotrowski J (2004) MOCVD growth of $Hg_{1-x}Cd_xTe$ heterostructures for uncooled infrared photodetectors. Opto-Electron Rev 12(4):453–458
153. Janik E, Triboulet R (1983) Ohmic contacts to p-type cadmium telluride and cadmium mercury telluride. J Phys D Appl Phys 16(12):2333–2340. https://doi.org/10.1088/0022-3727/16/12/011 [Crossref]
154. Bubulac LO, Lo DS, Tennant WE, Edwall DD, Chen JC, Ratusnik J, Robinson JC, Bostrup G (1987) Ion implanted junction formation in $Hg_{1-x}Cd_xTe$. J Vac Sci Technol A 5(5):3166–3170. https://doi.org/10.1116/1.574861 [Crossref]
155. Baker IM (2017) II-VI narrow bandgap semiconductors: optoelectronic. In: Kasap S, Capper P (eds) Handbook of electronic and photonic materials II-VI narrow bandgap semiconductors: optoelectronics, 2nd edn. Springer, Leipzig, p 867
156. Lei W, Antoszewski J, Faraone L (2015) Progress, challenges, and opportunities for HgCdTe infrared materials and detectors. Appl Phys Rev 2:041303. https://doi.org/10.1063/1.4936577 [Crossref]
157. Dutton DT, O'Keefe E, Capper P, Jones CL, Mugford S, Ard C (1993) Type conversion of $Cd_xHg_{1-x}Te$ grown by liquid phase epitaxy. Semicond Sci Technol 8:S266–S269. https://doi.

org/10.1088/0268-1242/8/1S/058
[Crossref]

158. Jenner MD, Blackman MV (1982) Method of manufacturing an infrared detector device. US Patent. 4,318,217, 9 March 1982

159. Blackman MV, Charlton DE, Jenner MD, Purdy DR, Wotherspoon JTM, Elliot CT, White AM (1987) Type conversion in $Hg_{1-x}Cd_xTe$ by ion beam treatment. Electron Lett 23(19:978–979. https://doi.org/10.1049/el:19870688
[Crossref]

160. Mynbaev KD, Ivanov-Omski VI (2003) Modification of $Hg_{1-x}Cd_xTe$ properties by low energy ions. Semiconductors 37(10):1127–1150. https://doi.org/10.1134/1.1619507
[Crossref]

161. Baker IM, Ballinga RA (1984) Photovoltaic CdHgTe-silicon hybrid focal planes. Proc SPIE 510:121–129. https://doi.org/10.1117/12.945014
[Crossref]

162. Agnihorti OP, Lee HC, Yang K (2002) Plasma induced type conversion in mercury cadmium telluride. Semicond Sci Technol 17:R11–R19
[Crossref]

163. Destefanis G (1988) Electrical doping of HgCdTe by ion implantation and heat treatment. J Cryst Growth 86(1–4):700–722. https://doi.org/10.1016/0022-0248(90)90798-P
[Crossref]

164. Marchishin IV, Sabinina IV, Sidorov GY, Yakushev MV, Varavin VS, Remesnik VG et al (2020) HgCdTe-based 640 × 512 matrix midwave infrared photodetector. J Commun Technol Electron 65(3):316–320. https://doi.org/10.1134/S1064226920030122
[Crossref]

165. Zverev AV, Suslyakov AO, Sabinina IV, Sidorov GY, Yakushev MV, Kuzmin VD et al (2019) Photodetectors with 384 × 288 matrix elements for the infrared range of 8–10 microns. J Commun Technol Electron 64(9):1024–1029. https://doi.org/10.1134/S1064226919090171
[Crossref]

166. Vuillermet M, Billon-Lanfrey D, Reibel Y, Manissadjian A, Mollard L, Baier N, Gravrand O, Destéfanis G (2012) Status of MCT focal plane arrays in France. Proc. of SPIE 8353:83532K
[Crossref]

167. Figgemeier H, Hanna S, Eich D, Fries P, Mahlein K-M, Wenisch J et al (2017) State-of-the-Art MCT photodiodes for cutting-edge sensor applications by AIM. Proc of SPIE 10177:101771K. https://doi.org/10.1117/12.2261925
[Crossref]

168. Foyt AG, Harman TC, Donnelly JP (1971) Type conversion and n–p junction formation in CdxHg1−xTe produced by proton bombardment. Appl Phys Lett 18(8):321–323. https://doi.org/10.1063/1.1653679
[Crossref]

169. Kozlowski LJ, Bailey RB, Cabelli SC, Cooper DE, McComas G, Vural K, Tennant WE (1992) 640×480 PACE HgCdTe FPA. Proc SPIE 1735:163–173. https://doi.org/10.1117/12.138620 [Crossref]
170. Lutz H, Breiter R, Rutzinger S, Schallenberg T, Wendler J, Ziegler J (2013) High-performance IR detector modules for army applications. Proc SPIE 8704:87040A. https://doi.org/10.1117/12.2015714/ [Crossref]
171. Bubulac LO (1988) Defects, diffusion and activation in ion implanted HgCdTe. J Cryst Growth 86(1–4):723–734. https://doi.org/10.1016/0022-0248(90)90799-Q [Crossref]
172. Bubulac LO, Tennant WE (1987) Role of Hg in junction formation in ion-implanted HgCdTe. Appl Phys Lett 51(5):355–357. https://doi.org/10.1063/1.98439 [Crossref]
173. Bubulac LO, Lo DS, Tennant WE, Edwall DD, Chen JC, Ratusnik J, Robinson JC, Bostrup G (1987) P on n ion-implanted junctions in liquid phase epitaxy HgCdTe layers on CdTe substrates. Appl Phys Lett 50:1586–1589. https://doi.org/10.1063/1.97788
174. Mollard L, Destefanis G, Baier N, Rothman J, Ballet P, Zanatta JP, Tchagaspanian M, Papon AM, Bourgeois G, Barnes JP (2009) Planar p-on-n HgCdTe FPAs by Arsenic Ion Implantation. J Electron Mater 38(9):1805–1813. https://doi.org/10.1007/s11664-009-0829-9 [Crossref]
175. Eich D, Schirmacher W, Hanna S, Mahlein KM, Fries P, Figgemeier H (2017) Progress of MCT detector technology at AIM towards smaller pitch and lower dark current. J Electron Mater 46(9):5448–5457. https://doi.org/10.1007/s11664-017-5596-4 [Crossref]
176. Kovchavtsev AP, Guzev AA, Tsarenko AV, Panova ZV, Yakushev MV, Marin DV et al (2015) The reverse current temperature dependences of SWIR CdHgTe “p-on-n” and “n-on-p” junctions. Infrared Phys Technol 73:312–315 [Crossref]
177. Varavin VS, Sabinina IV, Sidorov GY, Marin DV, Remesnik VG, Predein AV et al (2020) Photodiodes based on p-on-n junctions formed in MBE-grown n-type MCT absorber layers for the spectral region 8 to 11 μm. Infrared Phys Technol 105:103182. https://doi.org/10.1016/j.infrared.2019.103182 [Crossref]
178. Rogalski A (2005) HgCdTe infrared detector material: history, status and outlook. Rep Prog Phys 68:2267–2336 [Crossref]
179. Destefanis G, Baylet J, Ballet P, Castelein P, Rothan F, Gravrand O, Rothman J, Chamonal JP, Million A (2007) Status of HgCdTe bicolor and dual-band infrared focal plane arrays at LETI. J Electron Mater 36(8):1031–1044. https://doi.org/10.1007/s11664-007-0168-7 [Crossref]

180. Kinch MA (2000) Fundamental physics of infrared detector materials. J Electron Mater 29(6):809–817. https://doi.org/10.1007/s11664-000-0229-7 [Crossref]
181. Krishnamurthy S, Casselman TN (2000) A detailed calculation of the auger lifetime in p-type HgCdTe. J Electron Mater 29(6):828–831. https://doi.org/10.1007/s11664-000-0232-z [Crossref]
182. Wollrab R, Bauer A, Bitterlich H, Bruder M, Hanna S, Lutz H, Mahlein K-M, Schallenberg T, Ziegler J (2011) Planar n-on-p HgCdTe FPAs for LWIR and VLWIR applications. J Electron Mater 40(8):1618–1623. https://doi.org/10.1007/s11664-011-1659-0 [Crossref]
183. Haiml M, Eich D, Fick W, Figgemeier H, Hanna S, Mahlein M, Schirmacher W, Thöt R (2016) Low dark current LWIR HgCdTe focal plane arrays at AIM. Proc SPIE 9881:988116. https://doi.org/10.1117/12.2229027 [Crossref]
184. Hanna S, Eich D, Mahlein M, Fick W, Schirmacher W, Thöt R et al (2016) MCT-based LWIR and VLWIR 2D focal plane arrays for low dark currents application at AIM. J Electron Mater 45(9):4542–4551. https://doi.org/10.1007/s11664-016-4523-4 [Crossref]

OceanofPDF.com

© The Author(s), under exclusive license to Springer Nature Switzerland AG 2023
G. Korotcenkov (ed.), *Handbook of II-VI Semiconductor-Based Sensors and Radiation Detectors*
https://doi.org/10.1007/978-3-031-19531-0_16

16. II-VI Wide-Bandgap Semiconductor Device Technology: Deposition, Doping, and Etchig

Ghenadii Korotcenkov[1] ✉
(1) Department of Physics and Engineering, Moldova State University, Chisinau, Moldova

Keywords II-VI semiconductors – CdS – CdSe – CdTe – ZnS – ZnSe – ZnTe – Wide bandgap – Deposition – Influencing factors – Substrates – Doping – Acceptors – Donors – Doping strategy – Ion implantation – Limitations – p-n junction – Self-compensation – Etching – Wet etching – Br_2-CH_3OH solution – Dissolution rate – H_2O_2-HBr etchants – I_2-MeOH solution – Mechanism – Polishing effects – Dry etching – Advantages – Gas mixtures – Ion milling – Plasma etching – Reactive ion etching – Patterning – Surface stoichiometry – Cd-rich layer – Surface oxidation – Te-rich layer

16.1 Introduction

As shown in Chap. 2 of this volume, due to their unique properties, the use of wide-bandgap II-VI compounds has increased significantly in the last few decades. Based on these compounds, lasers, photodetectors for the spectral range from IR to UV, solar cells, photocatalysts, light-emitting diodes, thin film transistors, various sensors, and radiation detectors are being developed. The implementation of these and other developments based on II-VI compounds is based on the use of a variety of technological processes adapted to these compounds and taking into account the specifics of their properties. In this chapter, we will look at some of them.

16.2 Synthesis and Deposition of II-VI Semiconductors

16.2.1 Synthesis of Single Crystals

In Chap. 6 (Vol. 1), a detailed consideration was given of the features of the synthesis of CdTe and CdZnTe single crystals intended for the development of radiation detectors (Chap. 2, Vol. 3) and for use as substrates in the growth of HgCdTe epitaxial layers (Chap. 15, Vol. 1). It should be noted that for the growth of single crystals of other II-VI compounds, the same approaches are used that were described in Chap. 6 (Vol. 1).

16.2.2 Film Deposition

The approaches used to deposit films of II-VI compounds are discussed in sufficient detail in Chap. 10 (Vol. 1). Therefore, in this chapter, we indicate only some regularities common to all II-VI compounds.

Experience shows that in order to form films of II-VI compounds with given parameters using most of the methods developed for this, it is necessary to take into account the following factors:

- The choice of the substrate largely determines the morphology of the films grown on them.
- The stoichiometry of the deposited films, which determines most of the properties of the formed films of II-VI compounds, is very sensitive to the growth conditions, especially the temperature regimes of deposition.
- Film doping should be carried out taking into account the characteristics of each II-VI compound. II-VI compounds exhibit a strong tendency to self-compensate upon the introduction of impurities, especially in materials with a wide bandgap.
- The electrical properties of the polycrystalline films largely depend on the microstructure of the films and the properties of the grain boundaries. In such films, the mobility of charge carriers along the film, μ, is much smaller than the bulk values due to grain boundary effects.
- The application of high-temperature post-deposition treatments and their sequence require careful planning.

Based on general principles, the most efficient and stable devices should be those developed on the basis of films with the least crystalline disorder.

From this point of view, the layers grown in the process of homoepitaxy are the most perfect, followed by heteroepitaxy, where there is some lattice mismatch, and the worst case is deposition on an amorphous substrate. However, it must be recognized that deposition on amorphous substrates is economically the most preferable.

Homo- and heteroepitaxy of II-VI compounds are relatively easy to obtain on various crystalline substrates. In this case, the orientation of the film is determined by the orientation of the substrate, and the grain size strongly depends on the parameters of the growth process. As a result, both single-crystal layers and polycrystalline layers with oriented crystallites with grain sizes from nanometers to micrometers can be obtained. For most wide-gap II-VI compounds, the temperature at which epitaxial growth occurs exceeds 300–500 °C.

Oriented crystallite growth can also occur on amorphous substrates, which can either be directed toward the deposition source or perpendicular to the substrate. This effect is especially noticeable during vacuum deposition from a source with a small area. In both heteroepitaxy and deposition on an amorphous substrate, there is a transition region between the substrate and the layer being grown, where the crystallites are small and the disorder is large. The thickness and quality of this disordered layer strongly depend on the conditions of preparation of the substrate surface and temperature regimes of deposition. This transition region can be expected to have a very short carrier lifetime and a short diffusion length for photoexcited carriers. As the distance from the substrate increases, the grains become larger and their orientation more uniform. Linear and surface defects and grain boundaries are eliminated; the layers become more perfect.

The II-VI compounds evaporate congruently, and stoichiometry is maintained relatively automatically at elevated substrate temperatures because the vapor pressure of the elements is much higher over pure elements than over a compound. For example, at 500 °C, the pressures of Cd and Se are ~15 and ~40 torr over the elements and $\sim 3 \cdot 10^{-5}$ and $\sim 1.5 \cdot 10^{-5}$ torr over CdSe.

Because in an efficient photodetector series resistance must be kept to a minimum, it is important to be able to form highly conductive semiconductor layers. Studies have shown that n-type II-VI binary compounds CdS, CdSe, and CdTe can be easily grown with sufficiently

high conductivity (<1 Ω) either in the form of a single crystal or in the form of a thin film by various methods. Low-resistivity p-ZnTe can also be easily grown. With regard to binary semiconductors such as p-CdTe, n-ZnSe, and n-ZnS, there are significant difficulties.

For the manufacture of a large number of semiconductor devices, polycrystalline films of II-VI semiconductors are used. In such films, the electron mobility along the film, μ_e, is determined by grain boundary effects and, as a rule, is much smaller than bulk values (Chap. 2, Vol. 1). Therefore, to reduce the series resistance to a reasonable value in such devices, a high carrier concentration ($>10^{18}/cm^3$) may be required. However, doping of polycrystalline films is generally complicated by rapid diffusion along grain boundaries. Therefore, for devices designed for long-term operation, it is desirable not to use highly diffusible impurities such as lithium (Li). Doping of II-VI films can be carried out by depositing a thin layer of a dopant on the substrate before deposition, heat treatment in a controlled atmosphere, ion doping, and finally incorporating a film during deposition. The best results are obtained using the latter method. Doping by chemical vapor deposition has proven to be very successful for many II-VI compounds. More details about the process of doping II-VI compounds can be found in Chap. 2 (Vol. 1) and Sect. 16.3.

Finally, high-temperature processing sequences must be carefully considered, since ohmic contacts and Schottky barriers can be unstable at high temperatures (read Chap. 17, Vol. 1) and interdiffusion of dopants, as well as elements of II-VI compounds, can change their transport properties and form intermediate compounds.

16.3 Doping of II-VI Semiconductors

16.3.1 General Consideration

The ability to dope n- or p-type semiconductors by introducing suitable impurities is the basis of the semiconductor industry. As it is known, the applications and usefulness of semiconductors depend on their ability to be doped with p- or n-type impurities to change their properties.

For II-VI compounds, the elements of groups I and V can theoretically act as acceptors upon substitution of cations and anions, respectively, and

the elements of groups III and VII can act as donors (see Fig. 16.1). A typical substitutional doping strategy shown in Fig. 16.2.

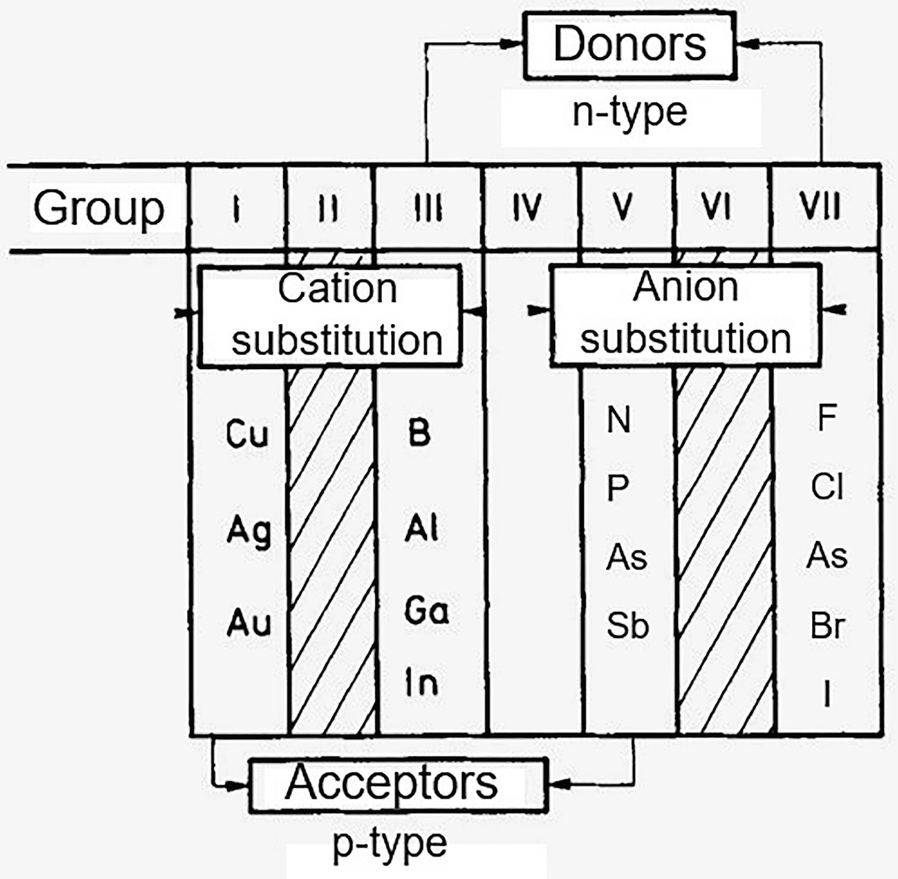

Fig. 16.1 Doping of II-VI compounds. In practice, V and VII elements are not electrically active. Cation excess gives n-type materials; cation vacancies give material of p-type

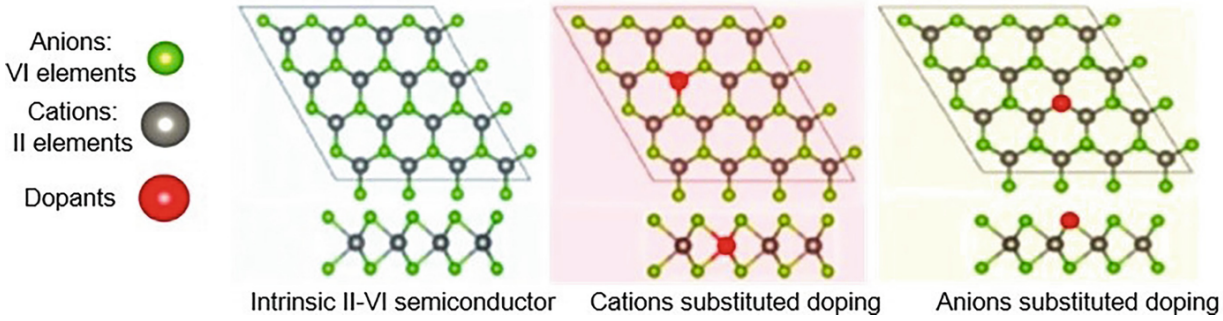

Fig. 16.2 A typical substitutional doping strategy. (Reprinted from [32]. Published 2021 by MDPI as open access)

Unfortunately, for a long time, it was not possible to find approaches that make it possible to introduce an electrically active additive instead of an anion [7]. Therefore, for a long time, the most important dopants of II-VI

compounds were copper, silver, and gold for p-type materials and gallium, indium, aluminum, and sometimes boron for n-type materials [9, 23, 47, 50, 53]. Notwithstanding the above, there are studies in which p-type doping of ZnS, ZnSe, ZnTe, CdTe, and CdS with N, P, As, and Li and n-type doping with Sb and Cl are reported [1, 6, 45, 48, 70, 78].

However, it should be noted that the relative ease of both n- and p-doping of III-V semiconductors is largely absent in II-VI semiconductors [13, 14, 94]. As shown in the chap. 2 (Vol. 1) and [7], the doping efficiency of these compounds is seriously limited by self-compensation phenomena, which considerably reduces the device potential of II-VI compounds. It was found that the tendency to self-compensation is a phenomenon characteristic of wide-gap materials, since the energy acquired during the formation of a compensating defect is of the order of the bandgap. As the energy gap increases, the self-compensation becomes energetically more and more favorable. However, this simple analysis does not really explain the doping behavior of II-VI semiconductors, when compounds with comparable energy bandgaps can differ drastically in the ability to control electrophysical properties via doping: for example, CdS and ZnTe are comparable in their energy bandgaps, but CdS can only be n-type doped, while ZnTe is only p-doped. CdSe can also easily be doped on the n-type, while CdTe can be doped on both on p- and n-type [13, 14, 94]. ZnSe can be relatively easily doped n-type, but p-type doping is very difficult to accomplish, and only doping with reactive nitrogen was successful in achieving p-type conductivity [66]. Real success in incorporating N as an acceptor into ZnSe was also obtained in the process of epitaxial layer growth using MBE, MOCVD, and VPE methods and implantation [12].

It was found that the behavior of doping additions also depends on the II-VI material used [7]. For example, experiments with P impurities showed that shallow acceptors were observed in ZnTe:P, but not in the sulfides and selenides. This behavior of II-VI compounds makes it difficult to use the regularities established for some II-VI compounds in the development of devices based on other II-VI compounds. For example, in contrast to CdTe, for most II-VI compounds, there are limitations in making homo- and some heterojunction devices. However, the dopability of CdTe is relatively low, especially for p-type doping.

Wei and Zhang [98] note that there are other factors besides self-compensation that could limit the dopability of II-VI compounds: (i) the

desired dopant may have a low solubility; (ii) the desired dopant has good solubility, but the defect transition energy level may be too deep; thus, the defect is not ionized at normal operating temperature. For example, Wei and Zhang [98] analyzing behavior of CdTe concluded that p-type doping in CdTe is mostly limited by not having a dopant with both high solubility and shallow acceptor level. For example, CdTe:N or CdTe:P have shallow acceptor levels, but their defect formation energies are too high. CdTe:Cu has a relatively low formation energy, but its acceptor level is too deep. According to Wei and Zhang [98], Ag and P are likely to be the best p-type dopants, and iodine should be the best n-type dopant for CdTe.

It should also not be forgotten that the stoichiometry of II-VI compounds has a strong influence on the results of their doping. An excess of cations leads to the formation of an n-type material, while with a deficiency of cations, the material becomes p-type of conductivity. During the growth of a single crystal, a high concentration of vacancies (cations) is usually observed. Therefore, they act as acceptors, and effective doping with donor impurities requires annealing in cation vapor.

In addition, the very high mobility of defect-related cations leads to very specific surface effects in II-VI compounds. So, with mechanical deformation, chipping, etc., it is possible to convert p-type material to n-type material in near-surface layer. Similarly, when using passivating layers, it is necessary take into account chemical reactions that can lead to the appearance of electrically active defects at the interface. For example, anodic oxide can invert the type of surface layer conductivity. Therefore, in the manufacture of devices, it is preferable to use insulators (SiO_2, Al_2O_3 or ZnS) deposited by low-temperature methods, which, among other things, make it possible to avoid diffusion of cations during the production process.

As for the other additives such as Mn, Ni, Co, Fe, Mo, and Cr [29, 49, 61, 71, 101], they are commonly used to control the optical, luminescent, and magnetic properties of II-VI compounds [12, 56].

As we noted earlier, the most effective is the doping of II-VI compounds in the process of their deposition or synthesis. How effective such doping can be can be judged from the results obtained for CdS layers grown by chemical bath deposition (CBD). While undoped CdS grown by CBD has reported resistivity values of ∼108–107 Ω cm, the reported values for doped CdS values with different dopants are the following [9]: Sn,

10^5 Ω·cm; In, 10^3 Ω·cm; Al, 10^7 Ω·cm; Cl, 10^7 Ω·cm; B, 10^5 Ω·cm; Cu, 10^{12} Ω·cm; Na, 10^5 Ω·cm; and Ga, 10^2 Ω·cm.

Depending on the method used for the synthesis of II-VI compounds, a wide variety of sources can be used for their doping. For example, when precipitating II-VI compounds by chemical methods, NaCl (Cl), $AlCl_3$ (Al), tris(dimethylamino)arsine (As), $AsCl_3$ (As), PCl_3 (P), $SbCl_3$ (Sb), $NiCl_2$ (Ni), and $AgNO_3$ (Ag) can be used as a source of doping impurities. When growing single crystals, elemental In, Sb, and As can also be used as dopants. In the vapor transport deposition (VTD) process, a high-purity dopant-containing compound, specifically Cd_3P_2 for phosphorous, Cd_3As_2 for arsenic, and CdSb for antimony, can be the source of impurities [47].

16.3.2 Ion Implantation

Doping of II-VI materials is often performed using ion implantation. In particular, ion implantation of CdTe crystals has long been used to convert their conduction type in order to create sharp p-n junctions [10, 77] and form a heavy-doped material in both p- and n-type [35, 42, 58]. Most often, group V acceptors, i.e., P, As, Bi, and Sb, and group III donors, i.e., B and In, respectively, are used for these purposes. In addition, heavy-doped CdTe layers with Mn and Cr have been obtained using ion implantation, resulting in the RT ferroelectricity of the as-prepared material [27, 64]. Cl, N, O, Al, Cu, and Co are also used for ion implantation in II-VI compounds [8, 54, 62, 104]. For example, the conversion of n-type CdS to p-type on implantation of N^+ ion has been reported by Shiraki et al. [75].

Ion implantation has several advantages over traditional doping methods [100]: (1) it is a process that depends only on current density, implanted ion energy, and time; (2) it is carried out at a relatively low temperature, which reduces the likelihood of uncontrolled doping with foreign impurities; (3) the process of irradiation is uniform in surface. It is easy to control the concentration of dopants introduced into depth; (4) implantation allows introducing non-soluble elements into the material; and (5) the implantation process is well modeled with Monte Carlo simulation. However, ion implantation can be accompanied by the generation of dislocations, which cannot always be cured using postimplantation procedures.

The typical setup for ion implantation consists of source of ions, magnet for ion selection, accelerator, scanning electrostatic plates, and beam diaphragm. The environment for all these parts/factors is high vacuum (10^{-7} torr). Typically, ion implantation in II-VI compounds occurs at room temperature with the energy from 50 to 500 keV at a dose level of 10^{14}–10^{18} ions/cm^2 [42]. The depth of the p-n junction increases with increasing implantation energy. Ions penetrate the near-surface layer up to 1 μm for high energy.

During implantation, a large concentration of structural defects, such as vacancies, interstices, formation of voids, etc., is generated in the volume of a semiconductor. In order to eliminate these defects or part of them, postimplantation annealing is required. Usually, for the annealing, the ion-implanted samples are coated with SiO_2 films and then annealed at various temperatures in the range of 150–800 °C. For the disappearance of implantation defects, annealing in saturated vapors of Zn and Cd can also be used [62]. It is important to keep in mind that implantation with higher energy causes more radiation damage, and therefore a higher annealing temperature is required to recover the radiation damage. The surface damage also increases significantly with the dose increase. However, annealing at high temperature can create new defects. It was also established that ion implantation and annealing of II-VI semiconductor-based quantum wells lead to an intermixing of barrier and well material, causing a change in quantum well characteristics [90].

However, several studies have shown that implantation at room temperature is not always effective. For example, Donnelly et al. [21] found that implantation in CdTe with As^+ at room temperature is inefficient, because the damage of the structure is so great that the sample becomes semi-insulating and the recovery of the crystal structure is not achieved even after 2 days of annealing at 650 °C. Thus, Donnelly et al. [21] consider that hot temperature implantation is preferable. To carry out such a process, encapsulation of samples must be carried out even before implantation. For these purposes, it is best to use SiO_2 layers. Encapsulating layers of SiO_2 are stable at temperatures not exceeding 525 °C [21]. Implantation at elevated temperature is not accompanied by layer amorphization [8], which is often observed after implantation at room temperature. This behavior indicates a significant reduction in lattice disorder due to elevated

temperature doping. Therefore, in most cases, implantation at elevated temperatures eliminates the need for postimplantation annealing.

In most cases, ion implantation is used to develop device structures based on epitaxial layers and single crystals. However, the use of ion implantation to control the properties of polycrystalline II-VI compounds has also been reported [2, 8, 103]. For example, Kutra et al. [43] used ion implantation of selenium to change the conduction type of n-CdSe layers deposited by thermal evaporation in vacuum to p-type after heat treatment in an inert atmosphere. Kraft et al. [42] used phosphorus (P) ion implantation to obtain enhanced p-type doping near the back contact of CdTe polycrystalline solar cells.

16.3.3 Formation of p-n Junction

p-n junction, i.e., a junction formed between p-type and n-type materials, is the basic building block of many electronic devices, including solar cells and photodetectors. As we pointed out above, materials with different types of conductivity are needed to form a p-n junction. This means that the formation of homojunctions based on II-VI compounds is possible only for CdTe and ZnSe, which can have both n- and p-type conductivity. For their formation, one can use the same approaches that are used for silicon and III-V compounds, i.e., diffusion and ion implantation, described earlier, as well as sequential deposition of compounds with different types of conductivity, achieved by doping or using different deposition modes. For the remaining II-VI compounds, p-n junction can be made only on the basis of heterojunctions. Moreover, one of the parts of these p-n junctions based on heterojunctions should be the same p-type CdTe or ZnSe compounds, plus ZnTe, which is characterized by only p-type conductivity, since other II-VI compounds can only have n-type of conductivity.

16.4 Etching of II-VI Semiconductor Compounds

16.4.1 Chemical Wet Etching

Chemical etching is one of the most commonly used methods for processing semiconductors in the production of devices based on them. There are several reasons why a semiconductor can be chemically etched. The most common are (1) removing a layer of material near a surface that has been damaged by mechanical cutting or mechanical polishing, (2)

obtaining a shiny flat surface, and (3) studying the defective structure of a semiconductor. Some chemical etchants impart features to the semiconductor surface that may be associated with defects in the crystal. This is especially true for dislocations, which often form etch pits at their intersections with the surface, providing an easy way to estimate dislocation density.The formation of the required surface morphology is another purpose of using chemical etching. For example, it has been found that etching in HCl textures the front surface of CdS films, which leads to a decrease in light reflection losses and, consequently, to an increase in photon absorption and an increase in photoconversion efficiency [3, 76].

A wide variety of solutions have been tried to etch II-VI compounds, some of which are listed in Table 16.1.

Table 16.1 Etches for II-VI semiconductors

Semiconductor	Etchant	Remarks
ZnS	0.5 M $K_2Cr_2O_7$ in 16 N H_2SO_4	10 min at 95 °C. High polish, with etch pits on (111). Shallow dishes on the other surface.
	Conc. HNO_3	2–5 min, boiling. Produces etch pits
ZnSe	0.5% Br_2 in CH_3OH	Soaked in CS_2 for 45 min after etching to remove deposit. Produces etch pits on (111)
	3 HNO_3: 1HCl	Produces pits on $(\overline{111})$. Wash in CS_2 after etching
	H_2SO_4 – $KMnO_4$ + H_2O	Polished surface
	$K_3[Fe(CN)]_6$ – isopropanol	Polished surface
	H_2O_2 –NaOH– H_2O	Polished surface
ZnTe	3HNO_3: 4HF	25 °C. Wash in conc. HCl after etching, to remove film
	2H_2O_2: 3HF: 1H_2O	Differentiates (111) from $(\overline{111})$
	0.5% Br_2 in CH_3OH	Produces etch pits on (111)
CdS	1 ml H_2SO_4 + 100 ml H_2O+ 0.08 g Cr_2O_3	Used for 10 min at 80 °C. Differentiates between (0001) and $(000\ \overline{1})$ surfaces
	6 fuming HNO_3: 6CH_3COOH: 1H_2O	Used for 2 min. Sharply defined hexagonal pits on $(000\ \overline{1})$
	0.5 M $K_2Cr_2O_7$ in 16 N H_2SO_4	5–10 min at 95 °C. High polish, with etch 30 pits on (111)

Semiconductor	Etchant	Remarks
CdSe	$30HNO_3$: 0.1HCI: $20H_2SO_4$: $10CH_3COOH$	8 sec at 40 °C. A thick film develops, which can be dissolved in conc. H_2SO_4
	$1HNO_3$: 1HCl	Pits on (0001)
CdTe	$2H_2O_2$: 3HF: $1H_2O$	Polishes (111) and ($\overline{111}$). Etch pits on ($\overline{111}$)
	0.5% Br_2 in CH_3OH	Polishes (111) and ($\overline{111}$). Etch pits on ($\overline{111}$)
	10 ml HNO_3 + 20 ml H_2O + 4 g $K_2Cr_2O_7$	Mirrorlike surface
	0.5% Br_2 in CH_3OH + (0.5–10) mg $AgNO_3$	Etch-pit formation
	$2HNO_3$: 2HCl + $1H_2O$	Polished surface
	I_2 in CH_3OH	Polished surface

Source: Data extracted from Gavrishchuk et al. [30], Tuck B. [91]

In addition to the etchants listed in Table 16.1, solutions of HNO_3-HPO_4-H_2O, HNO_3-HCl-H_2O, and HNO_3-CH_3COOH-H_2O were also used to treat CdTe [73].

In almost all chemical etching processes of semiconductors, the basic initial reaction is the oxidation of the material. Therefore, most etchant compositions for the treatment of semiconductor surfaces consist of an oxidant. The oxidants can be arranged in the following order: $H_2O_2 > K_2Cr_2O_7 > Br_2 > HNO_3 > I_2$ according to the diminution of their standard oxidizing potential. As a rule, surface atoms are oxidized at the stage of oxidation, but not pass into solution. Therefore, the etchant must have one more component that will react with the oxides formed by the elements of the compound to form a soluble complex. As a result, chemical etchants, primarily polishing ones, contain an oxidizing agent, of which HNO_3, H_2O_2 and bromine are most commonly used, as well as a complexing agent such as HF that promotes the dissolution of oxides (see Table 16.1). Many solutions also contain a component that simply dilutes the solution. Often it is water.

When etching semiconductors, it must be borne in mind that there is a significant difference between chemical etching and chemical polishing. Etching means removing material regardless of the final state of the surface,

while polishing means removing material so that the surface is smooth and shiny. At the same time, chemical etching is often accompanied by a violation of the flatness of the processed material and the appearance of etch pits, which are characteristic of each crystallographic plane. For II-VI compounds, this is due to the presence of two polar surfaces in these materials. Warekois et al. [95] etched a number of II-VI semiconductors in several different etches and established that the A-type basal planes have different etching properties to the B-type. The pronounced difference in the etching characteristics on the polar faces of most II-VI compounds is attributed to the higher amount of ionic character in the bonding; A and B surfaces have different concentrations of available bonds at the respective surfaces. There is also an explanation based on the large differences in electronegativity that exist between the components of the II-VI compounds [95]. The A components (Zn, Cd) have larger electronegativities than the B components (Se, S), and it seems reasonable to assume that at least some of the difference in behavior between A and B surfaces in these compounds is due to this fact [83, 91]. The features of etching lead to the formation of various etch figures, which makes it possible to determine the polarity of each plate by the shape of these etching patterns. Since the various II-VI compounds show much less similarity in their etching behavior than the III-V compounds, a specific etchant was found for each II-VI compound, which makes it possible to conveniently and unambiguously distinguish between surfaces A and B. This difference is based either on differences in the formation of dislocation pits or on differences in etching patterns [95]. The etchants and procedures for the polarity determination are summarized in Table 16.2.

Table 16.2 Chemical etchants to determine the polarity of the crystal wafers

Compound	Etchant	Remarks
ZnO (hex)	HNO_3 (20%)	Hexagonal etch pits on the (0001) face
	Conc. HCI	Specular (0001) face, matte (000 $\bar{1}$) face
ZnS (hex)	Conc. HCI	Specular (0001) face, matte (000 $\bar{1}$) face Hexagonal etch pits on the (0001) face
CdS (hex)	$HNO_3/CH_3COOH/H_2O$ at 25 °C	Sharply defined hexagonal etch pits on the (0001) face
	Conc. HCI, HNO_3	Hexagonal-shaped etch pits on the (0001) face

Compound	Etchant	Remarks
CdSe (hex)	$HNO_3/HCl/CH_3COOH/H_2SO_4$ at 40 °C	Hexagonal-shaped pits on the (0001) face
	Conc. HCI	Specular (0001) face, matte $(000\ \bar{1})$ face
ZnTe (cub)	$HF/H_2O_2/H_2O$ at 25 °C	Triangular etch figures on the $\{\overline{111}\}$face
	NaOH (at elev. temp.)	Specular reflecting $\{\overline{111}\}$ face with shallow triangular structures

Source: Reprinted with permission from [83]. Copyright 1969: AIP Publishing

The polarity of the planes also manifests itself during etching in polishing etchants. For example, at a given concentration of bromine in a solution of Br_2 in CH_3OH above 0.5%, the etch rates on the faces of various compounds increase in the following order [83]:

$$(0001)\mathrm{ZnO} < (0001)\mathrm{ZnS} < \left(000\ \bar{1}\right)\mathrm{ZnO} < \left(000\ \bar{1}\right)\mathrm{ZnS} \tag{16.1}$$

$$(0001)\mathrm{CdS} < (0001)\mathrm{CdSe} < \{111\}\,\mathrm{ZnTe} < \left(000\ \bar{1}\right)\mathrm{CdS} < \left(000\ \bar{1}\right)\mathrm{CdSe} \tag{16.2}$$

As a rule, the etch rate of a bromine-methanol solution on the anion faces of the compounds is larger than the etch rate observed on the cation faces. This is in agreement with the higher etch rates obtained with different etchants on the anion faces of ZnO [46] and CdS [84]. Figure 16.3 also shows an increase of the etch rates on all surfaces with the bromine concentration.

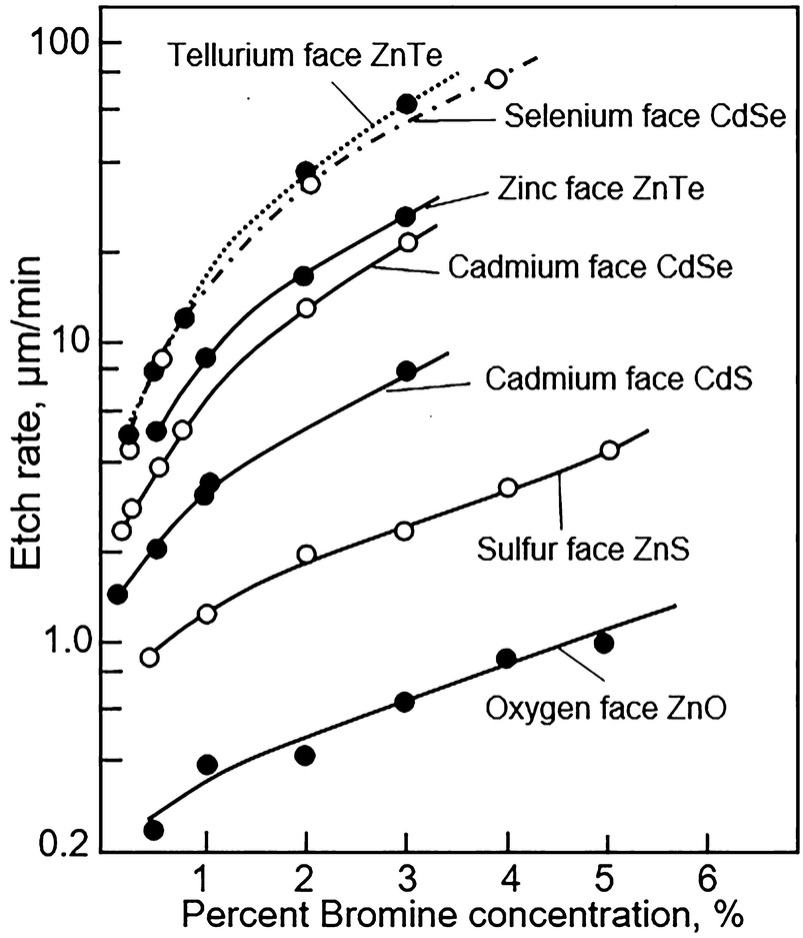

Fig. 16.3 Etch rate at room temperature on the anion faces of ZnO, ZnS, CdSe, and ZnTe and the cation faces of CdS, CdSe, and ZnTe versus the concentration of bromine dissolved in methanol. (Data extracted from Strehlow [83])

For polishing etchants, an important aspect is the surface finish obtained by etching the semiconductor. As noted in Table 16.1, there are several polishing solutions. However, etchants based on bromine and methanol were most widely used in the treatment of II-VI compounds [15, 68, 99, 108]. Some results related to II-VI semiconductor etching in Br_2-CH_3OH solution are presented in Table 16.3. It has been found that a 1–2% bromine solution provides a suitable etch rate on the (000 $\bar{1}$) faces of both ZnO and ZnS, and the damaged layers produced by mechanical polishing is removed in a reasonable time. The polished (000 $\bar{1}$) surface of ZnO and ZnS is smooth and shiny. Chemical polishing with 0.5% bromine in methanol results in excellent surface finish on both anionic and cationic CdSe and ZnTe surfaces. However, a satisfactory chemical polishing of the (0001) faces of ZnO and ZnS has not yet been found. Of the large number of chemical etchants that have been studied, only concentrated phosphoric

acid and dilute acetic acid have shown some promise. Despite a significant etching rate on both polar CdS surfaces, the bromine-methanol solution did not provide a high surface quality on either side.

Table 16.3 Etching and polishing effects of bromine dissolved in methanol

Compound	Remarks
ZnO	Excellent surface finish on (000 $\bar{1}$) face, no satisfactory chemical polish for the (0001) face, etch rate on this face was not detectable
ZnS	Good surface finish on the (0001) face, etch rate on the (0001) face was less than 0.1 μm/min
CdS	No satisfactory surface finish on both faces, etch rate of a 1% bromine-methanol solution on the (0001) face was 12 μm/min
CdSe	Smooth and shiny surface finish on both polar surfaces with a 0.5% bromine-methanol solution
ZnTe (cub)	Smooth and shiny surface finish on both polar surfaces with a 0.5% solution of bromine in methanol

Source: Reprinted with permission from [83]. Copyright 1960: AIP Publishing

Solutions based on Br_2 are also polishing etchants for ZnSe. To obtain more perfect polished surface of ZnSe crystals, bromine containing etching compositions such as Br_2 in methanol or ethanol with different bromine content has been used. It was shown that the polishing effect was observed when the concentration of Br_2 was changed from 0.4 vol.% [34] to 10 vol.% [72].

Brominated solutions, such as H_2O_2-HBr-citric acid [88], H_2O_2-HBr-tartaric acid [80, 81], and H_2O_2-HBr-lactic acid [82, 87], have also been used to etch CdTe and CdZnTe. The results obtained showed that H_2O_2-HBr etchants, containing from 2 to 10 vol.% H_2O_2, give a high-quality polished surface at moderate speeds and that dissolution in such etchants is diffusion limited [86]. The dissolution rate did not exceed 1.5–25 μm/min. This makes it possible to use such etchants for the controlled removal of thin layers from the surface of semiconductors. The etching of CdTe and CdZnTe of various compositions in aqueous solutions of H_2O_2-HBr also showed that the introduction of dopants into CdTe has a significant effect on the dissolution of the semiconductor matrix. The dissolution rate in such

solutions increases in the series CdTe < $Cd_{0.96}Zn_{0.04}Te$ < $Cd_{0.8}Zn_{0.2}Te$. Tomashyk et al. [85] have shown that H_2O_2-HBr-based solution is also polishing etchant for ZnSe. According to Tomashyk et al. [85], for chemical polishing of undoped and aluminum or tellurium-doped zinc selenide samples, the optimal etchant is a solution containing (in vol.%) 10 H_2O_2:10 HBr:80 EG. It was found that H_2O_2-HBr-ethylene glycol (EG) etchants are stable in time and keep their high polishing properties for 24 hours after preparation. For these solutions, the controlled polishing rate of II-VI compounds is in the range of 12–22 μm/min.

Instead of bromine, iodine can also be used in polishing etchants for II-VI compounds. However, according to De Wit and Kelly [15], the iodine-methanol solution is of limited use. De Wit and Kelly [15] found that CdS dissolves in I_2-CH_3OH solutions only in the presence of a high concentration of chloride ions. This behavior was explained by the fact that the radical I* is a much weaker oxidizing agent than bromine. However, in subsequent studies, this opinion about the prospects of iodine-based etchants was refuted. For example, Ivanits'ka et al. [37] have reported the etching of the CdTe single crystals in the I_2-MeOH solution even without the presence of chloride ions and found the dissolution is diffusion controlled. The iodine redox potential (($I_2 \rightarrow 2I^-$, 0.54 V) is lower than that of bromine ($Br_2 \rightarrow 2Br^-$, 1.09 V), but it is sufficient for CdTe surface oxidation [38]. Bastola et al. [5] noted that the Br_2-MeOH etch is very corrosive to metals and may penetrate the entire CdTe film and damage the front interface. At the same time, I_2-MeOH-based etchants are less corrosive and toxic and more technologically efficient compared with bromine. Ivanitska et al. [37] found that the studied compositions of I_2-methanol etching solutions have good polishing properties, and the quality of polishing improves with increasing iodine content in the etching solution. The polishing ability of solutions increases also with increasing viscosity of the solution. The etching rate of CdTe depends on the orientation of the plates and changes in the following sequence: CdTe (110) < CdTe (111)A < CdTe (111)B < CdTe (100). However, the difference between the dissolution rates for different orientations of CdTe was insignificant. The rate of dissolution of the (111)B plane was only slightly higher than the rate of etching of the (111)A plane of the polar crystallographic direction.

Besides elemental iodine (I_2), methylammonium iodide (CH_6IN) (MAI) [96], hydroiodic acid (HI) [4, 38, 52], potassium iodate (KIO_3) and potassium iodide (KI) [51], ammonium iodide (NH_4I), and formamidinium iodide (CH_5IN_2) (FAI) [5] can be used in etchants of II-VI compounds. Moravec et al. [52] studied CdTe and CdZnTe etching in HI-based solutions (H_2O_2-HI-tartaric/citric acid) and found that the results obtained were similar to those obtained for the I_2-methanol solution described above. Ivanitska et al. [36] have shown that KIO_3-KI-lactic acid solution also has highly polishing properties. An important advantage of this etchant is the low etching rate of CdTe and CdZnTe, which does not exceed 2 μm/min [51].

When using the above solutions, iodine and especially Br_2 can be released during the interaction of the etchant components, which leads to a change in the etching rate. This instability is one of the main problems for etching solutions based on Br_2 and HBr. Therefore, the controllability of etch depth is found relatively poor in the absence of an etch stopper. The experiment showed that the amount of iodine and bromine evolved can be controlled to some extent by the introduction of various solvents. The addition of water-organic acids to iodine- or bromine-forming mixtures helps to reduce the etching rate and improve their polishing properties due to more rapid dissolution of poorly soluble interaction products [38]. As previously stated, Tomashyk et al. [85] using this approach developed a H_2O_2-HBr-EG polishing etchant that is stable for 24 h.

Experiments performed by Tomashik et al. [89] showed that well-polished surfaces of CdTe and $Cd_{0.22}Hg_{0.78}Te$ single crystals can also be obtained using H_2O_2-HCl-$C_4H_6O_6$ solutions with the following compositions (5:95:0), (5:75:20), and (11:89:0). The maximum dissolution rate of CdTe (3.3 μm/min) was observed in the solutions of H_2O_2-HCl-$C_4H_6O_6$ at the volume ratio of the components 9.5:85.5:5, i.e., in the solutions enriched by hydrochloric acid. The minimum dissolution rate (1.4 μm/min) was observed at the component ratio in the etching composition H_2O_2-HCl-$C_4H_6O_6$ = 6.5:83.5:10, i.e., in the solutions with the greatest quantity of the tartaric acid, when the dissolution rate decreases

almost to zero during the following increase of the tartaric acid quantity in the etchant.

The experiment showed that the physicochemical state of the surface of II-VI semiconductors after etching is as important a parameter of the used etchant as the etching rate or surface flatness. As a result of a detailed analysis of the surfaces of CdTe and CdZnTe using modern methods of analytical control, it was found that a layer rich in Te is formed on the surface of these semiconductors after etching in bromine-alcohol and iodine solutions [5]. The mechanism of formation of such a layer is usually explained as follows. Br_2 molecules present in a Br_2 solution are adsorbed on the crystal surface and react with Te^{2-} anions to form Br^- and Te^0 anions. Br^- anions oxidize Cd cations, which leads to the formation of soluble Cd bromides. Dimethyl Cd, which can also be formed as a result of interaction with the etchant components (methanol/butanol/ethylene glycol), is apparently a volatile substance. The thermodynamic probability of Te^{4+} formation is low due to the large free energy barrier. Neutral Te^0 are removed in the form of atoms and accumulate on the crystal surface. Due to the heterophasic nature of CdTe etching, the surface uniformity and stoichiometry change. Te-rich layer is prone to oxidation over time in air [60].

Te-rich surface is also formed as a result of the wet chemical etching of CdTe in an acidic solution. For example, $K_2Cr_2O_7$-HNO_3 etch produces TeO_2 on the CdTe surface. According to Tomashik et al. [89], films of the ternary compounds $CdTeO_3$ or Cd_2TeO_5, with exception of mechanical mixtures containing CdO and TeO_2, are formed most probably on the surface of CdTe and $Cd_xHg_{1-x}Te$ as the result of the chemical etching in water solutions of H_2O_2. It turned out that the solubility of the oxidation products strongly depends on the acidity, i.e., the composition of the film can be controlled by changing the pH value. Table 16.4 summarizes the results of XPS evaluation of CdZnTe samples after etching in different solutions. It is seen that lower values of the Te/(Cd + Zn) atomic ratio on as-received surfaces were observed in samples treated with I_2-methanol and KIO_3-KI-based solutions compared with Br_2-methanol solution. According to Ivanitska et al. [36], the thickness of Te oxide layer for (211)B

$Cd_{0.96}Zn_{0.04}Te$ surfaces treated in KIO_3-KI-lactic acid solutions is equal to ~1.7 nm.

Table 16.4 Results of XPS evaluation for (211)B CdZnTe samples for different surface treatments

Surface treatment	Te overall/(Cd + Zn) atomic ratio	Te oxide/Te elemental atomic ratio
I_2-methanol	1.8	1.4
Annealed 330 °C/1 min	1.0	0.7
Br_2-methanol	2.2	2.1
Annealed 330 °C/1 min	1.6	1.3
KIO_3-KI-lactic acid	1.9	1.1
Annealed 330 °C/1 min	1.0	0.5
KIO_3-KI-citric acid	1.8	1.4
Annealed 330 °C/1 min	1.0	0.4

Source: Data extracted from and Ivanitska et al. [36, 37]

It is important to note that the improvement in the performances of CdTe solar cells after etching in most works is associated with the formation of the Te-rich layer [86, 87]. In the presence of the Te-rich layer, an increase in open-circuit voltage and fill factor (FF) of the device is observed. The presence of Te-rich layer on the CdTe surface also contributes to the formation of more low-resistance contacts (read Chap. 17, Vol. 1). However, at the same time, it was found that the formation of a tellurium layer on the surface of CdTe can change the conductivity of the surface causing an increase in leakage current [22, 107], thus inducing noise in the system. Surface leakage current can be minimized by passivating the surface, either by forming a native oxide layer [106] on the surface or by the application of a dielectric layer [67]. Several wet and dry passivation techniques [65] exist for the formation of native oxide film, which is believed to be TeO_2 and proved to reduce the leakage current [28] significantly.

A clean stoichiometric surface that does not contain native oxides is also required for the epitaxial growth of HgCdTe on the surface of CdTe/CdZnTe substrates, which makes it necessary to use additional treatments to remove them. For example, alkaline etch such as KOH-MeOH and an aqueous solution of KOH or KOH + KCl can be used to remove

them [5]. In addition, it was found that long-term etching in KOH or KOH/KCl helps to restore the surface stoichiometry ([28]; Zázvorka et al. [106]) that was disturbed during etching in bromine-containing etchants. After such treatments the crystalline quality of CdTe surface is comparable to that of a cleaved one [28]. Hage-Ali et al. [31] showed that the Te-rich layer could be controlled by quenching the etch with methanol (mirror coating). The Te-rich layer and Te oxide-rich layers can also be removed by long soaking in 10% KCN solution, thus maintaining the surface stoichiometry. It has also been found that the tellurium excess can be desorbed by heating. Several publications have reported on heat treatment of CdTe in ultrahigh vacuum [37, 74, 93, 102]. Such treatments considerably influenced the structural perfection and electrophysical properties of the surface. As it is shown in Table 16.5, a stoichiometric CdTe surface was achieved directly after the short heating in vacuum for the surfaces etched in I_2-methanol and KIO_3-KI solutions. This is a significant difference from the annealed Br_2-methanol-treated surface. To remove the tellurium excess in this case, longer annealing or annealing at a higher temperature are required. For example, according to the results published by Waag et al. [93], to reduce the oxygen contamination at the CdTe surface below the detection limit, annealing at temperatures above 350 °C is required. Based on these results, it can be concluded that for applications where native oxide-free surfaces are required, the use of I_2-methanol and KIO_3-KI-based etchants is preferred [37].

It is important to note that during the etching of II-VI compounds, the surface can be enriched not only with tellurium, as is observed during etching of CdTe in solutions based on bromine and acids, but also with cadmium [16, 19]. Studies have shown that similar phenomena are observed during ZnSe etching [16–18, 20]. This is clearly seen in the etching results of CdTe and ZnSe samples in commonly used etchants, which are shown in Table 16.5. The results shown in Table 16.5 are graphically shown in Fig. 16.4.

Table 16.5 Effect of etching on the surface stoichiometry of CdTe and ZnSe

Etchant	Etchant composition	CdTe	ZnSe
		Te/Cd	Se/Zn
1	1% bromine in methanol	2.33	1.84

Etchant	Etchant composition	CdTe	ZnSe
		Te/Cd	Se/Zn
2	1 g of $K_2Cr_2O_7$ in 10 ml H_2SO_4 + 20 ml H_2O	–	1.21
3	Vacuum cleaved for CdTe and Ar^+ ion bombarded for ZnSe (ref. surfaces)	1.43	0.72
4	0.5 g of NaOH +0.5 g of $Na_2S_2O_3$ in 100 ml H_2O	–	0.69
5	Etchant 2 followed by etchant 4	0.41	0.68
6	Etchant 1 followed by a wash in hot NaOH solution (80–90 °C)	1.25	0.58
7	1 g of NaOH in 20 ml H_2O + l ml H_2O_2	–	0.57
8	Etchant I followed by hydrazine-hydrate	0.95	–

Source: Data extracted from Dharmadasa et al. [18]

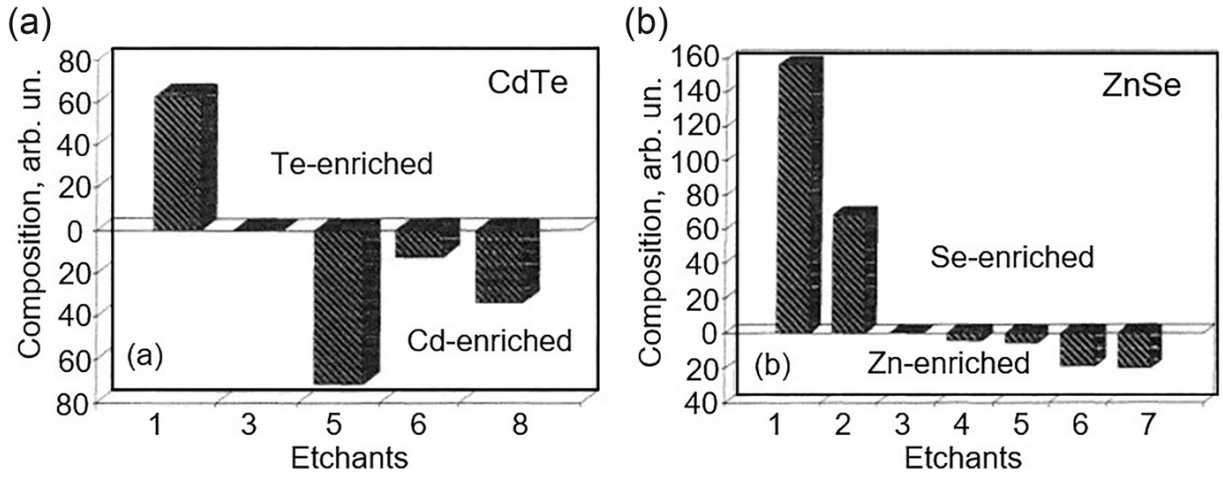

Fig. 16.4 Graphical representation of stoichiometry of chemically etched CdTe and ZnSe surfaces: (**a**) stoichiometry of chemically etched CdTe; (**b**) stoichiometry of chemically etched ZnSe. Vertical axis shows the stoichiometry, and horizontal axis shows the number corresponding to the chemical etchants listed in Table 16.5. When constructing these graphs, the vacuum cleavage surface for CdTe and the surface sputtered with Ar^+ ions for ZnSe were used as stoichiometric surfaces. It was assumed that the Cd/Te and Zn/Se ratios for these surfaces are equal to 1. (Adapted with permission from [18]. Copyright 1994: Taylor and Francis)

These results indicate that the stoichiometry of the II-VI semiconductor surface can be readily changed by chemical treatment [19]. In particular, bromine-containing or acid-based solutions preferentially remove the semiconductor cation, leaving a semiconductor anion-rich surface. As applied to ZnSe, this means that the surface treated in etchants 1 and 2 (Table 16.5) is rich in Se. This solution contains bromine and therefore

preferentially removes Zn from the material. The formation of an amorphous layer of Se on the ZnSe surface was also observed by Osinsky et al. [59] when etching ZnSe in a low-pH H_2SO_4:H_2O_2:H_2O solution. Osinsky et al. [59] showed that the Se layer can be dissolved in aqueous $(NH_4)_2S$ solution, resulting in a S-passivated surface that prevents ZnSe oxidation. If necessary, the S-passivated layer, which is volatile, can be desorbed by heating the sample to 300 °C. Osinsky et al. [59] found that this ZnSe treatment gives surfaces free of damage that is suitable for homoepitaxy. The efficiency of this process was demonstrated by the formation of 20 nm wide quantum nanowires of CdZnSe/ZnSe with good optical properties.

As can be seen from the previous results (see Fig. 16.4), in contrast, alkaline-based systems such as an etchant 5 preferentially remove the semiconductor anion to produce a semiconductor cation-rich surface, i.e., surfaces enriched with Zn (ZnSe) or Cd (CdTe). These effects should therefore have a strong influence on current transport across metal-semiconductor interfaces fabricated on these material surfaces. It is important that etchant 4 produces nearly stoichiometric surfaces as for polycrystalline and for MBE-grown ZnSe epilayers. Apparently, a similar change in the surface stoichiometry during etching should also be observed for other II-VI compounds, such as ZnTe and CdSe.

16.4.2 Dry Etching

The fabrication of II-VI semiconductor-based optical and electronic devices, especially those containing low-dimensional structures such as quantum well photodetectors, IR detector arrays, and quantum dot arrays, requires the use of high-resolution pattern definition and transfer techniques. While electron beam lithography is capable of 10–20 nm resolution, a high-resolution etching technique is required to transfer this pattern into the base material. Since the size of electronic devices and quantum structures is reduced to the nanometer scale, the need to create anisotropic profiles with good uniformity is of paramount importance in their fabrication, and therefore the development and use of dry etching methods is important.

In general, dry etching includes a range of different technologies, ranging from plasma etching to reactive ion etching (RIE) and ion milling.

An important difference between these technologies is the process pressure used in the etch chamber during etching (see Fig. 16.5).

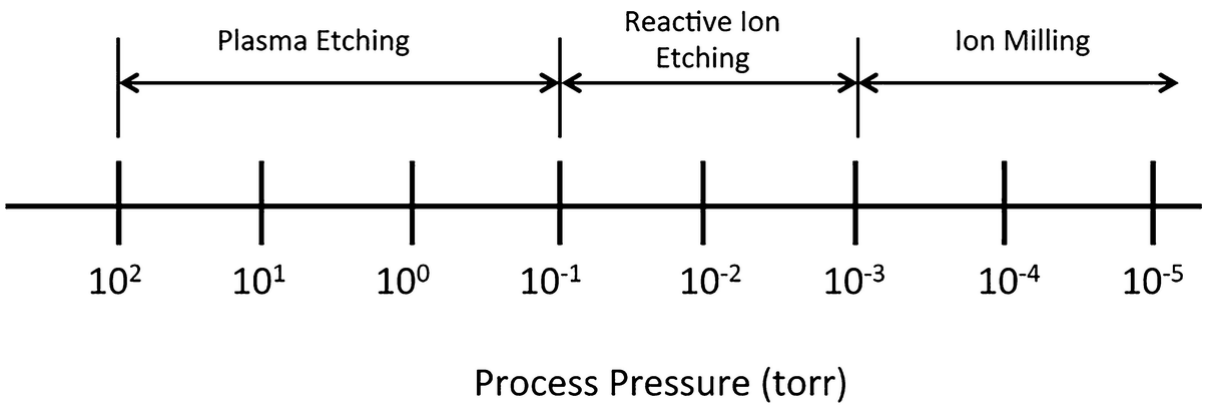

Fig. 16.5 Spectrum of dry etching processes and their relationship to the process pressure. (Reprinted from Huff M. [33]. Published 2021 by MDPI as open access)

Plasma etching is performed at comparatively higher process pressures (i.e., 10^{-1} to 10^{2} torr). Plasma components have relatively short mean free paths and experience multiple collisions before striking with the substrate. Because of these collisions, the etch particles collide with the substrate at different angles, making this form of dry etching more isotropic in nature. Plasma etching is mainly due to the chemical reactions of the plasma particles with the material to be etched, and not to physical effects. This means that like wet etching, plasma etching is not very directional, but this process tends to be material selective.

At the other end of the spectrum (Fig. 16.5), the process pressure is 10^{-3} torr or lower, and the mean free path of the particles is much longer, usually longer than the size of the reaction chamber. As a result, plasma particles do not experience collisions and are therefore able to maintain higher energy levels and transfer this kinetic energy to surface atoms when they collide with the substrate. This form of dry etching is called ion milling and relies solely on the mechanical bombardment of the substrate surface with plasma ions. Since the etch mechanism is solely physical, most materials have a similar etch rate, and consequently etch selectivity is poor. This means that ion milling is a highly anisotropic etching process with a minimum transverse etching rate. Typically, this method is used to etch materials that cannot be etched by other methods. The most common type of ion milling is ion sputtering with argon (Ar^{+}) or neon (Ne^{+}) ions, which are often used to clean the surface of semiconductors. However, this etching

method usually causes damage to the semiconductor (either a physical displacement of atoms or a change in near-surface stoichiometry). Therefore, in some cases, annealing after its use is required to restore the crystal lattice. Viswanathan et al. [92] used this method to clean the surface prior to back contact formation in the fabrication of CdTe solar cells. Gases utilized included N_2, Ar, and N_2/O_2. It has been established that in order to remove oxides from the CdTe surface and introduce minimal damage, which is required for the formation of low-resistance contacts, it is preferable to use etching in N_2 at low power levels and low O_2 concentration. At the other extreme, high power levels, long etch times, and low pressures are conditions that yield high-energy ions that cause significant damage to the surface of the CdTe. At higher levels of O_2 (20%), a barrier is present at back side, presumably due to the presence of oxides on the surface of CdTe. Nishimura and Aritome [55] have shown that Ar^+ sputtering can be used for fabrication of optical directional coupler.

At process pressures between 10^{-1} and 10^{-3} torr, reactive ion etching (RIE) occurs. RIE combines the properties of both plasma etching and ion milling. In RIE, plasma particles impart significant kinetic energy to substrate surface atoms to initiate etching, and chemically reacting particles react with substrate atoms, which are then desorbed from the surface as reaction by-products. As a result, RIE is more material specific than ion milling, while at the same time providing good anisotropy of etched features. RIE utilizes both the chemical and physical components of the etch mechanism to achieve anisotropic profiles, high etch rates, and dimensional control. RIE plasma is typically generated by applying 13.56 MHz radio frequency (RF) power between two parallel electrodes in a reactive gas.

A more detailed description of these methods and the devices used to implement them can be found in [33, 63]. Dry etching offers a number of advantages over wet chemical etching, including the anisotropic nature of the etching which is critical for dimensional control, improved uniformity, in situ processing, absence of surface tension effects, and smaller amounts of hazardous waste. However, at the same time, this process is longer and requires more sophisticated equipment.

There are two basic classes of gas mixtures used for dry etching of II-VI compounds. By analogy with III-V compounds, the first is based on

chlorine and bromine since group II and group VI chlorides and bromides are volatile at relatively low temperatures, as opposed to some stable fluorides. From the literature [97], it is speculated that tellurium fluoride is volatile and zinc fluoride is nonvolatile compound. Some of the gas mixtures used for dry etching of II-VI compounds include Cl_2 [69], $SiCl_2$ [26], BCl_3 [11, 40], BCl_3-Cl_2 [44], or Cl_2-CF_4 [41, 105] with additions of Ar.

According to the conducted abovementioned research, dry etching in chlorine and bromine gas mixtures provides the required high-quality etched films. However, Foad [26], who studied dry etching of ZnTe and ZnSe in $SiCl_2$ and CHF_3 plasma, found that SEM micrographs taken after CHF_3 etching and removal of the photoresist showed some evidence of redeposition on the etched surface, possibly polymer. The deposit was treated in O_2 plasma for 30 minutes, but even this etching did not remove all of the deposit. The same result was observed after etching in $SiCl_2$ plasma. Although the etch rate in $SiCl_2$ plasma was found to be about 20 nm/min, deposition was observed on the etched surface. It is possible that the problem with etching Zn-containing II-VI semiconductors is that there are very few volatile Zn compounds that can be produced in a successfully designed plasma etching chemistry and almost all of them are organometallics [97]. For example, the melting point of $ZnCl_2$ is 290 °C (see Fig. 16.6). It was also found that when etching ZnS:Mn and ZnMnS in BCl_3/Ar plasma, Mn had been detected on the surface [40]. The same effect was observed after etching of ZnS:Mn in Cl_2/CF_4/Ar plasma [41, 105]. Such behavior was explained as follows: it is well-known that some of the components for ZnS:Mn form low-volatile chloride such as $MnCl_2$ (melting point = 650 °C) (Fig. 16.6). Among them, $MnCl_2$ has extremely low-volatile compound. This fact supposes a negligible role of the thermal desorption of $MnCl_2$ during etching. At the same time, sulfur, which is formed in the form of sulfur chloride and fluoride, is easily removed from the surface due to their high volatility. As a result, Mn accumulates on the surface. Yun et al. [105] also established that Cl_2 gas is more effective than CF_4 gas for etching ZnS films due to the higher vapor pressure of chloride

compounds and higher ionization rate of Cl_2 gas. Contrarily, pure Cl_2 plasma could not etch Mn.

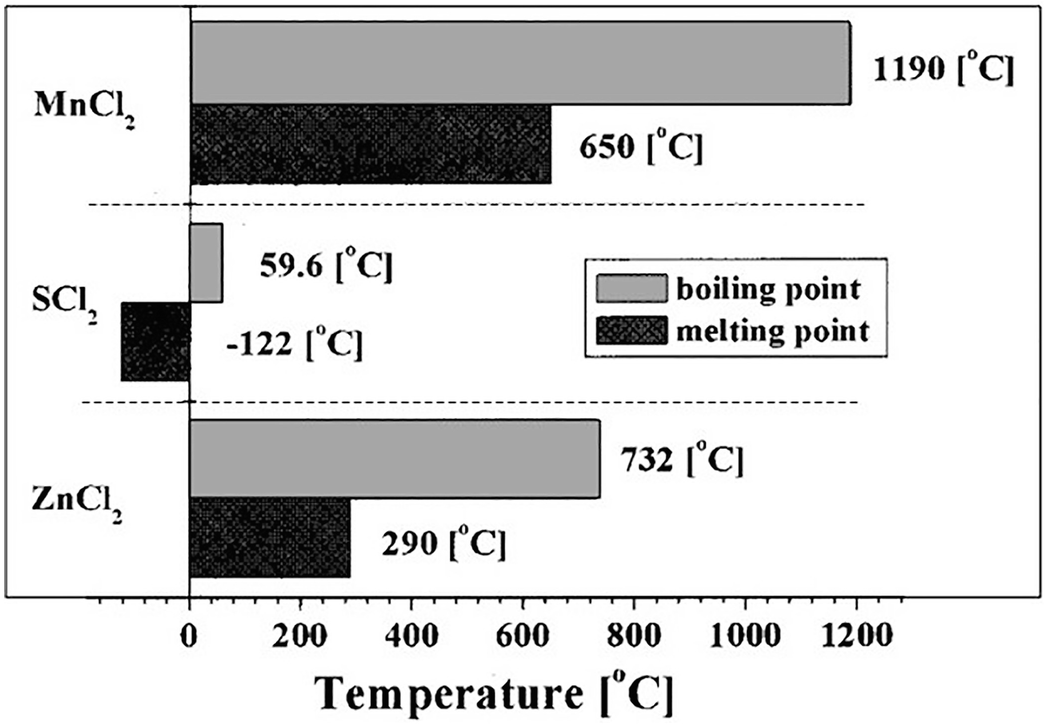

Fig. 16.6 Melting point and boiling point of ZnS:Mn etching byproducts. (Reprinted from [40]. Published 2008 by the Korean Institute of Electrical and Electronic Material Engineers as open access)

The second general class of gas mixture is based on methane [24, 25] or ethane [57] and hydrogen. It was found that RIE using CH_4/H_2 is a high-resolution dry etching technique which is suitable for a variety of II-VI semiconductors. In particular, using a mixture of methane and hydrogen, binary II-VI compound, e.g., ZnTe, ZnSe, CdTe, ZnS, and CdS, and ternary compounds, e.g., CdMnTe and ZnSSe, have been etched. This non-chlorinated mixture showed controlled smooth and highly anisotropic etching of all II-VI semiconductors. The most vertical etching and smooth surfaces were obtained for the 1:8 mixture of CH_4/H_2. The etch rates and the anisotropy factors estimated at the optimum conditions are presented in Table 16.6. During etching, the flow rates of hydrogen and methane were 40 and 5 sec, respectively, and the total pressure was in the range of 22–25 mTorr. The anisotropy factor was defined as [1- (horizontal etch rate)/(vertical etch rate)]. As for the change in the surface properties of II-VI compounds, XPS analysis of the etched surfaces showed no change in

the binding of the zinc, but there was reduction in the tellurium and selenium oxide over the range of the escape depth of the photoelectrons (~3 nm) [24].

Table 16.6 The etch rates and anisotropy factors for the II-VI semiconductors

Material	Thickness (μm)	Source of material	Etch rate (nm/min)	Anisotropy factor
(100) ZnTe	1–2	MOCVD	72	0.91
(100) ZnSe	0.53	MOCVD	34	~1
(100) ZnSSe	>3	MOCVD	25	0.89
(111) CdTe	Bulk	Single crystal	72	0.92
CdMnTe	1.98	MOCVD	41	0.91
ZnS	Bulk	Polycrystalline	160	0.85
CdS	Bulk	Polycrystalline	115	0.88

Source: Reprinted with permission from [24]. Copyright 1992: IOP

It is important to note that the use of CH_4-based gas mixture gives the smoothest surface of II-VI compounds compared to etching using H_2 [39] or Ar/H_2 [79] plasma. However, some papers note that the use of gases, such as methane (CH_4), can cause hydrocarbon polymer deposition on the sidewall of a plasma reactor and the etched film [39]. To solve this problem, Keller et al. [39] proposed the use of a new technique for dry etching II-VI material that involves the addition of N_2 to the $CH_4/H_2/Ar$ process gases. Keller et al. [39] using this technique prepared CdZnTe substrates with excellent surface properties for a subsequent MBE growth of HgCdTe.

Acknowledgments

G.K. is grateful to the State Program of the Republic of Moldova (project 20.80009.5007.02) for supporting his research.

References

1. Ablekim T, Swain SK, Yin WJ, Zaunbrecher K, Burst J, Barnes TM et al (2017) Self-compensation in arsenic doping of CdTe. Sci Rep 7:1–9
2. Al-Achkar M, Scott CG (1994) Influence of ion implantation of the surface characteristics of polycrystalline CdS layers. Surf Rev Lett 1(4):665–668

3. Amith A (1978) Thickness dependence of structural and electrical properties of CdS films for solar cells. J Vac Sci Technol 15(2):353
4. Awni RA, Li DB, Grice CR, Song Z, Razooqi MA, Phillips AB et al (2019) The effects of hydrogen iodide back surface treatment on CdTe solar cells. Sol RRL 3:1800304
5. Bastola E, Alfadhili FK, Phillips AB, Heben MJ, Ellingson RJ (2019) Wet chemical etching of cadmium telluride photovoltaics for enhanced open-circuit voltage, fill factor, and power conversion efficiency. J Mater Res 34:3988–3997
6. Chadi DJ (1999) Predictor of p-type doping in II-VI semiconductors. Phys Rev B 59(23):15181–15183
7. Chadi DJ (1994) The problem of doping in II-VI semiconductors. Annu Rev Mater Sci 24:45–62
8. Chandramohan S, Kanjilal A, Sarangi SN, Majumder S, Sathyamoorthy R, Hong C-H, Som T (2010) Effect of substrate temperature on implantation doping of Co in CdS nanocrystalline thin films. Nanoscale 2:1155–1159
9. Chavez-Urbiola IR, Pintor-Monroy MI, Willars-Rodriguez FJ, Vorobiev YV, Ramírez-Bon R, Quevedo-Lopéz MA (2019) Effects of aluminum doping upon properties of cadmium sulfide thin films and its effect on ITO/CdS:Al/NiO_X/Ni/Au diodes. J Appl Phys 126:115702
10. Chu TL, Chu SS, Ang ST (1988) Electrical properties of CdS/CdTe heterojunctions. J Appl Phys 64:1233
11. Clausen EM Jr, Craighead HG, Tamargo MC, de Miguel JL, Schiavone LM (1988) Etching and cathodoluminescence studies of ZnSe. Appl Phys Lett 53:690
12. Colak S (1993) Devices and applications of II-VI compounds. In: Mukesh J (ed) II—VI Semiconductor Compounds. World Scientific, pp 397–426
13. Desnica VU (1998) Doping limits in II-VI compounds – challenges, problems and solutions. Prog. Crystal Growth Charact 36(4):291–357
14. Desnica UV (1998) Wide band-gap II–VI compounds—can efficient doping be achieved? Vacuum 50(3–4):463
15. De Wit AR, Kelly JJ (1991) Etching of CdS in aqueous halogen solutions. Ber Bunsenyes Phys Chem 95(6):670–674
16. Dharmadasa IM (1998) Recent developments and progress on electrical contacts to CdTe, CdS and ZnSe with special reference to barrier contacts to CdTe. Prog Crystal Growth Charact 36(4):249–290
17. Dharmadasa IM, Blomfield CJ, Coratger R, Ajustron E, Beauvillain J, Simpson J et al (1996) Microscopic and macroscopic investigation of electrical contacts to n type and p type ZnSe. Mater Sci Technol 12(1):86–89

18. Dharmadasa IM, Blomfield CJ, Gregory GE, Young J (1994) Influence of chemical etching on metal contacts to 11-VI compounds: CdTe and ZnSe. Intern J Electron 76(5):961–967
19. Dharmadasa IM, Thorton JH, Williams RH (1989) Effects of surface treatments on Schottky barrier formation at metal n-type CdTe contacts. Appl Phys Lett 54:137–139
20. Dharmadasa IM, Blomfield CJ, Gregory GE, Cavenett BC, Prior KA, Simpson J (1964) Microscopic and macroscopic investigation of electrical contacts to n-ZnSe. Surf Interface Anal 21:718–723
21. Donnelly JP, Foyt AG, Hinkley ED, Lindley WT, Dimmock JO (1968) Type conversion and p-n junctions in n-CdTe produced by ion implantation. Appl Phys Lett 12:303
22. Duff MC, Hunter DB, Burger A, Groza M, Buliga V, Black DR (2008) Effect of surface preparation technique on the radiation detector performance of CdZnTe. Appl Surf Sci 254(9):2889–2892
23. Fanhrenbruch AL (1977) Il-VI compounds in solar energy conversion. J Crystal Growth 39:73–91
24. Foad MA, Wilkinson CDW, Dunscomb C, Williams RH (1992) CH_4/H_2: a universal reactive ion etch for Il-VI semiconductors? Appl Phys Lett 60(20):2531–2533
25. Foad MA, Smart AP, Watt M, Sotomayor Torres CM, Wilkinson CDW (1991) Reactive ion etching of II-VI semiconductors using a mixture of methane and hydrogen. Electron Lett 27(1):73–75
26. Foad MA (1990) Characterisation of Dry Etching Damage in III-V and II-VI Semiconductors. PhD thesis, University of Glasgow
27. Fu DJ, Lee JC, Chou SW, Park CS, Panin GN, Kang TW, Fan XJ (2003) Ferroelectricity in Mn-implanted CdTe. Appl Phys Lett 83:2214–2216
28. García-García J, González-Hernández J, Mendoza-Alvarez JG, Cruz EL, Contreras-Puente G (1990) Photoluminescence characterization of the surface layer of chemically etched CdTe. J Appl Phys 67(8):3810–3814
29. Gautam G, Thilini KE, Andrew JY, Tula RP (2019) Absorption enhancement by transition metal doping in ZnS. Mater Res Express 6:126550
30. Gavrishchuk EM, Timofeev OV, Pogorelko AA, Suchkov AI (2004) Effect of polishing conditions on the optical properties of Zinc Selenide surfaces. Inorg Mater 40(3):217–220
31. Hage-Ali M, Stuck R, Saxena AN, Siffort P (1979) Studies of CdTe surfaces with secondary ion mass spectrometry, Rutherford backscattering and ellipsometry. Appl Phys Lett 19:25–33
32. Hocheon Y, Keun H, Hasan RA, Seongjae C (2021) Recent advances in electrical doping of 2D semiconductor materials: methods, analyses, and applications. Nano 2021(11):832
33. Huff M (2021) Recent advances in reactive ion etching and applications of high-aspect-ratio microfabrication. Micromachines 12:991

34. Hughes WC, Boney C, Johnson MAL, Cook JW, Schetzina JF (1997) Surface preparation of ZnSe substrates for MBE growth of V-VI light emitters. J Cryst Growth 175(176):546–551
35. Hwang HL, Hsu KYJ, Ueng HY (1996) Fundamental studies of p-type doping of CdTe. J Cryst Growth 161:73–81
36. Ivanitska VG, Moravec P, Tomashik VM, Masek K, Tomashik ZF, Franc J et al (2013) A slightly oxidizing etchant for polishing of CdTe and CdZnTe surfaces. J Electron Mater 42:3059–3065
37. Ivanitska VG, Moravec P, Franc J, Tomashik VM, Tomashik ZF, Masek K et al (2011) Chemical polishing of CdTe and CdZnTe in Iodine–Methanol etching solutions. J Electron Mater 40(8):1802–1808
38. Ivanits'ka V, Moravec P, Franc J, Tomashik Z, Feychuk P, Tomashik V et al (2007) Chemical etching of CdTe in aqueous solutions of H_2O_2–HI-citric acid. J Electron Mater 36:1021–1024
39. Keller RC, Zimmerman H, Seelmann-Eggebert M, Richter HJ (1997) Surface cleaning and etching of CdZnTe and CdTe in H_2/Ar, CH_4/H_2/Ar, and $CH_4/H_2/N_2$/Ar electron cyclotron resonance plasmas. J Electron Mater 26:542–551
40. Kim G-H, Woo J-C, Kim K-T, Kim D-P, Kim C-I (2008) Etching properties of ZnS:Mn thin films in an inductively coupled plasma. Trans Electric Electron Mater 9(1):1–5
41. Kim D-P, Kim C-I, Kwon K-H (2004) Etching properties of ZnS thin films in Cl_2/CF_4/Ar plasma. Thin Solid Films 459:131–136
42. Kraft C, Brömel A, Schönherr S, Hädrich M, Reislöhner U, Schley P et al (2011) Phosphorus implanted cadmium telluride solar cells. Thin Solid Films 519:7153–7155
43. Kutra J, Sakalas A, Zindulis A, Kapsukas VV (1978) Electrical properties of p-CdSe layers obtained by the ion implantation of selenium. Thin Solid Films 55:421–425
44. Legge M, Bacher G, Bader S, Kummell T, Forchel A, Nurnberger J et al (2001) Selective ultrahigh vacuum dry etching process for ZnSe-based II–VI semiconductors. J Vac Sci Technol B 19(3):692–694
45. Ma X (2011) Study of the p-type doping properties of ZnS nanocrystals. J Nanomater 2011:952616
46. Mariano AN, Hanneman RE (1963) Crystallographic polarity of ZnO crystals. J Appl Phys 34:384
47. McCandless BE, Buchanan WA, Thompson CP, Sriramagiri G, Lovelett RJ, Duenow J et al (2018) Overcoming carrier concentration limits in polycrystalline CdTe thin films with in situ doping. Sci Rep 8:1–13
48. Metzger WK, Grover S, Lu D, Colegrove E, Moseley J, Perkins CL et al (2019) Exceeding 20% efficiency with in situ group V doping in polycrystalline CdTe solar cells. Nat Energy 4:837–845

49. Mirov S, Fedorov V, Moskalev I, Mirov M, Martyshkin D (2013) Frontiers of mid-infrared lasers based on transition metal doped II-VI semiconductors. J Lumin 133:268–275
50. Mondal P, Chakraborty S, Grandhi GK, Viswanatha R (2020) Copper doping in II-VI semiconductor nanocrystals: single-particle fluorescence study. J Phys Chem Lett 11:367–372
51. Moravec P, Tomashik Z, Ivanits'ka V., Tomashik V., Franc J., Mašek K., Höschl P. (2012) Slow-polishing iodine-based etchant for CdTe and CdZnTe single crystals. J Electron Mater 41:2838–2845
52. Moravec P, Ivanits'ka V, Franc J, Tomashik Z, Tomashik V, Mašek K et al (2009) Chemical interaction of CdTe and CdZnTe with aqueous solutions of H_2O_2-HI-tartaric acid. J Electron Mater 38:1645–1651
53. Nagamani K, Prathap P, Lingappa Y, Miles RW, Reddy KTR (2012) Properties of Al-doped ZnS films grown by chemical bath deposition. Phys Procedia 25:137–142
54. Nair RM, Khadar MA, Kumar SS, Rajalakshmi M, Arora AK, Nair KGM (2007) Effect of N^+ ion implantation on the optical properties of nanostructured CdS thin film prepared by CBD technique. Nucl Instr Meth Phys Res B 254:131–138
55. Nishimura T, Aritome H (1990) Fabrication of an optical directional coupler of CdTe by electron beam lithography and ion etching. J Quantum Electron QE-16(12):1337–1340
56. Norris DJ, Efros AL, Erwin SC (2008) Doped nanocrystals. Science 319:1776
57. Ohtsuka K, Imaizumi M, Sugimoto H, Isu T, Endoh Y (1992) Reactive ion etching of ZnSe by gas mixture of ethane and hydrogen. Appl Phys Lett 60:3025
58. Oldekop E, Hermann S, Sulzer G, Niedermeyer F, Wienecke M, Zeitz W-D (1996) Boron implantation into CdTe. J Cryst Growth 159:359–362
59. Osinsky A, Qiu Y, Mahan J, Temkin H, Gurevich SA, Nesterov SI et al (1997) Novel wet chemical etch for nanostructures based on II-VI compounds. Appl Phys Lett 71(4):509–511
60. Özsan ME, Sellin PJ, Veeramani P, Hinder SJ, Monnier MLT, Prekas G et al (2010) Chemical etching and surface oxidation studies of cadmium zinc telluride radiation detectors. Surf Interface Anal 42(6–7):795–798
61. Pandey A, Sarma DD (2016) Recent advances in manganese doped II-VI semiconductor quantum dots. Zeitschrift Anorg Allg Chem 642:1331–1339
62. Pautrat JL, Bensahel D, Katircioglu B, Pfister JC, Revoil L (1976) Ion implantation in ZnTe: defect generation, migration and annealing. Radiat Eff 30:107–121
63. Peatron SJ (1994) Reactive ion etching of III-V semiconductors. Intern J Modern Phys B 8(14):1781–1876
64. Popovych VD, Böttger R, Heller R, Zhou S, Bester M, Cieniek B et al (2018) Heavy doping of CdTe single crystals by Cr ion implantation. Nuclear Inst Methods Phys Res B 419:26–31

65. Prettyman TH, Hoffbauer MA, Rennie AR, Cook S, Gregory C, George MA et al (1999) Performance of CdZnTe detectors passivated with energetic oxygen atoms. Nucl Instruments Methods Phys Res Sect A 422(1–3):179–184
66. Qiu J, DePuydt JM, Cheng H, Haase MA (1989) Heavily doped *p*-ZnSe:N grown by molecular beam epitaxy heavily doped *p*-ZnSe:N grown by molecular beam epitaxy. Appl Phys Lett 59:2992
67. Ruzin A, Nemirovsky Y (1997) Passivation and surface leakage in CdZnTe spectrometers. Appl Phys Lett 71(15):2214–2215
68. Sagar A, Lehman W, Faust JW (1968) Etchants for ZnSe. J Appl Phys 39:5336
69. Saitoh T, Yokogawa T, Narusawa T (1990) Reactive ion beam etching of ZnSe and ZnS epitaxial films using Cl_2 electron cyclotron resonance plasma. Appl Phys Lett 56:839
70. Sangsu K, Deok K, Jinki H, Abdallah E, Alima M, Jung-Yeol Y et al (2022) Performance comparison of CdTe:Na, CdTe:As, ands CdTe:P single crystals for solar cell applications. Materials 15:1408
71. Sanjeev KR, Veeravazhuthi V, Muthukumarasamy N, Thambidurai M, Vishnu SD (2015) Effect of nickel doping on structural and optical properties of ZnS nanoparticles. Superlattice Microst 86:552–558
72. Sankar N, Ramachandrana K, Sanjeeviraja C (2002) Growth and characterization of ZnSe and phosphorus-doped ZnSe single crystals. J Cryst Growth 235:195–200
73. Sarlund J, Ritala M, Leskelä M, Siponmaa E, Zilliacus R (1996) Characterization of etching procedure in preparation of CdTe solar cells. Sol Energy Mater Sol Cells 44:177–190
74. Shaw JL, Brillson LJ, Sivananthan S, Faurie JP (1990) Deep level photoluminescence spectroscopy of CdTe epitaxial layer surfaces. Appl Phys Lett 56:1266
75. Shiraki Y, Shimada T, Komatsubara KF (1972) Ion implantation of nitrogen into Cadmium Sulfide. J Appl Phys 43:710
76. Shirland FA (1980) Etching of CdS films. Solar Cells 1:183–197
77. Simashkevich AV, Gorchak LV, Gilan EV, Sushkevich KD (1989) Study of p-n junctions fabricated by Phosphorus-ion implantation into CdTe. Phys Status Solidi A 112:305–309
78. Sivaraman T, Narasimman V, Nagarethinam VS, Balu AR (2015) Effect of chlorine doping on the structural, morphological, optical and electrical properties of spray deposited CdS thin films. Prog Nat Sci Mater Int 25:392–398
79. Stoltz AJ, Benson JD, Thomas M, Boyd PR, Martinka M, Dinan JH (2002) Development of a high-selectivity process for electron cyclotron resonance plasma etching of II-VI semiconductors. J Electron Mater 31(7):749–753
80. Stratiichuk IB, Tomashik ZF, Tomashik VM (2005) Dissolution behavior of undoped and doped CdTe with H_2O_2–HBr–Tartaric acid solutions. Fiz Khim Tverd Tela 6(1):99–103

81. Stratiichuk IB, Tomashik VN, Tomashik ZF, Feichuk PI (2004a) Dynamic chemical polishing of CdTe based semiconductor materials with H_2O_2–HBr–Tartaric acid solutions. Nov Tekhnol 3(6):29–33
82. Stratiichuk IB, Tomashik ZF, Tomashik VN, Feichuk PI (2004b) Doping effect on the dissolution behavior of Cadmium Telluride in H_2O_2–HBr solutions. Zh Neorg Khim 49(12):2095–2100
83. Strehlow WH (1969) Chemical polishing of II-VI compounds. J Appl Phys 40(7):2928–2932
84. Sullivan MV, Bracht WR (1967) Chemical polishing of Cadmium Sulfide. J Electrochem Soc 114:295
85. Tomashyk VM, Kravtsova AS, Tomashyk ZF, Stratiychuk IB, Galkin SM (2013) Optimization of conditions for treatment of ZnSe crystal surfaces by chemical etching. Semicond Phys Quantum Electron Optoelectron 16(2):140–145
86. Tomashik VN, Kravtsova AS, Tomashik ZF, Stratiichuk IB, Galkin SN (2013) Dynamic chemical polishing of undoped and doped ZnSe crystals with H_2O_2–HBr–H_2O solutions. Inorg Mater 49(10):971–974
87. Tomashik ZF, Tomashik VN, Gnativ II, Stratiichuk IB (2006) Etching behavior of CdTe and $Zn_xCd_{1-x}Te$ single crystals in aqueous H_2O_2–HBr–lactic acid solutions. Inorg Mater 42(8):859–862
88. Tomashik VN, Stratiichuk IB, Tomashik ZF, Feichuk PI (2005) Chemical etching of undoped and doped CdTe with H_2O_2–HBr–citric acid solutions. Voprosy Khim Khim Tekhnol 1:43–46
89. Tomashik ZF, Lukiyanchuk EM, Tomashik VM (2004) Chemical dynamic polishing CdTe and $Cd_xHg_{1-x}Te$ single crystals by using solutions of H_2O_2–HCl–tartaric acid system. Semicond Phys Quant Electron Optoelectron 7(4):452–455
90. Tonnies D, Bacher G, Eisert D, Forchel A (1994) Ion-implantation induced interdiffusion in CdTe/CdMgTe quantum wells. Appl Phys Lett 65(25):3194–3196
91. Tuck B (1975) Review. The chemical polishing of semiconductors. J Mater Sci 10:321–339
92. Viswanathan V, Morel DL, Ferekides CS (2005) RF Sputter etch as a surface cleaning process for CdTe solar cells, In: Conference Record of the Thirty-first IEEE Photovoltaic Specialists Conference, 03-07 January 2005, Lake Buena Vista, FL, USA, p. 8487512
93. Waag A, Wu YS, Bicknell-Tassius RN, Landwehr G (1989) Investigation of CdTe surfaces by x-ray photoelectron spectroscopy. Appl Phys Lett 54:2662
94. Walukiewicz W (2001) Intrinsic limitations to the doping of wide-gap semiconductors. Physica B 302–303:123–134
95. Warekois EP, Lavine MC, Mariano AN, Gatos HC (1962) Crystallographic polarity in the II-VI compounds. J Appl Phys 33:690

96. Watthage SC, Phillips AB, Liyanage GK, Song Z, Gibbs JM, Alfadhili FK et al (2018) Selective cd removal from CdTe for high-efficiency Te back-contact formation. IEEE J Photovolt 8:1125
97. Weast RC (ed) (1990) Handbook of chemistry and physics, 70th edn. CRC Press, Ohio
98. Wei SH, Zhang SB (2002) Chemical trends of defect formation and doping limit in II–VI semiconductors: the case of CdTe. Phys Rev B 66:155211
99. Werthen JG, Haring JP, Fahrenbruch AL, Bube RH (1983) Surface effects on metal/CdTe junctions and CdTe heterojunctions. J Phys D Appl Phys 16(12):2391–2404
100. Wiecek T, Popovich V, Bester M, Kuzma M (2017) Ion implantation of CdTe single crystals. EPJ Web of Conferences 133:03002
101. Wu M, Wei Z, Zhao W, Wang X, Jiang J (2017) Optical and magnetic properties of Ni doped ZnS diluted magnetic semiconductors synthesized by hydrothermal method. J Nanomater 2017:1603450
102. Wu YS, Becker CR, Waag A, Schmiedl R, Einfeldt S, Landwehr G (1993) Oxygen on the (100) CdTe surface. J Appl Phys 73:7385–7388
103. Yakushev M.V., Martin R.W., Holman D., Pilkington R.D., Hill A.E., Tomlinson R.D., et al. (2000) Effects of D^+ implantation on the properties of CdS/CIGS and ZnO/CdS/CIGS heterostructures, In: Conference Record of the 28th IEEE Photovoltaic Specialists Conference, 15–22 Sept. 2000, Anchorage, AK, USA, p. 7004966
104. Yu KM, Ager JW III, Bourret ED, Walker J, Walukiewicz W (1994) High dose Cl implantation in ZnSe: impurity incorporation and radiation damage. J Appl Phys 75(3):1378–1383
105. Yun SJ, Kwon K-H, Lee Y-E, Kim CI (2004) Etching characteristics of Manganese-doped Zinc Sulfide film using Cl_2/CF_4 inductively coupled plasma. Jpn J Appl Phys 43(5A):2716–2720
106. Zázvorka J, Franc J, Statelov M, Pekarek J, Veis M, Moravec P, Masek K (2016) Optical and electrical study of CdZnTe surfaces passivated by KOH and NH_4F solutions. Appl Surf Sci 389:1214–1219
107. Zha G, Jie W, Tan T, Li P (2007) The surface leakage currents of CdZnTe wafers. Appl Surf Sci 253(7):3476–3479
108. Zia R, Saleemi F, Naseem S, Kayani Z (2015) Study the efficiency of single crystal CdTe/ZnCdS solar cell at various temperatures and illumination levels. Energy Rep 1(1):58–61

OceanofPDF.com

© The Author(s), under exclusive license to Springer Nature Switzerland AG 2023
G. Korotcenkov (ed.), *Handbook of II-VI Semiconductor-Based Sensors and Radiation Detectors*
https://doi.org/10.1007/978-3-031-19531-0_17

17. II-VI Wide-Bandgap Semiconductor Device Technology: Schottky Barrier, Ohmic Contacts, and Heterostructures

Ghenadii Korotcenkov[1] ✉, Nikolay P. Simonenko[2], Fedor S. Fedorov[3] and Victor V. Sysoev[4]

(1) Department of Physics and Engineering, Moldova State University, Chisinau, Moldova
(2) Kurnakov Institute of General and Inorganic Chemistry, Russian Academy of Sciences, Moscow, Russia
(3) Laboratory of Nanomaterials, Skolkovo Institute of Science and Technology, Moscow, Russia
(4) Yuri Gagarin State Technical University of Saratov, Saratov, Russia

Keywords Aging – Exchange reactions – Leakage current – Metal diffusion – Oxygen diffusion – Heterojunction – Advantages – Energy-band diagram – Metal-semiconductor junctions – Schottky diodes – Bandgap – Electronegativity – Fermi level pinning – Formation – Ideality factor – Potential barrier – Schottky barrier – Surface states – Work function – Surface – Air-cleaved – Cd-rich – Chemically etched – Native oxides – Se-rich – Te-rich layer – Vacuum-cleaved – Ohmic contacts – Annealing – Approaches – Doping – Etching – n-CdS – n-ZnS – p-CdTe – Tunneling effect – ZnSe

17.1 Introduction

Due to the difficulty of doping II-VI compounds and forming p-n junctions on their basis, the use of heterojunctions, i.e., structures formed by various semiconductors, and Schottky barriers, i.e., metal-semiconductor contacts,

is one of the main approaches used in the development of various devices based on these compounds.

Metal-semiconductor junctions can be classified as ohmic or rectifier contacts (frequently called as Schottky diodes or Schottky barriers), depending on the relative work function difference between a metal and a semiconductor including its nature of conductivity, p-type or n-type. An ohmic contact works like a conventional resistor with a linear I-V characteristic, while the rectifying one behaves like a p-n junction diode to yield a current-voltage curve, typical for such junctions. However, unlike a p-n diode, the current transfer via a metal-semiconductor junction always involves only the major charge carriers, electrons for n-type semiconductors and holes for p-type ones. Schottky barriers are useful for application in transistors, solar cells, photo- and radiation detectors, and materials which cannot easily be made of p-type or n-type one. It is believed that the contacts become rectifying when the height of the potential barrier is more than a few kT. However, the numerous experiments show that at room temperature the contacts begin to exhibit an ohmic behavior at a potential barrier with a height of less than 0.3 eV.

17.2 Schottky Diodes

A Schottky diode is ordinarily fabricated with an n-type semiconductor when a metal is deposited on the top of semiconductor under the condition that the metal has a higher work function (i.e., $\Phi_m > \Phi_s$, as depicted in Fig. 17.1). When the two materials are brought together, electrons diffuse into the metal from the semiconductor devoid of its interface layer by majority charge carriers, i.e., electrons. This equally corresponds to an equal and opposite (negative) charge on the surface of the metal. Since the Fermi levels of both materials are equalized in stationary conditions, the conduction and valence energy bands of the semiconductor at the interface with the metal must be shifted by an amount caused by the difference between the work functions of the metal and the semiconductor. In the case of an n-type semiconductor, the electrostatic potential rises that leads to appearance of a potential barrier in the interface, frequently called as the Schottky barrier. The height of an ideal Schottky barrier at the semiconductor-metal junction can be determined as Eq. (17.1) [74], where χ is an “electron affinity” of the semiconductor.

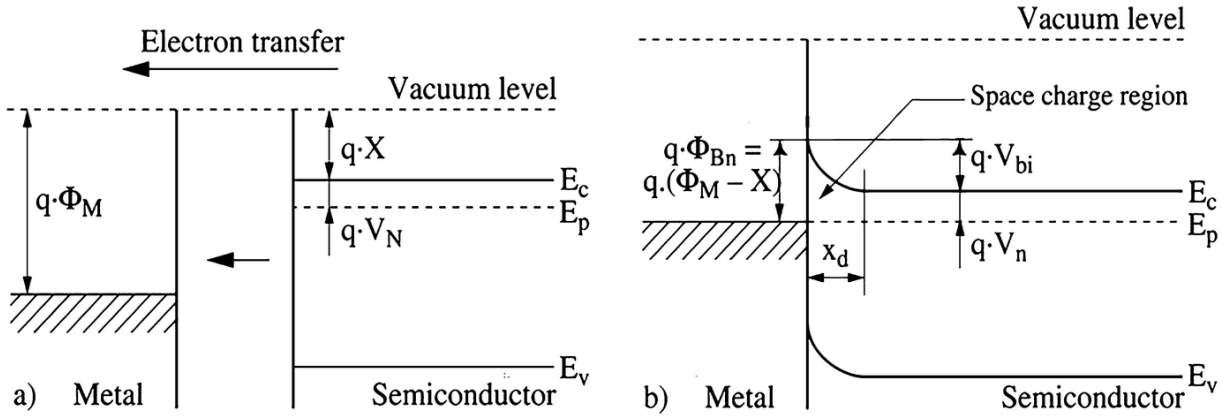

Fig. 17.1 (**a**, **b**) Formation of a Schottky barrier at the contact of a metal and a n-type semiconductor

On the contrary, for a p-type semiconductor, a rectifying contact will be formed when a metal with a lower work function is deposited on the surface of the semiconductor (i.e., $\Phi_m < \Phi_s$).

$$\Phi_b = \Phi_m - \chi \tag{17.1}$$

However, it should be noted that such a behavior, when the potential barrier is defined by the work function of metal, is typical only in case of ideal Schottky barriers that do not contain surface states at the interface. When a large concentration of such bandgap states appears, a completely different situation may arise. In this situation, the Fermi level could be pinned at these states and the height of the potential barrier would cease to depend on metal properties. If the concentration of surface states is insufficient to pin the Fermi level, then the work function can influence the height of the potential barrier, but not as strong as in the case of an ideal surface. According to the theory of linear interface potential, the effect of surface states on the barrier height can be expressed using the expression of Eq. (17.2):

$$\partial \Phi_{bS} = S \cdot \partial \Phi_m, \tag{17.2}$$

where S is a parameter that determines the degree of influence of surface states on the height of the potential barrier and depends both on the type of semiconductor and on the surface treatment used. For an ideal metal-semiconductor interface $S = 1$, while $S = 0$ at the Fermi level pinning by the interface states [32, 56, 80]. Let us now consider the properties of Schottky barriers designed from II-VI compounds in more detail.

17.2.1 II-VI Semiconductor-Based Schottky Barriers

Studies have shown that the major feature of Schottky barriers prepared with II-VI compounds is a significant difference in the behavior of contacts prepared on air-cleaved or vacuum surfaces and chemically treated ones. For cleavage surfaces, the height of the potential barrier is primarily defined by the work function of the metals, and this dependence is strengthened with increasing bond ionicity in the compound. For example, in case of a CdTe compound, where the covalent nature of the bond prevails, S does not exceed 0.2, while for ZnS and CdS compounds, where the ionic nature of the bond predominates, S approaches 1.0 [6, 76]. In other words, CdTe has a dependence characteristic for III-V compounds, while ZnS and CdS exhibit a dependence similar to metal oxide ones. The graphs illustrating these dependencies are shown in Fig. 17.2.

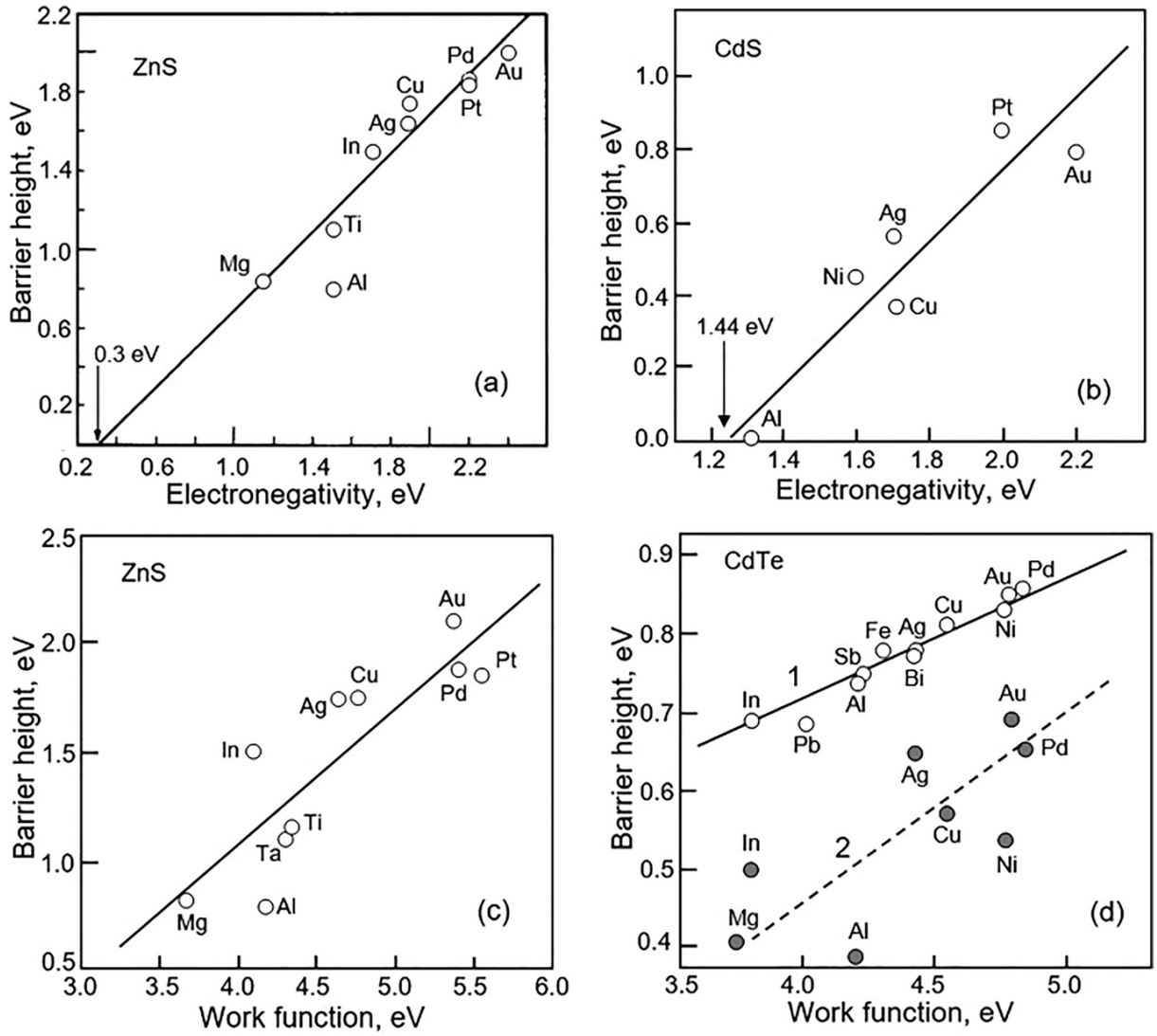

Fig. 17.2 (**a**, **b**) Barrier heights of various metals on (**a**) n-ZnS and (**b**) n-CdS as a function of the electronegativity of the metal. Contacts were formed by deposition of a layer of the desired metal on a vacuum-cleaved surface of single crystals (adapted with permission from [6]. Copyright 1965: AIP Publishing); (**c**) dependence of the height of the Schottky barrier formed on the vacuum-cleaved n-ZnS surface on the metal work function (data extracted from Adachi S. [3]). (**d**) Barrier height at the interface M-n-CdTe: 1, chemically etched samples (data extracted from [67]); 2, vacuum-cleaved samples (data extracted from [63])

For the chemically prepared surfaces of II-VI compounds, the situation is somewhat different. Depending on the surface treatment, one can observe both the influence of the work function of metals on the potential barrier height, as displayed in Fig. 17.3 [7], and Fermi level pinning, where the height of potential barrier is not defined by the work function of the deposited metal; see Fig. 17.4 [50]. In the last case, the height of the barrier matures entirely from the bandgap of the semiconductor (Fig. 17.5) and the type of defects generated at the interface.

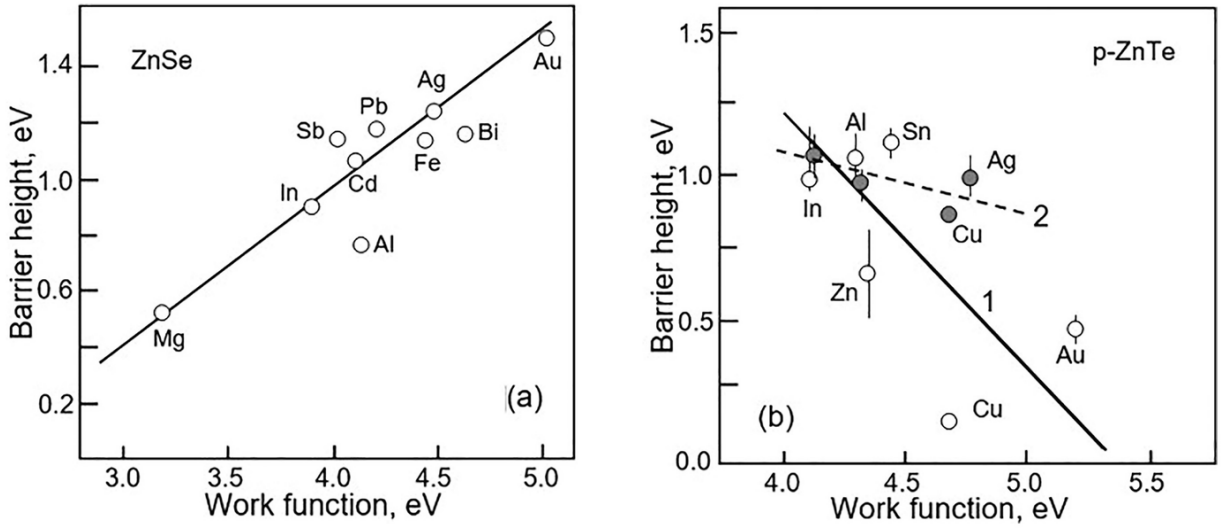

Fig. 17.3 (**a**) Barrier height values for metal-n-ZnSe Schottky contacts plotted against the values of metal work function. Single-crystal n-ZnSe was etched in a 1% solution of bromine in methanol for 5 min, followed by immersion for 0.5 min in a hot NaOH solution (adapted with permission from [83]. Copyright 1975: Wiley); (**b**) the relation of the Schottky barrier height at the interface M-p-ZnTe and the metal work function. Samples were etched in Br_2-methanol solution: 1, data extracted from [71], Fig. 17.10; 2, data extracted from [8]

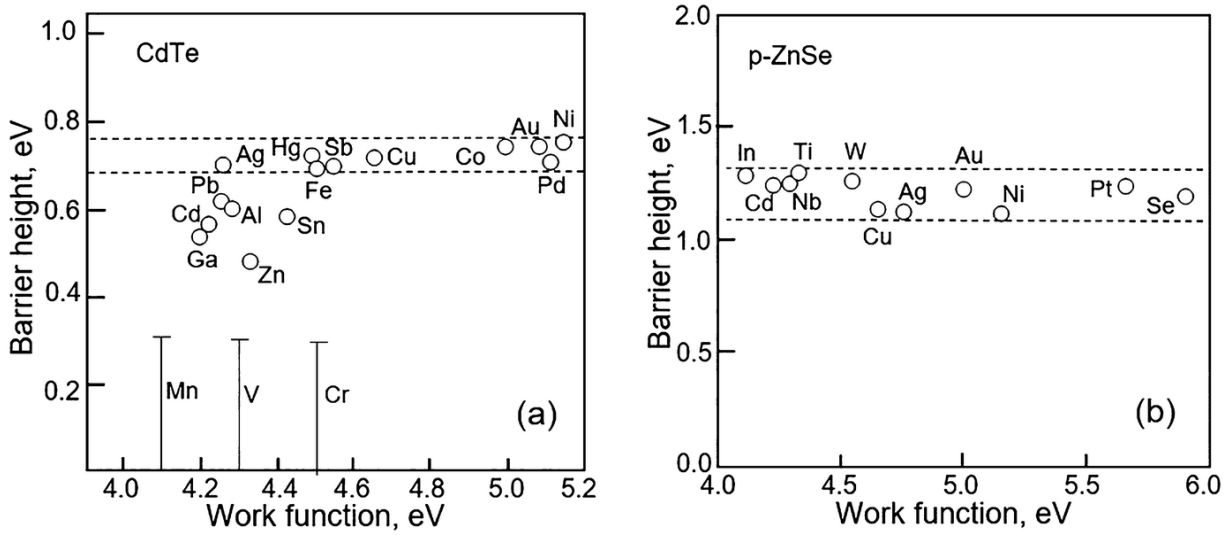

Fig. 17.4 Plot of barrier heights versus metal work functions for various metals on chemically etched (**a**) CdTe and (**b**) p-ZnSe surfaces. ((**a**) Adapted with permission from [25]. Copyright 1987: IOP Science. (**b**) Adapted with permission from [50]. Copyright 1997: AIP Publishing)

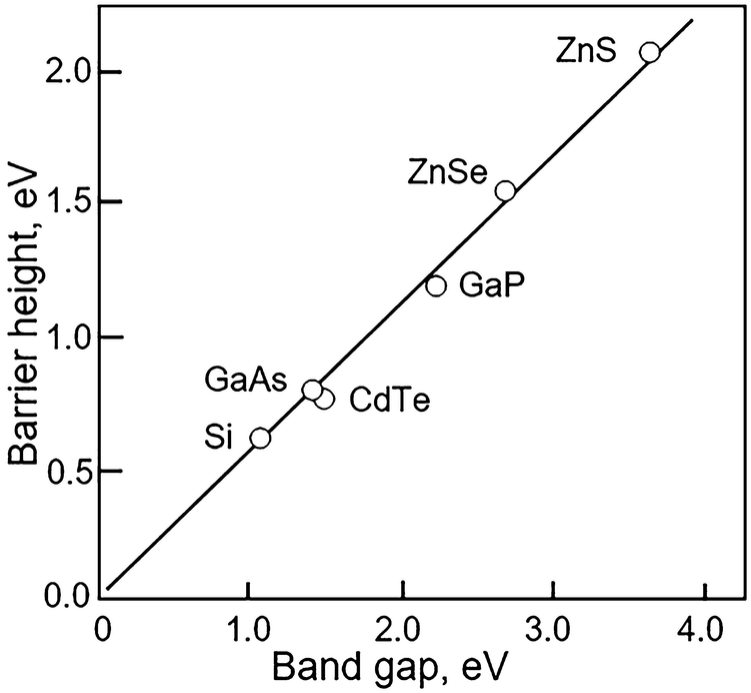

Fig. 17.5 Φ_{Bn} of Ni Schottky contacts formed on various semiconductors (Si, CdTe, GaAs, GaP, ZnSe, ZnS) after chemical etching, depending on the E_g of these materials. (Adapted with permission from [12]. Copyright 1982: Wiley)

An analysis of the surface properties of II-VI compounds allows us to conclude that the indicated difference in the properties of Schottky barriers is associated with the influence of the method of surface preparation on the surface states of the II-VI compounds. If the cleaved surfaces are close to

the stoichiometric state [25], i.e., are quasi-ideal with a minimum density of surface states in the bandgap of the semiconductor, then the surface, subjected to a chemical treatment, is characterized by the presence of its native oxides and a significant deviation from stoichiometry. It is the deviation from a stoichiometry that causes a generation of structural defects that induce surface states in the bandgap to further contribute to the pinning of the surface Fermi level. At that, according to Dharmadasa et al. [23], the energy range of Fermi level pinning depends on the nature of the defects to be generated at the interface. According to Dharmadasa et al. [24, 25], the strong Fermi pinning appears due to the states created by the Te-rich or Cd-deficient surface layer. Furthermore, while studying CdTe-based Schottky contacts, Dharmadasa et al. [23] argued that surfaces, rich in Te, tend to exhibit lower Schottky barriers, of 0.74 ± 0.02 eV, but those rich in Cd yield higher Schottky barriers, of 0.93 ± 0.02 eV. The Te-rich surface was produced by etching in a bromine-methanol solution, and the Cd-rich surface was produced by etching in an oxidized agent followed by an alkaline solution. The thickness of the Te-rich layer on the CdTe surface can vary up to 4 nm depending on such parameters as the employed concentration of bromine-methanol solution and the duration of the chemical treatment. For a 1% solution of bromine in methanol, the suggested Te thickness is less than 1.0 nm [29]. These results are very similar to CdS and ZnSe surfaces. Acidic solutions remove preferentially the semiconductor cations leaving a semiconductor anion-rich surface, whereas strong alkaline solutions primarily etch the semiconductor anions making a semiconductor cation-rich surface [21].

The properties of Schottky barriers are also significantly affected by native oxides of the II-VI compounds, which are formed on the surface during etching and subsequent contact with the surrounding atmosphere. The presence of native oxides at the interface leads to enhancing the ideality factor (n) of I-V curves (Eq. 17.3). For example, the ideality factors observed in contacts fabricated on chemically etched CdTe single crystals typically range from n = 1.05 to n = 1.40 [23]. The same values of *n* are typical for Schottky barriers that appeared with other II-VI semiconductors. For diodes prepared with polycrystalline films, the ideality factors can go to values higher than 3 [28]. At the same time, the ideality factor does not usually exceed 1.1 in Schottky diodes based on vacuum-cleaved surfaces. It

is worth noting that the ideal Schottky barrier, where the thermionic emission mechanism fully dominates, yields n = 1 [69].

$$I = I_0 \exp\left(\frac{qV}{nkT} - 1\right), \text{and} \tag{17.3}$$

$$I_0 = AA^{**}T^2 \exp\left(-\frac{q\varphi_b}{kT}\right), \tag{17.4}$$

where A is the active area of contact, A^{**} is the Richardson constant, T is temperature, k is the Boltzmann constant, and φ_b is the height of Schottky barrier.

When the tunneling and recombination effects substantially contribute to the current transport, the ideality factor is further increased. In diodes fabricated on chemically etched surfaces, there is also a large scatter in the parameters of Schottky barriers depending on various methods. As a rule, the height of the potential barrier, to be estimated from the volt-farad curves, exceeds significantly the value of the Schottky barrier which is calculated from the I-V data. The alkaline treatment can be used to remove a native oxide. Amirtharaj and Pollack [4] and Feldman et al. [29] argued that this treatment also removes an excessive tellurium from the surface of CdTe that appears after etching in 1% bromine in methanol.

17.2.2 Aging of II-VI Semiconductor-Based Schottky Diodes

Another feature that distinguishes Schottky barriers based on II-VI compounds from similar devices based on III-V compounds is the tendency to vary their parameters over time. Moreover, as shown in Fig. 17.6, these variations can be significant and frequently lead to growing or reducing the height of the potential barrier. Dharmadasa [21] also noted that the degradation of some devices is accompanied by a gradual increase in both series resistance and recombination and generation current components. These contacts become highly resistive and ohmic with time with complete loss of their rectifying properties after a while.

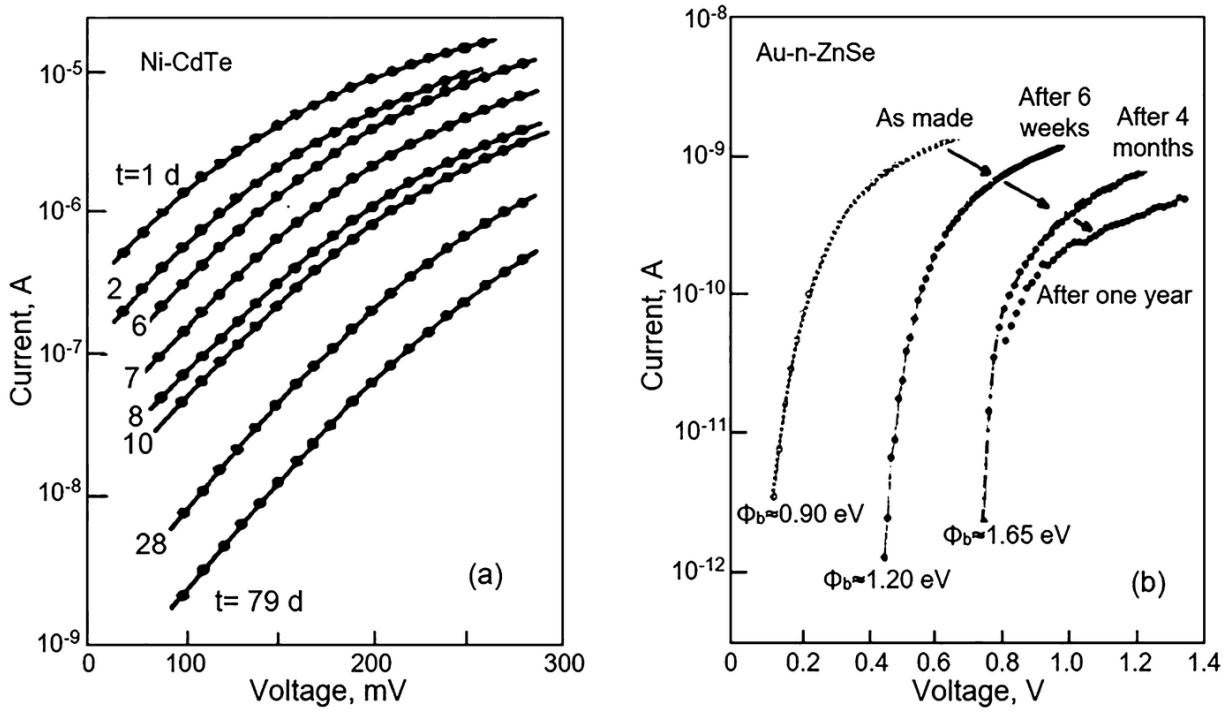

Fig. 17.6 (**a**) Forward I-V characteristics of Ni-CdTe contact (air-cleaved) as a function of time spent in room air (adapted with permission from [12]. Copyright 1982: Wiley); (**b**) aging of a typical Au/n-ZnSe (100) contact. (Adapted with permission from [22]. Copyright 1996: Taylor and Francis)

Some experiments showed that the modifications of the parameters of Schottky barriers under the operation are observed for all the II-VI compounds, and these changes can be accelerated when the electric fields are applied at elevated temperatures [21]. For example, the degradation of Ag-ZnSe diodes was observed when heated for several hours at a temperature of 250 °C and higher. The observed processes were accompanied by great increase in the leakage current and, at the same time, by reduction of the φ_b value. The same effect was also observed for contacts based on $ZnS_{0.07}Se_{0.93}$ [85]. Thermal annealing tests have shown that Pd-$ZnS_{0.07}Se_{0.93}$ contacts retain their electrical properties up to T = 250 °C, while Au-$ZnS_{0.07}Se_{0.93}$ contacts are stable enough up to T = 150 °C. However, a dramatic degradation was observed after higher-temperature annealing to be attributed to the interaction between metals and $ZnS_{0.07}Se_{0.93}$ as revealed by characterization of samples with Auger electron spectroscopy. Devine et al. [20] also reported that a significant decline in the barrier height of Au-CdTe contacts, from 0.9 eV to 0.64 eV, occurs after annealing at 200 °C in vacuum. As example, the thermal

stability data characterizing Pd/n-$ZnS_{0.07}Se_{0.93}$ contact after annealing at temperatures from RT to 350 °C are collected in Table 17.1.

Table 17.1 Influence of the annealing on the height of Schottky barriers at the Pd/n-$ZnS_{0.07}Se_{0.93}$ interface

T °C	As-dep.	100	150	200	250	300	350
φ_{bn} (IV), eV	1.49	1.49	1.486	1.486	1.485	0.782	0.76
φ_{bn} (CV), eV	1.51	1.51	1.506	1.506	1.505	0.80	0.78

Source: Reprinted with permission from [85]. Copyright 1996: Springer

The phenomenon of barrier height degradation, lowering the barrier height value and increasing the leakage current, which are observed following a heating at the temperature of 250 °C, is characteristic of even the most stable II-VI compounds such as CdS and ZnS. In addition to a decrease in φ_b, the enhancing of the ideality factor of I-V curves, n, and an increase in the series resistance of the diode were observed in experiments as collected in Table 17.2. However, these temperature-induced modifications do not necessarily occur in all the M-ZnS and M-CdS barriers and not always to the same extent. For example, at the initial studies of ZnS-metal barriers, it was found that heat treating does not alter the Pt-ZnS barriers, while the Ni-ZnS barriers reacted inconsistently, and the Ag-ZnS barriers constantly degraded.

Table 17.2 Properties of Schottky barriers fabricated on the chemically prepared ZnS surface

Barrier	n	R (Ohm)	φ_b (I-V), eV	φ_b (C-V), eV
Ag-ZnS	1.10	36	1.701	1.85
Ag-ZnS after heating at 250 °C	>2	7000	1.689	1.75
Au-ZnS	1.16	125	1.728	1.93
Au-ZnS after heating at 250 °C	>2	5500	1.678	1.80

Source: Data extracted from Cohen et al. [13]

It is worth noting that the temporal instability of Schottky barrier's parameters is observed for both air-cleaved and chemically etched diodes; these data are given in Table 17.3. At the same time, an interesting features

were noted [12]: (i) for samples that were subjected to a chemical etching prior the metal deposition, as GaP, GaAs, and ZnSe, and had an oxide layer at the interface, “saturated” barrier heights were achieved almost immediately after forming the metal-semiconductor contacts; (ii) for the contacts prepared with cleaved semiconductor surfaces, as CdTe and ZnS, “saturated” barrier heights were normally reached after a rather long time. These data are drawn in Fig. 17.6. According to Dharmadasa [21], the observed changes mature from interactions at the interface and so depend on the density of interface states within the contact. The clarification of appeared interactions and then elimination of the undesirable changes present a real challenge for researchers in this area.

Table 17.3 Summary of parameters of Ni-semiconductor contacts

Semiconductor	**n-GaAs**	**n-GaP**	**n-CdTe**	**n-ZnSe**	**n-ZnS**
Surface treatment	CE in NH_4OH: H_2O = 1:l	CE in HCl (38%)	AC	CE in methanol (1% Br_2)	AC
Variation with time of exposure to air of Φ_B	Little	Little	Significant	Intermediate	Significant: Φ_{Bn} (2 days) = 1.70 eV; Φ_{Bn} (83 days) = 2.00 eV
n	<1.15	<1.15	<1.10	<1.10	<1.05
Φ_{Bn} (saturated), (eV)	0.77	1.16	0.74	1.55	2.00

Source: Reprinted with permission from [12]. Copyright 1982: Wiley

Experimental data show that a great number of metals interact with II-VI semiconductors when the electrical contact is made. It was established that exchange reactions between the metal and the semiconductor, chemical reactions between the metal and the native oxide of the semiconductor, and the in- and out-diffusions of various elements present at the interface occur during and after the fabrication of the metal contact [23, 33, 64]. For example, in a 6-month-aged Sb-CdTe contact, both Cd and Te elements were found on the surface of the Sb layer, indicating interdiffusion of elements at the interface [26]. Cordes and Schmid-Fetzer [15, 17, 18] studied thermodynamics and kinetics of chemical reactions at the metal/CdTe interfaces and found that Au, Ag, Pt, and Ti are reactive metals

that form very reactive interfaces. It was clarified that Au, Ag, and Pt contacts contain $AuTe_2$, Ag_2Te, PtTe, and PtCd, respectively. At the same time, Ti creates a thermodynamically unstable contact on CdTe. The reaction zone comprised various tellurides such as Ti_3Te_4 and Ti_5Te_4. Cd has moved from the reacted CdTe toward the Ti layer, and Ti_2Cd can be found closer to the metallic Ti layer. It was argued that V, Al, Mn, and Cr form oxides to be more stable than either Cd or Te and may therefore be expected to reduce the oxide layer on CdTe [22]. This, however, is not expected for Au, Ag, Hg, Ir, and Cu. In addition, planar interfaces for these contacts were not observed, and the interface region was highly intermixed. In contrast to these reactive metals, three metals, namely, W, Mo, and Ta, yielded nonreactive interfaces with CdTe [16]. These metals had abrupt interfaces even after annealing at 800 °C for 2 days; that means these contacts should advance the stability of devices based on CdTe. Still, the diffusion of oxygen from the surrounding atmosphere through the metal film [66] with its subsequent adsorption at the interface cannot be excluded from consideration as well. That is why Chot [12] believes that this phenomenon does make a significant contribution to the change in φ_b during the operation of unencapsulated Schottky diodes. In addition to out-diffusion of Cd and Te atoms, the properties of CdTe Schottky diodes can also be significantly affected by in-diffusion of metal atoms. It is known that in the bulk of CdTe, In and Al are known to act as shallow donors with energies at 0.014 eV below the conduction band edge. At the same time, Au, Ag, and Cu induce deep acceptor levels, when introduced as dopants into the CdTe bulk, at 0.3–0.4 eV above the valence band.

Dharmadasa et al. [24, 25] concluded after analyzing the properties of Schottky barriers made on chemically etched CdTe surfaces that all the metals employed to generate Schottky barriers could be divided into three groups:

(i) Highly reactive metals, like Cr, Mn, and V, completely reduce the surface oxide; react with the Te-rich, or Cd-deficient, underlying layer; and gain an access to CdTe bulk; thus, these metals create barriers very similar to those on clean CdTe surfaces.

(ii) Nonreactive metals, like Au, Ag, Hg, Cu, Ni, Co, Sb, Fe, and Pd, as predicted by the heat of formation of tellurides, are completely

separated from CdTe by the interfacial layer, of TeO_2, and provide a constant barrier height, equal to 0.72 ± 0.03 eV; Au, Ag, Hg, and Cu do not reduce the TeO_2 present on the surface, while other metals consume the TeO_2 and lead to enhancing the height of the potential barrier.

(iii) A group of metals with intermediate properties, as Cd, Zn, Ga, Al, Sn, and Pb, produces a barrier height lower than 0.7 eV with a poor reproducibility; these metals partially react with the intermediate layer and do not completely separate the metal from the CdTe; the degree of reaction is determined by the kinetic features and the thickness of the oxide layer present on the surface and, therefore, is difficult to control.

It is important to note that all the processes mentioned above occur also at the interface between the metal and other II-VI compounds. For example, Forsyth et al. [33] considered these processes to be the major origin for the aging effects in metal-CdS contacts. In particular, they found that Pd bonds with S to form a palladium sulfide. It has been observed that Al reacts similarly to Pd, forming metal sulfides and releasing Cd from interfaces. Sn also binds to the surface but “free” Cd is not observed. It is believed that Sn binds to S at the interface without disrupting the CdS surface. A subsequent deposition of Sn following this initial layer leads to the formation of structures like islands on the surface. According to Forsyth et al. [33], Sb and Ag do not appear on CdS to react with the pure sulfide, although it can be assumed that Sb reacts with the oxide on the air-cleaved surface. Au appears to disrupt the CdS surface and to cause some diffusion of S. Patterson and Williams [64] have shown that interfaces are not abrupt under depositing the active metals over CdS and CdSe surfaces and the interface widths can be considerable.

It was established that interface interactions can be helpful in some cases but detrimental to most device applications. The formation of a high-resistive layer or the loss of the rectifying properties in the Schottky barriers can lead to a fast degradation of the device. All of the above indicates that in order to achieve the required reproducibility and stability of the parameters of devices fabricated on the surface of II-VI semiconductor compounds, a special attention is required to the choice of surface treatment methods, its passivation, and modification. Since almost all the metals react

with II-VI semiconductors and oxygen, the creation of diffusion barrier for oxygen, the incorporation of suitable reaction barriers at the interface that prevent or inhibit reactions at the metal-semiconductor interface, and the use of materials that do not interact with II-VI compounds will undoubtedly be necessary to increase the service life of the devices, being developed.

17.3 Ohmic Contacts

Ohmic contact is basically a junction which exhibits a linear I-V curve and provides the same carrier conduction in both directions from the metal to the semiconductor and vice versa. In an efficient photodetector, the series resistance must be kept to a minimum, which means that the ohmic contacts must be of low resistance.

Ohmic contacts can be achieved in various ways [35, 48, 51]:

1. As a rule, Schottky barriers with a barrier height, less than 0.3 eV, have characteristics close to ohmic contacts, i.e., their I-V dependence is close to a linear function. Therefore, the simplest method to design ohmic contacts is utilizing a metal with an appropriate work function. To form an ideal ohmic contact with n-type semiconductor, the condition $\Phi_M < \Phi_S$ must be satisfied. In such a contact, electrons do not find a barrier to flow from a semiconductor to a metal or vice versa under the applied electric field. While analyzing the properties of metals, it is found that very electronegative elements such as In, Ga, or Al should create the lowest Schottky barriers for II-VI n-type semiconductors, as discussed in the previous section, thereby facilitating a formation of ohmic contacts with these semiconductors. For p-type semiconductors, when making ohmic contacts, it is necessary to give a preference to metals, which satisfy the condition of $\Phi_M > \Phi_S$.

2. It is known that the tunneling effect in the Schottky barrier significantly reduces its resistance. Therefore, an increase in the concentration of free charge carriers at the contact interface due to a doping of this region is the second approach that promotes forming a low-resistance contact. To achieve the desired result, the carrier concentration must fall into 10^{18}–10^{19} cm^{-3} range. Studies have shown that high

conductive, below 1 Ω resistance, n-type II-VI binary compounds such as CdS, CdSe, and CdTe can be easily grown either in the form of a single crystal or in the form of a thin film by various methods. Low-resistivity p-ZnTe can also be easily grown. With regard to binary semiconductors such as p-CdTe, p-ZnSe, and n-ZnS, there are significant difficulties in achieving the desired conductivity. The doping can be carried out while growing or synthesizing the compounds, and/or with the help of ion implantation. The band diagram of such a contact is schematically shown in Fig. 17.7.

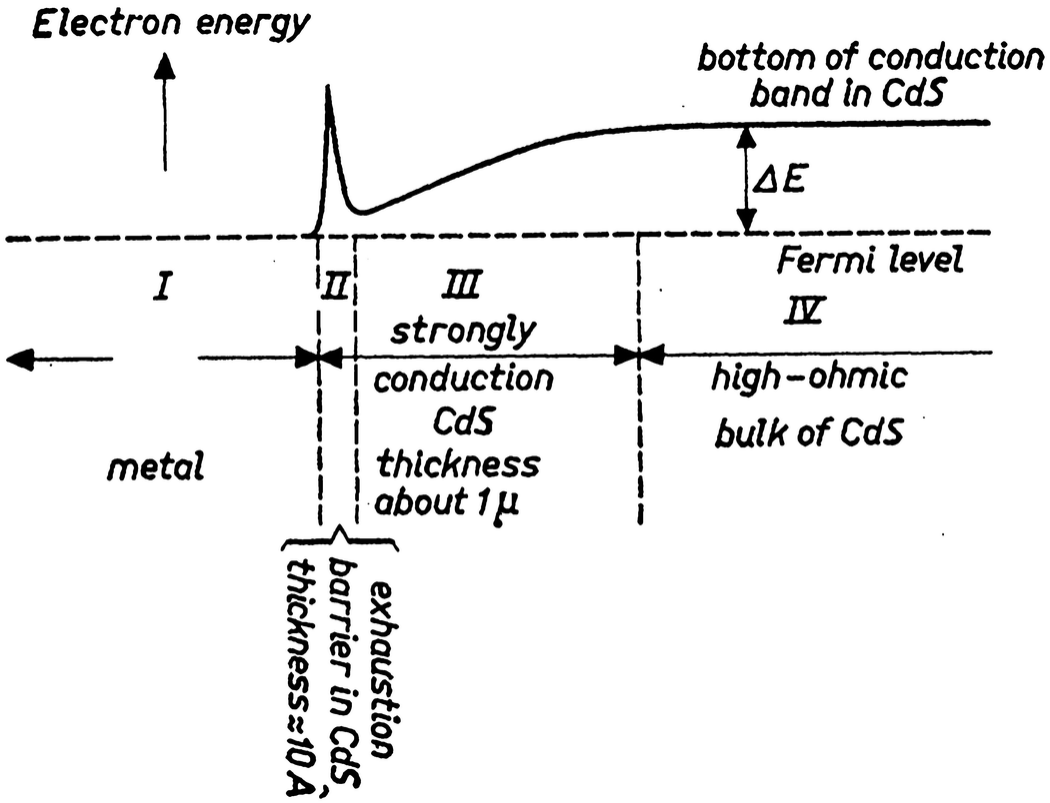

Fig. 17.7 Proposed band model of an ohmic contact between a highly resistive n-type bulk IV and a metal electrode I. III is a thin layer of strongly n-type semiconductor, and II is an exhaustion barrier due to the difference in work function between the material III and the electrode I. (Reprinted with permission from [51]. Copyright 1956: American Physical Society)

1. Previously, it was shown that some metals such as In, Ga, and Al create shallow donor states in II-VI compounds of n-type. This means that due to the post-deposition treatment of the metallic layer, which promotes the diffusion of the metal into the semiconductor, it is possible to provide the necessary doping of the contacting interface. To achieve this effect, alloys containing In and Al can be also used. The same

metals can be applied in a hybrid metallization as a sublayer for more refractory metals.

2. Introducing defects into the M-S interface to facilitate the transport of charge carriers through the interface is another approach to help reduce contact resistance.

3. The experimental data show that to form a low-resistance contact one can also employ an approach based on the formation of a heterojunction on the surface of a wide-gap semiconductor with the corresponding energy-band diagram. To achieve the desired result in such a heterojunction, (i) there should be no restrictions for the transition of the major charge carriers from the wide-gap semiconductor to the narrow-gap one, and (ii) the formation of a low-resistance ohmic contact to the upper narrow-gap semiconductor should not be difficult. One should note that the first and third methods can complement each other with the appropriate choice of contacting metals.

17.3.1 p-CdTe

The electron affinity of CdTe is of the order of 4.7 eV, which requires the electrode materials to have higher work function than this value in order to generate a barrier-less contact. In principle, materials like Ni, Au, Pd, and Pt may have a possibility to match with such a large electron affinity of CdTe to form a contact [35, 38]. The above metals are usually deposited by vacuum evaporation, sputtering, and electroplating methods. However, even using the listed metals does not always result in creating low-resistance contacts due to the presence of surface states in CdTe, which further contribute to the formation of a potential barrier at the interface. The surface doping is usually adopted to resolve this problem. This type of contact is known as M-p^+-p ohmic contact.

Scientists and technologists recommend for M-p^+-p CdTe contacts to employ the Au-Cu alloy as the contacting material. The added Cu diffuses into the CdTe and produces the p^+-region at the back surface of CdTe/CdS solar cells [65]. However, the high diffusivity of Au and Cu in CdTe results in the formation of Cu-Cd complex. This complex acts as the killer centers

to the carriers to degrade the interface performance. It was found that Cu diffuses into the bulk of CdTe with a very high rate [37], so it was suggested that diffusion along grain boundaries in the case of thin-film materials is a very likely mechanism for the observed degradation of CdTe-CdS solar cells. Diffusion of Cu at the cell junction leads to the appearance of recombination centers and the generation of shunting pathways that limit the lifetime of the solar cell. Therefore, solutions are being developed to allow designing either a back contact without copper or a contact based on a stable low-diffusive copper compound [84].

Ni:P fulfills the above requirements for CdTe, as Ni is a very hard material with very low diffusivity and dissolution in CdTe. Ni:P can be deposited using the electroless technique on the CdTe substrates [36]. While depositing a few percentage of P over Ni, free P may diffuse into the contacting interface and dope the CdTe surface to transform the p-CdTe surface to hole-enriched region of p^+-type. Moreover, the phosphorus's presence in Ni might form various phases like Ni_2P and Ni_3P which have a low or even zero diffusion probability in CdTe [57]. Thus, the choice of electroless Ni for contacting CdTe is a justified option. The only problem with Ni contact is that the bulk resistivity of Ni-P composite is high and it increases the series resistance of the device.

An introduction of an intermediate semiconducting layer between CdTe and metal is also utilized to form ohmic contacts [38]. For these purposes, low-resistance films of HgTe [5], Sb_2Te_3 [71], or ZnTe [54, 79] are frequently applied. Sb_2Te_3 is a p-type semiconductor with a low optical bandgap of 0.2–0.3 eV. The mechanism of contact formation using Sb_2Te_3 is not properly understood due to the lack of sufficient knowledge of the material properties. However, Sb_2Te_3 contacts have been successfully fabricated [71]. Sb_2Te_3 films were deposited on CdTe solar cells at substrate temperatures of 300 °C, by RF sputtering of a compound target of Sb_2Te_3. However, the Ni/Sb_2Te_3 interface was found to be in nonequilibrium leading to a spontaneous formation of $NiTe_X$, $NiSb_X$, and Sb_2O_3. This seems to suggest that the long-term reliability could be in question as the nonequilibrium state could cause reaction products which enhance the contact resistivity thereby reducing the cell efficiency [73].

Mercury telluride, a semimetal, with a reported work function of 5.9 eV is ideally appropriate for forming ohmic contacts to CdTe [45]. In addition, it has a nearly matched lattice parameter with CdTe, of −0.3% mismatch [5], that allows one to make a solid solution over the whole composition range. HgTe has been employed successfully as low-resistive contact to p-type single-crystalline CdTe by Janik and Triboulet [45], using the close-spaced isothermal technique. The contacts obtained via this technique possessed a room temperature R_c to be about 0.1 Ω-cm^2. However, despite the desired low value of such a contact resistance, this technique could not be used for polycrystalline CdTe solar cells because of rather high processing temperatures applied to make the HgTe layer. The working temperature of 550 °C under such a deposition causes structural changes in the CdTe crystals.

Another alloy, p-ZnTe, provides on the one hand a negligibly small valence-band discontinuity with the p-CdTe (see Fig. 17.8), while, on the other hand, it easily dopes to a high carrier concentration which promotes a free carrier's tunneling in contact with the metal. According to [34], the valence-band discontinuity is only about of −0.14 eV. Thus, it provides no hindrance to the flow of holes toward the contact. In addition, ZnTe has a low work function. Zinc telluride films have been fabricated by a variety of techniques like molecular beam epitaxy, chemical vapor deposition, electrodeposition, and RF sputtering. The p-ZnTe can be doped by elements of group V like P, As, and Sb. However, copper is often considered to be the optimal dopant in the formation of ZnTe for contact applications. The carrier concentrations of 10^{19}–10^{20} cm^{-3} have been reached in ZnTe:Cu films [78]. Studies performed on the ZnTe contacts indicate the stability of these cells varies depending on the kind of a final metal layer to be over-deposited; furthermore, it is critically dependent on the free Cu content in the ZnTe [79]. The cells containing Cu in excess of 6 at.% in ZnTe exhibit greater degradation due to the migration of copper atoms to the junction.

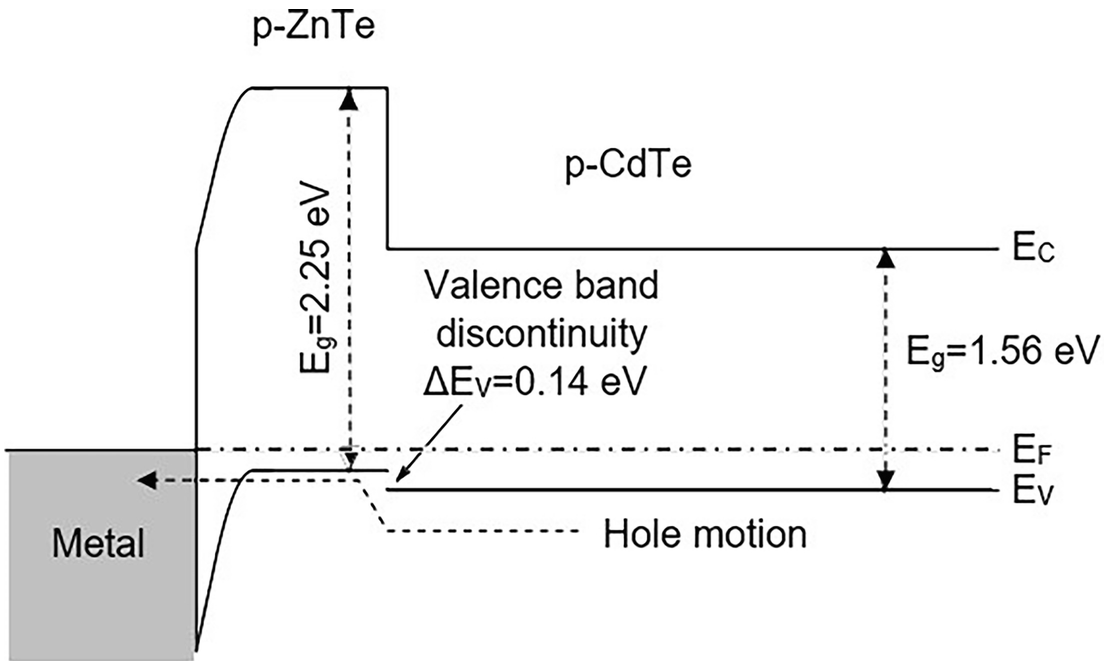

Fig. 17.8 Band diagram of CdTe/ZnTe interlayer

The formation of a Te-rich surface at CdTe prior to depositing the contact metal also helps to reduce the contact resistance. When Te is present, a degenerate Cu_xTe semiconducting layer may be formed in contact of (Au-Cu)-CdTe depending on the reaction temperature [90]. Recently, the Te layer had been shown to allow one to fabricate a device with a good performance even without using additional Cu [59]. As it was shown before, the Te-rich surface is typically prepared by wet chemical etching processes that may include a dilute solution of bromine in methanol (Br_2:MeOH) or a mixture of nitric and phosphoric acid in water (NP). A thin layer of Te on the back surface of CdTe can be also formed by a vacuum deposition [38].

For the same target, the incorporation of a thin layer of Cu_xO between the metal and CdTe [35] is used. This thin layer of Cu_xO grown on CdTe plays a dual role. It protects the CdTe surface from oxidation and builds up stress due to mismatching of lattice parameters. The stress field develops a piezo charge polarization as well as a spontaneous polarization effect in an intermediated semiconducting layer that ultimately enhances a carrier density at the metal-CdTe interface. These additional carriers create a chain of charge carrier flows into the bulk semiconductor and establish a barrier-free current linkage from the bulk semiconductor to the metal underacting the inherent drift field. In general, the oxide layers are very stable, so the

nature of the contact is very stable. This approach was applied for the development of thin film CdTe-CdS solar cells [35].

Other approaches being developed to reduce resistance and improve the stability of ohmic contacts to p-CdTe, such as applying metal oxides and organic materials, can be found in [38]. It is worth noting here that the search for an ideal back contact for p-type CdTe solar cells has not yet found a single solution.

17.3.2 ZnSe

The research data support rather easy fabricating of an ohmic contact to n-ZnSe because its electron affinity is equal to ca. 4.09 eV; moreover, n-ZnSe could be doped to get the free carrier concentration higher than 10^{19} cm^{-3} [30]. As discussed before, the ionic bonding in ZnSe-based systems results in an unpinned E_F. Consequently, formation of ohmic contacts to ZnSe can be predicted based on the value of the metal work function versus the semiconductor electron affinity. This means that it is easy to select a metal with a work function less than or nearly equal to 4.09 eV and to obtain an ohmic contact, which can be improved by high surface doping via building the n^+-surface layer. For example, ohmic contacts to n-ZnSe with In (Φ_{In} = 4.2 eV) and In-Sn alloys plus to Ti/Pt/Au alloys (Φ_{Ti} = 4.3 eV) have been demonstrated [31, 86]. However, heating of a deposited metal layer is normally required even in this case in order to observe an ohmic behavior [41]. After heat treatment at T > 200 °C, the contacts commonly switch from rectifying to ohmic one. The heating assists presumably in an interfacial reaction whose purpose is eliminating or penetrating any interfacial contamination layer which may be present. Liu et al. [54] have discussed the surface preparation methods for ZnSe to minimize such a contamination. The characterization of In layer with secondary ion mass spectrometry (SIMS) proved that the interface between the In and ZnSe was quite diffusive after annealing. This is consistent with interdiffusion of In and/or roughening of the interface [54]. An upper limit to the specific contact resistance of In layer over n-ZnSe was reported by Wang and Holloway [86] to be 10^{-3} $\Omega \cdot cm^2$. However, it must be kept in mind that in most cases the heat treatment of the metal/ZnSe contacts at temperatures above 350 °C resulted in degrading of I-V curves and even in returning the

rectifying properties of contacts that were ohmic at lower processing temperatures [30].

In the case of ohmic contacts to p-ZnSe, the situation is completely different. In this material, the sum of the electron affinity (4.09 eV) and the bandgap (2.67 eV) is so large (6.76 eV) that it is impossible to find a metal with a sufficiently large work function to create an ohmic contact. As a result, all the studies where authors have attempted to employ simple metals or multiple-layer metallization schemes have failed [31]. Simple metallization schemes should, in principle, still be able to yield an ohmic contact, if they could be used to create a p^{++}-doped surface layer. However, the maximum free hole concentrations observed in ZnSe have been only at the mid of 10^{17} cm^{-3} level [62], which is not sufficient to allow one to switch the interface transport from thermionic to tunneling one. In addition, no dopant or regrowth scheme has been found which could force advancing the surface doping under the contact formation because of interfacial reactions.

It was found that heterostructures of the p^{+}-ZnTe/p-ZnSe type turned out, as in the case of p-CdTe, to be the most successful ones in terms of their ohmic properties [27, 40]. The p-ZnTe was applied in these heterostructure because it can be doped to very high densities of free holes during the growth, and the band edges of ZnTe and ZnSe align properly to facilitate resonant tunneling bandgap states. This means that to create an ohmic contact to p-ZnSe, it is sufficient to form an ohmic contact to p-ZnTe, which does not cause any difficulties. Trexler et al. [82] demonstrated that Au could be used to make good ohmic contacts to p-ZnTe with free hole concentrations of $3 \cdot 10^{18}$ cm^{-3}. As in the case of n-ZnSe, as-deposited Au contacts yielded a rectifying contact, but the thermal processing at 200 °C led to an ohmic contact due to the destruction of the interfacial layer of ZnTe contamination and in-diffusion of Au without making an interfacial phase. Under heat treating at temperatures higher than 250 °C, the contact resistance increased, and an interface phase was detected by Auger and SIMS depth profiles. The quality of the ohmic contact to p-ZnTe-p-ZnSe was improved considerably if the metallization via introducing bilayer, as Au/Pd; trilayer, as Au/Pt/Pd, Au/Pt/Ti, or Au/Mo/Pd; or quaternary layer, as Au/Pt/Ti/Ni, was utilized [49, 58, 60, 61]. Using two- and three-layer metallization, the specific contact resistances were reported as low as

$6 \cdot 10^{-6}$ Ω·cm^2 due to advanced surface doping of p-ZnTe in combination with reduced Schottky barrier heights [49]. A surface cleaning in saturated bromine water solution also gave a significant improvement in the parameters of ohmic contacts to p-ZnSe [43].

There were also attempts to create low-resistive contacts based on HgSe-p-ZnSe heterostructures via employing molecular beam epitaxy (MBE) [53]. Films of HgSe result in low barrier contacts to p-ZnSe and p-$ZnSe_xTe_{1-x}$ because it is a semimetal with an electron affinity of about 6.1 eV. The predicted interfacial barrier for this film on p-ZnSe was 0.4–0.6 eV [31]. However, this interfacial barrier is too high to consider this as an ohmic contact. As a result, contact resistance was rather large [30]. In addition, making a contact in frames of the MBE growth requires a deposition of rig into the system.

For more details on the approaches employed to design ohmic contacts to ZnSe, the readers could look at [30].

17.3.3 n-ZnS

Despite on advances in the development of ZnS-based devices, there are a number of technological problems in their fabrication. Among them, the selection and development of compatible low-resistive and thermally stable ohmic contacts to ZnS films are two of the most important and difficult tasks [9, 46]. First, zinc sulfide has a very low electron affinity, approximately 1 Ev less than that of CdS, and a very large energy barrier that exists at the metal-semiconductor interface as discussed in the previous subsection. Second, there are difficulties with the formation of low-resistive near-contact areas without a simultaneous introduction of extensive concentrations of defects.

It should be noted that the same approaches are used for fabricating ohmic contacts to n-ZnS to be previously described for other n-type II-VI compounds. In principle, a metal contact whose work function is closer to that of ZnS and/or greater than the electron affinity of ZnS can generate an ohmic or non-rectifying contact with ZnS. However, the practice shows that the potential barrier at the M-ZnS interface appears to be too high, even for these metals. Therefore, the major emphasis in efforts to make the ohmic contacts to n-ZnS was given to using the metals which can act as shallow donors in its crystal lattice under subsequent heat treatment due to a diffusion in ZnS [77]. These metals could be Al, Ga, and In [14] which

could indeed yield ohmic contacts following a thermal processing. The only differences between ZnS and other II-VI compounds regarding to contacts to become ohmic are (i) annealing at a much higher temperature is required [9] and (ii) the available temperature range to facilitate appearing ohmic contacts is very narrow (see Fig. 17.9). Figure 17.9 shows the temperature dependence of V_D for ZnSe, $ZnS_{0.5}Se_{0.5}$, and ZnS contacts with In where ohmic contacts are formed at 220 °C, 320 °C, and 420 °C, respectively [46], under heating in an inert atmosphere. The similar results were reported by Blount et al. [9]. Ohmic electrical contacts to high-resistive ZnS single crystals were fabricated by annealing crystals at 400–475 °C. The dashed portion of curves in Fig. 17.9 indicates that contacts are degrading to be a subject of overheating. A low-conductivity layer where a photoconductivity is still observed starts forming both over entire crystal surface and under the contact. Kaufman and Dowbor [46] assumed that contacts degrade due to in-diffusion of zinc vacancies from the surface. According to Blount et al. [9], the reasons for a deterioration of the contact quality are (i) a thermal generation of an extensive number of vacancies and (ii) a significant diffusion of the electrode metal into the crystal.

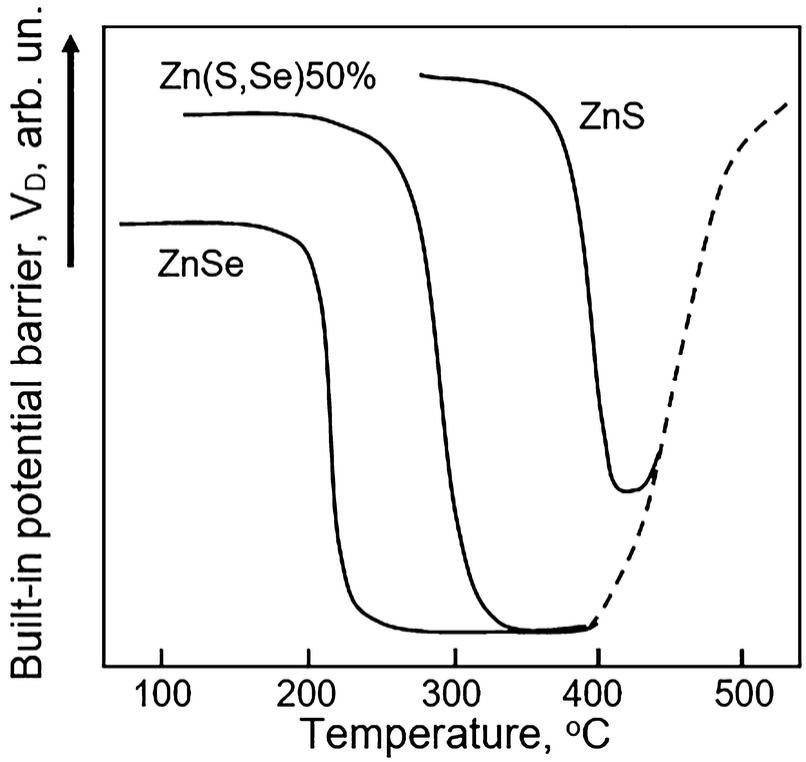

Fig. 17.9 A graph of V_D for ZnSe, $ZnS_{0.5}Se_{0.5}$, and ZnS contacts with In versus annealing temperature. V_D is the voltage under a reverse bias necessary to pass the current I_D. (Adapted with permission from [46]. Copyright 1974: AIP Publishing)

Kaufman and Dowbor [46] argued also that alloys of In with Cd, Au, Cu, Ag, Hg, TI, Ga, and Sn on the addend-rich side of the eutectic would all result in appropriate ohmic contacts, whereas alloys of In with Zn, AI, or Mg would not. Zn, AI, and Mg are lower than In at Pauling's electronegativity scale, while all the other metals are higher than In. This suggests that Zn, AI, and Mg will replace indium in the compound formed between In and Se.

Regarding the contact resistance, it was found out that the specific contact resistance of In/ZnS contacts is better when compared to Al/ZnS ones. For example, Abbas and Slewa [1] reported that the In/ZnS contacts exhibited R_c value of ~5 Ω.cm^2 after annealing at 300 °C in air for 90 min, while the Al/ZnS contacts had R_c ~ 50 Ω.cm^2. Contacts like Au/ZnS and Ag/ZnS remained rectifying even after annealing at 400 °C [14].

There are also attempts to create an ohmic transparent contact based on indium oxide layers (In_2O_3:Sn) [88]. It was found that the deposition of In_2O_3:Sn over a crystal with an appropriate follow-up heat treating gives much better results than a direct effort to force shallow donor impurities into the crystal lattice. It has been shown that the area with relatively high conductivity in ZnS arises as a result of the In diffusion into the crystal under heating to be carried out just after the deposition. As it is well-known [x], indium has a high diffusion rate into ZnS single crystals.

17.3.4 n-CdS

When we consider facilitating ohmic contacts to n-CdS, we should account that most of the regularities found in other II-VI compounds of n-type conductivity are observed, too. In particular, as for other compounds, the contacts based on In, Ga, and Al [75, 89], which play a role of shallow donor impurities under diffusion into CdS, have the minimum resistance. However, In- or Ga-based ohmic contacts on CdS, similar to other II-VI compounds, are unstable at temperatures above 100 °C. At the same time, Al can serve as an ohmic contact to CdS and does not noticeably diffuse into CdS up to 350 °C. But Boer and Hall [10] found that only a small percentage of attempts to create an ohmic contact by Al evaporation yield ohmic electrodes. This occurs, apparently, due to the formation of an

insulating layer of Al_2O_3 during the interaction of deposited Al with oxygen chemisorbed on the surface of the semiconductor. Therefore, to achieve ohmic characteristics, such contacts require additional annealing. A partial success was achieved due to the desorption of oxygen from the surface applying pre-evaporative heating of the CdS crystal under high vacuum conditions or taking vacuum-cleaved crystal surfaces [81]. The first approach was successful only for a fraction of the investigated CdS crystals, while the second one, to be completely successful though, does not match the practical conditions in most of the technically interesting cases. Boer and Hall [10] found a more efficient solution via depositing a thin Ti sublayer, close to a monolayer, followed by a simultaneous evaporating of Al and Ti. After heating at 200 °C, the contacts were ohmic with a low contact noise. Moreover, in half of the cases studied, the heat treatment after applying the Ti sublayer was not even required. This result indicates that Ti being co-evaporated with Al allows one to yield an ohmic Al-CdS contact under conditions where Al alone would otherwise facilitate blocking contacts. This can be explained by influence of Ti via (i) decreasing a partial oxygen pressure during evaporation and (ii) its chemical reaction with a chemisorbed oxide layer at the CdS surface. The heat treatment was also not required if the Ti-Al contact was sputtered only to a thickness of ca. 5.0 nm and then covered with a sputtered Pt layer. Apparently, the heating during the deposition of Pt was sufficient to initiate the reduction of Al_2O_3 with titanium and/or to ensure the diffusion of Al through TiO_X:Ti into the CdS surface. The electrical properties of the obtained electrodes after the heat processing in vacuum, up to 300 °C, do not noticeably change.

Experiment has shown that the contacts based on Cu, Au, Ag, and Ni can also have ohmic characteristics after heating [11]. To impart ohmic properties to these contacts, the annealing is required at temperatures of 200–450 °C, preferably in a vacuum or a neutral atmosphere. However, it is worth noting that these contacts are of quite high resistance. By using a heavily doped material, the requirements to the metals to form the contacts could be reduced. Interestingly, to achieve the minimum resistance of In-CdS contacts over chemically treated surfaces, the annealing at the temperature of 300–350 °C is required [89]. With a further increase in the annealing temperature, like other II-VI compounds, the resistance of the contacts goes up.

If we analyze the published works related to the development of photodetectors based on CdS, then the most common approach to create an ohmic contact is employing a combination of Cr-Au, of ca. 10/100 nm thick [19]; Ti-Au, of ca. 10–20/50–300 nm thick [39, 92]; or Pt:Ga [87]. These contacts provide an acceptable contact resistance and stability of parameters.

17.4 Heterojunctions

Heterojunction is fundamentally a junction between two unlike n-type and p-type semiconductor materials. The values of permittivity (ε_s), energy gap (E_g), electron affinities (χ), and work functions (Φ_S) of these two semiconductors are also supposed to be different in addition to their lattice constants. Based on various construction strategies, core-shell heterojunctions, crossed nanowire heterojunctions, one-dimensional axial heterojunctions, and one-dimensional nanostructure/thin film or Si substrate heterojunctions are studied incessantly for optoelectronic application. The difference in energies of conduction-band (CB) edge and valence-band (VB) edge, ΔE_C and ΔE_V, are denoted as $\Delta E_C = q\,(\Delta\chi)$ and $\Delta E_V = \Delta E_g - \Delta E_C$, where the χ, E_g are the electron affinity and bandgap of semiconductors. A typical band diagram of II-VI semiconductor heterojunction and CB and VB of extensively used elements is shown in Fig. 17.10.

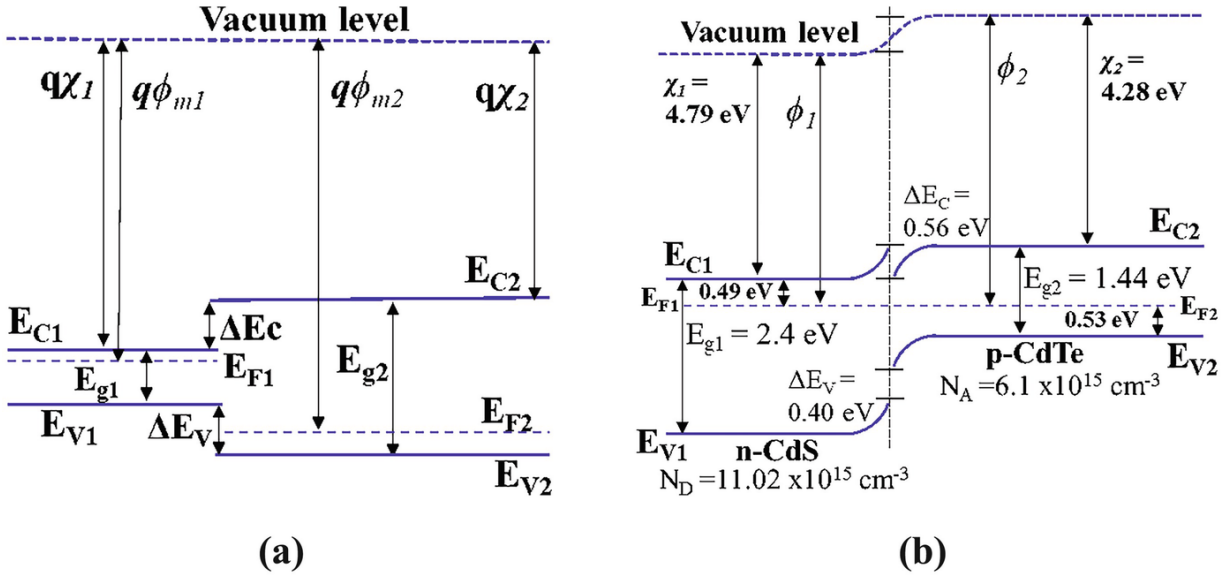

Fig. 17.10 (**a**) Typical energy-band diagram of two isolated semiconductors with the smaller bandgap n-type semiconductor. (**b**) Equilibrium energy-band diagram of n-CdS/p-CdTe heterojunction. (Reprinted from [2]. Published 2000 by World Academy of Science, Engineering and Technology as open access)

When developing various devices based on II-VI compounds, a special attention is paid to heterojunctions because of the following:

1. Heterojunctions make it possible to form transparency windows in the desired spectral range and to develop multicolor photodetectors.

2. The heterojunction backwall configuration of photodetectors can significantly reduce the effects of surface recombination.

3. Low-series resistance losses are easier to implement in backwall heterojunctions.

4. In polycrystalline homojunctions, a fast diffusion along grain boundaries makes it difficult to obtain n- or p-layers by doping via diffusion processes.

When designing heterojunctions intended for use in photodetectors, the following should be taken into account:

- The material used in photodetectors as an absorber is selected accounting for the required spectral sensitivity region, since the forbidden gap of materials determines the part of the solar spectrum received by photodetectors. In this case, it is desirable to have the diffusion length of photogenerated carriers in this material at the maximum value. Therefore, a *p*-type material is usually employed as an absorber, since the mobility of electrons is much greater than the one of holes in most II-VI semiconductors.
- The II-VI semiconducting layer on the top of heterojunction plays normally the role of the window. Increasing the forbidden gap of a given material with respect to the absorber opens a “window” on the high-energy side that yields more light-generated current J_L. However, a very large value of the forbidden gap, ordinarily higher than ca. 2.6 eV, is frequently accompanied by appearing difficulties to ensure a sufficient conductivity of the semiconductor.

- For a p-type absorber, the difference in the electron affinities of the two components forming the heterojunction, $\Delta X = X_1 - X_2$, must be equal to zero. If $\Delta X > 0$, then this leads to a surge in the conduction band which can interfere with the photogenerated transport of carriers through the junction, while $\Delta X < 0$ reduces the resulting diffusion voltage V_b.
- A lattice mismatch in the heterostructure introduces interface states which could enhance the reverse saturation current J_0 and decrease the open-circuit voltage V_{oc}, fill factor, and also the light current J_L due to the interfacial recombination. Therefore, a minimum lattice mismatch between heterojunction components is desirable to minimize losses due to the interfacial recombination. However, it should be taken into account that the state of the substrate surface is critical in the fabrication of a heterojunction even at zero lattice mismatch. These interface states will occur due to surface contamination, oxides, and surface defects. Therefore, the most scrupulous conditions must be observed in the fabrication of heterostructures.
- As for the coefficients of thermal expansion, they must be approximately equal for semiconductors forming a heterojunction in order to allow high-temperature processing.

It is important to note that most of the methods described earlier in the Chaps. 10 and 11 can be used to fabricate heterojunctions. Taking these methods, a wide variety of heterojunctions were fabricated, and highly efficient optoelectronic devices such as photodetectors, solar cells, light-emitting diodes, and junction field-effect transistors were developed accounting for the reported technology protocols [44]. For example, the efficiencies as high as $\eta \sim 22.1\%$ with a module efficiency of 19.0% (experimental) and 25–29% (theoretical) are observed for the CdS/CdTe heterostructure [42, 70]. A theoretical study on II-VI semiconductor-based heterostructure of CdTe/ZnS/ZnTe shows the efficiency of 21.38%, while the efficiency of 21.4% is for ZnS/SnS, 24% for ZnS/CdTe/ZnSe heterostructure with distributed Bragg reflector and back surface field, and 44% for CdS/CdTe solar cell with Sb_2Se_3 BSF layer ([47, 52, 68]). Besides, Xie et al. [91] reported a high-performance photodetector made of a p-CdTeNR/n-SiNW array heterojunction which exhibits a fast response speed under the white light illumination with an intensity of 62.5 μW cm^{-2} with high stability and sensitivity.

Acknowledgments

This work was supported by the Russian Science Foundation, project No. 21-73-10251, https://rscf.ru/en/project/21-73-10251/.

References

1. Abbas T, Slewa L (2015) Transmission line method (TLM) measurement of (metal/ZnS) contact resistance. Int J Nanoelectron Mater 8:111–120
2. Abdullah RA, Razooqi MA, Al-Ajili ANH (2013) Characterization of the energy band diagram of fabricated SnO_2/CdS/CdTe solar cells. Intn J Phys Mathem Sci 79:418–422
3. Adachi S (2004) Handbook of physical properties of semiconductors, II-VI compounds semiconductors, vol 3. Kluwer Academic Publishers, Boston
4. Amirtharaj and Pollack (1984) Raman scattering study of the properties and removal of excess Te on CdTe surfaces. Appl Phys Lett 45:789
5. Asa G, Nemirovsky Y (1995) Properties of metal-organic chemical-vapor-deposition mercury telluride contacts on *p*-type cadmium telluride. J Appl Phys 77:4417
6. Aven M, Mead CA (1965) Electrical transport and contact properties of low resistivity n-type zinc sulfide crystals. Appl Phys Lett 7(1):8–10
7. Baker WD, Milnes AG (1972) Schottky barriers on ZnTe. J Appl Phys 43:5152
8. Bhunia S, Bose DN (2000) Schottky barrier studies on single crystal ZnTe and determination of interface index. J Appl Phys 87(6):2931–2935
9. Blount GH, Fisher MW, Morrison RG, Bube RH (1966) Ohmic electrical contacts to high-resistivity ZnS crystals. J Electrochem Soc 113(7):690–693
10. Boer KW, Hall RB (1966) Multilayer Ohmic contacts on CdS. J Appl Phys 37(13):4739–4742
11. Chakraborty M (2012) Optimum metal-semiconductor contact for Cadmium Sulphide thin film. Intn J Eng Res Appl (IJERA) 2(6):793–799
12. Chot T (1982) Some new experimental results of a study of metal-n-type semiconductor Schottky barrier contacts. Phys Stat Sol (a) 70:311–316
13. Cohen J, Vilms J, Archer RJ (1968) Investigation of semiconductor Schottky barriers for optical detection and cathodic emission. Final Report. AFCRL-68-0651. Air Force Cambridge Research Laboratories
14. Cooke I (1963) Ohmic contact to Zinc Sulfide single crystals. J Chem Phys 38(2):291–292
15. Cordes H, Schmid-Fetzer R (1995a) Thermodynamics and kinetics of Ti/CdTe contact metallurgy. J Mat Sci: Mater Electron 6:118–126

16. Cordes H, Schmid-Fetzer R (1995b) Thermochemically stable metal contacts on CdTe: tungsten, molybdenum and tantalum. Z Metallkd 86(5):304–309
17. Cordes H, Schmid-Fetzer R (1994) The role of interfacial reactions in Pt/CdTe contact formation. Semicond Sci Technol 9:2085
18. Cordes H, Schmid-Fetzer R (1992) Interfacial reactions in noble metal M/CdTe contacts and the related ternary Cd-Te-M phase stabilities (M = Ag, Au). Z Metallkd 83(8):601–608
19. Deng K, Li L (2014) CdS nanoscale photodetectors. Adv Mater 26:2619–2635
20. Devine P, Matthews GW, Sands D, Scott CG, Yousaf M, Blomfield CJ et al (1994) Structural and electrical stability of metal contacts to MBE CdTe layers. Surf Rev Lett 1(4):669–672
21. Dharmadasa IM (1998) Recent developments and progress on electrical contacts to CdTe, CdS and ZnSe with special reference to barrier contacts to CdTe. Prog Crystal Growth Charact 36(4):249–290
22. Dharmadasa IM, Blomfield CJ, Coratger R, Ajustron F, Beauvillain J, Simpson J et al (1996) Microscopic and macroscopic investigation of electrical contacts to n type and p type ZnSe. Mat Sci Technol 12:86–89
23. Dharmadasa IM, Blomfield CJ, Gregory GE, Young J (1994) Influence of chemical etching on metal contacts to 11-VI compounds: CdTe and ZnSe. Intern J Electron 76(5):961–967
24. Dharmadasa IM, I. M., Thorton J. H., Williams R.H. (1989) Effects of surface treatments on Schottky barrier formation at metal n-type CdTe contacts. Appl Phys Lett 54:137–139
25. Dharmadasa IM, McLean AB, Patterson MH, Williams RH (1987) Schottky barriers and interfaces on chemically etched n-CdTe single crystals. Semicond Sci Technol 2(1987):404–412
26. Dharmadasa IM, Herrenden-Harker WG, Williams RH (1986) Metals on cadmium telluride: Schottky barriers and interface reactions. Appl Phys Lett 48:1802–1804
27. Fan T, Han J, He L, Saraie J, Gunshor R, Hagerott M et al (1993) Ohmic contact to *p*-Zn(S,Se) using a pseudograded Zn(Te,Se) structure. J Vac Sci Technol B 11:1748–1751
28. Farag AAM, Yahia IS, Fadel M (2009) Electrical and photovoltaic characteristics of Al/n-CdS Schottky diode. Intern J Hydrogen Energy 34:4906–4913
29. Feldman RD, Opila RL, Bridenbaugh PM (1985) Auger electron spectroscopic study of the etching of cadmium telluride and cadmium manganese telluride. J Vac Sci Technol A 3:1988–1991
30. Fijol JE, Holloway PH (1996) Ohmic contacts to ZnSe-based materials. Crit Rev Solid State Mater Sci 21(2):77–128
31. Fijol JJ, Trexler JT, Calhoun L, Park RM, Holloway PH (1996) Ex situ formation of HgSe electrical contacts to p-ZnSe. J Vac Sci Technol 14:159
32. Flores F, Tejedor C (1987) On the formation of semiconductor interfaces. J Phys C 20:145

33. Forsyth NM, Dharmadasa IM, Sobiesierski Z, Williams RH (1989) Schottky barriers to CdS and their importance in Schottky barriers theories. Semicond Sci Technol 4:57–59
34. Gessert TA, Mason AR, Reedy RC (1995) Development of rf sputtered, Cu-doped ZnTe for use as a contact interface layer to p-CdTe. J Electron Mater 24:1443
35. Ghosh B (2009) Electrical contacts for II-VI semiconducting devices. Microelectron Eng 86:2187–2206
36. Ghosh B, Purakayastha S, Datta PK, Miles RW, Carter MJ, R. Hill R. (1995) Formation of a stable ohmic contact to CdTe thin films through the diffusion of P from Ni-P. Semicond Sci Tech 10:71–76
37. Grecu D, Compann AD (1999) Photoluminescence study of Cu diffusion and electromigration in CdTe. Appl Phys Lett 75:361–363
38. Hall RS, Lamb D, Curzon Irvine SJ (2021) Back contacts materials used in thin film CdTe solar cells—a review. Energy Sci Eng 9:606–632
39. Heo K, Lee H, Park Y, Park J, Lim HJ, Yoon D et al (2012) Aligned networks of cadmium sulfide nanowires for highly flexible photodetectors with improved photoconductive responses. J Mater Chem 22:2173–2179
40. Hiei F, Ikeda M, Ozawa M, Miyajima T, Ishibashi A, Akimoto K (1993) Ohmic contacts to p-type ZnSe using ZnTe/ZnSe multiquantum wells. Electron Lett 29:878–879
41. Holloway PH, Kim T-J, Trexler JT, Miller S, Fijol JJ, Lampert WV, Haas TW (1997) Interfacial reactions in the formation of ohmic contacts to wide bandgap semiconductors. Appl Surf Sci 117(118):362–372
42. Hu A, Zhou J, Zhong P, Qin X, Zhang M, Jiang Y, Wu X, Yang D (2021) High-efficiency CdTe-based thin-film solar cells with ultrathin CdS:O window layer and processes with post annealing. Sol Energy 214:319–325
43. Ishikawa H, Tsukai K, Koide Y, Teraguchi N, Tomomura Y, Suzuki A, Murakami M (1996) Effects of surface cleaning on electrical properties for Ni contacts to p-type ZnSe. J Vac Sci Technol B Microelectron Nanom Struct 14:1812
44. Isahiki M, Wang J (2017) II-IV semiconductors for optoelectronics: CdS, CdSe, CdTe. In: Kasap S, Capper P (eds) Springer handbook of electronic and photonic materials. Springer Handbooks. Springer, Cham
45. Janik E, Triboulet R (1983) Ohmic contacts to p-type cadmium telluride and cadmium mercury telluride. J Physics D: Appl Phys 16:2333
46. Kaufman RG, Dowbor P (1974) Mechanism of formation of Ohmic contacts to ZnSe, ZnS, and mixed crystals ZnS_XSe_{1-X}. J Appl Phys 45:4487–4490
47. Kazmi SAA, Khan AD, Khan AD, Rauf A, Farooq W, Noman M, Ali H (2020) Efficient materials for thin-film CdTe solar cell based on back surface field and distributed Bragg reflector. Appl Phys A Mater Sci Process 126:46

48. Kim TJ, Houoway PH (2000) Ohmic contacts to II-VI and III–V compound semiconductors, processing of wide band gap semiconductors growth. In: Pearton SJ (ed) Processing of wide band gap semiconductors. William Andrew Inc., New York, pp 80–150
49. Kim D-W, Kwak JS, Park H-S, Kim HN, Lee S-M, Sim C-S et al (1997) Interfacial reaction and electrical property of Ge/Ni/ZnSe for blue laser diode. J Electron Mater 26:83–89
50. Koide Y, Kawakami T, Teraguchi N, Tomomura Y, Suzuki A, Murakami M (1997) Schottky barrier heights of metals contacting to p-ZnSe. J Appl Phys 82:2393–2399
51. Kroger FA, Diemer G, Klasens HA (1956) Nature of an Ohmic metal-semiconductor contact. Phys Rev 103(2):279
52. Kuddus A Md, Ismail AB, Hossain J (2021) Design of a highly efficient CdTe-based dual-heterojunction solar cell with 44% predicted efficiency. Solar Cells 221:488–501
53. Lansari Y, Cook J, Schetzina J (1993) Growth of HgSe and $Hg_{1-x}Cd_xSe$ thin films by molecular beam epitaxy. J Electron Mater 22:809–813
54. Li JV, Duenow JN, Kuciauskas D, Kanevce A, Dhere RG, Young MR, Levi DH (2013) Electrical characterization of Cu composition effects in CdS/CdTe thin-film solar cells with a ZnTe:Cu back contact preprint. IEEE J Photovolt 3:1095–1099
55. Liu L-M, Lindauer G, Alexander WB, Holloway PH (1995) Surface preparation of ZnSe by chemical methods. J Vac Sci Technol B 13:2238
56. Mead CA, Spitzer WG (1964) Fermi level position at metal-semiconductor interfaces. Phys Rev A 134:713–716
57. Miles RW, Ghosh B, Duke S, Bates JR, Carter MJ, Datta PK, Hill R (1996) Formation of low resistance contacts to p-CdTe by annealing autocatalytically deposited Ni-P alloy coatings. J Crystal Growth 161:148–152
58. Mochizuki K, Jerano A, Momose M, Taike A, Kawata M, Gotoh J, Nakatsuka S (1995) Crystallographic microstructure and electrical characteristics of au/Pt/Ti/Ni Ohmic contacts on *p*-type (001) ZnTe layers. J Appl Phys 78:3216
59. Moore A, Song T, Sites J (2017) Improved CdTe solar-cell performance with an evaporated Te layer before the back contact. MRS Adv 2:3195–3201
60. Ohtsuka T, Yoshimura M, Morita K, Koyama M, Yao T (1995) Low resistance ohmic contact for p-type ZnTe using Au electrode. Appl Phys Lett 67:1277
61. Ozawa M, Hiei F, Takasu M, Isibashi A, Akimoto K (1994) Low resistance Ohmic contacts for *p*-type ZnTe. Appl Phys Lett 64:1120
62. Park RM (1992) Low-resistivity *p*-type ZnSe:N grown by molecular beam epitaxy using a nitrogen free-radical source. J Vac Sci Technol A 10:701–704
63. Parker GH, Mead CA (1969) Tunneling in CdTe Schottky barriers. Phys Rev 184(3):780–787

64. Patterson MH, Williams RH (1981) Schottky barriers at metal-CdTe interfaces. Vacuum 31(10–12):639–643
65. Paudel NR, Wieland KA, Compaan AD (2012) Ultrathin CdS/CdTe solar cells by sputtering. Sol Energy Mater Sol Cells 105:109–112
66. Ponpon JP, Siffert P (1978) Role of oxygen in the mechanism of formation of Schottky diodes. J Appl Phys 49:6004
67. Ponpon JP, Siffert P (1977) Barrier heights on cadmium telluride Schottky solar cells. Rev Phys Appl (EDP) 12(2):427–430
68. Rashel AAS, Ferdous J, Suruz MM (2018) Development of a novel CdTe/ZnS/ZnTe heterojunction thin-film solar cells: a numerical approach. IOP SciNotes 1:024802
69. Rhoderick EH, Williams RH (1988) Metal Semiconductor Contacts, 2nd edn. Clarendon Press, Oxford, U.K.
70. Romeo A, Artegiani E (2021) CdTe-based thin film solar cells: past, present and future. Energies 14:1684
71. Romeo N, Bosio A, Tedeschi R, Canevari V (2000) Back contacts to CSS CdS/CdTe solar cells and stability of performances. Thin Solid Films 361:327–329
72. Saji M, Matsumoto K, Fujimoto H (1978) Properties of Schottky barrier diodes and ohmic contacts on ZnTe single crystal. Electrical Eng Jpn 98(6):1–9
73. Schmidt T, Durose K, Rothenhausler C, Lerch M (2000) Chemical stability of Sb_2Te_3 back contacts to CdS/CdTe solar cells. Thin Solid Films 361:383–387
74. Schottky W (1942) Vereinfachte und erweiterte theorie der randschicht-gleichrichter. Z Phys 118:539–592
[zbMATH]
75. Smith RW (1955) Properties of Ohmic contacts to Cadmium Sulfide single crystals. Phys Rev 97(6):1525–1530
76. Spitzer WG, Mead CA (1963) Barrier height studies on metal-semiconductor systems. J Appl Phys 34:3061
77. Stavitski N, Van Dal MJH, Wolters RAM, Kovalgin AY, Schmitz J (2006) Specific contact resistance measurements of metal semiconductor-junctions. In: Proceedings of the IEEE International Conference on Microelectronic Test Structures (ICMTS), 6–9 March 2006, Austin, TX, USA, 8902792, pp. 13–17.
78. Tang J, Mao D, Ohno TR, Kaydanov V, Trefny JU (1997) Properties of ZnTe:Cu thin films and CdS/CdTe/ZnTe solar cells. In Proceedings of the 26th IEEE Photovoltaic Specialists Conference, 29 September–3 October 1997, Anaheim, CA, pp. 439–442
79. Tang J, Mao D, Feng L, Song W, Trefny JU (1996) The properties and optimization of ZnTe:Cu Back contacts on CdTelCdS thin film solar cells. In proceedings of the 25th IEEE photovoltaic

specialists conference, may 13–17 1996, Washington D.C USA, pp. 925–928
80. Tersoff J (1986) Band lineups at II-VI heterojunctions: failure of the common-anion rule. Phys Rev Lett 56:2755
81. Thompson MJ, Cornwall MG (1972) Low resistance Ohmic contacts to photoconductive CdS. Solid State Electron 15:861–864
82. Trexler JT, Fijol JJ, Calhoun LC, Park RM, Holloway PH (1996) Formation of ohmic contacts to p-ZnTe. J Electron Mater 25:1474–1477
83. Tyagi MS, Arora SN (1975) Metal Zinc Selenide Schottky barriers. Phys Stat Sol (a) 38:165–172
84. Viswanathan V (2004) Study of Cu free back contacts to thin film CdTe Solar Cells. PhD Thesis. University of South Florida, USA
85. Wang A, Anderson WA (1996) Metal-semiconductor contacts to n-$ZnS_{0.07}Se_{0.93}$. J Electron Mater 25:201–205
86. Wang Y-X, Holloway PH (1992) Indium ohmic contacts to *n*-ZnSe. Vacuum 43:1149–1151
87. Wei TY, Huang CT, Hansen BJ, Lin YF, Chen LJ, Lu SY, Wang ZL (2010) Large enhancement in photon detection sensitivity via Schottky-gated CdS nanowire nanosensors. Appl Phys Lett 96:013508
88. Williams VA (1966) High conductivity transparent contacts to ZnS. J Electrochem Soc 113(3):234–237
89. Yamaguchi M (1974) Ohmic contacts to CdS. Jpn J Appl Phys 13(8):1325–1326
90. Xia W, Lin H, Wu HN, Tang CW, Irfan I, Wang C et al (2014) Te/Cu bi-layer: a low-resistance back contact buffer for thin film CdS/CdTe solar cells. Solar Energy Mater Solar Cells 128:411–420
91. Xie C, Luo LB, Zeng LH, Zhu L, Chen J-J, Nie B et al (2012) P-CdTe nanoribbon/n-silicon nanowires array heterojunctions: photovoltaic devices and zero-power photodetectors. CrystEngComm 14:7222–7228
92. Zhou W, Peng Y, Yin Y, Zhou Y, Zhang Y, Tanga D (2014) Broad spectral response photodetector based on individual tin-doped CdS nanowire. AIP Adv 4:123005

OceanofPDF.com

© The Author(s), under exclusive license to Springer Nature Switzerland AG 2023
G. Korotcenkov (ed.), *Handbook of II-VI Semiconductor-Based Sensors and Radiation Detectors*
https://doi.org/10.1007/978-3-031-19531-0_18

18. II-VI Wide-Bandgap Semiconductor Device Technology: Stability and Oxidation

Ghenadii Korotcenkov[1] ✉
(1) Department of Physics and Engineering, Moldova State University, Chisinau, Moldova

Keywords II-VI semiconductors – Wide bandgap – Native oxides – CdO – $CdSeO_3$ – $CdTeO_3$ – Composition – TeO_2 – Thickness – ZnO – $ZnSeO_3$ – Stability – Back contacts – $CdCl_2$ treatment – Contact degradation – Cu diffusion – Device performance – Quantum dots – Surface oxidation – Surface passivation – Advantages – Al_2O_3 – Disadvantages – SiO_2 – SiN_x – Stability – ZnS – Thermal oxidation – CdS – CdSe – CdTe – Phase dissociation – Oxide composition – Oxidation temperature – Surface stoichiometry – ZnS – ZnSe – ZnTe

18.1 Introduction

The problem of parameter instability has always been one of the most important in the development of any semiconductor devices. This also applies to devices based on II-VI compounds.

18.2 Stability of II-VI Semiconductor-Based Devices

18.2.1 Stability of CdTe/CdS Solar Cells

The most detailed studies in this area have been carried out for CdS/CdTe solar cells. It has been found that the degradation of solar cell parameters, which usually shows up in the current-voltage characteristics and, in particular, in a decrease in the open-circuit voltage (Voc), an increase in the internal resistance of the cell, and a decrease in the fill factor (FF), is mainly controlled by the following processes.

First, it is the degradation of ohmic contacts. Early studies used carbon layers as ohmic back contact (BC) in glass/CdS/CdTe/Ag solar cells [82]. Studies of such cells showed that the main reason for the degradation of such solar cells (an increase in series resistance and a drop in open-circuit voltage) was the degradation of ohmic contacts (a decrease in the adhesion of the carbon layer), which increased with increasing temperature and humidity.

Zeng et al. [95] also believes that an efficient back contact layer and a composite front electrode are the indispensable structural elements to achieve high stability in the CdS/CdTe solar cell. At that, the back contact layer, as well as the presence of buffer layers, is critical for the stability of the CdS/CdTe solar cells. In particular, the main junction of the glass/FTO/CdS/CdTe/Au solar cell was destroyed in the absence of buffer layers close to front and back electrodes. Zeng et al. [95] also showed that optimized front contact also improves stability of the cells. They achieved this by using an SnO_2:F (FTO)/magnesium-doped zinc oxide (MZO) as a front contact.

The second mechanism involved in the process of degradation of solar cells is the diffusion and drift of Cu in CdTe solar cells [17, 34]. It is generally accepted that Cu aids the formation of better ohmic contacts by increasing the p-doping of CdTe near/at the back contact interface. An anneal step at temperatures around 150 °C is generally used in the back contact formation process for the diffusion and activation of the dopant [28]. This process leads not only to the formation of a good back contact but also, by increasing the acceptor concentration of the absorber layer, to an increased built-in field and consequently higher open-circuit voltage of the solar cell devices. It is, however, at the same time considered to be the principal component responsible for the degradation of solar cells which is ascribed to its ability to diffuse especially along the grain boundaries through the polycrystalline CdTe film to the cell junction. It is found that Cu rapidly diffuses through the cell structure during the annealing of back

contact and accumulates in the CdS layer. As it accumulates, copper, together with chlorine, dopes CdS, forming high-resistance photoconductive CdS. An increase in the photoconductivity of CdS leads to increased crossover in the light-dark current-voltage characteristic of the device. A schematic of the proposed roles of Cu in CdTe/CdS cells is presented in Fig. 18.1. Improvements in initial cell performance are proposed to be due to the formation of a favorable Cu_2Te back contact from the reaction of Cu with a Te-rich CdTe surface. This material is also an excellent diffusion source for Cu into the cell structure [17].

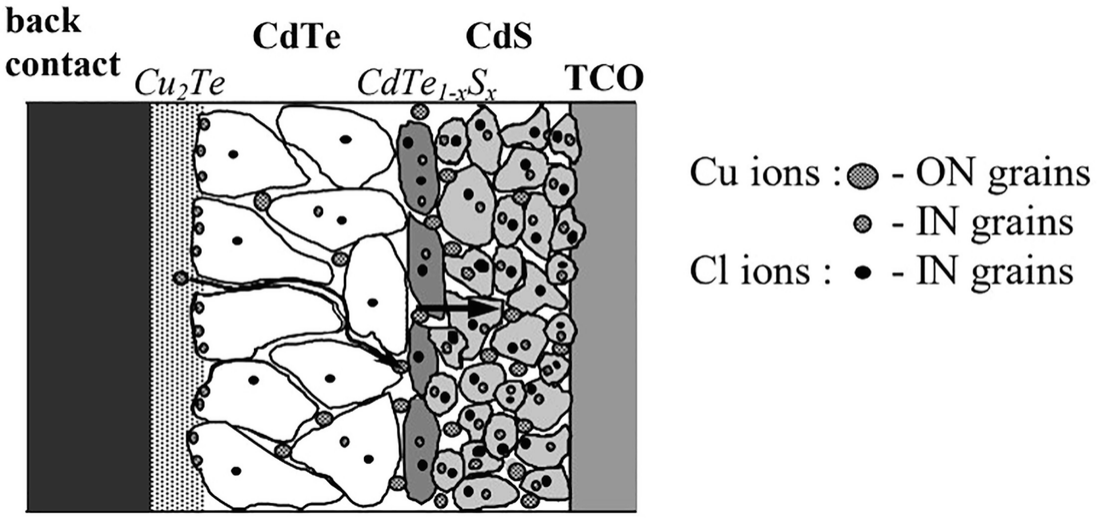

Fig. 18.1 Schematic illustration of the behavior of Cu and Cl within CdTe/CdS solar cells. Processes shown are formation of Cu_2Te at back contact/CdTe interface, GB diffusion of Cu from the Cu_2Te to the intermixed and CdS layers, accumulation of Cu and Cl ions in the GBs in this region, and further GB diffusion to, and possibly penetrating, the TCO interface. (Reprinted with permission from Ref. [16]. Copyright 2000: Elsevier)

Grecu et al. [28] have shown in their studies that the degradation of some CdTe solar cell devices that use Cu to form back contact can also be related to the instability of Cu acceptor states in CdTe. They found that copper-doped CdTe samples show a significant change in their luminescent properties when stored at room temperature. The observed behavior indicates the decay of the Cu_{Cd} and $Cu_i^+ - V_{cd}^-$ states with the formation of nonradiative recombination centers. Grecu et al. [28] also found that applied external electric fields can significantly change the diffusion profile of Cu in CdTe due to electromigration effects, which then can lead to degraded device performance as well. Gretener et al. [29] also considers

that the loss in net acceptor concentration in CdTe may be one of the reasons for the observed degradation of solar cell parameters.

This situation undoubtedly requires new approaches to cell design. In particular, copper-free back contacts are needed, which will allow the development of solar cells that are significantly more stable than their copper-containing counterparts under the same stress conditions [34]. However, research in this direction has not yet been successful, as in general cells with these copper-free back contacts show lower initial photovoltaic (PV) characteristics [18, 83]. But at the same time, encouraging results obtained in the development of cells with Sb_2Te_3 back contacts indicate that acceptable performance and cell stability can be achieved without the use of Cu [67]. At that, it was found that the most encouraging results are obtained when using Sb_2Te_3/Mo back contacts [5]. Figure 18.2 shows the efficiencies of CdTe/CdS solar cells for a variety of back contact combinations. Solid squares represent the initial efficiencies and open triangles with central dots represent efficiencies after annealing at 200 °C for 30 min. It is seen that performance degradation occurs for cells with Al, Au, or Cu at the back contact, while cells with Mo metallization do not degrade when a buffer layer of Sb or Sb_2Te_3 is applied. Cells with a Mo metallization and Sb and Sb_2Te_3 buffers also showed no long-term performance degradation during an accelerated lifetime test using a climate chamber where the cells are kept at 65 °C cell temperature in air at 1 sun illumination in open-circuit condition. Thus, cells with a Sb_2Te_3/Mo buffer showed excellent stability, and stress tests suggested that these cells will not degrade when properly encapsulated. Cells with Sb/Mo back contacts showed a small degradation. However, according to Batzner et al. [5], for industrial production, the application of an Sb buffer would be preferred over an Sb_2Te_3 buffer because of lower cost and less stringent process control requirements.

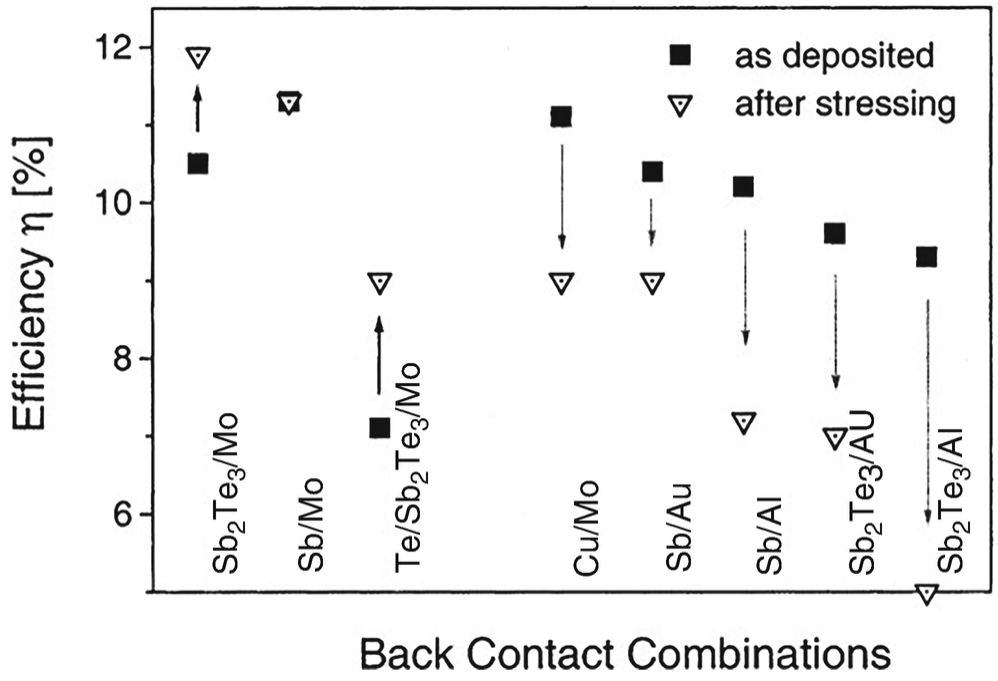

Fig. 18.2 Efficiencies of CdTe cells with different back contacts in as-deposited conditions and after annealing at 200 °C. Contacts containing fast diffuser impurities (Cu, Al, Au; right part of graph) degraded severely. The diffused impurities tend to accumulate in CdS and at the front contact CdS/TCO interface. (Reprinted with permission from Ref. [5]. Copyright 2004: Elsevier)

There is also suggestion that the replacement of CdTe by CdS_xTe_{1-x} in cells can also improve stability. This will be facilitated by the formation of Cu_2S inside the alloy, which will prevent the penetration of Cu into CdS [16]. The use of a different fluxing agent for CdTe (and CdS) post-deposition treatment (activation process), such as CdI_2, may also limit the possible detrimental symbiotic behavior related to the presence of Cl and Cu within the cell and, hence, may be beneficial to both cell performance and stability. Studies have shown that reducing copper concentration in back contacts [29], increasing the thickness of the CdTe layer [6, 34], and optimizing the CdTe etching process before deposition of back contacts [66] also improve the stability of CdTe/CdS solar cells. In particular, Rimmaudo et al. [66] showed that etching changes the way in which Cu interacts with CdTe surface: in fact, by means of a 40 s Br-MeOh etching of CdTe and 2 nm of Cu deposited on top of it, it is possible to obtain a CuTe and an extremely limit the diffusion of copper. In the absence of etching, during the back contact annealing, Cu reacts and generates Cu_2Te at the surface, which is unstable and may be the main supplier of Cu^+ to the solar cell during annealing. Moreover, Rimmaudo et al. [66] believe that with a suitable

optimization of the etching conditions it is possible to obtain a rather stable device even with a simple Cu-based back contact. Also, it has been shown that the thickness of the back contact ZnTe:Cu affects the amount of Cu accumulation at CdTe/CdS interface, e.g., more Cu accumulation with thicker contacts.

Among other proposals to reduce the influence of Cu on the degradation of CdTe/CdS parameters of solar cells, we can highlight the optimization of the $CdCl_2$ treatment process [22]. It has been found that small changes such as process time, $CdCl_2$ concentration, or temperature during processing can lead to significant differences in device stability [23]. To improve the stability of CdTe/CdS solar cells, Enzenroth et al. [21] proposed before back contact forming to carry out the $CdCl_2$ treatment at 400 °C followed by exposure of the CdTe layer to a copper halide vapor flux with the substrate temperature in the range of 200 °C. The copper profile measured by SIMS in structures with the proposed $CdCl_2$ treatment showed that the copper concentration gradient at the back of the CdTe/CdS device does not change significantly, and there is no significant increase in copper concentration in the CdS layer at open-circuit bias and a temperature of 65 °C. This indicates that, with proper $CdCl_2$ processing, Cu can be used to form a back contact for CdTe/CdS devices with acceptable stability.

Another strategy to overcome the problem mentioned above is to change the Cu solubility and the acceptor formation energy by doping CdTe with isovalent elements [50]. Another approach is to introduce alternative, possibly less diffuse additives such as As or P [29]. For these purposes, ion implantation can be used. The importance of using low-diffusivity dopants can be judged from the results shown in Fig. 18.3. Kim et al. [43] studied CdTe/CdS solar cells (Fig. 18.3a) fabricated using CdTe doped with group V elements (phosphorus and arsenic) and group I element (sodium). These cells were annealed at 100 °C for 10 days. It is seen that the sodium-doped sample exhibited poor interfacial properties, and its performance decreased rapidly during annealing. The samples doped with group V elements exhibited stable characteristics even during long-term annealing. It was assumed that more extensive degradation compared to samples containing group V dopants occurs due to increased surface recombination caused by diffusion of Na and Cu into the transition region. It was concluded, therefore, that group V elements dopants such as As and P are more suitable

for CdTe single-crystal-based solar cell applications involving thermal stress conditions, such as space missions or extreme fabrication temperature environments. Apparently, this requirement also applies to other II-VI semiconductors. For example, Sasaki et al. [68] have shown that the Li acceptor in ZnSe is unstable and migrates to an interstitial site, remaining a vacancy.

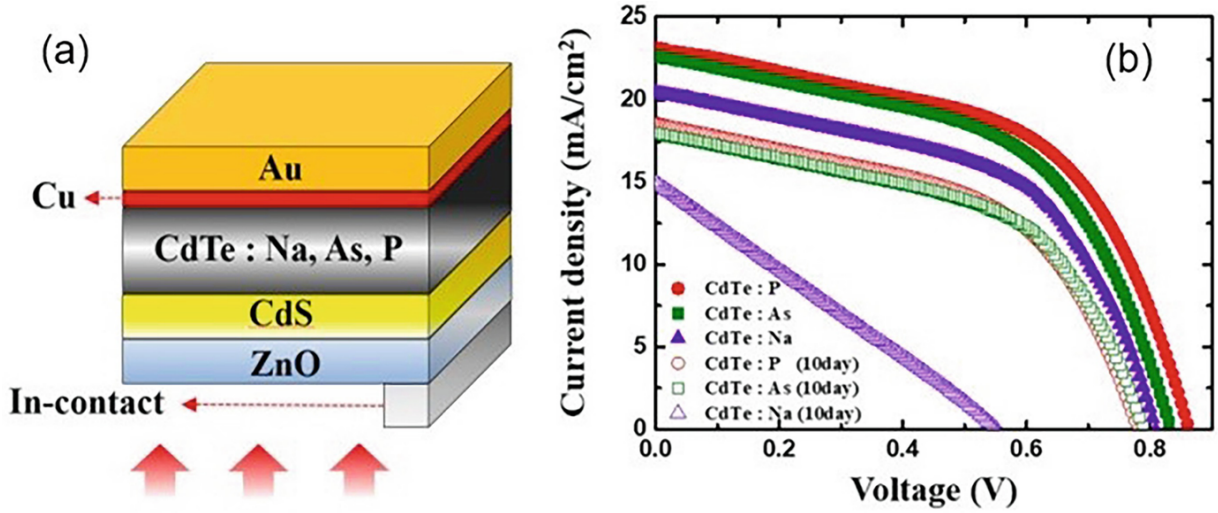

Fig. 18.3 (**a**) Schematic diagram of the device structure, (**b**) J-V curve of CdTe:P, CdTe:As, and CdTe:Na solar cell devices. The solid symbols represent the as-deposited samples, and the hollow symbols represent the samples annealed at 100 °C for 10 days. (Reprinted from Ref. [43]. Published 2022 by MDPI as open access)

It is important to note that there are suggestions [17] that the oxygen also plays a significant role in both contact degradation and copper diffusion. Studies have shown that these processes are significantly slowed down in encapsulated solar cells. Dobson et al. [17] believe that air oxidation of the cell creates Cd and/or Te oxide barriers at the back contact interface and possibly other deeper changes in the solar cell structure. For example, Visoly-Fisher et al. [85] suggested that the oxygen can migrate through the back contact and interact with Te atoms. The result is the formation of a thin layer of oxide of tellurium that increases the series resistance of the cells. This may explain why encapsulated modules exhibit higher stability compared to non-encapsulated lab solar cells and highlights the need to protect the cells/modules from the atmosphere during working stress to obtain high device stability.

18.2.2 Stability of II-VI Semiconductor-Based Quantum Dots

As for the instability of the properties of II-VI semiconductors, especially if they are formed in the form of quantum dots, numerous studies have shown that this instability is directly related to the surface oxidation process, which is enhanced in the presence of UV irradiation [34, 73]. For example, Singh and Roy [73] in the process of studying the effect of thermal annealing on the properties of CdSe/CdS core-shell nanocrystals found that the formation of oxide layers on the surfaces of the particles and generation of defect states occur during thermal annealing under the action of radiation. This process is accompanied by a significant decrease in the intensity of photoluminescence. At the same time, a decrease in the particle size is observed, which is directly related to their oxidation. Moreover, both the CdS forming the shell and the CdSe core are oxidized. Singh and Roy [73] consider that the oxidation of the CdSe core through the CdS layer indicates that the shells in the core/shell particles are not closed epitaxial layers but are layers with grain boundaries. These grain boundaries are formed where the CdS islands, which start to grow at different places on the CdSe nanocrystal surfaces, meet. At these boundaries, the oxygen can diffuse to the CdSe core inside the CdS shell.

At the same time, an important feature of the process of QD oxidation was established. The stability of the properties of nanodots is directly related to the stoichiometry of their surface. For example, Sharma et al. [71] studied the effect of oxidation on the properties of Cd-rich, Se-rich, and stoichiometric CdSe QDs that were stored in an ordinary atmosphere for 6 months. Long-term stability studies showed that the Se-rich CdSe nanoparticle exhibited the blueshift in photoluminescence (PL) position and a considerable decrease in PL intensity associated with surface states. Cd-rich CdSe nanoparticles also showed broadening of PL spectrum with significant enhancement of surface states. At the same time, the CdSe nanoparticles having stoichiometric Cd/Se composition were stable against oxidation with no shift in PL position and absence of signatures of surface-related states.

It is important to note that the instability of QDs drastically worsens the performance of quantum dot-sensitized solar cells. It has been established that the degradation of unencapsulated solar cells with CdSe QDs occurs rather fast, and when the cell was left in the room atmosphere for only 1 day, a loss of efficiency of 40% was observed, and a loss of efficiency of more than 80% was observed for a 3-day exposure. Wang et al. [87] found

that surface oxidation and phase separation of CdSe QDs are the cause of a sharp deterioration in the performance of quantum dot-sensitized solar cells. Wang et al. [87] proposed to use ZnS passivation of CdSe quantum dots to solve this problem. They found that the rate of degradation was significantly slowed compared to cells without ZnS passivation. However, it was also found that ZnS passivation could not completely prevent the degradation of solar cells.

Oxidation of a semiconductor material, accompanied by the formation of an oxide layer and trap sites at grain boundaries, is also the cause of a change in the mobility of charge carriers in polycrystalline films [45].

Of course, the incorporation of nanodots into a polymer or inorganic monolith significantly increases the stability of their parameters, since it ensures that QDs do not come into contact with the atmosphere [48]. How effective this approach can be seen from the results shown in Fig. 18.4. These results were obtained in the study of the stability of CdSe/CdS/ZnS QDs. It can be seen that the stability of CdSe/CdS/ZnS QDs incorporated into SiO_2/Al_2O_3 monolith (SAM) is dramatically improved. But this option is not acceptable in the development of photodetectors, solar cells, and sensors, where it is necessary either to provide conductivity between quantum dots or to provide contact of QDs with the atmosphere or the object under test.

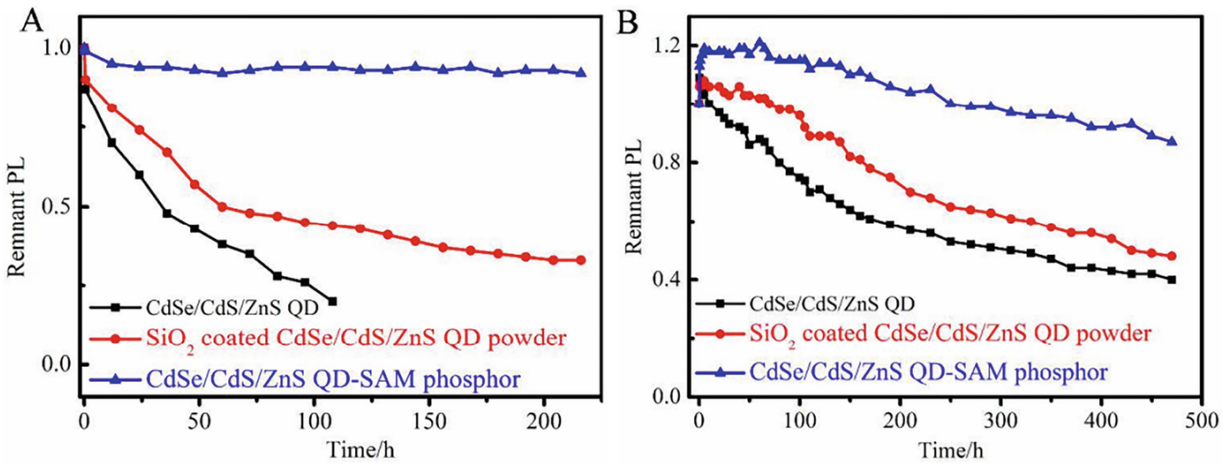

Fig. 18.4 (**a**) Thermal stability of the CdSe/CdS/ZnS QD, SiO_2-coated CdSe/CdS/ZnS QD powders, and CdSe/CdS/ZnS QD-SAM phosphors at 100 °C. (**b**) Photostability of corresponding samples sealed with optical adhesive on the LED chip. (Reprinted with permission from Ref. [47]. Copyright 2018: ACS)

Taking into account the above, in this chapter, we will consider in more detail the main processes that occur during the interaction of II-VI compounds with oxygen. Moreover, the results of research in this area draw a direct parallel between the stability of the properties of semiconductors and their resistance to oxidation. We will also discuss coatings that can be used to encapsulate the surface of II-VI compounds in order to stabilize their properties.

Taking into account the above, in this chapter, we will consider in more detail the main processes.

18.3 Native Oxides

On the surface of II-VI compounds, as well as on the surface of silicon and III-V compounds, a layer of native oxides is formed upon contact with the atmosphere. However, unlike III-V compounds, more ionic II-VI compounds are much less active in an oxygen atmosphere. Therefore, although thermodynamic data indicate the possibility of interaction between II-VI semiconductors and oxygen, the rate of this reaction at room temperature is evidently very low [7].

Studies performed in high vacuum on cleaved surfaces of II-VI compounds such as ZnSe, ZnTe, CdSe, and CdTe, using ultraviolet photoelectron (UPS) and electron energy loss (ELS) spectroscopies [19], showed that during oxidation of CdTe the oxygen at the initial stage of interaction seems to be adsorbed onto the surface Te atoms, breaking the back bonds, which leads to the formation of TeO_2 on the CdTe surface. Tari et al. [77] also believe that a TeO_2 layer is formed on the CdZnTe surface. According to Yi and Liou [93], the TeO_2 layer on the surface of a polycrystalline CdTe film after exposure to air at room temperature for 6 months has a thickness of ~2 nm.

In the case of chemically etched surfaces, the situation is somewhat different. Zázvorka et al. [94] studied the growth of the surface oxide layer on the CdTe and CdZnTe crystals after chemical etching in bromine solutions and found that a rapid growth was visible within 5 days after the chemical treatment followed by semi-saturation and a decrease in the growth rate after the first week. After 1 month all the samples showed an oxide layer about 3 nm thick (see Fig. 18.5). Interestingly, CdTe samples

exhibited almost no surface layer right after the surface treatment, whereas CdZnTe samples with 10% zinc concentration showed a surface layer with the thickness approx. 0.5 nm right after the surface etching. According to Tari et al. [77], the thickness of the TiO_2 layer formed on the surface of $Cd_{0.9}Zn_{0.1}Te$ approximately 1 h after etching is about 3–4 nm.

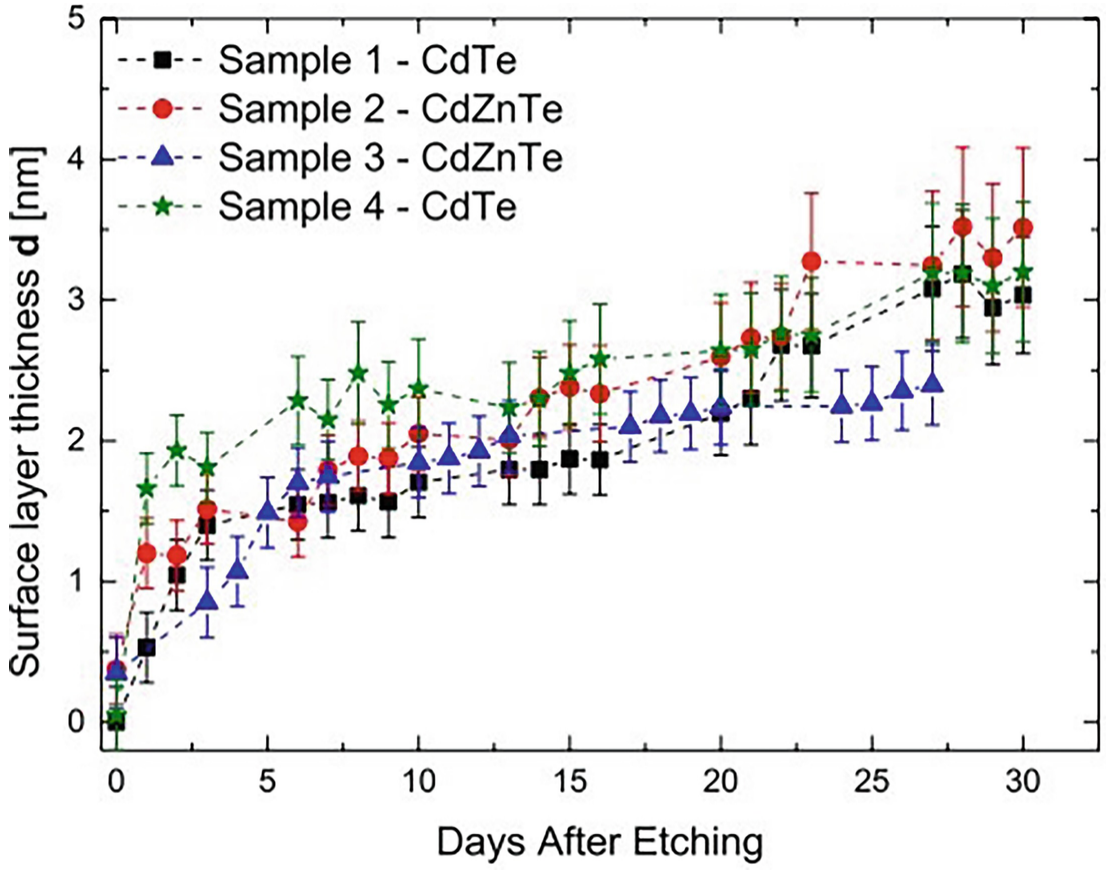

Fig. 18.5 Evolution of surface layer thickness d after the surface preparation treatment. (Reprinted from Ref. [92]. Published 2016 by National Institute for Materials Science as open access)

However, not everyone agrees with the statement that there is a TeO_2 layer on the surface. Choi and Lucovsky [9] believe that native air-grown CdTe oxide is a complex oxide of the form $Cd_xTe_yO_x$, probably $CdTeO_3$, and not a mixture of binary oxides CdO and TeO_2. Moreover, they state that the chemical composition of the native oxide can vary considerably depending on the oxidation conditions.

According to Ebina et al. [19], for the case of ZnTe, the TeO_2 appears at the oxygen coverage, θ, of about 0.5 of a monolayer. However, at the oxygen coverage $\theta > 1$, ZnO begins to appear on the surface ZnO. Thus, the

oxide overlayer on ZnTe is composed of TeO_2 and ZnO and, in addition, a complex oxide, such as $ZnTeO_3$, for the heavy-oxidized surface. On further oxygen exposures and beam irradiation of this oxide, tellurium oxides sublime away from the surface, leaving an oxide layer rich in ZnO. The dissociative evaporation of the complex oxide might help the formation of the ZnO overlayer. Ebina et al. [20] assumed that the dominance of ZnO on the heavy-oxidized ZnTe surface is due to the fact that ZnO is more stable than TeO_2 and therefore Zn can reduce TeO_2 to a loner level oxide (Eq. 18.1), which sublimes away from the surface, leaving ZnO on the surface. The existence of gaseous TeO is known [55].

$$TeO_2 + Zn \rightarrow TeO \uparrow + ZnO \tag{18.1}$$

As regards the dominance of TeO_2 on the surface of heavy-oxidized CdTe, according to Ebina et al. [20], this result is very reasonable because TeO_2 is more stable than CdO. The thermodynamic data for TeO_2 and CdO reported are presented in Table 18.1, where ΔH is the standard heat of formation of a given substance from its elements at 25 °C and ΔS is the variation of standard entropy for a substance. ΔH and ΔS are related to the standard Gibbs free energy of formation ΔG as ΔG = ΔH - TΔS, where T is the absolute temperature. Using the data in Table 18.1 and setting T = 298.17 K, we found that TeO_2 has a higher Gibbs free energy of formation (−64.6 Kcal/mol) than CdO (−54.6 Kcal/mol). Thus, the CdTe film exposed to the air prefers the formation of TeO_2 over CdO.

Table 18.1 Thermodynamic data of TeO_2 and CdO (at 25 °C)

Material	ΔH (Kcal/mol)	ΔS (cal/deg.mol)
Cd	0	12.37
Te	0	11.88
O_2	0	49.0
CdO	−61.7	13.1
TeO_2	−77.1	19.0

Source: Data extracted from Ref. [93]

Ebina et al. [19] have found that in the case of the Se compounds, the oxygen adsorbs on the surface Se atoms without breaking the back bonds at the initial stages of oxidation ($\theta < 0.5$). For $\theta > 0.5$, back bonds are broken, resulting in the formation of the bulklike cation oxide, ZnO and CdO, and, perhaps, the anion oxide, SeO_2. Ebina et al. [19] do not exclude that the formation of complex oxides, such as $ZnSeO_3$ and $CdSeO_3$, also occurs during the oxidation process. The presence of $ZnSeO_3$ and $CdSeO_3$ is possible, since these oxides are more stable than binary oxides based on Zn, Cd, and Se. Because of its high vapor pressure, the SeO_2 may sublime away from the surface, leaving the overlayer rich in ZnO for ZnSe and rich in CdO for CdSe. Thus, for very heavy oxidation, the following oxides were found: TeO_2 on CdTe, CdO on CdSe, and ZnO on ZnTe and ZnSe. For each II-VI semiconductor, the single oxide listed above was that with the largest heat of formations.

At the same time, studies by Hellgren et al. [33] showed that the composition of the oxide on the surface of ZnSe is indeed very sensitive to the method of surface treatment, and in the presence of water or its vapor, hydroxyls such as SeOH and ZnOH can also be present on the surface. The relative concentrations of elements present on the ZnSe surface after various treatments are given in Table 18.2. After etching, the samples were immediately washed with deionized water and dried in nitrogen gas.

Table 18.2 Atomic concentrations of C, O, Se, and Zn, as well as Zn/Se ratio for ZnSe after various surface treatments

Sample treatment	**C 1S**	**O 1S**	**Se 3d**			**Zn 3d**			**Zn/Se**
			ZnSe	**SeO_2**	**SeOH**	**ZnSe**	**ZnO**	**ZnOH**	
Vacuum cleaved	0.0	0.0	50.0	0.0	0.0	50.0	0.0	0.0	1.0
Air cleaved	14.4	7.7	38.0	0.0	0.0	38.6	0.9	0.0	1.05
HCl	39.1	14.8	18.1	0.0	8.0	19.2	0.6	0.0	0.76
HCl + O_3	12.3	15.7	2.1	13.3	3.7	6.5	5.7	0.7	0.67
$KMnO_4 + H_2SO_4$	25.0	19.6	22.9	0.0	7.9	23.8	0.5	0.0	0.80
$KMnO_4 + H_2SO_4 + O_3$	10.5	59.6	1.0	12.8	3.0	3.9	7.1	2.1	0.79
NH_4OH	17.7	28.7	22.7	0.0	7.0	22.1	1.3	0.0	0.80
$NH_4OH + O_3$	15.3	39.7	5.3	1.0	15.6	6.5	4.0	12.5	1.06
Native oxide	29.0	51.8	2.6	1.5	2.6	4.8	4.7	3.0	1.85

Sample treatment	C 1S	O 1S	Se 3d			Zn 3d			Zn/Se
			ZnSe	SeO_2	SeOH	ZnSe	ZnO	ZnOH	
Native oxide+O_3	13.7	51.0	5.1	5.6	4.9	9.8	7.5	2.4	1.25

Source: Reprinted with permission from Ref. [33]. Copyright 2020: Elsevier

Results obtained showed that all etches preferentially remove Zn, leaving an amorphous and presumably porous Se-rich top layer. According to Hellgren et al. [33], the thickness of Se top layer is ~1 nm, or 3–4 monolayer. The main difference between the etches is the effect on carbon and oxygen. The surface oxygen concentration is lowest on the HCl-etched sample and highest on the NH_4OH:C_2H_6O-etched sample. The overall oxygen concentration is less than half of that on the sample with native oxide, but still significantly higher than the air-cleaved sample. For carbon, the trend is reversed; the HCl etch does not appear to remove much of the native carbon contamination, while both the other etches do. Hellgren et al. [33] have also found that after UV-O_3 treatment, on the HCl- and $KMnO_4$:H_2SO_4-etched samples, the Se-rich top layer is converted to SeO_2, as can be expected as the ozone breaks apart and reacts with the Se top layer. Some ZnO is also formed, which is possible since the Se top layer is relatively thin. The Zn/Se atomic ratio, however, remains relatively unchanged. Based on the total oxygen concentration, the thickness of the resulting oxide layer is comparable to that of the native sample, which we estimate to be ~3–4 nm. However, for the NH_4OH:C_2H_6O-etched sample, hydrogen-containing species are trapped, resulting in the formation of a surface layer consisting of SeOH and ZnOH, rather than SeO_2 and ZnO.

If we now turn to the consideration of natural oxides on the surface of S compounds, CdS, and ZnS, then we can assume that the composition of the oxide on the surface of these compounds will be the same as in the case of Se compounds. Those, the surface of heavy-oxidized CdS and ZnS, will be dominated by CdO and ZnO, respectively. This is due to the fact that these oxides have higher heat of formations compared to SO_2. In addition, SO_2 is a gas under normal conditions.

18.4 Thermal Oxidation of II-VI Compounds

II-VI compounds during the fabrication of devices in most cases are subjected to thermal treatments in an oxygen-containing atmosphere. These treatments can affect the surface and bulk properties, since this process can be accompanied by both the dissociation of II-VI compounds, i.e., generation of point defects that affect the optical and electrical properties of the compounds, and its oxidation [7, 62, 79]. Oxygen can also diffuse into II-VI compounds and fill anion vacancies [74], which leads to a significant increase in the resistivity of the semiconductor. Therefore, it is important to know in what temperature range II-VI compounds remain stable and what oxides are formed on their surface.

The latter is of great interest, since it can be used both for the synthesis of oxides through the oxidation of the corresponding II-VI compounds [88] and for the formation of core-shell structures based on II-VI compounds [47, 51], in which the top layer is formed by oxides that have better stability and lower toxicity compared to II-VI compounds (read Chap. 8, Vol. 1). In other words, the oxides formed on the surface of II-VI compounds can act as protective coatings for these compounds. Through oxidation, it is also possible to influence the catalytic properties of II-VI compounds [81].

18.4.1 CdS

CdS is the most studied compound. Studies, performed by Dimitrov et al. [15], using both differential thermal (DTA) and thermogravimetric analysis (TGA), as well as chemical, mineralogical, X-ray phase analysis, and scanning electron microscopy (SEM), showed that the oxidation of CdS is a complex heterogeneous exothermic process, which is affected by a number of complex processes such as reaction kinetics, crystal chemistry, adsorption, mass transfer, heat transfer, and others. It was found that up to 400–450 °C the compound CdS remains stable (see Table 18.3). Trenczek-Zajaca [81] also did not observe any change in X-ray diffraction (XRD) patterns of nanostructured CdS up to 300 °C. Only at a temperature of 400 °C did the first qualitative changes in the X-ray diffraction pattern begin, as evidenced by the appearance of new diffraction peaks and a decrease in the width of the peaks. The latter indicated an increase in the crystallite size. However, Somorjai [75] established that single crystals remain stable only in the absence of illumination. When the single crystal

was heated in oxidizing atmosphere over 300 °C in UV irradiation, the illuminated area was darkened visibly after short exposure times. It was found that the darkening was caused by the presence of precipitated cadmium and cadmium oxide of particle sizes 0.2–400 nm. At that, no Cd precipitation and subsequent oxidation could be detected in the absence of light under identical conditions. The results were interpreted assuming that charge transfer is the rate-determining step in the studied evaporation and oxidation surface reactions. Light of greater than bandgap energy (1) changed the charge concentration at the CdS crystal surface and (2) slowly changed the composition of the crystal. According to Somorjai [75], both of these effects could influence the evaporation and oxidation rates.

Table 18.3 Characteristic temperatures of the CdS and ZnS oxidation

Sulfide	**Temperature,°C**				**Δm at 1000,°C%**
	T1	**T2**	**T3**	**T4**	
CdS-Merck 1	505	635	770	790	+1.0
CdS-Merck 2	505	535	630, 755	820	−6.0
CdS	450	495	595, 680	725	0.0
CdS-monocrystal	660	725	790	830	−11.6
ZnS-Fluka	520	530	660	685	−13.5
ZnS-monocrystal	590	625	745	835	−15.0

Source: Data extracted from Refs. [13, 14]
T1 = temperature of the beginning of the oxidation process (the first change in DTA curves, the appearance of SO_2 in gas phase); T2 = temperature of the beginning of intense oxidation of the sulfide (the sharp bend of the DTA curve); T3 = temperature at which intense oxidation takes place (T3 is close to the temperature of completion of the process of oxidation with time); T4 = minimum temperature above which processes take place at a high rate up to the stage of desulfurization (T4 is determined by DTA, gas-phase analysis, and measuring the change in the sample weight)

The experiment showed that at higher temperatures, the oxidation of CdS with the formation of oxide and sulfate occurs even in the dark. Dimitrov et al. [15] established that in static air atmosphere the mass of polycrystalline sample decreases in the interval from 500 to 1000 °C. The sample mass loss is 16%, while, theoretically, if the whole quantity of CdS

turns into CdO, Δm would be 11%. The probable reason for this is the sublimation of CdS, as well as oxidation. The sublimation and dissociation of CdS which resulted in the emission of sulfur vapor have been confirmed by Yazawa [92]. The process of CdS dissociation, under isothermal conditions, most probably begins in the temperature interval 600–800 °C. In flowing air, the processes occur at the lower temperatures with the emission of considerably larger quantities of sulfur.

According to Dimitrov and Boyanov [14], the following reactions are possible during the oxidation of CdS:

$$\mathrm{CdS} + 2\mathrm{O_2} \rightarrow \mathrm{CdSO_4} \tag{18.2}$$

$$3\mathrm{CdS} + 5\mathrm{O_2} \rightarrow 2\mathrm{CdO}\cdot \mathrm{CdSO_4} + 2\mathrm{SO_2} \tag{18.3}$$

$$\mathrm{CdSO_4} \rightarrow \mathrm{CdO} + \mathrm{SO_2} + 1/2\mathrm{O_2} \tag{18.4}$$

$$2\mathrm{CdS} + 3\mathrm{O_2} \rightarrow 2\mathrm{CdO} + 2\mathrm{SO_2} \tag{18.5}$$

$$\mathrm{CdS} + \mathrm{CdSO_4} \rightarrow 2\mathrm{CdO} + 2\mathrm{SO_2} \tag{18.6}$$

From a theoretical point of view, the oxidation of CdS should give rise to $CdSO_4$ (reaction 18.2). The experiment confirms this conclusion. According to XPS data, the initial formation of sulfate begins at temperatures below 500 °C; at 500 °C, its concentration is negligible; and after the sample is oxidized at 600 °C, $CdSO_4$ becomes the main component present on the CdS surface. In addition to $CdSO_4$, Trenczek-Zajaca [81] observed the appearance of $Cd(S_2O_7)$ and $Cd_5S_3O_6$ in this temperature range. Heiba [32] believes that, in addition to $CdSO_4$, $Cd_3O_2SO_4$, i.e., $2CdO{\cdot}CdSO_4$ (reaction 18.3), is also present on the CdS surface (see Fig. 18.6).

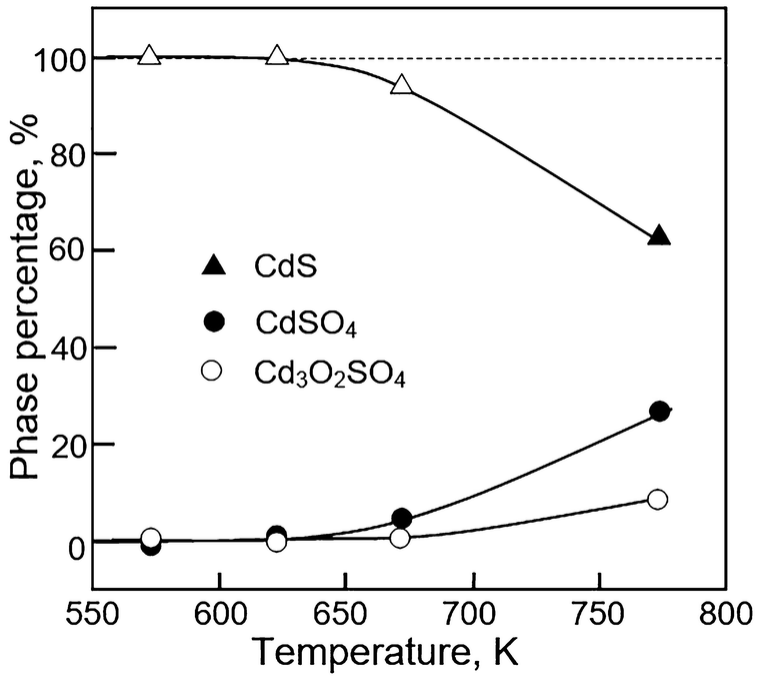

Fig. 18.6 The phase percentage of the oxidation products of CdS after annealing at different temperatures. (Reprinted with permission from Ref. [32]. Copyright 2002: Cambridge University Press)

However, Dimitrov and Boyanov [14] believe that CdS is not completely oxidized to $CdSO_4$ or $2CdO{\cdot}CdSO_4$. According to Dimitrov and Boyanov [14], the decomposition of $CdSO_4$ begins before the completion of sulfate formation (reaction 18.4). At temperatures >800 °C, the dissociation of $CdSO_4$ to CdO is quite intense. As a result, at temperatures above 800 °C, cadmium oxide CdO appears on the CdS surface, resulting in both an increase in the bandgap and a significant increase in the Cd/S ratio. Figure 18.7 shows the dependence of the bandgap energy values and atomic ratio of Cd/S in nanopowders as a function of oxidation temperature. These data were reported by [81]. As can be seen, an increase in temperature is accompanied be an increase in Eg from 2.27 eV for RT to 2.41 eV for samples annealed at 650 °C. The latter value is typical for bulk CdS. This may confirm that at lower temperatures only the recrystallization of CdS occurs. At T_{an} > 600 °C, an additional bandgap energy was observed and found to be 3.19 eV, increasing to 3.48 eV at 900 °C. Trenczek-Zajaca [81] believe that the appearance of the Eg more than 3.0 eV may be connected with the crystallization of $Cd_3O_2SO_4$ at this temperature. The rise in Eg is likely associated with the growth of its contribution in the oxidized material. As for the increase in the Cd/S ratio, according to Trenczek-Zajaca

[81], this is a consequence of the oxidation of sulfur to gaseous products such as SO_2 and SO_3 (reactions 18.3, 18.4, 18.5, and 18.6). However, even at temperatures 800–900 °C, Dimitrov and Boyanov [14] observed the presence of $CdSO_4$. True, the presence of sulfates at these temperatures in the experiments of Dimitrov and Boyanov [14] may be due to the oxidation conditions used: a large amount of CdS used and the absence of air flow. In this case, intermediate sulfate products can be formed due to the lack of oxygen and the large mass of CdS in a small volume reactor [14]. During oxidation in a flow reactor, the presence of $CdSO_4$ may not be detected.

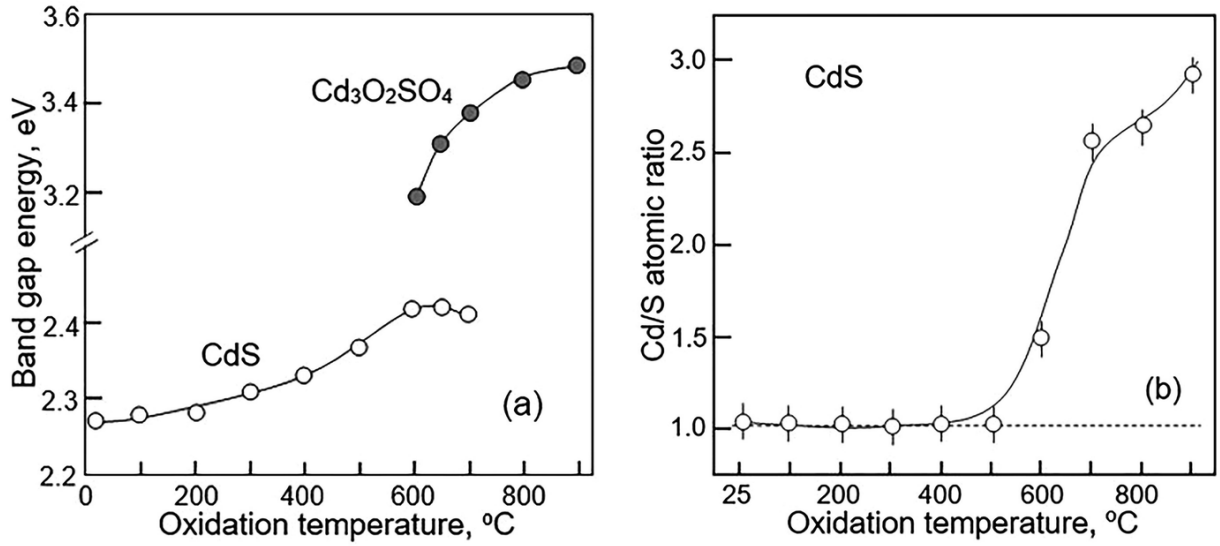

Fig. 18.7 (**a**) Bandgap energy of the investigated samples. (**b**) Atomic ratio of Cd/S in nanopowders as a function of oxidation temperature. (Reprinted with permission from Ref. [81]. Copyright 2019: RSC Publishing)

It was also established that the CdO obtained from the oxidation of CdS has larger crystallographic unit cell and is more porous, compared to the ZnO [12] obtained from the oxidation of ZnS. The oxide crust is mechanically weaker, and there is no joint between the oxide crust and the unoxidized sulfide core. The adhesion is very weak. It is possible that the high vapor pressure over the base CdS has an effect [84]. Thus, according to Dimitrov et al. [15], the thermal oxidation of polycrystalline CdS results in a very porous and mechanically fragile CdO shell, which does not prevent the diffusion of the gaseous reagent (O_2).

Dimitrov and Boyanov [14] also found that the stability of single-crystal CdS is markedly better than that of polycrystalline material. In addition, the behavior of CdS, obtained as a monocrystal, is very different from the

behavior of polycrystalline CdS. In the case of single crystals, the oxidation takes place in one stage. The thermogravimetric (TG) curve for single-crystal CdS does not change until about 660 °C, after which the mass begins to decrease. The change in Δm obtained at 1000 °C (Δm = −11.6%) is quite close to the theoretical value (−11.1%) when reaction (18.5) is complete.

18.4.2 ZnS

ZnS is another well-studied II–VI compound. Studies by Dimitrov and Bonev [12] showed that the oxidation of ZnS is very similar to the process of oxidation of CdS considered earlier. Like CdS, ZnS remains stable in air at low temperatures of 400–600 °C. Yamamoto et al. [91] reported that below the oxidizing temperature of 400 °C, only diffraction peaks corresponding to ZnS were observed in XRD patterns. By the oxidation of 600 °C, however, small peaks corresponding to ZnO were detected in addition to those of ZnS, suggesting the oxidation of small amount of ZnS. This is also quite obvious from the thermogravimetric (TG) curves for ZnS, which are almost horizontal until the beginning of the oxidation process [69].

According to Dimitrov and Boyanov [14], the following reactions are possible during the oxidation of ZnS:

$$\mathrm{ZnS} + 2\mathrm{O_2} \rightarrow \mathrm{ZnSO_4} \tag{18.7}$$

$$\mathrm{ZnSO_4} \rightarrow \mathrm{ZnO} + \mathrm{SO_2} + 1/2\mathrm{O_2} \tag{18.8}$$

$$\mathrm{ZnS} + 3/2\mathrm{O_2} \rightarrow \mathrm{ZnO} + \mathrm{SO_2} \tag{18.9}$$

Based on the thermodynamic analysis of the Zn-S-O system and the study of hexagonal ZnS oxidized in a quasi-closed volume, Dimitrov and Bonev [12] found that the following phases can be present on the surface of ZnS:

(a) ZnS, ZnO, $ZnSO_4$ and Zn at 527 °C;

(b) ZnS, ZnO, $ZnSO_4$ at 580–875 °C;

(c) ZnO, $ZnSO_4$ at 875 °C;

(d) ZnO at 850–1000 °C;

However, they also showed that $ZnSO_4$ is only stable at high partial pressures of SO_2 (P_{SO2}). According to Narayan et al. [57], decomposition of zinc sulfate starts at ~600 °C. Oxysulfites are more stable, but under quasi-stationary conditions, they should completely decompose at temperatures of ~800–850 °C. And this means that under real conditions at temperatures above 600 °C, $ZnSO_4$ should decompose. This has been confirmed experimentally. X-ray analysis of ZnS powders oxidized in an air flow at 600 °C for 5 h did not find sulfate. Based on the analysis of the mass loss of ZnS at 1000 °C, Dimitrov and Bonev [12] concluded that the product of ZnS high-temperature oxidation is zinc oxide, and zinc oxide is obtained directly (reaction 18.9). This conclusion is in good agreement with the results obtained by Schultze et al. [69], who studied the oxidation in the temperature range of 560–1000 ^oC of various modifications of ZnS: sphalerite and wurtzite. Schultze et al. [69] reported that wurtzite, the high-temperature hexagonal modification, is oxidized directly to ZnO without any detectable side reactions or intermediate products (reaction 18.9). Sphalerite, the low-temperature cubical modification of ZnS, starts to oxidize at lower temperature, and this reaction involves intermediates. $ZnSO_4$ and $Zn_3O(SO_4)_2$ ($ZnO{\cdot}2ZnSO_4$) are formed as intermediates in side reactions but yielded ZnO finally (reactions 18.8, 18.11, and 18.12). Schultze et al. [69] believe that the higher reactivity of sphalerite is eventually due to the Hedvall effect (the increased reactivity of a solid during and as a consequence of a crystalline transformation) and correlated with the sphalerite-wurtzite transformation:

$$ZnSO_4 \rightarrow Zn_3O(SO_4)_2 + SO_3 \quad (18.10)$$

$$Zn_3O(SO_4)_2 \rightarrow 3ZnO + 2SO_3 \quad (18.11)$$

$$2SO_3 \rightleftarrows 2SO_2 + O_2 \quad (18.12)$$

However, it should be borne in mind that the above ZnS oxidation temperatures are not strictly established but depend on the material

properties and experimental conditions. For example, ZnO formation has been reported to occur at 400 °C [58], 500 °C [47], or 600 °C [88]. Moreover, with a decrease in the size of ZnS crystallites, this temperature decreased. For example, Kanti Kole et al. [39] observed complete oxidation of ZnS nanobelts 450 × 20 × 20 nm in size at 600 °C, while Murugadoss [56] reported that ZnS 3–5 nm nanoparticles were oxidized at 300 °C. The kinetics of zinc sulfide oxidation also depends on the porosity of the material [64]. The activation energy of ZnS oxidation, depending on its porosity, can vary from 353 kJ/mol to 146 kJ/mol, decreasing with increasing porosity. This means that these factors must be taken into account when choosing the modes of ZnS oxidation, which are especially used in the formation of ZnO/ZnS core-shell structures.

It should also be taken into account that the oxidation process is accompanied by a significant change in the film morphology and crystallite size (see Fig. 18.8). For example, Dengo et al. [11] studied the oxidation of ZnS nanopowders obtained using miniemulsion (ME) and hydrothermal (HT) synthesis, which had an average size of 7 nm and 21 nm, respectively. Data from X-ray diffraction analysis, near-edge X-ray absorption spectra (XANES), and transmission electron microscopy (TEM) images are shown in Fig. 18.9 and Table 18.4. These studies have shown that smaller nanoparticles are prone to more intense oxidation at low temperatures, and complete conversion of ZnS to ZnO is achieved already at 550 °C, regardless of the initial properties of the crystallites. A significant amount of sulfates on the surface of the particles was detected using FT-IR, Raman spectroscopy, and XPS only at temperatures of about 400 °C. It is important to note that the size of crystallites began to increase already at temperatures (450 °C), at which intensive oxidation did not yet occur (Fig. 18.9a). After annealing at 800 °C, the crystallite size approaches 100 nm.

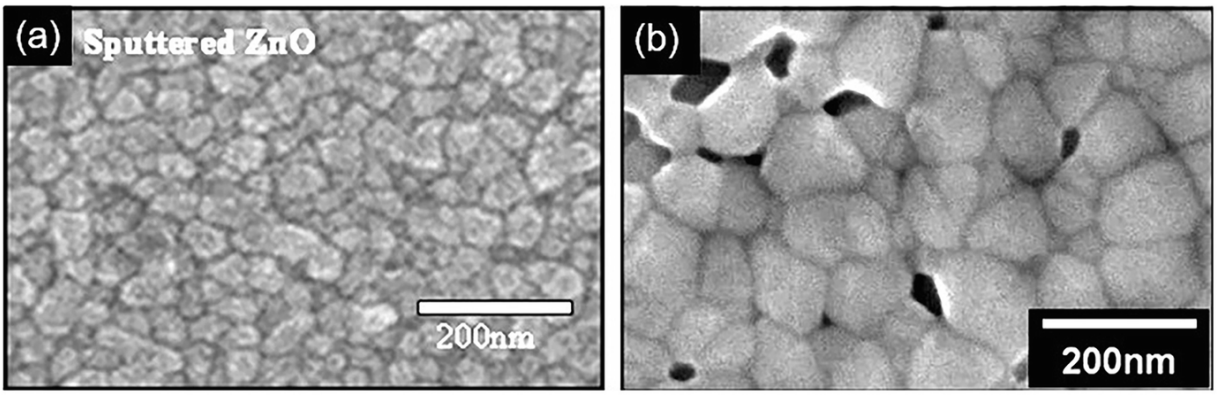

Fig. 18.8 SEM micrographs of the ZnS films after (**a**) sputtering and (**b**) after annealing at 800°C for 2 h in air. (Reprinted from Ref. [62]. Published 2013 by Korean Photovoltaic Society as open access)

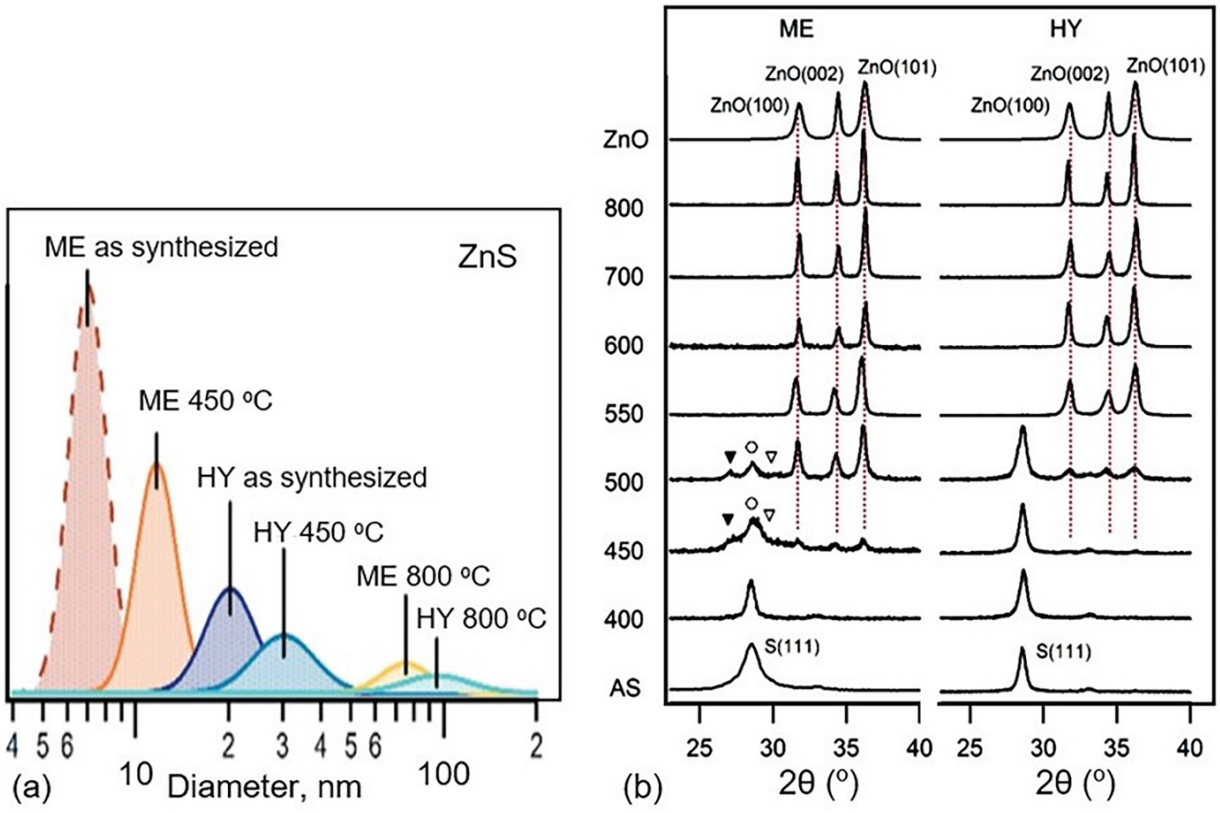

Fig. 18.9 (**a**) Log-normal fitted equivalent diameter numerical distribution obtained from the TEM image; (**b**) evolution of the XRD diffractograms at different calcination temperatures. The S(111) index is referred to sphalerite-phase ZnS. The dotted lines emphasize the presence of the three main reflections of ZnO. Markers show the presence of the wurtzite ZnS reflections: (▼) = (100), (○) = (100), (▽) = (100). AS = as-synthesized. Temperatures are indicated in degrees Celsius. (Reprinted with permission from Ref. [11]. Copyright 2018: ACS)

Table 18.4 Sample composition as weight percentages obtained from XRD and XAS analysis

T (°C)	ME				HT			
	%ZnS		%ZnO		%ZnS		%ZnO	
	XRD	XAS	XRD	XAS	XRD	XAS	XRD	XAS
as-syn.	100	100	0	0	100	100	0	0
400	100	97	0	3	100	98	0	2
500	34	44	66	56	65	42	35	58
600	0	0	100	100	0	0	100	100
700	0	0	100	100	0	0	100	100
800	0	0	100	100	0	0	100	100

Source: Reprinted with permission from Ref. [11]. Copyright 2018: ACS

18.4.3 ZnTe and CdTe

Studies of the process of thermal oxidation of ZnTe have shown that a two-phase system is formed on the surface of ZnTe during oxidation. Kaito et al. [38] found that ZnO and tellurium crystallites were present on the surface of ZnTe after oxidation in air at 300 °C. At the same time, there are no epitaxial relations between the oxides and the substrate. ZnO crystallites are formed everywhere, while tellurium crystallites appear at the corner of the ZnTe crystal. Kaito et al. [38] also concluded that the (110) plane oxidized more slowly than any other plane. Since the surface (110) plane contains Zn and Te atoms and the (001) plane contains only Zn or Te, the (001) surface may more easily be attacked by the oxygen. Therefore, the oxidation predominantly takes place at ZnTe boundary surfaces such as (111) or (100) planes, which is accompanied by the generation of Zn vacancies, formed by the diffusion of Zn atoms to the surface. Lu et al. [49] also consider that during low-temperature (260 °C) thermal oxidation of polycrystalline ZnTe in air, the main phases present at the surface are crystals of ZnO and metallic Te. They usually form layered surface formations in the ZnTe/Te/ZnO sequence, with large (up to 100 nm) Te crystals in epitaxial relationship with bulk ZnTe and small ZnO (5 nm) crystals in random orientations. Lu et al. [49] also believe that process of oxidation involves the diffusion of Zn from the bulk ZnTe to the surface followed by reaction with oxygen in air to form ZnO.

A similar conclusion was made by Gas et al. [25] during oxidation at 300 °C of ZnTe and ZnTe/Zn nanowires grown by MBE. The energy

dispersive X-ray analysis (EDX) data obtained unequivocally showed that upon the oxidation these NWs have lost their original ZnTe nature and transformed into Te-enriched cores decorated with ZnO nanocrystals. At that the actual form of ZnO depended on the initial state of the NW surface. In the case of the oxidation of bare ZnTe NWs, only separated and relatively large ZnO nanocrystals form. After long-term oxidation (4 h) at 300 °C, the size of ZnO nanoparticle reached 60 nm. At the same time, the presence of the additional Zn coverage of ZnTe NWs results in a relatively smooth ZnO shell, but only of an amorphous or a fine-crystalline form. The total diameter of this particular NW measured at a half-height was approximately 90 nm, while the thickness of the shell was approximately 25 nm. In addition, the analogous long-term oxidation process did not lead to significant changes in the morphology of the NWs. Here, only a slight increase in the sizes of the crystallites building the NWs' shells and an increase in NWs' diameters to 80–90 nm can be noticed. This means that ZnO/ZnTe core-shell structures can only be formed after thin Zn shells are deposited on bare ZnTe NWs prior to oxidation.

Gas et al. [25] also concluded that the low-temperature oxidation of ZnTe and zinc-coated ZnTe NWs is not a promising method for obtaining homogeneous and high-quality ZnO-based nanostructures, since the oxidation process rather leads to the formation of a ZnTe/Te/ZnO sequence, which at sufficiently long oxidation time turns into a sequence of Te/ZnO. The formation of ZnO crystals on the surface is more likely than formation of TeO_2 ones, due to the lower free energy of the ZnO formation (−323.9 kJ/mol) than of the TeO_2 (−347.8 kJ/mol).

In this regard, anodic oxidation of ZnTe [72] can be a very effective method for forming ZnO/ZnTe structures. This method ensures the uniform formation of the ZnO oxide layer over the film surface, and in the case of anodic oxidation of nanowires, it can provide the formation of core-shell structures. Moreover, Sher et al. [72] demonstrated the diode-like behavior of the p-n junction between p-type ZnTe and its anodic oxide. After annealing at 400–450 °C in nitrogen, the anodic oxide had n-type conductivity with a charge carrier concentration of 5×10^{18} cm^{-3}. Diodes formed between epitaxial p-ZnTe and annealed n-type anode oxide showed good rectifying properties at low turn-on voltages. It is important that, as in the case of thermal oxidation, during anodic oxidation, a region enriched in

tellurium is formed near the ZnTe-oxide interface. This indicates that the Te oxide tends to segregate at the ZnTe-oxide interface.

With an increase in the oxidation temperature, the situation somewhat changes. De Melo et al. [10], studying the oxidation of polycrystalline ZnTe in wet Ar (3 wt.% H_2O) at temperatures of 450–550 °C, found that the process of oxidation of ZnTe films in the presence of wet Ar leads to the transformation into ZnO with a small amount of TeO_2. More complex oxides were also not detected. De Melo et al. [10] reported that the process is relatively slow at 450 °C: during 6 h only around 30 nm of the starting ZnTe material was converted to ZnO. At 550 °C, during the same time, around 90 nm was converted. This means that a ZnTe film of 90 nm should be completely converted to ZnO at this temperature. It was assumed that the oxidation reaction occurs in competition with the sublimation of ZnTe. During ZnTe sublimation the ZnTe bonds break and Zn becomes free to react with O to form ZnO in the degraded surface. Second, the fact that the atom density of ZnO is 1.6 times larger than that of ZnTe implies that the same number of Zn atoms will occupy in ZnO a smaller volume than in ZnTe. Then during the conversion of ZnTe to ZnO, voids should be necessarily formed. The sublimation of the ZnTe starting material can also contribute to the degradation of the surface at the annealing temperatures used. This explains the large roughness of the oxidized layers revealed in the Rutherford backscattering spectrometry (RBS) spectra. De Melo et al. [10] observed also that during the oxidation process, the morphology of the films changed abruptly from a relatively flat surface to a network of ZnO nanosheets.

As for the oxidation of CdTe at elevated temperatures (250–550 °C), Bai and Wang [3], analyzing the surface properties of polycrystalline CdTe coated with and without a $CdCl_2$ layer, found that when coated with a $CdCl_2$ layer, the CdTe film showed a much stronger oxidation after annealing at 550 °C. According to analysis of Raman spectra (Fig. 18.10), the main oxides formed on the surface of CdTe were $CdTeO_3$, Te, TeO_2, and Te_2O_5. The dominant oxide was $CdTeO_3$. All the Raman peaks in the energy range of 600–800 cm^{-1} are attributed to the vibration of the TeO_3^{2-} ion from the $CdTeO_3$ oxide. Earlier, a similar conclusion was made by [30]: CdTe oxidizes to $CdTeO_3$ without forming cadmium oxide. At the same

time, Bai and Wang [3] found that intense oxidation of CdTe begins only at temperatures above 400 °C. At temperatures <400 °C, the amount of oxides formed was not large enough to be detected using the XRD and Raman scattering techniques. It is important to note that after annealing at 550 °C, two Raman peaks appear in the spectra, located at 92 and 102 cm^{-1} and related to Te. This indicates the presence of an increased amount of Te both inside and on the surface of the film after annealing at 550 °C. Apparently, at this temperature, most of the detected Te was formed as a result of the decay of CdTe.

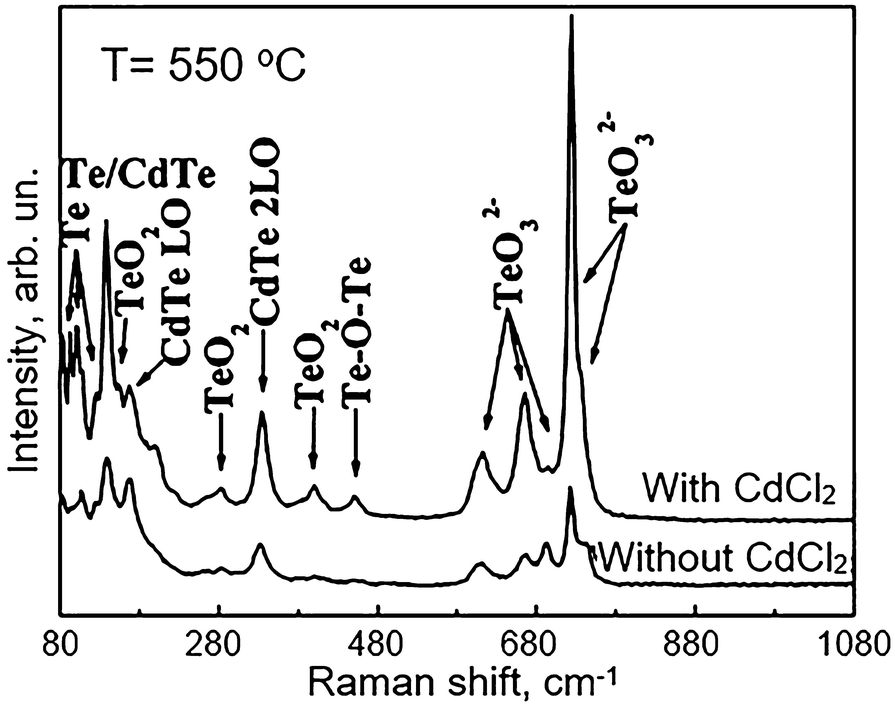

Fig. 18.10 Raman spectra recorded at room temperature after CdTe films were annealed at a temperature of 550 °C without and with the presence of a $CdCl_2$ coating layer. (Reprinted with permission from Ref. [3]. Copyright 2012: Wiley)

18.4.4 ZnSe and CdSe

ZnSe, like ZnS, is a compound that, unlike ZnTe and CdTe, can be used to form chalcogen-free ZnO [80]. In addition, among zinc chalcogenides such as ZnS, ZnSe, and ZnTe, only ZnSe is easily and successfully oxidized to ZnO at a relatively low temperature in accordance with the reaction:

$$\mathrm{ZnSe} + 3/2\mathrm{O_2} \rightarrow \mathrm{ZnO} + \mathrm{SeO_2} \uparrow \qquad (18.13)$$

The dissociation energy of ZnS, ZnSe, and ZnTe decreases in this order [80], so that, when the heat treatment between 300 and 600 °C is done, ZnS is stable but ZnSe and ZnTe are easily oxidized into ZnO, SeO_2, and TeO_2 by diffused oxygen. However, as it was shown before, in the temperature range mentioned above, SeO_2 is gaseous while TeO_2 is solidus. Therefore, TeO_2 remains with ZnO and then it is impossible to get pure ZnO. On the other hand, SeO_2 evaporates and we obtain ZnO thin film without SeO_2. The kinetics and mechanism of ZnSe oxidation at high temperatures were described by Stepanova et al. [76]. However, it was established that the oxidation of ZnSe is a more complex heterogeneous process, which involves a series of chemical reactions taking place during the decomposition of the initial material and formation of the final product [44]. For example, according to Gunchenko et al. [30] and Khlopochkina et al. [41], the appearance of Se is possible during the oxidation of ZnSe. But certain conditions must be created for this. Khlopochkina et al. [41] and Tikhonova et al. [78] suggested that when SeO_2, which is a highly active oxidizing agent, passes through a layer of ZnSe, the following reaction between these compounds is possible:

$$2ZnSe + SeO_2 \rightarrow 2ZnO + 3Se \tag{18.14}$$

Reaction (18.15) is also possible [30]:

$$2ZnSe + O_2 \rightarrow 2ZnO + 2Se \tag{18.15}$$

However, under normal oxidation conditions, the content in the gas phase of such forms of selenium as Se, Se_2, Se_3, etc. is several orders of magnitude lower than the content of selenium dioxide. Gunchenko et al. [30] and Khlopochkina et al. [40] also believe that at low temperatures such as 300 °C, zinc selenite ($ZnSeO_3$) can be formed (reaction 18.16). However, the concentration of this oxide, in comparison with zinc oxide, should noticeably decrease with an increase in the oxidation temperature. The same conclusion was reached earlier by Gunchenko et al. [30]. This means that at temperatures above 550 °C, the presence of $ZnSeO_3$ should no longer be observed.

$$2ZnSe + 3O_2 \rightarrow 2ZnSeO_3 \tag{18.16}$$

This conclusion was confirmed in the results of studies performed by Jabri et al. [36] and Heiba [32]. Jabri et al. [36], studying the oxidation of ZnO-ZnSe nanowires, have found that if at a temperature below 550 °C the ZnSe shell transforms into a ZnO-$ZnSeO_3$ shell dominated by ZnO, which is associated with the incorporation of oxygen into the shell after annealing, then at annealing temperatures above 580 °C, the $ZnSeO_3$ oxide phase is not detected (see Fig. 18.11a). As a result, only the strong hexagonal ZnO (0002) diffraction peak was observed in the XRD patterns. According to the results reported by Heiba [32], at 500 °C, the content of $ZnSeO_3$ in the formed oxide is about 10% (Fig. 18.11b). Apparently, the content of the ZnO phase is higher than that of $ZnSeO_3$, because the formation of ZnO is thermodynamically more favorable than the formation of $ZnSeO_3$ at 470 °C. This is consistent with thermodynamic calculations, which showed that the free energy (ΔG) of ZnO formation is 242.6 kJ/mol and that of $ZnSeO_3$ is 393 kJ/mol [32]. Therefore, the rate of ZnO formation, especially at elevated temperatures, is much higher than that of $ZnSeO_3$.

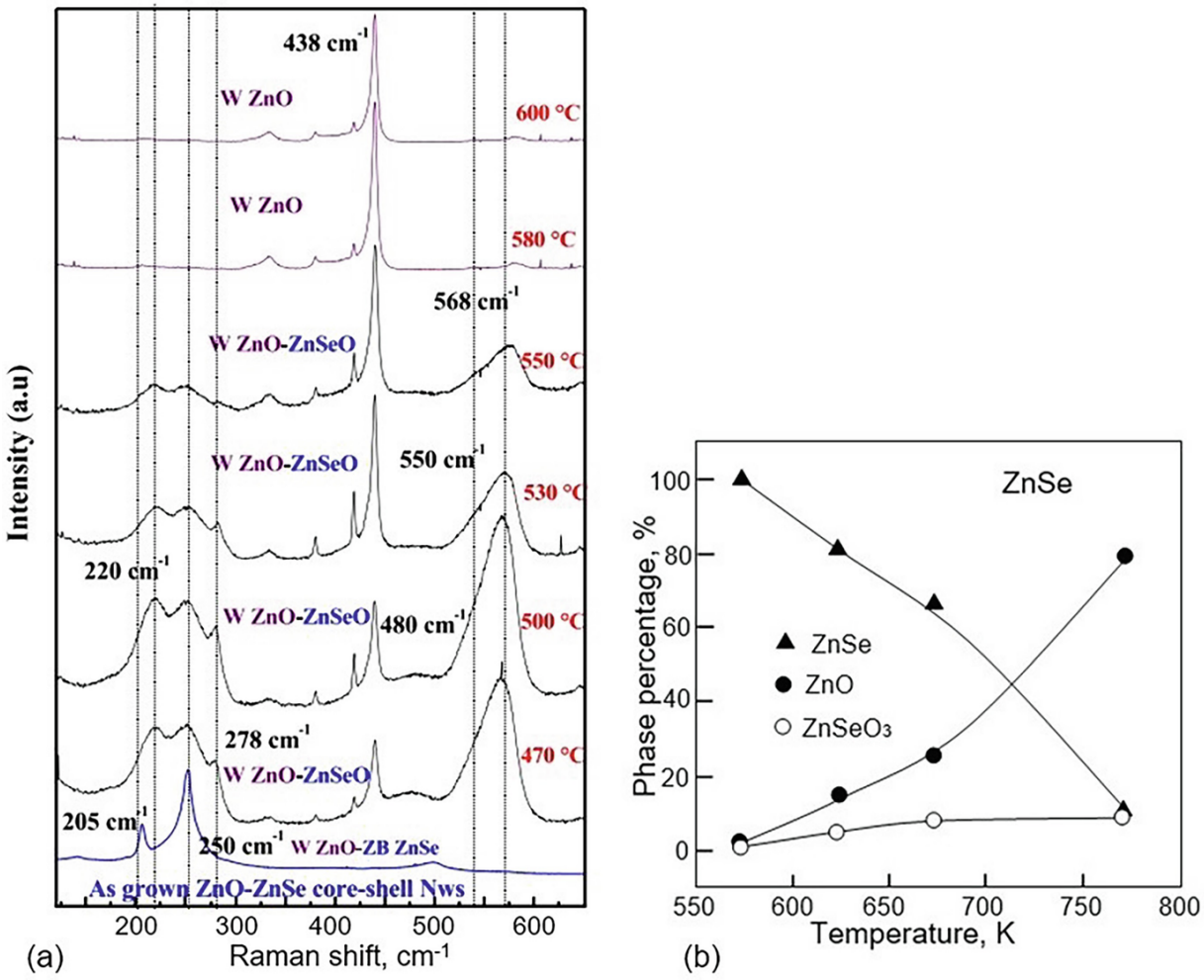

Fig. 18.11 (**a**) Raman spectra of ZnO-ZnSe nanowires on a sapphire substrate, as a function of annealing temperature under O_2. (Reprinted with permission from Ref. [36]. Copyright 2017: AIP Publishing); (**b**) the phase percentage of the oxidation products of ZnSe after annealing at different temperatures. (Reprinted with permission from Ref. [32]. Copyright 2002: Cambridge University Press)

Polukarov and Makhmetove [63] and Khlopochkina et al. [40], analyzing the process of oxidation of polycrystalline ZnSe in the temperature range of 400–700 °C, showed that the oxidation rate depends on the oxidation time, particle size, and temperature. At the same time, the oxidation process under consideration is controlled by internal diffusion. They also showed that already at a temperature of 550 °C, complete oxidation of ZnSe particles with a size of 0.20–6.50 nm takes place within an acceptable time (see Fig. 18.12a). As established by Tikhonova et al. [78], there is also a sharp increase in the oxidation rate with increasing air flow in the reactor. In Fig. 18.12b, it can be seen that with an increase in air flow, the time for complete oxidation decreases significantly, being 260, 66,

and 11 h at the flow rates of 9.5, 40, and 110 ml/min, respectively. Tikhonova et al. [78] also found that the rate of oxidation is increased by the addition of an oxidizing agent, such as nitric acid vapor, to the air stream. Reducing the crystallite size also helps to reduce the oxidation time.

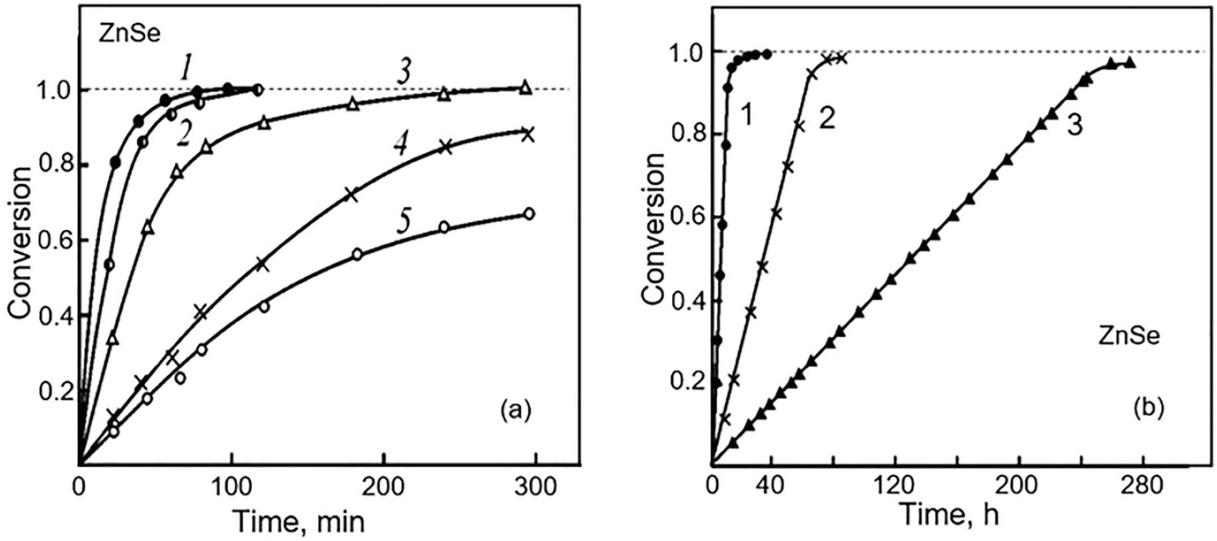

Fig. 18.12 (a) Kinetic curves of zinc selenide oxidation: (**a**) conversion and (t) time. Temperature of oxidation (°C): (1) 700, (2) 600, (3) 550, (4) 500, and (5) 430. (Reprinted with permission from Ref. [40]. Copyright 2001: Springer); (**b**) kinetic curves of ZnSe oxidation at 600 °C in a forced air flow: (α) degree of zinc selenide conversion and (τ) time. Flow rate, ml/min: (1) 110, (2) 40, and (3) 9.5. (Reprinted with permission from Ref. [78]. Copyright 2003: Springer)

Tomura et al. [80] also found that by doping the starting material, ZnSe, it is possible to control the properties of the formed ZnO. They noted that the resistivity in ZnO films made from ZnSe doped with lithium or aluminum was much higher than in films made from undoped ZnSe. It was also shown that the doping of ZnSe films with aluminum or lithium enhanced the crystallization of the ZnO film.

As for CdSe, the results of studying the properties of polycrystalline CdSe after 24–26 h of oxidation at 300–550 °C in open air [32] show that, unlike ZnSe, the formation of CdO oxide does not occur during the oxidation of CdSe in the specified temperature range. These studies also indicate that the process of CdSe oxidation does not follow the regularities established for CdS. CdSe and CdS crystallize with a hexagonal lattice with two molecules per unit cell. Each atom is surrounded by a tetrahedron of atoms of opposite sort. Both have the same space group and the same atomic sites; however, they are found to have different resistance for oxidation and different oxidation products. It can be seen in Fig. 18.13; CdS

is more resistible for oxidation with a lower rate of phase dissociation than CdSe and ZnSe. For CdS no oxidation takes place until at temperature of 400 °C, while CdSe oxidizes at T > 300 °C. Moreover, CdSe oxidizes into only one phase, $CdSeO_3$, which dominates at least up to 550 °C. At 500 °C, the content of $CdSeO_3$ in polycrystalline CdSe reaches 87% (see Fig. 18.13). At the same time, the oxidation products of CdS are two phases $CdSO_4$ and $Cd_3O_2SO_4$ ($2CdO{\cdot}CdSO_4$) where the first is the predominant as shown in Fig. 18.6. In both cases, no cadmium oxide was found in the oxidation products, and accordingly, an increase in the sample weight should be found upon oxidation, in contrary to ZnSe case.

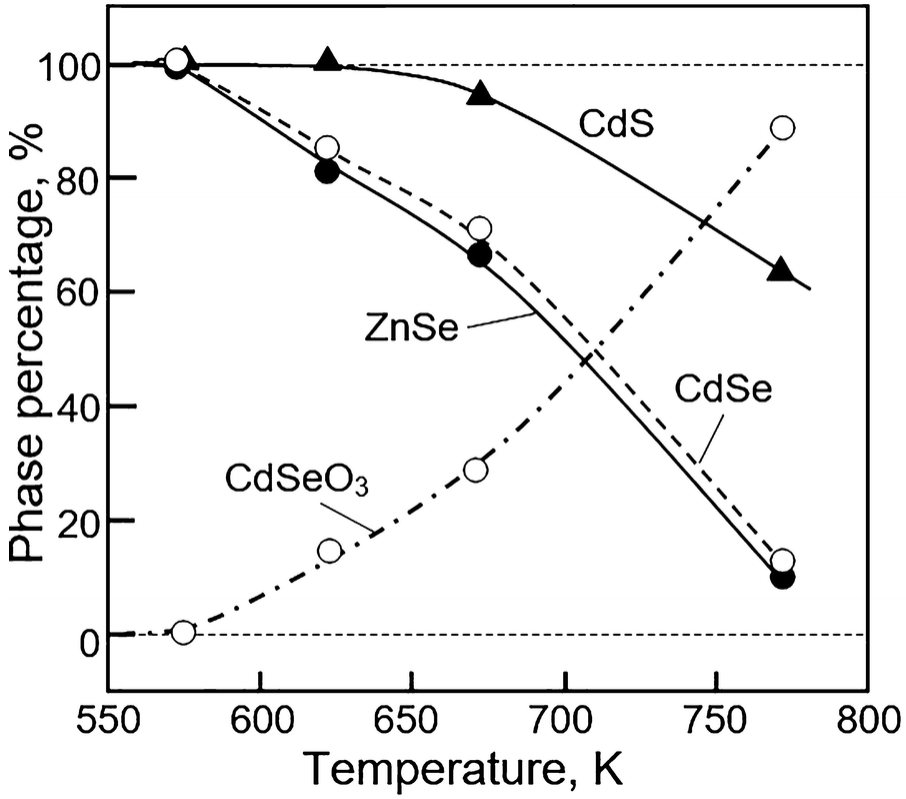

Fig. 18.13 The rate of phase dissociation of ZnSe, CdSe, and CdS with temperature. (Reprinted with permission from Ref. [32]. Copyright 2002: Cambridge University Press)

It should be noted that there are data indicating the presence of CdO on the thermally oxidized CdSe surface [24, 54]. However, these results were obtained during short-term oxidation of CdSe at temperatures of 100–400 °C, at which intensive oxidation of CdSe does not yet occur. Therefore, it can be assumed that the species present on the CdSe surface, apparently, do not yet form a separate phase but are chemisorbed particles. For

example, Masson et al. [54] after annealing a CdSe (0001) single crystal in dry air at 350 °C (2 h) found that the surface concentration of oxygen atoms determined by the XPS method is 1.3×10^{15} cm^{-2}, which is comparable to concentration of atoms on the (0001) plane in wurtzite CdSe crystal. At the same time, about 60% of this oxygen is bound to Se. Masson et al. [54] found that the thickness of the oxide layer is ~0.9 nm and the oxide contains two separate layers. The top of the oxide layer contains primarily Se oxide species. The oxygen bound to cadmium is within the next two or three atomic planes below at the Se substitution sites. Raman measurements confirm the existence of O at the Se substitution sites. Regarding the results published by Eom et al. [24], they were obtained in the study of 5 nm CdSe QDs synthesized at low temperatures and containing an excess of Cd. Therefore, the appearance of CdO in this case is quite natural.

18.5 Surface Passivation

As shown earlier, the state of the surface of II-VI compounds is very sensitive to the ambient atmosphere, especially at elevated temperatures. Like other semiconductor materials, II-VI compounds are oxidized in an oxygen-containing atmosphere. II-VI compounds are also strongly affected by humidity. In addition, due to the high vapor pressure of the elements forming II-VI compounds, at elevated temperatures, the dissociation of compounds is possible, accompanied by a change in the stoichiometry of the surface layer. Such changes lead to instability of the characteristics of devices developed on their basis. This makes it extremely necessary to carry out encapsulation at the final stage of device fabrication in order to prevent such undesirable changes in surface properties.

Studies have shown that the semiconductor-passivating layer interface, as well as the dielectric properties of the passivating layers, plays an important and very often dominant role in determining the characteristics of devices based on II-VI semiconductors [1, 59]. For example, CdTe surface defects have been found to be one of the main limitations for increasing the efficiency of CdTe solar cells. It is known that the performance of a photoconductive detector is limited by carrier recombination at the surface, which affects the lifetime of minority carriers. Surface recombination is mainly controlled by surface states, the concentration of which is directly related to the concentration of surface defects, the presence of which on the

CdTe surface was confirmed experimentally [27]. Due to surface passivation, it is possible to significantly reduce the concentration of surface defects and thus improve the parameters of photodetectors. For example, Reese et al. [65] showed that while the surface recombination velocity (SRV) for as-prepared p-CdTe was about 10^5–10^6 cm/s, after surface passivation, the SRV decreased to less than 2.5×10^4 cm/s.

An important feature of the surface passivation process of II-VI compounds using dielectric layers is that dielectric films and the process of their deposition must meet the following requirements [59]:

(i) The deposition process must be low temperature and must not introduce damage to the II-VI semiconductors or its interface.

(ii) Films must exhibit thermal stability and excellent adhesion, and the film must be mechanically stable.

(iii) The film must be electrically insulating, as well as chemically stable.

(iv) The passivation film must be thick enough to provide adequate environmental protection.

(v) For specific applications, coatings may also have requirements such as high dielectric constant for MIS devices, an appropriate index of refraction (n) for an antireflection coating, and a high transmission for front-illuminated devices.

Considering the above, at present, several approaches have been proposed for surface passivation of II-VI compounds, which are based on the use of coatings such as ZnS, SiO_2, and SiN_x and native oxides of II-VI compounds [59, 89]. Native oxides are typically used in the formation of two-layer passivating coatings, including a thin film of natural oxide and a thick deposited dielectric film. Such coatings are often used for passivating photoconductors and photodiodes.

ZnS is currently the most common coating used to stabilize parameters of devices and especially the properties of colloidal particles based on II-VI compounds [35, 60]. ZnS is even used to passivate ZnO nanostructures [4]. It was found that the ZnS layer not only inhibited the ZnO dissolving

process in water but additionally improved its mechanical and electrical properties. After the passivation process, ZnO/ZnS films remained stable in water for over 7 days. The electrical conductivity of the ZnO films increased about 500-fold as a result of surface defect passivation and the removal of oxygen molecules which can trap free carriers. In addition to high stability, ZnS presents a much lower toxicity than Cd-based compounds, and therefore ZnS-coated Cd-based semiconductor QDs may be more suitable for biological applications (see Chap. 8, Vol. 1). The ZnS coating can be formed using vacuum deposition, MBE, and various methods of chemical synthesis. For example, Huang et al. [35] and Pan and Zhong [60] used deposition of ZnS layer via a reproducible and controlled successive ionic layer adsorption and reaction (SILAR) method for passivation of CdS/CdSe and CdSeTe QDs, correspondingly. Deposition by magnetron sputtering improves adhesion but may introduce damage. ZnS forms high-quality interface with very low fixed surface charges. Usually the coating has excellent adhesion on freshly etched surfaces. ZnS films exhibit good insulating properties and high bulk resistivity, which, however, are worse compared to SiO_2. In addition, ZnS layers are relatively inert. However, they are sensitive to water and etched with concentrated HCl. In addition, mechanical properties of these films are relatively poor and may crack during ultrasonic bonding on overlaying metallization.

SiO_2 is also widely used to protect the surface of II-VI compounds [8, 40] and quantum dots [86, 90]. In particular, Xiong et al. [90] have shown that the silica coating protects the surface of ZnSe nanowires from oxidation and greatly improves its thermal stability. There are currently a number of different low-temperature methods for the deposition of SiO_2. The low-temperature SiO_2 layer is a protective coating, but more porous and structurally different than thermally grown SiO_2 on Si. The electrical properties of the SiO_2-II-VI semiconductor interface are very sensitive to the presence of native oxides on the surface of II-VI compounds prior to the SiO_2 deposition [8, 40]. Best results are obtained when a few layers of native oxide are present on the II-VI compounds before deposition. SiO_2 layer is an excellent insulator. Bulk resistivity of SiO_2 films exceeds 10^{13} ohm·cm. They exhibit good chemical properties and excellent mechanical properties when adhesion is adequate. However, adhesion problems are

observed and are probably associated with the different coefficients of thermal expansion of II-VI compounds ((2–8)·10^{-6} K^{-1}) and SiO_2 (0.5·10^{-6} K^{-1}).

SiN_x is another coating with excellent insulating properties. Dense SiNx layers can be deposited using the plasma chemical vapor deposition process. Dense SiN_x films can be deposited even at temperatures <95 °C. The deposited films have excellent uniformity and high resistivity. Tunable near-zero mechanical stress can be obtained by modifying the deposition conditions. Due to low porosity, the SiN_x as protective covering has an excellent moisture resistance. It is a more moisture-resistant covering than ZnS or SiO_x and acts as an effective barrier to external contaminants. Therefore, the application of the SiN_x film stabilizes the diodes and photodetectors in humid condition.

Uda et al. [82] found that a significant improvement in the performance stability of CdS/CdTe solar cells can also be achieved by using an epoxy resin coating as a back protector.

In addition to the dielectrics mentioned above, other materials were also used to passivate the surface of II-VI compounds and its QDs. Materials tested for this purpose include Al_2O_3 [2, 89], Nb_2O_5 [61], Ta_2O_5 [40], TiO_2 [61, 70], V_2O_5, NiO [89], $Mg_xCd_{1-x}Te$ [96], amorphous Zn_2SiO_4 [46], and hydrothermal carbonation carbon (HTCC) [53]. But these coatings, with the exception of Al_2O_3 [40], have not received such widespread use compared to the above SiO_2, SiN_x, and especially ZnS passivation layers. In addition, Kephart et al. [40], analyzing the passivation effect of various coatings, have found that Ta_2O_5 and TiO_2 layers at the interface of CdTe/$Zn_xMg_{1-x}O$ exhibited no passivation effect. The same conclusion was made by Wu et al. [89] regarding the NiO coating on the CdTe surface. At the same time, Pareek et al. [61] have shown that TiO_2-modified CdS films are more stable than Nb_2O_5-modified CdS films. Pareek et al. [61] also concluded that surface modification with metal oxide nanoparticles is the best and most economical way to stabilize the CdS photoanode for hydrogen production technology.

It is important to note that in addition to property stabilization, the application of a passivation coating generally improves the performance of the photovoltaic devices [8, 60]. For example, Kim et al. [42] established

that the surface trap states of CdTe are reduced by the CdZnTe and ZnS passivation, which results in the increase in the surface lifetime of CdTe. Alfadhili et al. [2] concluded that the performance enhancement of CdTe solar cells after back-surface passivation by Al_2O_3 is due to a reduction in the interface recombination current at the back surface. It is interesting that the open-circuit voltage (V_{oc}) was increased and the fill factor (FF) and photoconversion efficiency (PCE) were optimized when the thickness of Al_2O_3 layer corresponded to ∼1 monolayer. Wu et al. [89] also found that very thin coatings are sufficient for surface passivation. It was established that the CdTe surface was effectively passivated by a 3-nm-thick V_2O_5 or Al_2O_3 coating layer. The simulation and experimental results indicated that the passivation was ascribed to the electric field effect induced by negative fixed charges in V_2O_5 and Al_2O_3.

However, it must be borne in mind that the improvement in the parameters of photovoltaic devices after surface passivation does not always correlate with the protective properties of the coatings used. For example, Budhraja [8] compared the parameters of CdTe solar cells with SiO_2 and SiN_x passivating coatings and found that there is no large increase in solar cell performance when using SiN_x, while such an effect was observed when using SiO_2. Layers of SiO_2 and SiN_x were deposited by plasma chemical vapor deposition. Solar cells after deposition were annealed at 200 °C for 30 min. Such a difference in the effect of passivating coatings on device characteristics indicates that in CdTe solar cells with a SiN_x passivating layer, the effect of rear surface recombination cannot be neglected.

Studies have also shown that in order to achieve the required parameters of photovoltaic (PV) devices based on II-VI compounds, it is necessary not only to choose the right protective coating and its deposition technology but also to properly prepare the surface before its deposition [65]. As mentioned earlier, depending on their stoichiometry, a large number of defects with different properties can be generated in II-VI compounds. For example, according to theoretical modeling of defect chemistry [31, 52], the V_{Te} in CdTe is a shallow donor, Te antisites (Te_{Cd}) and Te interstitials (Te_i) are the dominant mid-gap deep levels, and the Cd vacancy (V_{Cd}) is a deeper acceptor (0.36 eV above the valence band maximum) [31]. This theoretical

framework was then supported with experimentally grown off-stoichiometric samples that exhibited higher bulk recombination in Te-rich samples than Cd-rich ones [52]. Band diagrams of Te-rich and Cd-rich CdTe surfaces are shown in Fig. 18.14. Experimental results have shown that exposing the back surface of a CdTe PV device to Te was correlated with a drop in minority carrier lifetime and device performance [26]. Moreover, Reese et al. [65] found that CdTe samples with a Te-rich surface were characterized by significant temporal instability, while samples with stoichiometric or Cd-rich surface were stable. This means that when preparing the CdTe surface, the use of treatments (see Table 18.5) that favor the formation of a Te-rich surface should be avoided. Reese et al. [65] also showed that a thermal reconstruction step (250 °C) that restores surface crystallinity (in an inert atmosphere, UHV, or Cd ambient) also contributes to a significant reduction in SRV. According to Reese et al. [65], when using the Br_2:MeOH etchant, which is usually recommended for etching II-VI compounds, to achieve a significant reduction in surface recombination, the CdTe surface after etching in Br_2:MeOH should be subjected to short-term etching in KOH followed by thermal annealing. It is important that if, after such treatment, the CdTe surface was again etched in Br_2:MeOH, then surface recombination velocity (SRV) increased sharply.

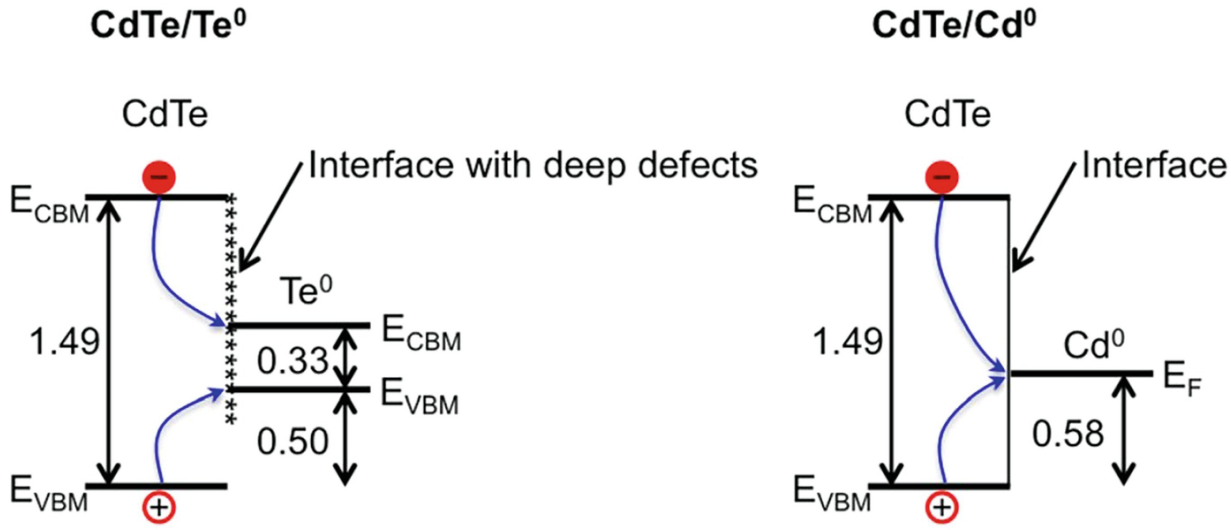

Fig. 18.14 Band alignment of CdTe with elemental tellurium (left panel) and of CdTe and elemental cadmium (right panel). Both cases show a significant potential gradient favoring movement of both electrons and holes to the interface where the presence of defects can enable their recombination. (Reprinted with permission from Ref. [65]. Copyright 2015: AIP Publishing)

Table 18.5 Summary of surface compositions of CdTe extracted by XPS of various samples examined by Reese et al. [65]

Sample treatment	Cd/Te
As-received	0.59
Br_2:MeOH	0.73
3 kV Ar^+	1.08
Atomic H	1.10
Ar^+, 250 °C UHV	1.09
Cd ampoule anneal	1.29
Te ampoule anneal	1.05
UV/O_3	1.81
NaOH:$Na_2S_2O_4$	1.35
KOH	1.12
Hydrazine	0.86
CH_3COOH:HNO_3:H_2SO_4	0.004
$FeCl_3$	0.03
HNO_3:$K_2Cr_2O_7$:$Cu(NO_3)_2$	0.08
HNO_3:$K_2Cr_2O_7$	0.06

Source: Reprinted with permission from Ref. [65]. Copyright 2015: AIP Publishing

Acknowledgments

G.K. is grateful to the State Program of the Republic of Moldova (project 20.80009.5007.02) for supporting his research.

References

1. Agnihotri OP, Musca CA, Faraone L (1998) Current status and issues in the surface passivation technology of mercury cadmium telluride infrared detectors. Semicond Sci Technol 13:839–845
2. Alfadhili FK, Phillips AB, Subedi KK, Perkins CL, Halaoui AI, Jamarkattel MK et al (2020) Back-surface passivation of CdTe solar cells using solution-processed oxidized Aluminum. ACS Appl Mater Interfaces 12:51337–51343

3. Bai Z, Wang D (2012) Oxidation of CdTe thin film in air coated with and without a $CdCl_2$ layer. Phys Status Solidi A 209(10):1982–1987
4. Baranowska-Korczyc A, Koscinski M, Coy EL, Grzeskowiak BF, Jasiurkowska-Delaporte M, Peplinska B, Jurga S (2018) ZnS coating for enhanced environmental stability and improved properties of ZnO thin films. RSC Adv 8:24411–24421
5. Batzner DL, Romeo A, Terheggen M, Dobeli M, Zogg H, Tiwari AN (2004) Stability aspects in CdTe/CdS solar cells. Thin Solid Films 451–452:536–543
6. Bertoncello M, Casulli F, Barbato M, Artegiani E, Romeo A, Trivellin N et al (2020) Influence of CdTe solar cell properties on stability at high temperatures. Microelectron Reliab 114:113847
7. Bootsma GA (1968) Gas adsorption on Cadmium Sulphide. Surf Sci 9:396–406
8. Budhraja V (2015) Effect of SiO_2 and SiN_X passivation on CdTe based solar cells. Intern J Eng Res Technol 4(7):10–12
9. Choi SS, Lucovsky G (1988) Native oxide formation on CdTe. J Vac Sci Technol B 6:1198–1203
10. de Melo O, Larramendi S, Contreras-Puente G, Behar M, Rodríguez-López S, Trabada DG, Hernández-Vélez M (2012) ZnO nanosheet network formation by ZnTe oxidation in humid argon atmosphere annealing. Mater Lett 81:202–204
11. Dengo N, De Fazio AF, Weiss M, Marschall R, Dolcet P, Fanetti M, Gross S (2018) Thermal evolution of ZnS nanostructures: effect of oxidation phenomena on structural features and photocatalytical performances. Inorg Chem 57(21):13104–13114
12. Dimitrov R, Bonev I (1986) Mechanism of zinc sulphide oxidation. Thermochim Acta 106:9–15
13. Dimitrov R, Boyanov B (1983) Investigation of the oxidation of metal sulphides and sulphide concentrates. Thermochim Acta 64:27–37
14. Dimitrov R, Boyanov B (2000) Oxidation of metal sulphides and determination of characteristic temperatures by DTA and TG. J Therm Anal Calorimet 61(2000):181–189
15. Dimitrov RI, Moldovanska N, Bonev IK (2002) Cadmium Sulphide oxidation. Thermochim Acta 385:41–49
16. Dobson KD, Visoly-Fisher I, Hodes G, Cahen D (2000) Stability of CdTe/CdS thin-film solar cells. Sol Energy Mater Sol Cells 62:295–235
17. Dobson KD, Visoly-Fisher I, Jayakrishnan R, Gartsman K, Hodes G, Cahen D (2001) When, why and where are CdTe/CdS solar cells stable? MRS Proc 668:H8.24
18. Durose K, Boyle D, Abken A, Ottley CJ, Nollet P, Degrave S, Burgelman M, Wendt R, Beier J, Bonnet D (2002) Key aspects of CdTe/CdS solar cells. Phys Status Solidi B 229(2):1055–1064
19. Ebina A, Asano K, Suda Y, Takahaski T (1980) Oxidation properties of II–VI compound surfaces studied by low energy electron loss spectroscopy and 21 eV photoemission spectroscopy citation. J Vac Sci Technol 17:1074–1979

20. Ebina A, Suda Y, Takahashi T (1982) Oxidation of ZnSe (110) and ZnTe (110). Int Electron 52(1):77–88
21. Enzenroth RA, Barth KL, Sampath WS (2004) Continuous, In Line processing of CdS/CdTe devices: progress towards consistent stability. In: Proceedings of 19th European photovoltaic solar energy conference, 7–11 June, Paris, France, pp 1980–1983
22. Enzenroth RA, Barth KL, Sampath WS (2005) Correlation of stability to varied $CdCl_2$ treatment and related defects in CdS/CdTe PV devices as measured by thermal admittance spectroscopy. J Phys Chem Solids 66:1883–1886
23. Enzenroth RA, Barth KL, Sampath WS, Manivannan V, Kirkpatrick AT, Noronha P (2009) Stable Cu-based Back contacts for CdTe thin film photovoltaic devices. J Sol Energy Eng 131:021012
24. Eom NSA, Kim T-S, Choa Y-H, Kim W-B, Kim BS (2014) Surface oxidation behaviors of Cd-rich CdSe quantum dot phosphors at high temperature. J Nanosci Nanotechnol 14:8024–8027
25. Gas K, Kret S, Zaleszczyk W, Kaminska E, Sawicki M, Wojtowicz T, Szuszkiewicz W (2021) Oxidation of MBE-grown ZnTe and ZnTe/Zn nanowires and their structural properties. Materials 14:5252
26. Gessert TA, Burst JM, Wei S-H, Ma J, Kuciauskas D, Rance WL et al (2013) Pathways toward higher performance CdS/CdTe devices: Te exposure of CdTe surface before ZnTe:Cu/Ti contacting. Thin Solid Films 535:237–240
27. Gorji NE (2014) Modeling the defect distribution and degradation of CdTe ultrathin films. J Semicond 35(12):122001
28. Grecu D, Compaan AD, Young D, Jayamaha U, Rose DH (2000) Photoluminescence of Cu-doped CdTe and related stability issues in CdS/CdTe solar cells. J Appl Phys 88(5):2490–2496
29. Gretener C, Perrenoud J, Kranz L, Cheah E, Dietrich M, Buecheler S, Tiwari AN (2016) New perspective on the performance stability of CdTe solar cells. Sol Energy Mater Sol Cells 146:51–57
30. Gunchenko NN, Dronova GN, Maksimova IA, Mironova IA, Pavlova VN, Pevtsova NI (1988) Oxidation of polycrystalline materials based on zinc and cadmium chalcogenides. Izv Akad Nauk SSSR Neorg Mater 24:36–40
31. Hegedus S, McCandless BE (2005) CdTe contacts for CdTe/CdS solar cells: effect of Cu thickness, surface preparation and recontacting on device performance and stability. Sol Energy Mater Sol Cells 88:75–95
32. Heiba ZK (2002) X-ray quantitative analysis of the phases developed upon air annealing of ZnSe, CdSe, and CdS semiconductors. Powder Diffract 17(3):191–195
33. Hellgren N, Steves MA, Shallenberger J, O'Boyle SK, Mellott E, Noble AR (2020) Effect of etching on the oxidation of zinc selenide surfaces characterized by X-ray photoelectron spectroscopy. Appl Surf Sci 528:146604

34. Hiltner JF, Sites JR (1999) Stability of CdTe solar cells at elevated temperatures: Bias, temperature, and Cu dependence. AIP Conference Proc 462, 170
35. Hosnedlova B, Vsetickova M, Stankova M, Uhlirova D, Ruttkay-Nedecky B, Ofomaja A et al (2020) Study of physico-chemical changes of CdTe QDs after their exposure to environmental conditions. Nano 10:865
36. Huang F, Zhang Q, Xu B, Hou J, Wang Y, Masse R et al (2016) A comparison of ZnS and ZnSe passivation layers on CdS/CdSe cosensitized quantum dot solar cells. J Mater Chem A 4:14773–14780
37. Jabri S, Amiri G, Hassani S, Lusson A, Sallet V, Meftah A et al (2017) Zinc blende-oxide phase transformation upon oxygen annealing of ZnSe shell in ZnO-ZnSe core-shell nanowires. Appl Phys Lett 110(10):101601
38. Kaito C, Nakamura N, Saito Y (1985) High resolution microscopic studies of the oxidadtion process of ZnTe films. Appl Surf Sci 22/23:604–612
39. Kanti Kole A, Sekhar Tiwary C, Kumbhakar P (2014) Morphology controlled synthesis of wurtzite ZnS nanostructures through simple hydrothermal method and observation of white light emission from ZnO obtained by annealing the synthesized ZnS nanostructures. J Mater Chem C 2:4338–4346
40. Kephart JM, Kindvall A, Williams D, Kuciauskas D, Dippo P, Munshi A, Sampath WS (2018) Sputter-deposited oxides for interface passivation of CdTe photovoltaics. IEEE J Photovoltaics 8(2):587–593
41. Khlopochkina EL, Gaivoronskii PE, Gavrishchuk EM, Elliev YE, Yashina EV (2001) Oxidation of polycrystalline Zinc Selenide with atmospheric oxygen. Russ J Appl Chem 74(7):1079–1081
42. Kim Y-H, An S-Y, Lee J-Y, Kim IJ, Oh K-N, Kim S-U et al (1999) Photoluminescence study on the effects of the surface of CdTe by surface passivation. J Appl Phys 85(10):7370–7373
43. Kim S, Kim D, Hong J, Elmughrabi A, Melis A, Yeom J-Y et al (2022) Performance comparison of CdTe:Na, CdTe:As, and CdTe:P single crystals for solar cell applications. Materials 15:1408
44. Kulakov MP, Fadeev AV (1983) Oxidation of mechanically polished zinc selenide upon heating in air. Izv Akad Nauk SSSR Neorg Mater 19:347–351
45. Kumaki D, Umeda T, Tokito S (2008) Influence of H_2O and O_2 on threshold voltage shift in organic thin-film transistors: deprotonation of SiOH on SiO_2 gate-insulator surface. Appl Phys Lett 92:093309
46. Lee HJ, Lee SI (2006) Surface passivation of CdS/Zn_2SiO_4 nanocomposites prepared by a wet chemical route. J Nanosci Nanotechnol 6:3369–3372
47. Li X, Li X, Zhu B, Wang J, Lan H, Chen X (2017) Synthesis of porous ZnS, ZnO and ZnS/ZnO nanosheets and their photocatalytic properties. RSC Adv 7:30956–30962

48. Li Z, Kong L, Sun H, Huang S, Li L (2018) Effect of electronic structure on the stability of CdSe/CdS and CdSe/CdS/ ZnS quantum dot phosphor incorporated into silica/alumina monolith. ACS Appl Nano Mater 1(7):3086–3090
49. Lu P, Smith DJ, Przezdziecka E, Kaminska E, Dynowska E, Dobrowolski W et al (1988) P-type ZnO and ZnMnO by oxidation of Zn(Mn)Te films. Phys Status Solidi 1988(107):681–691
50. Ma J, Wei S-H (2013) Bowing of the defect formation energy in semiconductor alloys. Phys Rev B 87:241201
51. Ma H, Han J, Fu Y, Song Y, Yu C, Dong X (2011) Synthesis of visible light responsive ZnO−ZnS/C photocatalyst by simple carbothermal reduction. Appl Catal B 102:417–423
52. Ma J, Kuciauskas D, Albin D, Bhattacharya R, Reese M, T. Barnes T., et al. (2013) Dependence of the minority-carrier lifetime on the stoichiometry of CdTe using time-resolved photoluminescence and first-principles calculations. Phys Rev Lett 111:067402–067406
53. Ma Y, Zhao Z, Shen Z, Cai Q, Ji H, Meng L (2017) Hydrothermal carbonation carbon-coated CdS nanocomposite with enhanced photocatalytic activity and stability. Catalysts 7: 194
54. Masson DP, Lockwood DJ, Graham MJ (1997) Thermal oxide on CdSe. J Appl Phys 82:1632–1639
55. Mills KC (1974) Thermodynamic data for inorganic Sulphides, Selenides and Tellurides. Butterworthes, London, p 494
56. Murugadoss G (2011) Synthesis, optical, structural and thermal characterization of Mn^{2+} doped ZnS nanoparticles using reverse micelle method. J Lumin 131:2216–2223
57. Narayan R, Tabatabaie-Raissi A, Antal MJ Jr (1988) A study of Zinc Sulfate decomposition at low heating rates. Ind Eng Chem Res 27:1050–1058
58. Nasi L, Calestani D, Besagni T, Ferro P, Fabbri F, Licci F, Mosca R (2012) ZnS and ZnO nanosheets from $ZnS(en)_{0.5}$ precursor: nanoscale structure and photocatalytic properties. J Phys Chem C 116:6960–6965
59. Nemirovsky Y, Bahir G (1989) Passivation of mercury cadmium telluride surfaces. J Vac Sci Technol A 7(2):450–459
60. Pan Z, Zhong X (2016) A ZnS and metal hydroxide composite passivation layer for recombination control in high efficiency quantum dot sensitized solar cells. J Mater Chem A 4:18976–18982
61. Pareek A, Gopalakrishnan A, Borse PH (2016) Efficiency and stability aspects of CdS photoanode for solar hydrogen generation technology. J Phys Conf Ser 755:012006
62. Park DH, Cho YH, Shin DH, Ahn BT (2013) Preparation of intrinsic ZnO films at low temperature using oxidation of ZnS precursor and characterization of the films. Curr Photovolt Res 1(2):115–121

63. Polukarov AN, Makhmetove MZ (1972) Dissociation pressure of zinc selenite. Zh Fiz Khim 46:1059
64. Prabhu GM, Ulrichson DL, Pulsifer (1984) Kinetics of the oxidation of Zinc Sulfide. Ind Eng Chem Fundam 23:271–273
65. Reese MO, Perkins CL, Burst JM, Farrell S, Barnes TM, Johnston SW et al (2015) Intrinsic surface passivation of CdTe. J Appl Phys 118:155305
66. Rimmaudo I, Salaveia A, Artegiani E, Menossi D, Giarola M, Mariotto G, Gasparotto A, Romeo A (2017) Improved stability of CdTe solar cells by absorber surface etching. Sol Energy Mater Sol Cells 162:127–133
67. Romeo N, Bosio A, Tedeschi R, Romeo A, Canevari V (1999) A highly efficient and stable CdTe/CdS thin film solar cell. Sol Energy Mater Sol Cells 58:209–218
68. Sasaki T, Oguchi T, Katayama-Yoshida H (1991) Li impurity in ZnSe: electronic structure and the stability of the acceptor. Phys Rev B 43(11):9362–9364
69. Schultze D, Steinike U, Kussin J, Kretzschmar U (1995) Thermal oxidation of ZnS modifications sphalerite and wurtzite. Cryst Res Technol 30(4):553–558
70. Shalom M, Dor S, Ruhle S, Grinis L, Zaban A (2009) Core/CdS quantum dot/shell mesoporous solar cells with improved stability and efficiency using an amorphous TiO_2 coating. J Phys Chem C 113(9):3895–3898
71. Sharma H, Sharma SN, Singh G, Shivaprasad SM (2007) Effect of oxidation induced surface state formation on the properties of colloidal CdSe quantum dots. J Nanosci Nanotechnol 7:1953–1959
72. Sher A, Feldman RD, Austin RF, Opila RL, Masaitis RL, Zyskind JL, Sulhoff JW (1992) Fabrication of n-native oxide/p-ZnTe heterojunctions the anodic oxidation of ZnTe MBE layers. J Electron Mater 21(6):653–657
73. Singh A, Roy A (2006) Quantitative analysis of thermal stability of CdSe/CdS core-shell nanocrystals under infrared radiation. J Mater Res 21(6):1385–1389
74. Somorjai GA (1963) Charge transfer controlled surface interactions between oxygen and CdSe films. J Phys Chem Solids 24:175–186
75. Somorjai GA (1964) Effect of light on the evaporation and oxidation of CdS single crystals. Surf Sci 2:298–306
76. Stepanova ND, Kalinkin IP, Sokolov VA (1975) Oxidation of ZnSe in air. Izv Akad Nauk SSSR Neorg Mater 11:1030–1034
77. Tari S, Aqariden F, Chang Y, Grein C, Li J, Kiossis N (2013) Impact of surface treatment on the structural and electronic properties of polished CdZnTe surfaces for radiation detectors. J Electron Mater 42:3252–3258

78. Tikhonova EL, Gaivoronskii PE, Elliev YE, Gavrischuk EM, Mazavin SM, Yashina EV (2003) Influence of conditions of Zinc Selenide oxidation with atmospheric oxygen on the composition of volatile products. Russ J Appl Chem 76(11):1724–1727
79. Tomas SA, Vigil O, Alvarado-Gil JJ, Lozada-Morales R, Zelaya-Angel O, Vargas H et al (1995) Influence of thermal annealing in different atmospheres on the band-gap shift and resistivity of CdS thin films. J Appl Phys 78(4):2204–2207
80. Tomura K, Ohnishi M, Yashizawa M (1974) ZnO films formed by oxidation of ZnSe films. Jpn J Appl Phys 13:939–943
81. Trenczek-Zajaca A (2019) Thermally oxidized CdS as a photoactive material. New J Chem 43:8892–8902
82. Uda H, Nakano A, Kuribayashi K, Komatsu Y, Matsumoto H, Ikegami S (1983) Stability of screen printed CdS/CdTe solar cells. Jpn J Appl Phys 22:1822–1827
83. Ulicna S, Isherwood PJM, Kaminski PM, Walls JM, Li J, Wolden CA (2017) Development of ZnTe as a back contact material for thin film cadmium telluride solar cells. Vacuum 139:159–163
84. Vanjukov A, Issakova R, Bistrov V (1978) Thermal dissociation of metal sulphides. Nauka, Alma-Ata, p 135. (in Russian)
85. Visoly-Fisher I, Dobson K, Nair J, Bezalel E, Hodes G, Cahen D (2003) Factors affecting the stability of CdTe/CdS solar cells deduced from stress tests at elevated temperature. Adv Funct Mater 13:289–299
86. Volodin DO, Bozrova SV, Dovzhenko DS, Zvaigzne MA, Linkov PA, Nifontova GO, et al (2018) Highly stable, water-soluble CdSe/ZnS/CdS/ZnS quantum dots with additional SiO_2 shell, In: MEPhI's Section of the Scientific Session on "Breakthrough directions of scientific research at MEPhI: development prospects within the Strategic Academic Units", KnE Eng. 2018, p 449–456
87. Wang K, He W, Wu L, Xu G, Ji S, Ye C (2014) On the stability of CdSe quantum dot-sensitized solar cells. RSC Adv 4:15702
88. Wu X, Li K, Wang H (2010) Facile fabrication of porous ZnO microspheres by thermal treatment of ZnS microspheres. J Hazard Mater 174:573–580
89. Wu L, Li Z, Wang D, Lei X, Cai Y, Zeng H et al (2021) CdTe surface passivation by electric field induced at the metal-oxide/ CdTe interface. Sol Energy 225:83–90
90. Xiong S, Xi B, Wang W, Zhou H, Zhang S, Qian Y (2007) Preparation and characterization of silica-coated ZnSe nanowires with thermal stability and photoluminescence. J Nanosci Nanotechnol 7:4494–4500
91. Yamamoto O, Sawai J, Ishimura N, Kojima H, Sasamoto T (1999) Change of antibacterial activity with oxidation of ZnS powder. J Ceram Soc Jpn 107(9):853–856
92. Yazawa A (1979) Thermodynamic evaluations of extractive metallurgical processes. Metall Trans B 10B:307–321

93. Yi X, Liou JJ (1995) Surface oxidation of polycrystalline Cadmium telluride thin films for Schottky barriers junction solar cells. Solid-State Electron 38(6):1151–1154
94. Zázvorka J, Franc J, Beran L, Moravec P, Pekárek J, Veis M (2016) Dynamics of native oxide growth on CdTe and CdZnTe X-ray and gamma-ray detectors. Sci Technol Adv Mater 17(1):792–798
95. Zeng G, Liu X, Zhao Y, Shi Y, Li B, Zhang J et al (2019) Study on the stability of unpackaged CdS/CdTe solar cells with different structures. Intern J Photoenergy 2019:3579587
96. Zhao X, Liu S, Campbell CM, Yuan Z, Lassise MB, Zhang Y (2017) Ultralow interface recombination velocity (~1 cm/s) at CdTe/$Mg_xCd_{1-x}Te$ heterointerface. IEEE J Photovoltaics 7(3):913–918

OceanofPDF.com

© The Author(s), under exclusive license to Springer Nature Switzerland AG 2023
G. Korotcenkov (ed.), *Handbook of II-VI Semiconductor-Based Sensors and Radiation Detectors*
https://doi.org/10.1007/978-3-031-19531-0_19

19. II-VI Wide-Bandgap Semiconductor Device Technology: Post-Deposition Treatments

Ghenadii Korotcenkov[1] ✉
(1) Department of Physics and Engineering, Moldova State University, Chisinau, Moldova

Keywords II-VI semiconductors – Wide bandgap – Post-deposition treatment – $CdCl_2$ treatment – Activation process – CdS/CdTe solar cell – Defect distribution – Homogeneity – Interface defects – Solar cell performances – Stoichiometry – Chemical etching – Br_2:MeOH solution – CdSe/CdS core-shell – CdTe solar cells – Nitric-phosphoric (NP) etching – Laser treatment – CdTe – Heavy doping – K_2S and Na_2Te sources – Laser-induced defects – Nd:YAG laser – Ohmic back contact – Pulse laser treatment – Recrystallization – Treatment with alkalis – CsF – KF – NaF – RbF – Thermal treatment – Crystallinity – Grain size – Oxygen desorption

19.1 Introduction

In the previous chapters, we considered the problems associated with the deposition; doping; etching of II-VI compounds (Chap. 16); the formation of Schottky barriers, ohmic contacts, and heterostructures based on these compounds (Chap. 17); and stability and oxidation of II-VI compounds (Chap. 18). In this chapter, we will continue to cover topics related to II-VI wide-bandgap semiconductor device technology. Post-deposition treatments of II-VI semiconductor compounds will be the topic of this chapter.

19.2 Thermal Treatments

Post-deposition treatments (PDTs) are an important step in the fabrication of any devices based on II-VI compounds. Typically, these treatments include chemical or thermal treatments [36, 79]. Thermal treatment of II-VI compounds after deposition in the temperature range of 100–450 °C is the most common method for improving the crystallinity of the formed films [29, 104, 113, 117], for reproducible control of the nanocrystal size [52], and also to confirm the stability of the crystal at a given temperature, which is important for device purposes [36, 91].

Experiment has shown that the most pronounced effect of annealing is observed for initially amorphous films obtained by magnetron sputtering [92]. During the annealing process, the material crystallizes and transforms into a nanocrystalline or polycrystalline form. This recrystallization may also result in a notable change in the grain orientation as well as the texture of the material [117]. If the films are initially polycrystalline, which is usually observed when films are deposited on heated substrates, then this effect is much smaller, although even in this case there is an increase in the size of crystallites. For example, Trenczek-Zajaca [103] have found that during the annealing of nanocrystalline CdS in the temperature range of 400–900 °C, the crystallite size increased from 20–35 nm to 1.5–10 μm. Maticiuc et al. [64] studied the effect of annealing in the range of 250–400 °C on the properties of chemical bath deposited (CBD) CdS:Cl_2 thin films and found that the main changes in the structural, optical, and electrical properties of CBD CdS layers in the annealing process were connected with (i) decomposition of OH group incorporated in CdS lattice in the deposition process, (ii) outdiffusion of H_2O, and (iii) creation of Cd excess resulting in transition from $CdS_{1-x}(OH)_x$ to $CdS_{1-y}Oy$ solid solution.

In addition to improving the crystallinity, annealing also promotes a more uniform distribution of impurities and improves the optical transparency of coatings based on II-VI compounds [29]. In many cases, thermal treatment of films of II-VI compounds is also accompanied by a change in the bandgap, which can be used to optimize the spectral characteristics of photodetectors. The resistivity of both doped and undoped films of II-VI compounds is also sensitive to the applied heat treatments. For example, Bayhan and Ercelebi [9] reported that the resistance of CdTe

films systematically decreased when the films were annealed at 300–400 °C for 5–10 min.

The post-deposition treatment is also necessary to activate the impurities used to dope II-VI semiconductors. How effective this process is can be seen from the results shown in Fig. 19.1. These results were obtained by McCandless et al. [67]. CdTe samples deposited using the vapor-phase deposition (VTD) process were in situ doped with Sb, As, and P. These impurities are of interest because they are low-diffusion impurities. Annealing after deposition was carried out in sealed quartz ampoules at 550–600 °C for 4 min with quench cooling at a controlled Cd partial pressure. For comparison, the same figure shows the results obtained after $CdCl_2$ treatment (see next section). It can be seen that doping with Sb and P, and especially with As, makes it possible to significantly increase the concentration of charge carriers in CdTe from historical limits of 10^{14} to levels of 10^{16}–10^{17} cm^{-3} without compromising the service life in thin polycrystalline CdTe films. This opens up opportunities for improving the performances of CdTe/CdS solar cells and reducing their cost. Device modeling indicates that increasing CdTe hole density while retaining carrier lifetimes of several nanoseconds can increase solar cell efficiency to 25% [67].

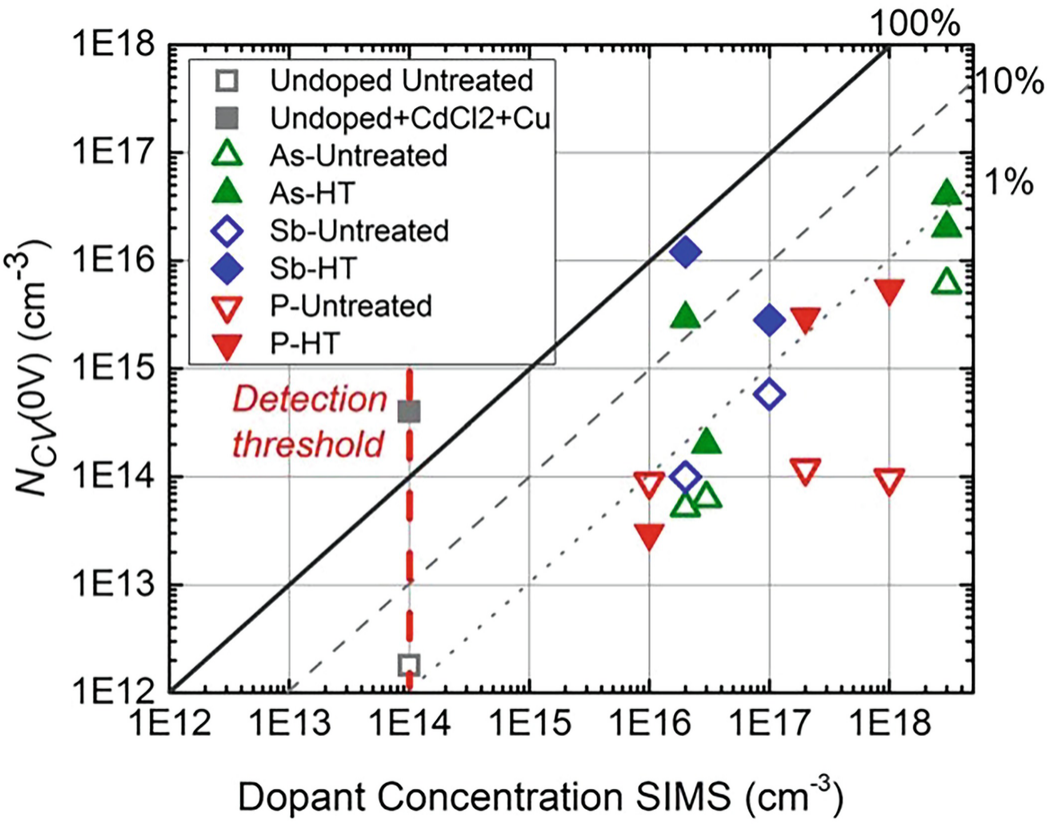

Fig. 19.1 N_{CV} at zero volts versus SIMS concentration of dopants. The red dotted line indicates the SIMS detection threshold for the group V dopants and used as a reference for undoped CdTe. The square symbols indicate the range of raw and fully optimized CdTe films using $CdCl_2$:O_2 treatment and diffused Cu contact. (Reprinted from [67]. Published 2018 by Nature as open access)

The atmosphere used in the heat treatment process also has a significant influence on the effect of annealing on the II-VI layer parameter. For example, the neutral (N_2, Ar containing) annealing, as it was reported before, brings reorientation of as-deposited CdS films with a significantly improved crystalline quality and diminishes their resistivity by increasing the grain size and decreasing the number of grain boundaries in CdS films [102]. Also, such an annealing leads to phase transition from the metastable cubic phase to a stable hexagonal phase of CdS [70], which is undesirable when stacking CdS film with a cubic CdTe absorber. Annealing in an oxidizing atmosphere also leads to an increase in the grain size and an improvement in the crystallinity of the CdS films. In addition, there are reports that such annealing is accompanied by a significant decrease in the bandgap [35], due to creating stable $CdS_{1-y}O_y$ solid solution [64]. Thermal treatment in a reducing atmosphere of H_2 promotes the removal of chemisorbed oxygen and oxides. It is important that the traces of oxygen

were present even in H_2-annealed CdS, and only at 450 °C annealing did the main peak reached the position of pure cubic modification of CdS. At the same time, annealing of CdS in the presence of H_2 retains the same structural cubic phase during the entire thermal process [106] and reduces the resistivity by four orders of magnitude [65] compared to the neutral case [102].

As for annealing in an oxygen atmosphere, as was shown in the previous chapter, this annealing is accompanied by the oxidation of the semiconductor, with a corresponding change in all its properties. An example of the influence of such annealing on the structural properties of ZnS nanocrystals prepared by chemical precipitation method is shown in Fig. 19.2. These results were obtained by Shanmugam et al. [91]. From Fig. 19.2 it is seen that at 200 °C the sample is still in the cubic phase with an average particle size of ~6 nm. As the temperature rises to 400 °C, a phase transformation of ZnS from cubic phase into hexagonal phase takes place. It can also be seen that at 400 °C a small part of ZnO wurtzite was also formed. With a following increase in temperature up to 500 °C, the ZnS wurtzite phase completely disappears, and the ZnO wurtzite phase appears. This result shows that 500 °C is the temperature essential to convert ZnS nanoparticles to ZnO nanoparticles in the presence of air. The average particle size of ZnO nanoparticles at these temperatures was ~23 nm. With a further increase in the annealing temperature up to 800 °C, the diffraction peaks are found to narrow down as compared to those of the samples annealed at 500 °C indicating the growth of bulk crystallites. The average sizes of ZnO nanocrystallites are 33 and 66 nm for samples annealed at 600 and 800 °C, respectively. Similar results were previously reported by Amaranatha Reddy et al. [2].

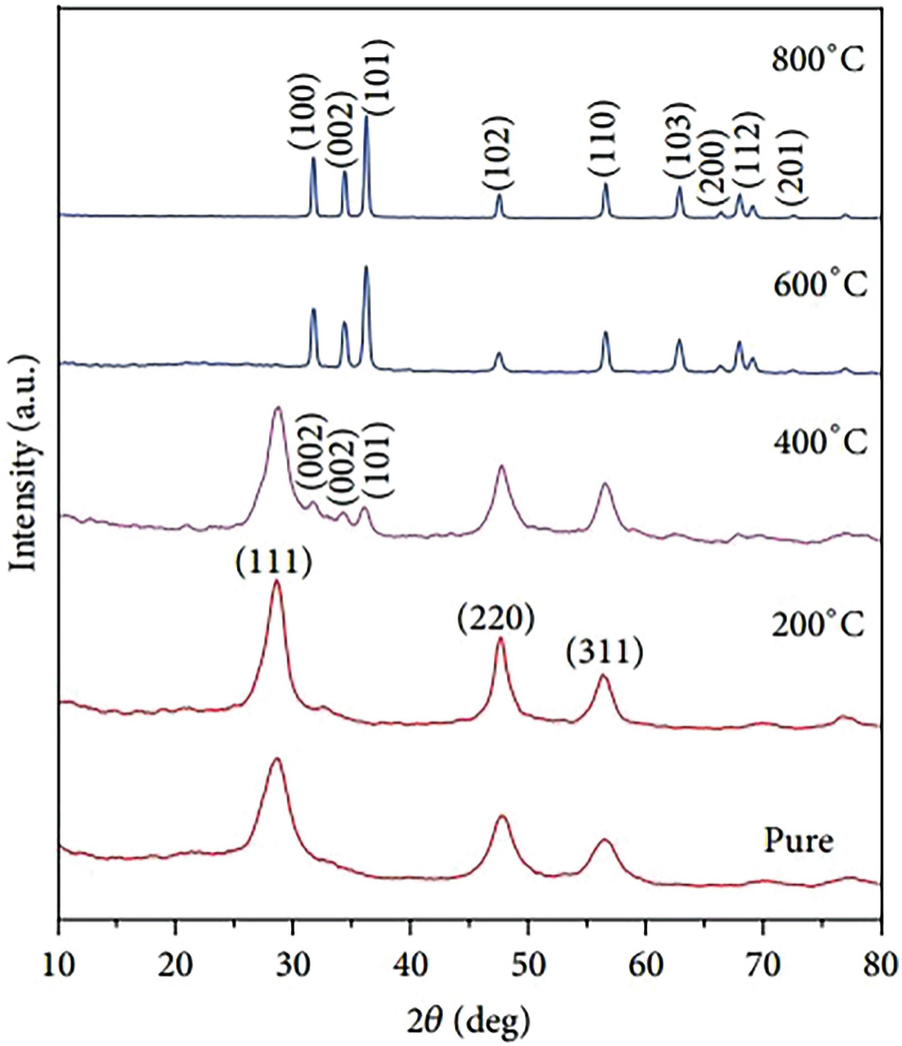

Fig. 19.2 XRD patterns of as-synthesized and annealed ZnS. (Reprinted from [91]. Published 2013 by Hindawi as open access)

It is important to note that these transformations are observed for all II-VI semiconductor compounds. But, unlike ZnS, these processes occur at lower temperatures. For example, ZnSe nanoparticles 4–5 nm in size transform from the ZnSe phase to the ZnO phase at 442 °C [105]. Verma et al. [105] also concluded that the optimal temperature used in the fabrication of solar cells with ZnSe QDs should be below 325 °C, since the samples annealed at 325 °C did not show any phase changes, except for an improvement in the crystallinity of the ZnSe nanoparticles. Dhage et al. [20] showed that CdS nanoparticles with an average diameter of about 10 nm, obtained via chemical bath method, are thermally stable up to 300 °C. Similar experiments were carried out by Reichert et al. [79]. They showed that CdSe and CdS nanorods are relatively stable for a long time in

air at temperatures up to 350 °C and 400 °C, respectively (see Fig. 19.3). Particle coalescence begins at 500 °C and continues up to 700 °C and above. Reichert et al. [79] also found that when CdSe is heated in air at 600 °C, polycrystalline rock salt CdO is formed. However, neither CdO nor CdSe nanorods are reduced to Cd in the presence of H_2 at elevated temperatures.

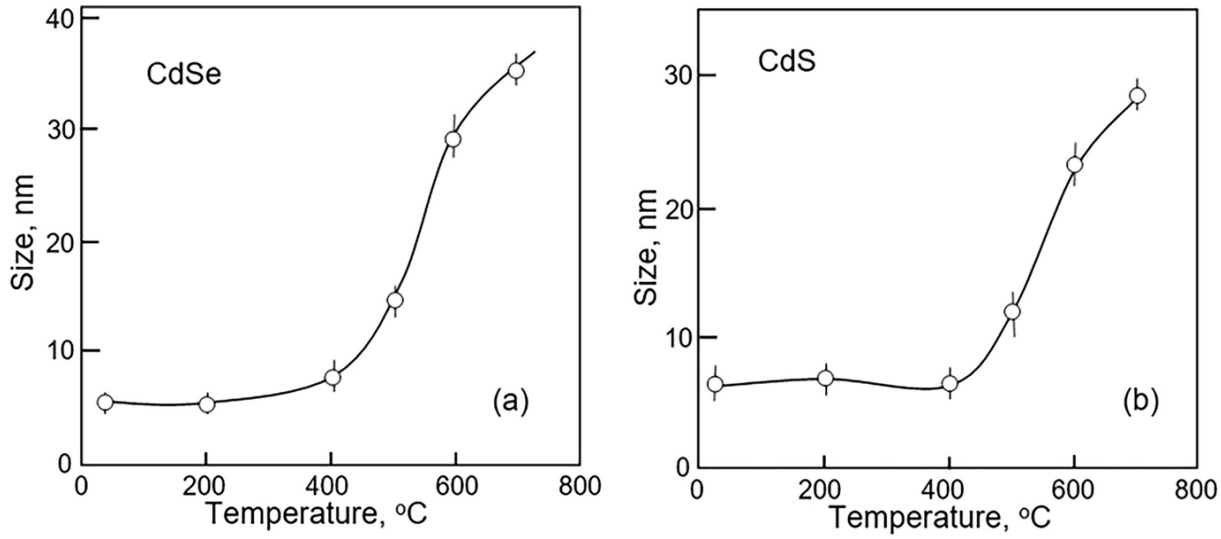

Fig. 19.3 Thermal stability of (**a**) CdSe and (**b**) CdS nanorods. Crystallite sizes for the main diffraction planes were calculated using Scherrer equation. (Adapted with permission from [79]. Copyright 2014: ACS)

Post-deposition treatment is also an important step in the fabrication of heterojunctions based on II-VI compounds [33]. For example, Rohatgi [83] found that thermal treatment of CdS in a hydrogen atmosphere at temperatures above 400 °C prior to CdTe deposition removes oxygen-related defects from CdS films but creates a Cd-deficient CdS surface. Oxygen in CdS grain boundaries is known to be a detrimental recombination center [27]. It was found that such annealing of CdS films at 450 °C significantly improved the performance of the CdTe/CdS photocell. It was concluded that the observed improvement is due to increased interdiffusion between CdTe and CdS and a decrease in the bandgap of CdTe to 1.47 eV when growing CdTe films on CdS under Te-rich conditions. For comparison, when CdTe films were grown under Cd-rich conditions, the CdTe bandgap remained at 1.5 eV. Chu et al. [15] showed that thermal treatment of CdS in a hydrogen atmosphere also changes the transport mechanism at the CdTe/CdS heterojunction from interface recombination/tunneling to depletion region recombination.

Kobayashi et al. [48] showed that the processes occurring during heat treatments, especially at low temperatures, are significantly affected by lighting. Kobayashi et al. [48] fabricated ZnO/ZnS(O,OH)/CIGS solar cells and subjected them to three treatments:

- HS: the solar cells were annealed on a heating stage at 130 °C for 80 min in the air.
- LS: light soaking under AM1.5, 100 mW/cm^2 illumination using a solar simulator for 80 min without intentional heating, the device temperature was increased from 25 °C to the saturated temperature of 40 °C in 10 min by the radiation during light soaking.
- HLS: a combination of one-sun LS and annealing on a heating stage at 130 °C for 80 min in the air.

The basic cell parameters of the as-fabricated and post-treated solar cells are shown in Fig. 19.4. The open and filled symbols represent the as-fabricated and post-treated (HS, LS, and HLS) solar cells, respectively. Although the cell efficiency showed slight increase after the HS treatment, the cell efficiency increase was much more important after the LS (from η = 8.0 to 12.0%) and HLS treatments (from η = 7.8% to 16.0%), respectively. All parameters especially FF increased drastically after HLS treatment. XPS analysis by Kobayashi et al. [48] showed that after HLS treatment, the S/(S + O) atomic ratio decreased in the surface region to about 0.6. On this basis, they hypothesized that HLS treatment through changing the composition in the ZnS(O,OH) buffer layer changes the S/(S + O) atomic ratio at the interface and thus optimizes the conduction band offset (CBO) at the ZnS(O,OH)/CIGS interface [49].

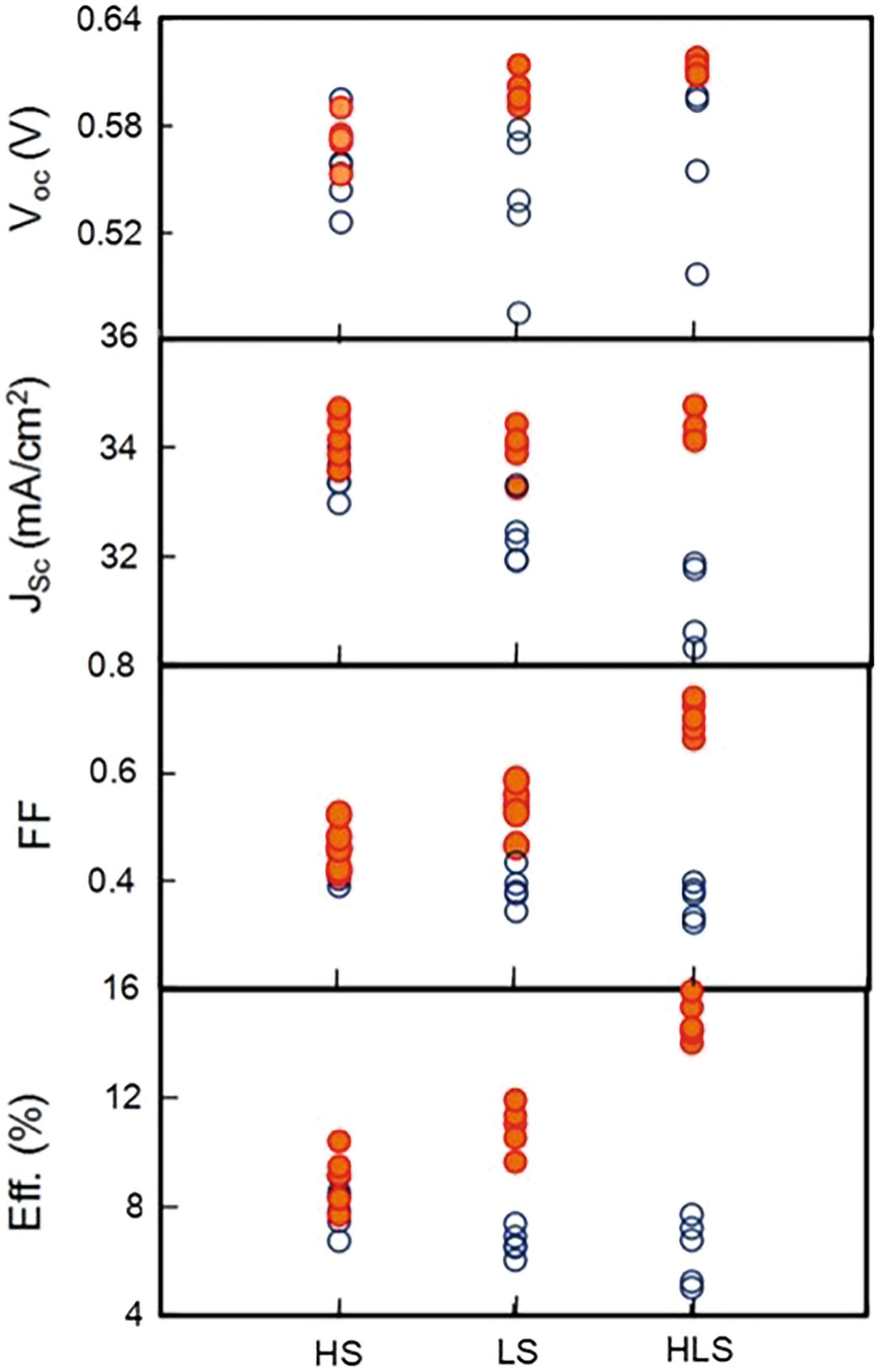

Fig. 19.4 The basic cell parameters of the as-fabricated (open symbols) and post-treated (filled symbols) solar cells for a processing time of 80 min (without antireflection coating). (Reprinted with permission from [48]. Copyright 2014: Elsevier)

In addition to the above post-deposition treatments, Nakada et al. [73] for ZnO/ZnS(O,OH)/CIGS solar cells used the treatment such as ammonia rinsing. ZnS(O,OH)/CIGS stacked layers were rinsed with a 7–10% NH_3 aqueous solution at room temperature for 1 min immediately after buffer

deposition. Post-annealing was then performed in air at 200 °C for 10 min. It was found that FF improved significantly after this treatment of the ZnS(O,OH) buffer layers. According to Nakada et al. [73], this is due to the removal of weakly bound ZnO, $Zn(OH)_2$ in the ZnS(O,OH) surface layer.

Another factor influencing the effect of heat treatment is pressure. In [117] polycrystalline ZnS taken from an industrial chemical vapor deposition (CVD) process was thermally treated with and without hot isostatic pressing (HIP). Post-deposition treatment was performed by hot isostatic pressing at about 1000 °C and about 100 MPa for more than 24 h and annealing CVD-ZnS for the same time at 850 °C in an Ar atmosphere of normal pressure. It was found that both annealed materials showed an increased light transmittance in the visible range, a recrystallized and reorganized microstructure, as well as an absence of the Zn-H bonds observed in CVD-ZnS. However, the increased light transmission essential for most optical applications is only observed in the HIP-ZnS (see Fig. 19.5). Zscheckel et al. [117] explained this effect by a significantly reduced porosity of the material after HIP. The majority of pores initially forms at grain boundaries during thermal treatment, and the application of simultaneous high pressure reduces their number to a minimum.

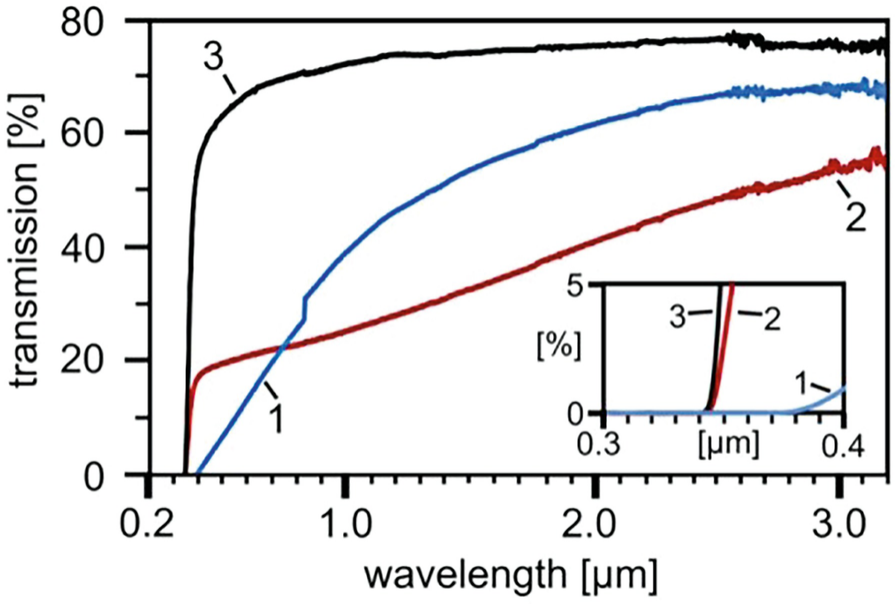

Fig. 19.5 UV-Vis transmission spectra of (1) CVD-ZnS, (2) annealed ZnS, and (3) HIP-ZnS. (Reprinted from [117]. Published 2014 by Optica Publishing Group as open access)

19.3 $CdCl_2$ Treatment

Rohatgi [83] has shown that post-deposition processing of CdTe, such as a post-deposition $CdCl_2$ treatment (also called an activation process), also plays a critical role in CdS/CdTe thin-film solar cell technology to achieve desired solar cell performance. Importantly, post-deposition treatment (PDT) of CdTe is necessary to obtain high efficiency, regardless of the deposition method or solar cell configuration [30, 84]. The $CdCl_2$ layer deposition on the CdTe is made by either physical vapor deposition or dipping in a $CdCl_2$-methanol solution. Subsequently annealing can be applied in air or in controlled atmosphere at a temperature in the range of 350–440 °C. Handling of $CdCl_2$ is an issue at laboratory scale since it is a volatile and at the same time carcinogen material. In any case in large-scale fabrication lines, wet deposition is mainly applied in order to avoid contamination and ease the cleaning of the chambers. In superstrate configuration, the $CdCl_2$ treatment is done after the deposition of CdTe, meaning it affects the CdTe absorber layer as well as the n-type CdS layer. In substrate configuration the treatment can be applied after the deposition of CdTe, after the deposition of CdS, or after each.

In general, $CdCl_2$ improves the short circuit current and open circuit voltage through enhancing the crystallite grain nucleation in CdTe, recrystallization, surface amendment, grain boundary passivation, doping concentration modification, assisting interdiffusion at the interface, defect density amending, and boosting lifetime of charge carriers in CdTe layer [3, 30, 84]. The recrystallization of the structure is evidenced by a change in the predominant orientation of grains, different shapes and sizes of crystallites, as well as a different structure of the grain boundaries. Chlorine acts as sintering flux enhancing the growth and the coalescence of the grains [101]. Also the stacking faults in CdTe are reduced and the texture changes [86, 100]. The improvement in crystallinity actually contributes to a decrease in the concentration of defects, thereby reducing the number of recombination centers [16]. As a rule, these processes are accompanied by an increase in the mobility of charge carriers (see Fig. 19.6). It is seen that post-deposition treatments using $CdCl_2$ increase the mobility of CdSe significantly. It is important that this phenomenon is observed not only for

CdTe but also for other II-VI compounds. For example, Leoncini et al. [56] and Romeo et al. [86] reported that treatment of CdS with chlorine increased grain size and changed grain orientation. It was found that the presence of oxygen during annealing is crucial because it leads to an increase of the absorber carrier concentration as needed for high-performance devices [26]. Post-deposition treatment also reinforces the ionic bonding between atoms as well as increases the hole concentration from 10^{13} cm^{-3} limits to 10^{16} cm^{-3} without compromising the carrier lifetime in CdTe thin films [4].

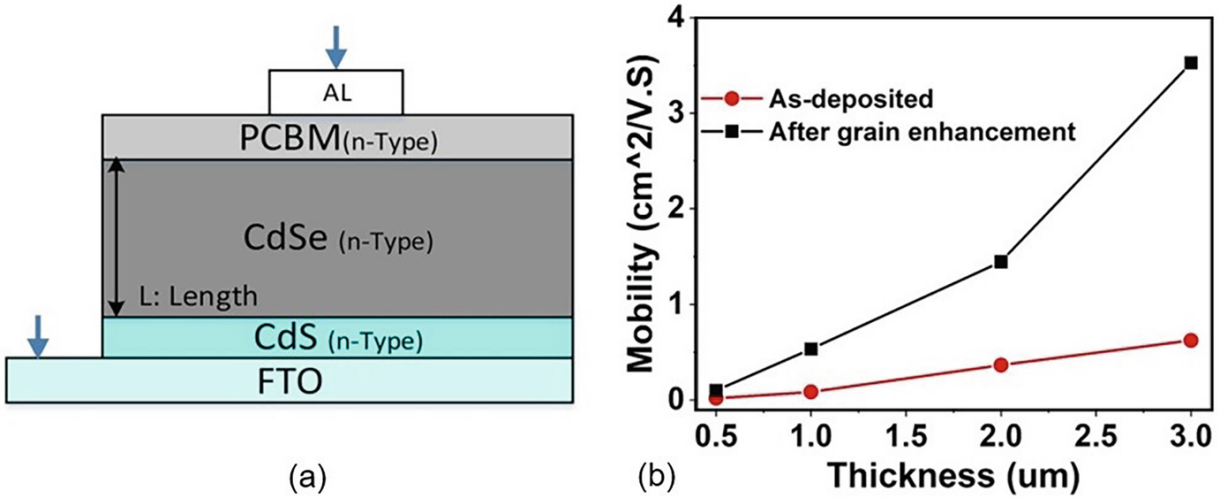

Fig. 19.6 (**a**) Schematic diagram of the n+-n-n+ structure to measure mobility of the CdSe thin film using the SCLC technique. (**b**) Electron mobility vs film thickness showing an increase in mobility with the grain size. CdSe thin films were deposited using physical vapor deposition at a temperature of ~400 °C. The $CdCl_2$ treatment consisted of spin coating of a 2 wt.% solution of $CdCl_2$ in deionized (DI) water (2 g/100 ml) followed by thermal annealing under a nitrogen atmosphere at 450 °C for 30 min inside a quartz tube. (Reprinted from [6]. Published 2019 by AIP as open access)

Dharmadasa et al. [22] also found that $CdCl_2$ treatment done on CdTe layers tends to remove any excess of Te from the layer and make the CdTe material more stoichiometric. The presence of $CdCl_2$ on the surface also prevents material loss during sublimation. In other words, this treatment converts Te-rich CdTe layers into stoichiometric CdTe more suitable for device fabrication. Dharmadasa et al. [21–23] believe that this effect is responsible for the change in solar cell parameters observed after thermal treatment with $CdCl_2$. It has previously been shown that when the grown material was rich in Te and had p-type electrical conductivity, the devices produced had poor performance [25]. However, when the material reached

the stoichiometric composition or the composition with low ppm Cd enrichment, the performance of the solar cell device improved, and the efficiency reached its highest values. Thus, it was concluded that treatment with $CdCl_2$ improves the stoichiometry of the material; turns the CdTe layer into Cd enriched at the ppm level, which drastically improves the electronic properties; and therefore helps in the production of high-efficiency solar cells. This conclusion is consistent with the results of studies reported in [21, 23], which showed that $CdCl_2$ treatment reduces the defect concentration and transforms a very broad defect distribution in the middle of the bandgap to a relatively narrow defect level at ~0.74 eV (see Fig. 19.7).

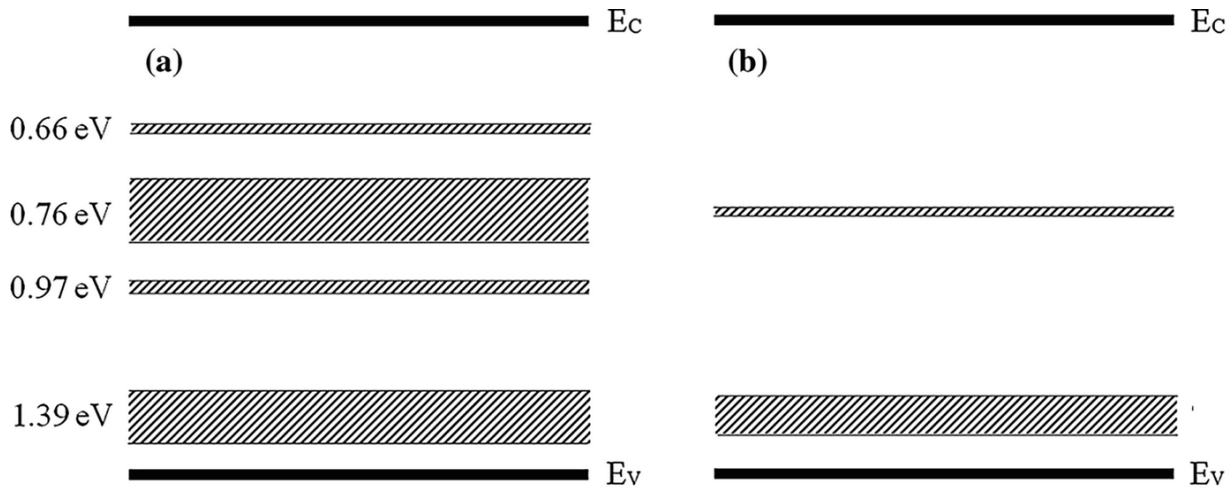

Fig. 19.7 A graphical summary of defect fingerprint observed at 80 K for (**a**) as-deposited and (**b**) $CdCl_2$-treated thin films of CdTe grown by electroplating. (Reprinted with permission from [23]. Copyright 2015: Springer)

The $CdCl_2$ treatment has also a strong influence on the interface in CdTe/CdS structure. The lattice constants of CdTe and CdS differ by about 10% possibly leading to interface defects [101]. This effect can be moderated by intermixing of CdTe and CdS caused by the $CdCl_2$ treatment where $CdS_{1-x}Te_x$ forms at the interface [54]. The $CdS_{1-x}Te_x$ solid solution has a reduced lattice parameter. Chlorine diffuses predominantly along grain boundaries, since its solubility in CdTe is very limited at temperatures below 520 °C. Therefore, chlorine very quickly reaches the junction. The intermixing partially consumes the CdS layer. This is beneficial as it enhances the spectral response in the short wavelength region. It was also found that cells treated with $CdCl_2$ not only exhibited higher quantum

efficiency at all relevant wavelengths but also markedly lower penetration loss, and the shape was consistent with the classical “window response” expected for such a heterostructure. However, it should be kept in mind that an improvement in the spectral response is observed as long as the CdS coating layer remains. When intermixing becomes excessive and in some places all CdS is converted to $CdS_{1-x}Te_x$, weak junctions are formed, which reduces the performance of the device [100]. Galloway et al. [30] found that the presence of $CdCl_2$ flux also had a significant effect on microscopic homogeneity. According to the results of their studies, the recombination losses in the depletion region and at the grain boundaries are small and, if they occur at the junction, then with a significant uniformity over the device area.

As for the atmosphere optimal for carrying out the $CdCl_2$ treatment process, there is no consensus. Some propose to carry out heat treatment in a vacuum [90], others in a neutral atmosphere [87], third in hydrogen [45], and fourth in an atmosphere containing oxygen [110]. As a result of these studies, it was found that the vacuum annealing process increases open circuit voltage (V_{oc}) and J_{sc}, as well as efficiency [66]. Samoilenko et al. [90] demonstrated that the vacuum ambient $CdCl_2$ treatment leads to CdTe absorbers with grain refinement, recrystallization, and grain boundary passivation. Jain et al. [44] studied the annealing in a nitrogen glovebox with less than 0.01 parts per million and in atmosphere containing oxygen (21%) and nitrogen (78%) using the standard method for device fabrication. The authors concluded that both devices exhibit diode characteristics, but the device annealed in air exhibits photovoltaic behavior, whereas the device annealed in an oxygen-deficient atmosphere does not show any photoresponse. At the same time, Chander and Dhaka [11] reported that the treatment in air ambient was found to increase the surface oxidation with a lot of chlorine residues left in CdTe surface causing increased resistivity, and reduced acceptor density resulted in a reduction of efficiency. In contrast, Wang et al. [110] demonstrated that air ambient $CdCl_2$ treatment not only improved the grain size and quality but also incorporated Cl and more O into the film, both of which can significantly improve the heterojunction quality and device performance. Ambient oxygen was also studied as a p-type dopant in CdTe leading to type conversion [89], and it was found that the annealing at temperatures from 350 to 450 °C during 10–

20 min is the best for thermal treatment of $CdCl_2$ [61]. In addition, oxygen annealing has been reported to be accompanied by (a) recrystallization and grain growth, (b) interaction at the CdS/CdTe interface, (c) life span extension, (d) grain boundary passivation, and (e) improved solar cell efficiency [22]. Dharmadasa [24] concluded from the recent $CdCl_2$ treatment studies that three main elements to consider in this process are Cd, Cl, and O. Air-treated devices followed by vacuum annealing process presented better cell performance as O_2 may introduce CdO into CdS and CdTe layers and completely change the wetting properties, growth behavior, or electrical properties of these layers.

It should be noted that $CdCl_2$ treatment can be combined with other treatments. For example, Bagheri et al. [6] proposed post-deposition selenization of CdSe films after $CdCl_2$ treatment. The post-selenization step was performed at 450 °C on three samples for 30–120 min under a nitrogen flow inside the quartz tube. Bagheri et al. [6] have found that selenization after grain enhancement was shown to improve the photoconductivity and the photo-to-dark conductivity ratio. The mobility-lifetime product for electrons was measured and was found to increase with selenization time and be in the range of 5×10^{-6} cm^2/V (see Fig. 19.8). Tail-state densities and the Urbach energy of the tail states near the valence band were measured, and it was found that selenization reduced the tail-state densities and also reduced the mid gap densities.

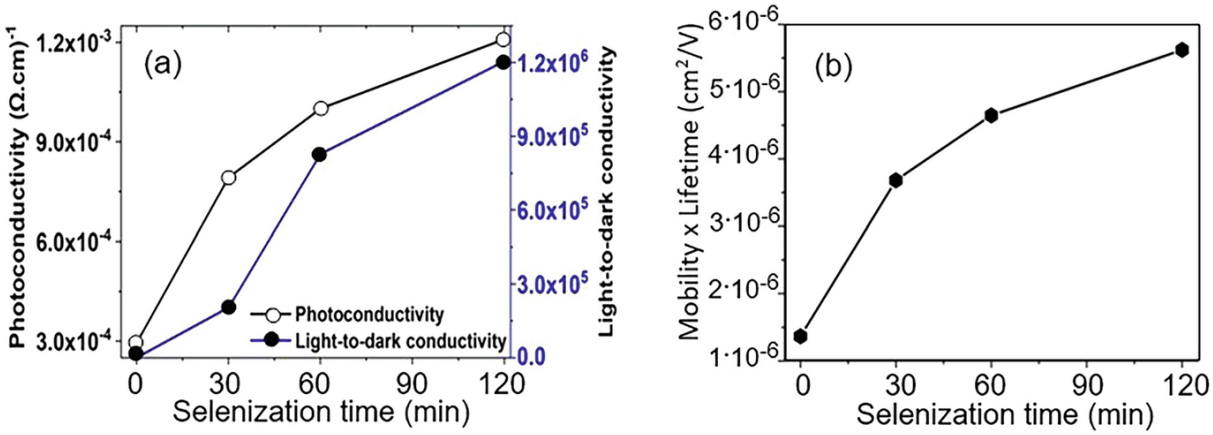

Fig. 19.8 (**a**) Results for the photoconductivity and light-to-dark conductivity ratio of CdSe thin films for as-deposited and after post-deposition selenization. (**b**) Mobility-lifetime product vs post-selenization time for CdSe thin films. (Reprinted from [6]. Published 2019 by AIP as open access)

Li et al. [57] proposed another option of post-deposition treatments. As shown earlier, in order to achieve high efficiency of CdTe/CdS solar cells, in addition to $CdCl_2$ treatment (~400 °C), it is also necessary to dope CdTe with copper, which is carried out in the process of ohmic contact forming (~200 °C). However, Cu doping is one of the reasons for the observed temporal instability of CdTe/CdS solar cells. A low-temperature ex situ doping of CdTe with V elements developed by Li et al. [57] is one of the promising routes to solve this problem. Ex situ doping is carried out in chlorinated CdTe (i.e., CdTe treated with $CdCl_2$), which provides the formation of vacancies at Te sites (V_{Te}), facilitating diffusion. Solutions of group V chlorides (PCl_3, $AsCl_3$, $SbCl_3$, and $BiCl_3$) were applied directly to the CdSeTe surface by spin coating with various solution concentrations (1–100 mg/l) at a spin-coating speed of 1000 rpm for 30 seconds. The samples were dried to form the group V chloride layer on the CdSeTe surface. This process was performed in the N_2-filled glovebox. After applying carbon electrode, the CdSeTe devices were heated to diffuse the group V ions into the CdSeTe absorber. The dopants were thermally activated by annealing at temperatures 200–240 °C for 10–30 min. The annealing conditions significantly impact device performance. Li et al. [57] have shown that this low-temperature ex situ doping process produces an activation ratio as high as 5.88%, leading to both high hole density (on the order of 10^{15} cm^{-3}) and a long carrier lifetime (~22 ns). The best CdSeTe solar cell achieved a V_{OC} of 863 mV and a power conversion efficiency (PCE) exceeding 18% through ex situ As doping, which is better than its Cu-doped counterparts. More importantly, such a low-cost and low-temperature group V diffusion doping process is similar to the traditional Cu doping process and thus can be easily integrated with the manufacturing line, which can further make the CdTe-based solar cell technology more competitive in the solar market.

Experiment has shown that in addition to $CdCl_2$, chlorine-containing gases and other chloride compounds can also be used as a source of chlorine. For example, CdTe can be processed in an atmosphere of chlorinated gases belonging to the Freon© family. In this case, CdTe is placed in a vacuum chamber, and then a mixture of argon and a nontoxic chlorine-containing gas is introduced. Both chlorofluorocarbons and hydrochlorofluorocarbons can be used. When the system is brought to 400 °C, the following reaction occurs [85]:

$$CdTe + 2Cl_2 \rightleftarrows CdCl_2 + TeCl_2 \quad (19.1)$$

This process does not require the surface to be etched after treatment, since chlorine residues are removed by evacuating the chamber after completion of the reaction, while maintaining the same substrate temperature. In addition, it was demonstrated that a Te-rich layer is formed on the surface after treatment [87].

As for chloride compounds, Major et al. [62] tested various chloride compounds such as $MgCl_2$, NaCl, KCl, and $MnCl_2$ as possible substitutes for $CdCl_2$. Other alternative chloride compounds that have been tried for CdTe post-deposition treatment are $ZnCl_2$, Na_2ZnCl_4, $(NH_4)_2ZnCl_4$, $MgZnCl_4$, $CaZnCl_4$ [86], NH_4Cl, and $MgCl_2$ [63, 111]. The need for new sources is due to the fact that the widespread use of $CdCl_2$ treatment requires additional safety procedures to avoid contamination for both people and the environment, since this compound is very toxic [63, 111]. This is why great efforts are being made to develop nontoxic and inexpensive treatments. Major et al. [62] have shown that the best results were obtained with $MgCl_2$. The solar cells had an efficiency of 13.5%, comparable to similar devices made with standard $CdCl_2$ treatment [62]. $MgCl_2$ can be deposited by physical vapor deposition or using "solution" process [62, 68]. It is important to note that when using the above sources of chlorine, the same effects were observed as when treated with $CdCl_2$. Harif et al. [36] also tested several different post-deposition treatments. CdTe/CdS samples were treated with $CdCl_2$, $MgCl_2$, $CuCl_2$, and $AgNO_3$. To perform these treatments, $CdCl_2$, $MgCl_2$, $AgNO_3$, and $CuCl_2$ powders were dissolved in deionized water with the concentration of 0.3 M, 0.3 M, 0.01 M, and 0.01 M, respectively. Afterward, CdTe surface was treated by immersing the glass/CdS/CdTe structure into the solutions for 30 s. The annealing process was done into a furnace in an open-air atmosphere at 390 °C for 15 min. Upon the completion of the annealing process, the films were dipped into hot deionized water (80 °C) to remove any possible residue from the films' surface. Results of these studies are shown in Fig. 19.9. The XRD result showed that all the CdTe films had marginally better crystallinity after post-deposition treatment, whereby $AgNO_3$-treated films indicated a larger grain size than other treatments (Fig. 19.9a). The average

grain sizes were in the range 4–7 μm. The $CuCl_2$ treatment showed a higher carrier concentration of 10^{15} cm^{-3} compared to the other treatments, while the maximum mobility was observed after the $CdCl_2$ treatment (Fig. 19.9b).

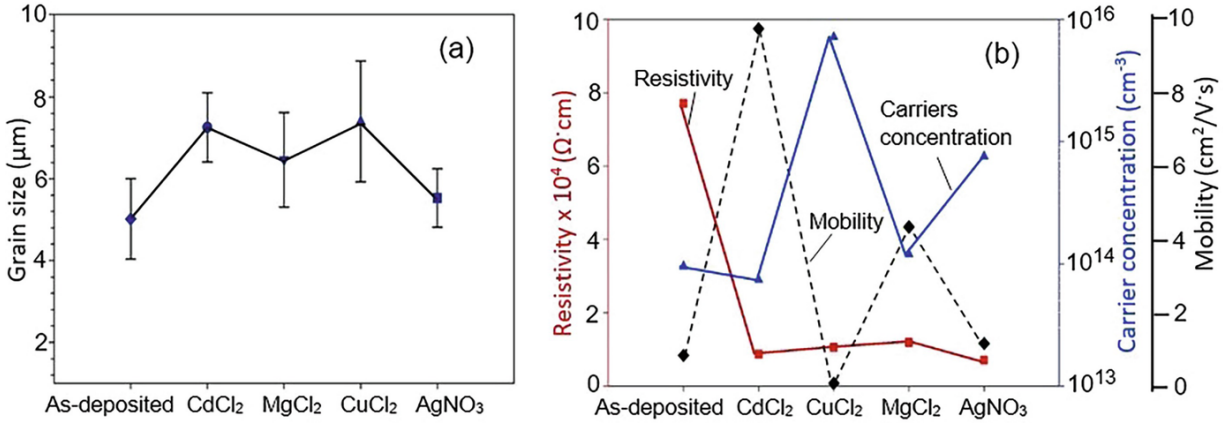

Fig. 19.9 (**a**) SEM grain size comparison of CdTe thin films for different treatments. (**b**) Carrier concentration, resistivity, and mobility variation with different treatments. (Reprinted with permission from [36]. Copyright 2020: Elsevier)

19.4 Post-Deposition Treatment with Alkalis

Among other post-deposition treatments that have become widespread in the manufacture of solar cells, it is necessary to highlight post-deposition treatment with alkalis. It is well-known that alkaline metals such as sodium are crucial for the performance of $Cu(In,Ga)Se_2$ (CIGSe)/CdS solar cells. For example, Chirila et al. [13] have shown that the use of a combined NaF and KF post-deposition treatment of a $Cu(In,Ga)Se_2$ (CIGSe) absorber prior to CdS deposition contributes to a significant increase in photoconversion efficiency in CdS/CIGSe photocells. During this treatment NaF and KF layers were deposited on the CIGSe surface. By using this PDT of a CIGSe absorber grown on polyimide foil, Chirila et al. [13] were able to prepare a world record device at that time with a cell efficiency of 20.4%. Subsequently, thin-film solar cells based on $Cu(In,Ga)Se_2$ polycrystalline absorbers achieved a record energy conversion efficiency of 23.35% [74]. With surface-sensitive X-ray photoelectron spectroscopy (XPS), Chirila et al. [13] observed a much stronger Cu and Ga depletion of the surface region compared to the untreated absorber. They concluded that the increased deficiency of Cu at the CIGSe surface leads to an enhanced Cd diffusion

into the absorber during the chemical bath deposition (CBD) of the CdS buffer layer even at low process temperatures. In addition, it was found that (i) the amount of Cd diffusing into the interface region of the absorber during the CBD of CdS is dependent on the Cu concentration [71], and the penetration of Cd into the CIGSe absorber becomes even more pronounced upon annealing in ultrahigh vacuum (UHV) at 350 °C [13]. This indicates that the Cd diffusion in CIGSe might be correlated with the Cu migration in this material which is directly connected to the formation of Cu vacancies (V_{Cu}) [109]. Later, this conclusion was confirmed by the results of theoretical [47] and experimental studies [108]. Umsur et al. [108] carried out such treatment in a separate ultrahigh vacuum evaporation chamber for 20 min at a substrate temperature of 330 °C in the presence of KF and Se molecular beams. In particular, Umsur et al. [108] suggested that due to Cd diffusion during CdS deposition, excess electrons are able to overcome the building-up potential barrier at the CIGSe/CdS interface. This improves the band alignment of the CIGSe/CdS heterojunction, resulting in improved efficiency of CIGSe/CdS thin-film solar cell devices.

Studies have shown that post-deposition treatment with alkalis such as NaF and KF also has a significant impact on the performance of solar cells based on $Cu_2ZnSnSe_4$ (CZTSe), sulfide (CZTS), and sulfo-selenide (CZTSSe) counterparts of CIGSe [42]. As in CIGSe, the inclusion of alkali metals in the above semiconductors causes a profound modification of its morphological and electro-optical properties. The most efficient CZTSe-based solar cells were fabricated using additional supply of Na [55]. In both CZTSe and CZTS, Na tends to segregate at grain boundaries [99] and provides an increase in the crystallite size [40, 97]. Na increases the lifetime of minority carriers both in single crystals [77] and in thin polycrystalline films [58]. The incorporation of Na also reduces the activation energy of the acceptor and increases the hole mobility and the carrier concentration [58, 72].

Ray et al. [80] compared the effects of NaF and KF treatment on the performance of CZTSe-based solar cells. They found that both PDTs resulted in higher solar cell conversion efficiency driven by a simultaneous increase in fill factor (FF), Voc, and Jsc (see Fig. 19.10). Ray et al. [80] attributed the improvement in V_{oc} to a decrease in diode quality factor (A) and J_0, as well as to better radiation efficiency. The best V_{oc} improvement

was obtained with NaF-PDT, which showed the highest radiation efficiency and lowest activation energy of doping defects, whereas for KF-PDT, the V_{oc} improvement was limited to redshift photoluminescence, higher band-tail density of states, and deeper acceptors. At the same time, the largest value of J_{sc} was achieved with KF-PDT associated with a larger width of the space charge region.

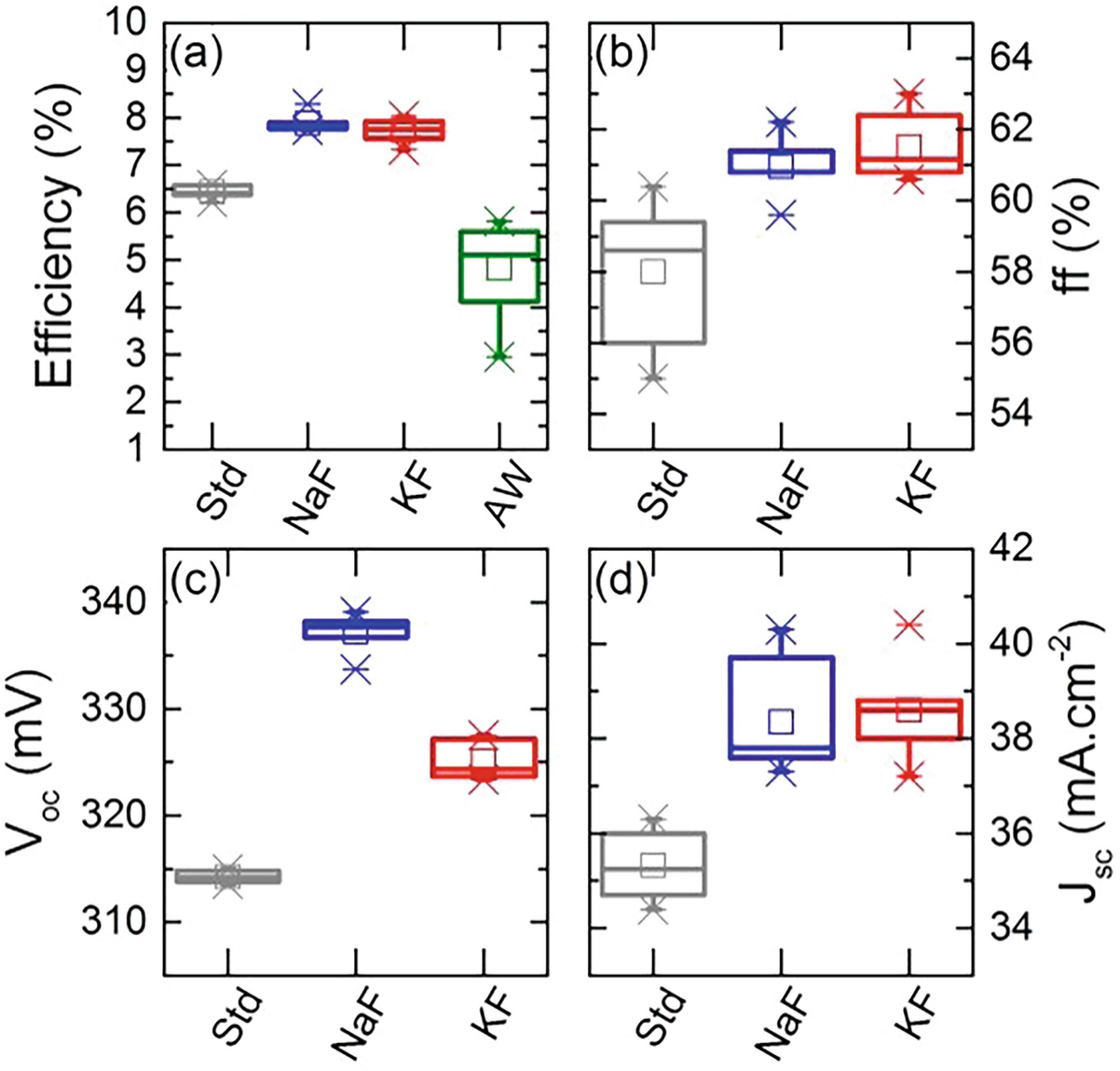

Fig. 19.10 (**a–d**) Performances of CZTSe-based solar cells made with untreated, NaF-treated, and KF-treated absorbers. CZTSe thin films were grown on a Mo-coated soda lime glass (SLG) substrate heated at 470 °C in a molecular beam epitaxial system. An optional two-step PDT was applied to the CZTSe thin films. The first step consisted of an approximately 5-nm-thick alkaline fluoride layer deposition by electron beam evaporation. The second step was an annealing in a tube furnace at atmospheric pressure and 100 °C for 1 h under a N_2 atmosphere. Prior to solar cell processing, the

samples, which underwent a PDT, were washed with deionized water. AW-PDT without supply of alkaline fluoride. (Reprinted with permission from [80]. Copyright 2017: Elsevier)

The same effect of optimizing the parameters of CIGSe/CdS-based photodetectors was also observed when using for PDT of other heavy alkali fluorides such as RbF or CsF [98, 107]. Moreover, the latest record-breaking efficiencies have been achieved with RbF-PDT for co-evaporated CIGSe [43] and CsF-PDT for sequentially deposited/selenized CIGSe [74], respectively. Kodalle et al. [50] analyzed and compared the effects of two different post-deposition alkaline fluorine treatments (KF and RbF) on the growth of chemical bath-deposited CdS buffer layers on Cu(In, Ga)Se_2 absorbing layers for thin-film solar cells. They found that both PDTs resulted in better CdS coverage of the CIGS surface, leading to improved heterojunction quality in the early stages of growth compared to untreated devices. Therefore, they concluded that the quality of the p-n junction at early growth stages of the CdS is mostly determined by the lateral homogeneity of the CdS layer. It was also found that RbF-treated devices had more stable behavior, while KF-treated devices suffered from a decrease in fill factor and open-circuit voltage. In addition, RbF treatment is accompanied by a higher CdS growth rate [28], increased Cd diffusion [108], accumulation of Rb at the CdS/CIGSe interface [78], and formation of the $RbInSe_2$ compound at the interface [41, 78]. Ümsür et al. [107] suggested that the observed effects are associated with the Rb-Cd exchange mechanism in the $RbInSe_2$ compound and the formation of a (Cu,Cd)-In-S-Se mixed compound at the CdS/CIGSe interface, accompanied by the incorporation of Cd into the remaining V_{Cu} sites in the matrix. It is important that the interface between CdS and CIGSe with lower V_{Cu} concentration was not affected by the RbF-PDT in terms of Cd incorporation.

However, because of the toxicity of Cd, the CdS buffer layer is desired to be eliminated from the cell structure. The Zn(O,S) buffer material is an attractive candidate due to its nontoxic nature and a larger tunable bandgap energy [69], reducing the parasitic absorption in the buffer layer. However, similar studies for CIGSe/ZnS solar cells carried out by Ümsür et al. [107] have shown that the incorporation of Zn atoms into the CIGSe does not occur as much as Cd atoms during the chemical bath deposition, i.e., the donor-like Zn_{Cu} states do not form as easily as the Cd_{Cu} states. The

available V_{Cu} concentration and RbF-PDT have limited effects on the CIGSe/ZnS interface in comparison to its CdS counterpart. This means that the ZnS buffer layer forms a more stable and well-defined interface with CIGSe.

19.5 Chemical Etching

It was found that the stage of nitric-phosphoric (NP) etching [62, 111] is also as important as the activation process for improving the performance of a CdS/CdTe photocell. Several studies have shown that bromine methanol (BrMeOH) can be used as an alternative to NP etchant. However, the Br_2:MeOH solution has been found to have some problems. Bätzner et al. [8] reported that etching with a Br_2:MeOH solution broadens the grain boundaries, and the tellurium layer formed along these boundaries provides a conductive bond between the grains. Also, when a Br_2:MeOH solution is used, bromine accumulates at the CdS/CdTe interface [17]. Therefore, NP etching has been favored in recent years. At that Cho et al. [14] have shown that the most successful way to optimize the parameters of CdS/CdTe photocells is a combination of $CdCl_2$ treatment with NP etching (Fig. 19.11). When using them, the best parameters of photodetectors were achieved (see Fig. 19.12). Improvement of photovoltaic parameters can be attributed to the removal of the oxide and the formation of Te-rich layer, which benefit the activation process. These changes were observed by Major et al. [62] and Williams et al. [111] in CdS/CdTe structures after combining NP etching process with the $CdCl_2$ activation process.

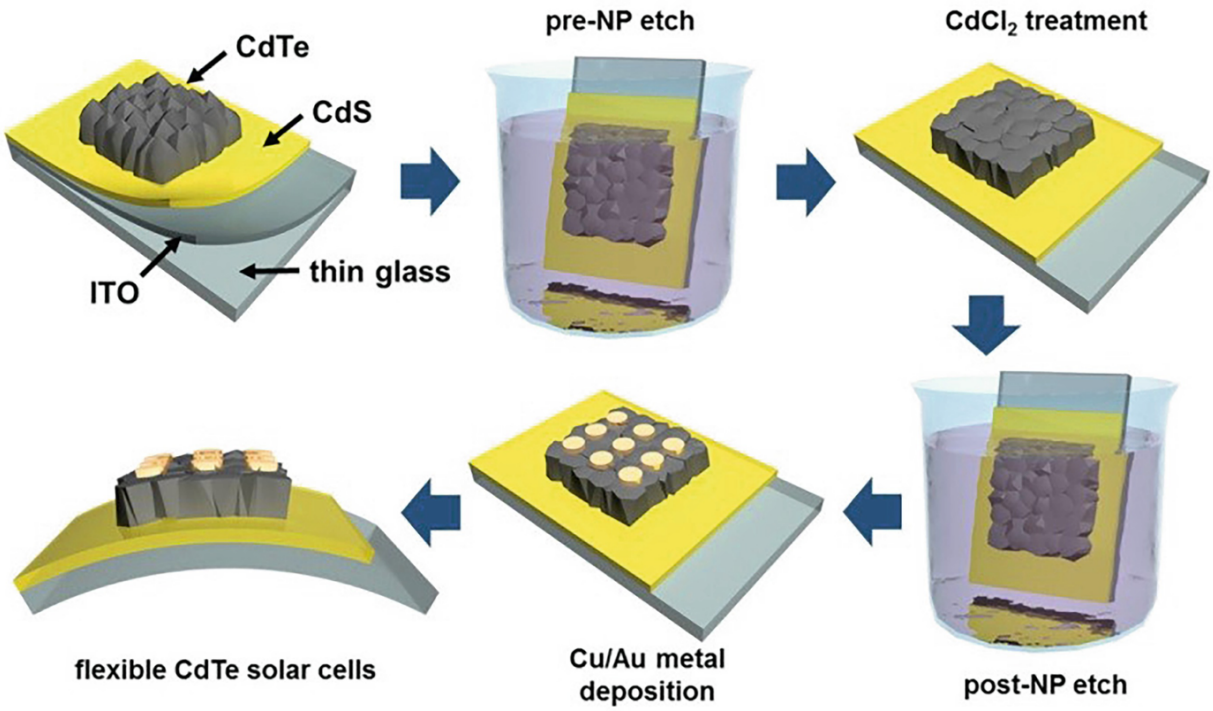

Fig. 19.11 Schematic diagram of fabrication of a flexible and ultralightweight CdTe thin-film solar cell with superstrate configuration. (Reprinted from [14]. Published 2016 by Optica Publishing Group as open access)

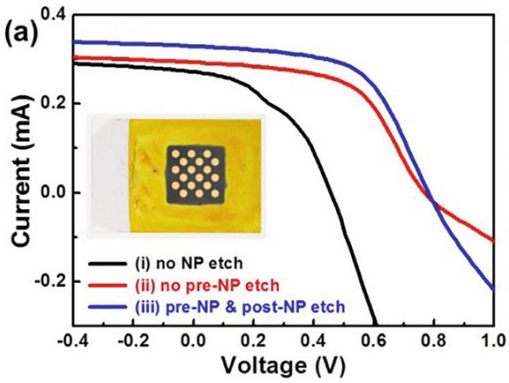

(b)

process	V_{OC} (mV)	J_{SC} (mA/cm^2)	fill factor (%)	efficiency (%)
(i) no NP etch	456.9	24.72	43.39	4.9
(ii) post-NP etch only	767.6	26.70	55.92	11.46
(iii) both pre-NP and post-NP etch	780.7	29.95	58	13.56

Fig. 19.12 (**a**) Light I-V curves of the CdTe solar cells with the highest efficiencies of each process, (inset) photograph of the fabricated ultralightweight, flexible CdTe thin-film solar cell, (**b**) summary of the best photovoltaic parameters of each type of cells. (Reprinted from [14]. Published 2016 by Optica Publishing Group as open access)

It should be noted that chemical etching of synthesized nanocrystals and nanoparticles in order to control their properties can also be attributed to post-deposition treatments. Etching technology is considered to be a particularly important process to resize semiconductor NPs (see Fig. 19.13) and to tune their luminescence and catalytic properties. Chemical etching of colloidal nanoparticles can also help to obtain the necessary forms of

nanocrystals. For example, Lim et al. [60] have shown that the shape and size of colloidal CdSe NCs can be tailored by chemical and photochemical etchings in chloromethane solvents. Yang et al. [114] used copper acetate etching of colloidal CdSe nanocrystals for this purpose. Along with the etching time, both the absorption and photoluminescence spectra of etched CdSe NCs showed blueshift, while the transmission electron microscopy images indicated that the size of the NCs became from 5.6 nm to 2.6 nm. Li et al. [59] found that the slow chemical etching process of CdSe NCs in a 3-amino-1-propanol/water mixture can remove surface irregularities and disperse grain boundaries. Lam et al. [53] obtained CdSe nanowires with controlled diameters by acid treatment and subsequent Se thermal desorption. Khon et al. [46] showed that chemical etching of CdSe/CdS core-shell structures promotes partial dissolution of the CdS shell from the surface of the CdSe core, which allows CdSe to come into direct contact with the environment and thus enhances the catalytic activity of such structures. Hydrogen production tests confirmed the improved catalytic activity of CdSe/CdS dimers, which was enhanced 3–4 times upon etching treatment. Examples of other post-deposition treatments of II-VI NPS that used chemical etching are listed in Table 19.1.

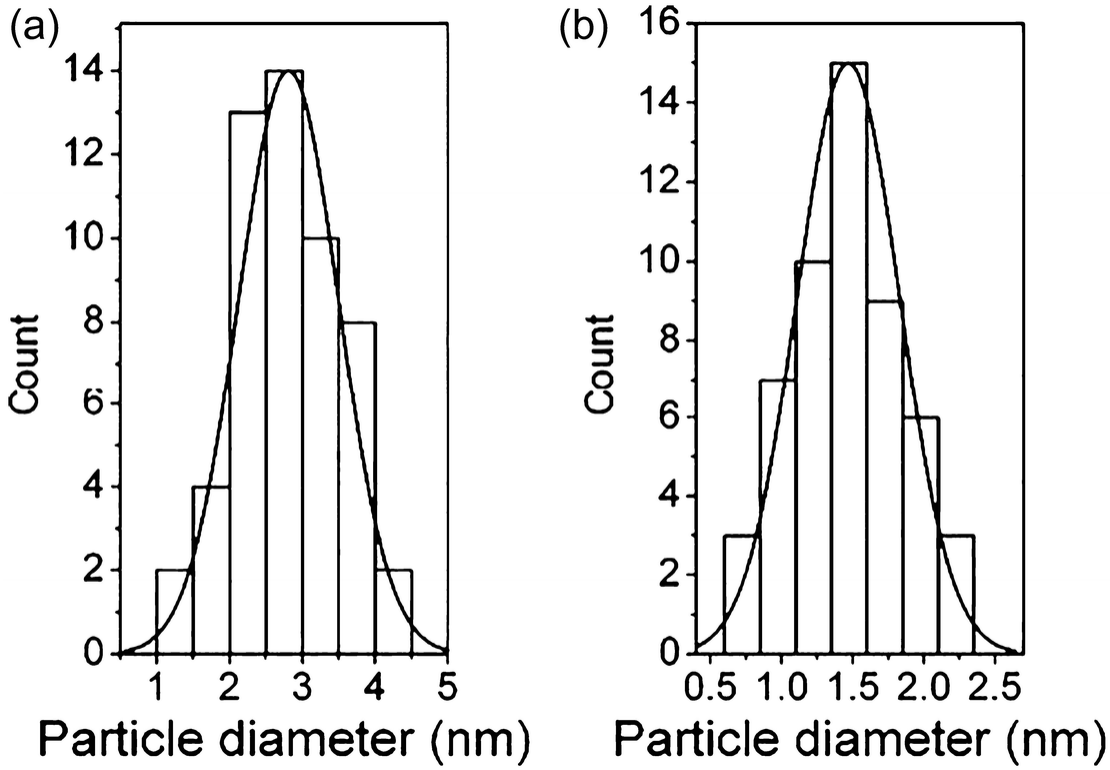

Fig. 19.13 Size distribution of CdS NPs (**a**) before and (**b**) after enzymatic etching process of CdS NPs by HRP in the presence of H_2O_2. (Reprinted with permission from [34]. Copyright 2015: RSC)

Table 19.1 Examples of post-deposition chemical treatments of II-VI NPs

NPs	Synthesis	Etchant	Application	Ref.
CdS	Chemical synthesis in aqueous buffered solutions	Enzyme horseradish peroxidase +H_2O_2	Optical chemical and biosensing	[34]
CdS	Solvothermal reaction	$AgNO_3$ + ethanol	Porous photoelectrode	[115]
CdSe	Hot injection method	$CuAC_2$/tri-n-butylphosphine	N/A	[114]
CdSe	High-temperature pyrolysis of organometallic precursors	3-Amino-1-propanol (APOssL)/water (v/v) 10:1) mixture at 80 °C in the presence of O_2	N/A	[59]
CdSe/CdS	Two-step chemical synthesis	Mild solution of benzoyl peroxide	Catalysis	[46]

Yang et al. [115] showed that chemical etching can also control the porosity of synthesized nanocrystals of II-VI compounds. The fabrication of mesoporous materials is of increasing interest due to their potential applications in electrode materials, solar cells, or catalysts. For preparing porous CdS nanorods, Yang et al. [115] proposed to use a simple Ag^+ etching chemical reaction at room temperature. Because the solubility of Ag_2S is much lower than that of CdS, $AgNO_3$ was chosen as the etch agent to modify the morphology of CdS nanorods. In a typical procedure, 0.002 mol fresh CdS and 0.0002 mol $AgNO_3$ were dispersed in 50 ml absolute ethanol using ultrasound. Then the two solutions were mixed together and violently stirred for 2 h at room temperature. Absolute ethanol, the only organic solvent that can dissolve $AgNO_3$, was used to substitute distilled water for the modification of nanorods. As a result of such processing, mesoporous CdS nanorods with the average diameter of approximately 2 nm were obtained.

Wet oxidation in a hydrogen peroxide can also be attributed to the considered method of post-deposition treatment. A hydrogen peroxide solution (15 wt % H_2O_2/distilled water) was used by Chen et al. [12] as an oxidizing agent at room temperature to avoid deviation from stoichiometry and to maintain a smooth surface of ZnTe. This wet chemical oxidation

process was confirmed to form an oxide layer (TiO_2 and $CdTeO_3$) with a thickness in the range of 2–4 nm. This thickness reached a saturation level after 5 min of oxidation. Chen et al. [12] have shown that this treatment reduced the surface leakage current by about 37% and improved the photoresponse of CZT ($Cd_{0.9}Zn_{0.1}Te$) detector to low-energy X-rays. The same result was obtained by Zázvorka et al. [116]. It was found that the formation of native oxides on the surface of CdZnTe significantly reduces surface leakage currents in radiation detectors. Zazvorka et al. [116] found that the leakage current decreased simultaneously with oxide growth. A thicker oxide layer correlated with a lower leakage current.

19.6 Laser Treatment

Surface treatment of as-prepared II-VI compounds using excimer laser radiation is another method of post-deposition treatments. A typical schematic of a laboratory scale apparatus for laser treatment is shown in Fig. 19.14a. The samples to be treated can be placed in a gastight chamber to control the annealing environment. This chamber can be mounted on a motion stage to allow for scanning of the sample in the beam line.

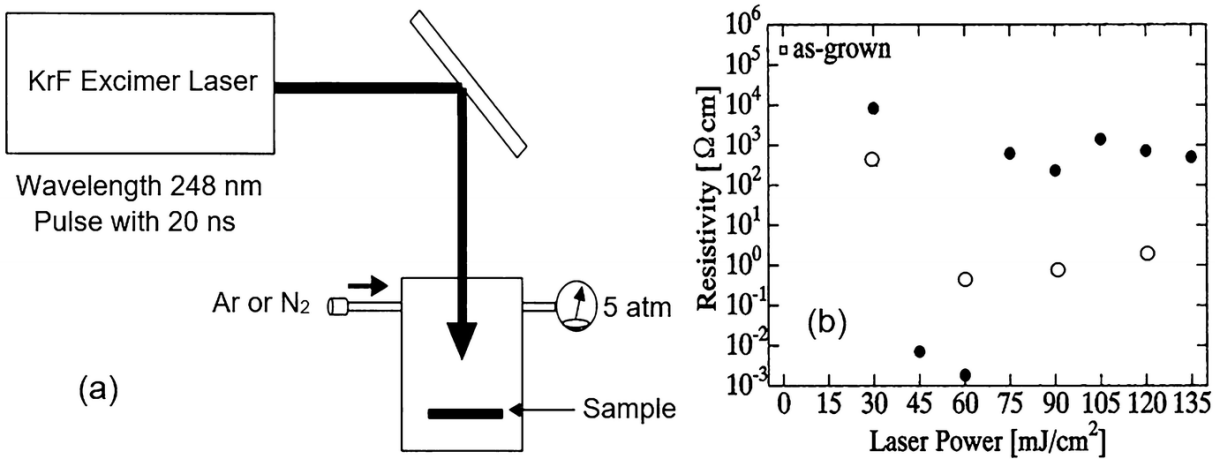

Fig. 19.14 (**a**) A schematic of excimer laser doping setup; (**b**) Dependence of CdTe resistivity on the power density of excimer laser radiation using various doping precursors: ●, Sb; ○, Na_2Te. (Reprinted with permission from [37]. Copyright 2001: Elsevier)

As a result of experimental studies, it was found that laser treatment of the surface of II-VI compounds can be used for the following purposes [93].

First, the pulse laser treatment (PLT) can be used for heavy doping of II-VI semiconductors, for which it is rather difficult to achieve bipolar conductivity. For example, it was reported that p-type heavy-doped CdTe, ZnSe, and ZnO layers with the resistivity in the range from 10^{-2} to 10^{-3} Ω cm and the hole concentration of 10^{17}–10^{19} cm^{-3} with carrier mobility of 10–100 cm^2/V s can be obtained using dopant atoms such as Na, K, Sb, In, or P and by diffusing them inside the crystals by irradiating with an excimer laser [32, 37]. In particular, when Na_2Se was deposited on the ZnSe surface as a material including dopant atom, Hatanaka et al. [39] obtained remarkably heavy p-type doping with the hole carrier concentration of 4.8 x 10^{19} cm^{-3}. In these experiments the laser light with an energy of 350 mJ and pulse width of 20 ns was irradiated through a quartz window. The effective laser energy irradiation on the sample was estimated as 110 mJ. Alkaline metal compounds such as K_2S and Na_2Te were used as a source of other impurities. The thickness of these layers deposited on the surface of II-VI compounds was around 50 nm.

Highly conductive n-type CdTe layers with low resistivity, high electron concentration, and mobility, 5×10^{-3} Ω cm, 8.9×10^{18} cm^{-3}, and 140 $cm^2/V{\cdot}s$, respectively, can also be obtained using an appropriate dopant and laser treatment. These results have been presented in several papers [37–39]. The dependence of CdTe resistivity on the irradiation power density of excimer laser is shown in Fig. 19.14b.

Very fast, nonequilibrium and nonstationary processes such as laser-induced defect formation, heating, melting, and following fast cooling of a thin surface layer of the semiconductor under irradiation can provide the conditions for heavy doping of CdTe with impurity concentrations which cannot be achieved by traditionally used equilibrium methods. In particular, this causes a laser-stimulated increase in the impurity diffusion rate as well as freezing of a large number of nonequilibrium point defects [31, 32]. Furthermore, laser implantation of impurities is a promising procedure for doping because the irradiation of semiconductors with high-absorbed laser pulses of nanosecond duration allows us to avoid heating the bulk of crystals and modifies only thin surface layer crystals and modifies only a thin surface layer.

Second, laser processing can be used to create an ohmic back contact to II-VI compounds [94, 95]. Figure 19.15 shows the dependence of specific

resistivity of Mo-CdTe contact for single pulses of UV laser at various energy fluences. As shown earlier, the formation of an ohmic contact with CdTe at the final stage of metallization has been a difficult task for a long time due to the high electron affinity of CdTe and its tendency to form surface dipoles pinning the Fermi level [19]. The experiment showed that the use of PLT can solve this problem. An ohmic back contact is created with PLT by exploiting the difference in vapor pressure between Cd and Te; Cd is a more volatile substance [7, 10]. When a pulsed UV laser is used, the surface quickly heats up to very high temperatures, resulting in slightly more Cd loss than Te. This can either leave a Te-rich surface that effectively dopes the surface of CdTe to a high degree of p-type due to the increased presence of Cd vacancy acceptors or form a thin film of Te or some combination of both [96]. Elemental Te is a degenerate p-type semiconductor, and thin layers on a CdTe surface have been shown to lead to ohmic behavior of contacts formed on such a surface [75], although there are suggestions that this may be more related to the formation of metal tellurides than to the properties of Te itself, as discussed in [51].

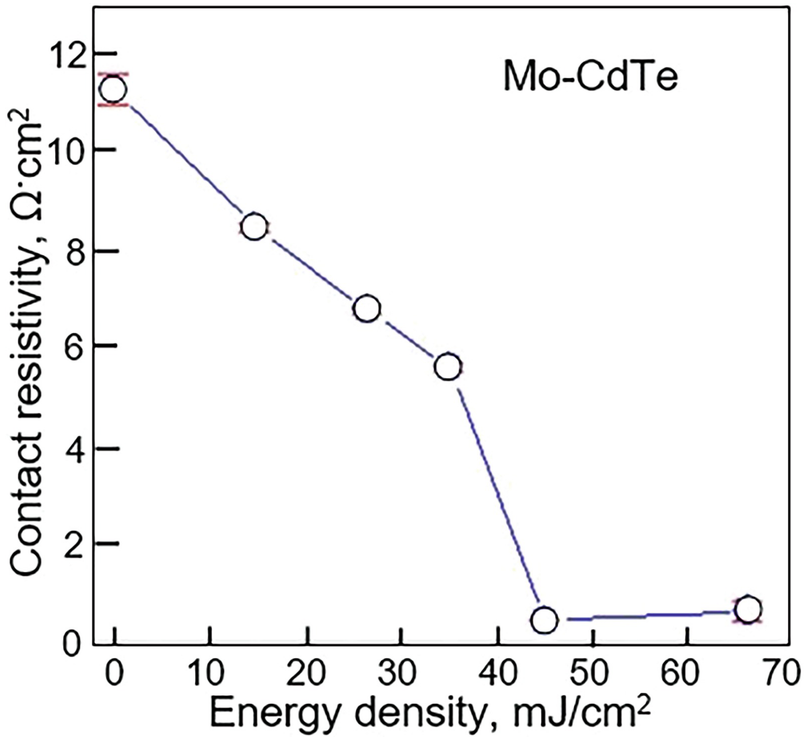

Fig. 19.15 Contact resistivity as a function of energy density of samples treated with single laser pulse. The laser anneals were carried out by a KrF excimer laser emitting 248 nm pulses of about 25 ns duration. (Reprinted with permission from [96]. Copyright 2014: AIP Publishing)

The doping method described in the previous paragraph can also be used to form ohmic contacts. Hatanaka et al. [38] used this approach to form p-type ohmic contact in ZnSe and CdTe diodes. They used Na_2Se or Na_2Te deposited on the surface with ZnSe and CdTe before PLT as a dopant source.

Third, PLT can be used to recrystallize grown films [1]. The deposition of high-quality polycrystalline CdTe is currently one of the slowest steps in the fabrication of a solar cell module [112]. Thus, the CdTe fast deposition method, although of low quality of films grown, in combination with PLT, which allows a fast recrystallization process accompanied by grain size increase and defect annealing, has the potential to save capital costs and increase the productivity of solar cell production. The PLT of polycrystalline CdTe was first studied by Dawar et al. [18], who used a Nd:YAG laser with a wavelength of 1064 nm and a wavelength of 700 nm. By increasing the energy and the number of pulses, they showed that it was possible to achieve grain growth from 45 to 103 nm, as well as more than double the mobility. Laser recrystallization of grown CdTe films was also studied by As and Palmetshofer [5], who showed a rapid increase in grain size after only 2 seconds of exposure of CdTe:In films to continuous light at a wavelength of 647 nm. A more promising way to use PLT for the rapid production of thin-film CdTe from an inexpensive precursor is the sintering of CdTe nanoparticles, which can be easily and cheaply synthesized chemically. This approach has been tried by Ricky et al. [82]. Unfortunately, optoelectronic characterization was not carried out, and the films were far from optimal.

Simonds et al. [93] believe that laser processing offers unique opportunities to address technological issues affecting CdTe device efficiencies as well as lowering manufacturing costs by increasing module throughput. However, it must be recognized that the use of laser processing in large-scale production, especially solar panels, will be difficult.

Based on the features of PLT, it can be assumed that the use of PLT can have maximum prospects when it is necessary to locally change the properties of II-VI compounds on the surface of manufactured devices [76], for example, based on one-dimensional structures [81]. In the development of flexible devices, PLT can also be used, since the use of PLT drastically reduces the requirements for the substrates used.

Acknowledgments

G.K. is grateful to the State Program of the Republic of Moldova (project 20.80009.5007.02) for supporting his research.

References

1. Al-Mebir AA, Harrison P, Kadhim A, Zeng G, Wu J (2016) Effect of in situ thermal annealing on structural, optical, and electrical properties of CdS/CdTe thin film solar cells fabricated by pulsed laser deposition. Adv Condens Matter Phys 2016:8068396
2. Amaranatha RD, Murali G, Poornaprakash B, Vijayalakshmi RP, Reddy BK (2012) Effect of annealing temperature on optical and magnetic properties of Cr doped ZnS nanoparticles. Solid State Commun 152(7):596–602
3. Amin N, Karim MR, ALOthman Z.A. (2021) Impact of $CdCl_2$ treatment in CdTe thin film grown on ultra-thin glass substrate via close spaced sublimation. Crystals 11:390
4. Angeles-Ordonez G, Regalado-Perez E, Reyes-Banda M, Mathews N, Mathew X (2017) CdTe/CdS solar cell junction activation: study using $MgCl_2$ as an environment friendly substitute to traditional $CdCl_2$. Sol Energy Mater Sol Cell 160:454–462
5. As DJ, Palmetshofer L (1985) Laser annealing of defects in CdTe epitaxial layers. J Cryst Growth 72:246–251
6. Bagheri B, Kottokkaran R, Poly L-P, Reichert B, Sharikadze S, Noack M, Dalal V (2019) Influence of post-deposition selenization and cadmium chloride assisted grain enhancement on electronic properties of cadmium selenide thin films. AIP Adv 9:125012
7. Baidullaeva A, Vlasenko AI, Mozol PE, Smirnov A (2001) CdTe polycrystalline surface subjected to pulsed laser irradiation. Semiconductors 35(6):745–748
8. Bätzner D, Wendt R, Romeo A, Zogg H, Tiwari A (2000) A study of the back contacts on CdTe/CdS solar cells. Thin Sol Films 361–362:463–467
9. Bayhan H, Ercelebi C (1998) Effects of post deposition treatments on vacuum evaporated CdTe thin films and CdS/CdTe heterojunction devices. Tr J Physics 22:441–451
10. Brewer PD, Zinck JJ, Olson GL (1990) Reversible modification of CdTe surface composition by excimer laser irradiation. Appl Phys Lett 57(24):2526
11. Chander S, Dhaka M (2017) Time evolution to $CdCl_2$ treatment on Cd-based solar cell devices fabricated by vapor evaporation. Sol Energy 150:577–583
12. Chen K-T, Shi DT, Chen H, Granderson B, George MA, Collin WE et al (1997) Study of oxidized cadmium zinc telluride surfaces. J Vac Sci Technol A 15(3):850–853
13. Chirila A, Reinhard P, Pianezzi F, Bloesch P, Uhl AR, Fella C et al (2013) Potassium-induced surface modification of $Cu(In,Ga)Se_2$ thin films for high-efficiency solar cell. Nat Mater

12:1107–1111

14. Cho E, Kang Y, Kim D, Kim J (2016) Post-growth process for flexible CdS/CdTe thin film solar cells with high specific power. Opt Express 24:A791–A796

15. Chu TL, Chu SS, Ang ST (1988) Electrical properties of CdS/CdTe heterojunctions. J Appl Phys 64:1233

16. Consonni V, Feuillet G, Renet S (2006) Spectroscopic analysis of defects in chlorine doped polycrystalline CdTe. J Appl Phys 99:53502–53507

17. Danaher W, Lyons L, Marychurch M, Morris G (1986) Chemical etching of crystal and thin film cadmium telluride. Appl Surf Sci 27(3):338–354

18. Dawar AL, Jagadish C, Ferdinand KV, Kumar A, Mathur PC (1985) Effect of laser annealing on the structural, electrical, and optical properties of CdTe thin films. Appl Surf Sci 22(23):846–858

19. Demtsu SH, Sites JR (2006) Effect of back-contact barrier on thin-film CdTe solar cells. Thin Solid Films 510(1–2):320–324

20. Dhage SR, Colorado HA, Hahn HT (2013) Photoluminescence properties of thermally stable highly crystalline CdS nanoparticles. Mater Res 16:504–507

21. Dharmadasa IM, Alam AE, Ojo AA, Echendu OK (2019) Scientific complications and controversies noted in the feld of CdS/ CdTe thin film solar cells and the way forward for further development. J Mater Sci Mater Electron 30:20330–20344

22. Dharmadasa IM, Echendu OK, Fauzi F, Abdul-Manaf NA, Olusola OI, Salim HI et al (2017) Improvement of composition of CdTe thin films during heat treatment in the presence of $CdCl_2$. J Mater Sci Mater Electron 28:2342–2352

23. Dharmadasa IM, Echendu OK, Fauzi F, Abdul-Manaf NA, Salim HI, Druffel T et al (2015) Effects of $CdCl_2$ treatment on deep levels in CdTe and their implications on thin film solar cells: a comprehensive photoluminescence study. J Mater Sci Mater Electron 26:4571–4583

24. Dharmadasa IM (2014) Review of the $CdCl_2$ treatment used in CdS/CdTe thin film solar cell development and new evidence towards improved understanding. Coatings 4:282–307

25. Diso DG, Fauzi F, Echendu OK, Dharmadasa IM (2016) Optimisation of CdTe electrodeposition voltage for development of CdS/CdTe solar cells. J Mater Sci Mater Electron 27:12464–12472

26. Drayton J, Geisthardt R, Raguse J, Sites JR (2013) Metal chloride passivation treatments for CdTe solar cells. MRS Proc 1538(2013):269–274

27. Ferrer IJ, Salvador P (1989) Photoluminescence and electroluminescence mechanisms at polycrystalline CdS in air and in contact with aqueous electrolytes. J Appl Phys 66:2568

28. Friedlmeier TM, Jackson P, Kreikemeyer-lorenzo D, Hauschild D, Kiowski O, Hariskos D, et al (2016) A closer look at initial CdS growth on high-efficiency $Cu(In,Ga)Se_2$ absorbers using

surface-sensitive methods. In: Proceedings of IEEE 43rd Photovoltaic Specialists Conference, 05–10 June 2016, Portland, OR, USA, 16484084

29. Fuh A, Gallinger RP, Schuster P, Adolph J, Caporaletti O (1992) The effects of post-deposition annealing on ZnS:Mn film crystalline structure and electroluminescent characteristics. Thin Solid Films 207:202–205

30. Galloway SA, Brinkman AW, Durose K (1996) A study of the effects of post-deposition treatments on CdS/CdTe thin film solar cells using high resolution optical beam induced current. Appl Phys Lett 68:3725–3727

31. Gnatyuka VA, Aoki T, Hatanaka Y (2006) Laser-induced shock wave stimulated doping of CdTe crystals. Appl Phys Lett 88:242111

32. Gnatyuk VA, Aoki T, Niraula M, Hatanaka Y (2003) Influence of laser irradiation and laser-induced in doping on the photoluminescence of CdTe crystals. Semicond Sci Technol 18:560–565

33. Gorji NE (2015) Deposition and doping of CdS/CdTe thin film solar cells. J Semicond 36(5):054001

34. Grinyte R, Saa L, Garai-Ibabe G, Pavlov V (2015) Biocatalytic etching of semiconductor cadmium sulfide nanoparticles as a new platform for optical detection of analytes. Chem Commun 51:17152–17155

35. Haider AJ, Mousa AM, Al-Jawad SMH (2008) Annealing effect on structural, electrical and optical properties of CdS films prepared by CBD method. Semicond Sci Technol 8(4):326–332

36. Harif MN, Rahman KS, Rosly HN, Chelvanathan P, Doroody C, Misran H, Amin N (2020) An approach to alternative post-deposition treatment in CdTe thin films for solar cell application. Superlatt Microstruct 147:106687

37. Hatanaka Y, Niraula M, Nakamura A, Aoki T (2001) Excimer laser doping techniques for II-VI semiconductors. Appl Sursf Sci 175–176:462–467

38. Hatanaka Y, Aoki T, Niraula M, Aoki Y, Nakanishi Y (1999) Laser doping technique for II-VI semiconductors, ZnSe and CdTe. In: Proceedings of 5th Asian Symp. Infrared Display, ASID 1999, pp. 65–68

39. Hatanaka Y, Aoki T, Niraula M, Aoki Y, Nakanishi Y (1998) Heavy p-type doping of ZnSe-based II-VI semicondsuctors using an excimer laser. Proc SPIE 3283:79–86

40. Hlaing OW, Johnson J, Bhatia A, Lund E, Nowell M, Scarpulla M (2011) Grain size and texture of Cu_2ZnSnS_4 thin films synthesized by cosputtering binary sulfides and annealing: effects of processing conditions and sodium. J Electron Mater 40:2214–2221

41. Ishizuka S, Taguchi N, Fons PJ (2019) Similarities and critical differences in heavy alkali-metal rubidium and cesium effects on chalcopyrite $Cu(In,Ga)Se_2$ thin film solar cells. J Phys Chem C 123:17757–17764

42. Ito K, Nakazawa N (1988) Electrical and optical properties of stannite-type quaternary semiconductor thin films. Jpn J Appl Phys 27:2094

43. Jackson P, Wuerz R, Hariskos D, Lotter E, Witte W, Powalla M (2016) Effects of heavy alkali elements in Cu(In,Ga)Se_2 solar cells with efficiencies up to 22.6%. Phys Status Solidi (RRL) 10(8):583–586
44. Jain G, Ahnood A, Chanaewa A, Fox K, Mulvaney P (2019) The role of $CdCl_2$ treatments and annealing in the formation of sintered CdTe nanocrystal solar cells. Phys Lett A 383:1199–1202
45. Kartopu G, Barrioz V, Irvine SJC, Clayton AJ, Monir S, Lamb D (2014) Inline atmospheric pressure metal-organic chemical vapour deposition for thin film CdTe solar cells. Thin Solid Films 558:374–377
46. Khon E, Lambright K, Khnayzer RS, Moroz P, Perera D, Butaeva E et al (2013) Improving the catalytic activity of semiconductor nanocrystals through selective domain etching. Nano Lett 13:2016–2023
47. Kiss J, Gruhn T, Roma G, Felser C (2013) Theoretical study on the diffusion mechanism of Cd in the Cu-poor phase of $CuInSe_2$ solar cell material. J Phys Chem C 117:25933–25938
48. Kobayashi T, Kumazawa T, Kao ZJL, Nakada T (2014) Post-treatment effects on ZnS(O,OH)/Cu(In,Ga)Se_2 solar cells deposited using thioacetamide-ammonia based solution. Solar Energy Mater Solar Cells 123:197–202
49. Kobayashi T, Yamaguchi H, Nakada T (2014) Effects of combined heat and light soaking on device performance of Cu(In,Ga)Se_2 solar cells with ZnS(O,OH) buffer layer. Prog Photovoltaics 22(1):115–121
50. Kodalle T, Choubra L, Arzel L, Schlatmann R, Barreau N, Kaufmann CA (2019) Effects of KF and RbF post deposition treatments on the growth of the CdS buffer layer on CIGS thin films – a comparative study. Solar Energy Mater Solar Cells 200:109997
51. Kraft D, Thissen A, Broetz J, Flege S (2003) Characterization of tellurium layers for back contact formation on close to technology treated CdTe surfaces. J Appl Phys 94(5):3589
52. Kuzuya T, Tai Y, Yamamuro S, Sumiyama K (2005) Synthesis of copper and zinc sulfide nanocrystals via thermolysis of the polymetallic thiolate cage. Sci Technol Adv Mater 6(1):84–90
53. Lam NS, Wong KW, Li Q, Zheng Z, Lau WM (2007) Controllable size reduction of CdSe nanowires through the intermediate formation of Se-coated CdSe nanowires using acid and thermal treatment. Nanotechnology 18:415607
54. Lane DW, Conibeer GJ, Wood DA, Rogers KD, Capper P, Romani S, Hearne S (1999) Sulphur diffusion in CdTe and the phase diagram of the CdS–CdTe pseudo-binary alloy. J Cryst Growth 197:743–748
55. Lee YS, Gershon T, Gunawan O, Todorov TK, Gokmen T, Virgus Y, Guha S (2014) $Cu_2ZnSnSe_4$ thin-film solar cells by thermal co-evaporation with 11.6% efficiency and improved minority carrier diffusion length. Adv Energy Mater 5:1401372

56. Leoncini M, Artegiani E, Lozzi L, Barbato M, Meneghini M, Meneghesso G et al (2019) Difluorochloromethane treated thin CdS buffer layers for improved CdTe solar cells. Thin Solid Films 672:7–13
57. Li D-B, Yao C, Vijayaraghavan SN, Awni RA, Subedi KK, Ellingson RJ et al (2021) Low-temperature and effective ex situ group V doping for efficient polycrystalline CdSeTe solar cells. Nat Energy 6:715–722
58. Li JV, Kuciauskas D, Young MR, Repins IL (2013) Effects of sodium incorporation in co-evaporated $Cu_2ZnSnSe_4$ thin-film solar cells. Appl Phys Lett 102:163905
59. Li R, Lee J, Yang B, Horspool DN, Aindow M, Papadimitrakopoulos F (2005) Amine-assisted facetted etching of CdSe nanocrystals. J Am Chem Soc 127:2524–2532
60. Lim SJ, Kim W, Jung S, Seo J, Shin SK (2011) Anisotropic etching of semiconductor nanocrystals. Chem Mater 23:5029–5036
61. Major JD, Al TM, Bowen L, Brossard M, Li C, Lagoudakis P et al (2016) In-depth analysis of chloride treatments for thin-film CdTe solar cells. Nat Commun 7:13231
62. Major JD, Treharne RE, Phillips LJ, Durose K (2014) A low-cost non-toxic post-growth activation step for CdTe solar cells. Nature 511(7509):334–337
63. Maniscalco B, Abbas A, Bowers J, Kaminski P, Bass K, West G, Walls J (2015) The activation of thin film CdTe solar cells using alternative chlorine containing compounds. Thin Solid Films 582:115–119
64. Maticiuc N, Kukk M, Spalatu N, Potlog T, Krunks M, Valdna V, Hiie J (2014) Comparative study of CdS films annealed in neutral, oxidizing and reducing atmospheres. Energy Procedia 44:77–84
65. Maticiuc N, Hiie J, Potlog T, Valdna V, Gavrilov A (2012) Influence of annealing in H_2 atmosphere on the electrical properties of thin film CdS. Mater Res Soc Symp Proc 1324:69–74
66. McCandless B, Metzger WK, Buchanan W, Sriramagiri G, Thompson C, Duenow J et al (2019) Enhanced p-type doping in polycrystalline CdTe films: deposition and activation. IEEE J Photovolt 9:912–917
67. McCandless BE, Buchanan WA, Thompson CP, Sriramagiri G, Lovelett RJ, Duenow J et al (2018) Overcoming carrier concentration limits in polycrystalline CdTe thin films with in situ doping. Sci Rep 8:14519
68. Menossi D, Artegiani E, Salavei A, Di Mare S, Romeo A (2017) Study of $MgCl_2$ activation treatment on the defects of CdTe solar cells by capacitance-voltage, drive level capacitance profiling and admittance spectroscopy techniques. Thin Solid Films 633:97–100
69. Meyer BK, Polity A, Farangis B, He Y, Hasselkamp D, Kramer T, Wang C (2004) Structural properties and bandgap bowing of $ZnO_{1-x}S_x$ thin films deposited by reactive sputtering. Appl Phys Lett 85:4929–4931

70. Mishra S, Ingale A, Roy UN, Gupta A (2007) Study of annealing-induced changes in CdS thin films using X-ray diffraction and Raman spectroscopy. Thin Solid Films 516:91–98
71. Monig H, Fischer CH, Grimm A, Johnson B, Kaufmann CA, Caballero R et al (2010) Surface Csu-depletion of Cu(In,Ga)Se_2 thin films: further experimental evidence for a defect-induced surface reconstruction. J Appl Phys 107:113540
72. Nagaoka A, Miyake H, Taniyama T, Kakimoto K, Nose Y, Scarpulla MA, K. Yoshino K. (2014) Effects of sodium on electrical properties in Cu_2ZnSnS_4 single crystal. Appl Phys Lett 104:152101
73. Nakada T, Kobayashi T, Kumazawa T, Yamaguchi H (2013) Impacts of post-treatments on cell performance of CIGS solar cells with Zn-compound buffer layers. IEEE J Photovoltaics 3(1):461–466
74. Nakamura M, Yamaguchi K, Kimoto Y, Yasaki Y, Kato T, Sugimoto H (2019) Cd-free Cu(In,Ga)$(Se,S)_2$ thin-film solar cell with record efficiency of 23.35%. IEEE J Photovoltaics 9:1863–1867
75. Niles DW, Li X, Albin D, Rose D, Gessert T (1996) Evaporated Te on CdTe: a vacuum-compatible approach to making back contact to CdTe solar cell devices. Prog Photovolt Res Appl 4:225–229
76. Niraula M, Agata Y, Yasuda K, Nakamura A, Aoki T, Hatanaka Y (2004) Surface processing of CdTe crystals by an excimer laser and its application in fabricating nuclear radiation detectors. Phys Stat Sol (c) 1(4):1071–1074
77. Phuong LQ, Okano M, Yamashita G, Nagai M, Ashida M, Nagaoka A, Yoshino K, Kanemitsu Y (2015) Photocarrier dynamics in undoped and Na-doped Cu_2ZnSnS_4 single crystals revealed by ultrafast time-resolved terahertz spectroscopy. Appl Phys Exp 8:062303
78. Raghuwanshi M, Vilalta-Clemente A, Castro C, Duguay S, Cadel E, Jackson P et al (2019) Influence of RbF post deposition treatment on heterojunction and grain boundaries in high efficient (21.1%) cu(in,Ga)Se_2 solar cells. Nano Energy 60:103–110
79. Reichert MD, Lin C-C, Vela J (2014) How robust are semiconductor nanorods? Investigating the stability and chemical decomposition pathways of photoactive nanocrystals. Chem Mater 26(13):3900–3908
80. Rey G, Babbe F, Weiss TP, Elanzeery H, Melchiorre M, Valle N, El Adib B, Siebentritt S (2017) Post-deposition treatment of $Cu_2ZnSnSe_4$ with alkalis. Thin Solid Film 633:162–165
81. Rickey KM, Nian Q, Zhang G, Chen L, Suslov S, Bhat SV et al (2015) Welding of semiconductor nanowires by coupling laser induced peening and localized heating. Sci Rep 5:16052
82. Rickey KM, Nian Q, Zhang G, Chen L, Venkataprasad BS, Wu T et al (2012) Effects osf rapid thermal processing and pulse-laser sintering on CdTe nanofilms for photovoltaic applications. Proc SPIE 8465:846505.

83. Rohatgi A (1992) A study of efficiency limiting defects in polycrystalline CdTe/CdS solar cell. Int J Solar Energy 12:37–49
84. Romeo A, Artegioni E (2021) CdTe-based thin film solar cells: past, present and future. Energies 14(6):1684
85. Romeo N, Bosio A, Romeo A, Mazzamuto S, Canevari V (2006) High efficiency CdTe/CdS thin film solar cells prepared by treating CdTe films with a Freon gas in substitution of $CdCl_2$. In: Proceedings of the 21st European Photovoltaic Solar Energy Conference, Dresden, Germany, 4–8 September 2006, pp. 1857–1860
86. Romeo A, Bätzner DL, Zogg H, Tiwari AN (2000) Recrystallization in cd-Te/CdS. Thin Solid Films 361–362:420–425
87. Rugen-Hankey SL, Clayton AJ, Barrioz V, Kartopu G, Irvine SJC, McGettrick JD, Hammond D (2015) Improvement to thin film CdTe solar cells with controlled back surface oxidation. Sol Energy Mater Sol Cell 136:213–217
88. Salavei A, Rimmaudo I, Piccinelli F, Zabierowski P, Romeo A (2013) Study of difluorochloromethane activation treatment on low substrate temperature deposited CdTe solar cells. Sol Energy Mater Sol Cells 112:190–195
89. Salavei A, Rimmaudo I, Piccinelli F, Menossi D, Romeo N, Bosio A, et al. (2012) Flexible CdTe solar cells by a low temperature process on ITO/ZnO coated polymers. In: Proceedings of the 27th European Photovoltaic Solar Energy Conference and Exhibition, Frankfurt, Germany, 24 September 2012, pp. 24–28
90. Samoilenko Y. Yeung G. Munshi A.H. Abbas A. Reich C.L. Walker M., et al. (2020) Stable magnesium zinc oxide by reactive co-sputtering for CdTe-based solar cells. Sol Energy Mater Sol Cells 210, 110521
91. Shanmugam N, Cholan S, Kannadasan N, Sathishkumar K, Viruthagiri G (2013) Effect of annealing on the ZnS nanocrystals prepared by chemical precipitation method. J Nanomater 2013:351798
92. Simandan I-D, Sava F, Buruiana A-T, Burducea I, Becherescu N, Mihai C et al (2011) The effect of the deposition method on the structural and optical properties of ZnS thin films. Coatings 11:1064
93. Simonds BJ, Meadows HJ, Misra S, Ferekides C, Dale PJ, Scarpulla MA (2015) Laser processing for thin film chalcogenide photovoltaics: a review and prospectus. J Photon Energ 5:050999–050991
94. Simonds BJ, Palekis V, Van Devener B, Ferekides C, Scarpulla MA (2014) Te-rich CdTe surface by pulsed UV laser treatment for Ohmic back contact formation, In: Proceedings of IEEE 40th Photovoltaic Specialist Conference (PVSC), 08–13 June 2014, Denver, CO, USA, 14683753
95. Simonds BJ et al (2014) Pulsed laser induced ohmic back contact in CdTe solar cells. Appl Phys Lett 104:141604

96. Simonds BJ, Palekis V, Van Devener B, Ferekides C, Scarpulla MA (2014) Surface stoichiometry of pulsed ultraviolet laser treated polycrystalline CdTe surface stoichiometry of pulsed ultraviolet laser treated polycrystalline CdTe. J Appl Phys 116:013506
97. Singh OP, Gour KS, Parmar R, Singh VN (2016) Sodium induced grain growth, defect passivation and enhancement in the photovoltaic properties of Cu_2ZnSnS_4 thin film solar cell. Mater Chem Phys 177:293–298
98. Taguchi N, Tanaka S, Ishizuka S (2018) Direct insights into $RbInSe_2$ formation at cu(in,Ga)Se_2 thin film surface with RbF post deposition treatment. Appl Phys Lett 113:113903
99. Tajima S, Asahi R, Isheim D, Seidman DN, Itoh T, Ohishi KI (2015) Sodium distribution in solar-grade Cu_2ZnSnS_4 layers using atom-probe tomographic technique. Jpn J Appl Phys 54:112302
100. Terheggen M, Heinrich H, Kostorz G, Baetzner D, Romeo A, Tiwari AN (2004) Analysis of bulk and interface phenomena in CdTe/CdS thin-film solar cells. Interface Sci 12:259
101. Terheggen M, Heinrich H, Kostorz G, Romeo A, Baetzner D, Tiwari AN et al (2003) Structural and chemical interface characterization of CdTe solar cells by transmission electron microscopy. Thin Solid Films 431–432:262–266
102. Tomas SA, Vigil O, Alvarado-Gil JJ, Lozada-Morales R, Zelaya-Angel O, Vargas H et al (1995) Influence of thermal annealings in different atmospheres on the band-gap shift and resistivity of CdS thin films. J Appl Phys 78(4):2204–2207
103. Trenczek-Zajaca A (2019) Thermally oxidized CdS as a photoactive material. New J Chem 43:8892–8902
104. Verma M, Patidar D, Sharma KB, Saxena NS (2016) Phase transformations and thermal stability of CdSe quantum dots: cubic to hexagonal. J Inorg Organomet Polym 26:75–80
105. Verma M, Kaswan A, Patidar D, Sharma KB, Saxena NS (2016) Phase transformation and thermal stability of ZnSe QDs due to annealing: emergence of ZnO. J Mater Sci Mater Electron 27:8871–8878
106. Vigil O, Zelaya-Angel O, Rodriguez Y (2000) Changes of the structural and optical properties of cubic CdS films on annealing in H_2 and air atmospheres. Semicond Sci Technol 15:259–262
107. Ümsür B, Maticiuc N, Kodalle T, Wenisch R, Majumdar I, Wang Y et al (2021) Impact of RbF post deposition treatment on CdS/CIGSe and Zn(O,S)/CIGSe interfaces – A comparative HAXPES study. Renew Energ 180:626–636
108. Umsur B, Calvet W, Steigert A, Lauermann I, Gorgoi M, Prietzel K et al (2016) Investigation of the potassium fluoride post deposition treatment on the CIGSe/CdS interface using hard X-ray photoemission spectroscopy – a comparative study. Phys Chem Chem Phys 18:14129–14138
109. Umsur B, Calvet W, Hopfner B, Steigert A, Lauermann I, Gorgoi M et al (2015) Investigation of Cu-poor and Cu-rich Cu(In,Ga)Se_2/CdS interfaces using hard X-ray photoelectron spectroscopy. Thin Solid Films 582:366–370

110. Wang L, Luo M, Qin S, Liu X, Chen J, Yang B et al (2015) Ambient $CdCl_2$ treatment on CdS buffer layer for improved performance of Sb_2Se_3 thin film photovoltaics. Appl Phys Lett 107:143902
111. Williams BL, Major JD, Bowen L, Keuning W, Creatore M, Durose K (2015) A comparative study of the effects of nontoxic chloride treatments on CdTe solar cell microstructure and stoichiometry. Adv Energy Mater 5(21):1500554
112. Woodhouse M, Goodrich A, Redlinger M, Lokanc M, Eggert R (2013) The present, mid-term, and long-term supply curves for tellurium; and updates in the results from NREL's CdTe PV module manufacturing cost model. NREL/PR-6A20–60430, Golden, Colorado
113. Yadav K, Dwivedi Y, Jaggi N (2015) Effect of annealing temperature on the structural and optical properties of ZnSe nanoparticles. J Mater Sci Mater Electron 26:2198–2204
114. Yang B, Zhang H, Zhang J (2016) Copper acetate etching of colloidal CdSe nanocrystals. NANO: Brief Rep Rev 11(2):1650021
[MathSciNet]
115. Yang L, Yang J, Wang Z-H, Zeng J-H, Yang L, Qian Y-T (2003) Fabrication of mesoporous CdS nanorods by chemical etching. J Mater Res 18(2):396–401
116. Zázvorka J, Franc J, Beran L, Moravec P, Pekárek J, Veis M (2016) Dynamics of native oxide growth on CdTe and CdZnTe X-ray and gamma-ray detectors. Sci Technol Adv Mater 17(1):792–798
117. Zscheckel T, Wisniewski W, Gebhardt A, Rüssel C (2014) Recrystallization of CVD-ZnS during thermal treatment. Opt Mater Express 4(9):1886–1894

OceanofPDF.com

Index

A

Aging
  exchange reactions 498
  leakage current 497, 498
  metal diffusion 501
  oxygen diffusion 500
Alloy QDs 183
Alloys 110–115, 118, 120
Annealing
  recrystallization 229
Artificial atoms 181

B

Band alignments 7–8
Bandgap engineering 109, 110
  tunability of bandgaps 98
Bandgaps 3, 5–12, 14, 109–113, 115–122, 125, 126
Binary semiconductors 110, 111
Biocompatibility 184, 185, 187–194, 198, 204

C

Capping agents 185
Carrier dynamics 143, 145–146
Catalysis 330, 339
CdTe 215–229
CdTe-based alloys
  CdHgTe 368–371, 378
  CdMnTe 368
  CdSeTe
    graduated 377
    homogeneous 377
  CdSTe 377
  CdZnTe 368, 376
CdZnTe (CZT) 216–229
Charge transfer 158

Chemical sensors 261, 265
Colloidal quantum dots 159
Colloidal stability 348, 349
Colloidal synthesis 158–164, 170
Comet assay 196
Core/shell quantum dots 181, 184, 197
Core-shell structures
  $CdTe/Cd_{1-x}Hg_xTe$ 371
  CdTe/CdMnTe 368
  CdTe/CdS 378
  CdTe/CdS/ZnS 378
  CdTe/CdSe 378
  CdTe/HgTe 370
  CdTe/HgTe/CdTe 370
  CdTe/ZnS 376, 377
  CdTe/ZnTe 378
  cores 378
  hybrid 378
  microwave-assisted 379
  shell 366, 368–373, 377–379
  SILAR 379
  synthesis 366, 368, 379
Crystallographic structure
  cubic 22, 30
  hexagonal 30
  space group F43m 22
  space group P63mc 22
  sphalerite 22, 23
  wurtzite 22
  zinc blende 22
Cytotoxicity 184, 187, 194, 196–198, 204

D

Deposition
  influencing factors 466
  substrates 466, 467, 485
Detectors 109, 111, 119

Device technology
contact
Au 446
ohmic contacts 446, 453
doping
As 432, 447
In 447
etching
dry etching 453
Schottky barrier 444–446
surface passivation
Al_2O_3 442, 443
anodic oxide 442, 443, 448
SiN_x 442, 443
SiO_2 443
ZnS 441–443
Dimensionality 101–102
Displays 109, 110, 112, 116, 121, 124, 125
Doping 8–9, 95, 96, 110, 114–117, 121, 126
acceptors 468, 469
chlorine 229
compensation 229
donors 468, 469
doping strategies 468
indium 229
ion implantation 470–472
limitations 469
p-n junction 472
self-compensation 468, 469

E

Endocytosis 189, 191–194
Energy spectrum 122
Etching
dry etching
advantages 477, 483
gas mixtures 483–485

ion milling 482, 483
plasma etching 482, 483
reactive ion etching 482, 483
patterning 474
wet etching
Br_2-CH_3OH solution 475
dissolution rates 476–478
H_2O_2–HBr 476
I_2–MeOH solution 477
mechanism 478, 482, 483
polishing effects 476

F

Fluorescence imaging 182
Functionalization of II-VI QDs
application
biofunctionalization 390, 396, 406–415
biolabeling 394, 410, 416
biology 412
biosensor 413–415
drug delivery 408, 415
medicine 402
bioconjugation
covalent linkage 407
electrostatic 390, 391, 401, 402, 405, 407, 408
non-covalent linkage 407
biomolecules
biotin 405, 407, 408, 414
DNA 394, 406, 410–412, 414–416
peptides 406, 410–412, 415
RNA 406, 410, 411, 414
functional groups
amines 391, 397, 401, 402, 404, 405, 414
carboxylic acids 401, 414
poly(ethylene glycol) (PEG) 402–403
thiol groups 391, 401, 407

G

Genotoxicity 194–196, 204

H

Heterojunction
  energy-band diagram 502
Heterostructures 96, 98, 101, 110, 118–121, 124
Hg-based II-VI semiconductors
  band diagram 72, 73
  chemical bond 71
  chemical properties 69
  doping
    acceptor 77
    donor 77
  electrophysical parameters
    chalcogen vacancies 76
    interstices 76
    mobility 76
  HgS 67, 69, 71, 73, 76, 79, 81
  HgSe 67, 68, 70–72, 74, 76–81, 83
  HgTe 67–74, 76–81, 83
  physical parameters 74
  stability 69, 71
  stoichiometry 75
  synthesis 68
Hg-based II-VI semiconductors applications
  IR detectors 79
    superlattices 78, 79
  limitations 83
  magnetoelectronics 80
  optoeletronics 81
  quantum electronics 81
  spintronics 81
  thermoelectric converters 81
  topological insulator 81
HgCdTe
  conductivities 427, 429, 432, 436, 437, 441, 446

growth 423, 425–433, 435–437, 443, 446, 447, 453
impurities 432, 437, 445, 447, 449, 452, 453
layers 424, 427–438, 440–443, 445–447, 449–453
n-type 425, 427, 429, 432, 436, 437, 442, 444, 445, 448, 449, 452, 453
p-type 425, 427, 429, 432, 435–437, 444–446, 448, 449, 451–453
technologies 423–453
HgCdTe epilayer technologies
epitaxy 446, 453
LPE 427, 429, 430, 441, 450, 452, 453
MBE 431–433, 437, 447, 450, 453
MOCVD 430–432, 447, 450, 453
temperatures 423, 425, 427, 431, 433, 437, 441, 446, 448, 449, 451, 453
HgCdTe material technology
Bridgman methods 425–427
bulk crystals 424
recrystallization 425
traveling heater method 425, 426

I

II-VI alloys
application
photodetectors 87–102
photovoltaic devices 93, 94
ternary II-VI semiconductors
CdHgTe 87
CdZnTe 87, 96
HgZnTe 87, 96
II-VI compounds 110, 111, 114, 116, 121–123
CdS 364
CdTe
applications 367
luminescence 359, 362, 367, 373, 374
quantum yield 362, 367, 368, 378
II-VI QDs
advantages 397, 403, 407–409, 414
biocompatibility
improvement 394, 395

CdSe 385
CdSe/ZnS 386, 391, 392, 395, 398, 412
photostability
improvement 392
stability
improvement 392, 394–396
II-VI semiconductor applications
light emitting devices 58
optoelectronics 56
phosphors 57
photodetectors 56, 57, 59
quantum electronics 59
scintillators 58
solar cells 57–59
substrates 60
X-ray detectors 59
II-VI semiconductor properties
band gap 27, 29, 38
band structure 26, 27
catalytic properties 54, 55
chemical bond
iconicity 52
chemical properties 35
electrophysical properties
acceptors 39, 41–43
defects 39–41, 45, 46
donors 39, 40, 42–44
doping 42, 43, 45, 46
self-compensation 40, 44, 45
heat treatment 33, 41
mobility 38–40, 56
n-type 40, 41, 44, 53
physical properties
II-VI semiconductor properties 28
physicochemical properties 29, 35
p-type 40, 41, 44, 53
resistivity 30, 37, 42

stability
dissociation 31
oxidation 31–34
surface properties
adsorption 37, 47, 49–51, 53
oxidation 54
oxygen 47, 48, 51, 53
pinning 52
surface Fermi level 52, 53
surface state 52
II-VI semiconductors 109–126
alloys
$Cd_{1-x}Zn_xTe$ 6, 11
CdS_xSe_{1-x} 13
CdZnS 14
$Hg_{1-x}Cd_xTe$ 6, 7, 9, 10
applications
biosensors 13
focal plane arrays 10
gas sensor 10, 14
lasers 11, 12
light emitting devices 12
phosphors 12
photocatalysis 14
THz emitters and detectors 11
UV detectors 12
cadmium selenide (CdSe) 5, 7–10, 13–15, 235–237, 245, 249, 252–256, 261, 264, 267, 287, 469
cadmium sulfide (CdS) 5–9, 12–14, 235–239, 242, 244–246, 249, 251–259, 261, 263, 264, 267–269, 287, 469
cadmium telluride (CdTe) 7–14, 235, 237, 239, 245, 246, 248, 252, 255, 261, 263, 264, 267–269, 287, 469
HgS 303
HgTe 10, 12
history 3, 4
wide-band gap 466, 517–544, 551–571

zinc selenide (ZnSe) 5, 7–9, 12, 237, 239, 245, 246, 249–256, 259, 264, 267, 287, 303, 469, 483
zinc sulfide (ZnS) 5, 6, 8, 10, 12–15, 236, 237, 239–242, 244–246, 249–257, 260–262, 264–266, 287, 303, 483
zinc telluride (ZnTe) 6, 8, 11, 12, 235, 237, 245, 250–252, 264, 266, 267, 269, 303, 469, 483
II-VI semiconductor technology
polycrystals 38
single crystals 36
thin films 36, 37
Infrared 133, 134, 136, 142, 143, 147–149
Ingots
diameters 219, 224–226
single crystals 219, 220, 223, 226

L

Lasers 109, 110, 120, 124
Lattice strain 121
Ligands 133–135, 138, 140, 141, 144, 145, 147, 149
Light emission 134, 147–148

M

Macropinocytosis 189, 192
Mercury chalcogenide
doping 136
electronic structure 133–149
HgS 136
HgSe 136
HgTe 136
Metal oxides 157–172
Metal-semiconductor junctions 491
Methods of deposition
aerosol spray pyrolysis (ASP) 260–263
atomic layer deposition 249–251
chemical bath deposition (CBD) 255–259, 269
chemical vapor deposition (CVD) 234, 244–246
electrochemical deposition 263–266
ion beam sputtering (IBS) 243

magnetron sputtering 238–240
metalorganic vapor phase epitaxy 248
molecular-beam epitaxy 246
pulsed laser deposition (PLD) technique 234, 240–243
successive ionic layer adsorbtion and reaction (SILAR) 234, 251–254
vacuum thermal sputtering 234, 235, 237
Molecular beam epitaxy 120

N

Nanocomposites 158, 167–172
Nanocrystal heterostructures 158–164
Nanocrystals 133–149
Nanocrystals synthesis
co-precipitation methods
advantage 284
disadvantages 284
precursor 281, 282
supersaturation 281
green synthesis
advantage 312
microorganisms 308–310, 312
plant extractions 308
hot-injection method
capping agents 305
solvent 305
temperature 305, 306
hydrothermal technique
autoclave 290, 291, 293
pressure 290–292
water 290
mechanochemical method
ball milling 279, 280
milling time 279
microemulsion technique
disadvantages 302
micelles 300
microemulsion scheme 300, 301

oil 300
surfactant 300, 301
microwave-assisted method
advantages 303
limitations 304
microwave irradiation 303, 304
one-step colloidal method
advantages 306
photochemical synthesis
advantages 306
duration, high pressure indium lamp 307
light irradiation 306, 307
low-pressure mercury lamp, duration 306
silica matrix, sol-gel processing
SiO2:CdS 287
SiO2:CdSe 287, 289
SiO2:CdTe 287, 289
SiO2:ZnS 287
sol-gel processing
advantages 289
capping agents 287
disadvantages 289
gel 284–289
mineralizers 287
polymerization 285
precursor 285, 286
sol 284–289
solvothermal technique 294
limitations 294
precursors 294, 295, 297
temperatures 294, 295
sonochemical method
acoustic cavitation 298
advantages 299
free radicals 298
solvents 298
sonochemistry 298, 302

Nanomaterials
core-shell nanoparticles 325, 332, 335–337, 339–341, 343, 344, 350
hollow nanostructures 346
nanobelts 339, 343, 348, 349
nanoparticles 345
nanosheets 330–332
nanowires 327–330, 343
quantum dots 334–336, 344, 351
Nanoparticles 110, 121, 122, 157–167, 170–172
Nanosensors 182
Nanostructures
core-shells 7, 8, 10
quantum dots (QDs) 10, 15
Nanotechnology 181, 204
Native oxides
CdO 525–530, 539, 540
$CdSeO_3$ 526, 539
$CdTeO_3$ 525, 536
composition 525–527
TeO_2 524–526, 535–537
thickness 527, 540
ZnO 525–527, 530–539, 542
$ZnSeO_3$ 526, 537, 538
Natural minerals
cinnabar 67
coloradoite 68
methacinnabarite 67
timannite 67
NC synthesis
aqueous 360, 362–368, 370, 372, 375, 377–379
colloidal NPs 360
organic synthesis 360, 378
Ostwald ripening 366
precursors 360, 361, 365, 368, 369, 373, 375–378
shape 360, 361, 363, 366, 367
solvents 360, 362, 367

stabilizers 360, 361
surfactants 360, 367
thiol capping ligands 364

O

Ohmic contacts
annealing 505, 507, 509
approaches 505–507, 509
doping 505, 506
n-CdS 508
n-ZnS 507
p-CdTe 505, 506
tunneling effect 501
ZnSe 506, 507
1d structures 125
Optical absorption 90–93
Oxidative stress 196–199, 202

P

Phagocytosis 189, 191–193
Phase transfer QDs
encapsulation 397
ligand bilayer 400
ligand exchange 395, 397, 398, 400, 403, 404
ligand modification 397, 400
polymer coating 403, 404, 406
Photodetector 233, 234, 238, 243, 251, 257, 261, 269
C-V characteristic 441–443
FPAs 424
junctions 424, 437, 446–450, 452
n-on-p 452, 453
p-n 424, 437, 446–450, 453
p-on-n 449, 452, 453
Photoexcited charges 158, 167, 169, 170
Photo-induced toxicity 198, 204
Photonics 233, 255, 259, 265
Photovoltaic cells 109, 110
P-n junction technology

ion etching 448
ion implantation
As 449
B 449
iron 449, 450
mercury diffusion 447
reactive ion etching 448
Polymer coatings 185–187, 198
Post-deposition treatment
$CdCl_2$ treatment
activation process 557
CdS/CdTe solar cell 557
defect distribution 559
homogeneity 560
interface defects 559
solar cells performances 557
stoichiometry 559
chemical etching
Br_2
MeOH solution 566
CdSe/CdS core-shell 566
CdTe solar cells 567
nitric-phosphoric (NP) etching 566
laser treatment
CdTe 552, 557, 558, 562, 569–571
heavy doping 569
K_2S and Na_2Te sources 570
laser-induced defects 570
Nd
YAG laser 571
Ohmic back contact 570
pulse laser treatment 569
recrystallization 558
thermal treatment
crystallinity 558, 562
grain sizes 558, 562
treatment with alkalis

CsF 564
KF 564
NaF 564
RbF 564
Producers of CdZnTe (CdTe)
Acrorad 219, 227
CEA-Leti 220
Eurorad 224, 227
eV PRODUCTS 216, 217, 224
5NPlus 220, 227
Giredmet 224, 227
Institute of Solid State Physics RAS 227
Kromek 216, 218, 227
NII Materialovedeniya 218, 227
Orbotech 225, 227
Redlen 219, 228
Saint-Gobain Crystals 224
Yinnel Tech, Inc. 225

Q

Quantum confinement 134, 137, 140, 149
Quantum dots (QDs) 101, 111, 118, 122–125, 181–204
molecular orbital (MO) theory 386
size-quatization 386
synthesis 390, 394, 416
Quantum size effect 123, 125
Quantum wells 101, 118–119

R

Reactive oxygen species 194, 196, 198–199, 201

S

Schottky diodes
band gap 493, 503, 510
electronegativity 494, 507
Fermi level pinning 493, 494
formation 492, 500–505, 507, 509
ideality factors 496

potential barrier 492
Schottky barriers 491, 496
surface states 492, 493
work functions 491
Seed plates
CdZnTe 219
GaAs 219
Seeded growth 163
Semiconductor 87, 90–92, 95–97, 101, 109, 110, 113, 116, 118, 120–124, 126, 181–184, 194
GaAs 5, 12
GaN 12
Ge 4, 5
InAs 14
PbS 4
selenide 336
Si 4
sulfides 327
ZnO 12, 14
Semiconductor heterojunction 166
Silanization 187
Simulations 119, 125
Single crystals
dislocations
dislocation density 216
electrical conductivity 228, 229
inclusion
mechanical strains 217
resistance 217, 219
Te 216, 220, 225
thermal conductivity 216
precipitates 216, 225
the twins 217
Solar cells 109, 111, 113, 115, 116, 119, 124
Spectral range
infrared 453
LWIR 423, 433, 435–437, 450–453

MWIR 453
Stability
back contacts 517, 519–521
$CdCl_2$ treatment 520
contact degradation 521
Cu diffusion 518
device performance 519, 544
quantum dots 522–523
surface oxidation 522
Substrate
CdTe 429, 431, 433–435, 453
CdZnTe 427, 429, 431, 433–437, 452, 453
GaAs 430, 431, 433–435, 453
orientation 431, 433
Si 431, 453
Successive ionic layer adsorption and reaction 164, 167
Superlattices 110, 118–121
Surface
air-cleaved 500
Cd-rich 494
chemically etched 494, 496
native oxides 494, 496, 499
Te-rich layer 495
vacuum-cleaved 494, 496, 509
Surface modifications 184–188, 190, 192, 193
Surface passivation 170
Al_2O_3 543
SiN_x 541–543
SiO_2 541–543
stability 541–543
ZnS 541, 542
Surface states 502
Surface stoichiometry
Cd-rich layer 481
surface oxidation 477
Te-rich layer 478, 479

Synthesis
ion exchange 337, 350
PVD 328, 330
solvothermal synthesis 330
Synthesis methods
from tellurium solution – melt
process by solvent evaporation (PBSE) 221
traveling heater method (THM) 219
from the melt
Bridgeman method 222–224
high pressure Bridgman 224, 225
high-pressure vertical zone melting (HPVZM) 227
horizontal zone melting (HZM) 227
Obreimov-Shubnikov method 221
vertical gradient freezing (VGF) method 221, 225, 226
from the vapor phase
chemical vapor deposition (CVD) 218
Markov-Davydov 218
Piper-Polich method 218
sublimation 218, 224

T

Technology
thick film 277
thin films 277
Thermal oxidation
CdS 530
CdSe 522, 539, 540
$CdTeO_3$ 536
oxidation temperature 530, 535, 537
oxide composition 527
phase dissociation 539, 540
surface stoichiometry 522
ZnS 530
ZnTe 534
Thin films 102, 115, 116, 121, 126, 233–269
THz 135, 138, 145, 149

Toxicities 182, 184, 185, 187, 188, 190, 194–199, 202–204
Transport characteristics
carrier mobility 219
charge carrier lifetime 219
Tunability of bandgaps 111

W

Wide band gap II-VI semiconductors
CdS 21, 23–25, 28–31, 34–37, 39–44, 46, 49–51, 53–58
CdSe 21, 23–25, 28–31, 33, 35, 36, 39, 40, 43, 44, 47–49, 54, 57, 60
CdTe 21, 23–25, 27–31, 33, 34, 36, 38–41, 43, 44, 46–49, 53, 54, 57, 59, 60
ZnS 21, 23–25, 27–33, 35, 36, 38, 39, 42–44, 51–54, 57
ZnSe 21, 23–25, 28–31, 33, 36, 39, 43, 44, 47–49, 53, 54, 57, 58
ZnTe 21, 24, 25, 28–31, 35, 36, 39, 42–44, 47–49, 53, 54, 59

Z

0D structures 124
Zone diagrams 333, 334

OceanofPDF.com